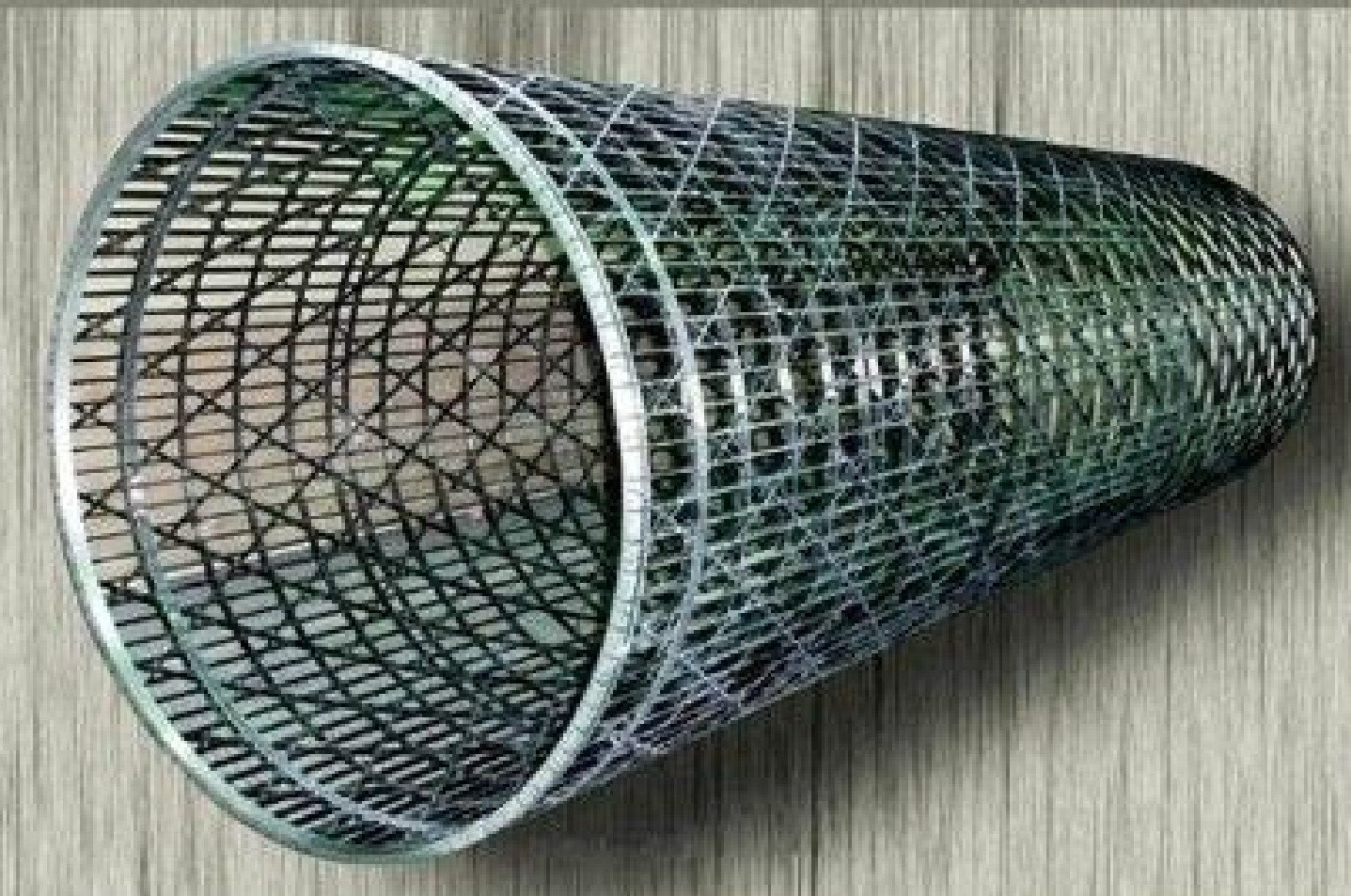
Valery V. Vasiliev
Evgeny V. Morozov

ELSEVIER

Advanced Mechanics of

COMPOSITE MATERIALS AND STRUCTURAL ELEMENTS

THIRD EDITION



Advanced Mechanics of Composite Materials and Structural Elements

Third Edition

Valery V. Vasiliev

Professor of Structural Mechanics
Institute for Problems in Mechanics
Russian Academy of Sciences, Moscow

Evgeny V. Morozov

Professor of Mechanical Engineering
School of Engineering & IT
The University of New South Wales
Canberra, Australia



ELSEVIER

AMSTERDAM • BOSTON • HEIDELBERG • LONDON
NEW YORK • OXFORD • PARIS • SAN DIEGO
SAN FRANCISCO • SINGAPORE • SYDNEY • TOKYO

Elsevier
The Boulevard, Langford Lane, Kidlington, Oxford, OX5 1GB
225 Wyman Street, Waltham, MA 02451, USA

First published 2001
Second edition 2007
Third edition 2013

Copyright © 2013, 2007, 2001 Elsevier Ltd. All rights reserved.

No part of this publication may be reproduced or transmitted in any form or by any means, electronic or mechanical, including photocopying, recording, or any information storage and retrieval system, without permission in writing from the publisher. Details on how to seek permission, further information about the Publisher's permissions policies and our arrangement with organizations such as the Copyright Clearance Center and the Copyright Licensing Agency, can be found at our website: www.elsevier.com/permissions.

This book and the individual contributions contained in it are protected under copyright by the Publisher (other than as may be noted herein).

Notices
Knowledge and best practice in this field are constantly changing. As new research and experience broaden our understanding, changes in research methods, professional practices, or medical treatment may become necessary.

Practitioners and researchers must always rely on their own experience and knowledge in evaluating and using any information, methods, compounds, or experiments described herein. In using such information or methods they should be mindful of their own safety and the safety of others, including parties for whom they have a professional responsibility.

To the fullest extent of the law, neither the Publisher nor the authors, contributors, or editors, assume any liability for any injury and/or damage to persons or property as a matter of products liability, negligence or otherwise, or from any use or operation of any methods, products, instructions, or ideas contained in the material herein.

British Library Cataloguing in Publication Data
A catalogue record for this book is available from the British Library

Library of Congress Cataloguing in Publication Data
A catalog record for this book is available from the Library of Congress

ISBN: 978-0-08-098231-1

For information on all Elsevier publications visit our website at **store.elsevier.com**

Printed and bound in the United Kingdom

13 14 15 16 10 9 8 7 6 5 4 3 2 1



Preface to the Third Edition

This book is concerned with describing, analyzing, and discussing topical problems in the mechanics of advanced composite materials and structural elements whose mechanical properties are controlled by high-strength and/or high-stiffness continuous fibers embedded in a polymeric, metal, or ceramic matrix. Although the idea of combining two or more components to produce materials with controlled properties has been known and used from time immemorial, modern composites have been developed only over the last five or six decades and now have widespread applications in many different fields of engineering, but are of particular importance in aerospace structures for which high strength-to-weight and stiffness-to-weight ratios are required.

Due to these widespread existing and potential applications, composite technology has been developed very intensively over recent decades, and there exist publications that cover anisotropic elasticity, mechanics of composite materials, design, analysis, fabrication, and application of composite structures. A particular feature of this book, which distinguishes it from the existing publications, is that it addresses a wide range of advanced problems in the mechanics of composite materials, such as the physical statistical aspects of fiber strength, stress diffusion in composites with damaged fibers, nonlinear elasticity, plasticity and creep of composite materials, hybrid and two-matrix composites, spatial fibrous structures, tensor strength criteria, progressive failure, and environmental and manufacturing effects, as well as the traditional basic composite material mechanics. In addition to classical lamination theory and its application to beams and plates, this book covers the problems of consistency of non-classical theories, buckling and postbuckling behavior of symmetrically and non-symmetrically laminated plates, and applied theories of composite cylindrical shells. Since the advantages of composite materials are best demonstrated by the optimal fibrous structures, we have particularly addressed the issues of optimality criteria and the analysis of the most significant optimal composite structures: filament-wound pressure vessels, rotating disks, and lattice cylindrical shells.

The authors of this book are experienced designers of composite structures who over the last 40 years have been involved in practically all the main Russian projects in composite technology. This experience has led us to carefully select the problems addressed in our book, which can be referred to as material problems challenging design engineers. Our discussions are illustrated with composite parts and structures designed and built within the frameworks of these projects. In connection with this, the authors appreciate the permission of the Russian Composite Center – Central Institute of Special Machinery (CRISM) – to use in our book several pictures of structures developed and fabricated at CRISM as part of the joint research and design projects.

The primary aim of the book is the combined coverage of mechanics, technology, and analysis of composite materials and structural elements at an advanced level. Such an approach enables an engineer to take into account the essential mechanical properties of the material itself and the special features of practical implementation, including manufacturing technology, experimental results, and design characteristics.

The book consists of twelve chapters and can be divided into two main parts: the first part, including Chapters 3–7, is devoted to composite materials, whereas the second part, Chapters 8–12, covers the analysis and design of typical composite structural elements.

Chapter 1 is an introduction in which typical reinforcing and matrix materials, as well as the typical manufacturing processes used in composite technology, are described.

Chapter 2 is an introduction to the fundamentals of mechanics of solids, i.e., stress, strain, and constitutive theories, governing equations, and principles that are used in the subsequent chapters for the analysis of composite materials and structures.

Chapter 3 is devoted to the basic structural element of a composite material: a unidirectional composite ply. In addition to the conventional description of micromechanical models and experimental results, the physical nature of fiber strength, its statistical characteristics, and the interaction of damaged fibers through the matrix are discussed, and we show that fibrous composites comprise a special class of man-made materials utilizing the natural potentials of material strength and structure.

Chapter 4 contains a description of typical composite layers made of unidirectional, fabric, and spatially reinforced composite materials. Conventional linear elastic models are supplemented in this chapter with nonlinear elastic and elastic-plastic analyses demonstrating specific types of the behavior of composites with metal and thermoplastic matrices.

Chapter 5 is concerned with the mechanics of laminates and includes a conventional description of the laminate stiffness matrix, coupling effects in typical laminates, and procedures for stress calculations for in-plane and interlaminar stresses.

Chapter 6 presents a practical approach to the evaluation of laminate strength. Three main types of failure criteria, i.e., structural criteria indicating the modes of failure, approximation polynomial criteria treated as formal approximations of experimental data, and tensor-polynomial criteria are discussed and compared with available experimental results for unidirectional and fabric composites. A combined elastoplastic damage model and a strain-driven implicit integration procedure for fiber reinforced composite materials and structures that involves a consideration of their mechanical response prior to the initiation of damage, prediction of damage initiation, and modeling of postfailure behavior are discussed.

Chapter 7 deals with environmental and special loading effects and includes analysis of thermal conductivity, hydrothermal elasticity, material aging, creep, and durability under long-term loading, fatigue, damping, and impact resistance of typical advanced composites. The effect of manufacturing factors on material properties and behavior is demonstrated for filament winding accompanied by nonuniform stress distribution between the fibers and ply waviness and laying-up processing of nonsymmetric laminate exhibiting warping after curing and cooling.

Composite beams are discussed in Chapter 8. Along with the general solutions for static and buckling problems, refined beam theories are considered and evaluated.

Chapter 9 is devoted to laminated composite plates and covers traditional and specific problems of the plate theory, particularly, Kirchhoff and Thomson-Tait transformation of boundary conditions in classical plate theory and the interaction of penetrating and boundary-layer solutions in the theory of shear deformable plates. Exact solution of the problem of bending of a clamped plate is presented. Buckling and postbuckling problems are discussed with application to composite plates with symmetrically and unsymmetrically laminated structures.

Chapter 10 is concerned with laminated thin-walled composite beams. Free and restrained bending and torsion problems are considered for composite beams with closed, open, and multi-cell contours of the beam cross section. Coupling effects in anisotropic beams are discussed with application to composite beams with controlled properties. Practical methods for the analysis of beams stiffened with ribs and loaded with surface forces are presented.

Chapter 11 deals with composite cylindrical shells and covers applied theories and practical methods of analysis, particularly the problems of engineering and semi-membrane shell theories.

A new approach to the study of shell buckling under axial compression, which results in simple and boundary-condition-independent analytical solutions, is presented.

Chapter 12 is devoted to optimal composite structures, particularly to laminates of uniform strength, numerical optimization of laminates, and structural elements: composite pressure vessels, rotating disks, and geodesic lattice structures for which the appropriate combination of directional material properties, design concepts, and manufacturing methods provides a dramatic improvement in structural performance.

This third edition is a revised, updated and much extended version of the second edition, with extended and new sections on: fiber metal laminates (Section 5.6.4), progressive failure analysis (Section 6.5), durability (Section 7.3.2) and impact loading (Section 7.3.4), composite beams (Chapter 8) including the analysis of refined beam and plate theories (Section 8.7), composite plates (Chapter 9) with the exact solution for the problem of bending of clamped rectangular plates and comprehensive analysis of the classical Poisson-Kirchhoff reconciliation boundary problem (Section 9.4), in-plane loading and buckling of unsymmetrically laminated plates (Section 9.7), modern theory of thin-walled composite beams (Chapter 10) including the analysis of free and restrained bending and torsion of orthotropic beams with closed (Section 10.4) and open (Section 10.6) cross-sectional contours and coupling effects in anisotropic beams (Section 10.4.8), applied linear and nonlinear theories of composite cylindrical shells (Chapter 11) with a new approach to the problem of buckling (Section 11.5) and numerical optimization of laminated composites under strength and buckling constraints (Section 12.3). More than 280 new pages, 200 new illustrations, and 19 new tables have been added to form the third edition.

A new title, "Advanced Mechanics of Composite Materials and Structural Elements," has been adopted for the third edition, since this provides a better reflection of the overall contents and improvements, extensions, and revisions introduced in the present version.

This book offers a comprehensive coverage of the topic over a wide range, from basics and fundamentals to advanced modeling and analysis including practical design and engineering applications, and can be used as an up-to-date introductory text book aimed at senior undergraduates and graduate students. At the same time it includes a detailed and comprehensive coverage of the contemporary theoretical models at the micro and macro levels of material structure, practical methods and approaches, experimental results, and optimization of composite material properties and component performance that can be used by researchers and engineers.

The authors would like to thank several people for their time and effort in making this book a reality. Specifically, we would like to thank our Elsevier editors who have encouraged and participated in the preparation of the third edition. These include Graham Nisbet and Steve Merken (Publishing Editors of the third edition), Jeffrey Freeland (Editorial Project Manager), and Lisa Jones (Senior Project Manager). Special thanks are due to Prof. Leslie Henshall, for his work on the text improvements.

Valery V. Vasiliev
Evgeny V. Morozov

CHAPTER

Introduction 1

1.1 STRUCTURAL MATERIALS

Materials are the basic elements of all natural and man-made structures. Technological progress is associated with continuous improvement of existing material properties, as well as with the expansion of structural material classes and types. Usually, new materials emerge due to the need to improve structural efficiency and performance. In addition, as a rule, new materials themselves in turn provide new opportunities to develop updated structures and technology, which then challenge materials science with new problems and tasks. One of the best manifestations of this interrelated process in the development of materials, structures, and technology is associated with composite materials and structural elements, to which this book is devoted.

Structural materials possess a great number of physical, chemical and other types of properties, but at least two principal characteristics are of primary importance. These characteristics are stiffness and strength. They provide the structure with the ability to maintain its shape and dimensions under loading or any other external action.

High stiffness means that material exhibits low deformation under loading. However, by saying that stiffness is an important property, we do not necessarily mean that it should be high. The ability of a structure to have controlled deformation (compliance) can also be important for some applications (e.g., springs; shock absorbers; and pressure, force, and displacement gauges).

Lack of material strength causes an uncontrolled compliance, i.e., a failure after which a structure does not exist any more. Usually, we need to have as high strength as possible, but there are some exceptions (e.g., controlled failure of explosive bolts is used to separate rocket stages).

Thus, without controlled stiffness and strength, the structure cannot exist. Naturally, both properties depend greatly on the structure's design, but are ultimately determined by the stiffness and strength of the structural material, because a good design is only a proper utilization of material properties.

To evaluate material stiffness and strength, consider the simplest test: a bar with cross-sectional area A loaded with tensile force F, as shown in Fig. 1.1. Obviously, the higher the force causing the bar rupture, the higher the bar's strength. However, this strength does not only depend on the material properties; it is proportional to the cross-sectional area A. Thus, it is natural to characterize material strength by the ultimate stress

$$\overline{\sigma} = \frac{\overline{F}}{A} \tag{1.1}$$

Advanced Mechanics of Composite Materials and Structural Elements. http://dx.doi.org/10.1016/B978-0-08-098231-1.00001-7
Copyright © 2013 Elsevier Ltd. All rights reserved.

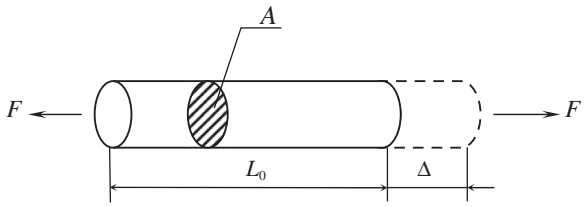


FIGURE 1.1

A bar under tension.

where $\overline{F}$ is the force causing the bar failure (here and subsequently we use the overbar notation to indicate the ultimate characteristics). As follows from Eq. (1.1), stress is measured as force divided by area, i.e., according to international (SI) units, in pascals (Pa), such that 1 Pa = 1 N/m^2. Since the loading of real structures induces relatively high stresses, we also use kilopascals (1 kPa = 10^3 Pa), megapascals (1 MPa = 10^6 Pa), and gigapascals (1 GPa = 10^9 Pa). Conversion of old metric (kilogram per square centimeter) and English (pound per square inch) units to pascals can be done using the following relations: 1 kg/cm^2= 98 kPa and 1 psi = 6.89 kPa.

For some special (e.g., aerospace or marine) applications, i.e., for which material density, ρ, is also important, a normalized characteristic

$$k_\sigma = \frac{\overline{\sigma}}{\rho} \tag{1.2}$$

is also used to describe the material. This characteristic is called the "specific strength" of a material. If we use old metric units, i.e., measure force and mass in kilograms and dimensions in meters, substitution of Eq. (1.1) into Eq. (1.2) yields k_σ in meters. This result has a simple physical sense, namely k_σ is the length of the vertically hanging fiber under which the fiber will be broken by its own weight.

The stiffness of the bar shown in Fig. 1.1 can be characterized by an elongation Δ corresponding to the applied force F or acting stress $\sigma = F/A$. However, Δ is proportional to the bar's length L_0. To evaluate material stiffness, we introduce strain

$$\varepsilon = \frac{\Delta}{L_0} \tag{1.3}$$

Since ε is very small for structural materials, the ratio in Eq. (1.3) is normally multiplied by 100, and ε is expressed as a percentage.

Naturally, for any material, there should be some interrelation between stress and strain, i.e.,

$$\varepsilon = f(\sigma), \quad \text{or} \quad \sigma = \varphi\,(\varepsilon) \tag{1.4}$$

These equations specify the so-called constitutive law and are referred to as constitutive equations. They allow us to introduce an important concept of the material model which represents some idealized object possessing only those features of the real material that are essential for the problem under study. The point is that when performing design or analysis, we always operate with models rather than with real materials. Particularly for strength and stiffness analysis, such a model is described by constitutive equations, Eqs. (1.4), and is specified by the form of the function $f(\sigma)$ or $\varphi\,(\varepsilon)$.

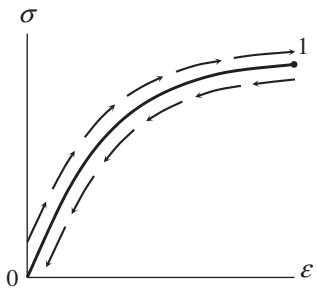


FIGURE 1.2

Stress-strain curve for an elastic material.

The simplest is the elastic model, which implies that $f(0) = 0$, $\varphi\,(0) = 0$, and that Eqs. (1.4) are the same for the processes of an active loading and an unloading. The corresponding stress-strain diagram (or curve) is presented in Fig. 1.2. The elastic model (or elastic material) is characterized by two important features. First, the corresponding constitutive equations, Eqs. (1.4), do not include time as a parameter. This means that the form of the curve shown in Fig. 1.2 does not depend on the rate of loading (naturally, it should be low enough to neglect inertial and dynamic effects). Second, the active loading and the unloading follow one and the same stress-strain curve as in Fig. 1.2. The work performed by force F in Fig. 1.1 is accumulated in the bar as potential energy, which is also referred to as strain energy or elastic energy. Consider some infinitesimal elongation $d\Delta$, and calculate the elementary work performed by the force F in Fig. 1.1 as $dW = Fd\Delta$. Then, work corresponding to point 1 of the curve in Fig. 1.2 is

$$W = \int_0^{\Delta_1} Fd\Delta$$

where Δ_1 is the elongation of the bar corresponding to point 1 of the curve. The work W is equal to the elastic energy of the bar, which is proportional to the bar's volume and can be presented as

$$E = L_0\, A \int_0^{\varepsilon_1} \sigma d\varepsilon$$

where $\sigma = F/A$, $\varepsilon = \Delta/L_0$ and $\varepsilon_1 = \Delta_1/L_0$. Integral

$$U = \int_0^{\varepsilon_1} \sigma d\varepsilon = \int_0^{\varepsilon_1} \varphi\,(\varepsilon) d\varepsilon \tag{1.5}$$

is a specific elastic energy (energy accumulated in a unit volume of the bar) that is referred to as an elastic potential. It is important that U does not depend on the history of loading. This means that irrespective of the way we reach point 1 of the curve in Fig. 1.2 (e.g., by means of continuous loading,

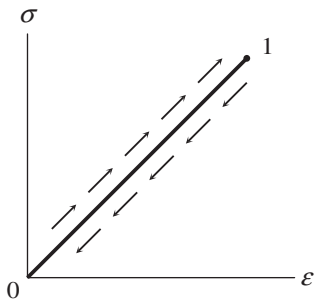


FIGURE 1.3

Stress-strain diagram for a linear elastic material.

increasing force F step by step, or using any other loading program), the final value of U will be the same, and will depend only on the value of final strain ε_1 for the given material.

A very important particular case of the elastic model is the linear elastic model described by the well-known Hooke's law,

$$\sigma = E\varepsilon \tag{1.6}$$

(see Fig. 1.3). Here, E is the modulus of elasticity. It follows from Eqs. (1.3) and (1.6), that $E = \sigma$ if $\varepsilon = 1$, i.e., if $\Delta = L_0$. Thus, modulus can be interpreted as the stress causing the elongation of the bar in Fig. 1.1 to be the same as the initial length. Since the majority of structural materials fail before such a high elongation can occur, the modulus is usually much higher then the ultimate stress $\overline{\sigma}$.

Similar to specific strength k_σ in Eq. (1.2), we can introduce the corresponding specific modulus

$$k_E = \frac{E}{\rho} \tag{1.7}$$

which describes a material's stiffness with respect to its density.

Absolute and specific values of mechanical characteristics for typical materials discussed in this book are listed in Table 1.1.

After some generalization, modulus can be used to describe nonlinear material behavior of the type shown in Fig. 1.4. For this purpose, the so-called secant, E_s, and tangent, E_t, moduli are introduced as

$$E_s = \frac{\sigma}{\varepsilon} = \frac{\sigma}{f(\sigma)} \qquad E_t = \frac{d\sigma}{d\varepsilon} = \frac{d\varphi\,(\varepsilon)}{d\varepsilon} \tag{1.8}$$

While the slope α in Fig. 1.4 determines the conventional modulus E, the slopes β and γ determine E_s and E_t, respectively. As can be seen, E_s and E_t, in contrast to E, depend on the level of loading, i.e., on σ or ε. For a linear elastic material (see Fig. 1.3), $E_s = E_t = E$.

Hooke's law, Eq. (1.6), describes rather well the initial part of a stress-strain diagram for the majority of structural materials. However, under a relatively high level of stress or strain, materials exhibit nonlinear behavior.

One of the existing models is the nonlinear elastic material model introduced earlier (see Fig. 1.2). This model allows us to describe the behavior of highly deformable rubber-type materials.

TABLE 1.1 Mechanical Properties of Structural Materials and Fibers.

Material	Ultimate Tensile Stress, $\overline{\sigma}$ (MPa)	Modulus, E (GPa)	Specific Gravity	Maximum Specific Strength, $k_\sigma \times 10^3$(m)	Maximum Specific Modulus, $k_E \times 10^3$(m)
Metal alloys					
Steel	400–2200	180–210	7.8–7.85	28.8	2750
Aluminum	140–700	69–72	2.7–2.85	26.5	2670
Titanium	420–1200	110	4.5	26.7	2440
Magnesium	220–320	40	1.8	14.4	2220
Beryllium	620	320	1.85	33.5	17,300
Nickel	400–500	200	8.9	5.6	2250
Metal wires (diameter, μm)					
Steel (20–1500)	1500–4400	180–200	7.8	56.4	2560
Aluminum (150)	290	69	2.7	10.7	2550
Titanium (100–800)	1400–1500	120	4.5	33.3	2670
Beryllium (50–500)	1100–1450	240–310	1.8–1.85	80.5	17,200
Tungsten (20–50)	3300–4000	410	19–19.3	21.1	2160
Molybdenum (25–250)	1800–2200	360	10.2	21.5	3500
Thermoset polymeric resins					
Epoxy	60–90	2.4-4.2	1.2–1.3	7.5	350
Polyester	30–70	2.8–3.8	1.2–1.35	5.8	310
Phenol-formaldehyde	40–70	7–11	1.2–1.3	5.8	910
Organosilicone	25–50	6.8–10	1.35–1.4	3.7	740
Polyimide	55–110	3.2	1.3–1.43	8.5	240
Bismaleimide	80	4.2	1.2	6.7	350
Thermoplastic polymers					
Polyethylene	20–45	6-8.5	0.95	4.7	890
Polystyrene	35–45	30	1.05	4.3	2860
Teflon	15–35	3.5	2.3	1.5	150
Nylon	80	2.8	1.14	7.0	240
Polyester (PC)	60	2.5	1.32	4.5	190
Polysulfone (PSU)	70	2.7	1.24	5.6	220
Polyamide-imide (PAI)	90–190	2.8–4.4	1.42	13.4	360
Polyetheretherketone (PEEK)	90–100	3.1–3.8	1.3	7.7	300
Polyphenylene sulfide (PPS)	80	3.5	1.36	5.9	250

(*continued on next page*)

TABLE 1.1 Mechanical Properties of Structural Materials and Fibers. *(continued)*

Material	Ultimate Tensile Stress, $\overline{\sigma}$ (MPa)	Modulus, E (GPa)	Specific Gravity	Maximum Specific Strength, $k_\sigma \times 10^3$(m)	Maximum Specific Modulus, $k_E \times 10^3$(m)
Synthetic fibers					
Capron	680–780	4.4	1.1	70	400
Dacron	390–880	4.9–15.7	1.4	60	1430
Teflon	340–440	2.9	2.3	190	130
Nitron	390–880	4.9–8.8	1.2	70	730
Polypropylene	730–930	4.4	0.9	100	480
Viscose	930	20	1.52	60	1300
Fibers for advanced composites (diameter, μm)					
Glass (3–19)	3100–5000	72–95	2.4–2.6	200	3960
Quarts (10)	6000	74	2.2	270	3360
Basalt (9–13)	3000–3500	90	2.7–3.0	130	3300
Aramid (12–15)	3500–5500	140–180	1.4–1.47	390	12,800
Polyethylene (20–40)	2600–3300	120–170	0.97	310	17,500
Carbon (5–11)					
High-Strength	7000	300	1.75	400	17,100
High-Modulus	2700	850	1.78	150	47,700
Boron (100–200)	2500–3700	390–420	2.5–2.6	150	16,800
Alumina–Al_2O_3 (20–500)	2400–4100	470–530	3.96	100	13,300
Silicon Carbide–SiC (10–15)	2700	185	2.4–2.7	110	7700
Titanium Carbide–TiC (280)	1500	450	4.9	30	9100
Boron Carbide–B_4C (50)	2100–2500	480	2.5	100	10,000
Boron Nitride–BN (7)	1400	90	1.9	70	4700

Another model developed to describe metals is the so-called elastic-plastic material model. The corresponding stress-strain diagram is shown in Fig. 1.5. In contrast to an elastic material (see Fig. 1.2), the processes of active loading and unloading are described with different laws in this case. In addition to elastic strain, ε_e, which disappears after the load is taken off, the residual strain (for the bar shown in Fig. 1.1, it is plastic strain, ε_p) remains in the material. As for an elastic material, the stress-strain curve in Fig. 1.5 does not depend on the rate of loading (or time of loading). However, as opposed to an elastic material, the final strain of an elastic-plastic material can depend on the history of loading, i.e., on the law according to which the final value of stress was reached.

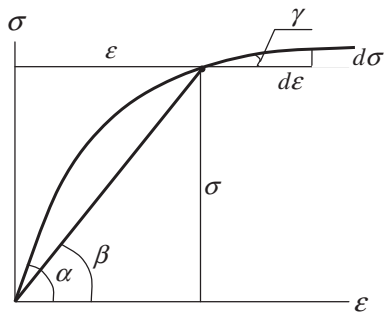


FIGURE 1.4

Introduction of secant and tangent moduli.

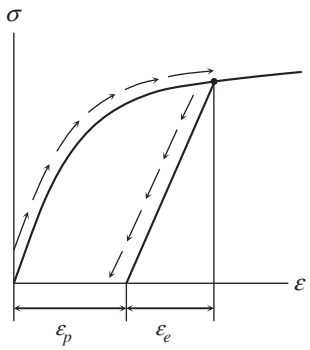


FIGURE 1.5

Stress-strain diagram for elastic-plastic material.

Thus, for elastic or elastic-plastic materials, constitutive equations, Eqs. (1.4), do not include time. However, under relatively high temperature practically all the materials demonstrate time-dependent behavior (some of them do it even under room temperature). If we apply some force F to the bar shown in Fig. 1.1 and keep it constant, we can see that for a time-sensitive material the strain increases under a constant force. This phenomenon is called the creep of the material.

So, the most general material model that is used in this book can be described with a constitutive equation of the following type:

$$\varepsilon = f(\sigma, t, T) \tag{1.9}$$

where t indicates the time moment, whereas σ and T are stress and temperature corresponding to this moment. In the general case, constitutive equation Eq. (1.9) specifies strain that can be decomposed into three constituents corresponding to elastic, plastic, and creep deformation, i.e.,

$$\varepsilon = \varepsilon_e + \varepsilon_p + \varepsilon_c \tag{1.10}$$

However, in application to particular problems, usually this model can be substantially simplified. To show this, consider the bar in Fig. 1.1 and assume that a force F is applied at the moment $t = 0$ and is taken off at moment $t = t_1$, as shown in Fig. 1.6a. At the moment $t = 0$, elastic and plastic strains that do not depend on time appear, and while time is running, the creep strain is developed. At the moment $t = t_1$, the elastic strain disappears, while the reversible part of the creep strain, ε_c^t, disappears with time. Residual strain consists of the plastic strain, ε_p, and the residual part of the creep strain, ε_c^r.

Now assume that $\varepsilon_p << \varepsilon_e$, which means that either the material is elastic, or the applied load does not induce high stress and, hence, plastic strain. Then, we can neglect ε_p in Eq. (1.10) and simplify the model. Furthermore, let $\varepsilon_c << \varepsilon_e$, which in turn means that either the material is not susceptible to creep, or the force acts for a short time (t_1 is close to zero). Thus, we arrive at the simplest elastic model, which is the case for the majority of practical applications. It is important that the appropriate choice of the material model depends not only on the material nature and properties, but also on the operational conditions of the structure. For example, a shell-type structure made of aramid-epoxy composite material that is susceptible to creep and designed to withstand internal gas pressure should be analyzed with due regard to the creep, if this structure is a pressure vessel for long term gas storage. At the same time, for a solid propellant rocket motor case working only for seconds, the creep strain can be ignored.

A very important feature of material models under consideration is their phenomenological nature. This means that these models ignore the actual material microstructure (e.g., crystalline structure of metals or molecular structure of polymers) and represent the material as some uniform continuum possessing some effective properties that are the same irrespective of how small the material volume is. This allows us, first, to determine material properties testing material samples (as in Fig. 1.1). Second, this formally enables us to apply methods of *Mechanics of Solids* that deal with equations derived for

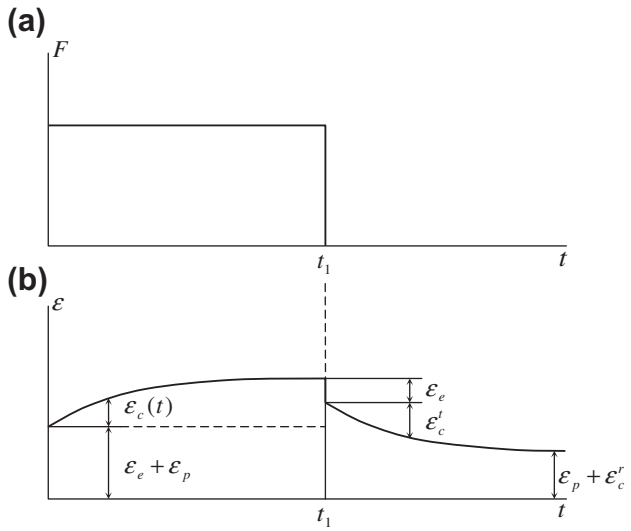


FIGURE 1.6

Dependence of force (a) and strain (b) on time.

infinitesimal volumes of material. And third, this allows us to simplify the strength and stiffness evaluation problem and to reduce it to a reasonable practical level, not going into analysis of the actual mechanisms of material deformation and fracture.

1.2 COMPOSITE MATERIALS

This book is devoted to composite materials that emerged in the middle of the twentieth century as a promising class of engineering materials providing new prospects for modern technology. Generally speaking, any material consisting of two or more components with different properties and distinct boundaries between the components can be referred to as a composite material. Moreover, the idea of combining several components to produce a material with properties that are not attainable with the individual components has been used by man for thousands of years. Correspondingly, the majority of natural materials that have emerged as a result of a prolonged evolution process can be treated as composite materials.

With respect to the problems covered in this book, we can classify existing composite materials (composites) into two main groups.

The first group comprises composites that are known as "filled materials." The main feature of these materials is the existence of some basic or matrix material whose properties are improved by filling it with some particles. Usually the matrix volume fraction is more than 50% in such materials, and material properties, being naturally modified by the fillers, are governed mainly by the matrix. As a rule, filled materials can be treated as homogeneous and isotropic, i.e., traditional models of mechanics of materials developed for metals and other conventional materials can be used to describe their behavior. This group of composites is not touched on in the book.

The second group of composite materials that is under study here involves composites that are called "reinforced materials." The basic components of these materials (sometimes referred to as "advanced composites") are long, thin fibers possessing high strength and stiffness. The fibers are bound with a matrix material whose volume fraction in a composite is usually less than 50%. The main properties of advanced composites (which grant these materials a wide application in engineering) are governed by fibers whose types and characteristics are considered later. The following sections provide a concise description of typical matrix materials and fiber-matrix compositions. Two comments should be made with respect to the data presented in these sections. First, only brief information concerning material properties that are essential for the topics covered in this book is presented there, and second, the given data are of a broad nature and are not expected to be used in design or analysis of particular composite structures. More complete descriptions of composite materials and their components, including the history of development and advancement, chemical compositions, physical characteristics, manufacturing and applications, can be found elsewhere (Peters, 1998).

1.2.1 Fibers for advanced composites

Continuous glass fibers (the first type of fibers used in advanced composites) are made by pulling molten glass (at a temperature of about 1300°C) through 0.8–3.0 mm diameter dies and then high-speed stretching the glass to a diameter of 3–19 μm. Usually, glass fibers have solid circular cross sections. However, there exist fibers with rectangular (square or plane), triangular, and hexagonal cross

sections, as well as hollow circular fibers. Typical mechanical characteristics and density of glass fibers are listed in Table 1.1, whereas a typical stress-strain diagram is shown in Fig. 1.7.

Important properties of glass fibers as components of advanced composites for engineering applications are their high strength, which is maintained in humid environments but degrades under elevated temperatures (see Fig. 1.8), relatively low stiffness (about 40% of the stiffness of steel), high chemical and biological resistance, and low cost. As elements of monolithic glass, the fibers do not absorb water and do not change their dimensions in water. For the same reason, they are brittle and sensitive to surface damage.

Quartz fibers are similar to glass fibers and are obtained by high-speed stretching of quartz rods made (under a temperature of about 2200°C) of fused quartz crystals or sand. The original process developed for manufacturing glass fibers cannot be used because the viscosity of molten quartz is too

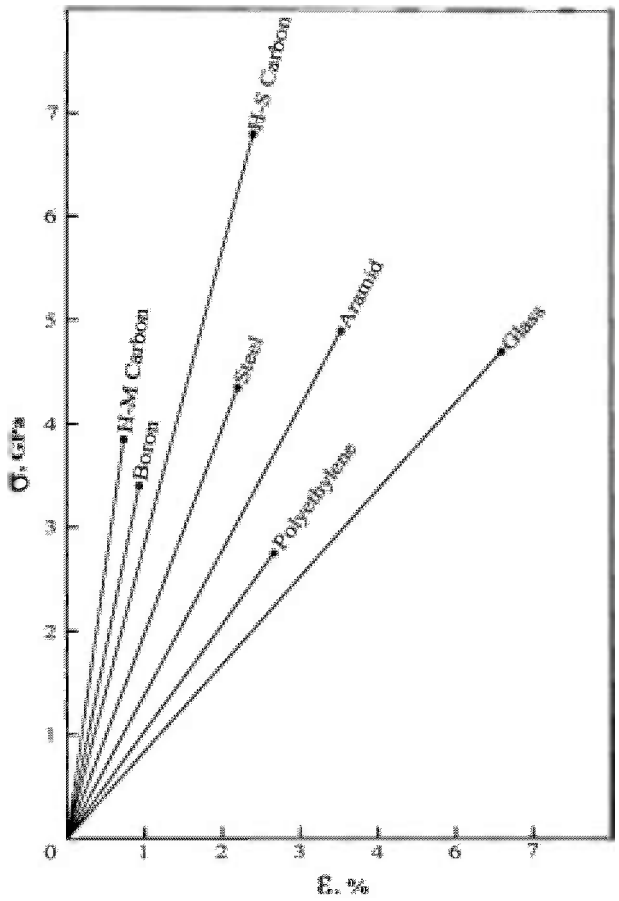


FIGURE 1.7

Stress-strain diagrams for typical fibers of advanced composites.

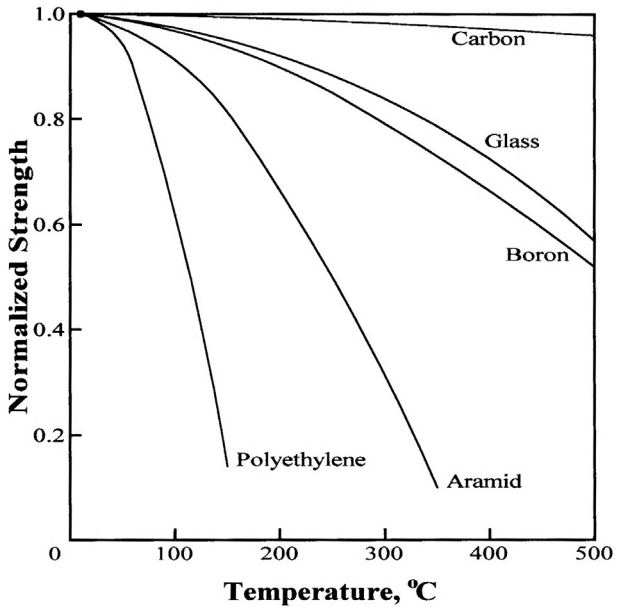


FIGURE 1.8

Temperature degradation of fiber strength normalized by the strength at 20°C.

high to make thin fibers directly. However, this more complicated process results in fibers with higher thermal resistance than glass fibers.

The same process that is used for glass fibers can be employed to manufacture mineral fibers, e.g., basalt fibers made of molten basalt rocks. Having relatively low strength and high density (see Table 1.1), basalt fibers are not used for high-performance structures, e.g., aerospace structures, but are promising reinforcing elements for pre-stressed reinforced concrete structures in civil engineering.

Substantial improvement of a fiber's stiffness in comparison with glass fibers has been achieved with the development of carbon (or graphite) fibers. Modern high-modulus carbon fibers have a modulus that is a factor of about four higher than the modulus of steel, whereas the fiber density is lower by the same factor. Although the first carbon fibers had lower strength than glass fibers, modern high-strength carbon fibers have a 40% higher tensile strength than the best glass fibers, whereas the density of carbon fibers is 30% less than that of glass fibers.

Carbon fibers are made by pyrolysis of organic fibers, of which there exist two main types–PAN-based and pitch-based fibers. For PAN-based fibers, the process consists of three stages: stabilization, carbonization, and graphitization. In the first step (stabilization), a system of polyacrylonitrile (PAN) filaments is stretched and heated up to about 400°C in an oxidation furnace, while in the subsequent step (carbonization under 900°C in an inert gas media), most elements of the filaments other than carbon are removed or converted into carbon. During the successive heat treatment at a temperature reaching 2800°C (graphitization), a crystalline carbon structure oriented along the fiber's length is formed, resulting in PAN-based carbon fibers. The same process is used for rayon organic filaments (instead of PAN), but it results in carbon fibers with lower modulus and strength

because rayon contains less carbon than PAN. For pitch-based carbon fibers, the initial organic filaments are made in approximately the same manner as for glass fibers from molten petroleum or coal pitch, and they pass through the carbonization and graphitization processes. Since pyrolysis is accompanied with a loss of material, carbon fibers have a porous structure and their specific gravity (about 1.8) is less than that of graphite (2.26). The properties of carbon fibers are affected by the crystallite size, crystalline orientation, porosity, and purity of the carbon structure.

Typical stress-strain diagrams for high-modulus (HM) and high-strength (HS) carbon fibers are plotted in Fig. 1.7. As components of advanced composites for engineering applications, carbon fibers are characterized by very high modulus and strength, high chemical and biological resistance, high electric conductivity and very low coefficient of thermal expansion. The strength of carbon fibers practically does not change with temperatures up to 1500°C (in an inert media preventing oxidation of the fibers).

The exceptional strength of 7.06 GPa is reached in Toray T-1000 carbon fibers, whereas the highest modulus of 850 GPa is obtained in Carbonic HM-85 fibers. Carbon fibers are anisotropic, very brittle and sensitive to damage. They do not absorb water and do not change their dimensions in humid environments.

There exist more than 50 types of carbon fibers with a broad spectrum of strength, stiffness, and cost, and the process of fiber advancement is not over; one may expect fibers with strength up to 10 GPa and modulus up to 1000 GPa within a few years.

Organic fibers commonly encountered in textile applications can be employed as reinforcing elements of advanced composites. Naturally, only high performance fibers, i.e., fibers possessing high stiffness and strength, can be used for this purpose. The most widely used organic fibers that satisfy these requirements are known as aramid (aromatic polyamide) fibers. They are extruded from a liquid crystalline solution of the corresponding polymer in sulfuric acid with subsequent washing in a cold water bath and stretching under heating. Some properties of typical aramid fibers are listed in Table 1.1, and the corresponding stress-strain diagram is presented in Fig. 1.7. As components of advanced composites for engineering applications, aramid fibers are characterized by low density providing high specific strength and stiffness, low thermal conductivity resulting in high heat insulation, and a negative thermal expansion coefficient allowing us to construct hybrid composite elements that do not change their dimensions under heating. Consisting of a system of very thin filaments (fibrils), aramid fibers have very high resistance to damage. Their high strength in the longitudinal direction is accompanied by relatively low strength under tension in the transverse direction. Aramid fibers are characterized by pronounced temperature (see Fig. 1.8) and time dependence for stiffness and strength. Unlike the inorganic fibers discussed earlier, they absorb water, resulting in moisture content up to 7% and degradation of material properties by 15–20%.

The list of organic fibers has been supplemented recently with extended chain polyethylene fibers demonstrating outstanding low density (less than that of water) in conjunction with relatively high stiffness and strength (see Table 1.1 and Fig. 1.7). Polyethylene fibers are extruded from the corresponding polymer melt in a similar manner to glass fibers. They do not absorb water and have high chemical resistance, but demonstrate relatively low temperature and creep resistance (see Fig. 1.8).

Boron fibers were developed to increase the stiffness of composite materials when glass fibers were mainly used to reinforce composites of the day. Being followed by high-modulus carbon fibers with higher stiffness and lower cost, boron fibers now have rather limited application. Boron fibers are

manufactured by chemical vapor deposition of boron onto about 12 μm diameter tungsten or carbon wire (core). As a result, boron fibers have a relatively large diameter, 100–200 μm. They are extremely brittle and sensitive to surface damage. Typical mechanical properties of boron fibers are presented in Table 1.1 and Figs 1.7 and 1.8. Mainly used in metal matrix composites, boron fibers degrade on contact with aluminum or titanium matrices at the temperature that is necessary for processing (above 500°C). To prevent this degradation, chemical vapor deposition is used to cover the fiber surface with about a 5 μm-thick layer of silicon carbide, SiC (such fibers are called Borsic), or boron carbide, B_4C.

There exists a special class of ceramic fibers for high-temperature applications, composed of various combinations of silicon, carbon, nitrogen, aluminum, boron, and titanium. The most commonly used are silicon carbide (SiC) and alumina (Al_2O_3) fibers.

Silicon carbide is deposited on a tungsten or carbon core-fiber by the reaction of a gas mixture of silanes and hydrogen. Thin (8–15 μm in diameter) SiC fibers can be made by pyrolysis of polymeric (polycarbosilane) fibers at temperatures of about 1400°C in an inert atmosphere. Silicon carbide fibers have high strength and stiffness, moderate density (see Table 1.1), and very high melting temperature (2600°C).

Alumina (Al_2O_3) fibers are fabricated by sintering of fibers extruded from the viscous alumina slurry with rather complicated composition. Alumina fibers, possessing approximately the same mechanical properties as SiC fibers, have relatively large diameter and high density. The melting temperature is about 2000°C.

Silicon carbide and alumina fibers are characterized by relatively low reduction in strength at elevated temperatures (see Fig. 1.9).

Boron carbide (B_4C) fibers that can be obtained either as a result of reaction of a carbon fiber with a mixture of hydrogen and boron chloride at high temperature (around 1800°C) or by pyrolysis of

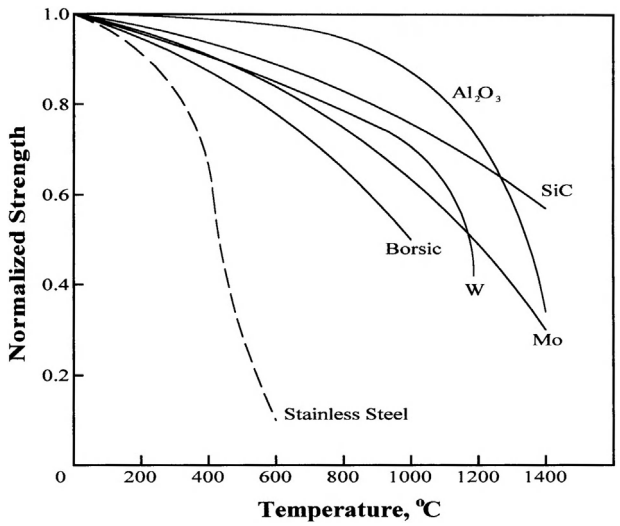


FIGURE 1.9

Temperature dependence of high-temperature fibers' normalized strength (in comparison with stainless steel).

cellulosic fibers soaked with boric acid solution are promising ceramic fibers for high-temperature applications. Possessing high stiffness and strength and moderate density (see Table 1.1), boron carbide fibers have very high thermal resistance (up to 2300°C).

Metal fibers (thin wires) made of steel, beryllium, titanium, tungsten, and molybdenum are used for special (e.g., low-temperature and high-temperature) applications. Typical characteristics of metal fibers are presented in Table 1.1 and Figs. 1.7 and 1.9.

In advanced composites, fibers provide not only high strength and stiffness but also a possibility to tailor the material so that the directional dependence of its mechanical properties matches that of the loading environment. The principle of directional properties can be traced in all natural materials that have emerged as a result of a prolonged evolution and, in contrast to man-made metal alloys, are neither isotropic nor homogeneous. Many natural materials have fibrous structures and utilize the high strength and stiffness of natural fibers listed in Table 1.2. As can be seen (Tables 1.1 and 1.2), natural fibers, having lower strength and stiffness than man-made fibers, can compete with modern metals and plastics.

Before being used as reinforcing elements of advanced composites, the fibers are normally subjected to special surface finish treatments, undertaken to prevent any fiber damage under contact with processing equipment, provide surface wetting when the fibers are combined with matrix materials, and improve the interface bond between fibers and matrices. The most commonly used surface treatments are chemical sizing performed during the basic fiber formation operation and resulting in a thin layer applied to the surface of the fiber; surface etching by acid, plasma, or corona discharge; and coating of the fiber surface with thin metal or ceramic layers.

With only a few exceptions (e.g., metal fibers), individual fibers, being very thin and sensitive to damage, are not used in composite manufacturing directly, but in the form of tows (rovings), yarns, and fabrics.

TABLE 1.2 Mechanical Properties of Natural Fibers.

Fiber	Diameter (μm)	Ultimate Tensile Stress, $\bar{\sigma}$ (MPa)	Modulus, *E* (GPa)	Specific Gravity
Wood	15–20	160	23	1.5
Bamboo	15–30	550	36	0.8
Jute	10–50	580	22	1.5
Cotton	15–40	540	28	1.5
Wool	75	170	5.9	1.32
Coir	10–20	250	5.5	1.5
Bagasse	25	180	9	1.25
Rice	5–15	100	6	1.24
Natural Silk	15	400	13	1.35
Spider Silk	4	1750	12.7	–
Linen	–	270	–	–
Sisal	–	560	–	–
Asbestos	0.2	1700	160	2.5

A unidirectional tow (roving) is a loose assemblage of parallel fibers usually consisting of thousands of elementary fibers. Two main designations are used to indicate the size of the tow, namely the K number that gives the number of fibers in the tow (e.g., $3K$ tow contains 3000 fibers) and the tex number, which is the mass in grams of 1000 m of the tow. The tow tex number depends not only on the number of fibers but also on the fiber diameter and density. For example, an AS4-6K tow consisting of 6000 AS4 carbon fibers has 430 tex.

A yarn is a fine tow (usually it includes hundreds of fibers) slightly twisted (about 40 turns per meter) to provide the integrity of its structure necessary for textile processing. Yarn size is indicated in tex numbers or in textile denier numbers (den) such that 1 tex = 9 den. Continuous yarns are used to make fabrics with various weave patterns. There exists a wide variety of glass, carbon, aramid, and hybrid fabrics whose nomenclature, structure, and properties are described elsewhere (Chou and Ko, 1989; Tarnopol'skii et al., 1992; Bogdanovich and Pastore, 1996; Peters, 1998).

An important characteristic of fibers is their processability, which can be evaluated as the ratio $K_p = \overline{\sigma}_S/\overline{\sigma}$, of the strength demonstrated by fibers in the composite structure $\overline{\sigma}_S$ to the strength of fibers before they were processed $\overline{\sigma}$. This ratio depends on the fibers' ultimate elongation, on their sensitivity to damage, and on manufacturing equipment causing damage to the fibers. The most sensitive to operational damage are boron and high-modulus carbon fibers possessing relatively low ultimate elongation $\overline{\varepsilon}$ (less than 1%, see Fig. 1.7). For example, for filament wound pressure vessels $K_p = 0.96$ for glass fibers, whereas for carbon fibers $K_p = 0.86$.

To evaluate fiber processability under real manufacturing conditions, three simple tests are used: tension of a straight dry tow, tension of tows with loops, and tension of a tow with a knot (see Fig. 1.10). Similar tests are used to determine the strength of individual fibers (Fukuda et al., 1997). For carbon tows, the normalized strength obtained in these tests is presented in Table 1.3 (for appropriate comparison, the tows should be of the same size). As follows from this table, the tow processability depends on the fiber's ultimate strain (elongation). The best processability is observed for aramid tows, whose fibers have high elongation and low sensitivity to damage (they are not monolithic and consist of thin fibrils).

1.2.2 Matrix materials

To utilize high strength and stiffness of fibers in a monolithic composite material suitable for engineering applications, fibers are bound with a matrix material whose strength and stiffness are, naturally, much lower than those of fibers (otherwise, no fibers would be necessary). Matrix materials provide the final shape of the composite structure and govern the parameters of the manufacturing process. The optimal combination of fiber and matrix properties should satisfy a set of operational and manufacturing requirements that are sometimes of a contradictory nature, and have not been completely met yet in existing composites.

First of all, the stiffness of the matrix should correspond to the stiffness of the fibers and be sufficient to provide uniform loading of fibers. The fibers are usually characterized by relatively high scatter in strength that may be increased due to damage of the fibers caused by the processing equipment. Naturally, fracture of the weakest or damaged fiber should not result in material failure. Instead, the matrix should evenly redistribute the load from the broken fiber to the adjacent ones and then load the broken fiber at a distance from the cross section at which it failed. The higher the matrix stiffness, the smaller is this distance, and the less is the influence of damaged fibers on material

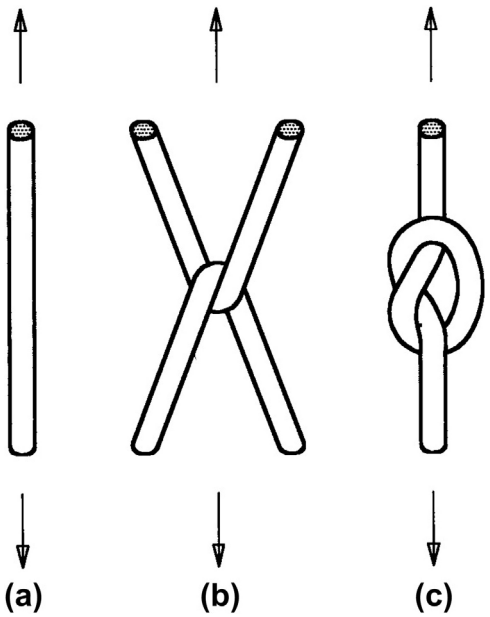


FIGURE 1.10

Testing of a straight tow (a), tows with a loop (b), and a tow with a knot (c).

TABLE 1.3 Normalized Strength of Carbon Tows.

	Normalized Strength		
Ultimate Strain, $\bar{\varepsilon}$ (%)	**Straight Tow**	**Tow with a Loop**	**Tow with a Knot**
0.75	1	0.25	0.15
1.80	1	0.53	0.18

strength and stiffness (which should be the case). Moreover, the matrix should provide the proper stress diffusion (this is the term traditionally used for this phenomenon in the analysis of stiffened structures (Goodey, 1946) in the material at a given operational temperature. That is why this temperature is limited, as a rule, by the matrix rather than by the fibers. On the other hand, to provide material integrity up to the failure of the fibers, the matrix material should possess high compliance. Obviously, for a linear elastic material (see Fig. 1.3), a combination of high stiffness and high ultimate strain $\bar{\varepsilon}$ results in high strength (which is not the case for modern matrix materials). Thus, close to optimal (with respect to the foregoing requirements) and realistic matrix material should have a nonlinear stress-strain diagram (of the type shown in Fig. 1.5) and possess high initial modulus of elasticity and high ultimate strain.

However, matrix properties, even though being optimal for the corresponding fibers, do not manifest in the composite material if the adhesion (the strength of fiber-matrix interface bonding) is

not high enough. High adhesion between fibers and matrices, providing material integrity up to the failure of the fibers, is a necessary condition for high-performance composites. Proper adhesion can be reached for appropriately selected combinations of fiber and matrix materials under some additional conditions. First, a liquid matrix should have viscosity low enough to allow the matrix to penetrate between the fibers of such dense systems of fibers as tows, yarns, and fabrics. Second, the fiber surface should have good wettability with the matrix. Third, the matrix viscosity should be high enough to retain the liquid matrix in the impregnated tow, yarn, or fabric in the process of fabrication of a composite part. Finally, the manufacturing process providing the proper quality of the resulting material should not require high temperature and pressure to make a composite part.

At present, typical matrices are made from polymeric, metal, carbon, and ceramic materials.

Polymeric matrices are divided into two main types, thermoset and thermoplastic. Thermoset polymers, which are the most widely used matrix materials for advanced composites, include polyester, epoxy, polyimide, and other resins (see Table 1.1) cured under elevated or room temperature. A typical stress-strain diagram for a cured epoxy resin is shown in Fig. 1.11. Being cured (polymerized), a thermoset matrix cannot be reset, dissolved, or melted. Heating of a thermoset material results first in degradation of its strength and stiffness, and then in thermal destruction.

In contrast to thermoset resins, thermoplastic matrices (PSU, PEEK, PPS, and others – see Table 1.1) do not require any curing reaction. They melt under heating and convert to a solid state under cooling. The possibility to re-melt and dissolve thermoplastic matrices allows us to reshape the composite parts forming them under heating, and it simplifies their recycling, which is a problem for thermoset materials.

Polymeric matrices can be combined with glass, carbon, organic, or boron fibers to yield a wide class of polymeric composites with high strength and stiffness, low density, high fatigue resistance, and excellent chemical resistance. The main disadvantage of these materials is their relatively low temperature resistance (in comparison with metals) limited by the matrix. The so-called thermomechanical curves are plotted to determine this important (for applications) characteristic of the matrix. These curves, presented for typical epoxy resins in Fig. 1.12, show the dependence of some

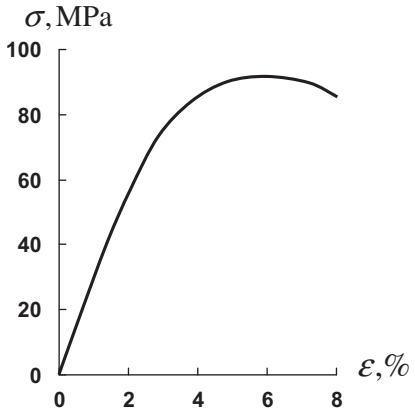


FIGURE 1.11

Stress-strain diagram for a typical cured epoxy matrix.

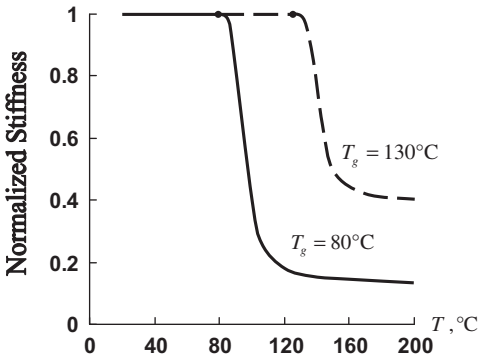


FIGURE 1.12

Typical thermo-mechanical diagrams for cured epoxy resins with glass transition temperatures of 80°C (solid line) and 130°C (dashed line).

stiffness parameters on the temperature, and allow us to find the so-called glass transition temperature, T_g, which indicates a dramatic reduction in material stiffness. There exist several standard methods to obtain a material's thermo-mechanical diagram. The one used to plot the curves presented in Fig. 1.12 involves compression tests of heated polymeric discs. Naturally, to retain the complete set of properties of polymeric composites, the operating temperature should not (in general) exceed T_g. However, the actual material behavior depends on the type of loading. As follows from Fig. 1.13, heating above the glass transition temperature only slightly influences material properties under tension in the fiber direction and dramatically reduces its strength in longitudinal compression and transverse bending. The glass transition temperature depends on the processing temperature, T_p, at which a material is fabricated, and higher T_p results, as a rule, in higher T_g. Thermoset epoxy matrices cured at a temperature in the range 120−160°C have $T_g = 60-140°C$. There also exist a number of high temperature thermoset matrices (e.g., organosilicone, polyimide, and bismaleimide resins) with $T_g = 250-300°C$ and curing temperatures of up to 400°C. Thermoplastic matrices are also characterized by a wide range of glass transition temperatures: from 90°C for PPS and 140°C for PEEK, to 190°C for PSU and 270°C for PAI (see Table 1.1 for abbreviations). The processing temperature for different thermoplastic matrices varies from 300°C to 400°C.

Further enhancement in temperature resistance of composite materials is associated with application of metal matrices in combination with high temperature boron, carbon, ceramic fibers, and metal wires. The most widespread metal matrices are aluminum, magnesium, and titanium alloys possessing high plasticity (see Figure 1.14), whereas for special applications nickel, copper, niobium, cobalt, and lead matrices can be used. Fiber reinforcement essentially improves the mechanical properties of such metals. For example, carbon fibers increase strength and stiffness of a soft metal such as lead by an order of magnitude.

As noted earlier, metal matrices allow us to increase operational temperatures for composite structures. The dependencies of longitudinal strength and stiffness of boron-aluminum unidirectional composite material on temperature, corresponding to the experimental results that can be found in Karpinos (1985) and Vasiliev and Tarnopol'skii (1990), are shown in Fig. 1.15. Clearly, higher temperature resistance requires higher processing temperature, T_p. Indeed, aluminum matrix composite materials are processed at $T_p = 550°C$, whereas for magnesium, titanium, and nickel

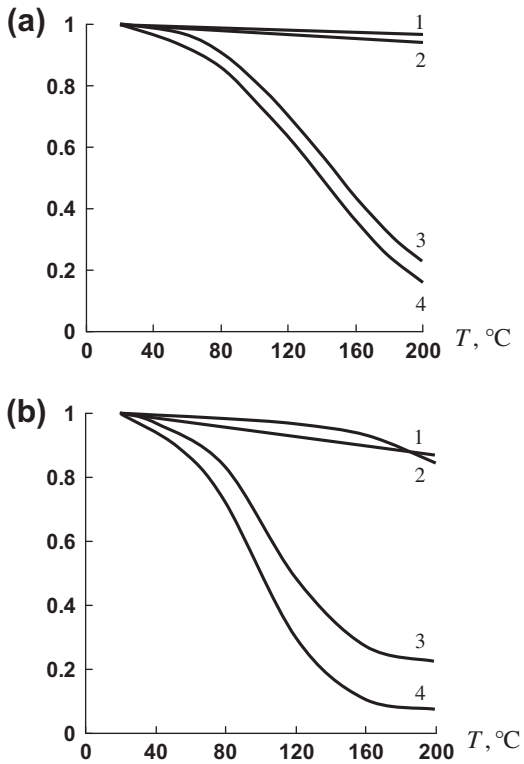


FIGURE 1.13

Dependence of normalized longitudinal moduli (1), strength under longitudinal tension (2), bending (3), and compression (4) on temperature for unidirectional carbon composites with epoxy matrices having $T_g = 130°C$ (a) and $T_g = 80°C$ (b).

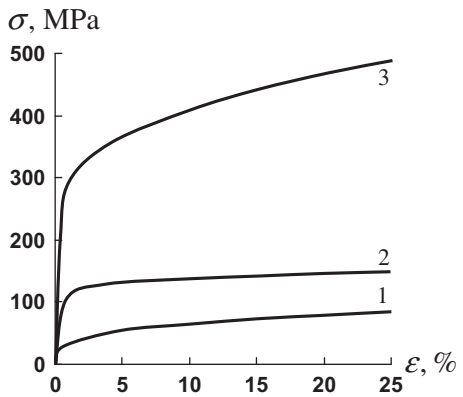


FIGURE 1.14

Typical stress-strain curves for aluminum (1), magnesium (2), and titanium (3) matrices.

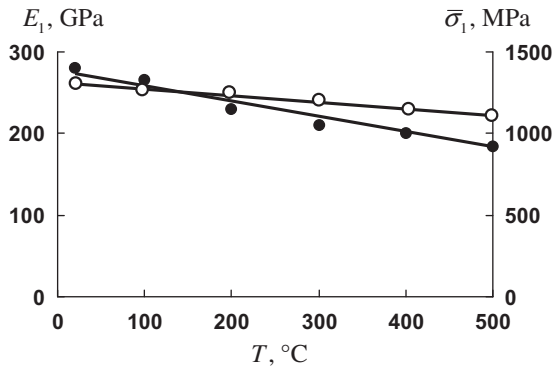


FIGURE 1.15

Temperature dependence of tensile strength (●) and stiffness (○) along the fibers for unidirectional boron-aluminum composite.

matrices the appropriate temperature is about 800, 1000, and 1200°C respectively. Some processes also require rather high pressure (up to 150 MPa).

In polymeric composites, the matrix materials play an important but secondary role of holding the fibers in place and providing good load dispersion into the fibers, whereas material strength and stiffness are controlled by the reinforcements. In contrast, the mechanical properties of metal matrix composites are controlled by the matrix to a considerably larger extent, though the fibers still provide the major contribution to the strength and stiffness of the material.

The next step in the development of composite materials that can be treated as matrix materials reinforced with fibers rather than fibers bonded with matrix (which is the case for polymeric composites) is associated with ceramic matrix composites possessing very high thermal resistance. The stiffness of the fibers which are usually metal (steel, tungsten, molybdenum, niobium), carbon, boron, or ceramic (SiC, Al_2O_3) and the ceramic matrices (oxides, carbides, nitrides, borides, and silicides) are not very different, and the fibers do not carry the main fraction of the load in ceramic composites. The function of the fibers is to provide strength and (mainly) toughness (resistance to cracks) of the composite, because non-reinforced ceramic materials are very brittle. Ceramic composites can operate under very high temperatures depending on the melting temperature of the matrix, which varies from 1200 to 3500°C. Naturally, the higher the temperature, the more complicated is the manufacturing process. The main shortcoming of ceramic composites is associated with a low ultimate tensile elongation of the ceramic matrix resulting in cracks appearing in the matrix under relatively low tensile stress applied to the material.

An outstanding combination of high mechanical characteristics and temperature resistance is demonstrated by carbon-carbon composites in which both components (fibers and matrix) are made from one and the same material, but with different structures. A carbon matrix is formed as a result of carbonization of an organic resin (phenolic and furfural resin or pitch) with which carbon fibers are impregnated, or of chemical vapor deposition of pyrolitic carbon from a hydrocarbon gas. In an inert atmosphere or in a vacuum, carbon-carbon composites can withstand very high temperatures (more than 3000°C). Moreover, their strength increases under heating up to 2200°C, while the modulus

degrades at temperatures above 1400°C. However, in an oxygen atmosphere, they oxidize and sublime at relatively low temperatures (about 600°C). To use carbon-carbon composite parts in an oxidizing atmosphere, they must have protective coatings, usually made from silicon carbide. Manufacturing of carbon-carbon parts is a very energy- and time-consuming process. To convert an initial carbon-phenolic composite into carbon-carbon, it should receive a thermal treatment at 250°C for 150 h, carbonization at about 800°C for about 100 h, and several cycles of densification (one-stage pyrolysis results in high porosity of the material), each including impregnation with resin, curing, and carbonization. To refine the material structure and to provide oxidation resistance, a further high-temperature graphitization (at 2700°C) and coating (at 1650°C) can be required. Vapor deposition of pyrolitic carbon is also a time-consuming process, performed at 900–1200°C under a pressure of 150–2000 kPa.

1.2.3 Processing

Composite materials do not exist separately from composite structures and are formed while the structure is fabricated. Being a heterogeneous media, a composite material has two levels of heterogeneity. The first level represents a microheterogeneity induced by at least two phases (fibers and matrix) that form the material microstructure. At the second level, the material is characterized by a macroheterogeneity caused by the laminated or more complicated macrostructure of the material, which consists usually of a set of layers with different orientations. A number of technologies have been developed to manufacture composite structures, all of which involve two basic processes during which material microstructure and macrostructure are formed.

The first basic process yielding material microstructure involves the application of a matrix material to the fibers. The simplest way to do this, normally utilized in the manufacturing of composites with thermosetting polymeric matrices, is a direct impregnation of tows, yarns, fabrics, or more complicated fibrous structures with liquid resins. Thermosetting resin has relatively low viscosity, which can be controlled using solvents or heating, and good wetting ability for the majority of fibers.

There exist two versions of this process. According to the so-called wet process, impregnated fibrous material (tows, fabrics, etc.) is used to fabricate composite parts directly, without any additional treatment or interruption of the process. In contrast to that, in "dry" or "prepreg" processes, impregnated fibrous material is dried (partially cured) and thus preimpregnated tapes (prepregs) are stored for further utilization (usually under low temperature to prevent uncontrolled premature polymerization of the resin). An example of a machine for making prepregs is shown in Fig. 1.16. Both processes, having similar advantages and shortcomings, are widely used for composites with thermosetting matrices. For thermoplastic matrices, application of direct impregnation (wet processing) is limited by the relatively high viscosity of thermoplastic polymer solutions or melts. For this reason, prepreg processes with preliminary fabricated tapes or sheets in which fibers are already combined with the thermoplastic matrix are used to manufacture composite parts.

There also exist other processes that involve application of heat and pressure to hybrid materials, including reinforcing fibers and a thermoplastic polymer in the form of powder, films, or fibers. A promising process (called fibrous technology) utilizes tows, tapes, or fabrics with two types of fibers – reinforcing and thermoplastic. Under heat and pressure, thermoplastic fibers melt and form the matrix of the composite material. Metal and ceramic matrices are applied to fibers by means of casting,

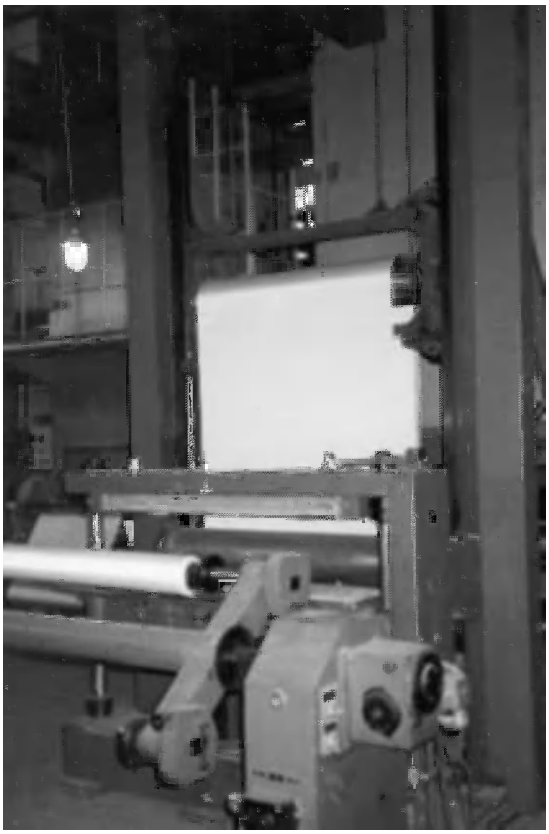


FIGURE 1.16

Machine making a prepreg from fiberglass fabric and epoxy resin.

Courtesy of CRISM.

diffusion welding, chemical deposition, plasma spraying, processing by compression molding, or with the aid of powder metallurgy methods.

The second basic process provides the appropriate macrostructure of a composite material corresponding to the loading and operational conditions of the composite part that is fabricated. There exist three main types of material macrostructure: linear structure, which is appropriate for bars, profiles, and beams; plane laminated structure, suitable for thin-walled plates and shells; and spatial structure, which is necessary for thick-walled and bulk solid composite parts.

A linear structure is formed by pultrusion, table rolling, or braiding and provides high strength and stiffness in one direction coinciding with the axis of a bar, profile, or a beam. Pultrusion results in a unidirectionally reinforced composite profile, made by pulling a bundle of fibers impregnated with resin through a heated die to cure the resin and to provide the desired shape of the profile cross section. Profiles made by pultrusion and braiding are shown in Fig. 1.17. Table rolling is used to fabricate small diameter tapered tubular bars (e.g., ski poles or fishing rods) by rolling preimpregnated fiber tapes in

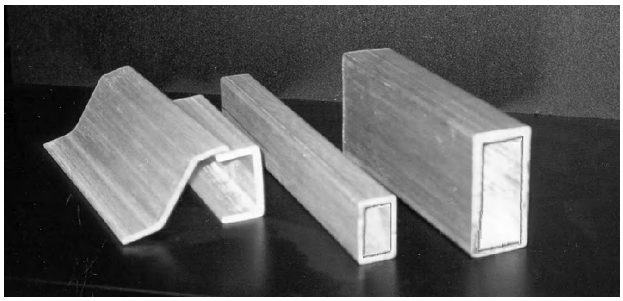


FIGURE 1.17

Composite profiles made by pultrusion and braiding.

Courtesy of CRISM.

the form of flags (triangular sheets) around the metal mandrel, which is pulled out of the composite bar after the resin is cured. Fibers in the flags are usually oriented along the bar axis or at an angle to the axis, thus providing more complicated reinforcement than the unidirectional one typical of pultrusion. Even more complicated fiber placement with orientation angle varying from 5 to 85° along the bar axis can be achieved using two-dimensional (2D) braiding, which results in a textile material structure consisting of two layers of yarns or tows interlaced with each other while they are wound onto the mandrel.

A plane laminated structure consists of a set of composite layers providing the necessary stiffness and strength in at least two orthogonal directions in the plane of the laminate. Such a plane structure would be formed by hand or machine lay-up, fiber placement, or filament winding.

Lay-up and fiber placement technology provides fabrication of thin-walled composite parts of practically arbitrary shape by hand or automated placing of preimpregnated unidirectional or fabric tapes onto a mold. Layers with different fiber orientations (and even with different fibers) are combined to result in the laminated composite material exhibiting the desired strength and stiffness in given directions. Lay-up processes are usually accompanied by pressure applied to compact the material and to remove entrapped air. Depending on the required quality of the material, as well as on the shape and dimensions of a manufactured composite part, compacting pressure can be provided by rolling or vacuum bags, in autoclaves, or by compression molding. A catamaran yacht (length 9.2 m, width 6.8 m, tonnage 2.2 t) made from carbon-epoxy composite by hand lay-up is shown in Fig. 1.18.

Filament winding is an efficient automated process of placing impregnated tows or tapes onto a rotating mandrel (Fig. 1.19) that is removed after curing of the composite material. Varying the winding angle, it is possible to control the material strength and stiffness within the layer and through the thickness of the laminate. Winding of a pressure vessel is shown in Fig. 1.20. Preliminary tension applied to the tows in the process of winding induces pressure between the layers, providing compaction of the material. Filament winding is the most advantageous in manufacturing thin-walled shells of revolution, though it can also be used in building composite structures with more complicated shapes (Fig. 1.21).

Structural elements of rather complicated shapes can be fabricated by braiding, which is a sort of combination of weaving and filament winding. In braiding, two or more tows come from spools that



FIGURE 1.18

Catamaran yacht Ivan-30 made from carbon-epoxy composite by hand lay-up.

Courtesy of CRISM.

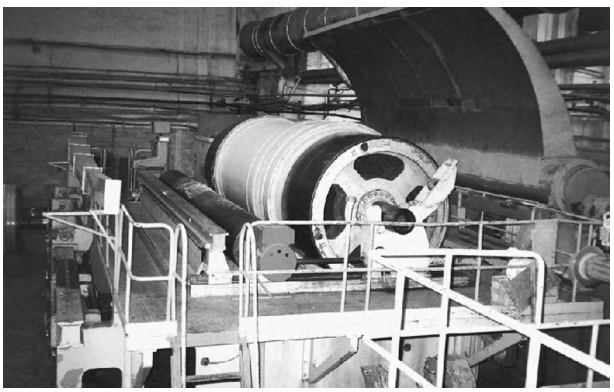


FIGURE 1.19

Manufacturing of a pipe by circumferential winding of preimpregnated fabric.

Courtesy of CRISM.

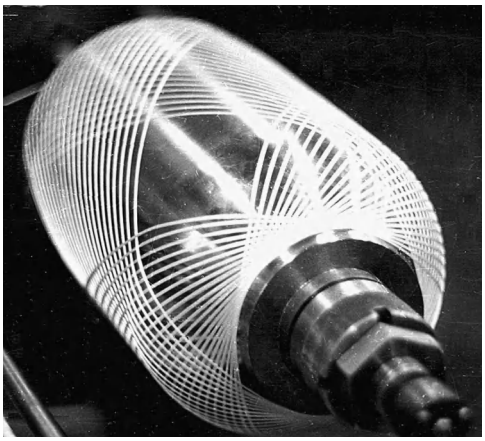


FIGURE 1.20

Geodesic winding of a pressure vessel.

rotate in opposite directions around a mandrel that moves in the axial direction. The tows interlace with one another making flat, tubular, shell-like, or solid structural elements. Braiding over shaped mandrels allows us to fabricate the structures with curvature and cross sections varying along the axes.

Spatial macrostructure of the composite material that is specific for thick-walled and solid members requiring fiber reinforcement in at least three directions (not lying in one plane) can be formed by 3D braiding (with three interlaced yarns) or using such textile processes as weaving, knitting, or stitching. Spatial (3D, 4D, etc.) structures used in carbon-carbon technology are assembled

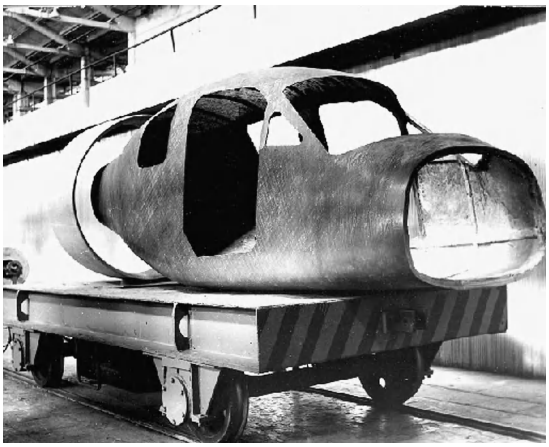


FIGURE 1.21

A body of a small plane made by filament winding.

Courtesy of CRISM.



FIGURE 1.22

A 4D spatial structure.

Courtesy of CRISM.

from thin carbon composite rods fixed in different directions. Such a structure that is prepared for carbonization and deposition of a carbon matrix is shown in Fig. 1.22.

There are two specific manufacturing procedures that have an inverse sequence of the basic processes described earlier, i.e., first the macrostructure of the material is formed, and then the matrix is applied to fibers.

The first of these procedures is the aforementioned carbon-carbon technology that involves chemical vapor deposition of a pyrolytic carbon matrix on sometimes rather complicated preliminary assembled structures made from dry carbon fabric. A carbon-carbon shell made by this method is shown in Fig. 1.23.

The second procedure is the well-known resin transfer molding (RTM). Fabrication of a composite part starts with a preform that is assembled in the internal cavity of a mold from dry fabrics, tows, yarns, etc., and which forms the macrostructure of a composite part. The shape of this part is governed by the shape of the mold cavity into which liquid resin is transferred under pressure through injection ports. Vacuum-assisted RTM (VARTM), in contrast to RTM, requires a single-sided tool on which a dry fiber preform is placed and covered with a vacuum bag. Inlet and exit resin feed pipes go through the bag, and vacuum is drawn at the exit to facilitate an infusion of the preform with resin.

VARTM in combination with an autoclave processing results in resin infusion (RI) processes. Low-viscosity resins can be infused into fiber preforms by vacuum, whereas high-viscosity resins can be applied in the form of solid films placed within the fiber preform (e.g., alternating with the dry reinforcement layers) and subsequently melted under heating. Temperature and pressure profiles during the curing process are controlled by relevant autoclave programs.

The basic processes described earlier are normally accompanied by a thermal treatment resulting in the solidification of the matrix. Heating is applied to cure thermosetting resins, cooling is used to transfer thermoplastic, metal, and ceramic matrices to a solid phase, and a carbon matrix is made by pyrolysis. The final stages of the manufacturing procedure involve removal of mandrels and molds, or other tooling and machining of a composite part as required.



FIGURE 1.23

A carbon-carbon conical shell.

Courtesy of CRISM.

The fabrication processes are described in more detail elsewhere (e.g., Peters, 1998; Baker et al., 2004; Long, 2005; Mortensen, 2007).

1.3 References

Baker, A., Dutton, S., & Kelly, D. (2004). *Composite Materials for Aircraft Structures* (2nd ed.). AIAA Education Series, AIAA, USA.

Bogdanovich, A. E., & Pastore, C. M. (1996). *Mechanics of Textile and Laminated Composites*. London: Chapman & Hall.

Chou, T. W., & Ko, F. K. (1989). Textile Structural Composites. In T. W. Chou, & F. K. Ko (Eds.). New York: Elsevier.

Fukuda, H., Yakushiji, M., & Wada, A. (1997). Loop test for the strength of monofilaments. In M. L. Scott (Ed.), *Proc. 11th Int. Conf. on Comp. Mat. (ICCM-11), Vol. 5: Textile Composites and Characterization* (pp. 886–892). Gold Coast, Australia: Woodhead Publishing Ltd.

Goodey, W. J. (1946). Stress diffusion problems. *Aircraft Eng*. June, 195–198; July, 227–234; August, 271–276; September, 313–316; October, 343–346; November, 385–389.

Karpinos, D. M. (1985). Composite Materials. In D. M. Karpinos (Ed.), *Handbook*. Kiev: Naukova Dumka [in Russian].

Long, A. C. (Ed.). (2005). *Design and Manufacture of Textile Composites*. Cambridge, England: CRC Press, Woodhead Publishing Ltd.

Mortensen, A. (Ed.). (2007). *Concise Encyclopedia of Composite Materials* (2nd ed.). Elsevier.

Peters, S. T. (1998). Handbook of Composites. In S. T. Peters (Ed.) (2nd ed.). London: Chapman & Hall.

Tarnopol'skii, Yu. M., Zhigun, I. G., & Polyakov, V. A. (1992). *Spatially Reinforced Composites*. Pennsylvania: Technomic.

Vasiliev, V. V., Tarnopol'skii, Yu. M. (1990). Composite Materials. In V. V. Vasiliev, & M. Yu Tarnopol'skii (Eds.), *Handbook*. Moscow: Mashinostroenie [in Russian].

CHAPTER

Fundamentals of mechanics of solids

2

The behavior of composite materials whose micro and macrostructures are much more complicated than those of traditional structural materials such as metals, concrete, and plastics is nevertheless governed by the same general laws and principles of mechanics briefly described below.

2.1 STRESSES

Consider a solid referred to Cartesian coordinates as in Fig. 2.1. The solid is fixed at the part S_u of the surface and loaded with body forces q_v having coordinate components q_x, q_y, and q_z, and with surface

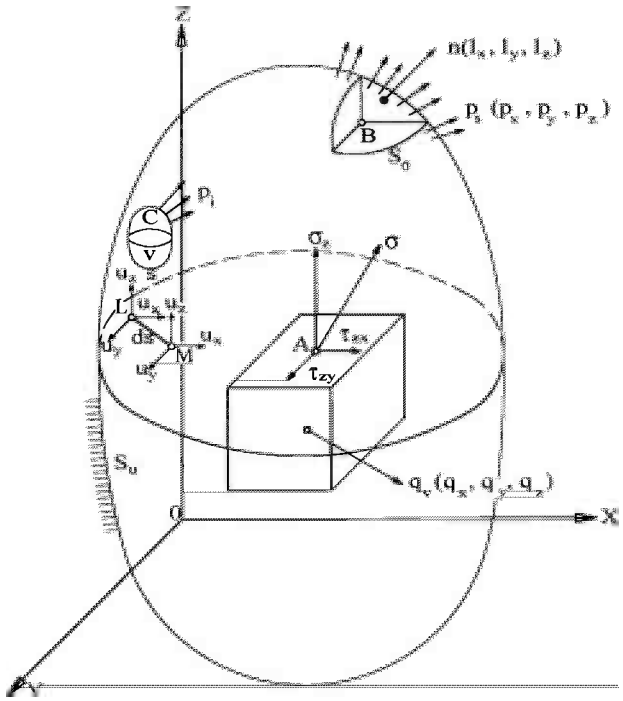


FIGURE 2.1

A solid loaded with body and surface forces and referred to Cartesian coordinates.

Advanced Mechanics of Composite Materials and Structural Elements. http://dx.doi.org/10.1016/B978-0-08-098231-1.00002-9
Copyright © 2013 Elsevier Ltd. All rights reserved.

tractions p_s specified by coordinate components p_x, p_y, and p_z. Surface tractions act on surface S_σ which is determined by its unit normal n with coordinate components l_x, l_y, and l_z that can be referred to as directional cosines of the normal, i.e.,

$$l_x = \cos(n,x) \qquad l_y = \cos(n,y) \qquad l_z = \cos(n,z) \tag{2.1}$$

Introduce some arbitrary cross section formally separating the upper part of the solid from its lower part. Assume that the interaction of these parts in the vicinity of some point A can be simulated with some internal force per unit area or stress σ distributed over this cross section according to some yet unknown law. Since the mechanics of solids is a phenomenological theory (see the closure of Section 1.1), we do not care about the physical nature of stress, which is only a parameter of our model of the real material (see Section 1.1) and, in contrast to forces F, has never been observed in physical experiments. Stress is referred to the plane on which it acts and is usually decomposed into three components: normal stress (σ_z in Fig. 2.1) and two shear stresses (τ_{zx} and τ_{zy} in Fig. 2.1). The subscript of the normal stress and the first subscript of the shear stress indicate the plane on which the stresses act. For stresses shown in Fig. 2.1, this is the plane whose normal is parallel to the z-axis. The second subscript of the shear stress shows the axis along which the stress acts. If we single out a cubic element in the vicinity of point A (see Fig. 2.1), we should apply stresses to all its sides as in Fig. 2.2, which also shows notations and positive directions of all the stresses acting inside the solid referred to Cartesian coordinates.

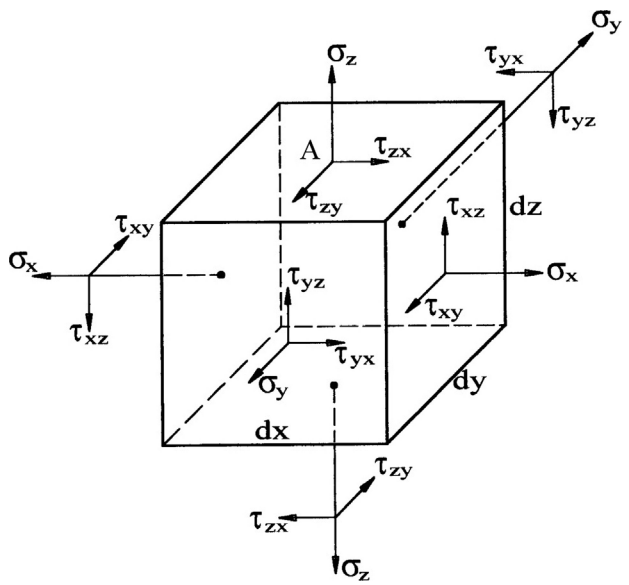


FIGURE 2.2

Stresses acting on the planes of the infinitely small cubic element.

2.2 EQUILIBRIUM EQUATIONS

Now suppose that the solid in Fig. 2.1 is in a state of equilibrium. If so, we can write equilibrium equations for any part of this solid. In particular, we can do this for an infinitely small tetrahedron singled out in the vicinity of point B (see Fig. 2.1) in such a way that one of its planes coincides with S_σ and the other three planes are coordinate planes of the Cartesian frame. Internal and external forces acting on this tetrahedron are shown in Fig. 2.3. The equilibrium equation corresponding, for example, to the x-axis can be written as

$$-\sigma_x dS_x - \tau_{yx} dS_y - \tau_{zx} dS_z + p_x dS_\sigma + q_x dV = 0$$

Here, dS_σ and dV are the elements of the body surface and volume, whereas $dS_x = dS_\sigma l_x$, $dS_y = dS_\sigma l_y$, and $dS_z = dS_\sigma l_z$. When the tetrahedron is infinitely diminished, the term including dV, which is of the order of the cube of the linear dimensions, can be neglected in comparison with terms containing dS, which is of the order of the square of the linear dimensions. The resulting equation is

$$\sigma_x l_x + \tau_{yx} l_y + \tau_{zx} l_z = p_x \qquad (x, y, z) \tag{2.2}$$

The symbol (x, y, z), which is widely used in this chapter, denotes permutation with the aid of which we can write two more equations corresponding to the other two axes changing x for y, y for z, and z for x.

Consider now the equilibrium of an arbitrary finite part C of the solid (see Fig. 2.1). If we single this part out of the solid, we should apply to it body forces q_v and surface tractions p_i whose coordinate components p_x, p_y, and p_z can be expressed, obviously, by Eq. (2.2) in terms of stresses acting inside the volume C. Since the sum of the components corresponding, for example, to the x-axis must be equal to zero, we have

$$\iiint_v q_x dv + \iint_s p_x ds = 0$$

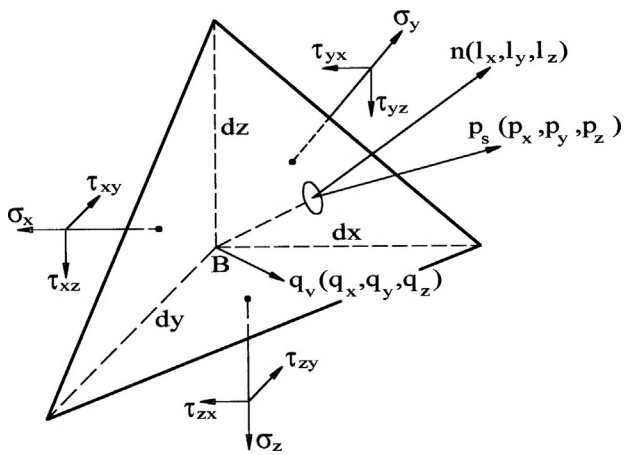


FIGURE 2.3

Forces acting on an elementary tetrahedron.

where v and s are the volume and the surface area of the part of the solid under consideration. Substituting p_x from Eq. (2.2) we get

$$\iint_s (\sigma_x l_x + \tau_{yx} l_y + \tau_{zx} l_z) ds + \iiint_v q_x \, dv = 0 \qquad (x, y, z) \tag{2.3}$$

Thus, we have three integral equilibrium equations, Eqs. (2.3), which are valid for any finite part of the solid. To convert them into the corresponding differential equations, we use Green's integral transformation

$$\iint_s (f_x l_x + f_y l_y + f_z l_z) ds = \iiint_v \left(\frac{\partial f_x}{\partial x} + \frac{\partial f_y}{\partial y} + \frac{\partial f_z}{\partial z} \right) dv \tag{2.4}$$

which is valid for any three continuous, finite, and single-valued functions $f(x, y, z)$ and allows us to transform a surface integral into a volume one. Taking $f_x = \sigma_x, f_y = \tau_{yx}$, and $f_z = \tau_{zx}$ in Eq. (2.4) and using Eqs. (2.3), we arrive at

$$\iiint_v \left(\frac{\partial \sigma_x}{\partial x} + \frac{\partial \tau_{yx}}{\partial y} + \frac{\partial \tau_{zx}}{\partial z} + q_x \right) dv = 0 \qquad (x, y, z)$$

Since these equations hold whatever the part of the solid may be, provided only that it is within the solid, they yield

$$\frac{\partial \sigma_x}{\partial x} + \frac{\partial \tau_{yx}}{\partial y} + \frac{\partial \tau_{zx}}{\partial z} + q_x = 0 \qquad (x, y, z) \tag{2.5}$$

Thus, we have arrived at three differential equilibrium equations that could also be derived from the equilibrium conditions for the infinitesimal element shown in Fig. 2.2.

However, in order to keep part C of the solid in Fig. 2.1 in equilibrium the sum of the moments of all the forces applied to this part about any axis must be zero. By taking moments about the z-axis, we get the following integral equation

$$\iiint_v (q_x y - q_y x) dv + \iint_s \left(p_x y - p_y x \right) ds = 0$$

Using again Eqs. (2.2) and (2.4) and taking into account Eq. (2.5), we finally arrive at the symmetry conditions for shear stresses, i.e.,

$$\tau_{xy} = \tau_{yx} \qquad (x, y, z) \tag{2.6}$$

So, we have three equilibrium equations, Eq. (2.5), which include six unknown stresses σ_x, σ_y, and σ_z, and τ_{xy}, τ_{xz}, and τ_{yz}.

Eq. (2.2) can be treated as force boundary conditions for the stressed state of a solid.

2.3 STRESS TRANSFORMATION

Consider the transformation of a stress system from one Cartesian coordinate frame to another. Suppose that the elementary tetrahedron shown in Fig. 2.3 is located inside the solid and that point B coincides with the origin 0 of Cartesian coordinates x, y, and z in Fig. 2.1. Then, the oblique plane of

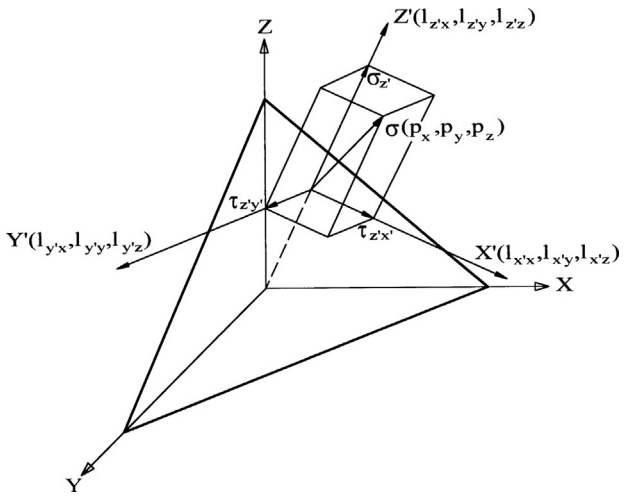


FIGURE 2.4

Rotation of the coordinate frame.

the tetrahedron can be treated as a coordinate plane $z' = 0$ of a new coordinate frame x', y', z' shown in Fig. 2.4 such that the normal element to the oblique plane coincides with the z'-axis, whereas axes x' and y' are located in this plane. Component p_x of the surface traction in Eq. (2.2) can now be treated as the projection on the x-axis of stress σ acting on plane $z' = 0$. Then, Eq. (2.2) can be presented in the following explicit form specifying projections of stress σ

$$\begin{aligned} p_x &= \sigma_x l_{z'x} + \tau_{yx} l_{z'y} + \tau_{zx} l_{z'z} \\ p_y &= \sigma_y l_{z'y} + \tau_{zy} l_{z'z} + \tau_{xy} l_{z'x} \\ p_z &= \sigma_z l_{z'z} + \tau_{xz} l_{z'x} + \tau_{yz} l_{z'y} \end{aligned} \tag{2.7}$$

Here, l are directional cosines of axis $z'$with respect to axes x, y, and z (see Fig. 2.4, in which the corresponding cosines of axes x' and y' are also presented). The normal stress $\sigma_{z'}$ can be found now as

$$\begin{aligned} \sigma_{z'} &= p_x l_{z'x} + p_y l_{z'y} + p_z l_{z'z} \\ &= \sigma_x l_{z'x}^2 + \sigma_y l_{z'y}^2 + \sigma_z l_{z'z}^2 + 2\tau_{xy} l_{z'x} l_{z'y} + 2\tau_{xz} l_{z'x} l_{z'z} + 2\tau_{yz} l_{z'y} l_{z'z} \qquad \left(x', y', z'\right) \end{aligned} \tag{2.8}$$

The final result was obtained with the aid of Eqs. (2.6) and (2.7). Changing x' for y', y' for z', and z' for x', i.e., performing the appropriate permutation in Eq. (2.8), we can write similar expressions for $\sigma_{x'}$and $\sigma_{y'}$.

The shear stress in the new coordinates is

$$\begin{aligned} \tau_{z'x'} &= p_x l_{x'x} + p_y l_{x'y} + p_z l_{x'z} \\ &= \sigma_x l_{x'x} l_{z'x} + \sigma_y l_{x'y} l_{z'y} + \sigma_z l_{x'z} l_{z'z} + \tau_{xy}(l_{x'x} l_{z'y} + l_{x'y} l_{z'x}) \\ &\quad + \tau_{xz}(l_{x'x} l_{z'z} + l_{x'z} l_{z'x}) + \tau_{yz}(l_{x'y} l_{z'z} + l_{x'x} l_{z'y}) \qquad \left(x', y', z'\right) \end{aligned} \tag{2.9}$$

Permutation yields expressions for $\tau_{x'y'}$ and $\tau_{y'z'}$.

2.4 PRINCIPAL STRESSES

The foregoing equations, Eqs. (2.8) and (2.9), demonstrate stress transformations under rotation of a coordinate frame. There exists a special position of this frame in which the shear stresses acting on the coordinate planes vanish. Such coordinate axes are called the principal axes, and the normal stresses that act on the corresponding coordinate planes are referred to as the principal stresses.

To determine the principal stresses, assume that coordinates x', y', and z' in Fig. 2.4 are the principal coordinates. Then, according to the aforementioned property of the principal coordinates, we should take $\tau_{z'x'} = \tau_{z'y'} = 0$ and $\sigma_{z'} = \sigma$ for the plane $z' = 0$. This means that $p_x = \sigma l_{z'x}$, $p_y = \sigma l_{z'y}$, and $p_z = \sigma l_{z'z}$ in Eqs. (2.7). Introducing new notations for directional cosines of the principal axis, i.e., taking $l_{z'x} = l_{px}$, $l_{z'y} = l_{py}$, $l_{z'z} = l_{pz}$, we have from Eqs. (2.7)

$$\begin{aligned}(\sigma_x - \sigma)l_{px} + \tau_{xy}l_{py} + \tau_{xz}l_{pz} &= 0\\ \tau_{xy}l_{px} + (\sigma_y - \sigma)l_{py} + \tau_{yz}l_{pz} &= 0\\ \tau_{xz}l_{px} + \tau_{yz}l_{py} + (\sigma_z - \sigma)l_{pz} &= 0\end{aligned} \tag{2.10}$$

These equations were transformed with the aid of symmetry conditions for shear stresses, Eq. (2.6). For some specified point of the body in the vicinity of which the principal stresses are determined in terms of known stresses referred to some fixed coordinate frame x, y, z, Eqs. (2.10) comprise a homogeneous system of linear algebraic equations. Formally, this system always has the trivial solution, i.e., $l_{px} = l_{py} = l_{pz} = 0$ which we can ignore because directional cosines should satisfy an evident condition following from Eqs. (2.1), i.e.,

$$l_{px}^2 + l_{py}^2 + l_{pz}^2 = 1 \tag{2.11}$$

So, we need to find a nonzero solution of Eqs. (2.10) which can exist if the determinant of the set is zero. This condition yields the following cubic equation for σ

$$\sigma^3 - I_1\sigma^2 - I_2\sigma - I_3 = 0 \tag{2.12}$$

in which

$$\begin{aligned}I_1 &= \sigma_x + \sigma_y + \sigma_z\\ I_2 &= -\sigma_x\sigma_y - \sigma_x\sigma_z - \sigma_y\sigma_z + \tau_{xy}^2 + \tau_{xz}^2 + \tau_{yz}^2\\ I_3 &= \sigma_x\sigma_y\sigma_z + 2\tau_{xy}\tau_{xz}\tau_{yz} - \sigma_x\tau_{yz}^2 - \sigma_y\tau_{xz}^2 - \sigma_z\tau_{xy}^2\end{aligned} \tag{2.13}$$

are invariant characteristics (invariants) of the stressed state. This means that if we refer the body to any Cartesian coordinate frame with directional cosines specified by Eqs. (2.1), take the origin of this frame at some arbitrary point, and change stresses in Eqs. (2.13) with the aid of Eqs. (2.8) and (2.9), the values of I_1, I_2, I_3 at this point will be the same for all such coordinate frames. Eq. (2.12) has three real roots that specify three principal stresses σ_1, σ_2, and σ_3. There is a convention according to which $\sigma_1 \geq \sigma_2 \geq \sigma_3$, i.e., σ_1 is the maximum principal stress and σ_3 is the minimum one. If, for example, the roots of Eq. (2.12) are 100 MPa, −200 MPa, and 0, then σ_1 =100 MPa, $\sigma_2 = 0$, and $\sigma_3 = -200$ MPa.

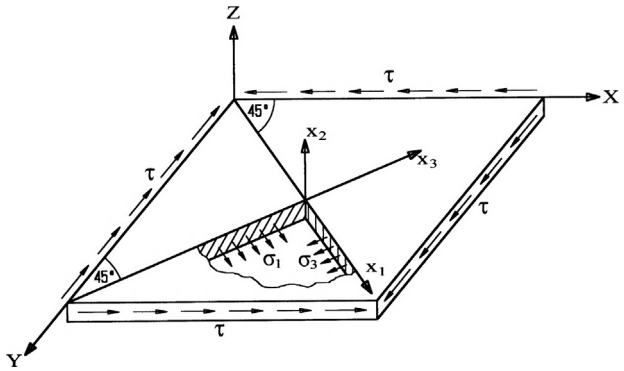


FIGURE 2.5

Principal stresses under pure shear.

To demonstrate the procedure, consider a particular state of stress relevant to several applications, namely, pure shear in the xy-plane. Let a thin square plate referred to coordinates x, y, z be loaded with shear stresses τ uniformly distributed over the plate thickness and along the edges (see Fig. 2.5).

One principal plane is evident; it is plane $z = 0$, which is free of shear stresses. To find the two other planes, we should take in Eqs. (2.13) $\sigma_x = \sigma_y = \sigma_z = 0$, $\tau_{xz} = \tau_{yz} = 0$, and $\tau_{xy} = \tau$. Then, Eq. (2.12) takes the form

$$\sigma^3 - \tau^2\sigma = 0$$

The first root of this equation gives $\sigma = 0$ and corresponds to plane $z = 0$. The other two roots are $\sigma = \pm\tau$. Thus, we have three principal stresses, i.e., $\sigma_1 = \tau$, $\sigma_2 = 0$, and $\sigma_3 = -\tau$. To find the planes corresponding to σ_1 and σ_3 we should put $l_{pz} = 0$, substitute $\sigma = \pm\tau$ into Eqs. (2.10), write them for the state of stress under study, and supplement this set with Eq. (2.11). The final equations allowing us to find l_{px} and l_{py} are

$$\mp\tau\, l_{px} + \tau\, l_{py} = 0, \qquad l_{px}^2 + l_{py}^2 = 1$$

Solution of these equations yields $l_{px} = \pm 1/\sqrt{2}$ and $l_{py} = \mp 1/\sqrt{2}$, and this means that principal planes (or principal axes) make 45° angles with axes x and y. Principal stresses and principal coordinates x_1, x_2, and x_3 are shown in Fig. 2.5.

2.5 DISPLACEMENTS AND STRAINS

For any point of a solid (e.g., L or M in Fig. 2.1), coordinate component displacements u_x, u_y, and u_z can be introduced which specify the point displacements in the directions of coordinate axes.

Consider an arbitrary infinitely small element LM characterized with its directional cosines

$$l_x = \frac{dx}{ds}, \qquad l_y = \frac{dy}{ds}, \qquad l_z = \frac{dz}{ds} \tag{2.14}$$

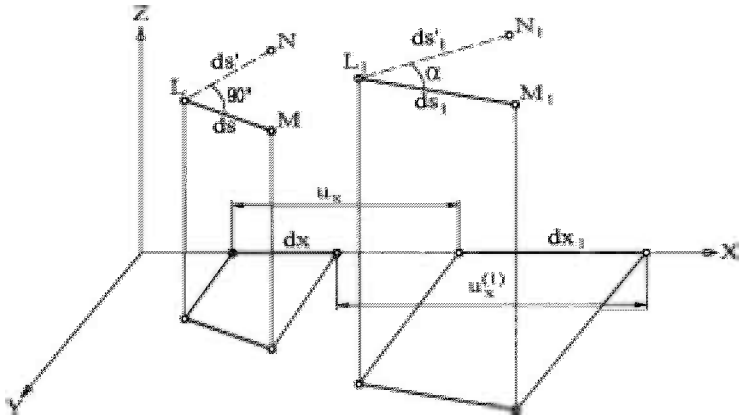


FIGURE 2.6

Displacement of an infinitesimal linear element.

The positions of this element before and after deformation are shown in Fig. 2.6. Suppose that the displacements of the point L are u_x, u_y, and u_z. Then, the displacements of the point M should be

$$u_x^{(1)} = u_x + du_x, \qquad u_y^{(1)} = u_y + du_y, \qquad u_z^{(1)} = u_z + du_z \tag{2.15}$$

Since u_x, u_y, and u_z are continuous functions of x, y, z, we get

$$du_x = \frac{\partial u_x}{\partial x}dx + \frac{\partial u_y}{\partial y}dy + \frac{\partial u_z}{\partial z}dz \qquad (x, y, z) \tag{2.16}$$

It follows from Fig. 2.6 and Eqs. (2.15) and (2.16) that

$$dx_1 = dx + u_x^{(1)} - u_x = dx + du_x = \left(1 + \frac{\partial u_x}{\partial x}\right)dx + \frac{\partial u_x}{\partial y}dy + \frac{\partial u_x}{\partial z}dz \qquad (x, y, z) \tag{2.17}$$

Introduce the strain of element LM as

$$\varepsilon = \frac{ds_1 - ds}{ds} \tag{2.18}$$

After some rearrangements we arrive at

$$\varepsilon + \frac{1}{2}\varepsilon^2 = \frac{1}{2}\left[\left(\frac{ds_1}{ds}\right)^2 - 1\right]$$

where

$$ds_1^2 = (dx_1)^2 + (dy_1)^2 + (dz_1)^2$$

Substituting for dx_1, dy_1, dz_1 their expressions from Eqs. (2.17) and taking into account Eqs. (2.14), we finally get

$$\varepsilon + \frac{1}{2}\varepsilon^2 = \varepsilon_{xx}l_x^2 + \varepsilon_{yy}l_y^2 + \varepsilon_{zz}l_z^2 + \varepsilon_{xy}l_x l_y + \varepsilon_{xz}l_x l_z + \varepsilon_{yz}l_y l_z \tag{2.19}$$

where

$$\varepsilon_{xx} = \frac{\partial u_x}{\partial x} + \frac{1}{2}\left[\left(\frac{\partial u_x}{\partial x}\right)^2 + \left(\frac{\partial u_y}{\partial x}\right)^2 + \left(\frac{\partial u_z}{\partial x}\right)^2\right] \qquad (x, y, z)$$
$$\varepsilon_{xy} = \frac{\partial u_x}{\partial y} + \frac{\partial u_y}{\partial x} + \frac{\partial u_x}{\partial x}\frac{\partial u_x}{\partial y} + \frac{\partial u_y}{\partial x}\frac{\partial u_y}{\partial y} + \frac{\partial u_z}{\partial x}\frac{\partial u_z}{\partial y} \qquad (x, y, z) \tag{2.20}$$

Assuming that the strain is small, we can neglect the second term in the left-hand side of Eq. (2.19). Moreover, we further suppose that the displacements are continuous functions that change rather slowly with the change of coordinates. This allows us to neglect the products of derivatives in Eqs. (2.20). As a result, we arrive at the following equation:

$$\varepsilon = \varepsilon_x l_x^2 + \varepsilon_y l_y^2 + \varepsilon_z l_z^2 + \gamma_{xy} l_x l_y + \gamma_{xz} l_x l_z + \gamma_{yz} l_y l_z \tag{2.21}$$

in which

$$\varepsilon_x = \frac{\partial u_x}{\partial x}, \qquad \varepsilon_y = \frac{\partial u_y}{\partial y}, \qquad \varepsilon_z = \frac{\partial u_z}{\partial z}$$
$$\gamma_{xy} = \frac{\partial u_x}{\partial y} + \frac{\partial u_y}{\partial x}, \qquad \gamma_{xz} = \frac{\partial u_x}{\partial z} + \frac{\partial u_z}{\partial x}, \qquad \gamma_{yz} = \frac{\partial u_y}{\partial z} + \frac{\partial u_z}{\partial y} \tag{2.22}$$

can be treated as linear strain-displacement equations. Taking $l_x = 1$, $l_y = l_z = 0$ in Eqs. (2.22), i.e., directing element LM in Fig. 2.6 along the x-axis, we can readily see that ε_x is the strain along the same x-axis. Similar reasoning shows that ε_y and ε_z in Eqs. (2.22) are strains in the directions of axes y and z. To find the physical meaning of strains γ in Eqs. (2.22), consider two orthogonal line elements LM and LN and find the angle α that they make with each other after deformation (see Fig. 2.6), i.e.,

$$\cos\alpha = \frac{dx_1 dx_1' + dy_1 dy_1' + dz_1 dz_1'}{ds_1 ds_1'} \tag{2.23}$$

Here, dx_1, dy_1, and dz_1 are specified with Eqs. (2.17), ds_1 can be found from Eq. (2.18), and

$$dx_1' = \left(1 + \frac{\partial u_x}{\partial x}\right)dx' + \frac{\partial u_x}{\partial y}dy' + \frac{\partial u_x}{\partial z}dz' \qquad (x, y, z)$$
$$ds_1' = ds'\left(1 + \varepsilon'\right) \tag{2.24}$$

Introduce directional cosines of element LN as

$$l_x' = \frac{dx'}{ds'}, \qquad l_y' = \frac{dy'}{ds'}, \qquad l_z' = \frac{dz'}{ds'} \tag{2.25}$$

Since elements LM and LN are orthogonal, we have

$$l_x l_x' + l_y l_y' + l_z l_z' = 0$$

Using Eqs. (2.14), (2.18), and (2.24)–(2.26) and introducing the shear strain γ as the difference between angles $M_1L_1N_1$ and MLN, i.e., as

$$\gamma = \frac{\pi}{2} - \alpha$$

we can write Eq. (2.23) in the following form:

$$\sin\gamma = \frac{1}{(1+\varepsilon)(1+\varepsilon')}\Big[2\Big(\varepsilon_{xx}l_x l'_x + \varepsilon_{yy}l_y l'_y + \varepsilon_{zz}l_z l'_z\Big) + \varepsilon_{xy}\Big(l_x l'_y + l'_x l_y\Big) + \varepsilon_{xz}(l_x l'_z + l'_x l_z) + \varepsilon_{yz}(l_y l'_z + l'_y l_z)\Big] \tag{2.26}$$

Linear approximation of Eq. (2.26) similarly to Eq. (2.21) yields

$$\gamma = 2\Big(\varepsilon_x l_x l'_x + \varepsilon_y l_y l'_y + \varepsilon_z l_z l'_z\Big) + \gamma_{xy}\Big(l_x l'_y + l'_x l_y\Big) + \gamma_{xz}\Big(l_x l'_z + l'_x l_z\Big) + \gamma_{yz}\Big(l_y l'_z + l'_y l_z\Big) \tag{2.27}$$

Here, ε_x, ε_y, ε_z and γ_{xy}, γ_{xz}, γ_{yz} components are determined with Eqs. (2.22). If we now direct element *LM* along the *x*-axis and element *LN* along the *y*-axis putting $l_x = 1$, $l_y = l_z = 0$ and $l'_y = 1$, $l'_x = l'_z = 0$, Eq. (2.27) yields $\gamma = \gamma_{xy}$. Thus, γ_{xy}, γ_{xz}, and γ_{yz} are shear strains that are equal to the changes of angles between axes *x* and *y*, *x* and *z*, and *y* and *z*, respectively.

2.6 TRANSFORMATION OF SMALL STRAINS

Consider small strains in Eqs. (2.22) and study their transformation under rotation of the coordinate frame. Suppose that x', y', z' in Fig. 2.4 form a new coordinate frame rotated with respect to the original frame *x*, *y*, *z*. Since Eqs. (2.22) are valid for any Cartesian coordinate frame, we have

$$\varepsilon_{x'} = \frac{\partial u_{x'}}{\partial x'}, \qquad \gamma_{x'y'} = \frac{\partial u_{x'}}{\partial y'} + \frac{\partial u_{y'}}{\partial x'} \qquad (x, y, z) \tag{2.28}$$

Here, $u_{x'}$, $u_{y'}$, and $u_{z'}$ are displacements along the axes x', y', z' which can be related to displacements u_x, u_y, and u_z of the same point by the following linear equation

$$u_{x'} = u_x l_{x'x} + u_y l_{x'y} + u_z l_{x'z} \qquad (x, y, z) \tag{2.29}$$

Similar relations can be written for the derivatives of displacement with respect to variables x', y', z' and *x*, *y*, *z*, i.e.,

$$\frac{\partial u}{\partial x'} = \frac{\partial u}{\partial x}l_{x'x} + \frac{\partial u}{\partial y}l_{x'y} + \frac{\partial u}{\partial z}l_{x'z} \qquad (x, y, z) \tag{2.30}$$

Substituting displacements, Eqs. (2.29), into Eqs. (2.28), and transforming to variables *x*, *y*, *z* with the aid of Eqs. (2.30), and taking into account Eqs. (2.22), we arrive at

$$\begin{aligned}
\varepsilon_{x'} &= \varepsilon_x l^2_{x'x} + \varepsilon_y l^2_{x'y} + \varepsilon_z l^2_{x'z} + \gamma_{xy} l_{x'x} l_{x'y} + \gamma_{xz} l_{x'x} l_{x'z} + \gamma_{yz} l_{x'y} l_{x'z} \qquad (x, y, z) \\
\gamma_{x'y'} &= 2\varepsilon_x l_{x'x} l_{y'x} + 2\varepsilon_y l_{x'y} l_{y'y} + 2\varepsilon_z l_{x'z} l_{y'z} + \gamma_{xy}\big(l_{x'x} l_{y'y} + l_{x'y} l_{y'x}\big) \\
&\quad + \gamma_{xz}\big(l_{x'x} l_{y'z} + l_{x'z} l_{y'x}\big) + \gamma_{yz}\big(l_{x'y} l_{y'z} + l_{x'z} l_{y'y}\big) \qquad (x, y, z)
\end{aligned} \tag{2.31}$$

These strain transformations are similar to the stress transformations determined by Eqs. (2.8) and (2.9).

2.7 COMPATIBILITY EQUATIONS

Consider strain-displacement equations, Eqs. (2.22), and try to determine displacements u_x, u_y, and u_z in terms of strains ε_x, ε_y, ε_z and γ_{xy}, γ_{xz}, γ_{yz}. As can be seen, there are six equations containing only three unknown displacements. In general, such a set of equations is not consistent, and some compatibility conditions should be imposed on the strains to provide the existence of a solution. To derive these conditions, decompose derivatives of the displacements as follows

$$\frac{\partial u_x}{\partial x} = \varepsilon_x, \qquad \frac{\partial u_x}{\partial y} = \frac{1}{2}\gamma_{xy} - \omega_z, \qquad \frac{\partial u_x}{\partial z} = \frac{1}{2}\gamma_{xz} + \omega_y \qquad (x, y, z) \tag{2.32}$$

Here

$$\omega_z = \frac{1}{2}\left(\frac{\partial u_y}{\partial x} - \frac{\partial u_x}{\partial y}\right) \qquad (x, y, z) \tag{2.33}$$

is the angle of rotation of a body element (such as the cubic element shown in Fig. 2.1) around the z-axis. Three equations, Eqs. (2.32), including one and the same displacement u_x allow us to construct three couples of mixed second-order derivatives of u_x with respect to x and y or y and x, x and z or z and x, and y and z or z and y. As long as the sequence of differentiation does not influence the result, and since there are two other groups of equations in Eqs. (2.32), we arrive at nine compatibility conditions that can be presented as

$$\begin{gathered} \frac{\partial \omega_x}{\partial x} = \frac{1}{2}\left(\frac{\partial \gamma_{xz}}{\partial y} - \frac{\partial \gamma_{xy}}{\partial z}\right) \qquad (x, y, z) \\ \frac{\partial \omega_x}{\partial y} = \frac{1}{2}\frac{\partial \gamma_{yz}}{\partial y} - \frac{\partial \varepsilon_y}{\partial z} \qquad (x, y, z), \qquad \frac{\partial \omega_x}{\partial z} = -\frac{1}{2}\frac{\partial \gamma_{yz}}{\partial z} + \frac{\partial \varepsilon_z}{\partial y} \qquad (x, y, z) \end{gathered} \tag{2.34}$$

These equations are similar to Eqs. (2.32), i.e., they allow us to determine rotation angles only if some compatibility conditions are valid. These conditions compose the set of compatibility equations for strains and have the following final form

$$k_{xy}(\varepsilon, \gamma) = 0, \qquad r_x(\varepsilon, \gamma) = 0 \qquad (x, y, z) \tag{2.35}$$

where

$$\begin{aligned} k_{xy}(\varepsilon, \gamma) &= \frac{\partial^2 \varepsilon_x}{\partial y^2} + \frac{\partial^2 \varepsilon_y}{\partial x^2} - \frac{\partial^2 \gamma_{xy}}{\partial x \partial y} \qquad (x, y, z) \\ r_x(\varepsilon, \gamma) &= \frac{\partial^2 \varepsilon_x}{\partial y \partial z} - \frac{1}{2}\frac{\partial}{\partial x}\left(\frac{\partial \gamma_{xy}}{\partial z} + \frac{\partial \gamma_{xz}}{\partial y} - \frac{\partial \gamma_{yz}}{\partial x}\right) \qquad (x, y, z) \end{aligned} \tag{2.36}$$

If strains ε_x, ε_y, ε_z and γ_{xy}, γ_{xz}, γ_{yz} satisfy Eqs. (2.35), we can find rotation angles ω_x, ω_y, ω_z integrating Eqs. (2.34) and then determine displacements u_x, u_y, u_z integrating Eqs. (2.32).

The six compatibility equations, Eqs. (2.35), derived formally as compatibility conditions for Eqs. (2.32), have a simple physical meaning. Suppose that we have a continuous solid as shown in Fig. 2.1 and divide it into a set of pieces that perfectly match each other. Now, apply some strains to each of these pieces. Obviously, for arbitrary strains, the deformed pieces cannot be assembled

into a continuous deformed solid. This will happen only under the condition that the strains satisfy Eqs. (2.35). However, even if the strains do not satisfy Eqs. (2.35), we can assume that the solid is continuous but in a more general Riemannian (curved) space rather than in the traditional Euclidean space in which the solid existed before the deformation (Vasiliev and Gurdal, 1999). Then, six quantities k and r in Eqs. (2.36), being nonzero, specify curvatures of the Riemannian space caused by small strains ε and γ. The compatibility equations, Eqs. (2.35), require these curvatures to be equal to zero, which means that the solid should remain in the Euclidean space under deformation.

2.8 ADMISSIBLE STATIC AND KINEMATIC FIELDS

In solid mechanics, we introduce static field variables which are stresses and kinematic field variables which are displacements and strains.

The static field is said to be statically admissible if the stresses satisfy equilibrium equation Eq. (2.5), and are in equilibrium with surface tractions on the body surface S_σ where these tractions are given (see Fig. 2.1), i.e., if Eq. (2.2) is satisfied on S_σ.

The kinematic field is referred to as kinematically admissible if displacements and strains are linked by strain-displacement equations, Eq. (2.22), and displacements satisfy kinematic boundary conditions on the surface S_u where displacements are prescribed (see Fig. 2.1).

Actual stresses and displacements belong, naturally, to the corresponding admissible fields, though actual stresses must in addition provide admissible displacements, whereas actual displacements should be associated with admissible stresses. Mutual correspondence between static and kinematic variables is established through the so-called constitutive equations that are considered in the next section.

2.9 CONSTITUTIVE EQUATIONS FOR AN ELASTIC SOLID

Consider a solid loaded with body and surface forces as in Fig. 2.1. These forces induce some stresses, displacements, and strains that compose the fields of actual static and kinematic variables. Introduce some infinitesimal additional displacements du_x, du_y, and du_z such that they belong to a kinematically admissible field. This means that there exist equations that are similar to Eqs. (2.22), i.e.,

$$d\varepsilon_x = \frac{\partial}{\partial x}(du_x), \qquad d\gamma_{xy} = \frac{\partial}{\partial y}(du_x) + \frac{\partial}{\partial x}(du_y) \qquad (x, y, z) \tag{2.37}$$

and specify additional strains.

Since additional displacements are infinitely small, we can assume that external forces do not change under such variation of the displacements (here we do not consider special cases in which external forces depend on displacements of the points at which these forces are applied). Then we can calculate the work performed by the forces, multiplying forces by the corresponding increments of the displacements, and write the total work of body forces and surface tractions as

$$dW = \iiint_V (q_x du_x + q_y du_y + q_z du_z) dV + \iint_S (p_x du_x + p_y du_y + p_z du_z) dS \tag{2.38}$$

Here, V and S are the body volume and external surface of the solid in Fig. 2.1. Actually, we must write the surface integral in Eq. (2.38) only for the surface S_σ on which the forces are given. However, since the increments of the displacements belong to a kinematically admissible field, they are equal to zero on S_u, and the integral can be written for the whole surface of the solid. To proceed, we express p_x, p_y, and p_z in terms of stresses with the aid of Eq. (2.2) and transform the surface integral into a volume one using Eq. (2.4). For the sake of brevity, consider only x-components of forces and displacement in Eq. (2.38). We have in several steps

$$\begin{aligned}
&\iiint_V q_x du_x + \iint_S p_x\, du_x\, ds = \iiint_V q_x\, du_x + \iint_S \left(\sigma_x l_x + \tau_{yx} l_y + \tau_{zx}\, l_z\right) du_x dS \\
&= \iiint_V \left[q_x du_x + \frac{\partial}{\partial x}(\sigma_x du_x) + \frac{\partial}{\partial y}(\tau_{yx} du_x) + \frac{\partial}{\partial z}(\tau_{zx} du_x) \right] dV \\
&= \iiint_V \left[\left(q_x + \frac{\partial \sigma_x}{\partial x} + \frac{\partial \tau_{yx}}{\partial y} + \frac{\partial \tau_{zx}}{\partial z} \right) du_x + \sigma_x \frac{\partial}{\partial x}(du_x) + \tau_{yx} \frac{\partial}{\partial y}(du_x) + \tau_{zx} \frac{\partial}{\partial z}(du_x) \right] dV \\
&= \iiint_V \left[\sigma_x d\varepsilon_x + \tau_{xy} \frac{\partial}{\partial y}(du_x) + \tau_{xz} \frac{\partial}{\partial z}(du_x) \right] dV
\end{aligned}$$

The last transformation step has been performed with due regard to Eqs. (2.5), (2.6), and (2.37). Finally, Eq.(2.38) takes the form

$$dW = \iiint_V \left(\sigma_x d\varepsilon_x + \sigma_y d\varepsilon_y + \sigma_z d\varepsilon_z + \tau_{xy} d\gamma_{xy} + \tau_{xz} d\gamma_{xz} + \tau_{yz} d\gamma_{yz}\right) dV \tag{2.39}$$

Since the right-hand side of this equation includes only internal variables, i.e., stresses and strains, we can conclude that the foregoing formal rearrangement actually allows us to transform the work of external forces into the work of internal forces or into potential energy accumulated in the solid. For further derivation, let us introduce for the sake of brevity new notations for coordinates and use subscripts 1, 2, 3 instead of x, y, z, respectively. We also use the following notations for stresses and strains

$$\begin{gathered}
\sigma_x = \sigma_{11}, \qquad \sigma_y = \sigma_{22}, \qquad \sigma_z = \sigma_{33} \\
\tau_{xy} = \sigma_{12} = \sigma_{21}, \qquad \tau_{xz} = \sigma_{13} = \sigma_{31}, \qquad \tau_{yz} = \sigma_{23} = \sigma_{32} \\
\varepsilon_x = \varepsilon_{11}, \qquad \varepsilon_y = \varepsilon_{22}, \qquad \varepsilon_z = \varepsilon_{33} \\
\gamma_{xy} = 2\varepsilon_{12} = 2\varepsilon_{21}, \qquad \gamma_{xz} = 2\varepsilon_{13} = 2\varepsilon_{31}, \qquad \gamma_{yz} = 2\varepsilon_{23} = 2\varepsilon_{32}
\end{gathered}$$

Then, Eq. (2.39) can be written as

$$dW = \iiint_V dU dV \tag{2.40}$$

where

$$dU = \sigma_{ij}\, d\varepsilon_{ij} \tag{2.41}$$

This form of equation implies summation over repeated subscripts $i, j = 1, 2, 3$.

It should be emphasized that by now dU is just a symbol, which does not mean that there exists function U and that dU is its differential. This meaning for dU is correct only if we restrict ourselves to the consideration of an elastic material described in Section 1.1. For such a material, the difference between the body potential energy corresponding to some initial state A and the energy corresponding to some other state B does not depend on the way used to transform the solid from state A to state B. In other words, the integral

$$\int_A^B \sigma_{ij} d\varepsilon_{ij} = U(B) - U(A)$$

does not depend on the path of integration. This means that the element of integration is a complete differential of function U depending on ε_{ij}, i.e., that

$$dU = \frac{\partial U}{\partial \varepsilon_{ij}} d\varepsilon_{ij}$$

Comparing this result with Eq. (2.41), we arrive at Green's formulas

$$\sigma_{ij} = \frac{\partial U}{\partial \varepsilon_{ij}} \tag{2.42}$$

that are valid for any elastic material. The function $U(\varepsilon_{ij})$can be referred to as specific strain energy (energy accumulated in the unit of body volume) or elastic potential. The potential U can be expanded into a Taylor series with respect to strains, i.e.,

$$U(\varepsilon_{ij}) = s_0 + s_{ij}\,\varepsilon_{ij} + \frac{1}{2} s_{ijkl}\,\varepsilon_{ij}\,\varepsilon_{kl} + \cdots \tag{2.43}$$

where

$$s_0 = U(\varepsilon_{ij} = 0), \quad s_{ij} = \left.\frac{\partial U}{\partial \varepsilon_{ij}}\right|_{\varepsilon_{ij}=0}, \quad s_{ijkl} = \left.\frac{\partial^2 U}{\partial \varepsilon_{ij}\,\partial \varepsilon_{kl}}\right|_{\varepsilon_{ij}=0,\ \varepsilon_{kl}=0} \tag{2.44}$$

Assume that for the initial state of the solid, corresponding to zero external forces, we have $\varepsilon_{ij} = 0$, $\sigma_{ij} = 0$, $U = 0$. Then, $s_0 = 0$ and $s_{ij} = 0$, according to Eq. (2.42). For small strains, we can neglect high-order terms in Eq. (2.43) and restrict ourselves to the first system of nonzero terms taking

$$U = \frac{1}{2} s_{ijkl}\,\varepsilon_{ij}\,\varepsilon_{kl}$$

Then, Eq. (2.42) yields

$$\sigma_{ij} = s_{ijkl}\,\varepsilon_{kl} \tag{2.45}$$

These linear equations correspond to a linear elastic model of the material (see Section 1.1) and, in general, include $3^4 = 81$ coefficients s. However, since $\sigma_{ij} = \sigma_{ji}$ and $\varepsilon_{ij} = \varepsilon_{ji}$, we have the following equations $s_{ijkl} = s_{jikl} = s_{ijlk}$ which reduce the number of independent coefficients to 36. Then, taking

into account that the mixed derivative specifying coefficients s_{ijkl} in Eqs. (2.44) does not depend on the sequence of differentiation, we get 15 equations $s_{ijkl} = s_{klij} (ij \neq kl)$ using which we can reduce the number of independent coefficients to 21. Returning to coordinates x, y, z, we can write Eq. (2.45) in the following explicit form:

$$\{\sigma\} = [S]\{\varepsilon\} \tag{2.46}$$

where

$$\{\sigma\} = \begin{Bmatrix} \sigma_x \\ \sigma_y \\ \sigma_z \\ \tau_{xy} \\ \tau_{xz} \\ \tau_{yz} \end{Bmatrix} \quad \{\varepsilon\} = \begin{Bmatrix} \varepsilon_x \\ \varepsilon_y \\ \varepsilon_z \\ \gamma_{xy} \\ \gamma_{xz} \\ \gamma_{yz} \end{Bmatrix} \quad [S] = \begin{bmatrix} S_{11} & S_{12} & S_{13} & S_{14} & S_{15} & S_{16} \\ S_{21} & S_{22} & S_{23} & S_{24} & S_{25} & S_{26} \\ S_{31} & S_{32} & S_{33} & S_{34} & S_{35} & S_{36} \\ S_{41} & S_{42} & S_{43} & S_{44} & S_{45} & S_{46} \\ S_{51} & S_{52} & S_{53} & S_{54} & S_{55} & S_{56} \\ S_{61} & S_{62} & S_{63} & S_{64} & S_{65} & S_{66} \end{bmatrix} \tag{2.47}$$

Being written in the explicit form, the matrix equation, Eq. (2.46), gives six constitutive equations. They relate stresses and strains through 21 stiffness coefficients $S_{ij} = S_{ji}$ that specify material mechanical properties within the framework of a linear elastic model of the material. The inverse form of Eq. (2.46) is

$$\{\varepsilon\} = [C]\{\sigma\} \tag{2.48}$$

Strains are expressed in terms of stresses via the matrix of compliance coefficients that can be written as

$$[C] = \begin{bmatrix} \frac{1}{E_x} & -\frac{\nu_{xy}}{E_y} & -\frac{\nu_{xz}}{E_z} & \frac{\eta_{x,xy}}{G_{xy}} & \frac{\eta_{x,xz}}{G_{xz}} & \frac{\eta_{x,yz}}{G_{yz}} \\ -\frac{\nu_{yx}}{E_x} & \frac{1}{E_y} & -\frac{\nu_{yz}}{E_z} & \frac{\eta_{y,xy}}{G_{xy}} & \frac{\eta_{y,xz}}{G_{xz}} & \frac{\eta_{y,yz}}{G_{yz}} \\ -\frac{\nu_{zx}}{E_x} & -\frac{\nu_{zy}}{E_y} & \frac{1}{E_z} & \frac{\eta_{z,xy}}{G_{xy}} & \frac{\eta_{z,xz}}{G_{xz}} & \frac{\eta_{z,yz}}{G_{yz}} \\ \frac{\eta_{xy,x}}{E_x} & \frac{\eta_{xy,y}}{E_y} & \frac{\eta_{xy,z}}{E_z} & \frac{1}{G_{xy}} & \frac{\lambda_{xy,xz}}{G_{xz}} & \frac{\lambda_{xy,yz}}{G_{yz}} \\ \frac{\eta_{xz,x}}{E_x} & \frac{\eta_{xz,y}}{E_y} & \frac{\eta_{xz,z}}{E_z} & \frac{\lambda_{xz,xy}}{G_{xy}} & \frac{1}{G_{xz}} & \frac{\lambda_{xz,yz}}{G_{yz}} \\ \frac{\eta_{yz,x}}{E_x} & \frac{\eta_{yz,y}}{E_y} & \frac{\eta_{yz,z}}{E_z} & \frac{\lambda_{yz,xy}}{G_{xy}} & \frac{\lambda_{yz,xz}}{G_{xz}} & \frac{1}{G_{yz}} \end{bmatrix} \tag{2.49}$$

This matrix is symmetric, and the following 15 symmetry conditions are valid

$$\begin{aligned}
&\frac{\nu_{xy}}{E_y}=\frac{\nu_{yx}}{E_x}, \qquad \frac{\nu_{xz}}{E_z}=\frac{\nu_{zx}}{E_x}, \qquad \frac{\nu_{yz}}{E_z}=\frac{\nu_{zy}}{E_y}\\
&\frac{\eta_{x,xy}}{G_{xy}}=\frac{\eta_{xy,x}}{E_x}, \qquad \frac{\eta_{x,xz}}{G_{xz}}=\frac{\eta_{xz,x}}{E_x}, \qquad \frac{\eta_{x,yz}}{G_{yz}}=\frac{\eta_{yz,x}}{E_x}\\
&\frac{\eta_{y,xy}}{G_{xy}}=\frac{\eta_{xy,y}}{E_y}, \qquad \frac{\eta_{y,xz}}{G_{xz}}=\frac{\eta_{xz,y}}{E_y}, \qquad \frac{\eta_{y,yz}}{G_{yz}}=\frac{\eta_{yz,y}}{E_y}\\
&\frac{\eta_{z,xy}}{G_{xy}}=\frac{\eta_{xy,z}}{E_z}, \qquad \frac{\eta_{z,xz}}{G_{xz}}=\frac{\eta_{xz,z}}{E_y}, \qquad \frac{\eta_{z,yz}}{G_{yz}}=\frac{\eta_{yz,z}}{E_z}\\
&\frac{\lambda_{xy,xz}}{G_{xz}}=\frac{\lambda_{xz,xy}}{G_{xy}}, \qquad \frac{\lambda_{xy,yz}}{G_{yz}}=\frac{\lambda_{yz,xy}}{G_{xy}}, \qquad \frac{\lambda_{xz,yz}}{G_{yz}}=\frac{\lambda_{yz,xz}}{G_{xz}}
\end{aligned} \tag{2.50}$$

The compliance matrix, Eq. (2.49), includes the following engineering constants:

E_x is the modulus of elasticity in the x direction (x, y, z); ν_{xy} is the Poisson's ratio that determines the strain in the x direction induced by normal stress acting in the orthogonal y direction (x, y, z); G_{xy} is the shear modulus in the xy-plane (x, y, z); $\eta_{x,yz}$ is the extension-shear coupling coefficient indicating normal strain in the x direction induced by shear stress acting in the yz-plane (x, y, z); $\eta_{xy,z}$ is the shear-extension coupling coefficient characterizing shear strain in the xy-plane caused by normal stress acting in the z direction (x, y, z); and $\lambda_{xy,yz}$ is the shear-shear coupling coefficient that determines the shear strain taking place in the xy-plane under shear stress acting in the yz-plane (x, y, z).

Having constitutive equations, Eq. (2.46), we can now write the finite expression for elastic potential, U. Substituting stresses into Eq. (2.41) and integrating the resulting equation with respect to strains, we get the following equation–after some transformation with the aid of Eq. (2.46):

$$U=\frac{1}{2}(\sigma_x\varepsilon_x+\sigma_y\varepsilon_y+\sigma_z\varepsilon_z+\tau_{xy}\gamma_{xy}+\tau_{xz}\gamma_{xz}+\tau_{yz}\gamma_{yz}) \tag{2.51}$$

The potential energy of the solid can be found as

$$W=\iiint_V U dV \tag{2.52}$$

The compliance matrix, Eq. (2.49), containing 21 independent elastic constants corresponds to the general case of material anisotropy that practically never occurs in real materials. The most common particular case corresponds to an orthotropic (orthogonally anisotropic) material which has three orthogonal orthotropy (coordinate) axes such that normal stresses acting along these axes do not induce shear strains, whereas shear stresses acting in coordinate planes do not cause normal strains in the direction of these axes. As a result, the stiffness and compliance matrices become uncoupled with respect to normal stresses and strains on one side and shear stresses and strains on the other side. For

the case of an orthotropic material, with axes x, y, and z coinciding with the orthotropy axes, Eq. (2.49) takes the form

$$[C] = \begin{bmatrix} \frac{1}{E_x} & -\frac{\nu_{xy}}{E_y} & -\frac{\nu_{xz}}{E_z} & 0 & 0 & 0 \\ -\frac{\nu_{yx}}{E_x} & \frac{1}{E_y} & -\frac{\nu_{yz}}{E_z} & 0 & 0 & 0 \\ -\frac{\nu_{zx}}{E_x} & -\frac{\nu_{zy}}{E_y} & \frac{1}{E_z} & 0 & 0 & 0 \\ 0 & 0 & 0 & \frac{1}{G_{xy}} & 0 & 0 \\ 0 & 0 & 0 & 0 & \frac{1}{G_{xz}} & 0 \\ 0 & 0 & 0 & 0 & 0 & \frac{1}{G_{yz}} \end{bmatrix} \tag{2.53}$$

Symmetry conditions, Eqs. (2.50), reduce to

$$\nu_{xy}E_x = \nu_{yx}E_y, \qquad \nu_{xz}E_x = \nu_{zx}E_z, \qquad \nu_{yz}E_y = \nu_{zy}E_z$$

These equations have a simple physical meaning. The higher the stiffness, demonstrated by the material in some direction, the less is the strain in this direction under loading in the orthogonal directions. Taking into account the foregoing symmetry conditions, we can conclude that an orthotropic material is characterized by nine independent elastic constants.

The simplest material model corresponds to the isotropic material, whose mechanical properties are the same for any direction or plane of loading. As a result, subscripts indicating coordinate directions and planes in Eq. (2.53) disappear, and it reduces to

$$[C] = \begin{bmatrix} \frac{1}{E} & -\frac{\nu}{E} & -\frac{\nu}{E} & 0 & 0 & 0 \\ -\frac{\nu}{E} & \frac{1}{E} & -\frac{\nu}{E} & 0 & 0 & 0 \\ -\frac{\nu}{E} & -\frac{\nu}{E} & \frac{1}{E} & 0 & 0 & 0 \\ 0 & 0 & 0 & \frac{1}{G} & 0 & 0 \\ 0 & 0 & 0 & 0 & \frac{1}{G} & 0 \\ 0 & 0 & 0 & 0 & 0 & \frac{1}{G} \end{bmatrix} \tag{2.54}$$

The compliance matrix, Eq. (2.54), contains three elastic constants, E, G, and ν. However, only two of them are independent. To show this, consider the case of pure shear for a plate discussed in Section 2.4 (see Fig. 2.5). For this problem, $\sigma_x = \sigma_y = \sigma_z = \tau_{xz} = \tau_{yz} = 0$, $\tau_{xy} = \tau$, and Eqs. (2.48) and (2.54) yield

$$\gamma_{xy} = \frac{\tau}{G}$$

The specific strain energy in Eq. (2.51) can be written as

$$U = \frac{1}{2}\tau_{xy}\gamma_{xy} = \frac{1}{2G}\tau^2 \tag{2.55}$$

However, as discussed in Section 2.4, pure shear can be reduced to tension and compression in the principal directions (see Fig. 2.5). For these directions, Eqs. (2.48) and (2.54) give

$$\varepsilon_1 = \frac{\sigma_1}{E} - \nu\frac{\sigma_3}{E}, \qquad \varepsilon_3 = \frac{\sigma_3}{E} - \nu\frac{\sigma_1}{E}$$

Here $\sigma_1 = \tau$, $\sigma_3 = -\tau$, and the remaining stresses are equal to zero. The strain energy, Eq. (2.51), can be presented now in the following form:

$$U = \frac{1}{2}(\sigma_1\varepsilon_1 + \sigma_3\varepsilon_3) = \frac{1+\nu}{E}\tau^2 \tag{2.56}$$

Since Eqs. (2.55) and (2.56) specify one and the same quantity, we get

$$G = \frac{E}{2(1+\nu)} \tag{2.57}$$

Thus, an isotropic material is characterized within the linear elastic model with two independent elastic constants: E and ν.

2.10 FORMULATIONS OF THE PROBLEM

The problem of solid mechanics is reduced, as follows from the foregoing derivation, to a set of 15 equations, i.e., three equilibrium equations, Eqs. (2.5), six strain-displacement equations, Eqs. (2.22), and six constitutive equations, Eq. (2.46) or (2.48). This set of equations is complete, i.e., it contains 15 unknown functions among which there are six stresses, six strains, and three displacements. Solution of a particular problem should satisfy three boundary conditions that can be written at any point of the body surface. Static or force boundary conditions have the form of Eqs. (2.2), whereas kinematic or displacement boundary conditions are imposed on three displacement functions.

There exist two classical formulations of the problem–displacement formulation and stress formulation.

According to the displacement formulation, we first determine displacements u_x, u_y, and u_z from three equilibrium equations, Eqs. (2.5), written in terms of displacements with the aid of constitutive equations, Eq. (2.46), and strain-displacement equations, Eqs. (2.22). Having found the displacements, we use Eqs. (2.22) and (2.46) to determine strains and stresses.

The stress formulation is much less straightforward than the displacement one. Indeed, we have only three equilibrium equations, Eqs. (2.5), for six stresses which means that the problem of solid

mechanics is not, in general, a statically determinate problem. All possible solutions of the equilibrium equations (there is an infinite number of them because the number of equations is less than the number of unknown stresses) satisfying force boundary conditions (solutions that do not satisfy them do not belong to the problem under study) comprise the class of statically admissible stress fields (see Section 2.8). Suppose that we have one such stress field. We can now readily find strains using constitutive equations, Eq. (2.48), but to determine displacements, we need to integrate a set of six strain-displacement equations, Eqs. (2.22). Having only three unknown displacements these equations are, in general, not compatible. As shown in Section 2.7, this set can be integrated if strains satisfy six compatibility equations, Eqs. (2.35). We can write these equations in terms of stresses using constitutive equations, Eq. (2.48). Thus, the stress formulation of the problem is reduced to a set of nine equations consisting of three equilibrium equations and six compatibility equations in terms of stresses. At first glance, it looks like this set is not consistent because it includes only six unknown stresses. However, this is not the case because of the special properties of the compatibility equations. As was noted in Section 2.7, these equations provide the existence of Euclidean space inside the deformed body. But this space automatically exists if strains can be expressed in terms of three continuous displacements as in Eqs. (2.22). Indeed, substituting strains, Eqs. (2.22), into the compatibility equations, Eqs. (2.35), we can readily see that they are identically satisfied for any three functions u_x, u_y, and u_z. This means that the solution of six equations, Eqs. (2.35), including six strains is not unique. The uniqueness is ensured by three equilibrium equations.

2.11 VARIATIONAL PRINCIPLES

The equations of *Solid Mechanics* considered in the previous sections can be derived also from variational principles that establish the energy criteria according to which the actual state of the body under loading can be singled out of a system of admissible states (see Section 2.8).

Consider a linear elastic solid and introduce two mutually independent fields of variables: a statically admissible stress field σ'_x, σ'_y, σ'_z, σ'_{xy}, τ'_{xz}, τ'_{yz} and a kinematically admissible field characterized with displacements u''_x, u''_y, u''_z and corresponding strains ε''_x, ε''_y, ε''_z, γ''_{xy}, γ''_{xz}, γ''_{yz}. To construct the energy criteria allowing us to distinguish the actual variables from admissible ones, consider the following integral similar to the energy integral in Eqs. (2.51) and (2.52):

$$I = \iiint_V \left(\sigma'_x\varepsilon''_x + \sigma'_y\varepsilon''_y + \sigma'_z\varepsilon''_z + \tau'_{xy}\gamma''_{xy} + \tau'_{xz}\gamma''_{xz} + \tau'_{yz}\gamma''_{yz}\right)dV \tag{2.58}$$

Here, in accordance with the definition of a kinematically admissible field (see Section 2.8),

$$\varepsilon''_x = \frac{\partial u''_x}{\partial x}, \qquad \gamma''_{xy} = \frac{\partial u''_x}{\partial y} + \frac{\partial u''_y}{\partial x} \qquad (x, y, z) \tag{2.59}$$

Substituting Eqs. (2.59) into Eq. (2.58) and using the following evident relationships between the derivatives

$$\sigma'_x\frac{\partial u''_x}{\partial x} = \frac{\partial}{\partial x}(\sigma'_x u''_x) - u''_x\frac{\partial \sigma'_x}{\partial x}, \qquad \tau'_{xy}\frac{\partial u''_x}{\partial y} = \frac{\partial}{\partial y}(\tau'_{xy}u''_x) - u''_x\frac{\partial \tau'_{xy}}{\partial y},$$

etc., we arrive at

$$I = \iiint_V \left[\frac{\partial}{\partial x}(\sigma'_x u''_x + \tau'_{xy} u''_y + \tau'_{xz} u''_z) + \frac{\partial}{\partial y}(\tau'_{xy} u''_x + \sigma'_y u''_y + \tau'_{yz} u''_z) \right.$$
$$+ \frac{\partial}{\partial z}(\tau'_{xz} u''_x + \tau'_{yz} u''_y + \sigma'_z u''_z) - \left(\frac{\partial \sigma'_x}{\partial x} + \frac{\partial \tau'_{xy}}{\partial y} + \frac{\partial \tau'_{xz}}{\partial z} \right) u''_x \tag{2.60}$$
$$\left. - \left(\frac{\partial \sigma'_y}{\partial y} + \frac{\partial \tau'_{xy}}{\partial x} + \frac{\partial \tau'_{yz}}{\partial z} \right) u''_y - \left(\frac{\partial \sigma'_z}{\partial z} + \frac{\partial \tau'_{xz}}{\partial x} + \frac{\partial \tau'_{yz}}{\partial y} \right) u''_z \right] dV$$

Applying Green's integral transformation, Eq. (2.4), to the first three terms under the integral and taking into account that statically admissible stresses should satisfy equilibrium equations, Eqs. (2.5) and (2.6), and force boundary conditions, Eqs. (2.2), we obtain from Eqs. (2.58) and (2.60)

$$\iiint_V \left(\sigma'_x \varepsilon''_x + \sigma'_y \varepsilon''_y + \sigma'_z \varepsilon''_z + \tau'_{xy} \gamma''_{xy} + \tau'_{xz} \gamma''_{xz} + \tau'_{yz} \gamma''_{yz} \right) dV$$
$$= \iint_S \left(p_x u''_x + p_y u''_y + p_z u''_z \right) dS + \iiint_V \left(q_x u''_x + q_y u''_y + q_z u''_z \right) dV \tag{2.61}$$

For actual stresses, strains, and displacements, Eq. (2.61) reduces to the following equation:

$$\iiint_V (\sigma_x \varepsilon_x + \sigma_y \varepsilon_y + \sigma_z \varepsilon_z + \tau_{xy} \gamma_{xy} + \tau_{xz} \gamma_{xz} + \tau_{yz} \gamma_{yz}) dV$$
$$= \iint_S \left(p_x u_x + p_y u_y + p_z u_z \right) dS + \iiint_V (q_x u_x + q_y u_y + q_z u_z) dV \tag{2.62}$$

known as Clapeyron's theorem.

2.11.1 Principle of minimum total potential energy

This principle allows us to distinguish the actual displacement field of the body from kinematically admissible fields. To derive it, assume that the stresses in Eq. (2.61) are actual stresses, i.e., $\sigma' = \sigma$ and $\tau' = \tau$, whereas the displacements and the corresponding strains differ from the actual values by small kinematically admissible variations, i.e., $u'' = u + \delta u$, $\varepsilon'' = \varepsilon + \delta\varepsilon$, and $\gamma'' = \gamma + \delta\gamma$. Substituting these expressions into Eq. (2.61) and subtracting Eq. (2.62) from the resulting equation, we arrive at

$$\iiint_V (\sigma_x \delta\varepsilon_x + \sigma_y \delta\varepsilon_y + \sigma_z \delta\varepsilon_z + \tau_{xy} \delta\gamma_{xy} + \tau_{xz} \delta\gamma_{xz} + \tau_{yz} \delta\gamma_{yz}) dV$$
$$= \iint_S (p_x \delta u_x + p_y \delta u_y + p_z \delta u_z) dS + \iiint_V (q_x \delta u_x + q_y \delta u_y + q_z \delta u_z) dV$$

Assume that under small variation of displacements and strains belonging to the kinematically admissible fields the surface tractions and body forces do not change. Then, we can write the foregoing result in the following form

$$\delta W_\varepsilon - \delta A = 0 \tag{2.63}$$

Here

$$\delta W_\varepsilon = \iiint_V \left(\sigma_x \delta\varepsilon_x + \sigma_y \delta\varepsilon_y + \sigma_z \delta\varepsilon_z + \tau_{xy}\delta\gamma_{xy} + \tau_{xz}\delta\gamma_{xz} + \tau_{yz}\delta\gamma_{yz}\right) dV \tag{2.64}$$

is the variation of the strain energy (internal potential energy of an elastic solid) associated with small kinematically admissible variations of strains and

$$A = \iint_S (p_x u_x + p_y u_y + p_z u_z) dS + \iiint_V (q_x u_x + q_y u_y + q_z u_z) dV \tag{2.65}$$

can be formally treated as work performed by surface tractions and body forces on the actual displacements. Expressing stresses in Eq. (2.64) in terms of strains with the aid of the constitutive equations, Eq. (2.46), and integrating, we can determine W_ε, which is the body strain energy written in terms of strains. The quantity $T = W_\varepsilon - A$ is referred to as the total potential energy of the body. This name historically came from problems in which external forces had a potential function $F = -A$ so that $T = W_\varepsilon + F$ was the sum of internal and external potentials, i.e., the total potential function. Then, the condition in Eq. (2.63) reduces to

$$\delta T = 0 \tag{2.66}$$

which means that T has a stationary (actually, minimum) value under small admissible variation of displacements in the vicinity of actual displacements. Thus, we arrive at the following variational principle of minimum total potential energy: the actual displacement field, in contrast to all kinematically admissible fields, delivers the minimum value of the body total potential energy. This principle is a variational form of the displacement formulation of the problem discussed in Section 2.10. As can be shown, the variational equations ensuring the minimum value of the total potential energy of the body coincide with the equilibrium equations written in terms of displacements.

2.11.2 Principle of minimum strain energy

This principle is valid for a linear elastic body and establishes the criterion according to which the actual stress field can be singled out of all statically admissible fields. Suppose that displacements and strains in Eq. (2.61) are actual, i.e. $u'' = u$, $\varepsilon'' = \varepsilon$, and $\gamma'' = \gamma$, whereas stresses differ from the actual values by small statically admissible variations, i.e., $\sigma' = \sigma + \delta\sigma$, and $\tau' = \tau + \delta\tau$. Substituting these expressions in Eq. (2.61) and subtracting Eq. (2.62) for the actual state, we get

$$\delta W_\sigma = 0 \tag{2.67}$$

where

$$\delta W_\sigma = \iiint_V \left(\varepsilon_x \delta\sigma_x + \varepsilon_y \delta\sigma_y + \varepsilon_z \delta\sigma_z + \gamma_{xy}\delta\tau_{xy} + \gamma_{xz}\delta\tau_{xz} + \gamma_{yz}\delta\tau_{yz}\right) dV \tag{2.68}$$

is the variation of the strain energy associated with the variation of stresses. Expressing strains in terms of stresses with the aid of constitutive equations, Eq. (2.48), and integrating, we can determine W_σ, which is the body strain energy written in terms of stresses. As before, Eq. (2.67) indicates that strain

energy, W_σ, has a stationary (in fact, minimum) value under admissible variation of stresses. As a result, we arrive at the following variational principle of minimum strain energy: the actual stress field, in contrast to all statically admissible fields, delivers the minimum value of the body strain energy. This principle is a variational form of the stress formulation of the problem considered in Section 2.10. As can be shown, the variational equations providing the minimum value of the strain energy are compatibility equations written in terms of stresses. It is important that the stress variation in Eq. (2.68) should be performed within the statically admissible field, i.e., within stresses that satisfy equilibrium equations and force boundary conditions.

To derive another useful result that will be used further in Section 10.4.4, we can generalize the foregoing concept of a statically admissible stress field. In particular, assume that the statically admissible stresses satisfy only the equilibrium equations, whereas to satisfy the force boundary conditions, the acting loads must be slightly changed. Assume that a solid is loaded with a concentrated force P whose direction is specified by the directional cosines of the angles between the force direction and axes x, y, and z, i.e.,

$$n_x = \cos\big(P,\, x\big), \qquad n_y = \cos\big(P,\, y\big), \qquad n_z = \cos\big(P,\, z\big)$$

Assume also that the projections of the displacement u_p of the point of application of this force on the axes x, y, and z are u_x^P, u_y^P, and u_z^P. For a new formulation of a statically admissible stress field, to satisfy the force boundary conditions, we need to apply the force $P + \delta P$ in which δP is a small variation of the force P. Then, the variational equation, Eq. (2.67), can be generalized as

$$\delta W_\sigma = \delta P\Big(u_x^P n_x + u_y^P n_y + u_z^P n_z\Big)$$

where

$$u_x^P n_x + u_y^P n_y + u_z^P n_z = u^P$$

in which $u^P$is the projection of the displacement u_P of the point of the force application on the direction of the force P. Taking into account that variation is analogous to differentiation, we arrive at

$$\frac{\partial W_\sigma}{\partial P} = u^P \tag{2.69}$$

This equation specifies so-called Castigliano's theorem, according to which the derivative of the strain energy with respect to the force is equal to the projection of the displacement of the point at which the force is applied on the direction of the force.

Applying a concentrated moment M, we get in a similar way

$$\frac{\partial W_\sigma}{\partial M} = \theta^M \tag{2.70}$$

Here, $\theta^M$is the rotation angle in the plane and direction in which the moment M is applied.

2.11.3 Mixed variational principles

The two variational principles described above imply variations with respect to either displacements only or stresses only. There exist also the so-called mixed variational principles in which variation is performed with respect to both kinematic and static variables. The first principle from this group

follows from the principle of minimum total potential energy considered in Section 2.11.1. Let us expand the class of admissible kinematic variables and introduce displacements that are continuous functions satisfying displacement boundary conditions and strains that are not related to these displacements by strain-displacement equations, Eqs. (2.22). Then we can apply the principle of minimum total potential energy performing a conditional minimization of the total potential energy and introduce Eqs. (2.22) as additional constraints imposed on strains and displacements with the aid of Lagrange's multipliers. Using stresses as these multipliers, we can construct the following augmented functional

$$T_L = W_\varepsilon - A + \iiint_V \left[\sigma_x \left(\frac{\partial u_x}{\partial x} - \varepsilon_x \right) + \sigma_y \left(\frac{\partial u_y}{\partial y} - \varepsilon_y \right) + \sigma_z \left(\frac{\partial u_z}{\partial z} - \varepsilon_z \right) + \tau_{xy} \left(\frac{\partial u_x}{\partial y} + \frac{\partial u_y}{\partial x} - \gamma_{xy} \right) \right.$$
$$\left. + \tau_{xz} \left(\frac{\partial u_x}{\partial z} + \frac{\partial u_z}{\partial x} - \gamma_{xz} \right) + \tau_{yz} \left(\frac{\partial u_y}{\partial z} + \frac{\partial u_z}{\partial y} - \gamma_{yz} \right) \right] dV$$

According to the initial principle, Eq. (2.66), $\delta T_L = 0$. Variation of displacements yields, as earlier, equilibrium equations, variation of stresses results in strain-displacement equations, and variation of strains gives constitutive equations (W_ε should be expressed in terms of strains).

The second form of the mixed variational principle can be derived from the principle of minimum strain energy discussed in Section 2.11.2. Again, expand the class of admissible static fields and introduce stresses that satisfy force boundary conditions but do not satisfy equilibrium equations, Eqs. (2.5). Then, we can apply the principle of minimum strain energy if we construct an augmented functional adding Eqs. (2.5) as additional constraints. Using displacements as Lagrange's multipliers, we obtain

$$W_L = W_\sigma + \iiint_V \left[u_x \left(\frac{\partial \sigma_x}{\partial x} + \frac{\partial \tau_{xy}}{\partial y} + \frac{\partial \tau_{xz}}{\partial z} + q_x \right) + u_y \left(\frac{\partial \sigma_y}{\partial y} + \frac{\partial \tau_{xy}}{\partial x} + \frac{\partial \tau_{yz}}{\partial z} + q_y \right) \right.$$
$$\left. + u_z \left(\frac{\partial \sigma_z}{\partial z} + \frac{\partial \tau_{xz}}{\partial x} + \frac{\partial \tau_{yz}}{\partial y} + q_z \right) \right] dV$$

According to the original principle, Eq. (2.67), $\delta W_L = 0$. The variation with respect to stresses (W_σ should be expressed in terms of stresses) yields constitutive equations in which strains are expressed in terms of displacements via strain-displacement equations, Eqs. (2.22), whereas variation of displacements gives equilibrium equations.

The equations and principles considered in this chapter will be used in the following chapters in the book for the analysis of the mechanics of composite materials and structural elements.

2.12. Reference

Vasiliev, V. V., & Gurdal, Z. (1999). Optimal structural design. In V. V. Vasiliev, & Z. Gurdal (Eds.), *Optimal Design* (pp. 1–29). Lancaster PA: Technomic.

CHAPTER

Mechanics of a unidirectional ply 3

A ply or lamina is the simplest element of a composite material, an elementary layer of unidirectional fibers in a matrix (see Fig. 3.1) formed when a unidirectional tape impregnated with resin is placed onto the surface of a tool, thus providing the shape of a composite part.

3.1 PLY ARCHITECTURE

As the tape consists of tows (bundles of fibers), the ply thickness (whose minimum value is about 0.1 mm for modern composites) is much higher than the fiber diameter (about 0.01 mm). In an actual ply, the fibers are randomly distributed, as in Fig. 3.2. Since the actual distribution is not known and can hardly be predicted, some typical idealized regular distributions (i.e., square (Fig. 3.3), hexagonal (Fig. 3.4), and layer-wise (Fig. 3.5)) are used for the analysis.

A composite ply is generally taken to consist of two constituents: fibers and a matrix whose quantities in the materials are specified by volume, v, and mass, m, fractions

$$v_f = \frac{V_f}{V_c},\ v_m = \frac{V_m}{V_c} \tag{3.1}$$

$$m_f = \frac{M_f}{M_c},\ m_m = \frac{M_m}{M_c} \tag{3.2}$$

Here, V and M are volume and mass, whereas subscripts f, m, and c correspond to fibers, matrix, and composite material, respectively. Since $V_c = V_f + V_m$ and $M_c = M_f + M_m$, we have

$$v_f + v_m = 1,\ m_f + m_m = 1 \tag{3.3}$$

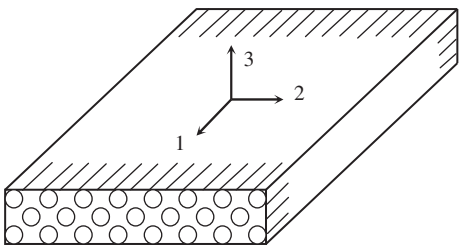


FIGURE 3.1

A unidirectional ply.

Advanced Mechanics of Composite Materials and Structural Elements. http://dx.doi.org/10.1016/B978-0-08-098231-1.00003-0
Copyright © 2013 Elsevier Ltd. All rights reserved.

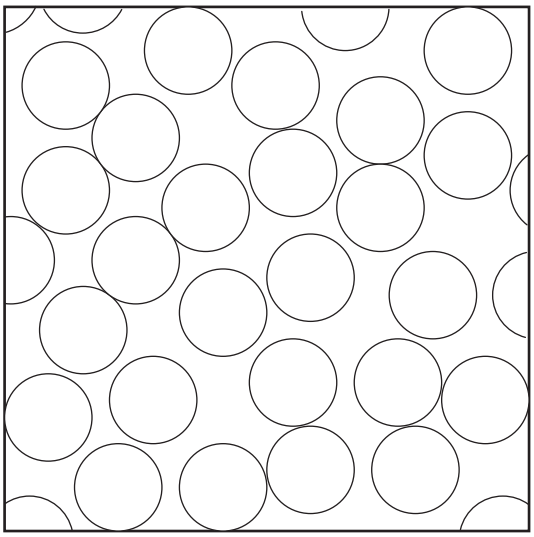


FIGURE 3.2

Actual fiber distribution in the cross section of a ply ($v_f = 0.65$).

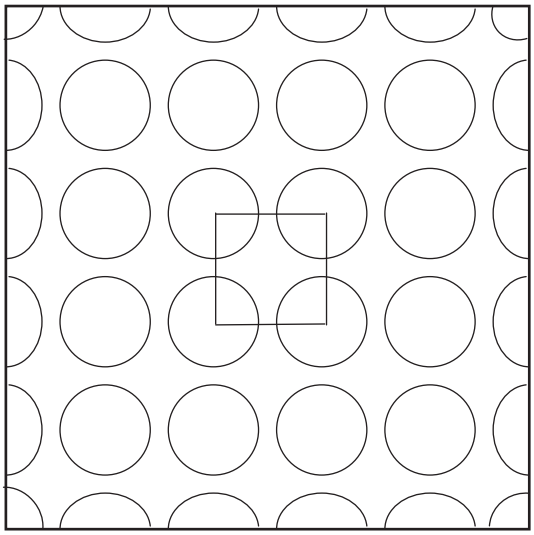


FIGURE 3.3

Square fiber distribution in the cross section of a ply ($v_f = 0.65$).

There exist the following relationships between volume and mass fractions

$$v_f = \frac{\rho_c}{\rho_f} m_f,\ v_m = \frac{\rho_c}{\rho_m} m_m \tag{3.4}$$

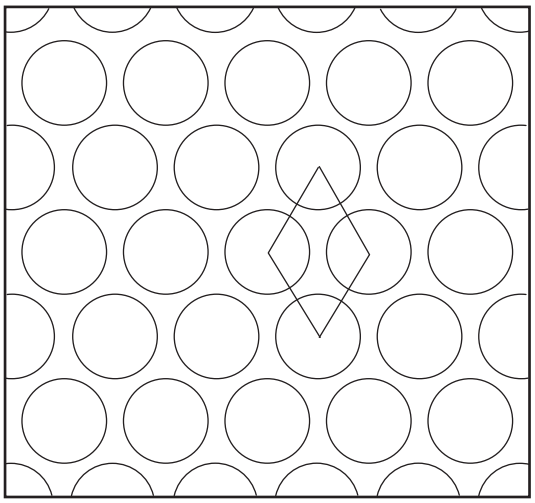


FIGURE 3.4

Hexagonal fiber distribution in the cross section of a ply ($v_f = 0.65$).

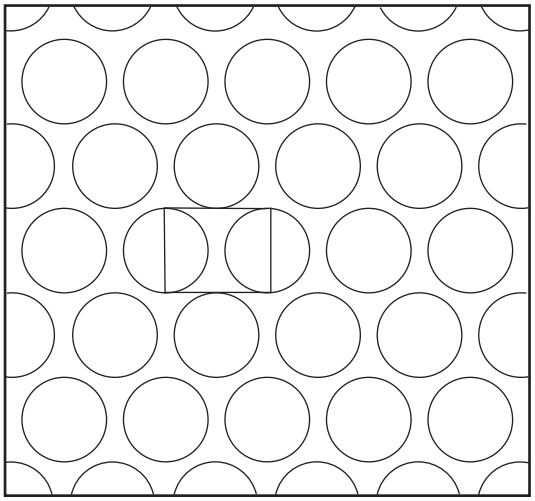


FIGURE 3.5

Layer-wise fiber distribution in the cross section of a ply ($v_f = 0.65$).

where ρ_f, ρ_m, and ρ_c are the densities of fibers, the matrix, and the composite respectively. In analysis, volume fractions are used because they enter the stiffness coefficients for a ply, whereas mass fractions are usually measured directly during processing or experimental study of the fabricated material.

Two typical situations usually occur. The first situation implies that we know the mass of the fibers used to fabricate a composite part and the mass of the part itself. The mass of the fibers can be found if we weigh the spools with fibers before and after they are used or calculate the total length of tows and multiply it by the tow tex-number that is the mass in grams of a 1000 m long tow. So, we know the values of M_f and M_c and can use the first equations of Eqs. (3.2) and (3.4) to calculate v_f.

The second situation takes place if we have a sample of a composite material and know the densities of the fibers and the matrix used for its fabrication. Then, we can find the experimental value of material density, ρ_c^e, and use the following equation for theoretical density

$$\rho_c = \rho_f v_f + \rho_m v_m \tag{3.5}$$

Putting $\rho_c = \rho_c^e$ and taking into account Eqs. (3.3), we obtain

$$v_f = \frac{\rho_c^e - \rho_m}{\rho_f - \rho_m} \tag{3.6}$$

Consider, for example, a carbon-epoxy composite material with fibers *AS*4 and matrix EPON DPL-862, for which $\rho_f = 1.79\ \text{g/cm}^3$ and $\rho_m = 1.2\ \text{g/cm}^3$. Let $\rho_c^e = 1.56\ \text{g/cm}^3$. Then, Eq. (3.6) yields $v_f = 0.61$.

This result is approximate because it ignores possible material porosity. To determine the actual fiber fraction, we should remove the resin using matrix destruction, solvent extraction, or burning the resin out in an oven. As a result, we get M_f, and having M_c, can calculate m_f and v_f with the aid of Eqs. (3.2) and (3.4). Then we find ρ_c using Eq. (3.5) and compare it with ρ_c^e. If $\rho_c > \rho_c^e$, the material includes voids whose volume fraction (porosity) can be calculated using the following equation:

$$v_p = 1 - \frac{\rho_c^e}{\rho_c} \tag{3.7}$$

For the carbon-epoxy composite material considered above as an example, assume that the foregoing procedure results in $m_f = 0.72$. Then, Eqs. (3.4), (3.5), and (3.7) give $v_f = 0.63$, $\rho_c = 1.58\ \text{g/cm}^3$, and $v_p = 0.013$, respectively.

For real unidirectional composite materials, we normally have $v_f = 0.50-0.65$. Lower fiber volume content results in lower ply strength and stiffness under tension along the fibers, whereas higher fiber content, close to the ultimate value, leads to reduction of the ply strength under longitudinal compression and in-plane shear due to poor bonding of the fibers.

Since the fibers usually have uniform circular cross sections, there exists the ultimate fiber volume fraction, v_f^u which is less than unity and depends on the fiber arrangement. For typical arrangements shown in Figs. 3.3–3.5, the ultimate arrays are presented in Fig. 3.6, and the corresponding ultimate fiber volume fractions are:

Square array

$$v_f^u = \frac{1}{d^2}\left(\frac{\pi d^2}{4}\right) = \frac{\pi}{4} = 0.785$$

Hexagonal array

$$v_f^u = \frac{2}{d^2\sqrt{3}}\left(\frac{\pi d^2}{4}\right) = \frac{\pi}{2\sqrt{3}} = 0.907$$

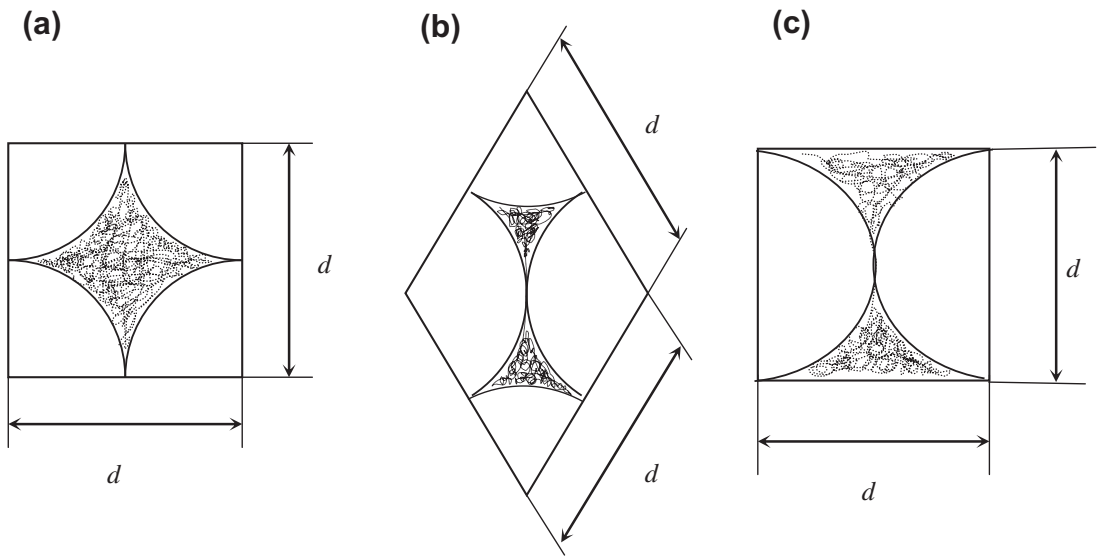


FIGURE 3.6

Ultimate fiber arrays for square (a), hexagonal (b), and layer-wise (c) fiber distributions.

Layer-wise array

$$v_f^u = \frac{1}{d^2}\left(\frac{\pi d^2}{4}\right) = \frac{\pi}{4} = 0.785$$

3.2 FIBER-MATRIX INTERACTION

Composite materials consist of fibers and matrix acting together, and the material properties are governed by the properties of fibers and matrix as the result of their interaction.

3.2.1 Theoretical and actual strength

The most important property of advanced composite materials is associated with the very high strength of a unidirectional ply, accompanied with relatively low density. This advantage of the material is provided mainly by the fibers. Correspondingly, a natural question arises as to how such traditional lightweight materials like glass or graphite, which were never utilized as primary load-bearing structural materials, can be used to make fibers with a strength exceeding the strength of such traditional structural materials as aluminum or steel (see Table 1.1). The general answer is well-known: the strength of a thin wire is usually much higher than the strength of the corresponding bulk material. This is demonstrated in Fig. 3.7, showing that the wire strength increases as the wire diameter is reduced.

In connection with this, two questions arise. First, what is the upper limit of strength that can be predicted for an infinitely thin wire or fiber? And second, what is the nature of this phenomenon?

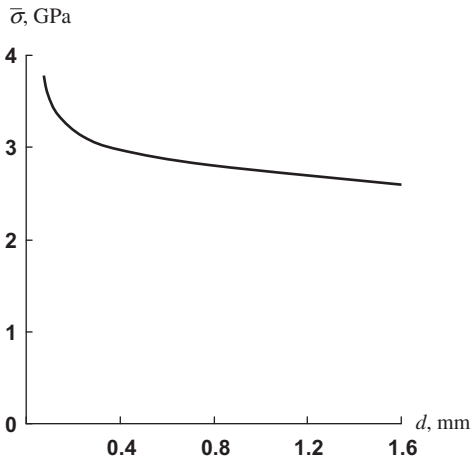


FIGURE 3.7

Dependence of high-carbon steel wire strength on the wire diameter.

The answer to the first question is given in *The Physics of Solids* (Feynman et al., 1964). Consider an idealized model of a solid, namely a regular system of atoms located as shown in Fig. 3.8, and find the stress, σ, that destroys this system. The dependence of σ on the atomic spacing is presented in Fig. 3.9. Point O of the curve corresponds to the equilibrium of the unloaded system, whereas point U specifies the ultimate theoretical stress, $\overline{\sigma}_t$. The initial tangent angle, α, characterizes the material's modulus of elasticity, E. To evaluate $\overline{\sigma}_t$, we can use the following sine approximation (Gilman, 1959) for the OU segment of the curve

$$\sigma = \overline{\sigma}_t \ \sin 2\pi \frac{a - a_0}{a_0}$$

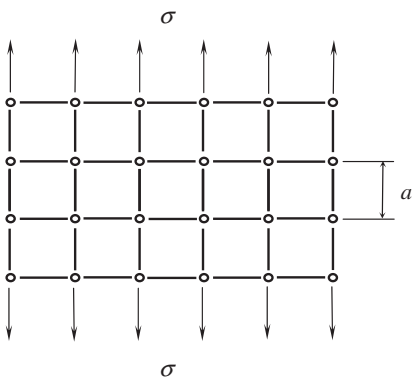


FIGURE 3.8

Material model.

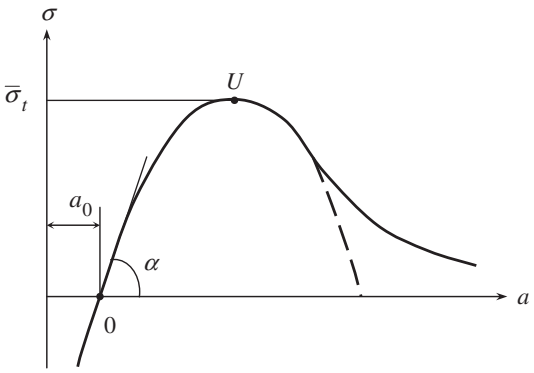


FIGURE 3.9

Atoms' interaction curve (solid line) and its sine approximation (dashed line).

Introducing strain

$$\varepsilon = \frac{a - a_0}{a_0}$$

we arrive at

$$\sigma = \overline{\sigma}_t \ \sin 2\pi\varepsilon$$

Now, we can calculate the modulus as

$$E = \left(\frac{d\sigma}{d\varepsilon}\right)\Big|_{\varepsilon=0} = 2\pi\overline{\sigma}_t$$

Thus,

$$\overline{\sigma}_t = \frac{E}{2\pi} \tag{3.8}$$

This equation yields a very high value for the theoretical strength. For example, for a steel wire, $\overline{\sigma}_t =$ 33.4 GPa. Until now, the highest strength reached in 2 μm-diameter monocrystals of iron (whiskers) is about 12 GPa.

The model under study allows us to introduce another important characteristic of the material. The specific energy that should be spent to destroy the material can be presented in accordance with Fig. 3.9 as

$$2\gamma = \int_{a_0}^{\infty} \sigma(a)da \tag{3.9}$$

As material fracture results in the formation of two new free surfaces, γ can be referred to as the specific surface energy (energy spent to form the surface of the unit area).

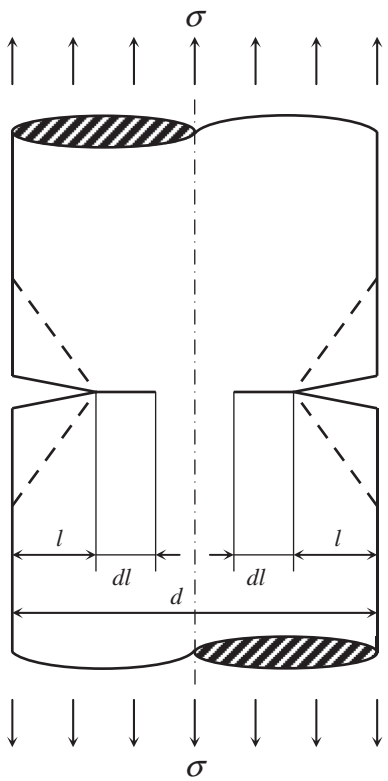


FIGURE 3.10

A fiber with a crack.

The answer to the second question (why the fibers are stronger than the corresponding bulk materials) was in fact given by Griffith (1920), whose results have formed the basis of fracture mechanics.

Consider a fiber loaded in tension and having a thin circumferential crack as shown in Fig. 3.10. The crack length, l, is much less than the fiber diameter, d.

For a linear elastic fiber, $\sigma = E\varepsilon$, and the elastic potential in Eq. (2.51) can be presented as

$$U = \frac{1}{2}\sigma\varepsilon = \frac{\sigma^2}{2E}$$

When the crack appears, the strain energy is released in a material volume adjacent to the crack. Suppose that this volume is comprised of a conical ring whose generating lines are represented in Fig. 3.10 by dashed lines and whose heights are proportional to the crack length, l. Then, the total released energy, Eq. (2.52), is

$$W = \frac{1}{2}k\pi\frac{\sigma^2}{E}l^2 d \tag{3.10}$$

where k is some constant coefficient of proportionality. On the other hand, the formation of new surfaces consumes the energy

$$S = 2\pi\,\gamma\,ld \tag{3.11}$$

where γ is the surface energy, Eq. (3.9). Now assume that the crack length is increased by an infinitesimal increment, dl. Then, if for some value of acting stress, σ

$$\frac{dW}{dl} > \frac{dS}{dl} \tag{3.12}$$

the crack will propagate, and the fiber will fail. Substituting Eqs. (3.10) and (3.11) into inequality (3.12) we arrive at

$$\sigma > \overline{\sigma}_c = \sqrt{\frac{2\gamma E}{kl}} \tag{3.13}$$

The most important result that follows from this condition specifying some critical stress, σ_c, beyond which the fiber with a crack cannot exist, is the fact that $\overline{\sigma}_c$ depends on the absolute value of the crack length (not on the ratio l/d). Now for a continuous fiber, $2l < d$, so the thinner the fiber, the smaller the length of the crack that can exist in this fiber and the higher is the critical stress, $\overline{\sigma}_c$. More rigorous analysis shows that, reducing l to a in Fig. 3.8, we arrive at $\overline{\sigma}_c = \overline{\sigma}_t$.

Consider, for example, glass fibers that are widely used as reinforcing elements in composite materials and have been studied experimentally to support the fundamentals of fracture mechanics (Griffith, 1920). The theoretical strength of glass, Eq. (3.8), is about 14 GPa, whereas the actual strength of 1 mm diameter glass fibers is only about 0.2 GPa, and for 5 mm diameter fibers, this value is much lower (about 0.05 GPa). The fact that such low actual strength is caused by surface cracks can be readily proved if the fiber surface is smoothed by etching the fiber with acid. Then the strength of 5 mm diameter fibers can be increased up to 2 GPa. If the fiber diameter is reduced by heating and stretching the fibers to a diameter of about 0.0025 mm, the strength is increased to 6 GPa. Theoretical extrapolation of the experimental curve, showing the dependence of the fiber strength on the fiber diameter for very small fiber diameters, yields $\overline{\sigma} = 11$ GPa, which is close to $\overline{\sigma}_t = 14$ GPa.

Thus, we arrive at the following conclusion, clarifying the nature of the high performance of advanced composites and their place among modern structural materials. The actual strength of advanced structural materials is much lower than their theoretical strength. This difference is caused by defects in the material microstructure (e.g., crystalline structure) or macrocracks inside the material and on its surface. Using thin fibers, we reduce the influence of cracks and thus increase the strength of materials reinforced with these fibers. So, advanced composites comprise a special class of structural materials in which we try to utilize the natural potential properties of the material, rather than the capabilities of technology as we do developing high-strength alloys.

3.2.2 Statistical aspects of fiber strength

Fiber strength, being relatively high, is still less than the corresponding theoretical strength, which means that fibers of advanced composites have microcracks or other defects randomly distributed along the fiber length. This is supported by the fact that the fiber strength depends on the length of the tested fiber. The dependence of strength on length for boron fibers (Mikelsons and Gutans, 1984) is shown in Fig. 3.11.

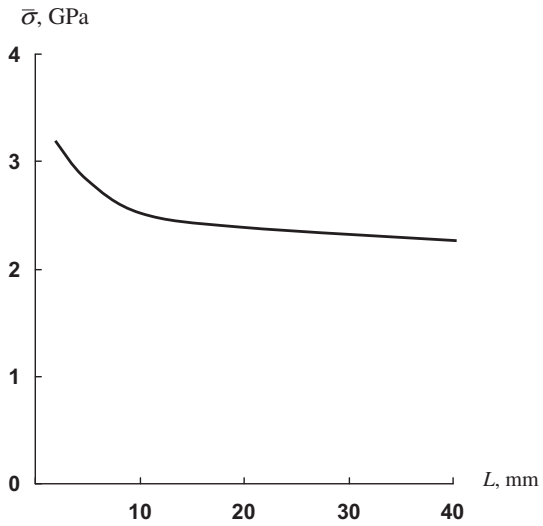


FIGURE 3.11

Dependence of strength of boron fibers on the fiber length.

The longer the fiber, the higher is the probability of a deleterious defect to exist within this length, and the lower the fiber strength. The tensile strengths of fiber segments with the same length but taken from different parts of a long continuous fiber, or from different fibers, also demonstrate the strength deviation. A typical strength distribution for boron fibers is presented in Fig. 3.12.

The first important characteristic of the strength deviation is the strength scatter, $\Delta\overline{\sigma} = \overline{\sigma}_{\max} - \overline{\sigma}_{\min}$. For the case corresponding to Fig. 3.12, $\overline{\sigma}_{\max} = 4.2$ GPa, $\overline{\sigma}_{\min} = 2$ GPa, and $\Delta\overline{\sigma} = 2.2$ GPa. To plot the diagram presented in Fig. 3.12, $\Delta\overline{\sigma}$ is divided into a set of increments, and a normalized number of fibers $n = N_\sigma/N$ (N_σ is the number of fibers failing at that stress within the increment, and N is the total number of tested fibers) is calculated and shown on the vertical axis. Thus, the so-called frequency histogram can be plotted. This histogram allows us to determine the mean value of the fiber strength as

$$\overline{\sigma}_m = \frac{1}{N}\sum_{i=1}^{N}\overline{\sigma}_i \tag{3.14}$$

and the strength dispersion as

$$d_\sigma = \sqrt{\frac{1}{N-1}\sum_{i=1}^{N}(\overline{\sigma}_m - \sigma_i)^2} \tag{3.15}$$

The deviation of fiber strength is characterized by the coefficient of the strength variation, which is presented as follows

$$r_\sigma = \frac{d_\sigma}{\overline{\sigma}_m}100\% \tag{3.16}$$

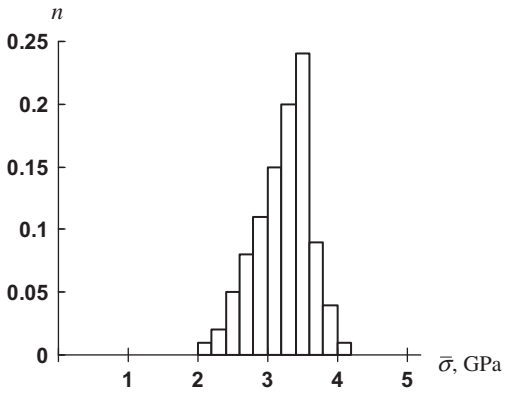


FIGURE 3.12

Strength distribution for boron fibers.

For the boron fibers under consideration, Eqs. (3.14)–(3.16) yield $\overline{\sigma}_m = 3.2$ GPa, $d_\sigma = 0.4$ GPa, and $r_\sigma = 12.5\%$.

To demonstrate the influence of fiber strength deviation on the strength of a unidirectional ply, consider a bundle of fibers, i.e., a system of approximately parallel fibers with different strengths and slightly different lengths as in Fig. 3.13. Typical stress-strain diagrams for fibers tested under tension in a bundle are shown in Fig. 3.14 (Vasiliev and Tarnopol'skii, 1990). As can be seen, the diagrams have two nonlinear segments. The nonlinearity in the vicinity of zero stresses is associated with different lengths of fibers in the bundles, whereas the nonlinear behavior of the bundle under stresses close to the ultimate values is caused by fracture of the fibers with lower strength.

Useful qualitative results can be obtained if we consider model bundles consisting of five fibers with different strengths. Five such bundles are presented in Table 3.1, showing the normalized strength

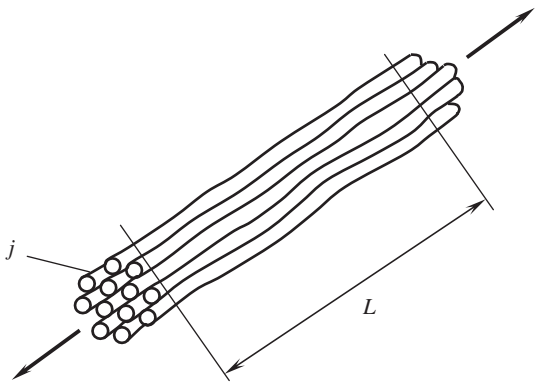


FIGURE 3.13

Tension of a bundle of fibers.

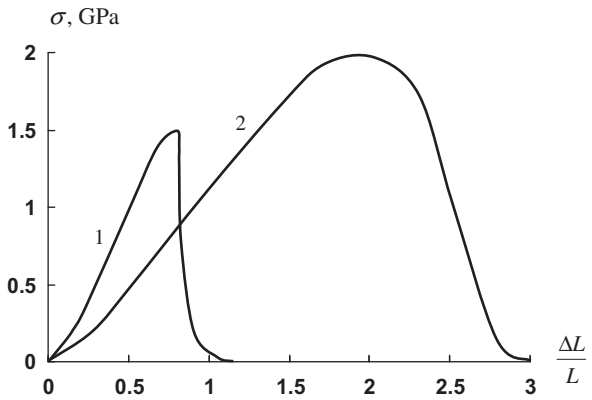


FIGURE 3.14

Stress-strain diagrams for bundles of carbon (1) and aramid (2) fibers.

of each fiber. As can be seen, the deviation of fiber strength is such that the mean strength, $\overline{\sigma}_m = 1$, is the same for all the bundles, whereas the variation coefficient, r_σ, changes from 31.6% for bundle No.1 to zero for bundle No.5. The last row in the table shows the effective (observed) ultimate force, $\overline{F}$, for a bundle. Consider, for example, the first bundle. When the force is increased to $F = 3$, the stresses in all the fibers become $\sigma_j = 0.6$, and fiber No.1 fails. After this happens, the force, $F = 3$, is taken by four fibers, and $\sigma_j = 0.75$ ($j = 2, 3, 4, 5$). When the force reaches the value $F = 3.2$, the stresses become $\sigma_j = 0.8$, and fiber No.2 fails. After that, $\sigma_j = 1.07$ ($j = 3, 4, 5$). This means that fiber No.3 also fails at force $F = 3.2$. Then, for the two remaining fibers, $\sigma_4 = \sigma_5 = 1.6$, and they also fail. Thus, $\overline{F} = 3.2$ for bundle No.1. In a similar way, $\overline{F}$ can be calculated for the other bundles in the table. As can be seen, the lower the fiber strength variation, the higher the $\overline{F}$, which reaches its maximum value, $\overline{F} = 5$, for bundle No.5 consisting of fibers with the same strength.

Table 3.2 demonstrates that strength variation can be more important than the mean strength. In fact, while the mean strength, $\overline{\sigma}_m$, goes down for bundles No.1–5, the ultimate force, $\overline{F}$, increases. So, it

TABLE 3.1 Strength of Bundles Consisting of Fibers with Different Strengths.

	Bundle No.				
Fiber No.	**1**	**2**	**3**	**4**	**5**
1	0.6	0.7	0.85	0.9	1.0
2	0.8	0.9	0.9	0.95	1.0
3	1.0	1.0	1.0	1.0	1.0
4	1.2	1.1	1.1	1.05	1.0
5	1.4	1.3	1.15	1.1	1.0
$\overline{\sigma}_m$	1.0	1.0	1.0	1.0	1.0
r_σ (%)	31.6	22.4	12.8	7.8	0
$\overline{F}$	3.2	3.6	4.25	4.5	5.0

TABLE 3.2 Strength of Bundles Consisting of Fibers with Different Strengths.

	Bundle No.				
Fiber no.	**1**	**2**	**3**	**4**	**5**
1	0.6	0.7	0.85	0.9	0.95
2	0.8	0.9	0.9	0.85	0.95
3	1.0	1.2	1.1	1.0	0.95
4	1.6	1.4	1.15	1.05	0.95
5	3.0	1.6	1.4	1.1	0.95
$\overline{\sigma}_m$	1.4	1.16	1.08	1.0	0.95
r_σ (%)	95.0	66.0	22.0	7.8	0
$\overline{F}$	3.2	3.6	4.25	4.5	4.75

can be better to have fibers with relatively low strength and low strength variation than high-strength fibers with high strength variation.

3.2.3 Stress diffusion in fibers interacting through the matrix

The foregoing discussion concerned individual fibers or bundles of fibers that are not joined together. This is not the case for composite materials in which the fibers are embedded in the matrix material. Usually, the stiffness of the matrix is much lower than that of the fibers (see Table 1.1), and the matrix practically does not take the load applied in the fiber direction. However, the fact that the fibers are bonded with the matrix even with relatively low stiffness changes the mechanism of fiber interaction and considerably increases their effective strength. To show this, the strength of dry fiber bundles can be compared with the strength of the same bundles after impregnating them with epoxy resin and curing. The results are listed in Table 3.3. As can be seen, composite bundles in which fibers are joined together by the matrix demonstrate significantly higher strength, and the higher the fiber sensitivity to damage, the higher the difference in strength of dry and composite bundles. The influence of a matrix on the variation of strength is even more significant. As follows from Table 3.4, the variation coefficients of composite bundles are lower by an order of magnitude than those of individual fibers.

To clarify the role of a matrix in composite materials, consider the simple model of a unidirectional ply shown in Fig. 3.15 and apply the method of analysis developed for stringer panels (Goodey, 1946).

TABLE 3.3 Strength of Dry Bundles and Composite Bundles.

Fibers	**Sensitivity of Fibers to Damage**	**Ultimate Tensile Load $\overline{F}$ (N)**		**Strength Increase (%)**
		Dry Bundle	**Composite Bundle**	
Carbon	High	14	26	85.7
Glass	Moderate	21	36	71.4
Aramid	Low	66	84	27.3

TABLE 3.4 Variation Coefficient for Fibers and Unidirectional Composites.

	Variation Coefficient r_σ (%)	
Fibers	**Fibers**	**Composite**
Glass	29	2.0
Carbon	30	4.7
Aramid	24	5.0
Boron	23	3.0

Let the ply of thickness δ consist of $2k$ fibers symmetrically distributed on both sides of the central fiber $n = 0$. The fibers are joined with layers of the matrix material, and the fiber volume fraction is

$$v_f = \frac{a_f}{a}, \quad a = a_f + a_m \tag{3.17}$$

Let the central fiber have a crack induced by the fiber damage or by the shortage of this fiber's strength. At a distance from the crack, the fibers are uniformly loaded with stress σ (see Fig. 3.15).

First, derive the set of equations describing the ply under study. Since the stiffness of the matrix is much less than that of fibers, we neglect the stress in the matrix acting in the x direction and assume that the matrix works only in shear. We also assume that there are no displacements in the y direction.

Considering equilibrium of the last ($n = k$) fiber, an arbitrary fiber, and the central ($n = 0$) fiber shown in Fig. 3.16, we arrive at the following equilibrium equations:

$$\begin{aligned} a_f\sigma_k' - \tau_k &= 0 \\ a_f\sigma_n' + \tau_{n+1} - \tau_n &= 0 \\ a_f\sigma_0' + 2\tau_1 &= 0 \end{aligned} \tag{3.18}$$

in which $(\ldots)' = d(\ldots)/dx$.

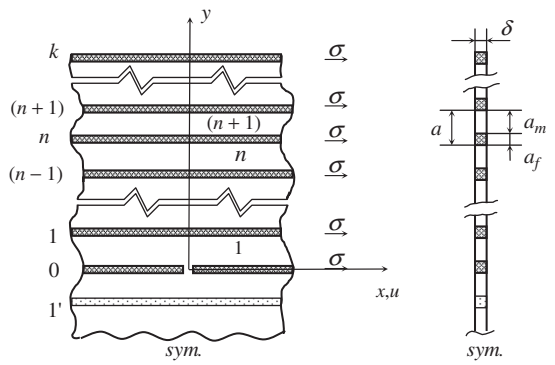


FIGURE 3.15

Model of a unidirectional ply with a broken fiber.

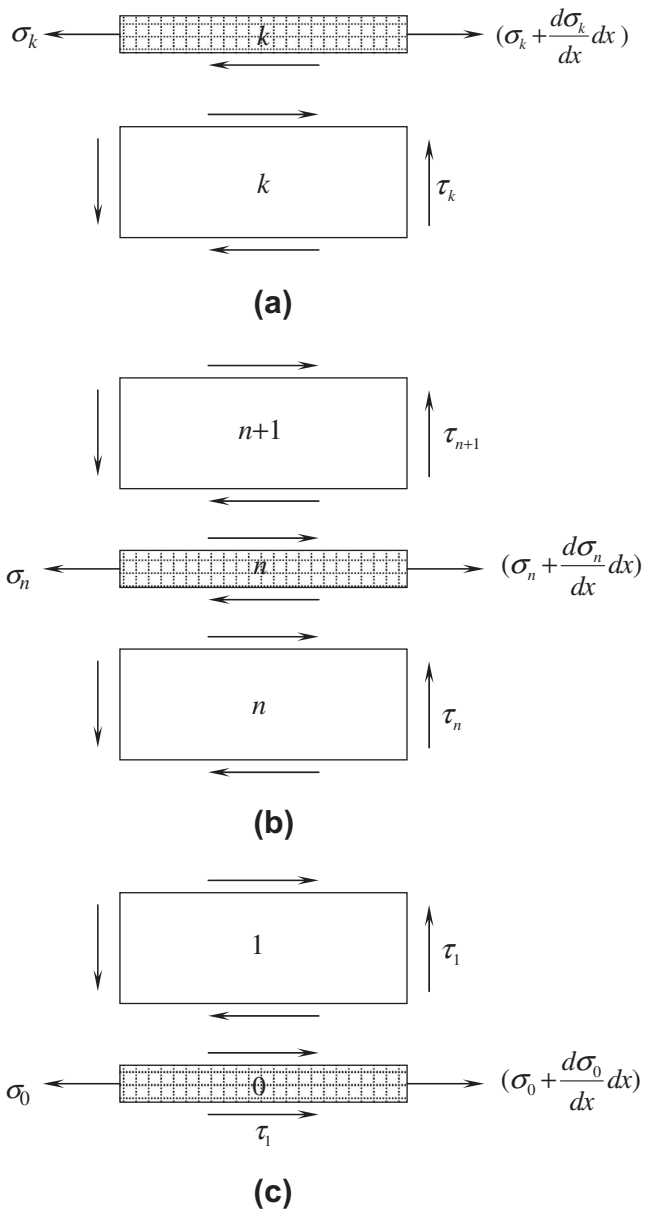


FIGURE 3.16

Stresses acting in fibers and matrix layers for the last (a), arbitrary n-th fiber (b), and the central $n = 0$ fiber (c).

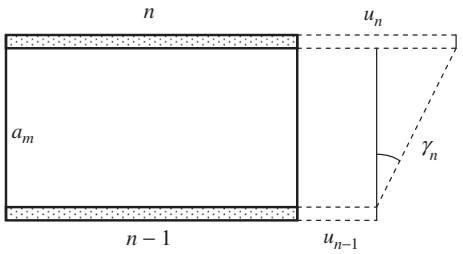


FIGURE 3.17

Shear strain in the matrix layer.

Constitutive equations for fibers and the matrix can be written as

$$\sigma_n = E_f \varepsilon_n, \quad \tau_n = G_m \gamma_n \tag{3.19}$$

Here, E_f is the fiber elasticity modulus and G_m is the matrix shear modulus, whereas

$$\varepsilon_n = u_n' \tag{3.20}$$

is the fiber strain expressed in terms of the displacement in the x direction. The shear strain in the matrix follows from Fig. 3.17, i.e.,

$$\gamma_n = \frac{1}{a_m}(u_n - u_{n-1}) \tag{3.21}$$

This set of equations, Eqs. (3.18)–(3.21), is complete – it includes $10k + 3$ equations and contains the same number of unknown stresses, strains, and displacements.

Consider the boundary conditions. If there is no crack in the central fiber, the solution of the problem is evident and has the form $\sigma_n = \sigma$, $\tau_n = 0$. Assuming that the perturbation of the stressed state induced by the crack vanishes at a distance from the crack, we arrive at

$$\sigma_n(x \to \infty) = \sigma, \quad \tau_n(x \to \infty) = 0 \tag{3.22}$$

As a result of the crack in the central fiber, we have

$$\sigma_0(x = 0) = 0 \tag{3.23}$$

For the remaining fibers, symmetry conditions yield

$$u_n(x = 0) = 0 \quad (n = 1,\ 2,\ 3\ \ldots k) \tag{3.24}$$

To solve the problem, we use the stress formulation and, in accordance with Section 2.10, should consider equilibrium equations in conjunction with compatibility equations expressed in terms of stresses.

First, transform equilibrium equations introducing the stress function, $F(x)$, such that

$$\tau_n = F_n', \quad F_n\big(x \to \infty\big) = 0 \tag{3.25}$$

Substituting Eqs. (3.25) into the equilibrium equations, Eqs. (3.18), integrating them from x to ∞, and taking into account Eqs. (3.22) and (3.25), we obtain

$$\begin{aligned}\sigma_k &= \sigma + \frac{1}{a_f}F_k \\ \sigma_n &= \sigma - \frac{1}{a_f}(F_{n+1} - F_n) \\ \sigma_0 &= \sigma - \frac{2}{a_f}F_1\end{aligned} \tag{3.26}$$

Compatibility equations follow from Eqs. (3.20) and (3.21), i.e.,

$$\gamma'_n = \frac{1}{a_m}(\varepsilon_n - \varepsilon_{n-1})$$

Using constitutive equations, Eqs. (3.19), we can write them in terms of stresses

$$\tau'_n = \frac{G_m}{a_m E_f}(\sigma_n - \sigma_{n-1})$$

Substituting stresses from Eqs. (3.25) and (3.26) and introducing the dimensionless coordinate $\bar{x} = x/a$ (see Fig. 3.15), we finally arrive at the following set of governing equations:

$$\begin{aligned}&F''_k - \mu^2\left(2F_k - F_{k-1}\right) = 0 \\ &F''_n + \mu^2\left(F_{n+1} - 2F_n + F_{n-1}\right) = 0 \\ &F''_1 + \mu^2\left(F_2 - 3F_1\right) = 0\end{aligned} \tag{3.27}$$

in which, in accordance with Eqns. (3.17),

$$\mu^2 = \frac{G_m a^2}{a_f a_m E_f} = \frac{G_m}{v_f(1 - v_f)E_f} \tag{3.28}$$

With due regard to the second equation in Eqs. (3.25), we can take the general solution of Eqs. (3.27) in the form

$$F_n(\bar{x}) = A_n e^{-\lambda\bar{x}} \tag{3.29}$$

Substitution in Eqs. (3.27) yields:

$$A_k\left(2 - \frac{\lambda^2}{\mu^2}\right) - A_{k-1} = 0 \tag{3.30}$$

$$A_{n+1} - A_n\left(2 - \frac{\lambda^2}{\mu^2}\right) + A_{n-1} = 0 \tag{3.31}$$

$$A_2 - A_1\left(3 - \frac{\lambda^2}{\mu^2}\right) = 0 \tag{3.32}$$

The finite-difference equation, Eq. (3.31), can be reduced to the following form:

$$A_{n+1} - 2A_n \cos\theta + A_{n-1} = 0 \tag{3.33}$$

where

$$\cos\theta = 1 - \frac{\lambda^2}{2\mu^2} \tag{3.34}$$

As can be readily checked, the solution for Eq. (3.33) is

$$A_n = B\cos n\theta + C\sin n\theta \tag{3.35}$$

whereas Eq. (3.34) yields, after some transformation,

$$\lambda = 2\mu\sin\frac{\theta}{2} \tag{3.36}$$

Substituting the solution, Eq. (3.35), into Eq. (3.30), we obtain, after some transformation,

$$B = -C\tan(k+1)\theta$$

Thus, Eq. (3.35) can be written as

$$A_n = C[\sin n\theta - \cos n\theta \cdot \tan(k+1)\theta] \tag{3.37}$$

Substituting Eq. (3.37) into Eq. (3.32) and performing rather cumbersome trigonometric transformations, we arrive at the following equation for θ:

$$\tan k\theta = -\tan\frac{\theta}{2} \tag{3.38}$$

The periodic properties of the tangent function in Eq. (3.38) mean that it has $k + 1$ different roots corresponding to intersection points of the curves $z = \tan k\theta$ and $z = -\tan\theta/2$. For the case $k = 4$, considered below as an example, these points are shown in Fig. 3.18. Further transformation allows us

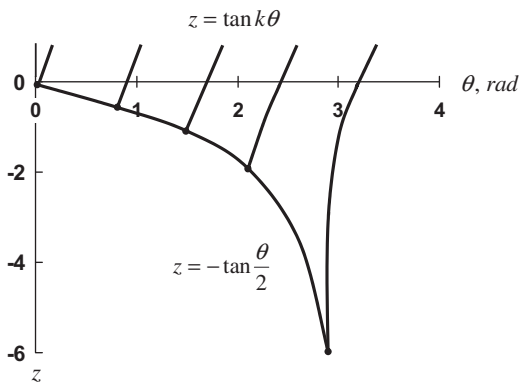


FIGURE 3.18

Geometric interpretation of Eq. (3.38) for $k = 4$.

to reduce Eq. (3.38) to

$$\sin\frac{2k+1}{2}\theta = 0$$

from which it follows that

$$\theta_i = \frac{2\pi i}{2k+1} \quad (i = 0,\ 1,\ 2\ \ldots\ k) \tag{3.39}$$

The first root, $\theta_0 = 0$, corresponds to $\lambda = 0$ and $F_n = const$, i.e., to a ply without a crack in the central fiber. So, Eq. (3.39) specifies k roots ($i = 1,\ 2,\ 3,\ \ldots,\ k$) for the ply under study, and the solution in Eqs. (3.29) and (3.37) can be generalized as

$$F_n(\overline{x}) = \sum_{i=1}^{k} C_i\left[\sin n\theta_i - \cos n\theta_i \bullet \tan\,(k+1)\theta_i\right] e^{-\lambda_i \overline{x}} \tag{3.40}$$

where, in accordance with Eq. (3.36),

$$\lambda_i = 2\mu \sin\frac{\theta_i}{2} \tag{3.41}$$

and θ_i is determined by Eq. (3.39).

Using Eq. (3.38), we can transform Eq. (3.40) to the following final form:

$$F_n(\overline{x}) = \sum_{i=1}^{k} C_i S_n(\theta_i) e^{-\lambda_i \overline{x}} \tag{3.42}$$

where

$$S_n(\theta_i) = \frac{\sin\dfrac{2n-1}{2}\theta_i}{\cos\dfrac{\theta_i}{2}} \tag{3.43}$$

Applying Eqs. (3.25) and (3.26), we can find shear and normal stresses, i.e.,

$$\tau_n(\overline{x}) = -\frac{1}{a}\sum_{i=1}^{k} \lambda_i C_i S_n(\theta_i) e^{-\lambda_i \overline{x}} \quad (n = 1,\ 2,\ 3\ldots\ k) \tag{3.44}$$

$$\sigma_k(\overline{x}) = \sigma + \frac{1}{a_f}\sum_{i=1}^{k} C_i S_k(\theta_i) e^{-\lambda_i \overline{x}} \tag{3.45}$$

$$\sigma_n(\overline{x}) = \sigma - \frac{1}{a_f}\sum_{i=1}^{k} C_i\left[S_{n+1}(\theta_i) - S_n(\theta_i)\right] e^{-\lambda_i \overline{x}} \quad (n = 1,\ 2,\ 3,\ 4\ \ldots\ k-1) \tag{3.46}$$

$$\sigma_0(\overline{x}) = \sigma - \frac{2}{a_f}\sum_{i=1}^{k} C_i S_1(\theta_i) e^{-\lambda_i \overline{x}} \tag{3.47}$$

Displacements can be determined with the aid of Eqs. (3.19), (3.21), and (3.25). Changing x for $\bar{x} = x/a$, we get

$$u_n(\bar{x}) = \frac{a_m}{aG_m} F_n'(\bar{x}) + u_{n-1}(\bar{x})$$

For the first fiber ($n = 1$), we have

$$u_1(\bar{x}) = \frac{a_m}{aG_m} F_1'(\bar{x}) + u_0(\bar{x})$$

Substituting Eq. (3.42) into these equations, we arrive at

$$u_n(\bar{x}) = -\frac{a_m}{aG_m} \sum_{i=1}^{k} C_i \lambda_i S_n(\theta_i) e^{-\lambda_i \bar{x}} + u_{n-1}(\bar{x}) \quad (n = 2,\ 3,\ 4 \ldots k) \tag{3.48}$$

$$u_1(\bar{x}) = -\frac{a_m}{aG_m} \sum_{i=1}^{k} C_i \lambda_i S_1(\theta_i) e^{-\lambda_i \bar{x}} + u_0(\bar{x}) \tag{3.49}$$

To determine coefficients C_i, we should apply the boundary conditions and write Eqs. (3.23) and (3.24) in the explicit form using Eqs. (3.47)–(3.49). Substituting S_n from Eq. (3.43) and λ_i from Eq. (3.41), we have

$$\sum_{i=1}^{k} C_i \tan\frac{\theta_i}{2} = \frac{\sigma a_f}{2}$$

$$\sum_{i=1}^{k} C_i \tan\frac{\theta_i}{2} \sin\frac{2n-1}{2}\theta_i = 0 \quad (n = 2,\ 3,\ 4 \ldots k)$$

$$\sum_{i=1}^{k} C_i \tan\frac{\theta_i}{2} \sin\frac{\theta_i}{2} = \frac{aG_m}{2\mu a_m} u_0(0)$$

Introducing new coefficients

$$D_i = C_i \tan\frac{\theta_i}{2} \tag{3.50}$$

we arrive at the final form of the boundary conditions, i.e.,

$$\sum_{i=1}^{k} D_i = \frac{\sigma a_f}{2} \tag{3.51}$$

$$\sum_{i=1}^{k} D_i \sin\frac{2n-1}{2}\theta_i = 0 \quad (n = 2,\ 3,\ 4 \ldots k) \tag{3.52}$$

$$\sum_{i=1}^{k} D_i \sin\frac{\theta_i}{2} = \frac{aG_m}{2\mu a_m} u_0(0) \tag{3.53}$$

This set contains $k + 1$ equations and includes k unknown coefficients D_i and displacement $u_0(0)$.

The foregoing set of equations allows us to obtain the exact analytical solution for any number of fibers, k. To find this solution, some transformations are required. First, multiply Eq. (3.52) by $\sin[(2n-1)\theta_s/2]$ and sum up all the equations from $n=2$ to $n=k$. Adding Eq. (3.53) for $n=1$ multiplied by $\sin(\theta_s/2)$, we obtain

$$\sum_{n=1}^{k}\sum_{i=1}^{k} D_i \sin\frac{2n-1}{2}\theta_i \sin\frac{2n-1}{2}\theta_s = \frac{aG_m}{2\mu a_m}u_0(0)\sin\frac{\theta_s}{2}$$

Now the sequence of summation can be changed, as follows

$$\sum_{i=1}^{k} D_i \sum_{n=1}^{k} \sin\frac{2n-1}{2}\theta_i \sin\frac{2n-1}{2}\theta_s = \frac{aG_m}{2\mu a_m}u_0(0)\sin\frac{\theta_s}{2} \tag{3.54}$$

Using the following known series

$$\sum_{n=1}^{k}\cos(2n-1)\theta = \frac{\sin 2k\theta}{2\sin\theta}$$

we get in several steps

$$\begin{aligned}
R_{is} &= \sum_{n=1}^{k} \sin\frac{2n-1}{2}\theta_i \sin\frac{2n-1}{2}\theta_s \\
&= \frac{1}{2}\sum_{n=1}^{k}\left[\cos\frac{2n-1}{2}(\theta_i-\theta_s) - \cos\frac{2n-1}{2}(\theta_i+\theta_s)\right] \\
&= \frac{1}{4}\left[\frac{\sin k(\theta_i-\theta_s)}{\sin\frac{1}{2}(\theta_i-\theta_s)} - \frac{\sin k(\theta_i+\theta_s)}{\sin\frac{1}{2}(\theta_i+\theta_s)}\right] \\
&= \frac{\cos\frac{\theta_i}{2}\cos k\theta_i \cos\frac{\theta_s}{2}\cos k\theta_s}{\cos\theta_s - \cos\theta_i}\left(\tan k\theta_i \tan\frac{\theta_i}{2} - \tan k\theta_s \tan\frac{\theta_s}{2}\right)
\end{aligned}$$

Using Eq. (3.38), we can conclude that $R_{is}=0$ for $i \neq s$. For the case $i=s$, we have

$$R_{ss} = \sum_{n=1}^{k}\sin^2\frac{2n-1}{2}\theta_s = \frac{1}{2}\sum_{n=1}^{k}[1-\cos(2n-1)\theta_s] = \frac{1}{2}\left(k - \frac{\sin 2k\theta_s}{2\sin\theta_s}\right)$$

As a result, Eq. (3.54) yields

$$D_s = \frac{2aG_m u_0(0)\sin\frac{\theta_s}{2}\sin\theta_s}{\mu a_m(2k\sin\theta_s - \sin 2k\theta_s)} \quad (s=1,\ 2,\ 3\ \ldots k) \tag{3.55}$$

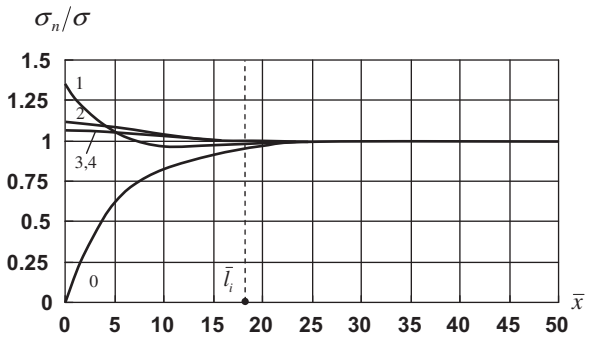


FIGURE 3.19

Distribution of normal stresses along the fibers $n = 0, 1, 2, 3, 4$ for $k = 4$, $E_f = 250$ GPa, $G_m = 1$ GPa.

Substituting these coefficients into Eq. (3.51), we can find $u_0(0)$, i.e.,

$$u_0(0) = \frac{\sigma \mu a_f a_m}{4aG_m} \left(\sum_{i=1}^{k} \frac{\sin \frac{\theta_i}{2} \sin \theta_i}{2k \sin \theta_i - \sin 2k\theta_i} \right)^{-1} \tag{3.56}$$

Thus, the solution for the problem under study is specified by Eqs. (3.44)–(3.50), (3.55), and (3.56).

For example, consider a carbon-epoxy ply with the following parameters: $E_f = 250$ GPa, $G_m = 1$ GPa, $\upsilon_f = 0.6$, and $k = 4$. The distribution of the normalized stresses in the fibers along the ply is shown in Fig. 3.19, whereas the same distribution of shear stresses in the matrix is presented in Fig. 3.20. As can be seen, in the vicinity of the crack in the central fiber, the load carried by this fiber is transmitted by shear through the matrix to adjacent fibers. At a distance from the end of the fiber, greater than $\bar{l}_i$, the stress in the broken fiber becomes close to σ, and for $\bar{x} > \bar{l}_i$, the fiber behaves as if there is no crack. A portion of the broken fiber corresponding to $0 \le \bar{x} \le \bar{l}_i$ is not fully effective in resisting the applied load, and $l_i = \bar{l}_i a$ is referred to as the fiber ineffective length. Since the fiber defects are randomly distributed along its length, their influence on the strength of the ply is minimal if there are no other defects in the central fiber and its adjacent fibers within distance l_i from the crack. To minimize the probability of such defects, we should minimize l_i which depends on fiber and matrix stiffness and material microstructure.

To evaluate l_i, consider Eq. (3.47) and assume that $\sigma_0(\bar{x})$ becomes close to σ if

$$e^{-\lambda_i \bar{l}_i} = k$$

where k is some small parameter indicating how close $\sigma_0(\bar{x})$ should be to σ to neglect the difference between them (as a matter of fact, this difference vanishes only for $\bar{x} \to \infty$). Taking approximately $\lambda_i = 2\mu$ in accordance with Eq. (3.41) and using Eq. (3.28) specifying μ, we arrive at

$$\bar{l}_i = -\frac{1}{2} \ln k \cdot \sqrt{\upsilon_f (1 - \upsilon_f) \frac{E_f}{G_m}}$$

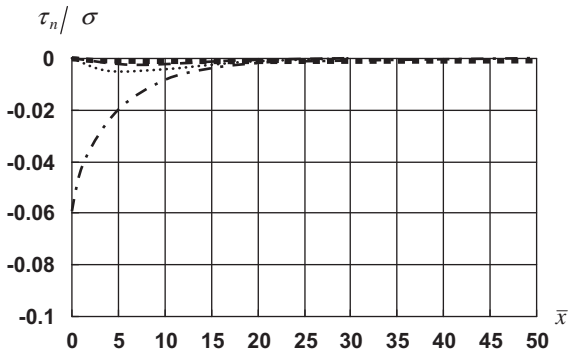


FIGURE 3.20

Distribution of shear stresses along the fibers for $k = 4$, $E_f = 250$ GPa, $G_m = 1$ GPa.
Numbers of the matrix layers:

- $n = 1$;
- $n = 2$;
- $n = 3$;
- $n = 4$.

For $k = 0.01$, we get

$$l_i = 2.3a \cdot \sqrt{\upsilon_f(1-\upsilon_f)\frac{E_f}{G_m}} \tag{3.57}$$

For a typical carbon-epoxy ply (see Fig. 3.19) with $a = 0.016$ mm and $\upsilon_f = 0.6$, Eq. (3.57) yields 0.29 mm.

Thus, for real composites, the length l_i is very small, and this explains why a unidirectional composite demonstrates much higher strength in longitudinal tension than a dry bundle of fibers (see Table 3.3). Reducing G_m, i.e., the matrix stiffness, we increase the fiber ineffective length which becomes infinitely large for $G_m \to 0$. This effect is demonstrated in Fig. 3.21 which corresponds to a material whose matrix shear stiffness is much lower than that in the foregoing example (see Fig. 3.19). For this case, $\bar{l}_i = 50$, and Eq. (3.57) yields $l_i = 0.8$ mm. The distribution of shear stresses in this material is shown in Fig. 3.22. Experiments with unidirectional glass-epoxy composites ($E_f = 86.8$ GPa, $\upsilon_f = 0.68$, and $a = 0.015$) have shown that reduction of the matrix shear modulus from 1.08 GPa ($l_i = 0.14$ mm) to 0.037 GPa ($l_i = 0.78$ mm) results in reduction of longitudinal tensile strength from 2010 MPa to 1290 MPa, i.e., by 35.8% (Chiao, 1979).

The ineffective length of a fiber in a matrix can be found experimentally by using the single-fiber fragmentation test. For this test, a fiber is embedded in a matrix, and tensile load is applied to the fiber through the matrix until the fiber breaks. Further loading results in fiber fragmentation, and the length of the fiber fragment that no longer breaks is the fiber ineffective length. For a carbon fiber in epoxy matrix, $l_i = 0.3$ mm (Fukuda et al., 1993).

According to the foregoing reasoning, it looks as though the stiffness of the matrix should be as high as possible. However, there exists an upper limit of this stiffness. Comparing Figs. 3.20 and 3.22,

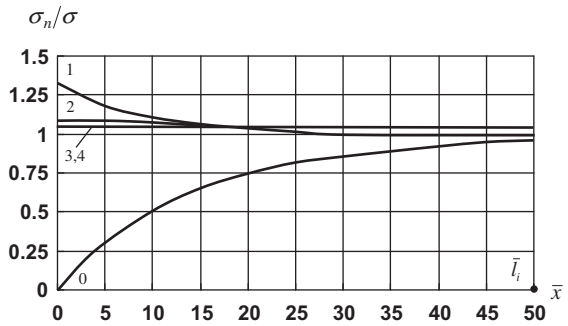


FIGURE 3.21

Distribution of normal stresses along the fibers $n = 0, 1, 2, 3, 4$ for $k = 4$, $E_f = 250$ GPa, $G_m = 0.125$ GPa.

we can see that the higher the value of G_m, the higher is the shear stress concentration in the matrix in the vicinity of the crack. If the maximum shear stress, τ_m, acting in the matrix reaches its ultimate value, $\overline{\tau}_m$, delamination will occur between the matrix layer and the fiber, and the matrix will not transfer the load from the broken fiber to the adjacent ones. This maximum shear stress depends on the fiber stiffness – the lower the fiber modulus, the higher the value of τ_m. This is shown in Figs. 3.23 and 3.24, where shear stress distributions are presented for aramid fibers ($E_f = 150$ GPa) and glass fibers ($E_f = 90$ GPa), respectively.

Finally, it should be emphasized that the plane model of a ply, considered in this section (see Fig. 3.15), provides only qualitative results concerning fibers and matrix interaction. In real materials,

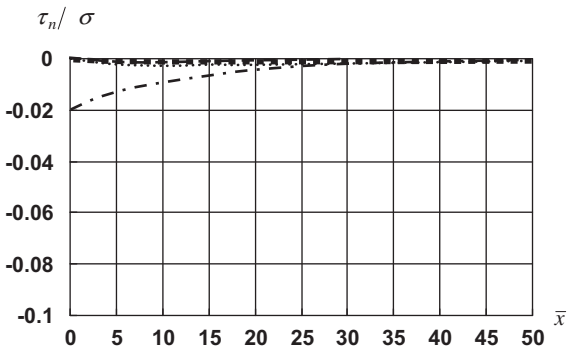


FIGURE 3.22

Distribution of shear stresses along the fibers for $k = 4$, $E_f = 250$ GPa, $G_m = 0.125$ GPa. Numbers of the matrix layers:

– · – · – $n = 1$;
····· $n = 2$;
– – – – $n = 3$;
■ ■ ■ ■ ■ ■ $n = 4$.

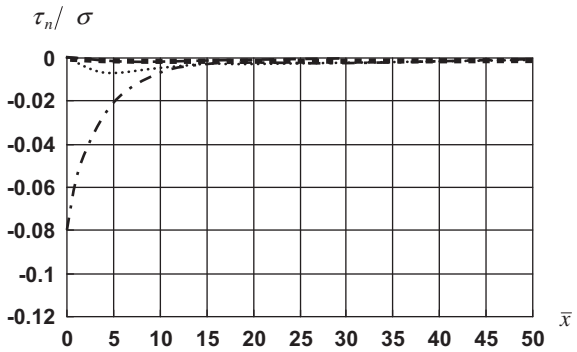


FIGURE 3.23

Distribution of shear stresses along the fibers for $k = 4$, $E_f = 150$ GPa, $G_m = 1$ GPa. Numbers of the matrix layers:

$n = 1$;
$n = 2$;
$n = 3$;
$n = 4$.

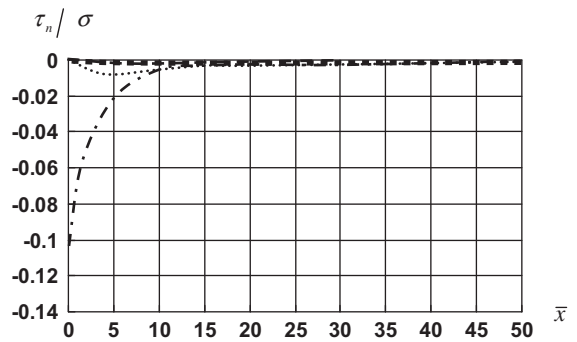


FIGURE 3.24

Distribution of shear stresses along the fibers for $k = 4$, $E_f = 90$ GPa, $G_m = 1$ GPa. Numbers of the matrix layers:

$n = 1$;
$n = 2$;
$n = 3$;
$n = 4$.

a broken fiber is surrounded with more than two fibers (at least five or six as can be seen in Fig. 3.2), so the stress concentration in these fibers and in the matrix is much lower than would be predicted by the foregoing analysis. For a hexagonal fiber distribution (see Fig. 3.4), the stress concentration factor for the fibers does not exceed 1.105 (Tikhomirov and Yushanov, 1980). The effect of fiber breakage on tensile strength of unidirectional composites has been studied by Abu-Farsakh et al. (2000).

3.2.4 Fracture toughness

Fracture toughness is a very important characteristic of a structural material indicating resistance of a material to cracks and governed by the work needed to fracture a material (work of fracture). It is well known that there exist brittle and ductile metal alloys, whose typical stress-strain diagrams are shown in Fig. 3.25. Comparing alloys with one and the same basic metal (e.g., steel alloys), we can see that while brittle alloys have higher strength, $\overline{\sigma}$, ductile alloys have higher ultimate elongation, $\overline{\varepsilon}$, and, as a result, higher work of fracture that is proportional to the area under the stress-strain diagram. Though brittle materials have, in general, higher strength, they are sensitive to cracks that, by propagating, can cause material failure for a stress that is much lower than the static strength. That is why design engineers usually prefer ductile materials with lower strength but higher fracture toughness. A typical dependence of fracture toughness on static strength for metals is shown in Fig. 3.26 (line 1). For composites, this dependence is entirely different (line 2) – a higher static strength corresponds usually to higher fracture toughness (Mileiko, 1982). This phenomenon is demonstrated for a unidirectional boron-aluminum composite in Fig. 3.27 (Mileiko, 1982). As can be seen, an increase in fiber volume fraction, v_f, results not only in higher static strength along the fibers (line 1), which is quite natural, but also is accompanied by an increase in the work of fracture (curve 2) and, consequently, in an increase in the material fatigue strength (bending under 10^6 cycles, line 3), which shows a material's sensitivity to cracks.

The reason for such a specific behavior in composite materials is associated with their inhomogeneous microstructure, particularly with fiber-matrix interfaces that restrain free propagation of a crack (see Fig. 3.28). Of some importance are also fiber defects, local delaminations, and fiber strength deviation, which reduce the static strength but increase the fracture toughness. As a result, by

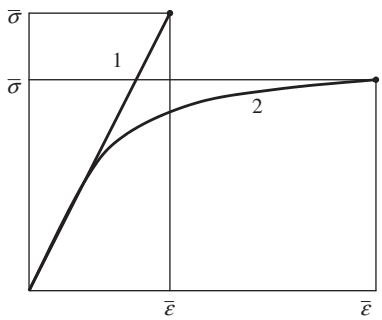


FIGURE 3.25

Typical stress-strain diagrams of brittle (1) and ductile (2) metal alloys.

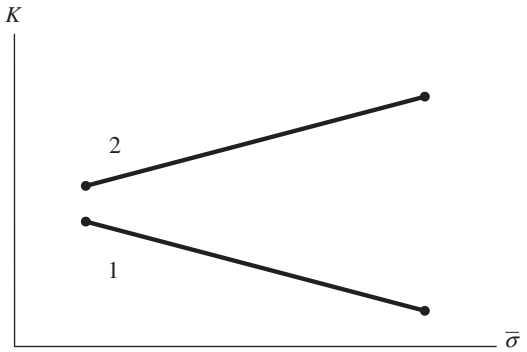


FIGURE 3.26

Typical relations between fracture toughness (K) and strength ($\overline{\sigma}$) for metals (1) and composites (2).

combining brittle fibers and brittle matrix, we usually arrive at a composite material whose fracture toughness is higher than that of its constituents.

Thus, we can conclude that composites comprise a new class of structural materials that are entirely different from traditional man-made materials for several reasons. Firstly, using thin fibers, we make an attempt to utilize the high strength capacity that is naturally inherent in all the materials. Secondly, this utilization is provided by the matrix material, which increases the fiber performance and makes it possible to manufacture composite structures. Thirdly, combination of fibers and matrices can result in new qualities of composite materials that are not inherent either in individual fibers or in the matrices,

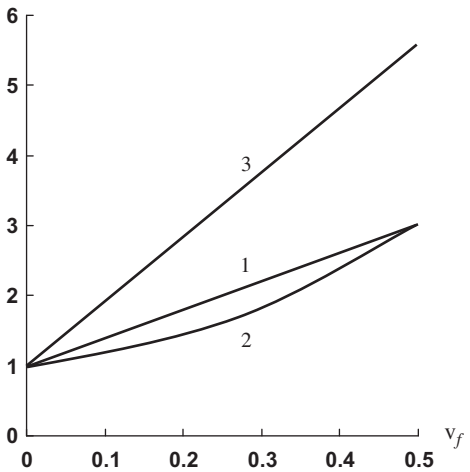


FIGURE 3.27

Dependence of static strength (1), work of fracture (2), and fatigue strength (3) on fiber volume fraction for a boron-aluminum composite material.

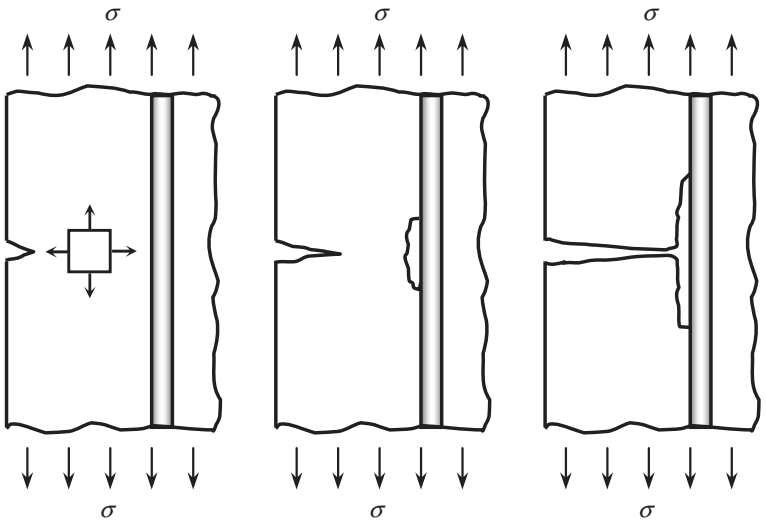


FIGURE 3.28

Mechanism of the crack stopping at the fiber-matrix interface.

and are not described by the laws of mechanical mixtures. For example, as noted above, brittle fiber and matrix materials, both having low fracture toughness on their own, can provide a heterogeneous composite material with higher fracture toughness.

3.3 MICROMECHANICS OF A PLY

Consider a unidirectional composite ply under the action of in-plane normal and shear stresses as in Fig. 3.29. Since the normal stresses do not change the right angle between axes 1 and 2, and shear stresses do not cause elongations in the longitudinal and transverse directions 1 and 2, the ply is

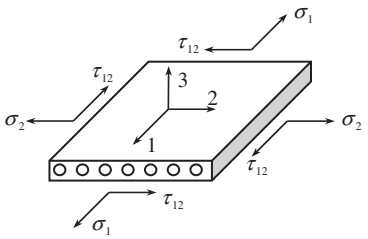


FIGURE 3.29

A unidirectional ply under in-plane loading.

orthotropic, and the corresponding constitutive equations, Eqs. (2.48) and (2.53), yield for the case under study

$$\begin{aligned}\varepsilon_1 &= \frac{\sigma_1}{E_1} - \nu_{12}\frac{\sigma_2}{E_2}\\ \varepsilon_2 &= \frac{\sigma_2}{E_2} - \nu_{21}\frac{\sigma_1}{E_1}\\ \gamma_{12} &= \frac{1}{G_{12}}\tau_{12}\end{aligned} \tag{3.58}$$

The inverse form of these equations is

$$\begin{aligned}\sigma_1 &= \overline{E}_1\left(\varepsilon_1 + \nu_{12}\varepsilon_2\right)\\ \sigma_2 &= \overline{E}_2\left(\varepsilon_2 + \nu_{21}\varepsilon_1\right)\\ \tau_{12} &= G_{12}\gamma_{12}\end{aligned} \tag{3.59}$$

where

$$\overline{E}_{1,2} = \frac{E_{1,2}}{1 - \nu_{12}\,\nu_{21}}$$

and the following symmetry condition is valid

$$E_1\nu_{12} = E_2\,\nu_{21} \tag{3.60}$$

The constitutive equations, Eqs. (3.58) and (3.59), include effective or apparent longitudinal, E_1, transverse, E_2, and shear, G_{12}, moduli of a ply and Poisson's ratios ν_{12} and ν_{21}, only one of which is independent, since the second one can be found from Eq. (3.60).

The elastic constants, E_1, E_2, and G_{12}, and ν_{12} or ν_{21}, are governed by fibers and matrix properties and the ply microstructure, i.e., the shape and size of the fibers' cross-sections, fiber volume fraction, distribution of fibers in the ply. The task of micromechanics is to derive the corresponding governing relationships, i.e., to establish the relation between the properties of a unidirectional ply and those of its constituents.

To achieve this, we should first know the mechanical characteristics of the fibers and the matrix material of the ply. To determine the matrix modulus, E_m, its Poisson's ratio, ν_m, and strength, $\overline{\sigma}_m$, conventional material specimens and testing procedures can be used (see Figs. 3.30 and 3.31). The shear modulus, G_m, can be calculated with the aid of Eq. (2.57). To find the fibers' properties is a more complicated problem. There exist several methods to test elementary fibers by bending or stretching 10–30 mm long fiber segments. All of them are rather specific because of the small (about 0.01 mm)



FIGURE 3.30

Specimens of matrix material.

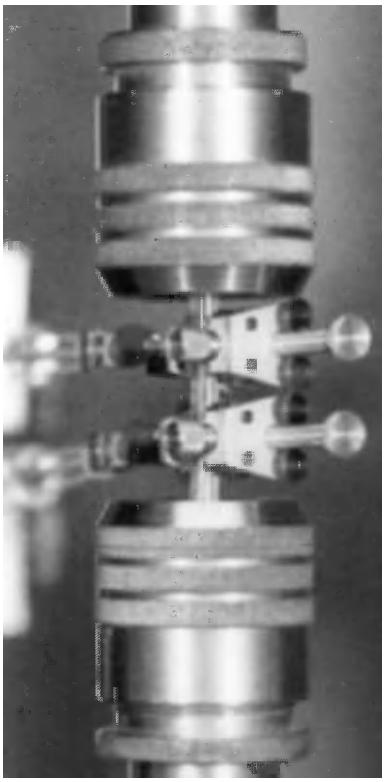


FIGURE 3.31

Testing of the matrix specimen.

fiber diameter, and, more important, the fiber properties in a composite material can be different from those of individual fibers (see Section 3.2.3) with the preassigned lengths provided by these methods.

It is worth knowing a fiber's actual modulus and strength, not only for micromechanics but also to check the fiber's quality before it is used to fabricate a composite part. For this purpose, a simple and reliable method has been developed to test the fibers in simulated actual conditions. According to this method, a fine tow or an assembly of fibers is carefully impregnated with resin, slightly stretched to avoid fiber waviness, and cured to provide a specimen of the so-called microcomposite material. The microcomposite strand is overwrapped over two discs as in Fig. 3.32, or fixed in special friction grips as in Fig. 3.33, and tested under tension to determine the ultimate tensile force $\overline{F}$ and strain ε corresponding to some force $F < \overline{F}$. Then, the resin is removed by burning it out, and the mass of fibers being divided by the strand length and fiber density yields the cross-sectional area of fibers in the strand, A_f. Fiber strength and modulus can be calculated as

$$\overline{\sigma}_f = \frac{\overline{F}}{A_f}, \quad E_f = \frac{F}{A_f \varepsilon}$$

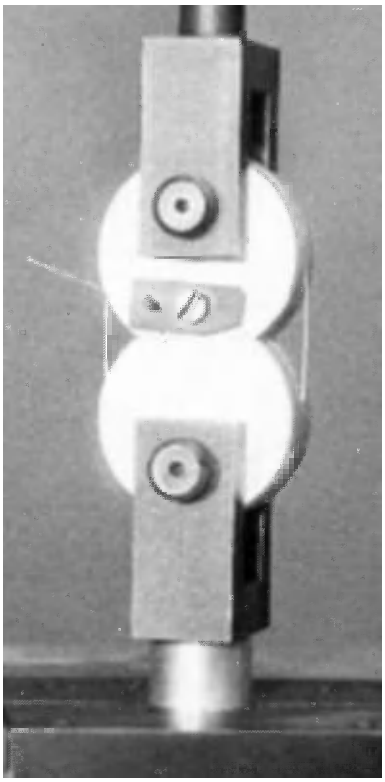


FIGURE 3.32

Testing of a microcomposite specimen overwrapped over discs.

In addition to fiber and matrix mechanical properties, micromechanical analysis requires information about the ply microstructure. Depending on the level of this information, there exist micromechanical models of different levels of complexity.

The simplest or zero-order model of a ply is a monotropic model ignoring the strength and stiffness of the matrix and assuming that the ply works only in the fiber direction. Taking $E_2 = 0$ and $G_{12} = 0$ in Eqs. (3.59) and putting $\nu_{12} = 0$ in accordance with Eq. (3.60), we arrive at the following equations describing this model:

$$\sigma_1 = E_1\varepsilon_1, \quad \sigma_2 = 0, \quad \tau_{12} = 0 \tag{3.61}$$

in which $E_1 = E_f v_f$. Being very simple and too approximate to be used in the stress-strain analysis of composite structures, Eqs. (3.61) are extremely efficient for the design of optimal composite structures in which the loads are carried mainly by the fibers (see Chapter 12).

First-order models allow for the matrix stiffness but require only one structural parameter to be specified: fiber volume fraction, v_f. Since the fiber distribution in the ply is not important for these models, the ply can be presented as a system of strips (shown in Fig. 3.34, simulating fibers (shaded

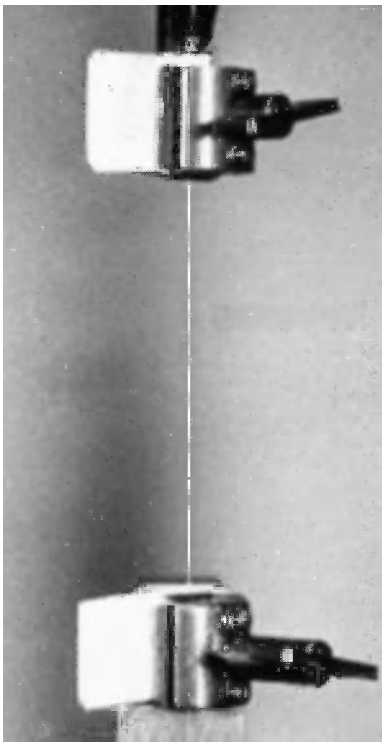


FIGURE 3.33

Testing of a microcomposite specimen gripped at the ends.

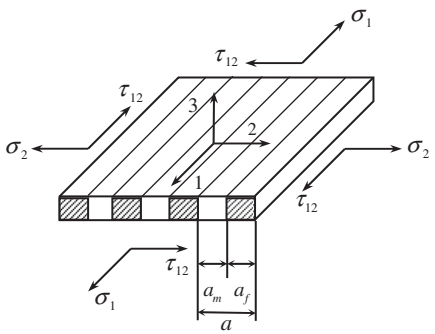


FIGURE 3.34

A first-order model of a unidirectional ply.

areas) and matrix (light areas)). The structural parameters of the model can be expressed in terms of fiber and matrix volume fractions only, i.e.,

$$\frac{a_f}{a} = v_f, \quad \frac{a_m}{a} = v_m, \quad v_f + v_m = 1 \tag{3.62}$$

Suppose that the ply is under in-plane loading with some effective stresses σ_1, σ_2, and τ_{12} as in Fig. 3.34, and find the corresponding effective elastic constants E_1, E_2, G_{12}, ν_{12}, and ν_{21} entering Eqs. (3.58). Constitutive equations for isotropic fiber and matrix strips can be written as

$$\begin{aligned}
\varepsilon_1^{f,m} &= \frac{1}{E_{f,m}}\left(\sigma_1^{f,m} - \nu_{f,m}\sigma_2^{f,m}\right) \\
\varepsilon_2^{f,m} &= \frac{1}{E_{f,m}}\left(\sigma_2^{f,m} - \nu_{f,m}\sigma_1^{f,m}\right) \\
\gamma_{12}^{f,m} &= \frac{1}{G_{f,m}}\tau_{12}^{f,m}
\end{aligned} \tag{3.63}$$

Here, f and m indices correspond, as earlier, to fibers and matrix, respectively.

Let us make some assumptions concerning the model behavior. First, it is natural to assume that effective stress resultant $\sigma_1 a$ is distributed between fiber and matrix strips and that the longitudinal strains of these strips are the same as the effective (apparent) longitudinal strain of the ply, ε_1, i.e.,

$$\sigma_1 a = \sigma_1^f a_f + \sigma_1^m a_m \tag{3.64}$$

$$\varepsilon_1^f = \varepsilon_1^m = \varepsilon_1 \tag{3.65}$$

Second, as can be seen in Fig. 3.34, under transverse tension the stresses in the strips are the same and are equal to the effective stress σ_2, whereas the ply elongation in the transverse direction is the sum of the fiber and matrix strips' elongations, i.e.,

$$\sigma_2^f = \sigma_2^m = \sigma_2 \tag{3.66}$$

$$\Delta a = \Delta a_f + \Delta a_m \tag{3.67}$$

Introducing transverse strains

$$\varepsilon_2 = \frac{\Delta a}{a}, \quad \varepsilon_2^f = \frac{\Delta a_f}{a_f}, \quad \varepsilon_2^m = \frac{\Delta a_m}{a_m}$$

we can write Eq. (3.67) in the following form:

$$\varepsilon_2 a = \varepsilon_2^f a_f + \varepsilon_2^m a_m \tag{3.68}$$

The same assumptions can be made for shear stresses and strains, so that

$$\tau_{12}^f = \tau_{12}^m = \tau_{12} \tag{3.69}$$

$$\gamma_{12} a = \gamma_{12}^f a_f + \gamma_{12}^m a_m \tag{3.70}$$

With due regard to Eqs. (3.65), (3.66), and (3.69), constitutive equations, Eqs. (3.63) can be reduced to

$$\varepsilon_1 = \frac{1}{E_f}\left(\sigma_1^f - \nu_f\sigma_2\right), \quad \varepsilon_1 = \frac{1}{E_m}\left(\sigma_1^m - \nu_m\sigma_2\right) \tag{3.71}$$

$$\varepsilon_2^f = \frac{1}{E_f}\left(\sigma_2 - \nu_f\sigma_1^f\right), \quad \varepsilon_2^m = \frac{1}{E_m}\left(\sigma_2 - \nu_m\sigma_1^m\right) \tag{3.72}$$

$$\gamma_{12}^f = \frac{1}{G_f}\tau_{12}, \quad \gamma_{12}^m = \frac{1}{G_m}\tau_{12} \tag{3.73}$$

The first two equations, Eqs. (3.71), allow us to find longitudinal stresses, i.e.,

$$\sigma_1^f = E_f\varepsilon_1 + \nu_f\sigma_2, \quad \sigma_1^m = E_m\varepsilon_1 + \nu_m\sigma_2 \tag{3.74}$$

Equilibrium equation, Eq. (3.64), can be rearranged with the aid of Eqs. (3.62) to the form

$$\sigma_1 = \sigma_1^f\upsilon_f + \sigma_1^m\upsilon_m \tag{3.75}$$

Substituting Eqs. (3.74) into this equation, we can express ε_1 in terms of σ_1 and σ_2. Combining this result with the first constitutive equation in Eqs. (3.58), we arrive at

$$E_1 = E_f\upsilon_f + E_m\upsilon_m \tag{3.76}$$

$$\frac{\nu_{12}}{E_2} = \frac{\nu_f\upsilon_f + \nu_m\upsilon_m}{E_f\upsilon_f + E_m\upsilon_m} \tag{3.77}$$

The first of these equations specifies the apparent longitudinal modulus of the ply and corresponds to the so-called rule of mixtures, according to which the property of a composite can be calculated as the sum of its constituent material properties multiplied by the corresponding volume fractions.

Now consider Eq. (3.68) that can be written as

$$\varepsilon_2 = \varepsilon_2^f\upsilon_f + \varepsilon_2^m\upsilon_m$$

Substituting strains ε_2^f and ε_2^m from Eqs. (3.72), stresses σ_1^f and σ_1^m from Eqs. (3.74), and ε_1 from Eqs. (3.58) with due regard to Eqs. (3.76) and (3.77), we can express ε_2 in terms of σ_1 and σ_2. Comparing this expression with the second constitutive equation in Eqs. (3.58), we get

$$\frac{1}{E_2} = \frac{\upsilon_f}{E_f} + \frac{\upsilon_m}{E_m} - \frac{\upsilon_f\upsilon_m\left(E_f\nu_m - E_m\nu_f\right)^2}{E_fE_m\left(E_f\upsilon_f + E_m\upsilon_m\right)} \tag{3.78}$$

$$\frac{\nu_{21}}{E_1} = \frac{\nu_f\upsilon_f + \nu_m\upsilon_m}{E_f\upsilon_f + E_m\upsilon_m} \tag{3.79}$$

Using Eqs. (3.76) and (3.79), we have

$$\nu_{21} = \nu_f\upsilon_f + \nu_m\upsilon_m \tag{3.80}$$

This result corresponds to the rule of mixtures. The second Poisson's ratio can be found from Eqs. (3.77) and (3.78). Finally, Eqs. (3.58), (3.70), and (3.73) yield the apparent shear modulus

$$\frac{1}{G_{12}} = \frac{v_f}{G_f} + \frac{v_m}{G_m} \tag{3.81}$$

This expression can be derived from the rule of mixtures if we use compliance coefficients instead of stiffness, as in Eq. (3.76).

Since the fiber modulus is typically many times greater than the matrix modulus, Eqs. (3.76), (3.78), and (3.81) can be simplified, neglecting small terms, and presented in the following approximate form:

$$E_1 = E_f v_f, \quad E_2 = \frac{E_m}{v_m(1-\nu_m^2)}, \quad G_{12} = \frac{G_m}{v_m}$$

Only two of the foregoing expressions, namely Eq. (3.76) for E_1 and Eq. (3.80) for ν_{21}, both following from the rule of mixtures, demonstrate good agreement with experimental results. Moreover, expressions analogous to Eqs. (3.76) and (3.80) follow practically from the numerous studies based on different micromechanical models. Comparison of predicted and experimental results is presented in Figs. 3.35–3.37, where theoretical dependencies of normalized moduli on the fiber volume fraction are shown with lines. The dots correspond to the test data for epoxy composites reinforced with different fibers that have been measured by the authors or taken from publications of Tarnopol'skii and Roze (1969), Kondo and Aoki (1982), and Lee et al. (1995). As can be seen in Fig. 3.35, not only the first-order model, Eq. (3.76), but also the zero-order model, Eqs. (3.61), provide fair predictions for E_1, whereas Figs. 3.36 and 3.37 for E_2 and G_{12} call for an improvement to the first-order model (the corresponding results are shown with solid lines).

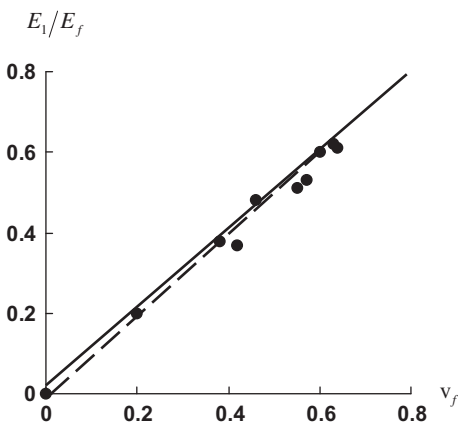


FIGURE 3.35

Dependence of the normalized longitudinal modulus on fiber volume fraction
– – – zero-order model, Eq. (3.61);
——— first-order model, Eq. (3.76);
● experimental data.

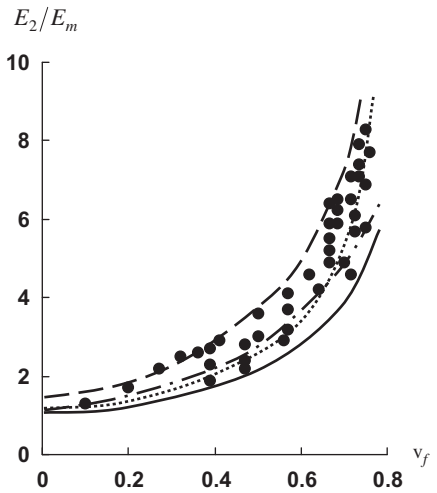


FIGURE 3.36

Dependence of the normalized transverse modulus on fiber volume fraction.
——— first-order model, Eq. (3.78);
····· second-order model, Eq. (3.89);
— · — higher-order model (elasticity solution) (Van Fo Fy , 1966);
– – – the upper bound;
● experimental data.

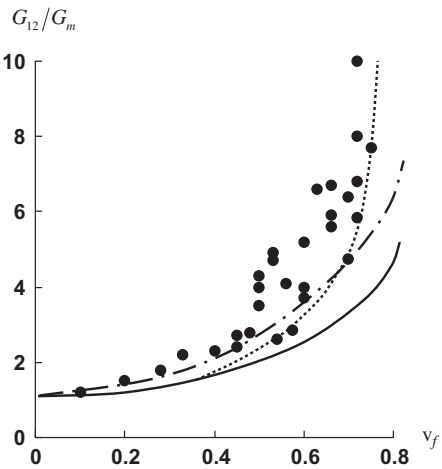


FIGURE 3.37

Dependence of the normalized in-plane shear modulus on fiber volume fraction.
——— first-order model, Eq. (3.81);
····· second-order model, Eq. (3.90);
— · — higher-order model (elasticity solution) (Van Fo Fy , 1966);
● experimental data.

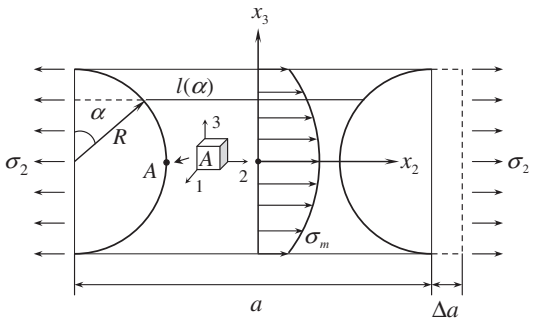


FIGURE 3.38

Microstructural model of the second order.

Second-order models allow for the fiber shape and distribution, but in contrast to higher-order models, ignore the complicated stressed state in the fibers and matrix under loading of the ply as shown in Fig. 3.29. To demonstrate this approach, consider a layer-wise fiber distribution (see Fig. 3.5) and assume that the fibers are absolutely rigid and the matrix is in the simplest uniaxial stressed state under transverse tension. The typical element of this model is shown in Fig. 3.38 from which we can obtain the following equation:

$$v_f = \frac{\pi R^2}{2Ra} = \frac{\pi R}{2a} \tag{3.82}$$

Since $2R < a$, $v_f < \pi/4 = 0.785$. The equilibrium condition yields

$$2R\sigma_2 = \int_{-R}^{R} \sigma_m \mathrm{d}x_3 \tag{3.83}$$

where $x_3 = R\cos\alpha$ and σ_2 is some average transverse stress that induces average strain

$$\varepsilon_2 = \frac{\Delta a}{a} \tag{3.84}$$

such that the effective (apparent) transverse modulus is calculated as

$$E_2 = \frac{\sigma_2}{\varepsilon_2} \tag{3.85}$$

The strain in the matrix can be determined with the aid of Fig. 3.38 and Eq. (3.84), i.e.,

$$\varepsilon_m = \frac{\Delta a}{l(\alpha)} = \frac{\Delta a}{a - 2R\sin\alpha} = \frac{\varepsilon_2}{1 - \lambda\sqrt{1 - \left(\frac{x_3}{R}\right)^2}} \tag{3.86}$$

where in accordance with Eq. (3.82),

$$\lambda = \frac{2R}{a} = \frac{4v_f}{\pi} \tag{3.87}$$

Assuming that there is no strain in the matrix in the fiber direction and there is no stress in the matrix in the x_3 direction, we have

$$\sigma_m = \frac{E_m \varepsilon_m}{1 - \nu_m^2} \tag{3.88}$$

Substituting σ_2 from Eq. (3.85) and σ_m from Eq. (3.88) into Eq. (3.83), and using Eq. (3.86) to express ε_m, we arrive at

$$E_2 = \frac{E_m}{2R(1 - \nu_m^2)} \int_{-R}^{R} \frac{dx_3}{1 - \lambda\sqrt{1 - \left(\frac{x_3}{R}\right)^2}}$$

Calculating the integral and taking into account Eq. (3.87), we finally get

$$E_2 = \frac{\pi E_m r(\lambda)}{2v_f(1 - \nu_m^2)} \tag{3.89}$$

where

$$r(\lambda) = \frac{1}{\sqrt{1 - \lambda^2}} \tan^{-1} \sqrt{\frac{1 + \lambda}{1 - \lambda}} - \frac{\pi}{4}$$

Similar derivation for an in-plane shear yields

$$G_{12} = \frac{\pi G_m}{2v_f} r(\lambda) \tag{3.90}$$

The dependencies of E_2 and G_{12} on the fiber volume fraction corresponding to Eqs. (3.89) and (3.90) are shown in Figs. 3.36 and 3.37 (dotted lines). As can be seen, the second-order model of a ply provides better agreement with the experimental results than the first-order model. This agreement can be further improved if we take a more realistic microstructure of the material. Consider the actual microstructure shown in Fig. 3.2 and single out a typical square element with size a as in Fig. 3.39. The dimension a should provide the same fiber volume fraction for the element as for the material under

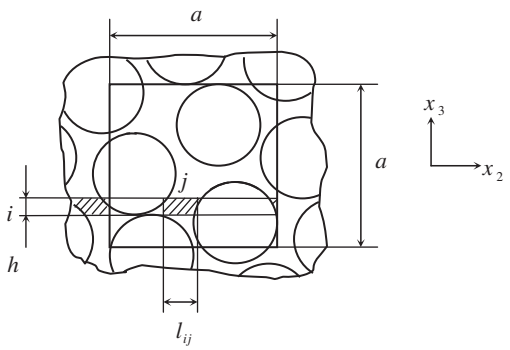


FIGURE 3.39

Typical structural element.

study. To calculate E_2, we divide the element into a system of thin ($h<<a$) strips parallel to axis x_2. The ith strip is shown in Fig. 3.39. For each strip, we measure the lengths, l_{ij}, of the matrix elements, the jth of which is shown in Fig. 3.39. Then, equations analogous to Eqs. (3.83), (3.88), and (3.86) take the form

$$\sigma_2 a = h\sum_i \sigma_m^{(i)}, \quad \sigma_m^{(i)} = \frac{E_m}{1-\nu_m^2}\varepsilon_m^{(i)}, \quad \varepsilon_m^{(i)} = \frac{\varepsilon_2 a}{\sum\limits_j l_{ij}}$$

and the final result is

$$E_2 = \frac{E_m \overline{h}}{1-\nu_m^2}\sum_i \left(\sum_j \overline{l}_{ij}\right)^{-1}$$

where $\overline{h} = h/a$, $\overline{l}_{ij} = l_{ij}/a$. The second-order models considered above can be readily generalized to account for the fiber transverse stiffness and matrix nonlinearity.

Numerous higher-order microstructural models and descriptive approaches have been proposed, including:

- Analytical solutions in the problems of elasticity for an isotropic matrix having regular inclusions: fibers or periodically spaced groups of fibers
- Numerical (finite element, finite difference methods) stress analysis of the matrix in the vicinity of fibers
- Averaging of stress and strain fields for a media filled in with regularly or randomly distributed fibers
- Asymptotic solutions of elasticity equations for inhomogeneous solids characterized by a small microstructural parameter (fiber diameter)
- Photoelasticity methods

An exact elasticity solution for a periodical system of fibers embedded in an isotropic matrix (Van Fo Fy (Vanin), 1966) is shown in Figs. 3.36 and 3.37. As can be seen, due to the high scatter in experimental data, the higher-order model does not demonstrate significant advantages with respect to elementary models.

Moreover, all the micromechanical models can hardly be used for practical analysis of composite materials and structures. The reason for this is that irrespective of how rigorous the micromechanical model is, it cannot describe adequately enough a real material microstructure governed by a particular manufacturing process, taking into account voids, microcracks, randomly damaged or misaligned fibers, and many other effects that cannot be formally reflected in a mathematical model. As a result of this, micromechanical models are mostly used for qualitative analysis, providing us with the understanding of how material microstructural parameters affect the mechanical properties rather than with quantitative information about these properties. In particular, the foregoing analysis should result in two main conclusions. First, the ply stiffness along the fibers is governed by the fibers and linearly depends on the fiber volume fraction. Second, the ply stiffness across the fibers and in shear is determined not only by the matrix (which is natural), but by the fibers as well. Although the fibers do not directly take the load applied in the transverse direction, they significantly increase the ply transverse stiffness (in comparison with the stiffness of a net matrix), acting as rigid inclusions in the

matrix. Indeed, as can be seen in Fig. 3.34, the higher the fiber fraction, a_f, the lower the matrix fraction, a_m, for the same a, and the higher stress σ_2 should be applied to the ply to cause the same transverse strain ε_2, because only matrix strips are deformable in the transverse direction.

Due to the aforementioned limitations of micromechanics, only the basic models were considered in the previous examples. Historical overview of micromechanical approaches and more detailed description of the corresponding results can be found elsewhere (Bogdanovich and Pastore, 1996; Jones, 1999).

To analyze the foregoing micromechanical models, we used the traditional approach based on direct derivation and solution of the system of equilibrium, constitutive, and strain-displacement equations. Alternatively, the same problems can be solved with the aid of variational principles discussed in Section 2.11. In their application to micromechanics, these principles allow us not only to determine the apparent stiffnesses of the ply, but also to establish the upper and the lower bounds on them.

Consider, for example, the problem of transverse tension of a ply under the action of some average stress σ_2 (see Fig. 3.29) and apply the principle of minimum strain energy (see Section 2.11.2). According to this principle, the actual stress field provides the value of the body strain energy, which is equal to or less than that of any statically admissible stress field. Equality takes place only if the admissible stress state coincides with the actual one. Excluding this case, i.e., assuming that the class of admissible fields under study does not contain the actual field, we can write the following strict inequality

$$W_\sigma^{adm} > W_\sigma^{act} \tag{3.91}$$

In the case of transverse tension, the fibers can be treated as absolutely rigid, and only the matrix strain energy needs to be taken into account. We can also neglect the energy of shear strain and consider the energy corresponding to normal strains only. With due regard to these assumptions, we use Eqs. (2.51) and (2.52) to get

$$W = \iiint\limits_{V_m} U dV_m \tag{3.92}$$

where V_m is the volume of the matrix, and

$$U = \frac{1}{2}\left(\sigma_1^m \varepsilon_1^m + \sigma_2^m \varepsilon_2^m + \sigma_3^m \varepsilon_3^m\right) \tag{3.93}$$

To find energy W_σ entering inequality (3.91), we should express strains in terms of stresses with the aid of constitutive equations, i.e.,

$$\begin{aligned}
\varepsilon_1^m &= \frac{1}{E_m}\left(\sigma_1^m - \nu_m \sigma_2^m - \nu_m \sigma_3^m\right) \\
\varepsilon_2^m &= \frac{1}{E_m}\left(\sigma_2^m - \nu_m \sigma_1^m - \nu_m \sigma_3^m\right) \\
\varepsilon_3^m &= \frac{1}{E_m}\left(\sigma_3^m - \nu_m \sigma_1^m - \nu_m \sigma_2^m\right)
\end{aligned} \tag{3.94}$$

Consider first the actual stress state. Let the ply in Fig. 3.29 be loaded with stress σ_2 inducing apparent strain ε_2 such that

$$\varepsilon_2 = \frac{\sigma_2}{E_2^{act}} \tag{3.95}$$

Here, E_2^{act} is the actual apparent modulus, which is not known. With due regard to Eqs. (3.92) and (3.93), we get

$$W = \frac{1}{2}\sigma_2\varepsilon_2 V, \quad W_\sigma^{act} = \frac{\sigma_2^2}{2E_2^{act}}V \tag{3.96}$$

where V is the volume of the material. As an admissible field, we can take any state of stress that satisfies the equilibrium equations and force boundary conditions. Using the simplest first-order model shown in Fig. 3.34, we assume that

$$\sigma_1^m = \sigma_3^m = 0, \quad \sigma_2^m = \sigma_2$$

Then, Eqs. (3.92)–(3.94) yield

$$W_\sigma^{adm} = \frac{\sigma_2^2}{2E_m}V_m \tag{3.97}$$

Substituting Eqs. (3.96) and (3.97) into the inequality (3.91), we arrive at

$$E_2^{act} > E_2^l$$

where, in accordance with Eqs. (3.62) and Fig. 3.34,

$$E_2^l = \frac{E_m V}{V_m} = \frac{E_m}{\upsilon_m}$$

This result, specifying the lower bound on the apparent transverse modulus, follows from Eq. (3.78) if we put $E_f \to \infty$. Thus, the lower (solid) line in Fig. 3.36 actually represents the lower bound on E_2.

To derive the expression for the upper bound, we should use the principle of minimum total potential energy (see Section 2.11.1), according to which (we again assume that the admissible field does not include the actual state)

$$T_{adm} > T_{act} \tag{3.98}$$

where $T = W_\varepsilon - A$. Here, W_ε is determined with Eq. (3.92), in which stresses are expressed in terms of strains with the aid of Eqs. (3.94), and A, for the problem under study, is the product of the force acting on the ply and the ply extension induced by this force. Since the force is the resultant of stress σ_2 (see Fig. 3.29) which induces strain ε_2, the same for actual and admissible states, A is also the same for both states, and we can present inequality (3.98) as

$$W_\varepsilon^{adm} > W_\varepsilon^{act} \tag{3.99}$$

For the actual state, we can write equations similar to Eqs. (3.96), i.e.,

$$W = \frac{1}{2}\sigma_2\varepsilon_2 V, \quad W_\varepsilon^{act} = \frac{1}{2}E_2^{act}\varepsilon_2^2 V \tag{3.100}$$

in which $V = 2Ra$ in accordance with Fig. 3.38. For the admissible state, we use the second-order model (see Fig. 3.38) and assume that

$$\varepsilon_1^m = 0, \quad \varepsilon_2^m = \varepsilon_m, \quad \varepsilon_3^m = 0$$

where ε_m is the matrix strain specified by Eq. (3.86). Then, Eqs. (3.94) yield

$$\sigma_1^m = \mu_m \sigma_2^m, \quad \sigma_3^m = \mu_m \sigma_2^m, \quad \sigma_2^m = \frac{E_m \varepsilon_m}{1 - 2\nu_m \mu_m} \tag{3.101}$$

where

$$\mu_m = \frac{\nu_m(1 + \nu_m)}{1 - \nu_m^2}$$

Substituting Eqs. (3.101) into Eq. (3.93) and performing integration in accordance with Eq. (3.92), we have

$$W_\varepsilon^{adm} = \frac{E_m \varepsilon_2^2}{1 - 2\nu_m \mu_m} \cdot \int_{-R}^{R} dx_3 \int_0^{\frac{a}{2}y} \frac{dx_2}{y^2} = \frac{\pi R a E_m \varepsilon_2^2 r(\lambda)}{2v_f(1 - 2\nu_m \mu_m)} \tag{3.102}$$

Here,

$$y = 1 - \lambda \sqrt{1 - \left(\frac{x_3}{R}\right)^2}$$

and $r(\lambda)$ is given above (see also Eq. (3.89)). Applying Eqs. (3.100) and (3.102) in conjunction with inequality (3.99), we arrive at

$$E_2^{act} < E_2^u$$

where

$$E_2^u = \frac{\pi E_m}{2v_f(1 - 2\nu_m \mu_m)}$$

is the upper bound on E_2, shown in Fig. 3.36 with a dashed curve.

Taking statically and kinematically admissible stress and strain fields that are closer to the actual state of stress and strain, one can increase E_2^l and decrease E_2^u, making the difference between the bounds smaller (Hashin and Rosen, 1964).

It should be emphasized that the bounds established thus are not the bounds imposed on the modulus of a real composite material but on the result of calculation corresponding to the accepted material model. Indeed, we can return to the first-order model shown in Fig. 3.34 and consider in-plane shear with stress τ_{12}. As can be readily proved, the actual stress-strain state of the matrix in this case is characterized by the following stresses and strains

$$\begin{aligned} &\sigma_1^m = \sigma_2^m = \sigma_3^m = 0, \quad \tau_{12}^m = \tau_{12}, \quad \tau_{13}^m = \tau_{23}^m = 0 \\ &\varepsilon_1^m = \varepsilon_2^m = \varepsilon_3^m = 0, \quad \gamma_{12}^m = \gamma_{12}, \quad \gamma_{13}^m = \gamma_{23}^m = 0 \end{aligned} \tag{3.103}$$

Assuming that the fibers are absolutely rigid and considering stresses and strains in Eqs. (3.103) as statically and kinematically admissible, we can readily find that

$$G_{12}^{act} = G_{12}^{l} = G_{12}^{u} = \frac{G_m}{v_m}$$

Thus, we have found the exact solution, but its agreement with experimental data is rather poor (see Fig. 3.37) because the material model is not sufficiently adequate.

As follows from the foregoing discussion, micromechanical analysis provides only qualitative prediction of the ply stiffness. The same is true for the ply strength. Although the micromechanical approach can be used in principle for strength analysis (Skudra et al., 1989), it mainly provides better understanding of the failure mechanism rather than the values of the ultimate stresses for typical loading cases. For practical applications, these stresses are determined by experimental methods described in the next section.

3.4 MECHANICAL PROPERTIES OF A PLY UNDER TENSION, SHEAR, AND COMPRESSION

As shown in Fig. 3.29, a ply can experience five types of elementary loading:

- Tension along the fibers
- Tension across the fibers
- In-plane shear
- Compression along the fibers
- Compression across the fibers

Actual mechanical properties of a ply under these loading cases are determined experimentally by testing of specially fabricated specimens. Since the thickness of an elementary ply is very small (0.1–0.2 mm), the specimen usually consists of tens of plies having the same fiber orientations.

Mechanical properties of composite materials depend on the processing method and parameters. So, to obtain the adequate material characteristics that can be used for analysis of structural elements, the specimens should be fabricated by the same processes that are used to manufacture the structural elements. In connection with this, there exist two standard types of specimens – flat ones that are used to test materials made by hand or machine lay-up and cylindrical (tubular or ring) specimens that represent materials made by winding.

Typical mechanical properties of unidirectional advanced composites are presented in Table 3.5 and in Figs. 3.40–3.43. More data relevant to the various types of particular composite materials can be found in Peters (1998).

We now consider typical loading cases.

3.4.1 Longitudinal tension

Stiffness and strength of unidirectional composites under longitudinal tension are determined by the fibers. As follows from Fig. 3.35, material stiffness linearly increases with increase in the fiber volume fraction. The same law following from Eq. (3.75) is valid for the material strength. If the fiber's

TABLE 3.5 Typical Properties of Unidirectional Composites.

Property	Glass-Epoxy	Carbon-Epoxy	Carbon-PEEK	Aramid-Epoxy	Boron-Epoxy	Boron-Al	Carbon-Carbon	Al_2O_3-Al
Fiber volume fraction, v_f	0.65	0.62	0.61	0.6	0.5	0.5	0.6	0.6
Density, ρ (g/cm^3)	2.1	1.55	1.6	1.32	2.1	2.65	1.75	3.45
Longitudinal modulus, E_1 (GPa)	60	140	140	95	210	260	170	260
Transverse modulus, E_2 (GPa)	13	11	10	5.1	19	140	19	150
Shear modulus, G_{12} (GPa)	3.4	5.5	5.1	1.8	4.8	60	9	60
Poisson's ratio, ν_{12}	0.3	0.27	0.3	0.34	0.21	0.3	0.3	0.24
Longitudinal tensile strength, $\overline{\sigma}_1^+$ (MPa)	1800	2000	2100	2500	1300	1300	340	700
Longitudinal compressive strength, $\overline{\sigma}_1^-$ (MPa)	650	1200	1200	300	2000	2000	180	3400
Transverse tensile strength, $\overline{\sigma}_2^+$ (MPa)	40	50	75	30	70	140	7	190
Transverse compressive strength, $\overline{\sigma}_2^-$ (MPa)	90	170	250	130	300	300	50	400
In-plane shear strength, $\overline{\tau}_{12}$ (MPa)	50	70	160	30	80	90	30	120

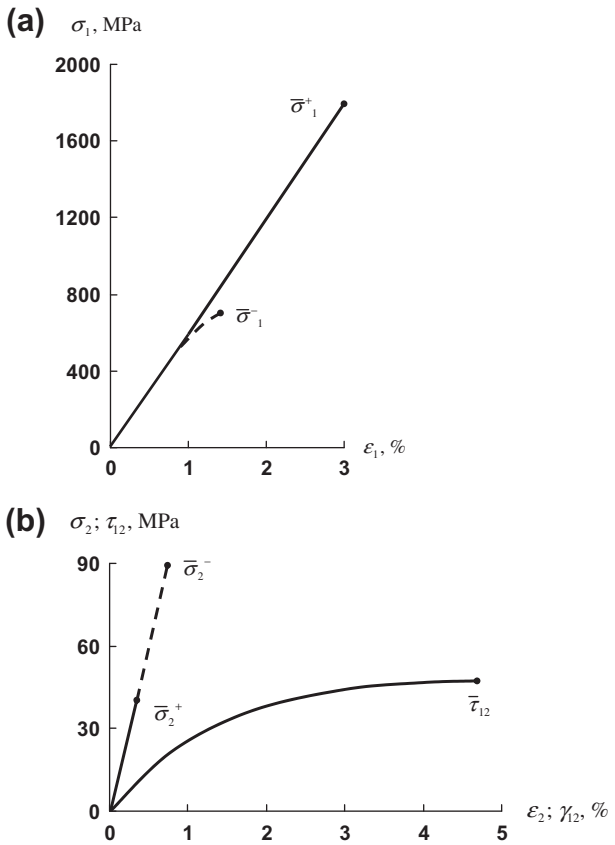


FIGURE 3.40

Stress-strain curves for unidirectional glass-epoxy composite material under longitudinal tension and compression (a), transverse tension and compression (b), and in-plane shear (b).

ultimate elongation, $\overline{\varepsilon}_f$, is less than that of the matrix (which is normally the case), the longitudinal tensile strength is determined as

$$\overline{\sigma}_1^{+} = \left(E_f \upsilon_f + E_m \upsilon_m\right)\overline{\varepsilon}_f \tag{3.104}$$

However, in contrast to Eq. (3.76) for E_1, this equation is not valid for very small and very high fiber volume fractions. The dependence of $\overline{\sigma}_1^{+}$ on υ_f is shown in Fig. 3.44. For very low υ_f, the fibers do not restrain the matrix deformation. Being stretched by the matrix, the fibers fail because their ultimate elongation is less than that of the matrix and the induced stress concentration in the matrix can reduce material strength below the strength of the matrix (point B). Line BC in Fig. 3.44 corresponds to Eq. (3.104). At point C, the amount of matrix reduces below the level necessary for a monolithic material, and the material strength at point D approximately corresponds to the strength of a dry bundle of fibers, which is less than the strength of a composite bundle of fibers bound with matrix (see Table 3.3).

Strength and stiffness under longitudinal tension are determined using unidirectional strips or rings. The strips are cut out of unidirectionally reinforced plates, and their ends are made thicker

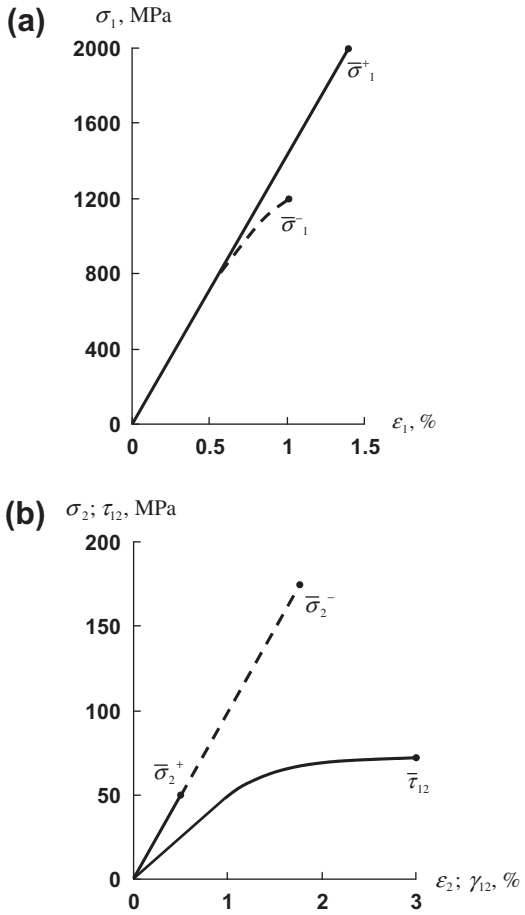


FIGURE 3.41

Stress-strain curves for unidirectional carbon-epoxy composite material under longitudinal tension and compression (a), transverse tension and compression (b), and in-plane shear (b).

(usually glass-epoxy tabs are bonded onto the ends) to avoid specimen failure in the grips of the testing machine (Jones, 1999; Lagace, 1985). Rings are cut out of a circumferentially wound cylinder or wound individually on a special mandrel, as shown in Fig. 3.45. The strips are tested using traditional approaches, whereas the rings should be loaded with internal pressure. There exist several methods to apply the pressure (Tarnopol'skii and Kincis, 1985), the simplest of which involves the use of mechanical fixtures with various numbers of sectors as in Figs. 3.46 and 3.47. The failure mode is shown in Fig. 3.48. Longitudinal tension yields the following mechanical properties of the material:

- Longitudinal modulus, E_1
- Longitudinal tensile strength, $\overline{\sigma}_1^+$
- Poisson's ratio, ν_{21}

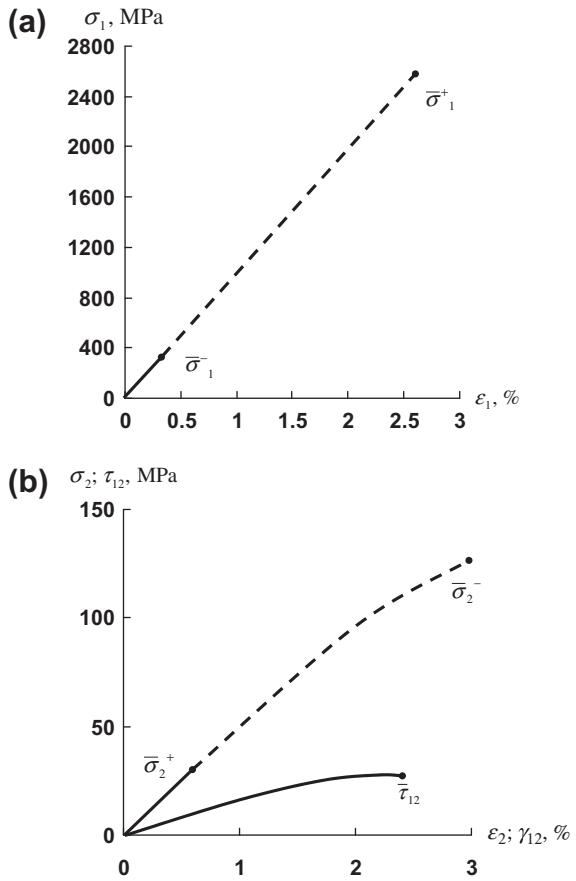


FIGURE 3.42

Stress-strain curves for unidirectional aramid-epoxy composite material under longitudinal tension and compression (a), transverse tension and compression (b), and in-plane shear (b).

Typical values of these characteristics for composites with various fibers and matrices are listed in Table 3.5. It follows from Figs. 3.40–3.43 that the stress-strain diagrams are linear practically up to failure.

3.4.2 Transverse tension

There are three possible modes of material failure under transverse tension with stress σ_2 shown in Fig. 3.49: failure of the fiber-matrix interface (adhesion failure), failure of the matrix (cohesion failure), and fiber failure. The last failure mode is specific for composites with aramid fibers, which consist of thin filaments (fibrils) and have low transverse strength. As follows from the

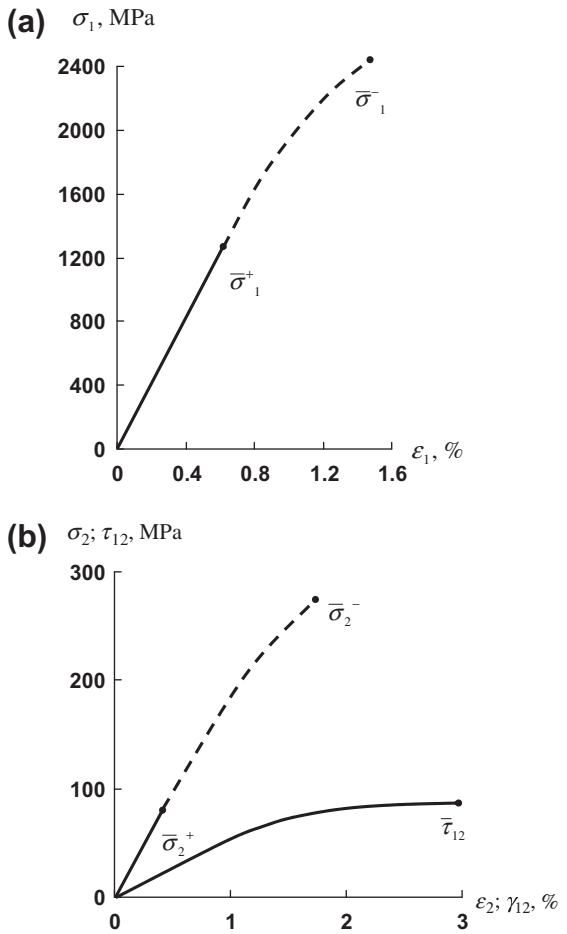


FIGURE 3.43

Stress-strain curves for unidirectional boron-epoxy composite material under longitudinal tension and compression (a), transverse tension and compression (b), and in-plane shear (b).

micromechanical analysis (Section 3.3), material stiffness under tension across the fibers is higher than that of a net matrix (see Fig. 3.36).

For qualitative analysis of transverse strength, consider again the second-order model in Fig. 3.38. As can be seen, the stress distribution $\sigma_m(x_3)$ is not uniform, and the maximum stress in the matrix corresponds to $\alpha = 90^\circ$. Using Eqs. (3.85), (3.86), and (3.88), we obtain

$$\sigma_m^{\max} = \frac{E_m \sigma_2}{(1-\nu_m^2)E_2(1-\lambda)}$$

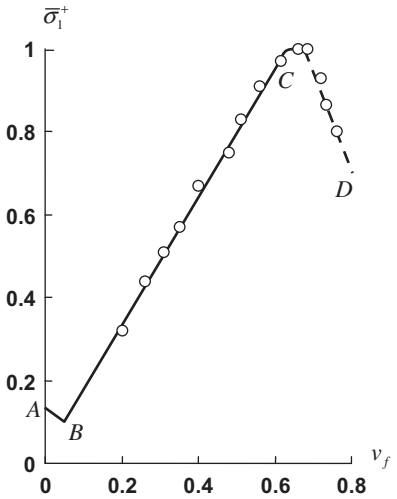


FIGURE 3.44

Dependence of normalized longitudinal strength on fiber volume fraction (○ – experimental results).

Taking $\sigma_m^{\max} = \overline{\sigma}_m$ and $\sigma_2 = \overline{\sigma}_2^+$, where $\overline{\sigma}_m$ and $\overline{\sigma}_2^+$ are the ultimate stresses for the matrix and composite material, respectively, and substituting for λ and E_2 their expressions given by Eqs. (3.87) and (3.89), we arrive at

$$\overline{\sigma}_2^+ = \overline{\sigma}_m \frac{r(\lambda)}{2v_f}(\pi - 4v_f) \tag{3.105}$$

The variation of the ratio $\overline{\sigma}_2^+/\overline{\sigma}_m$ for epoxy composites is shown in Fig. 3.50. As can be seen, the transverse strength of a unidirectional material is considerably lower than the strength of the matrix.

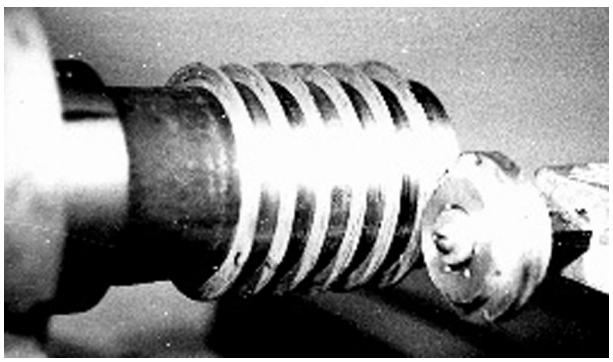


FIGURE 3.45

A mandrel for test rings.

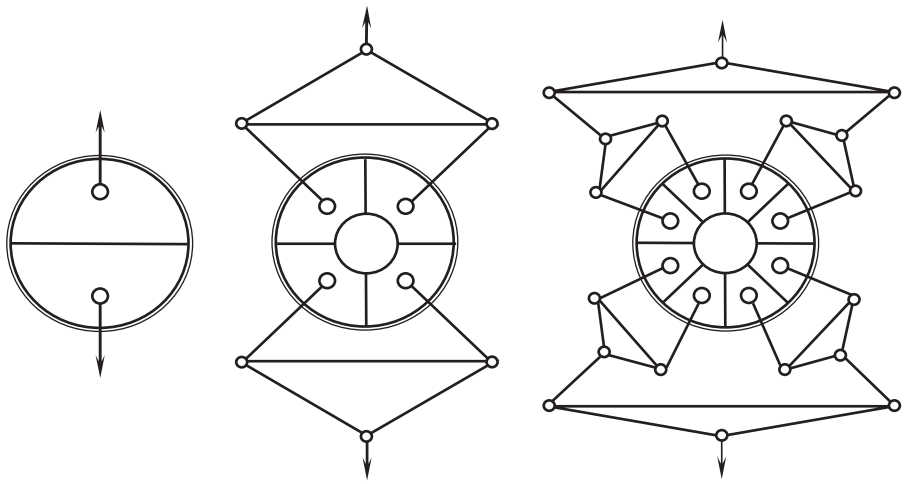


FIGURE 3.46

Two-, four-, and eight-sector test fixtures for composite rings.

It should be noted that for the first-order model, which ignores the shape of the fiber cross sections (see Fig. 3.34), $\overline{\sigma}_2^+$ is equal to $\overline{\sigma}_m$. Thus, the reduction of $\overline{\sigma}_2^+$ is caused by stress concentration in the matrix induced by cylindrical fibers.

However, both polymeric and metal matrices exhibit elastic-plastic behavior, as follows from Figs. 1.11 and 1.14, and it is known that plastic deformation reduces the effect of stress concentration. Nevertheless, the stress-strain diagrams $\overline{\sigma}_2^+ - \varepsilon_2$ shown in Figs. 3.40–3.43 are linear up to the

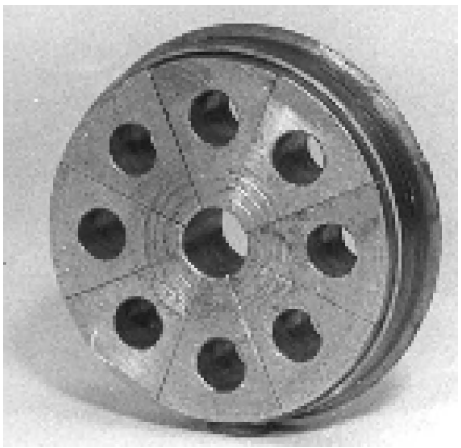


FIGURE 3.47

A composite ring on an eight-sector test fixture.



FIGURE 3.48

Failure modes of unidirectional rings.

failure point. To explain this phenomenon, consider element A of the matrix located in the vicinity of a fiber as in Fig. 3.38. Assuming that the fiber is absolutely rigid, we can conclude that the matrix strains in directions 1 and 3 are close to zero. Taking $\varepsilon_1^m = \varepsilon_3^m = 0$ in Eqs. (3.94), we arrive at Eqs. (3.101) for stresses, according to which $\sigma_1^m = \sigma_3^m = \mu_m \sigma_2^m$. The dependence of parameter μ_m on the matrix Poisson's ratio is presented in Fig. 3.51. As follows from this figure, in the limiting case $\nu_m = 0.5$, we have $\mu_m = 1$ and $\sigma_1^m = \sigma_2^m = \sigma_3^m$, i.e., the state of stress under which all the materials behave as absolutely brittle. For epoxy resin, $\nu_m = 0.35$ and $\mu_m = 0.54$ which, as can be expected, does not allow the resin to demonstrate its rather limited (see Fig. 1.11) plastic properties.

Strength and stiffness under transverse tension are experimentally determined using flat strips (see Fig. 3.52) or tubular specimens (see Fig. 3.53). These tests allow us to determine transverse modulus, E_2, and transverse tensile strength, $\overline{\sigma}_2^+$. For typical composite materials, these properties are given in Table 3.5.

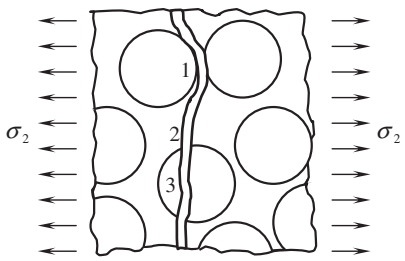


FIGURE 3.49

Modes of failure under transverse tension:

1 – Adhesion failure
2 – Cohesion failure
3 – Fiber failure

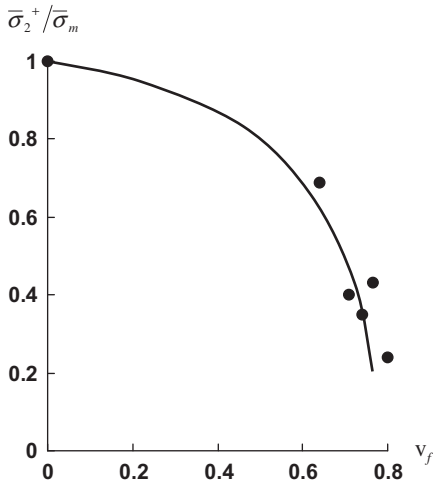


FIGURE 3.50

Dependence of material strength under transverse tension on fiber volume fraction: Eq. (3.105); (•) Experimental data.

3.4.3 In-plane shear

The failure modes in unidirectional composites under in-plane pure shear with stress τ_{12} shown in Fig. 3.29 are practically the same as those for the case of transverse tension (see Fig. 3.49). However, there is a significant difference in material behavior. As follows from Figs. 3.40–3.43, the stress-strain curves τ_{12}—γ_{12} are not linear, and $\overline{\tau}_{12}$ exceeds $\overline{\sigma}_2^+$. This means that the fibers do not restrict the free shear deformation of the matrix, and the stress concentration in the vicinity of the fibers does not significantly influence material strength because of matrix plastic deformation.

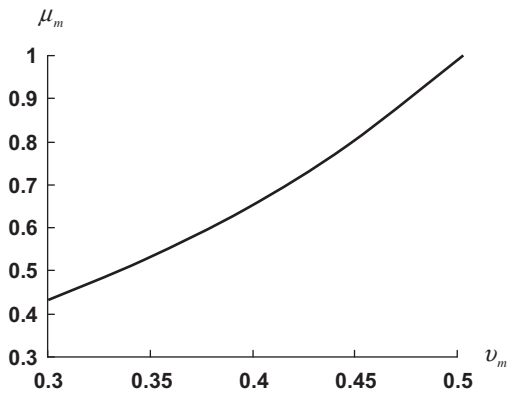


FIGURE 3.51

Dependence of parameter μ_m on the matrix Poisson's ratio.

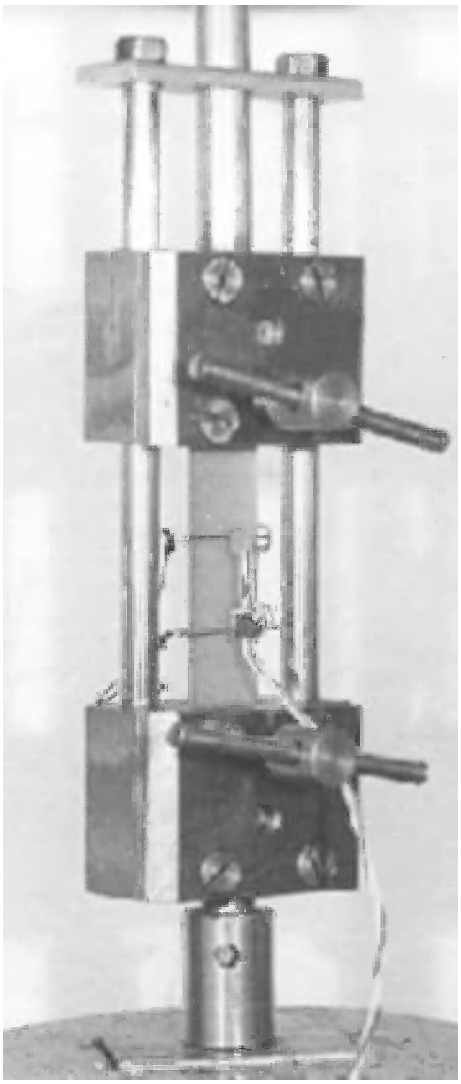


FIGURE 3.52

Test fixture for transverse tension and compression of unidirectional strips.

Strength and stiffness under in-plane shear are determined experimentally by testing plates and thin-walled cylinders. A plate is reinforced at 45° to the loading direction and is fixed in a square frame consisting of four hinged members, as shown in Fig. 3.54. Simple equilibrium consideration and geometric analysis with the aid of Eq. (2.27) yield the following equations:

$$\tau_{12} = \frac{P}{\sqrt{2}ah}, \quad \gamma_{12} = \varepsilon_y - \varepsilon_x, \quad G_{12} = \frac{\tau_{12}}{\gamma_{12}}$$

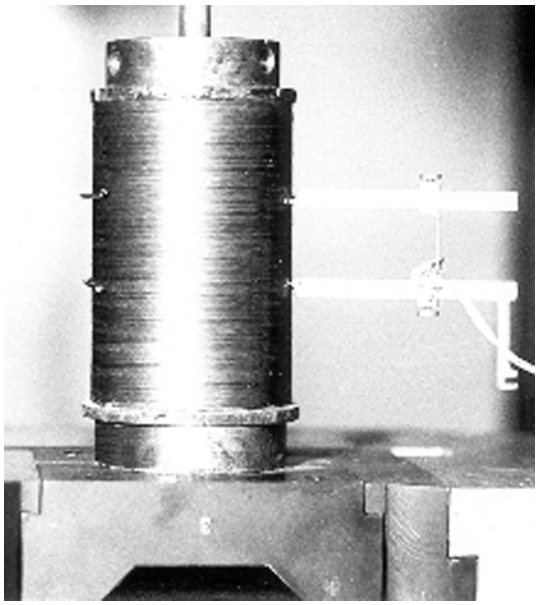


FIGURE 3.53

Test fixture for transverse tension or compression of unidirectional tubular specimens.

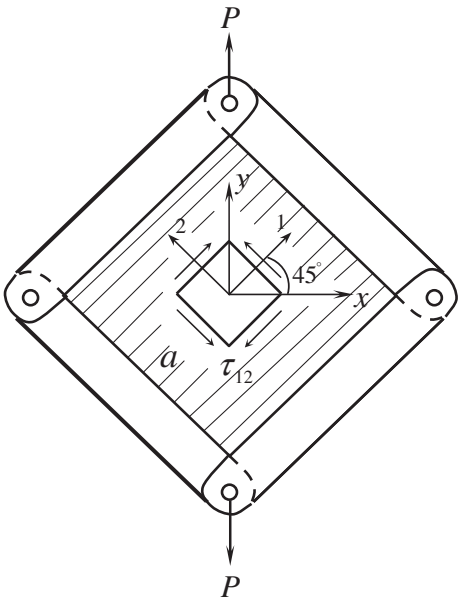


FIGURE 3.54

Simulation of pure shear in a square frame.

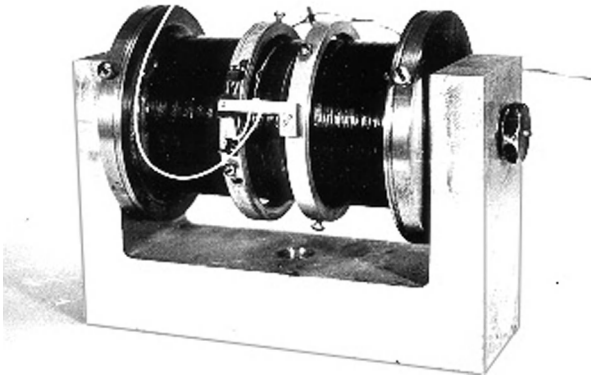


FIGURE 3.55

A tubular specimen for shear test.

in which h is the plate thickness. Thus, for given P and measured strains in the x and y directions, we can determine $\overline{\tau}_{12}$ and G_{12}. More accurate and reliable results can be obtained if we induce pure shear in a twisted tubular specimen reinforced in the circumferential direction (Fig. 3.55). Again, using simple equilibrium and geometric analysis, we get

$$\tau_{12} = \frac{M}{2\pi R^2 h}, \quad \gamma_{12} = \frac{\varphi R}{l}, \quad G_{12} = \frac{\tau_{12}}{\gamma_{12}}$$

Here, M is the torque, R and h are the cylinder radius and thickness, and φ is the twist angle between two cross-sections located at some distance l from each other. Thus, for given M and measured φ, we can find $\overline{\tau}_{12}$ and G_{12}.

3.4.4 Longitudinal compression

Failure under compression along the fibers can occur in different modes, depending on the material microstructural parameters, and can hardly be predicted by micromechanical analysis because of the rather complicated interaction of these modes. Nevertheless, useful qualitative results allowing us to understand material behavior and hence to improve properties can be obtained with microstructural models.

Consider typical compression failure modes. The usual failure mode under compression is associated with shear in some oblique plane as in Fig. 3.56. The shear stress can be calculated using Eq. (2.9), i.e.,

$$\tau = \sigma_1 \sin\alpha \cos\alpha,$$

and reaches its maximum value at $\alpha = 45^{\circ}$. Shear failure under compression is usually typical for unidirectional composites that demonstrate the highest strength under longitudinal compression. On the other hand, materials showing the lowest strength under compression exhibit a transverse extension failure mode typical of wood compressed along the fibers, as shown in Fig. 3.57. This failure is caused by tensile transverse strain, whose absolute value is

$$\varepsilon_2 = \nu_{21}\varepsilon_1 \tag{3.106}$$

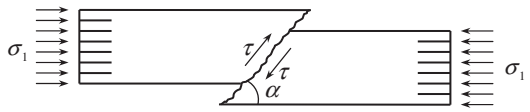


FIGURE 3.56

Shear failure under compression.

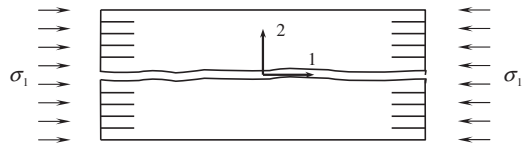


FIGURE 3.57

Transverse extension failure mode under longitudinal compression.

TABLE 3.6 Characteristics of Epoxy Composites.

	Characteristic				
Material	$\overline{\sigma}_1^-$ **(MPa)**	$\overline{\varepsilon}_1^-$ **(%)**	ν_{21}	$\overline{\varepsilon}_2^+$ **(%)**	$\overline{\varepsilon}_2 = \nu_{21}\overline{\varepsilon}_1^-$
Glass-epoxy	600	1.00	0.30	0.31	0.30
Carbon-epoxy	1200	0.86	0.27	0.45	0.23
Aramid-epoxy	300	0.31	0.34	0.59	0.11
Boron-epoxy	2000	0.95	0.21	0.37	0.20

where ν_{21} is Poisson's ratio and $\varepsilon_1 = \sigma_1/E_1$ is the longitudinal strain. Consider Table 3.6, showing some data taken from Table 3.5 and the results of calculations for epoxy composites. The fourth column displays the experimental ultimate transverse strains $\overline{\varepsilon}_2^+ = \overline{\sigma}_2^+/E_2$ calculated with the aid of data presented in Table 3.5, whereas the last column shows the results following from Eq. (3.106). As can be seen, the failure mode associated with transverse tension under longitudinal compression is not dangerous for the composites under consideration because $\overline{\varepsilon}_2^+ > \overline{\varepsilon}_2$. However, this is true only for fiber volume fractions $v_f = 0.50-0.65$, to which the data presented in Table 3.6 correspond. To see what happens for higher fiber volume fractions, let us use the second-order micromechanical model and the corresponding results in Figs. 3.36 and 3.50. We can plot the strain concentration factor k_ε (which is the ratio of the ultimate matrix elongation, $\overline{\varepsilon}_m$, to $\overline{\varepsilon}_2^+$ for the composite material) versus the fiber volume fraction. As can be seen in Fig. 3.58, this factor, being about 6 for $v_f = 0.6$, becomes as high as 25 for $v_f = 0.75$. This means that $\overline{\varepsilon}_2^+$ dramatically decreases for higher v_f, and the fracture mode shown in Fig. 3.57 becomes conventional for composites with high fiber volume fractions.

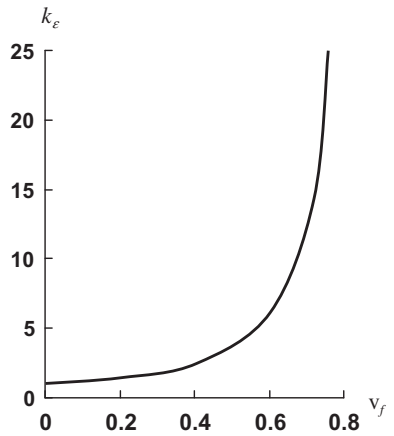


FIGURE 3.58

Dependence of the strain concentration factor on the fiber volume fraction.

Both fracture modes shown in Figs. 3.56 and 3.57 are accompanied with fibers bending, induced by local buckling of fibers. According to N.F. Dow and B.W. Rosen (Jones, 1999), there can exist two modes of fiber buckling, as shown in Fig. 3.59, i.e., a shear mode and a transverse extension mode. To study the fiber's local buckling (or microbuckling, which means that the material specimen is straight, whereas the fibers inside the material are curved), consider a plane model of a unidirectional ply, shown in Figs. 3.15 and 3.60, and take $a_m = a$ and $a_f = \delta = d$, where d is the fiber diameter. Then, Eqs. (3.17) yield

$$v_f = \frac{\overline{d}}{1+\overline{d}}, \quad \overline{d} = \frac{d}{a} \tag{3.107}$$

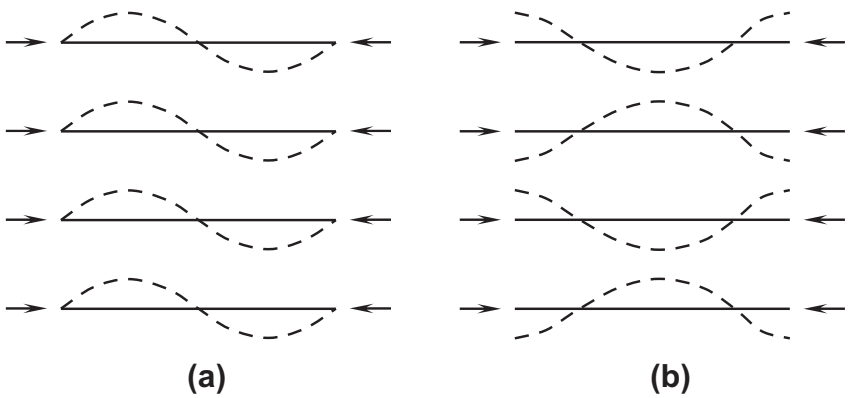


FIGURE 3.59

Shear (a) and transverse extension (b) modes of fiber local buckling.

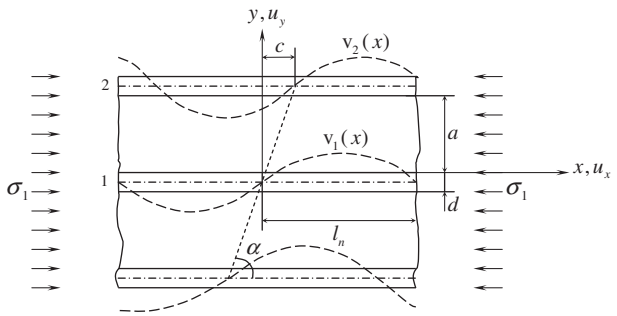


FIGURE 3.60

Local buckling of fibers in unidirectional ply.

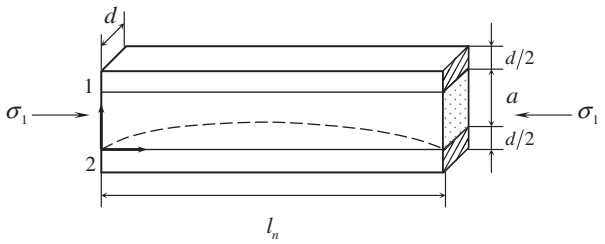


FIGURE 3.61

A typical ply element.

Due to the symmetry conditions, consider two fibers 1 and 2 in Fig. 3.60 and the matrix between these fibers. The buckling displacement, v, of the fibers can be represented with a sine function as

$$v_1(x) = V \sin \lambda_n x, \quad v_2(x) = V \sin \lambda_n (x - c) \tag{3.108}$$

where V is an unknown amplitude value, the same for all the fibers, $\lambda_n = \pi / l_n$, l_n is a half of a fiber wavelength (see Fig. 3.60), and $c = (a + d)\cot \alpha$ is a phase shift. Taking $c = 0$, we can describe the shear mode of buckling (Fig. 3.59a), whereas $c = l_n$ corresponds to the extension mode (Fig. 3.59b). To find the critical value of stress σ_1, we use the Timoshenko energy method (Timoshenko and Gere, 1961), yielding the following buckling condition:

$$A = W \tag{3.109}$$

Here, A is the work of external forces, and W is the strain energy accumulated in the material while the fibers undergo buckling. Work A and energy W are calculated for a typical ply element consisting of two halves of fibers 1 and 2 and the matrix between them (see Fig. 3.61). The work, A, can be calculated as

$$A = \sigma_1 (a + d) d \bullet \delta \tag{3.110}$$

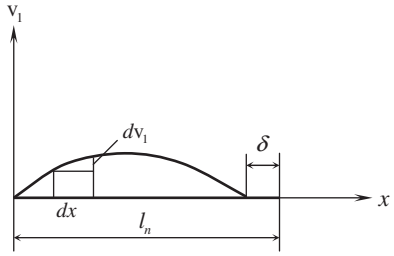


FIGURE 3.62

Deformation of a fiber.

with displacement δ following from Fig. 3.62, i.e.,

$$\delta = l_n - \int_0^{l_n-\delta} \sqrt{1 + \left(\frac{dv_1}{dx}\right)^2}\, dx$$

Using conventional assumptions, i.e., taking $(dv_1/dx) << 1$ and $\delta << l$ and substituting v_1 from Eqs. (3.108), we arrive at

$$\delta = \frac{1}{2}\int_0^{l_n} \left(\frac{dv_1}{dx}\right)^2 dx = \frac{1}{4}V^2\lambda_n^2 l_n$$

Thus, Eq. (3.110) yields

$$A = \frac{\pi^2}{4l_n}\sigma_1 V^2 ad(1+\overline{d}) \tag{3.111}$$

Strain energy consists of three parts, i.e.,

$$W = W_f + W_m^s + W_m^e \tag{3.112}$$

whereW_f is the energy of buckled fibers, whereas W_m^s and W_m^e correspond to shear strain and transverse extension of the matrix that supports the fibers. The strain energy of fibers deformed in accordance with Eqs. (3.108) and shown in Fig. 3.61 has the form

$$W_f = \frac{1}{4}D_f \int_0^{l_n} \left[\left(\frac{d^2v_1}{dx^2}\right)^2 + \left(\frac{d^2v_2}{dx^2}\right)^2\right] dx$$

where D_f is the fiber bending stiffness. Substituting Eqs. (3.108) and calculating the integrals, we get

$$W_f = \frac{\pi^4}{4l_n^3}D_f V^2 \tag{3.113}$$

To determine the strain energy of the matrix, we assume that the matrix element shown in Fig. 3.61 is in a state of plane stress (nonzero stresses are σ_x, σ_y, and τ_{xy}), and the equilibrium equations, Eqs. (2.5), can be written as

$$\frac{\partial \sigma_x}{\partial x} + \frac{\partial \tau_{xy}}{\partial y} = 0, \quad \frac{\partial \sigma_y}{\partial y} + \frac{\partial \tau_{xy}}{\partial x} = 0 \tag{3.114}$$

To simplify the solution, we assume that the longitudinal stress, σ_x, acting in the matrix can be neglected in comparison with the corresponding stress acting in the fibers. Thus, we can set $\sigma_x = 0$. Then, Eqs. (3.114) can be integrated and yield

$$\tau_{xy} = \tau(x), \quad \sigma_y = \sigma(x) - \tau'(x)y \tag{3.115}$$

Here, $\tau(x)$ and $\sigma(x)$ are arbitrary functions of integration and $(\quad)' = d(\quad)/dx$. Also neglecting the Poisson effects, we can express the strains as follows:

$$\gamma_{xy} = \frac{\tau(x)}{G_m}, \quad \varepsilon_y = \frac{1}{E_m}\left[\sigma(x) - \tau'(x)y\right] \tag{3.116}$$

which in turn can be expressed in terms of displacements with the aid of Eqs. (2.22), i.e.,

$$\gamma_{xy} = \frac{\partial u_x}{\partial y} + \frac{\partial u_y}{\partial x}, \quad \varepsilon_y = \frac{\partial u_y}{\partial y} \tag{3.117}$$

Substituting Eqs. (3.116) into Eqs. (3.117) and integrating, we can determine the displacements as

$$u_x = u(x) + \left[\frac{\tau(x)}{G_m} - \upsilon'(x)\right]y - \frac{1}{2E_m}\left[\sigma'(x)y^2 - \frac{1}{3}\tau''(x)y^3\right]$$

$$u_y = \upsilon(x) + \frac{1}{E_m}\left[\sigma(x)y - \frac{1}{2}\tau'(x)y^2\right]$$

Here, $u(x)$ and $\upsilon(x)$ are functions of integration that, in addition to the functions $\tau(x)$ and $\sigma(x)$, should be found using compatibility conditions at fiber-matrix interfaces. Using Fig. 3.63, we can write these conditions in the following form:

$$u_x(y=0) = -\frac{d}{2}\upsilon'_1(x), \quad u_x(y=a) = \frac{d}{2}\upsilon'_2(x)$$

$$u_y(y=0) = \upsilon_1(x), \quad u_y(y=a) = \upsilon_2(x)$$

Satisfying them, we can find $u(x)$ and $\upsilon(x)$ directly as

$$u(x) = -\frac{d}{2}V\lambda_n \cos\lambda_n x, \quad \upsilon(x) = V \sin\lambda_n x$$

and derive the following equations for $\sigma(x)$ and $\tau(x)$:

$$\sigma(x) = \frac{E_m}{a}V[\sin\lambda_n(x-c) - \sin\lambda_n x] + \frac{1}{2}\tau'(x)a \tag{3.118}$$

$$\frac{a^2}{6E_m}\tau''(x) - \frac{2}{G_m}\tau(x) = -V\lambda_n(1+\overline{d})[\cos\lambda_n(x-c) + \cos\lambda_n x] \tag{3.119}$$

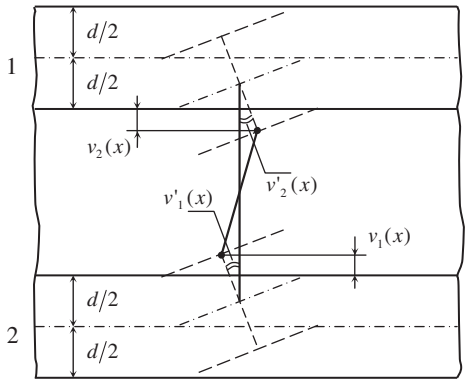


FIGURE 3.63

Compatible fiber-matrix deformation.

We need a periodic solution of Eq. (3.119), and can find it in the following form:

$$\tau(x) = C[\cos\lambda_n(x-c) + \cos\lambda_n x] \tag{3.120}$$

Substituting into Eq. (3.119) and taking into account that $\lambda_n = \pi/l_n$, we have

$$C = V\frac{\pi G_m(1+\overline{d})}{2l_n(1+\beta_n)}, \quad \beta_n = \frac{\pi^2 a^2 G_m}{12 l_n^2 E_m} \tag{3.121}$$

Now, using Eqs. (3.115), (3.118), and (3.120), we can write the final expressions for the stresses acting in the matrix

$$\begin{aligned}
\tau_{xy} &= C\left[\cos\lambda_n(x-c) + \cos\lambda_n x\right], \\
\sigma_y &= -\left[C\lambda_n\left(\frac{a}{2}-y\right) - \frac{E_m}{a}V\right]\sin\lambda_n(x-c) \\
&\quad -\left[C\lambda_n\left(\frac{a}{2}-y\right) + \frac{E_m}{a}V\right]\sin\lambda_n x
\end{aligned} \tag{3.122}$$

in which C is specified with Eqs. (3.121). The corresponding strain energies of the typical element in Fig. 3.61 are

$$W_m^s = \frac{ad}{2G_m}\int_0^{l_n}\tau_{xy}^2 dx, \quad W_m^e = \frac{ad}{2E_m}\int_0^{l_n}\sigma_y^2 dx$$

Substituting Eqs. (3.122) and integrating, we arrive at

$$W_m^s = \frac{adl_n}{2G_m}C^2(1+\cos\lambda_n c)$$

$$W_m^e = \frac{adl_n}{2E_m}\left[\frac{\pi^2 a^2}{12l_n^2}C^2(1+\cos\lambda_n c) + \frac{E_m^2}{a^2}V^2(1-\cos\lambda_n c)\right]$$

In conjunction with these results, Eqs. (3.109), (3.111)–(3.113), and (3.121) allow us to determine σ_1, which takes the following final form:

$$\sigma_1 = \frac{\pi^2 D_f}{\bar{l}_n^2\bar{d}\left(1+\bar{d}\right)a^4} + \frac{G_m\left(1+\bar{d}\right)}{2\left(1+\dfrac{\pi^2 G_m}{12\bar{l}_n^2 E_m}\right)}\left(1+\cos\frac{\pi\bar{c}}{\bar{l}_n}\right) + \frac{2E_m\bar{l}_n^2}{\pi^2\left(1+\bar{d}\right)}\left(1-\cos\frac{\pi\bar{c}}{\bar{l}_n}\right) \tag{3.123}$$

where $\bar{d} = d/a$, $\bar{l}_n = l_n/a$, and $\bar{c} = c/a$. The critical value of σ_1 can be found by minimization of the right-hand part of Eq. (3.123) with respect to $\bar{l}_n$ and $\bar{c}$. However, having in mind only qualitative analysis, we can omit this cumbersome procedure and use Eq. (3.123) for qualitative assessments and estimates.

As follows from this equation, the strength of a unidirectional composite under longitudinal compression should increase with an increase in the fiber bending stiffness. This prediction is definitely supported with experimental data presented in Table 3.6. The highest strength is demonstrated by composites reinforced with boron fibers that have relatively large diameter and high modulus, providing very high fiber bending stiffness. Carbon fibers, also having high modulus but smaller diameter than boron fibers, provide compressive strength that is 40% lower than that of boron composites, but is twice the strength of a composite reinforced with glass fibers having the same diameter but lower modulus. The lowest strength in compression is demonstrated by composites with aramid fibers. As was already noted, these fibers, although having high tensile stiffness, consist of a system of poorly bonded thin filaments and possess low bending stiffness. As can be seen in Eq. (3.123), compressive strength also increases with an increase in the matrix stiffness. Available experimental results (Woolstencroft et al., 1982; Crasto and Kim, 1993) show that the strength of carbon composites in compression increases linearly, while the matrix shear modulus rises up to $G_m =$ 1500 MPa, which is the value typical for epoxy resins. For higher values of G_m, the compressive strength does not change, and we can expect that there exists some maximum value of G_m beyond which the matrix does not allow fibers to buckle, and the material strength is controlled by the fiber strength in compression. Results listed in Table 3.5 support this conclusion. As can be seen, changing an epoxy matrix for an aluminum one with higher stiffness does not increase the compressive strength of boron fiber composites. Moreover, by increasing the matrix stiffness, we usually reduce its ultimate elongation. As a result, the material can fail under relatively low stress because of delamination (see Fig. 3.57). An example of such a material can also be found in Table 3.5. Carbon-carbon unidirectional composites with brittle carbon matrices possessing very high stiffness demonstrate very low strength under longitudinal compression.

Fracture of actual unidirectional composites usually occurs as a result of the interaction of fracture modes discussed above. Such fracture is shown in Fig. 3.64. The ultimate stress depends on material structural and manufacturing parameters, has considerable scatter, and can hardly be predicted theoretically. For example, the compressive strength of composites with the same fibers and matrices

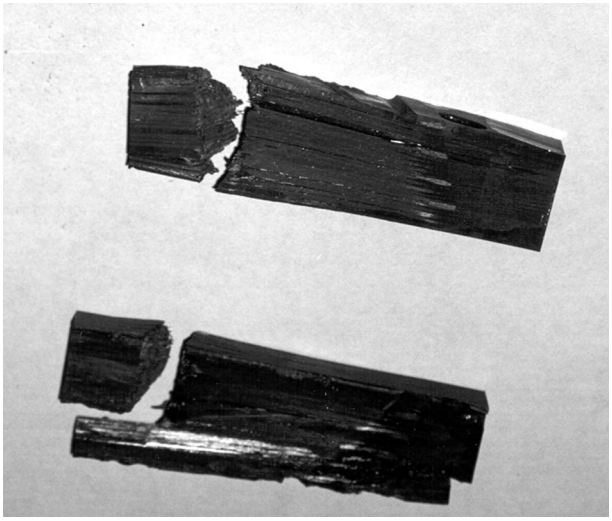


FIGURE 3.64

Failure mode of a unidirectional carbon-epoxy composite under longitudinal compression.

having the same stiffness but different nature (thermoset or thermoplastic) can be different (Crasto and Kim, 1993).

The strength of composites under longitudinal compression is determined experimentally using ring or flat specimens and special methods to prevent the specimen buckling (Tarnopol'skii and Kincis, 1985). The most accurate results are provided by compression of sandwich specimens with composite facings made from the material under study (Crasto and Kim, 1993).

3.4.5 Transverse compression

Under compression across the fibers, unidirectional composites exhibit a conventional shear mode of fracture of the type shown in Fig. 3.65. The transverse compression strength is higher than in-plane shear strength (see Table 3.5) due to two main reasons. Firstly, the area of the oblique failure plane is larger than the area of the orthogonal longitudinal ply cross-section in which the ply fails under in-plane shear. Secondly, additional compression across the oblique failure plane (see Fig. 3.65) increases the shear strength. Strength under transverse compression is measured using flat or tubular specimens (shown in Figs. 3.52 and 3.53).



FIGURE 3.65

Failure under transverse compression.

3.5 HYBRID COMPOSITES

The foregoing sections of this chapter are concerned with the properties of unidirectional plies reinforced with fibers of a certain type: glass, carbon, aramid, etc. In hybrid composites, the plies can include fibers of two or maybe more types, e.g., carbon and glass, glass and aramid, and so on. Hybrid composites provide wider opportunities to control material stiffness, strength, and cost. A promising application of these materials is associated with the so-called thermostable structures, which do not change their dimensions under heating or cooling. For some composites, e.g., with glass or boron fibers, the longitudinal coefficient of thermal expansion is positive, whereas for other materials, e.g., with carbon or aramid fibers, it is negative (see Table 7.1 and Section 7.1.2 of Chapter 7). So, the appropriate combination of fibers with positive and negative coefficients can result in material with zero thermal expansion.

Consider the problem of micromechanics for a unidirectional ply reinforced with two types of fibers. Naturally, the stiffness of these fibers should be different, and we assume that $E_f^{(1)} > E_f^{(2)}$. The first-order model of the ply that generalizes the model in Fig. 3.34 is presented in Fig. 3.66. For tension in the fiber direction, the apparent stress and strain, σ_1 and ε_1, are linked by Hooke's law

$$\sigma_1 = E_1 \varepsilon_1 \tag{3.124}$$

in which the effective modulus is specified by the following equation, generalizing Eq. (3.76)

$$E_1 = E_f^{(1)} v_f^{(1)} + E_f^{(2)} v_f^{(2)} + E_m v_m \tag{3.125}$$

Here, $v_f^{(1)}$ and $v_f^{(2)}$ are volume fractions of the fibers of the first and second type, and v_m is the matrix volume fraction, so that

$$v_f^{(1)} + v_f^{(2)} + v_m = 1$$

We also introduce the total volume fraction of the fibers

$$v_f = v_f^{(1)} + v_f^{(2)}$$

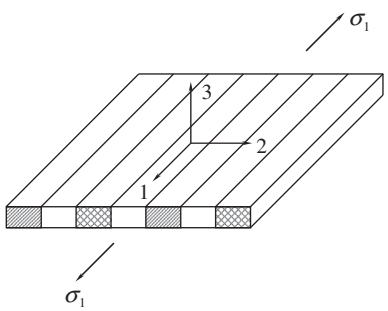


FIGURE 3.66

A first-order microstructural model of a hybrid unidirectional ply.

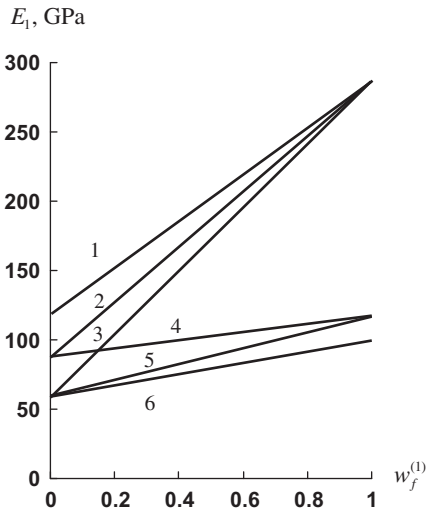


FIGURE 3.67

Experimental dependencies of longitudinal modulus on the volume fraction of the higher modulus fibers in hybrid unidirectional composites:
1 – boron-carbon, 2 – boron-aramid, 3 – boron-glass, 4 – carbon-aramid, 5 – carbon-glass, 6 – aramid-glass.

and normalized volume fractions of fibers as

$$w_f^{(1)} = \frac{v_f^{(1)}}{v_f},\ w_f^{(2)} = \frac{v_f^{(2)}}{v_f}$$

Obviously,

$$w_f^{(1)} + w_f^{(2)} = 1$$

Then, Eq. (3.125) can be written in the form

$$E_1 = v_f\left[E_f^{(1)} w_f^{(1)} + E_f^{(2)}\left(1 - w_f^{(1)}\right)\right] + E_m(1 - v_f) \tag{3.126}$$

The linear dependence of E_1 on $w_f^{(1)}$ predicted by Eq. (3.126) is in good correlation with the experimental data reported by Zabolotskii and Varshavskii (1984), and is presented in Fig. 3.67.

Since the fibers of hybrid composites have different stiffness, they are characterized as a rule with different ultimate elongations. As follows from Fig. 3.68, plotted with the data listed in Table 3.5, there exists an inverse linear dependence between the ply longitudinal modulus and the ultimate elongation $\overline{\varepsilon}_1$. So, assuming $E_f^{(1)} > E_f^{(2)}$, we should take into account that $\overline{\varepsilon}_f^{(1)} < \overline{\varepsilon}_f^{(2)}$. This means that Eq. (3.124) is valid for $\varepsilon_1 \le \overline{\varepsilon}_f^{(1)}$. Strain $\varepsilon_1 = \overline{\varepsilon}_f^{(1)}$ is accompanied by the failure of fibers

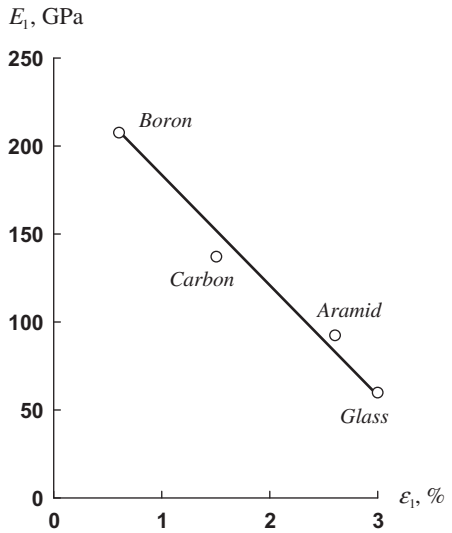


FIGURE 3.68

Longitudinal modulus versus ultimate tensile strain for advanced epoxy unidirectional composites.

of the first type. The corresponding part of a possible stress-strain diagram is shown in Fig. 3.69 with the line OA. The stress at point A is $\sigma_1^{(1)} = E_1\overline{\varepsilon}_f^{(1)}$. After the fibers of the first type fail, the material modulus reduces to

$$E_1^* = E_f^{(2)}\upsilon_f\left(1 - w_f^{(1)}\right) + E_m(1 - \upsilon_f)$$

This modulus determines the slope of line OC in Fig. 3.69.

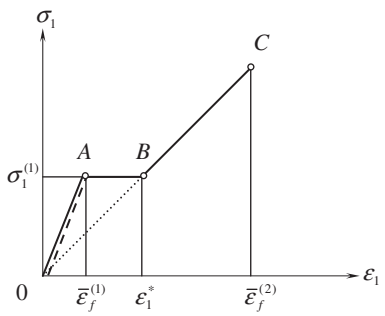


FIGURE 3.69

Typical stress-strain diagrams for hybrid unidirectional composites.

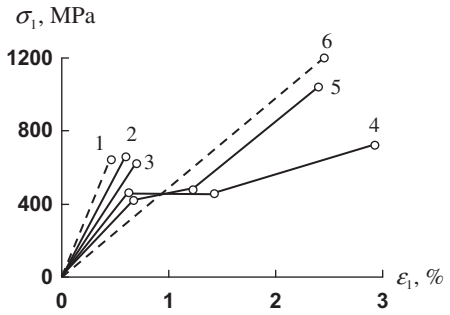


FIGURE 3.70

Experimental stress-strain diagrams for hybrid carbon-glass epoxy unidirectional composite with various volume fraction of glass fibers v_g and carbon fibers v_c: $1 - v_g = 0$; $2 - v_g = 0.07$; $3 - v_g = 0.14$; $4 - v_g = 0.25$; $5 - v_g = 0.5$; $6 - v_c = 0$.

Since $E_1^* < E_1$, the ply experiences a jump in strain under constant stress $\sigma_1 = \sigma_1^{(1)}$. As follows from Fig. 3.69, the final strain is

$$\varepsilon_1^* = \frac{\sigma_1^{(1)}}{E_1^*}$$

There are two possible scenarios of the further material behavior, depending on the relation between strain ε_1^* and the ultimate strain of the fibers of the second type, $\overline{\varepsilon}_f^{(2)}$. If $\varepsilon_1^* \geq \overline{\varepsilon}_f^{(2)}$, these fibers will also fail under stress $\sigma_1^{(1)}$, and the material stress-strain diagram corresponds to the dashed line OA in Fig. 3.69. If $\overline{\varepsilon}_f^{(2)} > \varepsilon_1^*$, the material would work up to point C in this figure. Experimental diagrams supporting this prediction are shown in Fig. 3.70 (Gunyaev, 1981).

The threshold value of $w_f^{(2)}$, indicating the minimum amount of the fibers of the second type that is sufficient to withstand the load after the failure of the first type fibers, can be found from the condition $\overline{\varepsilon}_1^* = \overline{\varepsilon}_f^{(2)}$(Skudra et al., 1989). The final result is as follows

$$\overline{w}_f^{(2)} = \frac{E_f^{(1)} v_f \overline{\varepsilon}_f^{(1)} - \left(1 - v_f\right) E_m \left(\overline{\varepsilon}_f^{(2)} - \overline{\varepsilon}_f^{(1)}\right)}{v_f \left[E_f^{(1)} \overline{\varepsilon}_f^{(1)} + E_f^{(2)} \left(\overline{\varepsilon}_f^{(2)} - \overline{\varepsilon}_f^{(1)}\right)\right]}$$

For $w_f^{(2)} < \overline{w}_f^{(2)}$, material strength can be calculated as $\overline{\sigma}_1 = E_1 \overline{\varepsilon}_f^{(1)}$, whereas for $w_f^{(2)} > \overline{w}_f^{(2)}$, $\overline{\sigma}_1 = E_1^* \overline{\varepsilon}_f^{(2)}$. The corresponding theoretical prediction of the dependence of material strength on $w_f^{(2)}$ is shown in Fig. 3.71 (Skudra et al., 1989).

3.6 COMPOSITES WITH HIGH FIBER FRACTION

We now return to Fig. 3.44, which shows the dependence of the tensile longitudinal strength of unidirectional composites on the fiber volume fraction v_f. As follows from this figure, the strength

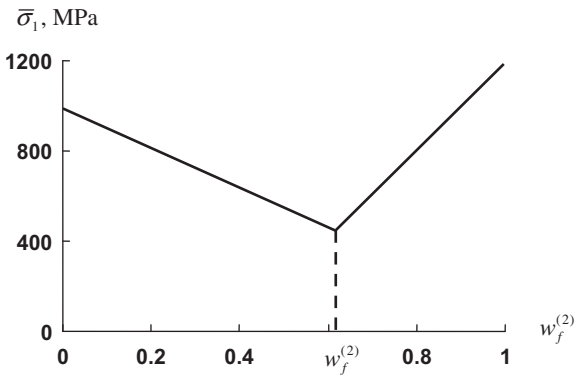


FIGURE 3.71

Dependence of the longitudinal strength of unidirectional carbon-glass epoxy composite on the volume fraction of glass fibers.

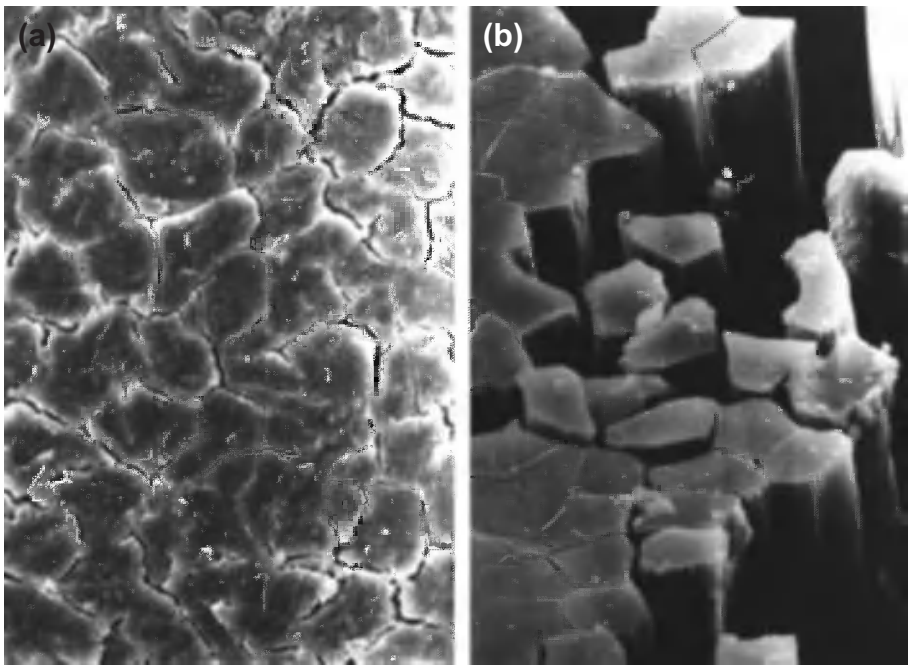


FIGURE 3.72

Cross section of aramid-epoxy composite with high fiber fraction: (a) initial structure; (b) structure with delaminated fibers.

TABLE 3.7 Properties of Aramid-epoxy Composites with High Fiber Fraction.

Property	Fiber Volume Fraction, v_f		
	0.65	**0.92**	**0.96**
Density, ρ (g/cm^3)	1.33	1.38	1.41
Longitudinal modulus, E_1 (GPa)	85	118	127
Transverse modulus, E_2 (GPa)	3.3	2.1	4.5
Shear modulus, G_{12} (GPa)	1.6	1.7	–
Longitudinal tensile strength, $\overline{\sigma}_1^+$ (MPa)	2200	2800	2800
Longitudinal compressive strength, $\overline{\sigma}_1^-$ (MPa)	293	295	310
Transverse tensile strength, $\overline{\sigma}_2^+$ (MPa)	22	12	–
Transverse compressive strength, $\overline{\sigma}_2^-$ (MPa)	118	48	–
In-plane shear strength, $\overline{\tau}_{12}$ (MPa)	41	28	18

increases up to v_f, which is close to 0.7 and becomes lower for higher fiber volume fractions. This is a typical feature of unidirectional fibrous composites (Andreevskaya, 1966). However, there are some experimental results (e.g., Roginskii and Egorov, 1966) showing that material strength can increase up to $v_f = 0.88$, which corresponds to the maximum theoretical fiber volume fraction discussed in Section 3.1. The reason that the material strength usually starts to decrease at higher fiber volume fractions is associated with material porosity, which becomes significant for materials with a shortage of resin. By reducing the material porosity, we can increase material tensile strength for high fiber volume fractions.

Moreover, applying the correct combination of compacting pressure and temperature to composites with organic (aramid or polyethylene) fibers, we can deform the fiber cross sections and reach a value of v_f that would be close to unity. Such composite materials studied by Golovkin (1985), Kharchenko (1999), and other researchers are referred to as Composites with High Fiber Fraction (CHFF). The cross section of a typical CHFF is shown in Fig. 3.72.

The properties of aramid-epoxy CHFF are listed in Table 3.7 (Kharchenko, 1999). Comparing traditional composites ($v_f = 0.65$) with CHFF, we can conclude that CHFF have significantly higher longitudinal moduli (up to 50%) and longitudinal tensile strengths (up to 30%), whereas their densities are only 6% higher. However, the transverse and shear strengths of CHFF are lower than those of traditional composites. Due to this, composites with high fiber fraction can be efficient in composite structures whose loading induces high tensile stresses acting mainly along the fibers, in cables, pressure vessels, etc.

3.7 PHENOMENOLOGICAL HOMOGENEOUS MODEL OF A PLY

It follows from the foregoing discussion that micromechanical analysis provides rather approximate predictions for the ply stiffness and only qualitative information concerning the ply strength. However, the design and analysis of composite structures require quite accurate and reliable information about the properties of the ply as the basic element of composite structures. This information is provided by experimental methods as discussed above. As a result, the ply is presented as an orthotropic homogeneous material possessing some apparent (effective) mechanical characteristics determined experimentally. This means that, on the ply level, we use a phenomenological model of a composite material (see Section 1.1) that ignores its actual microstructure.

It should be emphasized that this model, being quite natural and realistic for the majority of applications, sometimes does not allow us to predict actual material behavior. To demonstrate this, consider a problem of biaxial compression of a unidirectional composite in the 23-plane as in Fig. 3.73. Testing a glass-epoxy composite material described by Koltunov et al. (1977) shows a surprising result – its strength is about $\overline{\sigma} = 1200$ MPa, which is quite close to the level of material strength under longitudinal tension, and material failure is accompanied by fiber breakage typical for longitudinal tension.

The phenomenological model fails to predict this mode of failure. Indeed, the average stress in the longitudinal direction specified by Eq. (3.75) is equal to zero under loading (shown in Fig. 3.73), i.e.,

$$\sigma_1 = \sigma_1^f v_f + \sigma_1^m v_m = 0 \tag{3.127}$$

To apply the first-order micromechanical model considered in Section 3.3, we generalize constitutive equations, Eqs. (3.63), for the three-dimensional stress state of the fibers and the matrix as

$$\varepsilon_1^{f,m} = \frac{1}{E_{f,m}}\left[\sigma_1^{f,m} - \nu_{f,m}\left(\sigma_2^{f,m} + \sigma_3^{f,m}\right)\right] \quad \left(1,\ 2,\ 3\right) \tag{3.128}$$

Changing 1 for 2, 2 for 3, and 3 for 1, we can write the corresponding equations for ε_2 and ε_3.

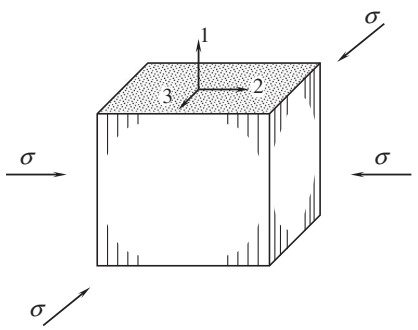


FIGURE 3.73

Biaxial compression of a unidirectional composite.

Suppose that the stresses acting in the fibers and in the matrix in the plane of loading are the same, i.e.,

$$\sigma_2^f = \sigma_3^f = \sigma_2^m = \sigma_3^m = -\sigma \tag{3.129}$$

and that $\varepsilon_1^f = \varepsilon_1^m$. Substituting ε_1^f and ε_1^m from Eqs. (3.128), we get (with due regard to Eqs. (3.129))

$$\frac{1}{E_f}\left(\sigma_1^f + 2\nu_f\sigma\right) = \frac{1}{E_m}\left(\sigma_1^m + 2\nu_m\sigma\right)$$

In conjunction with Eq. (3.127), this equation allows us to find σ_1^f, which has the form

$$\sigma_1^f = \frac{2\sigma\left(E_f\nu_m - E_m\nu_f\right)\upsilon_m}{E_f\upsilon_f + E_m\upsilon_m}$$

Simplifying this result for the situation $E_f >> E_m$, we arrive at

$$\sigma_1^f = 2\sigma\frac{\nu_m\upsilon_m}{\upsilon_f}$$

Thus, the loading shown in Fig. 3.73 indeed induces tension in the fibers as can be revealed using the micromechanical model. The ultimate stress can be expressed in terms of the fibers' strength $\overline{\sigma}_f$, as

$$\overline{\sigma} = \frac{1}{2}\overline{\sigma}_f\frac{\upsilon_f}{\nu_m\upsilon_m}$$

The actual material strength is not as high as follows from this equation, which is derived under the condition that the adhesive strength between the fibers and the matrix is infinitely high. Tension of fibers is induced by the matrix which expands in the 1 direction (see Fig. 3.73) due to Poisson's effect and interacts with fibers through shear stresses whose maximum value is limited by the fiber-matrix adhesion strength. Under high shear stress, debonding of the fibers can occur, reducing the material strength, which is, nevertheless, very high. This effect is utilized in composite shells with radial reinforcement designed to withstand an external pressure of high intensity (Koltunov et al., 1977).

3.8 References

Abu-Farsakh, G. A., Abdel-Jawad, Y. A., & Abu-Laila, Kh. M. (2000). Micromechanical characterization of tensile strength of fiber composite materials. *Mechanics of Composite Materials and Structures, 7*(1), 105–122.

Andreevskaya, G. D. (1966). *High-strength Oriented Fiberglass Plastics*. Moscow (in Russian): Nauka.

Bogdanovich, A. E., & Pastore, C. M. (1996). *Mechanics of Textile and Laminated Composites*. London: Chapman & Hall.

Chiao, T. T. (1979). Some interesting mechanical behaviors of fiber composite materials. In G. C. Sih, & V. P. Tamuzh (Eds.), *Proc. of 1st USA-USSR Symposium on Fracture of Composite Materials, Riga, USSR, 4–7 September, 1978* (pp. 385–392). Alphen aan den Rijn: Sijthoff and Noordhoff.

Crasto, A. S., & Kim, R. Y. (1993). An improved test specimen to determine composite compression strength. In *Proc. 9th Int. Conf. on Composite Materials (ICCM/9), Madrid, 12–16 July 1993, Vol. 6, Composite Properties and Applications* (pp. 621–630). Woodhead Publishing Ltd.

Feynman, R. P., Leighton, R. B., & Sands, M. (1964). *The Feynman Lectures on Physics. Vol. 2*. Reading, Massachusetts, Palo Alto, London: Addison-Wesley Publishing Company, Inc.

Fukuda, H., Miyazawa, T., & Tomatsu, H. (1993). Strength distribution of monofilaments used for advanced composites. In *Proc. 9th Int. Conf. on Composite Materials (ICCM/9), Madrid, 12–16 July 1993, Vol. 6, Composite Properties and Applications* (pp. 687–694). Woodhead Publishing Ltd.

Gilman, J. J. (1959). Cleavage, ductility and tenacity in Crystals. In *Fracture*. New York: Wiley.

Golovkin, G. S. (1985). Manufacturing parameters of the formation process for ultimately reinforced organic plastics. *Plastics, 4*, 31–33 [in Russian].

Goodey, W. J. (1946). Stress diffusion problems. *Aircraft Eng.* June 1946, 195–198; July 1946, 227–234; August 1946, 271–276; September 1946, 313–316; October 1946, 343–346; November 1946, 385–389.

Griffith, A. A. (1920). The phenomenon of rupture and flow in solids. *Philosophical Transactions of the Royal Society, A221*, 147–166.

Gunyaev, G. M. (1981). *Structure and Properties of Polymeric Fibrous Composites*. Moscow [in Russian]: Khimia.

Hashin, Z., & Rosen, B. W. (1964). The elastic moduli of fiber reinforced materials. *Journal of Applied Mechanics, 31E*, 223–232.

Jones, R. M. (1999). *Mechanics of Composite Materials* (2nd ed). Philadelphia, PA: Taylor & Francis.

Kharchenko, E. F. (1999). *High-strength Ultimately Reinforced Organic Plastics*. Moscow [in Russian].

Koltunov, M. A., Pleshkov, L. V., Kanovich, M. Z., Roginskii, S. L., & Natrusov, V. I. (1977). High-strength glass-reinforced plastic shells with radial orientation of the reinforcement. *Polymer Mechanics/Mechanics of Composite Materials, 13*(6), 928–930.

Kondo, K., & Aoki, T. (1982). Longitudinal shear modulus of unidirectional composites. In Kawata Hayashi, & Umeka. (Eds.), *Proc. 4th Int. Conf. on Composite Materials (ICCM-IV), Vol. 1, Progr. in Sci. and Eng. of Composites* (pp. 357–364), Tokyo, 1982.

Lagace, P. A. (1985). Nonlinear stress-strain behavior of graphite/epoxy laminates. *AIAA J, 223*(10), 1583–1589.

Lee, D. J., Jeong, T. H., & Kim, H. G. (1995). Effective longitudinal shear modulus of unidirectional composites. In *Proc. 10th Int. Conf. on Composite Materials (ICCM-10), Vol. 4, Characterization and Ceramic Matrix Composites* (pp. 171–178), Canada, 1995.

Mikelsons, M. Ya., & Gutans, Yu. A. (1984). Fracture of boron-aluminum under static and cyclic tension. *Mech. Comp. Mater, 1*, 52–59.

Mileiko, S. T. (1982). Mechanics of metal-matrix fibrous composites. In I. F. Obraztsov, & V. V. Vasiliev (Eds.), *Mechanics of Composites* (pp. 129–165). Moscow: Mir.

Peters, S. T. (1998). *Handbook of Composites* (2nd ed). London: Chapman & Hall.

Roginskii, S. L., & Egorov, N. G. (1966). Effect of fiber tension on strength of cylindrical shells reinforced with glass fibers. *Polim. Mech. 2*, 285–289 [in Russian].

Skudra, A. M., Bulavs, F. Ya., Gurvich, M. R., & Kruklinsh, A. A. (1989). *Elements of Structural Mechanics of Composite Truss Systems*. Riga: Zinatne [in Russian].

Tarnopol'skii, Yu. M., & Roze, A. V. (1969). *Specific Features of Analysis for Structural Elements of Reinforced Plastics*. Riga: Zinatne [in Russian].

Tarnopol'skii, Yu. M., & Kincis, T. Ya. (1985). *Static Test Methods for Composites*. New York: Van Nostrand Reinhold.

Tikhomirov, P. V., & Yushanov, S. P. (1980). Stress distribution after the fracture of fibers in a unidirectional composite. In *Mech. Composite Mater., Riga* (pp. 28–43) [in Russian].

Timoshenko, S. P., & Gere, J. M. (1961). *Theory of Elastic Stability* (2nd ed). New York: McGraw-Hill.

Van Fo Fy (Vanin), G. A. (1966). Elastic constants and state of stress of glass-reinforced strip. *J. Polym. Mech., 2*(4), 368–372.

Vasiliev, V. V., & Tarnopol'skii, Yu. M. (1990). *Composite Materials. Handbook*. Moscow: Mashinostroenie [in Russian].

Woolstencroft, D. H., Haresceugh, R. I., & Curtis, A. R. (1982). The compressive behavior of carbon fiber reinforced plastic. In Kawata Hayashi, & Umeka. (Eds.), *Proc. 4th Int. Conf. on Composite Materials (ICCM-IV), Vol. 1, Progr. in Sci. and Eng. of Composites* (pp. 439–446), Tokyo, 1982.

Zabolotskii, A. A., & Varshavskii, V. Ya (1984). Multireinforced (Hybrid) composite materials. In *Science and Technology Reviews, Composite Materials, Part 2*. Moscow.

CHAPTER

Mechanics of a composite layer

4

A typical composite laminate consists of individual layers (see Fig. 4.1), which are usually made of unidirectional plies with the same or regularly alternating orientations. A layer can also be made from metal, thermosetting or thermoplastic polymer, or fabric, or can have a spatial three-dimensionally reinforced structure. In contrast to a ply as considered in Chapter 3, a layer is generally referred to the global coordinate frame x, y, and z of the structural element rather than to coordinates 1, 2, and 3 associated with the ply orientation. Usually, a layer is much thicker than a ply and has a more complicated structure, but this structure does not change through its thickness, or this change is ignored. Thus, a layer can be defined as a three-dimensional structural element that is uniform in the transverse (normal to the layer plane) direction.

4.1 ISOTROPIC LAYER

The simplest layer that can be observed in composite laminates is an isotropic layer of metal or thermoplastic polymer that is used to protect the composite material (Fig. 4.2) and to provide tightness. For example, filament-wound composite pressure vessels usually have a sealing metal (Fig. 4.3) or thermoplastic (Fig. 4.4) internal liner, which can also be used as a mandrel for winding. Since the layer is isotropic, we need only one coordinate system and let it be the global coordinate frame shown in Fig. 4.5.

4.1.1 Linear elastic model

The explicit form of Hooke's law in Eqs. (2.48) and (2.54) can be written as

$$\begin{aligned}
\varepsilon_x &= \frac{1}{E}(\sigma_x - \nu\sigma_y - \nu\sigma_z), \quad \gamma_{xy} = \frac{\tau_{xy}}{G} \\
\varepsilon_y &= \frac{1}{E}(\sigma_y - \nu\sigma_x - \nu\sigma_z), \quad \gamma_{xz} = \frac{\tau_{xz}}{G} \\
\varepsilon_z &= \frac{1}{E}(\sigma_z - \nu\sigma_x - \nu\sigma_y), \quad \gamma_{yz} = \frac{\tau_{yz}}{G},
\end{aligned} \tag{4.1}$$

where E is the modulus of elasticity, ν Poisson's ratio, and G the shear modulus, which can be expressed in terms of E and ν with Eq. (2.57). Adding Eqs. (4.1) for normal strains we get

$$\varepsilon_0 = \frac{1}{K}\sigma_0 \tag{4.2}$$

Advanced Mechanics of Composite Materials and Structural Elements. http://dx.doi.org/10.1016/B978-0-08-098231-1.00004-2
Copyright © 2013 Elsevier Ltd. All rights reserved.



FIGURE 4.1

Laminated structure of a composite pipe.

where

$$\varepsilon_0 = \varepsilon_x + \varepsilon_y + \varepsilon_z \tag{4.3}$$

is the volume deformation (dilatation). For small strains, the volume dV_1 of an infinitesimal material element after deformation can be found knowing the volume dV before the deformation and ε_0 as

$$dV_1 = (1 + \varepsilon_0)dV$$

Volume deformation is related to the mean stress

$$\sigma_0 = \frac{1}{3}(\sigma_x + \sigma_y + \sigma_z) \tag{4.4}$$

through the volume or bulk modulus

$$K = \frac{E}{3(1 - 2\nu)} \tag{4.5}$$

It follows from Eq. (4.5) that for $\nu = 1/2$ we have $K \to \infty$. Then, Eq. (4.2) yields $\varepsilon_0 = 0$ and $dV_1 = dV$ for any stress. Such materials are called incompressible – they do not change their volume under deformation and can change only their shapes.

The foregoing equations correspond to the general three-dimensional stress state of a layer. However, working as a structural element of a thin-walled composite laminate, a layer is usually



FIGURE 4.2

Composite drive shaft with external metal protection layer.

Courtesy of CRISM.



FIGURE 4.3

Aluminum liner for a composite pressure vessel.



FIGURE 4.4

Thermoplastic liners for composite pressure vessels.

loaded with a system of stresses one of which, namely transverse normal stress σ_z, is much less than the other stresses. Bearing this in mind, we can neglect the terms in Eqs. (4.1) that include σ_z and write these equations in a simplified form

$$\varepsilon_x = \frac{1}{E}(\sigma_x - \nu\sigma_y), \quad \varepsilon_y = \frac{1}{E}(\sigma_y - \nu\sigma_x)$$
$$\gamma_{xy} = \frac{\tau_{xy}}{G}, \quad \gamma_{xz} = \frac{\tau_{xz}}{G}, \quad \gamma_{yz} = \frac{\tau_{yz}}{G} \tag{4.6}$$

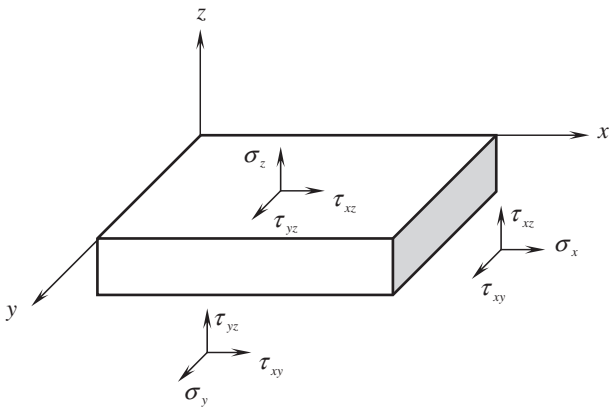


FIGURE 4.5

An isotropic layer.

or

$$\sigma_x = \overline{E}\left(\varepsilon_x + \nu\varepsilon_y\right), \quad \sigma_y = \overline{E}\left(\varepsilon_y + \nu\varepsilon_x\right)$$
$$\tau_{xy} = G\gamma_{xy}, \quad \tau_{xz} = G\gamma_{xz}, \quad \tau_{yz} = G\gamma_{yz} \tag{4.7}$$

where $\overline{E} = E/(1-\nu^2)$.

4.1.2 Nonlinear models

Materials of metal and polymeric layers considered in this section demonstrate linear response only under moderate stresses (see Figs. 1.11 and 1.14). Further loading results in nonlinear behavior, to describe which we need to apply one of the nonlinear material models discussed in Section 1.1.

A relatively simple nonlinear constitutive theory suitable for polymeric layers can be constructed using a nonlinear elastic material model (see Fig. 1.2). In the strict sense, this model can be applied to materials whose stress-strain curves are the same for active loading and unloading. However, normally structural analysis is undertaken only for active loading. If unloading is not considered, an elastic model can be formally used for materials that are not perfectly elastic.

There exist a number of models developed to describe the nonlinear behavior of highly deformable elastomers such as rubber (Green and Adkins, 1960). Polymeric materials used to form isotropic layers of composite laminates admitting, in principle, high strains usually do not demonstrate them in composite structures whose deformation is governed by fibers with relatively low ultimate elongation (1–3%). So, creating the model, we can restrict ourselves to the case of small strains, i.e., to materials whose typical stress-strain diagram is shown in Fig. 4.6.

A natural way is to apply Eqs. (2.41) and (2.42), i.e.,

$$dU = \sigma_{ij}d\varepsilon_{ij}, \quad \sigma_{ij} = \frac{\partial U}{\partial \varepsilon_{ij}} \tag{4.8}$$

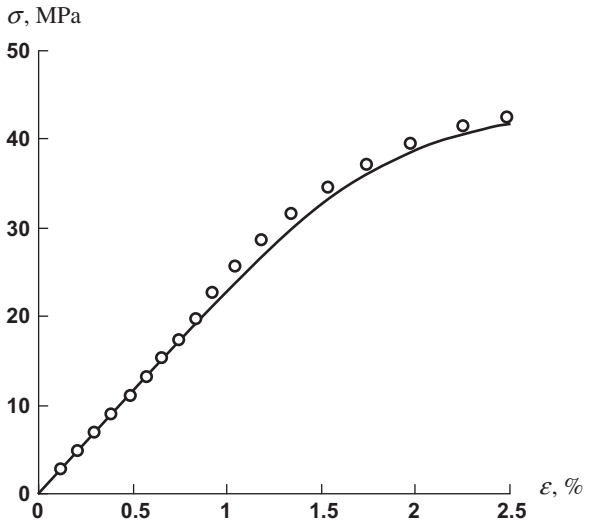


FIGURE 4.6

A typical stress-strain diagram (circles) for a polymeric film and its cubic approximation (solid line).

(we use tensor notations for stresses and strains introduced in Section 2.9 and the rule of summation over repeated subscripts). Approximation of elastic potential U as a function of ε_{ij} with some unknown parameters allows us to write constitutive equations directly using the second relation in Eqs. (4.8). However, the polynomial approximation similar to Eq. (2.43), which is the most simple and natural, results in a constitutive equation of the type $\sigma = S\varepsilon^n$, in which S is some stiffness coefficient and n is an integer. As can be seen in Fig. 4.7, the resulting stress-strain curve is not typical for the materials under study. Better agreement with nonlinear experimental diagrams presented (e.g., in Fig. 4.6) is demonstrated by the curve specified by the equation $\varepsilon = C\sigma^n$, in which C is some compliance coefficient. To arrive at this form of a constitutive equation, we need to have a relationship similar to the second one in Eqs. (4.8), but allowing us to express strains in terms of stresses. Such relationships exist and are known as Castigliano's formulae. To derive them, introduce the complementary elastic potential U_c in accordance with the following equation:

$$dU_c = \varepsilon_{ij} d\sigma_{ij} \tag{4.9}$$

The term "complementary" becomes clear if we consider a bar in Fig. 1.1 and the corresponding stress-strain curve in Fig. 4.8. The area 0BC below the curve represents U in accordance with the first equation in Eqs. (4.8), whereas the area 0AC above the curve is equal to U_c. As shown in Section 2.9, dU in Eqs. (4.8) is an exact differential. To prove the same for dU_c, consider the following sum

$$dU + dU_c = \sigma_{ij} d\varepsilon_{ij} + \varepsilon_{ij} d\sigma_{ij} = d\left(\sigma_{ij}\varepsilon_{ij}\right)$$

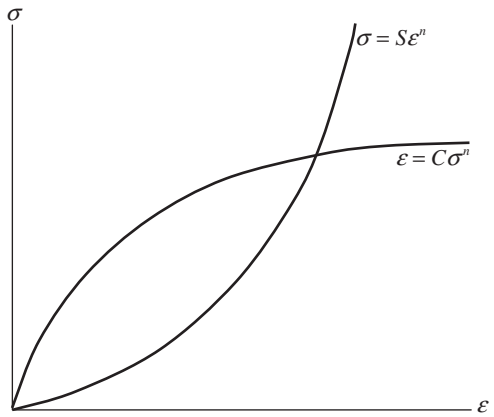


FIGURE 4.7

Two forms of approximation of the stress-strain curve.

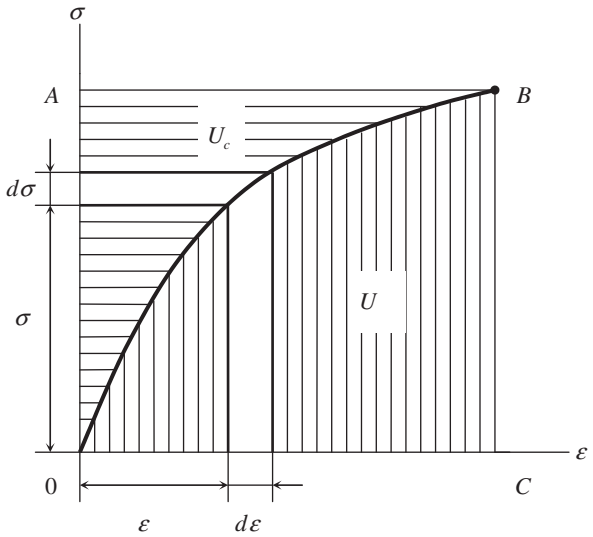


FIGURE 4.8

Geometric interpretation of elastic potential, U, and complementary potential, U_c.

which is obviously an exact differential. Since dU in this sum is also an exact differential, dU_c should have the same property and can be expressed as

$$dU_c = \frac{\partial U_c}{\partial \sigma_{ij}} d\sigma_{ij}$$

Comparing this result with Eq. (4.9), we arrive at Castigliano's formulae

$$\varepsilon_{ij} = \frac{\partial U_c}{\partial \sigma_{ij}} \tag{4.10}$$

which are valid for any elastic solid (for a linear elastic solid, $U_c = U$).

The complementary potential, U_c, in general, depends on stresses, but for an isotropic material, Eq. (4.10) should yield invariant constitutive equations that do not depend on the direction of coordinate axes. This means that U_c should depend on stress invariants I_1, I_2, and I_3 in Eqs. (2.13). Using different approximations for the function $U_c(I_1, I_2, I_3)$, we can construct different classes of nonlinear elastic models. Existing experimental verification of such models shows that the dependence of U_c on I_3 can be neglected. Thus, we can present the complementary potential in a simplified form $U_c(I_1, I_2)$ and expand this function as a Taylor series as follows

$$\begin{aligned} U_c = {} & c_0 + c_{11} I_1 + \frac{1}{2} c_{12} I_1^2 + \frac{1}{3!} c_{13} I_1^3 + \frac{1}{4!} c_{14} I_1^4 + \cdots \\ & + c_{21} I_2 + \frac{1}{2} c_{22} I_2^2 + \frac{1}{3!} c_{23} I_2^3 + \frac{1}{4!} c_{24} I_2^4 + \cdots \\ & + \frac{1}{2} c_{1121} I_1 I_2 + \frac{1}{3!} c_{1221} I_1^2 I_2 + \frac{1}{3!} c_{1122} I_1 I_2^2 + \cdots \\ & + \frac{1}{4!} c_{1321} I_1^3 I_2 + \frac{1}{4!} c_{1222} I_1^2 I_2^2 + \frac{1}{4!} c_{1123} I_1 I_2^3 + \cdots \end{aligned} \tag{4.11}$$

where

$$c_{in} = \left. \frac{\partial^n U_c}{\partial I_i^n} \right|_{\sigma_{ij}=0}, \quad c_{injm} = \left. \frac{\partial^{n+m} U_c}{\partial I_i^n \partial I_j^m} \right|_{\sigma_{ij}=0}$$

Constitutive equations follow from Eq. (4.10) and can be written in the form

$$\varepsilon_{ij} = \frac{\partial U_c}{\partial I_1} \frac{\partial I_1}{\partial \sigma_{ij}} + \frac{\partial U_c}{\partial I_2} \frac{\partial I_2}{\partial \sigma_{ij}} \tag{4.12}$$

Assuming that for zero stresses $U_c = 0$ and $\varepsilon_{ij} = 0$, we should take $c_0 = 0$ and $c_{11} = 0$ in Eq. (4.11).

Consider a plane stress state with stresses σ_x, σ_y, and τ_{xy} shown in Fig. 4.5. The stress invariants in Eqs. (2.13) to be substituted into Eq. (4.12) are

$$I_1 = \sigma_x + \sigma_y, \quad I_2 = -\sigma_x \sigma_y + \tau_{xy}^2 \tag{4.13}$$

A linear elastic material model is described with Eq. (4.11) if we take

$$U_c = \frac{1}{2} c_{12} I_1^2 + c_{21} I_2 \tag{4.14}$$

Using Eqs. (4.12)–(4.14) and engineering notations for stresses and strains, we arrive at

$$\varepsilon_x = c_{12}(\sigma_x + \sigma_y) - c_{21}\sigma_y, \quad \varepsilon_y = c_{12}(\sigma_x + \sigma_y) - c_{21}\sigma_x,$$
$$\gamma_{xy} = 2c_{21}\tau_{xy}$$

These equations coincide with the corresponding equations in Eqs. (4.6) if we take

$$c_{12} = \frac{1}{E}, \quad c_{21} = \frac{1+\nu}{E}$$

To describe a nonlinear stress-strain diagram of the type shown in Fig. 4.6, we can generalize Eq. (4.14) as

$$U_c = \frac{1}{2}c_{12}I_1^2 + c_{21}I_2 + \frac{1}{4!}c_{14}I_1^4 + \frac{1}{2}c_{22}I_2^2$$

Then, Eq. (4.12) yields the following cubic constitutive law

$$\varepsilon_x = c_{12}(\sigma_x + \sigma_y) - c_{21}\sigma_y + \frac{1}{6}c_{14}\left(\sigma_x + \sigma_y\right)^3 + c_{22}(\sigma_x\sigma_y - \tau_{xy}^2)\sigma_y$$

$$\varepsilon_y = c_{12}(\sigma_x + \sigma_y) - c_{21}\sigma_x + \frac{1}{6}c_{14}\left(\sigma_x + \sigma_y\right)^3 + c_{22}(\sigma_x\sigma_y - \tau_{xy}^2)\sigma_x$$

$$\gamma_{xy} = 2\left[c_{21} - c_{22}\left(\sigma_x\sigma_y - \tau_{xy}^2\right)\right]\tau_{xy}$$

The corresponding approximation is shown in Fig. 4.6 with a solid line. Retaining more higher-order terms in Eq. (4.11), we can describe the nonlinear behavior of any isotropic polymeric material.

To describe the nonlinear elastic-plastic behavior of metal layers, we should use constitutive equations of the theory of plasticity. There exist two basic versions of this theory – the deformation theory and the flow theory, which are briefly described later.

According to the deformation theory of plasticity, the strains are decomposed into two components – elastic strains (with superscript "e") and plastic strains (superscript "p"), i.e.,

$$\varepsilon_{ij} = \varepsilon_{ij}^e + \varepsilon_{ij}^p \tag{4.15}$$

We again use the tensor notations of strains and stresses (i.e., ε_{ij} and σ_{ij}) introduced in Section 2.9. Elastic strains are related to stresses by Hooke's law, Eqs. (4.1), which can be written with the aid of Eq. (4.10) in the form

$$\varepsilon_{ij}^e = \frac{\partial U_e}{\partial \sigma_{ij}} \tag{4.16}$$

where U_e is the elastic potential that for a linear elastic solid coincides with the complementary potential U_c in Eq. (4.10). An explicit expression for U_e can be obtained from Eq. (2.51) if we change strains for stresses with the aid of Hooke's law, i.e.,

$$\begin{aligned} U_e = {} & \frac{1}{2E}\left[\sigma_{11}^2 + \sigma_{22}^2 + \sigma_{33}^2 - 2\nu(\sigma_{11}\sigma_{22} + \sigma_{11}\sigma_{33} + \sigma_{22}\sigma_{33})\right] \\ & + \frac{1}{2G}(\sigma_{12}^2 + \sigma_{13}^2 + \sigma_{23}^2) \end{aligned} \tag{4.17}$$

Now represent the plastic strains in Eq. (4.15) in a form similar to Eq. (4.16)

$$\varepsilon_{ij}^p = \frac{\partial U_p}{\partial \sigma_{ij}} \tag{4.18}$$

where U_p is the plastic potential. To approximate the dependence of U_p on stresses, a special generalized stress characteristic, i.e., the so-called stress intensity σ, is introduced in the classical theory of plasticity as

$$\sigma = \frac{1}{\sqrt{2}}\left[(\sigma_{11}-\sigma_{22})^2 + (\sigma_{22}-\sigma_{33})^2 + (\sigma_{11}-\sigma_{33})^2 + 6\left(\sigma_{12}^2+\sigma_{13}^2+\sigma_{23}^2\right)\right]^{\frac{1}{2}} \tag{4.19}$$

Transforming Eq. (4.19) with the aid of Eqs. (2.13), we can reduce it to the following form

$$\sigma = \sqrt{I_1^2 + 3I_2}$$

This means that σ is an invariant characteristic of a stress state, i.e., that it does not depend on the orientation of a coordinate frame. For unidirectional tension as in Fig. 1.1, we have only one nonzero stress, e.g., σ_{11}. Then, Eq. (4.19) yields $\sigma = \sigma_{11}$. In a similar way, the strain intensity ε can be introduced as

$$\varepsilon = \frac{\sqrt{2}}{3}\left[(\varepsilon_{11}-\varepsilon_{22})^2 + (\varepsilon_{22}-\varepsilon_{33})^2 + (\varepsilon_{11}-\varepsilon_{33})^2 + 6\left(\varepsilon_{12}^2+\varepsilon_{13}^2+\varepsilon_{23}^2\right)\right]^{\frac{1}{2}} \tag{4.20}$$

The strain intensity is also an invariant characteristic. For uniaxial tension (Fig. 1.1) with stress σ_{11} and strain ε_{11} in the loading direction, we have $\varepsilon_{22} = \varepsilon_{33} = -\nu_p\varepsilon_{11}$, where ν_p is the elastic-plastic Poisson's ratio which, in general, depends on σ_{11}. For this case, Eq. (4.20) yields

$$\varepsilon = \frac{2}{3}(1+\nu_p)\varepsilon_{11} \tag{4.21}$$

For an incompressible material (see Section 4.1.1), $\nu_p = 1/2$ and $\varepsilon = \varepsilon_{11}$. Thus, the numerical coefficients in Eqs. (4.19) and (4.20) provide $\sigma = \sigma_{11}$ and $\varepsilon = \varepsilon_{11}$ for uniaxial tension of an incompressible material. The stress and strain intensities in Eqs. (4.19) and (4.20) have an important physical meaning. As known from experiments, metals do not demonstrate plastic properties under loading with stresses $\sigma_x = \sigma_y = \sigma_z = \sigma_0$ resulting only in a change of material volume. Under such loading, materials exhibit only elastic volume deformation specified by Eq. (4.2). Plastic strains occur in metals if we change material shape. For a linear elastic material, the elastic potential U in Eq. (2.51) can be reduced after rather cumbersome transformation with the aid of Eqs. (4.3) and (4.4), and (4.19) and (4.20) to the following form

$$U = \frac{1}{2}\sigma_0\varepsilon_0 + \frac{1}{2}\sigma\varepsilon \tag{4.22}$$

The first term in the right-hand part of this equation ($\sigma_0\varepsilon_0/2$) is the strain energy associated with the volume change, whereas the second term ($\sigma_\varepsilon/2$) corresponds to the change of material shape. Thus, σ and ε in Eqs. (4.19) and (4.20) are stress and strain characteristics associated with the change of a material's shape under which it demonstrates the plastic behavior.

In the theory of plasticity, the plastic potential U_p is assumed to be a function of stress intensity σ, and according to Eq. (4.18), the plastic strains are given by

$$\varepsilon_{ij}^p = \frac{dU_p}{d\sigma}\frac{\partial\sigma}{\partial\sigma_{ij}} \tag{4.23}$$

Consider further a plane stress state with stresses $\sigma_x,\ \sigma_y,$ and τ_{xy} in Fig. 4.5. For this case, Eq. (4.19) takes the form

$$\sigma = \sqrt{\sigma_x^2 + \sigma_y^2 - \sigma_x\sigma_y + 3\tau_{xy}^2} \tag{4.24}$$

Using Eqs. (4.15)–(4.17), (4.23), and (4.24), we finally arrive at the following constitutive equations

$$\begin{aligned}
\varepsilon_x &= \frac{1}{E}(\sigma_x - \nu\sigma_y) + \omega(\sigma)\left(\sigma_x - \frac{1}{2}\sigma_y\right) \\
\varepsilon_y &= \frac{1}{E}(\sigma_y - \nu\sigma_x) + \omega(\sigma)\left(\sigma_y - \frac{1}{2}\sigma_x\right) \\
\gamma_{xy} &= \frac{1}{G}\tau_{xy} + 3\omega(\sigma)\tau_{xy}
\end{aligned} \tag{4.25}$$

in which

$$\omega(\sigma) = \frac{1}{\sigma}\frac{dU_p}{d\sigma} \tag{4.26}$$

To find $\omega(\sigma)$, we need to specify the dependence of U_c on σ. The most simple and suitable for practical applications is the power approximation

$$U_p = C\sigma^n \tag{4.27}$$

where C and n are some experimental constants. As a result, Eq. (4.26) yields

$$\omega(\sigma) = Cn\sigma^{n-2} \tag{4.28}$$

To determine coefficients C and n, we introduce the basic assumption of the plasticity theory concerning the existence of a universal stress-strain diagram (master curve). According to this assumption, for any particular material, there exists a relationship between stress and strain intensities, i.e., $\sigma = \varphi(\varepsilon)$ (or $\varepsilon = f(\sigma)$), that is one and the same for all loading cases. This fact enables us to find coefficients C and n from a test under uniaxial tension and thus extend the obtained results to an arbitrary state of stress.

Indeed, consider uniaxial tension as in Fig. 1.1 with stress σ_{11}. For this case, $\sigma = \sigma_x$, and Eqs. (4.25) yield

$$\varepsilon_x = \frac{\sigma_x}{E} + \omega(\sigma_x)\sigma_x \tag{4.29}$$

$$\begin{aligned}
\varepsilon_y &= -\frac{\nu}{E}\sigma_x - \frac{1}{2}\omega(\sigma_x)\sigma_x \\
\gamma_{xy} &= 0
\end{aligned} \tag{4.30}$$

Solving Eq. (4.29) for $\omega(\sigma_x)$, we get

$$\omega(\sigma_x) = \frac{1}{E_s(\sigma_x)} - \frac{1}{E} \tag{4.31}$$

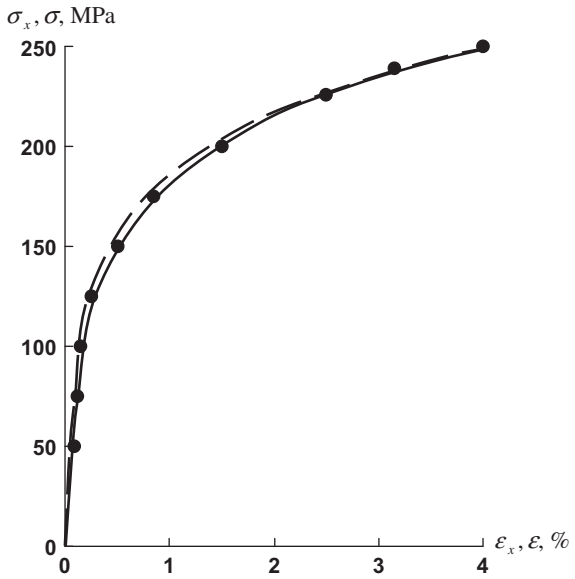


FIGURE 4.9

Experimental stress-strain diagram for an aluminum alloy under uniaxial tension (solid line); the universal stress-strain curve (dashed line), and its power approximation (dots).

where $E_s = \sigma_x/\varepsilon_x$ is the secant modulus introduced in Section 1.1 (see Fig. 1.4). Using now the assumption regarding the existence of the universal diagram for stress intensity σ and taking into account that $\sigma = \sigma_x$ for uniaxial tension, we can generalize Eq. (4.31) and write it for an arbitrary state of stress as

$$\omega(\sigma) = \frac{1}{E_s(\sigma)} - \frac{1}{E} \tag{4.32}$$

To determine $E_s(\sigma) = \sigma/\varepsilon$, we need to plot the universal stress-strain curve. For this purpose, we can use an experimental diagram $\sigma_x(\varepsilon_x)$ for the case of uniaxial tension, e.g., the one shown in Fig. 4.9 for an aluminum alloy with a solid line. To plot the universal curve $\sigma(\varepsilon)$, we should put $\sigma = \sigma_x$ and change the scale on the strain axis in accordance with Eq. (4.21). To do this, we need to know the plastic Poisson's ratio ν_p, which can be found from $\nu_p = -\varepsilon_y/\varepsilon_x$. Using Eqs. (4.29) and (4.30), we arrive at

$$\nu_p = \frac{1}{2} - \frac{E_s}{E}\left(\frac{1}{2} - \nu\right)$$

It follows from this equation that $\nu_p = \nu$ if $E_s = E$ and $\nu_p \to 1/2$ for $E_s \to 0$. The dependencies of E_s and ν_p on ε for the aluminum alloy under consideration are presented in Fig. 4.10. With the aid of this figure and Eq. (4.21) in which we should take $\varepsilon_{11} = \varepsilon_x$, we can calculate ε and plot the universal curve shown in Fig. 4.9 with a dashed line. As can be seen, this curve is slightly different from that in

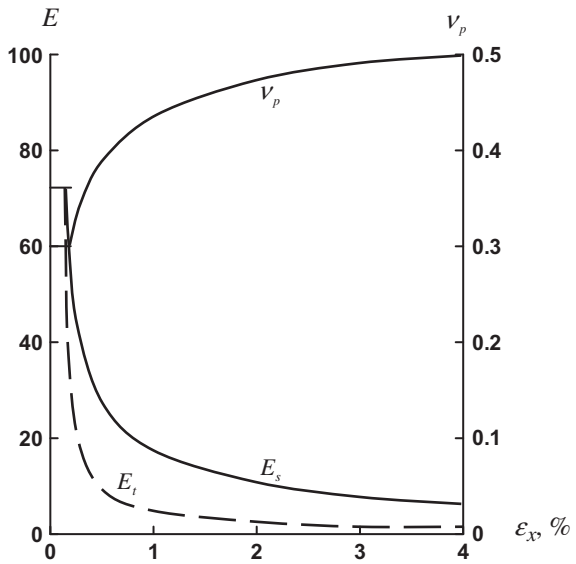


FIGURE 4.10

Dependencies of the secant modulus (E_s), tangent modulus (E_t), and the plastic Poisson's ratio (ν_p) on strain for an aluminum alloy.

the diagram corresponding to a uniaxial tension. For the power approximation in Eq. (4.27), we get from Eqs. (4.26) and (4.32) the following equations:

$$\omega(\sigma) = Cn\sigma^{n-2}, \quad \omega(\sigma) = \frac{\varepsilon}{\sigma} - \frac{1}{E}$$

Matching these results, we find

$$\varepsilon = \frac{\sigma}{E} + Cn\sigma^{n-1} \tag{4.33}$$

This is a traditional approximation for a material with a power hardening law. Now, we can find C and n using Eq. (4.33) to approximate the dashed line in Fig. 4.9. The results of this approximation are shown in this figure with dots that correspond to $E = 71.4$ GPa, $n = 6,$ and $C = 6.23 \cdot 10^{-15}(\text{MPa})^{-5}$.

Thus, constitutive equations of the deformation theory of plasticity are specified by Eqs. (4.25) and (4.32). These equations are valid only for active loading that can be identified by the condition $d\sigma > 0$. Applied for unloading (i.e., for $d\sigma < 0$), Eqs. (4.25) correspond to nonlinear elastic material with the stress-strain diagram shown in Fig. 1.2. For an elastic-plastic material (see Fig. 1.5), the unloading diagram is linear. So, if we reduce the stresses by some decrements $\Delta\sigma_x,\ \Delta\sigma_y,$ and $\Delta\tau_{xy}$, the corresponding decrements of strains will be

$$\Delta\varepsilon_x = \frac{1}{E}(\Delta\sigma_x - \nu\Delta\sigma_y), \quad \Delta\varepsilon_y = \frac{1}{E}(\Delta\sigma_y - \nu\Delta\sigma_x),$$

$$\Delta\gamma_{xy} = \frac{1}{G}\Delta\tau_{xy}$$

Direct application of the nonlinear equations (4.25) substantially hinders the problem of stress-strain analysis because these equations include function $\omega(\sigma)$ in Eq. (4.32) which, in turn, contains the secant modulus $E_s(\sigma)$. For the power approximation corresponding to Eq. (4.33), E_s can be expressed analytically, i.e.,

$$\frac{1}{E_s} = \frac{1}{E} + Cn\sigma^{n-2}$$

However, in many cases E_s is given graphically (as in Fig. 4.10) or numerically in the form of a table. Thus, Eqs. (4.25) sometimes cannot even be written in an explicit analytical form. This implies application of numerical methods in conjunction with iterative linearization of Eqs. (4.25).

There exist several methods of such linearization that will be demonstrated using the first equation in Eqs. (4.25), i.e.,

$$\varepsilon_x = \frac{1}{E}(\sigma_x - \nu\sigma_y) + \omega(\sigma)\left(\sigma_x - \frac{1}{2}\sigma_y\right) \tag{4.34}$$

In the method of elastic solutions (Ilyushin, 1948), Eq. (4.34) is used in the following form

$$\varepsilon_x^s = \frac{1}{E}\left(\sigma_x^s - \nu\sigma_y^s\right) + \eta_{s-1} \tag{4.35}$$

where s is the number of the iteration step and

$$\eta_{s-1} = \omega(\sigma_{s-1})\left(\sigma_x^{s-1} - \frac{1}{2}\sigma_y^{s-1}\right)$$

For the first step ($s = 1$), we take $\eta_0 = 0$ and solve the problem of linear elasticity with Eq. (4.35) in the form

$$\varepsilon_x^1 = \frac{1}{E}\left(\sigma_x^1 - \nu\sigma_y^1\right) \tag{4.36}$$

Finding the stresses, we calculate η_1 and write Eq. (4.35) as

$$\varepsilon_x^2 = \frac{1}{E}\left(\sigma_x^2 - \nu\sigma_y^2\right) + \eta_1$$

where the first term is linear, whereas the second term is a known function of coordinates. Thus we have another linear problem, resolving which we find stresses, calculate η_2, and switch to the third step. This process is continued until the strains corresponding to some step become sufficiently close within the stipulated accuracy to the results found at the previous step.

Thus, the method of elastic solutions reduces the initial nonlinear problem to a sequence of linear problems of the theory of elasticity for the same material, but with some initial strains that can be transformed into initial stresses or additional loads. This method readily provides a nonlinear solution for any problem that has a linear solution, analytical or numerical. The main shortcoming of the method is its poor convergence. Graphical interpretation of this process for the case of uniaxial tension with stress σ is presented in Fig. 4.11a. This figure shows a simple way to improve the convergence of the process. If we need to find the strain at the point of the curve that is close to point A, it is not necessary to start the process with initial modulus E. Taking $E' < E$ in Eq. (4.36) we can reach the result with many fewer steps.

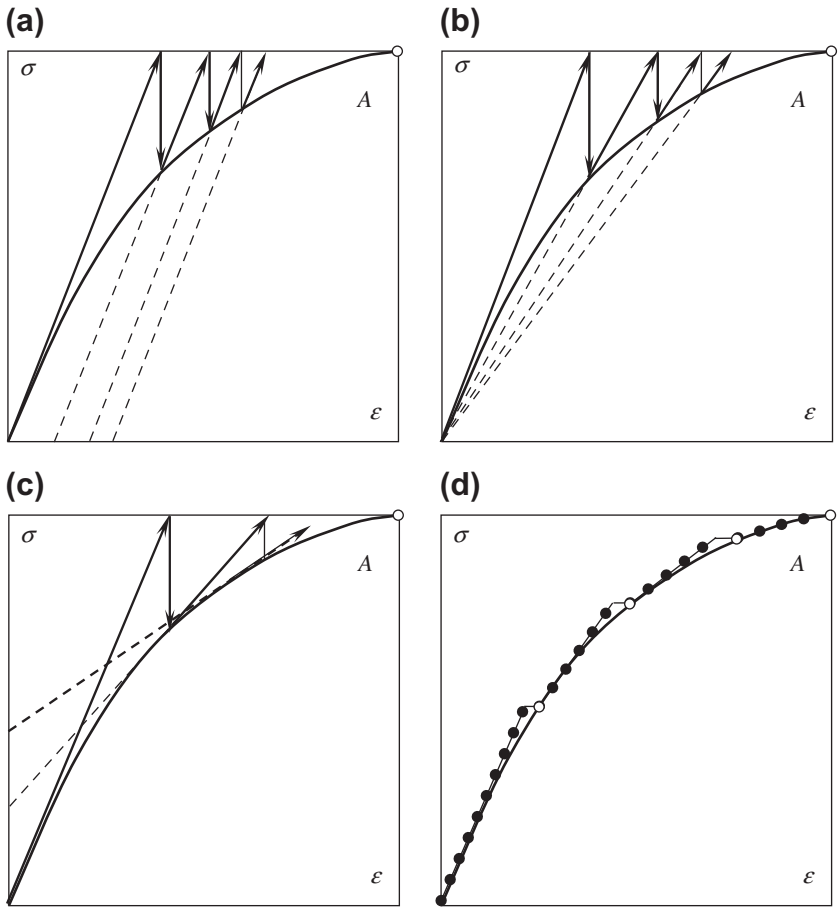


FIGURE 4.11

Geometric interpretation of (a) the method of elastic solutions, (b) the method of variable elasticity parameters, (c) Newton's method, and (d) method of successive loading.

According to the method of elastic variables (Birger, 1951), we should present Eq. (4.34) as

$$\varepsilon_x^s = \frac{1}{E}\left(\sigma_x^s - \nu\sigma_y^s\right) + \omega(\sigma_{s-1})\left(\sigma_x^s - \frac{1}{2}\sigma_y^s\right) \tag{4.37}$$

In contrast to Eq. (4.35), stresses σ_x^s and σ_y^s in the second term correspond to the current step rather than to the previous one. This enables us to write Eq. (4.37) in a form analogous to Hooke's law, i.e.,

$$\varepsilon_x^s = \frac{1}{E_{s-1}}\left(\sigma_x^s - \nu_{s-1}\sigma_y^s\right) \tag{4.38}$$

where

$$E_{s-1} = \left[\frac{1}{E} + \omega(\sigma_{s-1})\right]^{-1}, \quad \nu_{s-1} = E_{s-1}\left[\frac{\nu}{E} + \frac{1}{2}\omega(\sigma_{s-1})\right] \tag{4.39}$$

are elastic variables corresponding to the step with number $s-1$. The iteration procedure is similar to that described previously. For the first step we take $E_0 = E$ and $\nu_0 = \nu$ in Eq. (4.38). We then find σ_x^1, σ_y^1, and σ_1, determine E_1 and ν_1, switch to the second step, and so on. Graphical interpretation of the process is shown in Fig. 4.11b. Convergence of this method is by an order faster than that of the method of elastic solutions. However, elastic variables in the linear constitutive equation of the method, Eq. (4.38), depend on stresses, and hence, on coordinates whence the method has obtained its name. This method can be efficiently applied in conjunction with the finite element method, according to which the structure is modeled with the system of elements with constant stiffness coefficients. Being calculated for each step with the aid of Eqs. (4.39), stiffness will change only with transition from one element to another, which clearly would not practically hinder the calculation procedure for the finite element method.

The iteration process having the best convergence is provided by the classical Newton method, requiring the following form of Eq. (4.34)

$$\begin{aligned}\varepsilon_x^s = \varepsilon_x^{s-1} &+ c_{11}^{s-1}\left(\sigma_x^s - \sigma_x^{s-1}\right) \\ &+ c_{12}^{s-1}\left(\sigma_y^s - \sigma_y^{s-1}\right) + c_{13}^{s-1}\left(\tau_{xy}^s - \tau_{xy}^{s-1}\right)\end{aligned} \tag{4.40}$$

where

$$c_{11}^{s-1} = \frac{1}{E} + \omega(\sigma_{s-1}) + \left(\sigma_x^{s-1} - \frac{1}{2}\sigma_y^{s-1}\right)\frac{\partial}{\partial\sigma_x^{s-1}}\omega(\sigma_{s-1})$$

$$c_{12}^{s-1} = -\frac{\nu}{E} - \frac{1}{2}\omega(\sigma_{s-1}) + \left(\sigma_x^{s-1} - \frac{1}{2}\sigma_y^{s-1}\right)\frac{\partial}{\partial\sigma_y^{s-1}}\omega(\sigma_{s-1})$$

$$c_{13}^{s-1} = \left(\sigma_x^{s-1} - \frac{1}{2}\sigma_y^{s-1}\right)\frac{\partial}{\partial\tau_{xy}^{s-1}}\omega(\sigma_{s-1})$$

Since coefficients c are known from the previous step $(s-1)$, Eq. (4.40) is linear with respect to stresses and strains corresponding to step number s. Graphical interpretation of this method is presented in Fig. 4.11c. In contrast to the methods discussed previously, Newton's method has no physical interpretation and, being characterized with very high convergence, is rather cumbersome for practical applications.

The iteration methods discussed previously are used to solve direct problems of stress analysis, i.e., to find stresses and strains induced by a given load. However, there exists another class of problems requiring us to evaluate the load-carrying capacity of the structure. To solve these problems, we need to trace the evolution of stresses while the load increases from zero to some ultimate value. To do this, we can use the method of successive loading. According to this method, the load is applied with some increments, and for each s-step of loading the strain is determined as

$$\varepsilon_x^s = \varepsilon_x^{s-1} + \frac{1}{E_{s-1}}\left(\Delta\sigma_x^s - \nu_{s-1}\Delta\sigma_y^s\right) \tag{4.41}$$

where E_{s-1} and ν_{s-1} are specified by Eqs. (4.39) and correspond to the previous loading step. Graphical interpretation of this method is shown in Fig. 4.11d. To obtain reliable results, the load increments should be as small as possible, because the error of calculation is cumulative in this method. To avoid this effect, the method of successive loading can be used in conjunction with the method of elastic variables. Being applied after several loading steps (black circles in Fig. 4.11d), the latter method allows us to eliminate the accumulated error and to start the process of loading again from a "correct" initial state (light circles in Fig. 4.11d).

Returning to the constitutive equations of the deformation theory of plasticity, Eq. (4.25), it is important to note that these equations are algebraic. This means that strains corresponding to some combination of loads are determined by the stresses induced by these loads and do not depend on the history of loading, i.e., on what happened to the material before this combination of loads was reached.

However, existing experimental data show that, in general, strains should depend on the history of loading. This means that constitutive equations should be differential, rather than algebraic as they are in deformation theory. Such equations are provided by the flow theory of plasticity. According to this theory, decomposition in Eq. (4.15) is used for infinitesimal increments of stresses, i.e.,

$$d\varepsilon_{ij} = d\varepsilon_{ij}^e + d\varepsilon_{ij}^p \tag{4.42}$$

Here, increments of elastic strains are related to the increments of stresses by Hooke's law, e.g., for the plane stress state

$$\begin{aligned} &d\varepsilon_x^e = \frac{1}{E}(d\sigma_x - \nu d\sigma_y), \quad d\varepsilon_y^e = \frac{1}{E}(d\sigma_y - \nu d\sigma_x), \\ &d\gamma_{xy} = \frac{1}{G} d\tau_{xy} \end{aligned} \tag{4.43}$$

whereas increments of plastic strains

$$d\varepsilon_{ij}^p = \frac{\partial U_p}{\partial \sigma_{ij}} d\lambda$$

are expressed in the form of Eqs. (4.18) but include a parameter λ which characterizes the loading process.

Assuming that $U_p = U_p(\sigma)$, where σ is the stress intensity specified by Eqs. (4.19) or (4.24), we get

$$d\varepsilon_{ij}^p = \frac{dU_p}{d\sigma} \frac{\partial \sigma}{\partial \sigma_{ij}} d\lambda$$

The explicit form of these equations for the plane stress state is

$$\begin{aligned} d\varepsilon_x^p &= d\omega(\sigma)\left(\sigma_x - \frac{1}{2}\sigma_y\right) \\ d\varepsilon_y^p &= d\omega(\sigma)\left(\sigma_y - \frac{1}{2}\sigma_x\right) \\ d\gamma_{xy}^p &= 3d\omega(\sigma)\tau_{xy} \end{aligned} \tag{4.44}$$

where

$$d\omega(\sigma) = \frac{1}{\sigma}\frac{dU_p}{d\sigma}d\lambda \tag{4.45}$$

To determine the parameter λ, assume that the plastic potential U_p, being on the one hand a function of σ, can be treated as the work performed by stresses on plastic strains, i.e.,

$$dU_p = \frac{\partial U_p}{\partial \sigma}d\sigma = \sigma_x d\varepsilon_x^p + \sigma_y d\varepsilon_y^p + \tau_{xy} d\gamma_{xy}^p$$

Substituting strain increments from Eqs. (4.44) and taking into account Eq. (4.24) for σ, we have

$$\frac{\partial U_p}{\partial \sigma}d\sigma = \sigma^2 d\omega(\sigma)$$

With due regard to Eq. (4.45), we arrive at the following simple and natural relationship, $d\lambda = d\sigma/\sigma$. Thus, Eq. (4.45) takes the form

$$d\omega(\sigma) = \frac{d\sigma}{\sigma^2}\frac{dU_p}{d\sigma} \tag{4.46}$$

and Eqs. (4.42)–(4.44) result in the following constitutive equations for the flow theory

$$\begin{aligned} d\varepsilon_x &= \frac{1}{E}(d\sigma_x - \nu d\sigma_y) + d\omega(\sigma)\left(\sigma_x - \frac{1}{2}\sigma_y\right) \\ d\varepsilon_y &= \frac{1}{E}(d\sigma_y - \nu d\sigma_x) + d\omega(\sigma)\left(\sigma_y - \frac{1}{2}\sigma_x\right) \\ d\gamma_{xy} &= \frac{1}{G}d\tau_{xy} + 3d\omega(\sigma)\tau_{xy} \end{aligned} \tag{4.47}$$

As can be seen, in contrast to the deformation theory, stresses govern the increments of plastic strains rather than the strains themselves.

In the general case, irrespective of any particular approximation of plastic potential U_p, we can obtain for function $d\omega(\sigma)$ in Eqs. (4.47) an expression similar to Eq. (4.32). Consider uniaxial tension, for which Eqs. (4.47) yield

$$d\varepsilon_x = \frac{d\sigma_x}{E} + d\omega(\sigma_x)\sigma_x$$

Repeating the derivation of Eq. (4.32), we finally have

$$d\omega(\sigma) = \frac{d\sigma}{\sigma}\left(\frac{1}{E_t(\sigma)} - \frac{1}{E}\right) \tag{4.48}$$

where $E_t(\sigma) = d\sigma/d\varepsilon$ is the tangent modulus introduced in Section 1.1 (see Fig. 1.4). The dependence of E_t on strain for an aluminum alloy is shown in Fig. 4.10. Consider the power approximation for plastic potential

$$U_p = B\sigma^n \tag{4.49}$$

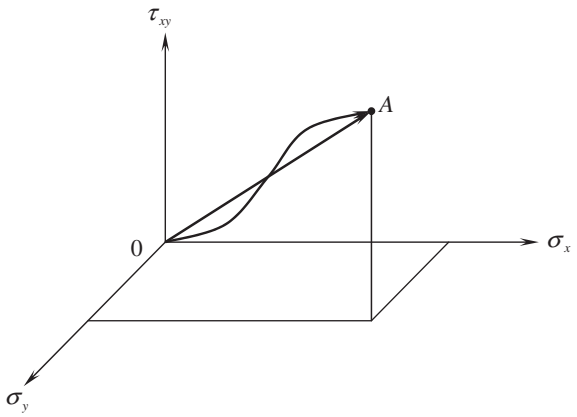


FIGURE 4.12

Loading path (0A) in the stress space.

Then, matching Eqs. (4.46) and (4.48), we arrive at the following equation

$$\frac{d\varepsilon}{d\sigma} = \frac{1}{E} + Bn\sigma^{n-2}$$

Upon integration, we get

$$\varepsilon = \frac{\sigma}{E} + \frac{Bn}{n-1}\sigma^{n-1} \tag{4.50}$$

As can be seen, this equation has the same form as Eq. (4.33). The only difference is in the form of coefficients C and B. As in the theory of deformation, Eq. (4.50) can be used to approximate the experimental stress-strain curve and to determine coefficients B and n. Thus, the constitutive equations for the flow theory of plasticity are specified by Eqs. (4.47) and (4.48).

For a plane stress state, introduce the stress space shown in Fig. 4.12 and referred to a Cartesian coordinate frame with stresses as coordinates. In this space, any loading can be presented as a curve specified by the parametric equations $\sigma_x = \sigma_x(p)$, $\sigma_y = \sigma_y(p)$, and $\tau_{xy} = \tau_{xy}(p)$, in which p is the loading parameter. To find strains corresponding to point A on the curve, we should integrate Eqs. (4.47) along this curve, thus taking into account the whole history of loading. In the general case, the obtained result will be different from what follows from Eqs. (4.25) of the deformation theory for point A. However, there exists one loading path (the straight line 0A in Fig. 4.12) that is completely determined by the location of its final point A. This is the so-called proportional loading during which the stresses increase in proportion to parameter p, i.e.,

$$\sigma_x = \sigma_x^0 p, \quad \sigma_y = \sigma_y^0 p, \quad \tau_{xy} = \tau_{xy}^0 p \tag{4.51}$$

where stresses with superscript "0" can depend on coordinates only. For such loading, $\sigma = \sigma_0 p$, $d\sigma = \sigma_0 dp$, and Eqs. (4.46) and (4.49) yield

$$d\omega(\sigma) = Bn\sigma^{n-3}d\sigma = Bn\sigma_0^{n-2}p^{n-3}dp \tag{4.52}$$

Consider, for example, the first equation of Eqs. (4.47). Substituting Eqs. (4.51) and (4.52), we have

$$d\varepsilon_x = \frac{1}{E}\left(\sigma_x^0 - \nu\sigma_y^0\right)dp + Bn\sigma_0^{n-2}\left(\sigma_x^0 - \frac{1}{2}\sigma_y^0\right)p^{n-2}dp$$

This equation can be integrated with respect to p. Again using Eqs. (4.51), we arrive at the constitutive equation of the deformation theory

$$\varepsilon_x = \frac{1}{E}(\sigma_x - \nu\sigma_y) + B\frac{n}{n-1}\sigma^{n-2}\left(\sigma_x - \frac{1}{2}\sigma_y\right)$$

Thus, for a proportional loading, the flow theory reduces to the deformation theory of plasticity. Unfortunately, before the problem is solved and the stresses are found we do not know whether the loading is proportional or not and which particular theory of plasticity should be used. There exists a theorem of proportional loading (Ilyushin, 1948), according to which the stresses increase proportionally and the deformation theory can be used if:

1. external loads increase in proportion to one loading parameter,
2. the material is incompressible and its hardening can be described with the power law $\sigma = S\varepsilon^n$.

In practice, both conditions of this theorem are rarely met. However, existing experience shows that the second condition is not very important and that the deformation theory of plasticity can be reliably (but approximately) applied if all the loads acting on the structure increase in proportion to one parameter.

4.2 UNIDIRECTIONAL ORTHOTROPIC LAYER

A composite layer with the simplest structure consists of unidirectional plies whose material coordinates, 1, 2, and 3, coincide with coordinates of the layer, x, y, and z, as in Fig. 4.13. An example of such a layer is presented in Fig. 4.14: the principal material axes of an outer circumferential unidirectional layer of a pressure vessel coinciding with global (axial and circumferential) coordinates of the vessel.

4.2.1 Linear elastic model

For the layer under study, the constitutive equations, Eqs. (2.48) and (2.53), yield

$$\begin{aligned}
\varepsilon_1 &= \frac{\sigma_1}{E_1} - \nu_{12}\frac{\sigma_2}{E_2} - \nu_{13}\frac{\sigma_3}{E_3} \\
\varepsilon_2 &= \frac{\sigma_2}{E_2} - \nu_{21}\frac{\sigma_1}{E_1} - \nu_{23}\frac{\sigma_3}{E_3} \\
\varepsilon_3 &= \frac{\sigma_3}{E_3} - \nu_{31}\frac{\sigma_1}{E_1} - \nu_{32}\frac{\sigma_2}{E_2} \\
\gamma_{12} &= \frac{\tau_{12}}{G_{12}}, \quad \gamma_{13} = \frac{\tau_{13}}{G_{13}}, \quad \gamma_{23} = \frac{\tau_{23}}{G_{23}}
\end{aligned} \tag{4.53}$$

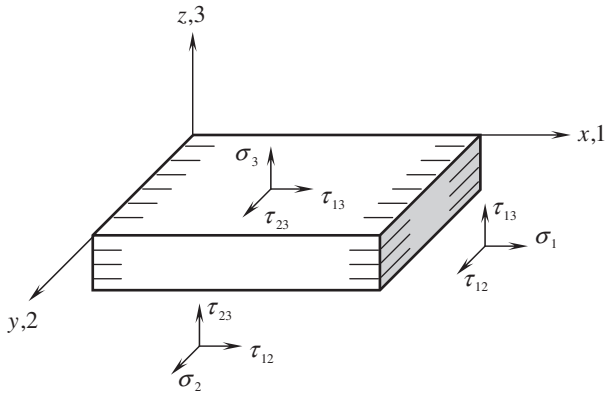


FIGURE 4.13

An orthotropic layer.

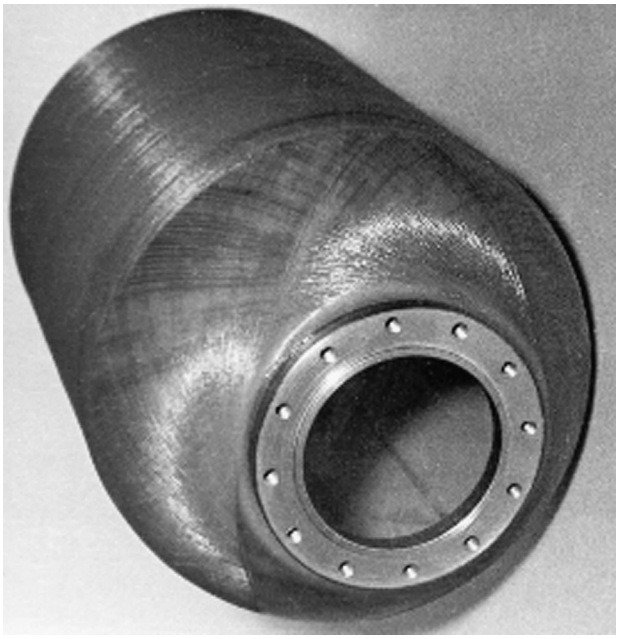


FIGURE 4.14

Filament-wound composite pressure vessel.

where

$$\nu_{12}E_1 = \nu_{21}E_2, \quad \nu_{13}E_1 = \nu_{31}E_3, \quad \nu_{23}E_2 = \nu_{32}E_3$$

The inverse form of Eqs. (4.53) is

$$\begin{aligned}
\sigma_1 &= A_1(\varepsilon_1 + \mu_{12}\varepsilon_2 + \mu_{13}\varepsilon_3) \\
\sigma_2 &= A_2(\varepsilon_2 + \mu_{21}\varepsilon_1 + \mu_{23}\varepsilon_3) \\
\sigma_3 &= A_3(\varepsilon_3 + \mu_{31}\varepsilon_1 + \mu_{32}\varepsilon_2) \\
\tau_{12} &= G_{12}\gamma_{12}, \quad \tau_{13} = G_{13}\gamma_{13}, \quad \tau_{23} = G_{23}\gamma_{23}
\end{aligned} \tag{4.54}$$

where

$$A_1 = \frac{E_1}{D}(1 - \nu_{23}\nu_{32}), \quad A_2 = \frac{E_2}{D}(1 - \nu_{13}\nu_{31}), \quad A_3 = \frac{E_3}{D}(1 - \nu_{12}\nu_{21})$$

$$D = 1 - \nu_{12}\nu_{23}\nu_{31} - \nu_{13}\nu_{21}\nu_{32} - \nu_{13}\nu_{31} - \nu_{12}\nu_{21} - \nu_{23}\nu_{32}$$

$$\mu_{12} = \frac{\nu_{12} + \nu_{13}\nu_{32}}{1 - \nu_{23}\nu_{32}}, \quad \mu_{21} = \frac{\nu_{21} + \nu_{23}\nu_{31}}{1 - \nu_{13}\nu_{31}}$$

$$\mu_{13} = \frac{\nu_{13} + \nu_{12}\nu_{23}}{1 - \nu_{23}\nu_{32}}, \quad \mu_{31} = \frac{\nu_{31} + \nu_{21}\nu_{32}}{1 - \nu_{12}\nu_{21}}$$

$$\mu_{23} = \frac{\nu_{23} + \nu_{13}\nu_{21}}{1 - \nu_{13}\nu_{31}}, \quad \mu_{32} = \frac{\nu_{32} + \nu_{12}\nu_{31}}{1 - \nu_{12}\nu_{21}}$$

As for an isotropic layer considered in Section 4.1, the terms including the transverse normal stress σ_3 can be neglected for a thin layer in Eqs. (4.53) and (4.54), and they can be written in the following simplified forms

$$\begin{aligned}
\varepsilon_1 &= \frac{\sigma_1}{E_1} - \nu_{12}\frac{\sigma_2}{E_2}, \quad \varepsilon_2 = \frac{\sigma_2}{E_2} - \nu_{21}\frac{\sigma_1}{E_1} \\
\gamma_{12} &= \frac{\tau_{12}}{G_{12}}, \quad \gamma_{13} = \frac{\tau_{13}}{G_{13}}, \quad \gamma_{23} = \frac{\tau_{23}}{G_{23}}
\end{aligned} \tag{4.55}$$

and

$$\begin{aligned}
\sigma_1 &= \overline{E}_1\big(\varepsilon_1 + \nu_{12}\varepsilon_2\big), \quad \sigma_2 = \overline{E}_2\big(\varepsilon_2 + \nu_{21}\varepsilon_1\big) \\
\tau_{12} &= G_{12}\gamma_{12}, \quad \tau_{13} = G_{13}\gamma_{13}, \quad \tau_{23} = G_{23}\gamma_{23}
\end{aligned} \tag{4.56}$$

where

$$\overline{E}_{1,2} = \frac{E_{1,2}}{1 - \nu_{12}\nu_{21}}$$

The constitutive equations presented earlier include elastic constants for a layer that are determined experimentally. For in-plane characteristics E_1, E_2, G_{12}, and ν_{12}, the corresponding test methods are discussed in Chapter 3. The transverse modulus E_3 is usually found by testing the layer under

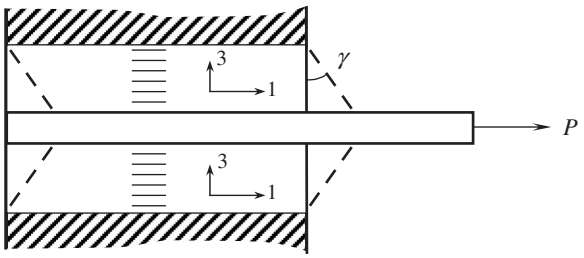


FIGURE 4.15

A test to determine transverse shear modulus.

compression in the z direction. The transverse shear moduli G_{13} and G_{23} can be obtained by various methods, e.g., by inducing pure shear in two symmetric specimens shown in Fig. 4.15 and calculating the shear modulus as $G_{13} = P/(2A\gamma)$, where A is the in-plane area of the specimen.

For unidirectional composites, $G_{13} = G_{12}$ (see Table 3.5), whereas typical values of G_{23} are listed in Table 4.1 (Herakovich, 1998).

Poisson's ratios ν_{31} and ν_{32} can be determined by measuring the change in the layer thickness under in-plane tension in directions 1 and 2.

4.2.2 Nonlinear models

Consider Figs. 3.40–3.43, showing typical stress-strain diagrams for unidirectional advanced composites. As can be seen, the materials demonstrate linear behavior only under tension. The curves corresponding to compression are slightly nonlinear, whereas the shear curves are definitely nonlinear. It should be emphasized that this does not mean that the linear constitutive equations presented in Section 4.2.1 are not valid for these materials. First, it should be taken into account that the deformations of properly designed composite materials are controlled by the fibers, and they do not allow the shear strain to reach the values at which the shear stress-strain curve is highly nonlinear. Second, the shear stiffness is usually very small in comparison with the longitudinal one, and so is its contribution to the apparent material stiffness. The material behavior is usually close to linear even if the shear deformation is nonlinear. Thus, a linear elastic model provides, as

TABLE 4.1 Transverse Shear Moduli of Unidirectional Composites (Herakovich, 1998).

Material	Glass-epoxy	Carbon-epoxy	Aramid-epoxy	Boron-Al
G_{23} (GPa)	4.1	3.2	1.4	49.1

a rule, a reasonable approximation to the actual material behavior. However, there exist problems to solve which we need to allow for material nonlinearity and apply one of the nonlinear constitutive theories discussed later.

First, note that material behavior under elementary loading (pure tension, compression, and shear) is specified by experimental stress-strain diagrams of the type shown in Figs. 3.40–3.43, and we do not need any theory. The necessity for a theory arises if we are to study the interaction of simultaneously acting stresses. Since for the layer under study this interaction usually takes place for in-plane stresses σ_1, σ_2, and τ_{12} (see Fig. 4.13), we consider further the plane state of stress.

In the simplest (but quite useful for practical engineering analysis) approach, the stress interaction is ignored completely, and the linear constitutive equations, Eqs. (4.55), are generalized as

$$\varepsilon_1 = \frac{\sigma_1}{E_1^s} - \nu_{12}^s \frac{\sigma_2}{E_2^s}, \quad \varepsilon_2 = \frac{\sigma_2}{E_2^s} - \nu_{21}^s \frac{\sigma_1}{E_1^s}, \quad \gamma_{12} = \frac{\tau_{12}}{G_{12}^s} \tag{4.57}$$

where the superscript "s" indicates the corresponding secant characteristics specified by Eqs. (1.8). These characteristics depend on stresses and are determined using experimental diagrams similar to those presented in Figs. 3.40–3.43. In particular, diagrams $\sigma_1(\varepsilon_1)$ and $\varepsilon_2(\varepsilon_1)$ plotted under uniaxial longitudinal loading yield $E_1^s(\sigma_1)$ and $\nu_{21}^s(\sigma_1)$, and secant moduli $E_2^s(\sigma_2)$ and $G_{12}^s(\tau_{12})$ are determined from experimental curves for $\sigma_2(\varepsilon_2)$ and $\tau_{12}(\gamma_{12})$, respectively, whereas ν_{12}^s is found from the symmetry condition in Eqs. (4.53). In a more rigorous model (Jones, 1977), the secant characteristics of the material in Eqs. (4.57) are also functions, but in this case they are functions of strain energy U in Eq. (2.51) rather than of individual stresses. Models of this type provide adequate results for unidirectional composites with moderate nonlinearity.

To describe pronounced nonlinear elastic behavior of a unidirectional layer, we can use Eq. (4.10). Expanding the complementary potential U_c into a Taylor series with respect to stresses, we have

$$\begin{aligned} U_c = c_0 + c_{ij}\sigma_{ij} + \frac{1}{2} c_{ijkl}\sigma_{ij}\sigma_{kl} + \frac{1}{3!} c_{ijklmn}\,\sigma_{ij}\sigma_{kl}\sigma_{mn} + \frac{1}{4!} c_{ijklmnpq}\,\sigma_{ij}\sigma_{kl}\sigma_{mn}\sigma_{pq} \\ + \frac{1}{5!} c_{ijklmnpqrs}\,\sigma_{ij}\sigma_{kl}\sigma_{mn}\sigma_{pq}\sigma_{rs} + \frac{1}{6!} c_{ijklmnpqrstw}\,\sigma_{ij}\sigma_{kl}\sigma_{mn}\sigma_{pq}\sigma_{rs}\sigma_{tw} + \ldots\ldots \end{aligned} \tag{4.58}$$

where

$$c_0 = U_c(\sigma_{ij} = 0), \quad c_{ij} = \left.\frac{\partial U_c}{\partial \sigma_{ij}}\right|_{\sigma_{ij}=0}, \quad c_{ijkl} = \left.\frac{\partial^2 U_c}{\partial \sigma_{ij}\partial \sigma_{kl}}\right|_{\sigma_{ij}=0,\sigma_{kl}=0}, \text{ etc.}$$

A sixth-order approximation with the terms presented in Eq. (4.58) (where summation over repeated subscripts is implied) allows us to construct constitutive equations including stresses in the fifth power. The coefficients "c" should be found from experiments with material specimens. Since these coefficients are partial derivatives that do not depend on the sequence of differentiation, the sequence of their subscripts is not important. As a result, the sixth-order polynomial in Eq. (4.58) includes 84 "c"-coefficients. This is clearly far too many for the practical analysis of composite materials. To reduce the number of coefficients, we can first use some general considerations. Namely, assume that $U_c = 0$ and $\varepsilon_{ij} = 0$ if there are no stresses ($\sigma_{ij} = 0$). Then, $c_0 = 0$ and $c_{ij} = 0$. Second, we should take into account that the material under study is orthotropic. This means that normal stresses do not induce shear strain, and shear stresses do not cause normal strains. Third, the direction of shear stresses should

influence only shear strains, i.e., shear stresses should have only even powers in constitutive equations for normal strains, whereas the corresponding equation for shear strain should include only odd powers of shear stresses. As a result, the constitutive equations will contain 37 coefficients and take the following form (in new notations for coefficients and stresses)

$$\begin{aligned}
\varepsilon_1 &= a_1\sigma_1 + a_2\sigma_1^2 + a_3\sigma_1^3 + a_4\sigma_1^4 + a_5\sigma_1^5 + d_1\sigma_1 \\
&\quad + 2d_2\sigma_1\sigma_2 + d_3\sigma_2^2 + 3d_4\sigma_1^2\sigma_2 + d_5\sigma_2^3 + d_6\sigma_1\sigma_2^2 + 4d_7\sigma_1^3\sigma_2 + 3d_8\sigma_1^2\sigma_2^2 + 2d_9\sigma_1\sigma_2^3 \\
&\quad + d_{10}\sigma_2^4 + 5d_{11}\sigma_1^4\sigma_2 + 4d_{12}\sigma_1^3\sigma_2^2 + 3d_{13}\sigma_1^2\sigma_2^3 + 2d_{14}\sigma_1\sigma_2^4 + d_{15}\sigma_2^5 + k_1\sigma_1\tau_{12}^2 + k_2\sigma_2\tau_{12}^2 \\
&\quad + 3k_3\sigma_1^2\tau_{12}^2 + 4k_4\sigma_1^3\tau_{12}^2 + 2k_5\sigma_1\tau_{12}^4 \\
\varepsilon_2 &= b_1\sigma_2 + b_2\sigma_2^2 + b_3\sigma_2^3 + b_4\sigma_2^4 + b_5\sigma_2^5 \\
&\quad + d_1\sigma_1 + d_2\sigma_1^2 + 2d_3\sigma_1\sigma_2 + d_4\sigma_1^3 + 3d_5\sigma_1\sigma_2^2 + d_6\sigma_1^2\sigma_2 + d_7\sigma_1^4 + 2d_8\sigma_1^3\sigma_2 \\
&\quad + 3d_9\sigma_1^2\sigma_2^2 + 4d_{10}\sigma_1\sigma_2^3 + d_{11}\sigma_1^5 + 2d_{12}\sigma_1^4\sigma_2 + 3d_{13}\sigma_1^3\sigma_2^2 + 2d_{14}\sigma_1^2\sigma_2^3 + 5d_{15}\sigma_1\sigma_2^4 \\
&\quad + m_1\sigma_2\tau_{12}^2 + k_2\sigma_1\tau_{12}^2 + 3m_2\sigma_2^2\tau_{12}^2 + 4m_3\sigma_2^3\tau_{12}^2 + 2m_4\sigma_2\tau_{12}^4 \\
\gamma_{12} &= c_1\tau_{12} + c_2\tau_{12}^3 + c_3\tau_{12}^5 + k_1\tau_{12}\sigma_1^2 + m_1\tau_{12}\sigma_2^2 \\
&\quad + 2k_2\tau_{12}\sigma_1\sigma_2 + 2k_3\tau_{12}\sigma_1^3 + 2m_2\tau_{12}\sigma_2^3 \\
&\quad + 2k_4\tau_{12}\sigma_1^4 + 4k_5\tau_{12}^3\sigma_1^2 + 2m_3\tau_{12}\sigma_2^4 + 4m_4\tau_{12}^3\sigma_2^2
\end{aligned} \tag{4.59}$$

For unidirectional composites, the dependence $\varepsilon_1(\sigma_1)$ is linear, which means that we should put $d_2 = \ldots\ d_{15} = 0,\ k_1 = \ldots\ k_5 = 0$. Then, the foregoing equations reduce to

$$\begin{aligned}
\varepsilon_1 &= a_1\sigma_1 + d_1\sigma_2 \\
\varepsilon_2 &= b_1\sigma_2 + b_2\sigma_2^2 + b_3\sigma_2^3 + b_4\sigma_2^4 + b_5\sigma_2^5 \\
&\quad + d_1\sigma_1 + m_1\sigma_2\tau_{12}^2 + 3m_2\sigma_2^2\tau_{12}^2 + 4m_3\sigma_2^3\tau_{12}^2 + 2m_4\sigma_2\tau_{12}^4 \\
\gamma_{12} &= c_1\tau_{12} + c_2\tau_{12}^3 + c_3\tau_{12}^5 + m_1\tau_{12}\sigma_2^2 \\
&\quad + 2m_2\tau_{12}\sigma_2^3 + 2m_3\tau_{12}\sigma_2^4 + 4m_4\tau_{12}^3\sigma_2^2
\end{aligned} \tag{4.60}$$

As an example, consider a specific unidirectional two-matrix fiberglass composite with high in-plane transverse and shear deformation (see Section 4.4.3 for further details). The stress-strain curves corresponding to transverse tension, compression, and in-plane shear are shown in Fig. 4.16. Solid lines correspond to Eqs. (4.60) used to approximate the experimental results (circles in Fig. 4.16). The coefficients a_1 and d_1 in Eqs. (4.60) are found using diagrams $\varepsilon_1(\sigma_1)$ and $\varepsilon_2(\sigma_2)$, which are linear and not shown here. The coefficients $b_1 \ldots b_5$ and c_1, c_2, and c_3 are determined using the least-squares method to approximate curves $\sigma_2^+(\varepsilon_2)$, $\sigma_2^-(\varepsilon_2)$, and $\tau_{12}(\gamma_{12})$. The other coefficients, i.e., $m_1 \ldots m_4$, should be determined with the aid of a more complicated experiment involving loading that induces both stresses σ_2 and τ_{12} acting simultaneously. This experiment is described in Section 4.3.

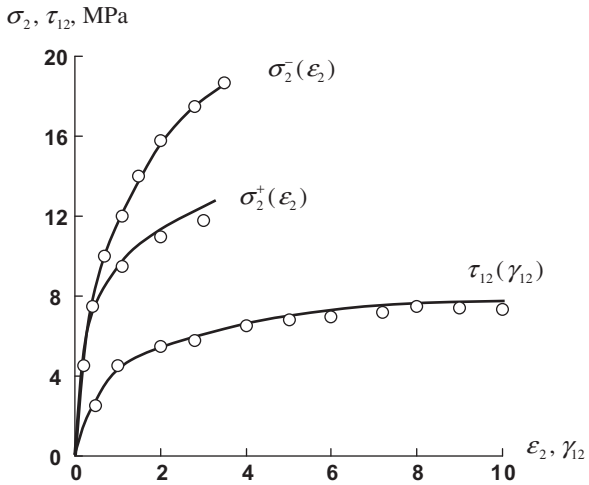


FIGURE 4.16

Calculated (solid lines) and experimental (circles) stress-strain diagrams for a two-matrix unidirectional composite under in-plane transverse tension (σ_2^+), compression (σ_2^-), and shear (τ_{12}).

As follows from Figs. 3.40–3.43, unidirectional composites demonstrate pronounced nonlinearity only under shear. Assuming that the dependence $\varepsilon_2(\sigma_2)$ is also linear, we can reduce Eqs. (4.60) to

$$\varepsilon_1 = a_1\sigma_1 + d_1\sigma_2, \quad \varepsilon_2 = b_1\sigma_2 + d_1\sigma_1, \quad \gamma_{12} = c_1\tau_{12} + c_2\tau_{12}^3 + c_3\tau_{12}^5$$

For practical analysis, an even simpler form of these equations (with $c_3 = 0$) can be used (Hahn and Tsai, 1973).

Nonlinear behavior in composite materials can also be described with the aid of the theory of plasticity, which can be constructed as a direct generalization of the classical plasticity theory developed for metals and described in Section 4.1.2.

To construct such a theory, we decompose strains in accordance with Eq. (4.15) and use Eqs. (4.16) and (4.18) to determine elastic and plastic strains as

$$\varepsilon_{ij}^e = \frac{\partial U_e}{\partial \sigma_{ij}}, \quad \varepsilon_{ij}^p = \frac{\partial U_p}{\partial \sigma_{ij}} \tag{4.61}$$

where U_e and U_p are elastic and plastic potentials. For elastic potential, elasticity theory yields

$$U = c_{ijkl}\sigma_{ij}\sigma_{kl}, \tag{4.62}$$

where c_{ijkl} are compliance coefficients, and summation over repeated subscripts is implied. The plastic potential is assumed to be a function of stress intensity, σ, which is constructed for a plane stress state as a direct generalization of Eq. (4.24), i.e.,

$$\sigma = a_{ij}\sigma_{ij} + \sqrt{a_{ijkl}\sigma_{ij}\sigma_{kl}} + \sqrt[3]{a_{ijklmn}\sigma_{ij}\sigma_{kl}\sigma_{mn}} + \cdots\cdots \tag{4.63}$$

where the coefficients "a" are material constants characterizing its plastic behavior. Finally, we use the power law in Eq. (4.27) for the plastic potential.

To write constitutive equations for a plane stress state, we return to engineering notations for stresses and strains and use conditions that should be imposed on an orthotropic material and which are discussed earlier in application to Eqs. (4.59). Finally, Eqs. (4.15), (4.27) and (4.61)–(4.63) yield

$$\begin{aligned}
\varepsilon_1 &= a_1\sigma_1 + d_1\sigma_2 + n\sigma^{n-1}\left[\frac{1}{R_1}(b_{11}\sigma_1 + c_{12}\sigma_2) + \frac{1}{R_2^2}\left(d_{11}\sigma_1^2 + 2e_{12}\sigma_1\sigma_2 + e_{21}\sigma_2^2\right)\right] \\
\varepsilon_2 &= b_1\sigma_2 + d_1\sigma_1 + n\sigma^{n-1}\left[\frac{1}{R_1}(b_{22}\sigma_2 + c_{12}\sigma_1) + \frac{1}{R_2^2}\left(d_{22}\sigma_2^2 + 2e_{21}\sigma_2\sigma_1 + e_{12}\sigma_1^2\right)\right] \\
\gamma_{12} &= c_1\tau_{12} + 2n\sigma^{n-1}\frac{b_{12}}{R_1}\tau_{12}
\end{aligned} \tag{4.64}$$

where

$$\sigma = R_1 + R_2$$

$$R_1 = \sqrt{b_{11}\sigma_1^2 + b_{22}\sigma_2^2 + b_{12}\tau_{12}^2 + 2c_{12}\sigma_1\sigma_2}, \quad R_2 = \sqrt[3]{d_{11}\sigma_1^3 + d_{22}\sigma_2^3 + 3e_{12}\sigma_1^2\sigma_2 + 3e_{21}\sigma_1\sigma_2^2}$$

Deriving Eqs. (4.64), we use new notations for coefficients and restrict ourselves to the three-term approximation for σ as in Eq. (4.63).

For independent uniaxial loading along the fibers, across the fibers, and in pure shear, Eqs. (4.64) reduce to

$$\begin{aligned}
\varepsilon_1 &= a_1\sigma_1 + n\left(\sqrt{b_{11}\sigma_1^2} + \sigma_1\sqrt[3]{d_{11}}\right)^{n-1}\left(\sqrt{b_{11}}\,\frac{\sigma_1}{\sqrt{\sigma_1^2}} + \sqrt[3]{d_{11}}\right) \\
\varepsilon_2 &= b_1\sigma_2 + n\left(\sqrt{b_{22}\sigma_2^2} + \sigma_2\sqrt[3]{d_{22}}\right)^{n-1}\left(\sqrt{b_{22}}\,\frac{\sigma_2}{\sqrt{\sigma_2^2}} + \sqrt[3]{d_{22}}\right) \\
\gamma_{12} &= \left[c_1 + 2n\sqrt{b_{12}^n}\left(\sqrt{\tau_{12}^2}\right)^{n-1}\right]\tau_{12}
\end{aligned} \tag{4.65}$$

If nonlinear material behavior does not depend on the sign of normal stresses, then $d_{11} = d_{22} = 0$ in Eqs. (4.65). In the general case, Eqs. (4.65) allow us to describe materials with high nonlinearity and different behaviors under tension and compression.

As an example, consider a boron-aluminum unidirectional composite whose experimental stress-strain diagrams (Herakovich, 1998) are shown in Fig. 4.17 (circles) along with the corresponding approximations (solid lines) plotted with the aid of Eqs. (4.65).

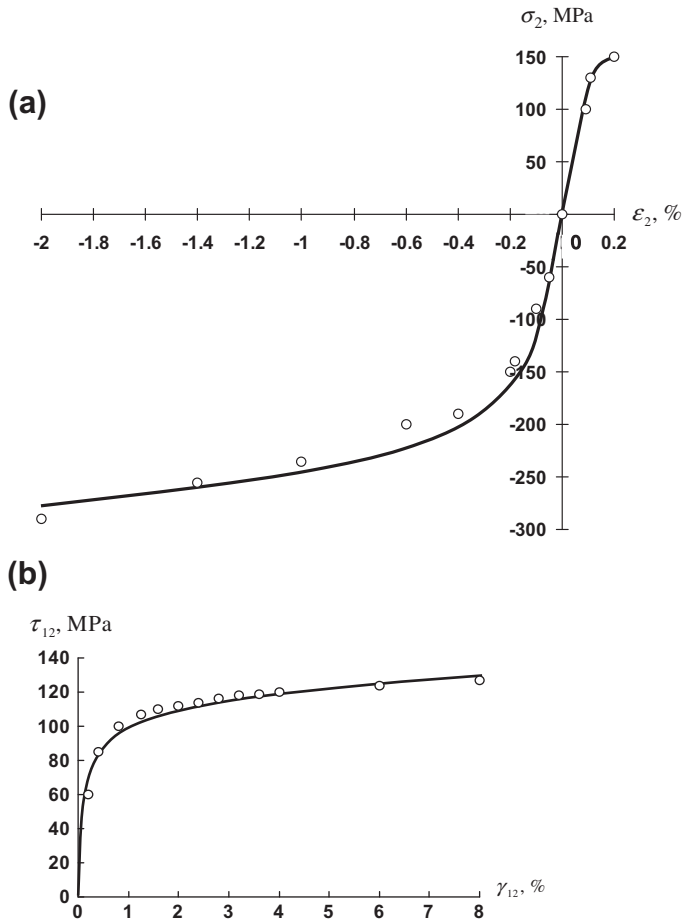


FIGURE 4.17

Calculated (solid lines) and experimental (circles) stress-strain diagrams for a boron-aluminum composite under transverse loading (a) and in-plane shear (b).

4.3 UNIDIRECTIONAL ANISOTROPIC LAYER

Consider now a unidirectional layer as studied in the previous section and assume that its principal material axis 1 makes some angle ϕ with the x-axis of the global coordinate frame (see Fig. 4.18). An example of such a layer is shown in Fig. 4.19.

4.3.1 Linear elastic model

Constitutive equations of the layer under study referred to the principal material coordinates are given by Eqs. (4.55) and (4.56). We now need to derive such equations for the global coordinate frame x, y, z (see Fig. 4.18). To do this, we should transfer stresses σ_1, σ_2, τ_{12}, τ_{13}, and τ_{23} acting in the layer and

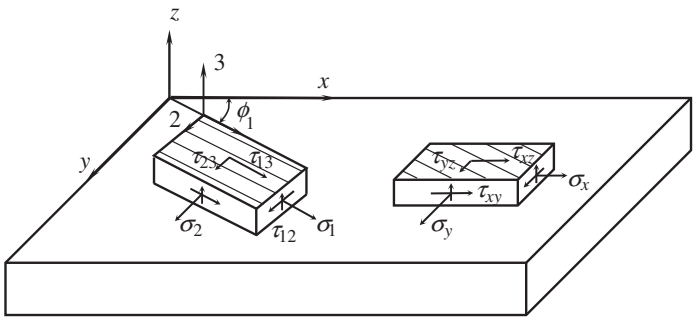


FIGURE 4.18

A composite layer consisting of a system of unidirectional plies with the same orientation.

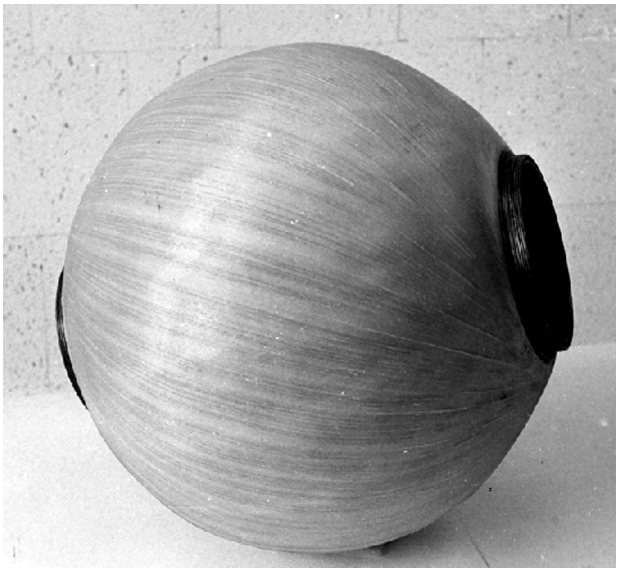


FIGURE 4.19

An anisotropic outer layer of a composite pressure vessel.

Courtesy of CRISM.

the corresponding strains ε_1, ε_2, γ_{12}, γ_{13}, and γ_{23} into stress and strain components σ_x, σ_y, τ_{xy}, τ_{xz}, and τ_{yz} and ε_x, ε_y, γ_{xy}, γ_{xz}, and γ_{yz} using Eqs. (2.8), (2.9), (2.21), and (2.27) for coordinate transformation of stresses and strains. According to Fig. 4.18, the directional cosines, Eqs. (2.1), for this transformation are (we take $x' = 1$, $y' = 2$, $z' = 3$)

$$\begin{aligned} l_{x'x} &= c, \quad l_{x'y} = s, \quad l_{x'z} = 0 \\ l_{y'x} &= -s, \quad l_{y'y} = c, \quad l_{y'z} = 0 \\ l_{z'x} &= 0, \quad l_{z'y} = 0, \quad l_{z'z} = 1 \end{aligned} \tag{4.66}$$

where $c = \cos\phi$ and $s = \sin\phi$. Using Eqs. (2.8) and (2.9), we get

$$\begin{aligned}
\sigma_1 &= \sigma_x c^2 + \sigma_y s^2 + 2\tau_{xy} cs \\
\sigma_2 &= \sigma_x s^2 + \sigma_y c^2 - 2\tau_{xy} cs \\
\tau_{12} &= (\sigma_y - \sigma_x) cs + \tau_{xy}(c^2 - s^2) \\
\tau_{13} &= \tau_{xz} c + \tau_{yz} s \\
\tau_{23} &= -\tau_{xz} s + \tau_{yz} c
\end{aligned} \tag{4.67}$$

The inverse form of these equations is

$$\begin{aligned}
\sigma_x &= \sigma_1 c^2 + \sigma_2 s^2 - 2\tau_{12} cs \\
\sigma_y &= \sigma_1 s^2 + \sigma_2 c^2 + 2\tau_{12} cs \\
\tau_{xy} &= (\sigma_1 - \sigma_2) cs + \tau_{12}(c^2 - s^2) \\
\tau_{xz} &= \tau_{13} c - \tau_{23} s \\
\tau_{yz} &= \tau_{13} s + \tau_{23} c
\end{aligned} \tag{4.68}$$

The corresponding transformation for strains follows from Eqs. (2.21) and (2.27), i.e.,

$$\begin{aligned}
\varepsilon_1 &= \varepsilon_x c^2 + \varepsilon_y s^2 + \gamma_{xy} cs \\
\varepsilon_2 &= \varepsilon_x s^2 + \varepsilon_y c^2 - \gamma_{xy} cs \\
\gamma_{12} &= 2(\varepsilon_y - \varepsilon_x) cs + \gamma_{xy}(c^2 - s^2) \\
\gamma_{13} &= \gamma_{xz} c + \gamma_{yz} s \\
\gamma_{23} &= -\gamma_{xz} s + \gamma_{yz} c
\end{aligned} \tag{4.69}$$

or

$$\begin{aligned}
\varepsilon_x &= \varepsilon_1 c^2 + \varepsilon_2 s^2 - \gamma_{12} cs \\
\varepsilon_y &= \varepsilon_1 s^2 + \varepsilon_2 c^2 + \gamma_{12} cs \\
\gamma_{xy} &= 2(\varepsilon_1 - \varepsilon_2) cs + \gamma_{12}(c^2 - s^2) \\
\gamma_{xz} &= \gamma_{13} c - \gamma_{23} s \\
\gamma_{yz} &= \gamma_{13} s + \gamma_{23} c
\end{aligned} \tag{4.70}$$

To derive constitutive equations for an anisotropic unidirectional layer, we substitute strains, Eqs. (4.69), into Hooke's law, Eqs. (4.56), and the resulting expressions for stresses σ_1, σ_2 and τ_{12} and into Eqs. (4.68). The final result is as follows

$$\begin{aligned}
\sigma_x &= A_{11}\varepsilon_x + A_{12}\varepsilon_y + A_{14}\gamma_{xy} \\
\sigma_y &= A_{21}\varepsilon_x + A_{22}\varepsilon_y + A_{24}\gamma_{xy} \\
\tau_{xy} &= A_{41}\varepsilon_x + A_{42}\varepsilon_y + A_{44}\gamma_{xy} \\
\tau_{xz} &= A_{55}\gamma_{xz} + A_{56}\gamma \\
\tau_{yz} &= A_{65}\gamma_{xz} + A_{66}\gamma_{yz}
\end{aligned} \tag{4.71}$$

The stiffness coefficients in these equations are

$$
\begin{aligned}
A_{11} &= \overline{E}_1 c^4 + \overline{E}_2 s^4 + 2E_{12} c^2 s^2 \\
A_{12} &= A_{21} = \overline{E}_1 \nu_{12} + \left(\overline{E}_1 + \overline{E}_2 - 2E_{12}\right) c^2 s^2 \\
A_{14} &= A_{41} = \left[\overline{E}_1 c^2 - \overline{E}_2 s^2 - E_{12}\left(c^2 - s^2\right)\right] cs \\
A_{22} &= \overline{E}_1 s^4 + \overline{E}_2 c^4 + 2E_{12} c^2 s^2 \\
A_{24} &= A_{42} = \left[\overline{E}_1 s^2 - \overline{E}_2 c^2 + E_{12}\left(c^2 - s^2\right)\right] cs \\
A_{44} &= \left(\overline{E}_1 + \overline{E}_2 - 2\overline{E}_1 \nu_{12}\right) c^2 s^2 + G_{12}\left(c^2 - s^2\right)^2 \\
A_{55} &= G_{13} c^2 + G_{23} s^2 \\
A_{56} &= A_{65} = (G_{13} - G_{23}) cs \\
A_{66} &= G_{13} s^2 + G_{23} c^2
\end{aligned}
\tag{4.72}
$$

where

$$
\overline{E}_{1,2} = \frac{E_{1,2}}{1 - \nu_{12}\nu_{21}}, \quad E_{12} = \overline{E}_1 \nu_{12} + 2G_{12}, \quad c = \cos\phi, \quad s = \sin\phi
$$

The dependence of stiffness coefficients A_{mn} in Eqs. (4.72) on ϕ has been studied by Tsai and Pagano (see, e.g., Tsai, 1987; Verchery, 1999). Changing the powers of $\sin\phi$ and $\cos\phi$ in Eqs. (4.72) for multiple-angle trigonometric functions, we can reduce these equations to the following form:

$$
\begin{aligned}
A_{11} &= S_1 + S_2 + 2S_3 \cos 2\phi + S_4 \cos 4\phi \\
A_{12} &= -S_1 + S_2 - S_4 \cos 4\phi \\
A_{14} &= S_3 \sin 2\phi + S_4 \sin 4\phi \\
A_{22} &= S_1 + S_2 - 2S_3 \cos 2\phi + S_4 \cos 4\phi \\
A_{24} &= S_3 \sin 2\phi - S_4 \sin 4\phi \\
A_{44} &= S_1 - S_4 \cos 4\phi \\
A_{55} &= S_5 + S_6 \cos 2\phi \\
A_{56} &= 4S_6 \sin 2\phi \\
A_{66} &= S_5 - S_6 \cos 2\phi
\end{aligned}
\tag{4.73}
$$

(Verchery, 1999). In these equations,

$$S_1 = \frac{1}{8}\left(A_{11}^0 + A_{22}^0 - 2A_{12}^0 + 4A_{44}^0\right)$$
$$S_2 = \frac{1}{4}\left(A_{11}^0 + A_{22}^0 + 2A_{12}^0\right)$$
$$S_3 = \frac{1}{4}\left(A_{11}^0 - A_{22}^0\right)$$
$$S_4 = \frac{1}{8}\left(A_{11}^0 + A_{22}^0 - 2A_{12}^0 - 4A_{44}^0\right)$$
$$S_5 = \frac{1}{2}\left(A_{55}^0 + A_{66}^0\right)$$
$$S_6 = \frac{1}{2}\left(A_{55}^0 - A_{66}^0\right)$$

where A_n^0 are stiffness coefficients corresponding to $\phi = 0$. It follows from Eqs. (4.72) that

$$A_{11}^0 = \overline{E}_1, \quad A_{12}^0 = \overline{E}_1\nu_{12}, \quad A_{14}^0 = A_{24}^0 = A_{56}^0 = 0$$
$$A_{22}^0 = \overline{E}_2, \quad A_{44}^0 = G_{12}, \quad A_{55}^0 = G_{13}, \quad A_{66}^0 = G_{23}$$

As can be seen in Eqs. (4.73), there exist the following differential relationships between tensile and coupling stiffnesses (Verchery and Gong, 1999)

$$\frac{dA_{11}}{d\phi} = -4A_{14}, \quad \frac{dA_{22}}{d\phi} = 4A_{24}$$

It can be directly checked that Eqs. (4.73) provide three invariant stiffness characteristics whose forms do not depend on ϕ, i.e.,

$$\begin{aligned} A_{11}(\phi) + A_{22}(\phi) + 2A_{12}(\phi) &= A_{11}^0 + A_{22}^0 + 2A_{12}^0 \\ A_{44}(\phi) - A_{12}(\phi) &= A_{44}^0 - A_{12}^0 \\ A_{55}(\phi) + A_{66}(\phi) &= A_{55}^0 + A_{66}^0 \end{aligned} \tag{4.74}$$

Any linear combination of these equations is also an invariant combination of stiffness coefficients.

The inverse form of Eqs. (4.71) can be obtained if we substitute stresses, Eqs. (4.67), into Hooke's law, Eqs. (4.55), and the derived strains in Eqs. (4.70). As a result, we arrive at the following particular form of Eqs. (2.48), (2.49)

$$\varepsilon_x = \frac{\sigma_x}{E_x} - \nu_{xy}\frac{\sigma_y}{E_y} + \eta_{x,xy}\frac{\tau_{xy}}{G_{xy}}, \quad \varepsilon_y = \frac{\sigma_y}{E_y} - \nu_{yx}\frac{\sigma_x}{E_x} + \eta_{y,xy}\frac{\tau_{xy}}{G_{xy}}$$

$$\gamma_{xy} = \frac{\tau_{xy}}{G_{xy}} + \eta_{xy,x}\frac{\sigma_x}{E_x} + \eta_{xy,y}\frac{\sigma_y}{E_y} \tag{4.75}$$

$$\gamma_{xz} = \frac{\tau_{xz}}{G_{xz}} + \lambda_{xz,yz}\frac{\tau_{yz}}{G_{yz}}, \quad \gamma_{yz} = \frac{\tau_{yz}}{G_{yz}} + \lambda_{yz,xz}\frac{\tau_{xz}}{G_{xz}}$$

in which the compliance coefficients are

$$\frac{1}{E_x}=\frac{c^4}{E_1}+\frac{s^4}{E_2}+\left(\frac{1}{G_{12}}-\frac{2\nu_{21}}{E_1}\right)c^2s^2$$

$$\frac{\nu_{xy}}{E_y}=\frac{\nu_{yx}}{E_x}=\frac{\nu_{21}}{E_1}-\left(\frac{1}{E_1}+\frac{1}{E_2}+\frac{2\nu_{21}}{E_1}-\frac{1}{G_{12}}\right)c^2s^2$$

$$\frac{\eta_{x,xy}}{G_{xy}}=\frac{\eta_{xy,x}}{E_x}=2\left[\frac{c^2}{E_1}-\frac{s^2}{E_2}-\left(\frac{1}{2G_{12}}-\frac{\nu_{21}}{E_1}\right)\left(c^2-s^2\right)\right]cs$$

$$\frac{1}{E_y}=\frac{s^4}{E_1}+\frac{c^4}{E_2}+\left(\frac{1}{G_{12}}-\frac{2\nu_{21}}{E_1}\right)c^2s^2 \tag{4.76}$$

$$\frac{\eta_{y,xy}}{G_{xy}}=\frac{\eta_{xy,y}}{E_y}=2\left[\frac{s^2}{E_1}-\frac{c^2}{E_2}+\left(\frac{1}{2G_{12}}-\frac{\nu_{21}}{E_1}\right)\left(c^2-s^2\right)\right]cs$$

$$\frac{1}{G_{xy}}=4\left(\frac{1}{E_1}+\frac{1}{E_2}+\frac{2\nu_{21}}{E_1}\right)c^2s^2+\frac{1}{G_{12}}\left(c^2-s^2\right)^2$$

$$\frac{1}{G_{xz}}=\frac{c^2}{G_{13}}+\frac{s^2}{G_{23}},\quad \frac{\lambda_{xz,yz}}{G_{yz}}=\frac{\lambda_{yz,xz}}{G_{xz}}=\left(\frac{1}{G_{13}}-\frac{1}{G_{23}}\right)cs,\quad \frac{1}{G_{yz}}=\frac{s^2}{G_{13}}+\frac{c^2}{G_{23}}$$

There exist the following dependencies between the coefficients of Eqs. (4.71) and (4.75)

$$\frac{1}{E_x}=\frac{1}{D_1}\left(A_{22}A_{44}-A_{24}^2\right),\quad \frac{\nu_{xy}}{E_y}=\frac{\nu_{yx}}{E_x}=\frac{1}{D_1}\left(A_{12}A_{44}-A_{14}A_{24}\right)$$

$$\frac{\eta_{x,xy}}{G_{xy}}=\frac{\eta_{xy,x}}{E_x}=\frac{1}{D_1}\left(A_{12}A_{24}-A_{22}A_{14}\right),\quad \frac{1}{E_y}=\frac{1}{D_1}\left(A_{11}A_{44}-A_{14}^2\right)$$

$$\frac{\eta_{y,xy}}{G_{xy}}=\frac{\eta_{xy,y}}{E_y}=\frac{1}{D_1}\left(A_{12}A_{14}-A_{11}A_{24}\right),\quad \frac{1}{G_{xy}}=\frac{1}{D_1}\left(A_{11}A_{22}-A_{12}^2\right)$$

$$\frac{1}{G_{xz}}=\frac{A_{66}}{D_2},\quad \frac{1}{G_{yz}}=\frac{A_{55}}{D_2},\quad \frac{\lambda_{xz,yz}}{G_{yz}}=\frac{\lambda_{yz,xz}}{G_{xz}}=-\frac{A_{56}}{D_2}$$

Here,

$$D_1=A_{11}A_{22}A_{44}-A_{11}A_{24}^2-A_{22}A_{14}^2-A_{44}A_{12}^2+2A_{12}A_{14}A_{24},\quad D_2=A_{55}A_{66}-A_{56}^2$$

and

$$A_{11} = \frac{1 - \eta_{y,xy}\eta_{xy,y}}{D_3 E_y G_{xy}}, \quad A_{12} = \frac{\nu_{xy} - \eta_{x,xy}\eta_{xy,y}}{D_3 E_y G_{xy}}$$

$$A_{14} = -\frac{\eta_{x,xy} + \nu_{xy}\eta_{y,xy}}{D_3 E_y G_{xy}}, \quad A_{22} = \frac{1 - \eta_{x,xy}\eta_{xy,y}}{D_3 E_x G_{xy}}$$

$$A_{24} = -\frac{\eta_{y,xy} + \nu_{yx}\eta_{x,xy}}{D_3 E_x G_{xy}}, \quad A_{44} = \frac{1 - \nu_{xy}\nu_{yx}}{D_3 E_x E_y}$$

$$A_{55} = \frac{1}{D_4 G_{yz}}, \quad A_{56} = -\frac{\lambda_{xz,yz}}{D_4 G_{yz}}, \quad A_{66} = \frac{1}{D_4 G_{xz}}$$

where

$$D_3 = \frac{1}{E_x E_y G_{xy}}\left(1 - \nu_{xy}\nu_{yx} - \eta_{x,xy}\eta_{xy,x} - \eta_{y,xy}\eta_{xy,y} - \nu_{xy}\eta_{y,xy}\eta_{xy,x} - \nu_{yx}\eta_{x,xy}\eta_{xy,y}\right)$$

$$D_4 = \frac{1}{G_{xz}G_{yz}}\left(1 - \lambda_{xz,yz}\lambda_{yz,xz}\right)$$

As can be seen in Eqs. (4.71) and (4.75), the layer under study is anisotropic in plane xy because the constitutive equations include shear-extension and shear-shear coupling coefficients η and λ. For $\phi = 0$, the foregoing equations degenerate into Eqs. (4.55) and (4.56) for an orthotropic layer.

The dependencies of stiffness coefficients on the orientation angle for a carbon-epoxy composite with properties listed in Table 3.5 are presented in Figs. 4.20 and 4.21.

Uniaxial tension of the anisotropic layer (the so-called off-axis test of a unidirectional composite) is often used to determine material characteristics that cannot be found in tests with orthotropic specimens or to evaluate constitutive and failure theories. Such a test is shown in Fig. 4.22. To study this loading case, we should take $\sigma_y = \tau_{xy} = 0$ in Eqs. (4.75). Then,

$$\varepsilon_x = \frac{\sigma_x}{E_x}, \quad \varepsilon_y = -\nu_{xy}\frac{\sigma_x}{E_x}, \quad \gamma_{xy} = \eta_{xy,x}\frac{\sigma_x}{E_x} \tag{4.77}$$

As can be seen in these equations, tension in the x direction is accompanied not only by transverse contraction, as in orthotropic materials, but also by shear. This results in the deformed shape of the sample shown in Fig. 4.23. This shape is expected because the material stiffness in the fiber direction is much higher than that across the fibers.

Such an experiment, in cases where it can be performed, allows us to determine the in-plane shear modulus, G_{12}, in principal material coordinates using a simple tensile test as opposed to the much more complicated tests described in Section 3.4.3 and shown in Figs. 3.54 and 3.55. Indeed, if we know E_x from the tensile test in Fig. 4.23 and find E_1, E_2, and ν_{21} from tensile tests along and across the fibers (see Sections 3.4.1 and 3.4.2), we can use the first equation of Eqs. (4.76) to determine

$$G_{12} = \frac{\sin^2\phi\cos^2\phi}{\dfrac{1}{E_x} - \dfrac{\cos^4\phi}{E_1} - \dfrac{\sin^4\phi}{E_2} + \dfrac{2\nu_{21}}{E_1}\sin^2\phi\cos^2\phi} \tag{4.78}$$

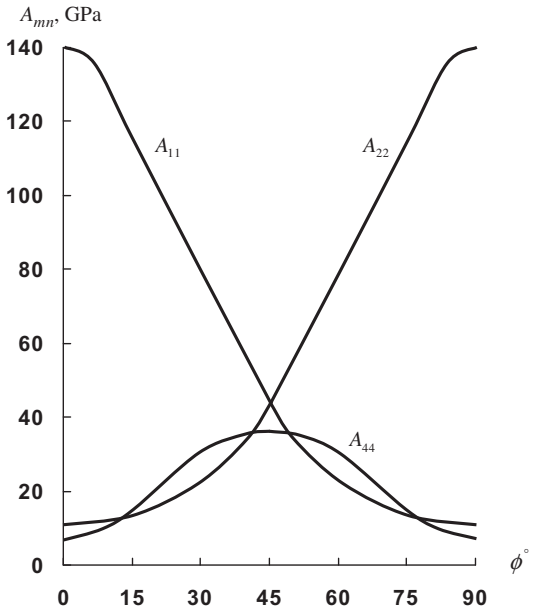


FIGURE 4.20

Dependencies of tensile (A_{11}, A_{22}) and shear (A_{44}) stiffnesses of a unidirectional carbon-epoxy layer on the orientation angle.

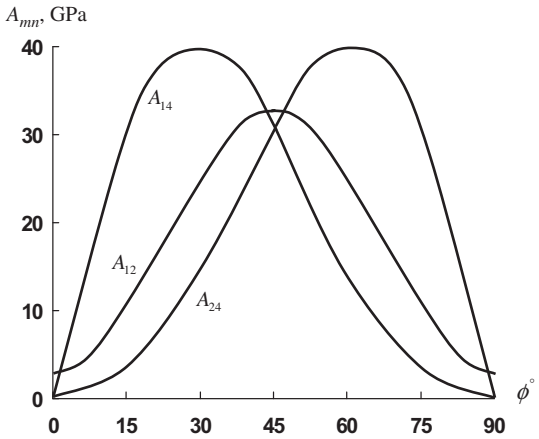


FIGURE 4.21

Dependencies of coupling stiffnesses of a unidirectional carbon-epoxy layer on the orientation angle.

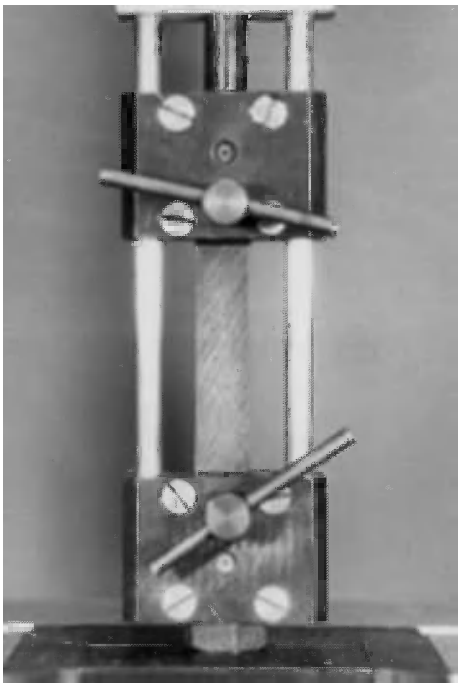


FIGURE 4.22

An off-axis test.

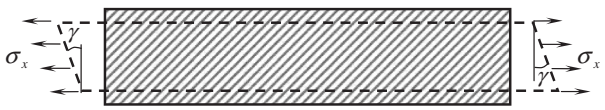


FIGURE 4.23

Deformation of a unidirectional layer loaded at an angle to fiber orientation.

In connection with this, a question arises as to what angle should be substituted into this equation to provide the most accurate result. The answer is given in Fig. 4.24, which displays the strains in principal material coordinates for a carbon-epoxy layer calculated with the aid of Eqs. (4.69) and (4.77). As can be seen in this figure, the most appropriate angle is about 10°. At this angle, the shear strain γ_{12} is much higher than normal strains ε_1 and ε_2, so that material deformation is associated mainly with shear. An off-axis test with $\phi = 10^\circ$ can be also used to evaluate material strength in shear $\overline{\tau}_{12}$ (Chamis, 1979). Stresses acting under off-axis tension in the principal material coordinates are statically determinate and can be found directly from Eqs. (4.67) as

$$\sigma_1 = \sigma_x \cos^2 \phi, \quad \sigma_2 = \sigma_x \sin^2 \phi, \quad \tau_{12} = -\sigma_x \sin \phi \cos \phi \tag{4.79}$$

Thus, applying stress σ_x and changing ϕ we can induce proportional loading with different combinations of stresses σ_1, σ_2, and τ_{12} to evaluate putative constitutive or failure theories for a material under study.

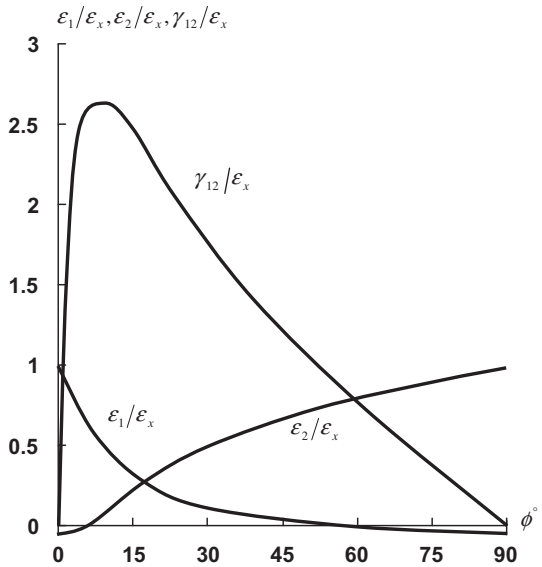


FIGURE 4.24

Dependencies of normalized strains in the principal material coordinates on the angle of the off-axis test.

However, the test shown in Fig. 4.23 can hardly be performed because the test fixture (see Fig. 4.22) restrains the shear deformation of the specimen and induces a corresponding shear stress. The constitutive equations for the specimen loaded with uniaxial tension as in Fig. 4.23 and fixed as in Fig. 4.22 follow from Eqs. (4.75) if we take $\sigma_y = 0$, i.e.,

$$\varepsilon_x = \frac{\sigma_x}{E_x} + \eta_{x,xy}\frac{\tau_{xy}}{G_{xy}} \tag{4.80}$$

$$\gamma_{xy} = \frac{\tau_{xy}}{G_{xy}} + \eta_{xy,x}\frac{\sigma_x}{E_x} \tag{4.81}$$

in which elastic constants are specified by Eqs. (4.76). The shear stress, being of a reactive nature, can be found from Eq. (4.81) if we put $\gamma_{xy} = 0$. Then,

$$\tau_{xy} = -\eta_{xy,x}\frac{G_{xy}}{E_x}\sigma_x$$

Substituting this result into Eq. (4.80), we arrive at

$$\varepsilon_x = \frac{\sigma_x}{E_x^{\mathrm{a}}} \tag{4.82}$$

Here,

$$E_x^{\mathrm{a}} = \frac{E_x}{1 - \eta_{x,xy}\eta_{xy,x}} \tag{4.83}$$

is the apparent elastic modulus that can be found from the test shown in Fig. 4.22. As follows from Eq. (4.83), E_x^{a}, in general, does not coincide with E_x as used in Eq. (4.78) for G_{12}.

Thus, measuring σ_x and ε_x we can determine E_x from Eq. (4.82) only under the condition $E_x^{\mathrm{a}} = E_x$, which means that the shear-extension coupling coefficient η must be zero. Applying Eqs. (4.76) and assuming that $\phi \neq 0$ and $\phi \neq 90^\circ$, we arrive at the following condition providing $\eta = 0$

$$\sin^2 \phi_0 = \frac{e_1}{e_2} \tag{4.84}$$

in which

$$e_1 = \frac{1+\nu_{21}}{E_1} - \frac{1}{2G_{12}}, \quad e_2 = \frac{1+\nu_{21}}{E_1} + \frac{1+\nu_{12}}{E_2} - \frac{1}{G_{12}}$$

Since $0 \leq \sin^2\phi \leq 1$, there exist two cases in which Eq. (4.84) is valid. The first case corresponds to the following set of inequalities

$$e_1 \geq 0, \quad e_2 > 0, \quad e_2 \geq e_1 \tag{4.85}$$

whereas for the second case,

$$e_1 \leq 0, \quad e_2 < 0, \quad e_2 \leq e_1 \tag{4.86}$$

To be specific, suppose that $E_1 > E_2$. Then, taking into account the symmetry condition $\nu_{12}E_1 = \nu_{21}E_2$ we have

$$\frac{1+\nu_{12}}{E_2} > \frac{1+\nu_{21}}{E_1} \tag{4.87}$$

Consider the first set of inequalities in Eqs. (4.85) and assume that the first of them, which has the following explicit form

$$\frac{1+\nu_{21}}{E_1} \geq \frac{1}{2G_{12}} \tag{4.88}$$

is valid. Then, Eq. (4.87) yields

$$\frac{1+\nu_{12}}{E_2} > \frac{1+\nu_{21}}{E_1} \geq \frac{1}{2G_{12}} \quad \text{or} \quad \frac{1+\nu_{12}}{E_2} > \frac{1}{2G_{12}}.$$

Matching this result with the last inequality in Eqs. (4.85) presented in the form

$$\frac{1+\nu_{12}}{E_2} \geq \frac{1}{2G_{12}} \tag{4.89}$$

we can conclude that if the first condition in Eqs. (4.85) is valid, then the last of these conditions holds too.

Consider the second condition in Eqs. (4.85) and write it in explicit form, i.e.,

$$\frac{1+\nu_{12}}{E_2} + \frac{1+\nu_{21}}{E_1} \geq \frac{1}{G_{12}} \tag{4.90}$$

Transforming Eq. (4.87) and using Eq. (4.89), we have

$$\frac{1+\nu_{12}}{E_2} + \frac{1+\nu_{21}}{E_1} > 2\frac{1+\nu_{21}}{E_1} \geq \frac{1}{G_{12}}$$

which means that the condition in Eq. (4.90) is valid.

So, the set of conditions in Eqs. (4.85) can be reduced to one inequality in Eq. (4.88), which can be written in a final form as

$$G_{12} \geq \frac{E_1}{2(1+\nu_{21})} \tag{4.91}$$

Consider conditions given by Eqs. (4.86) and assume that the last of them, which can be presented in the following explicit form

$$\frac{1+\nu_{12}}{E_2} \leq \frac{1}{2G_{12}} \tag{4.92}$$

is valid. Using Eqs. (4.87) and (4.92), we get

$$\frac{1+\nu_{21}}{E_1} < \frac{1+\nu_{12}}{E_2} \leq \frac{1}{2G_{12}} \quad \text{or} \quad \frac{1+\nu_{21}}{E_1} < \frac{1}{2G_{12}}$$

Since the first condition in Eqs. (4.86) can be presented as

$$\frac{1+\nu_{21}}{E_1} \leq \frac{1}{2G_{12}}$$

we can conclude that it is satisfied.

Consider the second inequality in Eqs. (4.86) and write it in an explicit form, i.e.,

$$\frac{1+\nu_{21}}{E_1} + \frac{1+\nu_{12}}{E_2} < \frac{1}{G_{12}} \tag{4.93}$$

Using Eqs. (4.87) and (4.92), we get

$$\frac{1+\nu_{21}}{E_1} + \frac{1+\nu_{12}}{E_2} < 2\frac{1+\nu_{12}}{E_2} \leq \frac{1}{G_{12}}$$

which means that the condition in Eqn. (4.93) is satisfied.

So, the set of conditions in Eqs. (4.86) is reduced to one inequality in Eq. (4.92), which can be written in the following final form

$$G_{12} \leq \frac{E_2}{2(1+\nu_{12})} \tag{4.94}$$

Thus, Eq. (4.84) determines the angle ϕ_0 for the orthotropic materials whose mechanical characteristics satisfy the conditions in Eqs. (4.91) or (4.94). Such materials, being loaded at an angle $\phi = \phi_0$, do not experience shear-stretching coupling. The shear modulus can be found from Eq. (4.78) in which $E_x = \sigma_x/\varepsilon_x$, where σ_x and ε_x are the stress and the strain determined in the off-axis tension test shown in Fig. 4.22.

Consider as examples unidirectional composites with typical properties (Table 3.5).

1. For fiberglass-epoxy composite, we have $E_1 = 60$ GPa, $E_2 = 13$ GPa, $G_{12} = 3.4$ GPa, $\nu_{12} = 0.065$, $\nu_{21} = 0.3$. Calculation in accordance with Eqs. (4.91) and (4.94) yields

$$\frac{E_1}{2(1+\nu_{21})} = 23.08 \text{ GPa} \qquad \frac{E_2}{2(1+\nu_{12})} = 6.1 \text{ GPa}$$

Thus, the condition in Eq. (4.94) is satisfied, and Eq. (4.84) gives $\phi_0 = 54.31°$.

2. For aramid-epoxy composite with $E_1 = 95$ GPa, $E_2 = 5.1$ GPa, $G_{12} = 1.8$ GPa, $\nu_{12} = 0.018$, $\nu_{21} = 0.34$, we have $\dfrac{E_1}{2(1+\nu_{21})} = 36.45$ GPa, $\dfrac{E_2}{2(1+\nu_{12})} = 2.5$ GPa, and $\phi_0 = 61.45^\circ$

3. For carbon-epoxy composite with $E_1 = 140$ GPa, $E_2 = 11$ GPa, $G_{12} = 5.5$ GPa $\nu_{12} = 0.021$, $\nu_{21} = 0.27$, we have $\dfrac{E_1}{2(1+\nu_{21})} = 55.12$ GPa, $\dfrac{E_2}{2(1+\nu_{12})} = 5.39$ GPa

As can be seen, the conditions in Eqs. (4.91) and (4.94) are not satisfied, and angle ϕ_0 does not exist for this material.

As can be directly checked with the aid of Eqs. (4.76), there exists the following relationship between the elastic constants of anisotropic materials (Verchery and Gong, 1999)

$$\frac{d}{d\phi}\left(\frac{1}{E_x}\right) = -2\frac{\eta_{x,xy}}{G_{xy}}$$

This equation means that $\eta_{x,xy} = 0$ for materials whose modulus E_x reaches the extremum in the interval $0 < \phi < 90^\circ$. The dependencies of E_x/E_1 on ϕ for the materials with properties listed in Table 3.5 are shown in Fig. 4.25.

As can be seen, curves 1 and 2 corresponding to glass and aramid composites reach the minimum value at $\phi_0 = 54.31^\circ$ and $\phi_0 = 61.45^\circ$, respectively, whereas curve 3 for carbon composite does not have a minimum at $0 < \phi < 90^\circ$.

The dependence $E_x(\phi)$ with the minimum value of E_x reached at $\phi = \phi_0$, where $0 < \phi < 90^\circ$, is typical for composites reinforced in two orthogonal directions. For example, for a fabric composite having $E_1 = E_2$ and $\nu_{12} = \nu_{21}$, Eq. (4.84) yields the well-known result $\phi_0 = 45^\circ$. For a typical fiberglass fabric composite with $E_1 = 26$ GPa, $E_2 = 22$ GPa, $G_{12} = 7.2$ GPa, $\nu_{12} = 0.11$, and $\nu_{21} = 0.13$, we have

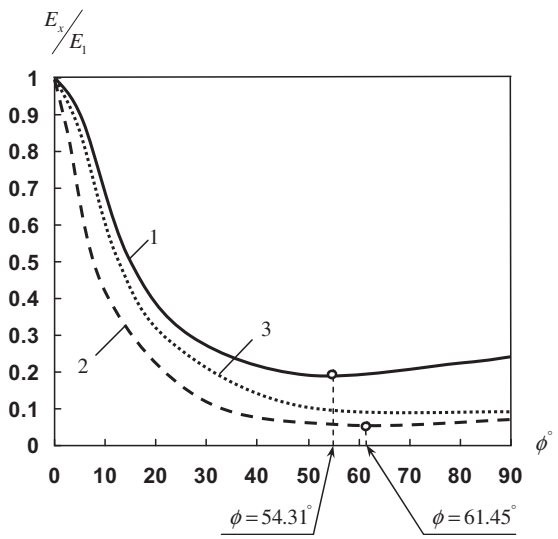


FIGURE 4.25

Dependencies of E_x/E_1 on ϕ for fiberglass- (1), aramid- (2), and carbon- (3) epoxy composites.

$$\frac{E_1}{2(1+\nu_{21})} = 11.5 \text{ GPa}, \quad \frac{E_2}{2(1+\nu_{12})} = 9.9 \text{ GPa}, \quad \text{and} \quad \phi_0 = 49.13^\circ$$

In conclusion, it should be noted that the actual application of Eq. (4.78) is hindered by the fact that the angle ϕ_0 specified by Eq. (4.84) depends on G_{12}, which is not known and needs to be determined from Eq. (4.78). To find G_{12}, we actually need to perform several tests for several values of G_{12} in the vicinity of the expected value and the corresponding values of ϕ_0 following from Eq. (4.84), and select the correct value of G_{12}, which satisfies in conjunction with the corresponding value of ϕ_0, both equations: Eqs. (4.78) and (4.84) (Morozov and Vasiliev, 2003).

Consider the general case of an off-axis test (see Fig. 4.22) for a composite specimen with an arbitrary fiber orientation angle ϕ (see Fig. 4.26). To describe this test, we need to study the coupled problem for an anisotropic strip in which shear is induced by tension but is restricted at the strip ends by the jaws of a test fixture as in Figs 4.22 and 4.26. As follows from Fig. 4.26, the action of the grip can be simulated if we apply a bending moment M and a transverse force V such that the rotation of the strip ends (γ in Fig. 4.23) will become zero. As a result, bending normal and shear stresses appear in the strip that can be analyzed with the aid of composite beam theory (Vasiliev, 1993).

To derive the corresponding equations, introduce the conventional assumptions of beam theory according to which axial, u_x, and transverse, u_y, displacements can be presented as

$$u_x = u(x) + y\theta, \quad u_y = v(x)$$

where u and θ are the axial displacement and the angle of rotation of the strip cross section, $x = constant$, and v is the strip deflection in the xy-plane (see Fig. 4.26). The strains corresponding to these displacements follow from Eqs. (2.22), i.e.,

$$\begin{aligned} \varepsilon_x &= \frac{\partial u_x}{\partial x} = u' + y\theta' = \varepsilon + y\theta' \\ \gamma_{xy} &= \frac{\partial u_x}{\partial y} + \frac{\partial u_y}{\partial x} = \theta + v' \end{aligned} \tag{4.95}$$

where $(\ldots)' = d(\ldots)/dx$, and ε is the deformation of the strip axis. These strains are related to stresses by Eqs. (4.75) which reduce to

$$\begin{aligned} \varepsilon_x &= \frac{\sigma_x}{E_x} + \eta_{x,xy}\frac{\tau_{xy}}{G_{xy}} \\ \gamma_{xy} &= \frac{\tau_{xy}}{G_{xy}} + \eta_{xy,x}\frac{\sigma_x}{E_x} \end{aligned} \tag{4.96}$$

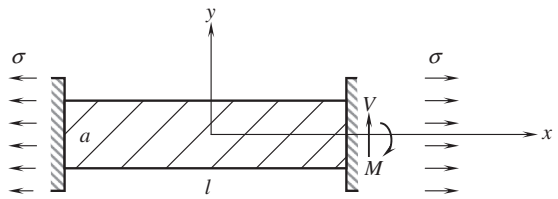


FIGURE 4.26

Off-axis tension of a strip fixed at the ends.

The inverse form of these equations is

$$\sigma_x = B_{11}\varepsilon_x + B_{14}\gamma_{xy}, \quad \tau_{xy} = B_{41}\varepsilon_x + B_{44}\gamma_{xy} \tag{4.97}$$

where

$$\begin{aligned} B_{11} &= \frac{E_x}{1-\eta_{x,xy}\eta_{xy,x}}, \quad B_{44} = \frac{G_{xy}}{1-\eta_{x,xy}\eta_{xy,x}} \\ B_{14} &= B_{41} = -\frac{E_x\eta_{x,xy}}{1-\eta_{x,xy}\eta_{xy,x}} = -\frac{G_{xy}\eta_{xy,x}}{1-\eta_{x,xy}\eta_{xy,x}} \end{aligned} \tag{4.98}$$

Now, decompose the strip displacements, strains, and stresses into two components corresponding to

1. free tension (see Fig. 4.23), and
2. bending.

For free tension, we have $\tau_{xy} = 0$ and $\upsilon = 0$. So, Eqs. (4.95) and (4.96) yield

$$\begin{aligned} \varepsilon_x^{(1)} &= \varepsilon_1 + y\theta_1', \quad \gamma_{xy}^{(1)} = \theta_1 \\ \varepsilon_x^{(1)} &= \frac{\sigma_x^{(1)}}{E_x}, \quad \gamma_{xy}^{(1)} = \eta_{xy,x}\frac{\sigma_x^{(1)}}{E_x} \end{aligned} \tag{4.99}$$

Here, $\varepsilon_1 = u_1'$ and $\sigma_x^{(1)} = \sigma = F/ah$, where F is the axial force applied to the strip, a is the strip width, and h is its thickness. Since $\sigma_x^{(1)} =$ constant, Eqs. (4.99) give

$$\theta_1 = \eta_{xy,x}\frac{\sigma}{E_x} = \text{constant}, \quad \varepsilon_x^1 = \varepsilon_1 = \frac{\sigma}{E_x} = \frac{F}{ah} \tag{4.100}$$

Adding components corresponding to bending (with index 2), we can write the total displacements and strains as

$$\begin{aligned} u_x &= u_1 + u_2 + y(\theta_1 + \theta_2), \quad u_y = \upsilon_2 \\ \varepsilon_x &= \varepsilon_1 + \varepsilon_2 + y\theta_2', \quad \gamma_{xy} = \theta_1 + \theta_2 + \upsilon_2' \end{aligned}$$

The total stresses can be expressed with the aid of Eqs. (4.97), i.e.,

$$\begin{aligned} \sigma_x &= B_{11}(\varepsilon_1 + \varepsilon_2 + y\theta_2') + B_{14}(\theta_1 + \theta_2 + \upsilon_2') \\ \tau_{xy} &= B_{41}(\varepsilon_1 + \varepsilon_2 + y\theta_2') + B_{44}(\theta_1 + \theta_2 + \upsilon_2') \end{aligned}$$

Transforming these equations with the aid of Eqs. (4.98) and (4.100), we arrive at

$$\begin{aligned} \sigma_x &= \sigma + B_{11}(\varepsilon_2 + y\theta_2') + B_{14}(\theta_2 + \upsilon_2') \\ \tau_{xy} &= B_{41}(\varepsilon_2 + y\theta_2') + B_{44}(\theta_2 + \upsilon_2') \end{aligned} \tag{4.101}$$

These stresses are statically equivalent to the axial force P, the bending moment M, and the transverse force V, which can be introduced as

$$P = h\int_{-a/2}^{a/2}\sigma_x dy, \quad M = h\int_{-a/2}^{a/2}\sigma_x y dy, \quad V = h\int_{-a/2}^{a/2}\tau_{xy}dy$$

Substitution of Eqs. (4.101) and integration yields

$$P = ah\left[\sigma + B_{11}\varepsilon_2 + B_{14}(\theta_2 + \upsilon_2')\right] \tag{4.102}$$

$$M = B_{11} h \frac{a^3}{12} \theta_2' \tag{4.103}$$

$$V = ah\left[B_{41}\varepsilon_2 + B_{44}\left(\theta_2 + v_2'\right)\right] \tag{4.104}$$

These forces and this moment should satisfy the equilibrium equation that follows from Fig. 4.27, i.e. ,

$$P' = 0, \quad V' = 0, \quad M' = V \tag{4.105}$$

Solution of the first equation is $P = F = \sigma\, ah$. Then, Eq. (4.102) gives

$$\varepsilon_2 = -\frac{B_{14}}{B_{11}}(\theta_2 + v_2') \tag{4.106}$$

The second equation of Eqs. (4.105) shows that $V = C_1$, where C_1 is a constant of integration. Then, substituting this result into Eq. (4.104) and eliminating ε_2 with the aid of Eq. (4.106), we have

$$\theta_2 + v_2' = \frac{C_1}{ah\overline{B}_{44}} \tag{4.107}$$

where $\overline{B}_{44} = B_{44} - B_{14}B_{41}$.

Taking in the third equation of Eqs. (4.105), $V = C_1$, and substituting M from Eq. (4.103), we arrive at the following equation for θ_2

$$\theta_2'' = \frac{12C_1}{a^3 h B_{11}}$$

Integration yields

$$\theta_2 = \frac{6C_1}{a^3 h B_{11}} + C_2 x + C_3$$

The total angle of rotation $\theta = \theta_1 + \theta_2$, where θ_1 is specified by Eqs. (4.100), should be zero at the ends of the strip, i.e., $\theta(x = \pm l/2) = 0$. Satisfying these conditions, we have

$$\theta_2 = \frac{3C_1}{a^3 h B_{11}}\left(2x^2 - \frac{l^2}{2}\right) - \eta_{xy,x}\frac{\sigma}{E_x} \tag{4.108}$$

Substitution into Eq. (4.107) and integration allows us to find the deflection

$$v_2 = \frac{C_1 x}{ah\overline{B}_{44}} - \frac{3C_1 x}{a^3 h B_{11}}\left(\frac{2x^2}{3} - \frac{l^2}{2}\right) + \eta_{xy,x}\frac{\sigma_0 x}{E_x} + C_4 \tag{4.109}$$

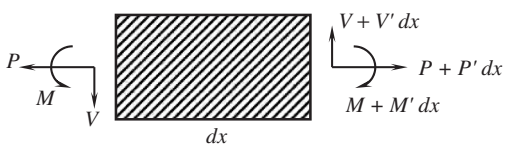


FIGURE 4.27

Forces and moments acting on the strip element.

This expression includes two constants, C_1 and C_4, which can be determined from the boundary conditions $v_2(x = \pm\, l/2) = 0$. The final result, following from Eqs. (4.100), (4.108), and (4.109), is

$$\begin{aligned} v &= l\eta_{xy,x}\frac{\sigma\bar{x}}{E_x}\left[1 - \frac{B_{11} + \bar{l}^2\bar{B}_{44}\left(3/2 - 2\bar{x}^2\right)}{B_{11} + \bar{l}^2\bar{B}_{44}}\right] \\ \theta &= \eta_{xy,x}\frac{3\sigma\bar{l}^2}{E_x}\frac{\bar{B}_{44}\left(2\bar{x}^2 - 1/2\right)}{B_{11} + \bar{l}^2\bar{B}_{44}} \end{aligned} \tag{4.110}$$

where $\bar{l} = l/a$ and $\bar{x} = x/l$. The deflection of a carbon-epoxy strip having $\phi = 45°$ and $\bar{l} = 10$ is shown in Fig. 4.28.

Now, we can write the relationship between modulus E_x corresponding to the ideal test shown in Fig. 4.23 and apparent modulus E_x^{a} that can be found from the real test shown in Figs. 4.22 and 4.26. Using Eqs. (4.98), (4.100), (4.106), and (4.110), we finally get

$$\sigma = E_x^{\mathrm{a}}\varepsilon$$

where

$$E_x^{\mathrm{a}} = \frac{E_x}{1 - \dfrac{E_x\eta_{x,xy}\eta_{xy,x}}{E_x + \bar{l}^2 G_{xy}(1 - \eta_{x,xy}\eta_{xy,x})}}$$

Consider two limiting cases. For an infinitely long strip ($\bar{l} \to \infty$), we have $E_x^{\mathrm{a}} = E_x$. This result corresponds to the case of free shear deformation specified by Eqs. (4.77). For an infinitely short strip ($\bar{l} \to 0$), taking into account Eqs. (4.98), we get

$$E_x^{\mathrm{a}} = \frac{E_x}{1 - \eta_{x,xy}\eta_{xy,x}} = B_{11}$$

In accordance with Eq. (4.97), this result corresponds to a restricted shear deformation ($\gamma_{xy} = 0$). For a strip with finite length, $E_x < E_x^{\mathrm{a}} < B_{11}$. The dependence of the normalized apparent modulus on the length-to-width ratio for a 45° carbon-epoxy layer is shown in Fig. 4.29. As can be seen, the difference between E_x^{a} and E_x becomes less than 5% for $l > 3a$.

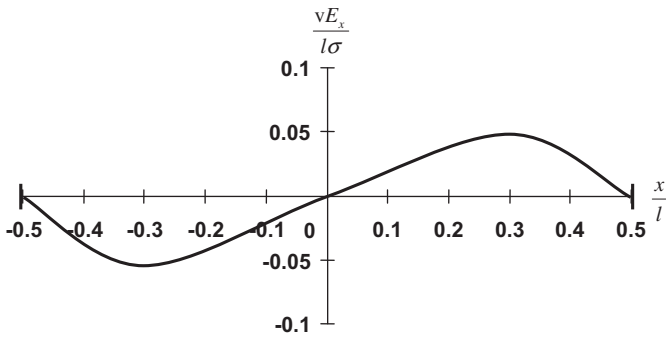


FIGURE 4.28

Normalized deflection of a carbon-epoxy strip ($\phi = 45°, \bar{l} = 10$).

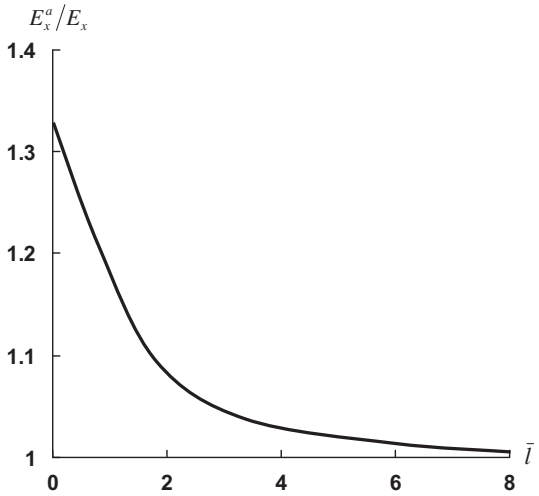


FIGURE 4.29

Dependence of the normalized apparent modulus on the strip length-to-width ratio for a 45° carbon-epoxy layer.

4.3.2 Nonlinear models

Nonlinear deformation of an anisotropic unidirectional layer can be studied rather straightforwardly because stresses σ_1, σ_2, and τ_{12} in the principal material coordinates (see Fig. 4.18) are statically determinate and can be found using Eqs. (4.67). Substituting these stresses into the nonlinear constitutive equations, Eqs. (4.60) or Eqs. (4.64), we can express strains ε_1, ε_2, and γ_{12} in terms of stresses σ_x, σ_y, and τ_{xy}. Further substitution of the strains ε_1, ε_2, and γ_{12} into Eqs. (4.70) yields constitutive equations that link strains ε_x, ε_y, and γ_{xy} with stresses σ_x, σ_y, and τ_{xy}, thus allowing us to find strains in the global coordinates x, y, and z if we know the corresponding stresses.

As an example of the application of a nonlinear elastic material model described by Eqs. (4.60), consider a two-matrix fiberglass composite (see Section 4.4.3) whose stress-strain curves in the principal material coordinates are presented in Fig. 4.16. These curves allow us to determine coefficients "b" and "c" in Eqs. (4.60). To find the coupling coefficients "m", we use a 45° off-axis test. Experimental results (circles) and the corresponding approximation (solid line) are shown in Fig. 4.30. Thus, the constructed model can be used now to predict material behavior under tension at any other angle (different from 0, 45, and 90° – the corresponding results are given in Fig. 4.31 for 60°) or to study more complicated material structures and loading cases (see Section 4.5).

As an example of the application of the elastic-plastic material model specified by Eq. (4.64), consider a boron-aluminum composite whose stress-strain diagrams in principal material coordinates are shown in Fig. 4.17. Theoretical and experimental curves (Herakovich, 1998) for 30 and 45° off-axis tension of this material are presented in Fig. 4.32.

4.4 ORTHOGONALLY REINFORCED ORTHOTROPIC LAYER

The simplest layer reinforced in two directions is the so-called cross-ply layer that consists of alternating plies with 0 and 90° orientations with respect to the global coordinate frame x, y, z as in

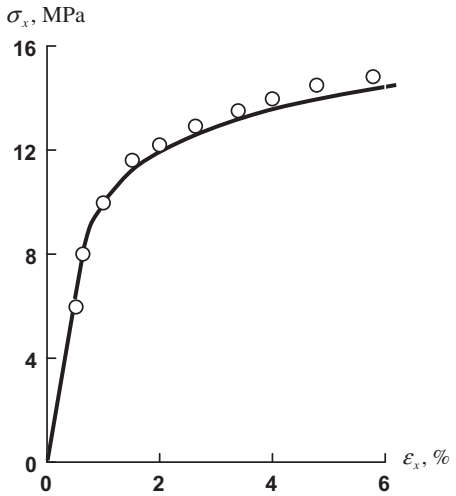


FIGURE 4.30

Calculated (solid line) and experimental (circles) stress-strain diagram for 45° off-axis tension of a two-matrix unidirectional composite.

Fig. 4.33. Actually, this is a laminated structure, but being formed with a number of plies, it can be treated as a homogeneous orthotropic layer (see Section 5.4.2).

4.4.1 Linear elastic model

Let the layer consist of m longitudinal (0°) plies with thicknesses $h_0^{(i)}$ ($i = 1,\ 2,\ 3,\ \ldots,\ m$) and n transverse (90°) plies with thicknesses $h_{90}^{(j)}$ ($j = 1,\ 2,\ 3,\ \ldots,\ n$) made from one and the same

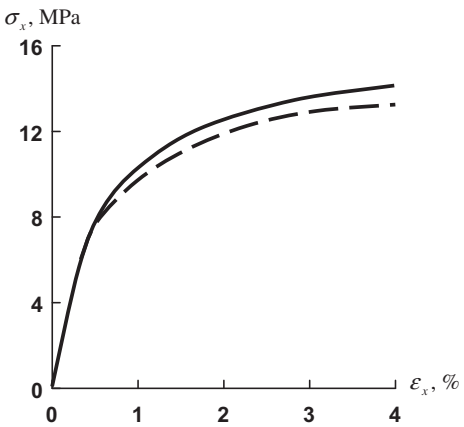


FIGURE 4.31

Theoretical (solid line) and experimental (dashed line) stress-strain diagrams for 60° off-axis tension of a two-matrix unidirectional composite.

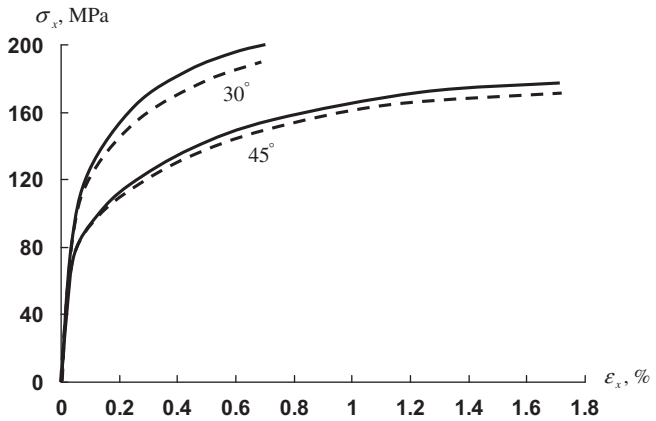


FIGURE 4.32

Theoretical (solid lines) and experimental (dashed lines) stress-strain diagrams for 30° and 45° off-axis tension of a boron-aluminum composite.

composite material. Then, stresses σ_x, σ_y, and τ_{xy} that comprise the plane stress state in the global coordinate frame can be expressed in terms of stresses in the principal material coordinates of the plies as

$$\begin{aligned}
\sigma_x h &= \sum_{i=1}^{m} \sigma_1^{(i)} h_0^{(i)} + \sum_{j=1}^{n} \sigma_2^{(j)} h_{90}^{(j)} \\
\sigma_y h &= \sum_{i=1}^{m} \sigma_2^{(i)} h_0^{(i)} + \sum_{j=1}^{n} \sigma_1^{(j)} h_{90}^{(j)} \\
\tau_{xy} h &= \sum_{i=1}^{m} \tau_{12}^{(i)} h_0^{(i)} + \sum_{j=1}^{n} \tau_{12}^{(j)} h_{90}^{(j)}
\end{aligned} \tag{4.111}$$

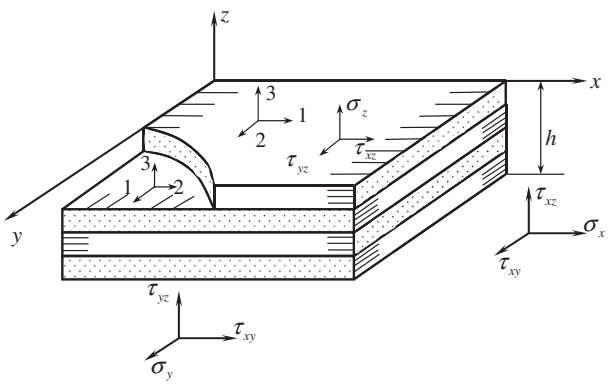


FIGURE 4.33

A cross-ply layer.

Here, h is the total thickness of the layer (see Fig. 4.33), i.e.,

$$h = h_0 + h_{90}$$

where

$$h_0 = \sum_{i=1}^{m} h_0^{(i)}, \quad h_{90} = \sum_{j=1}^{n} h_{90}^{(j)}$$

are the total thicknesses of the longitudinal and transverse plies.

The stresses in the principal material coordinates of the plies are related to the corresponding strains by Eqs. (3.59) or Eqs. (4.56)

$$\begin{aligned} \sigma_1^{(i,j)} &= \overline{E}_1\left(\varepsilon_1^{(i,j)} + \nu_{12}\varepsilon_2^{(i,j)}\right) \\ \sigma_2^{(i,j)} &= \overline{E}_2\left(\varepsilon_2^{(i,j)} + \nu_{21}\varepsilon_1^{(i,j)}\right) \\ \tau_{12}^{(i,j)} &= G_{12}\gamma_{12}^{(i,j)} \end{aligned} \tag{4.112}$$

in which, as earlier, $\overline{E}_{1,2} = E_{1,2}/(1 - \nu_{12}\nu_{21})$ and $E_1\nu_{12} = E_2\nu_{21}$. Now assume that the deformation of all the plies is the same as that of the deformation of the whole layer, i.e., that

$$\varepsilon_1^{(i)} = \varepsilon_2^{(j)} = \varepsilon_x, \quad \varepsilon_2^{(i)} = \varepsilon_1^{(j)} = \varepsilon_y, \quad \gamma_{12}^{(i)} = \gamma_{12}^{(j)} = \gamma_{xy}$$

Then, substituting the stresses, Eqs. (4.112), into Eqs. (4.111), we arrive at the following constitutive equations

$$\begin{aligned} \sigma_x &= A_{11}\varepsilon_x + A_{12}\varepsilon_y \\ \sigma_y &= A_{21}\varepsilon_x + A_{22}\varepsilon_y \\ \tau_{xy} &= A_{44}\gamma_{xy} \end{aligned} \tag{4.113}$$

in which the stiffness coefficients are

$$\begin{aligned} A_{11} &= \overline{E}_1\overline{h}_0 + \overline{E}_2\overline{h}_{90}, \quad A_{22} = \overline{E}_1\overline{h}_{90} + \overline{E}_2\overline{h}_0 \\ A_{12} &= A_{21} = \overline{E}_1\nu_{12} = \overline{E}_2\nu_{21}, \quad A_{44} = G_{12} \end{aligned} \tag{4.114}$$

and

$$\overline{h}_0 = \frac{h_0}{h}, \quad \overline{h}_{90} = \frac{h_{90}}{h}$$

The inverse form of Eqs. (4.113) is

$$\varepsilon_x = \frac{\sigma_x}{E_x} - \nu_{xy}\frac{\sigma_y}{E_y}, \quad \varepsilon_y = \frac{\sigma_y}{E_y} - \nu_{yx}\frac{\sigma_x}{E_x}, \quad \gamma_{xy} = \frac{\tau_{xy}}{G_{xy}} \tag{4.115}$$

where

$$\begin{aligned} &E_x = A_{11} - \frac{A_{12}^2}{A_{22}}, \quad E_y = A_{22} - \frac{A_{12}^2}{A_{21}}, \quad G_{xy} = A_{44} \\ &\nu_{xy} = \frac{A_{12}}{A_{11}}, \quad \nu_{yx} = \frac{A_{12}}{A_{22}} \end{aligned} \tag{4.116}$$

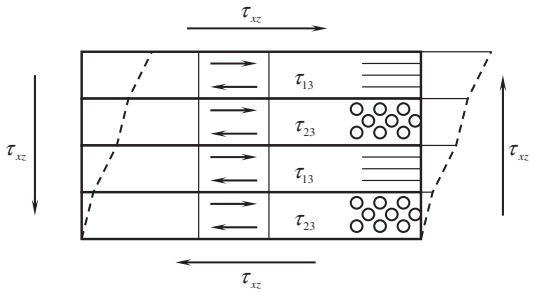


FIGURE 4.34

Pure transverse shear of a cross-ply layer.

To determine the transverse shear moduli G_{xz} and G_{yz}, consider, for example, pure shear in the xz–plane (see Fig. 4.34). It follows from the equilibrium conditions for the plies that

$$\tau_{13}^{(i)} = \tau_{23}^{(j)} = \tau_{xz}\,, \quad \tau_{23}^{(i)} = \tau_{13}^{(j)} = \tau_{yz} \tag{4.117}$$

The total shear strains can be found as

$$\begin{aligned} \gamma_{xz} &= \frac{1}{h}\left(\sum_{i=1}^{m}\gamma_{13}^{(i)}h_0 + \sum_{j=1}^{n}\gamma_{23}^{(j)}h_{90}\right) \\ \gamma_{yz} &= \frac{1}{h}\left(\sum_{i=1}^{m}\gamma_{23}^{(i)}h_0 + \sum_{j=1}^{n}\gamma_{13}^{(j)}h_{90}\right) \end{aligned} \tag{4.118}$$

where in accordance with Eqs. (4.56)

$$\gamma_{13}^{(i,j)} = \frac{\tau_{13}^{(i,j)}}{G_{13}}, \quad \gamma_{23}^{(i,j)} = \frac{\tau_{23}^{(i,j)}}{G_{23}} \tag{4.119}$$

Substituting Eqs. (4.119) into Eqs. (4.118) and using Eqs. (4.117), we arrive at

$$\gamma_{xz} = \frac{\tau_{xz}}{G_{xz}}\,, \quad \gamma_{yz} = \frac{\tau_{yz}}{G_{yz}}$$

where

$$\frac{1}{G_{xz}} = \frac{\overline{h}_0}{G_{13}} + \frac{\overline{h}_{90}}{G_{23}}\,, \quad \frac{1}{G_{yz}} = \frac{\overline{h}_0}{G_{23}} + \frac{\overline{h}_{90}}{G_{13}}$$

4.4.2 Nonlinear models

The nonlinear behavior of a cross-ply layer associated with nonlinear material response under loading in the principal material coordinates (e.g., see Figs. 4.16 and 4.17) can be described using nonlinear constitutive equations, Eqs. (4.60) or Eqs. (4.64), instead of linear equations, Eqs. (4.113).

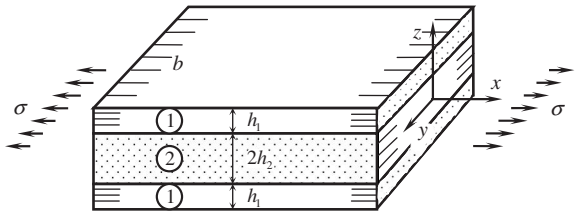


FIGURE 4.35

Tension of a cross-ply laminate.

However, this layer can demonstrate nonlinearity which is entirely different from that studied in the previous sections. This nonlinearity is observed in the cross-ply layer composed of linear elastic plies and is caused by microcracking of the matrix.

To study this phenomenon, consider a cross-ply laminate consisting of three plies as in Fig. 4.35. Equilibrium conditions yield the following equations

$$\begin{aligned} 2\left(\sigma_{x1}\overline{h}_1 + \sigma_{x2}\overline{h}_2\right) &= \sigma \\ 2\left(\sigma_{y1}\overline{h}_1 + \sigma_{y2}\overline{h}_2\right) &= 0 \end{aligned} \tag{4.120}$$

in which

$$\overline{h}_1 = h_1/h, \quad \overline{h}_2 = h_2/h, \quad h = 2\left(h_1 + h_2\right)$$

The constitutive equations are

$$\begin{aligned} \sigma_{x1,2} &= \overline{E}_{1,2}\left(\varepsilon_x + \nu_{12,21}\varepsilon_y\right) \\ \sigma_{y1,2} &= \overline{E}_{2,1}\left(\varepsilon_y + \nu_{21,12}\varepsilon_x\right) \end{aligned} \tag{4.121}$$

in which $\overline{E}_{1,2} = E_{1,2}/(1 - \nu_{12}\nu_{21})$. We assume that strains ε_x and ε_y do not change through the laminate thickness. Substituting Eqs. (4.121) into Eqs. (4.120), we can find strains and then stresses using again Eqs. (4.121). The final result is

$$\sigma_{x1,2} = \frac{\sigma E_{1,2}\left[E_2\overline{h}_1 + E_1\overline{h}_2 - E_{1,2}\nu_{12,21}^2\left(\overline{h}_1 + \overline{h}_2\right)\right]}{2\left[\left(E_1\overline{h}_1 + E_2\overline{h}_2\right)\left(E_2\overline{h}_1 + E_1\overline{h}_2\right) - E_1^2\nu_{12}^2(h_1 + h_2)^2\right]}$$

To simplify the analysis, neglect Poisson's effect, i.e. taking $\nu_{12} = \nu_{21} = 0$. Then

$$\sigma_{x1} = \sigma_1^0 = \frac{\sigma E_1}{2\left(E_1\overline{h}_1 + E_2\overline{h}_2\right)}, \quad \sigma_{x2} = \sigma_2^0 = \frac{\sigma E_2}{2\left(E_1\overline{h}_1 + E_2\overline{h}_2\right)} \tag{4.122}$$

Consider, for example, the case $\overline{h}_1 = \overline{h}_2 = 0.5$ and find the ultimate stresses corresponding to the failure of longitudinal plies or to the failure of the transverse ply. Putting $\sigma_1^0 = \overline{\sigma}_1^+$ and $\sigma_2^0 = \overline{\sigma}_2^+$, we get

$$\overline{\sigma}_x^{(1)} = \overline{\sigma}_1^+\left(1 + \frac{E_2}{E_1}\right), \quad \overline{\sigma}_x^{(2)} = \overline{\sigma}_2^+\left(1 + \frac{E_1}{E_2}\right)$$

The results of calculation for the composites listed in Table 3.5 are presented in Table 4.2.

TABLE 4.2 Ultimate stresses causing the failure of longitudinal $\left(\overline{\sigma}_x^{(1)}\right)$ or transverse $\left(\overline{\sigma}_x^{(2)}\right)$ plies and deformation characteristics of typical advanced composites.

σ(MPa); ε (%)	Glass-epoxy	Carbon-epoxy	Carbon-PEEK	Aramid-epoxy	Boron-epoxy	Boron-Al	Carbon-Carbon	Al_2O_3-Al
$\overline{\sigma}_x^{(1)}$	2190	2160	2250	2630	1420	2000	890	1100
$\overline{\sigma}_x^{(2)}$	225	690	1125	590	840	400	100	520
$\overline{\varepsilon}_1$	3	1.43	1.5	2.63	0.62	0.50	0.47	0.27
$\overline{\varepsilon}_2$	0.31	0.45	0.75	0.2	0.37	0.1	0.05	0.13
$\overline{\varepsilon}_1/\overline{\varepsilon}_2$	9.7	3.2	2	13.1	1.68	5	9.4	2.1

As can be seen, $\overline{\sigma}_x^{(1)} >> \overline{\sigma}_x^{(2)}$. This means that the first failure occurs in the transverse ply under stress

$$\sigma = \overline{\sigma} = 2\overline{\sigma}_2^{+}\left(\overline{h}_2 + \frac{E_1}{E_2}\overline{h}_1\right) \tag{4.123}$$

This stress does not cause failure of the whole laminate, because the longitudinal plies can carry the load, but the material behavior becomes nonlinear. Actually, the effect under consideration is the result of the difference between the ultimate elongations of the unidirectional plies along and across the fibers. From the data presented in Table 4.2 we can see that for all the materials listed in this table $\overline{\varepsilon}_1 >> \overline{\varepsilon}_2$. As a result, transverse plies drawn under tension by longitudinal plies that have much higher stiffness and elongation fail because their ultimate elongation is smaller. This failure is accompanied by a system of cracks parallel to the fibers which can be observed not only in cross-ply layers but also in many other laminates that include unidirectional plies experiencing transverse tension caused by interaction with the adjacent plies (see Fig. 4.36).

Now assume that the acting stress $\sigma \geq \overline{\sigma}$, where $\overline{\sigma}$ is specified by Eq. (4.123) and corresponds to the load causing the first crack in the transverse ply as in Fig. 4.37. To study the stress state in the vicinity of the crack, decompose the stresses in the three plies shown in Fig. 4.37 as

$$\sigma_{x1} = \sigma_{x3} = \sigma_1^0 + \sigma_1, \quad \sigma_{x2} = \sigma_2^0 - \sigma_2 \tag{4.124}$$

and assume that the crack also induces transverse through-the-thickness shear and normal stresses

$$\tau_{xzi} = \tau_i\,, \quad \sigma_{zi} = s_i\,, \quad i = 1,\ 2,\ 3 \tag{4.125}$$

The stresses σ_1^0 and σ_2^0 in Eqs. (4.124) are specified by Eqs. (4.122) with $\sigma = \overline{\sigma}$, corresponding to the acting stress under which the first crack appears in the transverse ply. Stresses σ_1 and σ_2 should be self-balanced, i.e.,

$$\sigma_1\overline{h}_1 = \sigma_2\overline{h}_2 \tag{4.126}$$

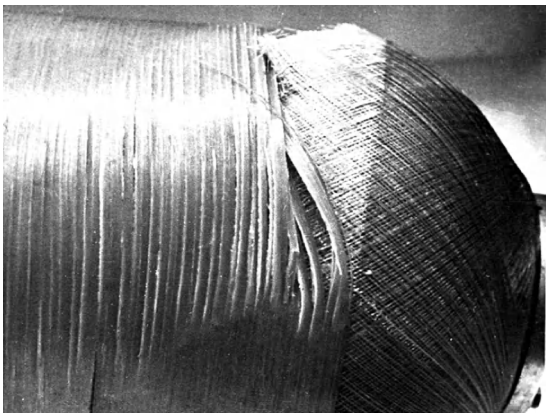


FIGURE 4.36

Cracks in the circumferential layer of a failed pressure vessel induced by transverse (for the vessel, axial) tension of the layer.

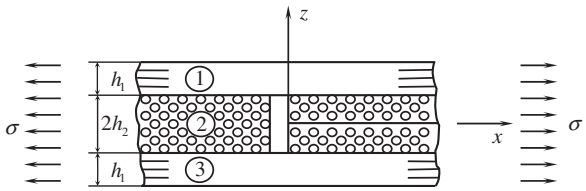


FIGURE 4.37

A cross-ply layer with a crack in the transverse ply.

The total stresses in Eqs. (4.124) and (4.125) should satisfy equilibrium equations, Eqs. (2.5), which yield for the problem under study

$$\frac{\partial \sigma_{xi}}{\partial x} + \frac{\partial \tau_{xzi}}{\partial z} = 0, \quad \frac{\partial \sigma_{zi}}{\partial z} + \frac{\partial \tau_{xzi}}{\partial x} = 0 \tag{4.127}$$

where $i = 1,\ 2,\ 3$.

To simplify the problem, suppose that the additional stresses σ_1 and σ_2 do not depend on z, i.e., that they are uniformly distributed through the thickness of longitudinal plies. Then, Eqs. (4.127) upon substitution of Eqs. (4.124) and (4.125) can be integrated with respect to z. The resulting stresses should satisfy the following boundary and interface conditions (see Fig. 4.37)

$$\begin{aligned}
&\tau_1(z = h_1 + h_2) = 0 && s_1(z = h_1 + h_2) = 0\\
&\tau_1(z = h_2) = \tau_2(z = h_2) && s_1(z = h_2) = s_2(z = h_2)\\
&\tau_2(z = -h_2) = \tau_3(z = -h_2) && s_2(z = -h_2) = s_3(z = -h_2)\\
&\tau_3(z = -h_1 - h_2) = 0 && s_3(z = -h_1 - h_2) = 0
\end{aligned}$$

Finally, using Eq. (4.126) to express σ_1 in terms of σ_2, we arrive at the following stress distribution (Vasiliev et al., 1970)

$$\begin{aligned}
&\sigma_{x1} = \sigma_{x3} = \sigma_1^0 + \sigma_2(x)\frac{h_2}{h_1}, \quad \sigma_{x2} = \sigma_2^0 - \sigma_2(x) \\
&\tau_1 = -\frac{h_2}{h_1}\sigma_2'(x)z_1, \quad \tau_2 = \sigma_2'(x)z, \quad \tau_3 = -\frac{h_2}{h_1}\sigma_2'(x)z_2 \\
&s_1 = \frac{h_2}{2h_1}\sigma_2''(x)z_1^2, \quad s_2 = -\frac{1}{2}\sigma_2''(x)(z^2 - h_1h_2 - h_2^2) \\
&s_3 = \frac{h_2}{2h_1}\sigma_2''(x)z_2^2
\end{aligned} \tag{4.128}$$

where

$$z_1 = z - h_1 - h_2\,, \quad z_2 = z + h_1 + h_2\,, \quad \text{and} \quad (\quad)' = d(\quad)/dx$$

Thus, we need to find only one unknown function: $\sigma_2(x)$. To do this, we can use the principle of minimum strain energy (see Section 2.11.2), according to which the function $\sigma_2(x)$ should deliver the minimum value of

$$W_\sigma = \frac{1}{2}\int_0^l \sum_{i=1}^{3} \int_{h_i} \left(\frac{\sigma_{xi}^2}{E_{xi}} + \frac{\sigma_{zi}^2}{E_{zi}} - 2\frac{\nu_{xzi}}{E_{zi}}\sigma_{xi}\sigma_{zi} + \frac{\tau_{xzi}^2}{G_{xzi}}\right)dx \tag{4.129}$$

where $E_{x1} = E_{x3} = E_1$, $E_{x2} = E_2$, $E_{zi} = E_2$, $G_{xz1} = G_{xz3} = G_{13}$, $G_{xz2} = G_{23}$, $\nu_{xz1} = \nu_{xz3} = \nu_{13}$, and $\nu_{xz2} = \nu_{23}$, whereas E_1, E_2, $G_{12}G_{23}$, ν_{13} and ν_{23} are elastic constants of a unidirectional ply. Substituting stresses, Eqs. (4.128), into the functional in Eq. (4.129), integrating with respect to z, and using the traditional procedure of variational calculus providing $\delta W_\sigma = 0$, we arrive at the following equation for $\sigma_2(x)$

$$\frac{d^4\sigma_2}{dx^4} - 2a^2\frac{d^2\sigma_2}{dx^2} + b^4\sigma_2 = 0$$

in which

$$a^2 = \frac{1}{d}\left[\frac{h_2}{3G_{23}} + \frac{h_1}{3G_{13}} - \frac{\nu_{23}}{E_2}\left(h_1 + \frac{2}{3}h_2\right) + \frac{h_1\nu_{23}}{3E_2}\right],$$

$$b^4 = \frac{1}{d}\left(\frac{1}{h_1E_1} + \frac{1}{h_2E_2}\right)$$

$$d = \frac{1}{2E_2}\left[\frac{1}{5}\left(h_1^3 + h_2^3\right) - \frac{2}{3}h_2^2(h_1 + h_2) + h_2(h_1 + h_2)^2\right]$$

The general solution for this equation is

$$\sigma_2 = e^{-k_1x}\left(c_1\sin k_2x + c_2\cos k_2x\right) + e^{k_1x}\left(c_3\sin k_2x + c_4\cos k_2x\right) \tag{4.130}$$

where

$$k_1 = \sqrt{\frac{1}{2}(a^2 + b^2)}, \quad k_2 = \sqrt{\frac{1}{2}(b^2 - a^2)}$$

Suppose that the strip shown in Fig. 4.37 is infinitely long in the x direction. Then, we should have $\sigma_1 \to 0$ and $\sigma_2 \to 0$ for $x \to \infty$ in Eqs. (4.124). This means that we should put $c_3 = c_4 = 0$ in Eq. (4.130). The other two constants, c_1 and c_2, should be determined from the conditions on the crack surface (see Fig. 4.37), i.e.,

$$\sigma_{x2}(x = 0) = 0, \quad \tau_{xz2}(x = 0) = 0$$

Satisfying these conditions, we obtain the following expressions for stresses

$$\begin{aligned}
\sigma_{x1} &= \sigma_{x3} = \sigma_1^0 + \sigma_2^0 \frac{h_2}{h_1} e^{-k_1 x}\left(\frac{k_1}{k_2}\sin k_2 x + \cos k_2 x\right) \\
\sigma_{x2} &= \sigma_2^0\left[1 - e^{-k_1 x}\left(\frac{k_1}{k_2}\sin k_2 x + \cos k_2 x\right)\right], \quad \tau_{xz2} = -\frac{\sigma_2^0}{k_2}\left(k_1^2 + k_2^2\right) z e^{-k_1 x}\sin k_2 x \\
\sigma_{z2} &= -\frac{\sigma_2^0}{2k_2}\left(k_1^2 + k_2^2\right)\left[z^2 - h_2(h_1 + h_2)\right] e^{-k_1 x}\left(k_1 \sin k_2 x - k_2 \cos k_2 x\right)
\end{aligned} \tag{4.131}$$

As an example, consider a glass-epoxy sandwich layer with the following parameters: $h_1 = 0.365$ mm, $h_2 = 0.735$ mm, $E_1 = 56$ GPa, $E_2 = 17$ GPa, $G_{13} = 5.6$ GPa, $G_{23} = 6.4$ GPa, $\nu_{13} = 0.095$, $\nu_{23} = 0.35$, and $\overline{\sigma}_2^+ = 25.5$ MPa. The distributions of stresses normalized to the acting stress σ are presented in Fig. 4.38. As can be seen, there is a stress concentration in the longitudinal plies in the vicinity of the crack, whereas the stress in the transverse ply, being zero on the crack surface, practically reaches σ_2^0 at a distance of about 4 mm (or about twice the thickness of the laminate) from the crack. The curves have the expected forms for this problem of stress diffusion. However, analysis of the second equation of Eqs. (4.131) allows us to reveal an interesting phenomenon which can be demonstrated if we increase the vertical scale of the graph in the vicinity of points A and B (see Fig. 4.38). It follows from this analysis that stress σ_{x2} becomes equal to σ_2^0 at point A with coordinate

$$x_A = \frac{1}{k_2}\left[\pi - \tan^{-1}\left(\frac{k_2}{k_1}\right)\right]$$

and reaches a maximum value at point B with coordinate $x_B = \pi/k_2$. This maximum value

$$\sigma_{x2}^{\max} = \sigma_2^0\left(1 + e^{-\pi\frac{k_1}{k_2}}\right)$$

is higher than stress σ_2^0, which causes failure of the transverse ply. This means that a single crack cannot exist. When stress σ_2^0 reaches its ultimate value $\overline{\sigma}_2^+$, a regular system of cracks located at a distance of $l_c = \pi/k_2$ from one to another appears in the transverse ply (see Fig. 4.39). For the previous example, $l_c = 12.6$ mm.

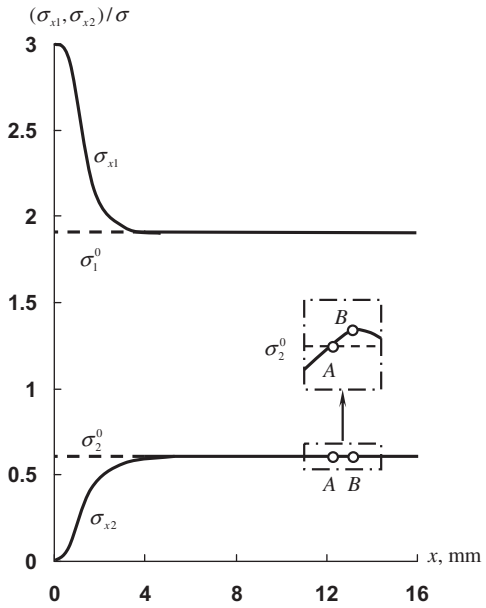


FIGURE 4.38

Variation of normalized normal stresses in longitudinal (σ_{x1}) and transverse (σ_{x2}) plies with distance from the crack.

To study the stress state of a layer with cracks shown in Fig. 4.39, we can use solution (4.130) but should write it in a different form, i.e.,

$$\begin{aligned}\sigma_2 = {} & C_1 \sinh k_1 x \sin k_2 x + C_2 \sinh k_1 x \cos k_2 x \\ & + C_3 \cosh k_1 x \sin k_2 x + C_4 \cosh k_1 x \cos k_2 x\end{aligned} \tag{4.132}$$

Since the stress state of an element $-l_c/2 \le x \le l_c/2$ is symmetric with respect to coordinate x, we should put $C_2 = C_3 = 0$ and find constants C_1 and C_4 from the following boundary conditions

$$\sigma_{x2}(x = l_c/2) = 0, \quad \tau_{xz2}(x = l_c/2) = 0 \tag{4.133}$$

where $l_c = \pi/k_2$.

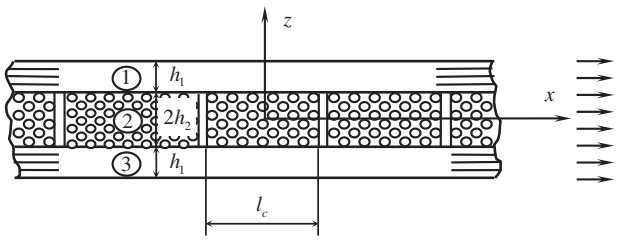


FIGURE 4.39

A system of cracks in the transverse ply.

The final expressions for stresses are

$$\begin{aligned}
\sigma_{x1} &= \sigma_{x3} = \sigma_1^0 + \sigma_2^0 \frac{h_2}{h_1 c}\left(\frac{k_1}{k_2}\cosh k_1 x \cos k_2 x + \sinh k_1 x \sin k_2 x\right) \\
\sigma_{x2} &= \sigma_2^0\left[1 - \frac{1}{c}\left(\frac{k_1}{k_2}\cosh k_1 x \cos k_2 x + \sinh k_1 x \sin k_2 x\right)\right] \\
\tau_{xz2} &= \frac{\sigma_2^0}{k_2 c}\left(k_1^2 + k_2^2\right) z \sinh k_1 x \cos k_2 x \\
\sigma_{z2} &= -\frac{\sigma_2^0}{2k_2 c}\left(k_1^2 + k_2^2\right)\left[z^2 - h_2\left(h_1 + h_2\right)\right]\left(k_1 \cosh k_1 x \cos k_2 x - k_2 \sinh k_1 x \sin k_2 x\right)
\end{aligned} \tag{4.134}$$

in which $c = \sinh(\pi k_1 / 2k_2)$.

For the layer under consideration, stress distributions corresponding to $\sigma = \overline{\sigma} = 44.7$ MPa are shown in Figs. 4.40 and 4.41. Under further loading ($\sigma > \overline{\sigma}$), two modes of the layer failure are possible. The first one is the formation of another transverse crack dividing the block with length l_c in Fig. 4.39 into two pieces. The second one is a delamination in the vicinity of the crack caused by stresses τ_{xz} and σ_z (see Fig. 4.41). Usually, the first situation takes place because stresses τ_{xz} and σ_z are considerably lower than the corresponding ultimate stresses, whereas the maximum value of σ_{x2} is close to the ultimate stress $\sigma_2^0 = \overline{\sigma}_2^+$. Indeed, the second equation of Eqs. (4.134) yields

$$\sigma_{x2}^{\max} = \sigma_{x2}\left(x = 0\right) = \sigma_2^0\left(1 - k\right)$$

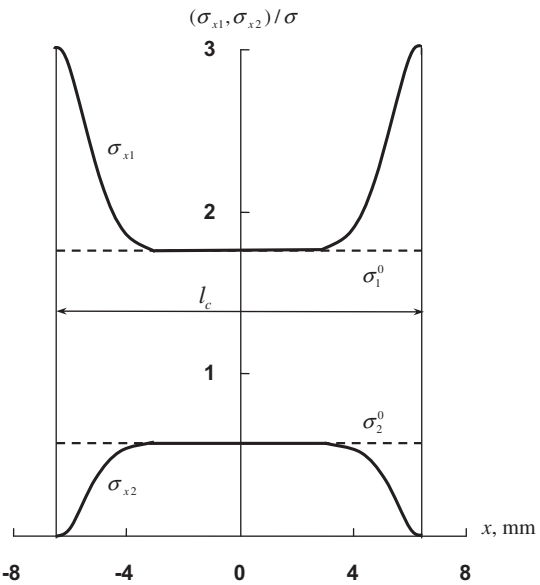


FIGURE 4.40

Distribution of normalized stresses in longitudinal (σ_{x1}) and transverse (σ_{x2}) plies between the cracks.

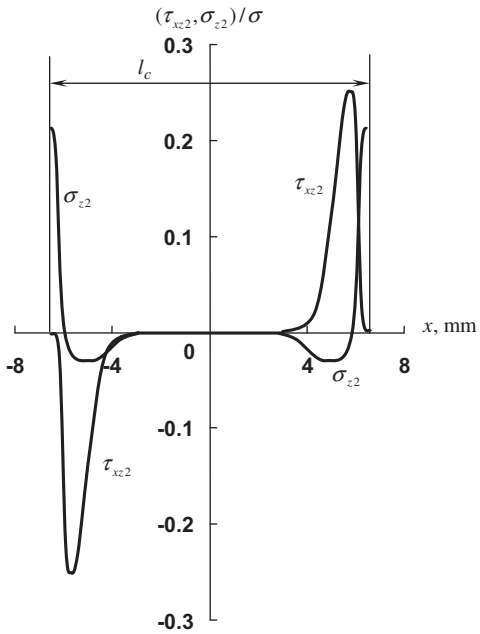


FIGURE 4.41

Distribution of normalized shear (τ_{xz2}) and transverse normal stresses (σ_{z2}) at the ply interface ($z = h_2$) between the cracks.

where $k = k_1/(k_2 c)$. For the foregoing example, $k = 3.85 \times 10^{-4}$. So, $\sigma_{x2}^{\max}$ is so close to σ_2^0 that we can assume that under practically the same load, another crack occurs in the central cross section $x = 0$ of the central block in Fig. 4.39 (as well as in all the other blocks). Thus, the distance between the cracks becomes $l_c = \pi/2k_2$ (6.4 mm for the example under study). The corresponding stress distribution can be determined with the aid of Eqs. (4.128) and (4.132), and boundary conditions (4.133) in which we should take $l_c = \pi/2k_2$. The next crack will again appear at the block center and this process will be continued until failure of the longitudinal plies.

To plot the stress-strain diagram of the cross-ply layer with allowance for the cracks in the transverse ply, we introduce the mean longitudinal strain

$$\varepsilon_x = \frac{2}{h_2 l_c} \int_0^{l_c/2} dx \int_0^{h_2} \varepsilon_{x2} dz$$

where

$$\varepsilon_{x2} = \frac{1}{E_2}(\sigma_{x2} - \nu_{23}\sigma_{z2})$$

For a layer with the properties given previously, such a diagram is shown in Fig. 4.42 with a solid line, and it is in good agreement with experimental results (circles). The formation of cracks is accompanied

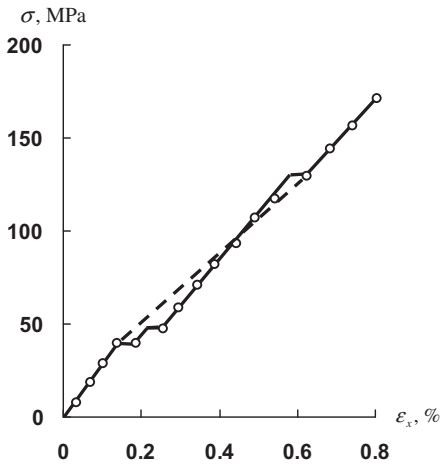


FIGURE 4.42

Stress-strain diagram for a glass-epoxy cross-ply layer:
○ experiment;
——— theoretical prediction;
– – – – · model.

by horizontal jumps and reduction in material stiffness. The stress-strain diagram for the transverse layer that is formally singled out of the diagram in Fig. 4.42 is presented in Fig. 4.43.

To develop a nonlinear phenomenological model of the cross-ply layer, we need to approximate the diagram in Fig. 4.43. As follows from this figure and numerous experiments, the most suitable and simple approximation is that shown by the dashed line. It implies that the ply is linear elastic until its transverse stress σ_2 reaches its ultimate value $\overline{\sigma}_2^+$, and after that, $\sigma_2 = \overline{\sigma}_2^+$, i.e., σ_2 remains constant up

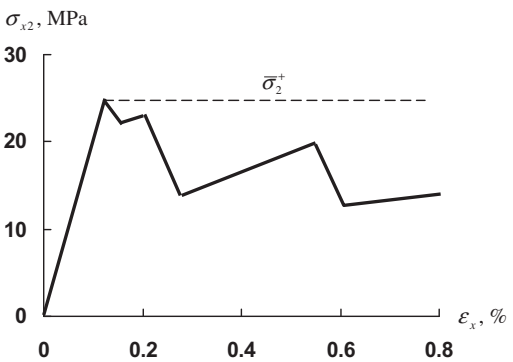


FIGURE 4.43

Stress-strain diagram for a transverse ply.

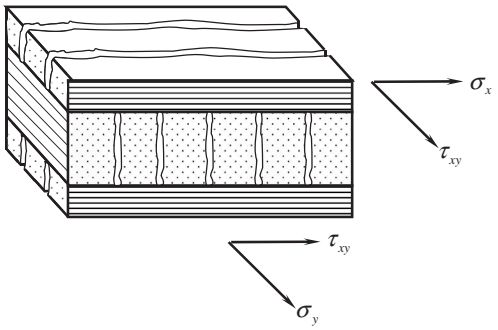


FIGURE 4.44

A cross-ply layer in a plane stress state.

to failure of the longitudinal plies. This means that under transverse tension, a unidirectional ply is in a state of permanent failure and takes from the longitudinal plies the necessary load to support this state (Vasiliev and Elpatievskii, 1967). The stress-strain diagram of the cross-ply layer corresponding to this model is shown in Fig. 4.42 with a dashed line.

Now consider a general plane stress state with stresses σ_x, σ_y, and τ_{xy} as in Fig. 4.44. As can be seen, stress σ_x induces cracks in the inner ply and stress σ_y causes cracks in the outer orthogonal plies, whereas shear stress τ_{xy} can give rise to cracks in all the plies. The ply model that generalizes the model introduced previously for a uniaxial tension is demonstrated in Fig. 4.45. To determine strains corresponding to a given combination of stresses σ_x, σ_y, and τ_{xy}, we can use the following procedure.

1. For the first stage of loading (before the cracks appear), the strains are calculated with the aid of Eqs. (4.114) and (4.115) providing $\varepsilon_x^{(1)}(\sigma)$, $\varepsilon_y^{(1)}(\sigma)$, and $\gamma_{xy}^{(1)}(\sigma)$, where $\sigma = (\sigma_x, \sigma_y, \tau_{xy})$ is the

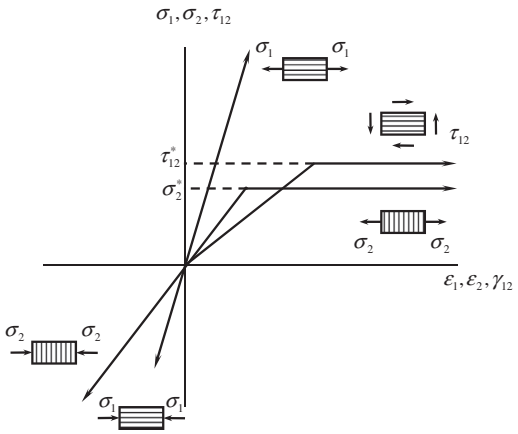


FIGURE 4.45

Stress-strain diagrams of a unidirectional ply simulating its behavior in the laminate and allowing for cracks in the matrix.

given combination of stresses. Using Eqs. (4.112), we find stresses σ_1, σ_2, and τ_{12} in principal material coordinates for all the plies.

2. We determine the combination of stresses σ_{1k}^*, σ_{2k}^*, and τ_{12k}^* which induce the first failure of the matrix in some ply and indicate the number of this ply, say k, applying the appropriate strength criterion (see Section 6.2). Then, the corresponding stresses $\sigma^* = (\sigma_x^*, \sigma_y^*, \tau_{xy}^*)$ and strains $\varepsilon_x^{(1)}(\sigma^*)$, $\varepsilon_y^{(1)}(\sigma^*)$, and $\gamma_{xy}^{(1)}(\sigma^*)$ are calculated.

3. To proceed, i.e., to study the material behavior for $\sigma > \sigma^*$, we need to consider two possible cases for the layer stiffnesses. For this purpose, we should write Eqs. (4.114) for stiffness coefficients in a more general form, i.e.,

$$A_{11} = \sum_{i=1}^{m} \overline{E}_1^{(i)} \overline{h}_0^{(i)} + \sum_{j=1}^{n} \overline{E}_2^{(j)} \overline{h}_{90}^{(j)}, \quad A_{22} = \sum_{i=1}^{m} \overline{E}_2^{(i)} \overline{h}_0^{(i)} + \sum_{j=1}^{n} \overline{E}_1^{(j)} \overline{h}_{90}^{(j)}$$

$$A_{12} = \sum_{i=1}^{m} \nu_{12}^{(i)} \overline{E}_1^{(i)} \overline{h}_0^{(i)} + \sum_{j=1}^{n} \nu_{12}^{(j)} \overline{E}_1^{(j)} \overline{h}_{90}^{(j)}, \quad A_{44} = \sum_{i=1}^{m} G_{12}^{(i)} \overline{h}_0^{(i)} + \sum_{j=1}^{n} G_{12}^{(j)} \overline{h}_{90}^{(j)} \tag{4.135}$$

where

$\overline{h}_0^{(i)} = h_0^{(i)}/h$ and $\overline{h}_{90}^{(j)} = h_{90}^{(j)}/h$.

a. If $\sigma_{2k} > 0$ in the kth ply, it can work only along the fibers, and we should calculate the stiffnesses of the degraded layer taking $E_2^k = 0$, $G_{12}^k = 0$, and $\nu_{12}^k = 0$ in Eqs. (4.135).

b. If $\sigma_{2k} < 0$ in the kth ply, it cannot work only in shear, so we should take $G_{12}^k = 0$ in Eqs. (4.135).

Thus, we find coefficients $A_{st}^{(2)}(st = 11, 12, 22, 44)$ corresponding to the second stage of loading (with one degraded ply). Using Eqs. (4.116) and (4.115) we can determine $E_x^{(2)}$, $E_y^{(2)}$, $G_{xy}^{(2)}$, $\nu_{xy}^{(2)}$, and $\nu_{yx}^{(2)}$ and express the strains in terms of stresses, i.e., $\varepsilon_x^{(2)}(\sigma)$, $\varepsilon_y^{(2)}(\sigma)$, and $\gamma_{xy}^{(2)}(\sigma)$. The final strains corresponding to the second stage of loading are calculated as

$$\varepsilon_x^f = \varepsilon_x^{(1)}(\sigma^*) + \varepsilon_x^{(2)}(\sigma - \sigma^*), \quad \varepsilon_y^f = \varepsilon_y^{(1)}(\sigma^*) + \varepsilon_y^{(2)}(\sigma - \sigma^*)$$
$$\gamma_{xy}^f = \gamma_{xy}^{(1)}(\sigma^*) + \gamma_{xy}^{(2)}(\sigma - \sigma^*)$$

To study the third stage, we should find σ_1, σ_2, and τ_{12} in all the plies, except the kth one, identify the next degraded ply, and repeat step 3 of the procedure which is continued up to failure of the fibers. The resulting stress-strain curves are multi-segmented broken lines with straight segments and kinks corresponding to degradation of particular plies.

The foregoing procedure was described for a cross-ply layer consisting of plies with different properties. For the layer made of one and the same material, there are only three stages of loading: first, before the plies' degradation; second, after the degradation of the longitudinal or the transverse ply only; and third, after the degradation of all the plies.

As a numerical example, consider a carbon-epoxy cylindrical pressure vessel consisting of axial plies with total thickness h_0 and circumferential plies with total thickness h_{90}. The vessel has the following parameters: radius $R = 500$ mm, and total thickness of the wall $h = 7.5$ mm, $h_0 = 2.5$ mm, and $h_{90} = 5$ mm. The mechanical characteristics of a carbon-epoxy unidirectional ply are $E_1 = 140$ GPa,

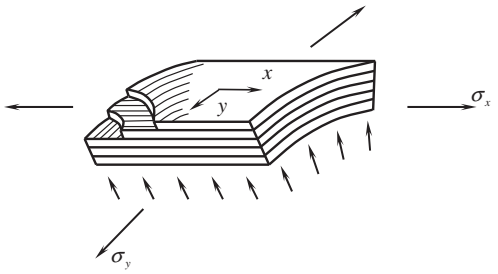


FIGURE 4.46

Element of a composite pressure vessel.

$E_2 = 11$ GPa, $\nu_{12} = 0.0212$, $\nu_{21} = 0.27$, $\overline{\sigma}_1^+ = 2000$ MPa, and $\overline{\sigma}_2^+ = 50$ MPa. Axial, σ_x, and circumferential, σ_y, stresses are expressed as (see Fig. 4.46)

$$\sigma_x = \frac{pR}{2h}, \quad \sigma_y = \frac{pR}{h} \tag{4.136}$$

where p is the internal pressure.

Using Eqs. (4.114) and (4.116), we calculate first the stiffness coefficients. The result is as follows:

$$\begin{aligned} &A_{11} = 54.1 \text{ GPa}, \quad A_{12} = 3 \text{ GPa}, \quad A_{22} = 97.1 \text{ GPa} \\ &E_x = 54 \text{ GPa}, \quad E_y = 97 \text{ GPa}, \quad \nu_{xy} = 0.055, \quad \nu_{yx} = 0.031 \end{aligned} \tag{4.137}$$

Substituting stresses, Eqs. (4.136), into the constitutive equations, Eqs. (4.115), we obtain

$$\varepsilon_x^{(1)}(p) = \frac{pR}{h}\left(\frac{1}{2E_x} - \frac{\nu_{xy}}{E_y}\right) = 0.58 \cdot 10^{-3} p, \quad \varepsilon_y^{(1)}(p) = \frac{pR}{h}\left(\frac{1}{E_y} - \frac{\nu_{yx}}{2E_x}\right) = 0.66 \cdot 10^{-3} p$$

where p is measured in megapascals. For axial plies, $\varepsilon_x = \varepsilon_{1,0}$ and $\varepsilon_y = \varepsilon_{2,0}$. The corresponding stresses are

$$\sigma_{1,0}^{(1)}(p) = \overline{E}_1(\varepsilon_{1,0} + \nu_{12}\varepsilon_{2,0}) = 83.2\, p, \quad \sigma_{2,0}^{(1)}(p) = \overline{E}_2(\varepsilon_{2,0} + \nu_{21}\varepsilon_{1,0}) = 9.04\, p$$

For circumferential plies, $\varepsilon_x = \varepsilon_{2,90}$, $\varepsilon_y = \varepsilon_{1,90}$ and

$$\sigma_{1,90}^{(1)}(p) = \overline{E}_1(\varepsilon_{1,90} + \nu_{12}\varepsilon_{2,90}) = 94.15\, p, \quad \sigma_{2,90}^{(1)}(p) = \overline{E}_2(\varepsilon_{2,90} + \nu_{21}\varepsilon_{1,90}) = 8.4\, p$$

As can be seen, $\sigma_{2,0}^{(1)} > \sigma_{2,90}^{(1)}$. This means that the cracks appear first in the axial plies under the pressure p^* that can be found from the equation $\sigma_{2,0}^{(1)}(p^*) = \overline{\sigma}_2^+$. The result is $p^* = 5.53$ MPa.

To study the second stage of loading for $p > p^*$, we should put $E_2 = 0$, and $\nu_{12} = 0$ in Eqs. (4.135) for the axial plies. Then, the stiffness coefficients and elastic constants become

$$\begin{aligned} &A_{11} = 54.06 \text{ GPa}, \quad A_{12} = 2 \text{ GPa}, \quad A_{22} = 93.4 \text{ GPa} \\ &E_x = 54 \text{ GPa}, \quad E_y = 93.3 \text{ GPa}, \quad \nu_{xy} = 0.037, \quad \nu_{yx} = 0.021 \end{aligned}$$

The strains and stresses in the plies are

$$\varepsilon_x^{(2)}(p) = 0.59\cdot 10^{-3}p, \quad \varepsilon_y^{(2)}(p) = 0.7\cdot 10^{-3}p$$
$$\sigma_{1,0}^{(2)}(p) = 82.6\,p, \quad \sigma_{1,90}^{(2)}(p) = 99.8\,p$$
$$\sigma_{2,90}^{(2)}(p) = 8.62\,p$$

The total transverse stress in the circumferential plies can be calculated as

$$\sigma_{2,90} = \sigma_{2,90}^{(1)}(p^*) + 8.62(p - p^*)$$

Using the condition $\sigma_{2,90}(p^{**}) = \overline{\sigma}_2^+$, we find the pressure $p^{**} = 5.95$ MPa at which cracks appear in the matrix of the circumferential plies.

For $p \geq p^{**}$, we should take $E_2 = 0$ and $\nu_{12} = 0$ for all the plies. Then

$$\begin{aligned} &A_{11} = 46.2 \text{ GPa}, \quad A_{12} = 0, \quad A_{22} = 93.4 \text{ GPa} \\ &E_x = 46.2 \text{ GPa}, \quad E_y = 93.4 \text{ GPa}, \quad \nu_{xy} = \nu_{yx} = 0 \\ &\varepsilon_x^{(3)}(p) = 0.72\cdot 10^{-3}p, \quad \varepsilon_y^{(3)}(p) = 0.71\cdot 10^{-3}p \\ &\sigma_{1,0}^{(3)}(p) = 100.8\,p, \quad \sigma_{1,90}^{(3)}(p) = 99.4\,p \end{aligned} \tag{4.138}$$

The total stresses acting along the fibers are

$$\sigma_{1,0}(p) = \sigma_{1,0}^{(1)}(p^*) + \sigma_{1,0}^{(2)}(p^{**} - p^*) + \sigma_{1,0}^{(3)}(p - p^{**}) = 100.8p - 105$$
$$\sigma_{1,90}(p) = \sigma_{1,90}^{(1)}(p^*) + \sigma_{1,90}^{(2)}(p^{**} - p^*) + \sigma_{1,90}^{(3)}(p - p^{**}) = 99.4p - 28.9$$

To determine the ultimate pressure, we can use two possible strength conditions – for axial fibers and for circumferential fibers. The criterion $\sigma_{1,0}(p) = \overline{\sigma}_1^+$ yields $p = 20.9$ MPa, whereas the criterion $\sigma_{1,90}(p) = \overline{\sigma}_1^+$ gives $p = 20.4$ MPa. Thus, the burst pressure governed by failure of the fibers in the circumferential plies is $\overline{p} = 20.4$ MPa.

The strains can be calculated for all three stages of loading using the following equations

- for $p \leq p^*$

$$\varepsilon_{x,y}(p) = \varepsilon_{x,y}^{(1)}(p)$$

- for $p^* < p \leq p^{**}$

$$\varepsilon_{x,y}(p) = \varepsilon_{x,y}^{(1)}(p^*) + \varepsilon_{x,y}^{(2)}(p - p^*)$$

- for $p^{**} < p \leq \overline{p}$

$$\varepsilon_{x,y}(p) = \varepsilon_{x,y}^{(1)}(p^*) + \varepsilon_{x,y}^{(2)}(p^{**} - p^*) + \varepsilon_{x,y}^{(3)}(p - p^{**})$$

For the pressure vessel under study, the dependency of the circumferential strain on pressure is shown in Fig. 4.47 (solid line). The circles correspond to failure of the matrix and fibers.

For comparison, consider two limiting cases. First, assume that no cracks occur in the matrix, and the material stiffness is specified by Eqs. (4.137). The corresponding diagram is shown in Fig. 4.47

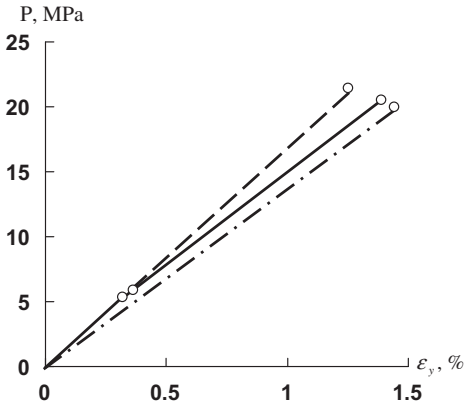


FIGURE 4.47

Dependence of the circumferential strain of the carbon-epoxy pressure vessel on pressure:
——— model allowing for cracks in the matrix;
– – – – model ignoring cracks in the matrix;
– · – · – model ignoring the matrix.

with a dashed line. Second, suppose that the load is taken by the fibers only, i.e., use the monotropic model of a ply introduced in Section 3.3. Then, the material stiffness is given by Eqs. (4.138). The corresponding result is also presented in Fig. 4.47. It follows from this figure that all three models give close results for the burst pressure (which is expected since $\overline{\sigma}_2^+ << \overline{\sigma}_1^+$), but provide different strains.

4.4.3 Two-matrix composites

The problem of the analysis of a cracked cross-ply composite laminate has been studied by Tsai and Azzi (1966), Vasiliev and Elpatievskii (1967), Vasiliev et al. (1970), Hahn and Tsai (1974), Reifsnaider (1977), Hashin (1987), and many other authors. In spite of this, the topic is still receiving repeated attention in the literature (Lungren and Gudmundson, 1999). Taking into account that matrix degradation leads to reduction of material stiffness and fatigue strength, absorption of moisture, and many other consequences that are difficult to predict but are definitely undesirable, it is surprising how many efforts have been undertaken to study this phenomenon rather than try to avoid it. At first glance, the problem looks simple; all we need is to synthesize a unidirectional composite whose ultimate elongations along and across the fibers, i.e. $\overline{\varepsilon}_1$ and $\overline{\varepsilon}_2$, are the same. Actually, the problem is even simpler, because $\overline{\varepsilon}_2$ can be less than $\overline{\varepsilon}_1$ by a factor that is equal to the safety factor of the structure. This means that matrix degradation can occur, but at the load that exceeds the operational level (the safety factor is the ratio of the failure load to the operational load and can vary from 1.25 up to 3 or more depending on the application of a particular composite structure). Returning to Table 4.2, in which $\overline{\varepsilon}_1$ and $\overline{\varepsilon}_2$ are given for typical advanced composites, we can see that $\overline{\varepsilon}_1 > \overline{\varepsilon}_2$ for all the materials and that for polymeric matrices the problem could be, in principle, solved if we could increase $\overline{\varepsilon}_2$ up to about 1%.

Two main circumstances hinder the direct solution of this problem. The first is that being locked between the fibers, the matrix does not show the high elongation that it has under uniaxial tension and behaves as a brittle material (see Section 3.4.2). To study this effect, epoxy resins were modified to

have different ultimate elongations. The corresponding curves are presented in Fig. 4.48 (only the initial part of curve 4 is shown in this figure; the ultimate elongation of this resin is 60%). Fiberglass composites that have been fabricated with these resins were tested under transverse tension. As can be seen in Fig. 4.49, the desired value of $\bar{\varepsilon}_2$ (that is, about 1%) is reached if the matrix elongation is about 60%. However, the stiffness of this matrix is relatively low, and the second circumstance arises; matrix material with low stiffness cannot provide sufficient stress diffusion in the vicinity of damaged or broken fibers (see Section 3.2.3). As a result, the main material characteristic – its longitudinal tensile strength – decreases. Experimental results corresponding to composites with resins 1, 2, 3, and 4 are presented in Fig. 4.50. Thus, a significant increase in transverse elongation is accompanied by an unacceptable drop in longitudinal strength (see also Chiao, 1979).

One of the possible ways for synthesizing composite materials with high transverse elongation and high longitudinal strength is to combine two matrix materials: one with high stiffness to bind the fibers and the other with high elongation to provide the appropriate transverse deformability (Vasiliev and Salov, 1984). The manufacturing process involves two-stage impregnation. At the first stage, a fine tow is impregnated with a high-stiffness epoxy resin (of the type 2 in Fig. 4.48) and cured. The properties of the composite fiber fabricated in this way are as follows:

- Number of elementary glass fibers in the cross section – 500
- Mean cross-sectional area—0.15 mm^2
- Fiber volume fraction—0.75
- Density—2.2 g/cm^3
- Longitudinal modulus—53.5 GPa
- Longitudinal strength—2100 MPa
- Longitudinal elongation—4.5%
- Transverse modulus—13.5 GPa
- Transverse strength—40 MPa
- Transverse elongation—0.32%

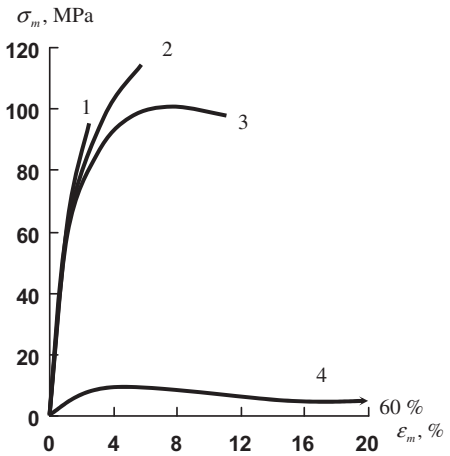


FIGURE 4.48

Stress-strain curves for epoxy matrices modified for various ultimate elongations.

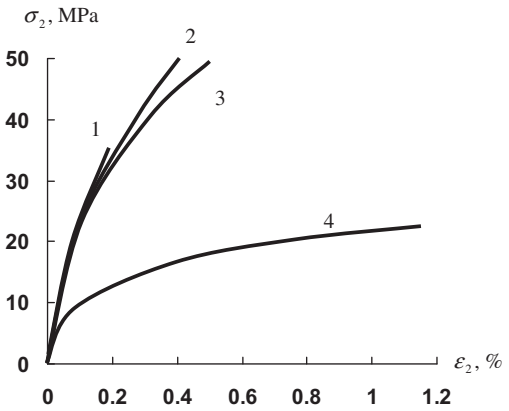


FIGURE 4.49

Stress-strain curves for transverse tension of unidirectional fiberglass composites with various epoxy matrices (numbers on the curves correspond to Figure 4.48).

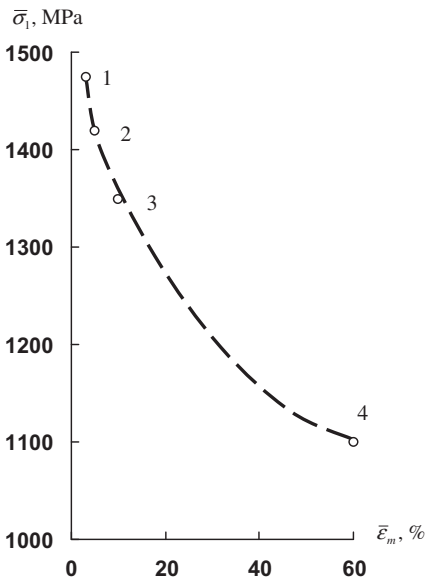


FIGURE 4.50

Dependence of the longitudinal strength on the matrix ultimate elongation (numbers on the curve correspond to Figs. 4.48 and 4.49).

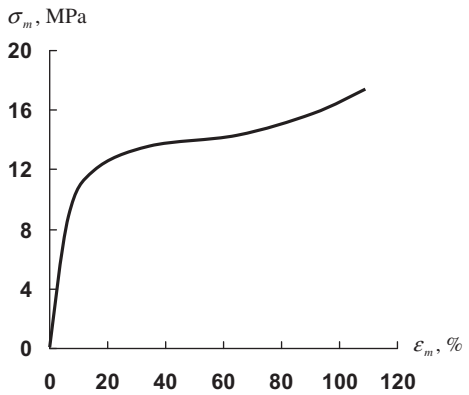


FIGURE 4.51

Stress-strain diagram of a deformable epoxy matrix.

At the second stage, a tape formed of composite fibers is impregnated with a highly deformable epoxy matrix whose stress-strain diagram is presented in Fig. 4.51. The microstructure of the resulting two-matrix unidirectional composite is shown in Fig. 4.52 (the dark areas are cross-sections of composite fibers; the magnification is not sufficient to see the elementary glass fibers). Stress-strain diagrams corresponding to transverse tension, compression, and in-plane shear of this material are presented in Fig. 4.16.

The main mechanical characteristics of the two-matrix fiberglass composite are listed in Table 4.3 (material No.1). As can be seen, two-stage impregnation results in relatively low fiber volume content (about 50%). Material No.2, composed of composite fibers and a conventional epoxy matrix, has also a low fiber fraction; however, its transverse elongation is 10 times lower than that of material No.1. Material No.3 is a conventional glass-epoxy composite that has the highest longitudinal strength and the lowest transverse strain. Comparing materials No.1 and No.3, we can see that although the fiber volume fraction of the two-matrix composite is lower by 24%, its longitudinal strength is less than that of a traditional composite by only 3.4% (because the composite fibers are not damaged in the processing of composite materials), whereas its specific strength is a bit higher (due to its lower density).

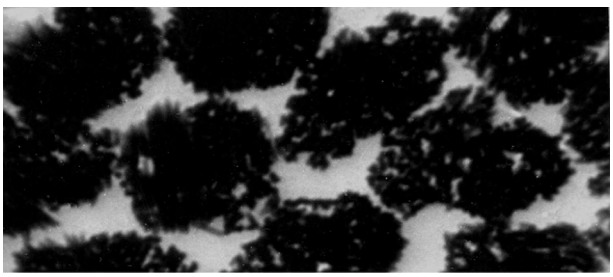


FIGURE 4.52

Microstructure of a unidirectional two-matrix composite.

TABLE 4.3 Properties of glass-epoxy unidirectional composites.

No	Material components	Fiber volume fraction	Longitudinal strength $\overline{\sigma}_1^+$ (MPa)	Ultimate transverse strain $\overline{\varepsilon}_2^+$ (%)	Density ρ (g/cm^3)	Specific strength $\overline{\sigma}_1^+/\rho\times10^3$(m)
1	Composite fibers and deformable matrix	0.51	1420	3.0	1.83	77.6
2	Composite fibers and high-stiffness matrix	0.52	1430	0.3	1.88	76.1
3	Glass fibers and high-stiffness matrix	0.67	1470	0.2	2.07	71.0
4	Glass fibers and deformable matrix	0.65	1100	1.2	2.02	54.4

Material No.4 demonstrates that direct application of a highly deformable matrix allows us to increase transverse strains but results in a 23% reduction in longitudinal specific strength.

Thus, two-matrix glass-epoxy composites have practically the same longitudinal strength as conventional materials but their transverse elongation is greater by an order of magnitude.

Comparison of a conventional cross-ply glass-epoxy layer and a two-matrix one is presented in Fig. 4.53. Line 1 corresponds to a traditional material and, typical for this material, has a kink corresponding to matrix failure in the transverse plies (see also Fig. 4.37). A theoretical diagram was plotted using the procedure described earlier. Line 2 corresponds to a two-matrix composite and was plotted using Eqs. (4.60). As can be seen, there is no kink on the stress-strain diagram. To prove that no cracks appear in the matrix of this material under loading, the intensity of acoustic emission was recorded during loading. The results are shown in Fig. 4.54.

Composite fibers of two-matrix materials can be also made from fine carbon or aramid tows, and the deformable thermosetting resin can be replaced with a thermoplastic matrix (Vasiliev et al., 1997). The resulting hybrid thermoset-thermoplastic unidirectional composite is characterized by high longitudinal strength and transverse strain exceeding 1%. Having high strength, composite fibers are not damaged in the process of laying-up or winding, and the tapes formed from these fibers are readily impregnated even with high-viscosity thermoplastic polymers.

4.4.4 Composites with controlled cracks

Now we return to the conventional composites discussed in Section 4.4.2. Since the transverse ultimate elongation of a ply, $\overline{\varepsilon}_2$, is less than the corresponding longitudinal elongation, $\overline{\varepsilon}_1$ (see Table 4.2), the stress σ in Eq. (4.123) induces a system of cracks in the matrix of the transverse ply as in Fig. 4.39.

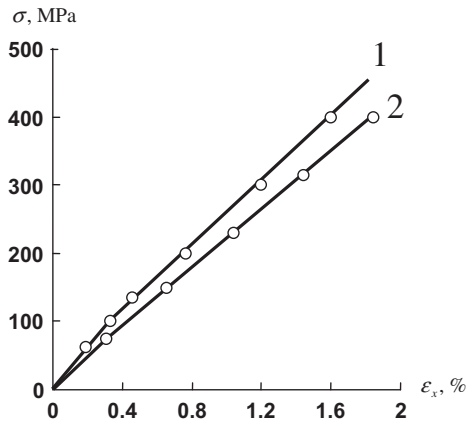


FIGURE 4.53

Stress-strain diagrams of a conventional (1) and two-matrix (2) cross-ply glass-epoxy layer under tension:
——— theoretical prediction;
○ experiment.

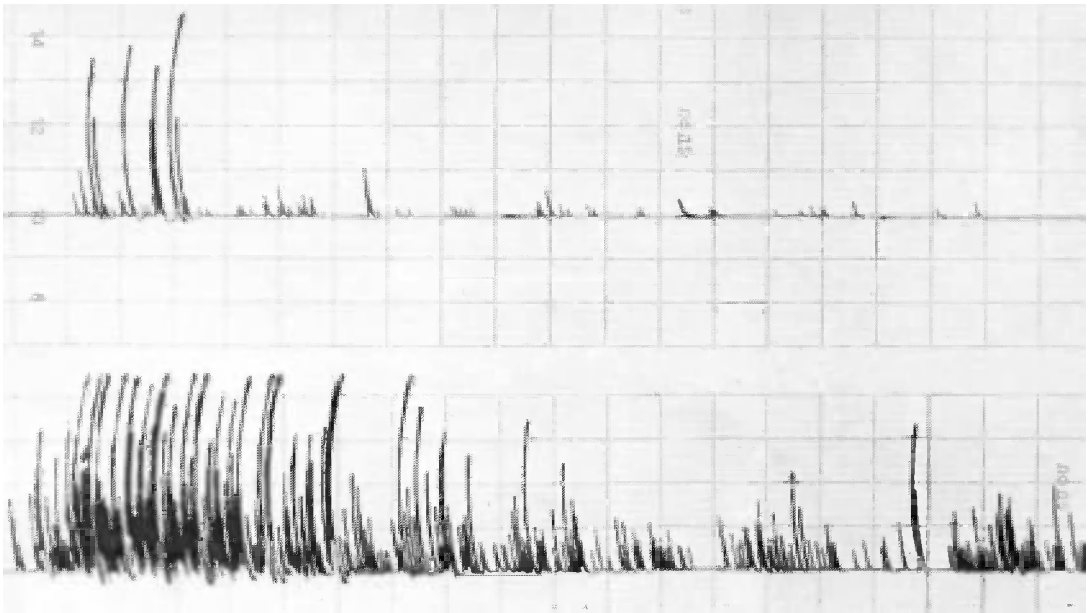


FIGURE 4.54

Intensity of acoustic emission for a cross-ply two-matrix composite (upper) and a conventional fiberglass composite (lower).

As has been already noted, these cracks do not cause laminate failure because strength is controlled by the longitudinal plies. What is actually not desirable is matrix failure in the process of laminate loading. So, since the cracks shown in Fig. 4.39 will occur anyway at some stress σ, suppose that the material has these cracks before loading, i.e., that the transverse ply consists of individual strips with width l_c as in Fig. 4.39. The problem is to find the width l_c for which no other cracks will appear in the transverse ply up to failure of the fibers in the longitudinal plies.

Consider the solution in Eq. (4.132), take $C_2 = C_3 = 0$, and find the constants C_1 and C_4 from the boundary conditions in Eqs. (4.133) in which l_c is some unknown width. The resulting expression for the stress in the transverse ply is

$$\sigma_{x2} = \sigma_2^0 \Bigg\{ 1 - \frac{1}{k_1 \sin\lambda_2 \cos\lambda_2 + k_2 \sinh\lambda_1 \cosh\lambda_1} [(k_2 \cosh\lambda_1 \sin\lambda_2 - k_1 \sinh\lambda_1 \cos\lambda_2) \sinh k_1 x \sin k_2 x + (k_1 \cosh\lambda_1 \sin\lambda_2 + k_2 \sinh\lambda_1 \cos\lambda_2) \cosh k_1 x \cos k_2 x] \Bigg\}$$

in which $\lambda_1 = k_1 l_c/2$ and $\lambda_2 = k_2 l_c/2$. The maximum stress acts at $x = 0$ (see Fig. 4.40) and can be presented as

$$\sigma_2^m = \sigma_2^0 [1 - F(l_c)] \tag{4.139}$$

where

$$F(l_c) = \frac{2(k_1 \cosh\lambda_1 \sin\lambda_2 + k_2 \sinh\lambda_1 \cos\lambda_2)}{k_1 \sin 2\lambda_2 + k_2 \sinh 2\lambda_1} \tag{4.140}$$

The stress σ_2^0 in Eq. (4.139) is specified by the second equation of Eqs. (4.122). Taking into account the first equation, we have

$$\sigma_2^0 = \frac{E_2}{E_1} \sigma_1^0$$

where σ_1^0 is the stress in the longitudinal plies. So, Eq. (4.139) can be written as

$$\sigma_2^m = \frac{E_2}{E_1} \sigma_1^0 [1 - F(l_c)] \tag{4.141}$$

Now suppose that $\sigma_1 = \overline{\sigma}_1$, i.e., that the longitudinal stress reaches the corresponding ultimate value. The cracks in the matrix of the transverse ply do not appear if $\sigma_2^m \le \overline{\sigma}_2$, where $\overline{\sigma}_2$ is the transverse tensile strength of the ply. Then, Eq. (4.141) yields

$$F(l_c) \ge t \tag{4.142}$$

Where

$$t = 1 - \frac{E_1 \overline{\sigma}_2}{E_2 \overline{\sigma}_1}$$

As an example, consider a cross-ply (see Fig. 4.35) carbon-epoxy composite with the following parameters

$$E_1 = 140\ \text{GPa},\quad E_2 = 11\ \text{GPa},\quad G_{13} = 5.5\ \text{GPa},\quad G_{23} = 4.1\ \text{GPa},$$
$$\nu_{23} = 0.3,\quad \overline{\sigma}_1 = 2000\ \text{MPa},\quad \overline{\sigma}_2 = 50\ \text{MPa}$$

for which $t = 0.68$. Introduce normalized thicknesses of the plies as

$$\overline{h}_1 = \frac{2h_1}{h},\quad \overline{h}_2 = \frac{2h_2}{h}$$

where $h = 2(h_1 + h_2)$ (see Fig. 4.37). Let $\overline{h}_1 = 1 - \alpha$ and $\overline{h}_2 = \alpha$, where the parameter α specifies the relative thickness of the transverse ply. The dependencies of the coefficients $\overline{k}_1 = k_1/h$ and $\overline{k}_2 = k_2/h$ (in which k_1 and k_2 are given in the notations to Eq. (4.130)) on the parameter α are shown in Fig. 4.55. The dependence of function F in Eq. (4.140) on the normalized distance between the cracks $\overline{l}_c = l_c/h$ is presented in Fig. 4.56 for $\alpha = 0.1,\ 0.5,$ and 0.9. The intersections of the horizontal line $F = t = 0.68$ give the values of $\overline{l}_c$ for which no new cracks appear in the transverse ply up to the fibers' failure. The final dependence of $\overline{l}_c$ on α is shown in Fig. 4.57. As can be seen, l_c varies from about two up to four thicknesses of the laminate. For $h_1 = h_2 = \delta$, where $\delta = 0.15$ mm is the thickness of the

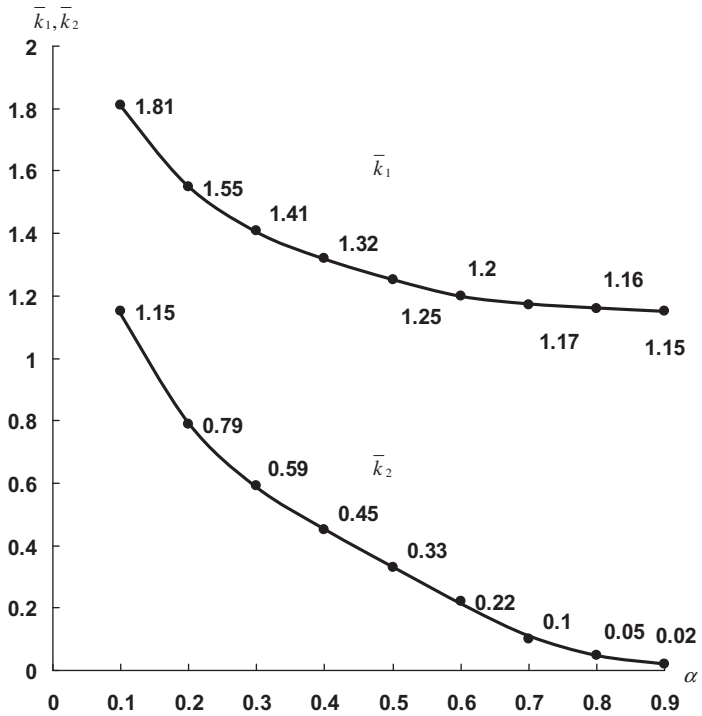


FIGURE 4.55

Dependencies of the coefficients $\overline{k}_1$ and $\overline{k}_2$ on the relative thickness of the transverse ply α.

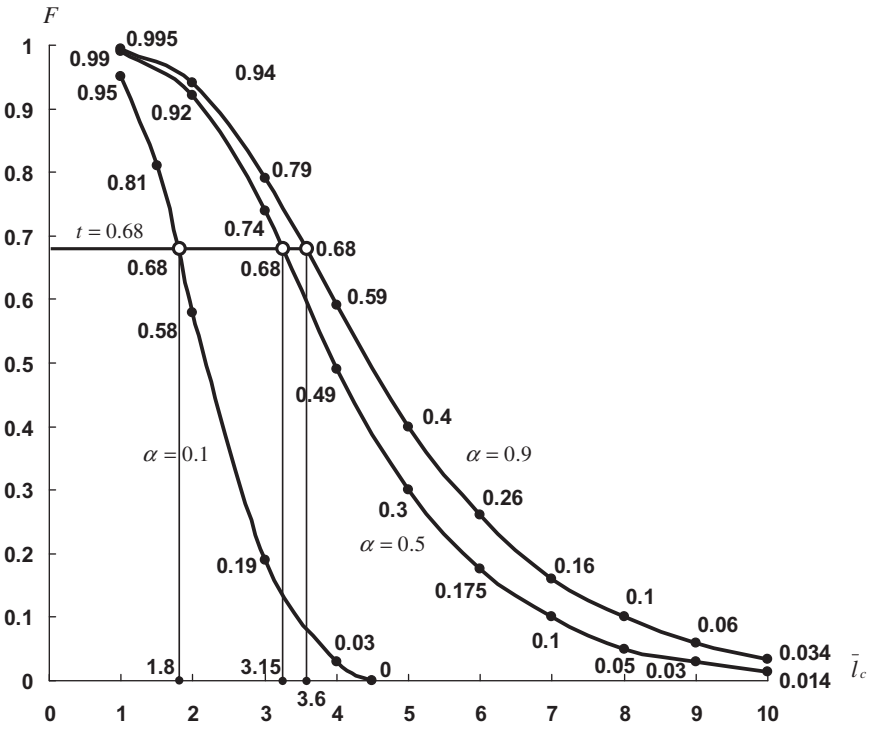


FIGURE 4.56

Dependencies of function F on the normalized width of the strip for $\alpha = 0.1$, 0.5, and 0.9.

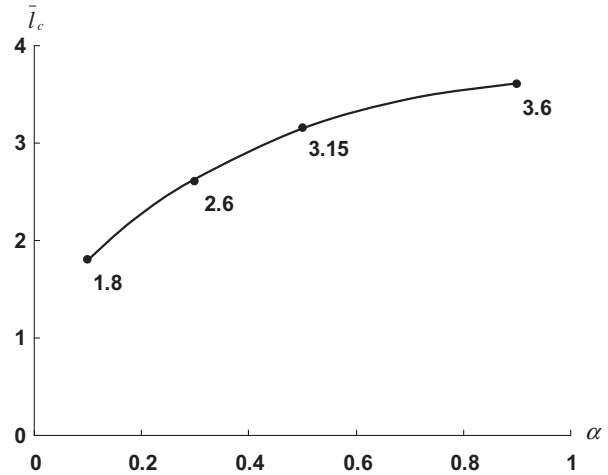


FIGURE 4.57

Normalized width of the strip $\bar{l}_c$ as a function of the relative thickness of transverse ply α.

unidirectional ply, we get $h = 4\delta$, $\alpha = 0.5$, and $l_c = 1.9$ mm. A yarn of such width is typical for carbon fabrics made of $3K$ carbon tows. Experiments with such fabric composites show that the tensile stress-strain diagram of the material is linear up to failure, and no cracks are observed in the matrix.

4.5 ANGLE-PLY ORTHOTROPIC LAYER

The angle-ply layer is a combination of an even number of alternating plies with angles $+\phi$ and $-\phi$ as in Fig. 4.58. The structure of this layer is typical for the process of filament winding (see Fig. 4.59). As for the cross-ply layer considered in the previous section, an angle-ply layer is actually a laminate, but for a large number of plies it can be approximately treated as a homogeneous orthotropic layer (see Section 5.6.3).

4.5.1 Linear elastic model

Consider two symmetric systems of unidirectional anisotropic plies (see Section 4.3) consisting of the same number of plies, made of one and the same material and having alternating angles $+\phi$ and $-\phi$.

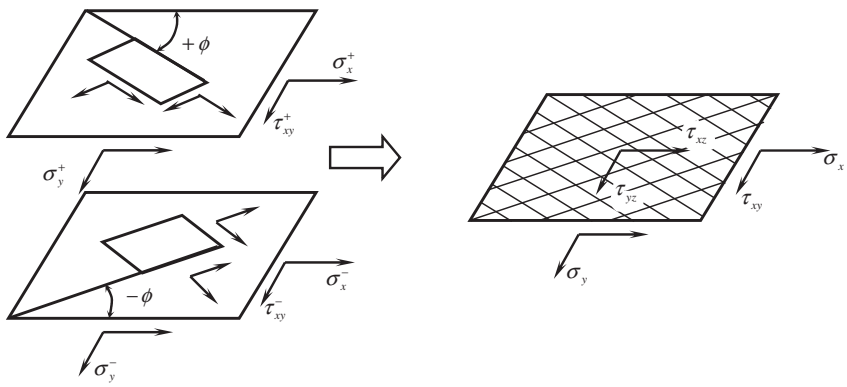


FIGURE 4.58

Two symmetric plies forming an angle-ply layer.

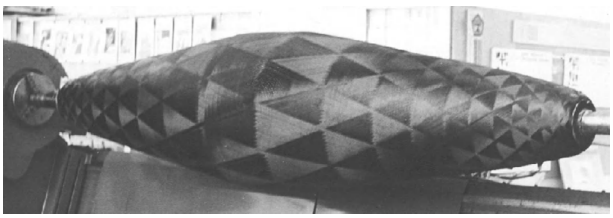


FIGURE 4.59

Angle-ply layer of a filament wound shell.

Courtesy of CRISM.

Then, the total stresses σ_x, σ_y, and τ_{xy} acting on the layer can be expressed in terms of the corresponding stresses acting in the $+\phi$ and $-\phi$ plies as

$$\begin{aligned}&\sigma_x h = \sigma_x^+ \frac{h}{2} + \sigma_x^- \frac{h}{2}, \quad \sigma_y h = \sigma_y^+ \frac{h}{2} + \sigma_y^- \frac{h}{2}\\ &\tau_{xy} h = \tau_{xy}^+ \frac{h}{2} + \tau_{xy}^- \frac{h}{2}\end{aligned} \tag{4.143}$$

where h is the total thickness of the layer. Stresses with superscripts "+" and "−" are related to strains ε_x, ε_y, and γ_{xy} (which are assumed to be the same for all the plies) by Eqs. (4.71), i.e.,

$$\begin{aligned}&\sigma_x^\pm = A_{11}^\pm \varepsilon_x + A_{12}^\pm \varepsilon_y + A_{14}^\pm \gamma_{xy}, \quad \sigma_y^\pm = A_{21}^\pm \varepsilon_x + A_{22}^\pm \varepsilon_y + A_{24}^\pm \gamma_{xy}\\ &\tau_{xy}^\pm = A_{41}^\pm \varepsilon_x + A_{42}^\pm \varepsilon_y + A_{44}^\pm \gamma_{xy}\end{aligned} \tag{4.144}$$

in which $A_{11}^+ = A_{11}^- = A_{11}$, $A_{12}^+ = A_{12}^- = A_{12}$, $A_{22}^+ = A_{22}^- = A_{22}$, $A_{14}^+ = -A_{14}^- = A_{14}$, $A_{24}^+ = -A_{24}^- = A_{24}$, and $A_{44}^+ = A_{44}^- = A_{44}$, where A_{mn} ($mn = 11, 12, 22, 14, 24, 44$) are specified by Eqs. (4.72). Substituting Eqs. (4.144) into Eqs. (4.143), we arrive at the following constitutive equations for an angle-ply layer

$$\begin{aligned}\sigma_x &= A_{11}\varepsilon_x + A_{12}\varepsilon_y\\ \sigma_y &= A_{21}\varepsilon_x + A_{22}\varepsilon_y\\ \tau_{xy} &= A_{44}\gamma_{xy}\end{aligned} \tag{4.145}$$

The inverse form of these equations is

$$\varepsilon_x = \frac{\sigma_x}{E_x} - \nu_{xy}\frac{\sigma_y}{E_y}, \quad \varepsilon_y = \frac{\sigma_y}{E_y} - \nu_{yx}\frac{\sigma_x}{E_x}, \quad \gamma_{xy} = \frac{\tau_{xy}}{G_{xy}} \tag{4.146}$$

where

$$\begin{aligned}&E_x = A_{11} - \frac{A_{12}^2}{A_{22}}, \quad E_y = A_{22} - \frac{A_{12}^2}{A_{11}}, \quad G_{xy} = A_{44}\\ &\nu_{xy} = \frac{A_{12}}{A_{11}}, \quad \nu_{yx} = \frac{A_{12}}{A_{22}}\end{aligned} \tag{4.147}$$

It follows from Eqs. (4.145) and (4.146) that the layer under study is orthotropic.

Now derive constitutive equations relating transverse shear stresses τ_{xz} and τ_{yz} and the corresponding shear strains γ_{xz} and γ_{yz}. Let the angle-ply layer be loaded by stress τ_{xz}. Then for all the plies, $\tau_{xz}^+ = \tau_{xz}^- = \tau_{xz}$, and because the layer is orthotropic, $\gamma_{xz}^+ = \gamma_{xz}^- = \gamma_{xz}$ and $\gamma_{yz}^+ = \gamma_{yz}^- = \gamma_{yz} = 0$. In a similar way, applying stress τ_{yz} we have $\tau_{yz}^+ = \tau_{yz}^- = \tau_{yz}$, $\gamma_{yz}^+ = \gamma_{yz}^- = \gamma_{yz}$, and $\gamma_{xz}^+ = \gamma_{xz}^- = \gamma_{xz} = 0$. Writing the last two constitutive equations of Eqs. (4.71) for these two cases, we arrive at

$$\tau_{xz} = A_{55}\gamma_{xz}, \quad \tau_{yz} = A_{66}\gamma_{yz} \tag{4.148}$$

where the stiffness coefficients A_{55} and A_{66} are specified by Eqs. (4.72).

The dependencies of E_x and G_{xy} on ϕ, plotted using Eqs. (4.147), are shown in Fig. 4.60 with solid lines. The theoretical curve for E_x is in very close agreement with experimental data shown with circles (Lagace, 1985). For comparison, the same moduli are presented for the $+\phi$ anisotropic layer considered in Section 4.3.1. As can be seen, $E_x(\pm\phi) \geq E_x^+$. To explain this effect, consider uniaxial tension of both layers in the x direction. Whereas tension of the $+\phi$ and $-\phi$ individual plies shown in Fig. 4.61 is accompanied with shear strain, the system of these plies does not demonstrate shear under tension and, as a result, has higher stiffness. Working as plies of a symmetric angle-ply layer, individual anisotropic $+\phi$ and $-\phi$ plies are loaded not only with a normal stress σ_x that is applied to the layer, but also with shear stress τ_{xy} that restricts the shear of individual plies (see Figure 4.61). In order to find the reactive shear stress, which is balanced between the plies, we can use Eqs. (4.75). Taking $\sigma_y = 0$, we can simulate the stress-strain state of the ply in the angle-ply layer putting $\gamma_{xy} = 0$. Then, the third equation yields

$$\tau_{xy} = -\eta_{xy,x}^{+} \frac{G_{xy}^{+}}{E_x^{+}} \sigma_x$$

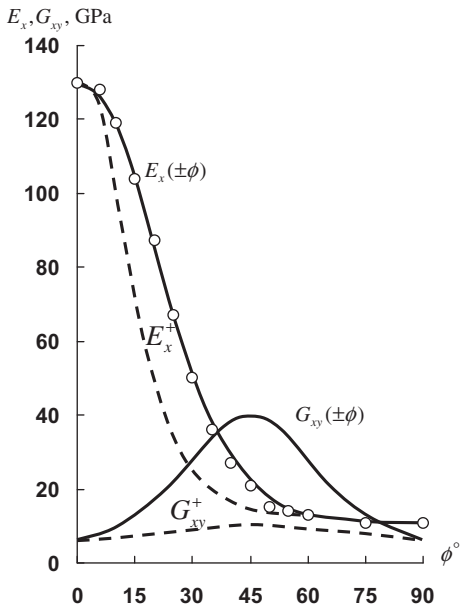


FIGURE 4.60

Dependencies of the moduli of a carbon-epoxy layer on the orientation angle:
——— orthotropic angle-ply $\pm\phi$ layer;
– – – – anisotropic $+\phi$ layer;
○ experiment for an angle-ply layer.

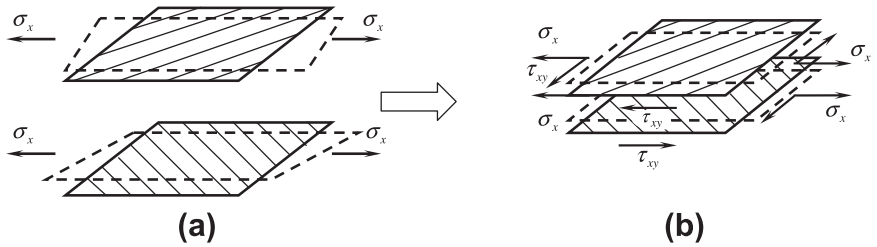


FIGURE 4.61

Deformation and stresses induced in individual plies (a) and bonded symmetric plies (b) by uniaxial tension.

Superscript "+" indicates that elastic constants correspond to an individual $+\phi$ ply. Substituting this shear stress into the first equation of Eqs. (4.75), we arrive at $\sigma_x = E_x\varepsilon_x$, where

$$E_x = \frac{E_x^+}{1-\eta_{x,xy}^+\eta_{xy,x}^+} = \frac{E_x^+}{1-\dfrac{G_{xy}^+}{E_x^+}\left(\eta_{xy,x}^+\right)^2} \tag{4.149}$$

is the modulus of the $\pm\phi$ angle-ply layer.

Under pure shear of an angle-ply layer, its plies are loaded with the additional normal stresses. These stresses can be found if we take $\varepsilon_x = 0$ and $\varepsilon_y = 0$ in the first two equations of Eqs. (4.75). The result is

$$\sigma_x = -\tau_{xy}\frac{E_x^+\left(\eta_{x,xy}^+ - \nu_{xy}^+\eta_{y,xy}^+\right)}{G_{xy}^+\left(1-\nu_{xy}^+\nu_{yx}^+\right)}, \quad \sigma_y = -\tau_{xy}\frac{E_y^+\left(\eta_{y,xy}^+ - \nu_{yx}^+\eta_{x,xy}^+\right)}{G_{xy}^+\left(1-\nu_{xy}^+\nu_{yx}^+\right)}$$

Substituting these expressions in the third equation, we get $\tau_{xy} = G_{xy}\gamma_{xy}$, where

$$G_{xy} = \frac{G_{xy}^+\left(1-\nu_{xy}^+\nu_{yx}^+\right)}{1-\nu_{xy}^+\nu_{yx}^+ - \eta_{x,xy}^+\eta_{xy,x}^+ - \eta_{y,xy}^+\eta_{xy,y}^+ - \nu_{xy}^+\eta_{y,xy}^+\eta_{xy,x}^+ - \nu_{yx}^+\eta_{x,xy}^+\eta_{xy,y}^+}$$

is the shear modulus of an angle-ply layer which is much higher than G_{xy}^+ (see Fig. 4.60).

Tensile loading of a $\pm 45^\circ$ angle-ply specimen provides a simple way to determine the in-plane shear modulus of a unidirectional ply, G_{12}. Indeed, for this layer, Eqs. (4.72) and (4.147) yield

$$A_{11}^{45} = A_{22}^{45} = \frac{1}{4}\left(\overline{E}_1 + \overline{E}_2 + 2\overline{E}_1\nu_{12} + 4G_{12}\right), \quad A_{12}^{45} = \overline{E}_1\nu_{12} + \frac{1}{4}\left(\overline{E}_1 + \overline{E}_2 - 2\overline{E}_1\nu_{12} - 4G_{12}\right)$$

and

$$E_{45} = \frac{1}{A_{11}^{45}}\left(A_{11}^{45} + A_{12}^{45}\right)\left(A_{11}^{45} - A_{12}^{45}\right), \quad 1+\nu_{45} = \frac{1}{A_{11}^{45}}\left(A_{11}^{45} + A_{12}^{45}\right)$$

Taking into account that $A_{11}^{45} - A_{12}^{45} = 2G_{12}$, we have

$$G_{12} = \frac{E_{45}}{2(1+\nu_{45})} \tag{4.150}$$

Thus, to find G_{12}, we can test a $\pm 45^\circ$ specimen under tension, measure ε_x and ε_y, determine $E_{45} = \sigma_x/\varepsilon_x$, $\nu_{45} = -\varepsilon_y/\varepsilon_x$, and use Eq. (4.150) rather than perform the cumbersome tests described in Section 4.3.1.

4.5.2 Nonlinear models

To describe nonlinear behavior of an angle-ply layer associated with material nonlinearity in its plies, we can use nonlinear constitutive equations, Eqs. (4.60) or (4.64), instead of Hooke's law. Indeed, assuming that the ply behavior is linear under tension or compression along the fibers, we can write these equations in the following general form

$$\varepsilon_1 = c_{11}\sigma_1 + c_{12}\sigma_2, \quad \varepsilon_2 = c_{12}\sigma_1 + c_{22}\sigma_2 + \omega_2(\sigma_2, \tau_{12}), \quad \gamma_{12} = c_{44}\tau_{12} + \omega_{12}(\sigma_2, \tau_{12})$$

Functions ω_2 and ω_{12} include all the nonlinear terms. The inverse form of these equations is

$$\begin{aligned} &\sigma_1 = C_{11}\varepsilon_1 + C_{12}\varepsilon_2 - C_{12}\omega_2, \quad \sigma_2 = C_{12}\varepsilon_1 + C_{22}\varepsilon_2 - C_{22}\omega_2, \\ &\tau_{12} = C_{44}\gamma_{12} - C_{44}\omega_{12} \end{aligned} \tag{4.151}$$

in which

$$C_{11} = \frac{c_{22}}{c}, \quad C_{22} = \frac{c_{11}}{c}, \quad C_{44} = \frac{1}{c_{44}}, \quad C_{12} = -\frac{c_{12}}{c}, \quad c = c_{11}c_{22} - c_{12}^2.$$

Repeating the derivation of Eqs. (4.145) and this time using Eqs. (4.151) as the constitutive equations for the ply, we arrive at

$$\begin{aligned} &\sigma_x = A_{11}\varepsilon_x + A_{12}\varepsilon_y - A_{11}^{\omega}, \quad \sigma_y = A_{21}\varepsilon_x + A_{22}\varepsilon_y - A_{22}^{\omega}, \\ &\tau_{xy} = A_{44}\gamma_{xy} - A_{44}^{\omega} \end{aligned}$$

where $s = \sin\phi$, and $c = \cos\phi$.

$$\begin{aligned} &A_{11}^{\omega} = \left(C_{22}s^2 + C_{12}c^2\right)\omega_2 - 2C_{44}cs\omega_{12}, \quad A_{22}^{\omega} = \left(C_{22}c^2 + C_{12}s^2\right)\omega_2 + 2C_{44}cs\omega_{12}, \\ &A_{44}^{\omega} = \left(C_{12} - C_{22}\right)cs\omega_2 + C_{44}\left(c^2 - s^2\right)\omega_{12} \end{aligned}$$

These equations can be used in conjunction with the method of elastic solutions described in Section 4.1.2.

As an example, consider the two-matrix glass-epoxy composite described in Section 4.4.3 (see also Figs. 4.16, 4.30, and 4.31). Theoretical (solid lines) and experimental (dashed lines) stress-strain diagrams for $\pm 30^\circ$, $\pm 45^\circ$, and $\pm 75^\circ$ angle-ply layers under tension along the x-axis are shown in Fig. 4.62.

Angle-ply layers demonstrate a specific type of material nonlinearity: structural nonlinearity that can occur in the layers composed of linear elastic plies due to the change of the plies' orientations caused by loading. Since this effect manifests itself at high strains, consider a geometrically nonlinear problem of the ply deformation. This deformation can be described with the longitudinal, ε_1,

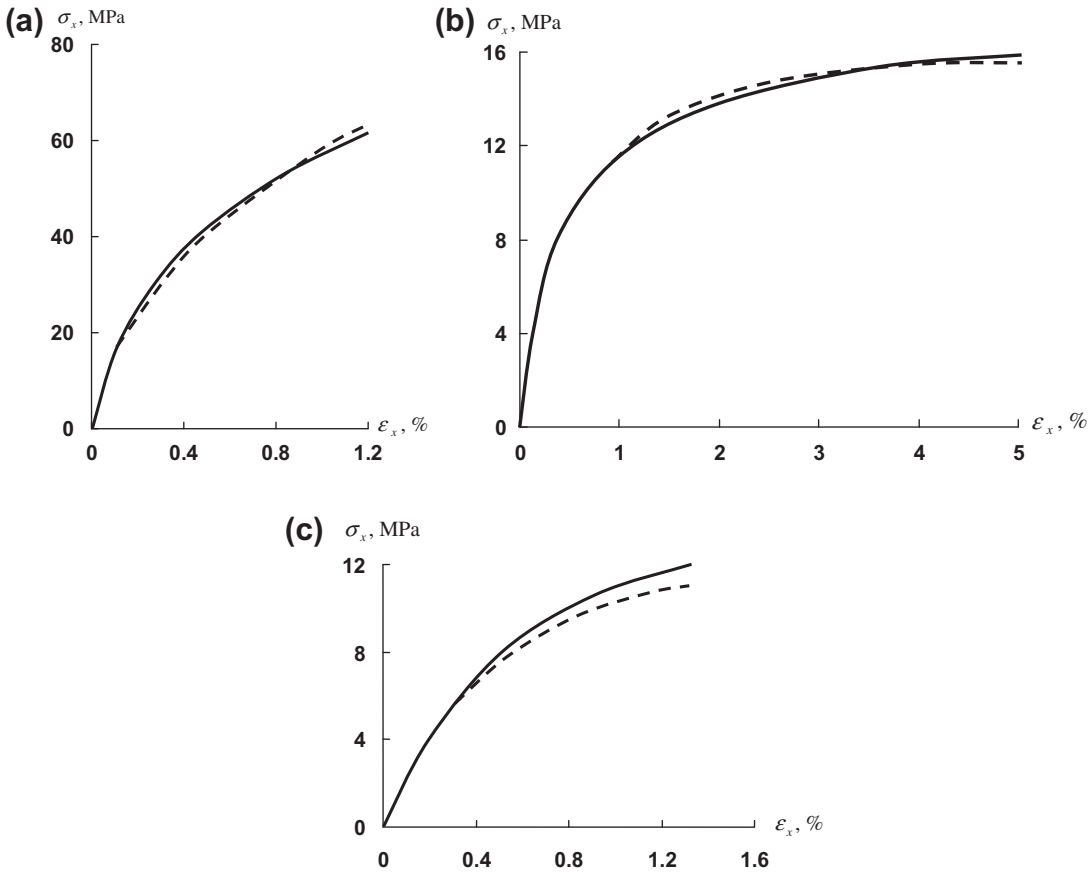


FIGURE 4.62

Theoretical (solid lines) and experimental (dashed lines) stress-strain diagrams for ±30°(a), ±45°(b), and ±75°(c) angle-ply two-matrix composites under uniaxial tension.

transverse, ε_2, and shear, γ_{12}, strains that follow from Fig. 4.63 and can be expressed as

$$\varepsilon_1 = \frac{1}{ds_1}\left(ds_1' - ds_1\right), \quad \varepsilon_2 = \frac{1}{ds_2}\left(ds_2' - ds_2\right), \quad \gamma_{12} = \frac{\pi}{2} - \psi \tag{4.152}$$

In addition to this, we introduce strain ε_2'' in the direction normal to the fibers

$$\varepsilon_2'' = \frac{1}{ds_2}\left(ds_2'' - ds_2\right) \tag{4.153}$$

and the angle of rotation of the element as a solid in the 12-plane

$$\omega_{12} = \frac{1}{2}\left(\omega_1 - \omega_2\right)$$

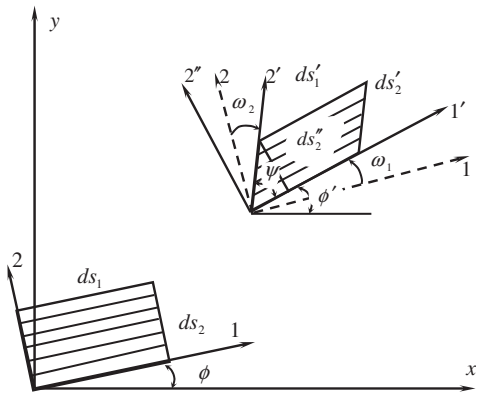


FIGURE 4.63

Ply element before and after deformation.

where $\omega_1 = \phi' - \phi, \quad \omega_2 = \dfrac{\pi}{2} + \phi - (\phi' + \psi)$

are the angles of rotation of axes $1'$ and $2'$ (see Fig. 4.63). Thus,

$$\omega_{12} = \phi' - \phi + \frac{\psi}{2} - \frac{\pi}{4} \tag{4.154}$$

Consider some arbitrary element ds_α, shown in Fig. 4.64, and introduce its strain

$$ds_\alpha = \frac{1}{ds_\alpha}(ds_\alpha' - ds_\alpha) \tag{4.155}$$

Repeating the derivation described in Section 2.5, we have

$$ds_\alpha^2 = dx^2 + dy^2$$

$$(ds_\alpha')^2 = (dx')^2 + (dy')^2 = (dx + du_x)^2 + (dy + du_y)^2$$

$$= (1 + \varepsilon_x)^2 dx^2 + (1 + \varepsilon_y)^2 dy^2 + 2\varepsilon_{xy} dx dy$$

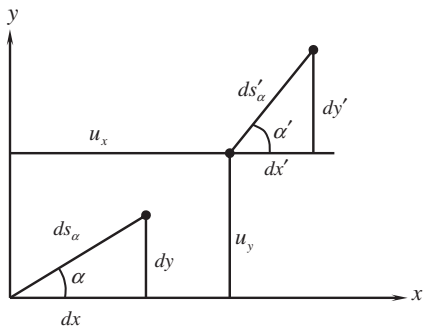


FIGURE 4.64

Linear element before and after deformation.

where

$$\begin{aligned}(1+\varepsilon_x)^2 &= 1+2\left[\frac{\partial u_x}{\partial x}+\frac{1}{2}\left(\frac{\partial u_x}{\partial x}\right)^2+\frac{1}{2}\left(\frac{\partial u_y}{\partial x}\right)^2\right]\\ \left(1+\varepsilon_y\right)^2 &= 1+2\left[\frac{\partial u_y}{\partial y}+\frac{1}{2}\left(\frac{\partial u_x}{\partial y}\right)^2+\frac{1}{2}\left(\frac{\partial u_y}{\partial y}\right)^2\right]\\ \varepsilon_{xy} &= \frac{\partial u_x}{\partial y}+\frac{\partial u_y}{\partial x}+\frac{\partial u_x}{\partial x}\frac{\partial u_x}{\partial y}+\frac{\partial u_y}{\partial x}\frac{\partial u_y}{\partial y}\end{aligned} \tag{4.156}$$

Using Eq. (4.155), we arrive at

$$(1+\varepsilon_\alpha)^2 = (1+\varepsilon_x)^2\cos^2\alpha+\left(1+\varepsilon_y\right)^2\sin^2\alpha+\varepsilon_{xy}\sin 2\alpha \tag{4.157}$$

where $\cos\alpha = dx/ds_\alpha$ and $\sin\alpha = dy/ds_\alpha$.

In a similar way, we can find the angle α' after the deformation, i.e.,

$$\begin{aligned}\sin\alpha' &= \frac{dy'}{ds_\alpha} = \frac{1}{1+\varepsilon_\alpha}\left[\left(1+\frac{\partial u_y}{\partial y}\right)\sin\alpha+\frac{\partial u_y}{\partial x}\cos\alpha\right]\\ \cos\alpha' &= \frac{dx'}{ds_\alpha} = \frac{1}{1+\varepsilon_\alpha}\left[\left(1+\frac{\partial u_x}{\partial x}\right)\cos\alpha+\frac{\partial u_x}{\partial y}\sin\alpha\right]\end{aligned} \tag{4.158}$$

Now return to the ply element in Fig. 4.63. Taking $\alpha = \phi$ in Eqs. (4.157) and (4.158), we obtain

$$\begin{aligned}(1+\varepsilon_1)^2 &= (1+\varepsilon_x)^2\cos^2\phi+\left(1+\varepsilon_y\right)^2\sin^2\phi+\varepsilon_{xy}\sin 2\phi\\ \sin\phi' &= \frac{1}{1+\varepsilon_1}\left[\left(1+\frac{\partial u_y}{\partial y}\right)\sin\phi+\frac{\partial u_y}{\partial x}\cos\phi\right]\\ \cos\phi' &= \frac{1}{1+\varepsilon_1}\left[\left(1+\frac{\partial u_x}{\partial x}\right)\cos\phi+\frac{\partial u_x}{\partial y}\sin\phi\right]\end{aligned} \tag{4.159}$$

Putting $\alpha = \dfrac{\pi}{2}+\phi$, we have

$$\begin{aligned}(1+\varepsilon_2)^2 &= (1+\varepsilon_x)^2\sin^2\phi+\left(1+\varepsilon_y\right)^2\cos^2\phi-2\varepsilon_{xy}\sin 2\phi\\ \sin\left(\phi'+\psi\right) &= \frac{1}{1+\varepsilon_2}\left[\left(1+\frac{\partial u_y}{\partial y}\right)\cos\phi-\frac{\partial u_y}{\partial x}\sin\phi\right]\\ \cos\left(\phi'+\psi\right) &= \frac{1}{1+\varepsilon_2}\left[-\left(1+\frac{\partial u_x}{\partial x}\right)\cos\phi+\frac{\partial u_x}{\partial y}\sin\phi\right]\end{aligned} \tag{4.160}$$

Using the last equation of Eqs. (4.152), we can find the shear strain as $\sin\gamma_{12} = \cos\psi$. After some rearrangement, with the aid of Eqs. (4.159) and (4.160), we arrive at

$$\sin\gamma_{12} = \frac{1}{(1+\varepsilon_1)(1+\varepsilon_2)}\left\{\left[\left(1+\varepsilon_y\right)^2-(1+\varepsilon_x)^2\right]\sin\phi\cos\phi+\varepsilon_{xy}\cos 2\phi\right\} \tag{4.161}$$

For $\phi = 0$, axes 1 and 2 coincide, respectively, with axes x and y (see Fig. 4.63), and Eq. (4.161) yields

$$\sin \gamma_{xy} = \frac{\varepsilon_{xy}}{(1+\varepsilon_x)(1+\varepsilon_y)} \tag{4.162}$$

Using this result to express ε_{xy}, we can write Eqs. (4.159)–(4.161) in the following final form

$$\begin{aligned}
(1+\varepsilon_1)^2 &= (1+\varepsilon_x)^2 \cos^2\phi + (1+\varepsilon_y)^2 \sin^2\phi \\
&\quad + (1+\varepsilon_x)(1+\varepsilon_y) \sin\gamma_{xy} \sin 2\phi \\
(1+\varepsilon_2)^2 &= (1+\varepsilon_x)^2 \sin^2\phi + (1+\varepsilon_y)^2 \cos^2\phi \\
&\quad - (1+\varepsilon_x)(1+\varepsilon_y) \sin\gamma_{xy} \sin 2\phi \\
\sin\gamma_{12} &= \frac{1}{(1+\varepsilon_1)(1+\varepsilon_2)} \left\{ \left[(1+\varepsilon_y)^2 - (1+\varepsilon_x)^2 \right] \sin\phi\cos\phi \right. \\
&\quad \left. + (1+\varepsilon_x)(1+\varepsilon_y) \sin\gamma_{xy} \cos 2\phi \right\}
\end{aligned} \tag{4.163}$$

It follows from Fig. 4.63 and the last equation of Eqs. (4.152) that $ds_2'' = ds_2' \sin\psi = ds_2' \cos\gamma_{12}$. So, in accordance with Eqs. (4.152) and (4.153),

$$1 + \varepsilon_2'' = (1+\varepsilon_2)\cos\gamma_{12}$$

Using Eqs. (4.163) to transform this equation, we get

$$1 + \varepsilon_2'' = \frac{(1+\varepsilon_x)(1+\varepsilon_y)}{1+\varepsilon_1} \cos\gamma_{xy} \tag{4.164}$$

To express ϕ' in terms of ϕ and strains referred to the global coordinate frame x, y, consider Eq. (4.154). After rather cumbersome transformation with the aid of Eqs. (4.159) and (4.160), we obtain

$$\begin{aligned}
\sin 2\omega_{12} = \frac{1}{(1+\varepsilon_1)(1+\varepsilon_2)} &\left\{ \left(\frac{\partial u_y}{\partial x} - \frac{\partial u_x}{\partial y} + \frac{\partial u_y}{\partial x}\frac{\partial u_y}{\partial y} - \frac{\partial u_x}{\partial x}\frac{\partial u_x}{\partial y} \right) \cos^2 2\phi \right. \\
&+ \left(\frac{\partial u_y}{\partial x} - \frac{\partial u_x}{\partial y} + \frac{\partial u_x}{\partial x}\frac{\partial u_y}{\partial x} - \frac{\partial u_x}{\partial y}\frac{\partial u_y}{\partial y} \right) \sin^2 2\phi \\
&\left. + \frac{1}{4} \left[\left(\frac{\partial u_x}{\partial x} - \frac{\partial u_y}{\partial y} \right)^2 - \left(\frac{\partial u_y}{\partial x} + \frac{\partial u_x}{\partial y} \right)^2 \right] \sin 4\phi \right\}
\end{aligned}$$

Taking $\phi = 0$, we can express rotation angle ω_z around the z-axis of the global coordinate frame, i.e.,

$$\sin 2\omega_z = \frac{1}{(1+\varepsilon_x)(1+\varepsilon_y)} \left(\frac{\partial u_y}{\partial x} - \frac{\partial u_x}{\partial y} + \frac{\partial u_y}{\partial x}\frac{\partial u_y}{\partial y} - \frac{\partial u_x}{\partial x}\frac{\partial u_x}{\partial y} \right) \tag{4.165}$$

Consider now Eqs. (4.156), (4.162), and (4.165) which form a set of four algebraic equations with respect to the derivatives of the displacements. Omitting the solution procedure, we can write the final outcome as

$$\frac{\partial u_x}{\partial x} = (1+\varepsilon_x)\cos\left(\frac{\gamma_{xy}}{2}+\omega_z\right) - 1, \quad \frac{\partial u_x}{\partial y} = (1+\varepsilon_y)\sin\left(\frac{\gamma_{xy}}{2}-\omega_z\right),$$
$$\frac{\partial u_y}{\partial x} = (1+\varepsilon_x)\sin\left(\frac{\gamma_{xy}}{2}+\omega_z\right), \quad \frac{\partial u_y}{\partial y} = (1+\varepsilon_y)\cos\left(\frac{\gamma_{xy}}{2}-\omega_z\right) - 1$$

Substituting these expressions in Eqs. (4.159), we have

$$\begin{aligned}\sin\phi' &= \frac{1}{1+\varepsilon_1}\left[(1+\varepsilon_x)\sin\left(\frac{\gamma_{xy}}{2}+\omega_z\right)\cos\phi\right.\\ &\quad \left.+(1+\varepsilon_y)\cos\left(\frac{\gamma_{xy}}{2}-\omega_z\right)\sin\phi\right.\\ \cos\phi' &= \frac{1}{1+\varepsilon_1}\left[(1+\varepsilon_x)\cos\left(\frac{\gamma_{xy}}{2}+\omega_z\right)\cos\phi\right.\\ &\quad \left.+(1+\varepsilon_y)\sin\left(\frac{\gamma_{xy}}{2}-\omega_z\right)\sin\phi\right.\end{aligned} \tag{4.166}$$

The derived nonlinear equations, Eqs. (4.163), generalize Eqs. (4.69) for the case of large strains, whereas Eqs. (4.166) allow us to find the fiber orientation angle after deformation.

The equilibrium equations, Eqs. (4.68), retain their form but should be written for the deformed state, i.e.,

$$\begin{aligned}\sigma_x &= \sigma_1'\cos^2\phi' + \sigma_2''\sin^2\phi' - \tau_{12}'\sin 2\phi'\\ \sigma_y &= \sigma_1'\sin^2\phi' + \sigma_2''\cos^2\phi' + \tau_{12}'\sin 2\phi'\\ \tau_{xy} &= (\sigma_1' - \sigma_1'')\sin\phi'\cos\phi' + \tau_{12}'\cos 2\phi'\end{aligned} \tag{4.167}$$

where σ_1', σ_2'', and τ_{12}' are stresses referred to coordinate frame $1'2''$ (see Fig. 4.63) and to the current thickness of the ply.

Consider a problem of uniaxial tension of a $\pm\phi$ angle-ply layer with stress σ_x. For this case, $\gamma_{xy} = 0$, $\omega_z = 0$, and Eqs. (4.163), (4.164), (4.166) take the form

$$(1+\varepsilon_1)^2 = (1+\varepsilon_x)^2\cos^2\phi + (1+\varepsilon_y)^2\sin^2\phi$$
$$(1+\varepsilon_2)^2 = (1+\varepsilon_x)^2\sin^2\phi + (1+\varepsilon_y)^2\cos^2\phi$$
$$\sin\gamma_{12} = \frac{\sin\phi\cos\phi}{(1+\varepsilon_1)(1+\varepsilon_2)}\left[(1+\varepsilon_y)^2 - (1+\varepsilon_x)^2\right]$$
$$1+\varepsilon_2'' = \frac{(1+\varepsilon_x)(1+\varepsilon_y)}{1+\varepsilon_1}$$
$$\sin\phi' = \frac{1+\varepsilon_y}{1+\varepsilon_1}\sin\phi, \quad \cos\phi' = \frac{1+\varepsilon_x}{1+\varepsilon_1}\cos\phi$$

For composite materials, the longitudinal strain ε_1 is usually small, and these equations can be further simplified as follows

$$\begin{aligned}
\varepsilon_1 &= \varepsilon_x \cos^2\phi + \varepsilon_y \sin^2\phi + \frac{1}{2}\left(\varepsilon_x^2 \cos^2\phi + \varepsilon_y^2 \sin^2\phi\right) \\
(1+\varepsilon_2)^2 &= (1+\varepsilon_x)^2 \sin^2\phi + \left(1+\varepsilon_y\right)^2 \cos^2\phi \\
\sin\gamma_{12} &= \frac{1}{1+\varepsilon_2}\left[\left(1+\varepsilon_y\right)^2 - (1+\varepsilon_x)^2\right] \sin\phi\cos\phi \\
1+\varepsilon_2'' &= \left(1+\varepsilon_x\right)\left(1+\varepsilon_y\right) \\
\tan\phi' &= \frac{1+\varepsilon_y}{1+\varepsilon_x}\tan\phi
\end{aligned} \tag{4.168}$$

As an example, consider a specially synthesized highly deformable composite material made from glass composite fibers and thermoplastic matrix as discussed in Section 4.4.3. Neglecting interaction of strains, we take constitutive equations for the unidirectional ply as

$$\sigma_1' = \frac{E_1\varepsilon_1}{1+\varepsilon_2''}, \quad \sigma_2' = \omega_2\left(\varepsilon_2''\right), \quad \tau_{12}' = \omega_{12}\left(\gamma_{12}\right) \tag{4.169}$$

where E_1 in the first equation is the longitudinal elasticity modulus, whereas ε_2 in the denominator takes account of the decrease of the ply stiffness due to the increase in the fiber spacing. The constant E_1 and functions ω_2 and ω_{12} are determined from the experimental stress-strain diagrams for 0, 90, and $\pm 45^\circ$ specimens that are shown in Fig. 4.65. The results of calculations with the aid of Eqs. (4.167)–(4.169) are presented together with the corresponding experimental data in Fig. 4.66.

The foregoing equations comprise the analytical background for a promising manufacturing process that allows us to fabricate composite parts with complicated shapes by deforming partially cured preforms of simple shapes made by winding or laying-up (see, e.g., Cherevatsky, 1999).

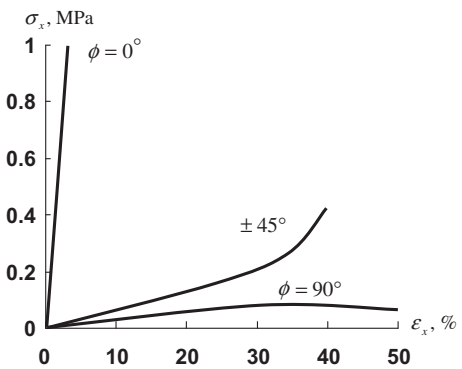


FIGURE 4.65

Experimental stress-strain diagrams for $0, \pm 45,$ and 90° angle-ply layers.

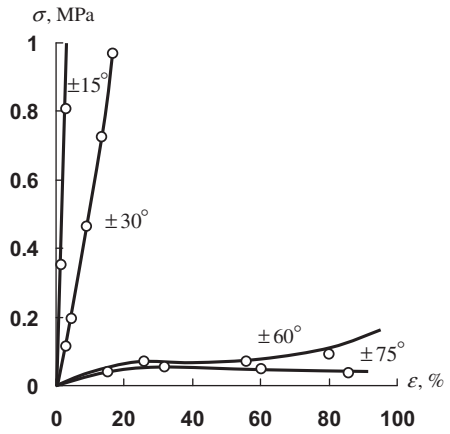


FIGURE 4.66

Calculated (circles) and experimental (solid lines) stress-strain diagrams for ±15, ±30, ±60, and ±75° angle-ply layers.



FIGURE 4.67

A curved angle-ply pipe made by deformation of a filament wound cylinder.

An example of such a part is presented in Fig. 4.67. The curved composite pipe shown in this figure was fabricated from a straight cylinder that was partially cured, loaded with pre-assigned internal pressure and end forces and moments, and cured completely in this state. The desired deformation of the part under loading is provided by the appropriate change of the fibers' orientation angles governed by Eqs. (4.163), (4.166), and (4.167).

Angle-ply layers can also demonstrate nonlinear behavior caused by the matrix cracking described in Section 4.4.2. To illustrate this type of nonlinearity, consider carbon-epoxy ±15, ±30, ±45, ±60, and ±75° angle-ply specimens studied experimentally by Lagace (1985). The unidirectional ply has the following mechanical properties: $E_1 = 131$ GPa, $E_2 = 11$ GPa, $G_{12} = 6$ GPa, $\nu_{21} = 0.28$, $\overline{\sigma}_1^+ = 1770$ MPa, $\overline{\sigma}_2^+ = 54$ MPa, $\overline{\sigma}_2^- = 230$ MPa, and $\overline{\tau}_{12} = 70$ MPa. The

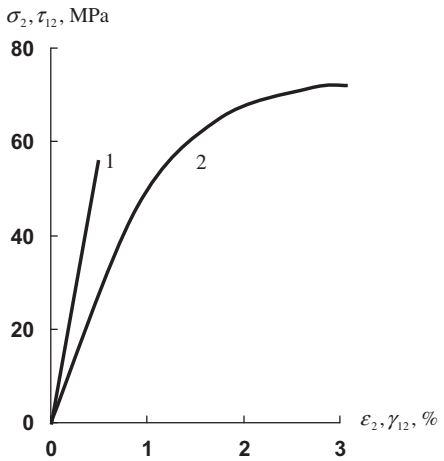


FIGURE 4.68

Experimental stress-strain diagrams for transverse tension (1) and in-plane shear (2) of a carbon-epoxy unidirectional ply.

dependencies $\sigma_1(\varepsilon_1)$ and $\sigma_2(\varepsilon_2)$ are linear, whereas for in-plane shear, the stress-strain diagram is not linear, and is shown in Fig. 4.68. To take into account the material nonlinearity associated with shear, we use the constitutive equation derived in Section 4.2.2, i.e.,

$$\gamma_{12} = c_1\tau_{12} + c_2\tau_{12}^3$$

in which $c_1 = 1/G_{12}$ and $c_2 = 5.2\cdot 10^{-8}(\text{MPa})^{-3}$.

The specimens were tested in uniaxial tension in the x direction. To calculate the applied stress σ_x that causes failure of the matrix, we use the simplest maximum stress strength criterion (see Chapter 6) which ignores the interaction of stresses, i.e.,

$$-\overline{\sigma}_2^- \le \sigma_2 \le \overline{\sigma}_2^+ , \quad |\tau_{12}| \le \overline{\tau}_{12}$$

Nonlinear behavior associated with ply degradation is predicted applying the procedure described in Section 4.4.2. Stress-strain diagrams are plotted using the method of successive loading (see Section 4.1.2).

Consider a $\pm 15^\circ$ angle-ply layer. Point 1 on the theoretical diagram, shown in Fig. 4.69, corresponds to cracks in the matrix caused by shear. These cracks do not result in complete failure of the matrix because the transverse normal stress σ_2 is compressive (see Fig. 4.70) and does not reach $\overline{\sigma}_2^-$ before the failure of fibers under tension (point 2 on the diagram). As can be seen, the theoretical prediction of the material stiffness is quite good, whereas the predicted material strength (point 2) is much higher than the experimental (dot on the solid line). The reasons for this are discussed in the next section.

The theoretical diagram corresponding to the $\pm 30^\circ$ layer (see Fig. 4.69) also has two specific points. Point 1 again corresponds to cracks in the matrix induced by the shear stress τ_{12}, whereas point 2 indicates complete failure of the matrix caused by the compressive stress σ_2, which reaches $\overline{\sigma}_2^-$ at this

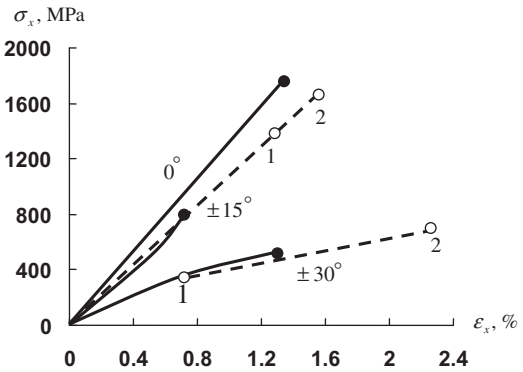


FIGURE 4.69

Experimental (solid lines) and calculated (dashed lines) stress-strain diagrams for 0, ±15, and ±30° angle-ply carbon-epoxy layers.

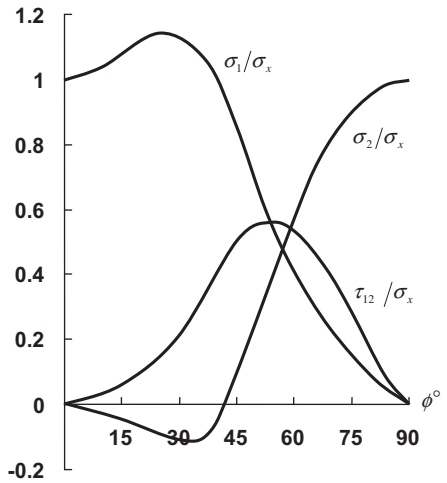


FIGURE 4.70

Dependencies of the normalized stresses in the plies on the ply orientation angle.

point. After the matrix fails, the fibers of an angle-ply layer cannot take the load. Indeed, putting $E_2 = G_{12} = \nu_{12} = 0$ in Eqs. (4.72), we obtain the following stiffness coefficients

$$A_{11} = E_1 \cos^4 \phi, \quad A_{22} = E_1 \sin^4 \phi, \quad A_{12} = E_1 \sin^2 \phi \cos^2 \phi$$

With these coefficients, the first equation of Eqs. (4.147) yields $E_x = 0$, which means that the system of fibers becomes a mechanism, and the stresses in the fibers, no matter how high they are, cannot balance the load. A typical failure mode for a ±30° angle-ply specimen is shown in Fig. 4.71.

Angle-ply layers with fiber orientation angles exceeding 45° demonstrate a different type of behavior. As can be seen in Fig. 4.70, the transverse normal stress σ_2 is tensile for $\phi \geq 45°$. This means

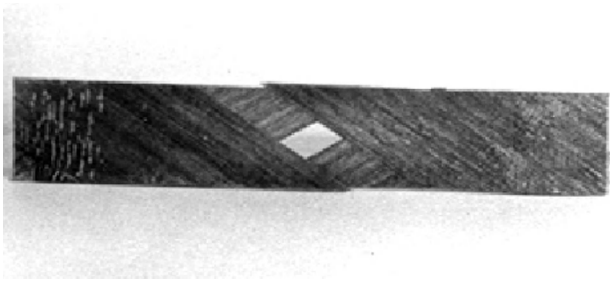


FIGURE 4.71

A failure mode of ±30° angle-ply specimen.

that the cracks induced in the matrix by normal, σ_2, or shear, τ_{12}, stresses cause failure of the layer. The stress-strain diagrams for ±60° and ±75° layers are shown in Fig. 4.72. As follows from this figure, the theoretical curves are linear and are close to the experimental ones, whereas the predicted ultimate stresses (circles) are again higher than the experimental values (dots).

Now consider the ±45° angle-ply layer, which demonstrates a very specific behavior. For this layer, the transverse normal stress, σ_2, is tensile but not high (see Fig. 4.70), and the cracks in the matrix are caused by the shear stress, τ_{12}. According to the ply model we use, to predict material response after the cracks' appearance, we should take $G_{12} = 0$ in the stiffness coefficients. Then, Eqs. (4.72) yield

$$A_{11} = A_{12} = A_{22} = \frac{1}{4}\left(\overline{E}_1 + \overline{E}_2\right) + \frac{1}{2}\overline{E}_1\nu_{12}$$

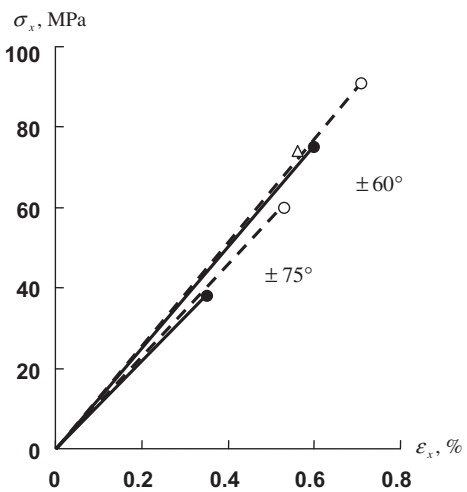


FIGURE 4.72

Experimental (solid lines) and calculated (dashed lines) stress-strain diagrams for ±60 and ±75° angle-ply carbon-epoxy layers.

whereas Eqs. (4.146) and (4.147) give

$$\varepsilon_x = \frac{A_{22}\sigma_x}{A_{11}A_{22} - A_{12}^2}, \quad \varepsilon_y = -\frac{A_{12}\sigma_x}{A_{11}A_{22} - A_{12}^2}$$

The denominator of both expressions is zero, so it looks as though the material becomes a mechanism and should fail under the load that causes cracks in the matrix. However, this is not the case. To explain why, consider the last equation of Eqs. (4.168), i.e.,

$$\tan\phi' = \frac{1+\varepsilon_y}{1+\varepsilon_x}\tan\phi$$

For the layer under study, $\tan\phi = 1$, $\varepsilon_y < 0$ and $\varepsilon_x > 0$, so $\tan\phi' < 1$ and $\phi' < 45^\circ$. However, in the plies with $\phi < 45^\circ$ the transverse normal stresses, σ_2, become compressive (see Fig. 4.70) and close the cracks. Thus, the load exceeding the level at which the cracks appear due to shear locks the cracks and induces compression across the fibers, thus preventing material failure. Since ϕ' is only slightly less than 45°, the material stiffness, E_x, is very low and slightly increases with the increase in strains and decrease of ϕ'. For the material under study, the calculated and experimental diagrams are shown in Fig. 4.73. The circle on the theoretical curve indicates the stress σ_x that causes cracks in the matrix. More pronounced behavior of this type is demonstrated by the glass-epoxy composites whose stress-strain diagram is presented via curve 1 in Fig. 4.74 (Alfutov and Zinoviev, 1982). A specific plateau on the curve and material hardening at high strain are the result of the angle variation as is also shown in Fig. 4.74 (line 2).

4.5.3 Free-edge effects

As shown in the previous section, there is a significant difference between the predicted and measured strength of an angle-ply specimen loaded in tension. This difference is associated with the stress

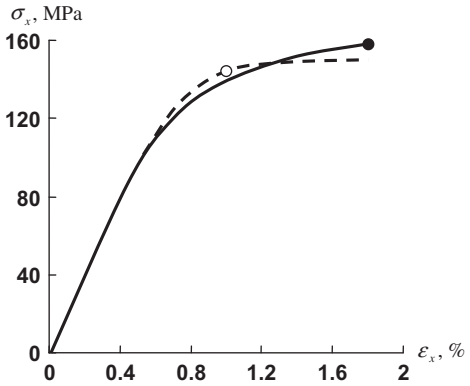


FIGURE 4.73

Experimental (solid line) and calculated (dashed line) stress-strain diagrams for a ±45° angle-ply carbon-epoxy layer.

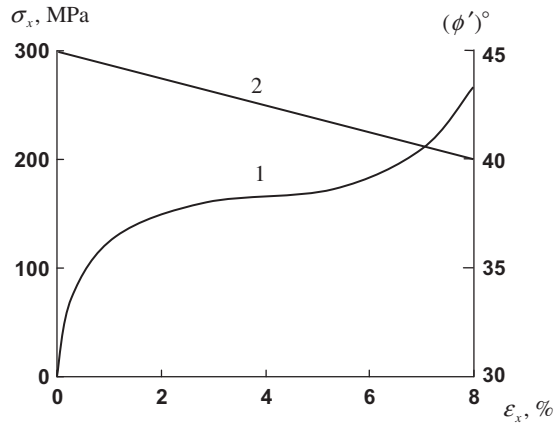


FIGURE 4.74

Experimental dependencies of stress (1) and ply orientation angle (2) on strain for ±45° angle-ply glass-epoxy composite.

concentration that occurs in the vicinity of the specimen longitudinal edges and was not taken into account in the analysis.

To study a free-edge effect in an angle-ply specimen, consider a strip whose initial width a is much smaller than the length l. Under tension with longitudinal stress σ, symmetric plies with orientation angles $+\phi$ and $-\phi$ tend to deform as shown in Fig. 4.75. As can be seen, deformation of the plies in the y direction is the same, whereas the deformation in the x direction tends to be different. This means that symmetric plies forming the angle-ply layer interact through the interlaminar shear stress τ_{xz} acting between the plies in the longitudinal direction. To describe the ply interaction, introduce the model shown in Fig. 4.76, according to which the in-plane stresses in the plies are applied to their middle surfaces, whereas transverse shear stresses act in some hypothetical layers introduced between these surfaces.

To simplify the problem, we further assume that the transverse stress can be neglected, i.e., $\sigma_y = 0$, and that the axial strain in the middle part of the long strip is constant, i.e., $\varepsilon_x = \varepsilon = \text{constant}$. Thus, the constitutive equations, Eqs. (4.75), for a $+\phi$ ply have the form

$$\varepsilon_x = \frac{\sigma_x}{E_x^+} + \eta_{x,xy}^+ \frac{\tau_{xy}}{G_{xy}^+} \tag{4.170}$$

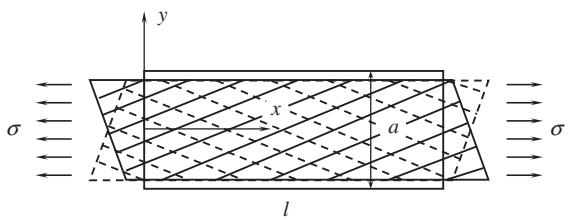


FIGURE 4.75

Deformation of symmetric plies under tension.

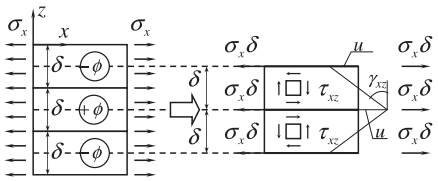


FIGURE 4.76

A model simulating the plies' interactions.

$$\varepsilon_y = -\nu_{yx}^{+}\frac{\sigma_x}{E_x^{+}} + \eta_{y,xy}^{+}\frac{\tau_{xy}}{G_{xy}^{+}} \tag{4.171}$$

$$\gamma_{xy} = \eta_{xy,x}^{+}\frac{\sigma_x}{E_x^{+}} + \frac{\tau_{xy}}{G_{xy}^{+}} \tag{4.172}$$

where the elastic constants for an individual ply are specified by Eqs. (4.76). The strain-displacement equations, Eqs. (2.22), for the problem under study are

$$\varepsilon_x = \varepsilon = \frac{\partial u_x}{\partial x}, \quad \varepsilon_y = \frac{\partial u_y}{\partial y}, \quad \gamma_{xy} = \frac{\partial u_x}{\partial y} + \frac{\partial u_y}{\partial x} \tag{4.173}$$

Integration of the first equation yields

$$u_x^{+\phi} = \varepsilon\cdot x + u(y), \quad u_x^{-\phi} = \varepsilon\cdot x - u(y) \tag{4.174}$$

for the $+\phi$ and $-\phi$ plies where $u(y)$ is the displacement shown in Fig. 4.76. This displacement results in the following transverse shear deformation and transverse shear stress

$$\gamma_{xz} = \frac{2}{\delta}u(y), \quad \tau_{xz} = G_{xz}\gamma_{xz}, \tag{4.175}$$

where G_{xz} is the transverse shear modulus of the ply specified by Eqs. (4.76). Consider the equilibrium state of the $+\phi$ ply element shown in Fig. 4.77. Equilibrium equations can be written as

$$\delta\frac{\partial\tau_{xy}}{\partial x} = 0, \quad \delta\frac{\partial\tau_{xy}}{\partial y} - 2\tau_{xz} = 0 \tag{4.176}$$

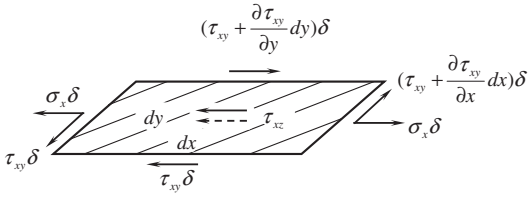


FIGURE 4.77

Forces acting on the infinitesimal element of a ply.

The first of these equations shows that τ_{xy} does not depend on x. Since the axial stress, σ_x, in the middle part of a long specimen also does not depend on x, Eqs. (4.171) and (4.173) allow us to conclude that ε_y, and hence u_y, do not depend on x. As a result, the last equation of Eqs. (4.173) yields, in conjunction with the first equation of Eqs. (4.174),

$$\gamma_{xy} = \frac{\partial u_x}{\partial y} = \frac{du}{dy}$$

Substituting this expression into Eq. (4.172) and taking into account the equation for ε, Eq. (4.170), we arrive at

$$\tau_{xy} = \frac{G_{xy}^{+}}{1-\eta}\left(\frac{du}{dy} - \eta_{xy,x}^{+}\varepsilon\right) \tag{4.177}$$

where $\eta = \eta_{x,xy}^{+}\eta_{xy,x}^{+}$.

Substitution of Eqs. (4.175) and (4.177) into the second equation of Eqs. (4.176) provides the following governing equation for the problem under study

$$\frac{d^2u}{dy^2} - k^2u = 0 \tag{4.178}$$

in which

$$k^2 = \frac{4G_{xz}(1-\eta)}{G_{xy}^{+}\delta^2}$$

Using the symmetry conditions, we can present the solution of Eq. (4.178) as

$$u = C\sinh ky$$

The constant C can be determined from the boundary conditions for the free longitudinal edges of the specimen (see Fig. 4.75), according to which $\tau_{xy}(y = \pm a/2) = 0$. Satisfying these conditions and using Eqs. (4.170), (4.171), (4.175), and (4.177), we finally obtain

$$\begin{aligned}
&\varepsilon_x = \varepsilon\\
&\varepsilon_y = \frac{\varepsilon}{1-\eta}\left[\eta_{y,xy}^{+}\eta_{xy,x}^{+}\left(\frac{\cosh\lambda\bar{y}}{\cosh\lambda} - 1\right) + \nu_{yx}^{+}\left(\eta\frac{\cosh\lambda\bar{y}}{\cosh\lambda} - 1\right)\right]\\
&\gamma_{xy} = \varepsilon\eta_{xy,x}^{+}\frac{\cosh\lambda\bar{y}}{\cosh\lambda},\\
&\sigma_x = \varepsilon E_x^{+}\left[1 - \frac{\eta}{1-\eta}\left(\frac{\cosh\lambda\bar{y}}{\cosh\lambda} - 1\right)\right]\\
&\tau_{xy} = \frac{G_{xy}^{+}\eta_{xy,x}^{+}}{1-\eta}\left(\frac{\cosh\lambda\bar{y}}{\cosh\lambda} - 1\right)\\
&\tau_{xz} = \frac{2\varepsilon}{k\delta}G_{xz}\eta_{xy,x}^{+}\frac{\sinh\lambda\bar{y}}{\cosh\lambda}
\end{aligned} \tag{4.179}$$

where

$$\lambda = \frac{ka}{2} = \frac{a}{\delta}\sqrt{(1-\eta)\frac{G_{xz}}{G_{xy}^{+}}}, \quad \overline{y} = \frac{2y}{a} \tag{4.180}$$

The axial stress, σ_x, should provide the stress resultant equal to σa (see Fig. 4.75), i.e.,

$$\int_{-a/2}^{a/2} \sigma_x dy = \sigma\, a$$

This condition allows us to determine the axial strain as

$$\varepsilon = \frac{\sigma}{E_x}$$

where

$$E_x = E_x^{+}\left[1 + \frac{\eta}{1-\eta}\left(1 - \frac{1}{\lambda}\tanh\lambda\right)\right] \tag{4.181}$$

is the apparent modulus of an angle-ply specimen.

Consider two limiting cases. First, suppose that $G_{xz} = 0$, i.e., that the plies are not bonded. Then $\lambda = 0$ and because

$$\lim_{\lambda \to 0} \frac{1}{\lambda}\tanh\lambda = 1,$$

$E_x = E_x^{+}$. Second, assume that $G_{xz} \to \infty$, i.e., that the interlaminar shear stiffness is infinitely high. Then $\lambda \to \infty$ and Eq. (4.181) yields

$$E_x = \frac{E_x^{+}}{1-\eta} \tag{4.182}$$

This result coincides with Eq. (4.149), which specifies the modulus of an angle-ply layer.

For finite values of G_{xz}, the parameter λ in Eqs. (4.180) is rather large because it includes the ratio of the specimen width, a, to the ply thickness, δ, which is, usually, a large number. Taking into account that $\tanh\lambda \leq 1$, we can neglect the last term in Eq. (4.181) in comparison with unity. Thus, this equation reduces to Eq. (4.182). This means that the tensile loading of angle-ply specimens allows us to measure material stiffness with good accuracy despite the fact that the fibers are cut on the longitudinal edges of the specimens.

However, this does not hold for the strength. The distribution of stresses over the half-width of the carbon-epoxy specimen with the properties given earlier and $a/\delta = 20$ and $\phi = 45^\circ$ is shown in Fig. 4.78. The stresses σ_x, τ_{xy}, and τ_{xz} were calculated with the aid of Eqs. (4.179), whereas stresses σ_1, σ_2, and τ_{12} in the principal material directions of the plies were found using Eqs. (4.69) for the corresponding strains and Hooke's law for the plies. As can be seen in Fig. 4.78, there exists a significant concentration of stress σ_2 that causes cracks in the matrix. Moreover, the interlaminar

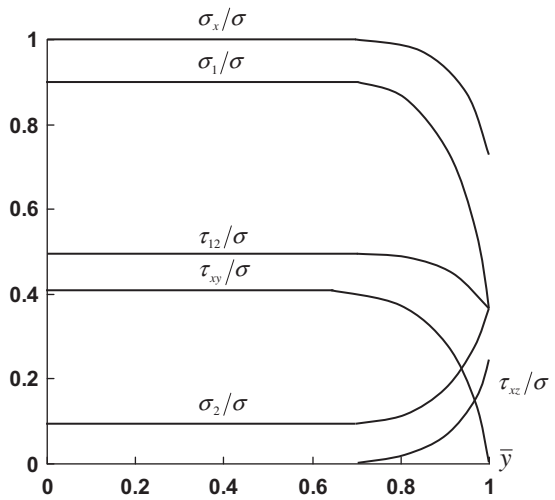


FIGURE 4.78

Distribution of normalized stresses over the width of a ±45° angle-ply carbon-epoxy specimen.

shear stress τ_{xz} that appears in the vicinity of the specimen edge can induce delamination of the specimen. The maximum value of stress σ_2 is

$$\sigma_2^{\max} = \sigma_2(\bar{y} = 1) = \overline{E}_2\varepsilon\left[(1 - \nu_{21}\nu_{yx}^{+})\sin^2\phi + (\nu_{21} - \nu_{yx})\cos^2\phi - (1 - \nu_{21})\eta_{xy,x}^{+}\sin\phi\cos\phi\right]$$

Using the modified strength condition, i.e., $\sigma_2^{\max} = \overline{\sigma}_2^{+}$, to evaluate the strength of the ±60° specimen, we arrive at the result shown with a triangular symbol in Fig. 4.72. As can be seen, the allowance for the stress concentration results in fair agreement with the experimental strength (dot).

Thus, the strength of angle-ply specimens is reduced by the free-edge effects, which causes a dependence of the observed material strength on the width of the specimen. Such dependence is shown in Fig. 4.79 for 105 mm diameter and 2.5 mm thick fiberglass rings made by winding at ±35° angles with respect to the axis and loading with internal pressure by two half-discs as in Fig. 3.46 (Fukui et al., 1966).

It should be emphasized that the free-edge effect occurs in specimens only and does not show itself in composite structures which, being properly designed, must not have free edges of such a type.

4.6 LAYER MADE BY ANGLE-PLY CIRCUMFERENTIAL WINDING

Composite materials with a special spatial structure can be fabricated using the so-called angle-ply circumferential winding process which is a combination of winding and weaving (shown in Fig. 4.80). The schematic of the process is shown in Fig. 4.81. A system of tows is placed on the rotating mandrel and moves in the axial direction. On the way to the mandrel, the tows are overwrapped with fine yarns drawn from the spools placed on the ring which rotates around the system of tows. The resulting

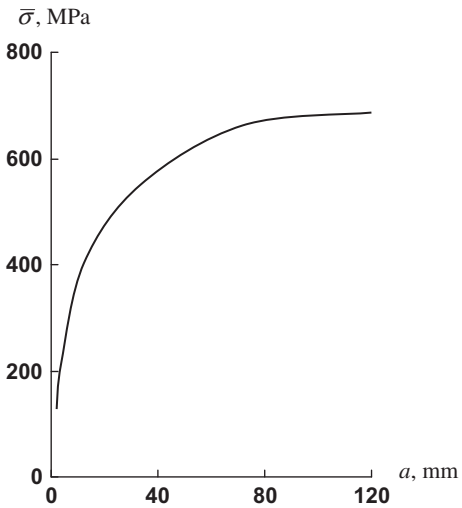


FIGURE 4.79

Experimental dependence of strength of a $\pm 35^\circ$ angle-ply layer on the width of the specimen.

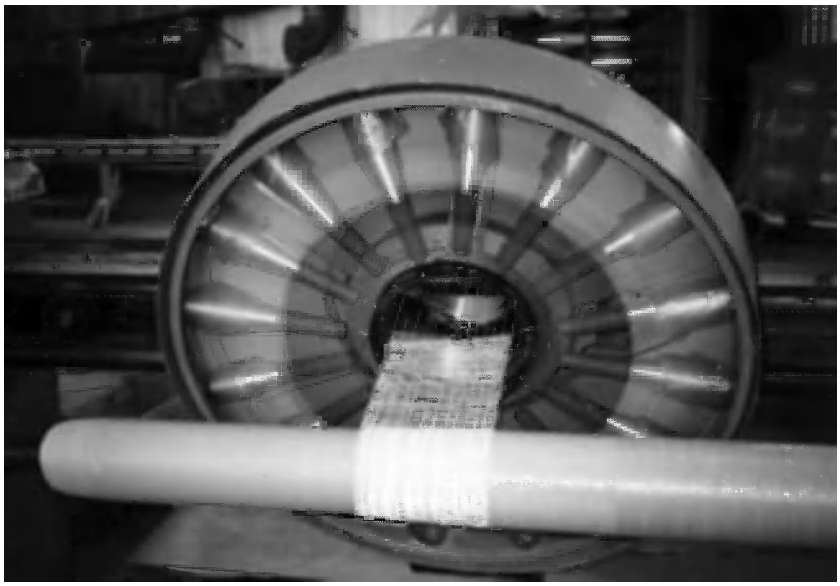


FIGURE 4.80

Angle-ply circumferential winding.

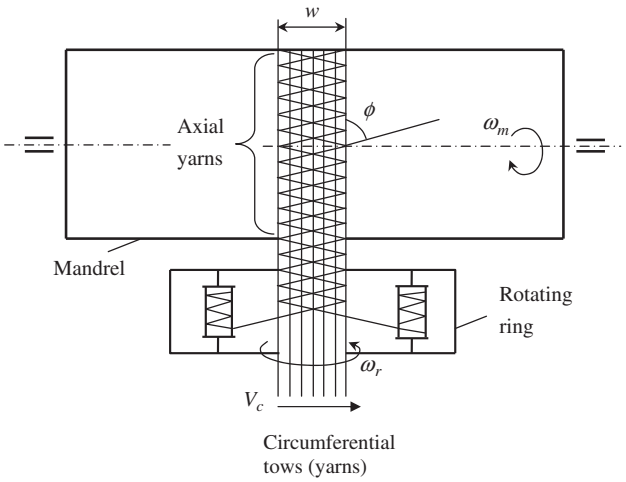


FIGURE 4.81

Parameters of angle-ply circumferential winding.

composite layer is reinforced in four directions. First, it has hoop tows; second, the $\pm\phi$ angle-ply structure is formed by the yarns drawn from the rotating ring; and finally, the yarns also provide through-the-thickness reinforcement of the layer. Composite materials made by angle-ply winding may have at least two applications. First, in composite pipes and pressure vessels made by continuous hoop filament winding (Vasiliev et al., 2003). Second, they can be utilized to fabricate wing and fuselage skin panels for composite aircraft structures using circular mandrels of large diameter or mandrels with rectangular cross-sections. For the panels, the primary tows should be oriented along the major loading direction of the panel. It is important that the panel with the material structure under consideration can be made as thick as required. This is achieved by controlling (reducing) the speed of the carriage V_c (see Fig. 4.81). Additional advantage is the higher resistance of the panel to the delaminations caused by impact. This is achieved due to the inherent through-the-thickness reinforcement introduced in the process of fabrication and the resulting non-laminated structure of the material.

Mechanical properties of the composite material made by angle-ply circumferential winding depend on the material structural parameters and normally could be determined experimentally. However, some theoretical predictions can also be made.

Assume that the circumferential tape (primary system of tows) consists of N_c fibers with cross-sectional areas f_c, modulus of elasticity E_c, and strength under tension $\overline{\sigma}_c$. Then, the total area of the fiber cross-section is

$$A_c = N_c f_c = n_t n_{ft} f_c$$

where n_t is the number of circumferential tows and n_{ft} is the number of fibers in the tow. The effective thickness of the resulting circumferential layer can be found by dividing the area A_c by the tape width w (see Fig. 4.81), i.e.,

$$h_c = \frac{A_c}{w} = \frac{f_c}{w} n_t n_{ft}$$

To find the corresponding parameter for the axial yarns, assume that the mandrel makes r_m rotations per minute, so that the time of one rotation is $t_m = 1/r_m$. Let the ring with n_r spools (see Fig. 4.80) make r_r rotations per minute. Taking into account that the ring places $2n_r$ yarns onto the hoop tape during one rotation, we can find the number of axial fibers N_a that are placed onto the mandrel while it makes this rotation, i.e.,

$$N_a = 2n_r n_{fa} r_r t_m = 2n_r n_{fa} \frac{r_r}{r_m}$$

where n_{fa} is the number of fibers in the yarn. Then, the total area of the fiber cross-sections becomes $A_a = N_a f_a$, where f_a is the area of the fiber cross section, and the effective thickness of the axial layer is

$$h_a = \frac{A_a}{2\pi R} = \frac{n_r n_{fa} r_r f_a}{\pi R r_m}$$

where R is the radius of the mandrel cross-section. Introduce the total effective thickness of the layer h and the normalized thickness as

$$h = h_c + h_a, \quad \overline{h}_c = \frac{h_c}{h}, \quad \overline{h}_a = \frac{h_a}{h}, \quad \overline{h}_c + \overline{h}_a = 1$$

Introducing parameter

$$\lambda = \frac{\overline{h}_a}{\overline{h}_c} = \frac{n_r n_{fa} r_r f_a w}{\pi R r_m f_c n_t n_{ft}}, \tag{4.183}$$

we arrive at

$$\overline{h}_c = \frac{1}{1+\lambda}, \quad \overline{h}_a = \frac{\lambda}{1+\lambda}, \tag{4.184}$$

The axial yarns make angles $\pm\phi$ with the tows' direction. The linear velocity of the circumferential tow is $v_c = \omega_m R$, where ω_m is the mandrel angular velocity $\omega_m = \pi r_m/30$, where, as earlier, r_m is the number of the mandrel rotations per minute. The time, t_r, over which the ring makes one complete rotation, is $t_r = 2\pi/\omega_r$, where $\omega_r = \pi r_r/30$ is the angular velocity of the ring. It follows from Fig. 4.81 that

$$a = v_c t_r = 2\pi R \frac{r_m}{r_r}, \quad \tan\phi = \frac{2w}{a} = \frac{w r_r}{\pi R r_m}$$

Effects of the manufacturing parameters on the mechanical properties of composite material have been studied experimentally. The materials under consideration have been manufactured using the angle-ply circumferential winding process shown in Fig. 4.80. The mandrel radius is $R = 75$ mm and the tape width is $w = 200$ mm. Fiberglass yarns are used to reinforce material in the circumferential and axial directions, so that $n_{fa} = n_{ft}$ and $f_a = f_c$. Correspondingly, the parameter λ in Eq. (4.183) becomes

$$\lambda = \frac{n_r r_r w}{\pi R r_m n_t}$$

The manufacturing parameters of five different versions of the fabrication process are presented in Table 4.4. Experimental mechanical properties are listed in Table 4.5. Dependencies of E_c and E_a, and $\overline{\sigma}_c$ and $\overline{\sigma}_a$ on the relative effective thickness of circumferential yarns $\overline{h}_c$ (see

TABLE 4.4 Manufacturing parameters of the process.

Process parameters	Process version				
	1	2	3	4	5
Number of circumferential yarns, n_t	154	132	132	132	132
Number of spools on the ring, n_r	5	7	9	3	11
Mandrel rotational speed, r_m (rpm)	31	34	33	10	32
Ring rotational speed, r_r (rpm)	220	220	220	220	220
Parameter λ	0.196	0.291	0.386	0.463	0.487
$\overline{h}_c$	0.836	0.774	0.721	0.683	0.673
$\overline{h}_a$	0.164	0.226	0.279	0.317	0.327
ϕ°	80.6	79.7	80	87.2	80.3

TABLE 4.5 Mechanical properties of the composite material.

Property	Process version				
	1	2	3	4	5
Circumferential modulus, E_c (GPa)	39.5	36.3	33.4	30.1	29.6
Axial modulus, E_a (GPa)	9.8	11.7	16.8	19.5	20.1
Poisson's ratio, v_{ac}	0.15	0.13	0.13	0.11	0.11
Circumferential strength, $\overline{\sigma}_c$ (MPa)	1070	1010	960	930	900
Axial strength, $\overline{\sigma}_a$ (MPa)	290	350	390	430	440

Eq. (4.184)) are given in Figs. 4.82 and 4.83. It follows from the graphs that the sums $E_c + E_a = E$ and $\overline{\sigma}_c + \overline{\sigma}_a = \overline{\sigma}$ do not depend on the material structure. For the material under study, $E = 49.5$ GPa and $\overline{\sigma} = 1350$ MPa. Compare these characteristics with the corresponding properties of the unidirectional composite. The glass fibers used to fabricate the material with properties as per Figs. 4.82 and 4.83 have the following modulus of elasticity and strength:

$$E_f = 85 \text{ GPa}, \quad \overline{\sigma}_f = 2350 \text{ MPa}$$

The fiber volume fraction in the composite material made by the angle-ply circumferential winding is usually lower than that typical for conventional composites fabricated by winding. For the material

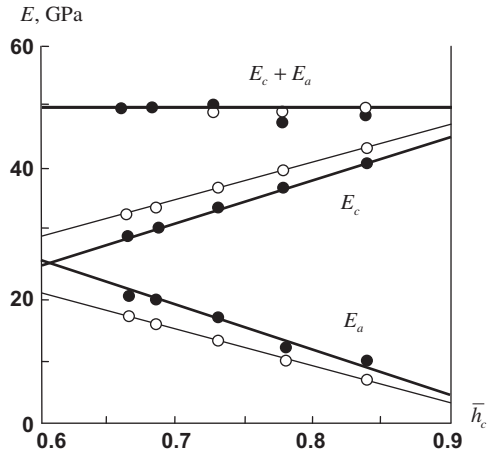


FIGURE 4.82

Dependencies of material moduli on parameter $\overline{h}_c$, —●— experiment, —○— analysis.

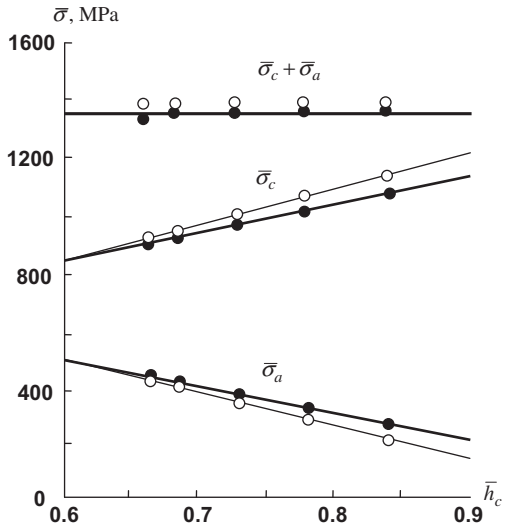


FIGURE 4.83

Dependencies of material tensile strength on parameter $\overline{h}_c$, —●— experiment, —○— analysis.

under consideration, it is $v_f = 0.59$. The products $E_f v_f = 50.15$ GPa and $\overline{\sigma}_f v_f = 1386$ MPa are slightly higher than E (by 1.3%) and $\overline{\sigma}$ (by 2.7%), respectively. This means that angle-ply circumferential winding, as opposed to weaving, allows us to utilize completely the original fiber stiffness and strength.

To evaluate approximately the stiffness and strength of the material under consideration, assume that it consists of two layers of fibers with relative thicknesses $\overline{h}_c$ and $\overline{h}_a$ in Eqs. (4.184) and apply the approach described in Sections 4.4 and 4.5. Neglecting the contribution of the matrix, we can present the stiffness coefficients of the layers using Eqs. (4.72), i.e.,

$$A_{11}^c = \upsilon_f E_f^c, \qquad A_{12}^c = A_{22}^c = A_{33}^c = 0$$
$$A_{11}^a = \upsilon_f E_f^a \cos^4\phi, \quad A_{12}^a = A_{33}^a = \upsilon_f E_f^a \sin^2\phi \cos^2\phi, \quad A_{22}^a = \upsilon_f E_f^a \sin^4\phi$$

Here, υ_f is the fiber volume fraction which can be found only experimentally and E_f^c and E_f^a are the fiber moduli of the circumferential and axial yarns. The stiffness coefficients of the material can be calculated using Eqs. (4.114), i.e.,

$$A_{11} = \upsilon_f \left(E_f^c \overline{h}_c + E_f^a \overline{h}_a \cos^4\phi \right)$$
$$A_{12} = A_{33} = \upsilon_f E_f^a \sin^2\phi \cos^2\phi$$
$$A_{22} = \upsilon_f E_f^a \sin^4\phi$$

whereas the elastic constants can be found from Eqs. (4.116)

$$E_c = A_{11} - \frac{A_{12}^2}{A_{22}}, \qquad E_a = A_{22} - \frac{A_{12}^2}{A_{11}}, \qquad G_{ca} = A_{33}$$
$$\upsilon_{ca} = \frac{A_{12}}{A_{11}}, \qquad \upsilon_{ac} = \frac{A_{12}}{A_{22}} \tag{4.185}$$

For $\upsilon_f = 0.59$, the results of the calculations are presented in Fig. 4.82 and qualitatively correlate with the experimental data.

To predict the strength, apply Eqs. (4.69) in conjunction with Hooke's law to find the stresses in the fibers

$$\sigma_f^c = E_f^c \varepsilon_c, \qquad \sigma_f^a = E_f^a \left(\varepsilon_c \cos^2\phi + \varepsilon_a \sin^2\phi \right) \tag{4.186}$$

The strains, ε_c and ε_a, specify the corresponding stresses

$$\sigma_c = \overline{E}_c (\varepsilon_c + \upsilon_{ca} \varepsilon_a), \qquad \sigma_a = \overline{E}_a (\varepsilon_a + \upsilon_{ac} \varepsilon_c) \tag{4.187}$$

where $\overline{E} = E/(1 - \upsilon_{ca}\upsilon_{ac})$, whereas E and ν are given by Eqs. (4.185). Substituting Eqs. (4.186) into Eqs. (4.187), we arrive at

$$\sigma_c = \overline{E}_c \left[\frac{\sigma_f^c}{E_f^c} \left(1 - \upsilon_{ca} \operatorname{cotan}^2 \phi \right) + \frac{\upsilon_{ca}}{\sin^2\phi} \frac{\sigma_f^a}{E_f^a} \right]$$

$$\sigma_a = \overline{E}_a \left[\frac{1}{\sin^2\phi} \frac{\sigma_f^a}{E_f^a} + \frac{\sigma_f^c}{E_f^c} \left(\upsilon_{ac} - \operatorname{cotan}^2 \phi \right) \right]$$

For the ultimate state, taking $\sigma_f^c = \overline{\sigma}_f^c$ and $\sigma_f^a = \overline{\sigma}_f^a$, we can find material strength, i.e., $\overline{\sigma}_c$ and $\overline{\sigma}_a$. The results of the calculations are presented in Fig. 4.83 and are in fair agreement with experimental data.

4.7 FABRIC LAYERS

Textile preforming plays an important role in composite technology, providing glass, aramid, carbon (see Fig. 4.84), and hybrid fabrics that are widely used as reinforcing materials. The main advantages of woven composites are their cost efficiency and high processability, particularly in lay-up manufacturing of large-scale structures (see Figs. 4.85 and 4.86). However, on the other hand, processing of fibers and their bending in the process of weaving results in substantial reduction of material strength and stiffness. As can be seen in Fig. 4.87, in which a typical woven structure is shown, the warp (lengthwise) and fill (crosswise) yarns forming the fabric make angle $\alpha \geq 0$ with the plane of the fabric layer.

To demonstrate how this angle influences material stiffness, consider the tension of the structure shown in Fig. 4.87 in the warp direction. The apparent modulus of elasticity can be expressed as

$$E_{\mathrm{a}}A_{\mathrm{a}} = E_f A_f + E_w A_w \tag{4.188}$$

where $A_{\mathrm{a}} = h(2t_1 + t_2)$ is the apparent cross-sectional area and

$$A_f = \frac{h}{2}(2t_1 + t_2), \quad A_w = \frac{h}{4}(4t_1 + t_2)$$

are the areas of the fill and warp yarns in the cross section. Substitution into Eq. (4.188) yields

$$E_{\mathrm{a}} = \frac{1}{2}\left[E_f + \frac{E_w(4t_1 + t_2)}{2(2t_1 + t_2)}\right]$$

Since the fibers of the fill yarns are orthogonal to the loading direction, we can take $E_f = E_2$, where E_2 is the transverse modulus of a unidirectional composite. The compliance of the warp yarn can be

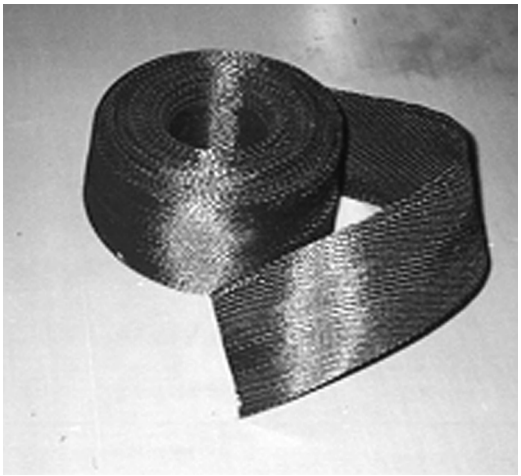


FIGURE 4.84

A carbon fabric tape.



FIGURE 4.85

A composite hull of a boat made of fiberglass fabric by lay-up method.

Courtesy of CRISM.

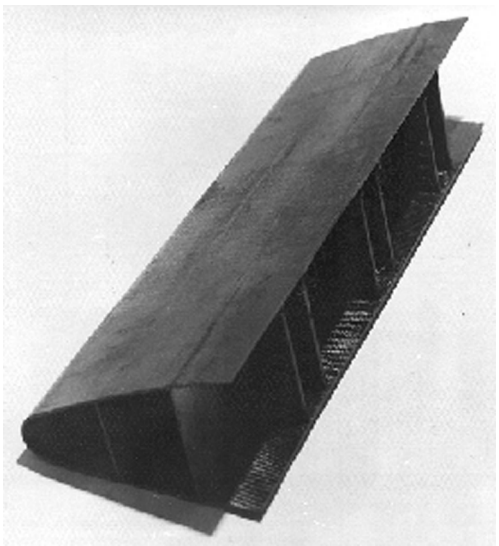


FIGURE 4.86

A composite leading edge of an aeroplane wing made of carbon fabric by lay-up method.

Courtesy of CRISM.

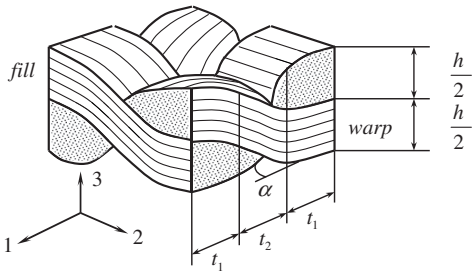


FIGURE 4.87

Unit cell of a fabric structure.

decomposed into two parts corresponding to t_1 and t_2 in Fig. 4.87, i.e.,

$$\frac{2t_1 + t_2}{E_w} = \frac{2t_1}{E_1} + \frac{t_2}{E_\alpha}$$

where E_1 is the longitudinal modulus of a unidirectional composite, whereas E_α can be determined with the aid of the first equation of Eqs. (4.76) if we change ϕ for α, i.e.,

$$\frac{1}{E_\alpha} = \frac{\cos^4\alpha}{E_1} + \frac{\sin^4\alpha}{E_2} + \left(\frac{1}{G_{12}} - \frac{2\nu_{21}}{E_1}\right)\sin^2\alpha\cos^2\alpha \tag{4.189}$$

The final result is as follows

$$E_a = \frac{E_2}{2} + \frac{E_1(4t_1 + t_2)}{4\left\{2t_1 + t_2\left[\cos^4\alpha + \frac{E_1}{E_2}\sin^4\alpha + \left(\frac{E_1}{G_{12}} - 2\nu_{21}\right)\sin^2\alpha\cos^2\alpha\right]\right\}} \tag{4.190}$$

For example, consider a glass fabric with the following parameters: $\alpha = 12^\circ$, $t_2 = 2t_1$. Taking elastic constants for a unidirectional material from Table 3.5, we get $E_a = 23.5$ GPa for the fabric composite. For comparison, a cross-ply $[0^\circ/90^\circ]$ laminate made of the same material has $E = 36.5$ GPa. Thus, the modulus of a woven structure is lower by 37% than the modulus of the same material reinforced with straight fibers. Typical mechanical characteristics of fabric composites are listed in Table 4.6.

The stiffness and strength of fabric composites depend not only on the yarns and matrix properties, but on the material structural parameters, i.e., on fabric count and weave. The fabric count specifies the number of warp and fill yarns per inch (25.4 mm), whereas the weave determines how the warp and the fill yarns are interlaced. Typical weave patterns are shown in Fig. 4.88 and include plain, twill, and triaxial woven fabrics. In the plain weave (see Fig. 4.88a), which is the most common and the oldest, the warp yarn is repeatedly woven over the fill yarn and under the next fill yarn. In the twill weave, the warp yarn passes over and under two or more fill yarns (as in Fig. 4.88b and c) in a regular way.

Being formed from one and the same type of yarns, plain and twill weaves provide approximately the same strength and stiffness of the fabric in the warp and the fill directions. Typical stress-strain diagrams for a fiberglass fabric composite of such a type are presented in Fig. 4.89. As can be seen, this material demonstrates relatively low stiffness and strength under tension at an angle of 45°

TABLE 4.6 Typical properties of fabric composites.

Property	Glass fabric-epoxy	Aramid fabric-epoxy	Carbon fabric-epoxy
Fiber volume fraction	0.43	0.46	0.45
Density (g/cm^3)	1.85	1.25	1.40
Longitudinal Modulus, GPa	26	34	70
Transverse modulus (GPa)	22	34	70
Shear modulus (GPa)	7.2	5.6	5.8
Poisson's ratio	0.13	0.15	0.09
Longitudinal tensile strength (MPa)	400	600	860
Longitudinal compressive strength (MPa)	350	150	560
Transverse tensile strength (MPa)	380	500	850
Transverse compressive strength (MPa)	280	150	560
In-plane shear strength (MPa)	45	44	150

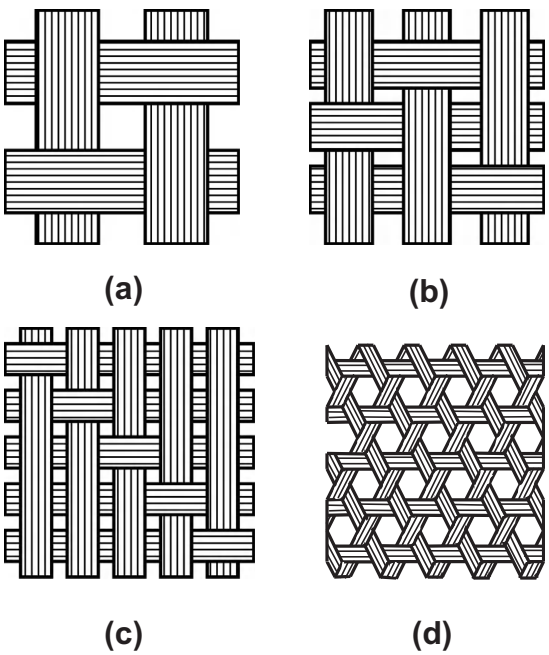


FIGURE 4.88

Plain (a), twill (b) and (c), and triaxial (d) woven fabrics.

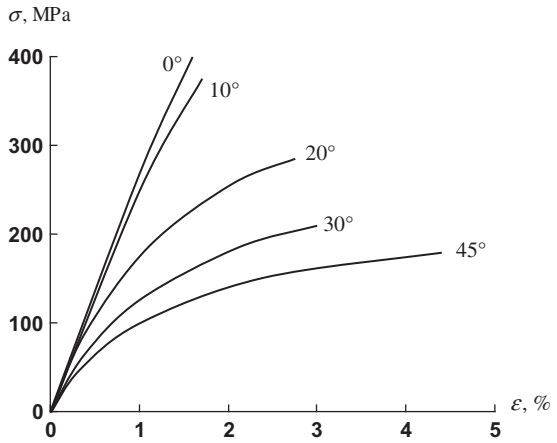


FIGURE 4.89

Stress-strain curves for fiberglass fabric composite loaded in tension at different angles with respect to the warp direction.

with respect to the warp or fill directions. To improve these properties, multiaxial woven fabrics, one of which is shown in Fig. 4.88d, can be used.

Fabric materials whose properties are closer to those of unidirectional composites are made by weaving a greater number of larger yarns in the longitudinal direction and fewer and smaller yarns in the orthogonal direction. Such a weave is called unidirectional. It provides materials with high stiffness and strength in one direction, which is specific for unidirectional composites and the high processability typical of fabric composites.

Being fabricated as planar structures, fabrics can be shaped on shallow surfaces using the material's high stretching capability under tension at 45° to the yarns' directions. Many more possibilities for such shaping are provided by the implementation of knitted fabrics whose strain to failure exceeds 100%. Moreover, knitting allows us to shape the fibrous preform in accordance with the shape of the future composite part. There exist different knitting patterns, some of which are shown in Fig. 4.90.

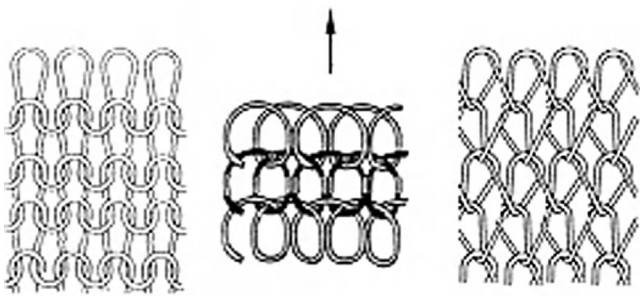


FIGURE 4.90

Typical knitted structures.

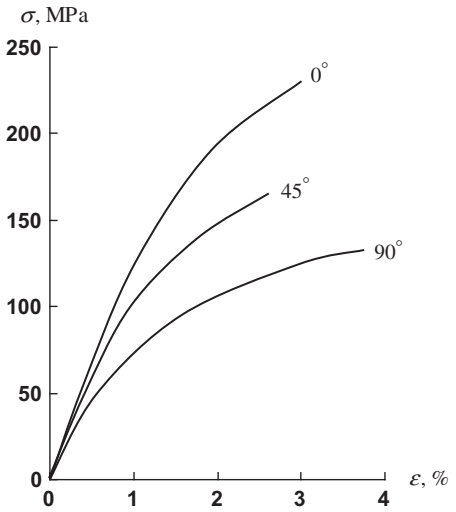


FIGURE 4.91

Typical stress-strain curves for fiberglass knitted composites loaded in tension at different angles with respect to direction indicated by the arrow in Fig. 4.90.

Relatively high curvature of the yarns in knitted fabrics, and possible fiber breakage in the process of knitting, result in materials whose strength and stiffness are less than those of woven fabric composites but whose processability is better and cost is lower. Typical stress-strain diagrams for composites reinforced by knitted fabrics are presented in Fig. 4.91.

Material properties close to those of woven composites are provided by braided structures which, being usually tubular in shape, are fabricated by mutual intertwining, or twisting of yarns about each other. Typical braided structures are shown in Fig. 4.92. The biaxial braided fabrics in Fig. 4.92 can

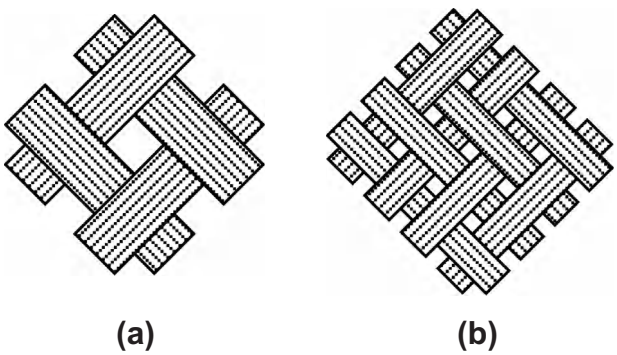


FIGURE 4.92

Diamond (a) and regular (b) braided fabric structures.

incorporate longitudinal yarns, forming a triaxial braid whose structure is similar to that shown in Fig. 4.88d. Braided preforms are characterized with very high processability providing near net-shape manufacturing of tubes and profiles with various cross-sectional shapes.

Although microstructural models of the type shown in Fig. 4.87 which lead to equations similar to Eq. (4.190) have been developed to predict the stiffness and even strength characteristics of fabric composites (e.g., Skudra et al., 1989), for practical design and analysis, these characteristics are usually determined by experimental methods. The elastic constants entering the constitutive equations written in principal material coordinates, e.g., Eqs. (4.55), are determined by testing strips cut out of fabric composite plates at different angles with respect to the orthotropy axes. The 0 and 90° specimens are used to determine moduli of elasticity E_1 and E_2 and Poisson's ratios ν_{12}, ν_{21} (or parameters for nonlinear stress-strain curves), whereas the in-plane shear stiffness can be obtained with the aid of off-axis tension described in Section 4.3.1. For fabric composites, the elastic constants usually satisfy conditions in Eqs. (4.85) and (4.86), and there exists the angle ϕ specified by Eq. (4.84) such that off-axis tension under this angle is not accompanied by shear-extension coupling.

Since Eq. (4.84) specifying ϕ includes the shear modulus G_{12}, which is not known, we can transform the results presented in Section 4.3.1. Using Eqs. (4.76) and assuming that there is no shear-extension coupling $(\eta_{x,xy} = 0)$, we can write the following equations

$$\begin{aligned}
\frac{1}{E_x} &= \frac{1+\nu_{21}}{E_1}\cos^4\phi + \frac{1+\nu_{12}}{E_2}\sin^4\phi - \frac{\nu_{21}}{E_1} + \frac{1}{G_{12}}\sin^2\phi\cos^2\phi \\
\frac{\nu_{yx}}{E_x} &= \frac{\nu_{21}}{E_1} - \left(\frac{1+\nu_{21}}{E_1} + \frac{1+\nu_{12}}{E_2} - \frac{1}{G_{12}}\right)\sin^2\phi\cos^2\phi \\
\frac{1+\nu_{21}}{E_1}\cos^2\phi &- \frac{1+\nu_{12}}{E_2}\sin^2\phi - \frac{1}{2G_{12}}\cos 2\phi = 0
\end{aligned} \tag{4.191}$$

Summing up the first two of these equations, we get

$$\frac{1+\nu_{yx}}{E_x} = \left(\frac{1+\nu_{21}}{E_1}\cos^2\phi - \frac{1+\nu_{12}}{E_2}\sin^2\phi\right)\cos 2\phi + \frac{2}{G_{12}}\sin^2\phi\cos^2\phi$$

Using the third equation, we arrive at the following remarkable result

$$G_{12} = \frac{E_x}{2(1+\nu_{yx})} \tag{4.192}$$

similar to the corresponding formula for isotropic materials, Eq. (2.57). It should be emphasized that Eq. (4.192) is valid for off-axis tension in the x direction making some special angle ϕ with the principal material axis 1. This angle is given by Eq. (4.84). Another form of this expression follows from the last equation of Eqs. (4.191) and (4.192), i.e.,

$$\sin^2\phi = \frac{\dfrac{1+\nu_{yx}}{E_x} - \dfrac{1+\nu_{21}}{E_1}}{2\dfrac{1+\nu_{yx}}{E_x} - \dfrac{1+\nu_{21}}{E_1} - \dfrac{1+\nu_{12}}{E_2}} \tag{4.193}$$

For fabric composites whose stiffness in the warp and the fill directions is the same $(E_1 = E_2)$, Eq. (4.193) yields $\phi = 45°$.

4.8 LATTICE LAYER

A layer with a relatively low density and high stiffness can be obtained with a lattice structure which can be made by a winding modified in such a way that the tapes are laid onto preceding tapes and not beside them, as in conventional filament winding (see Fig. 4.93). The lattice layer can be the single layer of the structure as in Fig. 4.94, or can be combined with a skin as in Fig. 4.95. As a rule, lattice structures have the form of cylindrical or conical shells in which the lattice layer is formed with two systems of ribs: a symmetric system of helical ribs and a system of circumferential ribs (see Figs. 4.94 and 4.95). However, there exist lattice structures with three systems of ribs, as shown in Fig. 4.96.

In general, a lattice layer can consist of k symmetric systems of ribs making angles $\pm\phi_j (j = 1,\ 2,\ 3 \ldots k)$ with the x-axis and having the geometric parameters shown in Fig. 4.97. Particularly, the lattice layer presented in this figure has $k = 2,\ \phi_1 = \phi,\ \phi_2 = 90^\circ$.

Since the lattice structure is often formed with dense and regular systems of ribs, the ribs can be smeared over the layer surface when modeled, which is simulated with a continuous layer having some effective (apparent) stiffness. Taking into account that the ribs work in their axial directions only, neglecting the ribs' torsion and bending in the plane of the lattice layer, and using Eqs. (4.72), we get

$$\begin{aligned} A_{11} &= \sum_{j=1}^{k} B_j \cos^4\phi_j, \quad A_{22} = \sum_{j=1}^{k} B_j \sin^4\phi_j, \\ A_{12} &= A_{21} = A_{44} = \sum_{j=1}^{k} B_j \sin^2\phi_j \cos^2\phi_j, \\ A_{44} &= \sum_{j=1}^{k} C_j \cos^2\phi_j, \quad A_{55} = \sum_{j=1}^{k} C_j \sin^2\phi_j \end{aligned} \tag{4.194}$$

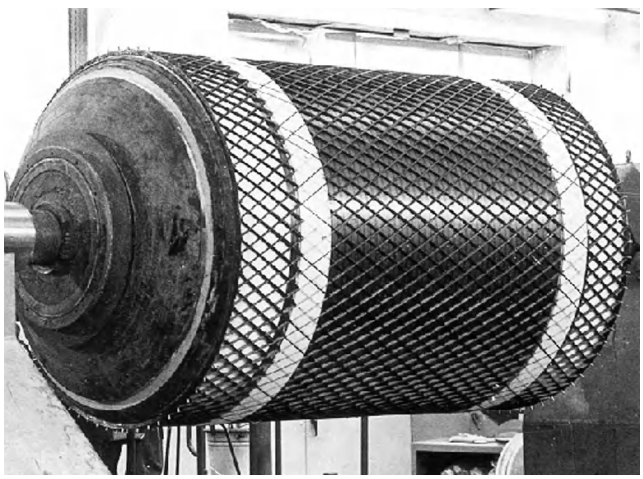


FIGURE 4.93

Winding of a lattice layer.

Courtesy of CRISM.

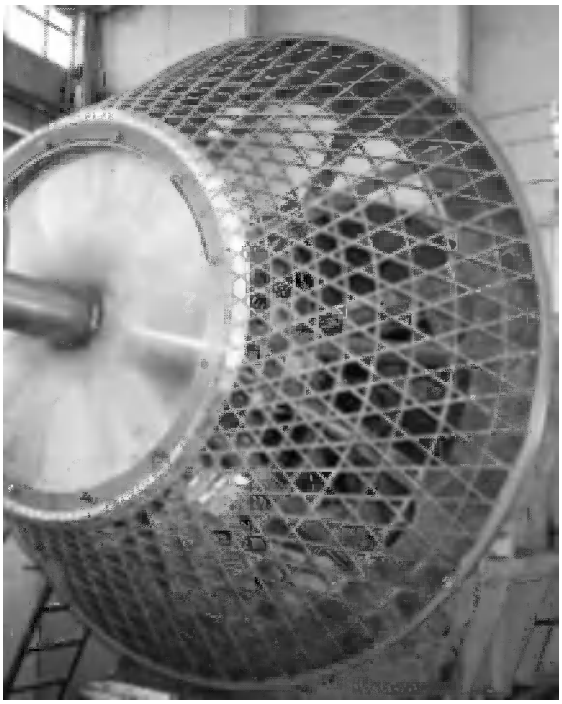


FIGURE 4.94

Carbon-epoxy lattice spacecraft adapter.

Courtesy of CRISM.

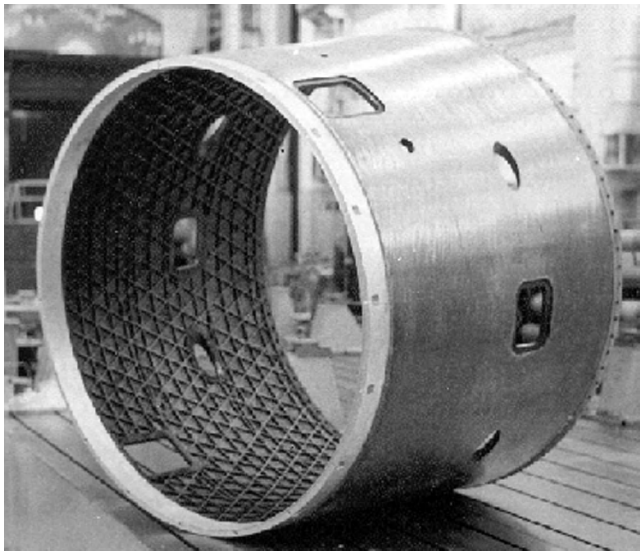


FIGURE 4.95

Interstage composite lattice structure.

Courtesy of CRISM.

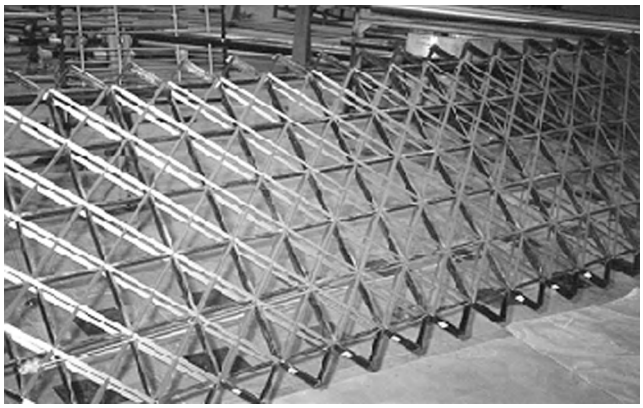


FIGURE 4.96

A composite lattice shear web structure.

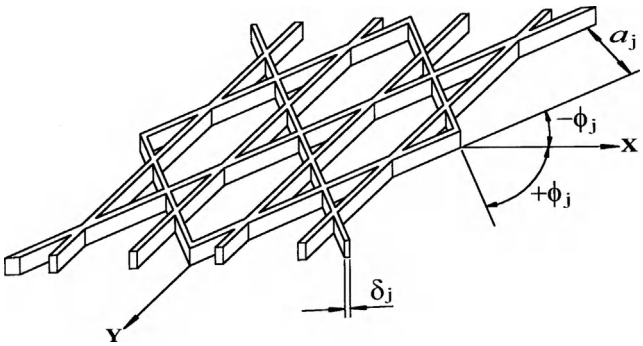


FIGURE 4.97

Geometric parameters of a lattice structure.

Here, $B_j = E_j\delta_j/a_j$ and $C_j = G_j\delta_j/a_j$, where E_j and G_j are the modulus of elasticity and the shear modulus of the ribs' materials, δ_j are the ribs' widths, and a_j are the ribs' spacings (see Figure 4.97).

4.9 SPATIALLY REINFORCED LAYERS AND BULK MATERIALS

The layers considered in the previous sections and formed of unidirectionally reinforced plies and tapes (Sections 4.2–4.5 and 4.8) or fabrics reinforced in the layer plane (Section 4.7) suffer from a serious shortcoming: their transverse (normal to the layer plane) stiffness and strength are substantially lower than the corresponding in-plane characteristics. To improve the material properties under tension or compression in the z direction and in shear in the xz- and the yz-planes (see, e.g., Fig. 4.18), the material should be additionally reinforced with fibers or yarns directed along the z-axis or making some angles (less than a right angle) with this axis.

A simple and natural way to gain such triaxial reinforcement is provided by the implementation of three-dimensionally woven or braided fabrics. Three-dimensional weaving or braiding is a variant of the corresponding planar process wherein some yarns are going in the thickness direction. An alternative method involves assembling elementary fabric layers or unidirectional plies into a three-dimensionally reinforced structure by sewing or stitching. Depending on the size of the additional yarn and frequency of sewing or stitching, the transverse mechanical properties of the two-dimensionally reinforced composite can be improved to a greater or lesser extent. A third way is associated with the introduction of composite or metal pins parallel to the z-axis that can be inserted in the material before or after it is cured. A similar effect can be achieved by so-called needle punching. The needles puncture the fabric, break the fibers that compose the yarns, and direct the broken fibers through the layer thickness. Short fibers (or whiskers) may also be introduced into the matrix with which the fabrics or the systems of fibers are impregnated.

Another class of spatially reinforced composites, used mainly in carbon-carbon technology, is formed by bulk materials multi-dimensionally reinforced with fine rectilinear yarns composed of carbon fibers bound with a polymeric or carbon matrix. The basic structural element of these materials is a parallelepiped, shown in Fig. 4.98. The simplest spatial structure is the so-called 3D (three-dimensionally reinforced), in which reinforcing elements are placed along the ribs AA_1, AB, and AD of the basic parallelepiped in Fig. 4.98. This structure is shown in Fig. 4.99 (Vasiliev and Tarnopol'skii, 1990). A more complicated 4D structure with reinforcing elements directed along the diagonals AC_1, A_1C, BD_1, and B_1D (see Fig. 4.98) is shown in Fig. 4.100 (Tarnopol'skii et al., 1987). An example of this structure is presented in Fig. 1.22. A cross section of a 5D structure reinforced along diagonals AD_1 and A_1D and ribs AA_1, AB, and AD is shown in Fig. 4.101 (Vasiliev and Tarnopol'skii, 1990). There exist structures with a greater number of reinforcing directions. For example, combination of a 4D structure (Fig. 4.100) with reinforcements along the ribs AB and AD (see Fig. 4.98)

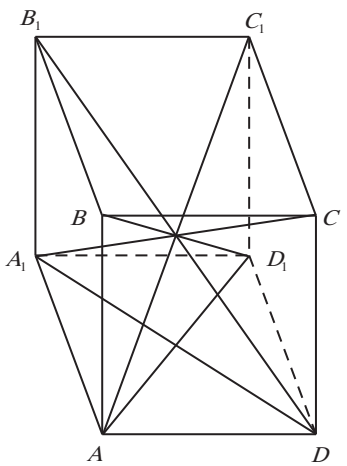


FIGURE 4.98

The basic structural element of multi-dimensionally reinforced materials.

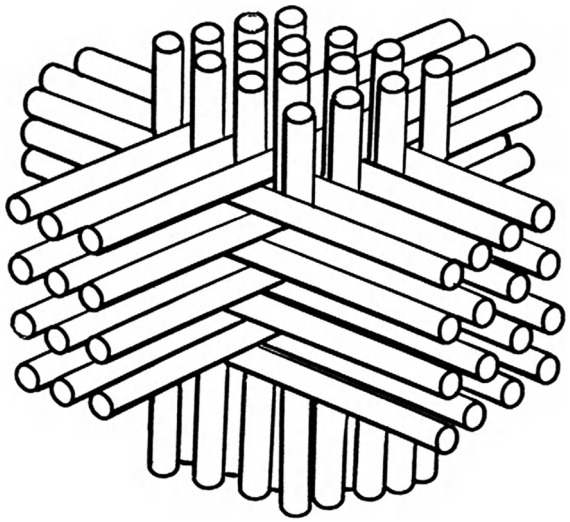


FIGURE 4.99

3D spatially reinforced structure.

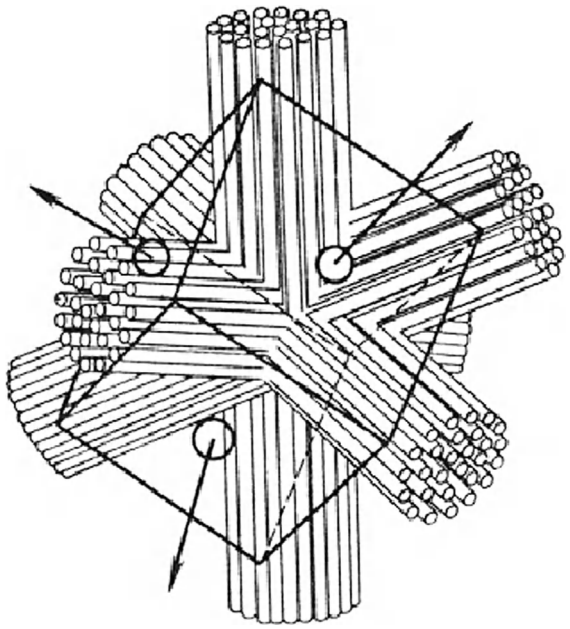


FIGURE 4.100

4D spatially reinforced structure.

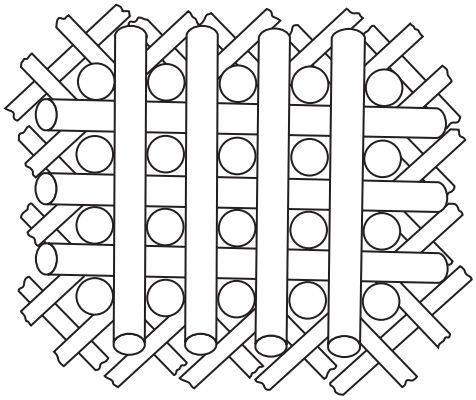


FIGURE 4.101

Cross section of a 5D spatially reinforced structure.

results in a 6D structure; addition of reinforcements in the direction of the rib AA_1 gives a 7D structure; and so on, up to 13D, which is the most complicated of the spatial structures under discussion.

The mechanical properties of multi-dimensional composite structures can be qualitatively predicted with the microstructural models discussed, e.g., by Tarnopol'skii et al. (1992). However, for practical applications these characteristics are usually obtained by experimental methods. Being orthotropic in the global coordinates of the structure x, y, and z, spatially reinforced composites are described within the framework of a phenomenological model, ignoring their microstructure by three-dimensional constitutive equations analogous to Eqs. (4.53) or Eqs. (4.54), in which 1 should be changed for x, 2 for y, and 3 for z. These equations include nine independent elastic constants. Stiffness coefficients in the basic plane, i.e., E_x, E_y, G_{xy}, and ν_{xy}, are determined using traditional tests developed for unidirectional and fabric composites as discussed in Sections 3.4, 4.2, and 4.7. The transverse modulus E_z and the corresponding Poisson's ratios ν_{xz} and ν_{yz} can be determined using material compression in the z direction. Transverse shear moduli G_{xz} and G_{yz} can be calculated using the results of a three-point beam bending test shown in Fig. 4.102. A specimen cut out of the material is loaded with force P, and the deflection at the central point, w, is measured. According to the theory of composite beams (Vasiliev, 1993),

$$w = \frac{Pl^3}{4bh^3E_x}\left(1 + \frac{h^2E_x}{l^2G_{xz}}\right).$$

For given P, the corresponding w, and modulus E_x (or E_y), we can calculate G_{xz} (or G_{yz}). It should be noted that for reliable calculation the beam should be rather short, because for high ratios of l/h the second term in parenthesis is small in comparison with unity.

The last spatially reinforced structure that is considered here is formed by a unidirectional composite material whose principal material axes 1, 2, and 3 make some angles with the global structural axes x, y, and z (see Fig. 4.103). In the principal material coordinates, the constitutive equations have the form of Eqs. (4.53) or Eqs. (4.54). Introducing directional cosines l_{xi}, l_{yi}, and l_{zi} which are cosines of the angles that the i-axis $(i = 1, 2, 3)$ makes with axes x, y, and z, respectively, applying Eqs. (2.8), (2.9), and (2.31) to transform stresses and strains in coordinates 1, 2, and 3 to

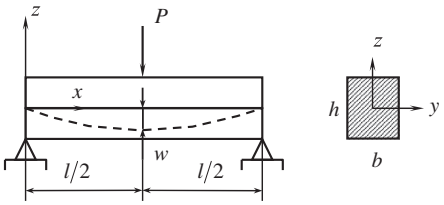


FIGURE 4.102

Three-point bending test.

stresses and strains referred to coordinates x, y, and z, and using the procedure described in Section 4.3.1, we finally arrive at the following constitutive equations in the global structural coordinate frame

$$\begin{Bmatrix} \sigma_x \\ \sigma_y \\ \sigma_z \\ \tau_{xy} \\ \tau_{xz} \\ \tau_{yz} \end{Bmatrix} = [S] \begin{Bmatrix} \varepsilon_x \\ \varepsilon_y \\ \varepsilon_z \\ \gamma_{xy} \\ \gamma_{xz} \\ \gamma_{yz} \end{Bmatrix} \tag{4.195}$$

in which

$$[S] = \begin{bmatrix} S_{1111} & S_{1122} & S_{1133} & S_{1112} & S_{1113} & S_{1123} \\ & S_{2222} & S_{2233} & S_{2212} & S_{2213} & S_{2223} \\ & & S_{3333} & S_{3312} & S_{3313} & S_{3323} \\ & & & S_{1212} & S_{1213} & S_{1223} \\ & sym & & & S_{1313} & S_{1323} \\ & & & & & S_{2323} \end{bmatrix}$$

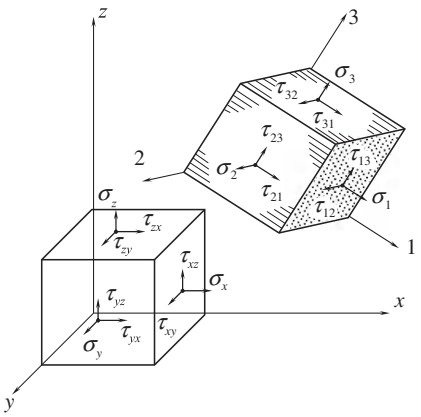


FIGURE 4.103

Material elements referred to the global structural coordinate frame *x, y, z* and to the principal material axes 1, 2, 3.

is the stiffness matrix where

$$
\begin{aligned}
S_{1111} &= A_1 l_{x1}^4 + A_2 l_{x2}^4 + A_3 l_{x3}^4 + 2A_{112} l_{x1}^2 l_{x2}^2 + 2A_{113} l_{x1}^2 l_{x3}^2 + 2A_{223} l_{x2}^2 l_{x3}^2 \qquad (1,\ 2,\ 3)\\
S_{1122} &= A_1 l_{x1}^2 l_{y1}^2 + A_2 l_{x2}^2 l_{y2}^2 + A_3 l_{x3}^2 l_{y3}^2 + A_1 \mu_{12}\left(l_{x1}^2 l_{y2}^2 + l_{x2}^2 l_{y1}^2\right) + A_1 \mu_{13}\left(l_{x1}^2 l_{y3}^2 + l_{x3}^2 l_{y1}^2\right)\\
&\quad + A_2 \mu_{23}\left(l_{x2}^2 l_{y3}^2 + l_{x3}^2 l_{y3}^2\right) + 4(G_{12} l_{x1} l_{x2} l_{y1} l_{y2} + G_{13} l_{x1} l_{x3} l_{y1} l_{y3}\\
&\quad + G_{23} l_{x2} l_{x3} l_{y2} l_{y3}) \qquad (1,\ 2,\ 3)\\
S_{1112} &= A_1 l_{x1}^3 l_{y1} + A_2 l_{x2}^3 l_{y2} + A_3 l_{x3}^3 l_{y3} + A_{112}\left(l_{x1} l_{y2} + l_{x2} l_{y1}\right) l_{x1} l_x^2 + A_{113}\left(l_{x1} l_{y3} + l_{x3} l_{y1}\right) l_{x1} l_{x3}\\
&\quad + A_{223}\left(l_{x2} l_{y3} + l_{x3} l_{y2}\right) l_{x2} l_{x3} \qquad (1,\ 2,\ 3)\\
S_{1113} &= A_1 l_{x3}^3 l_{z1} + A_2 l_{x2}^3 l_{z2} + A_3 l_{x3}^3 l_{z3} + A_{112}\left(l_{x1} l_{z2} + l_{x2} l_{z1}\right) l_{x1} l_{x2} + A_{113}\left(l_{x1} l_{z2} + l_{x3} l_{z1}\right) l_{x1} l_{x3}\\
&\quad + A_{223}\left(l_{x2} l_{z3} + l_{x3} l_{z2}\right) l_{x2} l_{x3} \qquad (1,\ 2,\ 3)\\
S_{1123} &= A_1 l_{x1}^2 l_{y1} l_{z1} + A_2 l_{x2}^2 l_{y2} l_{z2} + A_3 l_{x3}^2 l_{y3} l_{z3} + A_1 \mu_{12}\left(l_{x1}^2 l_{y2} l_{z2} + l_{x2}^2 l_{y1} l_{z1}\right) + A_1 \mu_{13}\left(l_{x1}^2 l_{y3} l_{z3}\right.\\
&\quad \left. + l_{x3}^2 l_{y1} l_{z1}\right) + A_2 \mu_{23}\left(l_{x2}^2 l_{y3} l_{z3} + l_{x3}^2 l_{y2} l_{z2}\right) + 2\left[G_{12}\left(l_{y1} l_{z2} + l_{z1} l_{y2}\right) l_{x1} l_{x2} + G_{13}\left(l_{y1} l_{z2}\right.\right.\\
&\quad \left.\left. + l_{z1} l_{y2}\right) l_{x1} l_{x3} + G_{23}\left(l_{y3} l_{z2} + l_{y2} l_{z3}\right) l_{x2} l_{x3}\right] \qquad (1,\ 2,\ 3)\\
S_{1212} &= A_1 l_{x1}^2 l_{y1}^2 + A_2 l_{x2}^2 l_{y2}^2 + A_3 l_{x3}^2 l_{y3}^2\\
&\quad + 2\left(A_1 \mu_{12} l_{x1} l_{x2} l_{y1} l_{y2} + A_1 \mu_{13} l_{x1} l_{x3} l_{y1} l_{y3} + A_2 \mu_{23} l_{x2} l_{x3} l_{y2} l_{y3}\right)\\
&\quad + G_{12}\left(l_{x1} l_{y2} + l_{x2} l_{y1}\right)^2 + G_{13}\left(l_{x1} l_{y3} + l_{x3} l_{y1}\right)^2 + G_{23}\left(l_{x2} l_{y3} + l_{x3} l_{y2}\right)^2 \qquad (1,\ 2,\ 3)
\end{aligned}
\tag{4.196}
$$

$$
\begin{aligned}
S_{1213} &= A_1 l_{x1}^2 l_{y1} l_{z1} + A_2 l_{x2}^2 l_{y2} l_{z2} + A_3 l_{x3}^2 l_{y3} l_{z3}\\
&\quad + A_1 \mu_{12}\left(l_{y1} l_{z2} + l_{y2} l_{z1}\right) l_{x1} l_{x2} + A_1 \mu_{13}\left(l_{y1} l_{z3} + l_{y2} l_{z1}\right) l_{x1} l_{x3}\\
&\quad + A_2 \mu_{23}\left(l_{y2} l_{z3} + l_{y3} l_{z2}\right) l_{x1} l_{x3} + G_{12}\left(l_{x1} l_{y2} + l_{x2} l_{y1}\right)\left(l_{x1} l_{y2} + l_{x2} l_{z1}\right)\\
&\quad + G_{13}\left(l_{x1} l_{y3} + l_{x3} l_{y1}\right)\left(l_{x1} l_{z3} + l_{x3} l_{z2}\right) + G_{23}\left(l_{x2} l_{y3} + l_{x3} l_{y2}\right)\left(l_{x2} l_{z3} + l_{x3} l_{z2}\right) \qquad (1,\ 2,\ 3)
\end{aligned}
$$

It should be noted that stiffness coefficients are symmetric with respect to the couples of subscripts ($S_{ijkl} = S_{klij}$) and that notation (1, 2, 3) means that performing permutation, i.e., changing 1 for 2, 2 for 3, and 3 for 1, we can use Eqs. (4.196) to write the expressions for all the stiffness coefficients entering Eq. (4.195). The coefficients A_i and μ_{ij} in Eqs. (4.196) are given in the notations to Eqs. (4.54) and

$$
A_{112} = A_1 \mu_{12} + 2G_{12}, \quad A_{113} = A_1 \mu_{13} + 2G_{13}, \quad A_{223} = A_2 \mu_{23} + 2G_{23}
$$

Resolving Eqs. (4.195) for strains, we arrive at Eq. (2.48) with the following coefficients for the compliance matrix in Eq. (2.49)

$$
\frac{1}{E_x} = \frac{l_{x1}^4}{E_1} + \frac{l_{y1}^4}{E_2} + \frac{l_{z1}^4}{E_3} + C_{122} l_{x1}^2 l_{y1}^2 + C_{133} l_{x1}^2 l_{z1}^2 + C_{233} l_{y1}^2 l_{z1}^2 \qquad (1,\ 2,\ 3),\ \ (x,\ y,\ z)
$$

$$\frac{\nu_{xy}}{E_y}=\frac{\nu_{yx}}{E_x}=\frac{\nu_{12}}{E_2}\left(l_{x1}^2l_{y2}^2+l_{x2}^2l_{y1}^2\right)+\frac{\nu_{13}}{E_3}\left(l_{x1}^2l_{z2}^2+l_{x2}^2l_{z1}^2\right)+\frac{\nu_{23}}{E_3}\left(l_{y1}^2l_{z2}^2+l_{y2}^2l_{z1}^2\right)$$
$$-\frac{l_{x1}^2l_{x2}^2}{E_1}-\frac{l_{y1}^2l_{y2}^2}{E_2}-\frac{l_{z1}^2l_{z2}^2}{E_3}-\frac{1}{G_{12}}l_{x1}l_{x2}l_{y1}l_{y2}-\frac{1}{G_{13}}l_{x1}l_{x2}l_{z1}l_{z2} \tag{4.197}$$
$$-\frac{1}{G_{23}}l_{y1}l_{y2}l_{z1}l_{z2}\qquad(1,\ 2,\ 3),\ \ (x,\ y,\ z)$$

$$\frac{\eta_{x,xy}}{G_{xy}}=\frac{\eta_{xy,x}}{E_x}$$
$$=2\left(\frac{l_{x1}^3l_{x2}}{E_1}+\frac{l_{y1}^3l_{y2}}{E_2}+\frac{l_{z1}^3l_{z2}}{E_3}\right)+C_{122}\left(l_{x1}l_{y2}+l_{x2}l_{y1}\right)l_{x1}l_{y1}+C_{133}(l_{x1}l_{z2}+l_{x2}l_{z1})l_{x1}l_{z1}$$
$$+C_{233}(l_{y1}l_{z2}+l_{y2}l_{z1})l_{y1}l_{z1}\qquad(1,\ 2,\ 3),\ \ (x,\ y,\ z)$$

$$\frac{\eta_{x,xz}}{G_{xz}}=\frac{\eta_{xz,x}}{E_x}=2\left(\frac{l_{x1}^3l_{x3}}{E_1}+\frac{l_{y1}^3l_{y3}}{E_2}+\frac{l_{z1}^3l_{z3}}{E_3}\right)$$
$$+C_{122}(l_{x1}l_{y3}+l_{y1}l_{x3})l_{x1}l_{y1}+C_{133}(l_{x1}l_{z3}+l_{x3}l_{z1})l_{x1}l_{z1}$$
$$+C_{233}(l_{y1}l_{z3}+l_{y3}l_{z1})l_{y1}l_{z1}\qquad(1,\ 2,\ 3),\ \ (x,\ y,\ z)$$

$$\frac{\eta_{x,yz}}{G_{yz}}=\frac{\eta_{yz,x}}{E_x}=2\left[\frac{l_{x1}^2l_{x2}l_{x3}}{E_1}+\frac{l_{y1}^2l_{y2}l_{y3}}{E_2}+\frac{l_{z1}^2l_{z2}l_{z3}}{E_3}-\frac{\nu_{12}}{E_2}\left(l_{x1}^2l_{y2}l_{y3}+l_{y1}^2l_{x2}l_{x3}\right)\right.$$
$$\left.-\frac{\nu_{13}}{E_3}\left(l_{x1}^2l_{z2}l_{z3}+l_{z1}^2l_{x2}l_{x3}\right)-\frac{\nu_{23}}{E_3}\left(l_{y1}^2l_{z2}l_{z3}+l_{z1}^2l_{y2}l_{y3}\right)\right]$$
$$+\frac{l_{x1}l_{y1}}{G_{12}}\left(l_{x2}l_{y3}+l_{x3}l_{y2}\right)+\frac{l_{x1}l_{z1}}{G_{13}}\left(l_{x2}l_{z3}+l_{x3}l_{z2}\right)$$
$$+\frac{l_{y1}l_{z1}}{G_{23}}\left(l_{y2}l_{z3}+l_{y3}l_{z2}\right)\qquad(1,\ 2,\ 3),\ \ (x,\ y,\ z)$$

$$\frac{1}{G_{xy}}=4\left[\frac{l_{x1}^2l_{x2}^2}{E_1}+\frac{l_{y1}^2l_{y2}^2}{E_2}+\frac{l_{z1}^2l_{z2}^2}{E_3}-2\left(\frac{\nu_{12}}{E_2}l_{x1}l_{x2}l_{y1}l_{y2}+\frac{\nu_{13}}{E_3}l_{x1}l_{x2}l_{z1}l_{z2}+\frac{\nu_{23}}{E_3}l_{y1}l_{y2}l_{z1}l_{z2}\right)\right]$$
$$+\frac{1}{G_{12}}\left(l_{x1}l_{y2}+l_{x2}l_{y1}\right)^2+\frac{1}{G_{13}}(l_{x1}l_{z2}+l_{x2}l_{z1})^2$$
$$+\frac{1}{G_{23}}\left(l_{y1}l_{z2}+l_{y2}l_{z1}\right)^2\qquad(1,\ 2,\ 3),\ \ (x,\ y,\ z)$$

$$\frac{\lambda_{xy,xz}}{G_{xz}} = \frac{\lambda_{xz,xy}}{G_{xy}} = 4\left[\frac{l_{x1}^2 l_{x2} l_{x3}}{E_1} + \frac{l_{y1}^2 l_{y2} l_{y3}}{E_2} + \frac{l_{z1}^2 l_{z2} l_{z3}}{E_3}\right.$$
$$\left. - \frac{\nu_{12}}{E_2}(l_{x3}l_{y2} + l_{x2}l_{y3})l_{x1}l_{y1} - \frac{\nu_{13}}{E_3}(l_{x2}l_{z3} + l_{z2}l_{x3})l_{x1}l_{z1} - \frac{\nu_{23}}{E_3}(l_{y2}l_{z3} + l_{y3}l_{z2})l_{y1}l_{z1}\right]$$
$$+ \frac{1}{G_{12}}(l_{x1}l_{y3} + l_{x3}l_{y1})(l_{x1}l_{y2} + l_{x2}l_{y1}) + \frac{1}{G_{13}}(l_{x1}l_{z3} + l_{x3}l_{z1})(l_{x1}l_{z2} + l_{x2}l_{z1})$$
$$+ \frac{1}{G_{23}}(l_{y1}l_{z3} + l_{y3}l_{z1})(l_{y1}l_{z2} + l_{y2}l_{z1}) \qquad (1,\ 2,\ 3),\ \ (x,\ y,\ z)$$

in which

$$C_{122} = \frac{1}{G_{12}} - \frac{2\nu_{12}}{E_2}, \quad C_{133} = \frac{1}{G_{13}} - \frac{2\nu_{13}}{E_3},$$
$$C_{233} = \frac{1}{G_{23}} - \frac{2\nu_{23}}{E_3}$$

Consider a special spatial structure (Pagano and Whitford, 1985) formed by a fabric composite in which the plies reinforced at angle ϕ (warp direction) with respect to the x-axis make angles α and β with the x-axis and the y-axis, respectively, as in Fig. 4.104. The directional cosines for this structure are

$$l_{x1} = \cos\lambda\cos\psi, \qquad l_{x2} = -\sin\lambda\cos\psi$$
$$l_{x3} = -\sin\psi, \qquad l_{y1} = \sin\lambda\cos\beta - \cos\lambda\sin\beta\sin\psi$$
$$l_{y2} = \cos\lambda\cos\beta + \sin\lambda\sin\beta\sin\psi, \qquad l_{y3} = -\sin\beta\cos\psi$$
$$l_{z1} = \sin\lambda\sin\beta + \cos\lambda\cos\beta\sin\psi$$
$$l_{z2} = \cos\lambda\sin\beta - \sin\lambda\cos\beta\sin\psi, \qquad l_{z3} = \cos\beta\cos\psi$$

where

$$\lambda = \phi + \tan^{-1}(\tan\beta\sin\psi), \quad \psi = \tan^{-1}(\tan\alpha\cos\beta)$$

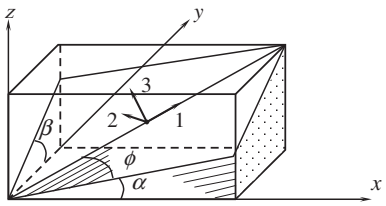


FIGURE 4.104

Orientation angles in a spatial composite structure.

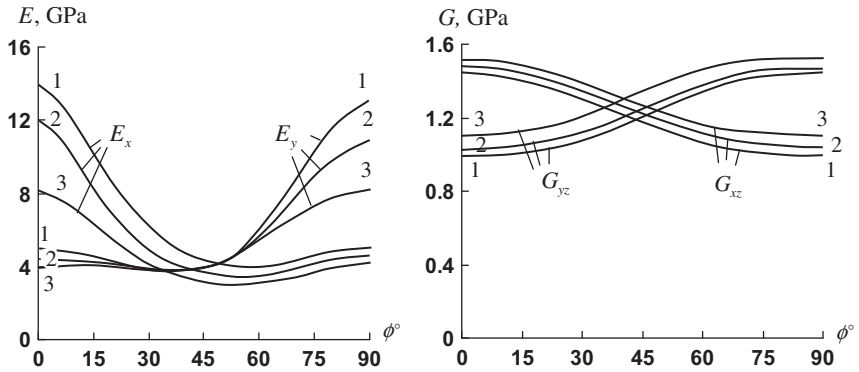


FIGURE 4.105

Dependencies of the elastic constants of a spatially reinforced composite on the orientation angles: (1) $\alpha = \beta = 0°$, (2) $\alpha = \beta = 8°$, (3) $\alpha = \beta = 16°$.

The dependencies of elastic constants E_x, E_y, G_{xz}, and G_{yz} calculated with the aid of Eqs. (4.197) for the material with $E_1 = 12.9$ GPa, $E_2 = 5.2$ GPa, $E_3 = 3$ GPa, $G_{12} = G_{13} = 1.5$ GPa, $G_{23} = 1$ GPa, $\nu_{21} = 0.15$, $\nu_{31} = 0.2$ and $\nu_{32} = 0.2$ are presented in Fig. 4.105 (Vasiliev and Morozov, 1988).

For planar structures $(\alpha = \beta = 0)$, Eqs. (4.196) and (4.197) generalize Eqs. (4.72) and (4.76) for a three-dimensional stress state of a layer.

4.10 References

Alfutov, N. A., & Zinoviev, P. A. (1982). Deformation and failure of fibrous composites with brittle polymeric matrix under plane stress. In I. F. Obraztsov, & V. V. Vasiliev (Eds.), *Mechanics of Composites* (pp. 166–185). Moscow: Mir.

Birger, I. A. (1951). General solutions of some problems of the plasticity theory. *Prikladnaya Matematika i Mekhanika, 15*(6), 765–770, (in Russian).

Chamis, C. C. (1979). Impetus of composite mechanics on test methods for fiber composites. In G. C. Sih, & V. P. Tamuzh (Eds.), *Proc. 1st USA-USSR Symp. Fracture of Composite Materials* (pp. 329–348). The Netherlands: Sijthoff & Noordhoff, Riga, USSR 4–7 Sept. 1978.

Cherevatsky, A. S. (1999). Manufacturing technology of wound structures by transformation of wound preforms. In *Proc. 12th Int. Conf. on Composite Materials (ICCM-12)* (p. 10), Paris, France, 5–9 July 1999(CD-ROM).

Chiao, T. T. (1979). Some interesting mechanical behaviors of fiber composite materials. In G. C. Sih, & V. P. Tamuzh (Eds.), *Proc. 1st USA-USSR Symp. Fracture of Composite Materials* (pp. 385–392). Alphen a/d Rijn: Sijthoff & Noordhoff, Riga, USSR 4–7 Sept. 1978.

Fukui, S., Kawata, K., Kobayashi, R., Takana, N., Hashimoto, S., Otani, N., & Hondo, A. (1966). Some theoretical and experimental studies on the width variation effects for the filament-wound cylinders. In: *Proc. 6th Int. Symp*. Tokyo: Space Technol. and Sci., pp. 467–470.

Green, A. E., & Adkins, J. E. (1960). *Large Elastic Deformations and Nonlinear Continuum Mechanics*. London: Oxford University Press.

Hahn, H. T., & Tsai, S. W. (1973). Nonlinear elastic behavior of unidirectional composite laminae. *Journal of Composite Materials, 7*, 102–118.

Hahn, H. T., & Tsai, S. W. (1974). On the behavior of composite laminates after initial failures. *Journal of Composite Materials, 8*, 288–305.

Hashin, Z. (1987). Analysis of orthogonally cracked laminates under tension. *Journal of Applied Mechanics, 54*, 872–879.

Herakovich, C. T. (1998). *Mechanics of Fibrous Composites*. New York: Wiley.

Ilyushin, A. A. (1948). *Plasticity.* Moscow (in Russian): Gostekhizdat.

Jones, R. M. (1977). A nonsymmetric compliance matrix approach to nonlinear multimodulus orthotropic materials. *AIAA Journal, 15*(10), 1436–1443.

Lagace, P. A. (1985). Nonlinear stress-strain behavior of graphite/epoxy laminates. *AIAA Journal, 23*(10), 1583–1589.

Lungren, J. E., & Gudmundson, P. (1999). Influence of matrix cracks and swelling on moisture absorption in cross-ply GFRP laminates. In *Proc. 12th Int. Conf. on Composite Materials (ICCM-12)* (p. 9), Paris, France, 5–9 July 1999, (CD-ROM).

Morozov, E. V., & Vasiliev, V. V. (2003). Determination of the shear modulus of orthotropic materials from off-axis tension tests. *Composite Structures, 62*, 379–382.

Pagano, N. J., & Whitford, L. E. (1985). On the solution for the elastic response of involute bodies. *Composite Science and Technology, 22*(4), 295–317.

Reifsnaider, K. L. (1977). Some fundamental aspects of the fatigue and fracture responses of composite materials. In *Proc. 14th Annual Meeting of Society of Engineering Science* (pp. 373–384), Nov. 14–16, Bethlehem, PA.

Skudra, A. M., Bulavs, F. Ya., Gurvich, M. R., & Kruklinsh, A. A. (1989). *Elements of Structural Mechanics of Composite Truss Systems*. Riga (in Russian): Zinatne.

Tarnopol'skii, Yu. M., Zhigun, I. G., & Polyakov, V. A. (1987). *Spatially Reinforced Composite Materials – Handbook*. Moscow (in Russian): Mashinostroenie.

Tarnopol'skii, Yu. M., Zhigun, I. G., & Polyakov, V. A. (1992). In *Spatially Reinforced Composites*. Lancaster PA, Technomic.

Tsai, S. W. (1987). *Composite Design* (3rd edn). Dayton: Think Composites.

Tsai, S. W., & Azzi, V. D. (1966). Strength of laminated composite materials. *AIAA Journal, 4*(2), 296–301.

Vasiliev, V. V. (1993). *Mechanics of Composite Structures*. Washington: Taylor & Francis.

Vasiliev, V. V., & Elpatievskii, A. N. (1967). Deformation of tape-wound cylindrical shells under internal pressure. *Polymer Mechanics/Mechanics of Composite Materials, 3*(5), 604–607.

Vasiliev, V. V., & Morozov, E. V. (1988). Applied theory of spatially reinforced composite shells. *Mechanics of Composite Materials, 24*(3), 393–400.

Vasiliev, V. V., & Salov, V. A. (1984). Development and examination of a two-matrix glass-fiber composite with high transverse strain. *Mechanics of Composite Materials, 20*(4), 463–467.

Vasiliev, V. V., Dudchenko, A. A., & Elpatievskii, A. N. (1970). Analysis of the tensile deformation of glass-reinforced plastics. *Polymer Mechanics/Mechanics of Composite Materials, 6*(1), 127–130.

Vasiliev, V. V., Krikanov, A. A., & Razin, A. F. (2003). New generation of filament-wound composite pressure vessels for commercial applications. *Composite Structures, 62*, 449–459.

Vasiliev, V. V., & Tarnopol'skii, Yu. M. (1990). *Composite Materials. Handbook*. Moscow (in Russian): Mashinostroenie.

Vasiliev, V. V., Salov, V. A., & Salov, O. V. (1997). Load-Carrying Shell of Revolution Made of Composite Materials. *Patent of Russian Federation*. No. 209197.

Verchery, G. (1999). Designing with anisotropy. Part 1: Methods and general results for laminates. In *Proc. 12th Int. Conf. on Composite Mater. (ICCM-12)* (p. 11), Paris, France, 5–9 July 1999, (CD-ROM).

Verchery, G., & Gong, X. J. (1999). Pure tension with off-axis tests for orthotropic laminates. In *Proc. 12th Int. Conf. on Composite Mater. (ICCM-12)* (p. 7), Paris, France, 5–9 July 1999, (CD-ROM).

CHAPTER

Mechanics of laminates

5

A typical composite structure consists of a system of layers bonded together. The layers can be made of different isotropic or anisotropic materials, and have different structures (see Chapter 4), thicknesses, and mechanical properties. In contrast to typical layers which are described in Chapter 4 and whose basic properties are determined experimentally, the laminate characteristics are usually calculated using information concerning the number of layers, their stacking sequence, and geometric and mechanical properties, which must be known. A finite number of layers can be combined to form so many different laminates that the concept of studying them using experimental methods does not seem realistic. Whereas the most complicated typical layer is described with nine stiffness coefficients A_{mn} ($mn = 11$, 22, 12, 14, 24, 44, 55, 56, and 66), some of which can be calculated, the laminate is characterized by 21 coefficients and demonstrates coupling effects that are difficult to simulate in experiments.

Thus, the topic of this chapter is to provide equations allowing us to predict the behavior of a laminate as a system of layers with given properties. The only restriction that is imposed on the laminate as an element of a composite structure concerns its total thickness, which is assumed to be much smaller than the other dimensions of the structure.

5.1 STIFFNESS COEFFICIENTS OF A NONHOMOGENEOUS ANISOTROPIC LAYER

Consider a thin nonhomogeneous layer, which is anisotropic in the xy-plane and whose mechanical properties are some functions of the normal coordinate z (see Fig. 5.1). A typical example of such a generalized layer is a laminate composed of different plies. Another practical example is a plate made of functionally graded material (FGM) which is characterized by gradual variation in

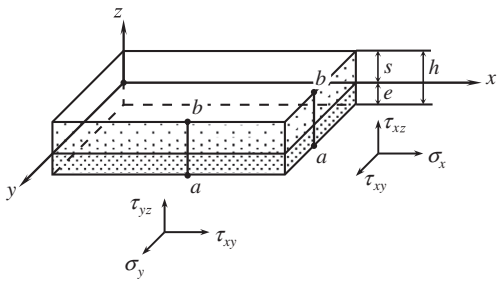


FIGURE 5.1

An element of a nonhomogeneous layer.

Advanced Mechanics of Composite Materials and Structural Elements. http://dx.doi.org/10.1016/B978-0-08-098231-1.00005-4
Copyright © 2013 Elsevier Ltd. All rights reserved.

composition and/or in microstructure over the material thickness, resulting in corresponding changes in the material properties. Coordinate axes x and y belong to some plane which is referred to as a reference plane such that $z = 0$ on this plane and $-e \le z \le s$ for the layer under study. There exist some special locations of the reference plane discussed later, but in this section its coordinates e and s are not specified. We introduce two assumptions, both based on the fact that the thickness $h = e + s$ is small.

First, it is assumed that the layer thickness, h, does not change under the action of stresses shown in Fig. 5.1. Actually, the thickness does change, but because it is small, this change is negligible. This means that there is no strain in the z direction, and in accordance with Eqs. (2.22),

$$\varepsilon_z = \frac{\partial u_z}{\partial z} = 0, \; u_z = w(x, y). \tag{5.1}$$

Here, $w(x, y)$ is the so-called normal deflection which is a translational displacement of a normal element a–b (see Fig. 5.1) as a solid in the z direction.

Second, we assume that in-plane displacements u_x and u_y are linear functions of the thickness coordinate z, i.e.,

$$\begin{aligned} u_x(x, y, z) &= u(x, y) + z\theta_x(x, y) \\ u_y(x, y, z) &= \upsilon(x, y) + z\theta_y(x, y) \end{aligned} \tag{5.2}$$

where u and υ are the displacements of the points of the reference plane $z = 0$ or, which is the same, the translational displacements of the normal element a–b (see Fig. 5.1) as a solid in the x and y direction, whereas θ_x and θ_y are the angles of rotations (usually referred to as "rotations") of the normal element a–b in the xz- and yz-planes. Geometric interpretation of the first expression in Eqs. (5.2) is presented in Fig. 5.2.

In-plane strains of the layer, $\varepsilon_x, \varepsilon_y$, and γ_{xy}, can be found using Eqs. (2.22), (5.1), and (5.2) as

$$\begin{aligned} \varepsilon_x &= \frac{\partial u_x}{\partial x} = \varepsilon_x^0 + z\kappa_x \\ \varepsilon_y &= \frac{\partial u_y}{\partial y} = \varepsilon_y^0 + z\kappa_y \\ \gamma_{xy} &= \frac{\partial u_x}{\partial y} + \frac{\partial u_y}{\partial x} = \gamma_{xy}^0 + z\kappa_{xy} \end{aligned} \tag{5.3}$$

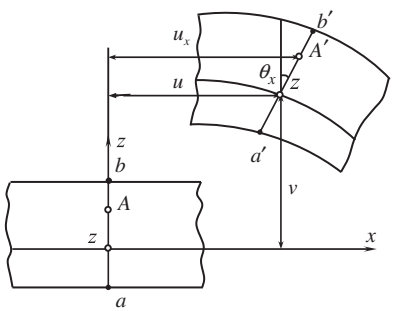


FIGURE 5.2

Decomposition of displacement u_x of point A into translational (u) and rotation ($z\theta_x$) components.

where

$$\varepsilon_x^0 = \frac{\partial u}{\partial x},\ \varepsilon_y^0 = \frac{\partial v}{\partial y},\ \gamma_{xy}^0 = \frac{\partial u}{\partial y} + \frac{\partial v}{\partial x}$$
$$\kappa_x = \frac{\partial \theta_x}{\partial x},\ \kappa_y = \frac{\partial \theta_y}{\partial y},\ \kappa_{xy} = \frac{\partial \theta_x}{\partial y} + \frac{\partial \theta_y}{\partial x}.$$

These generalized strains correspond to the following four basic deformations of the layer shown in Fig. 5.3:

- In-plane tension or compression $(\varepsilon_x^0, \varepsilon_y^0)$
- In-plane shear (γ_{xy}^0)
- Bending in the xz- and yz-planes (κ_x, κ_y) and
- Twisting (κ_{xy})

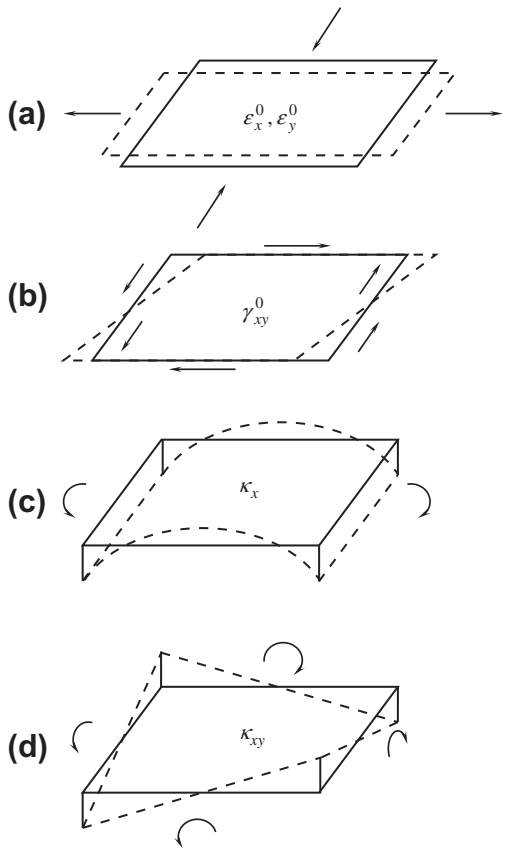


FIGURE 5.3

Basic deformations of the layer: (a) in-plane tension and compression $(\varepsilon_x^0, \varepsilon_y^0)$; (b) in-plane shear (γ_{xy}^0); (c) bending (κ_x); (d) twisting (κ_{xy}).

The constitutive equations for an anisotropic layer, Eqs. (4.71), upon substitution of Eqs. (5.3), yield

$$\begin{aligned}
\sigma_x &= A_{11}\varepsilon_x^0 + A_{12}\varepsilon_y^0 + A_{14}\gamma_{xy}^0 + z\left(A_{11}\kappa_x + A_{12}\kappa_y + A_{14}\kappa_{xy}\right)\\
\sigma_y &= A_{21}\varepsilon_x^0 + A_{22}\varepsilon_y^0 + A_{24}\gamma_{xy}^0 + z\left(A_{21}\kappa_x + A_{22}\kappa_y + A_{24}\kappa_{xy}\right)\\
\tau_{xy} &= A_{41}\varepsilon_x^0 + A_{42}\varepsilon_y^0 + A_{44}\gamma_{xy}^0 + z\left(A_{41}\kappa_x + A_{42}\kappa_y + A_{44}\kappa_{xy}\right)
\end{aligned} \tag{5.4}$$

where $A_{mn} = A_{nm}$ are the stiffness coefficients of the material that depend, in general, on the coordinate z.

It follows from Eqs. (5.4) that the stresses depend on six generalized strains $\varepsilon, \gamma,$ and κ, which are functions of coordinates x and y only. To derive the constitutive equations for the layer under study, we introduce the corresponding force functions as stress resultants and couples shown in Fig. 5.4 and specified as

$$N_x = \int_{-e}^{s} \sigma_x dz,\ N_y = \int_{-e}^{s} \sigma_y dz,\ N_{xy} = \int_{-e}^{s} \tau_{xy} dz$$

$$M_x = \int_{-e}^{s} \sigma_x z dz,\ M_y = \int_{-e}^{s} \sigma_y z dz,\ M_{xy} = \int_{-e}^{s} \tau_{xy} z dz$$

(see also Fig. 5.1). Substituting the stresses, Eqs. (5.4), into these equations, we arrive at the following constitutive equations that relate stress resultants and couples to the corresponding generalized strains, i.e.,

$$\begin{aligned}
N_x &= B_{11}\varepsilon_x^0 + B_{12}\varepsilon_y^0 + B_{14}\gamma_{xy}^0 + C_{11}\kappa_x + C_{12}\kappa_y + C_{14}\kappa_{xy}\\
N_y &= B_{21}\varepsilon_x^0 + B_{22}\varepsilon_y^0 + B_{24}\gamma_{xy}^0 + C_{21}\kappa_x + C_{22}\kappa_y + C_{24}\kappa_{xy}\\
N_{xy} &= B_{41}\varepsilon_x^0 + B_{42}\varepsilon_y^0 + B_{44}\gamma_{xy}^0 + C_{41}\kappa_x + C_{42}\kappa_y + C_{44}\kappa_{xy}\\
M_x &= C_{11}\varepsilon_x^0 + C_{12}\varepsilon_y^0 + C_{14}\gamma_{xy}^0 + D_{11}\kappa_x + D_{12}\kappa_y + D_{14}\kappa_{xy}\\
M_y &= C_{21}\varepsilon_x^0 + C_{22}\varepsilon_y^0 + C_{24}\gamma_{xy}^0 + D_{21}\kappa_x + D_{22}\kappa_y + D_{24}\kappa_{xy}\\
M_{xy} &= C_{41}\varepsilon_x^0 + C_{42}\varepsilon_y^0 + C_{44}\gamma_{xy}^0 + D_{41}\kappa_x + D_{42}\kappa_y + D_{44}\kappa_{xy}.
\end{aligned} \tag{5.5}$$

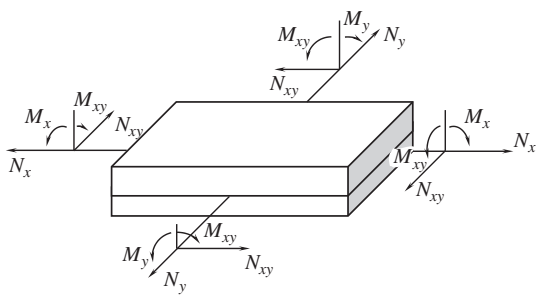


FIGURE 5.4

Stress resultants and couples applied to the reference plane of the layer.

These equations include membrane stiffness coefficients

$$B_{mn} = B_{nm} = \int_{-e}^{s} A_{mn} dz \tag{5.6}$$

which specify the layer stiffness under in-plane deformation (Figs. 5.3a and b), bending stiffness coefficients

$$D_{mn} = D_{nm} = \int_{-e}^{s} A_{mn} z^2 dz \tag{5.7}$$

which are associated with the layer bending and twisting (Figs. 5.3c and d), and membrane-bending coupling coefficients

$$C_{mn} = C_{nm} = \int_{-e}^{s} A_{mn} z dz \tag{5.8}$$

through which in-plane stress resultants are related to bending deformations, and stress couples are linked with in-plane strains.

Coefficients with subscripts 11, 12, 22, and 44 compose the basic set of the layer stiffnesses associated with in-plane extension, contraction, and shear (B_{11}, B_{12}, B_{22}, and B_{44}), bending and twisting (D_{11}, D_{12}, D_{22}, and D_{44}), and coupling effects (C_{11}, C_{12}, C_{22}, and C_{44}). For an anisotropic layer there also exists coupling between extension (a) and shear (b) in Fig. 5.3 (coefficients B_{14} and B_{24}), extension (a) and twisting (d) in Fig. 5.3 (coefficients C_{14} and C_{24}), and bending (c) and twisting (d) in Fig. 5.3 (coefficients D_{14} and D_{24}).

The forces and moments N and M specified by Eqs. (5.5) are resultants and couples of in-plane stresses σ_x, σ_y, and τ_{xy} (see Fig. 5.1). However, there also exist transverse shear stresses τ_{xz} and τ_{yz} which should be expressed in terms of the corresponding shear strains. Unfortunately, we cannot apply the direct approach that was used earlier to derive Eqs. (5.5) for this purpose. This direct approach involves strain-displacement equations, Eqs. (2.22),

$$\gamma_{xz} = \frac{\partial u_x}{\partial z} + \frac{\partial u_z}{\partial x}, \ \gamma_{yz} = \frac{\partial u_y}{\partial z} + \frac{\partial u_z}{\partial y} \tag{5.9}$$

in conjunction with Hooke's law

$$\tau_{xz} = A_{55}\gamma_{xz} + A_{56}\gamma_{yz}, \ \tau_{yz} = A_{65}\gamma_{xz} + A_{66}\gamma_{yz} \tag{5.10}$$

or

$$\gamma_{xz} = a_{55}\tau_{xz} + a_{56}\tau_{yz}, \ \gamma_{yz} = a_{65}\tau_{xz} + a_{66}\tau_{yz} \tag{5.11}$$

where A_{mn} and a_{mn} are stiffness and compliance coefficients, respectively. The problem is associated with Eqs. (5.2) which specify only approximate dependence of displacements u_x and u_y on coordinate z (the actual distribution of u_x and u_y through the layer thickness is not known) and must not be differentiated with respect to z. So, we cannot substitute Eqs. (5.2) into Eqs. (5.9) which include derivatives of u_x and u_y with respect to z. To see what can happen if we violate this well-known

mathematical restriction, consider a sandwich laminate shown in Fig. 5.5. It can be seen that while linear approximation of $u(z)$ (dashed line) looks reasonable, the derivatives of the actual displacements and the approximate ones have little in common.

To derive constitutive equations for transverse shear, consider Fig. 5.6. The actual distribution of shear stresses τ_{xz} and τ_{yz} across the layer thickness is not known, but we can assume that it is not important. Indeed, as follows from Eqs. (5.1), elements *a–b* (see Fig. 5.6) along which the shear stresses act are absolutely rigid. This means (in accordance with the corresponding theorem of *Statics of Solids*) that the displacements of these elements in the z direction depend only on the resultants of the shear stresses, i.e., on transverse shear forces

$$V_x = \int_{-e}^{s} \tau_{xz} dz,\ V_y = \int_{-e}^{s} \tau_{yz} dz \tag{5.12}$$

Since the particular distributions of τ_{xz} and τ_{yz} do not influence the displacements, we can introduce some average stresses having the same resultants as the actual ones, i.e.,

$$\tau_x = \frac{V_x}{h} = \frac{1}{h} \int_{-e}^{s} \tau_{xz} dz,\ \tau_y = \frac{V_y}{h} = \frac{1}{h} \int_{-e}^{s} \tau_{yz} dz$$

However, according to Eqs. (5.11), shear strains are linear combinations of shear stresses. So, we can use the same law to introduce average shear strains as

$$\gamma_x = \frac{1}{h} \int_{-e}^{s} \gamma_{xz} dz,\ \gamma_y = \frac{1}{h} \int_{-e}^{s} \gamma_{yz} dz \tag{5.13}$$

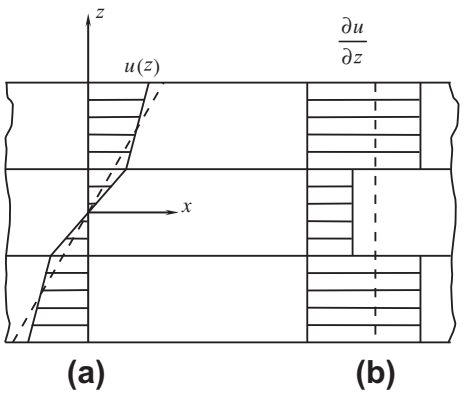


FIGURE 5.5

Actual (solid lines) and approximate (dashed lines) distributions of a displacement (a) and its derivative (b) through the thickness of a sandwich laminate.

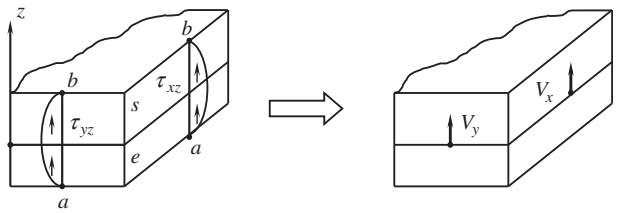


FIGURE 5.6

Reduction of transverse shear stresses to stress resultants (transverse shear forces).

Average shear strains γ_x and γ_y can be readily expressed in terms of displacements if we substitute Eqs. (5.9) into Eqs. (5.13), i.e.,

$$\gamma_x = \frac{1}{h}\left[u_x(s) - u_x(-e) + \int_{-e}^{s} \frac{\partial u_z}{\partial x} dz\right]$$

$$\gamma_y = \frac{1}{h}\left[u_y(s) - u_x(-e) + \int_{-e}^{s} \frac{\partial u_z}{\partial y} dz\right].$$

These equations, in contrast to Eqs. (5.9), do not include derivatives with respect to z. So, we can substitute Eqs. (5.1) and (5.2) to get the final result

$$\gamma_x = \theta_x + \frac{\partial w}{\partial x},\ \gamma_y = \theta_y + \frac{\partial w}{\partial y}. \tag{5.14}$$

Consider Eqs. (5.10) and (5.11). Integrating them over the layer thickness and using Eqs. (5.12) and (5.13), we get

$$V_x = \int_{-e}^{s} (A_{55}\gamma_{xz} + A_{56}\gamma_{yz})dz,\ V_y = \int_{-e}^{s} (A_{65}\gamma_{xz} + A_{66}\gamma_{yz})dz$$

$$\gamma_x = \frac{1}{h}\int_{-e}^{s} (a_{55}\tau_{xz} + a_{56}\tau_{yz})dz,\ \gamma_y = \frac{1}{h}\int_{-e}^{s} (a_{65}\tau_{xz} + a_{66}\tau_{yz})dz$$

Since the actual distribution of stresses and strains according to the foregoing reasoning is not significant, we can change them for the corresponding average stresses and strains:

$$V_x = S_{55}\gamma_x + S_{56}\gamma_y,\ V_y = S_{65}\gamma_x + S_{66}\gamma_y \tag{5.15}$$

$$\gamma_x = s_{55}V_x + s_{56}V_y,\ \gamma_y = s_{65}V_x + s_{66}V_y \tag{5.16}$$

where

$$S_{mn} = S_{nm} = \int_{-e}^{s} A_{mn} dz \tag{5.17}$$

$$s_{mn} = s_{nm} = \frac{1}{h^2} \int_{-e}^{s} a_{mn} dz \tag{5.18}$$

It should be emphasized that Eqs. (5.16) are not the inverse form of Eqs. (5.15). Indeed, solving Eqs. (5.16), using Eqs. (5.18), and taking into account that

$$a_{55} = \overline{A}_{66},\ a_{56} = -\overline{A}_{56},\ a_{66} = \overline{A}_{55},$$
$$\overline{A}_{mn} = \frac{A_{mn}}{A_{55}A_{66} - A_{56}^2}$$

we arrive at Eqs. (5.15) in which S_{mn} should be changed to

$$\overline{S}_{mn} = \frac{h^2 \int_{-e}^{s} \overline{A}_{mn} dz}{\left(\int_{-e}^{s} \overline{A}_{55} dz \right) \left(\int_{-e}^{s} \overline{A}_{66} dz \right) - \left(\int_{-e}^{s} \overline{A}_{56} dz \right)^2} \tag{5.19}$$

These expressions, in general, do not coincide with Eqs. (5.17).

Thus, the constitutive equations for transverse shear are specified by Eqs. (5.15), and there exist two–in general–different approximate forms of stiffness coefficients: Eqs. (5.17) and (5.19). The fact that equations obtained in this way are approximate is quite natural because the assumed displacement field, Eqs. (5.1) and (5.2), is also approximate.

To compare two possible forms of constitutive equations for transverse shear, consider for the sake of brevity an orthotropic layer for which

$$A_{56} = 0,\ a_{56} = 0,\ A_{55} = G_{xz},\ A_{66} = G_{yz},$$
$$a_{55} = \overline{A}_{66} = \frac{1}{G_{xz}},\ a_{66} = \overline{A}_{55} = \frac{1}{G_{yz}}$$

For transverse shear in the xz-plane, Eqs. (5.15) yield

$$V_x = S_{55}\gamma_x \quad \text{or} \quad V_x = \overline{S}_{55}\gamma_x \tag{5.20}$$

in which, in accordance with Eq. (5.17)

$$S_{55} = \int_{-e}^{s} G_{xz} dz \tag{5.21}$$

whereas Eq. (5.19) yields

$$\overline{S}_{55} = \frac{h^2}{\int_{-e}^{s} \frac{dz}{G_{xz}}} \tag{5.22}$$

If the shear modulus does not depend on z Eqs. (5.21) and (5.22) both, give the same result, $S_{55} = \overline{S}_{55} = G_{xz}h$. The same, of course, holds for the transverse shear in the yz-plane.

Using the energy method applied in Section 3.3, we can show that Eqs. (5.21) and (5.22) provide the upper and the lower bounds for the exact transverse shear stiffness. Indeed, consider a strip with unit width experiencing transverse shear induced by force V_x as in Fig. 5.7. Assume that Eq. (5.20) links the actual force V_x with the exact angle $\gamma_x = \Delta/l$ through the exact shear stiffness S^e_{55}, which we do not know, and which we would like to evaluate. To do this, we can use the two variational principles described in Section 2.11. According to the principle of minimum total potential energy

$$T_{ext} \le T_{adm} \tag{5.23}$$

where

$$T_{ext} = U^{\varepsilon}_{ext} - A_{ext}, \quad T_{adm} = U^{\varepsilon}_{adm} - A_{adm}$$

are the total energies of the exact state and some admissible kinematic state expressed in terms of the strain energy, U, and work A performed by force V_x on displacement Δ (see Fig. 5.7). For both states

$$A_{ext} = A_{adm} = V_x\Delta$$

and condition (5.23) reduces to

$$U^{\varepsilon}_{ext} \le U^{\varepsilon}_{adm} \tag{5.24}$$

For the exact state, with due regard to Eq. (5.20), we get

$$U_{ext} = \frac{l}{2}V_x\gamma_x = \frac{l}{2}S^e_{55}\gamma_x^2 \tag{5.25}$$

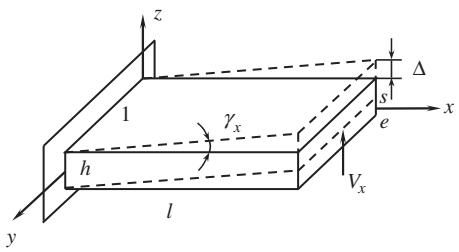


FIGURE 5.7

Transverse shear of a strip with unit width.

For the admissible state, we should use the following general equation

$$U = \frac{1}{2}\int_0^l dx \int_{-e}^{s} \tau_{xz}\gamma_{xz}dz = \frac{1}{2}\int_0^l dx \int_{-e}^{s} G_{xz}\gamma_{xz}^2 dz = U^{\varepsilon}$$

and admit some approximation for γ_{xz}. The simplest one is $\gamma_{xz} = \gamma_x$, so that

$$U_{adm}^{\varepsilon} = \frac{l}{2}\gamma_x^2 \int_{-e}^{s} G_{xz}dz \tag{5.26}$$

Then, Eqs. (5.24)–(5.26) yield

$$S_{55}^{e} \le \int_{-e}^{s} G_{xz}dz$$

Comparing this inequality with Eq. (5.21), we can conclude that this equation specifies the upper bound for S_{55}^{e}.

To determine the lower bound, we should apply the principle of minimum strain energy, according to which

$$U_{ext} \le U_{adm}^{\sigma} \tag{5.27}$$

where

$$U_{ext} = \frac{l}{2}V_x\gamma_x = \frac{l}{2}\cdot\frac{V_x^2}{S_{55}^{e}}$$

For the admissible state we should apply

$$U = \frac{1}{2}\int_0^l dx \int_{-e}^{s} \tau_{xz}\gamma_{xz}dz = \frac{1}{2}\int_0^l dx \int_{-e}^{s} \frac{\tau_{xz}^2}{G_{xz}}dz = U^{\sigma}$$

and use some admissible distribution for τ_{xz}. The simplest approximation is $\tau_{xz} = V_x/h$, so that

$$U_{adm}^{\sigma} = \frac{l}{2h^2}V_x^2 \int_{-e}^{s} \frac{dz}{G_{xz}}.$$

Substitution in the condition (5.27) yields

$$S_{55}^{e} \ge \frac{h^2}{\int_{-e}^{s} \frac{dz}{G_{xz}}}.$$

Thus, Eq. (5.22) provides the lower bound for S^e_{55}, and the exact stiffness satisfies the following inequality

$$\frac{h^2}{\int_{-e}^{s} \frac{dz}{G_{xz}}} \le S^e_{55} \le \int_{-e}^{s} G_{xz}\,dz$$

It should be emphasized that S^e_{55} in this analysis is not the actual shear stiffness coefficient of the laminate. It is the exact value of the stiffness coefficient which can be found using the exact stress and strain fields following from three-dimensional elasticity equations.

So, constitutive equations for the laminate under study are specified by Eqs. (5.5) and (5.15). Stiffness coefficients, which are given by Eqs. (5.6–5.8) and (5.17/5.19), can be written in a form more suitable for calculations. To do this, introduce the new coordinate $t = z + e$ such that $0 \le t \le h$ (see Fig. 5.8). Transforming the integrals to this new variable, we have

$$\begin{aligned} &B_{mn} = I^{(0)}_{mn}, \quad C_{mn} = I^{(1)}_{mn} - eI^{(0)}_{mn}, \\ &D_{mn} = I^{(2)}_{mn} - 2eI^{(1)}_{mn} + e^2 I^{(0)}_{mn} \end{aligned} \tag{5.28}$$

where $mn = 11$, 12, 22, 14, 24, and 44 and

$$I^{(r)}_{mn} = \int_0^h A_{mn} t^r\,dt, \quad r = 0,\ 1,\ 2 \tag{5.29}$$

The transverse shear stiffnesses, Eqs. (5.17) and (5.19), take the form

$$S_{mn} = I^{(0)}_{mn} \tag{5.30}$$

and

$$\overline{S}_{mn} = \frac{h^2 \overline{I}^{(0)}_{mn}}{\overline{I}^{(0)}_{55}\overline{I}^{(0)}_{66} - \left(\overline{I}^{(0)}_{56}\right)^2} \tag{5.31}$$

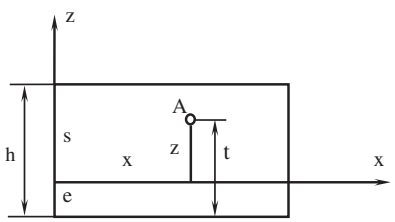


FIGURE 5.8

Coordinates of an arbitrary point *A*.

where $mn = 55$, 56, and 66 and

$$\overline{I}_{mn}^{(0)} = \int_0^h \overline{A}_{mn} dt. \tag{5.32}$$

The coefficients $\overline{A}_{mn}$ are specified by the expression given in notations to Eq. (5.19).

5.2 STIFFNESS COEFFICIENTS OF A HOMOGENEOUS LAYER

Consider a layer whose material stiffness coefficients A_{mn} do not depend on coordinate z. Then

$$I_{mn}^{(r)} = \frac{A_{mn}}{r+1} h^{r+1}, \; \overline{I}_{mn}^{(0)} = \overline{A}_{mn} h \tag{5.33}$$

and Eqs. (5.28), (5.30), and (5.31) yield the following stiffness coefficients for the layer

$$\begin{aligned} &B_{mn} = A_{mn} h, \; C_{mn} = A_{mn}\left(\frac{h}{2} - e\right), \\ &D_{mn} = A_{mn}\left(\frac{h^3}{3} - eh + e^2\right), \; S_{mn} = A_{mn} h \end{aligned} \tag{5.34}$$

Both Eqs. (5.30) and (5.31) give the same result for S_{mn}. It follows from the second of Eqs. (5.34) that the membrane-bending coupling coefficients C_{mn} become equal to zero if we take $e = h/2$, i.e., if the reference plane coincides with the middle-plane of the layer shown in Fig. 5.9. In this case, Eqs. (5.5) and (5.15) take the following decoupled form

$$\begin{aligned} &N_x = B_{11}\varepsilon_x^0 + B_{12}\varepsilon_y^0 + B_{14}\gamma_{xy}^0, \quad N_y = B_{21}\varepsilon_x^0 + B_{22}\varepsilon_y^0 + B_{24}\gamma_{xy}^0, \\ &N_{xy} = B_{41}\varepsilon_x^0 + B_{42}\varepsilon_y^0 + B_{44}\gamma_{xy}^0, \\ &M_x = D_{11}\kappa_x + D_{12}\kappa_y + D_{14}\kappa_{xy}, \quad M_y = D_{21}\kappa_x + D_{22}\kappa_y + D_{24}\kappa_{xy}, \\ &M_{xy} = D_{41}\kappa_x + D_{42}\kappa_y + D_{44}\kappa_{xy}, \\ &V_x = S_{55}\gamma_x + S_{56}\gamma_y, \; V_y = S_{65}\gamma_x + S_{66}\gamma_y \end{aligned} \tag{5.35}$$

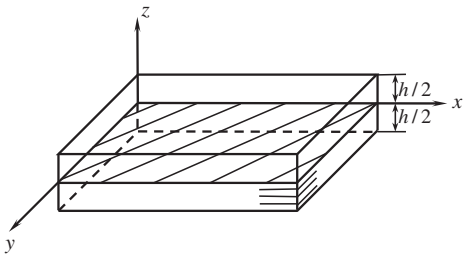


FIGURE 5.9

Middle plane of a laminate.

As can be seen, we have arrived at three independent groups of constitutive equations, i.e., for the in-plane stressed state of the layer, bending and twisting, and transverse shear. The stiffness coefficients, Eqs. (5.34), become

$$B_{mn} = A_{mn}h, \;\; D_{mn} = \frac{A_{mn}}{12}h^3, \;\; S_{mn} = A_{mn}h \tag{5.36}$$

For an orthotropic layer, there are no in-plane stretching-shear coupling ($B_{14} = B_{24} = 0$) and transverse shear coupling ($S_{56} = 0$). Then, Eqs. (5.35) reduce to

$$\begin{aligned} &N_x = B_{11}\varepsilon_x^0 + B_{12}\varepsilon_y^0, \quad N_y = B_{21}\varepsilon_x^0 + B_{22}\varepsilon_y^0, \; N_{xy} = B_{44}\gamma_{xy}^0 \\ &M_x = D_{11}\kappa_x + D_{12}\kappa_y, \quad M_y = D_{21}\kappa_x + D_{22}\kappa_y, \; M_{xy} = D_{44}\kappa_{xy} \\ &V_x = S_{55}\gamma_x, \; V_y = S_{66}\gamma_y \end{aligned} \tag{5.37}$$

In terms of engineering elastic constants, the material stiffness coefficients of an orthotropic layer can be expressed as

$$\begin{aligned} &A_{11} = \overline{E}_x, \; A_{12} = \nu_{xy}\overline{E}_x, \; A_{22} = \overline{E}_y, \; A_{44} = G_{xy}, \\ &A_{55} = G_{xz}, \; A_{66} = G_{yz} \end{aligned} \tag{5.38}$$

where $\overline{E}_{x,y} = E_{x,y}/(1 - \nu_{xy}\nu_{yx})$. Then, Eqs. (5.36) yield

$$\begin{aligned} &B_{11} = \overline{E}_x h, \; B_{12} = \nu_{xy}\overline{E}_x h, \; B_{22} = \overline{E}_y h, \; B_{44} = G_{xy}h \\ &D_{11} = \frac{1}{12}\overline{E}_x h^3, \; D_{12} = \frac{\nu_{xy}}{12}\overline{E}_x h^3, \; D_{22} = \frac{1}{12}\overline{E}_y h^3, \; D_{44} = \frac{1}{12}G_{xy}h^3 \\ &S_{55} = G_{xz}h, \; S_{66} = G_{yz}h \end{aligned} \tag{5.39}$$

Finally, for an isotropic layer, we have

$$E_x = E_y = E, \; \nu_{xy} = \nu_{yx} = \nu, \; G_{xy} = G_{xz} = G_{yz} = G = \frac{E}{2(1+\nu)}$$

and

$$\begin{aligned} &B_{11} = B_{22} = \overline{E}h, \;\; B_{12} = \nu\overline{E}h, \; B_{44} = S_{55} = S_{66} = Gh \\ &D_{11} = D_{22} = \frac{1}{12}\overline{E}h^3, \; D_{12} = \frac{\nu}{12}\overline{E}h^3, \; D_{44} = \frac{1}{12}Gh^3 \end{aligned} \tag{5.40}$$

where $\overline{E} = E/(1 - \nu^2)$.

5.3 STIFFNESS COEFFICIENTS OF A LAMINATE

Consider the general case, i.e., a laminate consisting of an arbitrary number of layers with different thicknesses h_i and stiffnesses $A_{mn}^{(i)}$ $(i = 1, \;\; 2, \;\; 3, \ldots, \;\; k)$. The location of an arbitrary ith layer of the laminate is specified by the coordinate t_i, which is the distance from the bottom plane of the laminate to the top plane of the ith layer (see Fig. 5.10). Assuming that the material stiffness coefficients do not

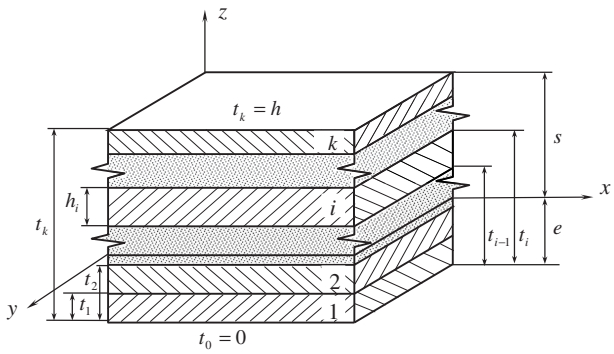


FIGURE 5.10

Structure of the laminate.

change within the thickness of the layer, and using piece-wise integration, we can write parameter I_{mn} in Eqs. (5.29) and (5.32) as

$$I_{mn}^{(r)} = \frac{1}{r+1}\sum_{i=1}^{k} A_{mn}^{(i)}\left(t_i^{r+1} - t_{i-1}^{r+1}\right), \quad \overline{I}_{mn}^{(0)} = \sum_{i=1}^{k} \overline{A}_{mn}^{(i)}\left(t_i - t_{i-1}\right) \tag{5.41}$$

where $r = 0, 1, 2$ and $t_0 = 0, t_k = h$ (see Fig. 5.10). For thin layers, Eqs. (5.41) can be reduced to the following form, which is more suitable for calculations

$$\begin{aligned} I_{mn}^{(0)} &= \sum_{i=1}^{k} A_{mn}^{(i)} h_i, \quad \overline{I}_{mn}^{(0)} = \sum_{i=1}^{k} \overline{A}_{mn}^{(i)} h_i \\ I_{mn}^{(1)} &= \frac{1}{2}\sum_{i=1}^{k} A_{mn}^{(i)}\, h_i(t_i + t_{i-1}) \\ I_{mn}^{(2)} &= \frac{1}{3}\sum_{i=1}^{k} A_{mn}^{(i)}\, h_i\left(t_i^2 + t_i t_{i-1} + t_{i-1}^2\right) \end{aligned} \tag{5.42}$$

in which $h_i = t_i - t_{i-1}$ is the thickness of the ith layer.

The membrane, coupling, and bending stiffness coefficients of the laminate are specified by Eqs. (5.28) and (5.42).

Consider transverse shear stiffnesses that have two different forms determined by Eqs. (5.30) and (5.31) in which

$$I_{mn}^{(0)} = \sum_{i=1}^{k} A_{mn}^{(i)} h_i, \quad \overline{I}_{mn}^{(0)} = \sum_{i=1}^{k} \overline{A}_{mn}^{(i)} h_i. \tag{5.43}$$

A particular case, important for practical applications, is an orthotropic laminate for which Eqs. (5.5) take the form

$$\begin{aligned} N_x &= B_{11}\varepsilon_x^0 + B_{12}\varepsilon_y^0 + C_{11}\kappa_x + C_{12}\kappa_y \\ N_y &= B_{21}\varepsilon_x^0 + B_{22}\varepsilon_y^0 + C_{12}\kappa_x + C_{22}\kappa_y \\ N_{xy} &= B_{44}\gamma_{xy}^0 + C_{44}\kappa_{xy} \\ M_x &= C_{11}\varepsilon_x^0 + C_{12}\varepsilon_y^0 + D_{11}\kappa_x + D_{12}\kappa_y \\ M_y &= C_{21}\varepsilon_x^0 + C_{22}\varepsilon_y^0 + D_{21}\kappa_x + D_{22}\kappa_y \\ M_{xy} &= C_{44}\gamma_{xy}^0 + D_{44}\kappa_{xy} \end{aligned} \tag{5.44}$$

Here, membrane, coupling, and bending stiffnesses B_{mn}, C_{mn}, and D_{mn}, are specified by Eqs. (5.28), i.e.,

$$\begin{aligned} B_{mn} &= I_{mn}^{(0)}, \quad C_{mn} = I_{mn}^{(1)} - eI_{mn}^{(0)}, \\ D_{mn} &= I_{mn}^{(2)} - 2eI_{mn}^{(1)} + e^2 I_{mn}^{(0)} \end{aligned} \tag{5.45}$$

where $mn = 11$, 12, 22, and 44 .

Transverse shear forces V_x and V_y are specified by equations similar to Eqs. (5.20)

$$V_x = S_{55}\gamma_x, \; V_y = S_{66}\gamma_y$$

in which the corresponding stiffness coefficients, Eqs. (5.30) and (5.31), reduce to ($mn = 55$, 66)

$$S_{mn} = \sum_{i=1}^{k} A_{mn}^{(i)} h_i, \quad \overline{S}_{mm} = \frac{h^2}{\sum_{i=1}^{k} \dfrac{h_i}{A_{mm}^{(i)}}} \tag{5.46}$$

Laminates composed of unidirectional plies have special stacking-sequence notations. For example, notation $[0_2^\circ/+45^\circ/-45^\circ/90_2^\circ]$ means that the laminate consists of a 0° layer having two plies, a ±45° angle-ply layer, and a 90° layer also having two plies. Notation $[0^\circ/90^\circ]_5$ means that the laminate has five cross-ply layers.

5.4 SYMMETRIC LAMINATES

Symmetric laminates are composed of layers that are symmetrically arranged with respect to the laminate's middle plane as shown in Fig. 5.11. Introduce the layer coordinate z_i (see Fig. 5.11). Since for any layer which is above the middle surface $z = 0$ and has the coordinate z_i there is a similar layer which is located under the middle surface and has the coordinate $(-z_i)$, the integration over the laminate thickness can be performed from $z = 0$ to $z = h/2$ (see Fig. 5.11). Then, the integrals for B_{mn} and D_{mn} similar to Eqs. (5.6) and (5.7) must be doubled, whereas the integral for C_{mn} similar to Eqs. (5.8) is equal to zero. Thus, the stiffness coefficients entering Eqs. (5.5) become

$$B_{mn} = 2\int_0^{h/2} A_{mn}dz, \quad D_{mn} = 2\int_0^{h/2} A_{mn}z^2 dz, \quad C_{mn} = 0 \tag{5.47}$$

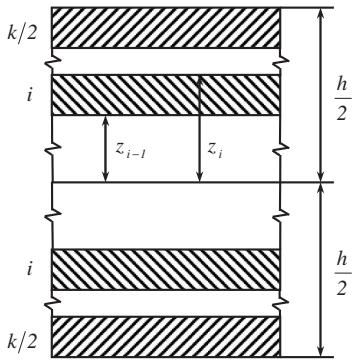


FIGURE 5.11

Layer coordinates of a symmetric laminate.

For a symmetric laminate (shown in Fig. 5.11), we get

$$\begin{aligned} B_{mn} &= 2\sum_{i=1}^{k/2} A_{mn}^{(i)}\left(z_i - z_{i-1}\right) = 2\sum_{i=1}^{k/2} A_{mn}^{(i)} h_i \\ C_{mn} &= 0 \\ D_{mn} &= \frac{2}{3}\sum_{i=1}^{k/2} A_{mn}^{(i)}\left(z_i^3 - z_{i-1}^3\right) = \frac{2}{3}\sum_{i=1}^{k/2} A_{mn}^{(i)} h_i\left(z_i^2 + z_i z_{i-1} + z_{i-1}^2\right) \end{aligned} \tag{5.48}$$

where $h_i = z_i - z_{i-1}$. The transverse shear stiffness coefficients are given by Eqs. (5.30) and (5.31) in which

$$I_{mn}^{(0)} = 2\sum_{i=1}^{k} A_{mn}^{(i)} h_i, \quad \overline{I}_{mn}^{(0)} = 2\sum_{i=1}^{k/2} \overline{A}_{mn}^{(i)} h_i, \quad \overline{A}_{mn}^{(i)} = \frac{A_{mn}^{(i)}}{A_{55}^{(i)} A_{66}^{(i)} - \left(A_{56}^{(i)}\right)^2}. \tag{5.49}$$

To indicate symmetric laminates, a contracted stacking-sequence notation is used, e.g., $[0°/90°/45°]_s$ instead of $[0°/90°/45°/45°/90°/0°]$. Symmetric laminates are characterized by a specific feature: their bending stiffness is higher than the bending stiffness of any asymmetric laminate composed of the same layers. To show this property of symmetric laminates, consider Eqs. (5.28) and (5.29) and apply them to calculate stiffness coefficients with some combination of subscripts, e.g., $m = 1$ and $n = 1$. Since the coordinate of the reference plane, e, is an arbitrary parameter, we can find it from the condition $C_{11} = 0$. Then,

$$e = \frac{I_{11}^{(1)}}{I_{11}^{(0)}} \tag{5.50}$$

and

$$D_{11} = I_{11}^{(2)} - \left[\frac{\left(I_{11}^{(1)}\right)^2}{I_{11}^{(0)}}\right]. \tag{5.51}$$

Introduce a new coordinate for an arbitrary point A in Fig. 5.12 as $z = t - (h/2)$. Changing t to z, we can present Eq. (5.29) in the form

$$I_{11}^{(r)} = \int_{-h/2}^{h/2} A_{11}\left(\frac{h}{2} + z\right)^r dz$$

Substituting these integrals into Eqs. (5.50) and (5.51), we have

$$e = \frac{h}{2} + \frac{J_{11}^{(1)}}{J_{11}^{(0)}} \tag{5.52}$$

and

$$D_{11} = J_{11}^{(2)} - \left[\frac{\left(J_{11}^{(1)}\right)^2}{J_{11}^{(0)}}\right] \tag{5.53}$$

where

$$J_{11}^{(r)} = \int_{-h/2}^{h/2} A_{11} z^r dz \tag{5.54}$$

and $r = 0, 1, 2$.

Now decompose A_{11} as a function of z into symmetric and antisymmetric components, i.e.,

$$A_{11}(z) = A_{11}^s(z) + A_{11}^a(z)$$

Then, Eq. (5.54) yields

$$J_{11}^{(0)} = \int_{-h/2}^{h/2} A_{11}^s dz, \quad J_{11}^{(1)} = \int_{-h/2}^{h/2} A_{11}^a z dz, \quad J_{11}^{(2)} = \int_{-h/2}^{h/2} A_{11}^s z^2 dz$$

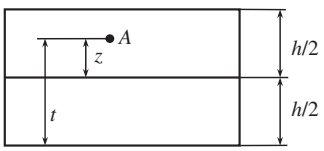


FIGURE 5.12

Coordinate of point *A* referred to the middle plane.

As can be seen from Eq. (5.53), D_{11} reaches its maximum value if $J_{11}^{(1)} = 0$. Then, $A_{11}^{a} = 0$ and $A_{11} = A_{11}^{s}$, which means that the laminate is symmetric. In this case, Eq. (5.52) gives $e = h/2$.

Thus, symmetric laminates provide the maximum bending stiffness for a given number and for mechanical properties of layers and, being referred to the middle-plane, do not have membrane-bending coupling effects. This essentially simplifies the behavior of the laminate under loading and constitutive equations which have the form specified by Eqs. (5.35).

5.5 ENGINEERING STIFFNESS COEFFICIENTS OF ORTHOTROPIC LAMINATES

It follows from Eqs. (5.28) that the laminate stiffness coefficients depend, in the general case, on the coordinate of the reference surface e. By changing e, we can change the bending stiffness coefficient D_{mn}. Naturally, the result of the laminate analysis undertaken with the aid of the constitutive equations, Eqs. (5.5), does not depend on the particular pre-assigned value of the coordinate e because of the coupling coefficients C_{mn} which also depend on e. To demonstrate this, consider an orthotropic laminated element loaded with axial forces N and bending moments M uniformly distributed over the element width as in Fig. 5.13. Suppose that the element displacement does not depend on coordinate y. Then, taking $N_x = N, M_x = M, \varepsilon_y^0 = 0$, and $\kappa_y = 0$ in Eqs. (5.44), we get

$$N = B_{11}\varepsilon_x^0 + C_{11}\kappa_x, \quad M = C_{11}\varepsilon_x^0 + D_{11}\kappa_x \tag{5.55}$$

where, in accordance with Eqs. (5.28),

$$\begin{aligned} B_{11} &= I_{11}^{(0)},\ C_{11} = I_{11}^{(1)} - eI_{11}^{(0)} \\ D_{11} &= I_{11}^{(2)} - 2eI_{11}^{(1)} + e^2 I_{11}^{(0)} \end{aligned} \tag{5.56}$$

Here, as follows from Eqs. (5.41),

$$I_{11}^{(r)} = \frac{1}{r+1}\sum_{i=1}^{k} A_{11}^{(i)}\left(t_i^{r+1} - t_{i-1}^{r+1}\right) \tag{5.57}$$

($r = 0, 1, 2$) are the coefficients which do not depend on the coordinate of the reference plane e.

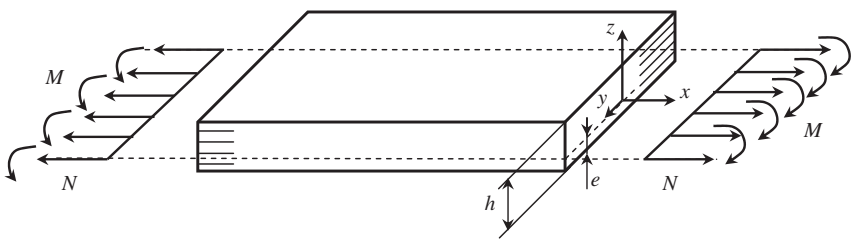


FIGURE 5.13

Laminated element under tension and bending.

It is important to emphasize that forces N in Fig. 5.13 act in the reference plane $z = 0$, and the strain ε_x^0 in Eqs. (5.55) is the strain of the reference plane. Solving Eqs. (5.55) for ε_x^0 and κ_x, we have

$$\varepsilon_x^0 = \frac{1}{D_1}\left(D_{11}N - C_{11}M\right), \quad \kappa_x = \frac{1}{D_1}\left(B_{11}M - C_{11}N\right) \tag{5.58}$$

where

$$D_1 = B_{11}D_{11} - C_{11}^2 \tag{5.59}$$

Substituting B, D, and C from Eqs. (5.56), we find

$$D_1 = I_{11}^{(0)}I_{11}^{(2)} - \left(I_{11}^{(1)}\right)^2$$

As can be seen, the parameter D_1 does not depend on e.

Consider now the same element but loaded with forces P applied to the middle plane of the element as in Fig. 5.14. As follows from Fig. 5.15 showing the element cross section, the forces and the moments in Fig. 5.13 induced by the forces shown in Fig. 5.14 are

$$N = P, \quad M = P\left(\frac{h}{2} - e\right) \tag{5.60}$$

Substitution of Eqs. (5.60) into Eqs. (5.58) yields

$$\varepsilon_x^0 = \frac{P}{D_1}\left[I_{11}^{(2)} - eI_{11}^{(1)} - \frac{h}{2}\left(I_{11}^{(1)} - eI_{11}^{(0)}\right)\right] \tag{5.61}$$

$$\kappa_x = \frac{P}{D_1}\left(\frac{h}{2}I_{11}^{(0)} - I_{11}^{(1)}\right) \tag{5.62}$$

It follows from Eq. (5.62) that κ_x does not depend on e, which is expected because the curvature induced by forces P in Fig. 5.14 is the same for all the planes $z = constant$ of the element. However, Eq. (5.61) includes e which is also expected because ε_x^0 is the strain in the plane $z = 0$ located at the distance e from the lower plane of the element (see Fig. 5.15). Let us find the strain ε_x^t at some arbitrary point A of the cross section for which $z = t - e$ (see Fig. 5.15). Using the first equation of Eqs. (5.3),

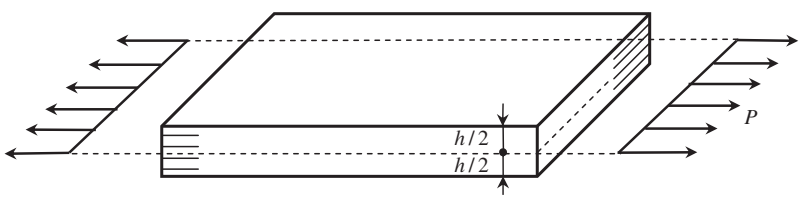


FIGURE 5.14

Laminated element under tension.

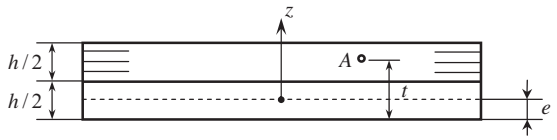


FIGURE 5.15

Cross-section of the element.

we have

$$\varepsilon_x^t = \varepsilon_x^0 + (t-e)\kappa_x = \frac{P}{D_1}\left[I_{11}^{(2)} - \frac{h}{2}\left(tI_{11}^{(0)} - I_{11}^{(1)}\right) - tI_{11}^{(1)}\right]$$

This equation includes the coordinate of point A and does not depend on e. Thus, taking an arbitrary coordinate of the reference plane, and applying Eqs. (5.56) for the stiffness coefficients, we arrive at values of C_{11} and D_{11}, the combination of which provides the final result that does not depend on e. However, the derived stiffness coefficient D_{11} is not the actual bending stiffness of the laminate which cannot depend on e.

To determine the actual stiffness of the laminate, return to Eqs. (5.58) for ε_x^0 and κ_x. Suppose that $C_{11} = 0$, which means that the laminate has no bending-stretching coupling effects. Then, Eq. (5.59) yields $D = B_{11}D_{11}$ and Eqs. (5.58) become

$$\varepsilon_x^0 = \frac{N}{B_{11}}, \quad \kappa_x = \frac{M}{D_{11}} \tag{5.63}$$

It is obvious that now B_{11} is the actual axial stiffness and D_{11} is the actual bending stiffness of the laminate. However, Eqs. (5.63) are valid only if $C_{11} = 0$. Using the second equation of Eqs. (5.56), we get

$$e = \frac{I_{11}^{(1)}}{I_{11}^{(0)}} \tag{5.64}$$

Substituting this result into Eqs. (5.56) and introducing new notations $B_x = B_{11}$ and $D_x = D_{11}$ for the actual axial and bending stiffnesses of the laminate in the x direction, we arrive at

$$B_x = I_{11}^{(0)}, \quad D_x = I_{11}^{(2)} - \frac{\left(I_{11}^{(1)}\right)^2}{I_{11}^{(0)}} \tag{5.65}$$

Here, coefficients $I_{11}^{(r)}$ $(r = 0, 1, 2)$ are specified by Eqs. (5.57). The corresponding stiffnesses in the y direction (see Fig. 5.13) are determined from similar equations, i.e.,

$$B_y = I_{22}^{(0)}, \quad D_y = I_{22}^{(2)} - \frac{\left(I_{22}^{(1)}\right)^2}{I_{22}^{(0)}} \tag{5.66}$$

in which

$$I_{22}^{(r)} = \frac{1}{r+1}\sum_{i=1}^{k} A_{22}^{(i)}\left(t_i^{r+1} - t_{i-1}^{r+1}\right)$$

For symmetric laminates, as discussed in Section 5.4, $C_{mn} = 0$ and coefficients D_{mn} in Eqs. (5.48) specify the actual bending stiffnesses of the laminate, i.e.,

$$\begin{aligned} D_x &= \frac{2}{3}\sum_{i=1}^{k/2} A_{11}^{(i)} h_i\left(z_i^2 + z_i z_{i-1} + z_{i-1}^2\right) \\ D_y &= \frac{2}{3}\sum_{i=1}^{k/2} A_{22}^{(i)} h_i\left(z_i^2 + z_i z_{i-1} + z_{i-1}^2\right) \end{aligned} \tag{5.67}$$

where coordinates z_i and z_{i-1} are shown in Fig. 5.11. Note that if the number of layers k is not even, the central layer is divided by the plane $z = 0$ into two identical layers so k becomes even.

To find the shear stiffness, consider the element in Fig. 5.13, but loaded with shear forces, S, and twisting moments H, uniformly distributed along the element edges as shown in Fig. 5.16. It should be recalled that forces and moments are applied to the element reference plane $z = 0$ (see Fig. 5.13). Taking $N_{xy} = S$ and $M_{xy} = H$ in the corresponding Eqs. (5.44), we get

$$S = B_{44}\gamma_{xy}^0 + C_{44}\kappa_{xy}, \quad H = C_{44}\gamma_{xy}^0 + D_{44}\kappa_{xy} \tag{5.68}$$

in which, in accordance with Eqs. (5.28) and (5.41),

$$B_{44} = I_{44}^{(0)}, \quad C_{44} = I_{44}^{(1)} - eI_{44}^{(0)}, \quad D_{44} = I_{44}^{(2)} - 2eI_{44}^{(1)} + e^2 I_{44}^{(0)} \tag{5.69}$$

where

$$I_{44}^{(r)} = \frac{1}{r+1}\sum_{i=1}^{k} A_{44}^{(i)}\left(t_i^{r+1} - t_{i-1}^{r+1}\right)$$

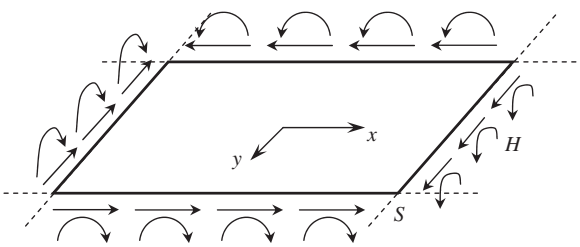


FIGURE 5.16

Shear and torsion of the element.

The solution of Eqs. (5.68) is

$$\gamma_{xy}^0 = \frac{1}{D_4}\left(D_{44}S - C_{44}H\right), \quad \kappa_{xy} = \frac{1}{D_4}\left(B_{44}M - C_{44}S\right) \tag{5.70}$$

in which $D_4 = I_{44}^{(0)} I_{44}^{(2)} - (I_{44}^{(1)})^2$.
A further transformation is used similar to that for Eqs. (5.58) and (5.59). Taking the coordinate of the reference plane as

$$e = \frac{I_{44}^{(1)}}{I_{44}^{(0)}} \tag{5.71}$$

we get $C_{44} = 0$, and Eqs. (5.70) reduce to

$$\gamma_{xy}^0 = \frac{S}{B_{44}}, \quad \kappa_{xy} = \frac{H}{D_{44}} \tag{5.72}$$

Using the new notations $B_{44} = B_{xy}$ and $D_{44} = D_{xy}$ and applying Eqs. (5.69) and (5.71), we arrive at

$$B_{xy} = I_{44}^{(0)}, \quad D_{xy} = I_{44}^{(2)} - \frac{\left(I_{44}^{(1)}\right)^2}{I_{44}^{(0)}} \tag{5.73}$$

where B_{xy} is the actual in-plane shear stiffness of the laminate, whereas D_{xy} needs some comments. The second equation of Eqs. (5.72) yields

$$H = D_{xy}\kappa_{xy} \tag{5.74}$$

where κ_{xy} is given in notations to Eqs. (5.3), i.e.,

$$\kappa_{xy} = \frac{\partial \theta_x}{\partial y} + \frac{\partial \theta_y}{\partial x} \tag{5.75}$$

The deformed state of the laminated element (see Fig. 5.16) loaded with twisting moments only is shown in Fig. 5.17. Consider the deflection of point A with coordinates x and y. It follows from Fig. 5.17 that $w = x\theta_x$ or $w = y\theta_y$. Introduce the gradient of the torsional angle

$$\theta' = \frac{\partial \theta_x}{\partial y} = \frac{\partial \theta_y}{\partial x}$$

Since θ' does not depend on x and y, $\theta_x = y\theta', \theta_y = x\theta'$, and $w = xy\theta'$. Using Eq. (5.75), we have $\kappa_{xy} = 2\theta'$. Then, Eq. (5.74) yields

$$H = D_t^p \theta' \tag{5.76}$$

where

$$D_t^p = 2D_{xy} \tag{5.77}$$

is the plate torsional stiffness specifying the stiffness of the element which is loaded with twisting moments applied to all four edges of the element, as shown in Fig. 5.16.

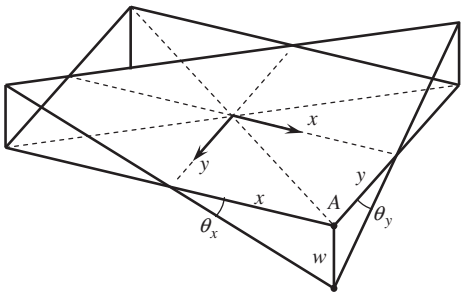


FIGURE 5.17

Deformation of the element under torsion.

However, in practice we usually need the torsional stiffness of the element loaded with twisting moments applied to only two opposite edges of the element, whereas the two other edges are free. Since such loading induces not only twisting moments (see Fig. 5.4) but also transverse shear forces V (see Fig. 5.6), we must first determine the actual transverse (through-the-thickness) stiffnesses of a laminate.

Consider an orthotropic laminated element loaded with transverse shear forces $V_x = V$ uniformly distributed over the element edge as in Fig. 5.18. From Eqs. (5.20), we have two possible constitutive equations, i.e.,

$$V = S_{55}\gamma_x, \quad V = \overline{S}_{55}\gamma_x \tag{5.78}$$

in which, in accordance with Eqs. (5.46),

$$S_{55} = \sum_{i=1}^{k} A_{55}^{(i)} h_i, \quad \overline{S}_{55} = \frac{h^2}{\sum_{i=1}^{k} \dfrac{h_i}{A_{55}^{(i)}}} \tag{5.79}$$

For the orthotropic material, $A_{55}^{(i)} = G_{xz}^{(i)}$, where $G_{xz}^{(i)}$ is the transverse shear modulus of the ith layer. Thus, Eqs. (5.79) take the form

$$S_{55} = \sum_{i=1}^{k} G_{xz}^{(i)} h_i, \quad \overline{S}_{55} = \frac{h^2}{\sum_{i=1}^{k} \dfrac{h_i}{G_{xz}^{(i)}}} \tag{5.80}$$

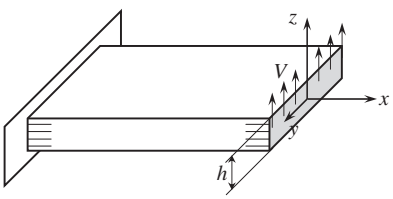


FIGURE 5.18

Laminated element loaded with transverse shear forces.

As shown in Section 5.1, S_{55} gives the upper bound and $\overline{S}_{55}$ gives the lower bound of the actual transverse shear stiffness of the laminate. For a laminate consisting of identical layers, i.e., for the case $G_{xz}^{(i)} = G_{xz}$ for all the layers, both equations of Eqs. (5.80) give the same result, $S_{55} = \overline{S}_{55} = G_{xz}h$. However, in some cases, the results following from Eqs. (5.80) can be dramatically different, whereas for engineering applications we must have a unique constitutive equation instead of Eqs. (5.78), i.e.,

$$V = S_x \gamma_x \tag{5.81}$$

and the question arises whether S_{55} or $\overline{S}_{55}$ should be taken as S_x in this equation. Since for a homogeneous material there is no difference between S_{55} and $\overline{S}_{55}$, we can expect that this difference shows itself in the laminates consisting of layers with different transverse shear moduli.

Consider, for example, sandwich structures composed of high-stiffness thin facing layers (facings) and low-stiffness light foam core (Fig. 5.19a). The facings (2 in Fig. 5.19a) are made of aluminum alloy with modulus $E_f = 70$ GPa and shear modulus $G_f = 26.9$ GPa. The foam core (1 in Fig. 5.19a) has $E_c = 0.077$ GPa and $G_c = 0.0385$ GPa. The geometric and stiffness parameters of two sandwich beams studied experimentally (Aleksandrov et al., 1960) are presented in Table 5.1. The beams with length $l = 280$ mm have been tested under transverse bending. The coefficient S_a in the table corresponds to the actual shear stiffness found from experimental results. Actually, experimental study allows us to determine the shear parameter (Vasiliev, 1993)

$$k_G = \frac{D}{S_a l^2} \tag{5.82}$$

which is presented in the third column of the table and depends on the bending stiffness, D, and the beam length, l. Since the sandwich structure is symmetric, we can use Eq. (5.67) for D_x in which $2k = 2$ (the core is divided into two identical layers as in Fig. 5.19a)

$$A_{11}^{(1)} = E_c,\ A_{11}^{(2)} = E_f,$$
$$h_1 = \frac{h_c}{2},\quad h_2 = h_f,\quad z_0 = 0,\quad z_1 = \frac{h_c}{2},\quad z_2 = \frac{h_c}{2} + h_f$$

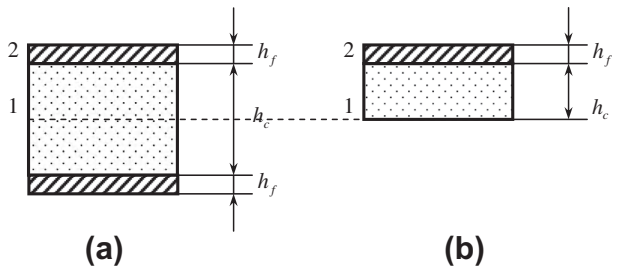


FIGURE 5.19

Three-layered (a) and two-layered (b) laminates.

TABLE 5.1 Parameters of Sandwich Structures.

h_f (mm)	h_c (mm)	k_G	Shear Stiffness (GPa × mm)			Bending Stiffness (GPa × mm^3)
			S_a	$\overline{S}_{55}$	S_{55}	
2.4	18.8	0.444	1.09	1.14	130	37,960
1.0	17.0	0.184	0.79	0.82	54.5	11,380

The final expression is

$$D_x = \frac{2}{3}\left[\frac{1}{8}E_c h_c^3 + E_f h_f\left(\frac{3}{4}h_c^2 + \frac{3}{2}h_c h_f + h_f^2\right)\right]$$

The results of the calculation are listed in the last column of Table 5.1. The shear stiffness coefficients S_{55} and $\overline{S}_{55}$ can be found from Eqs. (5.80) which for the structure in Fig. 5.19a take the form

$$S_{55} = h_c G_c + 2h_f G_f$$

$$\overline{S}_{55} = \frac{\left(h_c + 2h_f\right)^2}{\dfrac{h_c}{G_c} + \dfrac{2h_f}{G_f}}$$

The results of the calculation are presented in Table 5.1. As can be seen, coefficients $\overline{S}_{55}$ are in good agreement with the corresponding experimental data, whereas coefficients S_{55} are higher by an order of magnitude. Note that $\overline{S}_{55}$, providing the lower boundary for the exact shear stiffness, is higher than the actual stiffness S_a. The reason for this effect has been discussed in Section 5.1. Coefficient $\overline{S}_{55}$ specifies the lower boundary for the theoretical exact stiffness corresponding to the applied model of the laminate, but not for the actual stiffness following from experiment. For example, the actual shear stiffness of the sandwich beams described previously can be affected by the compliance of adhesive layers which bond the facings and the core and are not allowed for in the laminate model.

So, it can be concluded that the shear stiffness coefficient $\overline{S}_{55}$ specified by the corresponding equation of Eqs. (5.79) can be used to describe the transverse shear stiffness of composite laminates. However, there are special structures for which coefficient S_{55} provides a better approximation of shear stiffness than coefficient $\overline{S}_{55}$. Consider, for example, a two-layered structure shown in Fig. 5.19b and composed of a high-stiffness facing (2 in Fig. 5.19b) and a low-stiffness core (1 in Fig. 5.19b). Assume, as for the sandwich structure considered earlier, that $G_f = 26.9$ GPa and $G_c = 0.0385$ GPa, so that $G_f/G_c = 699$, and take $h_c = 9.9$ mm, and $h_f = 2.4$ mm. It is obvious that the core, having such a low-shear modulus, does not work, and the transverse shear stiffness of the laminate is governed by the facing layer. For this layer only, we get

$$S_{55} = \overline{S}_{55} = G_f h_f = 64.6 \text{ GPa}\cdot\text{mm}$$

whereas for the laminate, Eqs. (5.80) yield

$$S_{55} = h_c G_c + h_f G_f = 65 \text{ GPa}\cdot\text{mm}$$

$$\overline{S}_{55} = \frac{\left(h_c + h_f\right)^2}{\dfrac{h_c}{G_c} + \dfrac{h_f}{G_f}} = 0.59 \text{ GPa} \cdot \text{mm}$$

As can be seen, coefficient $\overline{S}_{55}$ is too far from the value that would be expected. However, structures of the type for which the stiffness coefficient S_{55} is more appropriate than the coefficient $\overline{S}_{55}$ are not typical in composite technology and, being used, they usually do not require the calculation of transverse shear stiffnesses. For laminated composites it can be recommended to use the coefficient $\overline{S}_{55}$ (Chen and Tsai, 1996). Thus, the transverse shear stiffness coefficient in Eq. (5.81) can be taken in the following form

$$S_x = \frac{h^2}{\sum_{i=1}^{k} \dfrac{h_i}{G_{xz}^{(i)}}} \tag{5.83}$$

For shear in the yz-plane (see Fig. 5.18), we get a similar expression, i.e.,

$$S_y = \frac{h^2}{\sum_{i=1}^{k} \dfrac{h_i}{G_{yz}^{(i)}}} \tag{5.84}$$

In engineering analysis of laminated composites, transverse shear stiffnesses are mainly used to study the problems of transverse bending of composite beams and plates. Note that the so-called classical theory of laminated beams and plates ignores the transverse shear deformation of the laminate. Consider the constitutive equations for the shear forces and write them in the following form:

$$\gamma_x = \frac{V_x}{S_x}, \quad \gamma_y = \frac{V_y}{S_y}$$

Taking $S_x \to \infty$ and $S_y \to \infty$, we get $\gamma_x = 0$ and $\gamma_y = 0$. Applying Eqs. (5.14) for γ_x and γ_y, we can express the rotation angles in terms of the deflection as

$$\theta_x = -\frac{\partial w}{\partial x}, \quad \theta_y = -\frac{\partial w}{\partial y}$$

Then, the expressions for curvatures entering Eqs. (5.3) take the form

$$\kappa_x = -\frac{\partial^2 w}{\partial x^2}, \quad \kappa_y = -\frac{\partial^2 w}{\partial y^2}, \quad \kappa_{xy} = -2\frac{\partial^2 w}{\partial x \partial y}$$

For actual laminates, the transverse shear stiffness coefficients are not infinitely high, but nevertheless, the classical theories ignoring the corresponding deformation are widely used in the analysis of composite structures. To evaluate the possibility of neglecting transverse shear deformation, we can use parameter k_G specified by Eq. (5.82) and compare it with unity. The effect of the transverse shear deformation is demonstrated in Table 5.2 for the problem of transverse bending of simply supported sandwich beams with various parameters k_G listed in the table. The right-hand column of the table shows the ratio of the maximum deflections of the beam, w, found with allowance for transverse shear

TABLE 5.2 The Effect of Transverse Shear Deformation on the Deflection of Sandwich Beams.

Beam No.	$k_G = \dfrac{D}{Sl^2}$	$\dfrac{w_G}{w_\infty}$
1	0.444	5.386
2	0.184	2.805
3	0.015	1.152
4	0.0015	1.014
5	0.0004	1.002

deformation (w_G) and corresponding to the classical beam theory (w_∞). As can be seen, for beams number 4 and 5, having parameter k_G which is negligible in comparison with unity, the shear deformation practically does not affect the beams' deflections.

Returning to the problem of torsion, we consider an orthotropic laminated strip with width b loaded with a torque M_t as in Fig. 5.20. In contrast to the laminate shown in Fig. 5.6, the strip in Fig. 5.20 is loaded only at the transverse edges, whereas the longitudinal edges $y = \pm\ b/2$ are free. The shear stresses τ_{xz} and τ_{yz} induced by torsion give rise to the shear forces N_{xy}, twisting moment M_{xy}, and transverse shear force V_x shown in Fig. 5.21. Applying the corresponding constitutive equations, Eqs. (5.44) and (5.81), we get

$$N_{xy} = B_{44}\gamma_{xy}^0 + C_{44}\kappa_{xy}, \quad M_{xy} = C_{44}\gamma_{xy}^0 + D_{44}\kappa_{xy} \tag{5.85}$$

$$V_x = S_x\gamma_x \tag{5.86}$$

where the stiffness coefficients B, C, D, and S are specified by Eqs. (5.69) and (5.82). Pre-assign the coordinate of the reference plane e in accordance with Eq. (5.71). Then, $C_{44} = 0$ and Eqs. (5.85) reduce to

$$N_{xy} = B_{xy}\gamma_{xy}^0 \tag{5.87}$$

$$M_{xy} = D_{xy}\kappa_{xy} \tag{5.88}$$

where B_{xy} and D_{xy} are given by Eqs. (5.73). Since the strip is loaded with a torque M_t only (see Fig. 5.20), $N_{xy} = 0$, and as follows from Eq. (5.87), $\gamma_{xy}^0 = 0$. So, we have only two constitutive equations, i.e., Eqs. (5.86) and (5.88), for V_x and M_{xy} which are expressed in terms of the transverse shear strain γ_x and the twisting deformation κ_{xy}. Applying Eqs. (5.14) and (5.75), we have

$$\gamma_x = \theta_x + \frac{\partial w}{\partial x}, \quad \kappa_{xy} = \frac{\partial \theta_x}{\partial y} + \frac{\partial \theta_y}{\partial x} \tag{5.89}$$

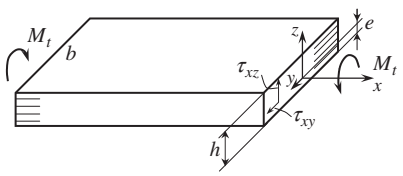


FIGURE 5.20

Torsion of a laminated strip.

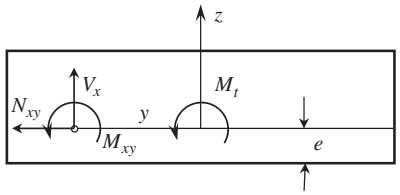


FIGURE 5.21

Forces and moments acting in the strip cross section.

Consider the deformation of the strip. Assume that the strip cross section rotates around the longitudinal axis x through an angle θ which depends only on x (Fig. 5.22). Then, as follows from Fig. 5.22,

$$w = -y\theta, \quad \theta_y = \theta$$

and the corresponding substitution in Eqs. (5.89) yields

$$\gamma_x = \theta_x - \theta' y, \quad \kappa_{xy} = \frac{\partial \theta_x}{\partial y} + \theta'$$

where $\theta' = d\theta/dx$. Using the first of these equations to transform the second one, we get

$$\kappa_{xy} = \frac{\partial \gamma_x}{\partial y} + 2\theta'$$

Thus, the constitutive equations, Eqs. (5.86) and (5.88), take the following final form

$$V_x = S_x \gamma_x, \quad M_{xy} = D_{xy}\left(\frac{\partial \gamma_x}{\partial y} + 2\theta'\right) \tag{5.90}$$

Consider the equilibrium of the strip element shown in Fig. 5.23. The equilibrium equations in this case are

$$\frac{\partial V_x}{\partial x} = 0, \quad \frac{\partial M_{xy}}{\partial x} = 0 \tag{5.91}$$

$$\frac{\partial M_{xy}}{\partial y} - V_x = 0 \tag{5.92}$$

The first two equations, Eqs. (5.91) show that $V_x = V_x(y)$ and $M_{xy} = M_{xy}(y)$. Then, as follows from Eq. (5.90) for V_x, $\gamma_x = \gamma_x(y)$. Substituting M_{xy} and V_x from Eqs. (5.90) into Eq. (5.92) and taking

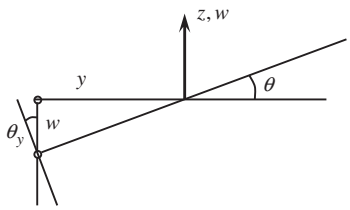


FIGURE 5.22

Rotation of the strip cross-section.

into account that θ' does not depend on y, we arrive at the following ordinary differential equation for γ_x

$$\frac{d^2\gamma_x}{dy^2} - k^2\gamma_x = 0$$

in which $k^2 = S_x/D_{xy}$. The general solution of this equation is

$$\gamma_x = C_1 \sinh ky + C_2 \cosh ky$$

Substitution in Eq. (5.90) for M_{xy} yields

$$M_{xy} = D_{xy}\left[2\theta' + k\left(C_1 \cosh ky + C_2 \sinh ky\right)\right]$$

The constants of integration C_1 and C_2 can be found from the boundary conditions according to which $M_{xy}(y = \pm b/2) = 0$ (see Fig. 5.20). The final solution is

$$V_x = -\frac{2S_x \sinh ky}{k \cosh \lambda}\,\theta', \quad M_{xy} = 2D_{xy}\theta'\left(1 - \frac{\cosh ky}{\cosh \lambda}\right) \tag{5.93}$$

in which

$$\lambda = \frac{1}{2}kb = \frac{b}{2}\sqrt{\frac{S_x}{D_{xy}}} \tag{5.94}$$

Consider Fig. 5.21 and express the applied torque M_t in terms of internal forces and moments V_x and M_{xy} as

$$M_t = \int_{-b/2}^{b/2} \left(M_{xy} - V_x y\right) dy$$

Substituting M_{xy} and V_x from Eqs. (5.93), we arrive at

$$M_t = D_t\theta'$$

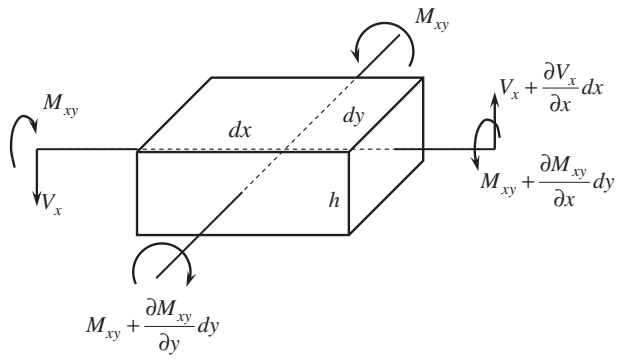


FIGURE 5.23

Forces and moments acting on the strip element.

where

$$D_t = 4D_{xy}b\left(1 - \frac{1}{\lambda}\tanh\lambda\right) \tag{5.95}$$

is the torsional stiffness of the strip. For a homogeneous orthotropic laminate (discussed in Section 5.2),

$$D_{xy} = \frac{1}{12}G_{xy}h^3, \quad S_x = G_{xz}h$$

and Eq. (5.95) reduces to

$$D_t = \frac{1}{3}bh^3G_{xy}\left(1 - \frac{1}{\lambda}\tanh\lambda\right) \tag{5.96}$$

where

$$\lambda = \frac{b}{h}\sqrt{\frac{3G_{xz}}{G_{xy}}}$$

The stiffness coefficient in Eq. (5.96) is in close agreement with the exact elasticity theory solutions (Vasiliev, 1993). Particularly, for $b/h \geq 3$ the difference between D_t given by Eq. (5.96) and the exact result is less than 2%. For a wide strip with relatively large b, the parameter λ in Eq. (5.94) is also large, and Eq. (5.95) can be approximately reduced to

$$D_t = 4D_{xy}b \tag{5.97}$$

Dividing D_t by b, we can find the stiffness of the laminate with a unit width, i.e.,

$$D_t^b = 4D_{xy} \tag{5.98}$$

This is a beam torsional stiffness which is twice as high as the plate stiffness specified by Eq. (5.77). The difference between Eqs. (5.77) and (5.98) is expected because Eq. (5.77) corresponds to torsion with the moments acting on all four edges of the element (see Fig. 5.16), whereas Eq. (5.98) describes torsion with only two moments applied at the transverse edges (see Fig. 5.20).

Thus, the laminate membrane, bending, transverse shear, and torsional stiffness coefficients are specified by Eqs. (5.65; 5.66; 5.82; 5.83 and 5.95).

5.6 QUASI-HOMOGENEOUS LAMINATES

Some typical layers considered in Chapter 4 were actually quasi-homogeneous laminates (see Sections 4.4 and 4.5), but being composed of a number of identical plies, they were treated as homogeneous layers. The accuracy of this assumption is evaluated ahead.

5.6.1 Laminate composed of identical homogeneous layers

Consider a laminate composed of layers with different thicknesses but the same stiffnesses, i.e., $A_{mn}^{(i)} = A_{mn}$ for all $i = 1, 2, 3, \ldots$ k. Then, Eqs. (5.29) and (5.32) yield

$$I_{mn}^{(r)} = \frac{A_{mn}}{r+1}h^{r+1}, \quad \overline{I}_{mn}^{(0)} = \overline{A}_{mn}h$$

This result coincides with Eqs. (5.33), which means that a laminate consisting of layers with the same mechanical properties is a homogeneous laminate (layer) as studied in Section 5.2.

5.6.2 Laminate composed of inhomogeneous orthotropic layers

Let the laminate have the following structure $[0°/90°]_p$, where $p = 1, 2, 3, \ldots$ specifies the number of elementary cross-ply couples of 0° and 90° plies. In Section 4.4, this laminate was treated as a homogeneous layer with material stiffness coefficients specified by Eqs. (4.114). Taking $\overline{h}_0 = \overline{h}_{90} = 0.5$ in these equations, we have

$$A_{11} = A_{22} = \frac{1}{2}\left(\overline{E}_1 + \overline{E}_2\right), \quad A_{12} = \overline{E}_1\nu_{12}, \quad A_{44} = G_{12} \tag{5.99}$$

In accordance with Eqs. (5.36), the stiffness coefficients of this layer should be

$$B^0_{mn} = A_{mn}h, \quad C^0_{mn} = 0, \quad D^0_{mn} = \frac{1}{12}A_{mn}h^3 \tag{5.100}$$

To calculate the actual stiffnesses of the laminate, we should put $h_i = \delta, t_i = i\delta, k = 2p, e = h/2$, and $h = 2p\delta$ (see Fig. 5.10), where δ is the thickness of a unidirectional ply. Then, Eqs. (5.28) and (5.42) yield

$$\begin{aligned} B_{mn} &= I^{(0)}_{mn}, \quad C_{mn} = I^{(1)}_{mn} - p\delta\, I^{(0)}_{mn}, \\ D_{mn} &= I^{(2)}_{mn} - 2p\delta\, I^{(1)}_{mn} + p^2\delta^2 I^{(0)}_{mn} \end{aligned} \tag{5.101}$$

Here,

$$\begin{aligned} &I^{(0)}_{11} = I^{(0)}_{22} = p\delta\,\overline{E}_1\left(1+\alpha\right) = \frac{h}{2}\overline{E}_1\left(1+\alpha\right), \quad I^{(0)}_{12} = 2p\delta\,\overline{E}_1\,\nu_{12} = \overline{E}_1\,\nu_{12}h, \\ &I^{(0)}_{44} = 2p\delta\,G_{12} = G_{12}h, \quad I^{(1)}_{11} = \frac{\delta^2}{2}\overline{E}_1\sum_{j=1}^{p}[4j(1+\alpha) - (3+\alpha)], \\ &I^{(1)}_{22} = \frac{\delta^2}{2}\overline{E}_1\sum_{j=1}^{p}[4j(1+\alpha) - (3\alpha+1)], \quad I^{(1)}_{12} = \frac{1}{2}\overline{E}_1\nu_{12}h^2, \\ &I^{(1)}_{44} = \frac{1}{2}G_{12}h^2, \\ &I^{(2)}_{11} = \frac{\delta^3}{3}\overline{E}_1\sum_{j=1}^{p}\left[12j^2\left(1+\alpha\right) - 6j\left(3+\alpha\right) + 7 + \alpha\right], \\ &I^{(2)}_{22} = \frac{\delta^3}{3}\overline{E}_1\sum_{j=1}^{p}\left[12j^2\left(1+\alpha\right) - 6j\left(3\alpha+1\right) + 7\alpha + 1\right], \\ &I^{(2)}_{12} = \frac{1}{3}\overline{E}_1\nu_{12}h^3, \quad I^{(2)}_{44} = \frac{1}{3}G_{12}h^3 \end{aligned} \tag{5.102}$$

where $\alpha = E_2/E_1$.

Matching Eqs. (5.99), (5.100), (5.101), and (5.102), we can see that $B_{mn} = B^0_{mn}$, i.e., membrane stiffnesses are the same for both models of the laminate. The coupling and bending stiffnesses are also the same for $mn = 12, 44$. There is no difference between the models for $\alpha = 1$ because the laminate reduces in this case to a homogeneous layer.

Summing up the series in Eqs. (5.102) and using Eqs. (5.101), we arrive at

$$\begin{aligned} C_{11} &= -C_{22} = \frac{1}{2}\overline{E}_1\delta^2 p(\alpha - 1), \quad C_{12} = C_{44} = 0, \\ D_{11} &= D_{22} = \frac{1}{3}\overline{E}_1\delta^3 p^3(1+\alpha), \quad D_{12} = D_{12}^0, \quad D_{44} = D_{44}^0 \end{aligned} \tag{5.103}$$

Taking into account that in accordance with Eqs. (5.100) and accepted notations

$$D_{11}^0 = D_{22}^0 = \frac{1}{3}\overline{E}_1\delta^3 p^3(1+\alpha)$$

we can conclude that the only difference between the homogeneous and the laminated models is associated with the coupling coefficients C_{11} and C_{22}, which are equal to zero for the homogeneous model and are specified by Eqs. (5.103) for the laminated one. Since $p\delta = h/2$, we can write these coefficients in the form

$$C_{11} = -C_{22} = \frac{1}{4}\overline{E}_1 h\delta\ (1+\alpha)$$

showing that $C_{mn} \to 0$ for $\delta \to 0$.

5.6.3 Laminate composed of angle-ply layers

Consider a laminate with the following structure $[+\ \phi\ /-\phi\ ]_p$, where p is the number of layers each consisting of $+\phi$ and $-\phi$ unidirectional plies. Taking the coordinate of the reference surface $e = h/2$, we can write the constitutive equations, Eqs. (5.5), as

$$\begin{aligned} N_x &= B_{11}\varepsilon_x^0 + B_{12}\varepsilon_y^0 + C_{14}\kappa_{xy} \\ N_y &= B_{21}\varepsilon_x^0 + B_{22}\varepsilon_y^0 + C_{24}\kappa_{xy} \\ N_{xy} &= B_{44}\gamma_{xy}^0 + C_{41}\kappa_x + C_{42}\kappa_y \\ M_x &= C_{14}\gamma_{xy}^0 + D_{11}\kappa_x + D_{12}\kappa_y \\ M_y &= C_{24}\gamma_{xy}^0 + D_{21}\kappa_x + D_{22}\kappa_y \\ M_{xy} &= C_{41}\varepsilon_x^0 + C_{42}\varepsilon_y^0 + D_{44}\kappa_{xy} \end{aligned} \tag{5.104}$$

in which

$$B_{mn} = A_{mn}h, \quad C_{mn} = -\frac{1}{2}A_{mn}h\delta, \quad D_{mn}\frac{1}{12}A_{mn}h^3$$

where, h is the laminate thickness, δ is the ply thickness, and A_{mn} are material stiffness coefficients specified by Eqs. (4.72). As can be seen, the laminate is anisotropic because $+\phi$ and $-\phi$ plies are located in different planes. The homogeneous model of the laminate ignores this fact and yields $C_{14} = C_{24} = 0$. Calculations show that these coefficients, although not actually equal to zero, have virtually no practical influence on the laminate behavior for $h/\delta \geq 20$.

Laminates in which any ply or layer with orientation angle $+\phi$ is accompanied by the same ply or layer but with angle $-\phi$ are referred to as balanced laminates. Being composed of only angle-ply layers, these laminates have no shear-extension $(B_{14} = B_{24} = 0)$, bending-stretching, and shear-twisting coupling $(C_{11} = C_{12} = C_{22} = C_{44} = 0)$. As follows from Eqs. (5.104), only

stretching-twisting and bending-shear coupling can exist in balanced laminates. These laminates can include also 0° and 90° layers; however, membrane-bending coupling can appear in such laminates.

5.6.4 Fiber metal laminates

Fiber metal laminates (FML) are composed of thin (0.3–0.5 mm thick) metal layers alternating with composite plies. To provide an appropriate adhesion, the metal layers are subjected to a special surface treatment, whereas the pre-impregnated with resin, high-strength fibers are used to form the composite layers having a unidirectional, cross-ply, or fabric structure. Fiber metal laminates are normally made by hot pressing, during which metal layers are formed to a required shape and composite plies are cured. To date, there exist a number of fiber metal laminates, e.g. ARALL (aramid fibers and aluminum), ALOR (aluminum and organic fibers), GLARE and SIAL (glass fibers and aluminum), and TIGR (titanium and graphite fibers), described elsewhere (Bucci et al., 1987, 1988; Vlot et al., 1992; Fridlyander et al., 1997; Vlot and Gunnik, 2001; Vermeeren, 2003). Being originally developed to increase the strength of bolted joints for composite laminates (Sirotkin, 1973; Vorobey and Sirotkin, 1985; Kolesnikov et al., 2008), fiber metal laminates are now used to fabricate the airframe skin of modern airplanes (Ohrloff and Horst, 1992). Reinforcement of carbon-epoxy laminate with titanium layers is shown in Fig. 5.24, whereas the GLARE skin of an airplane fuselage is presented in Fig. 5.25. Compared to monolithic metals, fiber metal laminates have the following advantages, partially combining the benefits of metals and composites:

- Considerably (by about 60%) higher tensile strength due to higher fiber strength
- Lower (by about 15–20%) density, since the density of composite materials is usually lower than that of metals included in the laminate
- Ability to demonstrate elastic-plastic behavior in contrast to pure composites which are normally linear elastic
- Higher (by an order of magnitude) fatigue strength, since transverse (through the thickness) cracks in metal layers are arrested by fibers of cross-ply or fabric composite layers
- Considerably higher damping properties which provide acoustic fatigue strength
- FML skin able to be efficiently joined with mechanical fasteners, such as bolts or rivets
- Impact damage resistance of FML usually higher than that of pure composite laminates
- Parts with variable thickness readily fabricated by terminating the layers (see Fig. 5.25)

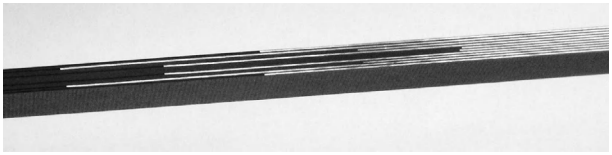


FIGURE 5.24

Titanium reinforcement of carbon-epoxy laminate. (This picture has been provided courtesy of B. Kolesnikov.)

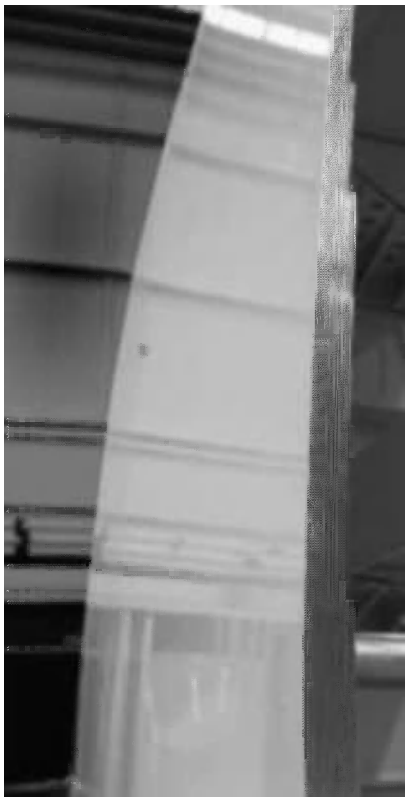


FIGURE 5.25

GLARE aircraft skin of variable thickness.

On the other hand, FMLs suffer from the following shortcomings:

- Since Young's and shear moduli of cross-ply or fabric glass or aramid plies are lower than the corresponding characteristics of aluminum, the stiffness of FML is also lower than the stiffness of aluminum. The same holds for FMLs composed of titanium and carbon-epoxy plies.
- In metal layers, yielding starts once the strain exceeds the yield limit, and lower modulus of FMLs results in lower effective yield stress.
- Hot pressing of FMLs induces residual interlaminar stresses.
- Delamination caused by the impact impedes the application of FMLs in compressed areas of the structure.
- The cost of FMLs is an order of magnitude higher than the cost of metals.

Consider the FML shown in Fig. 5.26. Since the thickness of individual layers is very small, the laminate can be treated as quasi-homogeneous and composed of the isotropic metal layer with total

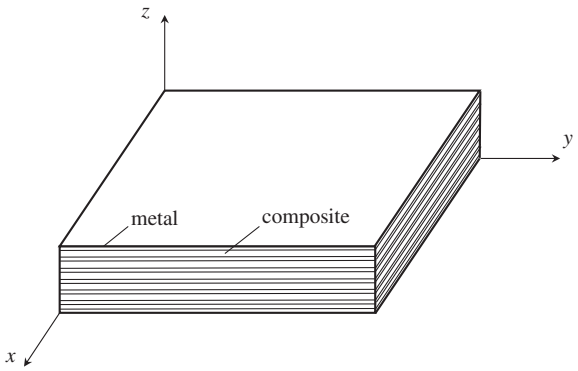


FIGURE 5.26

Fiber metal laminate.

thickness of h_m and the orthotropic composite layer of thickness h_c. The stiffness coefficients of the metal (m) and composite (c) layers are

$$A_{11}^c = \overline{E}_1,\ A_{12}^c = \overline{E}_1 \upsilon_{12},\ A_{22}^c = \overline{E}_2,\ A_{44}^c = G_{12},\ A_{55}^c = A_{66}^c = G_{xz}^c = G_{yz}^c$$
$$A_{11}^m = A_{22}^m = \overline{E},\ A_{12}^m = \overline{E}\upsilon,\ A_{44}^m = A_{55}^m = A_{66}^m = G = E/\big(2\big(1+\upsilon\big)\big)$$

(the subscripts 1, 2, 3 correspond to the x, y, and z coordinate axes shown in Fig. 5.26). Membrane stiffness coefficients of the laminate become

$$B_{11} = \overline{E}_1 h_c + \overline{E} h_m,\ B_{22} = \overline{E}_2 h_c + \overline{E} h_m,\ B_{12} = \overline{E}_1 \upsilon_{12} h_c + \overline{E}\upsilon h_m$$
$$B_{44} = G_{12} h_c + G h_m$$

where, as earlier, $\overline{E}_{1.2} = E_{1.2}/(1 - \upsilon_{12}\upsilon_{21})$ and $\overline{E} = E/(1 - \upsilon^2)$. The corresponding bending stiffness coefficients are expressed in terms of B_{mn} in accordance with Eqs. (5.100), i.e.,

$$D_{mn} = \frac{h^2}{12} B_{mn}$$

where $h = h_c + h_m$ is the total thickness of the laminate. Transverse shear stiffness coefficients are specified by Eqs. (5.83) and (5.84), which yield

$$S_x = S_y = \frac{h^2}{\dfrac{h_c}{G_{xz}} + \dfrac{h_m}{G}}$$

5.7 QUASI-ISOTROPIC LAMINATES IN THE PLANE STRESS STATE

The layers of a laminate can be arranged in such a way that the laminate will behave as an isotropic layer under in-plane loading. Actually, the laminate is not isotropic (that is why it is

called a quasi-isotropic laminate) because under transverse (normal to the laminate plane) loading and under interlaminar shear its behavior is different from that of an isotropic (e.g., metal) layer.

To derive the conditions that should be met by the structure of a quasi-isotropic laminate, consider in-plane loading with stresses σ_x, σ_y, and τ_{xy} that are shown in Fig. 5.1 and induce only in-plane strains $\varepsilon_x^0, \varepsilon_y^0$, and$\gamma_{xy}^0$. Taking $\kappa_x = \kappa_y = \kappa_{xy} = 0$ in Eqs. (5.5) and introducing average (through the laminate thickness h) stresses as

$$\sigma_x = N_x/h, \quad \sigma_y = N_y/h, \quad \tau_{xy} = N_{xy}/h$$

we can write the first three equations of Eqs. (5.5) in the following form

$$\begin{aligned} \sigma_x &= \overline{B}_{11}\varepsilon_x^0 + \overline{B}_{12}\varepsilon_y^0 + \overline{B}_{14}\gamma_{xy}^0 \\ \sigma_y &= \overline{B}_{21}\varepsilon_x^0 + \overline{B}_{22}\varepsilon_y^0 + \overline{B}_{24}\gamma_{xy}^0 \\ \tau_{xy} &= \overline{B}_{41}\varepsilon_x^0 + \overline{B}_{42}\varepsilon_y^0 + \overline{B}_{44}\gamma_{xy}^0 \end{aligned} \tag{5.105}$$

in which, in accordance with Eqs. (5.28) and (5.42),

$$\overline{B}_{mn} = \sum_{i=1}^{k} A_{mn}^{(i)}\overline{h}_i, \quad \overline{h}_i = h_i/h \tag{5.106}$$

where $\overline{h}_i$ is the thickness of the ith layer normalized to the laminate thickness and A_{mn} are the stiffness coefficients specified by Eqs. (4.72). For an isotropic layer, the constitutive equations analogous to Eqs. (5.105) are

$$\sigma_x = \overline{E}\left(\varepsilon_x^0 + \nu\varepsilon_y^0\right), \quad \sigma_y = \overline{E}\left(\varepsilon_y^0 + \nu\varepsilon_x^0\right), \quad \tau_{xy} = G\gamma_{xy}^0 \tag{5.107}$$

where

$$\overline{E} = \frac{E}{1-\nu^2}, \quad G = \frac{E}{2(1+\nu)} = \frac{1}{2}(1-\nu)\overline{E} \tag{5.108}$$

Comparing Eqs. (5.105) and (5.107), we can see that the shear-stretching coefficients of the laminate, i.e., $\overline{B}_{14} = \overline{B}_{41}$ and $\overline{B}_{24} = \overline{B}_{42}$, should be equal to zero. As follows from Eqs. (4.72) and Section 5.6.3, this means that the laminate should be balanced, i.e., it should be composed of $0°, \pm\phi_i$ (or ϕ_i and $\pi - \phi_i$), and 90° layers only. Since the laminate stiffness in the x- and the y-direction must be the same, we require that $\overline{B}_{11} = \overline{B}_{22}$. Using Eqs. (4.72), taking $\overline{h}_i = \overline{h}$ for all i, and performing the appropriate transformation, we arrive at the following condition

$$\sum_{i=1}^{k} \cos 2\phi_i = 0$$

As can be checked by direct substitutions, for $k = 1$ this equation is satisfied if $\phi_1 = 45°$ and for $k = 2$ if $\phi_1 = 0$ and $\phi_2 = 90°$. Naturally, such one- and two-layered materials cannot be isotropic even in one plane. So, consider the case $k \geq 3$, for which the solution has the form

$$\phi_i = (i-1)\frac{\pi}{k}, \quad i = 1, 2, 3, \ldots, k \tag{5.109}$$

Using the sums that are valid for angles specified by Eq. (5.109), i.e.,

$$\sum_{i=1}^{k} \sin^2\phi_i = \sum_{i=1}^{k} \cos^2\phi_i = \frac{k}{2}$$

$$\sum_{i=1}^{k} \sin^4\phi_i = \sum_{i=1}^{k} \cos^4\phi_i = \frac{3k}{8}$$

$$\sum_{i=1}^{k} \sin^2\phi_i \cos^2\phi_i = \frac{k}{8}$$

and calculating stiffness coefficients from Eqs. (5.106) and (4.72), we get

$$\overline{B}_{11} = \overline{B}_{22} = \frac{1}{8}\left[3\left(\overline{E}_1 + \overline{E}_2\right) + 2\left(\overline{E}_1\nu_{12} + 2G_{12}\right)\right]$$

$$\overline{B}_{12} = \frac{1}{8}\left[\overline{E}_1 + \overline{E}_2 + 2\left(3\overline{E}_1\nu_{12} - 2G_{12}\right)\right]$$

$$\overline{B}_{44} = \frac{1}{8}\left[\overline{E}_1 + \overline{E}_2 - 2\left(\overline{E}_1\nu_{12} - 2G_{12}\right)\right]$$

These stiffnesses provide constitutive equations in the form of Eqs. (5.107) and satisfy the conditions in Eqs. (5.108) which can be written as

$$\overline{B}_{11} = \overline{B}_{22} = \frac{E}{1-\nu^2}, \quad \overline{B}_{44} = G$$

if

$$E = \frac{\left(\overline{E}_1 + \overline{E}_2 + 2\overline{E}_1\nu_{12}\right)\left(\overline{E}_1 + \overline{E}_2 - 2\overline{E}_1\nu_{12} + 4G_{12}\right)}{3\left(\overline{E}_1 + \overline{E}_2\right) + 2\left(\overline{E}_1\nu_{12} + 2G_{12}\right)}$$

$$\nu = \frac{\overline{E}_1 + \overline{E}_2 + 2\left(3\overline{E}_1\nu_{12} - 2G_{12}\right)}{3\left(\overline{E}_1 + \overline{E}_2\right) + 2\left(\overline{E}_1\nu_{12} + 2G_{12}\right)}, \quad G = \frac{E}{2(1+\nu)} \tag{5.110}$$

Possible solutions to Eqs. (5.109) providing quasi-isotropic properties of the laminates with different number of layers are listed in Table 5.3 for $k \leq 6$.

TABLE 5.3 Angles Providing Quasi-isotropic Properties of the Laminates.

	Orientation Angle of the *i*th layer					
Number of Layers, *k*	ϕ_1°	ϕ_2°	ϕ_3°	ϕ_4°	ϕ_5°	ϕ_6°
3	0	60	120	–	–	–
4	0	45	90	135	–	–
5	0	36	72	108	144	–
6	0	30	60	90	120	150

TABLE 5.4 Modulus of Elasticity and Poisson's Ratio of Quasi-isotropic Laminates Made of Typical Advanced Composites.

Property	Glass-Epoxy	Carbon-Epoxy	Aramid-Epoxy	Boron-Epoxy	Boron-Al
Modulus, E (GPa)	27.0	54.8	34.8	80.3	183.1
Poisson's ratio, ν	0.34	0.31	0.33	0.33	0.28
Specific modulus $k_E \times 10^3$ (m)	1290	3530	2640	3820	6910

All quasi-isotropic laminates, having different structures determined by Eq. (5.109) for a given number of layers, k, possess the same apparent modulus and Poisson's ratio specified by Eqs. (5.110). For typical advanced composites with the properties listed in Table 3.5, these characteristics are presented in Table 5.4.

It follows from Tables 5.4 and 1.1 that the specific stiffness of quasi-isotropic composites with carbon and boron fibers exceeds the corresponding characteristic of traditional isotropic structural materials: steel, aluminum, and titanium.

Consider in more detail the behavior of the most popular quasi-isotropic laminate composed of the layers with angles $0°, 90°, +45°,$ and $-45°$ (second row in Table 5.3) and equal thicknesses. The laminate under study is made by filament winding of carbon tows HTS 5131 impregnated with epoxy resin on the flat mandrel. Material density is 1510 kg/m^3, fiber volume fraction 55%, and porosity 1.65%. Mechanical properties of unidirectional plies are: longitudinal modulus $E_1 = 105$ GPa, transverse modulus $E_2 = 8.9$ GPa, shear modulus $G_{12} = 5$ GPa, Poisson's ratios $\upsilon_{12} = 0.025$ and $\upsilon_{21} = 0.3$, tensile and compressive longitudinal ultimate stresses $\overline{\sigma}_1^+ = 1700$ MPa and $\overline{\sigma}_1^- = 1300$ MPa, tensile and compressive transverse ultimate stresses $\overline{\sigma}_2^+ = 35$ MPa and $\overline{\sigma}_2^- = 170$ MPa, and in-plane shear ultimate stress $\overline{\tau}_{12} = 35$ MPa.

The experimental stress-strain diagram for this laminate is shown in Fig. 5.27 with the solid line. As can be seen, the tensile diagram has two knees corresponding to the matrix failure (the so-called first and second ply failures) in the plies with angles 90° and ±45°. To describe analytically the laminate deformation under uniaxial tension in the x direction (see, e.g., Fig. 4.33), apply the model presented in Section 4.4. Stiffness coefficients of the plies specified by Eqs. (4.72) are

$$A_{11}^0 = \overline{E}_1, \quad A_{12}^0 = \overline{E}_1 \upsilon_{12}, \quad A_{22}^0 = \overline{E}_2$$

$$A_{11}^{45} = A_{22}^{45} = \frac{1}{4}(\overline{E}_1 + \overline{E}_2 + 2E_{12})$$

$$A_{11}^{45} = \overline{E}_1 \upsilon_{12} + \frac{1}{4}(\overline{E}_1 + \overline{E}_2 - 2E_{12})$$

$$A_{11}^{90} = \overline{E}_2, \quad A_{12}^{90} = \overline{E}_1 \upsilon_{12}, \quad A_{22}^{90} = \overline{E}_1$$

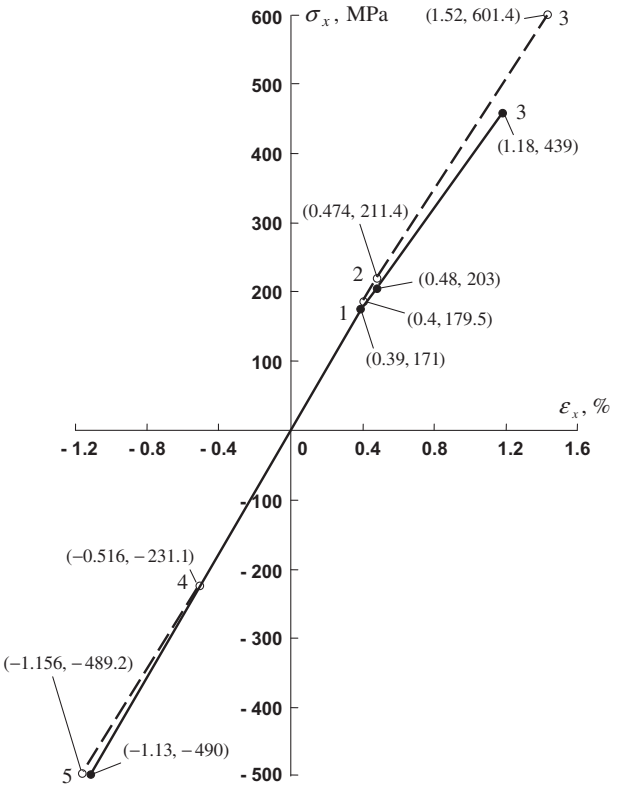


FIGURE 5.27

Stress-strain diagram for the quasi-isotropic carbon-epoxy laminate: analysis (○ – – – –), experiment (● ————).

in which, as earlier, $\overline{E}_{1.2} = E_{1.2}/(1 - \upsilon_{12}\upsilon_{21})$, $E_{12} = \overline{E}_1\upsilon_{12} + 2G_{12}$. Taking $\overline{h}_0 = \overline{h}_{90} = 0.25$, $\overline{h}_{45} = 0.5$, we can calculate the normalized membrane stiffness coefficients of the laminate using Eqs. (5.106), i.e.,

$$\overline{B}_{11} = \overline{B}_{22} = \frac{1}{4}\left[\overline{E}_1 + \frac{1}{2}\left(\overline{E}_1 + \overline{E}_2 + 2E_{12}\right) + \overline{E}_2\right]$$

$$\overline{B}_{12} = \frac{1}{4}\left[\overline{E}_1\upsilon_{12} + 2\overline{E}_1\upsilon_{12} + \frac{1}{2}\left(\overline{E}_1 + \overline{E}_2 - 2E_{12}\right) + \overline{E}_1\upsilon_{12}\right] = \overline{E}_1\upsilon_{12} + \frac{1}{8}\left(\overline{E}_1 + \overline{E}_2 - 2E_{12}\right) \tag{5.111}$$

For uniaxial tension in the x direction,

$$\sigma_x = \overline{B}_{11}\varepsilon_x + \overline{B}_{12}\varepsilon_y, \quad \sigma_y = \overline{B}_{12}\varepsilon_x + \overline{B}_{22}\varepsilon_y = 0, \quad \tau_{xy} = 0$$

Thus,

$$\sigma_x = E_x\varepsilon_x, \quad \varepsilon_y = -\upsilon_{xy}\varepsilon_x \tag{5.112}$$

where

$$E_x = \overline{B}_{11} - \frac{\overline{B}_{12}^2}{\overline{B}_{22}}, \quad \nu_{yx} = \frac{\overline{B}_{12}}{\overline{B}_{22}} \tag{5.113}$$

Strains in the principal ply directions are specified by Eqs. (4.69), according to which

$$\begin{aligned} &\varepsilon_1^0 = \varepsilon_x,\ \varepsilon_2^0 = \varepsilon_y,\ \varepsilon_{12}^0 = 0 \\ &\varepsilon_1^{45} = \varepsilon_2^{45} = \frac{1}{2}(\varepsilon_x + \varepsilon_y),\ \varepsilon_{12}^{45} = (\varepsilon_y + \varepsilon_x) \\ &\varepsilon_1^{90} = \varepsilon_y,\ \varepsilon_2^{90} = \varepsilon_x,\ \varepsilon_{12}^{90} = 0 \end{aligned} \tag{5.114}$$

The corresponding stresses can be found using Hooke's law, i.e.,

$$\sigma_1 = \overline{E}_1(\varepsilon_1 + \upsilon_{12}\varepsilon_2),\ \sigma_2 = \overline{E}_2(\varepsilon_2 + \upsilon_{21}\varepsilon_1),\ \tau_{12} = G_{12}\varepsilon_{12} \tag{5.115}$$

For the laminate under study, Eqs. (5.111) and (5.113) yield

$$\begin{aligned} &\overline{B}_{11} = \overline{B}_{22} = 49.39 \text{ GPa},\ \overline{B}_{12} = 15.02 \text{ GPa} \\ &E_x = 44.82 \text{ GPa},\ \upsilon_{yx} = 0.304 \end{aligned} \tag{5.116}$$

Then, it follows from Eqs. (5.112) and (5.114) that

$$\varepsilon_x = 2.23 \cdot 10^{-3}\sigma_x,\ \ \varepsilon_y = -0.68 \cdot 10^{-3}\sigma_x \tag{5.117}$$

Here and further in this section, stresses are measured in MPa, whereas strains are expressed in %.

The theoretical stress-strain diagram is shown in Fig. 5.27 by the dashed line. For the initial loading (before the first ply failure) the dashed line corresponding to the first equation of Eqs. (5.117) closely coincides with the experimental solid line.

To find the stress which causes the first ply failure, we apply the strength criterion, Eq. (6.17) derived in Section 6.1.2, i.e.

$$\left(\frac{\sigma_2}{\overline{\sigma}_2}\right)^2 + \left(\frac{\tau_{12}}{\overline{\tau}_{12}}\right)^2 = 1 \tag{5.118}$$

For the stresses in the plies, Eqs. (5.114) and (5.115) yield

$$\begin{aligned} &\sigma_1^0 = 2.51\sigma_x,\ \ \sigma_2^0 = -0.0009\sigma_x,\ \ \tau_{12}^0 = 0 \\ &\sigma_1^{45} = 0.9\sigma_x,\ \sigma_2^{45} = 0.097\sigma_x,\ \ \tau_{12}^{45} = -0.145\sigma_x \\ &\sigma_1^{90} = -0.71\sigma_x,\ \sigma_2^{90} = 0.195\sigma_x,\ \ \tau_{12}^{90} = 0 \end{aligned}$$

Substitution of these stresses in Eq. (5.118) allows us to conclude that the first ply failure occurs in the 90°-layer under the stress $\sigma_x^* = 179.5$ MPa. The corresponding strains which can be found from Eqs. (5.112) are $\varepsilon_x^* = 0.4\%$ and $\varepsilon_y^* = 0.122\%$. The experimental results are $\sigma_x = 171$ MPa and $\varepsilon_x = 0.39\%$. First ply failure is indicated in Fig. 5.27 by circle 1 (analysis) and dot 1 (experiment).

Now we consider further loading corresponding to $\sigma_x \geq \sigma_x^*$. According to the model described in Section 4.4, we should take in Eqs. (5.111) $E_2 = 0,\ G_{12} = 0,$ and $\upsilon_{12} = 0$ for the 90°-layer. Then, we arrive at the stiffness coefficients and elastic constants

$$\overline{B}_{11} = 46.98 \text{ GPa},\ \overline{B}_{12} = 14.3 \text{ GPa},\ \overline{B}_{22} = 49.39 \text{ GPa}$$
$$E_x = 42.83 \text{ GPa},\ \upsilon_{yx} = 0.29$$

Comparing E_x with Eq. (5.116), we can conclude that the first ply failure reduces the laminate stiffness. For $\sigma_x \geq \sigma_x^*$, the strains can be found as

$$\varepsilon_x = \varepsilon_x^* + 2.33(\sigma_x - \sigma_x^*)\cdot 10^{-3},\ \varepsilon_y = \varepsilon_y^* - 0.68(\sigma_x - \sigma_x^*)\cdot 10^{-3}$$

(see Section 4.4). The stresses acting in the plies are

$$\sigma_1^0 = 2.51\sigma_x^* + 2.63\left(\sigma_x - \sigma_x^*\right),\ \sigma_2^0 = -0.009\sigma_x^* - 0.0023\left(\sigma_x - \sigma_x^*\right),\ \tau_{12}^0 = 0$$
$$\sigma_1^{45} = 0.9\sigma_x^* + 0.96\left(\sigma_x - \sigma_x^*\right),\ \sigma_2^{45} = 0.097\sigma_x^* + 0.1\left(\sigma_x - \sigma_x^*\right)$$
$$\tau_{12}^{45} = -0.145\sigma_x^* - 0.151\left(\sigma_x - \sigma_x^*\right)$$

Substitution in Eq. (5.118) yields the stress $\sigma_x^{**} = 211.4$ MPa which induces the matrix failure in the 45° plies. The corresponding strain is $\varepsilon_x^{**} = 0.474\%$ (circle 2 in Fig. 5.27). The experimental results are $\sigma_x = 203$ MPa and $\varepsilon_x = 0.48\%$ (dot 2 in Fig. 5.27).

To describe further loading ($\sigma_x \geq \sigma_x^{**}$), we should take $E_2 = 0,\ G_{12} = 0,$ and $\upsilon_{12} = 0$ for the 45° layer and arrive at

$$\overline{B}_{11} = 42.57 \text{ GPa},\ \overline{B}_{12} = 14.9 \text{ GPa},\ \overline{B}_{22} = 44.97 \text{ GPa}$$
$$E_x = 37.63 \text{ GPa},\ \upsilon_{yx} = 0.33$$

The strains become

$$\varepsilon_x = \varepsilon_x^{**} + 2.66(\sigma_x - \sigma_x^{**})\cdot 10^{-3},\ \varepsilon_y = \varepsilon_y^{**} - 0.88(\sigma_x - \sigma_x^{**})\cdot 10^{-3}$$

and the stress along the fibers of the 0° layer is

$$\sigma_1^0 = 2.51\sigma_x^* + 2.63\left(\sigma_x^{**} - \sigma_x^*\right) + 2.99\left(\sigma_x - \sigma_x^{**}\right)$$

The ultimate stress can be found using the strength condition $\sigma_1^0 = \overline{\sigma}_1^+$ which yields $\overline{\sigma}_x = 601.4$ MPa and $\overline{\varepsilon}_x = 1.52\%$. This result corresponds to circle 3 in Fig. 5.27. It follows from this figure that the experimental ultimate stress (dot 3) is only 439 MPa, i.e., 27% lower. The reason for this difference is discussed in Section 4.5 (see Figs. 4.69 and 4.72). Whereas the theoretical results correspond to the laminate reinforced with continuous fibers, experimental data are obtained using 38 mm wide and 2.6 mm thick samples cut out of a 250 × 250 mm plate. Thus, the fibers of the 45° and 90° layers are not continuous and the edge effects discussed in Section 4.5 reduce the effective strength of the laminate. Intralaminar and interlaminar cracks in the matrix result in low efficiency of 45° plies. Indeed, if we assume that the load is taken by 0° plies only, we arrive at $\overline{\sigma}_x = 425$ MPa, which is fairly close to the experimental strength (439 MPa).

Under compression, the strains are specified by Eqs. (5.117) and the strength criterion, Eq. (5.118), in which $\overline{\sigma}_2 = \overline{\sigma}_2^-$ shows that the first ply failure occurs in the 45° layer under stress $\sigma_x^* = 231.3$ MPa and strain $\varepsilon_x^* = 0.516\%$ (circle 4 on the graph shown in Fig. 5.27). To describe further loading

($\sigma_x > \sigma_x^*$), we should take $G_{12} = 0$ for the 45° layer (see Section 4.4). Then, the stiffness coefficients become

$$\bar{B}_{11} = \bar{B}_{22} = 46.9 \text{ GPa}, \ \bar{B}_{12} = 17.52 \text{ GPa}$$
$$E_x = 40.34 \text{ GPa}, \ \upsilon_{yx} = 0.37$$

The modulus obtained is close to the initial one and the knee on the experimental diagram is usually not observed. For $\sigma_x > \sigma_x^*$, the strains become

$$\varepsilon_x = \varepsilon_x^* + 2.48(\sigma_x - \sigma_x^*)\cdot 10^{-3}, \ \varepsilon_y = \varepsilon_y^* - 0.93(\sigma_x - \sigma_x^*)\cdot 10^{-3}$$

These strains correspond to the dashed line between points 4 and 5 in Fig. 5.27. No other cracks in the matrix appear up to the failure of the 0° ply fibers. The corresponding stress is

$$\sigma_1^0 = 2.51\sigma_x^* + 2.79\left(\sigma_x - \sigma_x^*\right)$$

Putting $\sigma_1^0 = \overline{\sigma}_1^-$, we get $\overline{\sigma}_x = 489.2$ MPa and $\overline{\varepsilon}_x = 1.156\%$ (circle 5 in Fig. 5.27). The corresponding experimental results, i.e., $\overline{\sigma}_x = 490$ MPa and $\overline{\varepsilon}_x = 1.13\%$ (dot 5 in Fig. 5.27), are very close to the theoretical ones.

The quasi-isotropic laminate under discussion is widely used as the skin of modern composite airplanes. Demonstrating relatively high tensile and compressive strength and low density, this material is characterized, on the other hand, by relatively low stresses, inducing cracks in the matrix. Clearly, such cracks are not acceptable under limit loads for commercial airplanes. That is why the weight savings that such composite structures demonstrate in comparison with aluminum prototypes are relatively low (about 10–15%).

5.8 ANTISYMMETRIC LAMINATES

In antisymmetric laminates, symmetrically located layers have mutually reversed orientations. For example, whereas laminates $[0°/90°/90°/0°]$ and $[+\phi \ / -\phi \ / -\phi \ / +\phi]$ are symmetric, laminates $[0°/90°/0°/90°]$ or $[0°/0°/90°/90°]$ and $[+\phi/-\phi/+\phi/-\phi]$ are antisymmetric. In contrast to symmetric laminates which have maximum bending and zero coupling stiffness coefficients, antisymmetric laminates demonstrate pronounced coupling that can be important for some particular applications (robotic parts undergoing complicated deformation under simple loading, rotor blades that twist under centrifugal forces, airplane wings twisting under bending, etc.).

The simplest antisymmetric laminate is a cross-ply layer consisting of two plies with angles 0 and 90°, and the same thickness $h/2$ (see Fig. 5.28). Taking $e = h/2$ and using Eqs. (5.28) and (5.41), we arrive at the following stiffness coefficients entering Eqs. (5.44)

$$B_{11} = B_{22} = \frac{h}{2}(\overline{E}_1 + \overline{E}_2), \qquad B_{12} = \overline{E}_1\nu_{12}h, \qquad B_{44} = G_{12}h,$$
$$C_{11} = -C_{22} = \frac{h^2}{8}(\overline{E}_2 - \overline{E}_1), \qquad C_{12} = 0, \qquad C_{44} = 0,$$
$$D_{11} = D_{22} = \frac{h^3}{24}(\overline{E}_1 + \overline{E}_2), \qquad D_{12} = \frac{h^3}{12}\overline{E}_1\nu_{12}, \qquad D_{44} = \frac{h^3}{12}G_{12}$$

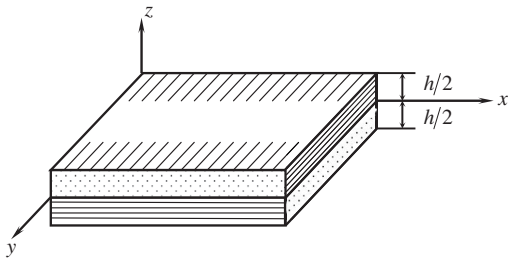


FIGURE 5.28

An antisymmetric cross-ply laminate.

Comparing these results with Eqs. (5.99) and (5.100), corresponding to a quasi-homogeneous cross-ply laminate, we can see that the antisymmetric cross-ply laminate has the same membrane and bending stiffnesses, but nonzero coupling coefficients C_{11} and C_{22}. This fact shows, in accordance with Eqs. (5.44), that in-plane tension or compression of this laminate induces bending.

As another typical example of an antisymmetric laminate, consider an angle-ply structure consisting of two plies with the same thickness $h/2$ and orientation angles $+\phi$ and $-\phi$, respectively (see Fig. 5.29). The plies (or layers) are characterized by the following stiffness coefficients

$$A_{11}^{(1)} = A_{11}^{(2)} = A_{11}, \quad A_{12}^{(1)} = A_{12}^{(2)} = A_{12}, \quad A_{22}^{(1)} = A_{22}^{(2)} = A_{22},$$
$$A_{14}^{(1)} = -A_{14}^{(2)} = A_{14}, \quad A_{24}^{(1)} = -A_{24}^{(2)} = A_{24}, \quad A_{44}^{(1)} = A_{44}^{(2)} = A_{44}$$

where coefficients A_{mn} are specified by Eqs. (4.72). Taking again $e = h/2$, we arrive at constitutive equations in Eqs. (5.104) in which

$$B_{mn} = A_{mn}h, \quad C_{mn} = -\frac{h^2}{4}A_{mn}, \quad D_{mn} = \frac{h^3}{12}A_{mn} \tag{5.119}$$

Comparing these coefficients with those entering Eqs. (5.104) and corresponding to a quasi-homogeneous angle-ply laminate, we can conclude that the antisymmetric laminate has much larger

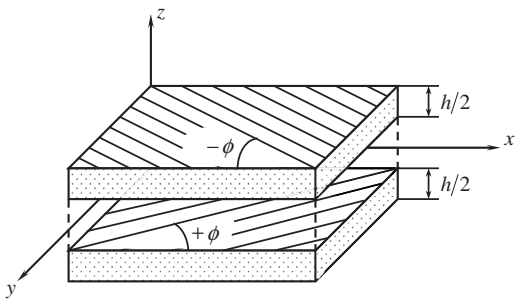


FIGURE 5.29

Unbonded view of an antisymmetric angle-ply laminate.

coupling coefficients C_{14} and C_{24}, and thus a much more pronounced extension-twisting coupling effect.

In composite technology, an antisymmetric $\pm\phi$ angle-ply laminate is usually fabricated by a continuous filament winding process. A typical structure made by filament winding is shown in Fig. 4.59 of Chapter 4. As can be seen in this figure, the angle-ply layer is composed from two plies with $+\phi$ and $-\phi$ orientation of the fibers and these plies are interlaced in the process of filament winding. As a result, the structure of the layer is characterized by the distinctive regular mosaic pattern consisting of triangular-shaped, two-ply segments (*T*-segments) repeating in chessboard fashion, with alternating $\pm\phi$ and $\mp\phi$ reinforcement. The *T*-segments are arranged in a regular geometric pattern around the circumference and along the axis forming the so-called cross-over circles (see Fig. 4.59). Depending on the parameters of the winding process, various numbers n_T of *T*-segments located along the circumference can be obtained. For a cylindrical shell, the structures corresponding to $n_T = 2,\ 4,\ 8,$ and 16 are shown in Fig. 5.30.

Each *T*-segment consists of two plies with either $[+\phi/-\phi]$ or $[-\phi/+\phi]$ structure, and the plies are not interlaced within the *T*-segment area. If, for instance, a *T*-segment consists of the top curvilinear-triangular-shaped ply, reinforced with fibers oriented at angle $+\phi$, and the bottom one reinforced with an angle $-\phi$, then the neighboring adjacent T-segments have an inverse structure: their top plies are reinforced at angle $-\phi$, and the bottom ones are reinforced at $+\phi$.



FIGURE 5.30

Filament-wound cylinders with various numbers n_T of *T*-segments: $n_T = 2$ (a), 4 (b), 8 (c), and 16 (d).

The traditional approach used to analyze the laminates under consideration is based on the model discussed in Section 4.5, according to which the laminate is treated as a homogeneous orthotropic layer with stiffness coefficients specified by Eqs. (4.72) and (4.147). The constitutive equations are taken in accordance with Eqs. (5.44), i.e.,

$$N_x = B_{11}\varepsilon_x^0 + B_{12}\varepsilon_y^0, \quad N_y = B_{21}\varepsilon_x^0 + B_{22}\varepsilon_y^0, \quad N_{xy} = B_{44}\gamma_{xy}^0,$$
$$M_x = D_{11}\kappa_x + D_{12}\kappa_y, \quad M_y = D_{21}\kappa_x + D_{22}\kappa_y, \quad M_{xy} = D_{44}\kappa_{xy}$$

where

$$B_{mn} = A_{mn}h, \quad D_{mn} = \frac{h^3}{12}A_{mn}$$

and A_{mn} are specified by Eqs. (4.72). The approach based on these constitutive equations corresponds to an infinite number of T-segments, i.e., to $n_T \to \infty$.

Considering a T-segment as an antisymmetric laminate, we must apply a more general version of Eqs. (5.44) including the coupling stiffness coefficients, i.e.,

$$\begin{aligned}
N_x &= B_{11}\varepsilon_x^0 + B_{12}\varepsilon_y^0 + C_{14}\kappa_{xy},\\
N_y &= B_{21}\varepsilon_x^0 + B_{22}\varepsilon_y^0 + C_{24}\kappa_{xy},\\
N_{xy} &= B_{44}\gamma_{xy}^0 + C_{41}\kappa_x + C_{42}\kappa_y,\\
M_x &= C_{14}\gamma_{xy}^0 + D_{11}\kappa_x + D_{12}\kappa_y,\\
M_y &= C_{24}\gamma_{xy}^0 + D_{21}\kappa_x + D_{22}\kappa_y,\\
M_{xy} &= C_{41}\varepsilon_x^0 + C_{42}\varepsilon_y^0 + D_{44}\kappa_{xy},
\end{aligned}$$

where the stiffness coefficients are specified by Eqs. (5.119). It is important that, whereas for the laminate with $[+\phi/-\phi]$ structure shown in Fig. 5.29 the coupling stiffness coefficient is negative, for the adjacent T-segment having $[-\phi/+\phi]$, this coefficient is positive. This difference results in the specific behavior of the two different laminate structures of T-segments that exhibit antisymmetric opposite anisotropic stretching-twisting and bending-shear coupling effects alternating along the circumference and axis of rotation of the shell. Due to the general alternating pattern of the T-segments (chessboard structure) and their interactions within a layer, the anisotropic effects are balancing each other inducing, at the same time, additional stresses in the plies.

To study the effect of the filament-wound mosaic pattern, the stress analysis of cylindrical shells has been performed (Morozov, 2006). The shells under consideration consist of one filament-wound $\pm\phi$ angle-ply layer and are loaded with internal pressure. The solid modelling (Solid Edge) and finite-element analysis (MSC NASTRAN) techniques have been employed to model the shells with different mosaic pattern structures. Each shell is partitioned into triangular-shaped T-segments according to the particular filament-wound pattern. Correspondingly, the finite elements are also combined into the respective alternating groups. The material structure of the finite elements for each of these groups is defined as either $[+\phi/-\phi]$ or $[-\phi/+\phi]$ laminate. The cylindrical shells under consideration are reinforced with a winding angle $\phi = \pm 60^\circ$ and loaded with internal pressure 1 MPa. The mechanical properties of the unidirectional glass-epoxy composite ply correspond to Table 3.5. The ends of the shells are clamped and the distance between the ends (length of the cylinder) is fixed

and equal to 140 mm. The diameter of the cylinder is 60 mm and the total thickness of the wall is $h = 1.4$ mm (with the thickness of the unidirectional ply being 0.7 mm). The stress analysis was performed for four types of shells.

The first cylinder is modeled with a homogeneous orthotropic angle-ply layer and analyzed using finite-element models available within the MSC NASTRAN software. This model corresponds to $n_T \to \infty$. The other three cylinders have 2, 4, and 8 triangular-shaped segments around the circumference ($n_T = 2,\ 4$ and 8) and are analyzed using the FE modelling of the shells with allowance for their mosaic structure. The finite-element models and the deformed shapes for $n_T \to \infty, n_T = 2,$ and $n_T = 4$ are shown in Fig. 5.31.

As can be seen, the deformation of the shells distinctively reflects the corresponding filament-wound mosaic texture. The calculated maximum values of stresses along and across fibers, σ_1 and σ_2, and shear stresses, τ_{12}, acting in the plies are presented in Table 5.5. It can be noted from this table that the maximum stresses strongly depend on the laminate structure. The traditional model ($n_T \to \infty$) significantly underestimated the stresses. With an increase in the structural parameter n_T, the stresses acting along the fibers reduce and approach the value following from the traditional laminate model.

Thus, it can be expected that the higher the parameter n_T, the higher the strength of $\pm\phi$ angle-ply filament-wound structures. This prediction is confirmed by the test results presented in Fig. 5.32 (Vorobey et al., 1992). Carbon-phenolic cylindrical shells with the geometrical parameters given previously have been loaded with internal pressure up to failure. As follows from Fig. 5.32, the increase of parameter n_T from 2 (Fig. 5.32a) to 16 (Fig. 5.32c) results in a significant increase in the burst pressure.

In conclusion, it should be noted that the effect under discussion shows itself mainly in $\pm\phi$ angle-ply structures consisting of two symmetric plies. For laminated structures consisting of a system of $\pm\phi$ angle-ply layers, the coupling stiffness coefficient which causes the specific behavior discussed earlier is given in notations to Eqs. (5.104) and has the form

$$C_{mn} = -\frac{1}{2} A_{mn} h \delta, \tag{5.120}$$

in which h is the laminate thickness and δ is the thickness of the ply. Since δ is relatively small, the coefficient C_{mn} in Eq. (5.120) is smaller than the corresponding coefficient in Eqs. (5.119), and the coupling effect caused by this coefficient is less pronounced.

5.9 SANDWICH STRUCTURES

Sandwich structures are three-layered laminates consisting of thin facings and a light-weight honeycomb or foam core as in Figs. 5.33 and 5.34. Since the in-plane stiffnesses of the facings are much higher than those of the core, whereas their transverse shear compliance is much lower than the same parameter of the core, the stiffness coefficients of sandwich structures are usually calculated presuming that the in-plane stiffnesses of the core are equal to zero. The transverse shear stiffnesses of the facings are assumed to be infinitely high. For the laminate shown in Fig. 5.35, this means that

$$A_{mn}^{(2)} = 0, \quad mn = 11, 12, 14, 24, 44,$$
$$A_{mn}^{(1,3)} \to \infty, \quad mn = 55, 56, 66$$

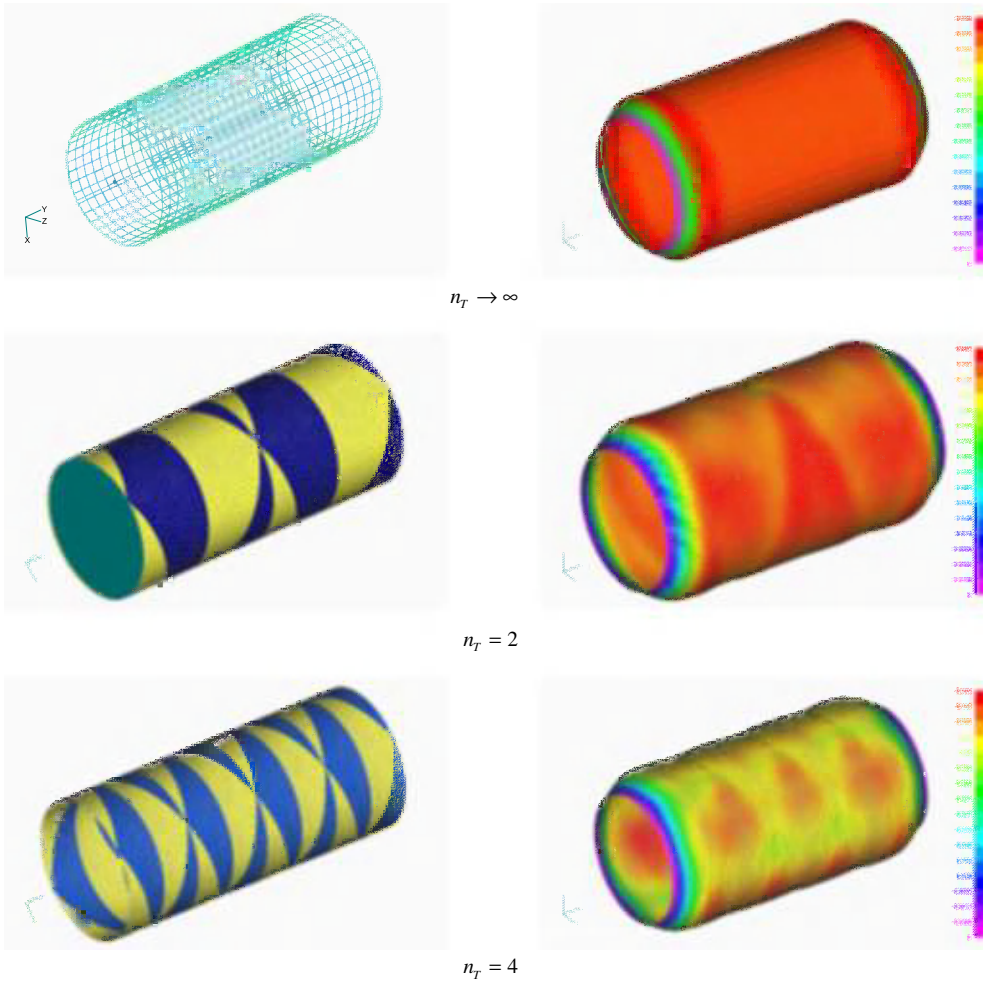


FIGURE 5.31

Finite-element models (a) and deformed shapes (b) of the cylinders with $n_T \to \infty$, $n_T = 2$, and $n_T = 4$.

TABLE 5.5 Maximum Stresses in the Plies of the Shells with Various Filament-wound Structures.

Structural Parameter, n_T	σ_1 (MPa)	σ_2 (MPa)	τ_{21} (MPa)
∞	24.9	3.79	1.98
2	40.99	17.7	4.82
4	33.2	20.3	5.33
8	27.30	18.2	4.94

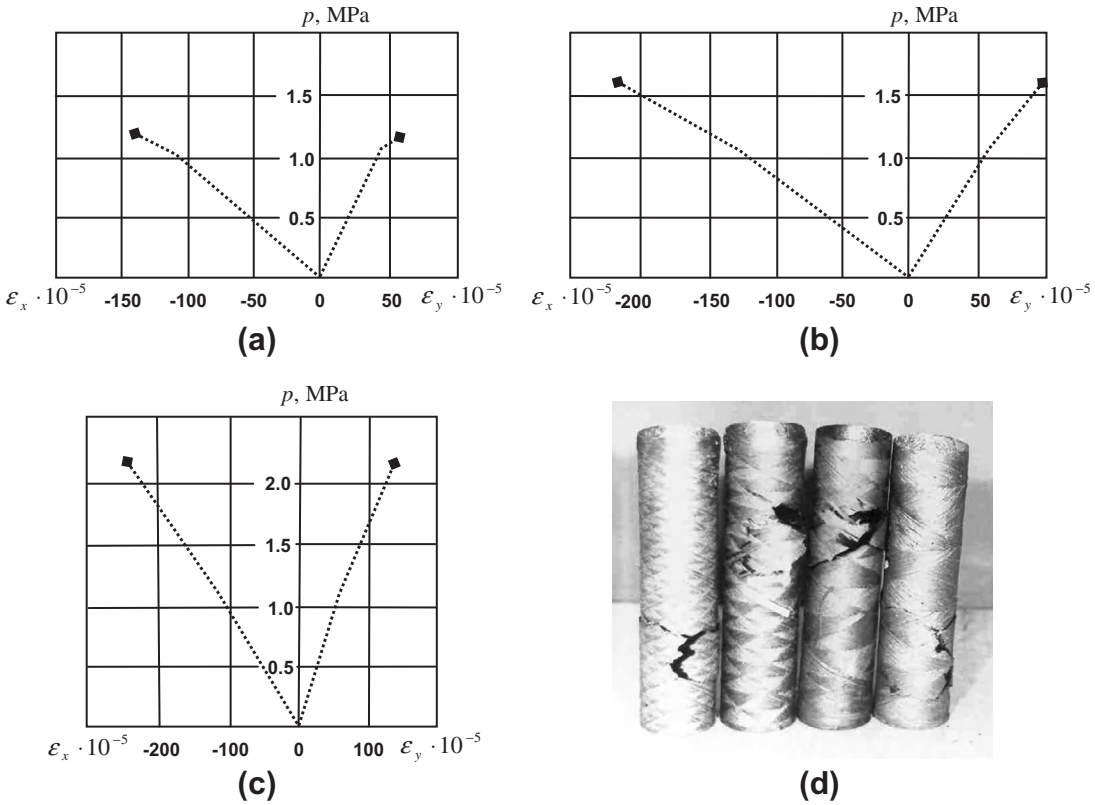


FIGURE 5.32

Dependencies of the axial (ε_x) and the circumferential (ε_y) strains on internal pressure (p) for cylindrical shells with $n_T = 2$- (*a*), $n_T = 4$- (*b*), $n_T = 16$- (*c*), and the corresponding failure modes (*d*).

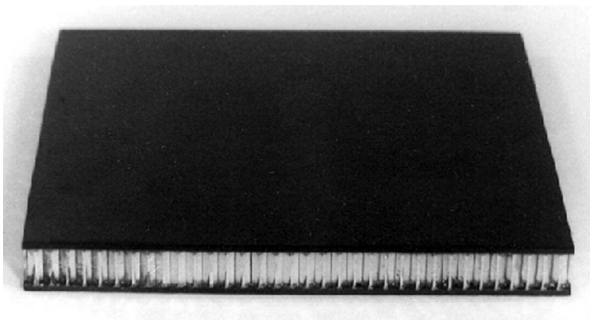


FIGURE 5.33

Composite sandwich panel with honeycomb core.



FIGURE 5.34

Composite sandwich rings with foam core.

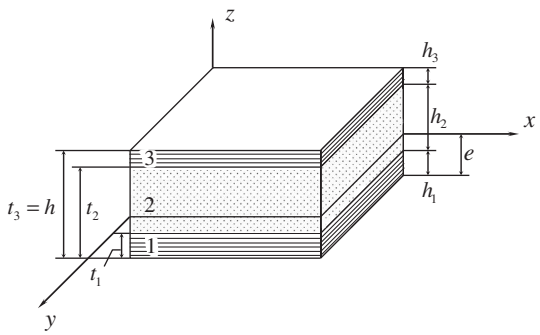


FIGURE 5.35

Sandwich laminate with two laminated facings (1 and 3) and foam core (2).

As a result, the coefficients in Eqs. (5.29) become

$$I_{mn}^{(r)} = \frac{1}{r+1}\left[A_{mn}^{(1)} t_1^{r+1} + A_{mn}^{(3)}\left(t_3^{r+1} - t_2^{r+1}\right)\right], \tag{5.121}$$

where $mn = 11$, 12, 22, 14, 24, and 44. Membrane, bending, and coupling stiffness coefficients can be determined using Eqs. (5.28). Transverse shear stiffnesses, Eqs. (5.83) and (5.84), for an orthotropic core, can be presented in the form

$$S_x = \frac{h^2}{h_2} G_{xz}, \quad S_y = \frac{h^2}{h_2} G_{yz}$$

where G_{xz} and G_{yz} are the shear moduli of the core.

5.10 COORDINATE OF THE REFERENCE PLANE

Stiffness coefficients specified by Eqs. (5.28) include the coordinate of the reference plane e (see Fig. 5.1) that, being appropriately pre-assigned, allows us to simplify the constitutive equations for the laminate. As was shown in Sections 5.2 and 5.4, taking the middle plane as the reference plane, i.e., putting $e = h/2$ for homogeneous and symmetric laminate, we have $C_{mn} = 0$, and the constitutive equations take their simplest form with zero membrane-bending coupling terms.

Now, a natural question as to whether it is possible to reduce Eqs. (5.5) to this form in the general case arises. Taking $C_{mn} = 0$ in Eqs. (5.28), we have

$$e = \frac{I_{mn}^{(1)}}{I_{mn}^{(0)}} \tag{5.122}$$

It is important that the reference plane should be one and the same for all $mn = 11$, 12, 22, 14, 24, and 44, and these six equations should give the same value of e. In the general case, this is not possible, so a universal reference plane providing $C_{mn} = 0$ cannot exist.

However, there are some other particular laminates (in addition to homogeneous and symmetric structures) for which this condition can be met. For example, consider a laminate composed of isotropic layers (see Sections 4.1 and 5.2). For such laminates,

$$A_{11}^{(i)} = A_{22}^{(i)} = \frac{E_i}{1-\nu_i^2}, \quad A_{12}^{(i)} = \frac{E_i\nu_i}{1-\nu_i^2}, \quad A_{44}^{(i)} = \frac{E_i}{2(1+\nu_i)}$$

and in accordance with Eqs. (5.42),

$$I_{11}^{(0)} = I_{22}^{(0)} = \sum_{i=1}^{k}\frac{E_i h_i}{1-\nu_i^2}, \quad I_{12}^{(0)} = \sum_{i=1}^{k}\frac{E_i\nu_i h_i}{1-\nu_i^2}, \quad I_{44}^{(0)} = \sum_{i=1}^{k}\frac{E_i h_i}{2(1+\nu_i)},$$

$$I_{11}^{(1)} = I_{22}^{(1)} = \frac{1}{2}\sum_{i=1}^{k}\frac{E_i h_i}{1-\nu_i^2}(t_i + t_{i-1}), \quad I_{12}^{(1)} = \frac{1}{2}\sum_{i=1}^{k}\frac{E_i\nu_i h_i}{1-\nu_i^2}(t_i + t_{i-1}),$$

$$I_{44}^{(1)} = \frac{1}{2}\sum_{i=1}^{k}\frac{E_i h_i}{2(1+\nu_i)}(t_i + t_{i-1})$$

As can be seen, these parameters, when substituted into Eqs. (5.122), do not provide one and the same value of e. However, if Poisson's ratio is the same for all the layers, i.e., $\nu_i = \nu$ ($i = 1, 2, 3, \ldots, k$), we get

$$e = \frac{\sum_{i=1}^{k} E_i h_i (t_i + t_{i-1})}{2\sum_{i=1}^{k} E_i h_i}$$

For practical analysis, this result is often used even if the Poisson's ratios of the layers are different. In these cases, it is assumed that all the layers can be approximately characterized with some average value of Poisson's ratio, i.e.,

$$\nu = \frac{1}{h}\sum_{i=1}^{k}\nu_i h_i$$

As another example, consider the sandwich structure described in Section 5.9 (see Fig. 5.35). In the general case, we again fail to find the desired reference plane. However, if we assume that the facings are made of one and the same material (only the thicknesses are different), Eqs. (5.121) and (5.122) yield

$$e = \frac{h_1^2 + h_3\left(h_3 + 2h_1 + 2h_2\right)}{2(h_1 + h_3)}$$

Returning to the general case, we should emphasize that the reference plane providing $C_{mn} = 0$ for all the mn values cannot be found in the general case only if the laminate structure is given. If the stacking-sequence of the layers is not pre-assigned and there is a sufficient number of layers, they can be arranged in such a way that $C_{mn} = 0$. Indeed, consider a laminate in Fig. 5.36 and suppose that its structure is, in general, not symmetric, i.e., that $z_i' \neq z_i$ and $k' \neq k$. Using plane $z = 0$ as the reference plane, we can write the membrane-bending coupling coefficients as

$$C_{mn} = \frac{1}{2}\sum_{i=1}^{k/2} A_{mn}^{(i)} h_i (z_i + z_{i-1}) - \frac{1}{2}\sum_{i'=1}^{k'/2} A_{mn}^{(i')} h_i' (z_i' + z_{i-1}')$$

where $z_i \geq 0$ and $z_i' \geq 0$. Introduce a new layer coordinate $\overline{z}_i = (z_i + z_{i-1})/2$, which is the distance between the reference plane of the laminate and the middle plane of the ith layer. Then, the condition $C_{mn} = 0$ yields

$$\sum_{i=1}^{k/2} A_{mn}^{(i)} h_i \overline{z}_i = \sum_{i'=1}^{k'/2} A_{mn}^{(i')} h_i' \overline{z}_i'$$

Now assume that we have a group of identical layers or plies with the same stiffness coefficients A_{mn} and thicknesses. For example, the laminate could include a 1.5 mm thick 0° unidirectional layer which

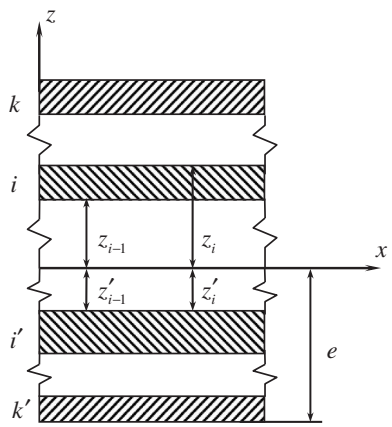


FIGURE 5.36

Layer coordinates with respect to the reference plane.

consists of 10 plies (the thickness of an elementary ply is 0.15 mm). Arranging these plies above ($\overline{z}_i$) and below ($\overline{z}'_i$) the reference plane in such a way that

$$\sum_{j=1}^{10}\left(\overline{z}_j - \overline{z}'_j\right) = 0 \tag{5.123}$$

we have no coupling for this group of plies. Doing the same with the other layers, we arrive at a laminate with no coupling. Naturally, some additional conditions following from the fact that the laminate is a continuous structure should be satisfied. However even with these conditions, Eq. (5.123) can be met with several systems of ply coordinates, and a symmetric arrangement of the plies ($\overline{z}_j = \overline{z}'_j$) is only one of these systems. The general analysis of the problem under discussion has been presented by Verchery (1999).

Return to laminates with pre-assigned stacking-sequences for the layers. It follows from Eqs. (5.122) that we can always make one of the coupling stiffness coefficients equal to zero, e.g., taking $e = e_{st}$ where

$$e_{st} = \frac{I^{(1)}_{st}}{I^{(0)}_{st}} \tag{5.124}$$

we get $C_{st} = 0$ (the rest of the coupling coefficients are not zero).

Another way to simplify the equations for stiffnesses is to take $e = 0$, i.e., to take the surface of the laminate as the reference plane. In this case, Eqs. (5.28) take the form

$$B_{mn} = I^{(0)}_{mn}, \quad C_{mn} = I^{(1)}_{mn}, \quad D_{mn} = I^{(2)}_{mn}$$

In practical analysis, the constitutive equations for laminates with arbitrary structure are often approximately simplified using the method of reduced or minimum bending stiffnesses described, e.g., by Ashton (1969), Karmishin (1974), and Whitney (1987). To introduce this method, consider the corresponding equation of Eqs. (5.28) for bending stiffnesses, i.e.,

$$D_{mn} = I^{(2)}_{mn} - 2eI^{(1)}_{mn} + e^2 I^{(0)}_{mn} \tag{5.125}$$

and find the coordinate e delivering the minimum value of D_{mn}. Using the minimum conditions

$$\frac{d}{de}D_{mn} = 0, \quad \frac{d^2}{de^2}D_{mn} > 0$$

we have

$$e = e_{mn} = \frac{I^{(1)}_{mn}}{I^{(0)}_{mn}} \tag{5.126}$$

This result coincides with Eq. (5.124) and yields $C_{mn} = 0$. Thus, calculating $I^{(1)}_{mn}$ and $I^{(0)}_{mn}$, we use for each $mn = 11,\ 12,\ 22,\ 14,\ 24$ and 44 the corresponding value e_{mn} specified by Eq. (5.126). Substitution yields

$$D^r_{mn} = I^{(2)}_{mn} - \frac{\left(I^{(1)}_{mn}\right)^2}{I^{(0)}_{mn}}, \quad C^r_{mn} = 0 \tag{5.127}$$

and the constitutive equations, Eqs. (5.5), become uncoupled. Naturally, this approach is only approximate because the reference plane coordinate should be the same for all stiffnesses, but it is not in the method under discussion. It follows from the foregoing derivation that the coefficients D^r_{mn} specified by Eqs. (5.127) do not exceed the actual values of bending stiffnesses, i.e., $D^r_{mn} \le D_{mn}$. So, the method of reduced bending stiffnesses leads to underestimation of the laminate bending stiffness. In conclusion, it should be noted that this method is not formally grounded and can yield both good and poor approximation of the laminate behavior, depending on the laminate structure.

5.11 STRESSES IN LAMINATES

The constitutive equations derived in the previous sections of this chapter relate forces and moments acting on the laminate to the corresponding generalized strains. For composite structures, forces and moments should satisfy equilibrium equations, whereas strains are expressed in terms of displacements. As a result, a complete set of equations is formed allowing us to find forces, moments, strains, and displacements corresponding to a given system of loads acting on the structure. We assume that this problem has already been solved, i.e., we know either generalized strains $\varepsilon, \gamma,$ and κ entering Eqs. (5.5) or forces and moments N and M. If the latter is the case, we can use Eqs. (5.5) to find $\varepsilon, \gamma,$ and κ. Now, to complete the analysis, we need to determine the stresses acting in each layer of the laminate.

To do this, we should first find strains in any ith layer using Eqs. (5.3) which yield

$$\varepsilon_x^{(i)} = \varepsilon_x^0 + z_i\kappa_x, \quad \varepsilon_y^{(i)} = \varepsilon_y^0 + z_i\kappa_y, \quad \gamma_{xy}^{(i)} = \gamma_{xy}^0 + z_i\kappa_{xy} \tag{5.128}$$

where z_i is the layer normal coordinate changing over the thickness of the ith layer. If the ith layer is orthotropic with principal material axes coinciding with axes x and y (e.g., made of fabric), Hooke's law provides the stresses we need, i.e.,

$$\sigma_x^{(i)} = \overline{E}_x^{(i)}\left(\varepsilon_x^{(i)} + \nu_{xy}^{(i)}\varepsilon_y^{(i)}\right), \quad \sigma_y^{(i)} = \overline{E}_y^{(i)}\left(\varepsilon_y^{(i)} + \nu_{yx}^{(i)}\varepsilon_x^{(i)}\right), \quad \tau_{xy}^{(i)} = G_{xy}^{(i)}\gamma_{xy}^{(i)} \tag{5.129}$$

where $\overline{E}_{x,y}^{(i)} = E_{x,y}^{(i)}/(1 - \nu_{xy}^{(i)}\nu_{yx}^{(i)})$ and $E_x^{(i)}, E_y^{(i)}, G_{xy}^{(i)}, \nu_{xy}^{(i)},$ and $\nu_{yx}^{(i)}$ are the elastic constants of the layer referred to the principal material axes. For an isotropic layer (e.g., metal or polymeric), we should take in Eqs. (5.129) $E_x^{(i)} = E_y^{(i)} = E_i$, $\nu_{xy}^{(i)} = \nu_{yx}^{(i)} = \nu_i,$ and $G_{xy}^i = G_i = E_i/2(1 + \nu_i)$.

Consider a layer composed of unidirectional plies with orientation angle ϕ_i. Using Eqs. (4.69), we can express strains in the principal material coordinates as

$$\begin{aligned}
\varepsilon_1^{(i)} &= \varepsilon_x^{(i)}\cos^2\phi_i + \varepsilon_y^{(i)}\sin^2\phi_i + \gamma_{xy}^{(i)}\sin\phi_i\cos\phi_i,\\
\varepsilon_2^{(i)} &= \varepsilon_x^{(i)}\sin^2\phi_i + \varepsilon_y^{(i)}\cos^2\phi_i - \gamma_{xy}^{(i)}\sin\phi_i\cos\phi_i,\\
\gamma_{12}^{(i)} &= 2\left(\varepsilon_y^{(i)} - \varepsilon_x^{(i)}\right)\sin\phi_i\cos\phi_i + \gamma_{xy}^{(i)}\cos 2\phi_i,
\end{aligned} \tag{5.130}$$

and find the corresponding stresses, i.e.,

$$\sigma_1^{(i)} = \overline{E}_1^{(i)}\left(\varepsilon_1^{(i)} + \nu_{12}^{(i)}\varepsilon_2^{(i)}\right), \quad \sigma_2^{(i)} = \overline{E}_2^{(i)}\left(\varepsilon_2^{(i)} + \nu_{21}^{(i)}\varepsilon_1^{(i)}\right), \quad \tau_{12}^{(i)} = G_{12}^{(i)}\gamma_{12}^{(i)} \tag{5.131}$$

where $\overline{E}_{1,2}^{(i)} = E_{1,2}^{(i)}/(1-\nu_{12}^{(i)}\nu_{21}^{(i)})$ and $E_1^{(i)}, E_2^{(i)}, G_{12}^{(i)}, \nu_{12}^{(i)}, \nu_{21}^{(i)}$ are the elastic constants of a unidirectional ply. Thus, Eqs. (5.128)–(5.131) allow us to find in-plane stresses acting in each layer or in an elementary composite ply.

Compatible deformation of the layers is provided by interlaminar stresses τ_{xz}, τ_{yz}, and σ_z. To find these stresses, we need to use the three-dimensional equilibrium equations, Eqs. (2.5), which yield

$$\frac{\partial \tau_{xz}}{\partial z} = -\left(\frac{\partial \sigma_x}{\partial x} + \frac{\partial \tau_{xy}}{\partial y}\right), \quad \frac{\partial \tau_{yz}}{\partial z} = -\left(\frac{\partial \sigma_y}{\partial y} + \frac{\partial \tau_{xy}}{\partial x}\right),$$
$$\frac{\partial \sigma_z}{\partial z} = -\left(\frac{\partial \tau_{xz}}{\partial x} + \frac{\partial \tau_{xz}}{\partial y}\right) \tag{5.132}$$

Substituting stresses σ_x, σ_y, and τ_{xy} from Eqs. (5.4), and integrating Eqs. (5.132) with due regard to the forces that can act on the laminate surfaces, we can calculate the transverse shear and normal stresses τ_{xz}, τ_{yz}, and σ_z.

5.12 References

Aleksandrov, A. Ya., Brukker, L. E., Kurshin, L. M., & Prusakov, A. P. (1960). *Analysis of Sandwich Plates*. Moscow (in Russian): Mashinostroenie.

Ashton, J. E. (1969). Approximate solutions for unsymmetrically laminated plates. *J. Composite Mater.,* 189–191.

Bucci, R. J., Mueller, L. N., Schulte, R. W., & Prohaska, J. L. (1987). ARALL laminates – results from a cooperative test program. In *Proc. 32nd Int. SAMPE Symp*., April 6–9, 1987, Anaheim, CA, USA, 902–916.

Bucci, R. J., & Mueller, L. N. (1988). ARALL™ laminates: properties and design update. In *Proc. 33rd Int. SAMPE Symp*. March 7–10, 1988, Anaheim, CA, USA, 1237–1248.

Chen, H.-J., & Tsai, S. W. (1996). Three-dimensional effective moduli of symmetric laminates. *J. Composite Mater., 30*(8), 906–917.

Fridlyander, I. N., Senatorova, O. G., Anihovskaya, L. I., Shokin, G. I., Gorushkin, V. A., Dementyeva, L. A., Sidelnikov, V. V., & Sandler, V. S. (1997). Laminated structural Al/Glass Epoxy SIAL composites. In: *Composite Materials, Technologies and Automation of Products Manufacturing*. Moscow: SAMPE. 1997, 78–85.

Karmishin, A. V. (1974). Equations for nonhomogeneous thin-walled elements based on minimum stiffnesses. *App. Mech. (Prikladnaya Mekhanika), 10*(6), 34–42 (in Russian).

Kolesnikov, B., Herbech, L., & Fink, A. (2008). GFRP/Titanium hybrid material for improving composite bolted joints. *Composite Structures, 83*, 368–380.

Morozov, E. V. (2006). The effect of filament-winding mosaic patterns on the strength of thin-walled composite shells. *Composite Structures, 76*, 123–129.

Ohrloff, N., & Horst, P. (1992). Feasibility study of the application of GLARE materials in wide body aircraft fuselage. In *Proc. 13th Int* (pp. 131–142). Hamburg, Germany: SAMPE European Conf, May 11–13, 1992.

Sirotkin, O. S. (1973). Design of mechanical joints for composite parts. In *Design, Analysis and Testing of Composite Structures, Issue 1, 1973* (pp. 144–151), TSAGI (in Russian).

Vasiliev, V. V. (1993). *Mechanics of Composite Structures*. Washington: Taylor & Francis.

Verchery, G. (1999). Designing with anisotropy. Part 1: Methods and general results for laminates. In *Proc. 12th International Conference on Composite Materials (ICCM-12)*, Paris, France, 5–9 July 1999, ICCM12/TCA (CD-ROM), p. 11.

Vermeeren, C. A. J. R. (2003). An historic overview of the development of fibre metal laminates. *Applied Composite Materials, 10*, 4–5, 189–205.

Vlot, A., Bulters, P. B. M., & Fredell, R. S. (1992). Low and high velocity impact loading on fiber/metal laminates, carbon/PEEK and monolithic aluminum 2024-T3. In *Proc. 13th Int* (pp. 347–360). Hamburg, Germany: SAMPE European Conf., May 11–13, 1992.

Vlot, A., & Gunnik, J. W. (2001). *Fibre Metal Laminates: an Introduction*. Dordrecht-Boston-London: Kluwer Academic Publishers.

Vorobey, V. V., & Sirotkin, O. S. (1985). *Joining of Composite Structures*. Moscow: Machinostroenie (in Russian).

Vorobey, V. V., Morozov, E. V., & Tatarnikov, O. V. (1992). *Analysis of Thermostressed Composite Structures*. Moscow: Mashinostroenie (in Russian).

Whitney, J. M. (1987). *Structural Analysis of Laminated Anisotropic Plates*. Lancaster, PA, USA: Technomic Publishing Co., Inc.

CHAPTER

Failure criteria and strength of laminates

6

Consider a laminate consisting of orthotropic layers or plies whose principal material axes 1, 2, and 3, in general, do not coincide with the global coordinates of the laminate (x, y, z) and assume that this layer or ply is in a state of plane stress as depicted in Fig. 6.1. It should be emphasized that, in contrast to a laminate that can be anisotropic and demonstrate coupling effects, the layer under consideration is orthotropic and is referred to its principal material axes. Using the procedure that is described in Section 5.11, we can find stresses σ_1, σ_2, and τ_{12} corresponding to a given system of loads acting on the laminate. The problem that we approach now is to evaluate the laminate load-carrying capacity, i.e., to calculate the loads that cause failure of the individual layers and of the laminate as a whole. For a layer, this problem can be readily solved if we have a failure or strength criterion

$$F(\sigma_1, \sigma_2, \tau_{12}) = 1 \tag{6.1}$$

specifying the combination of stresses that causes layer fracture. In other words, the layer functions while $F < 1$, fails if $F = 1$, and does not exist as a load-carrying structural element if $F > 1$. In the relevant stress space, i.e., σ_1, σ_2, and τ_{12}, Eq. (6.1) specifies the so-called failure surface (or failure envelope) shown in Fig. 6.2. Each point in this space corresponds to a particular stress state, and if a point is inside the surface, the layer withstands the corresponding combination of stresses without failure.

Thus, the problem of strength analysis is reduced to the construction of a failure criterion in its analytical, Eq. (6.1), or graphical, Fig. 6.2, form. Up to the present time, numerous variants of these forms have been proposed for traditional and composite structural materials (Gol'denblat and Kopnov,

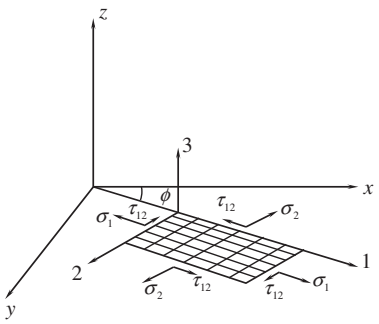


FIGURE 6.1

An orthotropic layer or ply in a plane stressed state.

Advanced Mechanics of Composite Materials and Structural Elements. http://dx.doi.org/10.1016/B978-0-08-098231-1.00006-6
Copyright © 2013 Elsevier Ltd. All rights reserved.

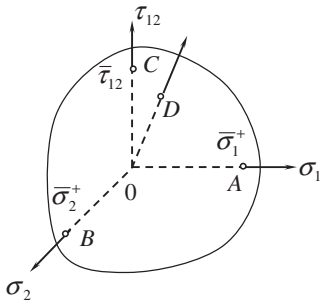


FIGURE 6.2

Failure surface in the stress space.

1968; Wu, 1974; Rowlands, 1975; Tsai and Hahn, 1975; Vicario and Toland, 1975; Hashin, 1980; etc.) and these have been described by the authors of many textbooks on composite materials. Omitting the history and comparative analysis of particular criteria that can be found elsewhere (Hinton et al., 2004), we mainly discuss here the practical aspects of the problem.

In addition, in many applications, a progressive failure analysis of composite laminates is required to predict their mechanical behavior under various loading conditions. We present a combined elastoplastic damage model and a strain-driven implicit integration procedure for fiber reinforced composite materials and structures that involves a consideration of their mechanical response prior to the initiation of damage, prediction of damage initiation, and modeling of postfailure behavior.

6.1 FAILURE CRITERIA FOR AN ELEMENTARY COMPOSITE LAYER OR PLY

There exist, in general, two approaches to construct the failure surface, the first of which can be referred to as the microphenomenological approach. The term "phenomenological" means that the actual physical mechanisms of failure at the microscopic material level are not considered and that we deal with stresses and strains, i.e., with conventional and not actually observed state variables introduced in Chapter 2. In the micro-approach, we evaluate the layer strength using microstresses acting in the fibers and in the matrix and failure criteria proposed for homogeneous materials. To a certain extent (see, e.g., Skudra et al., 1989), this approach requires the minimum number of experimental material characteristics, i.e., only those determining the strengths of fibers and matrices. As a result, the coordinates of all the points of the failure surface in Fig. 6.2 including points A, B, and C corresponding to uniaxial and pure shear loading are found by calculation. To do this, we should simulate the layer or the ply with a suitable microstructural model (see, e.g., Section 3.3), apply a pre-assigned system of average stresses σ_1, σ_2, and τ_{12} (e.g., corresponding to vector 0D in Fig. 6.2), find the stresses acting in the material components, specify the failure mode that can be associated with the fibers or with the matrix, and determine the ultimate combination of average stresses corresponding, for example, to point D in Fig. 6.2. Thus, the whole failure surface can be constructed. However, the uncertainty and approximate character of the existing micromechanical models discussed in Section 3.3 result in relatively poor accuracy using this method which, being in principle rather promising, has not found wide practical application at the present time.

The second basic approach, which can be referred to as the macrophenomenological one, deals with the average stresses σ_1, σ_2, and τ_{12} shown in Fig. 6.1 and ignores the ply's microstructure. For a plane stress state in an orthotropic ply, this approach requires at least five experimental results specifying material strength under:

- Longitudinal tension, $\overline{\sigma}_1^+$ (point A in Fig. 6.2)
- Longitudinal compression, $\overline{\sigma}_1^-$
- Transverse tension, $\overline{\sigma}_2^+$ (point B in Fig. 6.2)
- Transverse compression, $\overline{\sigma}_2^-$
- In-plane shear, $\overline{\tau}_{12}$ (point C in Fig. 6.2)

Obviously, these data are insufficient to construct the complete failure surface, and two possible ways leading to two types of failure criteria can be used.

The first type, referred to as structural failure criteria, involves some assumptions concerning the possible failure modes that can help us to specify the shape of the failure surface. According to the second type, which provides a failure surface of an approximate form, experiments simulating a set of complicated stress states (such that two or all three stresses σ_1, σ_2, and τ_{12} are induced simultaneously) are undertaken. As a result, a system of points, similar to point D in Fig. 6.2, is determined and approximated with some suitable surface.

The experimental data that are necessary to construct the failure surface are usually obtained by testing thin-walled tubular specimens such as those shown in Figs. 6.3 and 6.4. These specimens are loaded with internal or external pressure p, tensile or compressive axial forces P, and end torques T, providing a prescribed combination of axial stress σ_x, circumferential stress σ_y, and shear stress τ_{xy} that can be calculated as

$$\sigma_x = \frac{P}{2\pi Rh}, \quad \sigma_y = \frac{pR}{h}, \quad \tau_{xy} = \frac{T}{2\pi R^2 h}$$

Here, R is the cylinder radius and h is its thickness. For the tubular specimens shown in Fig. 6.4, which were made from unidirectional carbon-epoxy composite by circumferential winding, $\sigma_x = \sigma_2$, $\sigma_y = \sigma_1$, and $\tau_{xy} = \tau_{12}$ (see Fig. 6.1).

We shall now consider typical structural and approximation strength criteria developed for typical composite layers and plies.

6.1.1 Maximum stress and strain criteria

These criteria belong to a structural type and are based on the assumption that there can exist three possible modes of failure caused by stresses σ_1, σ_2, and τ_{12} or strains ε_1, ε_2, and γ_{12} when they reach the corresponding ultimate values.

The maximum stress criterion can be presented in the form of the following inequalities

$$\begin{aligned} &\sigma_1 \le \overline{\sigma}_1^+, \quad \sigma_2 \le \overline{\sigma}_2^+ \quad \text{if} \quad \sigma_1 > 0 \quad \sigma_2 > 0 \\ &|\sigma_1| \le \overline{\sigma}_1^-, \quad |\sigma_2| \le \overline{\sigma}_2^- \quad \text{if} \quad \sigma_1 < 0 \quad \sigma_2 < 0 \\ &|\tau_{12}| \le \overline{\tau}_{12} \end{aligned} \tag{6.2}$$

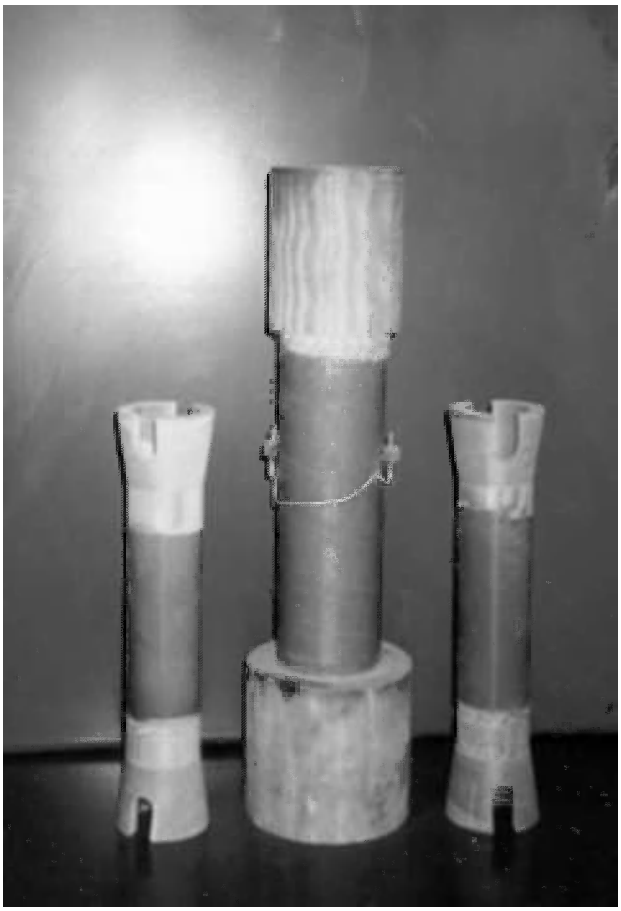


FIGURE 6.3

Glass-epoxy fabric test tubular specimens.

It should be noted here, and subsequently, that all the ultimate stresses $\overline{\sigma}$ and $\overline{\tau}$ including compressive strength values are taken as positive quantities. The failure surface corresponding to the criterion in Eqs. (6.2) is shown in Fig. 6.5. As can be seen, according to this criterion, failure is associated with independently acting stresses, and any possible stress interaction is ignored.

It can be expected that the maximum stress criterion adequately describes the behavior of those materials in which stresses σ_1, σ_2, and τ_{12} are taken by different structural elements. A typical example of such a material is the fabric composite layer discussed in Section 4.7. Indeed, warp and filling yarns (see Fig. 4.87) working independently provide material strength under tension and compression in two orthogonal directions (1 and 2), whereas the polymeric matrix controls the layer strength under in-plane shear. A typical failure envelope in the plane (σ_1, σ_2) for a glass-epoxy fabric composite is shown in Fig. 6.6. The corresponding results in the plane (σ_1, τ_{12}), but for a different glass fabric experimentally studied by Annin and Baev (1979), are presented in Fig. 6.7. It follows



FIGURE 6.4

Carbon-epoxy test tubular specimens made by circumferential winding (the central cylinder failed under axial compression and the right one under torsion).

from Figs. 6.6 and 6.7 that the maximum stress criterion provides a satisfactory prediction of the strength for fabric composites within the accuracy determined by the scatter of experimental results. As has been already noted, this criterion ignores the interaction of stresses. However, this interaction occurs in fabric composites that are loaded with compression in two orthogonal directions, because compression of the filling yarns increases the strength in the warp direction and vice versa. The corresponding experimental results from Belyankin et al. (1971) are shown in Fig. 6.8. As can be seen, there is a considerable discrepancy between the experimental data and the maximum stress criterion shown with solid lines. However, even in such cases, this criterion is sometimes used to design composite structures because it is simple and conservative, i.e., it underestimates material strength, thus increasing the safety factor for the structure under design. There exist fabric composites

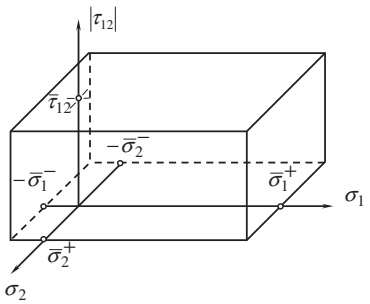


FIGURE 6.5

Failure surface corresponding to maximum stress criterion.

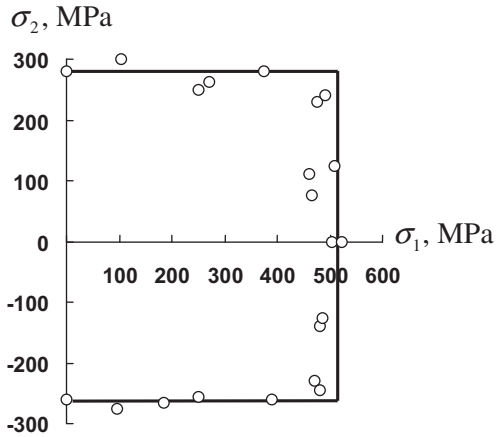


FIGURE 6.6

Failure envelope for glass-epoxy fabric composite in plane (σ_1, σ_2).
(——) maximum stress criterion, Eqs. (6.2);
(○) experimental data.

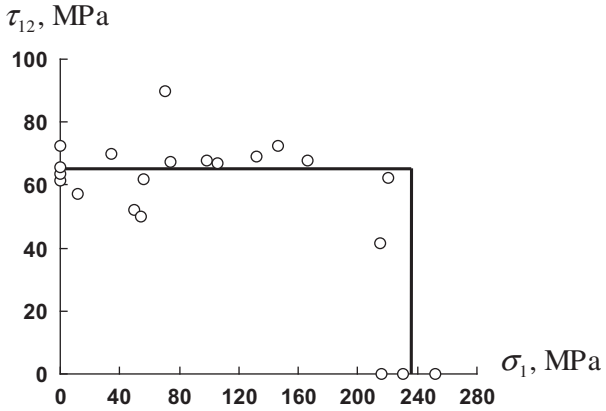


FIGURE 6.7

Failure envelope for glass-epoxy fabric composite in plane (σ_1, τ_{12}).
(——) maximum stress criterion, Eqs. (6.2);
(○) experimental data.

for which the interaction of normal stresses is exhibited in tension as well. An example of such a material is presented in Fig. 6.9 (experimental data from Gol'denblat and Kopnov (1968)). Naturally, the maximum stress criterion (solid lines in Fig. 6.9) should not be used in this case because it overestimates the material strength, and the structure can fail under loads that are lower than those predicted by this criterion.

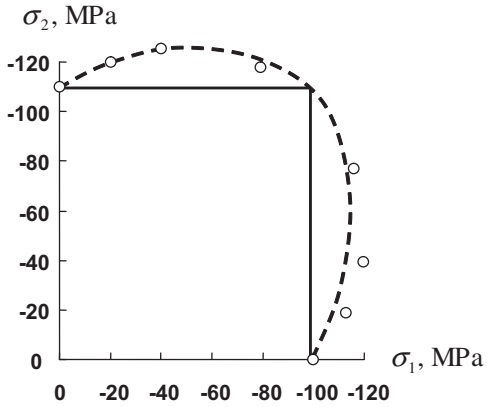


FIGURE 6.8

Failure envelope for glass-phenolic fabric composite loaded with compression in plane (σ_1, σ_2).
(——————) maximum stress criterion, Eqs. (6.2);
(– – – –) polynomial criterion, Eqs. (6.16);
(O) experimental data.

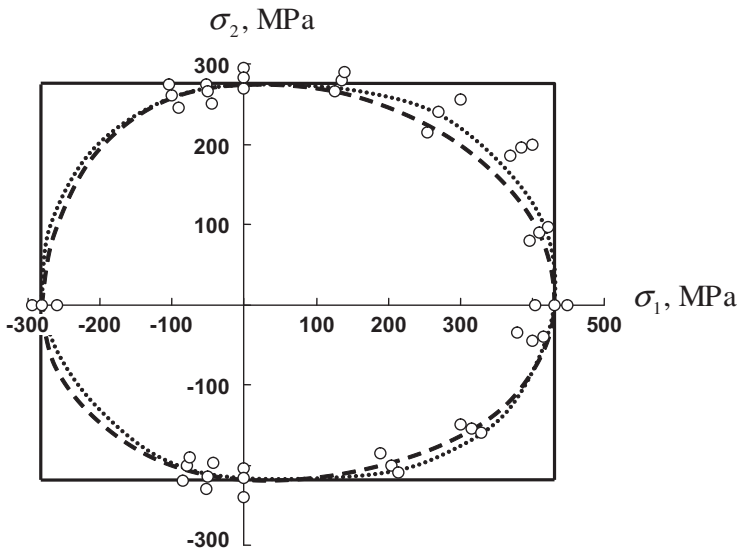


FIGURE 6.9

Failure envelope for glass-epoxy fabric composite in plane (σ_1, σ_2).
(——————) maximum stress criterion, Eqs. (6.2);
(– – – –) approximation criterion, Eqs. (6.11), (6.12);
(·····) approximation criterion, Eqs. (6.15);
(O) experimental data.

The foregoing discussion concerns fabric composites. Now consider a unidirectional ply and try to apply the maximum stress criterion in this situation. First of all, since the longitudinal strength of the ply is controlled by the fibers whose strength is much higher than that of the matrix, it is reasonable to neglect the interaction of stress σ_1 on one side and stresses σ_2 and τ_{12} on the other side. In other words, we can apply the maximum stress criterion to predict material strength under tension or compression in the fiber direction and, hence, use the first part of Eqs. (6.2), i.e.,

$$\begin{aligned} \sigma_1 &\le \overline{\sigma}_1^+ \quad \text{if} \quad \sigma_1 > 0 \\ |\sigma_1| &\le \overline{\sigma}_1^- \quad \text{if} \quad \sigma_1 < 0 \end{aligned} \tag{6.3}$$

Actually, there exist unidirectional composites with a very brittle matrix (carbon or ceramic) for which the other conditions in Eqs. (6.2) can be also applied. As an example, Fig. 6.10 displays the failure envelope for a carbon-carbon unidirectional material (experimental data from Vorobey et al., 1992). However, for the majority of unidirectional composites, the interaction of transverse normal and shear stresses is essential and should be taken into account. This means that we should apply Eq. (6.1) but can simplify it as follows

$$F(\sigma_2, \tau_{12}) = 1 \tag{6.4}$$

The simplest way to induce a combined stress state for a unidirectional ply is to use the off-axis tension or compression test as discussed in Section 4.3.1. Applying stress σ_x as in Figs. 4.22 and 4.23, we have stresses σ_1, σ_2, and τ_{12} specified by Eqs. (4.78). Then, Eqs. (6.2) yield the following ultimate stresses:

For $\sigma_x > 0$,

$$\overline{\sigma}_x = \frac{\overline{\sigma}_1^+}{\cos^2\phi}, \quad \overline{\sigma}_x = \frac{\overline{\sigma}_2^+}{\sin^2\phi}, \quad \overline{\sigma}_x = \frac{\overline{\tau}_{12}}{\sin\phi\,\cos\phi} \tag{6.5}$$

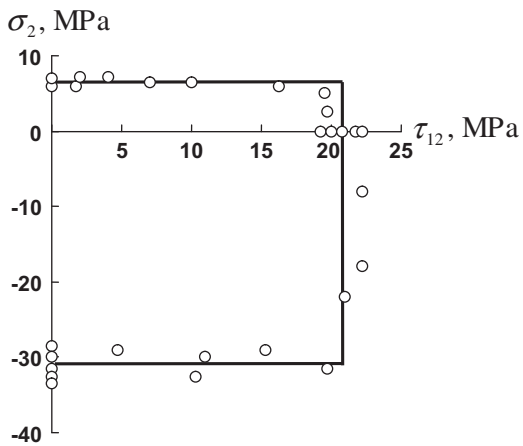


FIGURE 6.10

Failure envelope for carbon-carbon unidirectional composite in plane (σ_2, τ_{12}).
(——) maximum stress criterion, Eqs. (6.2);
(○) experimental data.

For $\sigma_x < 0$,

$$\overline{\sigma}_x = \frac{\overline{\sigma}_1^-}{\cos^2\phi}, \quad \overline{\sigma}_x = \frac{\overline{\sigma}_2^-}{\sin^2\phi}, \quad \overline{\sigma}_x = \frac{\overline{\tau}_{12}}{\sin\phi\,\cos\phi} \tag{6.6}$$

The actual ultimate stress is the minimum $\overline{\sigma}_x$ value of the three values provided by Eqs. (6.5) for tension or Eqs. (6.6) for compression. The experimental data of S.W. Tsai (taken from Jones (1999)) and corresponding to a glass-epoxy unidirectional composite are presented in Fig. 6.11. As can be seen, the maximum stress criterion (solid lines) demonstrates fair agreement with experimental results for angles close to 0 and 90° only. An important feature of this criterion belonging to a structural type is its ability to predict the failure mode. Curves 1, 2, and 3 in Fig. 6.11 correspond to the first, the second, and the third equations of Eqs. (6.5) and (6.6). It follows from Fig. 6.11a that fiber failure occurs only for $\phi = 0°$. For $0° < \phi < 30°$, material failure is associated with in-plane shear, whereas for $30° < \phi \leq 90°$, it is caused by the transverse normal stress σ_2.

The maximum strain failure criterion is similar to the maximum stress criterion discussed earlier, but is formulated in terms of strains, i.e.,

$$\begin{aligned} &\varepsilon \leq \overline{\varepsilon}_1^+, \quad \varepsilon_2 \leq \overline{\varepsilon}_2^+ \quad \text{if} \quad \varepsilon_1 > 0 \quad \varepsilon_2 > 0 \\ &|\varepsilon_1| \leq \overline{\varepsilon}_1^-, \quad |\varepsilon_2| \leq \overline{\varepsilon}_2^- \quad \text{if} \quad \varepsilon_1 < 0 \quad \varepsilon_2 < 0 \\ &\qquad\qquad |\gamma_{12}| \leq \overline{\gamma}_{12} \end{aligned} \tag{6.7}$$

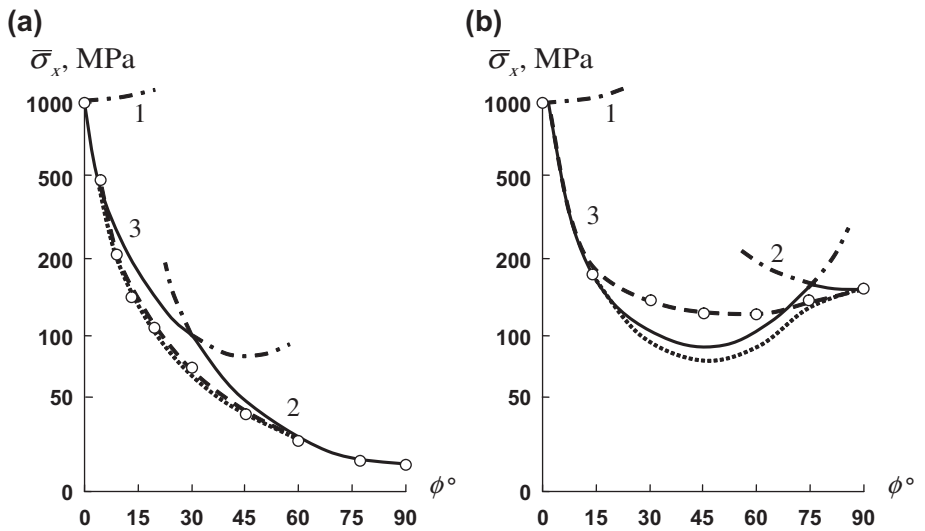


FIGURE 6.11

Dependence of the stress on the fiber orientation angle for off-axis tension (a) and compression (b) of glass-epoxy unidirectional composite.

——— · — maximum stress criterion, Eqs. (6.2);

····· approximation criterion, Eqs. (6.3) and (6.17);

— — — — approximation criterion, Eqs. (6.3) and (6.18).

where

$$\varepsilon_1 = \frac{\sigma_1}{E_1} - \nu_{12}\frac{\sigma_2}{E_2}, \quad \varepsilon_2 = \frac{\sigma_2}{E_2} - \nu_{12}\frac{\sigma_1}{E_1}, \quad \gamma_{12} = \frac{\tau_{12}}{G_{12}} \tag{6.8}$$

The maximum strain criterion ignores the strain interaction but allows for the stress interaction caused by Poisson's effect. This criterion provides results that are generally closely similar to those following from the maximum stress criterion.

There exists a unique stress state which can only be studied using the maximum strain criterion. This is longitudinal compression of a unidirectional ply as discussed earlier in Section 3.4.4. Under this type of loading, only longitudinal stress σ_1 is induced, whereas $\sigma_2 = 0$ and $\tau_{12} = 0$. Nevertheless, fracture is accompanied with cracks parallel to the fibers (see Fig. 6.12, showing tests performed by Katarzhnov (1982)). These cracks are caused by the transverse tensile strain ε_2 induced by Poisson's effect. The corresponding strength condition follows from Eqs. (6.7) and (6.8) and can be written as

$$|\sigma_1| \leq \overline{\varepsilon}_2^{+}\frac{E_1}{\nu_{21}}$$

It should be emphasized that the test shown in Fig. 6.12 can be misleading because transverse deformation of the ply is not restricted in this test, whereas it is normally restricted in actual laminated



FIGURE 6.12

Failure modes of a unidirectional glass-epoxy composite under longitudinal compression.

composite structural elements. Indeed, a long cylinder with material structure $[0^\circ_{11}]$ being tested under compression yields a material strength $\overline{\sigma}_1^- = 300$ MPa, whereas the same cylinder with material structure $[0^\circ_{10}/90^\circ]$ gives $\overline{\sigma}_1^- = 505$ MPa (Katarzhnov, 1982). Thus, if we change one longitudinal ply for a circumferential ply which practically does not bear any of the load in compression along the cylinder axis, but restricts its circumferential deformation, we increase the material strength in compression by 68.3%. Correspondingly, the failure mode becomes quite different (see Fig. 6.13).

6.1.2 Approximation strength criteria

In contrast to structural strength criteria, approximation criteria do not indicate the mode of failure and are constructed by approximation of available experimental results with some appropriate function depending on stresses σ_1, σ_2, and τ_{12}. The simplest and the most widely used criterion is a second-order polynomial approximation, typical forms of which are presented in Fig. 6.14. In the stress space shown in Fig. 6.2, the polynomial criterion corresponding to Fig. 6.14a can be written as

$$F(\sigma_1,\ \sigma_2,\ \tau_{12}) = R_{11}\sigma_1^2 + R_{22}\sigma_2^2 + S_{12}\tau_{12}^2 = 1 \tag{6.9}$$

To determine the coefficients R and S, we need to perform three tests providing material strength under uniaxial loading in 1 and 2 directions and in shear. Then, applying the following conditions

$$\begin{aligned} F(\sigma_1 = \overline{\sigma}_1,\ \sigma_2 = 0,\ \tau_{12} = 0) &= 1 \\ F(\sigma_1 = 0,\ \sigma_2 = \overline{\sigma}_2,\ \tau_{12} = 0) &= 1 \\ F(\sigma_1 = 0,\ \sigma_2 = 0,\ \tau_{12} = \overline{\tau}_{12}) &= 1 \end{aligned} \tag{6.10}$$

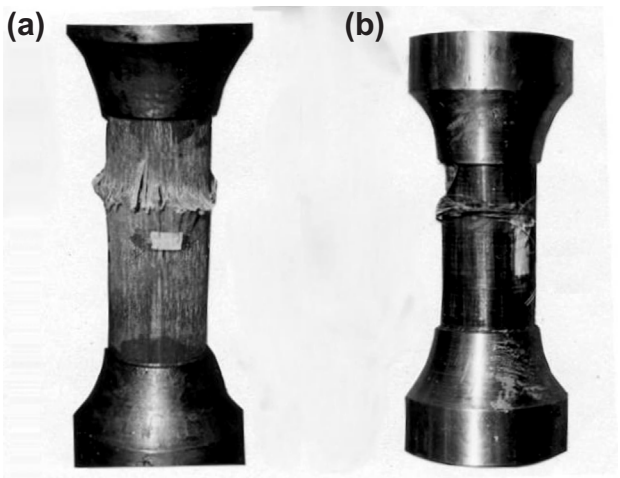


FIGURE 6.13

Failure mode of a glass-epoxy tubular specimen with 10 longitudinal plies and one outside circumferential ply:
(a) inside view;
(b) outside view.

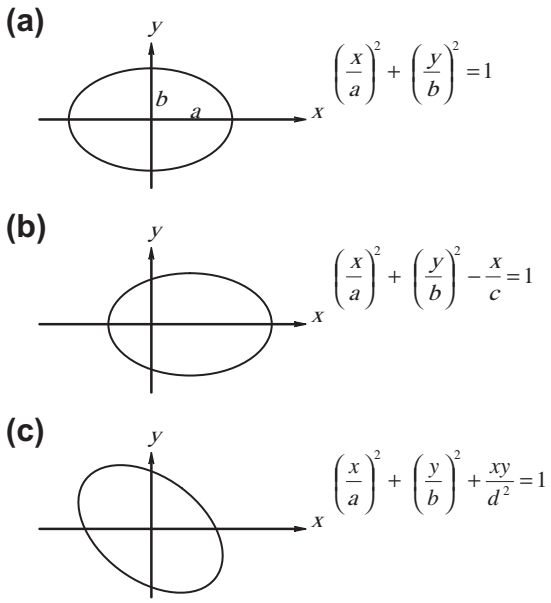


FIGURE 6.14

Typical shapes of the curves corresponding to the second-order polynomials specified by equations (a), (b) and (c).

we can find R and S and write Eq. (6.9) in its final form

$$\left(\frac{\sigma_1}{\overline{\sigma}_1}\right)^2+\left(\frac{\sigma_2}{\overline{\sigma}_2}\right)^2+\left(\frac{\tau_{12}}{\overline{\tau}_{12}}\right)^2=1 \tag{6.11}$$

It appears as though this criterion yields the same strength estimate in tension and compression. However, it can be readily made specific for tension or compression. It is important to realize that when evaluating a material's strength we usually know the stresses acting in this material. Thus, we can take in Eq. (6.10)

$$\begin{aligned}&\overline{\sigma}_1=\overline{\sigma}_1^+ \quad \text{if} \quad \sigma_1>0 \quad \text{or} \quad \overline{\sigma}_1=\overline{\sigma}_1^- \quad \text{if} \quad \sigma_1<0\\ &\overline{\sigma}_2=\overline{\sigma}_2^+ \quad \text{if} \quad \sigma_2>0 \quad \text{or} \quad \overline{\sigma}_2=\overline{\sigma}_2^- \quad \text{if} \quad \sigma_2<0\end{aligned} \tag{6.12}$$

describing in this way the cases of tension and compression. The failure criterion given by Eqs. (6.11) and (6.12) is demonstrated in Fig. 6.9 with application to a fabric composite loaded with stresses σ_1 and $\sigma_2(\tau_{12}=0)$. Naturally, this criterion requires different equations for different quadrants in Fig. 6.9.

For some problems, e.g., for the problem of design, for which we usually do not know the signs of the stresses, we may need to use a universal form of the polynomial criterion valid both for tension and for compression. In this case, we should apply an approximation of the type shown in Fig. 6.14b and generalize Eq. (6.9) as

$$F(\sigma_1,\ \sigma_2,\ \tau_{12})=R_1\sigma_1+R_2\sigma_2+R_{11}\sigma_1^2+R_{22}\sigma_2^2+S_{12}\tau_{12}^2=1 \tag{6.13}$$

Using criteria similar to Eqs. (6.10), i.e.,

$$\begin{aligned} &F\left(\sigma_1 = \overline{\sigma}_1^+,\ \sigma_2 = 0,\ \tau_{12} = 0\right) = 1 \quad \text{if} \quad \sigma_1 > 0 \\ &F\left(\sigma_1 = -\overline{\sigma}_1^-,\ \sigma_2 = 0,\ \tau_{12} = 0\right) = 1 \quad \text{if} \quad \sigma_1 < 0 \\ &F\left(\sigma_1 = 0,\ \sigma_2 = \overline{\sigma}_2^+,\ \tau_{12} = 0\right) = 1 \quad \text{if} \quad \sigma_2 > 0 \\ &F\left(\sigma_1 = 0,\ \sigma_2 = -\overline{\sigma}_2^-,\ \tau_{12} = 0\right) = 1 \quad \text{if} \quad \sigma_2 < 0 \\ &F(\sigma_1 = 0,\ \sigma_2 = 0,\ \tau_{12} = \overline{\tau}_{12}) = 1 \end{aligned} \tag{6.14}$$

we arrive at

$$\sigma_1\left(\frac{1}{\overline{\sigma}_1^+} - \frac{1}{\overline{\sigma}_1^-}\right) + \sigma_2\left(\frac{1}{\overline{\sigma}_2^+} - \frac{1}{\overline{\sigma}_2^-}\right) + \frac{\sigma_1^2}{\overline{\sigma}_1^+\overline{\sigma}_1^-} + \frac{\sigma_2^2}{\overline{\sigma}_2^+\overline{\sigma}_2^-} + \left(\frac{\tau_{12}}{\overline{\tau}_{12}}\right)^2 = 1 \tag{6.15}$$

Comparison of this criterion with the criteria discussed earlier and with experimental results is presented in Fig. 6.9. As can be seen, the criteria specified by Eqs. (6.11), (6.12), and (6.15) provide results which are in fair agreement with the experimental data for all the stress states except, possibly, biaxial compression for which there are practically no experimental results shown in Fig. 6.9. Such results are presented in Fig. 6.8 and allow us to conclude that the failure envelope can be approximated in this case by a polynomial of the type shown in Fig. 6.14c, i.e.,

$$F\left(\sigma_1,\ \sigma_2,\ \tau_{12}\right) = R_{11}\sigma_1^2 + R_{12}\sigma_1\sigma_2 + R_{22}\sigma_2^2 + S_{12}\tau_{12}^2 = 1$$

The coefficients R_{11}, R_{22}, and S_{12} can be found as earlier from Eqs. (6.10), and we need to use an additional strength condition to determine the coupling coefficient, R_{12}. A reasonable form of this condition is $F(\sigma_1 = -\overline{\sigma}_1^-,\ \sigma_2 = -\overline{\sigma}_2^-,\ \tau_{12} = 0) = 1$. This means that whereas for $|\sigma_1| < \overline{\sigma}_1^-$ and $|\sigma_2| < \overline{\sigma}_2^-$ the interaction of stresses increases material strength under compression, the combination of compressive failure stresses $|\sigma_1| = \sigma_1^-$ and $|\sigma_2| = \sigma_2^-$ results in material failure. Then

$$\left(\frac{\sigma_1}{\overline{\sigma}_1^-}\right)^2 - \frac{\sigma_1\sigma_2}{\overline{\sigma}_1^-\overline{\sigma}_2^-} + \left(\frac{\sigma_2}{\overline{\sigma}_2^-}\right)^2 + \left(\frac{\tau_{12}}{\overline{\tau}_{12}}\right)^2 = 1 \tag{6.16}$$

Comparison of this criterion with experimental data is presented in Fig. 6.8. The term allowing for the interaction of stresses σ_1 and σ_2 can be added to the strength criterion in Eq. (6.15), which is generalized as

$$\sigma_1\left(\frac{1}{\overline{\sigma}_1^+} - \frac{1}{\overline{\sigma}_1^-}\right) + \sigma_2\left(\frac{1}{\overline{\sigma}_2^+} - \frac{1}{\overline{\sigma}_2^-}\right) + \frac{\sigma_1^2}{\overline{\sigma}_1^+\overline{\sigma}_1^-} - \frac{\sigma_1\sigma_2}{\sqrt{\overline{\sigma}_1^+\overline{\sigma}_1^-\overline{\sigma}_2^+\overline{\sigma}_2^-}} + \frac{\sigma_2^2}{\overline{\sigma}_2^+\overline{\sigma}_2^-} + \left(\frac{\tau_{12}}{\overline{\tau}_{12}}\right)^2 = 1$$

(Tsai and Wu, 1971). Now consider unidirectional composites and return to Fig. 6.11. As can be seen, the maximum stress criterion (solid lines), ignoring the interaction of stresses σ_2 and τ_{12}, demonstrates

rather poor agreement with the experimental data. The simplest approximation criterion, Eqs. (6.11) and (6.12), takes, for the case under study, the form

$$F(\sigma_2,\ \tau_{12}) = \left(\frac{\sigma_2}{\overline{\sigma}_2}\right)^2 + \left(\frac{\tau_{12}}{\overline{\tau}_{12}}\right)^2 = 1 \tag{6.17}$$

and the corresponding failure envelope is shown in Fig. 6.11 with dotted lines. Although providing fair agreement with experimental results for tension (Fig. 6.11a), this criterion fails to predict material strength under compression (Fig. 6.11b). Moreover, for this case, the approximation criterion yields worse results than those demonstrated by the maximum stress criterion. There are simple physical reasons for this discrepancy. In contrast to the maximum stress criterion, Eq. (6.17) allows for stress interaction, but in such a way that the transverse stress σ_2 reduces the material strength under shear. However, this holds true only if the transverse stress is tensile. As can be seen in Fig. 6.15, in which the experimental results taken from Barbero's (1998) book are presented, a compressive stress σ_2 increases the ultimate value of shear stress τ_{12}. As a result, the simplest polynomial criterion in Eq. (6.17), being, as it has been already noted, quite adequate for $\sigma_2 > 0$, significantly underestimates material strength for $\sigma_2 < 0$ (solid line in Fig. 6.15). As also follows from Fig. 6.15, a reasonable approximation to the experimental results can be achieved if we use a curve of the type shown in Fig. 6.14b (but moved to the left with respect to the y-axis), i.e., if we apply for this case the criterion presented by Eq. (6.15) which can be written as

$$F(\sigma_2,\ \tau_{12}) = \sigma_2\left(\frac{1}{\overline{\sigma}_2^+} - \frac{1}{\overline{\sigma}_2^-}\right) + \frac{\sigma_2^2}{\overline{\sigma}_2^+\overline{\sigma}_2^-} + \left(\frac{\tau_{12}}{\overline{\tau}_{12}}\right)^2 = 1 \tag{6.18}$$

The corresponding approximations are shown in Figs 6.11 and 6.15 by dashed lines.

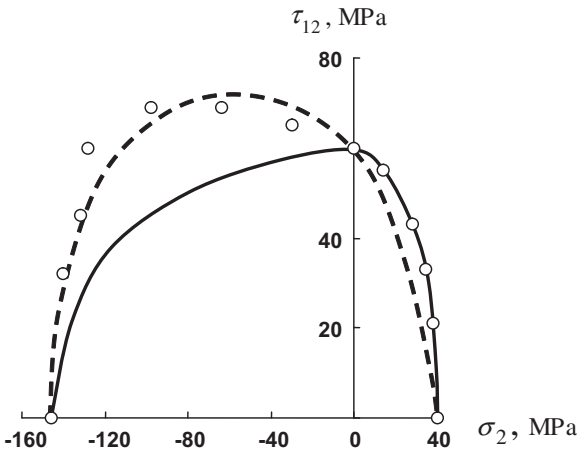


FIGURE 6.15

Failure envelope for glass-epoxy unidirectional composite in plane (σ_2, τ_{12}).
(——) approximation criterion, Eqs. (6.12), (6.17);
(– – – –) approximation criterion, Eqs. (6.18);
(○) experimental data.

In conclusion, it should be noted that there exist more complicated polynomial strength criteria than those considered earlier, e.g., the fourth-order criterion of Ashkenazi (1966) and cubic criterion proposed by Tennyson et al. (1980).

6.1.3 Tensor strength criteria

The polynomial approximation strength criteria discussed in Section 6.1.2 have been introduced as some formal approximations of the experimental data in the principal material coordinates. When written in some other coordinate frame, these criteria become much more complicated. Consider, for example, an orthotropic material shown in Fig. 6.16 and referred to the principal material axes 1 and 2, and to some axes $1'$ and $2'$ which make an angle $\phi = 45^\circ$ with the principal axes. For the principal material axes 1 and 2, apply a generalized form of the criterion in Eq. (6.13), i.e.,

$$F(\sigma_1,\ \sigma_2,\ \tau_{12}) = R_1\sigma_1 + R_2\sigma_2 + R_{11}\sigma_1^2 + R_{12}\sigma_1\sigma_2 + R_{22}\sigma_2^2 + S_{12}\tau_{12}^2 = 1 \tag{6.19}$$

Using the strength conditions in Eqs. (6.14) to determine the coefficients R and S, we arrive at

$$F(\sigma_1,\ \sigma_2,\ \tau_{12}) = \left(\frac{1}{\overline{\sigma}_1^+} - \frac{1}{\overline{\sigma}_1^-}\right)\sigma_1 + \left(\frac{1}{\overline{\sigma}_2^+} - \frac{1}{\overline{\sigma}_2^-}\right)\sigma_2 + \frac{\sigma_1^2}{\overline{\sigma}_1^+\overline{\sigma}_1^-} + R_{12}\sigma_1\sigma_2$$

$$+ \frac{\sigma_2^2}{\overline{\sigma}_2^+\overline{\sigma}_2^-} + \left(\frac{\tau_{12}}{\overline{\tau}_{12}}\right)^2 = 1 \tag{6.20}$$

This criterion is similar to the criterion in Eq. (6.15); however, it includes the coefficient R_{12}, which cannot be found from simple tests using Eqs. (6.14). Treating Eq. (6.20) as the approximation strength criterion, we can undertake some additional testing or adopt additional assumptions similar to those used for the derivation of Eq. (6.16) to determine the coefficient R_{12}. We can also simplify the problem and take $R_{12} = 0$, arriving at Eq. (6.15), i.e.,

$$F(\sigma_1,\ \sigma_2,\ \tau_{12}) = \left(\frac{1}{\overline{\sigma}_1^+} - \frac{1}{\overline{\sigma}_1^-}\right)\sigma_1 + \left(\frac{1}{\overline{\sigma}_2^+} - \frac{1}{\overline{\sigma}_2^-}\right)\sigma_2 + \frac{\sigma_1^2}{\overline{\sigma}_1^+\overline{\sigma}_1^-}$$

$$+ \frac{\sigma_2^2}{\overline{\sigma}_2^+\overline{\sigma}_2^-} + \left(\frac{\tau_{12}}{\overline{\tau}_{12}}\right)^2 = 1 \tag{6.21}$$

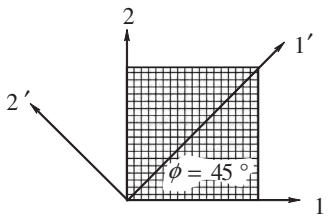


FIGURE 6.16

An orthotropic material referred to coordinates (1, 2) and $(1', 2')$.

which is in good agreement with experimental results (see Fig. 6.9). To simplify the analysis, assume that the material strength in tension and compression is the same for both principal directions 1 and 2, i.e.,

$$\overline{\sigma}_1^+ = \overline{\sigma}_1^- = \overline{\sigma}_2^+ = \overline{\sigma}_2^- = \overline{\sigma}_0, \qquad \overline{\tau}_{12} = \overline{\tau}_0 \tag{6.22}$$

Then, Eq. (6.21) reduces to

$$F(\sigma_1,\ \sigma_2,\ \tau_{12}) = \frac{\left(\sigma_1^2 + \sigma_2^2\right)}{\overline{\sigma}_0^2} + \left(\frac{\tau_{12}}{\overline{\tau}_0}\right)^2 = 1 \tag{6.23}$$

Now, let us write Eq. (6.23) in coordinates $1'$ and $2'$ (see Fig. 6.16). To transform the stresses σ_1, σ_2, and τ_{12} to the stresses σ_1^{45}, σ_2^{45}, and τ_{12}^{45} corresponding to coordinates $1'$ and $2'$, we can use Eqs. (4.68). Taking $\phi = 45^\circ$, $\sigma_x = \sigma_1$, $\sigma_y = \sigma_2$, and $\tau_{xy} = \tau_{12}$, and $\sigma_1 = \sigma_1^{45}$, $\sigma_2 = \sigma_2^{45}$, and $\tau_{12} = \tau_{12}^{45}$, we get

$$\begin{aligned}
\sigma_1 &= \frac{1}{2}\left(\sigma_1^{45} + \sigma_2^{45}\right) - \tau_{12}^{45} \\
\sigma_2 &= \frac{1}{2}\left(\sigma_1^{45} + \sigma_2^{45}\right) + \tau_{12}^{45} \\
\tau_{12} &= \frac{1}{2}\left(\sigma_1^{45} - \sigma_2^{45}\right)
\end{aligned} \tag{6.24}$$

Substitution in Eq. (6.23) yields

$$F(\sigma_1^{45},\ \sigma_2^{45},\ \tau_{12}^{45}) = \frac{1}{4}\left(\frac{2}{\overline{\sigma}_0^2} + \frac{1}{\overline{\tau}_0^2}\right)\left[\left(\sigma_1^{45}\right)^2 + \left(\sigma_2^{45}\right)^2\right] + \frac{1}{2}\left(\frac{2}{\overline{\sigma}_0^2} - \frac{1}{\overline{\tau}_0^2}\right)\sigma_1^{45}\sigma_2^{45}$$

$$+ \frac{2}{\overline{\sigma}_0^2}\left(\tau_{12}^{45}\right)^2 = 1 \tag{6.25}$$

For tension in the directions of axes $1'$ and $2'$ in Fig. 6.16 and for shear in plane $1'\,2'$, we can write Eq. (6.25) in the following forms similar to Eqs. (6.10)

$$\begin{aligned}
&F\left(\sigma_1^{45} = \overline{\sigma}_{45},\ \ \sigma_2^{45} = 0,\ \ \tau_{12}^{45} = 0\right) = 1 \\
&F\left(\sigma_1^{45} = 0,\ \ \sigma_2^{45} = \overline{\sigma}_{45},\ \ \tau_{12}^{45} = 0\right) = 1 \\
&F\left(\sigma_1^{45} = 0,\ \ \sigma_2^{45} = 0,\ \ \tau_{12}^{45} = \overline{\tau}_{45}\right) = 1
\end{aligned} \tag{6.26}$$

Here, $\overline{\sigma}_{45}$ and $\overline{\tau}_{45}$ determine material strength in coordinates $1'$ and $2'$ (see Fig. 6.16). Then, Eq. (6.25) can be reduced to

$$F(\sigma_1^{45},\ \sigma_2^{45},\ \tau_{12}^{45}) = \frac{1}{\overline{\sigma}_{45}^2}\left[\left(\sigma_1^{45}\right)^2 + \left(\sigma_2^{45}\right)^2\right] + \left(\frac{1}{\overline{\tau}_{45}^2} - \frac{2}{\overline{\sigma}_{45}^2}\right)\sigma_1^{45}\sigma_2^{45} + \left(\frac{\tau_{12}^{45}}{\overline{\tau}_{45}}\right) = 1 \tag{6.27}$$

where $\overline{\sigma}_{45}$ and $\overline{\tau}_{45}$ are given by

$$\frac{1}{\overline{\sigma}_{45}^2} = \frac{1}{4}\left(\frac{2}{\overline{\sigma}_0^2} + \frac{1}{\overline{\tau}_0^2}\right),\ \ \overline{\tau}_{45}^2 = \frac{1}{2}\overline{\sigma}_0^2$$

Comparing Eq. (6.27) with Eq. (6.23), we can see that Eq. (6.27), in contrast to Eq. (6.23), includes a term with the product of stresses σ_1^{45} and σ_2^{45}. So, the strength criterion under study changes its form with a transformation of the coordinate frame (from 1 and 2 to $1'$ and $2'$ in Fig. 6.16) which means that the approximation polynomial strength criterion in Eq. (6.23) and, hence, the original criterion in Eq. (6.21), is not invariant with respect to rotation of the coordinate frame.

Consider the class of invariant strength criteria which are formulated in a tensor-polynomial form as linear combinations of mixed invariants of the stress tensor σ_{ij} and the strength tensors of different ranks S_{ij}, S_{ijkl}, etc., i.e.,

$$\sum_{i,k} S_{ik}\sigma_{ik} + \sum_{i,k,m,n} S_{ikmn}\sigma_{ik}\sigma_{mn} + \cdots = 1 \tag{6.28}$$

Using the standard transformation for tensor components we can readily write this equation for an arbitrary coordinate frame. However, the fact that the strength components form a tensor induces some conditions that should be imposed on these components which do not necessarily correlate with experimental data.

To be specific, consider a second-order tensor criterion. Introducing contracted notations for tensor components and restricting ourselves to the consideration of orthotropic materials referred to the principal material coordinates 1 and 2 (see Fig. 6.16), we can present Eq. (6.22) as

$$F(\sigma_1,\ \sigma_2,\ \tau_{12}) = R_1^0\sigma_1 + R_2^0\sigma_2 + R_{11}^0\sigma_1^2 + 2R_{12}^0\sigma_1\sigma_2 + R_{22}^0\sigma_2^2 + 4S_{12}^0\tau_{12}^2 = 1 \tag{6.29}$$

which corresponds to Eq. (6.28) if we put

$$\sigma_{11} = \sigma_1, \quad \sigma_{12} = \tau_{12}, \quad \sigma_{22} = \sigma_2$$

and

$$S_{11} = R_1, \quad S_{22} = R_2,$$

$$S_{1111} = R_{11}^0, \quad S_{1122} = S_{2211} = R_{12}^0, \quad S_{2222} = R_{22}^0, \quad S_{1212} = S_{2121} = S_{1221} = S_{2112} = S_{12}^0$$

The superscript "0" indicates that the components of the strength tensors are referred to the principal material coordinates. Applying the strength conditions in Eqs. (6.14), we can reduce Eq. (6.29) to the following form

$$F(\sigma_1,\ \sigma_2,\ \tau_{12}) = \sigma_1\left(\frac{1}{\overline{\sigma}_1^+} - \frac{1}{\overline{\sigma}_1^-}\right) + \sigma_2\left(\frac{1}{\overline{\sigma}_2^+} - \frac{1}{\overline{\sigma}_2^-}\right) + \frac{\sigma_1^2}{\overline{\sigma}_1^+\overline{\sigma}_1^-} + 2R_{12}^0\sigma_1\sigma_2$$

$$+ \frac{\sigma_2^2}{\overline{\sigma}_2^+\overline{\sigma}_2^-} + \left(\frac{\tau_{12}}{\overline{\tau}_{12}}\right)^2 = 1 \tag{6.30}$$

This equation looks similar to Eq. (6.20); however, there is a difference in principle between them. Whereas Eq. (6.20) is only an approximation to the experimental results, and we can take any suitable value of coefficient R_{12} (in particular, we put $R_{12} = 0$), the criterion in Eq. (6.30) has an invariant tensor form, and coefficient R_{12}^0 should be determined using this characteristic of the criterion.

Following Gol'denblat and Kopnov (1968), consider two cases of pure shear in coordinates $1'$ and $2'$ shown in Fig. 6.17 and assume that $\tau_{45}^+ = \overline{\tau}_{45}^+$ and $\tau_{45}^- = \overline{\tau}_{45}^-$, where the overbar denotes, as earlier, the ultimate value of the corresponding stress. In the general case, $\overline{\tau}_{45}^+ \neq \overline{\tau}_{45}^-$. Indeed, for

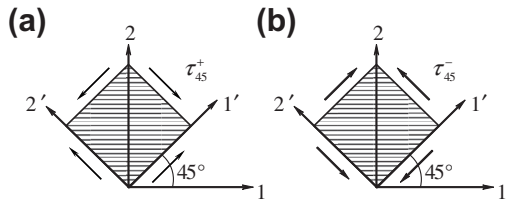


FIGURE 6.17

Two cases of pure shear in coordinates (1′, 2′) rotated by 45°with respect to the principal material coordinates (1, 2): (a) τ_{45}^{+}; (b) τ_{45}^{-}.

a unidirectional composite, stress τ_{45}^{+} induces tension in the fibers, whereas τ_{45}^{-} causes compression of the fibers, and the corresponding ultimate values can be different. Using the results presented in Section 2.4, we can conclude that for the loading case shown in Fig. 6.17a, $\sigma_1 = \tau_{45}^{+}$, $\sigma_2 = -\tau_{45}^{+}$, and $\tau_{12} = 0$, whereas for the case in Fig. 6.17b, $\sigma_1 = -\tau_{45}^{-}$, $\sigma_2 = \tau_{45}^{-}$, and $\tau_{12} = 0$. Applying the strength criterion in Eq. (6.30) for these loading cases, we arrive at

$$F(\sigma_1 = \overline{\tau}_{45}^{+},\ \sigma_2 = -\overline{\tau}_{45}^{+},\ \tau_{12} = 0)$$

$$= \overline{\tau}_{45}^{+}\left(\frac{1}{\overline{\sigma}_1^{+}} - \frac{1}{\overline{\sigma}_1^{-}} - \frac{1}{\overline{\sigma}_2^{+}} + \frac{1}{\overline{\sigma}_2^{-}}\right) + \left(\overline{\tau}_{45}^{+}\right)^2\left(\frac{1}{\overline{\sigma}_1^{+}\overline{\sigma}_1^{-}} + \frac{1}{\overline{\sigma}_2^{+}\overline{\sigma}_2^{-}} - 2R_{12}^{0}\right) = 1$$

$$F(\sigma_1 = -\overline{\tau}_{45}^{-},\ \sigma_2 = \overline{\tau}_{45}^{-},\ \tau_{12} = 0)$$

$$= \overline{\tau}_{45}^{-}\left(\frac{1}{\overline{\sigma}_1^{-}} - \frac{1}{\overline{\sigma}_1^{+}} + \frac{1}{\overline{\sigma}_2^{+}} - \frac{1}{\overline{\sigma}_2^{-}}\right) + \left(\overline{\tau}_{45}^{-}\right)^2\left(\frac{1}{\overline{\sigma}_1^{+}\overline{\sigma}_1^{-}} + \frac{1}{\overline{\sigma}_2^{+}\overline{\sigma}_2^{-}} - 2R_{12}^{0}\right) = 1$$

In general, these two equations give different solutions for R_{12}^{0}. A unique solution exists if the following compatibility condition is valid

$$\frac{1}{\overline{\sigma}_1^{+}} - \frac{1}{\overline{\sigma}_1^{-}} - \frac{1}{\overline{\sigma}_2^{+}} + \frac{1}{\overline{\sigma}_2^{-}} = \frac{1}{\overline{\tau}_{45}^{+}} - \frac{1}{\overline{\tau}_{45}^{-}} \tag{6.31}$$

If the actual material strength characteristics do not satisfy this equation, the strength criteria in Eq. (6.30) cannot be applied to this material. If they do, the coefficient R_{12}^{0} can be found as

$$R_{12}^{0} = \frac{1}{2}\left(\frac{1}{\overline{\sigma}_1^{+}\overline{\sigma}_1^{-}} + \frac{1}{\overline{\sigma}_2^{+}\overline{\sigma}_2^{-}} - \frac{1}{\overline{\tau}_{45}^{+}\overline{\tau}_{45}^{-}}\right) \tag{6.32}$$

For further analysis, consider for the sake of brevity a particular orthotropic material shown in Fig. 6.16 for which, in accordance with Eqs. (6. 22), $\overline{\sigma}_1^{+} = \overline{\sigma}_1^{-} = \overline{\sigma}_2^{+} = \overline{\sigma}_2^{-} = \overline{\sigma}_0$, $\overline{\tau}_{45}^{+} = \overline{\tau}_{45}^{-} = \overline{\tau}_{45}$, and $\overline{\tau}_{12} = \overline{\tau}_0$. As can be seen, Eq. (6.31) is satisfied in this case, and the strength criterion, Eq. (6.30), referred to the principal material coordinates (1, 2) in Fig. 6.16 takes the form

$$\frac{1}{\overline{\sigma}_0^2}\left(\sigma_1^2 + \sigma_2^2\right) + 2R_{12}^{0}\sigma_1\sigma_2 + \left(\frac{\tau_{12}}{\overline{\tau}_0}\right)^2 = 1 \tag{6.33}$$

where, in accordance with Eq. (6.32),

$$R_{12}^0 = \frac{1}{\overline{\sigma}_0^2} - \frac{1}{2\overline{\tau}_{45}^2} \tag{6.34}$$

Substituting Eq. (6.34) into Eq. (6.33), we arrive at the final form of the criterion under consideration

$$F(\sigma_1,\ \sigma_2,\ \tau_{12}) = \frac{\left(\sigma_1^2 + \sigma_2^2\right)}{\overline{\sigma}_0^2} + \left(\frac{2}{\overline{\sigma}_0^2} - \frac{1}{\overline{\tau}_{45}^2}\right)\sigma_1\sigma_2 + \left(\frac{\tau_{12}}{\overline{\tau}_0}\right)^2 = 1 \tag{6.35}$$

Now, present Eq. (6.33) in the following matrix form

$$\{\sigma\}^T \left[R^0\right]\{\sigma\} = 1 \tag{6.36}$$

where

$$\{\sigma\} = \begin{Bmatrix} \sigma_1 \\ \sigma_2 \\ \tau_{12} \end{Bmatrix}, \qquad \left[R^0\right] = \begin{bmatrix} R_{11}^0 & R_{12}^0 & 0 \\ R_{12}^0 & R_{11}^0 & 0 \\ 0 & 0 & 4S_{12}^0 \end{bmatrix}$$

$$R_{11}^0 = \frac{1}{\overline{\sigma}_0^2}, \quad R_{12}^0 = \frac{1}{\overline{\sigma}_0^2} - \frac{1}{2\overline{\tau}_{45}^2}, \quad S_{12}^0 = \frac{1}{4\overline{\tau}_0^2} \tag{6.37}$$

Superscript "T" means transposition, i.e. converting the column vector $\{\sigma\}$ into the row vector $\{\sigma\}^T$.

Let us transform stresses referred to axes $(1, 2)$ into stresses corresponding to axes $(1',\ 2')$ shown in Fig. 6.16. Such a transformation can be performed with the aid of Eqs. (6.24). The matrix form of this transformation is

$$\{\sigma\} = [T]\left\{\sigma^{45}\right\} \tag{6.38}$$

where

$$[T] = \begin{bmatrix} \frac{1}{2} & \frac{1}{2} & -1 \\ \frac{1}{2} & \frac{1}{2} & 1 \\ \frac{1}{2} & -\frac{1}{2} & 0 \end{bmatrix}$$

Substitution of the stresses in Eq. (6.38) into Eq. (6.36) yields

$$\left\{\sigma^{45}\right\}^T [T]^T \left[R^0\right][T]\left\{\sigma^{45}\right\} = 1$$

This equation, being rewritten as

$$\left\{\sigma^{45}\right\}^T \left[R^{45}\right]\left\{\sigma^{45}\right\} = 1 \tag{6.39}$$

specifies the strength criterion for the same material but referred to coordinates $(1', 2')$. The strength matrix has the following form

$$\left[R^{45}\right] = [T]^T \left[R^0\right][T] = \begin{bmatrix} R_{11}^{45} & R_{12}^{45} & 0 \\ R_{12}^{45} & R_{11}^{45} & 0 \\ 0 & 0 & 4S_{12}^{45} \end{bmatrix}$$

where

$$\begin{aligned} R_{11}^{45} &= \frac{1}{\overline{\sigma}_0^2} + \frac{1}{4}\left(\frac{1}{\overline{\tau}_0^2} - \frac{1}{\overline{\tau}_{45}^2}\right) \\ R_{12}^{45} &= \frac{1}{\overline{\sigma}_0^2} - \frac{1}{4}\left(\frac{1}{\overline{\tau}_0^2} + \frac{1}{\overline{\tau}_{45}^2}\right) \\ S_{12}^{45} &= \frac{1}{4\overline{\tau}_{45}^2} \end{aligned} \tag{6.40}$$

The explicit form of Eq. (6.39) is

$$\left[\frac{1}{\overline{\sigma}_0^2} + \frac{1}{4}\left(\frac{1}{\overline{\tau}_0^2} - \frac{1}{\overline{\tau}_{45}^2}\right)\right]\left[\left(\sigma_1^{45}\right)^2 + \left(\sigma_2^{45}\right)^2\right] + 2\left[\frac{1}{\overline{\sigma}_0^2} - \frac{1}{4}\left(\frac{1}{\overline{\tau}_0^2} + \frac{1}{\overline{\tau}_{45}^2}\right)\right]\sigma_1^{45}\sigma_2^{45} + \left(\frac{\tau_{12}^{45}}{\overline{\tau}_{45}}\right)^2 = 1 \tag{6.41}$$

Now apply the strength conditions in Eqs. (6.26) to give

$$\frac{1}{\overline{\sigma}_{45}^2} = \frac{1}{\overline{\sigma}_0^2} + \frac{1}{4}\left(\frac{1}{\overline{\tau}_0^2} - \frac{1}{\overline{\tau}_{45}^2}\right) \tag{6.42}$$

Then, the strength criterion in Eq. (6.41) can be presented as

$$F\left(\sigma_1^{45}, \sigma_2^{45}, \tau_{12}^{45}\right) = \frac{1}{\overline{\sigma}_{45}^2}\left[\left(\sigma_1^{45}\right)^2 + \left(\sigma_2^{45}\right)^2\right] + \left(\frac{2}{\overline{\sigma}_{45}^2} - \frac{1}{\overline{\tau}_0^2}\right)\sigma_1^{45}\sigma_2^{45} + \left(\frac{\tau_{12}^{45}}{\overline{\tau}_{45}}\right)^2 = 1 \tag{6.43}$$

Thus, we have two formulations of the strength criterion under consideration which are specified by Eq. (6.35) for coordinates (1, 2) and by Eq. (6.43) for coordinates $(1', 2')$ (see Fig. 6.16). As can be seen, Eqs. (6.35) and (6.43) have similar forms and follow from each other if we change the stresses in accordance with the following rule:

$$\sigma_1 \leftrightarrow \sigma_1^{45}, \quad \sigma_2 \leftrightarrow \sigma_2^{45}, \quad \tau_{12} \leftrightarrow \tau_{12}^{45}, \quad \overline{\sigma}_0 \leftrightarrow \overline{\sigma}_{45}, \quad \overline{\tau}_0 \leftrightarrow \overline{\tau}_{45}$$

However, such correlation is possible under the condition imposed by Eq. (6.42), which can be written in the form

$$I_s = \frac{1}{\overline{\sigma}_0^2} + \frac{1}{4\overline{\tau}_0^2} = \frac{1}{\overline{\sigma}_{45}^2} + \frac{1}{4\overline{\tau}_{45}^2} \tag{6.44}$$

This result means that I_s is the invariant of the strength tensor, i.e., that its value does not depend on the coordinate frame for which the strength characteristics entering Eq. (6.44) have been found.

If the actual material characteristics do not satisfy Eq. (6.44), the tensor strength criterion cannot be applied to this material. However, if this equation is consistent with experimental data, the tensor criterion offers considerable possibilities to study material strength. Indeed, restricting ourselves to two terms presented in Eq. (6.28), let us write this equation in coordinates $(1', 2')$ shown in Fig. 6.16 and assume that $\phi \neq 45^\circ$. Then

$$\sum_{i,k} S^{\phi}_{ik}\sigma^{\phi}_{ik} + \sum_{i,k,m,n} S^{\phi}_{ikmn}\sigma^{\phi}_{ik}\sigma^{\phi}_{mn} = 1 \tag{6.45}$$

Here, S^{ϕ}_{ik} and S^{ϕ}_{ikmn} are the components of the second and the fourth rank strength tensors which are transformed in accordance with tensor calculus as

$$\begin{aligned} S^{\phi}_{ik} &= \sum_{p,q} l_{ip}l_{kq}S^{0}_{pq} \\ S^{\phi}_{ikmn} &= \sum_{p,q,r,s} l_{ip}l_{kq}l_{mr}l_{ns}S^{0}_{pqrs} \end{aligned} \tag{6.46}$$

Here, l are directional cosines of axes $1'$ and $2'$ on the plane referred to coordinates 1 and 2 (see Fig. 6.16), i.e., $l_{11} = \cos\phi$, $l_{12} = \sin\phi$, $l_{21} = -\sin\phi$, $l_{22} = \cos\phi$. Substitution of Eqs. (6.46) into Eq. (6.45) yields the strength criterion in coordinates $(1', 2')$ but written in terms of strength components corresponding to coordinates (1, 2), i.e.,

$$\sum_{i,k}\sum_{p,q} l_{ip}l_{kq}S^{0}_{pq}\sigma^{\phi}_{ik} + \sum_{i,k,m,n}\sum_{p,q,r,s} l_{ip}l_{kq}l_{mr}l_{ns}S^{0}_{pqrs}\sigma^{\phi}_{ik}\sigma^{\phi}_{mn} = 1 \tag{6.47}$$

Apply Eq. (6.47) to the special orthotropic material studied earlier (see Fig. 6.16) and for which, in accordance with Eq. (6.22),

$$\begin{aligned} &S_{pq} = 0,\ S_{1111} = S_{2222} = R^{0}_{11} = R^{0}_{22} = \frac{1}{\overline{\sigma}^2_0} \\ &S_{1122} = S_{2211} = R^{0}_{12} = \frac{1}{\overline{\sigma}^2_0} - \frac{1}{2\overline{\tau}^2_{45}} \\ &S_{1212} = S_{2121} = S_{1221} = S_{2112} = S^{0}_{12} = \frac{1}{4\overline{\tau}^2_0} \end{aligned} \tag{6.48}$$

Following Gol'denblat and Kopnov (1968), consider the material strength under tension in the $1'$ direction and in shear in plane $(1', 2')$. Taking first $\sigma^{\phi}_{11} = \overline{\sigma}_{\phi}$, $\sigma^{\phi}_{22} = 0$, $\tau^{\phi}_{12} = 0$ and then $\tau^{\phi}_{12} = \overline{\tau}_{\phi}$, $\sigma^{\phi}_{11} = 0$, $\sigma^{\phi}_{22} = 0$, we get from Eq. (6.47)

$$\overline{\sigma}^2_{\phi} = \frac{1}{\sum\limits_{p,q,r,s} l_{1p}l_{1q}l_{1r}l_{1s}S^{0}_{pqrs}}, \quad \overline{\tau}^2_{\phi} = \frac{1}{\sum\limits_{p,q,r,s} l_{1p}l_{2q}l_{1r}l_{2s}S^{0}_{pqrs}}$$

or in explicit form,

$$\begin{aligned}\overline{\sigma}_{\phi}^{2} &= \left[R_{11}^{0}\left(\cos^{4}\phi+\sin^{4}\phi\right)+2\left(S_{12}^{0}+2R_{12}^{0}\right)\sin^{2}\phi\,\cos^{2}\phi\right]^{-1}\\ \overline{\tau}_{\phi}^{2} &= 4\left[2\left(R_{11}^{0}-R_{12}^{0}\right)\sin^{2}\phi\,\cos^{2}\phi+S_{12}^{0}\cos^{2}2\phi\right]^{-1}\end{aligned} \tag{6.49}$$

These equations allow us to calculate the material strength in any coordinate frame whose axes make angle ϕ with the corresponding principal material axes. Taking into account Eqs. (6.44) and (6.48), we can derive the following relationship from Eqs. (6.49)

$$\frac{1}{\overline{\sigma}_{\phi}^{2}}+\frac{1}{4\overline{\tau}_{\phi}^{2}}=\frac{1}{\overline{\sigma}_{0}^{2}}+\frac{1}{4\overline{\tau}_{0}^{2}}=I_{s} \tag{6.50}$$

So, I_s is indeed the invariant of the strength tensor whose value for a given material does not depend on ϕ.

Thus, tensor-polynomial strength criteria provide universal equations that can be readily written in any coordinate frame, but on the other hand, the material mechanical characteristics, particularly material strength in different directions, should follow the rules of tensor transformation, i.e., composed invariants (such as I_s) must be the same for all coordinate frames.

6.1.4 Interlaminar strength

The failure of composite laminates can also be associated with interlaminar fracture caused by transverse normal and shear stresses σ_3 and $\tau_{13},\ \tau_{23}$ or σ_z and $\tau_{xz},\ \tau_{yz}$ (see Fig. 4.18). Since $\sigma_3=\sigma_z$ and shear stresses in coordinates (1, 2, 3) are linked with stresses in coordinates (x, y, z) by simple relationships in Eqs. (4.67) and (4.68), the strength criterion is formulated here in terms of stresses $\sigma_z, \tau_{xz}, \tau_{yz}$ which can be found directly from Eqs. (5.132). Since the laminate strength in tension and compression across the layers is different, we can use the polynomial criterion similar to Eq. (6.15). For the stress state under study, we get

$$\sigma_z\left(\frac{1}{\overline{\sigma}_{3}^{+}}-\frac{1}{\overline{\sigma}_{3}^{-}}\right)+\left(\frac{\tau_r}{\overline{\tau}_i}\right)^{2}=1 \tag{6.51}$$

where

$$\tau_r=\sqrt{\tau_{13}^{2}+\tau_{23}^{2}}=\sqrt{\tau_{xz}^{2}+\tau_{yz}^{2}}$$

is the resultant transverse shear stress, and $\overline{\tau}_i$ determines the interlaminar shear strength of the material.

In thin-walled structures, the transverse normal stress is usually small and can be neglected in comparison with the shear stress. Then, Eq. (6.51) can be simplified and written as

$$\tau_r=\overline{\tau}_i \tag{6.52}$$

As an example, Fig. 6.18 displays the dependence of the normalized maximum deflection w/R on the force P for a fiberglass-epoxy cross-ply cylindrical shell of radius R loaded with a radial concentrated force P (Vasiliev, 1970). Failure of the shell was caused by delamination. The shaded interval shows the possible values of the ultimate force calculated with the aid of Eq. (6.52) (this value is not unique because of the scatter in interlaminar shear strength).

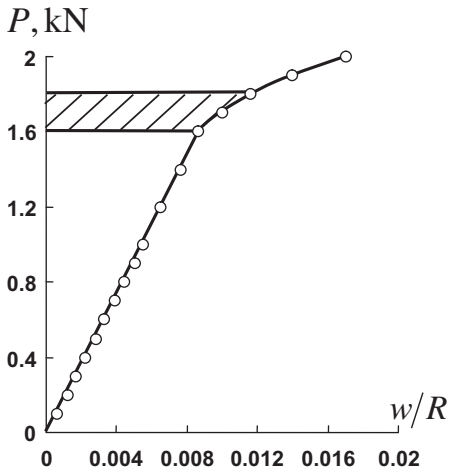


FIGURE 6.18

Experimental dependence of the normalized maximum deflection of a fiberglass-epoxy cylindrical shell on the radial concentrated force.

6.2 PRACTICAL RECOMMENDATIONS

It follows from the foregoing analysis that for the practical strength evaluation of fabric composites, we can use either the maximum stress criterion, Eqs. (6.2), or second-order polynomial criterion in Eq. (6.15) in conjunction with Eq. (6.16) for the case of biaxial compression. For unidirectional composites with polymeric matrices, we can apply Eqs. (6.3) and (6.4) in which the function F is specified by Eq. (6.18). It should be emphasized that the experimental data usually have rather high scatter, and the accuracy of more complicated and rigorous strength criteria can be more apparent than real.

Comparing the tensor-polynomial and approximation strength criteria, we can conclude the following. The tensor criteria should be used if our purpose is to develop a theory of material strength, because a consistent physical theory must be covariant, i.e., the constraints that are imposed on material properties within the framework of this theory should not depend on a particular coordinate frame. For practical applications, the approximation criteria are more suitable, however in the forms they are presented here they should be used only for orthotropic unidirectional plies or fabric layers in coordinates whose axes coincide with the fibers' directions.

To evaluate the laminate strength, we should first determine the stresses acting in the plies or layers (see Section 5.11), identify the layer that is expected to fail first, and apply one of the foregoing strength criteria. The fracture of the first ply or layer may not necessarily result in failure of the whole laminate. Then, simulating the failed element with a suitable model (see, e.g., Section 4.4.2), the strength analysis is repeated and continued up to failure of the last ply or layer.

In principle, failure criteria can be constructed for the whole laminate as a quasi-homogeneous material. This is not realistic for design problems, since it would be necessary to compare the solutions for numerous laminate structures which cannot practically be tested. However, this approach can be used successfully for structures that are well developed and in mass production. For example, the



FIGURE 6.19

Segments of composite drive shafts with test fixtures.

Courtesy of CRISM.

segments of two structures of composite drive shafts, one made of fabric and the other of unidirectional composite, are shown in Fig. 6.19. Testing these segments in tension, compression, and torsion, we can plot the strength envelope on the plane (M, T), where M is the bending moment and T is the torque, and thus evaluate the shaft strength for different combinations of M and T with high accuracy and reliability.

6.3 EXAMPLES

For the first example, consider a problem of torsion of a thin-walled cylindrical drive shaft (see Fig. 6.20) made by winding a glass-epoxy fabric tape at angles $\pm 45^\circ$. The material properties are $E_1 = 23.5$ GPa, $E_2 = 18.5$ GPa, $G_{12} = 7.2$ GPa, $\nu_{12} = 0.16$, $\nu_{21} = 0.2$, $\overline{\sigma}_1^+ = 510$ MPa,

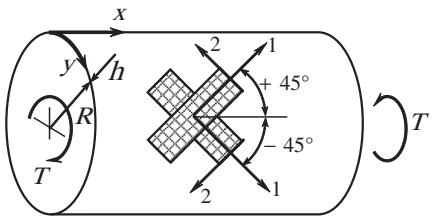


FIGURE 6.20

Torsion of a drive shaft.

$\overline{\sigma}_1^- = 460$ MPa, $\overline{\sigma}_2^+ = 280$ MPa, $\overline{\sigma}_2^- = 260$ MPa, and $\overline{\tau}_{12} = 85$ MPa. The shear strain induced by torque T is

$$\gamma_{xy} = \frac{T}{2\pi R^2 B_{44}}$$

(Vasiliev, 1993). Here, T is the torque, $R = 0.05$ m is the shaft radius, and B_{44} is the shear stiffness of the wall. According to Eqs. (5.39), $B_{44} = A_{44}h$, where $h = 5$ mm is the wall thickness, and A_{44} is specified by Eqs. (4.72) and can be written as

$$A_{44} = \frac{1}{4(1 - \nu_{12}\nu_{21})}(E_1 + E_2 - 2E_1\nu_{12})$$

($\phi = 45°$). Using Eqs. (5.130), we can determine the strains in the principal material coordinates 1 and 2 of $\pm 45°$ layers (see Fig. 6.20)

$$\varepsilon_1^{\pm} = \pm\frac{1}{2}\gamma_{xy}, \quad \varepsilon_2^{\pm} = \mp\frac{1}{2}\gamma_{xy}, \quad \gamma_{12}^{\pm} = 0$$

Applying Eqs. (5.131) and the foregoing results, we can express stresses in terms of T as

$$\sigma_1^{\pm} = \pm\frac{TE_1(1 - \nu_{12})}{\pi R^2 h(E_1 + E_2 - 2E_1\nu_{12})}$$

$$\sigma_2^{\pm} = \mp\frac{TE_2(1 - \nu_{21})}{\pi R^2 h(E_1 + E_2 - 2E_1\nu_{12})}$$

$$\tau_{12}^{\pm} = 0$$

The task is to determine the ultimate torque, $\overline{T}_u$.

First, use the maximum stress criterion, Eqs. (6.2), which gives the following four values of the ultimate torque corresponding to tensile or compressive failure of $\pm 45^{\circ}$ layers

$$\sigma_1^+ = \overline{\sigma}_1^+, \quad T_u = 34 \text{ kNm}$$
$$\sigma_1^- = \overline{\sigma}_1^-, \quad T_u = 30.7 \text{ kNm}$$
$$\sigma_2^+ = \overline{\sigma}_2^+, \quad T_u = 25.5 \text{ kNm}$$
$$\sigma_2^- = \overline{\sigma}_2^-, \quad T_u = 23.7 \text{ kNm}$$

The actual ultimate torque is the lowest of these values, i.e., $\overline{T}_u = 23.7$ kNm.

Now apply the polynomial criterion in Eq. (6.15), which has the form

$$\sigma_1^{\pm}\left(\frac{1}{\overline{\sigma}_1^{+}}-\frac{1}{\overline{\sigma}_1^{-}}\right)+\sigma_2^{\pm}\left(\frac{1}{\overline{\sigma}_2^{+}}-\frac{1}{\overline{\sigma}_2^{-}}\right)+\frac{\left(\sigma_1^{\pm}\right)^2}{\overline{\sigma}_1^{+}\overline{\sigma}_1^{-}}+\frac{\left(\sigma_2^{\pm}\right)^2}{\overline{\sigma}_2^{+}\overline{\sigma}_2^{-}}=1$$

For $+45$ and -45° layers, we get, respectively, $T_u = 21.7$ kNm and $T_u = 17.6$ kNm. Thus, $T_u = 17.6$ kNm.

As a second example, consider a two-layered cylindrical shell which consists of a $\pm 36^\circ$ angle-ply layer with total thickness $h_1 = 0.62$ mm and a 90° unidirectional layer with thickness $h_2 = 0.60$ mm. A 200 mm diameter cylinder is made by filament winding from glass-epoxy composite with the following mechanical properties: $E_1 = 44$ GPa, $E_2 = 9.4$ GPa, $G_{12} = 4$ GPa, and $\nu_{21} = 0.26$, and loaded with internal pressure p. Axial, N_x, and circumferential, N_y, stress resultants can be found as

$$N_x = \frac{1}{2}pR, \quad N_y = pR$$

where $R = 100$ mm is the shell radius. Applying the constitutive equations, Eqs. (5.44), and neglecting the change in the cylinder curvature ($\kappa_x = \kappa_y = 0$), we arrive at the following equations for strains

$$B_{11}\varepsilon_x^0 + B_{12}\varepsilon_y^0 = \frac{1}{2}pR, \quad B_{12}\varepsilon_x^0 + B_{22}\varepsilon_y^0 = pR \tag{6.53}$$

Using Eqs. (5.130) and (5.131) to determine strains and stresses in the principal material coordinates of the plies, we have

$$\begin{aligned}
\sigma_1^{(i)} &= \frac{pR}{2B}\overline{E}_1[(B_{22}-2B_{12})(\cos^2\phi_i + \nu_{12}\sin^2\phi_i) + (2B_{11}-B_{12})(\sin^2\phi_i + \nu_{12}\cos^2\phi_i)] \\
\sigma_2^{(i)} &= \frac{pR}{2B}\overline{E}_2[(B_{22}-2B_{12})(\sin^2\phi_i + \nu_{21}\cos^2\phi_i) + (2B_{11}-B_{12})(\cos^2\phi_i + \nu_{21}\sin^2\phi_i)] \\
\tau_{12}^{(i)} &= \frac{pR}{2B}G_{12}(2B_{11}+B_{12}-B_{22})\sin^2\phi_i
\end{aligned} \tag{6.54}$$

Here, $B = B_{11}B_{22} - B_{12}^2$, and the membrane stiffnesses B_{mn} for the shell under study are: $B_{11} = I_{11}^{(0)} = 21.2$ GPa mm, $B_{12} = I_{12}^{(0)} = 7.7$ GPa mm, and $B_{22} = I_{22}^{(0)} = 35.6$ GPa mm. Subscript "i" in Eqs. (6.54) denotes the helical plies for which $i = 1, \phi_1 = \phi = 36^\circ$ and circumferential plies for which $i = 2$ and $\phi_2 = 90^\circ$.

The task that we consider is to find the ultimate pressure $\overline{p}_u$. For this purpose, we use the strength criteria in Eqs. (6.3), (6.4), and (6.17), and the following material properties: $\overline{\sigma}_1^{+} = 1300$ MPa, $\overline{\sigma}_2^{+} = 27$ MPa, and $\overline{\tau}_{12} = 45$ MPa.

Calculation with the aid of Eqs. (6.54) yields

$$\begin{aligned}
\sigma_1^{(1)} &= 83.9p, \quad \sigma_2^{(1)} = 24.2p, \quad \tau_{12}^{(1)} = 1.9p \\
\sigma_1^{(2)} &= 112p, \quad \sigma_2^{(2)} = 19.5p, \quad \tau_{12}^{(2)} = 0
\end{aligned}$$

Applying Eqs. (6.3) to evaluate the plies' strength along the fibers, we get

$$\sigma_1^{(1)} = \overline{\sigma}_1^+, \quad p_u = 14.9 \text{ MPa}$$
$$\sigma_1^{(2)} = \overline{\sigma}_1^+, \quad p_u = 11.2 \text{ MPa}$$

The failure of the matrix can be identified using Eq. (6.17), i.e.,

$$\left(\frac{\sigma_2^{(1)}}{\overline{\sigma}_2^+}\right)^2 + \left(\frac{\tau_{12}^{(1)}}{\overline{\tau}_{12}}\right)^2 = 1, \quad p_u = 1.1 \text{ MPa}$$
$$\left(\frac{\sigma_2^{(2)}}{\overline{\sigma}_2^+}\right)^2 + \left(\frac{\tau_{12}^{(2)}}{\overline{\tau}_{12}}\right)^2 = 1, \quad p_u = 1.4 \text{ MPa}$$

Thus, we can conclude that failure occurs initially in the matrix of helical plies and takes place at an applied pressure $p_u^{(1)} = 1.1$ MPa. This pressure destroys only the matrix of the helical plies, whereas the fibers are not damaged and continue to work. According to the model of a unidirectional layer with failed matrix discussed in Section 4.4.2, we should take $E_2 = 0, G_{12} = 0$, and $\nu_{12} = 0$ in the helical layer. Then, the stiffness coefficients, Eqs. (4.72) for this layer, become

$$A_{11}^{(1)} = E_1 \cos^4\phi, \quad A_{12}^{(1)} = E_1 \sin^2\phi \cos^2\phi, \quad A_{22}^{(1)} = E_1 \sin^4\phi \tag{6.55}$$

Calculating again the membrane stiffnesses B_{mn} (see Eq. (5.28)) and using Eqs. (6.53), we get for $p \geq p_u^{(1)}$

$$\sigma_1^{(1)} = 92.1p, \quad \sigma_2^{(1)} = 24.2p_u^{(1)} = 26.6 \text{ MPa}, \quad \tau_{12}^{(1)} = 1.9p_u^{(1)} = 2.1 \text{ MPa},$$
$$\sigma_1^{(2)} = 134.6p, \quad \sigma_2^{(2)} = 22.6p, \quad \tau_{12}^{(2)} = 0$$

For a pressure $p \geq p_u^{(1)}$, three modes of failure are possible. The pressure causing failure of the helical plies under longitudinal stress $\sigma_1^{(1)}$ can be calculated from the following equation

$$\sigma_1^{(1)} = 83.9p_u^{(1)} + 92.1\left(p_u - p_u^{(1)}\right) = \overline{\sigma}_1^+$$

which yields $p_u = 14.2$ MPa. The analogous value for the circumferential ply is determined by the following condition

$$\sigma_1^{(2)} = 112p_u^{(1)} + 134.6\left(p_u - p_u^{(1)}\right) = \overline{\sigma}_1^+$$

which gives $p_u = 9.84$ MPa. Finally, the matrix of the circumferential layer can fail under tension across the fibers. Since $\tau_{12}^{(2)} = 0$, we put

$$\sigma_2^{(2)} = 19.5p_u^{(1)} + 22.6\left(p_u - p_u^{(1)}\right) = \overline{\sigma}_2^+$$

and find $p_u = 1.4$ MPa.

Thus, the second failure stage takes place at $p_u^{(2)} = 1.4$ MPa and is associated with cracks in the matrix of the circumferential layer (see Fig. 4.36).

For $p \geq p_u^{(2)}$, we should put $E_2 = 0, G_{12} = 0$, and $\nu_{12} = 0$ in the circumferential layer whose stiffness coefficients become

$$A_{11}^{(2)} = 0, \quad A_{12}^{(2)} = 0, \quad A_{22}^{(2)} = E_1 \tag{6.56}$$

The membrane stiffnesses of the structure now correspond to the monotropic model of a composite unidirectional ply (see Section 3.3) and can be calculated as

$$B_{mn} = A_{mn}^{(1)} h_1 + A_{mn}^{(2)} h_2$$

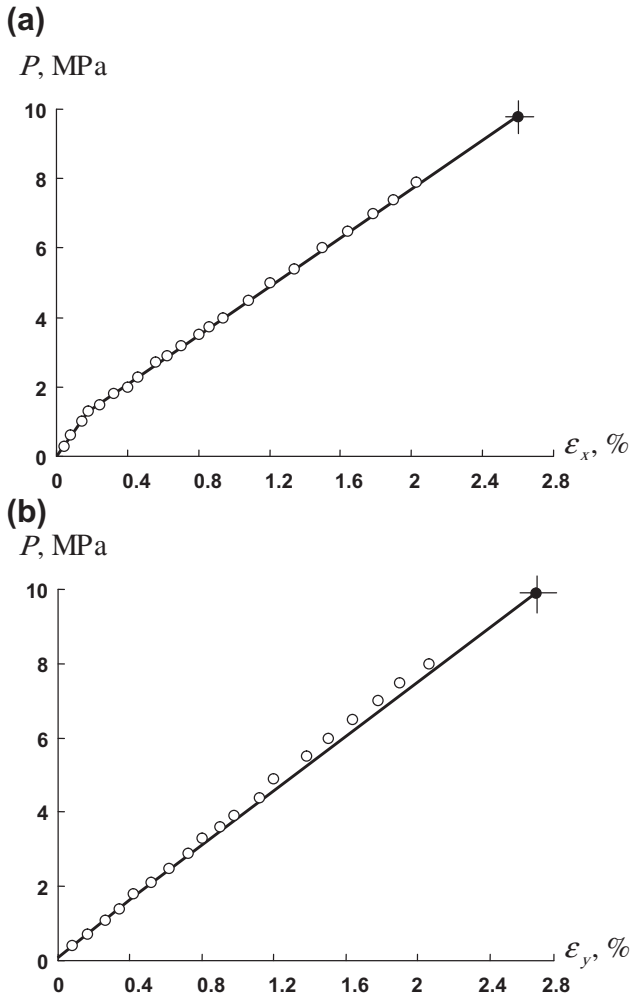


FIGURE 6.21

Dependence of the axial (a) and the circumferential (b) strains on internal pressure.
(——) analysis;
(○) experimental data.

Table 6.1 Burst Pressure for the Filament-Wound Fiberglass Pressure Vessels.

Diameter of the Vessel (mm)	Layer Thickness (mm)		Calculated Burst Pressure (MPa)	Number of Tested Vessels	Experimental Burst Pressure	
	h_1	h_2			Mean Value (MPa)	Variation Coefficient (%)
200	0.62	0.60	10	5	9.9	6.8
200	0.92	0.93	15	5	13.9	3.3

where A_{mn} are specified by Eqs. (6.55) and (6.56), and $h_1 = 0.62$ mm and $h_2 = 0.6$ mm are the thicknesses of the helical and the circumferential layers. Again using Eqs. (6.54), we have for $p \geq p_u^{(2)}$

$$\sigma_1^{(1)} = 137.7p, \quad \sigma_1^{(2)} = 122.7p$$

The cylinder's failure can now be caused by fracture of either helical fibers or circumferential fibers. The corresponding values of the ultimate pressure can be found from the following equations

$$\sigma_1^{(1)} = 83.9p_u^{(1)} + 92.1\left(p_u^{(2)} - p_u^{(1)}\right) + 137.7\left(p_u - p_u^{(2)}\right) = \overline{\sigma}_1^{+}$$

$$\sigma_1^{(2)} = 112p_u^{(1)} + 134.6\left(p_u^{(2)} - p_u^{(1)}\right) + 122.7\left(p_u - p_u^{(2)}\right) = \overline{\sigma}_1^{+}$$

in which $p_u^{(1)} = 1.1$ MPa and $p_u^{(2)} = 1.4$ MPa. The first of these equations yields $p_u = 10$ MPa, whereas the second gives $p_u = 10.7$ MPa.

Thus, failure of the structure under study occurs at $\overline{p}_u = 10$ MPa as a result of fiber fracture in the helical layer.

The dependencies of the strains, which can be calculated using Eqs. (6.53) and the appropriate values of B_{mn}, are shown in Fig. 6.21 (solid lines). As can be seen, the theoretical prediction is in fair agreement with the experimental results. The same conclusion can be drawn for the burst pressure which is listed in Table 6.1 for two types of filament-wound fiberglass pressure vessels. A typical example of the failure mode for the vessels presented in Table 6.1 is shown in Fig. 6.22.

6.4 ALLOWABLE STRESSES FOR LAMINATES CONSISTING OF UNIDIRECTIONAL PLIES

It follows from Section 6.3 (see also Section 4.4.2) that a unidirectional fibrous composite ply can experience two modes of failure associated with

- fiber failure, and
- cracks in the matrix.

The first mode can be identified using the strength criterion in Eqs. (6.3), i.e.,

$$\begin{aligned} &\sigma_1^{(i)} \leq \overline{\sigma}_1^{+} \quad \text{if} \quad \sigma_1^{(i)} > 0 \\ &\left|\sigma_1^{(i)}\right| \leq \overline{\sigma}_1^{-} \quad \text{if} \quad \sigma_1^{(i)} < 0 \end{aligned} \tag{6.57}$$

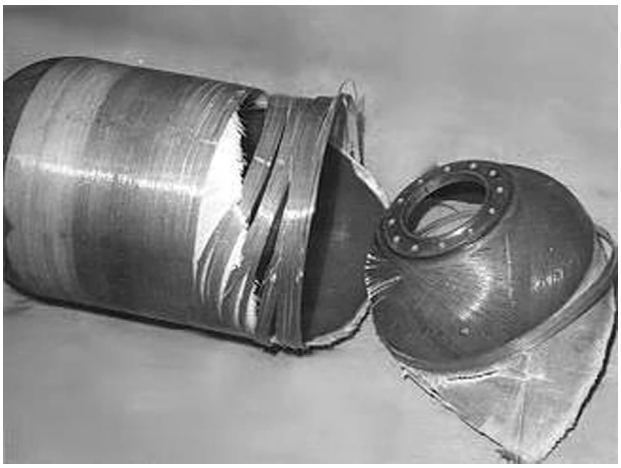


FIGURE 6.22

The failure mode of a composite pressure vessel.

in which $\overline{\sigma}_1^+$ and $\overline{\sigma}_1^-$ are the ultimate stresses of the ply under tension and compression along the fibers, and i is the ply number. For the second failure mode, we have the strength criterion in Eq. (6.18), i.e.,

$$\sigma_2^{(i)}\left(\frac{1}{\overline{\sigma}_2^+}-\frac{1}{\overline{\sigma}_2^-}\right)+\frac{\left(\sigma_2^{(i)}\right)^2}{\overline{\sigma}_2^+\overline{\sigma}_2^-}+\left(\frac{\tau_{12}^{(i)}}{\overline{\tau}_{12}}\right)^2=1 \tag{6.58}$$

in which $\overline{\sigma}_2^+$ and $\overline{\sigma}_2^-$ are the ultimate stresses of the ply under tension and compression across the fibers, and $\overline{\tau}_{12}$ is the ultimate in-plane shear stress.

Consider a laminate loaded with normal, σ_x and σ_y, and shear, τ_{xy}, stresses as in Fig. 6.23. Assume that the stresses are increased in proportion to some loading parameter p. Applying the strength criteria

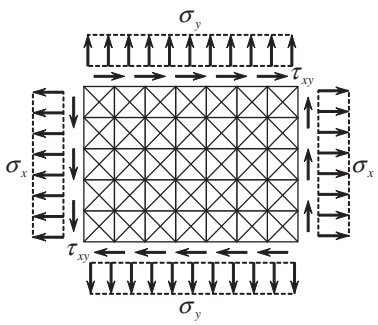


FIGURE 6.23

A laminate loaded with normal and shear stresses.

in Eqs. (6.57) and (6.58), we can find two values of this parameter, i.e., $p = p_f$ which corresponds to fiber failure in at least one of the plies and $p = p_m$ for which the loading causes a matrix failure in one or more plies. Since the parameters p_f and p_m usually do not coincide with each other for modern composites, a question concerning the allowable level of stresses acting in the laminate naturally arises. Obviously, the stresses under which the fibers fail must not be treated as allowable stresses. Moreover, the allowable value p_a of the loading parameter must be less than p_f by a specified safety factor s_f, i.e.,

$$p_a^f = p_f / s_f \tag{6.59}$$

However, for the matrix failure, the answer is not evident, and at least two different situations may take place.

First, failure of the matrix can result in failure of the laminate. As an example, we can take a $\pm\phi$ angle-ply layer discussed in Section 4.5 whose moduli in the x and y directions are specified by Eqs. (4.147), i.e.,

$$E_x = A_{11} - \frac{A_{12}^2}{A_{22}}, \qquad E_y = A_{22} - \frac{A_{12}^2}{A_{11}}$$

Ignoring the load-carrying capacity of the failed matrix, i.e., taking $E_2 = 0, G_{12} = 0$ and $\nu_{12} = \nu_{21} = 0$ in Eqs. (4.72) to get

$$A_{11} = E_1 \cos^4\phi, \qquad A_{12} = E_1 \sin^2\phi \ \cos^2\phi, \qquad A_{22} = E_1 \cos^4\phi$$

we arrive at $E_x = 0$ and $E_y = 0$, which means that the layer under consideration cannot work without the matrix. For such a mode of failure, we should take the allowable loading parameter as

$$p_a^m = p_m / s_m \tag{6.60}$$

where s_m is the corresponding safety factor.

Secondly, matrix fracture does not result in laminate failure. As an example of such a structure, we can take the pressure vessel considered in Section 6.3 (see Figs. 6.21 and 6.22). Now we have another question as to whether the cracks in the matrix are allowed even if they do not affect the structure's strength. The answer to this question depends on the operational requirements for the structure. For example, suppose that the pressure vessel in Fig. 6.22 is a model of a filament-wound solid propellant rocket motor case which works only once and for a short period of time. Then, it is appropriate to ignore the cracks appearing in the matrix and take the allowable stresses in accordance with Eq. (6.59). We can also suppose that the vessel may be a model of a pressurized passenger cabin in a commercial airplane for which no cracks in the material are allowed in flight. Then, in principle, we must take the allowable stresses in accordance with Eq. (6.60). However, it follows from the examples considered in Sections 4.4.2 and 6.3 that for modern composites the loading parameter p_m is reached at the initial stage of the loading process. As a result, the allowable loading parameter, p_a^m in Eq. (6.60), is so small that modern composite materials cannot demonstrate their high strength governed by the fibers and cannot compete with metal alloys. A more realistic approach allows the cracks in the matrix to occur only if p_m is higher than the operational loading parameter p_0. Using Eq. (6.60), we can assume that

$$p_0 = p_a^m = p_m / s_m$$

The ultimate loading parameter $\overline{p}$ is associated with fiber failure, so that $\overline{p} = p_f$. Thus, the actual safety factor for the structure becomes

$$s = \frac{\overline{p}}{p_0} = \frac{p_f}{p_m} s_m \tag{6.61}$$

and depends on the ratio p_f/p_m.

To be specific, consider a four-layered $[0°/45°/-45°/90°]$ quasi-isotropic carbon-epoxy laminate shown in Fig. 6.23 which is widely used in aircraft composite structures. The mechanical properties of quasi-isotropic laminates are discussed in Section 5.7. The constitutive equations for such laminates have the form typical for isotropic materials, i.e.,

$$\varepsilon_x = \frac{1}{E}(\sigma_x - \nu\sigma_y), \qquad \varepsilon_y = \frac{1}{E}(\sigma_y - \nu\sigma_x), \qquad \gamma_{xy} = \frac{\tau_{xy}}{G} \tag{6.62}$$

where E, ν, and G are given by Eqs. (5.110). For a typical carbon-epoxy fibrous composite, Table 5.4 yields $E = 54.8$ GPa, $\nu = 0.31$, and $G = 20.9$ GPa. The strains in the plies' principal coordinates (see Fig. 4.18) can be found using Eqs. (4.69) from which we have for the 0° layer,

$$\varepsilon_1 = \varepsilon_x, \quad \varepsilon_2 = \varepsilon_y, \quad \gamma_{12} = \gamma_{xy}$$

for the ±45°layer,

$$\varepsilon_1 = \frac{1}{2}(\varepsilon_x + \varepsilon_y \pm \gamma_{xy}), \quad \varepsilon_2 = \frac{1}{2}(\varepsilon_x + \varepsilon_y \mp \gamma_{xy}), \quad \gamma_{12} = \pm(\varepsilon_y - \varepsilon_x)$$

for the 90°layer,

$$\varepsilon_1 = \varepsilon_y, \quad \varepsilon_2 = \varepsilon_x, \quad \gamma_{12} = \gamma_{xy}$$

The stresses in the plies are

$$\sigma_1 = \overline{E}_1(\varepsilon_1 + \nu_{12}\varepsilon_2), \quad \sigma_2 = \overline{E}_2(\varepsilon_2 + \nu_{21}\varepsilon_1), \quad \tau_{12} = G_{12}\gamma_{12} \tag{6.63}$$

where $\overline{E}_{1,2} = E_{1,2}/(1 - \nu_{12}\nu_{21})$, $\nu_{12}E_1 = \nu_{21}E_2$, and the elastic constants E_1, E_2, ν_{21}, and G_{12} are given in Table 3.5. For given combinations of the acting stresses σ_x, σ_y, and τ_{xy} (see Fig. 6.23), the strains ε_x, ε_y, and γ_{xy} found with the aid of Eqs. (6.62) are transformed to the ply strains ε_1, ε_2 and γ_{12}, and then substituted into Eqs. (6.63) for the stresses σ_1, σ_2, and τ_{12}. These stresses are substituted into the strength criteria in Eqs. (6.57) and (6.58), the first of which gives the combination of stresses σ_x, σ_y, and τ_{xy} causing failure of the fibers, whereas the second one enables us to determine the stresses inducing matrix failure.

Consider biaxial loading with stresses σ_x and σ_y as shown in Fig. 6.23. The corresponding failure envelopes are presented in Fig. 6.24. The solid lines determine the domain within which the fibers do not fail, whereas within the area bound by the dashed lines no cracks in the matrix appear. Consider, for example, the cylindrical pressure vessel discussed in Section 6.3, for which

$$\sigma_x = \frac{pR}{2h}, \qquad \sigma_y = \frac{pR}{h} \tag{6.64}$$

are the axial and circumferential stresses expressed in terms of the vessel radius and thickness, R and h, and the applied internal pressure, p. Let us take $R/h = 100$. Then, $\sigma_x = 50p$ and $\sigma_y = 100p$, whereby $\sigma_y/\sigma_x = 2$. This combination of stresses is shown with the line 0BA in

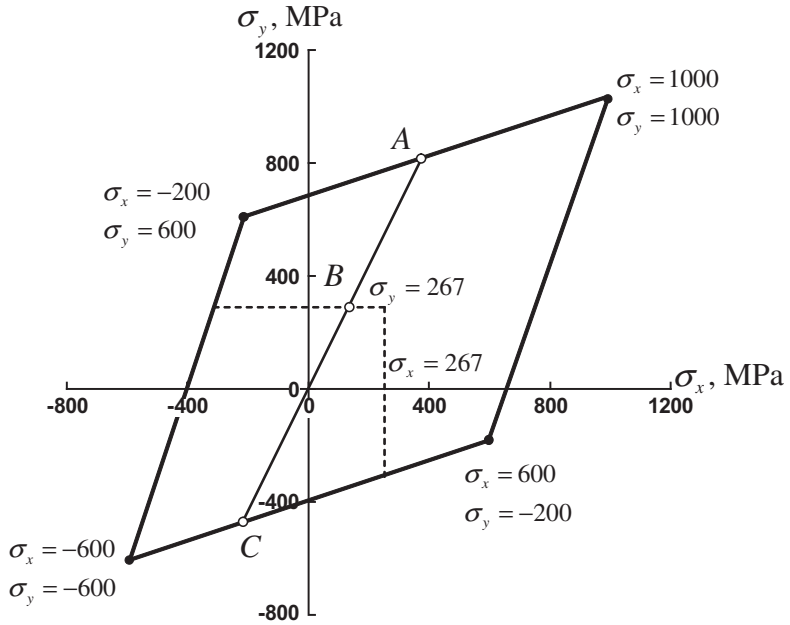


FIGURE 6.24

Failure envelops for biaxial loading corresponding to the failure criteria in Eqs. (6.57) (——————), and Eq. (6.58) (- - - - - - -).

Fig. 6.24. Point A corresponds to failure of the fibers in the circumferential (90°) layer and gives the ultimate loading parameter (which is the pressure in this case) $\overline{p} = p_f = 8$ MPa. Point B corresponds to matrix failure in the axial (0°) layer and to the loading parameter $p_m = 2.67$ MPa. Taking $s_m = 1.5$, which is a typical value for the safety factor preventing material damage under the operational pressure, we get $s = 4.5$ from Eq. (6.61). If such a high safety factor is not appropriate, then we should either allow the cracks in the matrix to appear under the operational pressure, or change the carbon-epoxy composite to some other material. It should be noted that the significant difference between the loading parameters p_f and p_m is typical mainly for tension. For compressive loads, the fibers usually fail before the matrix (see point C in Fig. 6.24).

Similar results for uniaxial tension with stresses σ_x combined with shear stresses τ_{xy} (see Fig. 6.23) are presented in Fig. 6.25. As can be seen, shear can induce the same effect as tension.

The problem of matrix failure discussed earlier significantly reduces the application of modern fibrous composites to structures subjected to long-term cyclic loading. It should be noted that Figs. 6.24 and 6.25 correspond to static loading at room temperature. Temperature, moisture, and fatigue can considerably reduce the areas bounded by the dashed lines in Figs. 6.24 and 6.25 (see Sections 7.1.2 and 7.3.3). Some methods developed to solve the problem of matrix failure are discussed in Sections 4.4.3 and 4.4.4.

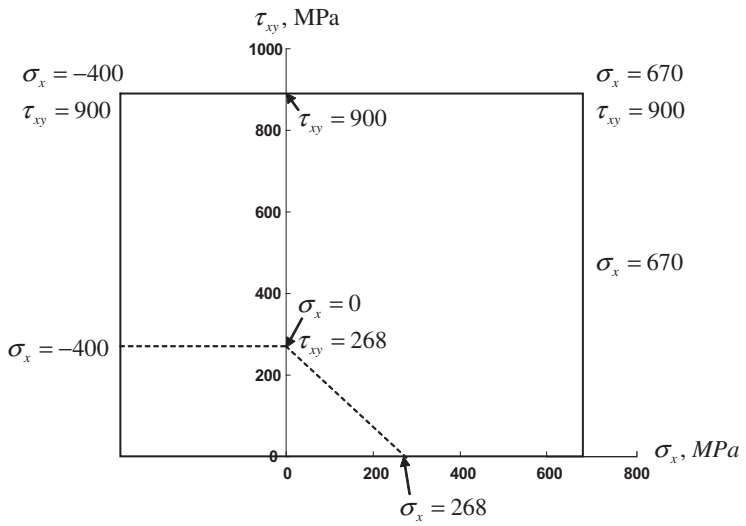


FIGURE 6.25

Failure envelops for uniaxial tension and compression combined with shear corresponding to the failure criteria in Eqs. (6.57) (——), and Eq. (6.58) (-------).

6.5 PROGRESSIVE FAILURE: MODELING AND ANALYSIS

The development of a representative constitutive model for fiber reinforced composite materials and structures should involve the consideration of their mechanical responses prior to the initiation of damage, the prediction of damage initiation, and the modeling of postfailure behavior. *Continuum Damage Mechanics* (CDM) provides a tractable framework for modeling damage initiation and development, as well as stiffness degradation. It is applied at the ply level and reflects on the corresponding failure modes. A number of material models employing continuum damage mechanics have been reported in the literature (see, e.g., Ladeveze and Le Dantec, 1992; Lapczyk and Hurtado, 2007; Maimi et al., 2007a, b; Matzenmiller et al., 1995; Van Der Meer and Sluys, 2009). Most of the CDM-based material approaches employ elastic-damage models which are suitable for modeling the mechanical behavior of elastic-brittle composites that do not exhibit noticeable nonlinearity or irreversible strains prior to the initiation of damage development. However, these models may be insufficient in describing the nonlinear or plastic behavior that some thermoset or thermoplastic composites might exhibit, particularly under transverse and/or shear loading.

The results of experiments reported by Lafarie-Frenot and Touchard (1994), Van Paepegem et al., (2006), Vogler and Kyriakides (1999) and Wang et al. (2004) show that some composite materials experience significant nonlinearity or plasticity before the collapse of the structures. In particular, such composites as carbon fiber reinforced epoxy T300/914, T300/1034-C, and AS4/3501-6, and fiber reinforced PEEK composite AS4/PEEK might manifest this type of mechanical behavior under certain conditions.

In addition to plasticity effects, the deterioration of material properties under loading is another significant feature of composite laminates. Defects such as fiber ruptures, matrix cracks, or fiber/matrix debonding developing in a ply do not lead to the collapse of a laminate immediately as they occur. These defects can accumulate gradually within the laminates. As a result, the material properties degrade progressively. Thus, the consideration of postfailure behavior is important for an accurate prediction of failure loads.

Physically, the nonlinearity and/or irreversible deformations of fiber reinforced composites stem from the various mechanisms, such as the nonlinearity of each individual constituent, damage accumulation resulting from fiber or matrix cracking, and fiber/matrix interface debonding. Drucker (1975) has proposed that such micromechanical phenomena can be described macroscopically within the framework of plasticity theory. In combined plasticity and damage theories, the plastic strain represents all the irreversible deformations, including those caused by microcracks. This approach has been employed by Morozov et al. (2011) and Chen et al. (2012) in the development of a combined elastoplastic damage model for progressive failure analysis that accounts for both the plasticity effects and material properties degradation of composite materials under loading and which is presented in this section. The plasticity effects are modeled using an equivalent form of Sun and Chen's (1989) plastic model. The prediction of the damage initiation and propagation in the laminated composites is performed taking into account various failure mechanisms employing Hashin's (1980) failure criterion.

Once the damage development process initiates in a material, the local stresses are redistributed in the undamaged area. As a result, the effective stresses in the undamaged area become higher than the nominal stresses in the damaged material. Plasticity is assumed to be developed in the undamaged area of the damaged material. Correspondingly, the effective stresses are used in the plastic model. Since the nominal stresses in the postfailure branch of the stress-strain curves decrease with an increase in strain, the use of these stresses in the failure criteria does not provide a prediction for further damage growth. Thus, the effective stresses are also used in the failure criterion (Hashin, 1980). It is assumed that under transverse and shear loading, the irreversible deformations are exhibited prior to the damage initiations, however, there is no stiffness degradation. Beyond the damage initiation points, both irreversible deformations and stiffness degradations are taken into account. Once the damage initiation is detected, both the damage development and plasticity evolve in the post-failure regime. In addition to the plastic strain accumulation at this stage, the material's stiffness degrades as well. The model accounts for both of these effects.

The plastic damage model is implemented in Abaqus/Standard using a user-defined subroutine (UMAT). The strain-driven implicit integration procedure for the proposed model is developed using equations of continuum damage mechanics, plasticity theory, and applying the return mapping algorithm. To ensure the algorithmic efficiency of the Newton-Raphson method in the finite element analysis, a tangent operator consistent with the developed integration algorithm is derived and implemented. The efficiency of the proposed model is verified by performing progressive failure analysis of various composite laminates subjected to in-plane tensile loads. The predicted results agree well with the test data reported in the literature and provide accurate estimates of the failure loads.

6.5.1 Constitutive equations

Damage development affects the behavior of fiber-reinforced composite materials considerably. Material properties, such as elastic moduli and Poisson's ratio, degrade due to damage accumulation

and growth. These effects are taken into account by introducing damage variables in the stiffness matrix using the CDM-based approach. According to this, the relation between the nominal stress and effective stress under uniaxial loading is given as

$$\sigma = (1 - d)\widehat{\sigma} \tag{6.65}$$

where $\sigma = P/A_0$ is the Cauchy nominal stress (P is the normal internal force applied to the resisting surface and A_0 is the original area), $\widehat{\sigma} = P/A_{eff}$ is the effective stress (A_{eff} is the effective resisting area of the damaged surface), and d is the damage variable.

For composite materials exhibiting plasticity response, the total strain tensor $\boldsymbol{\varepsilon}$ is presented as a sum of the elastic and plastic strain parts $\boldsymbol{\varepsilon}^e$ and $\boldsymbol{\varepsilon}^p$

$$\boldsymbol{\varepsilon} = \boldsymbol{\varepsilon}^e + \boldsymbol{\varepsilon}^p \tag{6.66}$$

where the plastic strain $\boldsymbol{\varepsilon}^p$ represents all the irreversible deformations, including those caused by microcracks.

According to the continuum damage mechanics theory, the stress-strain relationships for the damaged and undamaged composite materials are presented in the following forms:

$$\boldsymbol{\sigma} = \mathbf{S}(d)\colon \boldsymbol{\varepsilon}^e; \quad \widehat{\boldsymbol{\sigma}} = \mathbf{S}_0\colon \boldsymbol{\varepsilon}^e \tag{6.67}$$

where boldface symbols are used for variables of tensorial character and the symbol ":" denotes the inner product of two tensors with double contraction, e.g., $(\mathbf{S}(d)\colon \boldsymbol{\varepsilon}^e)_{ij} = \mathrm{S}(d)_{ijkl}\varepsilon^e_{kl}$, where the summation convention is applied to the subscripts; $\boldsymbol{\sigma}$ and $\widehat{\boldsymbol{\sigma}}$ are the Cauchy nominal stress tensor and the effective stress tensor (both are of the second order); $\mathbf{S}_0$ is the fourth-order constitutive tensor for linear-elastic undamaged unidirectional laminated composite (see Section 2.9); $\mathbf{S}(d)$ is the similar tensor for the associated damaged material. The explicit form of $\mathbf{S}_0$ is determined by elasticity theory for orthotropic materials (see, e.g., Eq. (2.41) and/or Eq. (4.195)). The Voigt form of $\mathbf{S}(d)$ adopted in the model under consideration is similar to that presented by Matzenmiller et al. (1995)

$$\boldsymbol{S}(d) = \frac{1}{D}\begin{bmatrix} (1-d_1)E_1^0 & (1-d_1)(1-d_2)\upsilon_{12}^0 E_1^0 & 0 \\ (1-d_1)(1-d_2)\upsilon_{21}^0 E_1^0 & (1-d_2)E_2^0 & 0 \\ 0 & 0 & D(1-d_3)G_{12}^0 \end{bmatrix} \tag{6.68}$$

where $\boldsymbol{S}(d)$ in italic is used to identify the Voigt form of $\mathbf{S}(d)$; $D = 1 - (1-d_1)(1-d_2)\upsilon_{12}^0\upsilon_{21}^0$; the parameters d_1, d_2, and d_3 denote damage developed in the fiber direction, transverse direction, and under shear stress, respectively (they are scalar damage variables that remain constant throughout the ply thickness); E_1^0, E_2^0, G_{12}^0 and υ_{12}^0, υ_{21}^0 are the elastic moduli and Poisson's ratios of undamaged unidirectional composite ply (as earlier, $E_1^0\upsilon_{12}^0 = E_2^0\upsilon_{21}^0$).

In order to differentiate between the effects of compression and tension on the failure modes, the damage variables are introduced as follows:

$$d_1 = \begin{cases} d_{1t} & \text{if } \widehat{\sigma}_1 \geq 0 \\ d_{1c} & \text{if } \widehat{\sigma}_1 < 0 \end{cases} \quad d_2 = \begin{cases} d_{2t} & \text{if } \widehat{\sigma}_2 \geq 0 \\ d_{2c} & \text{if } \widehat{\sigma}_2 < 0 \end{cases} \tag{6.69}$$

where d_{1t}, d_{1c} characterize the damage development caused by tension and compression in the fiber direction, and d_{2t}, d_{2c} reflect the damage development caused by tension and compression in the transverse direction, respectively; $\widehat{\sigma}_1$, $\widehat{\sigma}_2$ are the effective stresses in the fiber and transverse directions, respectively.

We assume that the shear stiffness reduction is caused by the fiber and matrix cracking. To take this effect into account, the corresponding damage variable d_3 is expressed as:

$$d_3 = 1 - (1 - d_6)(1 - d_{1t}) \tag{6.70}$$

where d_6 represents the damage effects on shear stiffness caused by matrix cracking.

As previously mentioned, all the irreversible deformations are represented by the plastic strain $\boldsymbol{\varepsilon}^p$. These effects are allowed for by the plastic model which includes the yield criterion, plastic flow rule, hardening rule, and the hardening law.

6.5.2 Plastic model

In the damaged materials, the internal forces are resisted by the effective area. Thus, it is reasonable to assume that plastic deformation occurs in the undamaged area of the damaged composites. According to this, the plastic flow rule and hardening law are expressed in terms of effective stresses $\widehat{\boldsymbol{\sigma}}$, equivalent plastic strain $\tilde{\varepsilon}^p$, and equivalent stress $\tilde{\sigma}$, which are based on the effective stress space concept.

The plastic yield function is expressed in terms of effective stresses as follows:

$$F(\widehat{\boldsymbol{\sigma}},\ \tilde{\varepsilon}^p) = F^p(\widehat{\boldsymbol{\sigma}}) - \kappa(\tilde{\varepsilon}^p) = 0 \tag{6.71}$$

where F^p is the plastic potential and k is the hardening parameter, which depends on the plastic deformations and is expressed in terms of equivalent plastic strain $\tilde{\varepsilon}^p$.

Due to its simplicity and accuracy, an equivalent form of the one-parameter plastic potential for the plane stress state proposed by Sun and Chen (1989) is adopted in this study to describe the irreversible strains exhibited by composites under transverse and/or shear loading:

$$F(\widehat{\boldsymbol{\sigma}},\ \tilde{\varepsilon}^p) = \sqrt{\frac{3}{2}\left(\widehat{\sigma}_2^2 + 2a\widehat{\sigma}_3^2\right)} - \tilde{\sigma}(\tilde{\varepsilon}^p) = 0 \tag{6.72}$$

where a is a material parameter which describes the level of plastic deformation developed under shear loading compared to the transverse loading; $\widehat{\sigma}_3$ is the effective in-plane shear stress; and $\tilde{\sigma}(\tilde{\varepsilon}^p)$ represents the isotropic hardening law. Note that the use of the yield criterion in the form of Eq. (6.72) in the model under consideration improves the efficiency and accuracy of the computational algorithm.

The equivalent stress is expressed in terms of $\widehat{\sigma}_2$ and $\widehat{\sigma}_3$ as follows (Sun and Chen, 1989):

$$\tilde{\sigma} = \left[\frac{3}{2}\left(\widehat{\sigma}_2^2 + 2a\widehat{\sigma}_3^2\right)\right]^{\frac{1}{2}} \tag{6.73}$$

Assuming the associated plastic flow rule for composite materials, the plastic strain rate $\dot{\varepsilon}^p$ is expressed as:

$$\dot{\varepsilon}^p = \dot{\lambda}^p \partial_{\widehat{\boldsymbol{\sigma}}} F \tag{6.74}$$

where $\dot{\lambda}^p \geq 0$ is a nonnegative plastic consistency parameter (hereafter in this section the following notations are used for the derivatives: $\partial_x y = \partial y/\partial x$ and $\dot{y} = \mathrm{d}y/\mathrm{d}t$).

Substituting Eq. (6.72) into Eq. (6.74), the following explicit form of plastic strain rate is derived:

$$\begin{bmatrix} \dot{\varepsilon}_1^p \\ \dot{\varepsilon}_2^p \\ \dot{\varepsilon}_3^p \end{bmatrix} = \dot{\lambda}^p \partial_{\widehat{\sigma}} F = \dot{\lambda}^p \begin{bmatrix} 0 \\ \dfrac{3}{2} \dfrac{\widehat{\sigma}_2}{\sqrt{\dfrac{3}{2}\left(\widehat{\sigma}_2^2 + 2a\widehat{\sigma}_3^2\right)}} \\ \dfrac{3a\widehat{\sigma}_3}{\sqrt{\dfrac{3}{2}\left(\widehat{\sigma}_2^2 + 2a\widehat{\sigma}_3^2\right)}} \end{bmatrix} \tag{6.75}$$

Also, the associated hardening rule is assumed for the equivalent plastic strain rate to have the following form:

$$\dot{\tilde{\varepsilon}}^p = \dot{\lambda}^p h^p = -\dot{\lambda}^p \partial_{\dot{\tilde{\varepsilon}}^p} F \tag{6.76}$$

where h^p defines the evolution direction of the equivalent plastic strain.

The equivalent plastic strain rate can be obtained from the equivalence of the rates of the plastic work per unit volume W^p presented as follows:

$$\dot{W}^p = \widehat{\boldsymbol{\sigma}} : \dot{\boldsymbol{\varepsilon}}^p = \partial_{\dot{\tilde{\varepsilon}}^p} \dot{\tilde{\varepsilon}}^p \tag{6.77}$$

Substituting Eq. (6.75) and Eq. (6.73) into Eq. (6.77), the following relation is derived

$$\dot{\tilde{\varepsilon}}^p = \dot{\lambda}^p \tag{6.78}$$

It follows from the comparison of Eqs. (6.76) and (6.78) that the value of h^p is unity. Note that this does not hold if the original quadratic form of the Sun and Chen yield criterion is adopted (Sun and Chen, 1989). As a result, the application of the original yield criterion leads to higher computational cost in the integration procedure. The current approach based on the use of Eq. (6.72) avoids this inefficiency.

For the sake of simplicity, an isotropic hardening law expressed in terms of equivalent plastic strain $\tilde{\varepsilon}^p$ is adopted in this study. The following formulation of this law proposed by Sun and Chen (1989) is employed in this work to represent the equivalent stress versus equivalent plastic strain hardening curve:

$$\kappa(\tilde{\varepsilon}^p) = \tilde{\sigma}(\tilde{\varepsilon}^p) = \beta(\tilde{\varepsilon}^p)^n \tag{6.79}$$

where β and n are coefficients that fit the experimental hardening curve. These parameters along with the material parameter a are determined using an approach based on linear regression analyses of the off-axis tensile tests performed on unidirectional composite specimens (Sun and Chen, 1989; Winn and Sridharan, 2001).

6.5.3 Damage model

The prediction of the damage initiation and progression in the laminated composites under consideration is performed taking into account various modes of failure, including those caused by tensile and compressive loading for the fibers and matrix, and also combined action of transverse and shear stresses.

6.5.3.1 Damage initiation and propagation criteria

In order to predict the damage initiation and propagation of each intralaminar failure of the material and evaluate the effective stress state, the damage initiation and propagation criteria f_I are presented in the following form:

$$f_I(\phi_1, r_I) = \phi_I - r_I \leq 0 \quad I = \{1t, 1c, 2t, 2c, 6\} \tag{6.80}$$

where ϕ_I are the loading functions for different failure mechanisms adopted in the form of Hashin's failure criterion (Hashin, 1980):

$$\begin{aligned}
\phi_{1t} &= \left(\frac{\widehat{\sigma}_1}{\overline{\sigma}_1^+}\right)^2 && (\widehat{\sigma}_1 \geq 0) && \text{(tensile fiber damage mode)} \\
\phi_{1c} &= \left(\frac{\widehat{\sigma}_1}{\overline{\sigma}_1^-}\right)^2 && (\widehat{\sigma}_1 < 0) && \text{(compressive fiber damage mode)} \\
\phi_{2t} &= \left(\frac{\widehat{\sigma}_2}{\overline{\sigma}_2^+}\right)^2 + \left(\frac{\widehat{\sigma}_3}{\overline{\tau}_{12}}\right)^2 && (\widehat{\sigma}_2 \geq 0) && \text{(tensile matrix damage mode)} \\
\phi_{2c} &= \left(\frac{\widehat{\sigma}_2}{\overline{\sigma}_2^-}\right)^2 + \left(\frac{\widehat{\sigma}_3}{\overline{\tau}_{12}}\right)^2 && (\widehat{\sigma}_2 < 0) && \text{(compressive matrix damage mode)}
\end{aligned} \tag{6.81}$$

where $\overline{\sigma}_1^+$ and $\overline{\sigma}_1^-$ are the tensile and compressive strengths in fiber direction; $\overline{\sigma}_2^+$ and $\overline{\sigma}_2^-$ are the transverse tensile and compressive strengths; and $\overline{\tau}_{12}$ is the shear strength. Each damage threshold parameter r_I controls the size of the expanding damage surface and depends on the loading history. The damage development in the material initiates when the value of ϕ_I exceeds the initial damage threshold $r_{I,0} = 1$. Further damage growth occurs when the value of ϕ_I in the current stress state exceeds the value of r_I in the previous loading history. As mentioned previously, the damage variable d_6 represents the damage effects on the shear stiffness due to matrix fracture caused by the combined action of transverse and shear stresses. However, the compressive transverse stress has beneficial effects on matrix cracking. Thus, it is reasonable to assume that the damage effects are governed by the tensile matrix cracking only, i.e., $f_6 = f_{2t}$, $r_6 = r_{2t}$.

Once the damage initiation criterion is satisfied, then further damage evolution could be developed. The way the damage would evolve depends on the level of the stress caused by the strain increment. The damage propagation criteria, Eq. (6.80), define the growing damage surfaces when the value of r_I corresponding to the current stress state in Eq. (6.80) is greater than unity. The modeling of the evolution of damage is discussed in the following subsection.

6.5.3.2 Damage evolution

The evolution of damage is possible only when the stresses reach the level corresponding to the damage surface, i.e., when Eq. (6.80) is converted to equality. In the further process of damage evolution, the following damage consistency condition should be satisfied: $\dot{f}(\phi_I, r_I) = \dot{\phi}_I - \dot{r}_I = 0$. Based on this condition, the values of the thresholds could be found by integrating equation $\dot{r}_I = \dot{\phi}_I$, i.e., $\int_0^t \dot{r}_I \mathrm{d}t = \int_0^t \dot{\phi}_I \mathrm{d}t$, and taking into account the initial condition $\phi_{I,0} = 0$. The following expressions for damage thresholds r_I can be derived:

$$r_I = \max\left\{1, \max\left\{\phi_I^\tau\right\}\right\} \quad I = \{1t, 1c, 2t, 2c, 6\} \quad \tau \in [0, t] \tag{6.82}$$

Since damage is irreversible, the damage evolution rate should satisfy the following condition: $\dot{d}_I \geq 0$. The exponential damage evolution law is adopted for each damage variable and expressed in the following form (Faria et al., 1998):

$$d_I = 1 - \frac{1}{r_I} \exp(A_I(1 - r_I)) \quad I = \{1t, 1c, 2t, 2c, 6\} \tag{6.83}$$

where A_I is the parameter that defines the exponential softening law. This parameter is determined by regularizing the softening branch of the stress-strain curve to ensure that the dissipated energy in the formation and opening of all microcracks per unit area of the fracture surface computed according to the numerical procedure proposed is independent of mesh size. This approach helps alleviate the mesh dependency of the finite element results. The regularization is based on Bazant's crack band theory (Bazant and Oh, 1983). According to this, the damage energy dissipated per unit volume g_I for a uniaxial or shear stress state is related to the critical strain energy release rate $G_{I,c}$ along with the characteristic length of the finite element l^* as follows:

$$g_I = \frac{G_{I,c}}{l^*} \quad I = \{1t, 1c, 2t, 2c, 6\} \tag{6.84}$$

where the parameters $G_{1t,c}$ and $G_{1c,c}$ are the mode I fracture toughness parameters related to fiber breakage under tension and compression. The critical strain energy release rates $G_{2t,c}$ and $G_{2c,c}$ are referred to as the intralaminar mode I fracture toughness parameters under transverse tension and compression. The parameter $G_{6,c}$ is the intralaminar mode II fracture toughness parameter. The identification of these parameters and the characteristic length l^* is discussed in Maimi et al. (2007b) and Pinho (2005).

The damage energy dissipated per unit volume for a uniaxial or shear stress state is obtained by integration of the damage energy dissipation during the process of damage development:

$$g_I(A_I) = \int_0^\infty Y_I \dot{d}_I(A_I)\mathrm{d}t; \quad Y_I = -\frac{\partial \psi}{\partial d_I}; \quad \psi = \frac{1}{2}\boldsymbol{\sigma}\colon\boldsymbol{\varepsilon} \quad I = \{1t, 1c, 2t, 2c, 6\} \tag{6.85}$$

where Y_I is the damage energy release rate; $\dot{d}_I$ is the rate of damage development defined as $\dot{d}_I = \mathrm{d}d_I/\mathrm{d}t$; and ψ is the Helmholtz free energy. The parameters A_I correspond to each uniaxial or shear loading condition applied to the elementary ply and these parameters should be determined for

a given material and a given finite element size to avoid mesh dependency in the finite element analysis. Equating Eq. (6.84) and Eq. (6.85), we can derive the following equation:

$$g_{I,c}(A_I) = \frac{G_{I,c}}{l^*} \quad I = \{1t, 1c, 2t, 2c, 6\} \tag{6.86}$$

The values of A_I for $I = \{1t, 1c, 2t, 2c, 6\}$ are found by solving Eq. (6.86) iteratively using a root-finding algorithm described in Chen et al. (2012). These parameters are determined for a given material and finite element size to avoid mesh dependency in the finite element analysis.

The loading/unloading stress-strain curves illustrating the combined elastoplastic damage model under consideration are shown in Fig. 6.26. It is assumed that under loading in the fiber direction the material exhibits linear elastic-brittle behavior and the irreversible strain is not developed. Note that the model can be easily extended to the case where the material would exhibit nonlinear inelastic behavior in the fiber direction, if required. After the damage initiation, the elastic modulus E_1 is assumed to degrade gradually. It is also assumed that under transverse and shear loading the irreversible deformations are exhibited prior to the damage initiations; however, there is no stiffness degradation at that stage. Beyond the damage initiation points, both irreversible deformations and stiffness degradations are taken into account.

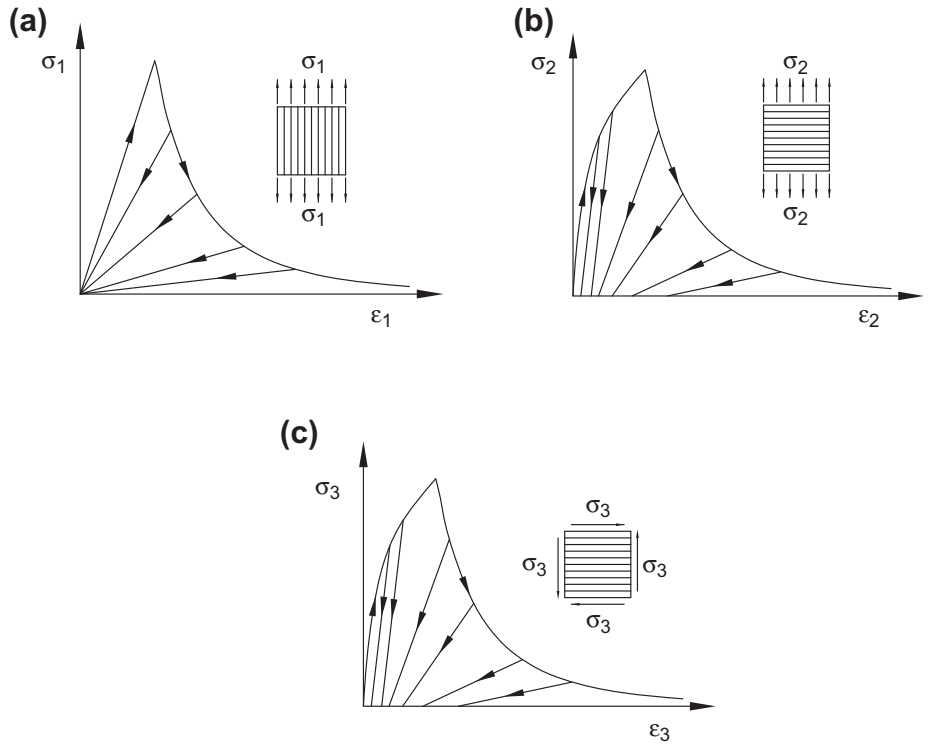


FIGURE 6.26

Loading/unloading stress-strain curves curves for in-plane loading along the fibers (a), in transverse direction (b), and shear (c).

6.5.4 Numerical implementation

The combined elastoplastic damage material model discussed earlier has been implemented in the Abaqus/Standard finite element software package using the user-defined subroutine UMAT. The numerical integration algorithms updating the Cauchy nominal stresses and solution-dependent state variables have been derived, as well as the tangent matrix that is consistent with the numerical integration algorithm ensuring the quadratic convergence rate of the Newton-Raphson method in the finite element analysis (Morozov et al., 2011; Chen et al., 2012).

6.5.4.1 Integration algorithm

The solution of the nonlinear inelastic problem under consideration is based on the incremental approach and is regarded as strain-driven. The loading history is discretized into a sequence of time steps $[t_n, t_{n+1}], n \in \{0, 1, 2, 3, \ldots\}$ where each step is referred to as the $(n+1)$th increment. Driven by the strain increment $\Delta\varepsilon_{n+1}$, the discrete problem in the context of a backward Euler scheme for the combined elastoplastic damage model can be stated as follows: for a given variable set $\{\boldsymbol{\varepsilon}_{n+1}, \boldsymbol{\varepsilon}^p_n, \tilde{\varepsilon}^p_n, \widehat{\boldsymbol{\sigma}}_n, \boldsymbol{\sigma}_n, \tilde{\sigma}_n, r_{I,n}, d_{I,n}\}$ at the beginning of the $(n+1)$th increment, find the updated variable set $\{\boldsymbol{\varepsilon}^p_{n+1}, \tilde{\varepsilon}^p_{n+1}, \widehat{\boldsymbol{\sigma}}_{n+1}, \boldsymbol{\sigma}_{n+1}, \tilde{\sigma}_{n+1}, r_{I,n+1}, d_{I,n+1}\}$ at the end of the $(n+1)$th increment. The updated stresses and solution-dependent state variables are stored at the end of the $(n+1)$th increment and are passed on to the user subroutine UMAT at the beginning of the next increment.

The effective stress-strain relationship, Eq. (6.67) yield criterion, Eq. (6.72), associated plastic flow rule, Eq. (6.74), and hardening power law, Eq. (6.79), represent the nonlinear plastic constitutive material model. Using the backward Euler implicit integration procedure, the corresponding integration algorithm is formulated as follows:

$$\begin{aligned}
\boldsymbol{\varepsilon}_{n+1} &= \boldsymbol{\varepsilon}_n + \Delta\boldsymbol{\varepsilon}_{n+1} \\
\boldsymbol{\varepsilon}^p_{n+1} &= \boldsymbol{\varepsilon}^p_n + \Delta\lambda^p_{n+1}\partial_{\widehat{\boldsymbol{\sigma}}_{n+1}} F^p_{n+1} \\
\tilde{\varepsilon}^p_{n+1} &= \tilde{\varepsilon}^p_n + \Delta\lambda^p_{n+1} \\
\widehat{\boldsymbol{\sigma}}_{n+1} &= \mathbf{S}_0 \colon (\boldsymbol{\varepsilon}_{n+1} - \boldsymbol{\varepsilon}^p_{n+1}) \\
F_{n+1} &= F\left(\widehat{\boldsymbol{\sigma}}_{n+1}, \tilde{\varepsilon}^p_{n+1}\right) \le 0
\end{aligned} \tag{6.87}$$

where $\Delta\lambda^p_{n+1} = \dot{\lambda}^p_{n+1}\Delta t$ is the increment of the plastic consistency parameter.

The closest point return mapping algorithm is employed to solve this nonlinear coupled system. The solutions $\{\boldsymbol{\varepsilon}^p_{n+1}, \tilde{\varepsilon}^p_{n+1}, \widehat{\boldsymbol{\sigma}}_{n+1}\}$ are the converged values at the end of the $(n+1)$th increment. They ensure that upon yielding, the determined stress state lies on the yield surface and they prevent drift from the yield surface due to the unconverged solutions obtained from the forward Euler integration scheme.

The nonlinear system, Eq. (6.87), is linearized and solved iteratively using the Newton-Raphson scheme. The iterations are performed until the final set of state variables $\{\widehat{\boldsymbol{\sigma}}^{(k+1)}_{n+1}, \boldsymbol{\varepsilon}^{p,(k+1)}_{n+1}, \tilde{\varepsilon}^{p,(k+1)}_{n+1}\}$ in the $(k+1)$th iteration fulfills the yield criterion $F(\widehat{\boldsymbol{\sigma}}^{(k+1)}_{n+1}, \tilde{\varepsilon}^{p,(k+1)}_{n+1}) \le$ TOL, where TOL is the error tolerance which was set to 1×10^{-6} in the analyses performed.

Substituting the effective stresses $\widehat{\boldsymbol{\sigma}}_{n+1}$ into the damage model, the damage variables are updated. According to Eq. (6.67), the Cauchy stresses are calculated as $\boldsymbol{\sigma}_{n+1} = \mathbf{S}(d_{n+1})\colon \boldsymbol{\varepsilon}^e_{n+1}$.

6.5.4.2 Consistent tangent stiffness matrix

The consistent tangent matrix for the proposed constitutive model is derived in the following form:

$$\frac{\mathrm{d}\boldsymbol{\sigma}_{n+1}}{\mathrm{d}\boldsymbol{\varepsilon}_{n+1}} = [\mathbf{M}_{n+1} + \mathbf{S}(d_{n+1})]\colon \mathbf{C}_0\colon \mathbf{S}^{\mathrm{alg}}_{\mathrm{n+1}} \tag{6.88}$$

in which the fourth-order tensor $\mathbf{M}_{n+1}$ can be presented in Voigt notation (in indicial form) as follows:

$$M_{ik}\big|_{n+1} = \frac{\partial S(d)_{ij}\varepsilon^e_j}{\partial \varepsilon^e_k}\bigg|_{n+1} = \varepsilon^e_j \frac{\partial S(d)_{ij}}{\partial d_p}\frac{\partial d_p}{\partial r_\xi}\frac{\partial r_\xi}{\partial \phi_\xi}\frac{\partial \phi_\xi}{\partial \widehat{\sigma}_q}\frac{\partial \widehat{\sigma}_q}{\partial \varepsilon^e_k}\bigg|_{n+1} \tag{6.89}$$
$$i,\ j,\ p,\ q,\ k = \{1,2,3\}; \quad \xi = \{1,2\}$$

where matrix $\mathbf{M}_{n+1} = [\mathrm{M}ik]_{n+1}$ is asymmetric. This results in the asymmetry of the consistent tangent matrix of the combined elastoplastic damage model. The explicit expression for matrix $\boldsymbol{M}$, along with the associated derivatives, can be found in Morozov et al. (2011) and Chen et al. (2012). In Eq. (6.88), $\mathbf{C}_0 = \mathbf{S}_0^{-1}$ is the fourth-order compliance tensor of the undamaged composite material and $\mathbf{S}^{\mathrm{alg}}_{n+1}$ is the consistent tangent tensor for the discrete plastic problem Eq. (6.87). The latter is expressed as:

$$\mathbf{S}^{\mathrm{alg}}_{n+1} = \frac{\mathrm{d}\widehat{\boldsymbol{\sigma}}_{n+1}}{\mathrm{d}\boldsymbol{\varepsilon}_{n+1}} = \tilde{\mathbf{S}}_{n+1} - \frac{\left(\tilde{\mathbf{S}}_{n+1}\colon \partial_{\overline{\sigma}} F^p_{n+1}\right) \otimes \left(\tilde{\mathbf{S}}_{n+1}\colon \partial_{\widehat{\boldsymbol{\sigma}}} F_{n+1}\right)}{\partial_{\widehat{\boldsymbol{\sigma}}} F_{n+1}\colon \tilde{\mathbf{S}}_{n+1}\colon \partial_{\widehat{\boldsymbol{\sigma}}} F^p_{n+1} - \partial_{\tilde{\varepsilon}^p} F_{n+1}} \tag{6.90}$$

where $\tilde{\mathbf{S}}_{n+1} = \left(\mathbf{C}_0 + \Delta\lambda^p_{n+1}\partial^2_{\widehat{\boldsymbol{\sigma}}\widehat{\boldsymbol{\sigma}}} F^p_{n+1}\right)^{-1}$, $\Delta\lambda^p_{n+1}$ denotes the increment of plastic consistency parameter λ^p in the $(n+1)$th increment, $\partial^2_{xx} y = \partial^2 y/\partial x^2$, and $(\otimes)$ denotes a tensor product. As the time increment Δt approaches zero, the increment of the plastic consistency parameter $\Delta\lambda^p_{n+1}$ also approaches zero. Thus, $\tilde{\mathbf{S}}_{n+1}$ approaches $\mathbf{S}_0$, and $\mathbf{S}^{\mathrm{alg}}_{n+1}$ reduces to the elastoplastic tangent operator when standard procedures of classical plasticity theory are applied.

6.5.4.3 Viscous regularization

Numerical simulations based on the implicit procedures, such as Abaqus/Standard, and the use of material constitutive models that are considering strain softening and material stiffness degradation often abort prematurely due to convergence problems. In order to alleviate these computational difficulties and improve convergence, a viscous regularization scheme has been implemented in the following form (Lapczyk and Hurtado, 2007):

$$\dot{d}^{\upsilon}_m = \frac{1}{\eta}\left(d_m - d^{\upsilon}_m\right), \quad m = \{1,2,3\} \tag{6.91}$$

where d_m is the damage variable obtained as described previously, d^{υ}_m is the regularized viscous damage variable, and η is the viscosity coefficient.

The regularized damage variable in the $(n+1)$th increment is derived as

$$d^{\upsilon}_{m,n+1} = \frac{\Delta t}{\eta + \Delta t} d_{m,n+1} + \frac{\eta}{\eta + \Delta t} d^{\upsilon}_{m,n} \tag{6.92}$$

The corresponding regularized consistent tangent matrix is derived as

$$\frac{\mathrm{d}\boldsymbol{\sigma}_{n+1}}{\mathrm{d}\boldsymbol{\varepsilon}_{n+1}}\bigg|_{\upsilon} = \left[\mathbf{M}^{\upsilon}_{n+1} + \mathbf{S}\left(d^{\upsilon}_{n+1}\right)\right]\colon \mathbf{C}_0\colon \mathbf{S}^{\mathrm{alg}}_{n+1} \tag{6.93}$$

where the fourth-order tensor $\mathbf{M}^{v}_{n+1}$ can be presented in Voigt notation (in indicial form) as follows:

$$\mathbf{M}^{v}_{ik}|_{n+1} = \left.\frac{\partial S(d^{v})ij\varepsilon^{e}_{j}}{\partial \varepsilon^{e}_{k}}\right|_{n+1} = \left[\varepsilon^{e}_{j}\frac{\partial S(d^{v})ij}{\partial d^{v}_{p}}\frac{\partial d_{p}}{\partial r_{\xi}}\frac{\partial r_{\xi}}{\partial \phi_{\xi}}\frac{\partial \phi_{\xi}}{\partial \widehat{\sigma}_{q}}\frac{\partial \widehat{\sigma}_{q}}{\partial \varepsilon^{e}_{k}}\right|_{n+1}.\frac{\Delta t}{\eta + \Delta t}\Bigg]$$

$$i,j,p,q,k = \{1,2,3\} \qquad \xi = \{1,2\}$$

6.5.4.4 Computational procedure

The user subroutine UMAT for the numerical algorithm based on the model discussed previously has been coded and is called by Abaqus/Standard at each material integration point of the elements where user-defined materials are used to update the Cauchy nominal stresses and provide the consistent tangent matrix of the material for the calculation of the element tangent stiffness matrix. This process includes the use of the elastic predictor, plastic corrector, damage corrector parts of the algorithm and calculation of the regularized consistent tangent matrix as follows:

1. Initial conditions:

$$\boldsymbol{\varepsilon}_{n+1},\ \Delta\boldsymbol{\varepsilon}_{n+1},\ \boldsymbol{\varepsilon}^{p}_{n},\ \tilde{\varepsilon}^{p}_{n},\ \widehat{\boldsymbol{\sigma}}_{n},\ \boldsymbol{\sigma}_{n},\ \tilde{\sigma}_{n},\ r_{I,n}\ d_{I,n},\ d_{m,n},\ d^{v}_{m,n}$$

2. Elastic predictor:
   a. Assign and compute the trial state variables:

$$\boldsymbol{\varepsilon}^{p,\text{trial}}_{n+1} = \boldsymbol{\varepsilon}^{p}_{n};\quad \tilde{\varepsilon}^{p,\text{trial}}_{n+1} = \tilde{\varepsilon}^{p}_{n};\quad \tilde{\sigma}^{p,\text{trial}}_{n+1} = \tilde{\sigma}_{n};$$

$$\widehat{\boldsymbol{\sigma}}^{\text{trial}}_{n+1} = \widehat{\boldsymbol{\sigma}}_{n} + \mathbf{S}_{0}\colon \Delta\boldsymbol{\varepsilon}_{n+1};\quad d^{\text{trial}}_{I,n+1} = d_{I,n}$$

   b. Check the yield criterion:

$$F^{\text{trial}}_{n+1} = F^{p,\text{trial}}_{n+1} - \tilde{\sigma}^{\text{trial}}_{n+1} \le 0$$

   If $F^{\text{trial}}_{n+1} \le 0$, then set $\widehat{\boldsymbol{\sigma}}_{n+1} = \widehat{\boldsymbol{\sigma}}^{\text{trial}}_{n+1}$. Otherwise, plasticity evolves, go to step 3.
3. Plastic corrector:
   The Newton-Raphson method is employed to solve the nonlinear problem $F_{n+1} = F(\widehat{\boldsymbol{\sigma}}(\Delta\lambda^{p}), \tilde{\varepsilon}^{p}(\Delta\lambda^{p})) = 0$ iteratively in order to compute the real plastic state variables $(\boldsymbol{\varepsilon}^{p}_{n+1}, \tilde{\varepsilon}^{p}_{n+1}, \tilde{\sigma}_{n+1})$:
   a. Initialize:

$$k = 0,\quad \widehat{\boldsymbol{\sigma}}^{(0)}_{n+1} = \widehat{\boldsymbol{\sigma}}^{\text{trial}}_{n+1},\quad \boldsymbol{\varepsilon}^{p,(0)}_{n+1} = \boldsymbol{\varepsilon}^{p}_{n},\quad \tilde{\varepsilon}^{p,(0)}_{n+1} = \tilde{\varepsilon}^{p}_{n},\quad \Delta\lambda^{p,(0)}_{n+1} = 0.$$

   b. Calculate $\delta(\Delta\lambda^{p})$, $\delta\boldsymbol{\varepsilon}^{p}$, $\delta\tilde{\varepsilon}^{p}$ in the $(k+1)$ iteration;
   c. Update the plastic state variables in the (k+1) iteration:

$$\Delta\lambda^{p,(k+1)}_{n+1} = \Delta\lambda^{p,(k)}_{n+1} + \delta(\Delta\lambda^{p});$$

$$\boldsymbol{\varepsilon}^{p,(k+1)}_{n+1} = \boldsymbol{\varepsilon}^{p,(k)}_{n+1} + \delta\boldsymbol{\varepsilon}^{p};$$

$$\tilde{\varepsilon}^{p,(k+1)}_{n+1} = \tilde{\varepsilon}^{p,(k)}_{n+1} + \delta\tilde{\varepsilon}^{p}$$

   d. Calculate $\widehat{\boldsymbol{\sigma}}^{(k+1)}_{n+1} = \mathbf{S}_{0}\colon \left(\boldsymbol{\varepsilon}_{n+1} - \boldsymbol{\varepsilon}^{p,(k+1)}_{n+1}\right)$

e. Calculate $F_{n+1}^{(k+1)} = F\left(\widehat{\boldsymbol{\sigma}}_{n+1}^{(k+1)}, \tilde{\varepsilon}_{n+1}^{p,(k+1)}\right)$, If $F_{n+1}^{(k+1)} = TOL$, then $\widehat{\boldsymbol{\sigma}}_{n+1} = \widehat{\boldsymbol{\sigma}}_{n+1}^{(k+1)}$, $\varepsilon_{n+1}^{p} = \boldsymbol{\varepsilon}_{n+1}^{p,(k+1)}$, $\tilde{\varepsilon}_{n+1}^{p} = \tilde{\varepsilon}_{n+1}^{p,(k+1)}$, calculate $\mathbf{S}_{n+1}^{\text{alg}}$. Otherwise, set $k = k + 1$, go to b.

4. Damage corrector (updating the nominal Cauchy stresses):

a. Calculate $\phi_{I,n+1}$, updating $r_{I,n+1} = \max\{1, \phi_{I,n+1}, r_{I,n}\}$

b. Calculate damage variables $d_{I,n+1}$, $d_{m,n+1}$, $d_{m,n+1}^{v}$ and $\mathbf{S}(d_{m,n+1}^{v})$

c. Update the nominal stresses: $\boldsymbol{\sigma}_{n+1} = \mathbf{S}(d_{m,n+1}^{v})$: $(\boldsymbol{\varepsilon}_{n+1} - \boldsymbol{\varepsilon}_{n+1}^{p})$

5. Calculation of the tensor $\mathbf{M}_{n+1}^{v}$ and the regularized consistent tangent matrix:

$$\frac{\mathrm{d}\boldsymbol{\sigma}_{n+1}}{\mathrm{d}\boldsymbol{\varepsilon}_{n+1}} = [\mathbf{M}_{n+1}^{v} + \mathbf{S}(d_{m,n+1}^{v})]\text{: } \mathbf{C}_0\text{: } \mathbf{S}_{n+1}^{\text{alg}}$$

The flow chart of this subroutine is shown in Fig. 6.27.

6.5.5 Numerical analyses

To illustrate the effectiveness of the model, numerical simulations of the progressive failure of flat composite laminates containing central through holes (see Fig. 6.28a) and subjected to uniform in-plane tensile loading have been undertaken. In addition, $[\pm 45^{\circ}]_{2s}$ laminate without cutouts under in-plane tensile loading has been analyzed.

6.5.5.1 Composite laminates with through holes

Two groups of different laminates are considered in this section. The rectangular laminates from the first group are composed of plies made from T300/1034-C carbon-epoxy composite and have the following dimensions: length $L = 203.2$ mm, thickness $H = 2.616$ mm, and widths $W = 19.05$, $38.1, 12.7,$ and 25.4 mm. The corresponding diameters of the central holes for this set of laminates are: $D = 3.175, 6.35, 3.175,$ and 6.35 mm.

The rectangular laminates from the second group are made from AS4/PEEK composite and have the length, width, and thickness of 100, 20, and 2 mm, respectively. The simulations have been performed for five different laminates having central through holes with the following diameters: $D = 2, 3, 5, 8,$ and 10 mm.

The laminates are modeled using the *Composite Layup* function available within Abaqus. Considering the symmetry of the laminate and loading, only one quarter of the laminate is simulated. The boundary conditions for the one quarter laminate FE model are illustrated in Fig. 6.28b. Nodes on the vertical central line are constrained to move along the vertical (x) direction. Nodes on the horizontal central line are restrained to move along the horizontal (y) direction. The laminates are subjected to tensile displacement-controlled loading. A reference point *RP* is appointed to the lower-left corner of the loaded surface (see Fig. 6.28b). Displacement-controlled loading is applied to this reference point. A linear constraint equation between this reference point and the loaded surface is implemented so that the displacements of all the nodes on the loaded surface are constrained to have equal displacements with the applied displacement on the reference point *RP*. By doing this, the reaction force and corresponding displacement on the loaded surface can be conveniently output to this reference point. The laminates are modeled using continuum shell elements SC8R available within Abaqus. The element size of the numerical simulations of the T300/1034-C carbon-epoxy composite laminates group is 0.635 mm; whereas the one for AS4/PEEK group is 0.5 mm.

As indicated earlier, both aforementioned materials could exhibit nonlinearity or plasticity under certain loading conditions. The details of the progressive failure analyses are discussed below.

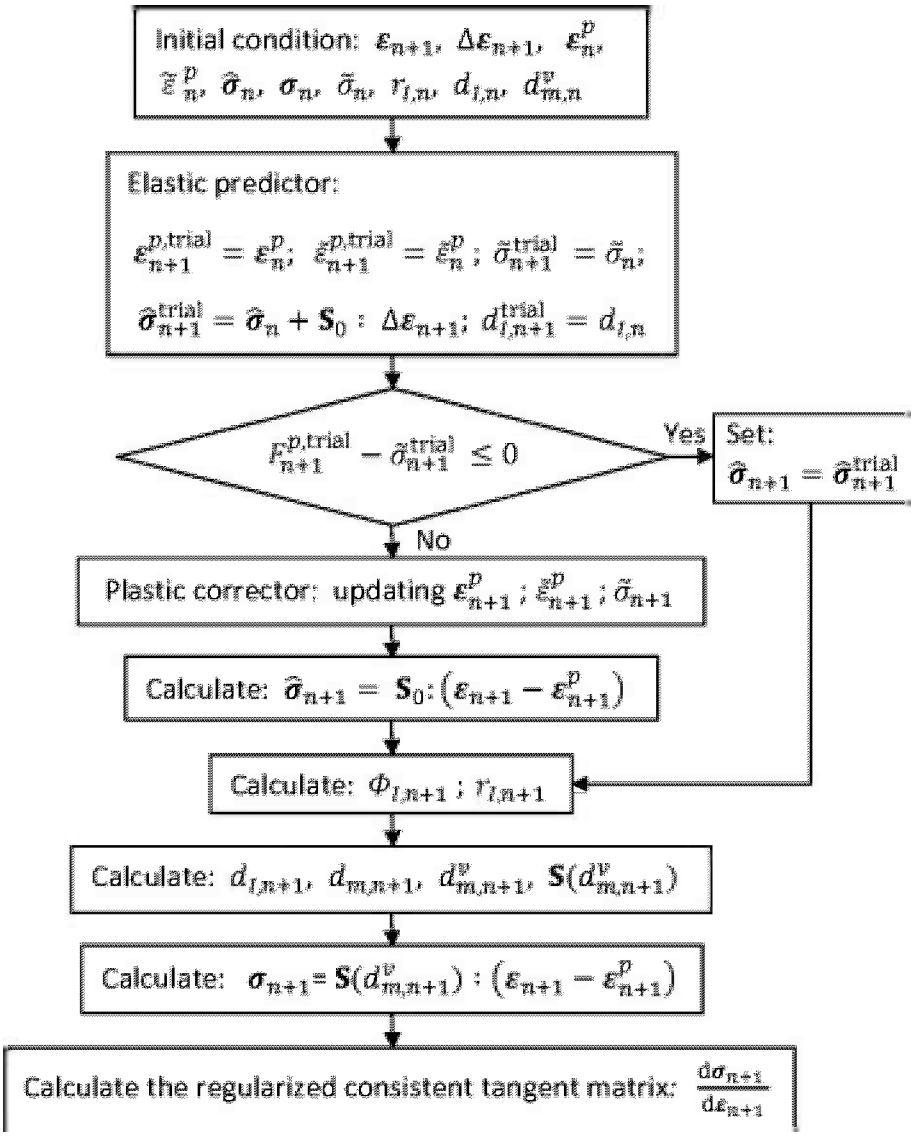


FIGURE 6.27

Flow chart of the user subroutine UMAT.

Three different material lay-ups were considered for the laminates made of T300/1034-C carbon-epoxy composite, namely $[0°/(\pm 45°)_3/90°_3]_s$, $[0°/(\pm 45°)_2/90°_5]_s$, and $[0°/(\pm 45°)_1/90°_7]_s$. The material properties along with model parameters used in the finite-element simulations are shown in Table 6.2. The material properties, strength characteristics, and critical strain energies were taken from Maimi et al. (2007b). The set of plastic model parameters reported by Chen and Sun (1987) for

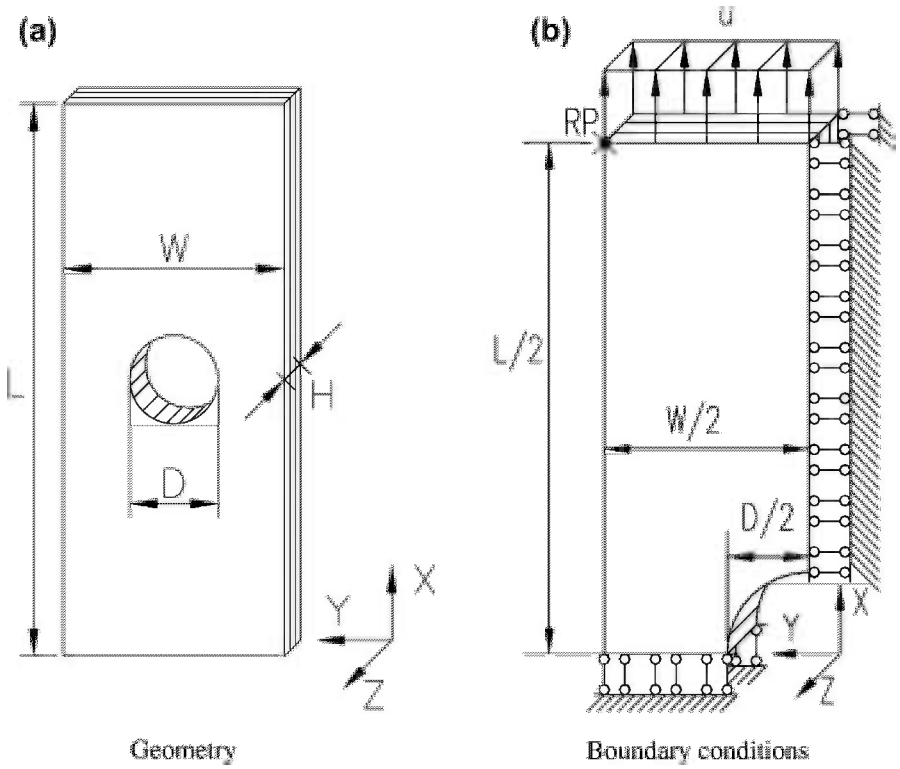


FIGURE 6.28

Geometry and boundary conditions of the composite laminate containing through hole ($L = 203.2$ mm, $H = 2.616$ mm).

AS/3501-5 graphite-epoxy composite have been adopted for the simulations. The appropriateness of such selection has been verified by comparison of the shear stress-strain curve predicted using these parameters and that generated by the shear stress-strain relation suggested by Maimi et al. (2007b) for the material under consideration. The corresponding geometric parameters (hole diameters D and

Table 6.2 Material Properties of T300/1034-C and Model Parameters.

E_1^0	E_2^0	G_{12}^0	ν_{21}^0	$\overline{\sigma}_{1t}$	$\overline{\sigma}_{1c}$	$\overline{\sigma}_{2t}$	$\overline{\sigma}_{2c}$	$\overline{\sigma}_s$
146.8 GPa	11.4 GPa	6.1 GPa	0.3	1730.0 MPa	1379.0 MPa	66.5 MPa	268.2 MPa	58.7 MPa

$G_{1t,c}$	$G_{1c,c}$	$G_{2t,c}$	$G_{2c,c}$	$G_{6,c}$	α	β	n	η
89.83 N/mm	78.27 N/mm	0.23 N/mm	0.76 N/mm	0.46 N/mm	1.25	567.9092	0.272405	0.0002

widths W) are presented in Table 6.3. According to the geometries, the laminates are grouped into four categories, labeled A, B, C, and D in Table 6.3.

The results of the simulations are shown in Table 6.3 and Fig. 6.29. The predicted failure stresses σ_u ($\sigma_u = P_u/(WH)$, where P_u is the failure load) obtained in this study, have been compared with the experimental results reported by Chang et al. (1984) along with the numerical results obtained by Chang and Chang (1987), Tan (1991), and Maimi et al. (2007b). It follows from Table 6.3 that the failure stresses predicted by the simulations performed in this study correlate well with the test data and generally are more accurate compared to the computational predictions made by Chang and Chang (1987), and Tan (1991). The comparison of load versus displacement curves obtained for the laminates from group D (see Table 6.3) using the model presented in this work and those reported by Maimi et al. (2007b) is shown in Fig. 6.29. The differences in the results could be attributable to the fact that in the model proposed by Maimi et al. (2007b) the nonlinear phenomenon observed under shear loading was simulated using only a nonlinear shear stress-strain relationship and the nonlinearity exhibited under transverse loading has been ignored. Also, different damage and failure criteria are adopted in the current model compared to those presented in Maimi et al. (2007b). It follows from these comparisons that the force versus displacement curves predicted by the present model are in good agreement with the experimental and computational results reported in the literature.

All five laminates made from AS4/ PEEK composite have the same lay-up: $[0^\circ/45^\circ/90^\circ/-45^\circ]_{2s}$. The material elastic properties and plastic model parameters were obtained from Sun and Yoon (1992). The compressive strengths were taken from Sun and Rui (1990), whereas the tensile strength and shear strength were obtained from Kawai et al. (2001). The values of the critical strain energies $G_{1t,c}$ and $G_{2t,c}$ were taken from the experimental data reported by Carlile et al. (1989). The value of the parameter $G_{6,c}$ was taken from Donaldson (1985). Using this value, the critical strain energy $G_{2c,c}$ was calculated approximately based on the equation proposed by Maimi et al. (2007b). The values for all these parameters are listed in Table 6.4.

The failure loads predicted by the simulations were compared with the experimental data reported by Maa and Cheng (2002) and also with the results of their numerical analyses based on the so-called "principal damage model" and modified "principal damage model" (see Maa and Cheng (2002)) referred to as Model 1 and Model 2 in this section. As shown in Table 6.5, the results obtained from the simulations based on the present model agree well with the test data. Moreover, it follows from Table 6.5 that these results are more accurate than those obtained using Model 1 and have similar accuracy to those based on Model 2. The corresponding force versus displacement curves are shown in Fig. 6.30. It follows from Table 6.5 that in Maa and Cheng's (2002) study the use of Model 2 substantially improves the predicted results compared to Model 1. This improvement can be attributed to the inclusion of the post-failure fiber damage development process simulation in Model 2. The current model is similar to Maa and Cheng's model in that the in-plane shear behavior is also allowed for using an isotropic hardening plastic model. However, the postfailure development of the shear failure was not considered by Maa and Cheng. In their work, the shear failure was assumed to occur once the shear stress reached the ultimate shear strength and no further damage progression was simulated. Also they did not include any plasticity evolution in the transverse direction, whereas this effect is taken into account by the present model. The comparable good accuracy of the present model and Model 2 (Maa and Cheng, 2002) provides some evidence that consideration of the two significant features, i.e., plasticity and damage development effects, is important when analyzing the progressive failure of composite materials and structures. Although both models provide accurate results in the simulations, it should be

Table 6.3 Comparison of the Tensile Failure Stresses of T300/1034-C Carbon/Epoxy Laminates.

				Failure stress σ_u MPa					Error %			
Lay-up	**Label**	**D (mm)**	**W (mm)**	**Present**	**Chang[a]**	**Tan[a]**	**Maimi**	**Test Data**	**Present**	**Chang**	**Tan**	**Maimi**
$[0/(\pm45)_3/90_3]_s$	A	3.175	19.05	293.07	227.53	275.75	—	277.17	5.74	-17.91	-0.5	—
$[0/(\pm45)_3/90_3]_s$	B	6.35	38.1	252.22	206.84	275.79	—	256.48	-1.66	-19.35	7.53	—
$[0/(\pm45)_3/90_3]_s$	C	3.175	12.7	269.05	206.84	262.00	—	226.15	18.97	-8.54	15.85	—
$[0/(\pm45)_3/90_3]_s$	D	6.35	25.4	238.30[b]	179.26	248.21	263.1[b]	235.80[b]	1.06	-23.98	5.26	11.6
$[0/(\pm45)_2/90_5]_s$	A	3.175	19.05	239.13	193.05	186.16	—	236.49	1.12	-18.37	-21.28	—
$[0/(\pm45)_2/90_5]_s$	B	6.35	38.1	214.30	172.37	186.16	—	204.08	5.00	-15.54	-8.78	—
$[0/(\pm45)_2/90_5]_s$	C	3.175	12.7	216.28	165.47	172.37	—	177.88	21.58	-6.98	-3.10	—
$[0/(\pm45)_2/90_5]_s$	D	6.35	25.4	205.83[b]	151.68	158.58	200.1[b]	185.47[b]	10.98	-18.22	-14.50	7.7
$[0/(\pm45)_1/90_7]_s$	A	3.175	19.05	171.03	144.79	227.53	—	190.98	-10.45	-24.19	19.13	—
$[0/(\pm45)_1/90_7]_s$	B	6.35	38.1	150.36	124.11	227.53	—	158.58	-5.18	-21.74	43.48	—
$[0/(\pm45)_1/90_7]_s$	C	3.175	12.7	154.96	124.11	213.74	—	134.45	15.25	-7.69	58.97	—
$[0/(\pm45)_1/90_7]_s$	D	6.35	25.4	135.67[b]	103.42	199.95	148.2[b]	159.96[b]	-15.19	-35.34	25.00	-7.4

[a] *Chang and Chang (1987) and Tan (1991).*
[b] *The load vs. displacement curves of these analyses using the present and Maimi models are shown in Fig. 6.29.*

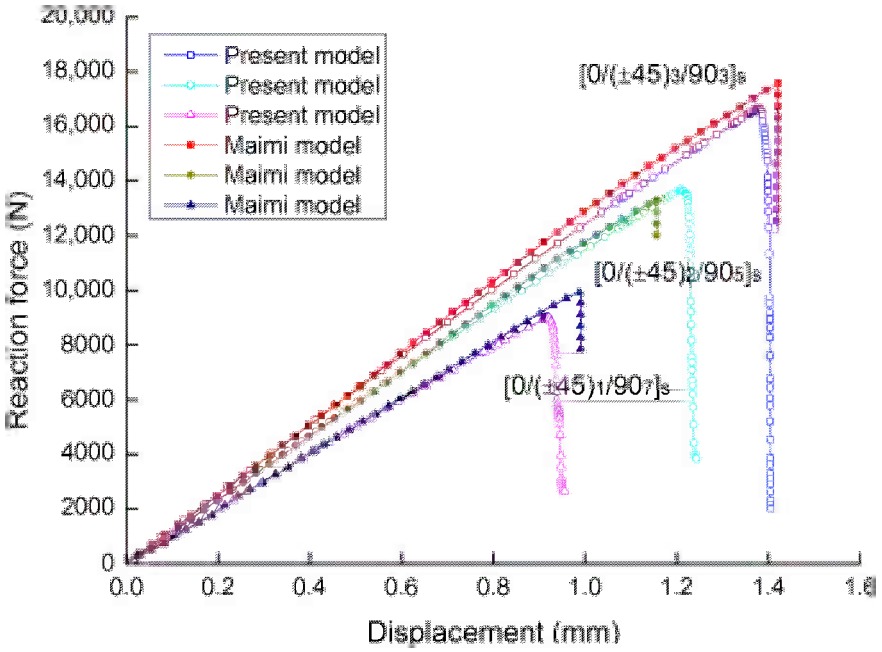


FIGURE 6.29

Comparison of load vs. displacement curves for T300/1034-C composite laminates.

noted that the damage accumulation parameter in Model 2 was obtained as a result of an inverse analysis to match the test data obtained for $[0°/45°/90°/-45°]_{2s}$ laminate with a hole diameter of 5 mm and then applied as an input parameter in the analyses of the other laminates with different hole diameters. From this point of view, one of the substantial advantages of the model presented in this section compared to Model 2 is that all the material properties or parameters are obtained independently for an elementary unidirectional ply. A graphical illustration of the damage evolution characterized by the variation of the damage variables d_1, d_2, d_6 and d_3 in each ply of the laminates under consideration can be found in Chen et al. (2012).

Table 6.4 Material Properties of AS4/PEEK and Model Parameters.

E_1^0	E_2^0	G_{12}^0	v_{21}^0	$\bar{\sigma}_{1t}$	$\bar{\sigma}_{1c}$	$\bar{\sigma}_{2t}$	$\bar{\sigma}_{2c}$	$\bar{\sigma}_s$
127.6 GPa	10.3 GPa	6.0 GPa	0.32	2023.0 MPa	1234.0 MPa	92.7 MPa	176.0 MPa	82.6 MPa

$G_{1t,c}$	$G_{1c,c}$	$G_{2t,c}$	$G_{2c,c}$	$G_{12,c}$	α	β	n	η
128.0 N/mm	128.0 N/mm	5.6 N/mm	9.31 N/mm	4.93 N/mm	1.5	295.0274	0.142857	0.0002

Table 6.5 Comparison of the Failure Loads between Experimental Data and the FE Analyses of AS4/PEEK $[0°/45°/90°/-45°]_{2s}$ Composite Laminates.

	Failure Load *P* (kN)				Error %		
D (mm)	**Test**	**Present**	**Model 1**	**Model 2**	**Present**	**Model 1**	**Model 2**
2	22.98	21.649	19.94	21.69	-5.792	-15.246	-5.614
3	19.31	18.122	13.63	17.65	-6.151	-41.673	-8.597
5	15.31	16.431	12.00	15.34	7.325	-27.583	0.196
8	11.67	13.105	10.06	12.46	12.296	-16.004	6.769
10	9.22	10.581	8.67	10.77	14.768	-6.344	16.811

6.5.5.2 AS4/PEEK $[\pm 45°]_{2s}$ composite laminates

In order to demonstrate the capability of the proposed model to represent the post-failure regime and to validate its ability to reflect on the plasticity behavior, a numerical analysis of the AS4/PEEK $[\pm 45°]_{2s}$ composite laminate subjected to tensile loading has been performed. The length, width, and thickness of the coupon are 230, 20, and 1 mm, respectively. The experimental stress-strain curve for this laminate was obtained by Lafarie-Frenot and Touchard (1994). The results of the simulation and testing are shown in Fig. 6.31. The material properties of the unidirectional AS4/PEEK CFRP material listed in Table 6.4 were adopted in the numerical analysis. It follows from Fig. 6.31 that the

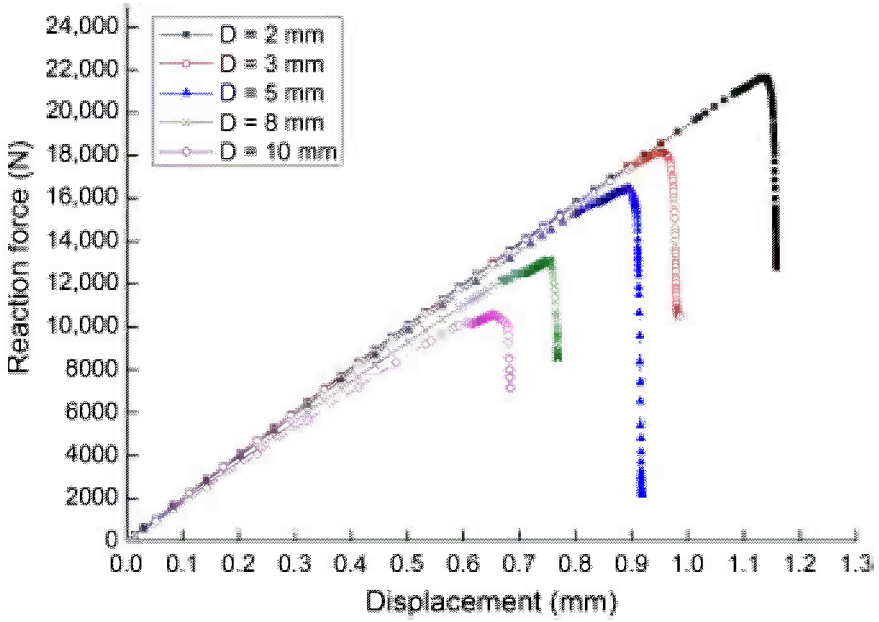


FIGURE 6.30

Predicted load vs. displacement curves of AS4/PEEK $[0°/45°/90°/-45°]_{2s}$ composite laminates.

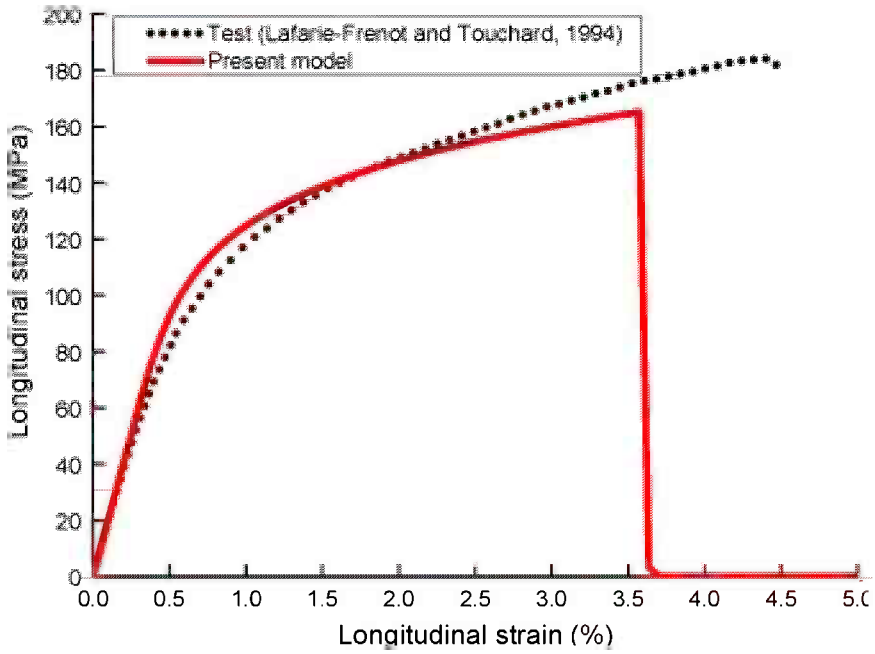


FIGURE 6.31

Comparison of the experimental and predicted stress vs. longitudinal strain curves of AS4/PEEK $[\pm 45^\circ]_{2s}$ composite laminates.

stress-strain curve predicted by the numerical simulation performed in this study correlates well with that obtained from the experimental study.

The aforementioned results of numerical simulations show the capability of the model and numerical procedure discussed in this section in simulating a progressive failure process for composite laminates and capturing and reflecting the key features of the damage initiation and progression.

6.6 References

Annin, B. D., & Baev, L. V. (1979). Criteria of composite material strength. In G. C. Sih, & V. P. Tamuzh (Eds.), *Proceedings of the First USA-USSR Symposium on Fracture of Composite Materials* (pp. 241–254). The Netherlands: Sijthoff & Noordhoff, Riga, USSR, Sept. 1978.

Ashkenazi, E. K. (1966). *Strength of Anisotropic and Synthetic Materials*. Moscow (in Russian): Lesnaya Promyshlennost.

Barbero, E. J. (1998). *Introduction to Composite Materials Design*. USA: West Virginia University.

Bazant, Z. P., & Oh, B. H. (1983). Crack band theory for fracture of concrete. *Materials and Structures, 16*(3), 155–177.

Belyankin, F. P., Yatsenko, V. F., & Margolin, G. G. (1971). *Strength and Deformability of Fiberglass Plastics under Biaxial Compression*. Kiev (in Russian): Naukova Dumka.

Carlile, D. R., Leach, D. C., Moore, D. R., & Zahlan, N. (1989). Mechanical properties of the carbon fiber/PEEK APC-2/AS-4 for structural applications. In *Advances in Thermoplastic Matrix Composite Materials* (pp. 199–212).

Chang, F. K., Scott, R. A., & Springer, G. S. (1984). Strength of bolted joints in laminated composites. *Technical Report AFWAL-TR-84–4029, Air Force Wright Aeronautical Laboratories*.

Chang, F. K., & Chang, K. Y. (1987). A progressive damage model for laminated composites containing stress concentrations. *Journal of Composite Materials, 21*(9), 834–855.

Chen, J. F., Morozov, E. V., & Shankar, K. (2012). A combined elastoplastic damage model for progressive failure analysis of composite materials and structures. *Composite Structures, 94*, 3478–3489.

Chen, J. K., & Sun, C. T. (1987). Nonlinear analysis of interlaminar stress in graphite/epoxy laminates with and without delamination cracks. *Composite Structures, 8*(4), 271–285.

Donaldson, S. L. (1985). Fracture toughness testing of graphite/epoxy and graphite/PEEK composites. *Composites, 16*(2), 103–112.

Drucker, D. C. (1975). Yielding, flow and failure. In C. T. Herakovich (Ed.), *AMD – Vol. 13, Inelastic Behavior of Composite Materials* (pp. 1–15). ASME, New York: ASME Winter Annual Meeting, Houston, TX.

Faria, R., Oliver, J., & Cervera, M. A. (1998). A strain-based plastic viscous-damage model for massive concrete structures. *Int. Journal of Solids and Structures, 35*(14), 1533–1558.

Gol'denblat, I. I., & Kopnov, V. A. (1968). *Criteria of Strength and Plasticity for Structural Materials*. Moscow (in Russian): Mashinostroenie.

Hashin, Z. (1980). Failure criteria for unidirectional fiber composites. *Journal of Applied Mechanics – Transactions of ASME, 47*(2), 329–334.

Hinton, M. J., Kaddour, A. S., & Soden, P. D. (Eds.). (2004). *Failure Criteria in Fibre Reinforced Polymer Composites: the World-Wide Failure Exercise*. Amsterdam: Elsevier.

Jones, R. M. (1999). *Mechanics of Composite Materials* (2nd ed.). Philadelphia, PA: Taylor and Francis.

Katarzhnov, Yu. I. (1982). *Experimental Study of Load Carrying Capacity of Hollow Circular and Box Composite Beams under Compression and Torsion*. Riga (in Russian): PhD thesis.

Kawai, M., Masuko, Y., Kawase, Y., & Negishi, R. (2001). Micromechanical analysis of the off-axis rate-dependent inelastic behavior of unidirectional AS4/PEEK at high temperature. *Int. Journal of Mechanical Sciences, 43*(9), 2069–2090.

Ladeveze, P., & Le Dantec, E. (1992). Damage modelling of the elementary ply for laminated composites. *Composite Science and Technology, 43*(3), 257–267.

Lafarie-Frenot, M. C., & Touchard, F. (1994). Comparative in-plane shear behaviour of long-carbon-fibre composites with thermoset or thermoplastic matrix. *Composite Science and Technology, 52*(3), 417–425.

Lapczyk, I., & Hurtado, J. A. (2007). Progressive damage modeling in fiber-reinforced materials. *Composites, Part A, 38*(11), 2333–2341.

Maa, R. H., & Cheng, J. H. (2002). A CDM-based failure model for predicting strength of notched composite laminates. *Composites, Part B, 33*(6), 479–489.

Maimi, P., Camanho, P. P., Mayugo, J. A., & Dávila, C. G. (2007a). A continuum damage model for composite laminates: Part I – Constitutive model. *Mechanics of Materials, 39*(10), 897–908.

Maimi, P., Camanho, P. P., Mayugo, J. A., & Dávila, C. G. (2007b). A continuum damage model for composite laminates: Part II – Computational implementation and validation. *Mechanics of Materials, 39*(10), 909–919.

Matzenmiller, A., Lubliner, J., & Taylor, R. L. (1995). A constitutive model for anisotropic damage in fiber-composites. *Mechanics of Materials, 20*(2), 125–152.

Morozov, E. V., Chen, J. F., & Shankar, K. (2011). Computational modelling of progressive failure of composite materials and structures including plasticity effects. In E. Oñate, D. R. J. Owen, D. Peric, & B. Suarez (Eds.), *Proceedings of the XI International Conference on Computational Plasticity.* Spain: Barcelona. Fundamentals and Applications (COMPLAS 2011), 7–9 September 2011.

Pinho, S. T. (2005). *Modelling failure of laminated composites using physically-based failure models. PhD thesis*. London, UK: Department of Aeronautics, Imperial College.

Rowlands, R. E. (1975). Flow and failure of biaxially loaded composites: experimental–theoretical correlation. In C. T. Herakovich (Ed.), *AMD – Vol. 13, Inelastic Behavior of Composite Materials* (pp. 97–125). ASME, New York: ASME Winter Annual Meeting, Houston, TX.

Skudra, A. M., Bulavs, F. Ya., Gurvich, M. R., & Kruklinsh, A. A. (1989). *Elements of Structural Mechanics of Composite Truss Systems*. Zinatne (in Russian): Riga.

Sun, C. T., & Chen, J. L. (1989). A simple flow rule for characterizing nonlinear behavior of fiber composites. *Journal of Composite Materials, 23*(10), 1009–1020.

Sun, C. T., & Rui, Y. (1990). Orthotropic elasto-plastic behavior of AS4/PEEK thermoplastic composite in compression. *Mechanics of Materials, 10*(1–2), 117–125.

Sun, C. T., & Yoon, K. J. (1992). Elastic-plastic analysis of AS4/PEEK composite laminate using a one-parameter plasticity model. *Journal of Composite Materials, 26*(2), 293–308.

Tan, S. C. (1991). A progressive failure model for composite laminates containing openings. *Journal of Composite Materials, 25*(5), 556–577.

Tennyson, R. C., Nanyaro, A. P., & Wharram, G. E. (1980). Application of the cubic polynomial strength criterion to the failure analysis of composite materials. *Journal of Composite Materials, 14*(suppl), 28–41.

Tsai, S. W., & Wu, E. M. (1971). A general theory of strength of anisotropic materials. *Journal of Composite Materials, 5*, 58–80.

Tsai, S. W., & Hahn, H. T. (1975). Failure analysis of composite materials. In C. T. Herakovich (Ed.), *AMD – Vol. 13, Inelastic Behavior of Composite Materials* (pp. 73–96). ASME, New York: ASME Winter Annual Meeting, Houston, TX.

Van Der Meer, F. P., & Sluys, L. J. (2009). Continuum models for the analysis of progressive failure in composite laminates. *Journal of Composte Materials, 43*(20), 2131–2156.

Van Paepegem, W., De Baere, I., & Degrieck, J. (2006). Modelling the nonlinear shear stress-strain response of glass fibre-reinforced composites. Part I: Experimental results. *Composite Science and Technology, 66*(10), 1455–1464.

Vasiliev, V. V. (1970). Effect of a local load on an orthotropic glass-reinforced plastic shell. *Polymer Mechanics/ Mechanics of Composite Materials, 6*(1), 80–85.

Vasiliev, V. V. (1993). *Mechanics of Composite Structures*. Washington: Taylor & Francis.

Vicario, A. A., Jr., & Toland, R. H. (1975). Failure criteria and failure analysis of composite structural components. In L. J. Broutman, & R. H. Krock (Eds.), *Composite Materials. Structural Design and Analysis. Part I*, Vol. 7 (pp. 51–97). New York: Academic Press (C.C. Chamis ed.).

Vogler, T. J., & Kyriakides, S. (1999). Inelastic behavior of an AS4/PEEK composite under combined transverse compression and shear. Part I: experiments. *International Journal of Plasticity, 15*(8), 783–806.

Vorobey, V. V., Morozov, E. V., & Tatarnikov, O. V. (1992). *Analysis of Thermostressed Composite Structures*. Moscow (in Russian): Mashinostroenie.

Wang, J., Callus, P. J., & Bannister, M. K. (2004). Experimental and numerical investigation of the tension and compression strength of un-notched and notched quasi-isotropic laminates. *Composite Structures, 64*(3–4), 297–306.

Winn, V. M., & Sridharan, S. (2001). An investigation into the accuracy of a one-parameter nonlinear model for unidirectional composites. *Journal of Composite Materials, 35*(16), 1491–1507.

Wu, E. M. (1974). Phenomenological anisotropic failure criterion. In L. J. Broutman, & R. H. Krock (Eds.), *Composite Materials. Mechanics of Composite Materials*, Vol. 2 (pp. 353–431). New York: Academic Press (G.P. Sendecky ed.).

CHAPTER

Environmental, special loading, and manufacturing effects

7

The properties of composite materials, as well as those of all structural materials, are affected by environmental and operational conditions. Moreover, for polymeric composites, this influence is more pronounced than for conventional metal alloys, because polymers are more sensitive to temperature, moisture, and time than are metals. There is also a specific feature of composites associated with the fact that they do not exist apart from composite structures and are formed while these structures are fabricated. As a result, the material characteristics depend on the type and parameters of the manufacturing process; e.g., unidirectional composites made by pultrusion, hand lay-up, and filament winding can demonstrate different properties.

This section of the book is concerned with the effect of environmental, loading, and manufacturing factors on the mechanical properties and behavior of composites.

7.1 TEMPERATURE EFFECTS

Temperature is the most important of the environmental factors affecting the behavior of composite materials. First of all, polymeric composites are rather sensitive to temperature and have relatively low thermal conductivity. This combination of properties allows us, on one hand, to use these materials in structures subjected to short-term heating, and on the other hand, requires the analysis of these structures to be performed with due regard to temperature effects. Secondly, there exist composite materials, e.g., carbon-carbon and ceramic composites that are specifically developed for operation under intense heating, and materials such as mineral-fiber composites, that are used to form heatproof layers and coatings. Thirdly, the fabrication of composite structures is usually accompanied by more or less intensive heating (e.g., for curing or carbonization), and the subsequent cooling induces thermal stresses and strains, to calculate which we need to utilize the equations of thermal conductivity and thermoelasticity as discussed below.

7.1.1 Thermal conductivity

Heat flow through a unit area of a surface with normal n is related to the temperature gradient in the n direction according to Fourier's law as

$$q = -\lambda \frac{\partial T}{\partial n} \tag{7.1}$$

Advanced Mechanics of Composite Materials and Structural Elements. http://dx.doi.org/10.1016/B978-0-08-098231-1.00007-8
Copyright © 2013 Elsevier Ltd. All rights reserved.

where λ is the thermal conductivity of the material. The temperature distribution along the n-axis is governed by the following equation:

$$\frac{\partial}{\partial n}\left(\lambda \frac{\partial T}{\partial n}\right) = c\rho \frac{\partial T}{\partial t} \tag{7.2}$$

in which c and ρ are the specific heat and density of the material, and t is time. For a steady (time-independent) temperature distribution, $\partial T/\partial t = 0$, and Eq. (7.2) yields

$$T = C_1 \int \frac{dn}{\lambda} + C_2 \tag{7.3}$$

Consider a laminated structure referred to coordinates x, z as shown in Fig. 7.1. To determine the temperature distribution along the x-axis only, we should take into account that λ does not depend on x, and assume that T does not depend on z. Using conditions $T(x = 0) = T_0$ and $T(x = l) = T_l$ to find the constants C_1 and C_2 in Eq. (7.3), in which $n = x$, we get

$$T = T_0 + \frac{x}{l}(T_l - T_0)$$

Introduce the apparent thermal conductivity of the laminate in the x direction, λ_x, and write Eq. (7.1) for the laminate as

$$q_x = -\lambda_x \frac{T_l - T_0}{l}$$

The same equation can be written for the ith layer, i.e.,

$$q_i = -\lambda_i \frac{T_l - T_0}{l}$$

The total heat flow through the laminate in the x direction is

$$q_x h = \sum_{i=1}^{k} q_i h_i$$

Combining the foregoing results, we arrive at

$$\lambda_x = \sum_{i=1}^{k} \lambda_i \overline{h}_i \tag{7.4}$$

where $\overline{h}_i = h_i/h$.

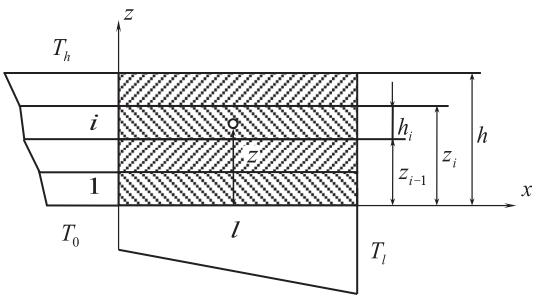


FIGURE 7.1

Temperature distribution in a laminate.

Consider the heat transfer in the z direction and introduce the apparent thermal conductivity λ_z in accordance with the following form of Eq. (7.1)

$$q_z = -\lambda_z \frac{T_h - T_0}{h} \tag{7.5}$$

Taking $n = z$ and $\lambda = \lambda_i$ for $z_{i-1} \le z \le z_i$ in Eq. (7.3) and using step-wise integration and the conditions $T(z = 0) = T_0$, $T(z = h) = T_h$ to find constants C_1, and C_2, we obtain for the ith layer

$$T_i = T_0 + \frac{T_h - T_0}{\sum_{i=1}^{k} \frac{h_i}{\lambda_i}} \left(\frac{z - z_{i-1}}{\lambda_i} + \sum_{j=1}^{i-1} \frac{h_j}{\lambda_j} \right) \tag{7.6}$$

The heat flow through the ith layer follows from Eqs. (7.1) and (7.6), i.e.,

$$q_i = -\lambda_i \frac{\partial T_i}{\partial z} = -\frac{T_h - T_0}{\sum_{i=1}^{k} \frac{h_i}{\lambda_i}}$$

Obviously, $q_i = q_z$ (see Fig. 7.1), and with due regard to Eq. (7.5)

$$\frac{1}{\lambda_z} = \sum_{i=1}^{k} \frac{\overline{h}_i}{\lambda_i} \tag{7.7}$$

where, as earlier, $\overline{h}_i = h_i/h$.

The results obtained, Eqs. (7.4) and (7.7), can be used to determine the thermal conductivity of a unidirectional composite ply. Indeed, comparing Fig. 7.1 with Fig. 3.34 showing the structure of the first-order ply model, we can write the following equations specifying thermal conductivity of a unidirectional ply along and across the fibers:

$$\begin{aligned} \lambda_1 &= \lambda_{1f} v_f + \lambda_m v_m \\ \frac{1}{\lambda_2} &= \frac{v_f}{\lambda_{2f}} + \frac{v_m}{\lambda_m} \end{aligned} \tag{7.8}$$

Here, λ_{1f} and λ_{2f} are the thermal conductivities of the fiber in the longitudinal and transverse directions (for some fibers they are different), λ_m is the corresponding characteristic of the matrix, and v_f, $v_m = 1 - v_f$ are the fiber and matrix volume fractions, respectively. The conductivity coefficients in Eqs. (7.8) are analogous to elastic constants specified by Eqs. (3.76) and (3.78), and the discussion presented in Section 3.3 is valid for Eqs. (7.8) as well. In particular, it should be noted that application of higher-order microstructural models has practically no effect on λ_1 but substantially improves λ_2, determined by Eqs. (7.8). Typical properties for unidirectional and fabric composites are listed in Table 7.1.

Consider heat transfer in an orthotropic ply or layer in coordinate frame x, y whose axes x and y make angle ϕ with the principal material coordinates x_1 and x_2, as in Fig. 7.2. Heat flows in coordinates x, y and x_1, x_2 are linked by the following equations:

$$q_x = q_1 \cos\phi - q_2 \sin\phi, \quad q_y = q_1 \sin\phi + q_2 \cos\phi \tag{7.9}$$

Table 7.1 Typical Thermal Conductivity and Expansion Coefficients of Composite Materials.

Property	Glass-epoxy	Carbon-epoxy	Aramid-epoxy	Boron-epoxy	Glass fabric-epoxy	Aramid fabric-epoxy
Longitudinal conductivity λ_1 (W/m K)	0.6	1	0.17	0.5	0.35	0.13
Transverse conductivity λ_2 (W/m K)	0.4	0.6	0.1	0.3	0.35	0.13
Longitudinal CTE 10^6 α_1 (1/°C)	7.4	−0.3	−3.6	4.1	8	0.8
Transverse CTE 10^6 α_2 (1/°C)	22.4	34	60	19.2	8	0.8

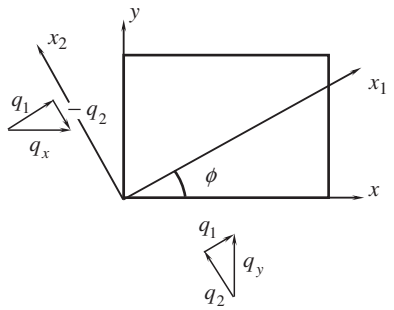


FIGURE 7.2

Heat flows in coordinates x, y and x_1, x_2.

Here, in accordance with Eq. (7.1)

$$q_1 = -\lambda_1 \frac{\partial T}{\partial x_1}, \quad q_2 = -\lambda_2 \frac{\partial T}{\partial x_2}$$

Changing variables x_1, x_2 to x, y with the aid of the following transformation relationships

$$x = x_1 \cos\phi - x_2 \sin\phi, \quad y = x_1 \sin\phi + x_2 \cos\phi$$

and substituting q_1 and q_2 into Eqs. (7.9), we arrive at

$$q_x = -\lambda_x \frac{\partial T}{\partial x} - \lambda_{xy} \frac{\partial T}{\partial y}, \quad q_y = -\lambda_y \frac{\partial T}{\partial y} + \lambda_{xy} \frac{\partial T}{\partial x}$$

where

$$\begin{aligned} \lambda_x &= \lambda_1 \cos^2\phi + \lambda_2 \sin^2\phi \\ \lambda_y &= \lambda_1 \sin^2\phi + \lambda_2 \cos^2\phi \\ \lambda_{xy} &= (\lambda_2 - \lambda_1) \sin\phi \cos\phi \end{aligned} \tag{7.10}$$

can be treated as the ply thermal conductivities in coordinates x, y. Since the ply is anisotropic in these coordinates, the heat flow in for example, the x direction induces a temperature gradient not only in the x direction, but in the y direction as well. Using Eq. (7.4), we can now determine the in-plane thermal conductivities of the laminate as

$$\Lambda_x = \sum_{i=1}^{k} \lambda_x^{(i)} \overline{h}_i, \quad \Lambda_y = \sum_{i=1}^{k} \lambda_y^{(i)} \overline{h}_i, \qquad \Lambda_{xy} = \sum_{i=1}^{k} \lambda_{xy}^{(i)} \overline{h}_i \tag{7.11}$$

where $\lambda_{x,y}^{(i)}$ are specified by Eqs. (7.10) in which $\lambda_{1,2} = \lambda_{1,2}^{(i)}$ and $\phi = \phi_i$. For $\pm\phi$ angle-ply laminates that are orthotropic, $\Lambda_{xy} = 0$.

As an example, consider the composite body of a space telescope, a section of which is shown in Fig. 7.3. The cylinder having diameter $D = 1$ m and total thickness $h = 13.52$ mm consists of four layers, i.e.,

- $\pm\phi_s$ angle-ply carbon-epoxy external skin with the following parameters:

$$\phi_s = 20^\circ, \quad h_s^e = 3.5 \text{ mm}, \quad E_1^e = 120 \text{ GPa},$$
$$E_2^e = 11 \text{ GPa}, \quad G_{12}^e = 5.5 \text{ GPa}, \quad \nu_{21}^e = 0.27,$$
$$\lambda_1^e = 1 \text{ W/m K}, \quad \lambda_2^e = 0.6 \text{ W/m K},$$
$$\alpha_1^e = -0.3 \cdot 10^{-6} \text{ 1/°C}, \quad \alpha_2^e = 34 \cdot 10^{-6} \text{ 1/°C},$$

- carbon-epoxy lattice layer (see Fig. 4.93) formed by a system of $\pm\phi_r$ helical ribs with

$$\phi_r = 26^\circ, \quad h_r = 9 \text{ mm}, \quad \delta_r = 4 \text{ mm}, \quad a_r = 52 \text{ mm}, \quad E_r = 80 \text{ GPa},$$
$$\lambda_r = 0.9 \text{ W/m K}, \quad \alpha_r = -1 \cdot 10^{-6} \text{ 1/°C},$$



FIGURE 7.3

A composite section of a space telescope.

Courtesy of CRISM.

- internal skin made of aramid fabric with

$$h_s^i = 1 \text{ mm}, \quad E_x^i = E_y^i = 34 \text{ GPa}, \quad G_{xy}^i = 5.6 \text{ GPa},$$
$$\nu_{xy}^i = \nu_{yx}^i = 0.15, \quad \lambda_x^i = \lambda_y^i = 0.13 \text{ W/m K},$$

  $\alpha_x^i = \alpha_y^i = 0.8 \cdot 10^{-6}$ 1/°C (x and y are the axial and the circumferential coordinates of the cylinder),
- internal layer of aluminum foil with

$$h_f = 0.02 \text{ mm}, \quad E_f = 70 \text{ GPa}, \quad \nu_f = 3.0,$$
$$\lambda_f = 210 \text{ W/m K}, \quad \alpha_f = 22.3 \cdot 10^{-6} \text{ 1/°C}$$

The apparent thermal conductivity of the cylinder wall can be found with the aid of Eqs. (7.10), (7.11), and the continuum model of the lattice layer described in Section 4.8 as

$$\Lambda_x = \frac{1}{h}\left[\left(\lambda_1^e \cos^2\phi_e + \lambda_2^e \sin^2\phi_e\right)h_s^e + \frac{2}{a_r} h_r \delta_r \lambda_r \cos^2\phi_r + \lambda_x^i h_s^i + \lambda_f h_f\right]$$

Calculation yields $\Lambda_x = 0.64$ W/m K. The thermal resistance of a unit length of this structure is

$$r_x = \frac{1}{\Lambda_x \pi D h} = 36.8 \frac{\text{K}}{\text{W m}}$$

7.1.2 Thermoelasticity

It is known that heating gives rise to thermal strains that, when restricted, induce thermal stresses. Assume that the temperature distribution in a composite structure is known, and consider the problem of thermoelasticity.

Consider first the thermoelastic behavior of a unidirectional composite ply studied in Section 3.3 and shown in Fig. 3.29. The generalized Hooke's law, Eqs. (3.58), allowing for temperature effects, can be written as

$$\varepsilon_{1T} = \varepsilon_1 + \varepsilon_1^T, \quad \varepsilon_{2T} = \varepsilon_2 + \varepsilon_2^T, \quad \gamma_{12T} = \gamma_{12} \tag{7.12}$$

Here and subsequently, the subscript "T" shows the strains that correspond to the problem of thermoelasticity, whereas the superscript "T" indicates temperature terms. Elastic strains ε_1, ε_2, and γ_{12} in Eqs. (7.12) are related to stresses by Eqs. (3.58). Temperature strains, to a first approximation, can be taken as linear functions of the temperature change, i.e.,

$$\varepsilon_1^T = \alpha_1 \Delta T, \quad \varepsilon_2^T = \alpha_2 \Delta T, \tag{7.13}$$

where α_1 and α_2 are the coefficients of thermal expansion (CTE) along and across the fibers, and $\Delta T = T - T_0$ is the difference between the current temperature T and some initial temperature T_0 at which thermal strains are zero. The inverse form of Eqs. (7.12) is

$$\begin{aligned}
\sigma_1 &= \overline{E}_1\left(\varepsilon_{1T} + \nu_{12}\varepsilon_{2T}\right) - \overline{E}_1\left(\varepsilon_1^T + \nu_{12}\varepsilon_2^T\right) \\
\sigma_2 &= \overline{E}_2\left(\varepsilon_{2T} + \nu_{21}\varepsilon_{1T}\right) - \overline{E}_2\left(\varepsilon_2^T + \nu_{21}\varepsilon_1^T\right) \\
\tau_{12} &= G_{12}\gamma_{12T}
\end{aligned} \tag{7.14}$$

where $\overline{E}_{1,2} = E_{1,2}/(1 - \nu_{12}\nu_{21})$.

To describe the thermoelastic behavior of a ply, apply the first-order micromechanical model shown in Fig. 3.34. Since the CTE (and elastic constants) of some fibers can be different in the longitudinal and transverse directions, generalize the first two equations of Eqs. (3.63) as

$$\begin{aligned}\varepsilon_{1T}^{f,m} &= \frac{1}{E_{f1,m}}\left(\sigma_1^{f,m} - \nu_{f2,m}\sigma_2^{f,m}\right) + \alpha_{f1,m}\Delta T \\ \varepsilon_{2T}^{f,m} &= \frac{1}{E_{f2,m}}\left(\sigma_2^{f,m} - \nu_{f1,m}\sigma_1^{f,m}\right) + \alpha_{f2,m}\Delta T\end{aligned} \tag{7.15}$$

Repeating the derivation of Eqs. (3.76)–(3.79), we arrive at

$$\begin{aligned}&E_1 = E_{f1}\upsilon_f + E_m\upsilon_m, \quad \nu_{21} = \nu_{f2}\upsilon_f + \nu_m\upsilon_m \\ &\frac{1}{E_2} = (1 - \nu_{f1}\nu_{f2})\frac{\upsilon_f}{E_{f2}} + \left(1 - \nu_m^2\right)\frac{\upsilon_m}{E_m} + \frac{\nu_{21}^2}{E_1} \\ &\alpha_1 = \frac{1}{E_1}(E_{f1}\alpha_{f1}\upsilon_f + E_m\alpha_m\upsilon_m) \\ &\alpha_2 = \left(\alpha_{f2} + \nu_{f2}\alpha_{f1}\right)\upsilon_f + \left(1 + \upsilon_m\right)\alpha_m\upsilon_m - \nu_{21}\alpha_1\end{aligned} \tag{7.16}$$

These equations generalize Eqs. (3.76)–(3.79) for the case of anisotropic fibers and specify the apparent CTE of a unidirectional ply.

As an example, consider the high-modulus carbon-epoxy composite tested by Rogers et al. (1977). The microstructural parameters for this material are as follows

$$E_{f1} = 411 \text{ GPa}, \quad E_{f2} = 6.6 \text{ GPa}, \quad \nu_{f1} = 0.06$$
$$\nu_{f2} = 0.35, \quad \alpha_{f1} = -1.2 \cdot 10^{-6}\ 1/^\circ\text{C}, \quad \alpha_{f2} = 27.3 \cdot 10^{-6}\ 1/^\circ\text{C}$$
$$E_m = 5.7 \text{ Gpa}, \quad \nu_m = 0.316, \quad \alpha_m = 45 \cdot 10^{-6}\ 1/^\circ\text{C}, \quad \upsilon_f = \upsilon_m = 0.5$$

($T = 27^\circ\text{C}$). For these properties, Eqs. (7.16) yield

$$E_1 = 208.3 \text{ GPa}, \quad E_2 = 6.5 \text{ GPa}, \quad \nu_{21} = 0.33$$
$$\alpha_1 = -0.57 \cdot 10^{-6}\ 1/^\circ\text{C}, \quad \alpha_2 = 43.4 \cdot 10^{-6}\ 1/^\circ\text{C}$$

whereas the experimental results were

$$E_1 = 208.6 \text{ GPa}, \quad E_2 = 6.3 \text{ GPa}, \quad \nu_{21} = 0.33$$
$$\alpha_1 = -0.5 \cdot 10^{-6}\ 1/^\circ\text{C}, \quad \alpha_2 = 29.3 \cdot 10^{-6}\ 1/^\circ\text{C}$$

Thus, it can be concluded that the first-order microstructural model provides good results for the longitudinal material characteristics, but fails to predict α_2 with the required accuracy. The discussion and conclusions concerning this problem presented in Section 3.3 for elastic constants are valid for thermal expansion coefficients as well. For practical applications, α_1 and α_2 are normally determined by experimental methods. However, in contrast to the elasticity problem for which the knowledge of experimental elastic constants and material strength excludes consideration of the micromechanical models, for the thermoelasticity problems these models provide us with useful information even if we know the experimental thermal expansion coefficients. Indeed, consider a unidirectional ply that is

subjected to uniform heating that induces only thermal strains, i.e., $\varepsilon_{1T} = \varepsilon_1^T$, $\varepsilon_{2T} = \varepsilon_2^T$, and $\gamma_{12T} = 0$. Then, Eqs. (7.14) yield $\sigma_1 = 0$, $\sigma_2 = 0$, and $\tau_{12} = 0$. For homogeneous materials, this means that no stresses occur under uniform heating. However, this is not the case for a composite ply. Generalizing Eqs. (3.74) that specify longitudinal stresses in the fibers and in the matrix, we obtain

$$\sigma_1^f = E_{f1}(\alpha_1 - \alpha_{f1})\Delta T, \quad \sigma_1^m = E_m(\alpha_1 - \alpha_m)\Delta T$$

where α_1 and α_2 are specified by Eqs. (7.16). Thus, because the thermal expansion coefficients of the fibers and the matrix are different from those of the material, there exist microstructural thermal stresses in the composite structural elements. These stresses are self-balanced.

Indeed,

$$\sigma_1 = \sigma_1^f v_f + \sigma_1^m v_m = 0$$

Consider an orthotropic layer referred to coordinate axes x, y making angle ϕ with the principal material coordinate axes (see Fig. 7.2). Using Eqs. (7.14) instead of Eqs. (4.56) and repeating the derivation of Eqs. (4.71), we arrive at

$$\begin{aligned}
\sigma_x &= A_{11}\varepsilon_{xT} + A_{12}\varepsilon_{yT} + A_{14}\gamma_{xyT} - A_{11}^T \\
\sigma_y &= A_{21}\varepsilon_{xT} + A_{22}\varepsilon_{yT} + A_{24}\gamma_{xyT} - A_{22}^T \\
\tau_{xy} &= A_{41}\varepsilon_{xT} + A_{42}\varepsilon_{yT} + A_{44}\gamma_{xyT} - A_{12}^T
\end{aligned} \tag{7.17}$$

where A_{mn} are specified by Eqs. (4.72) and the thermal terms are

$$\begin{aligned}
A_{11}^T &= \overline{E}_1\varepsilon_{12}^T \cos^2\phi + \overline{E}_2\varepsilon_{21}^T \sin^2\phi \\
A_{22}^T &= \overline{E}_1\varepsilon_{12}^T \sin^2\phi + \overline{E}_2\varepsilon_{21}^T \cos^2\phi \\
A_{12}^T &= \left(\overline{E}_1\varepsilon_{12}^T - \overline{E}_2\varepsilon_{21}^T\right) \sin\phi \cos\phi
\end{aligned} \tag{7.18}$$

Here,

$$\varepsilon_{12}^T = \varepsilon_1^T + \nu_{12}\varepsilon_2^T, \quad \varepsilon_{21}^T = \varepsilon_2^T + \nu_{21}\varepsilon_1^T$$

and ε_1^T, ε_2^T are determined by Eqs. (7.13). The inverse form of Eqs. (7.17) is

$$\varepsilon_{xT} = \varepsilon_x + \varepsilon_x^T, \quad \varepsilon_{yT} = \varepsilon_y + \varepsilon_y^T, \quad \gamma_{xyT} = \gamma_{xy} + \gamma_{xy}^T \tag{7.19}$$

Here, ε_x, ε_y, and γ_{xy} are expressed in terms of stresses σ_x, σ_y, and τ_{xy} by Eqs. (4.75), whereas the thermal strains are

$$\begin{aligned}
\varepsilon_x^T &= \varepsilon_1^T \cos^2\phi + \varepsilon_2^T \sin^2\phi \\
\varepsilon_y^T &= \varepsilon_1^T \sin^2\phi + \varepsilon_2^T \cos^2\phi \\
\gamma_{xy}^T &= \left(\varepsilon_1^T - \varepsilon_2^T\right) \sin 2\phi
\end{aligned}$$

Introducing thermal expansion coefficients in the xy coordinate frame with the following equations

$$\varepsilon_x^T = \alpha_x\Delta T, \quad \varepsilon_y^T = \alpha_y\Delta T, \quad \gamma_{xy}^T = \alpha_{xy}\Delta T \tag{7.20}$$

and using Eqs. (7.13), we obtain

$$\begin{aligned}\alpha_x &= \alpha_1 \cos^2\phi + \alpha_2 \sin^2\phi \\ \alpha_y &= \alpha_1 \sin^2\phi + \alpha_2 \cos^2\phi \\ \alpha_{xy} &= (\alpha_1 - \alpha_2) \sin 2\phi\end{aligned} \tag{7.21}$$

It follows from Eqs. (7.19) that, in an anisotropic layer, uniform heating induces not only normal strains, but also a shear thermal strain. As can be seen in Fig. 7.4, Eqs. (7.21) provide fair agreement with the experimental results of Barnes et al. (1989) for composites with carbon fibers and thermoplastic matrix (dashed line and light circles).

Consider a symmetric $\pm\phi$ angle-ply layer (see Section 4.5.1). This layer is orthotropic, and the corresponding constitutive equations of thermoelasticity have the form of Eqs. (7.17) in which $A_{14} = A_{41} = 0$, $A_{24} = A_{42} = 0$, and $A_{12}^T = 0$. The inverse form of these equations is

$$\varepsilon_{xT} = \varepsilon_x + \varepsilon_x^T, \quad \varepsilon_{yT} = \varepsilon_y + \varepsilon_y^T, \quad \gamma_{xyT} = \gamma_{xy}$$

where ε_x, ε_y, and γ_{xy} are expressed in terms of stresses by Eqs. (4.146), whereas the thermal strains are

$$\varepsilon_x^T = \frac{A_{11}^T A_{22} - A_{22}^T A_{12}}{A_{11}A_{22} - A_{12}^2}, \quad \varepsilon_y^T = \frac{A_{22}^T A_{11} - A_{11}^T A_{12}}{A_{11}A_{22} - A_{12}^2}$$

Using Eqs. (4.147), (7.13), (7.18), and (7.20), we arrive at the following expressions for apparent thermal expansion coefficients

$$\alpha_x = \frac{1}{E_x}\left(a_{11}^T - \nu_{yx} a_{22}^T\right), \quad \alpha_y = \frac{1}{E_y}\left(a_{22}^T - \nu_{xy} a_{11}^T\right) \tag{7.22}$$

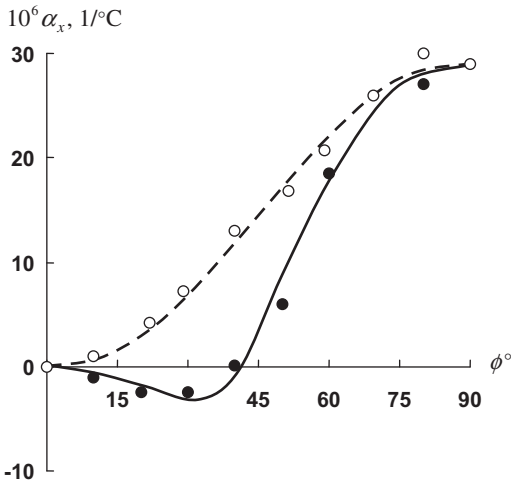


FIGURE 7.4

Calculated (dots) and experimental (circles) dependencies of thermal expansion coefficients on the ply orientation angle for unidirectional thermoplastic carbon composite (– – –, ○) and a $\pm\phi$ angle-ply layer (———, ●).

in which

$$a_{11}^T = \overline{E}_1(\alpha_1 + \nu_{12}\alpha_2)\cos^2\phi + \overline{E}_2(\alpha_2 + \nu_{21}\alpha_1)\sin^2\phi$$
$$a_{22}^T = \overline{E}_1(\alpha_1 + \nu_{12}\alpha_2)\sin^2\phi + \overline{E}_2(\alpha_2 + \nu_{21}\alpha_1)\cos^2\phi$$

Comparison of α_x with the experimental results of Barnes et al. (1989) for a thermoplastic carbon composite is presented in Fig. 7.4 (solid line and dots). As can be seen in this figure, there exists an interval $(0 \le \phi \le 40^\circ)$ within which the coefficient α_x of the angle-ply layer is negative. The same type of behavior is demonstrated by aramid-epoxy angle-ply composites. A comparison of calculated values based on Eqs. (7.22) with the experimental results of Strife and Prevo (1979) is presented in Fig. 7.5. Looking at Figs. 7.4 and 7.5, we can hypothesize that supplementing an angle-ply laminate with plies having small thermal elongations in the x direction, we can synthesize composite materials with zero thermal expansion in this direction. Such materials are important, for example, for space telescopes (Fig. 7.3), antennas, measuring instruments, and other high-precision, thermally stable structures (Hamilton and Patterson, 1993).

Consider laminates with arbitrary structural parameters (see Chapter 5). Repeating the derivation of Eqs. (5.5) and using the thermoelasticity constitutive equations, Eqs. (7.17), instead of Eqs. (4.71), we arrive at

$$\begin{aligned}
N_x &= B_{11}\varepsilon_{xT}^0 + B_{12}\varepsilon_{yT}^0 + B_{14}\gamma_{xyT}^0 + C_{11}\kappa_{xT} + C_{12}\kappa_{yT} + C_{14}\kappa_{xyT} - N_{11}^T \\
N_y &= B_{21}\varepsilon_{xT}^0 + B_{22}\varepsilon_{yT}^0 + B_{24}\gamma_{xyT}^0 + C_{21}\kappa_{xT} + C_{22}\kappa_{yT} + C_{24}\kappa_{xyT} - N_{22}^T \\
N_{xy} &= B_{41}\varepsilon_{xT}^0 + B_{42}\varepsilon_{yT}^0 + B_{44}\gamma_{xyT}^0 + C_{41}\kappa_{xT} + C_{42}\kappa_{yT} + C_{44}\kappa_{xyT} - N_{12}^T \\
M_x &= C_{11}\varepsilon_{xT}^0 + C_{12}\varepsilon_{yT}^0 + C_{14}\gamma_{xyT}^0 + D_{11}\kappa_{xT} + D_{12}\kappa_{yT} + D_{14}\kappa_{xyT} - M_{11}^T \\
M_y &= C_{21}\varepsilon_{xT}^0 + C_{22}\varepsilon_{yT}^0 + C_{24}\gamma_{xyT}^0 + D_{21}\kappa_{xT} + D_{22}\kappa_{yT} + D_{24}\kappa_{xyT} - M_{22}^T \\
M_{xy} &= C_{41}\varepsilon_{xT}^0 + C_{42}\varepsilon_{yT}^0 + C_{44}\gamma_{xyT}^0 + D_{41}\kappa_{xT} + D_{42}\kappa_{yT} + D_{44}\kappa_{xyT} - M_{12}^T
\end{aligned} \tag{7.23}$$

These equations should be supplemented with Eqs. (5.15) for transverse shear forces, i.e.,

$$V_x = S_{55}\gamma_{xT} + S_{56}\gamma_{yT}, \quad V_y = S_{65}\gamma_{xT} + S_{66}\gamma_{yT} \tag{7.24}$$

The temperature terms entering Eqs. (7.23) have the following form

$$N_{mn}^T = \int_{-e}^{s} A_{mn}^T dz, \quad M_{mn}^T = \int_{-e}^{s} A_{mn}^T z dz$$

where A_{mn}^T are specified by Eqs. (7.18). Performing the transformation that is used in Section 5.1 to reduce Eqs. (5.6), (5.7), and (5.8) to Eqs. (5.28) and (5.29), we get

$$N_{mn}^T = J_{mn}^{(0)}, \quad M_{mn}^T = J_{mn}^{(1)} - eJ_{mn}^{(0)} \tag{7.25}$$

Here (see Fig. 5.8),

$$J_{mn}^{(r)} = \int_0^h A_{mn}^T t^r dt, \tag{7.26}$$

where $r = 0,\ 1$ and $mn = 11,\ 12,\ 22$.

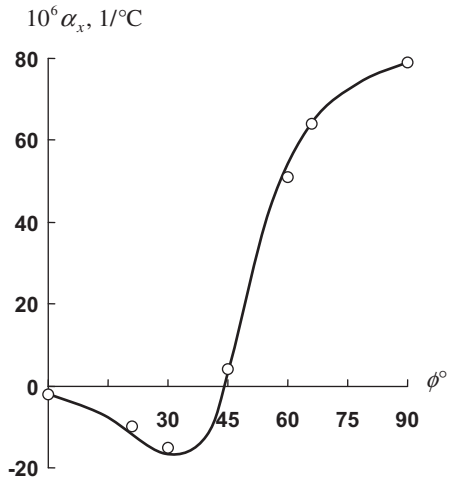


FIGURE 7.5

Calculated (line) and experimental (circles) dependencies of thermal expansion coefficient on the ply orientation angle for an aramid-epoxy $\pm\phi$ angle-ply layer.

For a laminate, the temperature governed by Eq. (7.6) is linearly distributed over the layers' thicknesses (see Fig. 7.1). The same law can obviously be assumed for the temperature coefficients in Eqs. (7.18), i.e., for the ith layer in Fig. 5.10

$$A_{mn}^{Ti} = \left(A_{mn}^{T}\right)_{i-1} + \frac{1}{h_i}\left[\left(A_{mn}^{T}\right)_{i} - \left(A_{mn}^{T}\right)_{i-1}\right](t - t_{i-1})$$

where $(A_{mn}^{T})_{i-1} = A_{mn}^{T}(t = t_{i-1})$ and $(A_{mn}^{T})_{i} = A_{mn}^{T}(t = t_i)$. Then, Eq. (7.26) takes the form

$$J_{mn}^{(r)} = \sum_{i=1}^{k} \frac{1}{h_i}\left\{\left[\left(A_{mn}^{T}\right)_{i-1} t_i - \left(A_{mn}^{T}\right)_{i} t_{i-1}\right]\frac{t_i^{r+1} - t_{i-1}^{r+1}}{r+1} + \left[\left(A_{mn}^{T}\right)_{i} - \left(A_{mn}^{T}\right)_{i-1}\right]\frac{t_i^{r+2} - t_{i-1}^{r+2}}{r+2}\right\}$$

If the temperature variation over the thickness of the ith layer can be neglected, we can introduce some average value

$$\left(\overline{A}_{mn}^{T}\right)_{i} = \frac{1}{2}\left[\left(A_{mn}^{T}\right)_{i-1} + \left(A_{mn}^{T}\right)_{i}\right]$$

and present Eq. (7.26) as

$$J_{mn}^{(r)} = \frac{1}{r+1}\sum_{i=1}^{k}\left(\overline{A}_{mn}^{T}\right)_{i}\left(t_i^{r+1} - t_{i-1}^{r+1}\right) \tag{7.27}$$

Total (elastic and thermal) generalized strains ε_T, γ_T, and κ_T entering Eqs. (7.23) and (7.24) can be expressed in terms of the displacements and rotational angles of the laminate element with the aid of Eqs. (5.3) and (5.14), i.e.,

$$\varepsilon_{xT}^0 = \frac{\partial u}{\partial x}, \quad \varepsilon_{yT}^0 = \frac{\partial v}{\partial y}, \quad \gamma_{xyT}^0 = \frac{\partial u}{\partial y} + \frac{\partial v}{\partial x} \tag{7.28}$$

$$\kappa_{xT} = \frac{\partial \theta_x}{\partial x}, \quad \kappa_{yT} = \frac{\partial \theta_y}{\partial y}, \quad \kappa_{xyT} = \frac{\partial \theta_x}{\partial y} + \frac{\partial \theta_y}{\partial x} \tag{7.29}$$

$$\gamma_{xT} = \theta_x + \frac{\partial w}{\partial x}, \quad \gamma_{yT} = \theta_y + \frac{\partial w}{\partial y} \tag{7.30}$$

It follows from Eqs. (7.23) that, in the general case, uniform heating of laminates induces, in contrast to homogeneous materials, not only in-plane strains but also changes to the laminate curvatures and twist. Indeed, assume that the laminate is free from edge and surface loads so that forces and moments in the left-hand sides of Eqs. (7.23) are equal to zero. Since the CTE of the layers, in the general case, are different, the thermal terms N^T and M^T in the right-hand sides of Eqs. (7.23) are not equal to zero even for a uniform temperature field, and these equations enable us to find ε_T, γ_T, and κ_T specifying the laminate in-plane and out-of-plane deformation. Moreover, using the approach described in Section 5.11, we can conclude that uniform heating of the laminate is accompanied, in the general case, by stresses acting in the layers and between the layers.

As an example, consider the four-layered structure of the space telescope described in Section 7.1.1. First, we calculate the stiffness coefficients of the layers, i.e.,

- for the internal layer of aluminum foil,

$$A_{11}^{(1)} = A_{22}^{(1)} = \overline{E}_f = 76.92 \text{ GPa}, \quad A_{12}^{(1)} = \nu_f \overline{E}_f = 23.08 \text{ GPa}$$

- for the inner skin,

$$A_{11}^{(2)} = A_{22}^{(2)} = \overline{E}_x^i = 34.87 \text{ GPa}, \quad A_{12}^{(2)} = \nu_{xy}^i \overline{E}_x^i = 5.23 \text{ GPa}$$

- for the lattice layer,

$$A_{11}^{(3)} = 2E_r \frac{\delta_r}{a_r} \cos^4 \phi_r = 14.4 \text{ GPa}$$

$$A_{22}^{(3)} = 2E_r \frac{\delta_r}{a_r} \sin^4 \phi_r = 0.25 \text{ GPa}$$

$$A_{12}^{(3)} = 2E_r \frac{\delta_r}{a_r} \sin^2 \phi \cos^2 \phi \ = 1.91 \text{ GPa}$$

- for the external skin,

$$A_{11}^{(4)} = \overline{E}_1^e \cos^4 \phi_e + \overline{E}_2^e \sin^4 \phi_e + 2\left(\overline{E}_1^e \nu_{12}^e + 2G_{12}^e\right) \sin^2 \phi_e \cos^2 \phi_e = 99.05 \text{ GPa}$$

$$A_{22}^{(4)} = \overline{E}_1^e \sin^4 \phi_e + \overline{E}_2^e \cos^4 \phi_e + 2\left(\overline{E}_1^e \nu_{12}^e + 2G_{12}^e\right) \sin^2 \phi_e \cos^2 \phi_e = 13.39 \text{ GPa}$$

$$A_{12}^{(4)} = \overline{E}_1^e \nu_{12}^e + \left[\overline{E}_1^e + \overline{E}_2^e - 2\left(\overline{E}_1^e \nu_{12}^e + 2G_{12}^e\right)\right] \sin^2 \phi_e \cos^2 \phi_e = 13.96 \text{ GPa}$$

Using Eqs. (7.18), we find the thermal coefficients of the layers (the temperature is uniformly distributed over the laminate thickness)

$$\left(A_{11}^T\right)_1 = \left(A_{22}^T\right)_1 = \overline{E}_f \alpha_f \Delta T = 1715 \cdot 10^{-6} \Delta T \text{ GPa}/^\circ\text{C}$$

$$\left(A_{11}^T\right)_2 = \left(A_{22}^T\right)_2 = \overline{E}_x^i \left(1 + \nu_{xy}^i\right) \alpha_x^i \Delta T = 32.08 \cdot 10^{-6} \Delta T \text{ GPa}/^\circ\text{C}$$

$$\left(A_{11}^T\right)_3 = 2E_r \frac{\delta_r}{a_r} \alpha_r \cos^2 \phi_r \Delta T = 4.46 \cdot 10^{-6} \Delta T \text{ GPa}/^\circ\text{C}$$

$$\left(A_{22}^T\right)_3 = 2E_r \frac{\delta_r}{a_r} \alpha_r \sin^2 \phi_r \Delta T = 1.06 \cdot 10^{-6} \Delta T \text{ GPa}/^\circ\text{C}$$

$$\left(A_{11}^T\right)_4 = \left[\overline{E}_1^e \left(\alpha_1^e + \nu_{12}^e \alpha_2^e\right) \cos^2 \phi + \overline{E}_2^e \left(\alpha_2^e + \nu_{21}^e \alpha_1^e\right) \sin^2 \phi\right] \Delta T$$

$$= 132.43 \cdot 10^{-6} \Delta T \text{ GPa}/^\circ\text{C}$$

$$\left(A_{22}^T\right)_4 = \left[\overline{E}_1^e \left(\alpha_1^e + \nu_{12}^e \alpha_2^e\right) \sin^2 \phi + \overline{E}_2^e \left(\alpha_2^e + \nu_{21}^e \alpha_1^e\right) \cos^2 \phi\right] \Delta T$$

$$= 317.61 \cdot 10^{-6} \Delta T \text{ GPa}/^\circ\text{C}$$

Since the layers are orthotropic, $A_{12}^T = 0$ for all of them. Specifying the coordinates of the layers (see Fig. 5.10), i.e.,

$$t_0 = 0 \text{ mm}, \quad t_1 = 0.02 \text{ mm}, \quad t_2 = 1.02 \text{ mm}, \quad t_3 = 10.02 \text{ mm}, \quad t_4 = 13.52 \text{ mm}$$

and applying Eq. (7.27), we calculate the parameters $J_{mn}^{(r)}$ for the laminate

$$J_{11}^{(0)} = \left(A_{11}^T\right)_1 (t_1 - t_0) + \left(A_{11}^T\right)_2 (t_2 - t_1) + \left(A_{11}^T\right)_3 (t_3 - t_2)$$
$$+ \left(A_{11}^T\right)_4 (t_4 - t_3) = 570 \cdot 10^{-6} \Delta T \text{ GPa mm}/^\circ\text{C}$$

$$J_{22}^{(0)} = 1190 \cdot 10^{-6} \Delta T \text{ GPa mm}/^\circ\text{C}$$

$$J_{11}^{(1)} = \frac{1}{2}\left[\left(A_{11}^T\right)_1 \left(t_1^2 - t_0^2\right) + \left(A_{11}^T\right)_2 \left(t_2^2 - t_1^2\right)\right.$$
$$\left. + \left(A_{11}^T\right)_3 \left(t_3^2 - t_2^2\right) + \left(A_{11}^T\right)_4 \left(t_4^2 - t_3^2\right)\right] = 5690 \cdot 10^{-6} \Delta T \text{ GPa mm}/^\circ\text{C}$$

$$J_{22}^{(1)} = 13150 \cdot 10^{-6} \Delta T \text{ GPa mm}/^\circ\text{C}$$

To determine M_{mn}^T, we need to specify the reference surface of the laminate. Assume that this surface coincides with the middle surface, i.e., that $e = h/2 = 6.76$ mm. Then, Eqs. (7.25) yield

$$N_{11}^T = J_{11}^{(0)} = 570 \cdot 10^{-6} \Delta T \text{ GPa mm}/^\circ\text{C}$$

$$N_{22}^T = J_{22}^{(0)} = 1190 \cdot 10^{-6} \Delta T \text{ GPa mm}/^\circ\text{C}$$

$$M_{11}^T = J_{11}^{(1)} - e J_{11}^{(0)} = 1840 \cdot 10^{-6} \Delta T \text{ GPa mm}/^\circ\text{C}$$

$$M_{22}^T = 5100 \cdot 10^{-6} \Delta T \text{ GPa mm}/^\circ\text{C}$$

Thus, the thermal terms entering the constitutive equations of thermoelasticity, Eqs. (7.23), are specified. Using these results, we can determine the apparent coefficients of thermal expansion for the space telescope section under study (see Fig. 7.3). We can assume that, under uniform heating, the curvatures do not change in the middle part of the cylinder so that $\kappa_{xT} = 0$ and $\kappa_{yT} = 0$. Since there are no external loads, the free body diagram enables us to conclude that $N_x = 0$ and $N_y = 0$. As a result, the first two equations of Eqs. (7.23) for the structure under study become

$$B_{11}\varepsilon_{xT}^0 + B_{12}\varepsilon_{yT}^0 = N_{11}^T$$
$$B_{21}\varepsilon_{xT}^0 + B_{22}\varepsilon_{yT}^0 = N_{22}^T$$

Solving these equations for thermal strains and taking into account Eqs. (7.20), we get

$$\varepsilon_{xT}^0 = \frac{1}{B}\left(B_{22}N_{11}^T - B_{12}N_{22}^T\right) = \alpha_x \Delta T$$
$$\varepsilon_{yT}^0 = \frac{1}{B}\left(B_{11}N_{22}^T - B_{12}N_{11}^T\right) = \alpha_y \Delta T$$

where $B = B_{11}B_{22} - B_{12}^2$. For the laminate under study, calculation yields

$$\alpha_x = -0.94 \cdot 10^{-6}\ \ 1/^\circ\mathrm{C}\,, \quad \alpha_y = 14.7 \cdot 10^{-6}\ \ 1/^\circ\mathrm{C}$$

Return to Eqs. (7.13) and (7.20) based on the assumption that the coefficients of thermal expansion do not depend on temperature. For moderate temperatures, this is a reasonable approximation. This conclusion follows from Fig. 7.6, in which the experimental results of Sukhanov et al. (1990)

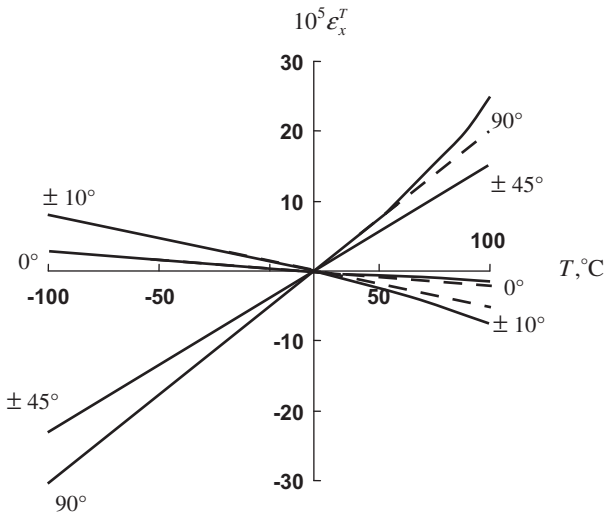


FIGURE 7.6

Experimental dependencies of thermal strains on temperature (solid lines) for $\pm\phi$ angle-ply carbon-epoxy composite and the corresponding linear approximations (dashed lines).

(shown by solid lines) are compared with Eqs. (7.20), in which $\Delta T = T - 20°C$ (dashed lines) represents carbon-epoxy angle-ply laminates. However, for relatively high temperatures, some deviation from linear behavior can be observed. In this case, Eqs. (7.13) and (7.20) for thermal strains can be generalized as

$$\varepsilon^T = \int_{T_0}^{T} \alpha(T)dT$$

Temperature variations can also result in a change in material mechanical properties. As follows from Fig. 7.7 in which the circles correspond to the experimental data of Ha and Springer (1987), elevated temperatures result in either higher or lower reduction of material strength and stiffness characteristics, depending on whether the corresponding material characteristic is controlled mainly by the fibers or by the matrix. The curves presented in Fig. 7.7 correspond to a carbon-epoxy composite, but they are typical for polymeric unidirectional composites. The longitudinal modulus and tensile strength, being controlled by the fibers, are less sensitive to temperature than longitudinal compressive strength, and transverse and shear characteristics. Analogous results for a more temperature sensitive thermoplastic composite studied by Soutis and Turkmen (1993) are presented in Fig. 7.8. Metal matrix composites demonstrate much higher thermal resistance, whereas ceramic and carbon-carbon composites have been specifically developed to withstand high temperatures. For example, carbon-carbon fabric composite under heating up to 2500°C demonstrates only a 7% reduction in tensile strength and about 30% reduction in compressive strength without significant change of stiffness.

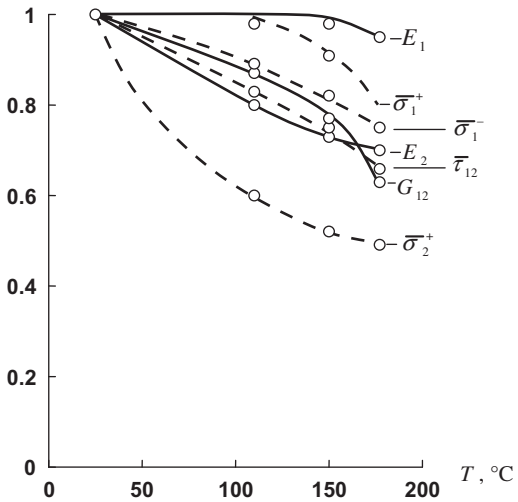


FIGURE 7.7

Experimental dependencies of normalized stiffness (solid lines) and strength (dashed lines) characteristics of unidirectional carbon-epoxy composite on temperature.

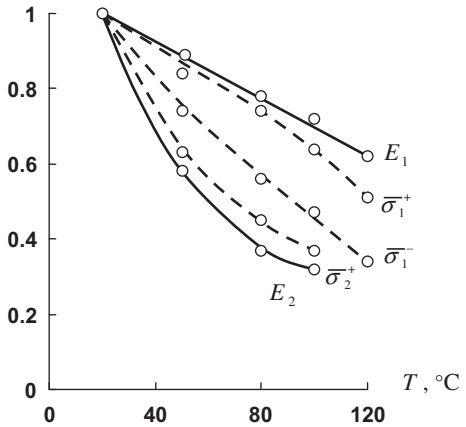


FIGURE 7.8

Experimental dependencies of normalized stiffness (solid lines) and strength (dashed lines) characteristics of unidirectional glass-polypropylene composite on temperature.

Analysis of thermoelastic deformation for materials whose stiffness characteristics depend on temperature presents substantial difficulties because thermal strains are caused not only by material thermal expansion, but also by external forces. Consider, for example, a structural element under temperature T_0 loaded with some external force P_0 and assume that the temperature is increased to a value T_1. Then the temperature change will cause a thermal strain associated with material expansion, and the force P_0, being constant, also induces additional strain because the material stiffness at temperature T_1 is less than its stiffness at temperature T_0. To determine the final stress and strain state of the structure, we should describe the process of loading and heating using, e.g., the method of successive loading (and heating) presented in Section 4.1.2.

7.2 HYGROTHERMAL EFFECTS AND AGING

Effects that are similar to temperature variations, i.e., expansion and degradation of properties, can also be caused by moisture. Moisture absorption is governed by Fick's law, which is analogous to Fourier's law, Eq. (7.1), for thermal conductivity, i.e.,

$$q_W = -D\frac{\partial W}{\partial n} \tag{7.31}$$

in which q_W is the diffusion flow through a unit area of surface with normal n, D is the diffusivity of the material whose moisture absorption is being considered, and W is the relative mass moisture concentration in the material, i.e.,

$$W = \frac{\Delta m}{m} \tag{7.32}$$

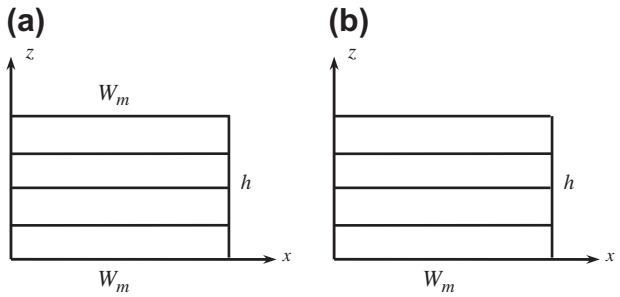


FIGURE 7.9

Composite material exposed to moisture on (a) both surfaces $z = 0$ and $z = h$, and (b) on the surface $z = 0$ only.

where Δm is the increase in the mass of a unit volume material element due to moisture absorption and m is the mass of the dry material element. Moisture distribution in the material is governed by the following equation, similar to Eq. (7.2) for thermal conductivity

$$\frac{\partial}{\partial n}\left(D\,\frac{\partial W}{\partial n}\right) = \frac{\partial W}{\partial t} \tag{7.33}$$

Consider a laminated composite material shown in Fig. 7.9 for which n coincides with the z-axis. Despite the formal correspondence between Eq. (7.2) for thermal conductivity and Eq. (7.32) for moisture diffusion, there is a difference in principle between these problems. This difference is associated with the diffusivity coefficient D, which is much lower than the thermal conductivity λ of the same material. As is known, there are materials, e.g., metals, with relatively high λ and practically zero D coefficients. Low D-value means that moisture diffusion is a rather slow process. As shown by Shen and Springer (1976), the temperature increase in time inside a surface-heated composite material reaches a steady (equilibrium) state temperature about 10^6 times faster than the moisture content approaching the corresponding stable state. This means that, in contrast to Section 7.1.1 in which the steady (time-independent) temperature distribution is studied, we must consider the time-dependent process of moisture diffusion. To simplify the problem, we can neglect the possible variation of the mass diffusion coefficient D over the laminate thickness, taking $D = constant$ for polymeric composites. Then, Eq. (7.33) reduces to

$$D\,\frac{\partial^2 W}{\partial z^2} = \frac{\partial W}{\partial t} \tag{7.34}$$

Consider the laminate in Fig. 7.9a. Introduce the maximum moisture content W_m that can exist in the material under the preassigned environmental conditions. Clearly, W_m depends on the material nature and structure, temperature, and relative humidity (RH) of the gas (e.g., humid air), or on the nature of the liquid (distilled water, salted water, fuel, lubricating oil, etc.) to the action of which the material is exposed. Introduce also the normalized moisture concentration as

$$w\,(z,t) = \frac{W(z,t)}{W_m} \tag{7.35}$$

Obviously, for $t \to \infty$, we have $w \to 1$. Then, the function $w(z, t)$ can be presented in the form

$$w(z,t) = 1 - \sum_{n=1}^{\infty} w_n(z) e^{-k_n t} \tag{7.36}$$

Substitution into Eq. (7.34), with due regard to Eq. (7.35), yields the following ordinary differential equation

$$w_n'' + r_n^2 w_n = 0$$

in which $r_n^2 = k_n/D$ and $(\ldots)' = d(\ )/dz$. The general solution is

$$w_n = C_{1n} \sin r_n z + C_{2n} \cos r_n z$$

The integration constants can be found from the boundary conditions on the surfaces $z = 0$ and $z = h$ (see Fig. 7.9a). Assume that on these surfaces $W = W_m$ or $w = 1$. Then, in accordance with Eq. (7.36), we get

$$w_n(0,t) = 0, \quad w_n(h,t) = 0 \tag{7.37}$$

The first of these conditions yields $C_{2n} = 0$, whereas from the second condition we have $\sin r_n h = 0$, which yields

$$r_n h = (2n-1)\pi \quad (n = 1,\ 2,\ 3, \ldots) \tag{7.38}$$

Thus, the solution in Eq. (7.36) takes the form

$$w(z,t) = 1 - \sum_{n=1}^{\infty} C_{1n} \sin\left(\frac{2n-1}{h}\pi z\right) \exp\left[-\left(\frac{2n-1}{h}\right)^2 \pi^2 D t\right] \tag{7.39}$$

To determine C_{1n}, we must use the initial condition, according to which

$$w(0 < z < h, t = 0) = 0$$

Using the following Fourier series:

$$1 = \frac{4}{\pi} \sum_{n=1}^{\infty} \frac{\sin(2n-1)z}{2n-1}$$

we get $C_{1n} = 4/(2n-1)\pi$, and the solution in Eq. (7.39) can be written in its final form

$$w(z,t) = 1 - \frac{4}{\pi} \sum_{n=1}^{\infty} \frac{\sin(2n-1)\pi\overline{z}}{2n-1} \exp\left[-\left(\frac{2n-1}{h}\right)^2 \pi^2 D t\right] \tag{7.40}$$

where $\overline{z} = z/h$.

For the structure in Fig. 7.9b, the surface $z = h$ is not exposed to moisture, and hence $q_W(z = h) = 0$. So, in accordance with Eq. (7.31), the second boundary condition in Eqs. (7.37) must be changed to $w'(h,t) = 0$. Then, instead of Eq. (7.38), we must use

$$r_n h = \frac{\pi}{2}(2n-1)$$

Comparing this result with Eq. (7.38), we can conclude that for the laminate in Fig. 7.9b, $w(z,t)$ is specified by the solution in Eq. (7.40) in which we must change h to $2h$.

The mass increase of the material with thickness h is

$$\Delta M = A \int_0^h \Delta m \, dz$$

where A is the surface area. Using Eqs. (7.32) and (7.35), we get

$$\Delta M = AmW_m \int_0^h w \, dz$$

Switching to a dimensionless variable $\overline{z} = z/h$ and taking the total moisture content as

$$C = \frac{\Delta M}{Amh} \tag{7.41}$$

we arrive at

$$C = W_m \int_0^1 w \, d\overline{z}$$

where w is specified by Eq. (7.40). Substitution of this equation and integration yields

$$\overline{C} = \frac{C}{W_m} = 1 - \frac{8}{\pi^2} \sum_{n=1}^{\infty} \frac{1}{(2n-1)^2} \exp\left[-\left(\frac{2n-1}{h} \right)^2 \pi^2 Dt \right] \tag{7.42}$$

For numerical analysis, consider a carbon-epoxy laminate for which $D = 10^{-3}$ mm^2/hour (Tsai, 1987) and $h = 1$ mm. The distributions of the moisture concentration over the laminate thickness are shown in Fig. 7.10 for $t = 1$, 10, 50, 100, 200, and 500 hours. As can be seen, complete impregnation of 1 mm thick material takes about 500 hours. The dependence of $\overline{C}$ on t found in accordance with Eq. (7.42) is presented in Fig. 7.11.

An interesting interpretation of the curve in Fig. 7.11 can be noted if we change the variable t to $\sqrt{t}$. The resulting dependence is shown in Fig. 7.12. As can be seen, the initial part of the curve is close to a straight line whose slope can be used to determine the diffusion coefficient of the material matching the theoretical dependence $C(t)$ with the experimental one. Note that experimental methods usually result in rather approximate evaluation of the material diffusivity D with possible variations up to 100% (Tsai, 1987). The maximum value of the function $C(t)$ which it tends to approach determines the maximum moisture content $C_m = W_m$.

Thus, the material behavior under the action of moisture is specified by two experimental parameters – D and C_m – which can depend on the ambient media, its moisture content, and temperature. The experimental dependencies of C in Eq. (7.41) on t for 0.6 mm thick carbon-epoxy composite exposed to humid air with various relative humidity (RH) levels are shown in Fig. 7.13 (Survey, 1984). As can be seen, the moisture content is approximately proportional to the air humidity. The gradients of the curves in Fig. 7.13 depend on the laminate thickness (Fig. 7.14, Survey, 1984).

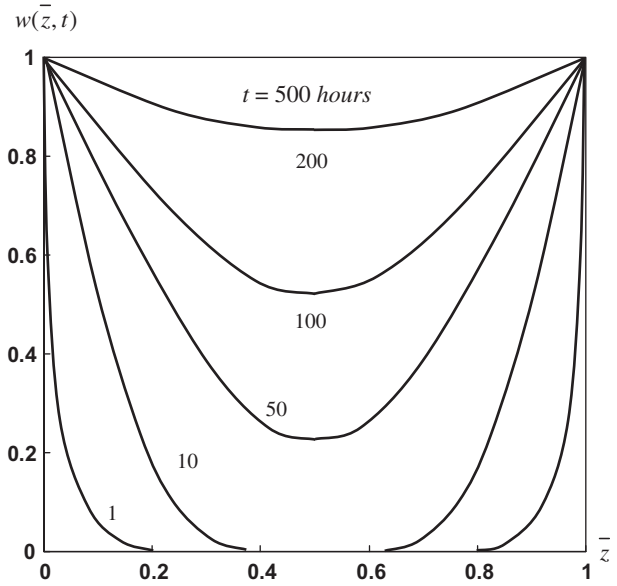


FIGURE 7.10

Distribution of the normalized moisture concentration w over the thickness of 1 mm thick carbon-epoxy composite for various exposure times t.

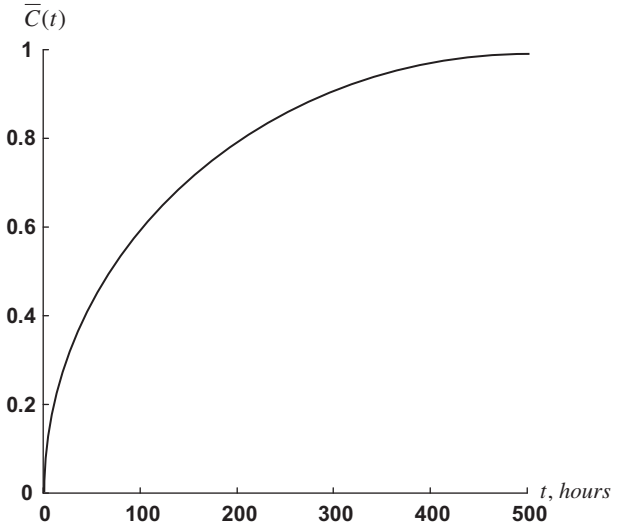


FIGURE 7.11

Dependence of the normalized moisture concentration $\overline{C}$ on time t.

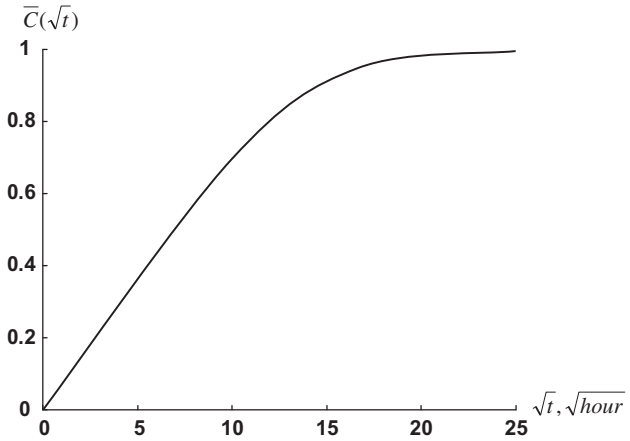


FIGURE 7.12

Dependence of the normalized moisture concentration on $\sqrt{t}$.

Among polymeric composites, the highest capacity for moisture absorption under room temperature is demonstrated by aramid composites ($7 \pm 0.25\%$ by weight) in which both the polymeric matrix and fibers are susceptible to moisture. Glass and carbon polymeric composites are characterized with moisture content $3.5 \pm 0.2\%$ and $2 \pm 0.75\%$, respectively. In real aramid-epoxy and carbon-epoxy composite structures, the moisture content is usually about 2% and 1%, respectively. The lowest susceptibility to moisture is demonstrated by boron composites. Metal matrix, ceramic, and carbon-carbon composites are not affected by moisture.

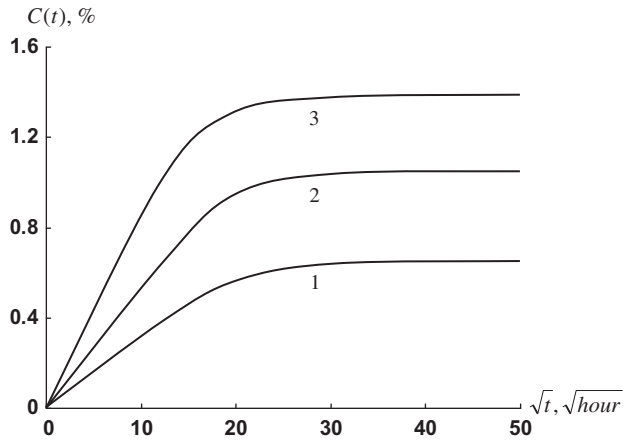


FIGURE 7.13

Dependence of the moisture content on time for a carbon-epoxy composite exposed to air with 45% *RH* (1), 75% *RH* (2), and 95% *RH* (3).

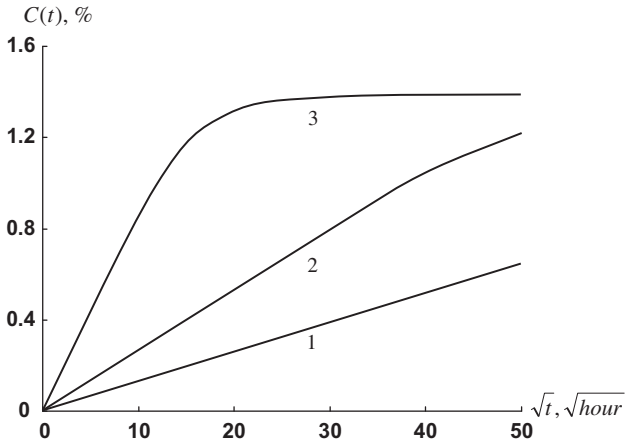


FIGURE 7.14

Dependencies of the moisture content on time for a carbon-epoxy composite with thickness 3.6 mm (1), 1.2 mm (2), and 0.6 mm (3) exposed to humid air with 75% *RH*.

The material diffusivity coefficient D depends on temperature in accordance with the Arrhenius relationship

$$D(T_a) = \frac{D_0}{e^{k/T_a}}$$

(Tsai, 1987) in which D_0 and k are some material constants and T_a is the absolute temperature. Experimental dependencies of the moisture content on time in a 1.2 mm thick carbon-epoxy composite exposed to humid air with 95% *RH* at various temperatures are presented in Fig. 7.15 (Survey, 1984). The most pronounced effect of temperature is observed for aramid-epoxy composites. The corresponding experimental results of Milyutin et al. (1989) are shown in Fig. 7.16.

When a material absorbs moisture it swells, demonstrating effects that are similar to thermal effects, which can be modeled using the equations presented in Section 7.1.2, if we treat α_1, α_2 and α_x, α_y as coefficients of moisture expansion and change ΔT for C. Similar to temperature, increase in moisture reduces material strength and stiffness. For carbon-epoxy composites, this reduction is about 12%, for aramid-epoxy composites, about 25%, and for glass-epoxy materials, about 35%. After drying out, the effect of moisture usually disappears.

The cyclic action of temperature, moisture, or sun radiation results in material aging, i.e., in degradation of the material properties during the process of material or structure storage. For some polymeric composites, exposure to elevated temperature, which can reach 70°C, and radiation, whose intensity can be as high as 1 kW/m^2, can cause more complete curing of the resin and some increase of material strength in compression, shear, or bending. However, under long-term action of the aforementioned factors, the material strength and stiffness decrease. To evaluate the effect of aging, testing under transverse bending (see Fig. 4.102) is usually performed. The flexural strength obtained

$$\overline{\sigma}_f = \frac{3\overline{P}l}{2bh^2}$$

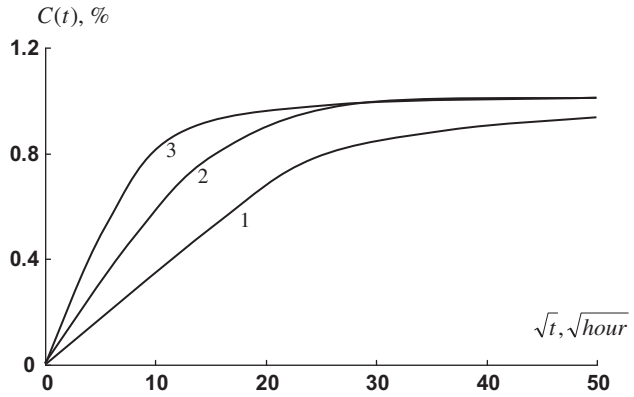


FIGURE 7.15

Dependencies of the moisture content on time for 1.2 mm thick carbon-epoxy composite exposed to humid air with 95% *RH* under temperatures 25°C (1), 50°C (2), and 80°C (3).

allows for both fiber and matrix material degradation in the process of aging. Experimental results showing the dependence of the normalized flexural strength on time for advanced composites are presented in Fig. 7.17. The most dramatic is the effect of aging on the ultimate transverse tensile deformation $\overline{\varepsilon}_2$ of unidirectional composites, the low value of which results in cracking of the matrix as discussed in Sections 4.4.2 and 6.4. After accelerated aging, i.e., long-term moisture conditioning at the temperature 70°C, a 0.75% moisture content in carbon-epoxy composites results in about a 20% reduction of $\overline{\varepsilon}_2$, whereas a 1.15% moisture content causes about a 45% reduction.

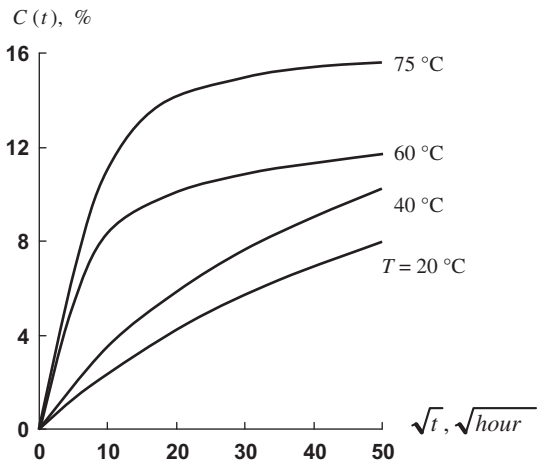


FIGURE 7.16

Moisture content as a function of time and temperature for aramid-epoxy composites.

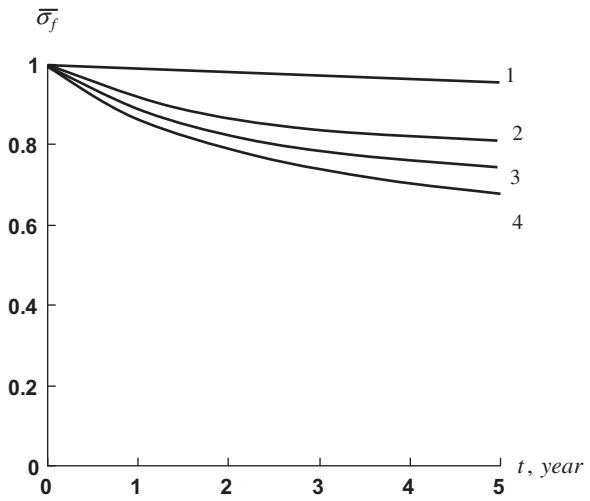


FIGURE 7.17

Dependence of the normalized flexural strength on the time of aging for boron- (1), carbon- (2), aramid- (3), and glass- (4) epoxy composites.

Environmental effects on composite materials are discussed in detail elsewhere (Tsai, 1987; Springer, 1981, 1984, 1988).

7.3 TIME-DEPENDENT LOADING EFFECTS

Polymeric matrices are characterized with pronounced viscoelastic properties resulting in time-dependent behavior of polymeric composites which is discussed below.

7.3.1 Viscoelasticity

Viscoelastic properties of composite materials manifest themselves in creep (see Section 1.1), stress relaxation, and dependence of the stress-strain diagram on the rate of loading. It should be emphasized that in composite materials, viscoelastic deformation of the polymeric matrix is restricted by the fibers that are usually linear elastic and do not demonstrate time-dependent behavior. The one exception to existing fibers is represented by aramid fibers that are actually polymeric themselves by their nature. The properties of metal matrix, ceramic, and carbon-carbon composites under normal conditions do not depend on time. Rheological (time-dependent) characteristics of structural materials are revealed in creep tests allowing us to plot the dependence of strain on time under constant stress. Such diagrams are shown in Fig. 7.18 for the aramid-epoxy composite described by Skudra et al. (1989). An important characteristic of the material can be established if we plot the so-called isochrone stress-strain diagrams shown in Fig. 7.19. Three curves in this figure are plotted for $t = 0$, $t = 100$, and $t = 1000$ days, and the points on these curves correspond to points 1, 2, and 3 in Fig. 7.18. As can be seen, the initial parts of the isochrone diagrams are linear, which means that under moderate stress, the

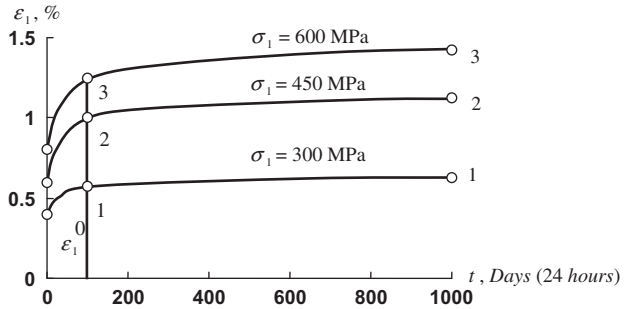


FIGURE 7.18

Creep strain response of unidirectional aramid-epoxy composite under tension in longitudinal direction with three constant stresses.

material under study can be classified as a linear-viscoelastic material. To characterize such a material, we need to have only one creep diagram, whereby the other curves can be plotted, increasing strains in proportion to stress. For example, the creep curve corresponding to $\sigma_1 = 450$ MPa in Fig. 7.18 can be obtained if we multiply strains corresponding to $\sigma_1 = 300$ MPa by 1.5.

Linear-viscoelastic material behavior is described with reasonable accuracy by the hereditary theory, according to which the dependence of strain on time is expressed as

$$\varepsilon(t) = \frac{1}{E}\left[\sigma(t) + \int_0^t C(t-\tau)\sigma(\tau)d\tau\right] \tag{7.43}$$

Here, t is the current time, τ is some moment of time in the past $(0 \le \tau \le t)$ at which stress $\sigma(\tau)$ acts, and $C(t-\tau)$ is the creep compliance (or creep kernel) depending on time passing from the moment τ to the moment t. The constitutive equation of hereditary theory, Eq. (7.43), is illustrated in Fig. 7.20.

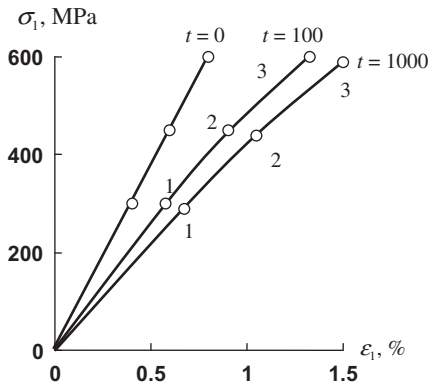


FIGURE 7.19

Isochrone stress-strain diagrams corresponding to creep curves in Fig 7.18.

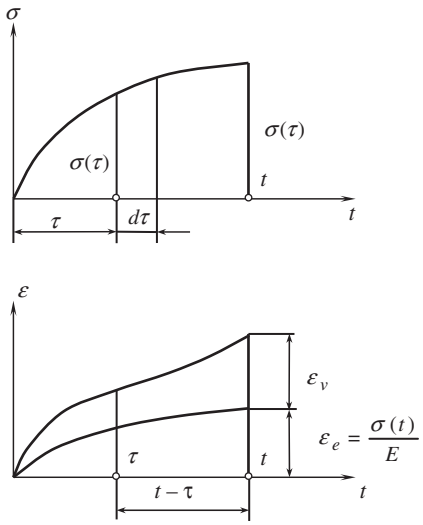


FIGURE 7.20

Geometric interpretation of the hereditary constitutive theory.

As can be seen, the total strain $\varepsilon(t)$ is composed of the elastic strain ε_e governed by the current stress $\sigma(t)$ and the viscous strain ε_v depending on the loading process as if the material "remembers" this process. Within the framework of this interpretation, the creep compliance is $C(\theta)$, where $\theta = t - \tau$ can be treated as some "memory function" that should, obviously, be infinitely high at $\theta = 0$ and tend to zero for $\theta \to \infty$ as in Fig. 7.21.

The inverse form of Eq. (7.43) is

$$\sigma(t) = E\left[\varepsilon(t) - \int_0^t R(t-\tau)\varepsilon(\tau)d\tau\right] \tag{7.44}$$

Here, $R(t-\tau)$ is the relaxation modulus or the relaxation kernel that can be expressed, as shown later, in terms of $C(t-\tau)$.

The creep compliance is determined using experimental creep diagrams. Transforming to a new variable $\theta = t - \tau$, we can write Eq. (7.43) in the following form

$$\varepsilon(t) = \frac{1}{E}\left[\sigma(t) + \int_0^t C(\theta)\sigma(\theta - t)d\theta\right] \tag{7.45}$$

For a creep test, the stress is constant, so $\sigma = \sigma^0$, and Eq. (7.44) yields

$$\varepsilon(t) = \varepsilon^0\left[1 + \int_0^t C(\theta)d\theta\right] \tag{7.46}$$

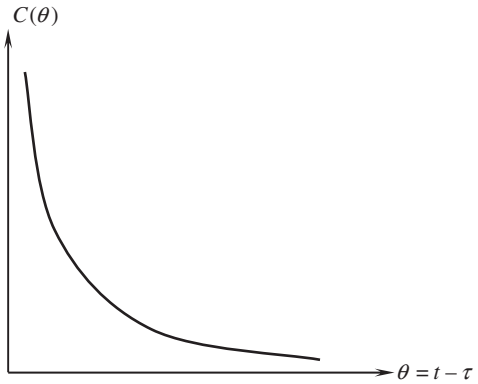


FIGURE 7.21

Typical form of the creep compliance function.

where $\varepsilon^0 = \sigma^0/E = \varepsilon(t=0)$ is the instantaneous elastic strain (see Fig. 7.18). Differentiating this equation with respect to t, we get

$$C(t) = \frac{1}{\varepsilon^0}\frac{d\varepsilon(t)}{dt}$$

This expression allows us to determine the creep compliance by differentiating the given experimental creep diagram or its analytical approximation. However, for practical analysis, $C(\theta)$ is usually determined directly from Eq. (7.46), introducing some approximation for $C(\theta)$ and matching the function obtained for $\varepsilon(t)$ with the experimental creep diagram. For this purpose, Eq. (7.46) is written in the form

$$\frac{\varepsilon(t)}{\varepsilon^0} = 1 + \int_0^t C(\theta)d\theta \tag{7.47}$$

Experimental creep diagrams for unidirectional glass-epoxy composite are presented in this form in Fig. 7.22 (solid lines).

The simplest form is an exponential approximation of the type

$$C(\theta) = \sum_{n=1}^{N} A_n e^{-\alpha_n \theta} \tag{7.48}$$

Substituting Eq. (7.48) into Eq. (7.47), we obtain

$$\frac{\varepsilon(t)}{\varepsilon^0} = 1 + \sum_{n=1}^{N} \frac{A_n}{\alpha_n}(1 - e^{-\alpha_n t})$$

For the curves presented in Fig. 7.22, calculation yields:

- Longitudinal tension: $N = 1,\ A_1 = 0$
- Transverse tension: $N = 1,\ A_1 = 0.04,\ \alpha_1 = 0.06\ \ 1/\text{day}$
- In-plane shear: $N = 2,\ A_1 = 0.033,\ \alpha_1 = 0.04\ \ 1/\text{day},\ A_2 = 0.06,\ \alpha_2 = 0.4\ \ 1/\text{day}$

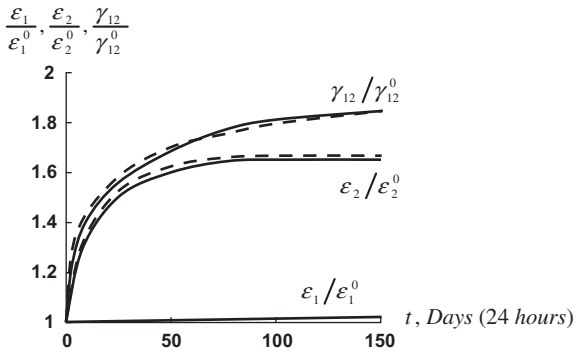


FIGURE 7.22

Creep strain diagrams for unidirectional glass-epoxy composite (solid lines) under tension in the longitudinal direction ($\varepsilon_1/\varepsilon_1^0$) and the transverse direction ($\varepsilon_2/\varepsilon_2^0$), and under in-plane shear ($\gamma_{12}/\gamma_{12}^0$) and the corresponding exponential approximations (dashed lines).

The corresponding approximations are shown in Fig. 7.22 with dashed lines. The main shortcoming of the exponential approximation in Eq. (7.48) is associated with the fact that, in contrast to Fig. 7.21, $C(\theta)$ has no singularity at $\theta = 0$ which means that it cannot properly describe material behavior in the vicinity of $t = 0$.

It should be emphasized that the one-term exponential approximation corresponds to a simple rheological mechanical model shown in Fig. 7.23. The model consists of two linear springs simulating material elastic behavior in accordance with Hooke's law

$$\sigma_1 = E_1\varepsilon_1, \quad \sigma_2 = E_2\varepsilon_2 \tag{7.49}$$

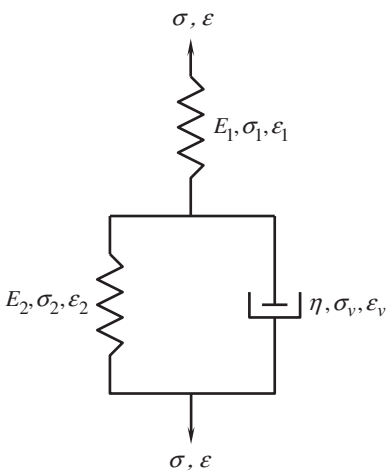


FIGURE 7.23

Three-element mechanical model.

and one dashpot simulating material viscous behavior obeying the Newton flow law

$$\sigma_v = \eta \frac{d\varepsilon_v}{dt} \tag{7.50}$$

Equilibrium and compatibility conditions for the model in Fig. 7.23 are

$$\sigma = \sigma_2 + \sigma_v, \quad \sigma_1 = \sigma$$
$$\varepsilon_v = \varepsilon_2, \quad \varepsilon_1 + \varepsilon_2 = \varepsilon$$

Using the first of these equations and Eqs. (7.49)–(7.50), we get

$$\sigma = E_2\varepsilon_2 + \eta \frac{d\varepsilon_v}{dt}$$

Taking into account that

$$\varepsilon_2 = \varepsilon_v = \varepsilon - \frac{\sigma}{E}$$

we finally arrive at the following constitutive equation relating the apparent stress σ to the apparent strain ε

$$\sigma\left(1 + \frac{E_2}{E_1}\right) + \frac{\eta}{E_1}\frac{d\sigma}{dt} = E_2\varepsilon + \eta\frac{d\varepsilon}{dt} \tag{7.51}$$

This equation allows us to introduce some useful material characteristics. Indeed, consider a very fast loading, i.e., such that stress σ and strain ε can be neglected in comparison with their rates. Then, integration yields $\sigma = E_i\varepsilon$, where $E_i = E_1$ is the instantaneous modulus of the material. Now assume that the loading is so slow that stress and strain rates can be neglected. Then, Eq. (7.51) yields $\sigma = E_l\varepsilon$, where

$$E_l = \frac{E_1E_2}{E_1 + E_2} \tag{7.52}$$

is the long-time modulus.

We can now apply the model under study to describe material creep. Taking $\sigma = \sigma_0$ and integrating Eq. (7.51) with initial condition $\varepsilon_0(0) = \sigma_0/E$, we get

$$\varepsilon = \frac{\sigma_0}{E_1}\left[1 + \frac{E_1}{E_2}\left(1 - e^{\frac{E_2}{\eta}t}\right)\right]$$

The corresponding creep diagram is shown in Fig. 7.24. As follows from this figure, $\varepsilon(t \to \infty) = \sigma_0/E_l$, where E_l is specified by Eq. (7.52). This means that there exists some limit for the creep strain, and materials that can be described with this model should possess the so-called limited creep.

Now assume that the model is loaded in such a way that the apparent strain is constant, i.e., that $\varepsilon = \varepsilon_0$. Then, the solution of Eq. (7.51) which satisfies the condition $\sigma(0) = E_1\varepsilon_0$ is

$$\sigma = \frac{E_1\varepsilon_0}{E_1 + E_2}\left(E_2 + E_1e^{-t/t_r}\right), \quad t_r = \frac{\eta}{E_1 + E_2}$$

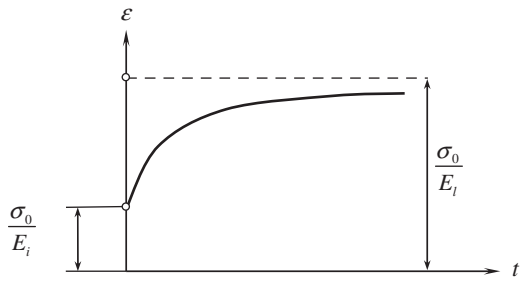


FIGURE 7.24

Creep diagram corresponding to the mechanical model in Fig. 7.23.

The corresponding dependence is presented in Fig. 7.25 and illustrates the process of stress relaxation. The parameter t_r is called the time of relaxation. During this time, the stress decreases by the factor of e.

Consider again Eq. (7.51) and express E_1, E_2, and η in terms of E_i, E_l, and t_r. The resulting equation is as follows

$$\sigma + t_r \frac{d\sigma}{dt} = E_l \varepsilon + E_i t_r \frac{d\varepsilon}{dt} \tag{7.53}$$

This first-order differential equation can be solved for ε in the general case. Omitting rather cumbersome transformations, we arrive at the following solution

$$\varepsilon(t) = \frac{1}{E_i}\left[\sigma(t) + \frac{1}{t_r}\left(1 - \frac{E_l}{E_i}\right)\int_0^t e^{-\frac{E_l}{E_i t_r}(t-\tau)}\sigma(\tau)d\tau\right]$$

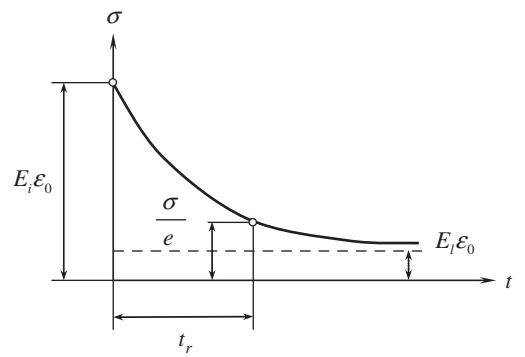


FIGURE 7.25

Relaxation diagram corresponding to the mechanical model in Fig. 7.23.

This result corresponds to Eq. (7.45) of the hereditary theory with one-term exponential approximation of the creep compliance in Eq. (7.48), in which $N = 1$. Taking more terms in Eq. (7.48), we get more flexibility in the approximation of experimental results with exponential functions. However, the main features of material behavior are, in principle, the same as that for the one-term approximation (see Figs. 7.23 and 7.24). In particular, there exists the long-time modulus that follows from Eq. (7.46) if we examine the limit for $t \to \infty$, i.e.,

$$\varepsilon(t) \to \frac{\sigma_0}{E_l}, \quad E_l = \frac{E}{1 + \int_0^\infty C(\theta) d\theta}$$

For the exponential approximation in Eq. (7.48),

$$I = \int_0^\infty C(\theta) d\theta = \sum_{n=1}^{N} \frac{A_n}{\alpha_n}$$

Since the integral I has a finite value, the exponential approximation of the creep compliance can be used only for materials with limited creep. There exist more complicated singular approximations, e.g.,

$$C(\theta) = \frac{A}{\theta^\alpha}, \quad C(\theta) = \frac{A}{\theta^\alpha} e^{-\beta\theta}$$

for which $I \to \infty$ and $E_l = 0$. This means that for such materials, the creep strain can be infinitely high.

A useful interpretation of the hereditary theory constitutive equations can be constructed with the aid of the integral Laplace transformation, according to which a function $f(t)$ is associated with its Laplace transform $f^*(p)$ as

$$f^*(p) = \int_0^\infty f(t) e^{-pt} dt$$

For some functions that we need to use for the examples presented below, we have

$$\begin{aligned} f(t) &= 1, \quad f^*(p) = \frac{1}{p} \\ f(t) &= e^{-\alpha t}, \quad f^*(p) = \frac{1}{\alpha + p} \end{aligned} \tag{7.54}$$

The importance of the Laplace transformation for the hereditary theory is associated with the existence of the so-called convolution theorem, according to which

$$\left[\int_0^t f_1(\theta) f_2(\theta - t) d\theta \right]^* = f_1^*(p) f_2^*(p)$$

Using this theorem and applying Laplace transformation to Eq. (7.45), we get

$$\varepsilon^*(p) = \frac{1}{E}\left[\sigma^*(p) + C^*(p)\sigma^*(p)\right]$$

This result can be presented in a form similar to Hookes's law, i.e.,

$$\sigma^*(p) = E^*(p)\varepsilon^*(p) \tag{7.55}$$

where

$$E^* = \frac{E}{1 + C^*(p)}$$

Applying Laplace transformation to Eq. (7.44), we arrive at Eq. (7.55) in which

$$E^* = E[1 - R^*(p)] \tag{7.56}$$

Comparing Eqs. (7.55) and (7.56), we can relate Laplace transforms of the creep compliance to the relaxation modulus, i.e.,

$$\frac{1}{1 + C^*(p)} = 1 - R^*(p)$$

With due regard to Eq. (7.55), we can formulate the elastic-viscoelastic analogy or the correspondence principle, according to which the solution of the linear viscoelasticity problem can be obtained in terms of the corresponding Laplace transforms from the solution of the linear elasticity problem if E is replaced with E^* and all the stresses, strains, displacements, and external loads are replaced with their Laplace transforms.

For an orthotropic material in a plane stress state, e.g., for a unidirectional composite ply or layer referred to the principal material axes, Eqs. (4.55) and (7.43) can be generalized as

$$\varepsilon_1(t) = \frac{1}{E_1}\left[\sigma_1(t) + \int_0^t C_{11}(t-\tau)\sigma_1(\tau)d\tau\right] - \frac{\nu_{12}}{E_2}\left[\sigma_2(t) + \int_0^t C_{12}(t-\tau)\sigma_2(\tau)d\tau\right]$$

$$\varepsilon_2(t) = \frac{1}{E_2}\left[\sigma_2(t) + \int_0^t C_{22}(t-\tau)\sigma_2(\tau)d\tau\right] - \frac{\nu_{21}}{E_1}\left[\sigma_1(t) + \int_0^t C_{21}(t-\tau)\sigma_1(\tau)d\tau\right]$$

$$\gamma_{12}(t) = \frac{1}{G_{12}}\left[\tau_{12}(t) + \int_0^t K_{12}(t-\tau)\tau_{12}(\tau)d\tau\right]$$

Applying Laplace transformation to these equations, we can reduce them to a form similar to Hooke's law, Eqs. (4.55), i.e.,

$$\begin{aligned}\varepsilon_1^*(p) &= \frac{\sigma_1^*(p)}{E_1^*(p)} - \frac{\nu_{12}^*(p)}{E_2^*(p)}\sigma_2^*(p)\\ \varepsilon_2^*(p) &= \frac{\sigma_2^*(p)}{E_2^*(p)} - \frac{\nu_{21}^*(p)}{E_1^*(p)}\sigma_1^*(p)\\ \gamma_{12}^*(p) &= \frac{\tau_{12}^*(p)}{G_{12}^*(p)}\end{aligned} \tag{7.57}$$

where

$$\begin{aligned}E_1^*(p) &= \frac{E_1}{1+C_{11}^*(p)}, \quad E_2^*(p) = \frac{E_2}{1+C_{22}^*(p)}, \quad G_{12}^*(p) = \frac{G_{12}}{1+K_{12}^*(p)}\\ \nu_{12}^*(p) &= \frac{1+C_{12}^*(p)}{1+C_{22}^*(p)}\nu_{12}, \quad \nu_{21}^*(p) = \frac{1+C_{21}^*(p)}{1+C_{11}^*(p)}\nu_{21}\end{aligned} \tag{7.58}$$

For the unidirectional composite ply whose typical creep diagrams are shown in Fig. 7.22, the foregoing equations can be simplified by neglecting material creep in the longitudinal direction ($C_{11} = 0$) and assuming that Poisson's effect is linear elastic and symmetric, i.e., that

$$\frac{\nu_{12}^*}{E_2^*} = \frac{\nu_{12}}{E_2}, \quad \frac{\nu_{21}^*}{E_1^*} = \frac{\nu_{21}}{E_1}$$

Then, Eqs. (7.57) take the form

$$\begin{aligned}\varepsilon_1^*(p) &= \frac{\sigma_1^*(p)}{E_1} - \frac{\nu_{12}}{E_2}\sigma_2^*(p)\\ \varepsilon_2^*(p) &= \frac{\sigma_2^*(p)}{E_2^*} - \frac{\nu_{21}}{E_1}\sigma_1^*(p)\\ \gamma_{12}^*(p) &= \frac{\tau_{12}^*(p)}{G_{12}^*(p)}\end{aligned} \tag{7.59}$$

Supplementing constitutive equations, Eqs. (7.57) or (7.59), with strain-displacement and equilibrium equations written in terms of Laplace transforms of stresses, strains, displacements, and external loads and solving the problem of elasticity, we can find Laplace transforms for all the variables. To represent the solution obtained in this way in terms of time t, we need to take the inverse Laplace transformation, and this is the most difficult stage of the problem solution. There exist exact and approximate analytical and numerical methods for performing inverse Laplace transformation discussed, for example, those by Schapery (1974). The most commonly used approach is based on approximation of the solution written in terms of the transformation parameter p with some functions for which the inverse Laplace transformation is known.

As an example, consider the problem of torsion for an orthotropic cylindrical shell similar to that shown in Fig. 6.20. The shear strain induced by torque T is specified by Eq. (5.171). Using the elastic-viscoelastic analogy, we can write the corresponding equation for the creep problem as

$$\gamma_{xy}^{*}(p) = \frac{T^{*}(p)}{2\pi R^{2} B_{44}^{*}(p)} \tag{7.60}$$

Here, $B_{44}^{*}(p) = A_{44}^{*}(p)h$, where h is the shell thickness.

Let the shell be made of glass-epoxy composite whose mechanical properties are listed in Table 3.5 and creep diagrams are shown in Fig. 7.22. To simplify the analysis, we assume that for the unidirectional composite under study $E_2/E_1 = 0.22$, $G_{12}/E_1 = 0.06$, $\nu_{12} = \nu_{21} = 0$ and introduce the normalized shear strain

$$\overline{\gamma} = \gamma_{xy}\left(\frac{T}{R^{2}hE_1}\right)^{-1}$$

Consider a $\pm 45^{\circ}$ angle-ply material discussed in Section 4.5 for which, with due regard to Eqs. (4.72), and (7.58), we can write

$$A_{44}^{*}(p) = \frac{1}{4}(E_1 + E_2^{*}) = \frac{1}{4}\left[E_1 + \frac{E_2}{1 + C_{22}^{*}(p)}\right]$$

Exponential approximation, Eq. (7.48), of the corresponding creep curve in Fig. 7.22 (the lower dashed line) is

$$C_{22} = A_1 e^{-\alpha_1 \theta}$$

where $A_1 = 0.04$ and $\alpha_1 = 0.06$ 1/day. Using Eqs. (7.54), we arrive at the following Laplace transforms of the creep compliance and the torque which is constant

$$C_{22}^{*}(p) = \frac{A_1}{\alpha_1 + p}, \quad T^{*}(p) = \frac{T}{p}$$

The final expression for the Laplace transform of the normalized shear strain is

$$\overline{\gamma}^{*}(p) = \frac{2E(\alpha_1 + A_1 + p)}{\pi p(\alpha_1 + A_1 E + p)} \tag{7.61}$$

where $E = E_1/(E_1 + E_2)$.

To use Eqs. (7.54) for the inverse Laplace transformation, we should decompose the right-hand part of Eq. (7.61) as

$$\overline{\gamma}^{*}(p) = \frac{2E}{\pi(\alpha_1 + A_1 E)}\left[\frac{\alpha_1 + A_1}{p} - \frac{A_1(1 - E)}{\alpha_1 + A_1 E + p}\right]$$

Applying Eqs. (7.54), we get

$$\overline{\gamma}(t) = \frac{2E}{\pi(\alpha_1 + A_1 E)}\left[\alpha_1 + A_1 - A_1(1 - E)e^{-(\alpha_1 + A_1 E)t}\right]$$

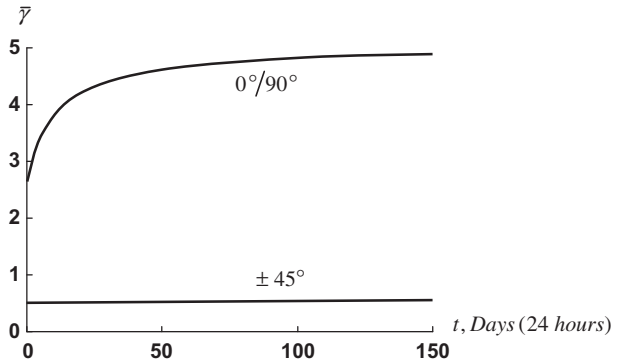


FIGURE 7.26

Dependencies of the normalized shear strain on time for 0°/90° cross-ply and ±45° angle-ply glass-epoxy composite cylinders under torsion.

This result is demonstrated in Fig. 7.26. As can be seen, there is practically no creep because the cylinder's deformation is controlled mainly by the fibers.

Quite different behavior is demonstrated by the cylinder made of 0°/90°cross-ply composite material discussed in Section 4.4. In accordance with Eqs. (4.114) and (7.58), we have

$$A_{44}^*(p) = G_{12}^*(p) = \frac{G_{12}}{1 + K_{12}^*(p)}$$

Exponential approximation, Eq. (7.48), of the shear curve in Fig. 7.22 (the upper dashed line) results in the following equation for the creep compliance

$$K_{12} = A_1 e^{-\alpha_1 \theta} + A_2 e^{-\alpha_2 \theta}$$

in which $A_1 = 0.033$, $\alpha_1 = 0.04$ 1/day, $A_2 = 0.06$, $\alpha_2 = 0.4$ 1/day. Omitting simple rearrangements, we finally get

$$\overline{\gamma} = \frac{E_1}{2\pi G_{12}} \left[1 + \frac{A_1}{\alpha_1}(1 - e^{-\alpha_1 t}) + \frac{A_2}{\alpha_2}\left(1 - e^{-\alpha_2 t}\right) \right]$$

The corresponding creep diagram is shown in Fig. 7.26.

Under relatively high stresses, polymeric composites demonstrate nonlinear viscoelastic behavior. The simplest approach to study nonlinear creep problems is based on experimental isochrone stress-strain diagrams of the type shown in Fig. 7.19. Using the curves corresponding to time moments $t_1 < t_2 < t_3$ etc., we can solve a sequence of nonlinear elasticity problems for these time moments and thus determine the change of strains and stresses with time. This approach, sometimes referred to as the aging theory, is approximate and can be used to study structures loaded with forces that do not change with time, or that change very slowly.

There exist also several variants of nonlinear hereditary theory, described, e.g., by Rabotnov (1980). According to the most common versions, Eq. (7.43) is generalized as

$$\varepsilon(t) = \frac{1}{E}\left[\sigma(t) + \int_0^t C_1(t-\tau)\sigma(\tau)d\tau + \int_0^t\int_0^t C_2(t-\tau_1, t-\tau_2)\sigma(\tau_1)\sigma(\tau_2)d\tau_1 d\tau_2 + \cdots\right]$$

or

$$\varepsilon(t) = \sum_k A_k\left[\sigma(t) + \int_0^t C(t-\tau)\sigma(\tau)d\tau\right]^k$$

or

$$f[\varepsilon(t)] = \frac{1}{E}\left[\sigma(t) + \int_0^t C(t-\tau)\sigma(\tau)d\tau\right]$$

or

$$\varepsilon(t) = \phi\left[\sigma(t)\right] + \int_0^t C(t-\tau)\psi\left[\sigma(\tau)\right]d\tau$$

In conclusion, it should be noted that correctly designed composite structures (see Chapter 12) in which the material behavior is controlled by fibers usually do not exhibit pronounced time-dependent behavior. For example, consider the filament-wound glass-epoxy pressure vessel studied in Section 6.3 (see Fig. 6.22 and the second row in Table 6.1 for parameters of the vessel). The vessel consists of $\pm 36^\circ$ helical plies and circumferential plies, and has structural parameters that are close to optimal (see Section 12.3.1). The experimental dependence of circumferential strain on time for step-wise loading with internal pressure p presented in Fig. 7.27 does not indicate any significant creep deformation. It should be noted that this conclusion is valid for composite materials reinforced with glass or carbon fibers and working under normal conditions (room temperature) whose creep is mainly associated with polymeric matrix.

Composite materials reinforced with aramid and other polymeric fibers can demonstrate significant creep associated with the creep of fibers, and under relatively high stress the behavior of these materials is not linear.

7.3.2 Durability

Composite materials, to be applied to structures with long service life, need to be guaranteed for the corresponding period of time from failure, which is usually a result of an evolutionary process of material degradation in the service environment. To provide adequate durability of the material we need, in turn, to study its long-term behavior under load and its endurance limits. The most widely used durability criteria establishing the dependence of material strength on the time of loading are based on the concept of the accumulation of material damage induced by acting stresses and intensified by the degrading influence of service conditions such as temperature and moisture. Particular criteria depend

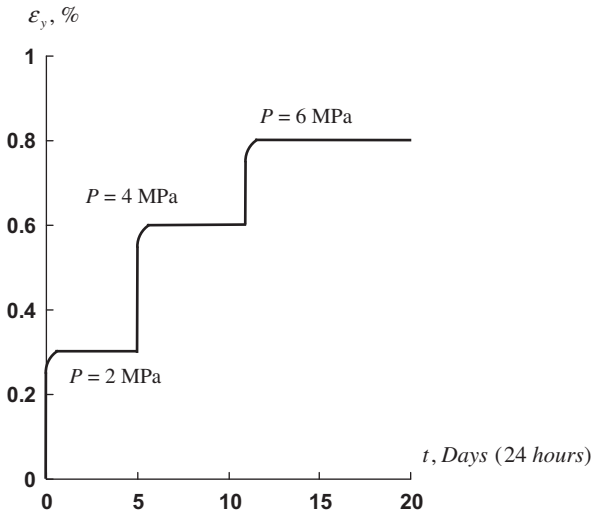


FIGURE 7.27

Dependence of the circumferential strain on time for a glass-epoxy cylindrical pressure vessel loaded in steps with internal pressure p.

on the accepted models simulating the material damage accumulation. Although there exist microstructural approaches to the durability evaluation of composite materials (see, e.g., Skudra et al. (1989)), for practical purposes, the experimental dependencies of the ultimate stresses on the time of their action are usually evaluated. In particular, these experiments allow us to conclude that fibers, which are the major load-carrying elements of composite materials, possess some residual strength $\overline{\sigma}_\infty = \overline{\sigma}(t \to \infty)$, which is about 50% to 70% of the corresponding static strength $\overline{\sigma}_0 = \overline{\sigma}(t = 0)$, depending on the fiber type. Typical dependencies of the long-term strength of composite materials on time are presented in Fig. 7.28. As can be seen, the time of loading dramatically affects material strength. However, being unloaded at any moment of time t, composite materials demonstrate practically the same static strength that they had before long-term loading.

Approximation of the curves shown in Fig. 7.28 can be performed using exponential functions as follows:

$$\overline{\sigma}(t) = \overline{\sigma}_\infty + \sum_n A_n e^{-\lambda_n t} \tag{7.62}$$

in which $\overline{\sigma}_\infty$, A_n, and λ_n are coefficients providing the appropriate approximation. The initial static strength is

$$\overline{\sigma}(0) = \overline{\sigma}_0 = \overline{\sigma}_\infty + \sum_n A_n$$

The simplest is a one-term approximation

$$\overline{\sigma}(t) = \overline{\sigma}_\infty + (\overline{\sigma}_0 - \overline{\sigma}_\infty) e^{-\lambda t} \tag{7.63}$$

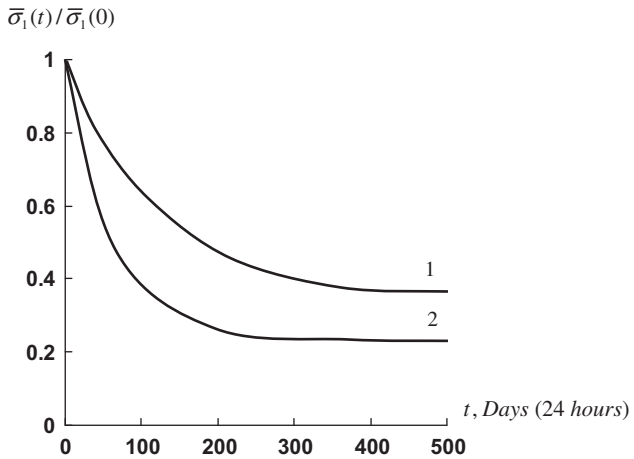


FIGURE 7.28

Normalized long-term longitudinal strength of aramid-epoxy (1) and glass-epoxy (2) unidirectional composites.

To approximate the initial part of the curve, we can put $\overline{\sigma}_\infty = 0$ and arrive at the following equation

$$\overline{\sigma}(t) = \overline{\sigma}_0 e^{-\lambda t} \tag{7.64}$$

Now assume that we can solve Eqs. (7.62), (7.63), or (7.64) for t and find the material durability $t_d(\sigma)$, i.e., the time during which the material can withstand stress σ. Consider the process of loading as a system of k stages such that the duration of each stage is t_i and the stress acting at this stage is σ_i $(i = 1, 2, 3, \ldots, k)$. Then, the whole period of time during which the material can withstand such step-wise loading can be calculated with the aid of the following equation

$$\sum_{i=1}^{k} \frac{t_i}{t_d(\sigma_i)} = 1$$

in which $t_d(\sigma_i)$ is material durability corresponding to stress σ_i.

The strength criteria discussed in Chapter 6 can be generalized for the case of long-term loading if we change the static ultimate stresses entering these criteria for the corresponding long-term strength characteristics.

Experimental study of material durability requires long-term testing that takes considerable time. This time can be substantially reduced by applying the Zhurkov equation (Zhurkov and Narzullaev, 1953), which links the material lifetime t with the stress level σ and absolute temperature T as

$$t = t_0 e^{\frac{1}{RT}(U_0 - \gamma\sigma)} \tag{7.65}$$

in which, originally, t_0 is the period of the atoms' thermal oscillations, U_0 is the energy activating material fracture, γ is the coefficient indicating the influence of stress on the fracture energy, and R is

Boltzmann's constant. However, irrespective of the physical meaning of the forgoing constants, we can treat them as some coefficients that can be found from direct experiments. For this purpose, rewrite Eq. (7.65) as

$$t = t_0 e^{\frac{1}{T}(a - b\sigma)} \tag{7.66}$$

in which t is the time to failure (lifetime), T is the absolute temperature, σ is the stress expressed as a percentage of the static ultimate stress, and t_0, a, and b are experimental constants. Thus, to determine these constants (t_0, a, and b), we need to perform three tests under different temperatures and loading levels.

Suppose that we have the results of these tests, i.e.,

$$\begin{array}{lll} \sigma = \sigma^{(1)}, & T = T_1, & t = t_1 \\ \sigma = \sigma^{(2)}, & T = T_2, & t = t_2 \\ \sigma = \sigma^{(3)}, & T = T_3, & t = t_3 \end{array}$$

Taking the logarithm of Eq. (7.66) and writing the result for the three test cases, we get

$$\ln t_i = \ln t_0 + \frac{1}{T_i}\left(a - b\sigma^{(i)}\right) \tag{7.67}$$

where $i = 1,\ 2,\ 3$. Solving Eqs. (7.67) for a, b, and t_0, we find

$$\begin{aligned} a &= \frac{1}{T_3 - T_2}\left[b\left(\sigma^{(2)} T_3 - \sigma^{(3)} T_2\right) - T_2 T_3 (\ln t_3 - \ln t_2)\right] \\ b &= T_1 \frac{\ln t_1 - \ln t_2}{\sigma^{(2)} - \sigma^{(1)}} \\ t_0 &= t_2 e^{-\frac{1}{T_2}\left(a - b\sigma^{(2)}\right)} \end{aligned}$$

Application of Eq. (7.65) to an organic fiber Kevlar 49 unidirectional composite material under tension along the fibers has been undertaken by Chiao et al. (1977). Composite materials with the static tensile strength $\overline{\sigma}_1 = 2280$ MPa have been tested under various temperatures and the loading levels σ. The results are presented in Fig. 7.29, which demonstrates dramatic effects of the temperature and stress on the lifetime t.

Using the test results shown in Fig. 7.29, Chiao et al. have arrived at the following form of Eq. (7.66) (Chiao et al., 1977):

$$t = 7.9 \cdot 10^{-11}\ e^{\frac{1}{T}(18246 - 123\sigma)} \tag{7.68}$$

in which t is measured in hours and σ in percentage. Comparison of the results calculated using Eq. (7.68) and those obtained from the experiment is presented in Table 7.2 (Chiao et al., 1977). As can be seen, the approach under consideration provides fair prediction of the material lifetime.

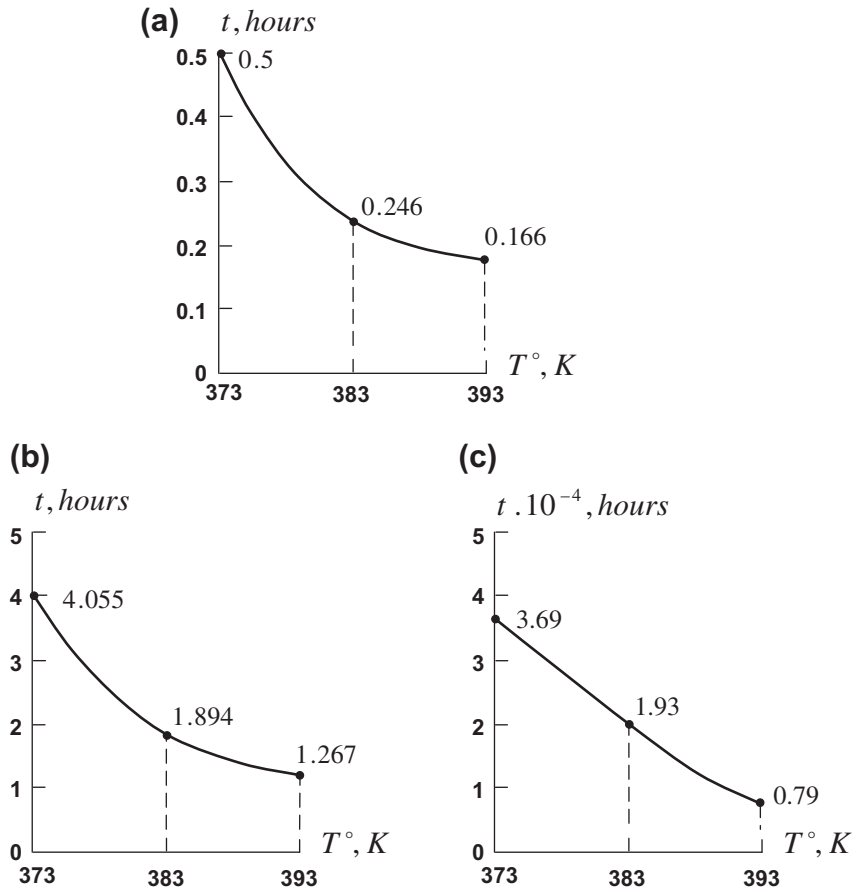


FIGURE 7.29

Dependencies of the material lifetime on temperature for loading levels of 80.4% (a), 73.2% (b), and 67.2% (c).

Table 7.2 Predicted (t_p) and Experimental (t_e) Lifetimes Under Room Temperature.

σ, %	70	75	80	85	90
t_p, hours	8725	1108	141	17.9	2.3
t_e, hours	8800	1150	150	7.6	0.8

7.3.3 Cyclic loading

Consider the behavior of composite materials under the action of loads periodically changing with time. For qualitative analysis, first consider a material that can be simulated with the simple mechanical model shown in Fig. 7.23. Applying stress acting according to the following form

$$\sigma(t) = \sigma_0 \sin \omega t \tag{7.69}$$

where σ_0 is the amplitude of stress and ω is the frequency, we can solve Eq. (7.53) that describes the model under study for strain $\varepsilon(t)$. The result is

$$\varepsilon(t) = \varepsilon_0 \sin(\omega t + \theta) \tag{7.70}$$

where

$$\begin{aligned} \varepsilon_0 &= \sigma_0 \sqrt{\frac{1 + t_r^2 \omega^2}{E_l^2 + E_i^2 t_r^2 \omega^2}} \\ \tan\theta &= -\frac{t_r \omega (E_i - E_l)}{E_l + E_i t_r^2 \omega^2} \end{aligned} \tag{7.71}$$

It follows from these equations that a viscoelastic material is characterized with a phase shift of strain with respect to stress. Eliminating the time variable from Eqs. (7.69) and (7.70), we arrive at the following relationship between stress and strain:

$$\left(\frac{\sigma}{\sigma_0}\right)^2 + \left(\frac{\varepsilon}{\varepsilon_0}\right)^2 - 2\cos\theta \frac{\sigma\varepsilon}{\sigma_0\varepsilon_0} = \sin^2\theta$$

This is the equation of an ellipse shown in Fig. 7.30a. The absolute value of the area A inside this ellipse (its sign depends on the direction of integration along the contour) determines the energy dissipation per single cycle of vibration, i.e.,

$$\Delta W = |A| = \pi \sigma_0 \varepsilon_0 |\sin\theta| \tag{7.72}$$

Following Zinoviev and Ermakov (1994), we can introduce the dissipation factor as the ratio of energy loss in a loading cycle, ΔW, to the value of the elastic potential energy in a cycle, W, as

$$\psi = \frac{\Delta W}{W}$$

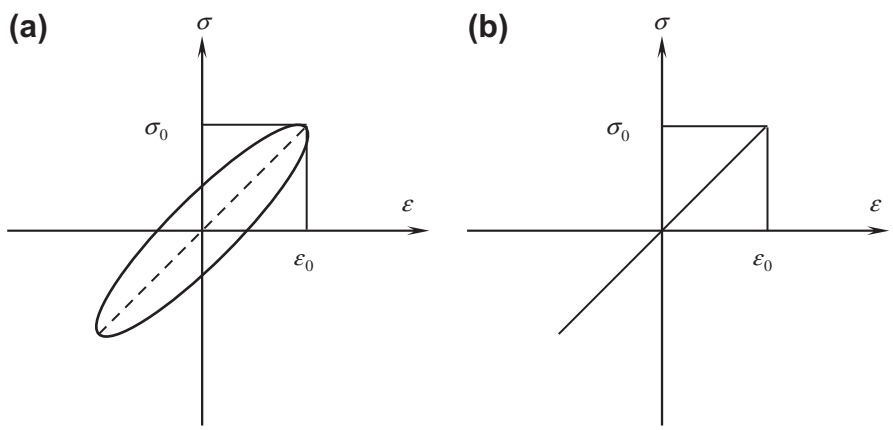


FIGURE 7.30

Stress-strain diagrams for viscoelastic (a) and elastic (b) materials.

where, in accordance with Fig. 7.30b, $W = (1/2)\sigma_0\varepsilon_0$. Transforming Eq. (7.72) with the aid of Eqs. (7.71), we arrive at

$$\psi = \frac{2\pi t_r \omega}{1 + t_r^2\omega^2}\left(1 - \frac{E_l}{E_i}\right)$$

As follows from this equation, ψ depends on the number of oscillations accomplished during the period of time equal to the material relaxation time, t_r, and reaches a maximum value for $t_r\omega = 1$.

As shown by Zinoviev and Ermakov (1994), for anisotropic materials the dissipation factor depends also on the direction of loading. Particularly, for a unidirectional composite ply, referred to axes x and y and making angle ϕ with the principal material axes 1 and 2 as in Fig. 4.18, the dissipation factors are

$$\psi_x = E_x\left[\left(\frac{\psi_1}{E_1}\cos^2\phi - \frac{\psi_2}{E_2}\sin^2\phi\right)\cos 2\phi + \psi_{45}\mu_{12}\sin^2\phi\cos^2\phi\right]$$

$$\psi_y = E_y\left[\left(\frac{\psi_2}{E_2}\cos^2\phi - \frac{\psi_1}{E_1}\sin^2\phi\right)\cos 2\phi + \psi_{45}\mu_{12}\sin^2\phi\cos^2\phi\right]$$

$$\psi_{xy} = G_{xy}\left[\left(\frac{2\psi_1}{E_1} + \frac{2\psi_2}{E_2} - \psi_{45}\mu_{12}\right)\sin^2\phi\cos^2\phi + \frac{\psi_{12}}{G_{12}}\cos^2 2\phi\right]$$

where

$$\mu_{12} = \frac{1 - \nu_{12}}{E_1} + \frac{1 - \nu_{21}}{E_2} + \frac{1}{G_{12}}$$

E_x, E_y and G_{xy} are specified by Eqs. (4.76) and ψ_1, ψ_2, ψ_{12}, and ψ_{45} are the ply dissipation factors corresponding to loading along the fibers, across the fibers, under in-plane shear and at 45° with respect to principal material axes 1 and 2. As follows from Fig. 7.31, calculations based on the foregoing equations provide fair agreement with experimental results of Ni and Adams (1984).

Energy dissipation in conjunction with the relatively low heat conductivity of composite materials induces their self-heating during cyclic loading. The dependence of an aramid-epoxy composite material's temperature on the number of cycles under tensile and compressive loading with frequency 10^3 cycles per minute is shown in Fig. 7.32 (Tamuzh and Protasov, 1986).

Under cyclic loading, structural materials experience a fatigue fracture caused by material damage accumulation. As already noted in Section 3.2.4, the heterogeneous structure of composite materials provides relatively high resistance of these materials to crack propagation resulting in their specific behavior under cyclic loading. It follows from Fig. 7.33 that stress concentration in aluminum specimens, which has practically no effect on the material's static strength due to plasticity of aluminum, dramatically reduces its fatigue strength. Conversely, the static strength of carbon-epoxy composites, which are brittle materials, is reduced by stress concentration that has practically no effect on the slope of the fatigue curve. On average, the residual strength of carbon composites after 10^6 loading cycles is 70–80% of the material's static strength, in comparison to 30–40% for aluminum alloys. Qualitatively, this comparative evaluation is true for all fibrous composites that are widely used in structural elements subjected to intensive vibrations, for example helicopter rotor blades, airplane propellers, drive shafts, automobile leaf springs.

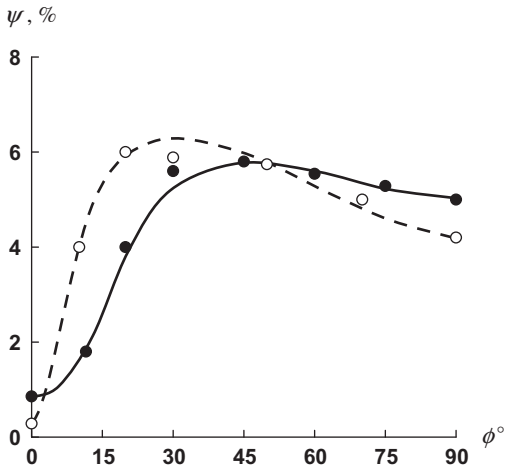


FIGURE 7.31

Calculated (dots) and experimental (circles) dependencies of dissipation factor on the ply orientation for glass-epoxy (——— ●) and carbon-epoxy (––– ○) unidirectional composites.

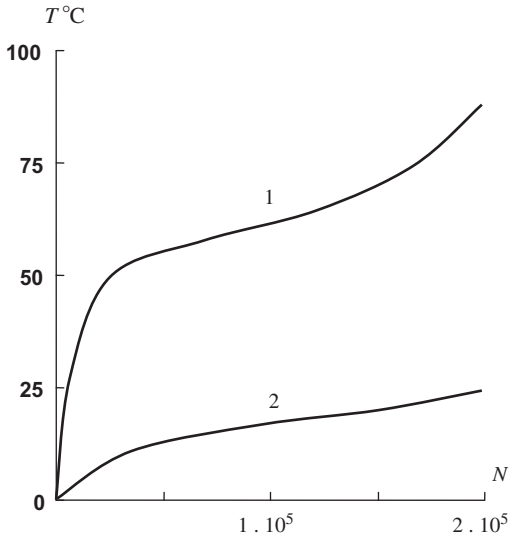


FIGURE 7.32

Temperature of an aramid-epoxy composite as a function of the number of cycles under tension (1) and compression (2).

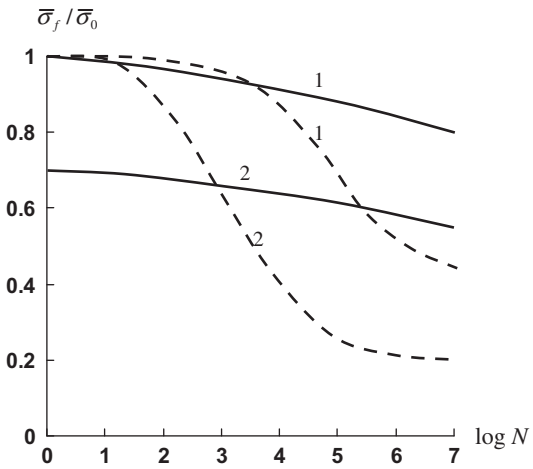


FIGURE 7.33

Typical fatigue diagrams for carbon-epoxy composite (solid lines) and aluminum alloy (dashed lines) specimens without (1) and with (2) stress concentration (fatigue strength is normalized to static strength of specimens without stress concentration).

The foregoing discussion concerns the fatigue strength of unidirectional composites loaded along the fibers. However, composites are anisotropic materials having different strengths in different directions and, naturally, different responses under cyclic loading. As shown in Fig. 7.34, presenting the approximations of the experimental results given by Tsai (1987), the degradation of material strength under tension across the fibers (line 2) is much higher than under tension along the fibers (line 1). Recall that the stress σ_2 induces the cracks in the matrix discussed in Sections 4.4.2 and 6.4.

A typical composite materials fatigue diagram, constructed from the experimental results of Apinis et al. (1991), is shown in Fig. 7.35. Standard fatigue diagrams usually determine the material strength for $10^3 \leq N \leq 10^6$ and are approximated as

$$\sigma_R = a - b \log N \tag{7.73}$$

Here, N is the number of cycles to failure under stress σ_R and a and b are experimental constants depending on frequency of cyclic loading, temperature, and other environmental factors, and on the stress ratio $R = \sigma_{\min}/\sigma_{\max}$, where $\sigma_{\max}$ and $\sigma_{\min}$ are the maximum and the minimum stresses. It should be taken into account that the results for fatigue tests are characterized, as a rule, with high scatter.

Factor R specifies the cycle type. The most common bending fatigue test provides a symmetric cycle for which $\sigma_{\min} = -\sigma$, $\sigma_{\max} = \sigma$, and $R = -1$. A tensile load cycle ($\sigma_{\min} = 0$, $\sigma_{\max} = \sigma$) has $R = 0$, whereas a compressive cycle ($\sigma_{\min} = -\sigma$, $\sigma_{\max} = 0$) has $R \rightarrow -\infty$. Cyclic tension with $\sigma_{\max} > \sigma_{\min} > 0$ corresponds to $0 < R < 1$, whereas cyclic compression with $0 > \sigma_{\max} > \sigma_{\min}$ corresponds to $1 < R < \infty$. Fatigue diagrams for unidirectional aramid-epoxy composite studied by Limonov and Anderson (1991) corresponding to various R-values are presented in Fig. 7.36. Similar results (Anderson et al., 1991) for carbon-epoxy composites are shown in Fig. 7.37.

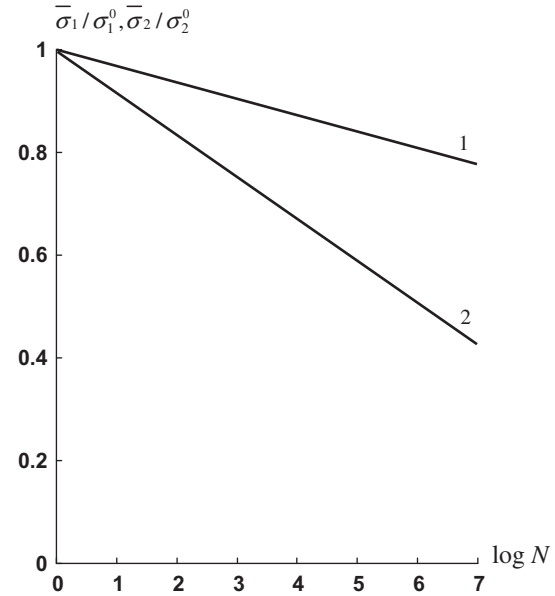


FIGURE 7.34

Normalized fatigue strength of carbon-epoxy composites loaded along (1) and across (2) the fibers.

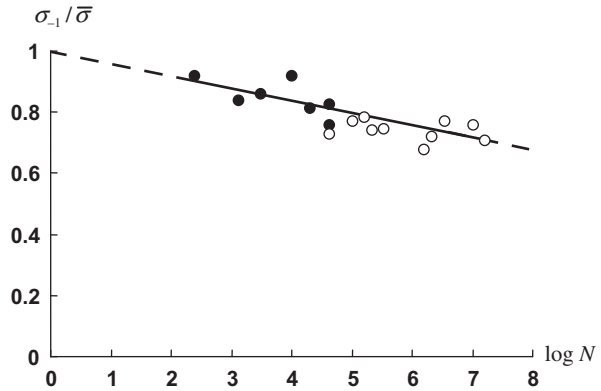


FIGURE 7.35

Normalized fatigue diagram for fabric carbon-carbon composite material ($\overline{\sigma}$-static strength), ● ——— ○ experimental part of the diagram loading frequency 6Hz (●) and 330Hz (○), ▬ ▬ ▬ extrapolation.

Since only σ_{-1} is usually available from standard tests under cyclic bending, fatigue strengths for other load cycles are approximated as

$$\sigma_R = \sigma_{-1} + \sigma_m\left(1 - \frac{\sigma_{-1}}{\overline{\sigma}_t}\right)$$

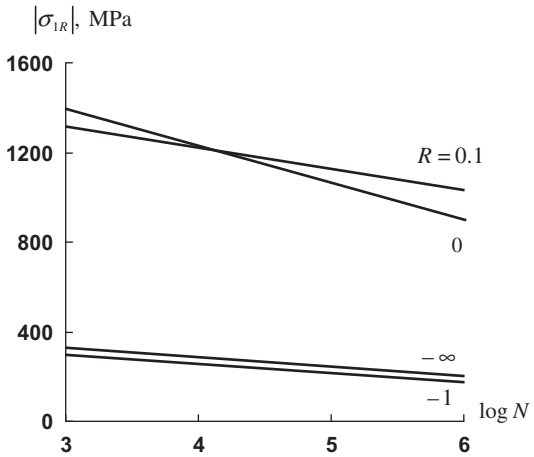


FIGURE 7.36

Fatigue diagrams for unidirectional aramid-epoxy composite loaded along the fibers with various stress ratios.

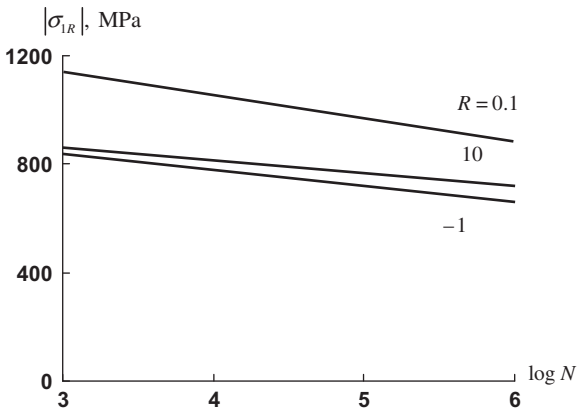


FIGURE 7.37

Fatigue diagrams for a unidirectional carbon-epoxy composite loaded along the fibers with various stress ratios.

where $\sigma_m = (\sigma_{\min} + \sigma_{\max})/2$ is the mean stress of the load cycle and $\overline{\sigma}_t$ is the material long-term strength (see Section 7.3.2) for the period of time equal to that of the cyclic loading.

Fabric composites are more susceptible to cyclic loading than materials reinforced with straight fibers. This fact is illustrated in Fig. 7.38, showing the experimental results of Schulte et al. (1987).

The foregoing discussion deals with high-cycle fatigue. The initial interval $1 \leq N \leq 10^3$ corresponding to so-called low-cycle fatigue is usually studied separately, because the slope of the approximation in Eq. (7.73) can be different for high stresses. A typical fatigue diagram for this case is shown in Fig. 7.39 (Tamuzh and Protasov, 1986).

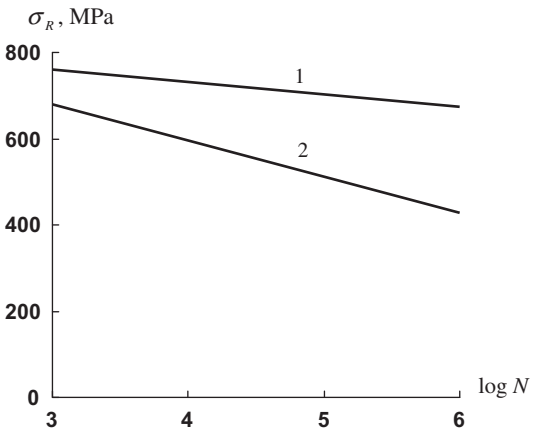


FIGURE 7.38

Tensile fatigue diagrams for cross-ply (1) and fabric (2) carbon-epoxy composites.

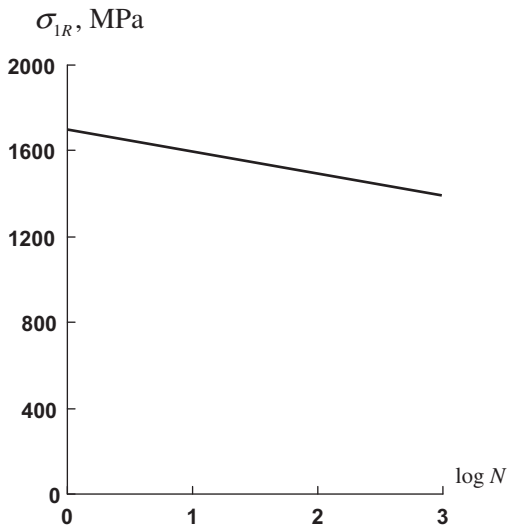


FIGURE 7.39

Low-cycle fatigue diagram for unidirectional aramid-epoxy composite loaded along the fibers with $R = 0.1$.

Fatigue has also some effect on the stiffness of composite materials. This can be seen in Fig. 7.40, demonstrating a reduction in the elastic modulus for a glass-fabric-epoxy-phenolic composite under low-cycle loading (Tamuzh and Protasov, 1986). This effect should be accounted for in the application of composites to the design of structural members such as automobile leaf springs that, being subjected to cyclic loading, are designed under stiffness constraints.

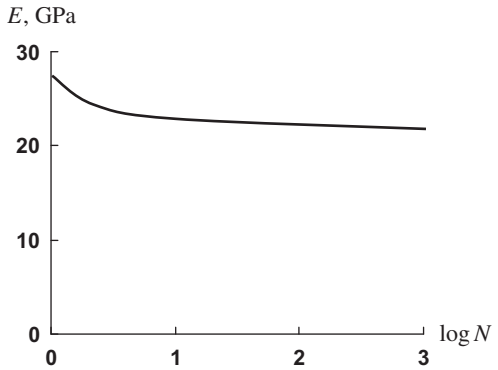


FIGURE 7.40

Dependence of elastic modulus of glass-fabric-epoxy-phenolic composite on the number of cycles at stress $\sigma = 0.5\overline{\sigma}$ ($\overline{\sigma}$ is the static ultimate stress).

Stiffness degradation can be used as an indication of material damage to predict fatigue failure. The most sensitive characteristic of the stiffness change is the tangent modulus E_t specified by the second equation in Eqs. (1.8). The dependence of E_t on the number of cycles, $\overline{N}$, normalized to the number of cycles that cause material fatigue fracture under the preassigned stress, is presented in Fig. 7.41, corresponding to a $\pm 45^\circ$ angle-ply carbon-epoxy laminate studied by Murakami et al. (1991).

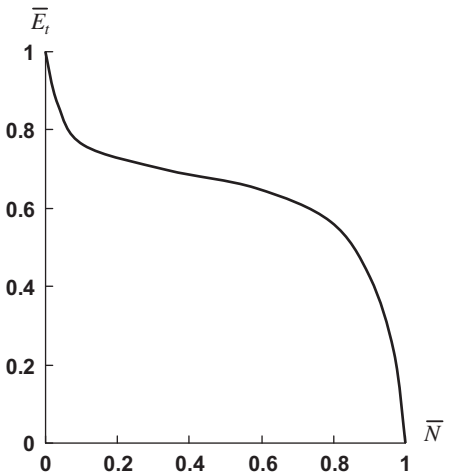


FIGURE 7.41

Dependence of the tangent modulus normalized to its initial value on the number of cycles related to the ultimate number corresponding to fatigue failure under stress $\sigma_{max} = 120$ MPa and $R = -1$ for $\pm 45^\circ$ angle-ply carbon-epoxy laminate.

7.3.4 Impact loading

Thin-walled composite laminates possessing high in-plane strength and stiffness are rather susceptible to damage initiated by transverse impact loads that can cause fiber breakage, cracks in the matrix, delamination, and even material penetration by the impactor. Depending on the impact energy determined by the impactor mass and velocity and the properties of laminate, impact loading can result in considerable reduction in material strength under tension, compression, and shear. One of the most dangerous consequences of an impact loading is an internal delamination in laminates (so-called barely visible impact damage (BVID)), which can sometimes be hardly noticed by visual examination.

Impact loading causing delamination of composite materials is critical for design of the laminated skin for modern composite airframe structures with load-carrying skin supported by stringers and rings as shown in Fig. 7.42. To study the impact loading, a special tool shown in Fig. 7.43 is recommended by ASTM Standard D7136. To model the impact loading, a rectangular 100×150 mm composite plate is fixed on a metal plate with a rectangular 75×125 mm cutout made in the center. The central part of the composite panel situated above the cutout is impacted by the steel drop-weight cylinder having a hemispherical nose of 8 mm in diameter. The mass of the cylinder is $m_W = 5.45$ kg. The cylinder moves inside the pipe as shown in Fig. 7.43.

The intensity of impact is specified by the given kinetic energy E_0, which is measured in joules ($1\ \text{J} = 1\ \text{N} \cdot \text{m}$) and is expressed in terms of the mass m_0 and velocity V_0 of the actual flying objects as

$$E_0 = \frac{1}{2} m_0 V_0^2 \tag{7.74}$$

The velocity of the drop-weight falling from the height H and the corresponding kinetic energy are

$$V_W = \sqrt{2gH}, \quad E_W = \frac{1}{2} m_W V_W^2 \tag{7.75}$$



FIGURE 7.42

Composite airframe structure with load carrying skin.



FIGURE 7.43

The test rig simulating the impact loading of a composite panel.

The real impact is simulated under condition $E_W = E_0$. Then the velocity and the height of the drop-weight following from Eqs. (7.74) and (7.75) are calculated as

$$V_W = V_0\sqrt{\frac{m_0}{m_W}}, \quad H = \frac{V_W^2}{2g}$$

After the impact, compressive strength of the composite plate is found using the test fixture shown in Fig. 7.44. The fixed metal parts, as well as the upper part that compresses the plate, have 5 mm deep grooves whose width is equal to the plate thickness. The plate is inserted into the grooves which fix the plate edges.

To perform the impact tests, quasi-isotropic $(0°/90°/\pm 45°)$ symmetric 8 mm thick carbon-epoxy plates have been fabricated by filament winding on the flat mandrel and tested as shown in Figs. 7.43 and 7.44. Relatively high impact energy causes complete delamination of the plate. Delamination area (black) for the plate after impact with energy $E = 90$ J is shown in Fig. 7.45a, whereas Fig. 7.45b demonstrates the interlaminar cracks in this plate. Reduction of the impact energy decreases the delamination area. This is illustrated in Fig. 7.46 where the contour of the delamination area is marked by the white line. This delamination was induced by the impact with energy $E = 35$ J and represents the BVID. The depth of the crater on the plate surface is only 0.3 mm, and this crater can hardly be detected by visual examination of the surface. Nevertheless, the diameter of the delamination area is about 70 mm, and further testing using the test rig shown in Fig. 7.44 results in reduction in the ultimate compressive force by a factor of four.

Dependence of the diameter of delamination area on the impact area plotted in accordance with experimental results of Hwang et al. (2000) for 2.3 mm thick carbon-epoxy plates, is shown in Fig. 7.47 (solid line). Extrapolation of the experimental curve to the axis $d = 0$ gives the minimum energy inducing material delamination: $E_m = 3$ J. This is a very low energy level, corresponding to a 1 kg mass falling from a 0.3 m height.

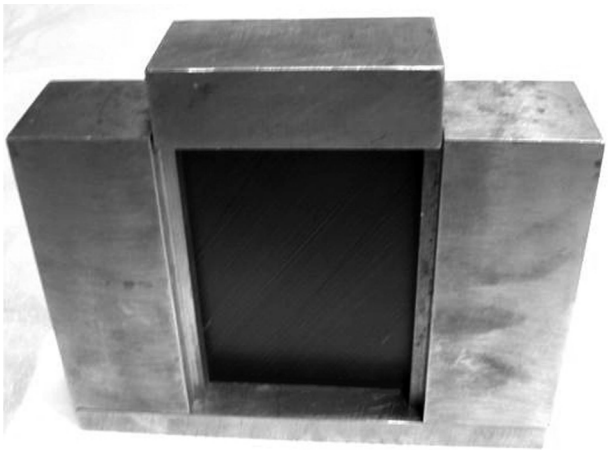


FIGURE 7.44

Composite plate in a clamping fixture for compression test.

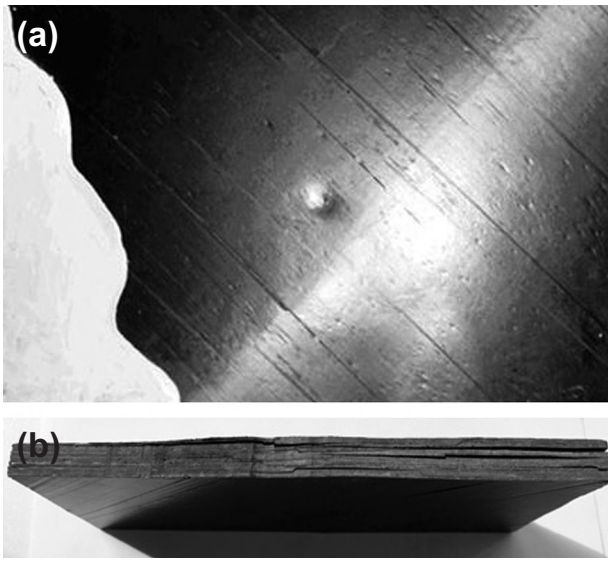


FIGURE 7.45

Delamination area (black); (a) and interlaminar cracks; (b) in the plate after impact with energy $E = 90$ J.

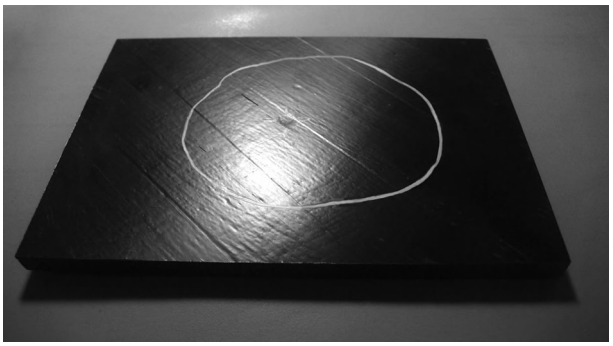


FIGURE 7.46

Delamination area of the plate after impact with energy $E = 35$ J.

It follows from the foregoing results and discussion that laminated composite materials have rather poor resistance to impact. This conclusion is supported by the experiments with relatively thin skin, the results of which are presented in Fig. 7.48. The skin with thickness of 1.6 mm has been made of carbon fabric by winding. As can be seen in Fig. 7.48, the skin is penetrated by the steel indenter with the energy exceeding just 15 J.

Thus, the obvious conclusion that composite material cannot be used in load-carrying structures subjected to impact suggests itself. However, this pessimistic conclusion relates more to the method of

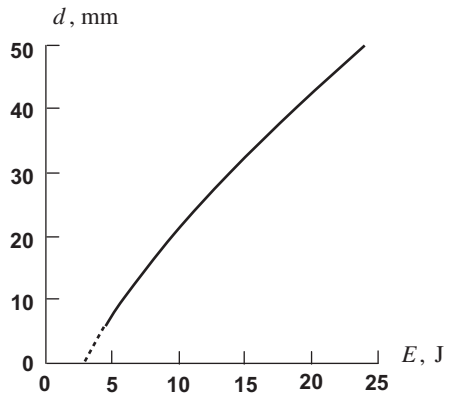


FIGURE 7.47

Dependence of diameter of delamination area on the impact energy for quasi-isotropic 2.3 mm-thick carbon-epoxy plates: experiment (——); extrapolation (·····).

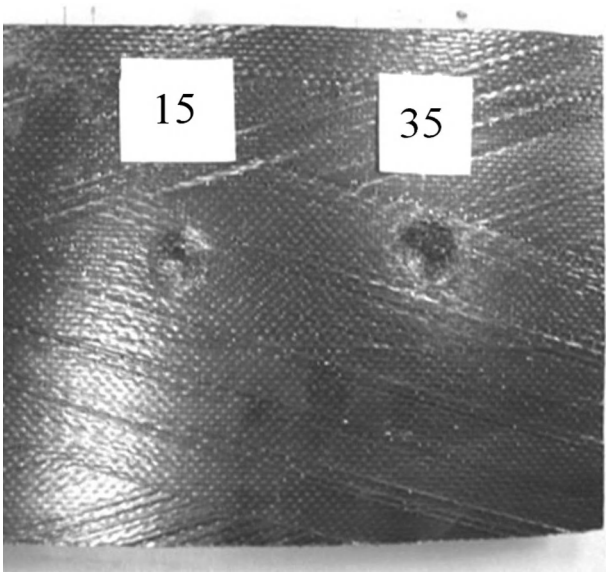


FIGURE 7.48

Damage of a thin fabric skin caused by impact loading with energies 15 J and 35 J.

impact test (see Fig. 7.43) than to the real ability of composite materials to resist impact loading. Indeed, the experiments with ice hail accelerated in a gas gun show that the damage demonstrated in Fig. 7.48 is caused by the hail ice with energy exceeding 400 J, which is by an order of magnitude higher than the energy of the steel indenter. The same is true for the delamination under impact

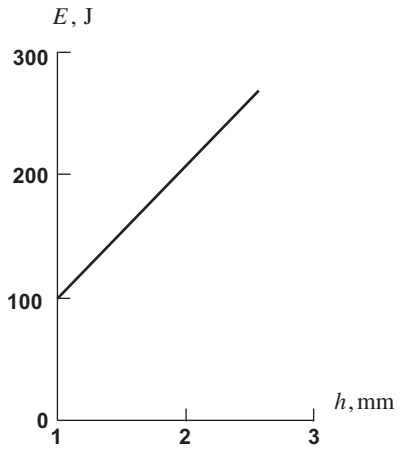


FIGURE 7.49

Dependencies of the delamination energy on the thickness of composite plates impacted by the hail ice with diameter $D = 47.2$ mm.

loading. Dependence of the energy causing material delamination on the thickness of the quasi-isotropic carbon-epoxy laminate plotted in accordance with experimental results of Kim and Kedward (1999a, b) who have studied the hail ice impact is presented in Fig. 7.49.

The difference between the steel impactor and the hail ice is in different masses and velocities of the impacting objects. The velocity of the steel impactor V_m can be found from Eqs. (7.75), whereas the velocity of the hail ice is specified by the following equation (Davis and Sakata, 1981):

$$V_h = 17.1\sqrt{D}$$

in which V_h is measured in m/sec and the hail ice pellet diameter D is substituted in mm. Parameters of the hail ice with density 850 kg/m^3 are listed in Table 7.3.

Compare now Fig. 7.47 and Fig. 7.49, both showing the energy of delamination under impact. For a 2.3 mm thick plate (see Fig. 7.47), the energy of the steel impactor with mass $m_W = 4.8$ kg which causes the plate delamination is $E_W = 3\ J$. For the plate of the same thickness and the hail ice with diameter $D = 42.7$ mm and $m_h = 0.035$ kg, it follows from Fig. 7.49 that $E_h = 240$ J, which is higher than E_W by a factor of 80. Thus, the higher the indenter mass, the lower the delamination energy.

Table 7.3 Mass, Velocity, and Kinetic Energy of Hail Ice with Various Diameters.

Hail ice diameter D, mm	Mass m_h, grams	Velocity V_h, m/s	Kinetic energy E, J
10	0.44	54.1	0.64
20	3.56	76.5	10.41
30	12.01	93.7	52.7
40	28.47	108.1	166.3
50	55.60	120.9	406.3

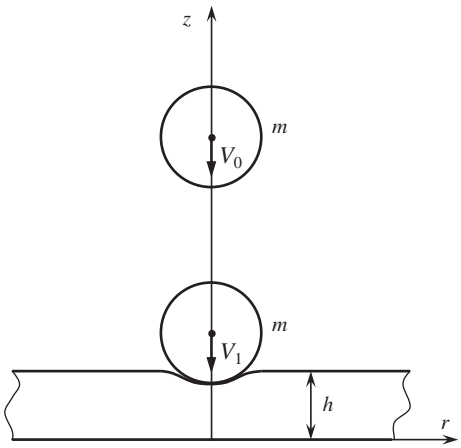


FIGURE 7.50

Interaction between the impactor and the plate.

To explain this effect, consider Fig. 7.50, which shows the impactor whose mass and initial velocity are m and V_0, respectively. Assume that V_0 is much less than the velocity of the shock wave propagation in the plate. Then, after the contact between the impactor and the plate, the contact velocity reduces to $V_1 < V_0$, whereas the velocity of the plate points becomes $V = V_1 f(r, z)$ in which $f(r = 0,\ z = h) = 1$ and $f(r \to \infty,\ z) = 0$. The balance of momentum is

$$mV_0 = V_1 \left(m + 2\pi\rho \int_0^\infty dr \int_0^h f(r,\ z) r dr \right) \tag{7.76}$$

where ρ is the density of plate material and h is the plate thickness. The balance equation, Eq. (7.76), allows us to determine V_1 as

$$V_1 = \frac{V_0}{1 + m_1/m}, \quad m_1 = 2\pi\rho \int_0^\infty dr \int_0^h f(r,\ z) r dr \tag{7.77}$$

in which m_1 is the reduced mass of the plate. Function $f(r, z)$ is not known; however, for qualitative analysis, it is not necessary to know it. Let $m_1/m \ll 1$, which means that the impactor mass is much higher than the reduced mass of the plate. In this case, which is typical for the test shown in Fig. 7.43, $V_1 \approx V_0$ and the plate practically does not reduce the kinetic energy of the impactor E_0. If $m_1/m \gg 1$, Eq. (7.77) gives $V_1 \ll V_0$ and the actual kinetic energy of the impactor, E_1, can be considerably lower than E_0. The energy dissipation $\Delta E = E_0 - E_1$ is absorbed by the impactor, which slows down and experiences deformation and sometimes fracture (this is typical for hail ice).

Thus, the conventional impact test (Fig. 7.43) based on the condition $E_W = E_0$ cannot provide adequate evaluation of the material impact resistance if the drop-weight mass in the experiment is considerably higher than the mass of the impactor in real conditions.

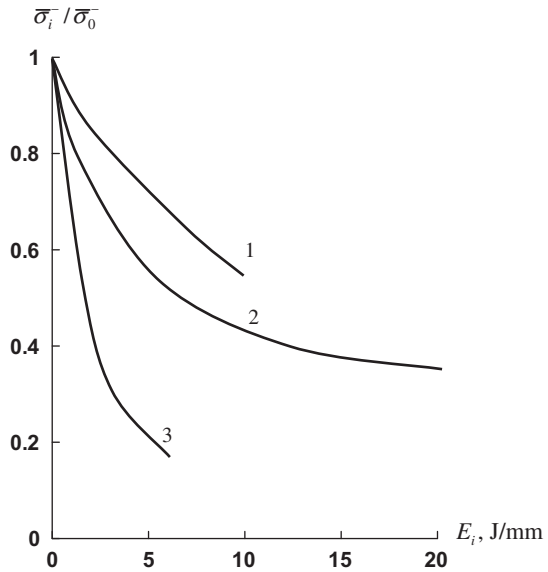


FIGURE 7.51

Dependence of compression strength after impact normalized to the initial compressive strength on the impact energy related to the plate thickness for glass-fabric-epoxy (1), unidirectional glass-epoxy (2), and carbon-epoxy composite plates (3).

The other comment concerns the conventional compression test (see Fig. 7.44). The results of this test are usually presented in the form shown in Fig. 7.51 which demonstrates the dependencies of the normalized ultimate compression stress on the impact energy referred to the plate thickness (Verpoest et al., 1989). As can be seen, the ultimate compression stress dramatically reduces with the increase in the impact energy. However, simple considerations allow us to conclude that the plate strength cannot depend on delamination induced by impact. Indeed, consider two plates, the first of which is monolithic and the second of which has interlaminar cracks parallel to the plate surfaces (see Fig. 7.45). Under in-plane compression, the cross-sectional area of both plates is the same, as well as the material strength. So, interlaminar cracks cannot reduce the plate compressive strength. The observed reduction of the ultimate compressive force for the delaminated plate is associated with local buckling of the plate surface layers (see Fig. 7.52). However, the buckling load, in contrast to strength, is not the material characteristic. The critical force depends on the relative thickness of the delaminated part of the plate, h_d/h (see Fig. 7.52), delamination size, a, and the boundary conditions (type of the plate support). Dependence of the load F (see Fig. 7.52) on the axial deformation ε calculated applying the finite-element method by Liang and Yuan (1993) for the plate with $h_d/h = 0.2$ and $a/l = 0.5$ is shown in Fig. 7.53. The diagram consists of two parts corresponding to pre-buckling and post-buckling deformation (as opposed to a compression diagram, which is usually linear up to failure). Thus, the conventional dependencies of the effective ultimate compression stress on the impact energy, like that shown in Fig. 7.51, are of a qualitative nature and cannot completely characterize material behavior after impact.

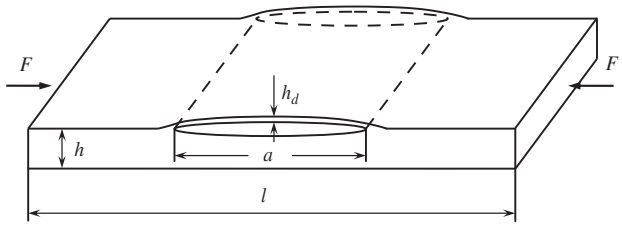


FIGURE 7.52

Local buckling of the surface layers under compression.

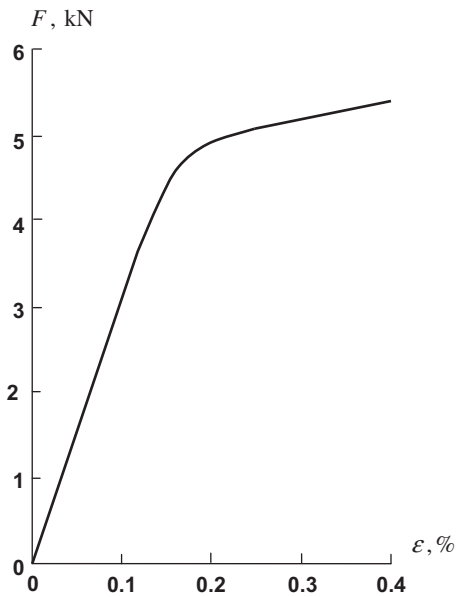


FIGURE 7.53

Load vs. plate shortening under compression for the plate with a crack.

Delamination discussed earlier is caused mainly by interlaminar shear stresses. Under high-velocity impact, delamination can be also caused by normal stresses induced by superposition of shock waves propagating through the thickness.

To study the mechanism of material delamination caused by transverse normal stresses, consider the problem of wave propagation through the thickness of the laminate shown in Fig. 7.54. The motion equation has the following well-known form

$$\frac{\partial}{\partial z}\left(E_z \frac{\partial u_z}{\partial z}\right) = \rho \frac{\partial^2 u_z}{\partial t^2} \tag{7.78}$$

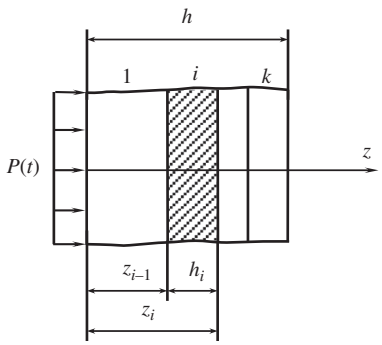


FIGURE 7.54

Laminate under impact load.

Here, u_z is the displacement in the z direction, E_z is material modulus in the same direction depending, in the general case, on z, and ρ is the material density. For the laminate in Fig. 7.54, the solution of Eq. (7.70) should satisfy the following boundary and initial conditions

$$\begin{gathered}\sigma_z(z=0,t)=-p(t)\\ \sigma_z(z=h,t)=0\end{gathered} \tag{7.79}$$

$$u_z(z,t=0)=0, \qquad \frac{\partial u_z}{\partial t}(z>0,t=0)=0 \tag{7.80}$$

in which

$$\sigma_z = E_z\frac{\partial u_z}{\partial z} \tag{7.81}$$

is the interlaminar normal stress.

Consider first a homogeneous layer such that E_z and ρ do not depend on z. Then, Eq. (7.78) takes the form

$$c^2\frac{\partial^2 u_z}{\partial z^2}=\frac{\partial^2 u_z}{\partial t^2}$$

where $c^2 = E_z/\rho$. Transform this equation introducing new variables, i.e., $x_1 = z + ct$ and $x_2 = z - ct$. Performing conventional transformation and rearrangement, we arrive at

$$\frac{\partial^2 u_z}{\partial x_1 \partial x_2}=0$$

The solution for this equation can be readily found and presented as

$$u_z=\phi_1(x_1)+\phi_2(x_2)=\phi_1(z+ct)+\phi_2(z-ct)$$

Here, ϕ_1 and ϕ_2 are some arbitrary functions. Using Eq. (7.81), we get

$$\sigma_z = E_z\Big[f_1(x+ct)+f_2(x-ct)\Big]$$

where

$$f_1 = \frac{\partial \phi_1}{\partial z}, \quad f_2 = \frac{\partial \phi_2}{\partial z}$$

Applying the boundary and initial conditions, Eqs. (7.79) and (7.80), we arrive at the following final result

$$\sigma_z = E\Big[f(x+ct)-f(x-ct)\Big] \tag{7.82}$$

in which the form of function f is governed by the shape of the applied pulse. As can be seen, the stress wave is composed of two components having opposite signs and moving in opposite directions with one and the same speed c, which is the speed of sound in the material. The first term in Eq. (7.82) corresponds to the applied pulse that propagates to the free surface $z = h$ (see Fig. 7.55, demonstrating the propagation of a rectangular pulse), whereas the second term corresponds to the pulse reflected from the free surface $z = h$. It is important that for a compressive direct pulse (which is usually the case), the reflected pulse is tensile and can cause material delamination since the strength of laminated composites under tension across the layers is very low.

Note that the speed of sound in a homogeneous material, i.e.,

$$c = \sqrt{\frac{E_z}{\rho}} \tag{7.83}$$

is the same for the tensile and compressive waves in Fig. 7.55. This means that the elastic modulus in Eq. (7.83) must be the same for both tension and compression. For composite materials, tensile and compressive tests sometimes produce modulus values that are slightly different. Usually, the reason for such a difference is that the different specimens and experimental techniques are used for tensile and compression tests. Testing of fiberglass fabric coupons (for which the difference in the experimental values of tensile and compressive moduli is sometimes observed) involving continuous loading from compression to tension through zero load does not show any "kink" in the stress-strain diagram at zero stress. Naturally, for heterogeneous materials, the apparent (effective) stiffness can

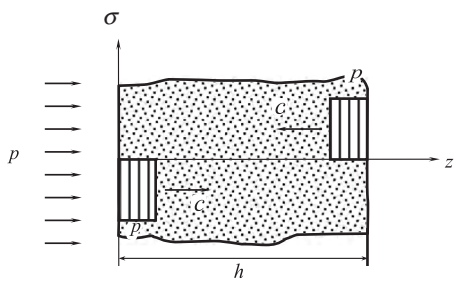


FIGURE 7.55

Propagation of direct and reflected pulses through the layer thickness.

be different for tension and compression as, for example, in materials with cracks which propagate under tension and close under compression. Sometimes stress-strain diagrams with a "kink" at the origin are used to approximate nonlinear experimental diagrams that actually do not have a "kink" at the zero stress level at all.

For laminates, such as that shown in Fig. 7.54, the boundary conditions, Eqs. (7.79), should be supplemented with the interlaminar conditions $u_z^{(i)} = u_z^{(i-1)}$ and $\sigma_z^{(i)} = \sigma_z^{(i-1)}$. Omitting the rather cumbersome solution that can be found elsewhere (Vasiliev and Sibiryakov, 1985), we present some numerical results.

Consider the two-layered structure: the first layer has thickness 15 mm and is made of aramid-epoxy composite material with $E_z^{(1)} = 4.2$ GPa, $\rho_1 = 1.4$ g/cm^3, and the second layer is made of boron-epoxy composite material and has $E_z^{(2)} = 4.55$ GPa, $\rho_2 = 2$ g/cm^3, and $h_2 = 12$ mm. The duration of a rectangular pulse of external pressure p acting on the surface of the first layer is $t_p = 5 \times 10^{-6}$ s. The dependence of the interlaminar ($z = 15$ mm) stress on time is shown in Fig. 7.56. As can be seen, at $t \approx 3t_p$ the tensile interface stress exceeds the intensity of the pulse of pressure by a factor of 1.27. This stress is a result of interaction of the direct stress wave with the waves reflected from the laminate's inner, outer, and interface surfaces. Thus, in a laminate, each interface surface generates elastic waves.

For laminates consisting of more than two layers, the wave interaction becomes more complicated and, what is more important, can be controlled by the appropriate stacking sequence of layers. As an example, consider a sandwich structure shown in Fig. 7.57a. The first (loaded) layer is made of aluminum and has $h_1 = 1$ mm, $E_z^{(1)} = 72$ GPa, $\rho_1 = 2.7$ g/cm^3; the second layer is a foam core with

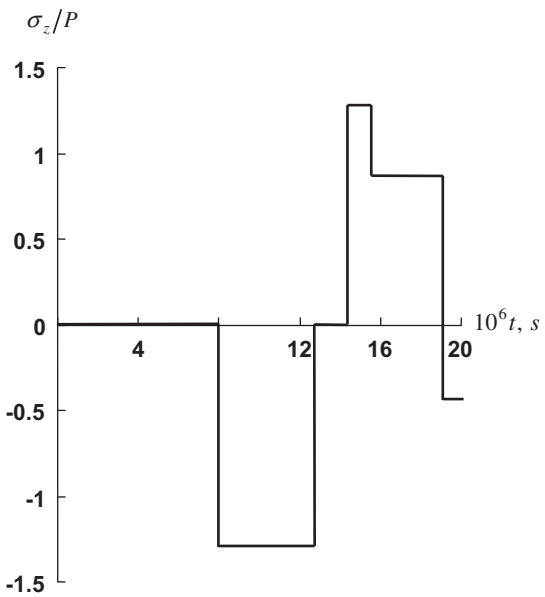


FIGURE 7.56

Dependence of the interlaminar stress referred to the acting pressure on time.

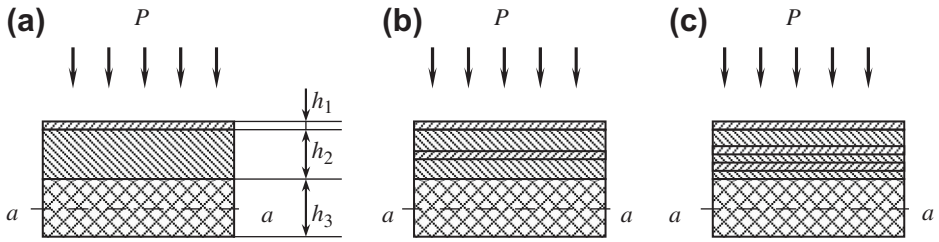


FIGURE 7.57

Structures of the original laminate (a) and the laminates with one (b) and two (c) additional aluminum layers in the foam core.

$h_2 = 10$ mm, $E_z^{(2)} = 0.28$ GPa, $\rho_2 = 0.25$ g/cm^3; and the third (load-carrying) composite layer has $h_3 = 12$ mm, $E_z^{(3)} = 10$ GPa, $\rho_3 = 1.4$ g/cm^3. The duration of a rectangular pulse of external pressure is 10^{-6} s. The maximum tensile stress occurs in the middle plane of the load-carrying layer (plane a–a in Fig. 7.57). The normal stress induced in this plane is presented in Fig. 7.58a. As can be

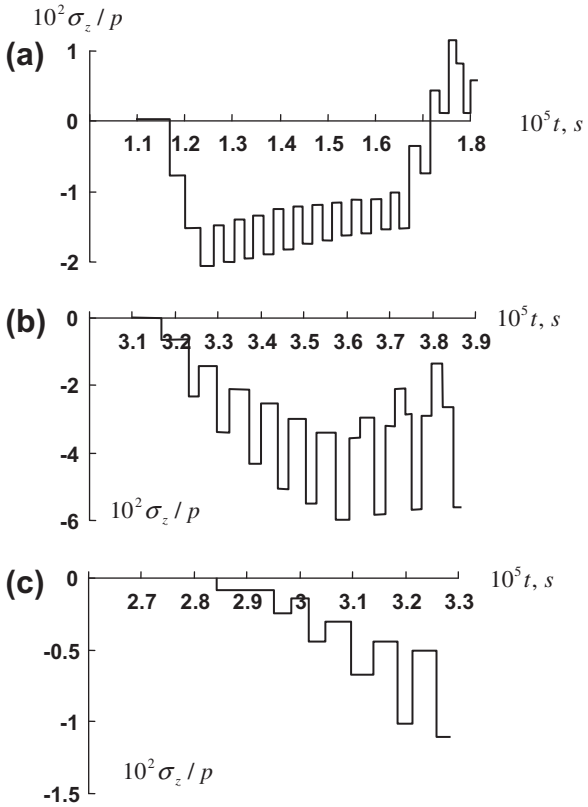


FIGURE 7.58

Normal stress related to external pressure acting in section a-a of the laminates in Fig. 7.57 (a)–(c), respectively.

seen, at the moment of time t equal to about 1.75×10^{-5} s, this stress is tensile and can cause delamination of the structure.

Now introduce an additional aluminum layer in the foam core as shown in Fig. 7.57b. As follows from Fig. 7.58b, this layer suppresses the tensile stress in section a–a. Two intermediate aluminum layers (Fig. 7.57c) working as generators of compressive stress waves eliminate the appearance of tensile stress in this section. Naturally, the effect under discussion can be achieved for a limited period of time. However, in reality, the impact-generated tensile stress is dangerous soon after the application of the pulse. The damping capacity of real structural materials (which is not taken into account in the foregoing analysis) dramatically reduces the stress amplitude in time.

A flying projectile with relatively high kinetic energy can penetrate through the laminate. As is known, composite materials, particularly high-strength aramid fabrics, are widely used for protection

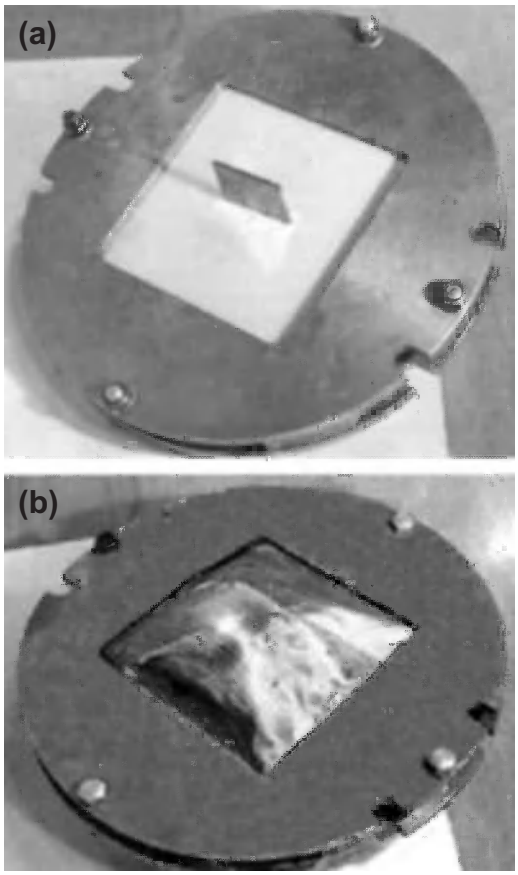


FIGURE 7.59

Plate No. 2 (see Table 7.2) after the impact test:
– (a) front view;
– (b) back view.

against flying objects. To demonstrate the mechanism of this protection, consider a square composite plate clamped in the steel frame shown in Fig. 7.59 and subjected to impact by a rectangular plane projectile (see Fig. 7.59) simulating the blade of the turbojet engine compressor. The plate consists of layers of thin aramid fabric impregnated with epoxy resin at a distance from the window in the frame (see Fig. 7.59) and co-cured together as shown in Fig. 7.60. The front (loaded) surface of the plate has a 1 mm thick cover sheet made of glass-fabric-epoxy composite. The results of ballistic tests are presented in Table 7.4. Front and back views of plate No. 2 are shown in Fig. 7.59, and the back view of plate No. 3 can be seen in Fig. 7.60. Since the mechanical properties of the aramid fabric used to make the plates are different in the warp and fill directions, the plates consist of couples of mutually orthogonal layers of fabric that are subsequently referred to as $0^\circ/90^\circ$ layers. All the plates listed in Table 7.4 have $n = 32$ of such couples.

To calculate the projectile velocity below which it fails to perforate the plate (the so-called ballistic limit), we use the energy conservation law, according to which

$$\frac{1}{2}m_p(V_s^2 - V_r^2) = n(W + T) \tag{7.84}$$

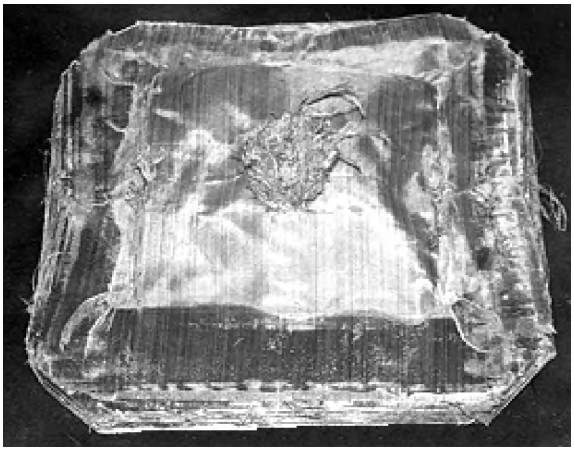


FIGURE 7.60

Back view of plate No. 3 (see Table 7.2) after the impact test.

Table 7.4 Ballistic Test of Plates Made of Aramid Fabric.

Plate No.	Projectile velocity (m/s)	Test results
1	315	No penetration
2	320	The projectile is "caught" by the containment
3	325	Penetration

where V_s is the projectile striking velocity, V_r is its residual velocity, $m_p = 0.25$ kg is the projectile mass, $n = 32$ is the number of the $0°/90°$ layers, W is the fracture work for the $0°/90°$ layers, and T is the kinetic energy of the layer. All other factors and the fiberglass cover of the plate are neglected.

The fracture work can be evaluated using the quasi-static test shown in Fig. 7.61. A couple of mutually orthogonal fabric layers is fixed along the plate contour and loaded by the projectile. The area under the force-deflection curve (solid line in Fig. 7.61) can be treated as the work of fracture which, for the fabric under study, has been found to be $W = 120$ Nm.

To calculate T, the deformed shape of the fabric membrane has been measured. Assuming that the velocities of the membrane points are proportional to deflections f and that $df_m/dt = V_s$, the kinetic energy of the fabric under study (the density of the layer unit surface is $0.2\ \text{kg/m}^2$) turns out to be $T_c = 0.0006\ V_s^2$.

To find the ballistic limit, we should take $V_r = 0$ in Eq. (7.84). Substituting the foregoing results in this equation, we get $V_b = 190.5$ m/s, which is much lower than the experimental result ($V_b = 320$ m/s) following from Table 7.4.

Let us change the model of the process and assume that the fabric layers fail one after another rather than all at once, as is assumed in Eq. (7.84). The result is expected to be different because the

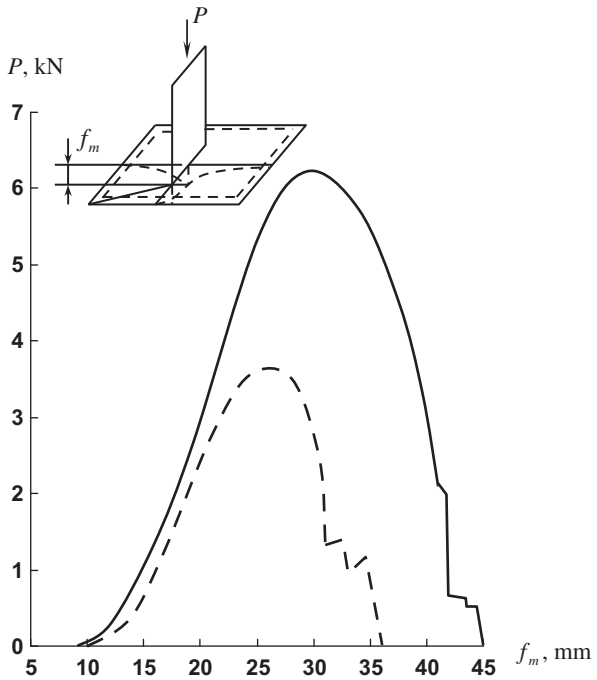


FIGURE 7.61

Force-deflection diagrams for square aramid fabric membranes, ——— couple of layers with orthogonal orientations, — — — superposition of the diagrams for individually tested layers.

problem under study is not linear, and the principle of superposition is not applicable. Bearing this in mind, we write Eq. (7.84) in the following incremental form

$$\frac{1}{2}m_p(V_{k-1}^2 - V_k^2) = W + T_{k-1} \tag{7.85}$$

Here, V_{k-1} and V_k are the projectile velocities before and after the failure of the kth couple of fabric layers, W is, as earlier, the fracture work consumed by the kth couple of layers, $T_{k-1} = 0.0006\ V_{k-1}^2$, and the last term in the right-hand side of Eq. (7.85) means that we account for the kinetic energy of only those fabric layers that have been already penetrated by the projectile. Solving Eq. (7.85) for V_k, we arrive at

$$V_k = \sqrt{[1 - 0.0048(k-1)]V_{k-1}^2 - \frac{2}{m_p}W} \tag{7.86}$$

For $k = 1$, we take $V_0 = 320$ m/s, in accordance with the experimental ballistic limit, and have $V_1 = 318.5$ m/s from Eq. (7.86). Taking $k = 2$, we repeat the calculation and find that, after the failure of the second couple of fabric layers, $V_2 = 316.2$ m/s. This process is repeated until $V_k = 0$, and the number k thus determined gives an estimate of the minimum number of $0°/90°$ layers that can stop a projectile with striking velocity $V_s = 320$ m/s. The result of the calculation is presented in Fig. 7.62, from which it follows that $k = 32$. This is exactly the same number of layers that have been used to construct the experimental plates.

Thus, it can be concluded that the high impact resistance of aramid fabrics is determined by two main factors. The first factor is the relatively high work of fracture, which is governed not only by high strength, but also by the interaction of the fabric layers. The dashed line in Fig. 7.61 shows the fracture process constructed as a result of the superposition of experimental diagrams for individual $0°$ and $90°$

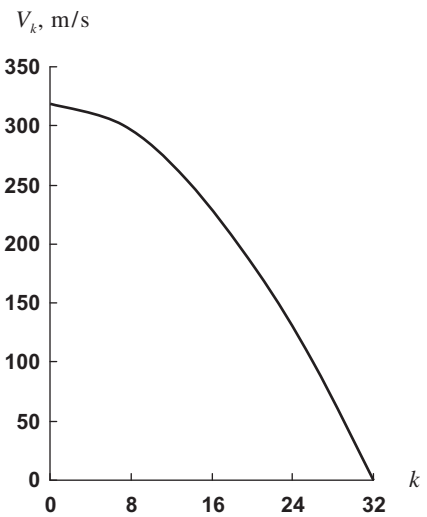


FIGURE 7.62

Dependence of the residual velocity of the projectile on the number of penetrated layers.

layers. The solid line corresponds, as noted, to 0° and 90° layers tested together (the ratio of the fabric strength under tension in the warp and the fill direction is 1.3). As can be seen, the area under the solid line is much larger that under the dashed one, which indicates the high contribution of the layers' interaction to the work of fracture. If this conclusion is true, we can expect that for layers with higher anisotropy and for laminates in which the principal material axes of the adjacent layers are not orthogonal, the fracture work would be higher than for the orthotropic laminate under study. The second factor increasing the impact resistance of aramid fabrics is associated with a specific process of the failure, during which the fabric layers fail one after another, but not all at once. Plates of the same number of layers, but consisting of resin-impregnated and co-cured layers that fail at once, demonstrate much lower impact resistance.

7.4 MANUFACTURING EFFECTS

As has been already noted, composite materials are formed in the process of fabrication of a composite structure, and their properties are strongly dependent on the type and parameters of the processing technology. This means that material specimens that are used to determine mechanical properties should be fabricated using the same manufacturing method that is expected to be applied to fabricate the structure under study.

7.4.1 Circumferential winding and tape overlap effect

To demonstrate the direct correlation that can exist between processing and material properties, consider the process of circumferential winding on a cylindrical surface as in Fig. 7.63. As a rule, the tapes are wound with some overlap w_0, shown in Fig. 7.64a. Introducing the dimensionless parameter

$$\lambda = \frac{w_0}{w} \tag{7.87}$$

we can conclude that for the case of complete overlap (Fig. 7.64b) we have $\lambda = 1$. The initial position of the tape placed with overlap w_0 as in Fig. 7.64a is shown in this figure with a dashed line, whereas the final position of the tapes is shown with solid lines. Assume that after the winding and curing are

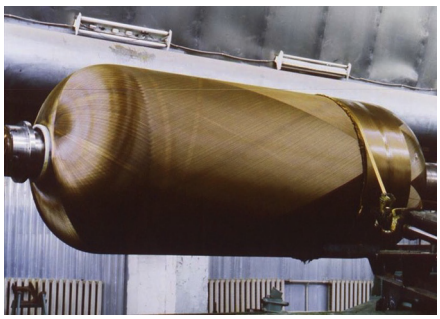


FIGURE 7.63

Winding of a circumferential layer.

Courtesy of CRISM.

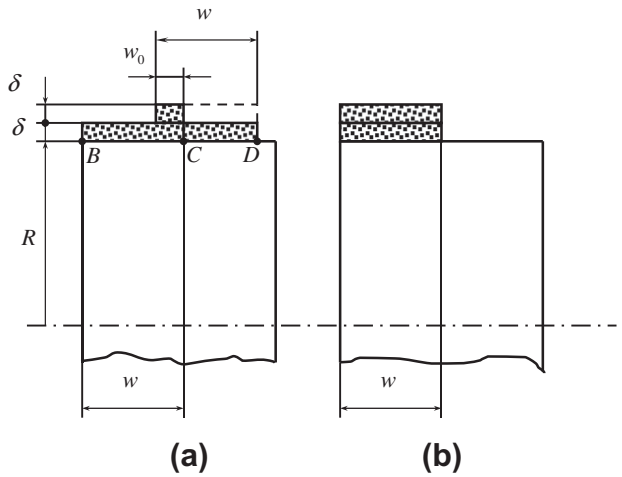


FIGURE 7.64

Circumferential winding with (a) partial overlap $w_0 < w$ and (b) complete overlap $w_0 = w$.

over, the resulting structure is a unidirectionally reinforced ring that is removed from the mandrel and loaded with internal pressure, so that the ring radius, being R before the loading, becomes R_1. Decompose the resultant force acting in the ring cross-section into two components, i.e.,

$$F = F' + F'' \tag{7.88}$$

and introduce the apparent stress acting along the fibers of the ring as

$$\sigma_1 = \frac{F}{A} \tag{7.89}$$

where $A = 2w\delta$ is the cross-sectional area of the ring made from two tapes as shown in Fig. 7.64. The force F' corresponds to part BC of the ring (Fig. 7.64a) and can be found as

$$F' = A'E_1\frac{R_1 - R}{R}$$

where $A' = (w + w_0)\delta$ is the cross-sectional area of this part of the ring and E_1 is the modulus of elasticity of the cured unidirectional composite. To calculate the force F'' that corresponds to part CD of the ring (Fig. 7.64a), we should take into account that the fibers start to take the load only when this part of the tape reaches the position indicated with dashed lines, i.e.,

$$F'' = A''E_1\frac{R_1 - (R + \delta)}{R}$$

where $A'' = (w - w_0)\delta$. With due regard to Eqs. (7.87), and (7.88)/(7.89), we can write the result of the foregoing analysis in the following form

$$\sigma_1 = E_1\left[\varepsilon_1 - \frac{\delta}{2R}(1 - \lambda)\right] \tag{7.90}$$

Here, $\varepsilon_1 = (R_1 - R)/R$ is the apparent strain in the fiber direction. For complete overlap in Fig. 7.64b, $\lambda = 1$ and $\sigma_1 = E_1\varepsilon_1$. It should be noted that there exists also the so-called tape-to-tape winding for which $\lambda = 0$. This case cannot be described by Eq. (7.90) because of assumptions introduced in the derivation, and the resulting equation for this case is $\sigma_1 = E_1\varepsilon_1$.

It follows from Eq. (7.89), which is valid for winding without tension, that overlap of the tape results in reduction of material stiffness. Since the levels of loading for the fibers in the *BC* and *CD* parts of the ring (Fig. 7.64a) are different, a reduction in material strength can also be expected.

Filament winding is usually performed with some initial tension of the tape. This tension improves the material properties because it straightens the fibers and compacts the material. However, high tension may result in fiber damage and reduction in material strength. For glass and carbon fibers, the preliminary tension usually does not exceed 5% of the tape strength, whereas for aramid fibers, which are less susceptible to damage, the level of initial tension can reach 20% of the tape strength. Preliminary tension reduces the effect of the tape overlap discussed earlier and described by Eq. (7.90). However, this effect can show itself in a reduction in material strength because the initial stresses which are induced by preliminary tension in the fibers can be different and some fibers can be overloaded or underloaded by the external forces acting on the structure in operational conditions. Strength reduction of aramid-epoxy unidirectional composites with tape overlap has been observed in the experiments of Rach and Ivanovskii (1986) for winding on a 200 mm diameter mandrel, as demonstrated in Fig. 7.65.

The absence of tape preliminary tension or low tension can cause ply waviness as shown in Fig. 7.66, which can occur in filament wound laminates as a result of the pressure exerted by the overwrapped plies on the underwrapped plies or in flat laminates due to material shrinkage in the process of curing.

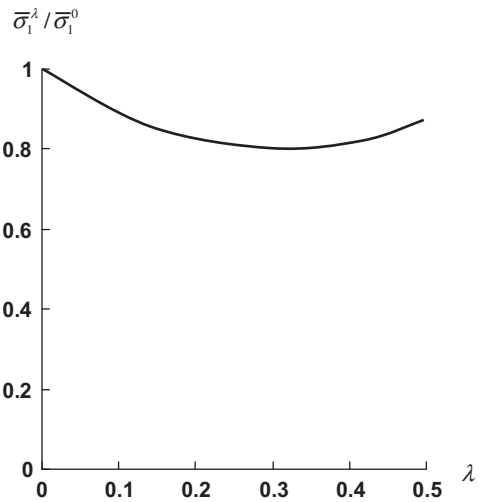


FIGURE 7.65

Dependence of the normalized longitudinal strength of unidirectional aramid-epoxy composite on the tape overlap.

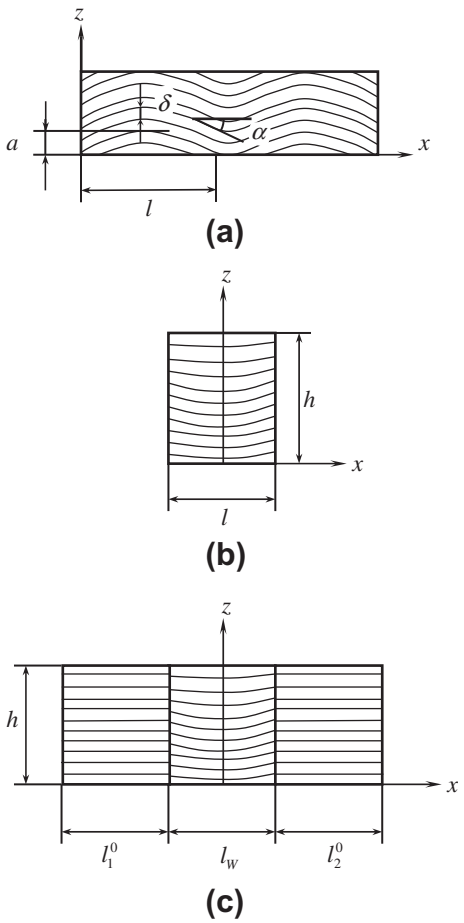


FIGURE 7.66

Regular (a), through-the-thickness (b), and local (c) ply waviness.

The simplest model for analysis is a regular waviness as presented in Fig. 7.66a. To determine the apparent modulus in the x direction, we can use an expression similar to the one presented in Eqs. (4.76), i.e.,

$$\frac{1}{E_x} = \frac{\cos^4\alpha}{E_1} + \frac{\sin^4\alpha}{E_3} + \left(\frac{1}{G_{13}} - \frac{2\nu_{31}}{E_1}\right)\sin^2\alpha\cos^2\alpha \tag{7.91}$$

Then, since the structure is periodic,

$$\frac{1}{E_x^{(r)}} = \frac{1}{l}\int_0^l \frac{dx}{E_x} \tag{7.92}$$

Approximating the ply wave as

$$z = a \sin \frac{\pi x}{l}$$

where a is the amplitude, we get

$$\tan \alpha = \frac{dz}{dx} = f \cos \frac{\pi x}{l}$$

where $f = \pi a/l$. Substitution into Eqs. (7.91) and (7.92) and integration yields

$$\frac{1}{E_x^{(r)}} = \frac{1}{2\lambda}\left[\frac{2+f^2}{E_1} + \frac{1}{E_3}(2\lambda - 2 - 3f^2) + \left(\frac{1}{G_{13}} - \frac{2\nu_{31}}{E_1}\right) f^2\right]$$

(Tarnopol'skii and Roze, 1969), where $\lambda = (1+f^2)^{3/2}$. Simplifying this result using the assumption that $f^2 << 1$, we arrive at

$$E_x^{(r)} = \frac{E_1}{1 + \dfrac{E_1 f^2}{2G_{13}}} \tag{7.93}$$

For glass-, carbon-, and aramid-epoxy composites with properties listed in Table 3.5, the dependencies corresponding to Eq. (7.93) are presented in comparison to the experimental results of Tarnopol'skii and Roze (1969) in Fig. 7.67.

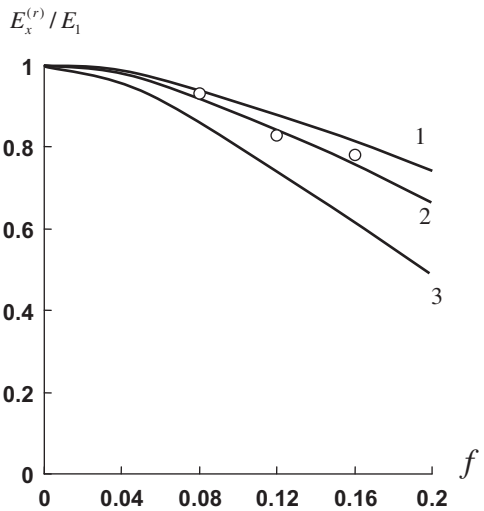


FIGURE 7.67

Reduction of the normalized modulus with the ply waviness parameter, *f*, for (1) glass-, (2) carbon-, and (3) aramid-epoxy composites. ——— Eqs. (7.93) ○ experiment for glass-epoxy composite.

If the ply waviness varies over the laminate thickness, as in Fig. 7.66b, Eq. (7.93) can be generalized as

$$E_x^{(t)} = \frac{E_1}{h} \int_0^h \frac{dz}{1 + \frac{E_1}{2G_{13}} f^2(z)} \tag{7.94}$$

Finally, for only local waviness (see Fig. 7.66c), we obtain

$$\frac{1}{E_x^{(l)}} = \frac{\bar{l}_1^0}{E_1} + \frac{\bar{l}_w}{E_x^{(t)}} + \frac{\bar{l}_2^0}{E_1}$$

where

$$\bar{l}_{1,2}^0 = \frac{l_{1,2}^0}{l_1^0 + l_w + l_2^0}, \quad \bar{l}_w = \frac{l_w}{l_1^0 + l_w + l_2^0}$$

and $E_x^{(t)}$ is specified by Eq. (7.94).

Even moderate ply waviness dramatically reduces material strength under compression along the fibers, as can be seen in Fig. 7.68, which illustrates the experimental results for a unidirectional carbon-epoxy composite. The other strength characteristics of unidirectional composites are only slightly affected by the ply waviness.

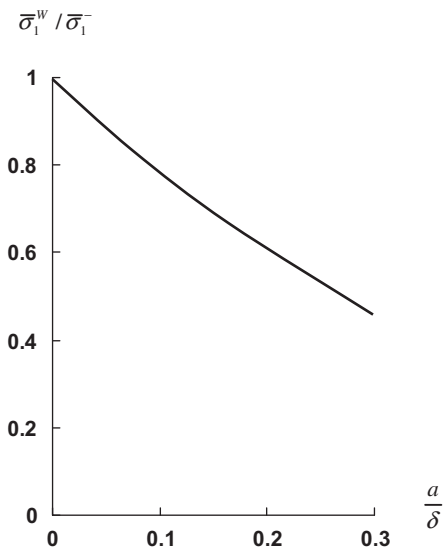


FIGURE 7.68

Experimental dependence of carbon-epoxy composite longitudinal compression strength related to the corresponding strength of material without ply waviness on the ratio of the waviness amplitude to the ply thickness.

7.4.2 Warping and bending of laminates in fabrication process

There exist also some manufacturing operations that are specific for composites that cause stresses and strains appearing in composite structural elements in the process of their fabrication.

As an example, consider the problem of bending and warping of asymmetric laminates during their fabrication. Assume that a laminated polymeric composite panel is cured at temperature T_c and cooled to room temperature T_0. Under slow cooling, the temperature change, $\Delta T = T_0 - T_c$, is the same for all the layers. Since the thus-fabricated panel is free of loading (i.e., no loads are applied to its edges or surfaces), the forces and moments in the left-hand sides of Eqs. (7.23) and (7.24) are zero, and these equations form a linear algebraic system for generalized strains ε_T, γ_T, and κ_T. Integration of the strain-displacement equations, Eqs. (7.28), allows us to determine the shape of the fabricated panel.

Analysis of Eqs. (7.25) and (7.26), similar to that performed in Section 5.4, shows that for symmetric laminates $M^T_{mn} = 0$. Since $C_{mn} = 0$ for such laminates, the last three equations of Eqs. (7.23) in which $M_x = M_y = M_{xy} = 0$ form a set of homogeneous equations whose solution is $\kappa_{xT} = \kappa_{yT} = \kappa_{xyT} = 0$. This means that a flat symmetric panel does not acquire curvature in the process of cooling. Naturally, the in-plane dimensions of the panel become different from those that the panel had before cooling. The corresponding thermal strains ε^0_{xT}, ε^0_{yT}, and γ^0_{xyT} can be found from the first three equations of Eqs. (7.23) in which $N_x = N_y = N_{xy} = 0$, but N^T_{11}, N^T_{22}, and N^T_{12} are not zero.

However, for asymmetric laminates, in general $M^T_{mn} \neq 0$, and these laminates experience bending and warping in the process of cooling. To demonstrate this, consider the two antisymmetric laminates studied in Section 5.8.

The first one is a two-layered orthotropic cross-ply laminate shown in Fig. 5.28. Using the stiffness coefficients calculated in Section 5.8, taking into account that for a cross-ply laminate $N^T_{12} = M^T_{12} = 0$, and applying Eqs. (7.23) for N_{xy} and M_{xy}, we get $\gamma^0_{xyT} = 0$ and $\kappa_{xyT} = 0$. Thus, cooling of such a cross-ply laminated panel does not induce in-plane shear or twisting in it. The other four parts of Eqs. (7.23) take the form

$$\begin{aligned} a_{xx}\varepsilon^0_{xT} + a_{xy}\varepsilon^0_{yT} - c_{xx}\kappa_{xT} &= n_x \\ a_{yx}\varepsilon^0_{xT} + a_{yy}\varepsilon^0_{yT} + c_{yy}\kappa_{yT} &= n_y \\ -c_{xx}\varepsilon^0_{xT} + b_{xx}\kappa_{xT} + b_{xy}\kappa_{yT} &= m_x \\ c_{yy}\varepsilon^0_{yT} + b_{xy}\kappa_{xT} + b_{yy}\kappa_{yT} &= m_y \end{aligned} \tag{7.95}$$

where

$$a_{xx} = a_{yy} = h\overline{E}, \quad a_{xy} = a_{yx} = \overline{E}_1\nu_{12}h$$

$$c_{xx} = c_{yy} = \frac{h^2}{8}(\overline{E}_1 - \overline{E}_2), \quad b_{xx} = b_{yy} = \frac{h^3\overline{E}}{12}$$

$$b_{xy} = b_{yx} = \frac{h^3}{12}\overline{E}_1\nu_{12}, \quad \overline{E} = \frac{1}{2}(\overline{E}_1 + \overline{E}_2)$$

$$n_x = n_y = \frac{h}{2}\Big[\overline{E}_1(\alpha_1 + \nu_{12}\alpha_2) + \overline{E}_2(\alpha_2 + \nu_{21}\alpha_1)\Big]\Delta T$$

$$-m_x = m_y = \frac{h^2}{8}\Big[\overline{E}_1(\alpha_1 + \nu_{12}\alpha_2) - \overline{E}_2(\alpha_2 + \nu_{21}\alpha_1)\Big]\Delta T$$

The solutions to Eqs. (7.95) can be written as

$$\varepsilon_{xT}^0 = \frac{n_x}{a_{xx}+a_{xy}} + \frac{c_{xx}}{a_{xx}^2 - a_{xy}^2}(a_{xx}\kappa_{xT} + a_{xy}\kappa_{yT})$$
$$\varepsilon_{yT}^0 = \frac{n_x}{a_{xx}+a_{xy}} - \frac{c_{xx}}{a_{xx}^2 - a_{xy}^2}(a_{xx}\kappa_{yT} + a_{xy}\kappa_{xT}) \tag{7.96}$$

where

$$\kappa_{xT} = -\kappa_{yT} = \frac{m_x(a_{xx}+a_{xy}) + n_x c_{xx}}{(a_{xx}+a_{xy})(b_{xx}-b_{xy}) - c_{xx}^2} \tag{7.97}$$

As follows from Eqs. (7.96) and (7.97), ε and κ do not depend on x and y.

To find the in-plane displacements, we should integrate Eqs. (7.28) which have the form

$$\frac{\partial u}{\partial x} = \varepsilon_{xT}^0, \quad \frac{\partial v}{\partial y} = \varepsilon_{yT}^0, \quad \frac{\partial u}{\partial y} + \frac{\partial v}{\partial x} = 0$$

Referring the panel to coordinates x and y shown in Fig. 7.69 and assuming that $u(x=0,\ y=0)=0$ and $v(x=0,\ y=0)=0$, we get

$$u = \varepsilon_{xT}^0 x, \quad v = \varepsilon_{yT}^0 y \tag{7.98}$$

Now consider Eqs. (7.24) in which $V_x = V_y = 0$. Thus, $\gamma_{xT} = \gamma_{yT} = 0$, and Eqs. (7.30) yield $\theta_x = -\partial w/\partial x$, $\theta_y = -\partial w/\partial y$. The plate deflection can be found from Eqs. (7.29), which reduce to

$$\frac{\partial^2 w}{\partial x^2} = -\kappa_{xT}, \quad \frac{\partial^2 w}{\partial y^2} = -\kappa_{yT}, \quad \frac{\partial^2 w}{\partial x \partial y} = 0$$

Assuming that $w(x=0,\ y=0)=0$, $\theta_x(x=0,\ y=0)=0$, $\theta_y(x=0,\ y=0)=0$, we can write the result of the integration as

$$w = -\frac{1}{2}(\kappa_{xT}x^2 + \kappa_{yT}y^2) \tag{7.99}$$

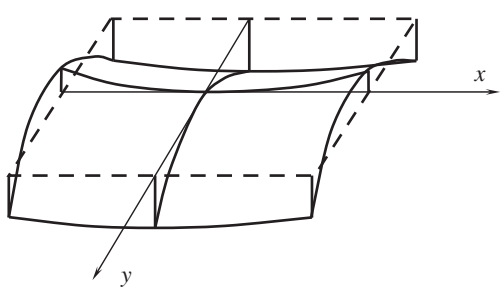


FIGURE 7.69

Deformed shape of a cross-ply antisymmetric panel.

To present this solution in an explicit form, consider, for the sake of brevity, material with zero Poisson's ratios ($\nu_{12} = \nu_{21} = 0$). Then, Eqs. (7.96)–(7.99) yield

$$u = \frac{\Delta T x}{E_1 + E_2}\left[E_1\alpha_1 + E_2\alpha_2 + 6(E_1 - E_2)\,\frac{E_1E_2(\alpha_2 - \alpha_1)}{E_1^2 + 14E_1E_2 + E_2^2}\right]$$

$$v = \frac{\Delta T y}{E_1 + E_2}\left[E_1\alpha_1 + E_2\alpha_2 + 6(E_1 - E_2)\,\frac{E_1E_2(\alpha_2 - \alpha_1)}{E_1^2 + 14E_1E_2 + E_2^2}\right] \tag{7.100}$$

$$w = -\frac{12\Delta T}{h}\cdot\frac{E_1E_2(\alpha_2 - \alpha_1)}{E_1^2 + 14E_1E_2 + E_2^2}(x^2 - y^2)$$

The deformed shape of the panel is shown in Fig. 7.69. Note that displacements u and v correspond to the panel reference plane, which is the contact plane of the 0^0 and 90° layers (see Fig. 5.28).

Compare the obtained results with experimental data of Papadopoulos and Bowles (1990). Experimental $0^0/90°$ cross-ply rectangular plate with sides $a = 204$ mm and $b = 76.5$ mm and thickness $h = 0.762$ mm is made of polyimide PMR-15 resin reinforced with Celion 6000 fibers. Characteristics of the unidirectional composite are $E_1 = 132$ GPa, $E_2 = 9.6$ GPa, $\alpha_1 = -1.03\cdot10^{-6}$ $1/°$C, and $\alpha_2 = 27.9\cdot10^{-6}$ $1/°$C. The glass transition temperature is 330°C, and the room temperature is taken as 23°C, so that $\Delta T = 307°$C. The maximum deflections in the $x = 0$ and $y = 0$ plane calculated in accordance with Eq. (7.100) are

$$W_x = w(x = 0, y = 0) - w\left(x = \frac{a}{2}, y = 0\right) = 52.25 \text{ mm}$$

$$W_y = w(x = 0, y = 0) - w\left(x = 0, y = \frac{b}{2}\right) = 7.37 \text{ mm}$$

The corresponding experimental results (Papadopoulos and Bowles, 1990) are

$$W_x = 38.1 \text{ mm}, \quad W_y = 4.5 \text{ mm}$$

The higher theoretical values can be explained by the high value of the transverse modulus E_2, which corresponds to the room temperature and is considerably lower under the elevated temperature (heating up to 300°C can reduce the stiffness of PMR-15 resin by 40%). To calculate the deflection W appearing under cooling, the process can be divided into a system of steps with different parameters, and the following equation can be used:

$$W = \sum_i W_i\left(\Delta T_i,\ E_1^{(i)},\ E_2^{(i)},\ \alpha_1^{(i)},\ \alpha_2^{(i)}\right) \tag{7.101}$$

in which "i" is the number of the cooling step, $\Delta T_i = T_{i+1} - T_i$, and $E^{(i)}$ and $\alpha^{(i)}$ are the material characteristics corresponding to the temperature T_i. Assume that the function $E_2(T)$ looks like that shown in Fig. 7.70, which is similar to the function shown in Fig. 1.12 for the resin, whereas the other

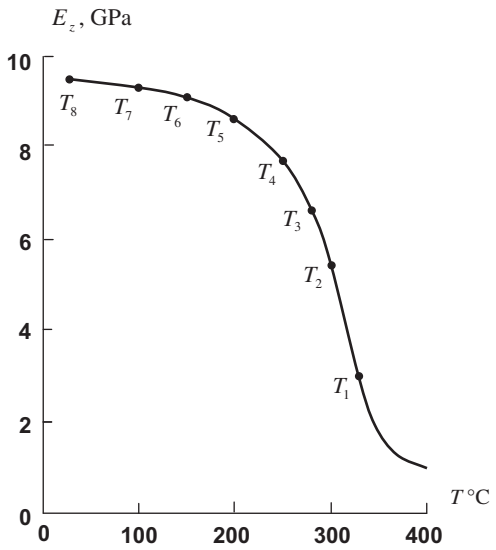


FIGURE 7.70

Dependence of the transverse modulus E_z on temperature.

parameters correspond to the room temperature. The process of cooling from temperature 325°C to 25°C is divided into 7 steps, for which

$$E_2^{(1)} = 3,\ E_2^{(2)} = 5.5,\quad E_2^{(3)} = 6.6,\ E_2^{(4)} = 7.6,\ E_2^{(5)} = 8.6,\quad E_2^{(6)} = 9.2,\ E_2^{(7)} = 9.5\ (\text{GPa});$$

$$\Delta T_1 = \Delta T_2 = \Delta T_3 = 25°\text{C}\,;\quad \Delta T_4 = \Delta T_5 = \Delta T_6 = 50°\text{C}\,;\quad \Delta T_7 = 75°\text{C}$$

Calculations using Eq. (7.101) yield

$$W_x = 40.1\ \text{mm}\,,\quad W_y = 5.6\ \text{mm}$$

As can be seen, these results are fairly close to the experimental data.

Another typical antisymmetric structure is the two-layered angle-ply laminate shown in Fig. 5.29. Using the stiffness coefficients for this laminate calculated in Section 5.8 and Eqs. (7.25) and (7.27), we can write Eqs. (7.23) in the following form

$$A_{11}\varepsilon_{xT}^0 + A_{12}\varepsilon_{yT}^0 - \frac{h}{4}A_{14}\kappa_{xyT} = A_{11}^T$$

$$A_{12}\varepsilon_{xT}^0 + A_{22}\varepsilon_{yT}^0 - \frac{h}{4}A_{24}\kappa_{xyT} = A_{22}^T$$

$$A_{44}\gamma_{xyT}^0 - \frac{h}{4}(A_{14}\kappa_{xT} + A_{24}\kappa_{yT}) = 0$$

$$-A_{14}\gamma_{xyT}^0 + \frac{h}{3}(A_{11}\kappa_{xT} + A_{12}\kappa_{yT}) = 0$$

$$-A_{24}\gamma_{xyT}^0 + \frac{h}{3}(A_{12}\kappa_{xT} + A_{22}\kappa_{yT}) = 0$$

$$A_{14}\varepsilon_{xT}^0 + A_{24}\varepsilon_{yT}^0 - \frac{h}{3}A_{44}\kappa_{xyT} = A_{12}^T$$

where

$$A_{11}^T = \left[\overline{E}_1(\alpha_1 + \nu_{12}\alpha_2)\cos^2\phi + \overline{E}_2(\alpha_2 + \nu_{21}\alpha_1)\sin^2\phi\right]\Delta T$$

$$A_{22}^T = \left[\overline{E}_1(\alpha_1 + \nu_{12}\alpha_2)\sin^2\phi + \overline{E}_2(\alpha_2 + \nu_{21}\alpha_1)\cos^2\phi\right]\Delta T$$

$$A_{12}^T = \left[\overline{E}_1(\alpha_1 + \nu_{12}\alpha_2) - \overline{E}_2(\alpha_2 + \nu_{21}\alpha_1\right]\Delta T \sin\phi\cos\phi$$

The solution is

$$\varepsilon_{xT}^0 = \frac{1}{A}\left[A_{11}^T A_{22} - A_{22}^T A_{12} + \frac{h}{4}(A_{14}A_{22} - A_{24}A_{12})\kappa_{xyT}\right]$$

$$\varepsilon_{yT}^0 = \frac{1}{A}\left[A_{22}^T A_{11} - A_{11}^T A_{12} + \frac{h}{4}(A_{24}A_{11} - A_{14}A_{22})\kappa_{xyT}\right]$$

$$\gamma_{xyT}^0 = 0, \quad \kappa_{xT} = 0, \quad \kappa_{yT} = 0$$

$$\kappa_{xyT} = \frac{A_{14}(A_{11}^T A_{22} - A_{22}^T A_{12}) + A_{24}(A_{22}^T A_{11} - A_{11}^T A_{12}) - A_{12}^T}{h\left[\frac{A}{3}A_{44} + \frac{1}{4}(2A_{14}A_{24}A_{12} - A_{14}^2 A_{22} - A_{24}^2 A_{11})\right]}$$

where $A = A_{11}A_{22} - A_{12}^2$.

Thus, the panel under study experiences only in-plane deformation and twisting. Displacements u and v can be determined by Eqs. (7.28), whereas the following equations should be used to find w

$$\frac{\partial^2 w}{\partial x^2} = 0, \quad \frac{\partial^2 w}{\partial y^2} = 0, \quad \frac{\partial^2 w}{\partial x \partial y} = -\kappa_{xyT}$$

The result is

$$w = -\kappa_{xyT}xy$$

The deformed shape of the panel is shown in Fig. 7.71.

Depending on the laminates' structures and dimensions, there exists a whole class of stable and unstable laminate configurations as studied by Hyer (1989).

7.4.3 Shrinkage effects and residual strains

Deformation and warping of laminates appearing after the manufacturing process is completed can occur not only due to cooling of the cured composite but also as a result of material shrinkage due to release of tension in the fibers after the composite part is removed from the mandrel or to chemical setting of the polymeric matrix.

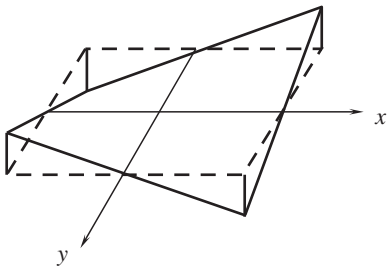


FIGURE 7.71

Deformed shape of an angle-ply antisymmetric panel.

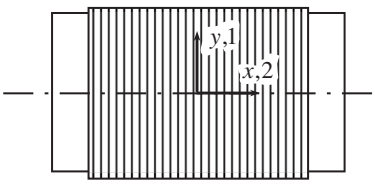


FIGURE 7.72

A unidirectional circumferential layer on a cylindrical mandrel.

To demonstrate these effects, consider a thin unidirectional layer formed from circumferential plies wound on a metallic cylindrical mandrel (see Fig. 7.72) under tension. Since the stiffness of the mandrel is much higher than that of the layer, we can assume that, on cooling from the curing temperature T_c to room temperature T_0, the strains in the principal material coordinates of the layer are governed by the mandrel with which the cured layer is bonded, i.e.,

$$\varepsilon_1^T = \varepsilon_2^T = \alpha_0 \, \Delta T \tag{7.102}$$

where α_0 is the CTE of the mandrel material and $\Delta \, T = T_0 - T_c$. On the other hand, if the layer is cooled after being removed from the mandrel, its strains can be calculated as

$$\varepsilon_1 = \alpha_1 \, \Delta T + \varepsilon_1^0, \quad \varepsilon_2 = \alpha_2 \, \Delta T + \varepsilon_2^0 \tag{7.103}$$

The first terms in the right-hand sides of these equations are the free temperature strains along and across the fibers (see Fig. 7.72), whereas ε_1^0 and ε_2^0 correspond to the possible layer shrinkage in these directions.

Using Eqs. (7.102) and (7.103), we can determine the strains that appear in the layer when it is removed from the mandrel, i.e.,

$$\begin{aligned} \overline{\varepsilon}_1 &= \varepsilon_1 - \varepsilon_1^T = \varepsilon_1^0 + (\alpha_1 - \alpha_0)\Delta T \\ \overline{\varepsilon}_2 &= \varepsilon_2 - \varepsilon_2^T = \varepsilon_2^0 + (\alpha_2 - \alpha_0)\Delta T \end{aligned} \tag{7.104}$$

These strains can be readily found if we measure the layer diameter and length before and after it is removed from the mandrel. Then, the shrinkage strains can be determined as

$$\varepsilon_1^0 = \overline{\varepsilon}_1 - (\alpha_1 - \alpha_0)\Delta T$$
$$\varepsilon_2^0 = \overline{\varepsilon}_2 - (\alpha_2 - \alpha_0)\Delta T$$

For a glass-epoxy composite with the following thermo-mechanical properties:

$$E_1 = 37.24\ \text{GPa}, \quad E_2 = 2.37\ \text{GPa}, \quad G_{12} = 1.2\ \text{GPa}$$
$$\nu_{12} = 0.26, \quad \alpha_1 = 3.1 \times 10^{-6}\ 1/^\circ\text{C}, \quad \alpha_2 = 25 \times 10^{-6}\ 1/^\circ\text{C}$$

the measurements of Morozov and Popkova (1987) gave $\varepsilon_1^0 = -93.6 \times 10^{-5}$, $\varepsilon_2^0 = -64 \times 10^{-5}$. Further experiments performed for different winding tensions and mandrel materials have shown that, although the strain ε_1^0 strongly depends on these parameters, the strain ε_2^0 practically has no variation. This supports the assumption that the strain ε_2^0 is caused by chemical shrinkage of the resin and depends only on the resin's characteristics and properties.

For a cylinder in which the fibers make angle ϕ with the x-axis in Fig. 7.72, the strains induced by removal of the mandrel can be found from Eqs. (4.70), i.e.,

$$\begin{aligned} \overline{\varepsilon}_x &= \overline{\varepsilon}_1 \cos^2\phi + \overline{\varepsilon}_2 \sin^2\phi \\ \overline{\varepsilon}_y &= \overline{\varepsilon}_1 \sin^2\phi + \overline{\varepsilon}_2 \cos^2\phi \\ \overline{\gamma}_{xy} &= (\overline{\varepsilon}_1 - \overline{\varepsilon}_2) \sin 2\phi \end{aligned} \tag{7.105}$$

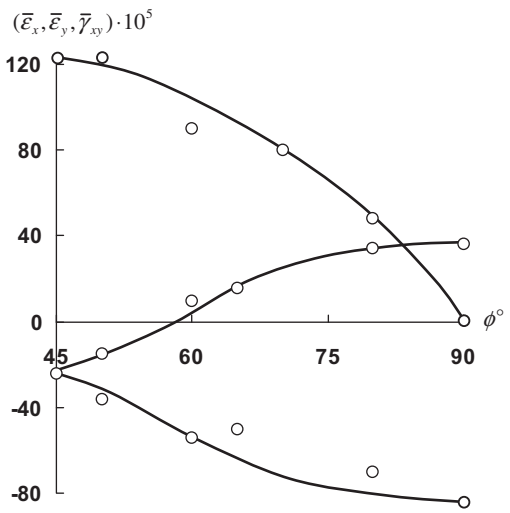


FIGURE 7.73

Dependence of residual strains in a glass-epoxy filament-wound cylinder on the winding angle, ——— calculation, ○ experiment.

where $\overline{\varepsilon}_1$ and $\overline{\varepsilon}_2$ are specified by Eqs. (7.104). The dependencies of $\overline{\varepsilon}_x$, $\overline{\varepsilon}_y$, and $\overline{\gamma}_{xy}$ on ϕ, plotted with the aid of Eqs. (7.105), are shown in Fig. 7.73 together with the experimental data of Morozov and Popkova (1987). As can be seen, the composite cylinder experiences, in the general case, not only a change in its length $(\overline{\varepsilon}_x)$ and diameter $(\overline{\varepsilon}_y)$, but also twist $(\overline{\gamma}_{xy})$.

To study the $\pm\,\phi$ angle-ply layer, we should utilize the thermoelasticity constitutive equations, Eqs. (7.23). Neglecting the bending and coupling stiffness coefficients, we can write for the case under study

$$\begin{aligned} N_x &= B_{11}\overline{\varepsilon}_x + B_{12}\overline{\varepsilon}_y - N_{1T} \\ N_y &= B_{21}\overline{\varepsilon}_x + B_{22}\overline{\varepsilon}_y - N_{2T} \end{aligned} \tag{7.106}$$

Applying these equations to an angle-ply composite cylinder removed from its mandrel, we should put $N_x = 0$ and $N_y = 0$ because the cylinder is free of loads, and take $\varepsilon_1^T = \overline{\varepsilon}_1$ and $\varepsilon_2^T = \overline{\varepsilon}_2$ in Eqs. (7.18) and (7.25)/(7.26) that specify N_{1T} and N_{2T}. Then, Eqs. (7.106) yield the following expressions for the strains that appear in the angle-ply cylinder after it is removed from the mandrel

$$\begin{aligned} \overline{\varepsilon}_x &= \frac{1}{B}\left(N_{1T}B_{22} - N_{2T}B_{12}\right) \\ \overline{\varepsilon}_y &= \frac{1}{B}\left(N_{2T}B_{11} - N_{1T}B_{12}\right) \end{aligned}$$

where $B = B_{11}B_{22} - B_{12}^2$,

$$\begin{aligned} N_{1T} &= h\left[\overline{E}_1(\overline{\varepsilon}_1 + \nu_{12}\overline{\varepsilon}_2)\cos^2\phi \;+ \overline{E}_2(\overline{\varepsilon}_2 + \nu_{21}\overline{\varepsilon}_1)\sin^2\phi\right] \\ N_{2T} &= h\left[\overline{E}_1(\overline{\varepsilon}_1 + \nu_{12}\overline{\varepsilon}_2)\sin^2\phi \;+ \overline{E}_2(\overline{\varepsilon}_2 + \nu_{21}\overline{\varepsilon}_1)\cos^2\phi\right]. \end{aligned}$$

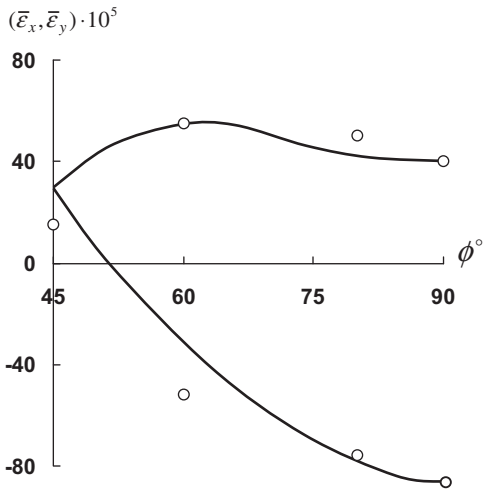


FIGURE 7.74

Residual strains in the $\pm\phi$ angle-ply filament wound glass-epoxy cylinder, ——— calculation, ○ experiment.

Here, $\overline{\varepsilon}_1$ and $\overline{\varepsilon}_2$ are given by Eqs. (7.104), $B_{mn} = A_{mn}h$, where A_{mn} are specified by Eqs. (4.72), and h is the thickness of cylinder. The results of calculations for the experimental cylinder studied by Morozov and Popkova (1987) are presented in Fig. 7.74.

As follows from Figs. 7.60 and 7.61, the approach described earlier, based on constitutive equations for laminates, Eqs. (7.23), with the shrinkage characteristics of a unidirectional ply or an elementary layer determined experimentally, provides fair agreement between the predicted results and the experimental data.

7.5 References

Anderson, J. A., Mikelsons, M. Ya., Tamuzh, V. P., & Tarashuch, I. V. (1991). Fatigue failure of laminated carbon-fiber-reinforced plastic. *Mechanics of Composite Materials, 27*(1), 74–78.

Apinis, R. P., Mikelsons, M. Ya., & Khonichev, V. I. (1991). Fatigue resistance of carbon material in symmetric tension-compression. *Mechanics of Composite Materials, 5*, 928–930 (in Russian).

ASTM Standard D7136 for Measuring the Damage Resistance of Fiber-Reinforced Polymer Matrix Composite to a Drop-Weight Impact Event.

Barnes, J. A., Simms, I. J., Farrow, G. J., Jackson, D., Wostenholm, G., & Yates, B. (1989). Thermal expansion behavior of thermoplastic composite materials. In *Proceedings of American Society for Composite Materials, Fourth Tech. Conf.* (pp. 717–725). Blacksburg, Virginia: Technomic Publ.

Chiao, C. C., Sherry, R. J., & Hetherington, N. W. (1977). Experimental verification of an accelerated tests for predicting the lifetime of organic fiber composite. *Journal of Composite Materials, 11*, 79–91 (January 1977).

Davis, G. W., & Sakata, I. F. (1981). *Design Considerations for Composite Fuselage Structure of Commercial Transport Aircraft*. NASA Report 159296, Washington.

Ha, S. K., & Springer, G. S. (1987). Mechanical properties of graphite epoxy composites at elevated temperatures. In F. L. Matthews, et al. (Eds.), *Proceedings of 6th International Conference on Composite Materials (ICCM-6),* July 1987, Vol. 4 (pp. 422–430). London: Elsevier Applied Science.

Hamilton, J. G., & Patterson, J. M. (1993). Design and analysis of near-zero *CTE* laminates and application to spacecraft. In *Proceedings of 9th International Conference on Composite Materials (ICCM/9),* Madrid, 12–16 July. *Composite Properties and Applications,* Univ. of Zaragoza, Vol. 6 (pp. 108–119). Woodhead Publ. Ltd.

Hwang., J. H., Kwon, D., Lee, C. S., & Hwang, W. (2000). Interlaminar fracture and low velocity impact on carbon/epoxy composite materials. *Journal of Composite Materials, Vol. 36*(No. 2), 195–214.

Hyer, M. W. (1989). Mechanics of unsymmetric laminates. Handbook of composites. In C. T. Herakovich, & Yu. M. Tarnopol'skii (Eds.), *Structure and Design*, Vol. 2 (pp. 86–114). Elsevier Applied Science.

Kim, H., & Kedward, K. T. (1999a). Experimental and numerical analysis correlation of hail ice impacting composite structures. In *Proceedings of 40th AIAA SDM Conference*. St. Louis, USA, Paper A99-24728, 1416–1426.

Kim, H., & Kedward, K. T. (1999b). Experimental measurement and numerical prediction of hail ice impact damage on composite panels. In *Proceedings of 12th International Conference on Composite Materials (ICCM-12)*. Paris, France (CD-ROM).

Liang, E. W., & Yuan, F. G. (1993). Delamination instability in composite laminates by a singular hybrid element method. In *Proceedings of 9th International Conference on Composite Materials (ICCM-9)* (pp. 409–416). Madrid: Spain.

Limonov, V. A., & Anderson, J. A. (1991). Effect of stress ratio on the strength of organic plastics. *Mechanics of Composite Materials, 27*(3), 276–283.

Milyutin, G. I., Bulmanis, V. N., Grakova, T. S., Popov, N. S., & Zakrzhevskii, A. M. (1989). Study and prediction of the strength characteristics of a wound epoxy organic-fiber plastic under different environmental effects. *Mechanics of Composite Materials, 25*(2), 183–189.

Morozov, E. V., & Popkova, L. K. (1987). Combined theoretical and experimental method of determining residual stresses in wound composite shells. *Mechanics of Composite Materials, 23*(6), 802–807.

Murakami, S., Kanagawa, Y., Ishida, T., & Tsushima, E. (1991). Inelastic deformation and fatigue damage of composite under multiaxial loading. In G. J. Dvorak (Ed.), *Inelastic Deformation of Composite Materials* (pp. 675–694). New York: Spring Verlag.

Ni, R. G., & Adams, R. D. (1984). The damping and dynamic moduli of symmetric laminated composite beams – theoretical and experimental results. *Journal of Composite Materials, 18*(2), 104–121.

Papadopoulos, D. S., & Bowles, K. J. (1990). Use of unbalanced laminates as a screening method for microcracking. In *Proceedings of 33th International SAMPE Symposium and Exhibition.* Book 2, Vol. 35. Anaheim, Ca. April 1990, 2127–2141.

Rabotnov, Yu. N. (1980). *Elements of Hereditary Solid Mechanics*. Moscow: Mir Publishers.

Rach, V. A., & Ivanovskii, V. S. (1986). On the effect of fiber length variation in filament wound structures. *Mechanics of Composite Materials*, 67–72 (in Russian).

Rogers, E. F., Phillips, L. M., Kingston-Lee, D. M., et al. (1977). The thermal expansion of carbon fiber-reinforced plastics. *Journal of Materials Science, 1*(12), 718–734.

Schapery, R. A. (1974). Viscoelastic behavior and analysis of composite materials. In L. J. Broutman, & R. H. Krock (Eds.), *Composite Materials. Mechanics of Composite Materials*, Vol. 2 (pp. 85–168). New York: Academic Press, (G.P. Sendeckyj ed.).

Schulte, K., Reese, E., & Chou, T.-W. (1987). Fatigue behavior and damage development in woven fabric and hybrid fabric composites. In F. L. Matthews, N. C. R. Buskel, J. M. Hodgkinson, & J. Morton (Eds.), *Proceedings of 6th International Conference on Composite Materials and 2nd European Conference on Composite Materials (ICCM and ECCM)*, Vol. 4 (pp. 89–99). London: Elsevier Science Ltd.

Shen, S. H., & Springer, G. S. (1976). Moisture absorption and desorption of composite materials. *Journal of Composite Materials, 10*, 2–20.

Skudra, A. M., Bulavs, F. Ya., Gurvich, M. R., & Kruklinsh, A. A. (1989). *Elements of Structural Mechanics of Composite Truss Systems*. Riga: Zinatne (in Russian).

Soutis, C., & Turkmen, D. (1993). High-temperature effects on the compressive strength of glass fiber-reinforced composites. In *Proceedings of 9th International Conference on Composite Materials (ICCM/9),* Madrid, 12–16 July. *Composite Properties and Applications,* Univ. of Zaragoza, Vol. 6 (pp. 581–588). Woodhead Publ. Ltd.

Springer, G. S. (Ed.) (1981). *Environmental Effects on Composite Materials*, Vol. 1. Westport CT: Technomic Publ.

Springer, G. S. (Ed.) (1984). *Environmental Effects on Composite Materials*, Vol. 2. Westport CT: Technomic Publ.

Springer, G. S. (Ed.) (1988). *Environmental Effects on Composite Materials*, Vol. 3. Westport CT: Technomic Publ.

Strife, J. R., & Prevo, K. M. (1979). The thermal expansion behavior of unidirectional kevlar/epoxy composites. *Journal of Composite Materials, 13*, 264–276.

Sukhanov, A. V., Lapotkin, V. A., Artemchuk, V. Ya., & Sobol', L. A. (1990). Thermal deformation of composites for dimensionally stable structures. *Mechanics of Composite Materials, 26*(4), 432–436.

Survey (1984). *Application of Composite Materials in Aircraft Technology.* Central Aero-hydrodynamics Institute (in Russian).

Tamuzh, V. P., & Protasov, V. D. (Eds.) (1986). *Fracture of Composite Structures*. Riga: Zinatne (in Russian).

Tarnopol'skii, Yu. M., & Roze, A. V. (1969). *Specific Features of Analysis for Structural Elements of Reinforced Plastics*. Riga: Zinatne (in Russian).

Tsai, S. W. (1987). *Composite Design*. Dayton OH: Think Composites Publ.

Vasiliev, V. V., & Sibiryakov, A. V. (1985). Propagation of elastic waves in a laminated strip. *Mechanics of Solids, 1*, 104–109.

Verpoest, I., Li, L., & Doxsee, L. (1989). A combined micro- and macromechanical study of the impact behavior of carbon and glass fiber epoxy composites. In W. Yunshu, G. Zhenlong, & W. Rrenjie (Eds.), *Proceedings of 7th International Conference on Composite Materials (ICCM-7),* November 1989, Guangzhou, China, Vol. 2 (pp. 316–321). Oxford: Pergamon Press.

Zhurkov, S. N., & Narzullaev, B. N. (1953). Time dependence of the strength of solids. *Journal of Technical Physics, Vol. 23*(No. 10), 1677–1689.

Zinoviev, P. A., & Ermakov, Yu. N. (1994). *Energy Dissipation in Composite Materials.* Lancaster PA: Technomic Publ.

CHAPTER

Laminated composite beams and columns

8

High modulus carbon fiber reinforced composites are successfully used to fabricate laminated composite beams loaded with axial and transverse forces and to reinforce traditional metal and concrete beam elements to increase their stiffness. Various approaches to the analysis and design of composite beams have been discussed by Vasiliev (1993), Gay et al. (2003), Kollar and Springer (2003), Dekker (2004), and Vinson and Sierakowski (2004). This chapter is concerned with the analysis of static, stability, and dynamic problems using elastic beam theory, allowing for transverse shear deformation.

8.1 BASIC EQUATIONS

Consider a beam as shown in Fig. 8.1 and loaded with a transverse distributed load (p, q) and/or-concentrated forces (R, F), and end forces and moment (V_l, N_l, M_l). The analysis of such a beam is based on a specific feature of the structure, namely, the height h is much smaller than its length l. This feature allows us to introduce some assumptions concerning the distribution of beam displacements through the beam height which, in turn, enables us to reduce the problem of the analysis of beams to a solution of ordinary differential equations. We also assume that the beam is loaded only in the xz-plane (see Fig. 8.1), so that the structure is in a state of plane stress.

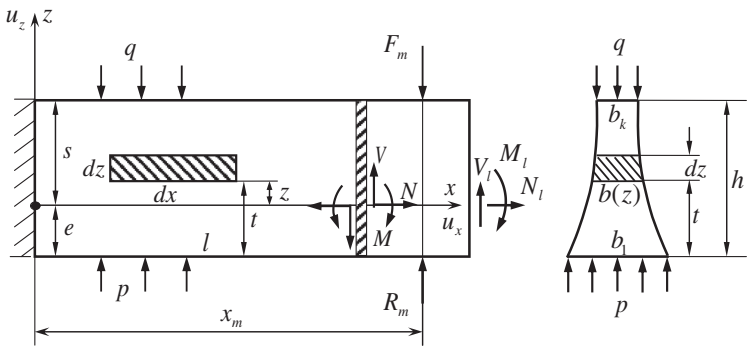


FIGURE 8.1

A beam loaded with surface and end forces and moment.

Advanced Mechanics of Composite Materials and Structural Elements. http://dx.doi.org/10.1016/B978-0-08-098231-1.00008-X
Copyright © 2013 Elsevier Ltd. All rights reserved.

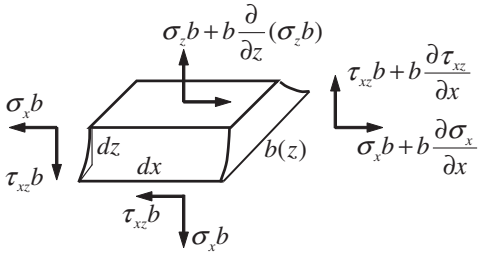


FIGURE 8.2

Stress state of a beam element.

Single out the shaded element of the beam as shown in Fig. 8.2 and assume that the stresses acting on this element are uniformly distributed over the element width b. The equilibrium equations for this element have the following form:

$$b\frac{\partial \sigma_x}{\partial x} + \frac{\partial}{\partial z}(b\tau_{xz}) = 0, \qquad \frac{\partial}{\partial z}(b\sigma_z) + b\frac{\partial \tau_{xz}}{\partial x} = 0 \tag{8.1}$$

in which $b(z)$ is the width of the beam cross-section (see Fig. 8.1). The stresses σ_z and τ_{xz} must satisfy the boundary conditions on the beam surfaces. Note that in accordance with Fig. 5.1 we measure the z-coordinate from some reference plane which is located at the distances e and s from the beam bottom and top surfaces (see Fig. 8.1). Then, the boundary conditions can be presented as

$$\begin{array}{ll} \sigma_z(x, z = -e) = -p, & \tau_{xz}(x, z = -e) = 0 \\ \sigma_z(x, z = s) = -q, & \tau_{xz}(x, z = s) = 0 \end{array} \tag{8.2}$$

Since the beam height h is relatively small, we assume that the beam deflection, u_z, does not depend on coordinate z (see Fig. 8.1), whereas the axial displacement, u_x, is a linear function of z. These assumptions are the same as those introduced in Section 5.1 for thin laminates. Thus, in accordance with Eqs. (5.1) and (5.2), we have

$$u_z = w(x), \quad u_x = u(x) + z\theta(x) \tag{8.3}$$

Here, w is the beam deflection, whereas u and θ are the axial displacement and the angle of rotation of the beam cross section, respectively. The axial strain is specified by the first equation of Eqs. (5.3), i.e.,

$$\varepsilon_x = u'(x) + z\theta'$$

in which $(\ldots)' = d(\ldots)/dx$. Using Hooke's law, we get

$$\sigma_x = E\varepsilon_x = E(u' + z\theta') \tag{8.4}$$

for the axial stress, where E is the axial modulus of the beam material. It follows from this equation that σ_x depends on two functions, $u'(x)$ and $\theta'(x)$, that can be replaced with the corresponding stress resultants, i.e., with the internal axial force N acting in the reference plane and directed along the beam axis, and the internal bending moment M exerted on the reference plane and acting in the xz-plane, i.e.,

$$N = \int_{-e}^{s} \sigma_x b dz, \quad M = \int_{-e}^{s} \sigma_x b z dz \tag{8.5}$$

(see Fig. 8.1). Substitution of Eq. (8.4) for σ_x into Eqs. (8.5) yields

$$N = B_{11}u' + C_{11}\theta', \quad M = C_{11}u' + D_{11}\theta' \tag{8.6}$$

where coefficients

$$B_{11} = \int_{-e}^{s} Ebdz, \quad C_{11} = \int_{-e}^{s} Ebzdz, \quad D_{11} = \int_{-e}^{s} Ebz^2dz \tag{8.7}$$

are similar to the stiffness coefficients specified by Eqs. (5.6)–(5.8).

The constitutive equations, Eqs. (8.6), can be simplified by a suitable choice of reference plane. Introduce a new coordinate of the shaded beam element

$$t = z + e \tag{8.8}$$

(see Fig. 8.1) which changes from $t = 0$ ($z = -e$) to $t = h$ ($z = s$). Then, the stiffness coefficients in Eqs. (8.7) become

$$B_{11} = I_0, \quad C_{11} = I_1 - eI_0, \quad D_{11} = I_2 - 2eI_1 + e^2I_0 \tag{8.9}$$

in which

$$I_n = \int_{0}^{h} Ebt^n dt, \quad n = 0, 1, 2 \tag{8.10}$$

Now assume that the coordinate of the reference plane e (see Fig. 8.1) determines the location of the beam neutral axis, so that the internal axial force N acting along this axis induces only an axial displacement u, whereas the bending moment M causes only a rotation of the cross section. Then, it follows from Eqs. (8.6) that $C_{11} = 0$, and the second equation of Eqs. (8.9) yields

$$e = \frac{I_1}{I_0} \tag{8.11}$$

Under this condition, Eqs. (8.6) reduce to

$$N = Bu', \qquad M = D\theta' \tag{8.12}$$

where

$$B = I_0, \qquad D = I_2 - \frac{I_1^2}{I_0} \tag{8.13}$$

are the axial and bending stiffnesses of the beam. Substituting Eqs. (8.12) into Eq. (8.4) and using Eq. (8.8), we arrive at the following final expression for the axial stress:

$$\sigma_x = E\left[\frac{N}{B} + (t - e)\frac{M}{D}\right] \tag{8.14}$$

Consider now the shear stress τ_{xz}. According to the first assumption in Eqs. (8.3), the beam height does not change with deformation of the beam. So, the distribution of the shear stress over the beam height

does not affect the beam behavior which is governed by the resultant transverse shear force V only. In accordance with Eqs. (5.12),

$$V = \int_{-e}^{s} \tau_{xz} b dz = \int_{0}^{h} \tau_{xz} b dt \tag{8.15}$$

The second part of this equation is written with the aid of Eq. (8.8). The transverse shear force V (see Fig. 8.1) is linked with the average shear strain γ (see Eq. 5.14) by the constitutive equation

$$V = S\gamma \tag{8.16}$$

in which

$$\gamma = \theta + w' \tag{8.17}$$

The shear stiffness coefficient S is defined and discussed in Section 5.5. To determine this coefficient, we average the shear strain γ_{xz} as

$$\gamma = \frac{1}{h} \int_{0}^{h} \gamma_{xz} dt = \frac{1}{h} \int_{0}^{h} \frac{\tau_{xz}}{G} dt \tag{8.18}$$

where $G = G_{xz}$ is the shear modulus of the beam material in the xz-plane. Since the actual distribution of shear stress over the beam height, as mentioned earlier, does not affect the beam deformation, we can introduce the averaged shear stress $\tau_a = V/bh$ which has the same resultant force V as the actual stress τ_{xz}. Taking $\tau_{xz} = \tau_a$ in Eq. (8.18), we arrive at Eq. (8.16) in which

$$S = \frac{h^2}{\int_{0}^{h} \frac{dt}{bG}} \tag{8.19}$$

For a homogeneous rectangular cross section with $b = constant$ and $G = constant$, we get

$$S = Gbh \tag{8.20}$$

The internal axial force N, bending moment M, and transverse shear force V must satisfy the equilibrium equations following from Eqs. (8.1) and boundary conditions in Eqs. (8.2). To derive these equations, consider the first equation of Eqs. (8.1) and using the transformation defined by Eq. (8.8) present it in the form

$$\frac{\partial}{\partial t}(b\tau_{xz}) = -b\frac{\partial \sigma_x}{\partial x}$$

Integrating with respect to t from $t = 0$ and taking into account the boundary conditions, Eqs. (8.2), according to which $\tau_{xz}(t = 0) = 0$, we get

$$\tau_{xz} = -\frac{1}{b} \int_{0}^{t} \frac{\partial \sigma_x}{\partial x} b dt$$

Substituting the axial stress specified by Eq. (8.14) into this equation, we have

$$\tau_{xz} = -\frac{1}{b}\left[\frac{N'}{B}\int_0^t Ebdt + \frac{M'}{D}\int_0^t E(t-e)bdt\right] \tag{8.21}$$

Now, take $t = h$ and again use the boundary conditions, Eq. (8.2) (according to which $\tau_{xz}(t = h) = 0$), to get

$$\frac{N'}{B}I_0 + \frac{M'}{D}(I_1 - eI_0) = 0$$

where the integrals $I_n (n = 0, 1, 2)$ are specified by Eq. (8.10). Applying Eq. (8.11), we can prove that the second term is zero, so that

$$N' = 0 \tag{8.22}$$

This is the first equilibrium equation for the beam under study showing that if the beam is not loaded with any distributed axial forces, which is the case, the internal axial force does not change along the beam axis. Thus, Eq. (8.21) reduces to

$$\tau_{xz} = -\frac{M'}{bD}\int_0^t E(t-e)bdt \tag{8.23}$$

Substitute this result into Eq. (8.15) for the transverse shear force to get

$$V = -\frac{M'}{D}\int_0^h dt\int_0^t E(t-e)bdt \tag{8.24}$$

Calculating the integral by parts and using Eqs. (8.10), (8.11), and (8.23), we get in several steps

$$\begin{aligned}\int_0^h dt\int_0^t E(t-e)bdt &= h\int_0^h Ebtdt - \int_0^h Ebt^2dt - e\left(h\int_0^h Ebdt - \int_0^h Ebtdt\right)\\ &= hI_1 - I_2 - e(hI_0 - I_1) = -I_2 + eI_1 + h(I_1 - eI_0) = -D\end{aligned} \tag{8.25}$$

Thus, Eq. (8.22) yields

$$V = M' \tag{8.26}$$

This is the moment equilibrium equation for the beam element. Using Eq. (8.26), we can present the following final form of Eq. (8.23) for the shear stress:

$$\tau_{xz} = -\frac{V}{bD}\int_0^t E(t-e)bdt \tag{8.27}$$

in which e is specified by Eq. (8.11).

Consider the so-called shear correction factor discussed, e.g., by Birman and Bert (2002). In its application to homogeneous beams with rectangular cross sections, Eq. (8.20) for the beam shear stiffness is modified as

$$S = kGbh \tag{8.28}$$

in which k is the shear correction factor which takes into account the actual distribution of shear stress over the beam height. The concept of the shear correction factor ($k = 2/3$ and $k = 0.889$) was introduced by Timoshenko (1921, 1922). Reissner (1945) actually used $k = 5/6$ as proposed by Goens (1931), whereas Mindlin (1951) proposed $k = \pi^2/12$.

Recall that Eq. (8.19) for S is derived under the condition that the shear stress τ_{xz} is averaged through the beam height. Now we have Eq. (8.27), which specifies the actual distribution for the shear stress. Substituting Eq. (8.27) into the second part of Eq. (8.18), we arrive at Eq. (8.16) in which

$$S = -\frac{Dh}{\int_0^h \frac{dt}{bG} \int_0^t E(t-e)bdt} \tag{8.29}$$

For a rectangular homogeneous beam, $D = Ebh^3/12$, $e = h/2$, and Eq. (8.29) yields $S = Gbh$.

Thus, $k = 1$ in Eq. (8.28). This result looks natural because, as follows from the corresponding theorem of statics, the force distribution over an absolutely rigid body does not affect the body motion.

The difference between Eq. (8.19) and Eq. (8.29) is most pronounced for sandwich beams with a lightweight core. Consider the cross section shown in Fig. 8.3 for which $b = h_0 = 25$ mm and $\delta = 2.5$ mm. The relevant parameters for aluminum facings are $E = 70$ GPa, $\upsilon = 0.3$, and $G = 26.9$ GPa, whereas for the core we take $E_0 = 140$ MPa, $\upsilon_0 = 0$, and $G_0 = 70$ MPa. Thus, $E/E_0 = 500$, $G/G_0 = 384$, and $h_0/\delta = 10$. For the beam shown in Fig. 8.3, Eq. (8.19) gives $S = 63$ kN, whereas Eq. (8.29) yields $S = 58.2$ kN, i.e., the difference is 8.2%. However, Eq. (8.19) is much simpler than Eq. (8.29) and for this reason it is recommended for practical analysis.

Return to the equilibrium equations and consider the second equation of Eqs. (8.1) which can be presented as

$$\frac{\partial}{\partial t}(b\sigma_z) = -b\frac{\partial \tau_{xz}}{\partial x}$$

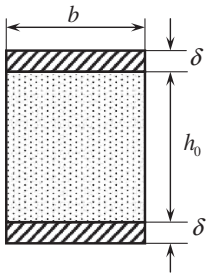


FIGURE 8.3

Cross section of a sandwich beam.

Substituting τ_{xz} from Eq. (8.24), integrating with respect to t from $t = 0$, and taking into account the boundary conditions in Eqs. (8.2) according to which $\sigma_z(t = 0) = -p$, we arrive at

$$\sigma_z = \frac{1}{b}\left[\frac{V'}{D}\int_0^t dt \int_0^t E(t-e)bdt - pb_1\right] \tag{8.30}$$

in which $b_1 = b(t = 0)$ (see Fig. 8.1). Taking $t = h$ and using the boundary conditions in Eqs. (8.2) according to which $\sigma_z(t = h) = -q$, we get

$$\frac{V'}{b}\int_0^h dt \int_0^t E(t-e)bdt = pb_1 - qb_k$$

where $b_k = b(t = h)$ (see Fig. 8.1). Using Eq. (8.25) for the integral in the left-hand side of this equation, we arrive at the last equilibrium equation for the beam element, i.e.,

$$V' + \overline{p} = 0, \quad \overline{p} = pb_1 - qb_k \tag{8.31}$$

Now, Eq. (8.30) allows us to determine the transverse normal stress as

$$\sigma_z = -\frac{1}{b}\left[\frac{\overline{p}}{D}\int_0^t dt \int_0^t E(t-e)bdt + pb_1\right] \tag{8.32}$$

Thus, we have constructed the theory of composite beams which includes the equilibrium equations, Eqs. (8.22), (8.26) and (8.31), that allow us to determine the stress resultants N, V, and M, and the constitutive equations, Eqs. (8.12) and (8.16), (8.17) that can be used to find the displacements u, w and the angle of rotation θ. These equations can be divided into two independent groups.

The first group describes the axial loading and includes Eqs. (8.22) and (8.12), i.e.,

$$N' = 0, \quad N = Bu' \tag{8.33}$$

This set of equations is of the second order and requires two boundary conditions (one for each end). At the fixed end $u = 0$, whereas at the free end $N = 0$. For the end $x = l$ loaded with an axial force N_l, $N = N_l$. Note that the force must be applied to the neutral axis of the beam. Otherwise, the force must be moved to the neutral axis and the additional bending moment must be applied in the end cross section.

The second group of equations, Eqs. (8.26) and (8.31) and Eqs. (8.12), (8.16), and (8.17), i.e.,

$$\begin{array}{ll} M' = V, & V' + \overline{p} = 0 \\ M = D\theta', & V = S(\theta + w') \end{array} \tag{8.34}$$

describes the beam bending. This set is of the fourth order and requires four boundary conditions (two for each end of the beam). At the clamped end $w = 0$ and $\theta = 0$, at the hinged end $w = 0$ and $M = 0$, whereas for the free end $V = 0$ and $M = 0$. For the end $x = l$ loaded with the transverse force V_l and the bending moment M_l, we have $V = V_l$ and $M = M_l$.

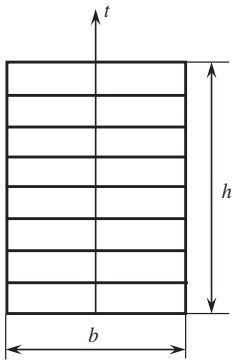


FIGURE 8.4

Rectangular cross section.

8.2 STIFFNESS COEFFICIENTS

The stiffness coefficients B, D, and S depend on the beam structure. For homogeneous or quasi-homogeneous (consisting of identical layers) beams with rectangular cross-sections (see Fig. 8.4), $E = constant$, $G = constant$, $b = constant$ and Eqs. (8.10), (8.11), and (8.20) yield

$$I_0 = Ebh, \quad I_1 = \frac{1}{2}Ebh^2, \quad I_2 = \frac{1}{3}Ebh^3$$
$$e = \frac{h}{2}, \quad B = Ebh, \quad D = \frac{1}{12}Ebh^3, \quad S = Gbh$$

Axial and shear stresses specified by Eqs. (8.14) and (8.27) are

$$\sigma_x = \frac{1}{bh}\left[N + \frac{12M}{h^2}\left(t - \frac{h}{2}\right)\right], \quad \tau_{xz} = \frac{6V}{bh^3}t(h-t)$$

For laminated beams (see Fig. 8.5), it follows from Eqs. (5.42) and (5.46) that

$$I_0 = \sum_{i=1}^{k} E_i b_i h_i, \quad I_1 = \frac{1}{2}\sum_{i=1}^{k} E_i b_i h_i (t_{i-1} + t_i)$$
$$I_2 = \frac{1}{3}\sum_{i=1}^{k} E_i b_i h_i \left(t_{i-1}^2 + t_{i-1}t_i + t_i^2\right) \tag{8.35}$$
$$e = \frac{I_1}{I_0}, \quad B = I_0, \quad D = I_2 - \frac{I_1^2}{I_0}, \quad S = \frac{h^2}{\sum_{i=1}^{k} \frac{h_i}{G_i b_i}}$$

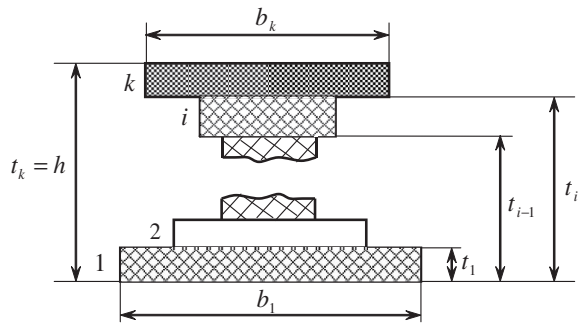


FIGURE 8.5

Laminated cross section.

where $h_i = t_i - t_{i-1}$ is the thickness of the i-th layer. The axial stress in the i-th ply is

$$\sigma_x^{(i)} = E_i\left[\frac{N}{B} + \frac{M}{D}(z_i - e)\right] \tag{8.36}$$

where $t_{i-1} - e \le z_i \le t_i - e$.

The shear stress acting between the i-th and the $(i+1)$-th layers is

$$\tau_{xz}^{(i,i+1)} = -\frac{V}{2Db_{i,i+1}}\sum_{j=1}^{i} E_j b_j h_j\left(t_{j-1} + t_j - 2e\right) \tag{8.37}$$

where $b_{i,i+1}$ is the lower value of b_i and b_{i+1}.

Composite tows can be used to reinforce metal profiles as shown in Fig. 8.6. In this case, Eq. (8.10) for coefficients I_n is generalized as

$$I_n = \int_0^h Ebt^n dt + \sum_{j=1}^{m} E_j A_j t_j^n \quad (n = 0, 1, 2)$$

Here m is the number of composite tows, E_j and A_j are the modulus and the cross-sectional area of the j-th tow, and t_j is the tow coordinate (see Fig. 8.6). The axial stress in the composite tow is

$$\sigma_x^{(j)} = E_j\left[\frac{N}{B} + \frac{M}{D}\left(t_j - e\right)\right]$$

Finally, consider a laminated beam whose layers are parallel to the plane of bending as shown in Fig. 8.7. The structure is symmetric with respect to the plane of bending (xz-plane). For such a beam,

$$e = \frac{h}{2}, \quad B = h\sum_{i=1}^{k} E_i b_i, \quad D = \frac{h^3}{12}\sum_{i=1}^{k} E_i b_i, \quad S = h\sum_{i=1}^{k} G_i b_i$$

The axial stress is

$$\sigma_x^{(i)} = E_i\left(\frac{N}{B} + \frac{M}{D}z\right)$$

Repeating the derivation of Eq. (8.27) for the shear stress, we arrive at

$$\tau_{xz}^{(i)} = E_i\frac{V}{2D}\left(\frac{h^2}{4} - z^2\right)$$

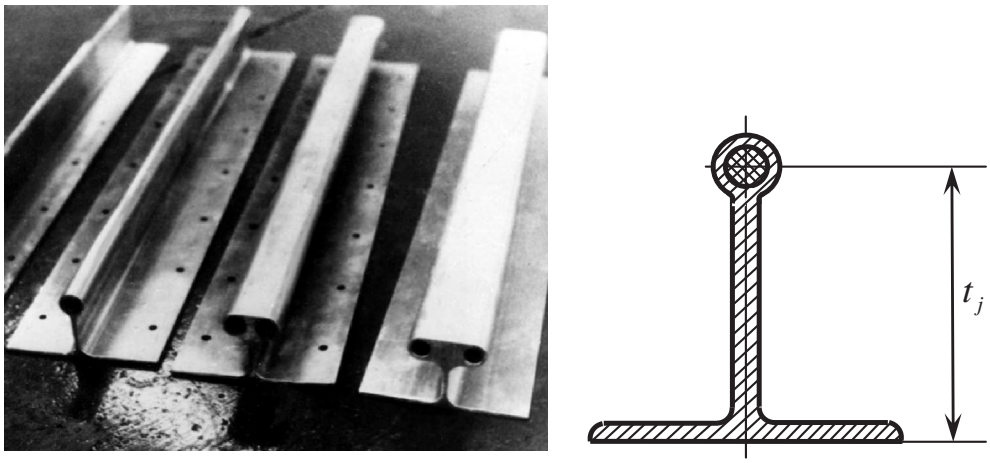


FIGURE 8.6

Metal profiles reinforced with composite tows.

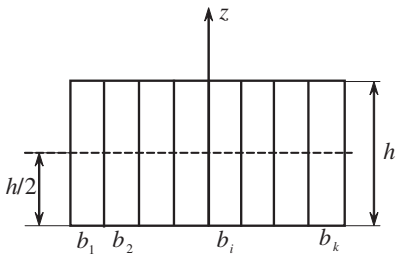


FIGURE 8.7

Laminated beam with layers parallel to the plane of bending.

8.3 BENDING OF LAMINATED BEAMS

Consider the problem of bending described by Eqs. (8.34). Integration of these equations with respect to x from $x = 0$ yields

$$\begin{aligned} V &= V_0 - V_p - V_R \\ M &= M_0 + V_0 x - M_p - M_R \\ \theta &= \theta_0 + \frac{M_0}{D}x + \frac{V_0}{2D}x^2 - \theta_p - \theta_R \\ w &= w_0 + \frac{1}{S}\left(V_0 x - M_p - M_R\right) - \theta_0 x - \frac{M_0}{2D}x^2 - \frac{V_0}{6D}x^3 + w_p + w_R \end{aligned} \tag{8.38}$$

where V_0, M_0, θ_0, and w_0 are the initial values of V, M, θ, and w corresponding to the cross section $x = 0$. These values can be found from the boundary conditions at the beam ends $x = 0$ and $x = l$ (see Fig. 8.1). The load terms with subscript "p" correspond to the distributed loads and have the following form:

$$V_p = \int_0^x \overline{p} dx, \quad M_p = \int_0^x V_p dx, \quad \theta_p = \frac{1}{D}\int_0^x M_p dx, \quad w_p = \int_0^x \theta_p dx \tag{8.39}$$

For uniform pressure $\overline{p} = \overline{p}_0$,

$$V_p = \overline{p}_0 x, \quad M_p = \frac{1}{2}\overline{p}_0 x^2, \quad \theta_p = \frac{1}{6D}\overline{p}_0 x^3, \quad w_p = \frac{1}{24D}\overline{p}_0 x^4 \tag{8.40}$$

The load terms with subscript "R" correspond to the concentrated forces R_m and F_m shown in Fig. 8.1. These terms can be written with the aid of Eqs. (8.39) if we present them in the form $\overline{p} = \overline{R}_m \delta(x - x_m)$ where $\overline{R}_m = R_m - F_m$ and δ is the delta function. Using the rules of integration of this function, we get from Eqs. (8.39)

$$V_R = \sum_{m=1}^{n} V_R^{(m)}, \quad M_R = \sum_{m=1}^{n} M_R^{(m)}, \quad \theta_R = \sum_{m=1}^{n} \theta_R^{(m)}, \quad w_R = \sum_{m=1}^{n} w_R^{(m)} \tag{8.41}$$

where n is the number of the beam cross sections in which the forces act and for $x_m < x$

$$V_R^{(m)} = 0, \quad M_R^{(m)} = 0, \quad \theta_R^{(m)} = 0, \quad w_R^{(m)} = 0 \tag{8.42}$$

and for $x \geq x_m$

$$V_R^{(m)} = \overline{R}_m, \quad M_R^{(m)} = \overline{R}_m (x - x_m), \quad \theta_R^{(m)} = \frac{\overline{R}_m}{2D}(x - x_m)^2, \quad w_R^{(m)} = \frac{\overline{R}_m}{6D}(x - x_m)^3 \tag{8.43}$$

The solution given by Eqs. (8.38) is universal and allows us to study both statically determinate and redundant beams using one and the same procedure. This solution can be applied also to multi-supported beams. Introducing forces F_m as the support reactions at the support cross sections $x = x_m$, we can find F_m using the conditions $w(x = x_m) = 0$.

The second term with S in Eq. (8.38) for w accounts for the transverse shear deformation. As can be seen, the allowance for this deformation practically does not hinder the analysis of the beam. If the shear deformation is neglected, we must take $S \to \infty$ in Eq. (8.38) for w. As a result, we arrive at the solution corresponding to classical beam theory.

To demonstrate the application of the general solution provided by Eqs. (8.38), consider the beam similar to that supporting the passenger floor of an airplane fuselage shown in Fig. 8.8. Since the cross section $x = 0$ is clamped, we must take $w_0 = 0$ and $\theta_0 = 0$ in Eqs. (8.38). The beam consists of two parts corresponding to $0 \leq x < c$ and $c \leq x \leq l$ (see Fig. 8.8). For the first part, $\overline{p} = -qb_k$ (see Fig. 8.1), so we take $\overline{p} = -Q$, where $Q = qb_k$. Then, Eqs. (8.39) and (8.42) yield

$$V_p^{(1)} = -Qx, \quad M_p^{(1)} = -\frac{1}{2}Qx^2, \quad \theta_p^{(1)} = -\frac{Q}{6D}x^3, \quad w_p^{(1)} = -\frac{Q}{24D}x^4$$

$$V_R = 0, \quad M_R = 0, \quad \theta_R = 0, \quad w_R = 0$$

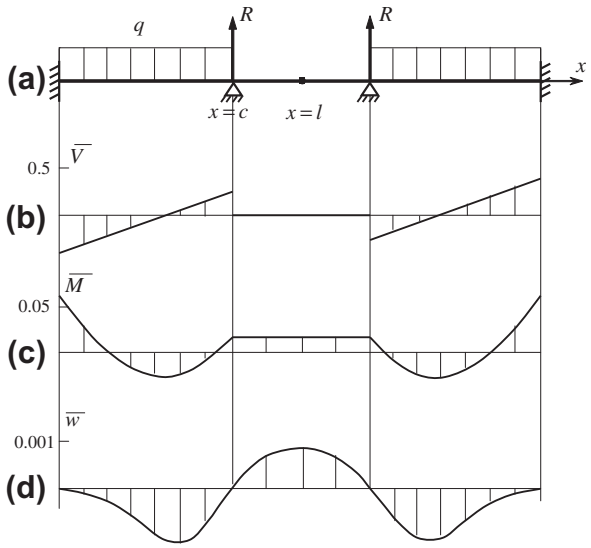


FIGURE 8.8

Distributions of the normalized shear force $\overline{V} = V/Ql$ (b), bending moment $\overline{M} = M/Ql^2$ (c), and deflection $\overline{w} = Dw/Ql^4$ (d) along the x-axis.

and the solution in Eqs. (8.38) can be written as

$$\begin{aligned} V_1 &= V_0 + Qx \\ M_1 &= M_0 + V_0 x + \frac{1}{2}Qx^2 \\ \theta_1 &= \frac{M_0}{D}x + \frac{V_0}{2D}x^2 + \frac{Q}{6D}x^3 \\ w_1 &= \frac{1}{S}\left(V_0 x + \frac{1}{2}Qx^2\right) - \frac{M_0}{2D}x^2 - \frac{V_0}{6D}x^3 - \frac{Q}{24D}x^4 \end{aligned} \tag{8.44}$$

Consider the second part for which $\overline{p} = 0$. Then, the load terms in Eqs. (8.39) become

$$V_p^{(2)} = \int_0^x \overline{p}dx = -\int_0^c Qdx = -Qc$$

$$M_p^{(2)} = \int_0^x V_p dx = \int_0^c V_p^{(1)}dx + \int_c^x V_p^{(2)}dx = -\frac{1}{2}Qc(2x - c)$$

$$\theta_p^{(2)} = \frac{1}{D}\int_0^x M_p dx = \frac{1}{D}\left(\int_0^c M_p^{(1)}dx + \int_0^x M_p^{(2)}dx\right) = -\frac{Qc}{6D}\left(c^2 + 3x^2 - 3cx\right)$$

$$w_p^{(2)} = \int_0^x \theta_p dx = \int_0^c \theta_p^{(1)}dx + \int_c^x \theta_p^{(2)}dx = -\frac{Qc}{24D}\left(4x^3 - c^3 + 4xc^2 - 6x^2c\right)$$

The support reaction R (see Fig. 8.8) is treated as the unknown concentrated force. Then, Eqs. (8.43) yield

$$V_R = R, \quad M_R = R(x-c), \quad \theta_R = \frac{R}{2D}(x-c)^2, \quad w_R = \frac{R}{6D}(x-c)^3$$

Finally, we get for the second part of the beam

$$\begin{aligned}
V_2 &= V_0 + Qc - R \\
M_2 &= M_0 + V_0 x + \frac{1}{2}Qc(2x-c) - R(x-c) \\
\theta_2 &= \frac{M_0}{D}x + \frac{V_0}{2D}x^2 + \frac{Qc}{6D}\left(c^2 + 3x^2 - 3cx\right) - \frac{R}{2D}(x-c)^2 \\
w_2 &= \frac{1}{S}\left[V_0 x + \frac{1}{2}Qc(2x-c) - R(x-c)\right] - \frac{M_0}{2D}x^2 - \frac{V_0}{6D}x^3 \\
&\quad -\frac{Qc}{24D}\left(4x^3 - c^3 + 4xc^2 - 6x^2 c\right) + \frac{R}{6D}(x-c)^3
\end{aligned} \tag{8.45}$$

The obtained solution, Eqs. (8.44) and (8.45), includes three unknown parameters: V_0, M_0, and R, which can be found from two symmetry conditions, i.e., $V_2(x=l)=0$ and $\theta_2(x=l)=0$, and the condition for the reaction force $w_1(x=c) = w_2(x=c) = 0$. The result is as follows

$$V_0 = R - Qc, \quad M_0 = \frac{1}{4}Qc^2(1-4k_s) - \frac{1}{3}Rc(1-6k_s) \tag{8.46}$$

$$R = \frac{1}{2}Qc\frac{3l(1+4k_s)-2c}{4l(1+3k_s-3c)}$$

where $k_s = D/Sc^2$.

For numerical analysis, neglect the shear deformation by taking $k_s = 0$. Then, the solution in Eqs. (8.46) reduces to

$$V_0 = -\frac{Qc(5l-4c)}{2(4l-3c)}, \quad M_0 = \frac{Qc^2(6l-5c)}{12(4l-3c)}, \quad R = \frac{Qc(3l-2c)}{2(4l-3c)}$$

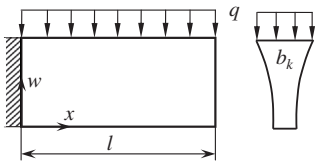
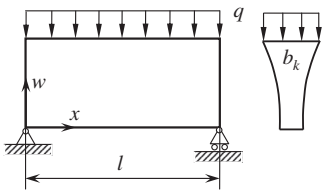
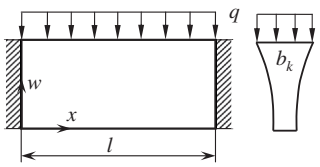
The dependencies of the normalized shear force, the bending moment, and the beam deflection on the axial coordinate are presented in Fig. 8.8.

Beam deflections are often used as approximation functions in the solutions of plate bending problems (see Chapter 9). Solutions of typical beam problems are presented in Table 8.1.

As an example, consider a simply supported I-beam loaded with uniform pressure q (see Fig. 8.9). The beam is made of an aluminum alloy for which $E = 70$ GPa and $G = 26.9$ GPa. At the bottom, where the maximum tensile stress acts, the beam is reinforced with a unidirectional carbon-epoxy layer with modulus of elasticity $E_c = 140$ GPa and shear modulus $G_c = 3.5$ GPa. The beam dimensions are

$$l = 1250 \text{ mm}, \quad \delta = 2.5 \text{ mm}, \quad h_0 = 100 \text{ mm}, \quad b = 50 \text{ mm} \tag{8.47}$$

TABLE 8.1 Solutions for the beams loaded with uniform pressure for typical boundary conditions.

Case	Beam Type	Solution
1		$V = -qb_k(l-x)$ $M = \frac{1}{2}qb_k(l-x)^2$ $\theta = \frac{qb_k}{6D}(3l^2 - 3lx + x^2)x$ $w = -\frac{qb_k}{24D}\left[x^3 - 4lx^2 + 6l^2x + 12\frac{D}{S}(2l-x)\right]x$
2		$V = \frac{1}{2}qb_k(2x-l)$ $M = -\frac{1}{2}qb_k(l-x)x$ $\theta = \frac{qb_k}{24D}(l^3 - 6lx^2 + 4x^3)$ $w = -\frac{qb_k}{24D}\left[l^3 - 2lx^2 + x^3 + 12\frac{D}{S}(l-x)\right]x$
3		$V = qb_k\left(x - \frac{l}{2}\right)$ $M = \frac{1}{12}qb_k(6x^3 - 6lx + l^2)x$ $\theta = \frac{qb_k}{12D}(2x^2 - 3lx + l^2)x$ $w = -\frac{qb_k}{24D}\left[x(l-x) + 12\frac{D}{S}\right](l-x)x$

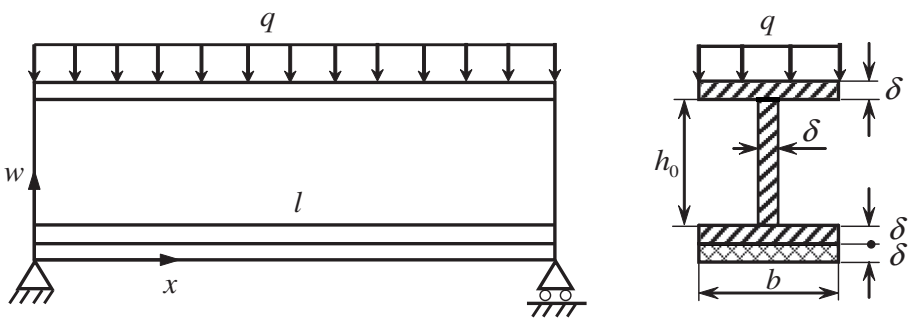


FIGURE 8.9

A simply supported *I*-beam.

The layer coordinates are shown in Fig. 8.10. The beam is composed of four layers with the following parameters:

$$\begin{aligned}
&b_1 = 50\ \text{mm}, \quad t_0 = 0, \quad t_1 = 2.5\ \text{mm}, \quad h_1 = 2.5\ \text{mm}, \quad E_1 = 140\ \text{GPa}, \quad G_1 = 3.5\ \text{GPa}\ \text{(layer 1)}\\
&b_2 = 50\ \text{mm}, \quad t_2 = 5\ \text{mm}, \quad h_2 = 2.5\ \text{mm}, \quad E_2 = 70\ \text{GPa}, \quad G_2 = 26.9\ \text{GPa} \quad \text{(layer 2)}\\
&b_3 = 2.5\ \text{mm}, \quad t_3 = 105\ \text{mm}, \quad h_3 = 100\ \text{mm}, \quad E_3 = 70\ \text{GPa}, \quad G_3 = 26.9\ \text{GPa} \quad \text{(layer 3)}\\
&b_4 = 50\ \text{mm}, \quad t_4 = h = 107.5\ \text{mm}, \quad h_4 = 2.5\ \text{mm}, \quad E_4 = 70\ \text{GPa}, \quad G_4 = 26.9\ \text{GPa} \quad \text{(layer 4)}
\end{aligned} \tag{8.48}$$

The beam strength is analyzed in accordance with the following procedure.

1. Determine the maximum shear force, bending moment, and deflection. The beam under study corresponds to Case 2 in Table 8.1, from which it follows that

$$\begin{aligned}
V_m &= V(x=0) = -\frac{1}{2}qbl\\
M_m &= M\left(x=\frac{l}{2}\right) = -\frac{1}{8}qbl^2\\
W_m &= w\left(x=\frac{l}{2}\right) = -\frac{5qbl^4}{384D}(1+\alpha), \quad \alpha = \frac{48D}{5Sl^2}
\end{aligned} \tag{8.49}$$

2. Determine the stiffness coefficients. First, calculate the I-coefficients specified by Eqs. (8.35), i.e.,

$$I_0 = \sum_{i=1}^{4} E_i b_i h_i = 5.25\cdot 10^4\ \text{GPa}\cdot\text{mm}^2$$

$$I_1 = \frac{1}{2}\sum_{i=1}^{4} E_i b_i h_i (t_{i-1} + t_i) = 1.95\cdot 10^6\ \text{GPa}\cdot\text{mm}^3$$

$$I_2 = \frac{1}{3}\sum_{i=1}^{4} E_i b_i h_i \left(t_{i-1}^2 + t_{i-1}t_i + t_i^2\right) = 1.66\cdot 10^8\ \text{GPa}\cdot\text{mm}^4$$

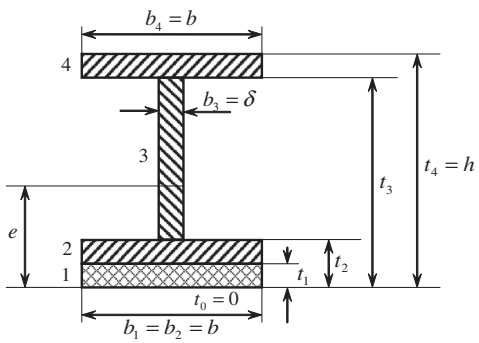


FIGURE 8.10

Coordinates of the layers.

The coordinate of the neutral axis can be found from Eq. (8.11), which yields

$$e = \frac{I_1}{I_0} = 37.14 \text{ mm}$$

The bending stiffness of the beam is calculated according to Eqs. (8.13) as

$$D = I_2 - \frac{I_1^2}{I_0} = 0.936 \cdot 10^8 \text{ GPa} \cdot \text{mm}^4$$

For a beam without the composite layer $D = 0.573 \cdot 10^8$ GPa·mm^4, i.e., the composite layer increases the beam bending stiffness by 63%.
The transverse shear stiffness of the beam is specified by Eqs. (8.35), which give

$$S = \frac{h^2}{\sum_{i=1}^{4} \frac{h_i}{G_i b_i}} = 7.68 \cdot 10^3 \text{ GPa} \cdot \text{mm}^2$$

3. Calculate the axial stress using Eqs. (8.36) and (8.49), according to which

$$\sigma_x^{(i)} = E_i \frac{M_m}{D}(t - e) = -E_i \frac{qbl^2 h}{8D}(\bar{t} - \bar{e})$$

where $\bar{t} = t/h$, $\bar{e} = e/h$ and $t_{i-1} \le t \le t_i$. For the beam with dimensions as per Eqs. (8.47) and (8.48), the maximum tensile stress in the composite layer corresponds to $t = 0$ and is equal to $\sigma_x^{(1)} = 542q$. The maximum tensile stress in the metal part is $\sigma_x^{(2)}(t = t_1) = 253q$. The maximum compressive stress in the metal part is $\sigma_x^{(4)}(t = h) = -514q$.

4. Calculate the shear stress. The most dangerous type is the shear stress which acts between composite layer 1 and metal layer 2 and can cause delamination. This stress is specified by Eq. (8.37), which yields

$$\tau_{xz}^{(1,2)} = -\frac{V_m}{2Db} E_1 b_1 h_1 (t_1 - 2e) = \frac{ql}{4D} E_1 b h_1 (h_1 - 2e)$$

For the beam under study, $\tau_{xz}^{(1,2)} = -4.2q$.

5. Calculate the maximum deflection. The deflection is specified by the third equation of Eqs. (8.49) in which $\alpha = 0.075$. Thus, the allowance for transverse shear deformation increases the maximum deflection by 7.5%.

8.4 NONLINEAR BENDING

To demonstrate the concept of nonlinear bending, consider Fig. 8.11. A conventional simply supported beam is shown in Fig. 8.11a. As can be seen, the beam deflection (dashed line) causes the displacements of the beam supports towards each other. The deflection is small and the curve slope is also so small that it can be neglected. In this case, the beam equations can be written for the initial rectilinear shape of the beam resulting in Eqs. (8.33) and (8.34). For the beam in Fig. 8.11b, in contrast to the beam in Fig. 8.11a, the ends do not move under bending. The

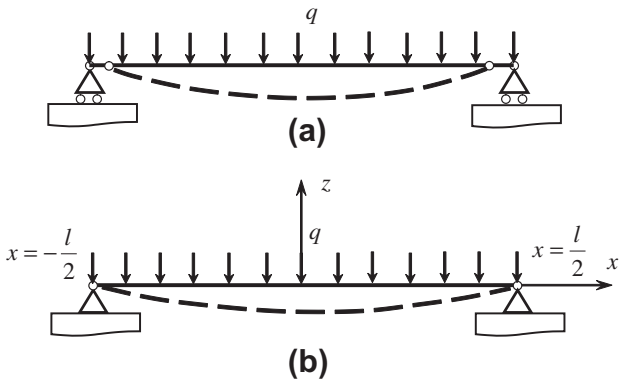


FIGURE 8.11

Bending (a) and bending-stretching (b) of the beam.

deflection of this beam is also small (it is even smaller than the deflection of the beam shown in Fig. 8.11a), however, the obvious difference between the length of the dashed curve and the initial length of the beam allows us to conclude that the beam axis experiences tension under bending. The slope of the beam axis shown in Fig. 8.11b is small, so that the first equation of Eqs. (8.33) is still valid and shows that the internal axial force N which appears as a result of the beam bending does not depend on the axial coordinate, so that $N = N_0 = constant$. To determine this force, consider a curved element of the beam axis shown in Fig. 8.12 from which it follows that

$$ds = \sqrt{dx^2 + dw^2} = \sqrt{1 + (w')^2}dx \cong \left[1 + \frac{1}{2}(w')^2\right]dx$$

The last part of this equation can be obtained if we take into account that $w' = dw/dx$ is much smaller than unity. So, the elongation of the beam axis due to bending is

$$\varepsilon = \frac{ds - dx}{dx} = \frac{1}{2}(w')^2$$

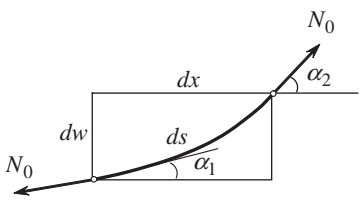


FIGURE 8.12

A curved element of the beam axis.

This elongation should be added to u' in Eqs. (8.33), and the final expression for the axial force becomes

$$N_0 = B\left[u' + \frac{1}{2}(w')^2\right] \tag{8.50}$$

Solving this equation for u' and integrating the resulting equation with respect to x from $x = -l/2$ (see Fig. 8.11b), the following expression for $u(x)$ is derived:

$$u = \frac{1}{B}N_0 x - \frac{1}{2}\int_{-l/2}^{x}(w')^2 dx + c$$

where c is the constant of integration. Since $u(x = -l/2) = 0$ (see Fig. 8.11b), $c = 0$. However, $u(x = l/2)$ is also zero, and we arrive at the following equation for N_0:

$$N_0 = \frac{B}{2}\int_{-l/2}^{l/2}(w')^2 dx \tag{8.51}$$

As can be seen, the dependence of N_0 on w is not linear. The axial force N_0 also affects the equilibrium equation, particularly the second equation of Eqs. (8.34) presenting the projection of the forces on the axis normal to the beam axis. The effect of N_0 can be simulated if we introduce some imaginary pressure shown in Fig. 8.13. Static equivalence of the forces in Figs. 8.12 and 8.13 gives

$$P_n dx = -N_0\alpha_1 + N_0\alpha_2$$

Here, α_1 and α_2 are small angles, such that $\alpha_1 \approx w'$ and $\alpha_2 \approx w' + w''dx$. Then, $P_n = N_0 w''$, and the second equation of Eqs. (8.34) can be generalized as

$$V' + N_0 w'' + \overline{p} = 0 \tag{8.52}$$

where $\overline{p}$ is the acting transverse load. The rest of Eqs. (8.34) remain the same, i.e.,

$$M' = V, \quad M = D\theta', \quad V = S(\theta + w') \tag{8.53}$$

Reduce the set of equations, Eqs. (8.52) and (8.53), to one equation for the beam deflection. For this purpose, first, substitute V from the first equation of Eqs. (8.53) into Eq. (8.52) to get

$$M'' + N_0 w'' + \overline{p} = 0 \tag{8.54}$$

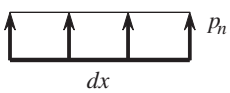


FIGURE 8.13

Imaginary pressure simulating the action of forces N_0.

Second, eliminate θ from the last two equations of Eqs. (8.53), i.e.,

$$M = D\left(\frac{V'}{S} - w''\right)$$

Third, substitute V' in this equation with its expression from Eq. (8.52) and determine

$$M = -D(1+\lambda)w'' - \frac{D}{S}\overline{p} \tag{8.55}$$

where $\lambda = N_0/S$. Substituting Eq. (8.55) into Eq. (8.54), we finally arrive at

$$w^{IV} - k^2 w'' = \frac{1}{D(1+\lambda)}\left(\overline{p} - \frac{D}{S}\overline{p}''\right), \quad k^2 = \frac{N_0}{D(1+\lambda)} \tag{8.56}$$

Consider the solution of this equation for the beam shown in Fig. 8.11b for which, as earlier, $\overline{p} = -qb_k = -Q$ (see Fig. 8.1). The solution of Eq. (8.56) is symmetric with respect to $x = 0$ and has the following form:

$$w = C_1 + C_2 \cosh kx + \frac{Q}{2N_0}x^2$$

The bending moment is specified by Eq. (8.55), which yields

$$M = -D\left[k^2 C_1(1+\lambda)\cosh kx + \frac{Q}{N_0}\right]$$

The constants of integration C_1 and C_2 can be found from the boundary conditions $w(x = \pm l/2) = 0$ and $M(x = \pm l/2) = 0$. The resulting solution is

$$w = \frac{Q}{N_0}\left[\frac{D}{N_0}\left(1 - \frac{\cosh kx}{\cosh \eta}\right) + \frac{x^2}{2} - \frac{l^2}{8}\right], \quad M = \frac{QD}{N_0}\left(\frac{\cosh kx}{\cosh \eta} - 1\right) \tag{8.57}$$

in which $\eta = kl/2$. To find N_0, apply Eq. (8.51). Substitution of the first equation of Eqs. (8.57) into Eq. (8.51) gives the following transcendental equation:

$$\frac{N_0 l}{2B} - \frac{Q^2}{2N_0^2}\left[\frac{l^3}{24} - \frac{2D}{N_0 \cosh \eta}\left(\frac{l}{2}\cosh \eta - \frac{1}{k}\sinh \eta\right) + \frac{D^2 k^2}{2N_0^2(\cosh \eta)^2}\left(\frac{1}{k}\sinh \eta \cosh \eta - \frac{l}{2}\right)\right] = 0 \tag{8.58}$$

Recall that in accordance with the foregoing derivation

$$\eta = \frac{l}{2}\sqrt{\frac{N_0}{D\left(1 + \frac{N_0}{S}\right)}}$$

To simplify the solution, neglect the shear deformation taking $S \to \infty$. Then, Eq. (8.58) can be transformed into the following dimensionless form:

$$\frac{\overline{q}^2}{\overline{N}^3}\left[\frac{1}{24} - \frac{1}{\overline{N}}\left(1 - \frac{1}{\eta}\tanh\eta\right) + \frac{1}{4\overline{N}(\cosh\eta)^2}\left(\frac{1}{\eta}\sinh\eta\cosh\eta - 1\right)\right] = 1$$

in which

$$\overline{q} = \frac{Ql^4}{D}\sqrt{\frac{B}{D}}, \quad \overline{N} = \frac{N_0 l^2}{D}, \quad \eta = \frac{1}{2}\sqrt{\overline{N}}$$

The function $\overline{N}(\overline{q})$ is presented in graphical form by Reismann (1988).

For the beam shown in Fig. 8.11b and having a square $(b = h)$ uniform cross section, the dependencies of the normalized maximum deflection $w_m = w(x = 0)$ on the loading parameter $\overline{q}$ are shown in Fig. 8.14. As can be seen, for relatively low loads $(\overline{q} \le 60)$ the nonlinear solution (curve 2) practically coincides with the linear one. The normalized maximum stress

$$\overline{\sigma}_m = \frac{\sigma_m l^2}{Eh^2}, \quad \sigma_m = E\left(\frac{N_0}{B} \pm \frac{M_m}{D}\frac{h}{2}\right)$$

is presented in Fig. 8.15. As can be seen, the loading parameter $\overline{q}$, for which the linear solution is valid, is much smaller for the maximum compressive stress than for the maximum tensile stress. It should be taken into account that the ultimate value of the loading parameter is limited by material strength. For example, for the aluminum beam with l/h =10, the material yields at $\overline{q} = 10$ for which the linear solution is valid. However, for composite beams, the situation can be different. For example, for a unidirectional glass-epoxy composite that has relatively low modulus and high strength (see Table 3.5), the ultimate value of $\overline{q}$ can reach 250, which is far beyond the limit for the linear solution.

In conclusion, consider another nonlinear problem. Suppose that the laminated beam in Fig. 8.16 is loaded with two tensile forces P applied at the beam ends $\chi = \pm l/2$. If the forces are applied to the beam

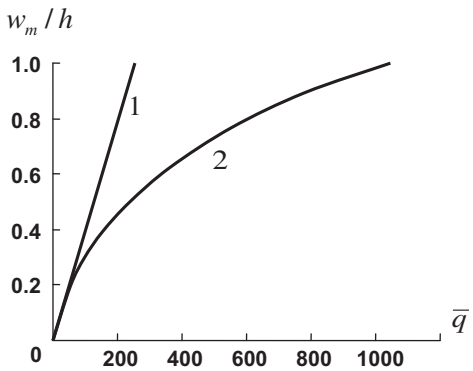


FIGURE 8.14

Dependencies of the normalized maximum deflection on the loading parameter corresponding to the linear (1) and nonlinear (2) solutions.

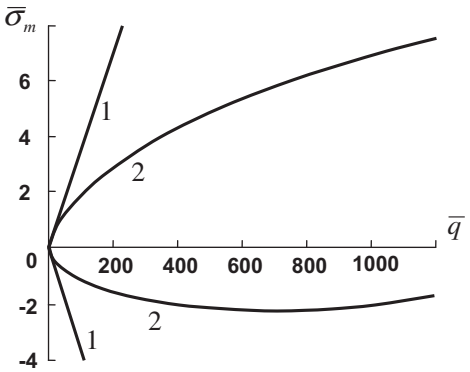


FIGURE 8.15

Dependencies of the normalized maximum stress on the loading parameter corresponding to the linear (1) and nonlinear (2) solutions.

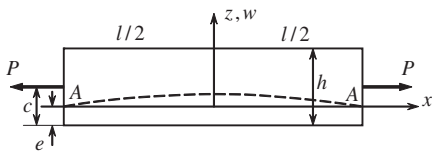


FIGURE 8.16

Eccentric tension of a laminated beam.

neutral axis, i.e., at points A with coordinate e, then no bending is observed. A natural question arises as to what happens if the forces are applied at some points with coordinate c which is not equal to e.

The problem of a beam subjected to eccentric tension (for a homogeneous rectangular beam $e = h/2$ and a force which does not induce any beam bending passes through the center of the cross section) can be studied using Eqs. (8.56) in which $\overline{p} = 0$ and $N_0 = P$, i.e.

$$w^{IV} - k^2 w'' = 0, \quad k^2 = \frac{P}{D(1+\lambda)}, \quad \lambda = \frac{P}{S} \tag{8.59}$$

The solution of this equation which satisfies the boundary conditions $w(x = \pm l/2) = 0$ is

$$w = -C(\cosh \eta - \cosh kx) \tag{8.60}$$

where $\eta = kl/2$. The rotation angle and the bending moment can be found with the aid of Eqs. (8.53) and (8.55), i.e.,

$$\theta = -kC(1+\lambda)\sinh kx, \quad M = -Dk^2 C(1+\lambda)\cosh kx \tag{8.61}$$

Assume that the beam in Fig. 8.16 is clamped, so that $\theta(x = \pm l/2) = 0$. Then, the first equation of Eqs. (6.61) yields $C = 0$ and $w = 0$. Thus, bending of a clamped beam does not occur irrespective of

the location of the force. Now assume that the beam ends are hinged and can rotate around points A (see Fig. 8.16) under a bending moment $M_0 = P(c - e)$. Taking $M(x = \pm l/2) = M_0$ in the second equation of Eqs. (8.61), we can present Eq. (8.60) as

$$w = (C - e)\left(1 - \frac{\cosh kx}{\cosh \eta}\right) \tag{8.62}$$

As an example, consider a two-layer beam composed of unidirectional glass-epoxy and carbon-epoxy layers with the following parameters: $h_1 = 1$ mm, $E_1 = 60$ GPa, $h_2 = 1$ mm, and $E_2 = 140$ GPa. The beam length and width are $l = 250$ mm and $b = 25$ mm. Calculate the I-coefficients in Eqs. (8.35), i.e.,

$$I_0 = 5 \cdot 10^3 \text{ GPa} \cdot \text{mm}^2, \quad I_1 = 6 \cdot 10^3 \text{ GPa} \cdot \text{mm}^3, \quad I_2 = 8.67 \cdot 10^3 \text{ GPa} \cdot \text{mm}^4$$

Then, the beam stiffness, Eq. (8.12), and the coordinate of the neutral axis, Eq. (8.11), become

$$B = 5 \cdot 10^3 \text{ GPa} \cdot \text{mm}^2, \quad D = 4.5 \cdot 10^3 \text{ GPa} \cdot \text{mm}^4, \quad e = 1.6 \text{ mm}$$

The axial strain of the beam under tension is specified by Eq. (8.12), i.e.,

$$\varepsilon = u' = \frac{P}{B} \tag{8.63}$$

The maximum strains of the carbon-epoxy and glass-epoxy composites are (see Table 3.5) $\varepsilon_c = 1.43\%$ and $\varepsilon_g = 3\%$. To find the ultimate force $\overline{P}$, we should substitute $\varepsilon = \varepsilon_c$ into Eq. (8.62) to get $\overline{P} = 71.5$ kN. Introduce the ratio $\alpha = P/\overline{P}$ and dimensionless coordinate $\overline{x} = x/l$ (see Fig. 8.16). Then, $\eta = 15.71\sqrt{\alpha}$ and in accordance with Eq. (8.62)

$$\overline{w} = \frac{w}{h} = (\overline{c} - \overline{e})\left(1 - \frac{\cosh 31.42\sqrt{\alpha}x}{\cosh 15.71}\right)$$

Let the force P be applied at the layers' interface, so that $c = h_1$, $\overline{c} = 0.5$, and $\overline{e} = e/h = 0.8$. Functions $\overline{w}(\overline{x})$ are presented in Fig. 8.17 for various values of the loading parameter. As can be seen, under a force equal to the ultimate value $(\alpha = 1)$, bending is concentrated in the vicinity of the beam ends.

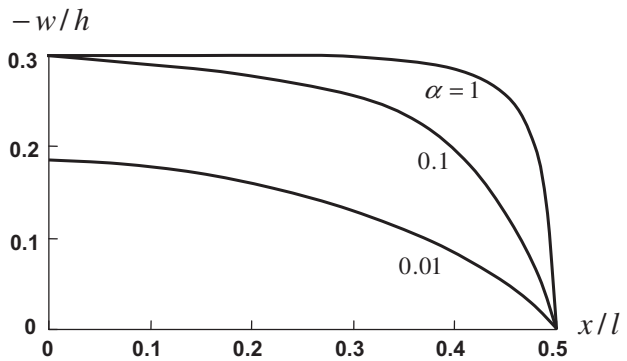


FIGURE 8.17

Deflection of the beam under eccentric tension.

8.5 BUCKLING OF COMPOSITE COLUMNS

Consider a column compressed by an axial force T as shown in Fig. 8.18. For a particular value of the force T, which is called the critical value, the initial rectilinear shape becomes unstable, and the column axis becomes curved as shown in Fig. 8.18 with dashed lines. According to the static buckling criterion, the critical force T_c is the minimum force under which two equilibrium states of the column are possible, i.e., the initial rectilinear shape and the slightly curved shape. To apply this criterion, we need to induce some deflection (see the dashed lines in Fig. 8.18) and to determine whether this deflection can be supported by the acting force T. Note that this small deflection is artificially induced because the column is analyzed assuming that it is "perfect" (it is perfectly straight, no transverse forces acting, etc.). In real structures, the tendency to bending always exists. For example, small eccentricity of the load application (see Fig. 8.16) causes bending from the very beginning of the loading process (see Fig. 8.17).

The equilibrium of a compressed column with some small deflection w can be described by Eq. (8.59) in which $P = -T$, i.e.,

$$w^{IV} + k^2 w'' = 0, \quad k^2 = \frac{T}{D(1-\lambda)}, \quad \lambda = \frac{T}{S} \tag{8.64}$$

Note that this equation has a trivial solution $w = 0$ which corresponds to the initial rectilinear shape of the column. We need to find out whether the critical force T_c exists, for which Eq. (8.69) has a nonzero solution. The general solution of Eq. (8.64) is

$$w = C_1 x + C_2 + C_3 \sin kx + C_4 \cos kx \tag{8.65}$$

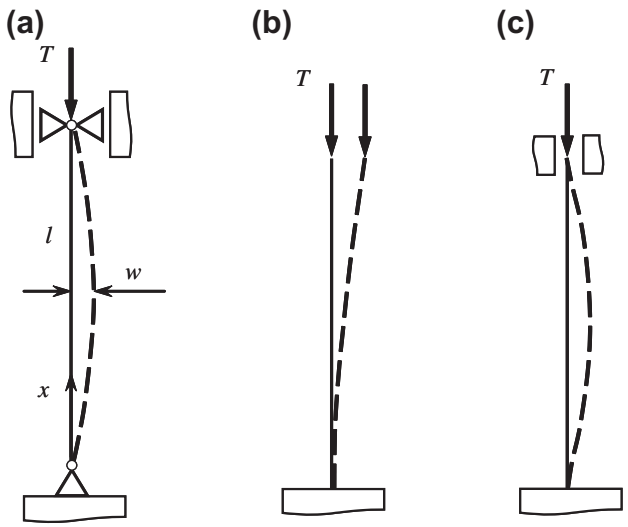


FIGURE 8.18

Axial compression and buckling modes of a column with simply-supported ends (a), with clamped end and free end (b), and with clamped ends (c).

Applying Eqs. (8.53) and (8.55), we can also find

$$\begin{aligned} \theta &= -k(1-\lambda)(C_3 \cos kx - C_4 \sin kx) - C_1 \\ M &= Dk^2(1-\lambda)(C_3 \sin kx + C_4 \cos kx) \\ V &= Dk^3(1-\lambda)(C_3 \cos kx - C_4 \sin kx) \end{aligned} \tag{8.66}$$

Consider the simply-supported column shown in Fig. 8.18a for which

$$w(x=0) = w(x=l) = 0, \quad M(x=0) = M(x=l) = 0 \tag{8.67}$$

For these boundary conditions, Eqs. (8.65) and (8.68) give the following algebraic equations written in terms of the constants of integration $C_i (i = 1, \ldots, 4)$:

$$\begin{aligned} C_2 + C_4 = 0, \quad & C_1 l + C_2 + C_3 \sin kl + C_4 \cos kl = 0 \\ C_4 = 0, \quad & C_3 \sin kl + C_4 \cos kl = 0 \end{aligned}$$

The last two equations yield

$$C_3 \sin kl = 0$$

Obviously, if $C_3 = 0$, then all the constants are zero and $w = 0$, which corresponds to the initial shape of the column. So, $C_3 \neq 0$ and

$$\sin kl = 0 \tag{8.68}$$

As can be readily seen, C_3 is the only nonzero constant and Eq. (8.65) reduces to

$$w = C_3 \sin kx \tag{8.69}$$

Note that within the approach under discussion the constant C_3 cannot be determined. Recall that Eq. (8.64) is valid for small deflections only. So, for the unknown C_3, we can formally assume that it is small enough so that the deflection, Eq. (8.69), is also small. The nonzero deflection given by Eq. (8.69) exists if the parameter k satisfies Eq. (8.68) from which $kl = n\pi (n = 1, 2, 3, \ldots)$. Using the corresponding Eq. (8.64) for k, we get the values of forces

$$T_n = \frac{\pi^2 n^2 D}{l^2 \left(1 + \dfrac{\pi^2 n^2 D}{Sl^2}\right)} \quad (n = 1, 2, 3, \ldots) \tag{8.70}$$

for which the nonzero deflection of the column can take place. Only one of these values, i.e., the smallest one, has a physical meaning and represents the critical force. If we neglect the shear deformation taking $S \to \infty$, the result is evident: the minimum value of T_n takes place when $n = 1$, i.e.,

$$T_E = \frac{\pi^2 D}{l^2} \tag{8.71}$$

This is a well known Euler formula for the critical load. In the general case, the situation looks more complicated. However, it can be proved that $n = 1$ for Eq. (8.70) as well. Indeed, using Eq. (8.71), the equation, Eq. (8.70), can be transformed as follows

$$T_n = \frac{n^2 T_E}{1 + n^2 \dfrac{T_E}{S}}$$

Consider the inequality $T_n > T_1$ for $n > 1$. This inequality reduces to $n > 1$ which is true. So, in the general case, $n = 1$ and the critical force is determined by

$$T_c = \frac{T_E}{1 + \dfrac{T_E}{S}} \tag{8.72}$$

For $n = 1$, Eq. (8.69) specifies the mode of buckling

$$w = C_3 \sin \frac{\pi x}{l}$$

shown in Fig. 8.18a with the dashed line.

In conclusion, consider the case $\lambda = 1$, or $T = S$, which is sometimes associated with the so-called shear mode of buckling. In this case, Eq. (8.64) reduces to $w'' = 0$ whose solution is $w = C_1 x + C_2$. Applying the boundary conditions in Eq. (8.67), we get $C_1 = C_2 = 0$ and $w = 0$. Thus, the case $\lambda = 1$ corresponds to the straight column and $T = S$ is not a critical load. Anyway, the force $T = S$ is always higher than T_c given by Eq. (8.72). Indeed, the inequality $T = S > T_c$ is equivalent to the inequality $S > 0$.

The result obtained for the critical force, i.e., Eq. (8.72), can be used for the columns with various boundary conditions substituting the corresponding expression for T_E instead of that given by Eq. (8.71). Particularly for the cantilever (see Fig. 8.18b) and clamped (see Fig. 8.18c) columns, we have, respectively,

$$T_E = \frac{\pi^2 D}{4l^2}, \quad T_E = \frac{4\pi^2 D}{l^2}$$

It should be noted that a buckling analysis must be accompanied by a study of stresses because composite beams can fail before buckling if the stresses in the layers reach the material ultimate compressive stresses. The stresses in the layers are specified by Eq. (8.36) in which $N = -T$ and $M = 0$, i.e.,

$$\sigma_x^{(i)} = -E_i \frac{T}{B}$$

Buckling can take place if these stresses calculated for $T = T_c$ are less than material strength.

8.6 FREE VIBRATIONS OF COMPOSITE BEAMS

Composite beams are good models allowing us to discuss some specific features of the dynamic behavior of laminated composite structures. The equations of motion of the beam element shown in Fig. 8.2 can be written adding the inertia terms to the equilibrium equations, Eqs. (8.1), i.e.,

$$b\frac{\partial \sigma_x}{\partial x} + \frac{\partial}{\partial z}(b\tau_{xz}) - \rho b \frac{\partial^2 u_x}{\partial t^2} = 0$$

$$b\frac{\partial \tau_{xz}}{\partial x} + \frac{\partial}{\partial z}(b\sigma_z) - \rho b \frac{\partial^2 u_z}{\partial t^2} = 0$$

in which t is the time and ρ is the material density. Applying assumptions introduced in Section 8.1, i.e., using Eqs. (8.3) for the displacements and Eqs. (8.5) and (8.15) for forces and moment, we can

arrive at the following equations for composite beams (these equations are generalizations of the equilibrium equations, Eqs. (8.22), (8.26), and (8.31))

$$\begin{aligned}
&\frac{\partial N}{\partial x} - B_\rho \frac{\partial^2 u}{\partial t^2} - C_\rho \frac{\partial^2 \theta}{\partial t^2} = 0 \\
&\frac{\partial M}{\partial x} - V - C_\rho \frac{\partial^2 u}{\partial t^2} - D_\rho \frac{\partial^2 \theta}{\partial t^2} = 0 \\
&\frac{\partial V}{\partial x} - B_\rho \frac{\partial^2 w}{\partial t^2} - \overline{p}(x,t) = 0
\end{aligned} \tag{8.73}$$

where

$$\begin{aligned}
&B_\rho = J_0, \quad C_\rho = J_0\left(e_\rho - e\right), \quad D_\rho = J_2 - 2eJ_1 + e^2 J_0 \\
&J_n = \int_0^h b\rho t^n dt \quad (n = 0, 1, 2)
\end{aligned} \tag{8.74}$$

are the inertia coefficients which are analogous to the stiffness coefficients in Eqs. (8.9). For laminated beams,

$$J_n = \frac{1}{n+1} \sum_{i=1}^{k} b_i \rho_i \left(t_i^{n+1} - t_{i-1}^{n+1}\right) \tag{8.75}$$

(see Fig. 8.5). The parameter e_ρ in Eqs. (8.74)

$$e_\rho = \frac{J_1}{J_0} \tag{8.76}$$

is similar to the coordinate of the neutral axis e defined by Eq. (8.11). In the general case, e_ρ does not coincide with e because the integrals I_n (see Eqs. (8.10)) depend on the stiffness distribution, whereas J_n determined by Eq. (8.75) are governed by the density distribution through the height of the beam cross section. For homogeneous beams ($E = constant$ and $\rho = constant$) we have

$$e_\rho = e = \frac{\int_0^h btdt}{\int_0^h bdt}, \quad C = 0$$

For beams with symmetric laminated structure,

$$e_\rho = e = \frac{h}{2}, \quad C = 0 \tag{8.77}$$

The forces and moments entering Eqs. (8.73) are linked with the corresponding deformations by the constitutive equations, Eq. (8.12), (8.16), and (8.17), i.e.,

$$N = Bu', \quad M = D\theta', \quad V = S(\theta + w') \tag{8.78}$$

Substituting Eqs. (8.78) into Eqs. (8.73), we can derive the motion equations in terms of displacements. Taking $\overline{p} = 0$ for the case of free vibrations, we get

$$B\frac{\partial^2 u}{\partial x^2} - B_\rho \frac{\partial^2 u}{\partial t^2} - C_\rho \frac{\partial^2 \theta}{\partial t^2} = 0 \tag{8.79}$$

$$D\frac{\partial^2 \theta}{\partial x^2} - S\left(\theta + \frac{\partial w}{\partial x}\right) - C_\rho \frac{\partial^2 u}{\partial t^2} - D_\rho \frac{\partial^2 \theta}{\partial t^2} = 0 \tag{8.80}$$

$$S\left(\frac{\partial \theta}{\partial x} + \frac{\partial^2 w}{\partial x^2}\right) - B_\rho \frac{\partial^2 w}{\partial t^2} = 0 \tag{8.81}$$

In the general case, $e_\rho \neq e$ and $C_\rho \neq 0$, so that Eq. (8.79) which describes the axial vibrations includes the rotation angle θ and is coupled through this term with Eqs. (8.80) and (8.81) which describe the flexural vibrations of the beam.

Specific features of longitudinal vibrations are discussed in Section 7.3.4. Consider here the flexural vibrations. For this purpose, assume that the beam has a symmetric structure, so that Eqs. (8.77) hold. Then, Eqs. (8.80) and (8.81) can be transformed to the following equation written in terms of the beam deflection

$$D\frac{\partial^4 w}{\partial x^4} - \left(D_\rho + \frac{B_\rho D}{S}\right)\frac{\partial^4 w}{\partial x^2 \partial t^2} + \frac{B_\rho D_\rho}{S}\frac{\partial^4 w}{\partial t^4} + B_\rho \frac{\partial^2 w}{\partial t^2} = 0 \tag{8.82}$$

In this equation, the terms including S allow us to take into account the shear deformation, whereas the terms with coefficient D_ρ allow for the rotation inertia of the beam cross section. Following Uflyand (1948), Eq. (8.82) can be presented in the form

$$\frac{\partial^4 w}{\partial x^4} - \left(\frac{1}{C_1^2} + \frac{1}{C_2^2}\right)\frac{\partial^4 w}{\partial x^2 \partial t^2} + \frac{1}{C_1^2 C_2^2}\frac{\partial^4 w}{\partial t^4} + C^2 \frac{\partial^2 w}{\partial t^2} = 0$$

or

$$\left(\frac{\partial^2}{\partial x^2} - \frac{1}{C_1^2}\frac{\partial^2}{\partial t^2}\right)\left(\frac{\partial^2 w}{\partial x^2} - \frac{1}{C_2^2}\frac{\partial^2 w}{\partial t^2}\right) + C^2 \frac{\partial^2 w}{\partial t^2} = 0$$

where

$$C_1 = \sqrt{\frac{D}{D_\rho}}, \quad C_2 = \sqrt{\frac{S}{B_\rho}}, \quad C = \sqrt{\frac{B_\rho}{B}}$$

To clarify the physical meaning of the coefficients C_1 and C_2, consider a beam with a rectangular cross section (see Fig. 8.19) for which

$$D = \frac{1}{12}Ebh^3, \quad S = Gbh, \quad B_\rho = bh\rho, \quad D_\rho = \frac{1}{12}\rho bh^3 \tag{8.83}$$

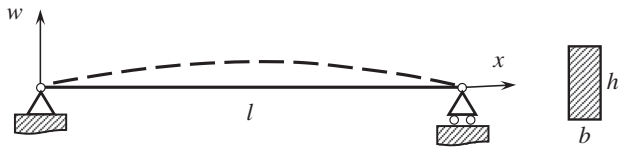


FIGURE 8.19

Free vibrations of a simply supported beam.

Then,

$$C_1 = \sqrt{\frac{E}{\rho}}, \quad C_2 = \sqrt{\frac{G}{\rho}}$$

are the velocities of normal stress (C_1) and shear stress (C_2) wave propagation along the beam axis. Neglecting rotatory inertia ($D_\rho = 0$) or shear deformation ($S \to \infty$) in Eq. (8.82), we actually assume that C_1 or C_2 becomes infinitely high.

For qualitative analysis, consider flexural vibrations of a simply supported beam shown in Fig. 8.19 and present the beam deflection as

$$w(x,t) = W_m \sin\frac{\pi m x}{l} \sin\omega_m t \tag{8.84}$$

where m is the number of the vibration mode (the mode corresponding to $m = 1$ is shown in Fig. 8.19 with a dashed line), W_m is the amplitude, and ω_m is the frequency of the m-th vibration mode. Recall that the number of the beam vibrations per 1 second (Hz) can be found as

$$\upsilon_m = \frac{\omega_m}{2\pi}$$

Substituting the deflection, Eq. (8.84), into Eq. (8.82) results in the following equation for the frequency:

$$\frac{B_\rho D_\rho}{S}\omega_m^4 - \left[B_\rho + \left(\frac{\pi m}{l}\right)^2\left(D_\rho + \frac{DB_\rho}{S}\right)\right]\omega_m^2 + D\left(\frac{\pi m}{l}\right)^2 = 0 \tag{8.85}$$

Neglecting both transverse deformation $S \to \infty$ and rotatory inertia ($D_\rho = 0$), we arrive at a result corresponding to classical beam theory, i.e.,

$$\omega_m^0 = \frac{\pi m}{l}\sqrt{\frac{D}{B_\rho}} \tag{8.86}$$

If we neglect the rotatory inertia ($D_\rho = 0$) and take into account the shear deformation, Eq. (8.85) yields

$$\omega_m = \frac{\omega_m^0}{\sqrt{1+\alpha_S}}$$

where ω_m^0 is specified by Eq. (8.86) and

$$\alpha_S = \frac{\pi^2 m^2 D}{l^2 S}$$

For a homogeneous beam with a rectangular cross section, using Eqs. (8.83), we get

$$\alpha_S = \frac{\pi^2 m^2 E h^2}{12 G l^2}$$

Thus, the shear correction factor reduces the frequency and is a function of the ratios E/G and h/l and the mode number m.

Consider now the effect of rotatory inertia. Taking $S \to \infty$ in Eq. (8.85), we have

$$\omega_m = \frac{\omega_m^0}{\sqrt{1 + \alpha_r}}$$

where

$$\alpha_r = \frac{\pi^2 m^2 D_\rho}{l^2 B_\rho}$$

Again, for a homogeneous beam with a rectangular cross section

$$\alpha_r = \frac{\pi^2 m^2 h^2}{12 l^2}$$

(see Fig. 8.19). As can be seen, the effect depends on the beam relative height and mode number.

Consider coupled longitudinal-transverse vibrations of the beams for which $C_\rho \neq 0$ described by Eqs. (8.79)–(8.81). Taking, for the sake of brevity, $D_\rho = 0$ and $S \to \infty$, we can transform these equations into the following form

$$BD\frac{\partial^6 w}{\partial x^6} - B_\rho D\frac{\partial^6 w}{\partial x^4 \partial t^2} - C_\rho^2 \frac{\partial^6 w}{\partial x^2 \partial t^4} + BB_\rho \frac{\partial^4 w}{\partial x^2 \partial t^2} - B_\rho^2 \frac{\partial^4 w}{\partial t^4} = 0$$

Substituting the deflection from Eq. (8.84), we arrive at the following equation for the frequency:

$$\left(B\lambda_m^2 - B_\rho \omega_m^2\right)\left(D\lambda_m^4 - B_\rho \omega_m^2\right) - C_\rho^2 \lambda_m^2 \omega_m^4 = 0$$

in which $\lambda_m = \pi m/l$. Taking into account Eq. (8.74) for C_ρ, we can present this equation in the form

$$\omega_m^4 B_\rho^2 \left[1 - \lambda_m^2 \left(e_\rho - e\right)^2\right] - B_\rho \lambda_m^2 \omega_m^2 \left(D\lambda_m^2 + B\right) + BD\lambda_m^6 = 0$$

It follows from this equation that the effect of vibration coupling can be evaluated by comparing parameter

$$\alpha_c = \frac{\pi^2 m^2}{l^2}\left(e - e_\rho\right)^2$$

with unity. If $\alpha_c \ll 1$, the coupling effect can be ignored.

Finally, consider flexural vibrations of beams loaded with axial compressive force T (see Fig. 8.18). For this purpose, we need to modify Eq. (8.81), adding to it the term with the axial force as in Eq. (8.52), i.e.,

$$S\left(\frac{\partial\theta}{\partial x}+\frac{\partial^2 w}{\partial x^2}\right)-T\frac{\partial^2 w}{\partial x^2}-B_\rho\frac{\partial^2 w}{\partial t^2}=0 \tag{8.87}$$

Taking, for the sake of brevity, $D_\rho=0$ and $C_\rho=0$ in Eq. (8.80), we get the second equation

$$D\frac{\partial^2\theta}{\partial x^2}-S\left(\theta+\frac{\partial w}{\partial x}\right)=0 \tag{8.88}$$

These two equations, Eqs. (8.87) and (8.88), can be transformed as follows

$$D\left(1-\frac{T}{S}\right)\frac{\partial^4 w}{\partial x^4}-\frac{DB_\rho}{S}\frac{\partial^4 w}{\partial x^2\partial t^2}+T\frac{\partial^2 w}{\partial x^2}+B_\rho\frac{\partial^2 w}{\partial t^2}=0$$

For a simply supported beam (see Fig. 8.18a), substituting the deflection in accordance with Eq. (8.84), we finally get

$$\omega_m=\omega_m^0\sqrt{\frac{1-\dfrac{T}{\alpha_m}\left(1+\dfrac{\alpha_m}{S}\right)}{1+\dfrac{\alpha_m}{S}}} \tag{8.89}$$

where $\alpha_m=\pi^2m^2D/l^2$. As can be seen, a compressive force reduces the frequency of flexural vibrations. For the first mode ($m=1$), $\alpha_1=T_E$ where T_E is the Euler critical force specified by Eq. (8.71) and Eq. (8.89) becomes

$$\omega_1=\omega_1^0\sqrt{\frac{1-\dfrac{T}{T_E}\left(1+\dfrac{T_E}{S}\right)}{1+\dfrac{T_E}{S}}}$$

For the critical force $T=T_c$ in Eq. (8.72), $\omega_1=0$, i.e., compressive loading up to the critical load results in zero frequency of flexural vibrations. A tensile force, naturally, increases the frequency.

8.7 REFINED THEORIES OF BEAMS AND PLATES

The composite beam, being a simple but representative model, allows us to consider the so-called "higher-order" theories of beams, plates, and shells intensively discussed in the literature. Note that although the equations presented in the text following are valid only for beams, the main references are made to plates, for which such theories originally have been constructed.

Consider two typical problems of beam theory, i.e., the cantilever beam shown in Fig. 8.20 and the simply supported beam shown in Fig. 8.21. Both beams are homogeneous and have rectangular cross sections.

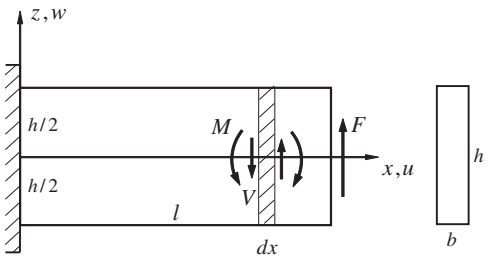


FIGURE 8.20

A cantilever beam.

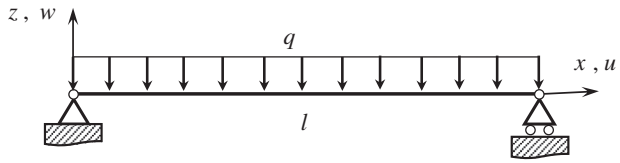


FIGURE 8.21

A simply supported beam.

The theory described in the foregoing sections is based on the approximations given by Eqs. (8.3) for the displacements which, for the case of bending, yield

$$u_x = z\theta(x), \quad u_z = w(x) \tag{8.90}$$

The corresponding static variables are the internal bending moment and the transverse shear force specified by Eqs. (8.5) and (8.15), i.e.,

$$M = \int_{-\frac{h}{2}}^{\frac{h}{2}} \sigma_x b z dz, \quad V = \int_{-\frac{h}{2}}^{\frac{h}{2}} \tau_{xz} b dz \tag{8.91}$$

This approximation reduces the theory to Eqs. (8.34), i.e.,

$$M' = V, \quad V' + \overline{p} = 0 \tag{8.92}$$

$$M = D\theta', \quad V = S\gamma, \quad \gamma = (\theta + w') \tag{8.93}$$

For a beam with a rectangular cross section

$$D = \frac{1}{12} E b h^3, \quad S = Gbh \tag{8.94}$$

(see Fig. 8.20). The normal and shear stresses are specified by Eqs. (8.12) and (8.27) which, for the stiffnesses in Eqs. (8.94), give

$$\sigma_x = \frac{12M}{bh^3}z, \quad \tau_{xz} = \frac{6V}{bh^3}\left(\frac{h^2}{4} - z^2\right) \tag{8.95}$$

For the cantilever beam (see Fig. 8.20), the solution of Eqs. (8.92) and (8.93) is

$$\begin{gathered} F = V, \quad M = -F(l-x), \quad \theta = -\frac{6F}{Ebh^3}(2l-x)x \\ w = \frac{2F}{Ebh^3}\left(3lx - x^2 + \frac{Eh^2}{2G}\right)x \end{gathered} \tag{8.96}$$

For the simply supported beam (see Fig. 8.21), the solutions are given in Table 8.1 (Case 2) and have the following form:

$$\begin{gathered} V = -\frac{1}{2}qb(l-2x), \quad M = -\frac{1}{2}qb(l-x)x \\ \theta = \frac{q}{2Eh^3}\left(l^3 - 6lx^2 + 4x^3\right), \quad w = -\frac{q}{2Eh^3}\left[l^3 - 2lx^2 + x^3 + \frac{Eh^2}{G}(1-x)\right]x \end{gathered} \tag{8.97}$$

Consider the "higher-order" beam and plate theories that are widely discussed in the literature and are based on the displacement approximations which generalize Eqs. (8.90) as

$$u_x = zu_1(x) + z^2u_2(x) + z^3u_3(x) + \cdots + z^ku_k(x) \tag{8.98}$$

$$u_z = w(x) \tag{8.99}$$

In accordance with Eq. (8.98), the theory based on Eqs. (8.90) is referred to as the "first-order" shear deformation theory (Reddy and Wang, 2000). The main shortcoming of this theory is usually associated with the shear stress distribution following from Eqs. (8.90). Indeed, the exact constitutive equation for the shear stress is

$$\tau_{xz} = G\gamma_{xz} = G\left(\frac{\partial u_x}{\partial z} + \frac{\partial u_z}{\partial x}\right) \tag{8.100}$$

Substituting Eqs. (8.90), we get

$$\tau_{xz} = G(\theta + w') \tag{8.101}$$

which does not depend on z. Thus, the stress τ_{xz} in Eq. (8.101) does not satisfy the boundary conditions (see Fig. 8.20), according to which

$$\tau_{xz}\left(z = \pm\frac{h}{2}\right) = 0 \tag{8.102}$$

However, as discussed in Section 5.1, Eq. (8.101) is not correct. Displacements in Eqs. (8.90) approximate the distribution of the actual displacements through the beam height. It is known that

approximate functions must not be differentiated, as has been done to derive Eq. (8.101). The second equation in Eqs. (8.90) states that u_z does not depend on z, which means that the beam element shaded in Fig. 8.20 is absolutely rigid in the z direction. As is known, the distribution of forces over the surface of an absolutely rigid body does not affect the body motion. Only the forces resultant, i.e., the transverse shear force V for the beam, affects the beam deflection. Integration in the second equation of Eqs. (8.91) allows us to avoid differentiation of u_x in Eq. (8.100) with respect to z. Indeed, using Eqs. (8.90), (8.91), and (8.100), we get in several steps

$$V = \int_{\frac{-h}{2}}^{\frac{h}{2}} \tau_{xz} b dz = bG \int_{\frac{-h}{2}}^{\frac{h}{2}} \left(\frac{\partial u_x}{\partial z} + \frac{\partial u_z}{\partial x} \right) dz$$

$$= bG \left[u_x\left(\frac{h}{2}\right) - u_x\left(-\frac{h}{2}\right) + hw' \right] = bGh(\theta + w')$$

Thus, in the theory under consideration, the constitutive equation exists for the shear force V only and does not exist for the shear stress τ_{xz}. The shear stress following from the equilibrium equation is specified by the second equation of Eqs. (8.95) and, naturally, satisfies the boundary conditions as per Eq. (8.102). The same situation occurs in classical beam theory in which Eq. (8.100) simply does not exist, so there is no temptation to use it and the shear stress is found from the equilibrium equation.

Now, return to Eqs. (8.98) and (8.99) and discuss the so-called "higher-order" theories. To derive the equations of the "third-order" theory, take $k = 3$ in Eq. (8.98), i.e.,

$$u_x = zu_1(x) + z^2 u_2(x) + z^3 u_3(x), \quad u_z = w(x) \tag{8.103}$$

Following the traditional procedure, substitute Eqs. (8.103) into Eq. (8.100) to get

$$\tau_{xz} = G\left(u_1 + w' + 2u_2 z + 3u_3 z^2\right)$$

Apply the boundary conditions in Eq. (8.102) and determine the functions u_2 and u_3. The resulting displacement field becomes

$$u_x = zu_1 - \frac{4z^3}{3h^2}(u_1 + w'), \quad u_z = w(x) \tag{8.104}$$

The displacements in Eqs. (8.104) have been originally proposed by Vlasov (1957) and Ambartsumyan (1958) and are used in numerous papers and books to construct the refined plate and shell theories (e.g., Reddy, 2004).

It seems, at first glance, that the displacements in Eqs. (8.103) are more accurate than the linear approximation given by Eqs. (8.90). However, this is not actually the case. In general, introduction of force constraints into the kinematic field is not the best way to improve it. To show this, apply the constitutive equations and find the stresses corresponding to displacements presented by

Eqs. (8.104), i.e.,

$$\sigma_x = E\varepsilon_x = E\frac{\partial u_x}{\partial x} = E\left[zu_1' - \frac{4z^3}{3h^2}(u_1' + w'')\right] \tau_{xz} = G\gamma_{xz} = G\left(\frac{\partial u_x}{\partial z} + \frac{\partial u_z}{\partial x}\right) = G(u_1 + w')\left(1 - \frac{4z^2}{h^2}\right) \tag{8.105}$$

Following Ambartsumyan (1987), introduce the bending moment and the shear force in Eqs. (8.91). Substituting the stresses in Eqs. (8.105), we get

$$M = E\frac{bh^3}{15}\left(u_1' - \frac{1}{4}w''\right), \quad V = \frac{2}{3}Gbh(u_1 + w') \tag{8.106}$$

Consider first the cantilever beam (see Fig. 8.20) for which the equilibrium equations, Eqs. (8.92) for $\overline{p} = 0$, have the solution given by Eqs. (8.96). Integration of Eqs. (8.106) yields

$$\begin{aligned} u_1 &= \frac{3F}{10Ghb} - \frac{12F}{Eh^3b}\left(lx - \frac{x^2}{2}\right) - C_1 \\ w &= \frac{6Fx}{5Ghb} + \frac{6F}{Eh^3b}\left(lx^2 - \frac{x^3}{3}\right) + C_1x + C_2 \end{aligned} \tag{8.107}$$

where C_1 and C_2 are the constants of integration which should be determined from the boundary conditions at $x = 0$ (see Fig. 8.20). According to these conditions, we should put $w(x = 0) = 0$ and, taking into account that u_1 is actually the angle of the cross section rotation, put $u_1(x = 0) = 0$. Then, Eqs. (8.107) reduce to

$$u_1 = -\frac{6F}{Eh^3b}(2l - x)x, \quad w = \frac{2F}{Eh^3b}\left(3lx - x^2 + \frac{3Eh^2}{4G}\right)x \tag{8.108}$$

Comparing this result with Eqs. (8.95), we can conclude that u_1 coincides with θ, whereas the deflection has a different coefficient in the term corresponding to the shear deformation (0.75 instead of 0.5). However, the main difference between the solutions is more significant. Indeed, for the clamped edge of the beam, Eqs. (8.96) of the "first-order" theory give $\theta = 0$ and $w = 0$, and Eqs. (8.90) for the displacements yield $u_x(x = 0) = 0$ and $u_z(x = 0) = 0$. Thus, the displacements are identically zero at the clamped edge of the beam. But for the "third-order" theory, Eqs. (8.104) and (8.108) give

$$u_x(x = 0) = -\frac{2Fz^3}{Gh^3b}, \quad u_z(x = 0) = 0$$

Thus the boundary conditions for the clamped end $(u_x = 0)$ cannot be satisfied within the framework of the "third-order" theory.

A similar conclusion can be derived for a simply supported beam, shown in Fig. 8.21. Substitution of the bending moment M and the shear force V (neither of which depends on the shear deformation) from Eqs. (8.97) into Eqs. (8.106) and integration yield the following solution:

$$u_1 = \frac{q}{2Eh^3}\left[l^3 - 6lx^2 + 4x^3 - \frac{3Eh^2}{10G}(l-2x)\right]$$
$$w = -\frac{q}{2Eh^3}\left[l^3 - 2lx^2 + x^3 - \frac{6Eh^2}{5G}(l-x)\right]x \tag{8.109}$$

in which the constants of integration are found from the boundary conditions $w(x=0) = w(x=l) = 0$ (see Fig. 8.21). Comparing this solution with the corresponding equation in Eqs. (8.97), we can conclude that the results coincide within the accuracy of the terms including the shear modulus G. The bending moment M specified by the first equation of Eqs. (8.106) and Eqs. (8.109) satisfies the boundary conditions (see Fig. 8.21), according to which $M(x=0) = M(x=l) = 0$. However, the axial stress is not zero at the beam ends. Substituting Eqs. (8.109) in the first equation of Eqs. (8.105), we arrive at

$$\sigma_x = -\frac{6q}{h^3}(l-x)xz + \frac{qE}{Gh^3}\left(\frac{3h^2}{10} - 2z^2\right)z \tag{8.110}$$

At the beam ends ($x = 0$ and $x = l$), the first term vanishes, but the second term gives nonzero stress, which cannot exist at the ends of a simply supported beam.

Usually, simply supported beams and plates are studied applying a trigonometric series, each term of which satisfies the boundary conditions $w(0) = w(l) = 0$ and $M(0) = M(l) = 0$, i.e.,

$$u_1 = \sum_m U_m \cos\lambda_m x, \quad w = \sum_m W_m \sin\lambda_m x \tag{8.111}$$

in which $\lambda_m = \pi m/l$ (see Fig. 8.21). Substituting expansions (8.111) into Eqs. (8.106), we get

$$M = E\frac{bh^3}{15}\sum_m\left(\frac{1}{4}\lambda_m W_m - U_m\right)\sin\lambda_m x$$
$$V = \frac{2}{3}Gbh\sum_m(\lambda_m W_m + U_m)\cos\lambda_m x \tag{8.112}$$

Decomposing the load $\overline{p} = -qb$ into a similar series

$$\overline{p} = -qb = -b\sum_m q_m \sin\lambda_m x \tag{8.113}$$

and substituting Eqs. (8.112) and (8.113) into the equilibrium equations, Eqs. (8.92), we arrive at the following set of algebraic equations derived in terms of W_m and U_m:

$$E\frac{h^2}{5}\lambda_m^2\left(\frac{1}{4}\lambda_m W_m - U_m\right) = 2G(\lambda_m W_m + U_m)$$
$$\frac{2}{3}Gh\lambda_m(\lambda_m W_m + U_m) = -q_m$$

Solving these equations for W_m and U_m, we have

$$W_m = -\frac{12q_m}{Eh^3\lambda_m^4}\left(1+\frac{Eh^2}{10G}\lambda_m^2\right), \quad U_m = \frac{12q_m}{Eh^3\lambda_m^3}\left(1-\frac{Eh^2}{40G}\lambda_m^2\right) \tag{8.114}$$

Substitution of Eqs. (8.111) and (8.114) into Eq. (8.105) yields the following equation for σ_x:

$$\sigma_x = -\frac{12z}{h^3}\sum_m \frac{q_m}{\lambda_m^2}\sin\lambda_m x + \frac{Ez}{Gh^3}\left(\frac{3h^2}{10}-2z^2\right)\sum_m q_m \sin\lambda_m x$$

Retaining a finite number of terms in the series of this equation, we can arrive at the conclusion that $\sigma_x(x=0)=\sigma_x(x=l)=0$. However, for an infinite number of terms, the second series converges, and in accordance with Eq. (8.113) becomes equal to the second term in Eq. (8.110), which means that σ_x is not zero at the beam ends.

Thus, the "third-order" theory does not allow one to satisfy the boundary conditions which are satisfied within the framework of the "first-order" theory. It is important that, following Ambartsumyan (1987), we used the displacements in Eqs. (8.104) in conjunction with the equilibrium equations, Eqs. (8.92), which follow from the free-body diagrams for the shaded element of the beam shown in Fig. 8.20. In more recent versions of the "third-order" theory (e.g., Reddy, 2004), the governing equations are derived with the aid of the variational principle. To discuss this approach, apply the minimum condition for the total potential energy of the beam, i.e., Eq. (2.63), according to which

$$\delta T = b\int_0^l dx \int_{-h/2}^{h/2}\left(\sigma_x\delta\varepsilon_x+\tau_{xz}\delta\gamma_{xz}\right)dz - b\int_0^l \overline{p}\delta w dx = 0 \tag{8.115}$$

Consider the "first-order" theory. Using Hooke's law and displacements as per Eqs. (8.90), we get the following equation for the axial stress:

$$\sigma_x = E\varepsilon_x = E\frac{\partial u_x}{\partial x} = E\theta' z \tag{8.116}$$

As has been noted earlier, the constitutive equation for the shear stress in the "first-order" theory exists only in the integral form. Eq. (8.99). To apply this form, we need to use Eqs. (8.91) for V and replace γ_{xz} with the average shear strain $\gamma=\theta+w'$. Taking into account Eq. (8.116) and Eqs. (8.91) for the bending moment, we can present Eq. (8.115) in the following form:

$$\int_0^l [M\delta\theta' + V(\delta\theta+\delta w') - \overline{p}\delta w]dx = 0$$

Integration by parts yields the following variational equations and natural boundary conditions

$$M' - V = 0, \quad V' + \overline{p} = 0 \tag{8.117}$$

$$[M\delta\theta]_{x=0}^{x=l} = 0, \quad [V\delta w]_{x=0}^{x=l} = 0 \tag{8.118}$$

As can be seen, Eqs. (8.117) coincide with equilibrium equations, Eqs. (8.92), whereas the boundary conditions, Eqs. (8.118) give $M = 0$ and $V = 0$ which are equivalent to $\sigma_x = 0$ and $\tau_{xz} = 0$ for the free end (see Eqs. (8.95)), and for the clamped end give $\theta = 0$ and $w = 0$ which are equivalent to $u_x = 0$ and $u_z = 0$ (see Eqs. (8.90)). Thus, the variational formulation of the "first-order" theory is equivalent to the direct formulation based on the equilibrium equations and the corresponding boundary conditions.

The situation is totally different for the "third-order" theory for which we have constitutive equations, Eqs. (8.105), for both normal and shear stresses. Substituting Eqs. (8.105) into Eq. (8.115), and integrating with respect to z, we get

$$\int_0^l \left[M\delta u_1' - H\left(\delta u_1' + \delta w''\right) + V(\delta u_1 + \delta w') - Q(\delta u_1 + \delta w') - \overline{p}\delta w\right]dx = 0$$

where M and V are specified by Eqs. (8.91) and

$$H = \frac{4b}{3h^2}\int_{-h/2}^{h/2} \sigma_x z^3 dz, \quad Q = \frac{4b}{h^2}\int_{-h/2}^{h/2} \tau_{xz} z^2 dz \tag{8.119}$$

The corresponding variational equations and the natural boundary conditions are

$$M' - H' - V + Q = 0, \quad V' - Q' + H'' + \overline{p} = 0 \tag{8.120}$$

$$[(M - H)\delta u_1]_{x=0}^{x=l} = 0, \quad [H\delta w']_{x=0}^{x=l} = 0, \quad [(V - Q)\delta w]_{x=0}^{x=l} = 0 \tag{8.121}$$

in which, in accordance with Eqs. (8.91), (8.105), and (8.119),

$$\begin{aligned} M &= \frac{Ebh^3}{60}\left(4u_1' - w''\right), \quad H = \frac{Ebh^3}{1260}\left(16u_1' - 5w''\right) \\ V &= \frac{2}{3}Gbh(u_1 + w'), \qquad Q = \frac{2}{15}Gbh(u_1 + w) \end{aligned} \tag{8.122}$$

These results look energy consistent. Indeed, Eqs. (8.120) in conjunction with Eqs. (8.122) are of the sixth-order which corresponds to three natural boundary conditions, Eqs. (8.121). For a cantilever beam shown in Fig. 8.20, at the clamped end $u_1 = 0$, $w' = 0$, and $w = 0$. Correspondingly, it follows from Eqs. (8.104) that $u_x = 0$ and $u_z = 0$ at $x = 0$. Thus, the boundary conditions at the clamped end can be satisfied. However, it follows from Eq. (8.105) that, under these conditions, $\tau_{xz}(x = 0) = 0$ and the force F acting at $x = l$ (see Fig. 8.20) is not balanced. This result is expected because the variational equations, Eqs. (8.120), do not coincide with equilibrium equations, Eqs. (8.92), and hence, the equilibrium equations of a beam element as a solid are violated. The reason for this is associated with the formulation of the displacement field. In contrast to Eqs. (8.90) of the "first-order" theory which allow for two mutually independent degrees of freedom for the shaded beam element shown in Fig. 8.20 (i.e., displacement w and rotation angle θ), in Eqs. (8.104) of the "third-order" theory the displacement and the rotation are not mutually independent, and the variational equations, Eqs. (8.120), cannot provide the equilibrium of the beam element as a solid.

Consistency conditions for the refined beam, plate, and shell theories have been proposed by Vasiliev and Lurie (1990a, b and 1992). According to these conditions, equilibrium equations following from the free-body diagram for the structure element must coincide with variational equations providing the minimum of the structure's total potential energy. Within the framework of this requirement, the "first-order" theory is consistent and the "third-order" theory is not.

Irrespective of the consistency of Eqs. (8.120) and (8.122), the corresponding governing equations have the specific structure which shows us a way to improve the "third-order" theory. Integrating Eqs. (8.120), substituting Eqs. (8.122), and performing some obvious transformations, we arrive at the following two equations with regard to u_1 and w:

$$\begin{aligned} u_1'' - k^2 u_1 &= -672\frac{G}{Eh^2}\left(30C_1x^2 + C_2x + C_3\right) - 1260C_1 \\ w' &= 4u_1 - 30C_1x^2 - C_2x - C_3 \end{aligned} \tag{8.123}$$

in which $k^2 = 840G/Eh^2$ and C_1, C_2, and C_3 are the constants of integration. As can be seen, Eqs. (8.123), in addition to the traditional polynomial solution, contain a solution which includes the exponential function $Exp(-kx)$ which rapidly vanishes at a distance from the beam end and corresponds to the so-called boundary-layer solution. Goldenveizer (1958) was the first who stated that the nonlinear approximation of the displacement distribution through the plate thickness (as in Eqs. (8.104)) must be supplemented with the boundary-layer solutions.

To do this, substitute Eqs. (8.108) for u_1 and w corresponding to the cantilever beam shown in Fig. 8.20 into Eqs. (8.104) for u_x and u_z to get the displacements

$$\begin{aligned} u_x^0 &= -\frac{6F}{Eh^3b}\left[(2b - x)xz + \frac{E}{3G}z^3\right] \\ u_z^0 &= \frac{2F}{Eh^3b}\left(3lx - x^2 + \frac{3Eh^2}{4G}\right)x \end{aligned} \tag{8.124}$$

which are treated now as the basic approximation. Following Vasiliev (2010) and Vasiliev and Lurie (1972), approximate the total displacements u_x and u_z supplementing the displacements in Eqs. (8.124) with a set of boundary-layer solutions which vanish at a distance from the clamped end of the beam (see Fig. 8.20), i.e.,

$$u_x = u_x^0 + \overline{u}_x, \quad u_z = u_z^0 + \overline{u}_z(x) \tag{8.125}$$

where

$$\overline{u}_x = C_0 f_0(z) + \sum_{k=1}^{\infty} e^{-s_k x} f_k(z) \tag{8.126}$$

Here, C_0 is a constant coefficient, $f_0(z) = z$, and $f_k(z)$ $(k = 0, 1, 2\ldots)$ is a complete system of functions which should be found (note that without f_0 the functions f_k do not form a complete system).

Substituting Eqs. (8.125) and (8.126) into Eqs. (8.105), find the stresses

$$\begin{aligned}\sigma_x &= E\frac{\partial u_x}{\partial x} = -\frac{12F}{bh^3}(l-x)z - E\sum_k s_k e^{-s_k x} f_k(z)\\ \tau_{xz} &= G\left(\frac{\partial u_x}{\partial z} + \frac{\partial u_z}{\partial x}\right) = G\left[C_0 + \frac{6F}{Gbh^3}\left(\frac{h^2}{4} - z^2\right) + \sum_k e^{-s_k x}\frac{df_k}{dz} + \frac{d\overline{u}_z}{dx}\right]\end{aligned} \tag{8.127}$$

Apply the equilibrium equation, i.e., the first equation of Eqs. (8.1) in which $b = constant$

$$\frac{\partial \sigma_x}{\partial x} + \frac{\partial \tau_{xz}}{\partial z} = 0 \tag{8.128}$$

Substituting for the stresses their expressions, Eqs. (8.127), we arrive at the following equation for $f_k(z)$ $(k = 1, 2, 3, \ldots)$:

$$\frac{d^2 f_k}{dz^2} + \alpha_k^2 f_k = 0$$

The antisymmetric solution with respect to z of this equation is

$$f_k(z) = C_k \sin \alpha_k z, \quad \alpha_k^2 = s_k^2 \frac{E}{G} \tag{8.129}$$

Now, Eqs. (8.127) for τ_{xz} becomes

$$\tau_{xz} = G\left[C_0 + \frac{6F}{Gbh^3}\left(\frac{h^2}{4} - z^2\right) + \sum_k C_k \alpha_k e^{-s_k x} \cos \alpha_k z + \frac{d\overline{u}_z}{dx}\right] \tag{8.130}$$

According to the boundary conditions, Eq. (8.102), $\tau_{xz}(z = \pm h/2) = 0$. Thus

$$\frac{d\overline{u}_z}{dx} = -C_0 - \sum_k C_k \alpha_k e^{-s_k x} \cos \lambda_k, \quad \lambda_k = \frac{1}{2}\alpha_k h \tag{8.131}$$

Integrating this equation and taking into account that for the clamped end (see Fig. 8.20) $\overline{u}_z(x = 0) = 0$, we get

$$\overline{u}_z = -C_0 x + \sum_k C_k \frac{\alpha_k}{s_k}\left(e^{-s_k x} - 1\right) \cos \lambda_k \tag{8.132}$$

Substituting Eq. (8.131) into Eq. (8.130), we arrive at the following expression for the shear stress

$$\tau_{xz} = G\left[\frac{6F}{Gbh^3}\left(\frac{h^2}{4} - z^2\right) - \sum_k C_k \alpha_k e^{-s_k x} \varphi_k(z)\right] \tag{8.133}$$

in which

$$\varphi_k(z) = \cos \lambda_k - \cos \alpha_k z \tag{8.134}$$

Apply the equilibrium equations, Eqs. (8.91) and (8.92), according to which

$$V = b \int_{-h/2}^{h/2} \tau_{xz} dz = F \tag{8.135}$$

for the cantilever beam (see Fig. 8.20) under consideration. Substituting Eq. (8.133) into Eq. (8.135), we derive the following equation for the parameter λ_k:

$$\tan \lambda_k = \lambda_k \tag{8.136}$$

As can be readily checked, the functions $\varphi_k(z)$ in Eqs. (8.134) and (8.136) are orthogonal on the interval $[-h/2, h/2]$, i.e.,

$$\int_{-h/2}^{h/2} \varphi_k \varphi_n dz = \begin{cases} \dfrac{h}{2}\sin^2 \lambda_k, & n = k \\ 0, & n \neq k \end{cases}, \quad \int_{-h/2}^{h/2} \varphi_k' \varphi_n' dz = \begin{cases} \dfrac{2}{h}\lambda_k^2 \sin^2 \lambda_k, & n = k \\ 0, & n \neq k \end{cases} \tag{8.137}$$

Moreover, the following integral conditions are also valid:

$$\int_{-h/2}^{h/2} \varphi_k dz = 0, \quad \int_{-h/2}^{h/2} \varphi_k' dz = 0, \quad \int_{-h/2}^{h/2} z\, \varphi_k' dz = 0 \tag{8.138}$$

It follows from Eqs. (8.138) that the system of functions $f_k = (C_k/\alpha_k)\varphi_k'$ is complete if it is supplemented with function $f_o = z$ (see Eq. (8.126)) in which this property of functions f_k is used.

To determine the constants C_0 and C_k, apply the boundary condition for the clamped end of the beam, i.e., $u_x(x = 0) = 0$. Using Eqs. (8.124) and (8.125), and (8.129) and (8.134), we have

$$u_x(x = 0) = -\frac{2F}{Gbh^3} z^3 + C_0 z + \sum_k \frac{C_k}{\alpha_k} \varphi_k'(z) = 0 \tag{8.139}$$

Multiplying this equation by z, integrating from –h/2 to h/2, and using Eqs. (8.138), we get $C_0 = 3F/(10Gbh)$. Multiplying by $\varphi_k'(z)$, integrating, and using Eqs. (8.137), we find $C_k = F/(Gb\lambda_k^2 \sin \lambda_k)$.

Thus, we have constructed the mathematically exact solution of the problem. To study the solution, present the explicit expressions for the displacements and the stresses. The final expression for the axial displacement follows from Eqs. (8.124) and (8.125), i.e.,

$$u_x = -\frac{6F}{Eh^3 b}(2l - x)xz + \frac{F}{Gb}\left(\frac{3z}{10h} - \frac{2z^3}{h^3} + \sum_k \frac{\sin \alpha_k z}{\lambda_k^2 \sin \lambda_k} e^{-s_k x}\right) \tag{8.140}$$

This displacement satisfies exactly the boundary conditions. We have two ways to simplify it. First, we can neglect the second term and arrive at the "first-order" theory, Eqs. (8.90) and (8.96). This approach looks attractive because all the boundary conditions are satisfied. Secondly, we can neglect the

boundary-layer part of the solution, i.e., omit the sum in Eq. (8.140). In this case, we arrive at the displacement that does not satisfy the boundary condition as per Eq. (8.139) and does not coincide with Eq. (8.124) for u_x^0 which corresponds to the "third-order" theory. Thus, the "third-order" theory displacement must be supplemented with the boundary-layer solution.

The beam deflection is specified by Eqs. (8.124), (8.125), and (8.132) which give

$$u_z = \frac{2F}{Eh^3b}\left(3lx - x^2 + \frac{3Eh^2}{5G}\right)x - \frac{F}{Gb}\sqrt{\frac{E}{G}}\sum_k \frac{\cos\lambda_k}{\lambda_k^2 \sin\lambda_k}\left(1 - e^{-s_k x}\right)$$

Direct calculation shows that the second term in this equation corresponding to the boundary-layer solution is negligible. Returning to the shear correction factor in Eq. (8.28), we can conclude that for the exact solution (without the boundary-layer part) $k = 5/6$, for the "first-order" theory (see Eqs. (8.96)), $k = 1$, and for the "third-order" theory (see Eqs. (8.108)), $k = 2/3$.

The stresses corresponding to the foregoing exact solution can be found from Eqs. (8.127) and (8.133) and presented in the following final form:

$$\sigma_x = -\frac{12F}{bh^3}(l - x)z - \frac{2F}{bh}\sqrt{\frac{E}{G}}\sum_k \frac{\sin\alpha_k z}{\lambda_k \sin\lambda_k}e^{-s_k x} \tag{8.141}$$

$$\tau_{xz} = \frac{6F}{bh^3}\left(\frac{h^2}{4} - z^2\right) - \frac{2F}{bh}\sum_k \frac{\cos\lambda_k - \cos\alpha_k z}{\lambda_k \sin\lambda_k}e^{-s_k x} \tag{8.142}$$

It follows from these equations that the solution contains a polynomial part, which is referred to as a penetrating solution because it does not vanish at a distance from the beam clamped end, and a boundary-layer part. It is important that as follows from Eqs. (8.138), the boundary-layer solution is self-balanced, i.e., it does not contribute to the bending moment and the shear force. Introduce the normalized normal stress and dimensionless coordinates as follows

$$\overline{\sigma} = \sigma_x \frac{bh^2}{6F}, \quad \overline{x} = \frac{x}{l}, \quad \overline{z} = \frac{z}{h}$$

and present Eq. (8.141) as

$$\overline{\sigma} = -2(1 - \overline{x})\overline{z} - \frac{\overline{h}}{3}\sqrt{\frac{E}{G}}\cdot\sum_k \frac{\sin 2\lambda_k \overline{z}}{\lambda_k \sin\lambda_k}e^{-\overline{s}_k\overline{x}} \tag{8.143}$$

where

$$\overline{s}_k = \frac{2l}{h}\sqrt{\frac{E}{G}}\lambda_k$$

and λ_k are the roots of Eq. (8.136) listed in Table 8.2. The higher roots corresponding to $k \gg 10$ can be approximately found as $\lambda_k \approx (2k + 1)/(2\pi)$. For a beam with parameters $h/l = 0.1$ and $E/G = 10$, Eq. (8.143) yields the following stress distribution

$$\overline{\sigma} = -\left\{(1 - \overline{x})\overline{\sigma}^{(0)}(\overline{z}) + 0.1054\left[\overline{\sigma}^{(1)}(\overline{z})e^{-\overline{s}_1\overline{x}} + \overline{\sigma}^{(2)}(\overline{z})e^{-\overline{s}_2\overline{x}} + \overline{\sigma}^{(3)}(\overline{z})e^{-\overline{s}_3\overline{x}} + \cdots\right]\right\} \tag{8.144}$$

TABLE 8.2 Nonzero roots of the equation $\tan \lambda_k = \lambda_k$ $(k = 1, 2, 3 \ldots 10)$.

k	**1**	**2**	**3**	**4**	**5**
λ_k	4.4934	7.7253	10.9041	14.0661	17.2208
k	**6**	**7**	**8**	**9**	**10**
λ_k	20.3713	23.5194	26.6661	29.8116	32.9563

Functions $\sigma^{(i)}(\overline{z})$ for $i = 0, 1, 2, 3$ and the corresponding values of parameter $\overline{s}_i$ are presented in Fig. 8.22. As can be seen, the higher the gradient of the function $\sigma^{(i)}(\overline{z})$, the higher the rate with which the corresponding boundary-layer solution vanishes at a distance from the clamped end $\overline{x} = 0$. For example, the contribution of the first boundary-layer solution $\sigma^{(1)}(\overline{z})$ to the maximum stress $\overline{\sigma}(\overline{z} = 0.5)$ at a distance from the clamped end $\overline{x} = 0.01$ (which is 0.1 of the beam thickness) does not exceed 0.2%. The distributions of the normalized normal stress over the height of the beam clamped edge corresponding to the exact solution (solid line) and to penetrating solution

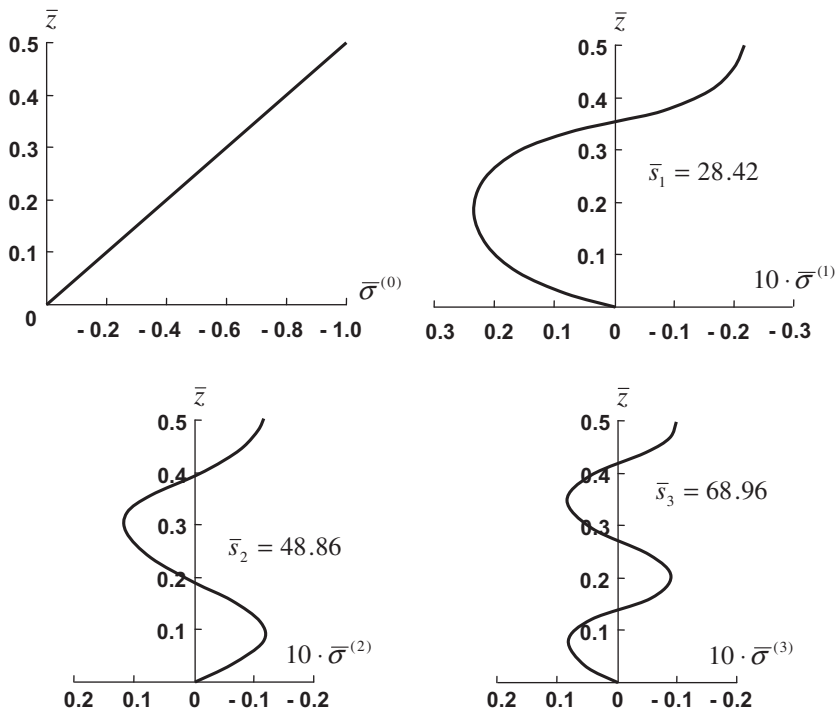


FIGURE 8.22

Functions $\overline{\sigma}^{(i)}(\overline{z})(i = 0, 1, 2, 3)$ and the corresponding values of parameter $\overline{s}_i$.

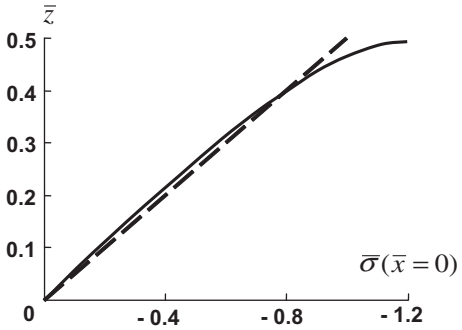


FIGURE 8.23

Distributions of the normalized normal stress over the height of the beam clamped edge corresponding to the exact solution (_____) and to the penetrating solution (_ _ _ _).

(dashed line) are shown in Fig. 8.23. It should be noted that the improvement of the penetrating solution provided by the boundary-layer solutions is more of a formal nature. Moreover, for practical analysis, the penetrating solution looks more realistic than the derived exact solution. Indeed, at the corner of the clamped edge ($x = 0, z = h/2$ in Fig. 8.20) the series in Eq. (8.144) does not converge, giving rise to infinitely high normal stresses at these corners. Note that practical analysis and design of cantilever beams is based on the penetrating solution which actually corresponds to the beam theory discussed in the *Strength of Materials* courses. According to the foregoing mathematically (but, naturally, not physically) exact solution, the cantilever beam cannot work because the maximum stress is infinitely high irrespective of the applied load. Clearly, this conclusion does not look realistic. The nature of the identified normal stress singularity is associated with a specific behavior of the shear stress in Eq. (8.142) in the vicinity of the clamped end of the beam (Vasiliev, 2010).

Consider the shear stress acting in the clamped cross section of the beam. Taking $x = 0$ in Eq. (8.142), we get

$$\tau_{xz}(x=0) = \frac{6F}{bh^3}\left(\frac{h^2}{4} - z^2\right) - \frac{2F}{bh}\sum_k \frac{\varphi_k(z)}{\lambda_k \sin \lambda_k} \tag{8.145}$$

where $\varphi_k(z)$ is given by Eq. (8.134). Since $\varphi_\kappa(z = \pm h/2) = 0$, we have $\tau_{xz}(z = \pm h/2) = 0$, so the boundary conditions are satisfied on the beam top and bottom surfaces. Now, use the orthogonality conditions in Eqs. (8.138) and decompose the quadratic function, entering the first term in Eq. (8.145) into a series with respect to functions $\varphi_k(z)$. Taking into account the fact that in accordance with Eqs. (8.138) the system of functions $\varphi_k(z)$ is complete only in conjunction with unity, we have

$$\frac{h^2}{4} - z^2 = C + \sum_k B_k \varphi_k(z)$$

where C and B_k are some constant coefficients. Multiplying this equation first by unity and second by $\varphi_n(z)$, integrating from $-h/2$ to $h/2$, and using Eqs. (8.137) and (8.138), we can determine C and B_k and finally arrive at

$$\frac{h^2}{4} - z^2 = \frac{h^2}{6}\left(1 + 2\sum_k \frac{\varphi_k(z)}{\lambda_k \sin \lambda_k}\right)$$

Substituting this result into Eq. (8.145), we get

$$\tau_{xz}(x = 0) = \frac{F}{bh} \tag{8.146}$$

As can be seen, the shear stress at the clamped end of the beam does not depend on z. This result is expected, because it follows directly from the constitutive equation, Eq. (8.100), for the shear stress. Indeed, at the clamped end of the beam (see Fig. 8.20) $u_x = 0$ and, hence, $(\partial u_x)/\partial z = 0$, whereas u_z does not depend on z. So, at $x = 0$ the shear stress does not change through the beam height and is specified by Eq. (8.146). However, this equation is valid only for the open interval $-h/2 < z < h/2$. At the interval ends $z = \pm h/2$, the shear stress must be zero due to the symmetry of the stress tensor ($\tau_{xz} = 0$ at $z = \pm h/2$ according to the boundary conditions). Thus, the distribution of the shear stress over the beam height for a clamped edge of the beam is not continuous, i.e., τ_{xz} is constant for $-h/2 < z < h/2$ and zero for $z = \pm h/2$. Naturally, the derivative $\partial \tau_{xz}/\partial z$ is infinitely high at the corner points ($x = 0$ and $z = \pm h/2$), and as follows from the equilibrium equation, Eq. (8.128), the normal stress σ_x is singular at the corner points.

The foregoing analysis allows us to formulate the following conclusions:

1. Boundary-layer solutions determine the stress state of the beam only in the close vicinity of the beam ends and depend on the particular boundary conditions which are usually not known exactly or can be hardly described mathematically for real beams.
2. Allowance for the boundary-layer solutions can cause mathematical problems which are physically not consistent and formally cause effects that do not exist in reality.
3. Analysis and design of beams should be based on the penetrating solutions which correspond to the "first-order" theory providing energy consistency of the boundary problem. The "third-order" and the other "higher-order" theories corresponding to the displacements in Eqs. (8.98) and (8.99) cannot be used for this purpose, because they require the boundary-layer solutions to satisfy the boundary conditions.

Consider laminated beams. The first solution for a laminated cantilever beam was obtained by S.G. Lekhnitskii in 1935 (Lekhnitskii, 1935) and reviewed by Carrera (2003). The bi-harmonic equation of the elasticity theory for a laminated beam was solved with the aid of polynomial presentation of the stress function for each layer. Thus, S.G. Lekhnitskii has constructed a penetrating solution ignoring boundary-layer solutions. Equations describing the combination of penetrating and boundary-layer solutions have been derived by Bolotin (1963). The laminate consists of a system of load-carrying layers alternating with core layers which take only transverse stresses (see Fig. 8.24). The axial displacements of the load-carrying layers correspond to the classical plate theory, according to which

$$u_x^{(i)} = u_i - z_i w_i', \quad u_x^{(i+1)} = u_{i+1} - z_{i+1} w_{i+1}' \tag{8.147}$$

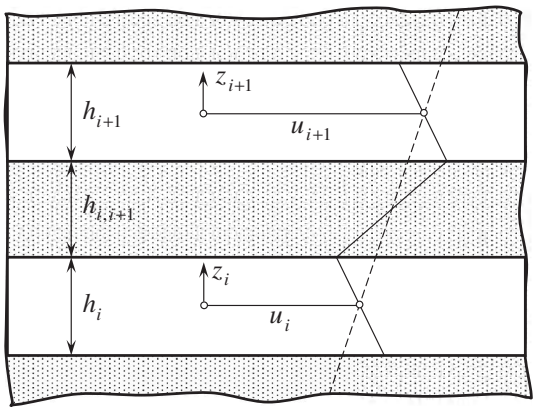


FIGURE 8.24

Distribution of the axial displacement over the height of a laminated beam.

(Bolotin and Novichkov, 1980), where $(\ldots)' = d(\ldots)/dx$, z_i is counted from the middle surface of the i-th layer $(-h_i/2 \le z_i \le h_i/2)$, and w_i is the deflection of the i-th layer. The axial stress in the i-th layer is

$$\sigma_x^{(i)} = A_{11}^{(i)} \varepsilon_x^{(i)} = A_{11}^{(i)} \left(u_i' - z_i w_i''\right)$$

For the core layers, the axial stress is zero and the shear strain does not depend on z, i.e.,

$$\gamma_{xz}^{(i,i+1)} = \frac{1}{h_{i,i+1}} \left[u_{i+1} - u_i + \frac{1}{2}\left(w_i' h_i + w_{i+1}' h_{i+1}\right)\right] + \frac{1}{2}\left(w_{i+1}' + w_i'\right)$$

The transverse normal strain of the core layers is

$$\varepsilon_z^{(i,i+1)} = \frac{1}{h_{i,i+1}} \left(w_{i+1} - w_i\right)$$

The governing equations for the functions u_i and w_i and the corresponding natural boundary conditions are derived with the aid of the variational principle. The total order of these equations depends on the number of layers. The solutions of numerous problems have been obtained by Bolotin and Novichkov (1980). They include the penetrating solutions and the system of boundary-layer solutions which describe local bending of load-carrying layers, as well as shear and normal strains of the core layers rapidly vanishing from the beam edge.

A theory that is more realistic for composite laminates (that do not have core layers) has been proposed by Grigolyuk and Chulkov (1964). In this theory, the axial stiffness of the core layers is not ignored. A similar theory with membrane load-carrying layers has been developed by Elpatievskii and Vasiliev (1965).

The main shortcoming of the theories under consideration is the high order of the governing equations (which depends on the number of layers) in which the penetrating solution is mixed with boundary-layer solutions. In modern versions of the theory (Reddy, 2004), the penetrating solution (the

corresponding displacement is shown in Fig. 8.24 with a dashed line) is singled out and the shear deformation of the layers is taken into account. The resulting expressions for the displacements become

$$\begin{aligned} u_x &= u(x) + z\theta(x) + \sum_i u_i(x)\varphi_i(z) \\ u_z &= w + \sum_i w_i\psi_i(z) \end{aligned} \tag{8.148}$$

where z is the global normal coordinate of the laminate and $\varphi_i(z)$ and $\psi_i(z)$ are some functions that provide the continuity of the displacements, the derivatives of which with respect to z are not continuous at the layer interfaces. Different forms of such functions have been presented by Carrera (2003). Since three functions for the whole laminate ($u, \theta,$ and w) are introduced in Eqs. (8.148), the number of functions u_i and w_i can be respectively reduced. For example, we can take for the first and the last (k-th) layers $u_1 = 0$, $w_1 = 0$, and $u_k = 0$ (Reddy, 2004).

In the simplest version of the theory, the deflection is assumed to be the same for all the layers, i.e., $u_z = w(x)$, whereas the functions $\varphi_i(z)$ in Eqs. (8.148) are some linear functions providing the continuity of the axial displacement u_x with respect to z (Carrera, 2003). Applying the continuity conditions for the shear stresses at the layer interface surfaces, we can express $u_i(x)$ in terms of two functions $\theta(x)$ and $w(x)$ (Carrera, 2003). As a result, the order of the governing equations for this theory does not depend on the number of layers. The theory constructed in such a way is similar to the "third-order" theory for homogeneous beams discussed earlier.

Return to the general theory based on Eqs. (8.147) or (8.148). The most pronounced difference between this theory and the theory based on the linear distribution of the axial displacement through the beam height is manifested in sandwich beams with stiff load-carrying layers and shear deformable lightweight cores.

Consider as an example the cantilever sandwich beam shown in Fig. 8.25. The axial displacements of the first and the second layers (see Fig. 8.25) following from Eqs. (8.147) and (8.148) are

$$\begin{aligned} u_1 &= u(x) - \left(\frac{H}{2} - z_1\right)\theta(x) - z_1 w'(x) \\ u_2 &= u(x) - \left(\frac{H}{2} - z_2\right)\theta(x) - z_2 w'(x) \end{aligned} \tag{8.149}$$

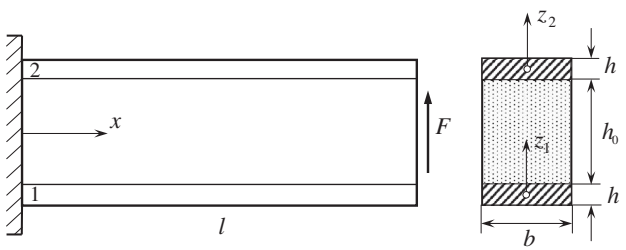


FIGURE 8.25

A cantilever sandwich beam.

Here, $u(x)$, $\theta(x)$, and $w(x)$ are the axial displacement, rotational angle, and the deflection (the same for both layers), $H = h_0 + h$, $-h/2 \le z_i \le h/2$, and $(i = 1, 2)$. The shear strain in the core is

$$\gamma = \frac{1}{h_0}\left[u_2\left(z_2 = -\frac{h}{2}\right) - u_1\left(z_1 = \frac{h}{2}\right)\right] + w' = \frac{H}{h_0}(\theta + w')$$

Then, the normal stresses in the layers and the shear stress in the core become

$$\begin{aligned}
\sigma^{(1)} &= E\left[u' - \left(\frac{H}{2} - z_1\right)\theta' - z_1 w''\right] \\
\sigma^{(2)} &= E\left[u' - \left(\frac{H}{2} - z_2\right)\theta' - z_2 w''\right] \\
\tau &= G\frac{H}{h_0}(\theta + w')
\end{aligned} \tag{8.150}$$

where E is the modulus of the layer and G is the shear modulus of the core material. The forces and the moments in the layers are

$$\begin{aligned}
N_1 &= b\int_{-h/2}^{h/2}\sigma^{(1)}dz_1 = B_l\left(u' - \frac{H}{2}\theta'\right) \\
N_2 &= b\int_{-h/2}^{h/2}\sigma^{(2)}dz_2 = B_l\left(u' + \frac{H}{2}\theta'\right) \\
M_1 &= b\int_{-h/2}^{h/2}\sigma^{(1)}z_1 dz_1 = -D_l(\theta' + w'') \\
M_2 &= b\int_{-h/2}^{h/2}\sigma^{(2)}z_2 dz_2 = D_l(\theta' - w'')
\end{aligned} \tag{8.151}$$

where

$$B_l = Ebh, \quad D_l = \frac{1}{12}Ebh^3 \tag{8.152}$$

are the membrane and bending stiffnesses of the layers. The equilibrium equations for the layers (see Fig. 8.26a) can be written as

$$M_1' - V_1 + \frac{1}{2}\tau bh = 0, \quad M_2' - V_2 + \frac{1}{2}\tau bh = 0 \tag{8.153}$$

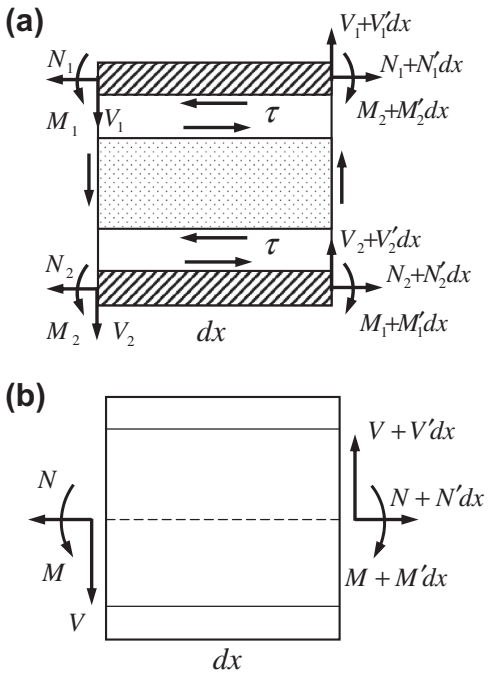


FIGURE 8.26

Free-body diagrams for a sandwich beam: equilibrium of the layers (a), and equilibrium of the beam element (b).

From Eqs. (8.150) for τ, (8.151) for M, and Eqs. (8.153) we can find the transverse forces in the layers, i.e.,

$$V_1 = M_1' + \frac{1}{2}\tau bh = -D_l(\theta'' + w''') + \frac{1}{2}GbhH(\theta + w')$$

$$V_2 = M_2' + \frac{1}{2}\tau bh = D_l(\theta'' - w''') + \frac{1}{2}GbhH(\theta + w')$$

Then, the total shear force

$$V = V_1 + V_2 + bh_0\tau$$

becomes

$$V = -2D_l w''' + S(w' + \theta) \tag{8.154}$$

where

$$S = GbH \tag{8.155}$$

is the shear stiffness of the beam. Finally, the total axial force and bending moment can be presented as

$$N = N_1 + N_2 = 2B_l u', \quad M = M_1 + M_2 = -2D_l w'' + \frac{1}{2}B_l H^2\theta' \tag{8.156}$$

The equilibrium equations of the beam element follow from Fig. 8.26b and have the form

$$N' = 0, \quad M' = V, \quad V' = 0 \tag{8.157}$$

The boundary conditions for the clamped end of the beam (see Fig. 8.25), i.e.,

$$u(x = 0) = 0, \quad \theta(x = 0) = 0, \quad w'(x = 0) = 0 \tag{8.158}$$

provide with regard to Eqs. (8.149) $u_1(x = 0) = 0$ and $u_2(x = 0) = 0$. For the end $x = l$ (see Fig. 8.25), we have

$$N = 0, \quad V = F, \quad M = 0 \tag{8.159}$$

The first equations in Eqs. (8.156)–(8.159) yield $N = 0$ and $u = 0$. Eq. (8.157) for V and the corresponding boundary condition in Eqs. (8.159) give $V = F$. Applying Eq. (8.154), we get

$$-2D_l w''' + S(w' + \theta) = F \tag{8.160}$$

Now, according to the second equilibrium equation in Eqs. (8.157), $M' = F$ and $M = Fx + C_1$. Since $M\ (x = l) = 0$, we arrive at $M = -F(l - x)$. Then, the second equation of Eqs. (8.156) yields

$$-2D_l w'' + \frac{1}{2} B_l H^2 \theta' = -F(l - x)$$

Integration gives

$$2D_l w' + \frac{1}{2} B_l H^2 \theta = F\left(lx - \frac{x^2}{2}\right) + C_2$$

Using the boundary conditions in Eqs. (8.158), we have $C_2 = 0$ and

$$2D_l w' + \frac{1}{2} B_l H^2 \theta = \frac{F}{2}\left(2lx - x^2\right) \tag{8.161}$$

Thus, the problem of a beam in bending is reduced to Eqs. (8.160) and (8.161). Eliminating θ from these equations and integrating the resulting equation, we arrive at

$$w'' - k^2 w = -\frac{FS}{2D_l B_l H^2}\left(lx^2 - \frac{x^3}{3} + \frac{B_l H^2}{S} x\right) + C_3 \tag{8.162}$$

where C_3 is the constant of integration and

$$k^2 = \frac{D_t S}{D_l B_l H^2}, \quad D_t = 2D_l + \frac{1}{2} B_l H^2 \tag{8.163}$$

Here, D_t is the total bending stiffness of the beam. The solution of Eq. (8.162) consists of two parts. The first part is the polynomial (i.e., penetrating solution) and the second part is the

boundary-layer solution. Retaining the boundary-layer solution in the vicinity of the clamped end only, we get

$$w = C_4 e^{-kx} + \frac{FB_l H^2}{2D_t S}\left(1 - \frac{2D_l}{D_t}\right)x + \frac{Fl}{2D_t}x^2 - \frac{F}{6D_t}x^3 + \frac{FSl}{2D_l B_l H^2} - C_3\frac{D_l B_l H^2}{D_t S}$$

The constants of integration C_3 and C_4 are found from the boundary conditions $w(0) = 0$ and $\theta = (0)0$. Then, the final expressions for w and θ become

$$\begin{aligned} w &= \frac{FB_l H^2}{2D_t S}\left(1 - \frac{2D_l}{D_t}\right)\left[H\sqrt{\frac{B_l D_l}{D_t S}}\left(e^{-kx} - 1\right) + x\right] + \frac{Fl}{2D_t}x^2 - \frac{F}{6D_t}x^3 \\ \theta &= \frac{F}{B_l H^2}\left(1 - \frac{2D_l}{D_t}\right)\left[\frac{2D_l B_l H^2}{D_t S}\left(1 - e^{-kx}\right) - 2lx + x^2\right] \end{aligned} \tag{8.164}$$

These expressions include the parameter $d = D_l/D_t$ which is the ratio of the bending stiffness of the layer to the total bending stiffness of the beam. Using Eqs. (8.152) and (8.163) for the stiffness coefficients, we get

$$d = \frac{h^2}{h^2 + 6H^2}, \quad H = h_0 + h$$

For practical sandwich beams, this parameter is normally rather small. For example, for $h_0 = 15$ mm, $h = 1$ mm (see Fig. 8.25) and $d = 0.00065$. Thus, we can simplify Eqs. (8.164) taking $d = 0$. Then,

$$w = \frac{F}{6D_t}\left(3lx - x^2 + \frac{6D_t}{S}\right)x, \quad \theta = -\frac{F}{2D_t}(2l - x)x$$

where $D_t = B_l H^2/2$. These equations coincide exactly with Eqs. (8.96) which correspond to a linear distribution of the axial displacement through the beam height.

Taking into account the transverse normal strain of the core ε_z, we arrive at an additional boundary-layer solution rapidly vanishing at a distance from the clamped end.

For simply supported sandwich beams (see Fig. 8.21) loaded with pressure $q = q_0 \sin(\pi x/l)$, the comparison of the maximum deflection w_m corresponding to various beam models with the experimental results w_m^e obtained by Alexandrov et al. (1960) is presented in Table 8.3. In this

TABLE 8.3 Normalized maximum deflections of sandwich beams.

E, GPa	G, MPa	l, mm	h, mm	h_0, mm	$\overline{w}_m^{(1)}$	$\overline{w}_m^{(2)}$	$\overline{w}_m^{(3)}$
70	55.7	280	0.7	3.7	0.990	0.992	1.027
70	915	480	0.7	4.8	0.969	0.983	1.020
70	915	280	0.7	5.1	0.856	0.986	1.033
70	38.5	280	1.0	17.0	0.329	0.923	0.985
70	38.5	280	2.4	18.8	0.171	0.921	1.053

table, $\overline{w}_m = w_m/w_m^e$, $\overline{w}_m^{(1)}$ corresponds to the classical beam theory for which $S \to \infty$, and $\overline{w}_m^{(2)}$ specifies the results corresponding to the displacements given by Eqs. (8.149), whereas deflections $\overline{w}_m^{(3)}$ show the solution based on the linear approximation of the axial displacement. It follows from Table 8.3 that $\overline{w}_m^{(2)}$ and $\overline{w}_m^{(3)}$ are characterized with a comparable accuracy for all the beams. Thus, the theory constructed in Section 8.1 allows us to describe the beam behavior with reasonable accuracy and is generalized in Chapter 9 for composite plates.

8.8 References

Alexandrov, A. Ya., Bryukker, L. E., Kurshin, L. M., & Prusakov, A. P. (1960). *Analysis of Sandwich Plates*. Moscow: Oborongiz, (in Russian).

Ambartsumyan, S. A. (1958). On a theory of bending of anisotropic plates. *Proc of USSR Academy of Sciences (Izvestia AN SSSR, Otdelenie Technicheskih Nauk)* (5), 69–77, (in Russian).

Ambartsumyan, S. A. (1987). *Theory of Anisotropic Plates*. Moscow: Nauka, (in Russian).

Birman, V., & Bert, C. W. (2002). On the choice of shear correction factor in sandwich structures. *Journal of Sandwich Structures and Materials, 4*, 83–95.

Bolotin, V. V. (1963). To the theory of laminated plates. *Proc of Russian Academy of Sciences (Izvestia AN SSSR, Otdelenie Technicheskih Nauk, Mechanika and Mashinostroenie)* (3), 65–72, (in Russian).

Bolotin, V. V., & Novichkov, Yu. N. (1980). *Mechanics of multilayered structures*. Moscow: Machinostroenie, (in Russian).

Carrera, E. (2003). Historical review of zig-zag theories for multilayered plates and shells. *Applied Mechanics Reviews, 56*(3), 287–308.

Dekker, M. (2004). *Structural Analysis of Polymeric Composite Materials*. New York: Marcell Dekker, Inc.

Elpatievskii, A. N., & Vasiliev, V. V. (1965). Analysis of the stress state of filament-wound fiberglass cylindrical shell. *Sov Engineering Journal, 5*(1), 129–142, (in Russian).

Gay, D., Hoa, S. V., & Tsai, S. W. (2003). *Composite Materials Design and Applications*. Boca Raton: CRC Press.

Goens, E. (1931). Uber die Bestimmung des Elastizitatsmodule von Staben mit Hilfe von Biegungsschwingungen. *Annalen der Physik, Ser, 5*(11), 649–678.

Goldenveizer, A. L. (1958). On Reissner's theory of plate bending. *Proc of USSR Academy of Sciences (Izvestia AN SSSR, Otdelenie Technicheskih Nauk)* (4), 102–109, (in Russian).

Grigolyuk, E. I., & Chulkov, P. P. (1964). Theory of viscoelastic multilayered shells with load-carrying core layers. *Applied Mechanics and Technical Physics (Prikladnaya Mechanika i Technicheskaya Phyzika)* (5), 109–117, (in Russian).

Kollar, L. P., & Springer, G. S. (2003). *Mechanics of Composite Structures*. Cambridge University Press.

Lekhnitskii, S. G. (1935). Strength calculation of composite beams. *Vestnik inzhenerov i tekhnikov* (9), (in Russian).

Mindlin, R. D. (1951). Influence of rotator inertia and shear on flexural motions of isotropic, elastic plates. *ASME Journal of Applied Mechanics, 18*, 31–38.

Reddy, J. N. (2004). *Mechanics of Laminated Composite Plates and Shells. Theory and Analysis* (2nd ed.). Boca Raton: CRC Press.

Reddy, J. N., & Wang, C. M. (2000). An overview of the relationships between solutions of the classical and shear deformation plate theories. *Composite Science and Technology, 60*, 2327–2335.

Reismann, H. (1988). *Elastic Plates: Theory and Application*. New York, USA: John Wiley and Sons.

Reissner, E. (1945). The effect of transverse shear deformation on the bending of elastic plates. *ASME Journal of Applied Mechanics, 12*, A69–A77.

Timoshenko, S. P. (1921). On the correction for shear of the differential equation for transverse vibrations of prismatic bars. *Philosophical Magazine, Ser, 6*(41), 742–746.

Timoshenko, S. P. (1922). On the transverse vibrations of bars of uniform cross-section. *Philosophical Magazine, Ser, 6*(43), 125–131.

Uflyand, Ya. S. (1948). Propagation of waves under transverse vibrations of beams and plates. *Applied Mechanics and Mathematics, 12*(8), 287–300, (in Russian).

Vasiliev, V. V. (1993). *Mechanics of Composite Structures*. Washington. USA: Taylor & Francis.

Vasiliev, V. V. (2010). Symmetry of stress tensor and singular solutions in the theory of elasticity. *Proceedings of Russian Academy of Sciences, Mechanics of Solids* (2), 62–72.

Vasililev, V. V., & Lurie, S. A. (1972). A version of refined beam theory for laminated plastics. *Mechanics of Polymers (Mechanika Polymerov), Riga, Zinatne* (4), 674–681, (in Russian).

Vasiliev, V. V., & Lurie, S. A. (1990a). To the problem of development of nonclassical plate theories. *Proceedings of Russian Academy of Sciences, Mechanics of Solids* (2), 158–167.

Vasiliev, V. V., & Lurie, S. A. (1990b). To the problem of refinement of the shallow shell theory. *Proceedings of Russian Academy of Sciences, Mechanics of Solids* (6), 139–146.

Vasiliev, V. V., & Lurie, S. A. (1992). On refined theories of beams, plates and shells. *Journal of Composite Materials, 26*(4), 546–557.

Vinson, J. R., & Sierakowski, R. L. (2004). *The Behavior of Structures Composed of Composite Materials*. Hingham MA: Kluwer Academic Publishers.

Vlasov, B. F. (1957). On the equations of theory of plate bending. *Proceedings of USSR Academy of Sciences (Izvestia AN SSSR, Otdelenie Technicheskih Nauk)* (12), 57–60, (in Russian).

CHAPTER

Laminated composite plates

9

Laminated composite plates possessing high strength and stiffness under in-plane loading and bending are widely used nowadays in composite aircraft and marine structures and have been discussed by many authors, particularly by Lekhnitskii (1957), Ambartsumian (1967, 1987), Ashton and Whitney (1970), Whitney (1987), Jones (1975, 1999), Pikul (1977, 1985), Vinson and Sierakovski (1986, 2004), Vasiliev (1993), Reddy (1997, 2004), Andreev and Nemirovskii (2001), Decolon (2002), Gay et al. (2003), Ye Jianqiao (2003), Kollar and Springer (2003), Vinson (2005) and Dekker (2009). This chapter is concerned with traditional and advanced specific problems and applications of the theory of anisotropic plates.

9.1 EQUATIONS OF THE THEORY OF ANISOTROPIC LAMINATED PLATES

Consider an anisotropic laminated plate referred to coordinates x, y, z as shown in Fig. 9.1. The reference plane $z = 0$ is located at distances e and s from the bottom and top surfaces (see Chapter 5). The displacement distributions over the plate thickness are specified by Eqs. (5.1) and (5.2), according to which

$$u_x = u(x, y) + z\theta_x(x, y), \qquad u_y = v(x, y) + z\theta_y(x, y), \qquad u_z = w(x, y) \tag{9.1}$$

Here u, v, and w are the displacements of the normal element cd (see Fig. 9.1) in the directions of the coordinate axes x, y, and z, respectively, whereas θ_x and θ_y are the rotation angles of the element in the xz and yz planes.

In plate theory, the displacements given by Eqs. (9.1) were originally introduced by Hencky (1947) and Bolle (1947) and later used by Uflyand (1948) and Mindlin (1951). Brief historical reviews of the problem have been presented by Reissner (1985), Vasiliev (1992, 1998, 2000), and Jemielita (1993).

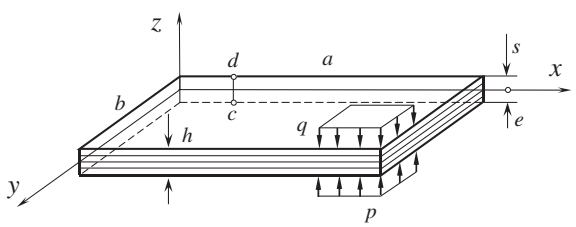


FIGURE 9.1

A laminated plate.

Advanced Mechanics of Composite Materials and Structural Elements. http://dx.doi.org/10.1016/B978-0-08-098231-1.00009-1
Copyright © 2013 Elsevier Ltd. All rights reserved.

For the displacements presented by Eqs. (9.1), the in-plane stresses σ_x, σ_y, and τ_{xy} can be found from Eqs. (5.4), i.e.,

$$\begin{aligned}
\sigma_x &= A_{11}\varepsilon_x^0 + A_{12}\varepsilon_y^0 + A_{14}\gamma_{xy}^0 + z\left(A_{11}\kappa_x + A_{12}\kappa_y + A_{14}\kappa_{xy}\right)\\
\sigma_y &= A_{21}\varepsilon_x^0 + A_{22}\varepsilon_y^0 + A_{24}\gamma_{xy}^0 + z\left(A_{21}\kappa_x + A_{22}\kappa_y + A_{24}\kappa_{xy}\right)\\
\tau_{xy} &= A_{41}\varepsilon_x^0 + A_{42}\varepsilon_y^0 + A_{44}\gamma_{xy}^0 + z\left(A_{41}\kappa_x + A_{42}\kappa_y + A_{44}\kappa_{xy}\right)
\end{aligned} \tag{9.2}$$

where $A_{mn} = A_{nm}$ are the stiffness coefficients of the material, which, in general, depend on the z-coordinate and

$$\begin{aligned}
\varepsilon_x^0 &= \frac{\partial u}{\partial x}, \quad \varepsilon_y^0 = \frac{\partial v}{\partial y}, \quad \gamma_{xy}^0 = \frac{\partial u}{\partial y} + \frac{\partial v}{\partial x}\\
\kappa_x &= \frac{\partial \theta_x}{\partial x}, \quad \kappa_y = \frac{\partial \theta_y}{\partial y}, \quad \kappa_{xy} = \frac{\partial \theta_x}{\partial y} + \frac{\partial \theta_y}{\partial x}
\end{aligned} \tag{9.3}$$

are in-plane and bending deformations of the reference surface $z = 0$. The stresses in Eqs. (9.2) are reduced to stress resultants and couples as follows

$$\begin{aligned}
N_x &= \int_{-e}^{s} \sigma_x dz, \quad N_y = \int_{-e}^{s} \sigma_y dz, \quad N_{xy} = \int_{-e}^{s} \tau_{xy} dz\\
M_x &= \int_{-e}^{s} \sigma_x z dz, \quad M_y = \int_{-e}^{s} \sigma_y z dz, \quad M_{xy} = \int_{-e}^{s} \tau_{xy} z dz
\end{aligned} \tag{9.4}$$

which are applied to the reference surface as shown in Fig. 9.2. Substitution of Eqs. (9.2) into Eqs. (9.4) yields the constitutive equations similar to Eqs. (5.5), i.e.,

$$\begin{aligned}
N_x &= B_{11}\varepsilon_x^0 + B_{12}\varepsilon_y^0 + B_{14}\gamma_{xy}^0 + C_{11}\kappa_x + C_{12}\kappa_y + C_{14}\kappa_{xy}\\
N_y &= B_{21}\varepsilon_x^0 + B_{22}\varepsilon_y^0 + B_{24}\gamma_{xy}^0 + C_{21}\kappa_x + C_{22}\kappa_y + C_{24}\kappa_{xy}\\
N_{xy} &= B_{41}\varepsilon_x^0 + B_{42}\varepsilon_y^0 + B_{44}\gamma_{xy}^0 + C_{41}\kappa_x + C_{42}\kappa_y + C_{44}\kappa_{xy}\\
M_x &= C_{11}\varepsilon_x^0 + C_{12}\varepsilon_y^0 + C_{14}\gamma_{xy}^0 + D_{11}\kappa_x + D_{12}\kappa_y + D_{14}\kappa_{xy}\\
M_y &= C_{21}\varepsilon_x^0 + C_{22}\varepsilon_y^0 + C_{24}\gamma_{xy}^0 + D_{21}\kappa_x + D_{22}\kappa_y + D_{24}\kappa_{xy}\\
M_{xy} &= C_{41}\varepsilon_x^0 + C_{42}\varepsilon_y^0 + C_{44}\gamma_{xy}^0 + D_{41}\kappa_x + D_{42}k_y + D_{44}\kappa_{xy}
\end{aligned} \tag{9.5}$$

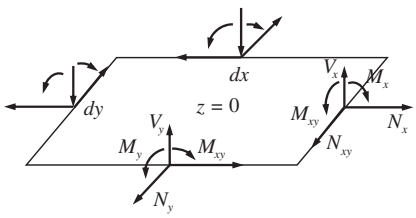


FIGURE 9.2

Stress resultants and couples acting on the reference plane of a plate.

in which

$$B_{mn} = \int_{-e}^{s} A_{mn} dz, \qquad C_{mn} = \int_{-e}^{s} A_{mn} z dz, \qquad D_{mn} = \int_{-e}^{s} A_{mn} z^2 dz \tag{9.6}$$

are membrane, coupling, and bending stiffness coefficients, respectively.

As discussed in Sections 5.1 and 8.7, for the displacements given by Eqs. (9.1), the distribution of the transverse shear stresses τ_{xz} and τ_{yz} over the plate thickness does not affect the plate behavior which is governed by the resultant shear forces

$$V_x = \int_{-e}^{s} \tau_{xz} dz, \qquad V_y = \int_{-e}^{s} \tau_{yz} dz \tag{9.7}$$

shown in Fig. 9.2. The constitutive equations for the shear forces, Eqs. (5.15), become

$$V_x = S_{55}\gamma_x + S_{56}\gamma_y, \qquad V_y = S_{66}\gamma_y + S_{56}\gamma_x \tag{9.8}$$

in which, in accordance with Eqs. (5.14)

$$\gamma_x = \theta_x + \frac{\partial w}{\partial x}, \qquad \gamma_y = \theta_y + \frac{\partial w}{\partial y} \tag{9.9}$$

are the shear strains averaged over the plate thickness. In accordance with Eq. (5.19), the stiffness coefficients in Eqs. (9.8) are calculated as follows

$$S_{mn} = \frac{h^2 \int_{-e}^{s} \overline{A}_{mn} dz}{\left(\int_{-e}^{s} \overline{A}_{55} dz\right)\left(\int_{-e}^{s} \overline{A}_{66} dz\right) - \left(\int_{-e}^{s} \overline{A}_{56} dz\right)^2} \tag{9.10}$$

where $mn = 55, 56, 66$ and

$$\overline{A}_{mn} = \frac{A_{mn}}{A_{55}A_{66} - A_{56}^2} \tag{9.11}$$

in which A_{mn} are the transverse shear stiffness coefficients specified by Eqs. (4.72). Since the stiffness coefficients A_{mn} in Eqs. (9.6) and (9.10) include the coordinates of the reference surface e and s as the integrals limits, we can simplify the expressions for these coefficients introducing the new coordinate $t = z + e$ (see Fig. 5.8) which changes from $t = 0$ to $t = h$, where h is the plate thickness (see Fig. 9.1). Then, Eqs. (9.6) reduce to the form specified by Eqs. (5.28) and (5.29). i.e.,

$$B_{mn} = I_{mn}^{0}, \qquad C_{mn} = I_{mn}^{(1)} - eI_{mn}^{(0)}, \qquad D_{mn} = I_{mn}^{(2)} - eI_{mn}^{(1)} + e^2 I_{mn}^{(0)} \tag{9.12}$$

where $mn = 11, 12, 22, 14, 24, 44$ and

$$I_{mn}^{(r)} = \int_{0}^{h} A_{mn} t^r dt, \qquad r = 0, 1, 2 \tag{9.13}$$

Equation (9.10) takes the form

$$S_{mn} = \frac{h^2 J_{mn}}{J_{55}J_{66} - J_{56}^2} \tag{9.14}$$

where $mn = 55, 56, 66$ and

$$J_{mn} = \int_0^h \overline{A}_{mn} dt \tag{9.15}$$

in which $\overline{A}_{mn}$ is given by Eq. (9.11). Typical composite material laminates are discussed in Sections 5.2 to 5.9.

For orthotropic plate $A_{14} = A_{24} = A_{56} = 0$ and Eqs. (9.5) and (9.8) are simplified as

$$\begin{aligned}
N_x &= B_{11}\varepsilon_x^0 + B_{12}\varepsilon_y^0 + C_{11}\kappa_x + C_{12}\kappa_y \\
N_y &= B_{21}\varepsilon_x^0 + B_{22}\varepsilon_y^0 + C_{21}\kappa_x + C_{22}\kappa_y \\
N_{xy} &= B_{44}\gamma_{xy}^0 + C_{44}\kappa_{xy} \\
M_x &= C_{11}\varepsilon_x^0 + C_{12}\varepsilon_y^0 + D_{11}\kappa_x + D_{12}\kappa_y \\
M_y &= C_{21}\varepsilon_x^0 + C_{22}\varepsilon_y^0 + D_{21}\kappa_x + D_{22}k_y \\
M_{xy} &= C_{44}\gamma_{xy}^0 + D_{44}\kappa_{xy} \\
V_x &= S_x\gamma_x, \quad V_y = S_y\gamma_y
\end{aligned} \tag{9.16}$$

Here, B_{mn}, C_{mn}, and D_{mn} are specified by Eqs. (9.12), whereas

$$S_x = \frac{h^2}{\int_0^h \frac{dt}{G_{xz}}}, \quad S_y = \frac{h^2}{\int_0^h \frac{dt}{G_{yz}}} \tag{9.17}$$

and G_{xz} and G_{yz} are the material shear moduli which, in the general case, vary through the plate thickness.

Consider the equilibrium equations, Eqs. (2.5), i.e.,

$$\frac{\partial \sigma_x}{\partial x} + \frac{\partial \tau_{xy}}{\partial y} + \frac{\partial \tau_{xz}}{\partial z} = 0 \quad (x, y) \tag{9.18}$$

$$\frac{\partial \sigma_z}{\partial z} + \frac{\partial \tau_{xz}}{\partial x} + \frac{\partial \tau_{yz}}{\partial y} = 0 \tag{9.19}$$

in which the notation (x, y) means that changing x to y and y to x we can obtain one more equation from the presented one. The boundary conditions on the plate surfaces are

$$\begin{aligned}
\sigma_z(z = -e) &= -p, \qquad \tau_{xz}(z = -e) = \tau_{yz}(z = -e) = 0 \\
\sigma_z(z = s) &= -q, \qquad \tau_{xz}(z = s) = \tau_{yz}(z = s) = 0
\end{aligned} \tag{9.20}$$

(see Fig. 9.1). We can reduce Eqs. (9.18) and (9.19), which include three independent variables, x, y, and z, to two-dimensional equations of plate theory. Integrating Eq. (9.18) from $t = 0$ to t and applying the boundary conditions, we get

$$\tau_{xz} = -\int_{-e}^{z}\left(\frac{\partial \sigma_x}{\partial x} + \frac{\partial \tau_{xy}}{\partial y}\right)dz \quad (x, y) \tag{9.21}$$

Putting $z = s$, taking into account that $\tau_{xz}(z = s) = 0$, and using Eqs. (9.4) for the stress resultants, we have

$$\frac{\partial N_x}{\partial x} + \frac{\partial N_{xy}}{\partial y} = 0 \quad (x, y) \tag{9.22}$$

These two equations correspond to the projections of the forces acting on the plate element shown in Fig. 9.2 on axes x and y, respectively. Integrating Eq. (9.19) and using the boundary conditions given by Eqs. (9.20) for σ_z, we can obtain

$$\sigma_z = -\int_{-e}^{z}\left(\frac{\partial \tau_{xz}}{\partial x} + \frac{\partial \tau_{yz}}{\partial y}\right)dz - p \tag{9.23}$$

Taking $z = s$ and applying the boundary condition for σ_z given in Eqs. (9.20) in conjunction with Eqs. (9.7) for the shear forces, we arrive at the third equilibrium equation which corresponds to the projection of the forces acting on the plate element shown in Fig. 9.2 on the z-axis

$$\frac{\partial V_x}{\partial x} + \frac{\partial V_y}{\partial_y} = \overline{p} = 0, \quad \overline{p} = p - q \tag{9.24}$$

Finally, substitute Eq. (9.19) for the shear stresses into Eq. (9.7) for the shear force, i.e.,

$$V_x = \int_{-e}^{s} dz \int_{-e}^{z}\left(\frac{\partial \sigma_x}{\partial x} + \frac{\partial \tau_{xy}}{\partial y}\right)dz \quad (x, y) \tag{9.25}$$

Integration by parts, taking into account Eqs. (9.4), yields

$$\int_{-e}^{s} dz \int_{-e}^{z} \frac{\partial \sigma_x}{\partial x}dz = s\int_{-e}^{s} \frac{\partial \sigma_x}{\partial x}dz - \int_{-e}^{s} z\frac{\partial \sigma_x}{\partial x}dz = s\frac{\partial N_x}{\partial x} - \frac{\partial M_x}{\partial x}$$

$$\int_{-e}^{s} dz \int_{-e}^{z} \frac{\partial \tau_{xy}}{\partial y}dz = s\int_{-e}^{s} \frac{\partial \tau_{xy}}{\partial y}dz - \int_{-e}^{s} z\frac{\partial \tau_{xy}}{\partial y}dz = s\frac{\partial N_{xy}}{\partial y} - \frac{\partial M_{xy}}{\partial y}$$

and Eq. (9.23) becomes

$$V_x = s\left(\frac{\partial N_x}{\partial x} + \frac{\partial N_{xy}}{\partial y}\right) - \frac{\partial M_x}{\partial x} - \frac{\partial M_{xy}}{\partial y}$$

Applying Eq. (9.22), we finally arrive at the following two moment equations for the plate element shown in Fig. 9.2:

$$\frac{\partial M_x}{\partial x}+\frac{\partial M_{xy}}{\partial y}-V_x=0 \quad (x,y) \tag{9.26}$$

Thus, the plate theory under consideration reduces to five equilibrium equations, Eqs. (9.22), (9.24), and (9.26), eight constitutive equations, Eqs. (9.16), and eight strain-displacement equations, Eqs. (9.3) and (9.9). This set consists of 21 equations in total which include the same number of unknown functions, i.e., eight forces and moments, N_x, N_y, N_{xy}, V_x, V_y, M_x, M_y, and M_{xy}, eight strains, ε_x^0, ε_y^0, γ_{xy}^0, κ_x, κ_y, κ_{xy}, γ_x, and γ_y, and five displacements and rotation angles, u, v, w, θ_x, and θ_y. The equilibrium equations can be obtained as the variational equations using the minimum conditions for the total potential energy functional (see Section 2.11.1) in the form

$$\begin{aligned}\delta T=\int_0^a\int_0^b\big(&N_x\delta\varepsilon_x^0+N_y\delta\varepsilon_y^0+N_{xy}\delta\gamma_{xy}^0+M_x\delta\kappa_x+M_y\delta\kappa_y\\&+M_{xy}\,\delta\kappa_{xy}+V_x\,\delta\gamma_x+V_y\,\delta\gamma_y-\overline{p}\delta w\big)dxdy=0\end{aligned} \tag{9.27}$$

The derived governing set of equations consists of two groups of equations describing the plane stress state of the plate and plate bending. Assume that for some of the reasons discussed, e.g., in Section 5.10, the coupling stiffness coefficients C_{mn} in Eqs. (9.16) are zero. Then, these equations link the in-plane forces with the corresponding strains, i.e., for an orthotropic plate,

$$N_x=B_{11}\varepsilon_x^0+B_{12}\varepsilon_y^0,\quad N_y=B_{21}\varepsilon_x^0+B_{22}\varepsilon_y^0,\quad N_{xy}=B_{44}\gamma_{xy}^0 \tag{9.28}$$

The forces satisfy the equilibrium equations, Eqs. (9.22)

$$\frac{\partial N_x}{\partial x}+\frac{\partial N_{xy}}{\partial y}=0,\quad \frac{\partial N_y}{\partial y}+\frac{\partial N_{xy}}{\partial x}=0 \tag{9.29}$$

and the strains are expressed in terms of the in-plane displacements by Eqs. (9.3), according to which

$$\varepsilon_x^0=\frac{\partial u}{\partial x},\quad \varepsilon_y^0=\frac{\partial v}{\partial y},\quad \gamma_{xy}^0=\frac{\partial u}{\partial y}+\frac{\partial v}{\partial x} \tag{9.30}$$

The obtained set of equations consisting of eight equations is of the overall fourth order and requires two boundary conditions for the plate edge. For the edges $x=constant$ and $y=constant$, respectively, the natural boundary conditions following from the energy condition given by Eq. (9.27) are

$$\begin{aligned}&N_x\delta u=0,\quad N_{xy}\delta v=0 \quad \text{for } x=constant\\&N_y\delta v=0,\quad N_{xy}\delta u=0 \quad \text{for } y=constant\end{aligned} \tag{9.31}$$

According to Eqs. (9.31), force, displacement, or mixed boundary conditions can be formulated at the plate edges.

For the problem of plate bending, the constitutive equations follow from Eqs. (9.16), i.e.,

$$\begin{gathered}M_x=D_{11}\kappa_x+D_{12}\kappa_y,\quad M_y=D_{21}\kappa_x+D_{22}\kappa_y,\quad M_{xy}=D_{44}\kappa_{xy}\\V_x=S_x\gamma_x,\quad V_y=S_y\gamma_y\end{gathered} \tag{9.32}$$

whereas the corresponding equilibrium equations are specified by Eqs. (9.24) and (9.26), i.e.,

$$\frac{\partial V_x}{\partial x}+\frac{\partial V_y}{\partial y}+\overline{p}=0,\quad \frac{\partial M_x}{\partial x}+\frac{\partial M_{xy}}{\partial y}-V_x=0,\quad \frac{\partial M_y}{\partial y}+\frac{\partial M_{xy}}{\partial x}-V_y=0 \tag{9.33}$$

The strain-displacement equations, Eqs. (9.3) and (9.9), become

$$\kappa_x=\frac{\partial \theta_x}{\partial x},\quad \kappa_y=\frac{\partial \theta_y}{\partial y},\quad \kappa_{xy}=\frac{\partial \theta_x}{\partial y}+\frac{\partial \theta_y}{\partial x},\quad \gamma_x=\theta_x+\frac{\partial w}{\partial x},\quad \gamma_y=\theta_y+\frac{\partial w}{\partial y} \tag{9.34}$$

The obtained set of 13 equations is of the overall sixth order and requires the following three boundary conditions for the plate edge:

$$\begin{aligned} &M_x\delta\theta_x=0,\quad M_{xy}\delta\theta_y=0,\quad V_x\delta w=0\quad \text{for } x=\textit{constant}\\ &M_y\delta\theta_y=0,\quad M_{xy}\delta\theta_x=0,\quad V_y\delta w=0\quad \text{for } y=\textit{constant}\end{aligned} \tag{9.35}$$

9.2 EQUATIONS FOR THE ORTHOTROPIC PLATES WITH SYMMETRIC STRUCTURE

It follows from the constitutive equations, Eqs. (9.5), that, in the general case, composite plates demonstrate a rather complicated behavior which involves various types of coupling effects, i.e., shear is coupled with tension and bending is coupled with torsion due to material anisotropy, whereas bending is coupled with in-plane deformation due to, in general, the nonsymmetrical laminated structure of the plate. Fortunately, plates with such a general structure are used rarely as composite structural elements.

First of all, it should be noted that the majority of real composite plates are orthotropic. Anisotropic composite plates are usually designed for special applications, e.g., for the so-called adaptive and/or passive control composite structures whose bending must be accompanied by controlled torsion. A unique example of such application is the composite panel of a forward swept airplane wing (Weisshaar, 1980, 1981). The anisotropic properties of such panels allow us to provide the appropriate aeroelastic tailoring of a wing's structure. In the vast majority of applications, plates designed as load-carrying structural elements are usually orthotropic.

Secondly, as shown in Section 5.4, the maximum bending stiffness of the plate composed of a given number and given properties of layers is reached if the plate structure is symmetric with respect to the plate middle plane. Note that the thickness of the elementary composite ply is normally rather small (0.1–0.2 mm) and that actual composite plates are usually composed of a large number of plies. Thus, it is practically always possible to arrange these plies symmetrically with respect to the plate middle plane. Note that homogeneous plates whose properties do not vary across the thickness represent one of the most widespread particular cases of plates with a balanced and symmetric structure. Typical examples of real nonsymmetrically laminated plates include sandwich panels with different facing layers and also stiffened panels.

Formally, the difference between symmetrically and nonsymmetrically laminated plates is associated with coupling stiffness coefficients C_{mn} in Eqs. (9.5) which are zero for plates with a symmetric structure. As shown in Section 5.10, the condition $C_{mn}=0$ can be approximately satisfied using the reduced bending stiffness method. Thus, formally, even nonsymmetric plates can sometimes be analyzed using the equations presented in this section.

For the foregoing reasons, we consider further mainly balanced and symmetrically laminated orthotropic plates. Plates with more complicated structures are discussed in the following sections of this chapter.

Thus, assume that the coupling stiffness coefficients $C_{mn} = 0$ and, hence, the problem of plate bending can be separated from the in-plane problem and described by Eqs. (9.32)–(9.34) derived in the previous section. Substitute the generalized strains, Eqs. (9.34), into the constitutive equations, Eqs. (9.32), and the resulting expressions for the moments and forces substitute into the equilibrium equations, Eqs. (9.33). As a result, we arrive at the following three equilibrium equations written in terms of the deflection, w, and rotation angles, θ_x and θ_y:

$$\begin{aligned} L_{1x}(\theta_x) + L_{1y}(\theta_y) + L_{1w}(w) &= 0 \\ L_{2x}(\theta_x) + L_{2y}(\theta_y) + L_{2w}(w) &= 0 \\ L_{3x}(\theta_x) + L_{3y}(\theta_y) + L_{3w}(w) &= -\overline{p} \end{aligned} \tag{9.36}$$

in which the differential operators L are

$$\begin{aligned} L_{1x}(\theta_x) &= \frac{1}{S_x}\left(D_{11}\frac{\partial^2\theta_x}{\partial x^2} + D_{44}\frac{\partial^2\theta_x}{\partial y^2}\right) - \theta_x \\ L_{1y}(\theta_y) &= \frac{\overline{D}}{S_x}\frac{\partial^2\theta_y}{\partial x\partial y}, \quad L_{1w}(w) = -\frac{\partial w}{\partial x} \\ L_{2x}(\theta_x) &= \frac{\overline{D}}{S_y}\frac{\partial^2\theta_x}{\partial x\partial y} \\ L_{2y}(\theta_y) &= \frac{1}{S_y}\left(D_{22}\frac{\partial^2\theta_y}{\partial y^2} + D_{44}\frac{\partial^2\theta_y}{\partial x^2}\right) - \theta_y, \quad L_{2w}(w) = -\frac{\partial w}{\partial y} \\ L_{3x}(\theta_x) &= S_x\frac{\partial\theta_x}{\partial x}, \quad L_{3y}(\theta_y) = S_y\frac{\partial\theta_y}{\partial y} \\ L_{3w}(w) &= S_x\frac{\partial^2 w}{\partial x^2} + S_y\frac{\partial^2 w}{\partial y^2} \end{aligned} \tag{9.37}$$

where $\overline{D} = D_{12} + D_{44}$.

We can reduce Eqs. (9.36) to one governing equation using the operational method (Vasiliev, 1992). According to this method, consider formally the determinant constructed of the operators given by Eqs. (9.37) and decompose it using the minors corresponding to the third row. Then, the functions θ_x, θ_y, and w can be expressed in terms of some resolving function $W(x, y)$ as

$$\begin{aligned} \theta_x &= \begin{vmatrix} L_{1y} & L_{1w} \\ L_{2y} & L_{2w} \end{vmatrix}(W) = \left(L_{1y}L_{2w} - L_{1w}L_{2y}\right)(W) \\ \theta_y &= -\begin{vmatrix} L_{1x} & L_{1w} \\ L_{2x} & L_{2w} \end{vmatrix}(W) = (L_{1w}L_{2x} - L_{1x}L_{2w})(W) \\ w &= \begin{vmatrix} L_{1x} & L_{1y} \\ L_{2x} & L_{2y} \end{vmatrix}(W) = \left(L_{1x}L_{2y} - L_{1y}L_{2x}\right)(W) \end{aligned} \tag{9.38}$$

Here, we use the formal multiplication operation for the differential operators with constant coefficients, e.g.,

$$L_{1y}L_{2w}(W) = L_{2w}L_{1y}(W) = -\frac{\overline{D}}{S_x}\frac{\partial^3 W}{\partial x \partial y^2}$$

As can be directly verified, substitution of Eqs. (9.38) into the first two equations of Eqs. (9.36) satisfies identically these equations, whereas the third equation takes the following operational form:

$$\left[L_{3x}\left(L_{1y}L_{2w} - L_{1w}L_{2y}\right) - L_{3y}(L_{1x}L_{2w} - L_{1w}L_{2x}) + L_{3w}\left(L_{1x}L_{2y} - L_{1y}L_{2x}\right)\right](W) = -\overline{p} \tag{9.39}$$

The left-hand part of this equation is actually the determinant composed of the operators given by Eqs. (9.37). The explicit form of Eq. (9.39) is

$$\begin{aligned} &D_{11}\frac{\partial^4 W}{\partial x^4} + 2(D_{12} + 2D_{44})\frac{\partial^4 W}{\partial x^2 \partial y^2} + D_{22}\frac{\partial^4 W}{\partial y^4} - \frac{D_{11}D_{44}}{S_y}\frac{\partial^6 W}{\partial x^6} - \frac{D_{22}D_{44}}{S_x}\frac{\partial^6 W}{\partial y^6} \\ &-\left\{\frac{D_{11}D_{44}}{S_x} + \frac{1}{S_y}\left[D_{11}D_{22} - D_{12}(D_{12} + 2D_{44})\right]\right\}\frac{\partial^6 W}{\partial x^4 \partial y^2} \\ &-\left\{\frac{D_{22}D_{44}}{S_y} + \frac{1}{S_x}\left[D_{11}D_{22} - D_{12}(D_{12} + 2D_{44})\right]\right\}\frac{\partial^6 W}{\partial x^2 \partial y^4} = \overline{p} \end{aligned} \tag{9.40}$$

The rotation angles and the deflection are expressed in terms of the resolving function W as

$$\begin{aligned} \theta_x &= \frac{\partial}{\partial x}\left[-W + \frac{D_{44}}{S_y}\frac{\partial^2 W}{\partial x^2} + \left(\frac{D_{22}}{S_y} - \frac{\overline{D}}{S_x}\right)\frac{\partial^2 W}{\partial y^2}\right] \\ \theta_y &= \frac{\partial}{\partial y}\left[-W + \frac{D_{44}}{S_x}\frac{\partial^2 W}{\partial y^2} + \left(\frac{D_{11}}{S_x} - \frac{\overline{D}}{S_y}\right)\frac{\partial^2 W}{\partial x^2}\right] \end{aligned} \tag{9.41}$$

$$\begin{aligned} w = W &- \left(\frac{D_{11}}{S_x} + \frac{D_{44}}{S_y}\right)\frac{\partial^2 W}{\partial x^2} - \left(\frac{D_{22}}{S_y} + \frac{D_{44}}{S_x}\right)\frac{\partial^2 W}{\partial y^2} \\ &+ \frac{1}{S_x S_y}\left\{D_{11}D_{44}\frac{\partial^4 W}{\partial x^4} + \left[D_{11}D_{22} - D_{12}(D_{12} + 2D_{44})\right]\frac{\partial^4 W}{\partial x^2 \partial y^2} + D_{22}D_{44}\frac{\partial^4 W}{\partial y^4}\right\} \end{aligned} \tag{9.42}$$

The equations obtained, Eqs. (9.41)–(9.42), have specific structures that are studied in the next section.

9.3 ANALYSIS OF THE EQUATIONS OF PLATE THEORY FOR TRANSVERSELY ISOTROPIC PLATES

To analyze the structure of the governing equations of plate theory, Eqs. (9.41) and (9.42), consider a transversely isotropic plate composed of identical isotropic layers. For such plates

$$D_{11} = D_{22} = D, \quad D_{12} = \upsilon D, \quad D_{44} = \frac{1}{2}(1 - \upsilon)D, \quad S_x = S_y = S \tag{9.43}$$

where D and S are the plate bending and transverse shear stiffnesses, and υ is the in-plane Poisson's ratio. For the stiffnesses presented by Eqs. (9.43), Eqs. (9.40)–(9.42) are markedly simplified and take the form

$$\begin{aligned} &D\Delta\Delta L(W) = \overline{p} \\ &\theta_x = -\frac{\partial}{\partial x}L(W), \quad \theta_y = -\frac{\partial}{\partial y}L(W) \\ &w = L(W) - \frac{D}{S}\Delta L(W) \end{aligned} \tag{9.44}$$

in which

$$L(W) = W - \frac{D(1-\upsilon)}{2S}\Delta W, \quad \Delta(\ldots) = \frac{\partial^2(\ldots)}{\partial x^2} + \frac{\partial^2(\ldots)}{\partial y^2} \tag{9.45}$$

9.3.1 Classical plate theory

Consider first classical plate theory which ignores the transverse shear deformation. Taking $S \to \infty$ in Eqs. (9.44) and (9.45), we get $L(W) = w$ and arrive at the following well-known equations in classical plate theory:

$$D\Delta\Delta w = \overline{p} \tag{9.46}$$

$$\theta_x = -\frac{\partial w}{\partial x}, \quad \theta_y = -\frac{\partial w}{\partial y} \tag{9.47}$$

in which w is the plate deflection. The bending moments are expressed in terms of the curvature changes as

$$M_x = D\big(\kappa_x + \upsilon\kappa_y\big), \quad M_y = D\big(\kappa_y + \upsilon\kappa_x\big), \quad M_{xy} = \frac{D}{2}(1-\upsilon)\kappa_{xy} \tag{9.48}$$

where, in accordance with Eqs. (9.47),

$$\kappa_x = -\frac{\partial^2 w}{\partial x^2}, \quad \kappa_y = -\frac{\partial^2 w}{\partial y^2}, \quad \kappa_{xy} = -2\frac{\partial^2 w}{\partial x \partial y} \tag{9.49}$$

The shear forces follow from the last two equilibrium equations in Eqs. (9.33), i.e.

$$V_x = \frac{\partial M_x}{\partial x} + \frac{\partial M_{xy}}{\partial y}, \quad V_y = \frac{\partial M_y}{\partial y} + \frac{\partial M_{xy}}{\partial x} \tag{9.50}$$

Substitution of these forces into the first equilibrium equation of Eqs. (9.33) yields

$$\frac{\partial^2 M_x}{\partial x^2} + 2\frac{\partial^2 M_{xy}}{\partial x \partial y} + \frac{\partial^2 M_y}{\partial y^2} + \overline{p} = 0 \tag{9.51}$$

If we express the moments in Eqs. (9.48) in terms of deflection with the aid of Eqs. (9.49) and substitute the resulting equations into Eq. (9.51), we arrive at the biharmonic equation, Eq. (9.46) for the plate deflection.

Specific features of classical plate theory follow from the variational formulation of the problem. For the classical theory, Eq. (9.27) can be presented as

$$\delta T = \int_0^a \int_0^b \left(M_x \delta\kappa_x + M_y \delta\kappa_y + M_{xy} \delta\kappa_{xy} - \overline{p}\delta w\right) dxdy = 0$$

Substituting for κ_x, κ_y, and κ_{xy} their expressions from Eqs. (9.49), we get

$$\int_0^a \int_0^b \left[M_x \delta\left(\frac{\partial^2 w}{\partial x^2}\right) + M_y \delta\left(\frac{\partial^2 w}{\partial y^2}\right) + 2M_{xy} \delta\left(\frac{\partial^2 w}{\partial x \partial y}\right) + \overline{p}\delta w \right] dxdy = 0 \tag{9.52}$$

Integration by parts for the first and the second terms of Eq. (9.32) yields in several steps

$$\int_0^a \int_0^b M_x \delta\left(\frac{\partial^2 w}{\partial x^2}\right) dxdy = \left[\int_0^b M_x \delta\left(\frac{\partial w}{\partial x}\right) dy \right]_x - \int_0^a \int_0^b \frac{\partial M_x}{\partial x} \delta\left(\frac{\partial w}{\partial x}\right) dxdy$$

$$= \left[\int_0^b M_x \delta\left(\frac{\partial w}{\partial x}\right) dy \right]_x - \left[\int_0^b \frac{\partial M_x}{\partial x} \delta w dy \right]_x + \int_0^a \int_0^b \frac{\partial^2 M_x}{\partial x^2} \delta w dxdy \quad (x, y)$$

The notations $[\ ]_x$ and $[\ ]_y$ mean that the term $[\ ]$ corresponds to either the plate edge $x = constant$ or $y = constant$. The third term in Eq. (9.52) can be transformed in two ways, i.e.,

$$\int_0^a \int_0^b M_{xy} \delta\left(\frac{\partial^2 w}{\partial x \partial y}\right) dxdy = \left[\int_0^b M_{xy} \delta\left(\frac{\partial w}{\partial y}\right) dy \right]_x - \int_0^a \int_0^b \frac{\partial M_{xy}}{\partial x} \delta\left(\frac{\partial w}{\partial y}\right) dxdy$$

$$= \left[\int_0^b M_{xy} \delta\left(\frac{\partial w}{\partial y}\right) dy \right]_x - \left[\int_0^a \frac{\partial M_{xy}}{\partial x} \delta w dy \right]_y + \int_0^a \int_0^b \frac{\partial^2 M_{xy}}{\partial x \partial y} \delta w dxdy$$

and

$$\int_0^a \int_0^b M_{xy} \delta\left(\frac{\partial^2 w}{\partial x \partial y}\right) dxdy = \left[\int_0^a M_{xy} \delta\left(\frac{\partial w}{\partial x}\right) dx \right]_y - \int_0^a \int_0^b \frac{\partial M_{xy}}{\partial y} \delta\left(\frac{\partial w}{\partial x}\right) dxdy$$

$$= \left[\int_0^a M_{xy} \delta\left(\frac{\partial w}{\partial x}\right) dx \right]_y - \left[\int_0^b \frac{\partial M_{xy}}{\partial y} \delta w dy \right]_x + \int_0^a \int_0^b \frac{\partial^2 M_{xy}}{\partial x \partial y} \delta w dxdy$$

Thus, using Eqs. (9.50) for the transverse forces, we can present the variational equation, Eq. (9.52), in the following form:

$$\int_0^a \int_0^b \left(\frac{\partial^2 M_x}{\partial x^2} + 2\frac{\partial^2 M_{xy}}{\partial x \partial y} + \frac{\partial^2 M_y}{\partial y^2} \right) \delta w dx dy$$

$$+ \left[\int_0^b M_x \delta \left(\frac{\partial w}{\partial y} \right) dy \right]_x + \left[\int_0^a M_y \delta \left(\frac{\partial w}{\partial y} \right) dx \right]_y - \left[\int_0^b V_x \delta w dy \right]_x - \left[\int_0^a V_y \delta w dx \right]_y \tag{9.53}$$

$$+ \left[\int_0^b M_{xy} \delta \left(\frac{\partial w}{\partial y} \right) dy \right]_x + \left[\int_0^a M_{xy} \delta \left(\frac{\partial w}{\partial x} \right) dx \right]_y = 0$$

To demonstrate some special features of classical plate theory, consider a simply supported plate loaded with a pressure

$$q = q_0 \sin \frac{\pi x}{a} \sin \frac{\pi y}{b} \tag{9.54}$$

as shown in Fig. 9.3. The boundary conditions for this plate

$$[w]_x = [w]_y = 0, \quad [M_x]_x = 0, \quad [M_y]_y = 0 \tag{9.55}$$

can be satisfied if the plate deflection has the form

$$w = w_0 \sin \frac{\pi x}{a} \sin \frac{\pi y}{b} \tag{9.56}$$

Substituting Eqs. (9.54) and (9.56) into the governing equation, Eq. (9.46), we arrive at the exact solution of the problem

$$w = -\frac{q_0 a^4 b^4}{\pi^4 D (a^2 + b^2)^2} \sin \frac{\pi x}{a} \sin \frac{\pi y}{b} \tag{9.57}$$

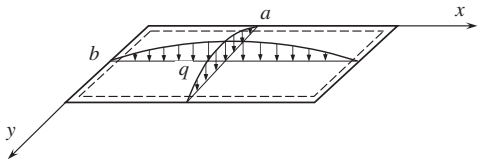


FIGURE 9.3

A simply supported plate loaded with sine pressure.

The transverse shear forces can be determined using Eqs. (9.48)–(9.50) and Eq. (9.57), to give

$$V_x = -D\frac{\partial}{\partial x}(\Delta w) = -\frac{q_0 ab^2}{\pi(a^2+b^2)}\cos\frac{\pi x}{a}\sin\frac{\pi y}{b}$$
$$V_y = -D\frac{\partial}{\partial y}(\Delta w) = -\frac{q_0 a^2 b}{\pi(a^2+b^2)}\sin\frac{\pi x}{a}\cos\frac{\pi y}{b} \tag{9.58}$$

Remove the plate shown in Fig. 9.3 from its supports and find the resultant of the edge reactions, i.e.,

$$R = \int_0^b [V_x(x=a) - V_x(x=0)]dy + \int_0^a [V_y(y=b) - V_y(y=0)]dx \tag{9.59}$$

Substitution of Eqs. (9.58) yields

$$R = \frac{4q_0 ab}{\pi^2} \tag{9.60}$$

The applied load, Eq. (9.54), gives, as expected, the same resultant.

Now returning to the variational equation, Eq. (9.53), the first integral in this equation gives Eq. (9.51). The next four integrals including bending moments and transverse forces are zero according to the boundary conditions, Eqs. (9.55). Moreover, the derivatives of the deflection given by Eq. (9.56) are zero along the plate edges and the last two integrals in Eq. (9.53) with the twisting moment are also zero. Thus, the variational equation, Eq. (9.53), is satisfied and the equilibrium equations are also satisfied along with the corresponding boundary conditions.

Note that actually the deflection determined by Eq. (9.57), being the solution of the fourth-order differential equation, Eq. (9.46), satisfies three boundary conditions at the plate edges. For example, for the edge $x = 0$ we have

$$w = 0, \quad M_x = 0, \quad \theta_y = 0 \tag{9.61}$$

The analysis for clamped plates is similar. Now, suppose that instead of θ_y we specify the twisting moment M_{xy} at the plate edge. Then, the last two integrals in Eq. (9.53) are not zero and the variational equation is not satisfied. The reason for this is associated with Eqs. (9.47) for the rotational angles, according to which the plate in-plane displacements are

$$u_x = z\theta_x = -z\frac{\partial w}{\partial x}, \quad u_y = z\theta_y = -z\frac{\partial w}{\partial y} \tag{9.62}$$

Torsion of the plate induces rotation of the plate element. The angle of in-plane rotation is specified by Eq. (2.33), according to which

$$\omega_z = \frac{1}{2}\left(\frac{\partial u_y}{\partial x} - \frac{\partial u_x}{\partial y}\right) \tag{9.63}$$

Substitution of Eqs. (9.62) yields $\omega_z = 0$, so no rotation can take place. The problem of plate torsion is considered in Section 5.5. The solution given by Eq. (5.93) depends on parameter λ, Eq. (5.94), which includes the transverse shear stiffness of the plate S_x. However, in classical plate theory $S_x \to \infty$ so this

solution does not exist. Thus, classical plate theory cannot be applied to the problems that involve plate torsion.

Nevertheless, some transformations traditionally have been introduced (Timoshenko and Woinowsky-Krieger, 1959) into classical plate theory that formally allow us to generalize the theory. Consider the last two integrals in Eq. (9.53) and apply integration by parts which gives

$$\left[\int_0^b M_{xy}\delta\left(\frac{\partial w}{\partial y}\right)dy\right]_x = \left[M_{xy}\delta w\right]_{x,y} - \left[\int_0^b \frac{\partial M_{xy}}{\partial y}\delta w dy\right]_x \quad (x,y) \tag{9.64}$$

The last term can be added to the integral including Q_x in Eq. (9.53) resulting in the so-called Kirchhoff's shear force

$$K_x = V_x + \frac{\partial M_{xy}}{\partial y} = -D\frac{\partial}{\partial x}\left[\frac{\partial^2 w}{\partial x^2} + (2-\upsilon)\frac{\partial^2 w}{\partial y^2}\right] \qquad (x,y) \tag{9.65}$$

whereby the first term in the right-hand part of Eq. (9.63) is treated as the force applied at the plate corner. Since the plate has four edges, the force $R_1 = -2M_{xy}$ is formally acting at each corner in the direction which is opposite to the direction of the forces K_x and K_y given by Eq. (9.65). As a result, the reactive forces of the plate shown in Fig. 9.3 become as those shown in Fig. 9.4. For the plate shown in Fig. 9.3, Eq. (9.65) yields

$$K_x = V_x\left[1 + \frac{(1-\upsilon)a^2}{a^2+b^2}\right], \quad K_y = V_y\left[1 + \frac{(1-\upsilon)b^2}{a^2+b^2}\right]$$

The distributions of the normalized forces $\overline{V}_x = V_x/V_x^m$ and $\overline{K}_x = K_x/V_x^m$ (in which V_x^m is the maximum shear force acting at the center) along the edge $x = 0$ for a square $(a = b)$ plate with $\upsilon = 0.3$ are presented in Fig. 9.5. As can be seen, K_x (the dashed line) is about 35% higher than V_x (Alfutov, 1992). The resultant force can be found from Eq. (9.59) if we replace V with K. The result

$$R_2 = \frac{4q_0ab}{\pi^2} + \frac{8(1-\upsilon)q_0a^3b^3}{\pi^2(a^2+b^2)^2}$$

shows that R_1 does not balance the applied pressure. The resulting force coincides with the actual force given by Eq. (9.60) if we add four concentrated forces

$$R_1 = -\frac{2(1-\upsilon)q_0a^3b^3}{\pi^2(a^2+b^2)^2}$$

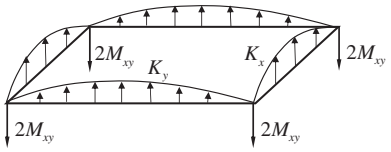


FIGURE 9.4

Support reactions corresponding to the classical plate theory.

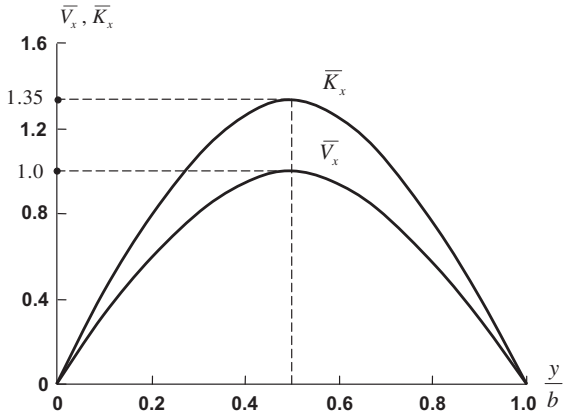


FIGURE 9.5

Distribution of the normalized transverse shear forces over the plate width coordinate y for $x = a$.

applied at the corners. However, for the plate shown in Fig. 9.3 the exact solution of the theory of elasticity equations is known (Galerkin, 1931). For an isotropic plate (see Fig. 9.1) whose surfaces $z = \pm h/2$ are free of shear stresses and for which the pressure is specified by Eq. (9.54), the shear, τ_{xz} and τ_{yz}, and normal, σ_z, transverse stresses are given by

$$\tau_{xz} = \frac{\partial}{\partial x}\left[(1-\upsilon)\Delta F - \frac{\partial^2 F}{\partial z^2}\right], \quad \tau_{yz} = \frac{\partial}{\partial y}\left[(1-\upsilon)\Delta F - \frac{\partial^2 F}{\partial z^2}\right]$$

$$\sigma_z = \frac{\partial}{\partial z}\left[(2-\upsilon)\Delta F - \frac{\partial^2 F}{\partial z^2}\right], \quad \Delta(\,) = \frac{\partial^2(\,)}{\partial x^2} + \frac{\partial^2(\,)}{\partial y^2} + \frac{\partial^2(\,)}{\partial z^2}$$

Here, F is the stress function which has the following form:

$$F = (C_1 \sinh \lambda z + C_2 \cosh \lambda z + C_3 z \cosh \lambda z + C_4 z \sinh \lambda z) \sin \frac{\pi x}{a} \sin \frac{\pi y}{b}, \quad \lambda = \pi\sqrt{\frac{1}{a^2} + \frac{1}{b^2}}$$

Constants C_1–C_4 can be found from the boundary conditions for the stresses σ_z and τ_{xz} (or τ_{yz}) at the plate surfaces $z = \pm h/2$. Omitting the determination of these constants, we can conclude anyway that the foregoing equations for τ_{xz} and τ_{yz} have no singularities at the plate corners and, hence, no corner forces exist at the plate corners. So, it seems that the transformation in Eq. (9.64), and the result given by Eq. (9.65) following from this transformation, are not correct for the plate under study.

Having derived the basic equations, consider the history of the problem. The boundary problem in classical plate theory was originally formulated by S.D. Poisson (1829), who arrived at the governing equation of the fourth order, Eq. (9.46), accompanied by three boundary conditions at the plate edge. No comments were given concerning the contradiction between the equation order and the number of boundary conditions, because Poisson considered the problems of bending of simply supported and clamped plates, for which three boundary conditions automatically reduce to two, and the problem of axisymmetric bending of circular plates, for which only two boundary conditions existed. The inconsistency of Poisson's theory was criticized by G. Kirchhoff (1850), who applied the variational

approach and arrived at two natural boundary conditions at the plate edge. For the free edge $x = constant$, Kirchhoff found that

$$\frac{\partial^2 w}{\partial x^2} + \upsilon \frac{\partial^2 w}{\partial y^2} = 0, \quad \frac{\partial}{\partial x}\left[\frac{\partial^2 w}{\partial x^2} + (2-\upsilon)\frac{\partial^2 w}{\partial y^2}\right] = 0 \tag{9.66}$$

It seems as though the first of these conditions corresponds to the bending moment M_x, whereas the second, in accordance with Eq. (9.65), provides the absence of Kirchhoff shear forces at the plate edges. However, Kirchhoff derived the conditions in Eqs. (9.66) from a variational equation similar to Eq. (9.52) which corresponds to the plate vibration problem. The resulting equation and the natural boundary conditions were not associated with any forces and moments. Kirchhoff forces, Eq. (9.65), were introduced later by Thomson and Tait (1883), who reduced the twisting moment acting at the plate edge to transverse shear forces (as per Eq. (9.65)), applying a static transformation which is valid, in general, for an absolutely rigid body. For an elastic plate, a moment cannot be reduced to forces (Zhilin, 1992, 1995). Thus, the transformation in Eq. (9.64) formally allows us to construct an energy-consistent theory for the plate with free edges or with force boundary conditions. However, this transformation cannot be used for the plates whose edges are fixed with respect to the deflection.

To show this, return to the functional in Eq. (9.53) and to the plate shown in Fig. 9.3 considered as an example. As can be readily seen, the plate deflection w, being zero at the plate edges, provides zero derivatives along the edges. This means that the last two integrals in Eq. (9.53) are zero, and their transformation in Eq. (9.64) has no physical meaning. Consequently, Kirchhoff and Thomson-Tait transformations are not valid for a simply supported plate for which the transverse shear forces are specified by Eqs. (9.58) and no generalized and corner forces following from these transformations can exist. The same is true for a clamped plate and for any plate whose deflection is zero at the boundary. For the force boundary conditions, the situation is different and the sixth-order plate theory discussed in the next section must be applied to study such plates.

9.3.2 Theory of shear deformable plates

Any plate theory which allows us to study those plates with force boundary conditions and not consistent with the Thomson-Tait transformation must result in governing equations of the sixth order. Such a theory has been proposed by E. Reissner (1944), who used a rather cumbersome stress formulation based on the through-the-thickness distribution of normal and shear stresses corresponding to classical plate theory and the variational principle of minimum complementary energy. In the displacement formulation based on Eq. (9.1), i.e.,

$$u_x = u(x,y) + z\theta_x(x,y), \quad u_y = \upsilon(x,y) + z\theta_y(x,y), \quad u_z = w(x,y) \tag{9.67}$$

this theory reduces to Eqs. (9.44) which are studied in this section.

Assume that $L(W) \neq 0$ in which case

$$L(W) = W - \frac{D(1-\upsilon)}{2S}\Delta W, \quad \Delta W = \frac{\partial^2 W}{\partial x^2} + \frac{\partial^2 W}{\partial y^2} \tag{9.68}$$

and introduce the new function $\varphi(x, y)$ such that $L(W) = \varphi$. Then, Eqs. (9.44) are transformed into the form

$$D\Delta\Delta\varphi = \overline{p} \tag{9.69}$$

$$\theta_x = -\frac{\partial\varphi}{\partial x}, \quad \theta_y = -\frac{\partial\varphi}{\partial y}, \quad w = \varphi - \frac{D}{S}\Delta\varphi \tag{9.70}$$

It follows from these equations that $\varphi(x, y)$ is a potential function for the rotation angles, whereas $z\varphi(x, y)$ is a potential function for the in-plane displacements in Eqs. (9.62). As is known, the potential displacement field cannot represent the continuum rotation. Indeed, substituting Eqs. (9.70) into Eq. (9.63), we get

$$\omega_z = \frac{1}{2}\left(\frac{\partial u_y}{\partial x} - \frac{\partial u_x}{\partial y}\right) = 0 \tag{9.71}$$

The potential function determines the so-called penetrating solution (see Eqs. (8.141) and (8.142) for those beams in which such solutions are introduced) that does not vanish at a distance from the plate edges. Note that Eq. (9.69) for φ and Eqs. (9.70) for θ_x and θ_y are similar to Eqs. (9.46) and (9.47) in classical plate theory and coincide with them if $\varphi = w$. However, in the theory under discussion, w is expressed by the last equation of Eqs. (9.70) in which the second term allows for the influence of the transverse shear deformation on the plate deflection.

We can expect that the theory described by Eqs. (9.69) and (9.70) is not complete and these equations must be supplemented with an additional equation for the following reasons:

1. The initial set of equations, Eqs. (9.44), is of the sixth order, whereas Eqs. (9.69) and (9.70) are only of the fourth order.
2. The equations obtained, Eqs. (9.69) and (9.70), cannot describe the plate torsion.
3. The initial equations, Eqs. (9.44), are reduced to Eqs. (9.69) and (9.70) under the condition that $L(W) \neq 0$. So, a natural question arises as to what happens if $L(W)$ in Eq. (9.68) is zero.

To derive the desired equation, return to the initial equations, Eqs. (9.36), and write them for a transversely isotropic plate. Note that because the pressure $\overline{p}$ is allowed for by the penetrating potential φ in accordance with Eq. (9.69), the equation under derivation must be homogeneous, i.e., correspond to $\overline{p} = 0$. So, taking $\overline{p} = 0$ and using Eqs. (9.43) for the stiffness coefficients, we can transform Eqs. (9.36) into the following form:

$$\frac{D}{S}\left(\frac{\partial^2\theta_x}{\partial x^2} + \frac{1-\upsilon}{2}\frac{\partial^2\theta_x}{\partial y^2}\right) + \frac{D(1+\upsilon)}{2S}\frac{\partial^2\theta_y}{\partial x\partial y} - \theta_x - \frac{\partial w}{\partial x} = 0 \tag{9.72}$$

$$\frac{D}{S}\left(\frac{\partial^2\theta_y}{\partial y^2} + \frac{1-\upsilon}{2}\frac{\partial^2\theta_x}{\partial x^2}\right) + \frac{D(1+\upsilon)}{2S}\frac{\partial^2\theta_x}{\partial x\partial y} - \theta_y - \frac{\partial w}{\partial y} = 0$$

$$\frac{\partial\theta_x}{\partial x} + \frac{\partial\theta_y}{\partial y} + \Delta w = 0 \tag{9.73}$$

As can be seen, Eq. (9.73) is satisfied if we take

$$\theta_x = \frac{\partial\psi}{\partial y}, \quad \theta_y = -\frac{\partial\psi}{\partial x}, \quad w = 0 \tag{9.74}$$

Then, Eqs. (9.72) become

$$\frac{\partial}{\partial y}L(\psi)=0,\quad \frac{\partial}{\partial x}L(\psi)=0 \tag{9.75}$$

in which operator L is specified by Eqs. (9.68). It follows from Eqs. (9.75) that $L(\psi)=c$. The solution of this equation is $\psi=\psi_0+c$ where ψ_0 is the solution for the corresponding homogeneous equation $L(\psi)=0$ and c is a constant. Since θ_x and θ_y are the derivatives of ψ, this constant is not important and we can take $c=0$. Thus, the final equation is

$$\Delta\psi-\frac{2S}{D(1-\upsilon)}\psi=0 \tag{9.76}$$

The function ψ can be referred to as the rotational potential. Indeed, substituting Eqs. (9.75) into Eqs. (9.67) for u_x and u_y and then the resulting expressions into Eq. (9.71) for ω_z, we get

$$\omega_z=-\frac{z}{2}\Delta\psi$$

For a homogeneous plate, $S=Gh=Eh/2(1+\upsilon)$ and $D=Eh^3/12(1-\upsilon^2)$. Introducing the normalized coordinates $\overline{x}=x/a$ and $\overline{y}=y/b$, we can transform Eq. (9.76) into the form

$$\frac{\partial^2\psi}{\partial\overline{x}^2}+\frac{a^2}{b^2}\frac{\partial^2\psi}{\partial\overline{y}^2}-k^2\psi=0,\quad k^2=\frac{12a^2}{h^2} \tag{9.77}$$

For relatively thin plates, i.e., for high ratios of *a/h*, the value of the parameter k is also high and the foregoing equation specifies the boundary-layer solution associated with plate torsion in the vicinity of the edges. Assume, for example, that $\psi=\psi(\overline{x})$. Then, Eq. (9.77) has the solution

$$\psi(\overline{x})=ce^{\left(2\sqrt{3}a\overline{x}\right)/h} \tag{9.78}$$

rapidly changing in the vicinity of the plate edge.

Historically, an equation analogous to Eqs. (9.76) and (9.77) was obtained by M. Lévy, M.J. Boussinesq, and W. Thomson and P. Tait at the end of the 19th century (Todhunter and Pearson, 1960), who formulated a theory of elasticity problem for a plate with particular boundary conditions. According to these conditions, the plate is loaded with edge forces that are statically equivalent to the transverse force V_x and twisting moment M_{xy} such that the Kirchhoff shear force K_x in Eq. (9.65) is zero. As a result, a second-order three-dimensional equation specifying the boundary-layer solution has been obtained. The two-dimensional version of this equation has been derived for plates by E. Reissner (1944).

Thus, the rotation angles of the plate element are composed of two functions specified by Eqs. (9.70) and (9.74), i.e.,

$$\theta_x=-\frac{\partial\varphi}{\partial x}+\frac{\partial\psi}{\partial y},\quad \theta_y=-\frac{\partial\varphi}{\partial y}-\frac{\partial\psi}{\partial x} \tag{9.79}$$

in which φ is the penetrating potential which satisfies the biharmonic equation

$$D\Delta\Delta\varphi=\overline{p} \tag{9.80}$$

and ψ is the rotational potential that can be found as the boundary-layer solution from Eq. (9.76), i.e.,

$$\Delta\psi-s^2\psi=0,\quad s^2=\frac{2S}{D(1-\upsilon)} \tag{9.81}$$

The plate deflection depends on the penetrating potential only, i.e.,

$$w = \varphi - \frac{D}{S}\Delta\varphi \tag{9.82}$$

The following equations for the bending and twisting moments are derived using Eqs. (9.48), (9.34), and (9.79):

$$\begin{aligned} M_x &= -D\left[\frac{\partial^2\varphi}{\partial x^2} + \upsilon\frac{\partial^2\varphi}{\partial y^2} - (1-\upsilon)\frac{\partial^2\psi}{\partial x\partial y}\right] \\ M_y &= -D\left[\frac{\partial^2\varphi}{\partial y^2} + \upsilon\frac{\partial^2\varphi}{\partial x^2} - (1-\upsilon)\frac{\partial^2\psi}{\partial x\partial y}\right] \\ M_{xy} &= -D(1-\upsilon)\left[\frac{\partial^2\varphi}{\partial x\partial y} + \frac{1}{2}\left(\frac{\partial^2\psi}{\partial x^2} - \frac{\partial^2\psi}{\partial y^2}\right)\right] \end{aligned} \tag{9.83}$$

Finally, the equations for the transverse shear forces follow from Eqs. (9.32), (9.34), and (9.82), i.e.,

$$V_x = S\left(\theta_x + \frac{\partial w}{\partial x}\right) = S\frac{\partial\psi}{\partial y} - D\frac{\partial}{\partial x}\Delta\varphi, \quad V_y = S\left(\theta_y + \frac{\partial w}{\partial y}\right) = S\frac{\partial\psi}{\partial x} - D\frac{\partial}{\partial y}\Delta\varphi \tag{9.84}$$

The variational equation

$$\begin{aligned} \int_0^a\int_0^b \Bigg[& M_x\delta\left(\frac{\partial\theta_x}{\partial x}\right) + M_y\delta\left(\frac{\partial\theta_y}{\partial y}\right) + M_{xy}\delta\left(\frac{\partial\theta_x}{\partial y} + \frac{\partial\theta_y}{\partial x}\right) \\ & + V_x\delta\left(\theta_x + \frac{\partial w}{\partial x}\right) + V_y\delta\left(\theta_y + \frac{\partial w}{\partial y}\right) - \overline{p}\delta w\Bigg] dxdy = 0 \end{aligned} \tag{9.85}$$

provides the equilibrium equations, Eqs. (9.33), and the following natural boundary conditions:

$$\begin{aligned} \left[\int_0^b \left(M_x\delta\theta_x + M_{xy}\delta\theta_y + V_x\delta w\right)dy\right]_x &= 0 \\ \left[\int_0^a \left(M_y\delta\theta_y + M_{xy}\delta\theta_x + V_y\delta w\right)dx\right]_y &= 0 \end{aligned} \tag{9.86}$$

Consider typical boundary conditions for the plate edge x=*constant*. First, consider the simply supported plates for which Eq. (9.86) provides two possible types of boundary conditions. The classical version of the boundary conditions is

$$w = 0, \quad M_x = 0 \quad \theta_y = 0 \tag{9.87}$$

The physical interpretation (see Fig. 9.6a) is that the plate is supported by the walls that are absolutely rigid in the wall plane providing the conditions $w = 0$ and $\theta_y = 0$, but have zero out-of-plane bending stiffness, so that $M_x = 0$. Substituting Eqs. (9.79), and (9.82), (9.83) in Eqs. (9.87), we get

$$\varphi - \frac{D}{S}\Delta\varphi = 0, \quad \frac{\partial^2\varphi}{\partial x^2} + \upsilon\frac{\partial^2\varphi}{\partial y^2} - (1-\upsilon)\frac{\partial^2\psi}{\partial x\partial y} = 0, \quad \frac{\partial\varphi}{\partial y} = -\frac{\partial\psi}{\partial x} \tag{9.88}$$

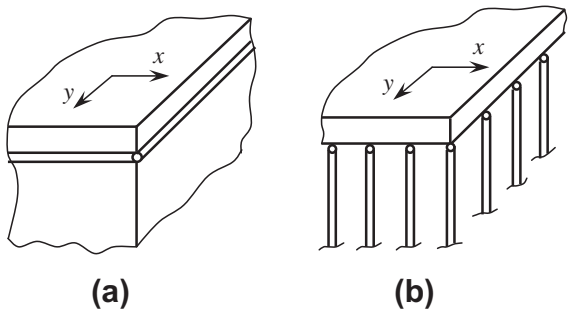


FIGURE 9.6

Two versions of a simply-supported plate edge corresponding to Eqs. (9.87) (a) and (9.92) (b).

Using the third of these equations to eliminate ψ from the second equation, we get $\Delta\varphi = 0$. Thus, it follows from the first equation of Eqs. (9.88) that $\varphi = 0$, and the boundary conditions given by Eqs. (9.88) reduce to

$$\varphi = 0, \quad \frac{\partial^2 \varphi}{\partial x^2} = 0, \quad \frac{\partial \psi}{\partial x} = 0 \tag{9.89}$$

For the edge $y = constant$, Eqs. (9.89) can be supplemented with

$$\varphi = 0, \quad \frac{\partial^2 \varphi}{\partial y^2} = 0, \quad \frac{\partial \psi}{\partial y} = 0 \tag{9.90}$$

Consider the last of the boundary conditions in Eqs. (9.89) and (9.90). The rotational potential ψ satisfies the homogeneous equation, Eq. (9.81), and the zero boundary conditions for the function normal derivatives at the plate contour. In this case, Eq. (9.81) has only a trivial solution, so that $\psi = 0$. Then, the boundary conditions (9.89) and (9.90) become

$$\begin{aligned} &\text{at} \quad x = constant \quad \varphi = 0, \quad \frac{\partial^2 \varphi}{\partial x^2} = 0 \\ &\text{at} \quad y = constant \quad \varphi = 0, \quad \frac{\partial^2 \varphi}{\partial y^2} = 0 \end{aligned} \tag{9.91}$$

Thus, for the conventional (classical) simply supported edge, the boundary layer solution does not exist (Pelekh, 1970; Vasiliev, 1992, 2000), and the plate bending is governed by the penetrating solution which is specified by the fourth-order equation, Eq. (9.80), with two boundary conditions, Eqs. (9.91), at the plate edge. The second term in Eq. (9.82) for the plate deflection allows for the transverse shear deformation. Clearly, no Kirchhoff or corner forces exist in this case.

It follows from the natural boundary condition given by Eqs. (9.86) that the other version of a simple support can exist if we replace the condition $\theta_y = 0$ with $M_{xy} = 0$, i.e.,

$$w = 0, \quad M_x = 0, \quad M_{xy} = 0 \tag{9.92}$$

The physical interpretation of these boundary conditions is presented in Fig. 9.6b. The plate is supported by absolutely rigid columns ($w = 0$) and has zero bending stiffnesses in the edge plane and in

the direction normal to the edge ($M_{xy} = 0$ and $M_x = 0$). Note that the boundary conditions in Eqs. (9.92) cannot exist in the classical plate theory based on Eqs. (9.62). Indeed, if $w = 0$ at the edge $x =$ *constant*, then $\theta_y = 0$ at this edge and M_{xy} cannot be zero. However, for the sixth-order theory, the boundary conditions given by Eqs. (9.92) can formally exist. Using Eqs. (9.82) and (9.83), we get

$$\varphi - \frac{D}{S}\Delta\varphi = 0 \tag{9.93}$$

$$\frac{\partial^2\varphi}{\partial x^2} + \upsilon\frac{\partial^2\varphi}{\partial y^2} - (1-\upsilon)\frac{\partial^2\psi}{\partial x\partial y} = 0 \tag{9.94}$$

$$2\frac{\partial^2\varphi}{\partial x\partial y} + \frac{\partial^2\psi}{\partial x^2} - \frac{\partial^2\psi}{\partial y^2} = 0 \tag{9.95}$$

These boundary conditions cannot be reduced to two equations and the set of the sixth-order equations, Eqs. (9.80) and (9.81), must be solved with these conditions. The problems of plate bending with boundary conditions in Eq. (9.92) have been solved by Schäfer (1952) for a rectangular plate under sine pressure (see Fig. 9.3), by Kromm (1955) for a square plate loaded with uniform pressure, and by Sheremetiev et al. (1968) for a square plate under the action of the central concentrated force.

As an example, consider a square plate loaded with cosine pressure as shown in Fig. 9.7. Placing the center of the coordinate frame at the plate center, we assume that

$$\overline{p} = -q = q_0 \cos\lambda_1 x \cos\lambda_1 y \tag{9.96}$$

where $\lambda_1 = \pi/a$. The boundary conditions in Eqs. (9.93)–(9.95) must be satisfied at $x = \pm a/2$. The penetrating potential φ satisfies Eq. (9.80) and can be decomposed as

$$\varphi = \varphi_h + \varphi_q \tag{9.97}$$

where

$$\varphi_q = \varphi_0 \cos\lambda_1 x \cos\lambda_1 y, \quad \varphi_0 = -\frac{q_0 a^4}{4\pi^4 D} \tag{9.98}$$

is the particular solution, whereas φ_h is the solution of the corresponding homogeneous equation

$$\Delta\Delta\varphi_h = 0 \tag{9.99}$$

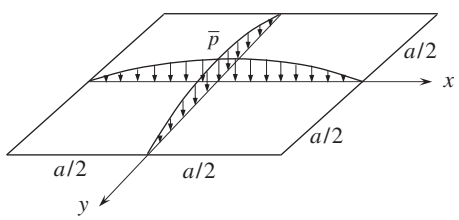


FIGURE 9.7

A square plate loaded with cosine pressure.

Taking into account the symmetry of the problem (see Fig. 9.7), the solution of this equation can be represented as

$$\varphi_h = \sum_m [\varphi_m(y) \cos \lambda_m x + \varphi_m(x) \sin \lambda_m y] \tag{9.100}$$

where $\lambda_m = (2m-1)\pi/a$ and φ_m is one and the same function of coordinates x or y. Substituting the solution, Eq. (9. 100), into Eq. (9.99), we arrive at the following equation for, e.g., $\varphi_m(y)$:

$$\varphi_m^{IV} - 2\lambda_m^2 \varphi_m'' + \lambda_m^4 \varphi_m = 0$$

The symmetric solution of this equation is

$$\varphi_m = C_1^m \cosh \lambda_m y + C_2^m y \sinh \lambda_m y$$

Thus, the penetrating solution becomes

$$\begin{aligned} \varphi = \varphi_0 \cos \lambda_1 x \cos \lambda_1 y + \sum_m \big[&\big(C_1^m \cosh \lambda_m y + C_2^m y \sinh \lambda_m y\big)\cos \lambda_m x \\ &+ \big(C_1^m \cosh \lambda_m x + C_2^m x \sinh \lambda_m x\big)\cos \lambda_m y\big] \end{aligned} \tag{9.101}$$

The rotational potential ψ can be found as the combination of antisymmetric functions, i.e.,

$$\psi = \sum_m [\psi_m(y) \sin \lambda_m x - \psi_m(x) \sin \lambda_m y]$$

Substituting this solution into Eq. (9.81), we get, e.g., for $\psi_m(y)$,

$$\psi_m'' + \big(\lambda_m^2 + s^2\big)\psi_m = 0$$

Thus, $\psi_m = B_m \sinh k_m y$ and the rotational potential becomes

$$\psi = \sum_m B_m(\sinh k_m y \cdot \sin \lambda_m x - \sinh k_m x \cdot \sin \lambda_m y) \tag{9.102}$$

Here,

$$k_m^2 = \lambda_m^2 + s^2 = \lambda_m^2 + \frac{2S}{D(1-\upsilon)} \tag{9.103}$$

To determine the constants C_1^m, C_2^m, and B_m in Eqs. (9.101) and (9.102), we must apply the boundary conditions, Eqs. (9.93)–(9.95) for the edge $x = a/2$. Substituting the solutions, Eqs. (9.101) and (9.102), into the boundary conditions, Eqs. (9.93) and (9.94), we arrive at the following two algebraic equations:

$$\begin{aligned} &\lambda_m C_1^m + \left(\overline{\lambda}_m \tanh \overline{\lambda}_m + 2\lambda_m^2 \frac{D}{S}\right) C_2^m = 0 \\ &\big(1-\upsilon\big) \cosh \overline{\lambda}_m \cdot C_1^m + \lambda_m \big[2 \cosh \overline{\lambda}_m + \big(1-\upsilon\big)\overline{\lambda}_m \sinh \overline{\lambda}_m\big] C_2^m \\ &+(1-\upsilon)\lambda_m k_m \cosh \overline{k}_m \cdot B_m = 0, \quad \overline{\lambda}_m = \frac{1}{2}\lambda_m a, \quad \overline{k}_m = \frac{1}{2} k_m a \end{aligned} \tag{9.104}$$

which allow us to express the constants C_1^m and C_2^m in terms of B_m. The third boundary condition, Eq. (9.95), yields the following equation:

$$\begin{aligned}2(1-\upsilon)\varphi_0\lambda_1^2 \sin \lambda_1 y - 2(1-\upsilon)\sum_m \Big[&\lambda_m^2\big(\sin \overline{\lambda}_m \cdot \sinh \lambda_m y + \sinh \overline{\lambda}_m \cdot \sin \lambda_m y\big)C_1^m \\ &+ \lambda_m\big(\sin \overline{\lambda}_m \cdot \sinh \lambda_m y + \lambda_m y \sin \overline{\lambda}_m \cdot \cosh \lambda_m y \\ &+ \sinh \overline{\lambda}_m \cdot \sin \lambda_m y + \overline{\lambda}_m \cosh \overline{\lambda}_m \cdot \sin \lambda_m y\big)C_2^m\Big] \\ -\sum_m \big(\lambda_m^2 + k_m^2\big)\big(\sin \overline{\lambda}_m \cdot \sinh k_m y + \sinh \overline{k}_m \cdot \sin \lambda_m y\big)B_m &= 0\end{aligned} \tag{9.105}$$

Multiplying this equation by $\sin \lambda_n y$, integrating with respect to y from *-a/2* to *a/2*, and using the following integrals:

$$\int_{-a/2}^{a/2} \sin^2 \lambda_n dy = a,$$

$$\int_{-a/2}^{a/2} \sinh \lambda_m y \cdot \sin \lambda_n y dy = \frac{2}{\lambda_m^2 + \lambda_n^2}\big(\lambda_m \cosh \overline{\lambda}_m \cdot \sin \overline{\lambda}_n - \lambda_n \sinh \overline{\lambda}_m \cdot \cos \overline{\lambda}_n\big),$$

$$\int_{-a/2}^{a/2} y \cdot \cosh \lambda_m y \cdot \sin \lambda_n y dy = \frac{2}{\lambda_m^2 + \lambda_n^2}\left(\overline{\lambda}_m \sinh \overline{\lambda}_m \cdot \sin \overline{\lambda}_n - \frac{\lambda_m^2 - \lambda_n^2}{\lambda_m^2 + \lambda_n^2} \cosh \overline{\lambda}_m \cdot \sin \overline{\lambda}_n\right),$$

we arrive at an infinite set of algebraic equations for constants B_m. Only the first of these equations includes φ_0, whereas the rest of the equations are homogeneous. For a one-term approximation of the acting pressure given by Eq. (9.96), we can retain in the foregoing series only the first term taking $m = 1$ and $\lambda_m = \lambda_1 = \pi/a$. Then, Eq. (9.105) yields

$$\begin{aligned}&2C_1\lambda_1^2 \cosh \overline{\lambda}_1\big(1 + 2\overline{\lambda}_1 \tanh \overline{\lambda}_1\big) + 2C_2\lambda_1 \cosh \overline{\lambda}_1 \cdot \Big(1 + 3\overline{\lambda}_1 \tanh \overline{\lambda}_1 + 2\overline{\lambda}_1^2 \tanh^2 \overline{\lambda}_1\Big) \\ &+B_1\big(\lambda_1^2 + k_1^2\big)\big(\cosh \overline{\lambda}_1 + 2\overline{\lambda}_1 \sinh \overline{k}_1\big) = 4\varphi_0\lambda_1^2\overline{\lambda}_1\end{aligned} \tag{9.106}$$

in which $\overline{\lambda}_1 = \lambda_1 a/2 = \pi/2$, $\overline{k}_1 = k_1 a/2$.

The equations obtained, Eqs. (9.104) and (9.106), allow us to determine the constants C_1, C_2, and B_1. The final result looks rather cumbersome; however, for relatively thin plates it can be significantly

simplified. Neglecting the effect of shear deformation on the penetrating potential (i.e., taking $\varphi = w$) and taking into account that $k_1 \gg \lambda_1$, we get

$$C_1 = \frac{(1-\upsilon)\lambda_1\overline{\lambda}_1 \tanh \overline{\lambda}_1}{k_1 \cosh \overline{\lambda}_1}\varphi_{0,} \quad C_2 = -\frac{(1-\upsilon)\lambda_1^2\varphi_0}{k_1 \cosh \overline{\lambda}_1}$$

$$B_1 = \frac{2\lambda_1^2\varphi_0}{k_1^2 \sinh \overline{k}_1}$$

The final approximate expression for the transverse shear force at the edge $x = a/2$ (see Fig. 9.7) becomes

$$\overline{V}_x^* = \frac{V_x^*}{V_x^m} = \cos \lambda_1 y - \frac{(1-\upsilon)}{\pi}\left(\frac{\sqrt{3}a}{h}\frac{\cosh k_1 y}{\sinh \overline{k}_1} - \frac{\pi}{2}\cos \lambda_1 y\right) \tag{9.107}$$

where the notation (*) shows that V_x^* corresponds to the theory of shear deformable plates and V_x^m is the maximum shear force at the edge corresponding to classical plate theory. The function $\overline{V}_x^*(y)$ is shown in Fig. 9.8. At the central part of the edge, the shear force specified by Eq. (9.107) coincides with the generalized Kirchhoff shear force K_x in Eq. (9.65) as per classical plate theory (this force is shown in Fig. 9.5). As discussed in Section 9.3.1, the force K_x is accompanied by a concentrated corner

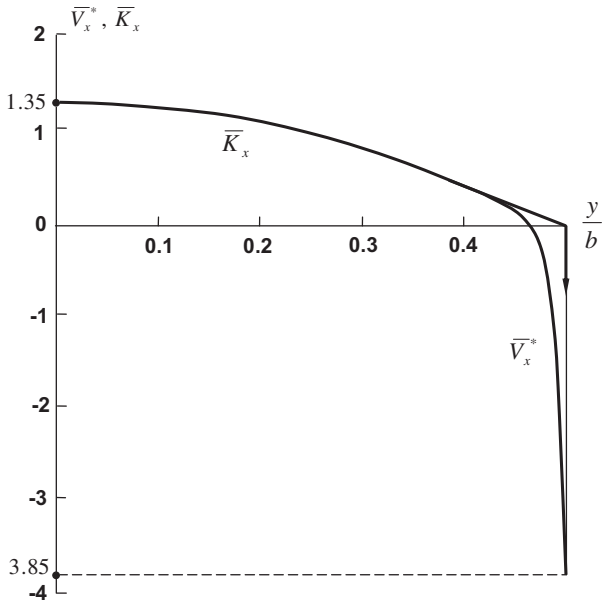


FIGURE 9.8

Distribution of the normalized transverse shear forces over the edge $x = \alpha/2$.

force which is also shown in Fig. 9.8. In the vicinity of the corner, the force V_x^* changes its sign (see the dashed line in Fig. 9.8). At the plate corner $\left(y = \frac{a}{2}\right)$, Eq. (9.107) yields

$$\overline{V}_x^*\left(\frac{a}{2}\right) = -\frac{(1-\upsilon)\sqrt{3}a}{\pi h}$$

If the relative thickness of the plate, $\overline{h} = h/a$, becomes infinitely small, $\overline{V}_x^*(a/2)$ becomes infinitely high and can be treated as a concentrated force. Thus, for the particular boundary conditions in Eq. (9.92), the Kirchhoff shear force is close to the actual reaction of the plate support and the corner force following from Kirchhoff and Thomson-Tait transformations corresponds to the asymptotic value of this reaction for an infinitely thin plate.

Thus, for a plate with the boundary conditions given by Eqs. (9.92), the solution corresponding to the theory of shear deformable plates demonstrates plate behavior which is asymptotically close to the traditional solution corresponding to classical theory which is shown in Fig. 9.4. However, it should be emphasized that this solution exists only for special boundary conditions, Eqs. (9.92), and the existing recommendation (Timoshenko and Woinovsky-Krieger, 1959) to use it for simply supported plates with classical boundary conditions, Eqs. (9.87), is not consistent.

Consider a clamped plate, for which

$$w = 0, \quad \theta_x = 0, \quad \theta_y = 0$$

at the edge $x = constant$. Applying Eqs. (9.79) and (9.82), we arrive at

$$\varphi - \frac{D}{S}\Delta\varphi = 0, \quad \frac{\partial\varphi}{\partial x} = \frac{\partial\psi}{\partial y}, \quad \frac{\partial\varphi}{\partial y} = -\frac{\partial\psi}{\partial x} \tag{9.108}$$

In contrast to a simply supported plate with classical boundary conditions, Eqs. (9.87), these three conditions cannot be exactly reduced to two. However, as demonstrated in the foregoing example, the boundary-layer effect hinders the solution considerably, and an attempt can be made to solve this problem using only the penetrating potential. So, take $\psi = 0$ and reduce Eqs. (9.108) to

$$\varphi - \frac{D}{S}\Delta\varphi = 0, \quad \frac{\partial\varphi}{\partial x} = 0, \quad \frac{\partial\varphi}{\partial y} = 0 \tag{9.109}$$

The third of these conditions can be integrated along the edge $x = constant$ which yields $\varphi = C$, where C is some constant. The same result can be obtained for the clamped edge $y = constant$. Thus, we can replace φ with $\varphi + C$. Since C is some arbitrary constant, it can be taken equal to zero. As a result, the boundary conditions for the penetrating solution become

$$\frac{\partial\varphi}{\partial x} = 0, \quad \varphi - \frac{D}{S}\Delta\varphi = 0 \tag{9.110}$$

and are consistent with the fourth order of the equation for the penetrating solution, Eq. (9.80). Thus, for clamped plates, the theory of shear deformable plates can be approximately reduced to the fourth-order equation, Eq. (9.80), for the penetrating potential and two boundary conditions at the plate edge.

To support the results obtained, consider the cylindrical bending of a plate. Taking $\varphi = \varphi(x)$, we arrive at the following equation and boundary conditions:

$$D\varphi^{IV} = \overline{p}, \quad [\varphi']_x = \left[\varphi - \frac{D}{S}\varphi''\right]_x = 0$$

where $(\quad)' = d(\quad)/dx$. As can be seen, four constants are required for the solution for constant pressure, i.e.,

$$\varphi = \frac{\overline{p}x^4}{24} + \frac{1}{3}C_1x^3 + \frac{1}{2}C_2x^2 + C_3x + C_4$$

which can be found from the four boundary conditions at $x = 0$ and $x = a$. We can formally add the constant C discussed earlier to φ, but it can be included into the unknown constant C_4.

For the free edge, as well as for any edge on which the twisting moment M_{xy} is preassigned, three boundary conditions cannot be reduced to two and the sixth-order equations of the theory of shear deformable plates should be used to study the problem.

As an example, consider a semi-infinite plate with simply supported longitudinal edges (see Fig. 9.9), for which the exact solutions can be found. Let the plate be loaded with pressure

$$\overline{p} = p = p_0 \sin \lambda y \tag{9.111}$$

where $\lambda = \pi/b$. For the longitudinal edges $y = 0$ and $y = b$, the boundary conditions are

$$w = 0, \quad M_y = 0, \quad \theta_x = 0$$

or exactly

$$\varphi - \frac{D}{S}\Delta\varphi = 0, \quad \frac{\partial^2\varphi}{\partial y^2} + \upsilon\frac{\partial^2\varphi}{\partial x^2} - (1-\upsilon)\frac{\partial^2\psi}{\partial x\partial y} = 0, \quad \frac{\partial\varphi}{\partial x} = \frac{\partial\psi}{\partial y}$$

These boundary conditions can be satisfied if we take

$$\varphi = \Phi(x)\sin\lambda y, \quad \psi = \Psi(x)\cos\lambda y \tag{9.112}$$

Substitution of Eqs. (9.112) into the governing equations, Eqs. (9.80) and (9.81), yields

$$D\left(\Phi^{IV} - 2\Phi'' + \Phi\right) = p_0 \tag{9.113}$$

$$\Psi'' - s^2\Psi = 0, \quad s^2 = \frac{2S}{D(1-\upsilon)} \tag{9.114}$$

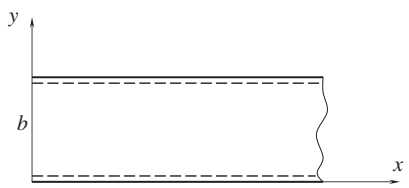


FIGURE 9.9

A semi-infinite simply supported plate.

The solutions of these equations in conjunction with Eqs. (9.112) for the plate shown in Fig.9.9 give

$$\varphi = \left[(C_1 + C_2 x)e^{-\lambda x} + \frac{p_0}{D\lambda^4}\right]\sin \lambda y \tag{9.115}$$

$$\psi = Be^{-kx}\cos \lambda y, \quad k^2 = \lambda^2 + s^2 \tag{9.116}$$

The following three cases are discussed.

1. Consider first a plate simply supported at the edge $x = 0$. The classical boundary conditions

$$w = 0, \quad M_x = 0, \quad \theta_y = 0 \tag{9.117}$$

can be represented as

$$\varphi - \frac{D}{S}\Delta\varphi = 0, \quad \frac{\partial^2 \varphi}{\partial x^2} + \upsilon\frac{\partial^2 \varphi}{\partial y^2} - (1-\upsilon)\frac{\partial^2 \psi}{\partial x \partial y} = 0, \quad \frac{\partial \varphi}{\partial y} = -\frac{\partial \psi}{\partial x}$$

Substitution of Eqs. (9.115) and (9.116) yields

$$C_1 = -\frac{p_0}{D\lambda^4}, \quad C_2 = -\frac{p_0}{2D\lambda^3}, \quad B = 0$$

Thus, $\psi = 0$ and the solution is governed by the penetrating potential φ only.
For an isotropic plate with parameters

$$\frac{h}{b} = 0.05, \quad \upsilon = 0.3, \quad \frac{E}{G} = 2.6, \quad \lambda = \frac{\pi}{b}, \quad k = \frac{69.4}{b} \tag{9.118}$$

the final solution specifies the following expressions for the plate deflection, moments, and transverse force:

$$\begin{aligned}
w^{(1)} &= 1.0059\frac{p_0}{D\lambda^4}\left[1 - e^{-\lambda x}\left(1 + 1.56\frac{x}{b}\right)\right]\sin \lambda y \\
M_x^{(1)} &= 0.3\frac{p_0}{\lambda^2}\left[1 - e^{-\lambda x}\left(1 - 3.66\frac{x}{b}\right)\right]\sin \lambda y \\
M_{xy}^{(1)} &= -0.35\frac{p_0}{\lambda^2}e^{-\lambda x}\left(1 + 3.14\frac{x}{b}\right)\cos \lambda y \\
V_x^{(1)} &= \frac{p_0}{\lambda}e^{-\lambda x}\sin \lambda y
\end{aligned} \tag{9.119}$$

Compare this solution with the results corresponding to classical plate theory which gives

$$w_c^{(1)} = \frac{p_0}{D\lambda^4}\left[1 - e^{-\lambda x}\left(1 + 1.57\frac{x}{b}\right)\right]\sin \lambda y$$

This deflection is close to that determined by the first equation in Eqs. (9.119), whereas the moments and the force are exactly the same as those given by Eqs. (9.119).

2. Consider the second version of the simple support, according to which at the edge $x = 0$ we have

$$w = 0, \quad M_x = 0, \quad M_{xy} = 0 \tag{9.120}$$

or

$$\varphi - \frac{D}{S}\Delta\varphi = 0, \quad \frac{\partial^2\varphi}{\partial x^2} + \upsilon\frac{\partial^2\varphi}{\partial y^2} - (1-\upsilon)\frac{\partial^2\psi}{\partial x\partial y} = 0, \quad 2\frac{\partial^2\varphi}{\partial x\partial y} + \frac{\partial^2\psi}{\partial x^2} - \frac{\partial^2\psi}{\partial y^2} = 0$$

The final solution is

$$w^{(2)} = 1.0057\frac{p_0}{D\lambda^4}\left[1 - e^{-\lambda x}\left(1 + 1.49\frac{x}{b}\right)\right]\sin\lambda y$$

$$M_x^{(2)} = 0.3\frac{p_0}{\lambda^2}\left[1 - 0.89e^{-\lambda x}\left(1 - 4.08\frac{x}{b}\right) - 0.11e^{-kx}\right]\sin\lambda y$$

$$M_{xy}^{(2)} = -0.36\frac{p_0}{\lambda^2}\left[e^{-\lambda x}\left(1 + 2.95\frac{x}{b}\right) - e^{-kx}\right]\cos\lambda y$$

$$V_x^{(2)} = 0.96\frac{p_0}{\lambda}\left(e^{-\lambda x} + 0.38e^{-kx}\right)\sin\lambda y$$

As can be seen, $w^{(2)}$ is rather close to $w^{(1)}$. The results of these calculations are presented in Figs. 9.10–9.12. The normalized bending moments $\overline{M}_x = M_x\lambda^2/p_0$ acting at $y = b/2$ (see Fig. 9.9) are shown in Fig. 9.10 as functions of x. It follows from the figure that the moment $\overline{M}_x^{(2)}$ corresponding to the boundary conditions given by Eqs. (9.120) is quite close to the moment $\overline{M}_x^{(1)}$ corresponding to the classical boundary conditions, Eqs. (9.117). The difference in the twisting moments $\overline{M}_{xy}^{(1)}$ and $\overline{M}_{xy}^{(2)}$ is significant only in the vicinity of the plate edge, where $\overline{M}_{xy}^{(2)} = 0$ in

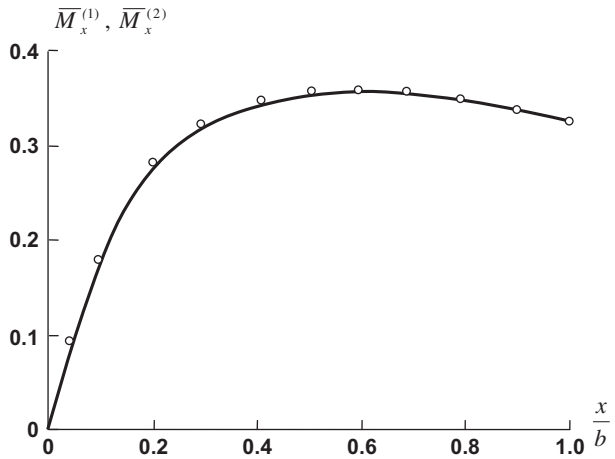


FIGURE 9.10

Distribution of the normalized bending moments $\overline{M}_x^{(1)}(y = b/2)$ (——) and $\overline{M}_x^{(2)}(y = b/2)$ (∘ ∘ ∘) along the x-axis.

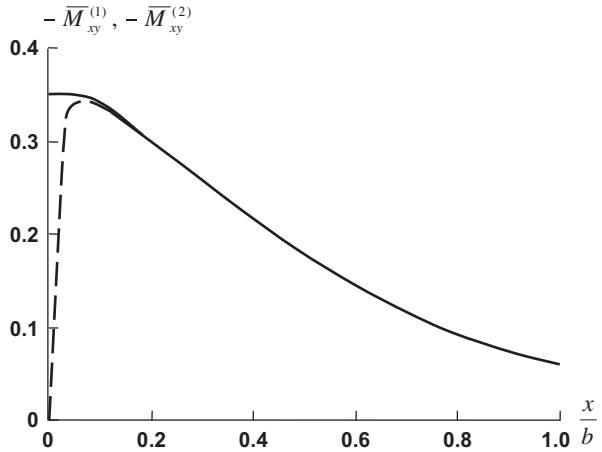


FIGURE 9.11

Distribution of the normalized twisting moments $\overline{M}_{xy}^{(1)}(y=0)$ (———) and $\overline{M}_{xy}^{(2)}(y=0)$ (— — —) along the x-axis.

accordance with Eqs. (9.120), whereas $\overline{M}_{xy}^{(1)}$ is a reactive moment. The distributions of the shear forces are presented in Fig. 9.12, where $\overline{V}_x^{(1)}$ and $\overline{V}_x^{(2)}$ correspond to the boundary conditions in Eqs. (9.117) and (9.120), respectively. For comparison, the Kirchhoff shear force

$$K_x^{(1)} = V_x^{(1)} + \frac{\partial M_{xy}^{(1)}}{\partial y} = \frac{p_0}{\lambda} e^{-\lambda x}\left(1.35 + 1.10\frac{x}{b}\right)\sin \lambda y$$

corresponding to the classical boundary conditions, Eqs. (9.117), is presented in Fig. 9.12. As can be seen, this force, being close to the force $V_x^{(2)}$ following from the sixth-order theory at the plate edge $x = 0$, does not represent the actual force $V_x^{(2)}$ at a distance from the plate edge, where $V_x^{(2)}$ is close to $V_x^{(1)}$. Thus, the force $K_x^{(1)}$ is a formal static variable allowing us to satisfy the boundary conditions and not reflecting the actual shear at a distance from the edge.

3. Consider a plate with the clamped edge $x = 0$. The boundary conditions

$$w = 0, \quad \theta_x = 0, \quad \theta_y = 0$$

can be presented as

$$\varphi - \frac{D}{S}\Delta\varphi = 0, \quad \frac{\partial \varphi}{\partial x} = \frac{\partial \psi}{\partial y}, \quad \frac{\partial \varphi}{\partial y} = -\frac{\partial \psi}{\partial x}$$

whereupon the solution becomes

$$\begin{aligned} w^{(3)} &= 1.0059\frac{p_0}{D\lambda^4}\left[1 - e^{-\lambda x}\left(1 + 3.12\frac{x}{b}\right)\right]\sin \lambda y \\ M_x^{(3)} &= -0.3\frac{p_0}{\lambda^2}\left[1 - 4.307e^{-\lambda x}\left(1 - 1.69\frac{x}{b}\right) + 0.0135e^{-kx}\right]\sin \lambda y \\ V_x^{(3)} &= 1.998\frac{p_0}{\lambda}\left(e^{-\lambda x} - 0.0225e^{-kx}\right)\sin \lambda y \end{aligned} \tag{9.121}$$

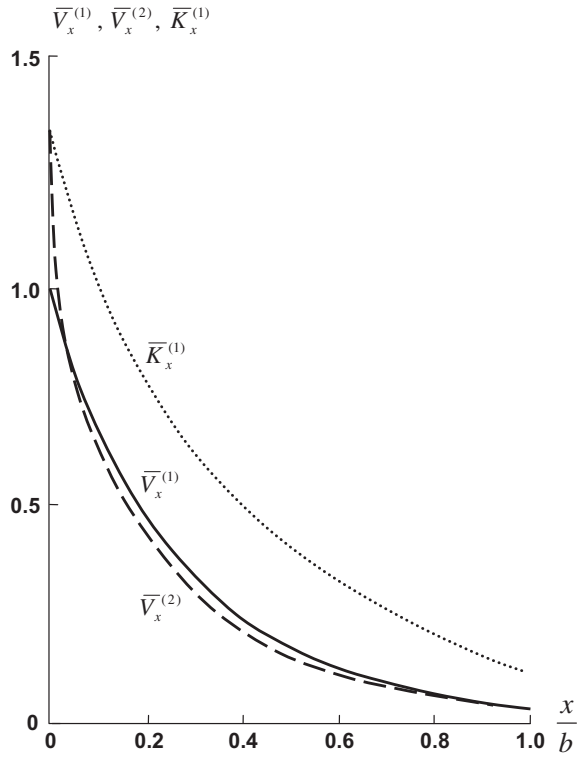


FIGURE 9.12

Distribution of the normalized shear forces $\overline{V}_x^{(1)}(y = b/2)$ (———), $\overline{V}_x^{(2)}(y = b/2)$ (— — —), and $\overline{K}_x^{(1)}(y = b/2)$ (·····) along the *x*-axis.

If we neglect the boundary-layer solution and satisfy two boundary conditions in Eqs. (9.110), i.e.,

$$\varphi - \frac{D}{S}\Delta\varphi = 0, \quad \frac{\partial\varphi}{\partial x} = 0$$

the solution reduces to

$$w^{(4)} = \frac{p_0}{D\lambda^4}\left[1 - e^{-\lambda x}\left(1 + 3.14\frac{x}{b}\right)\right]\sin\lambda y$$

$$M_x^{(4)} = 0.3\frac{p_0}{\lambda^2}\left[1 - 4.333e^{-\lambda x}\left(1 - 1.69\frac{x}{b}\right) + 0.0135e^{-kx}\right]\sin\lambda y$$

$$V_x^{(4)} = 2\frac{p_0}{\lambda}e^{-\lambda x}\sin\lambda y$$

These equations closely coincide with the corresponding Eqs. (9.121). Thus, clamped plates retaining the penetrating potential only can be studied.

This conclusion is valid for relatively thin plates for which the parameter k characterizing the rate of the boundary-layer solution is much higher than the corresponding parameter of the penetrating solution λ. Consider again the plate shown in Fig. 9.9 with the clamped edge $x = 0$ and having the following parameters:

$$\frac{h}{b} = 1, \quad \upsilon = 0, \quad \frac{E}{G} = 100, \quad \lambda = \frac{\pi}{b}, \quad k = \frac{5.82}{b} \tag{9.122}$$

In contrast to Eqs. (9.118), the plate with parameters given by Eqs. (9.122) is relatively thick and the ratio *E/G* is high. As a result, the parameter k is comparable with λ. Compare the following three solutions:

1. Exact solution
2. Penetrating solution
3. Solution corresponding to the classical plate theory.

The exact solutions for the plate deflection and the bending moment are

$$w^{(e)} = 1.823\frac{p_0}{D\lambda^4}\left[1 - \left(1 + 1.352\frac{x}{b}\right)e^{-\lambda x}\right]\sin\lambda y$$

$$M_x^{(e)} = -1.057\frac{p_0}{\lambda^2}\left[\left(1 - 2.375\frac{x}{b}\right)e^{-\lambda x} - 0.451e^{-kx}\right]\sin\lambda y$$

The dependencies of the normalized deflection and moment, i.e., $\overline{w}^{(e)} = D\lambda^4 w^{(e)}/p_0$ and $\overline{M}_x^{(e)} = \lambda^2 M_x^{(e)}/p_0$ corresponding to $y = b/2$ (see Fig. 9.9) on the longitudinal coordinate, are represented in Fig. 9.13 by solid lines.

The penetrating solution gives

$$w^{(p)} = 1.823\frac{p_0}{D\lambda^4}\left[1 - \left(1 + 1.187\frac{x}{b}\right)e^{-\lambda x}\right]\sin\lambda y$$

$$M_x^{(p)} = -0.689\frac{p_0}{\lambda^2}\left(1 - 3.14\frac{x}{b}\right)e^{-\lambda x}\sin\lambda y$$

As can be seen, the deflection corresponding to the penetration solution (shown with circles in Fig. 9.13a) practically coincides with the exact solution, whereas the bending moment (circles in Fig. 9.13b) is different. The maximum bending moment for the penetrating solution is 1.43 times higher than the exact moment.

The solution corresponding to classical plate theory

$$w^{(c)} = \frac{p_0}{D\lambda^4}\left[1 - \left(1 + 3.14\frac{x}{b}\right)e^{-\lambda x}\right]\sin\lambda y$$

$$M_x^{(c)} = -\frac{p_0}{\lambda^2}\left(1 - 3.14\frac{x}{b}\right)e^{-\lambda x}\sin\lambda y$$

is shown by the dashed lines and is, as expected, rather far from the exact solution.

In conclusion, we can formulate some practical recommendations. Note that they follow from experience and are not formally justified.

It follows from the foregoing discussion that the effect of transverse shear deformation provides two basic contributions to plate theory.

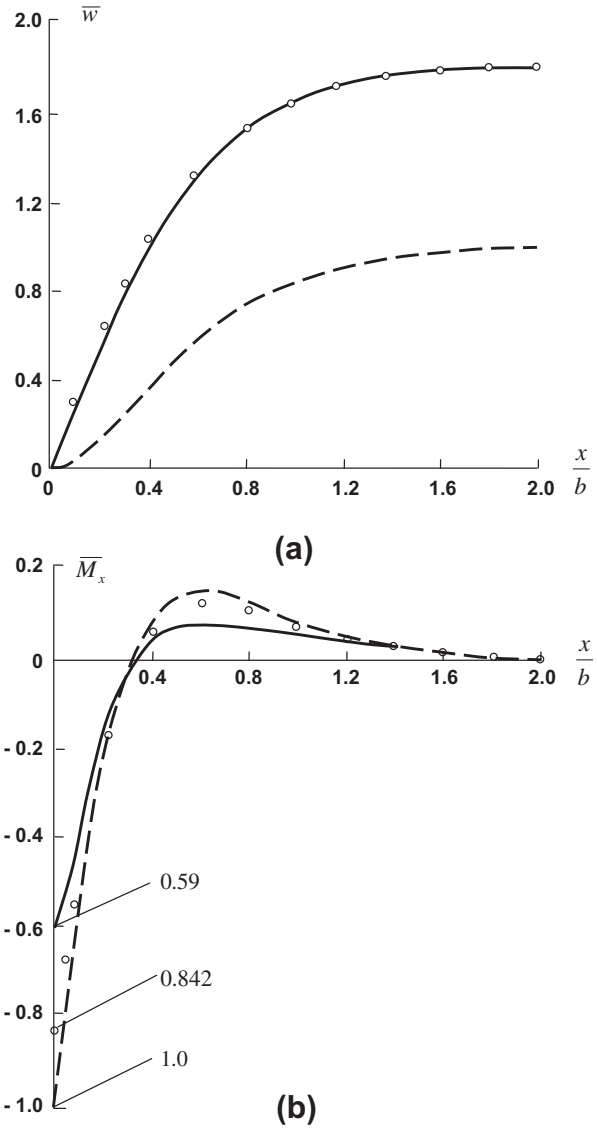


FIGURE 9.13

Dependencies of the normalized deflection (a) and bending moment (b) on the longitudinal coordinate: exact solution (———); penetrating solution (∘ ∘ ∘); classical plate theory (— — —).

Consider the first contribution. For the plates fixed at the edges (note that for the majority of the real boundary conditions, $w = 0$ at the plate edges), the shear deformation, first, affects the penetrating solution, i.e., the plate deflection specified by Eq. (9.82). This effect is the same as that discussed in Chapter 8 for beams and, as for the beams, it does not increase the fourth order of the governing equation, Eq. (9.80). Secondly, the allowance for transverse shear deformation gives rise to an

additional second-order differential equation, Eq. (9.81), which does not exist in the beam theory and describes the boundary layer solution corresponding to plate torsion.

The effect of the transverse shear deformation can be evaluated by comparing the parameter

$$r^2 = \frac{\pi^2 D m^2}{S l^2} \tag{9.123}$$

with unity. Here, m specifies the rate of the penetrating solution (e.g., the half-wave number) and l is the minimum in-plane dimension of the plate. If r^2 is of the order of unity, both shear effects must be taken into account (this is the case for the last example, the results of which are shown in Fig. 9.13). If the order of r^2 is 0.1, then the boundary-layer solution can be neglected. Finally, if the order of r^2 is 0.01, both shear effects can be neglected and classical plate theory can be used to study the plate.

The second basic contribution of the shear deformation is associated with the problems for which the sixth-order plate theory must be used irrespective of the order of the parameter r^2 given by Eq. (9.123). Such problems involve, particularly, plates loaded with twisting moments applied at the plate edges. Consider, for example, the plate shown in Fig. 5.20 loaded with moments M_{xy} distributed along the edges $x = constant$, whereas the edges $y = constant$ are free. The solution of this problem is given in Section 5.5, according to which the plate deflection is

$$w = -y\theta_y, \quad \theta_y = \alpha x \tag{9.124}$$

where α is the twisting angle per unit length. For $\overline{p} = 0$, the governing equation of the plate theory, Eq. (9.80), only has the trivial solution $\varphi = 0$. Thus, the penetrating solution is zero and the problem is reduced to Eq. (9.81), which takes the following form:

$$\psi'' - s^2\psi = 0$$

in which $(\ldots)' = d(\ldots)/dy$. The solution of this equation is studied in Section 5.5.

9.4 BENDING OF ORTHOTROPIC SYMMETRIC PLATES

The general set of equations obtained in Section 9.1 describes the plate with arbitrary structure. However, in the majority of applications, composite plates are orthotropic and the material structure is symmetric with respect to the plate middle plane. Such plates are considered in this Section.

9.4.1 Exact solutions of classical plate theory

The problem of bending of orthotropic symmetric plates is described by Eqs. (9.40)–(9.42). As noted towards the end of the previous section, thin plates with moderate ratio *E/G* can be studied using classical plate theory. Note that for the majority of real composite laminated plates, classical plate theory provides rather accurate results, assuming that the plate edges are fixed with respect to the plate deflection. Naturally (see Section 9.3), no generalized transverse shear forces and corner forces should be introduced into the analysis.

Neglecting transverse shear deformation, take $S_x \to \infty$ and $S_y \to \infty$ in Eqs. (9.40)–(9.42). Then, $W = w$ and Eq. (9.40) reduces to the well-known equation for plate deflection, i.e.,

$$D_1\frac{\partial^4 w}{\partial x^4} + 2D_3\frac{\partial^4 w}{\partial x^2 \partial y^2} + D_2\frac{\partial^4 w}{\partial y^4} = \overline{p} \tag{9.125}$$

where $\overline{p} = p - q$ (see Fig. 9.1) and

$$D_1 = D_{11}, \quad D_2 = D_{22}, \quad D_3 = D_{12} + 2D_{44} \tag{9.126}$$

The moments and the shear forces are expressed in terms of w as

$$\begin{gathered} M_x = -\left(D_{11}\frac{\partial^2 w}{\partial x^2} + D_{12}\frac{\partial^2 w}{\partial y^2}\right), \quad M_y = -\left(D_{12}\frac{\partial^2 w}{\partial x^2} + D_{22}\frac{\partial^2 w}{\partial y^2}\right), \quad M_{xy} = -2D_{44}\frac{\partial^2 w}{\partial x \partial y} \\ V_x = -\frac{\partial}{\partial x}\left(D_{11}\frac{\partial^2 w}{\partial x^2} + D_3\frac{\partial^2 w}{\partial y^2}\right), \quad V_y = -\frac{\partial}{\partial y}\left(D_{22}\frac{\partial^2 w}{\partial y^2} + D_3\frac{\partial^2 w}{\partial x^2}\right) \end{gathered} \tag{9.127}$$

For simply supported edges

$$\begin{gathered} w = 0, \quad \frac{\partial^2 w}{\partial x^2} = 0, \quad \text{for } x = constant \\ w = 0, \quad \frac{\partial^2 w}{\partial y^2} = 0, \quad \text{for } y = constant \end{gathered} \tag{9.128}$$

whereas for clamped edges

$$\begin{gathered} w = 0, \quad \frac{\partial w}{\partial x} = 0, \quad \text{for } x = constant \\ w = 0, \quad \frac{\partial w}{\partial y} = 0, \quad \text{for } y = constant \end{gathered} \tag{9.129}$$

Consider the exact solutions obtained for plates with various boundary conditions.

9.4.1.1 Simply supported plates

Plates supported at the contour by the walls that are absolutely rigid in-plane and flexible out-of-plane (see Fig. 9.14) are usually treated as simply supported plates with boundary conditions specified by Eqs. (9.128). The method of exact solution for such plates proposed in 1823 by L.M. Navier is based on the following trigonometric series for w:

$$w(x, y) = \sum_m \sum_n w_{mn} \sin \lambda_m x \sin \lambda_n y \tag{9.130}$$

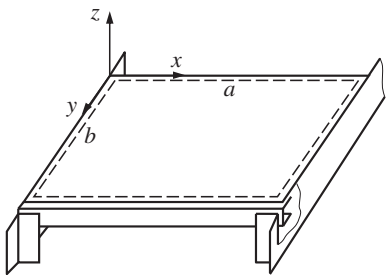


FIGURE 9.14

A simply supported plate.

in which w_{mn} are constant coefficients, $\lambda_m = \pi m/a$, $\lambda_n = \pi n/b$, and a, b are the plate in-plane dimensions (see Fig. 9.14). Each term of the series in Eq. (9.130) satisfies the boundary conditions given by Eqs. (9.128). In addition, the pressure $\overline{p}$ in Eq. (9.125) is also decomposed into a similar series, i.e.,

$$\overline{p}(x,y) = \sum_m \sum_n p_{mn} \sin \lambda_m x \sin \lambda_n y \tag{9.131}$$

in which

$$p_{mn} = \frac{4}{ab} \int_o^a \int_o^b \overline{p}(x,y) \sin \lambda_m x \sin \lambda_n y$$

For uniform pressure $\overline{p} = p_0$,

$$p_{mn} = \begin{cases} \dfrac{16p_0}{\pi^2 mn} & (m,n = 1,3,5\ldots) \\ 0 & (m,n = 2,4,6\ldots) \end{cases} \tag{9.132}$$

Substituting Eqs. (9.130) and (9.131) into Eq. (9.125), we can express w_{mn} in terms of p_{mn} and obtain finally the following solution

$$w(x,y) = \sum_m \sum_n \frac{p_{mn} \sin \lambda_m x \sin \lambda_n y}{D_1 \lambda_m^4 + 2D_3 \lambda_m^2 \lambda_n^2 + D_2 \lambda_n^4} \tag{9.133}$$

The moments and forces acting in the plate can be found using Eqs. (9.127).

Convergence of the series in Eq. (9.133) depends on the plate in-plane aspect ratio a/b (see Fig. 9.15). For square and close to square plates

$$1 \ll \frac{a}{b} \ll 1.5 \tag{9.134}$$

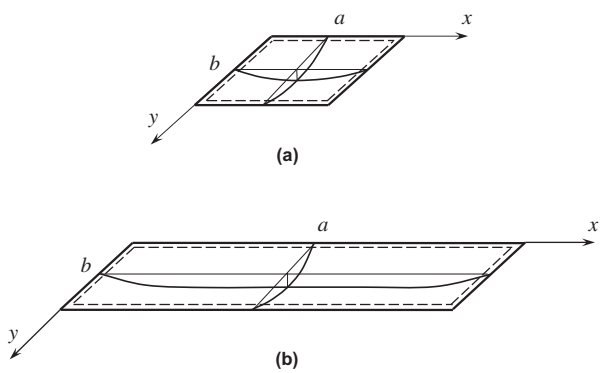


FIGURE 9.15

Close-to-square (a) and long (b) rectangular plates.

(see Fig. 9.15a). Using only the first term in Eq. (9.133) provides reasonable accuracy for the solution. Convergence of the corresponding series for the moment and the forces in Eqs. (9.127) which require differentiation of Eq. (9.133) is much slower than the convergence of Eq. (9.133), and to calculate the moments and the forces, we need to retain up to five terms in the series (Vasiliev, 1993).

For long plates (see Fig. 9.15b), with an aspect ratio

$$\frac{a}{b} > 3.5\sqrt{\frac{D_1}{D_2}}, \tag{9.135}$$

the convergence of the series is getting rather slow. It follows from Fig.9.15b that in the middle part of the plate the deflection is practically independent of x and is close to constant. To predict this deflection, we must retain a large number of terms in Eq. (9.133). For the $\pm 45^\circ$ composite plate with $D_1 = D_2 = D$ and $D_2 = 1.4D$, loaded with uniform pressure p_0, the dependence of the normalized maximum deflection $\overline{w}_m = w_m D/p_0 b^4$ on the plate aspect ratio a/b is shown in Fig. 9.16. As can be seen, for those ratios a/b which satisfy the condition given by Eq. (9.135), the plate can be considered as infinitely long. Taking $a/b \to \infty$, we get from Eq. (9.133) in which p_{mn} is specified by Eq. (9.132)

$$w = \frac{16p_0b^4}{\pi^6 D_2}\sum_m \frac{1}{m}\sin\lambda_m x \sum_n \frac{1}{n^5}\sin\lambda_n y = \frac{p_0}{24D_2}\left(y^4 - 2by^3 + b^3 y\right)$$

This result corresponds to the deflection of a beam of length b simply supported at its ends.

9.4.1.2 Plates simply supported at opposite edges

A more general method whose convergence does not depend on the aspect a/b ratio was proposed by M. Levy in 1899. Consider a plate with simply supported edges $y = 0$ and $y = b$ (see Fig. 9.17) and assume that $a \geq b$, i.e., that the plate is simply supported along the long edges, whereas the boundary

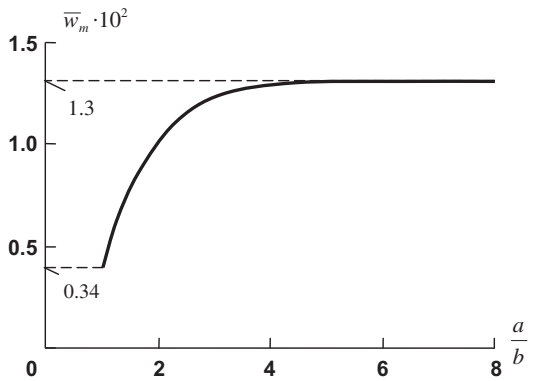


FIGURE 9.16

Dependence of the normalized deflection on the aspect ratio a/b.

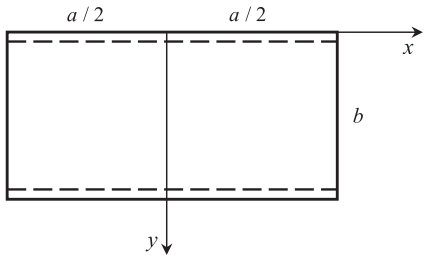


FIGURE 9.17

A rectangular plate with two simply supported opposite edges.

conditions for the short edges $x = \pm a/2$ can be arbitrary. The solution of Eq. (9.125) is presented in the form

$$w(x,y) = \sum_n W_n(x) \sin \lambda_n y \tag{9.136}$$

where, as earlier, $\lambda_n = \pi n/b$. The deflection given by Eq. (9.136) satisfies the boundary conditions, Eqs. (9.128) for the edges $y = 0$ and $= b$. The pressure $\overline{p}$ in Eq. (9.125) is decomposed into a similar series, i.e.,

$$\overline{p}(x,y) = \sum_n p_n(x) \sin \lambda_n y \tag{9.137}$$

where

$$p_n(x) = \frac{2}{b} \int_0^b \overline{p}(x,y) \sin \lambda_n y dy$$

For uniform pressure $\overline{p} = p_0$,

$$p_n = \begin{cases} \dfrac{4p_0}{b\lambda_n} & (n = 1,3,5\ldots) \\ 0 & (n = 2,4,6\ldots) \end{cases} \tag{9.138}$$

Substituting Eqs. (9.136) and (9.138) into Eq. (9.125), we arrive at the following ordinary differential equation for the function $W_n(x)$:

$$W_n^{IV} - 2k_{1n}^2 W_n'' + k_{2n}^4 W_n = k_{pn} \tag{9.139}$$

in which

$$k_{1n}^2 = \frac{D_3}{D_1}\lambda_n^2, \quad k_{2n}^4 = \frac{D_2}{D_1}\lambda_n^4, \quad k_{pn} = \frac{p_n}{D_1} \tag{9.140}$$

The solution of Eq. (9.139) is

$$W_n = \sum_{i=1}^{4} C_i \Phi_i(x) + W_{pn} \tag{9.141}$$

where C_i are the constants of integration and W_{pn} is the particular solution. For a uniform pressure with p_n specified by Eq. (9.138),

$$W_{pn} = \frac{p_n}{D_1 k_{2n}^4} \tag{9.142}$$

The functions $\Phi_i(x)$ have a form which depends on the relationship between the coefficients in Eqs. (9.140). Possible forms for these functions are presented in Table 9.1.

For orthotropic plates, it is usually the case that $k_2^2 > k_1^2$. In this case,

$$\begin{aligned} \Phi_1 &= \cosh rx \cos tx, \quad \Phi_2 = \sinh rx \sin tx \\ \Phi_3 &= \cosh rx \sin tx, \quad \Phi_4 = \sinh rx \cos tx \end{aligned} \tag{9.143}$$

TABLE 9.1 Solutions of the Differential Equation $W^{IV} - 2k_1^2 W'' + k_2^4 W = 0$

Relations Between Coefficients	Roots of the Characteristic Equation	Φ_1	Φ_2	Φ_3	Φ_4
$k_2^2 > k_1^2$	$x_1 = -x_2 = r + it$ $x_3 = -x_4 = r - it$	$\cosh rx \cos tx$	$\sinh rx \sin tx$	$\cosh rx \sin tx$	$\sinh rx \sin tx$
	$r = \sqrt{\frac{1}{2}(k_2^2 + k_1^2)}$	$e^{-rx} \cos tx$	$e^{-rx} \sin tx$	$e^{rx} \cos tx$	$e^{rx} \sin tx$
	$t = \sqrt{\frac{1}{2}(k_2^2 - k_1^2)}$				
$k_2^2 = k_1^2$	$x_1 = x_2 = r$ $x_3 = x_4 = -r$	$\cosh rx$	$x \sinh rx$	$\sinh rx$	$x \cosh rx$
	$r = k_1$	e^{-rx}	xe^{-rx}	e^{rx}	xe^{rx}
$k_2^2 < k_1^2$	$x_1 = -x_2 = r$ $x_3 = -x_4 = t$	$\cosh rx$	$\cosh tx$	$\sinh rx$	$\sinh tx$
	$r = \sqrt{k_1^2 - \sqrt{k_1^4 - k_2^4}}$	e^{-rx}	e^{-tx}	e^{rx}	e^{tx}
	$t = \sqrt{k_1^2 + \sqrt{k_1^4 - k_2^4}}$				

The derivatives of these functions are expressed in terms of the initial functions as

$$\begin{gathered}\Phi_1' = r\Phi_4 - t\Phi_3, \quad \Phi_2' = r\Phi_3 + t\Phi_4, \quad \Phi_3' = r\Phi_2 + t\Phi_1, \quad \Phi_4' = r\Phi_1 - t\Phi_2 \\ \Phi_1'' = \left(r^2 - t^2\right)\Phi_1 - 2rt\Phi_2, \quad \Phi_2'' = \left(r^2 - t^2\right)\Phi_2 + 2rt\Phi_1 \\ \Phi_3'' = \left(r^2 - t^2\right)\Phi_3 + 2rt\Phi_4, \quad \Phi_4'' = \left(r^2 - t^2\right)\Phi_4 - 2rt\Phi_3 \\ \Phi_1''' = r\left(r^2 - 3t^2\right)\Phi_4 + t\left(t^2 - 3r^2\right)\Phi_3, \quad \Phi_2''' = r\left(r^2 - 3t^2\right)\Phi_3 + t\left(t^2 - 3r^2\right)\Phi_4 \\ \Phi_3''' = r\left(r^2 - 3t^2\right)\Phi_2 - t\left(t^2 - 3r^2\right)\Phi_1, \quad \Phi_4''' = r\left(r^2 - 3t^2\right)\Phi_1 + t\left(t^2 - 3r^2\right)\Phi_2\end{gathered} \tag{9.144}$$

Consider the action of a uniform pressure p_0 on the plates whose boundary conditions are symmetric with respect to the x-coordinate (see Fig. 9.18). In this case, $C_3 = C_4 = 0$ and Eq. (9.141) becomes

$$W_n = C_1\Phi_1(x) + C_2\Phi_2(x) + W_p \tag{9.145}$$

in which W_p and Φ_1, Φ_2 are specified by Eqs. (9.142) and (9.143).

If the transverse edges $x = \pm a/2$ are simply supported (see Fig. 9.18a) and the boundary conditions correspond to Eq. (9.128), the solution is

$$W_n = W_p\left[1 - F_1(x)\right] \tag{9.146}$$

where

$$F_1(x) = \frac{\Phi_1(x)\Phi_2''(a/2) - \Phi_2(x)\Phi_1''(a/2)}{\Phi_1(a/2)\Phi_2''(a/2) - \Phi_2(a/2)\Phi_1''(a/2)}$$

and the derivatives of the functions Φ are specified by Eqs. (9.144). In contrast to the Navier solution given by Eq. (9.133), the series following from Eqs. (9.136), and (9.145), (9.146) rapidly converge for any aspect ratio b/a.

For a plate with clamped edges $x = \pm a/2$ (see Fig. 9.18b), the boundary conditions correspond to Eqs. (9.129) and

$$W_n(x) = W_p\left[1 - F_2(x)\right] \tag{9.147}$$

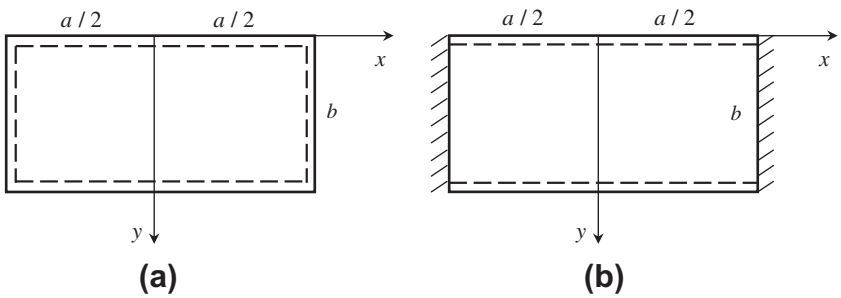


FIGURE 9.18

Plates with simply supported longitudinal edges and simply supported (a) and clamped (b) transverse edges.

where

$$F_2(x) = \frac{\Phi_1(x)\Phi_2'(a/2) - \Phi_2(x)\Phi_1'(a/2)}{\Phi_1(a/2)\Phi_2'(a/2) - \Phi_2(a/2)\Phi_1'(a/2)}$$

9.4.1.3 Clamped plates

The exact solution for a clamped plate has been found by S.A. Lurie (1982) with the aid of the method of homogeneous solutions developed by P.A. Shiff (1883), J. Dougall (1904), J.N.A. Brahtz (1935), F. Tolske (1938), I. Fadle (1941), and P.F. Papkovich (1941). The mathematical justification of the method and the exact solutions of biharmonic problems in the theory of elasticity are presented by S.A. Lurie and V.V. Vasiliev (1995).

Consider a plate clamped at its edges (see Fig. 9.19a) and introduce the normalized coordinates

$$\bar{x} = \frac{2x}{a}, \quad \bar{y} = \frac{2y}{b} \tag{9.148}$$

The initial rectangular plate (see Fig. 9.19a), being referred to the coordinates given in Eqs. (9.148), reduces to a square plate (see Fig. 9.19b) for which $-1 \le \bar{x} \le 1$ and $-1 \le \bar{y} \le 1$. Then, the governing equation, Eq. (9.125), is transformed as follows:

$$\frac{D_1 b^4 \partial^4 w}{D_2 a^4 \partial \bar{x}^4} + \frac{D_3 b^2}{D_2 b^2} \frac{\partial^4 w}{\partial \bar{x}^2 \partial \bar{y}^2} + \frac{\partial^4 w}{\partial \bar{y}^4} = \frac{\bar{p} b^4}{16 D_2} \tag{9.149}$$

The solution of Eq. (9.149) corresponding to a uniform pressure $\bar{p} = p_0$ has the form

$$w = w_0 + w_p \tag{9.150}$$

in which

$$w_p = \frac{p_0 b^4}{384 D_2} \left(1 - \bar{y}^2\right)^2 \tag{9.151}$$

satisfies the boundary condition, Eq. (9.129) for clamped edges, i.e., $w_p(\bar{y} = \pm 1) = w_p'(\bar{y} = \pm 1) = 0$, whereas w_0 satisfies the homogeneous equation corresponding to Eq. (9.149). The function w_0, which is symmetric with respect to the $\bar{x}$-coordinate, is given by

$$w_0(\bar{x}, \bar{y}) = \sum_m C_m \cosh\left(\lambda_m \bar{x}\right) F_m(\bar{y}) \tag{9.152}$$

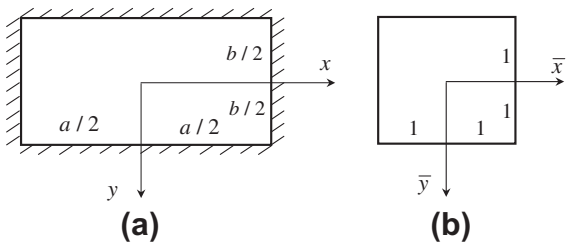


FIGURE 9.19

Clamped plate referred to coordinates x, y (a) and $\bar{x}$, $\bar{y}$ (b).

Here, C_m and λ_m are constants and $F_m(\overline{y})$ are the so-called homogeneous solutions which can be found if we substitute Eq. (9.152) into Eq. (9.149) where $\overline{p} = 0$. The resulting equation for $F_m(\overline{y})$ is

$$F_m^{IV} + 2\alpha^2 F_m'' + \beta^4 F_m = 0 \tag{9.153}$$

where $(\ldots)' = d(\ldots)/d\,\overline{y}$ and

$$\alpha^2 = \frac{D_3 b^2}{D_2 a^2}, \quad \beta^4 = \frac{D_1 b^4}{D_2 a^4}$$

The solution of Eq. (9.153), symmetric with respect to the $\overline{y}$ coordinate, is

$$F_m(\overline{y}) = C_{1m} \cos(r_1 \lambda_m \overline{y}) + C_{2m} \cos(r_2 \lambda_m \overline{y}) \tag{9.154}$$

where

$$\begin{aligned} r_{1,2} &= \sqrt{\alpha^2 \pm \sqrt{\alpha^4 - \beta^4}} \\ &= \frac{b}{a\sqrt{D_2}} \sqrt{D_3 \pm \sqrt{D_3^2 - D_1 D_2}} \end{aligned} \tag{9.155}$$

and r_1, r_2 are the roots of the characteristic equation.

Note that the solution given by Eq. (9.154) is valid if $D_3 > \sqrt{D_1 D_2}$. If $D_3 < \sqrt{D_1 D_2}$, then the roots $r_{1,2}$ are complex numbers, i.e.,

$$r_{1,2} = \frac{b}{a\sqrt{2}} \left(\sqrt{\sqrt{\frac{D_1}{D_2}} - \frac{D_3}{D_2}} \mp i \sqrt{\sqrt{\frac{D_1}{D_2}} + \frac{D_3}{D_2}} \right) \tag{9.156}$$

where i is the imaginary unit ($i^2 = -1$). For this case

$$F_m(\overline{y}) = C_{1m} \cosh(r_1 \lambda_m \overline{y}) \cos(r_2 \lambda_m \overline{y}) + C_{2m} \sinh(r_1 \lambda_m \overline{y}) \sin(r_2 \lambda_m \overline{y})$$

Further derivation is performed for the homogeneous solution, Eq. (9.154), because it is easier to differentiate this equation, although the roots r_1 and r_2 can be either real, Eqs. (9.155), or complex, Eq. (9.156), numbers.

To determine the parameter λ_m in Eq. (9.154), apply the boundary conditions, Eqs. (9.129), to the edges $\overline{y} = \pm 1$, i.e.,

$$F_m(\overline{y} = \pm 1) = 0, \quad F_m'(\overline{y} = \pm 1) = 0 \tag{9.157}$$

Substituting Eq. (9.154) into Eqs. (9.157), we arrive at the following two equations for the constants C_{1m} and C_{2m}:

$$C_{1m} \cos(r_1 \lambda_m) + C_{2m} \cos(r_2 \lambda_m) = 0$$

$$C_{1m} r_1 \sin(r_1 \lambda_m) + C_{2m} r_2 \sin(r_2 \lambda_m) = 0$$

The first of these equations yields

$$C_{2m} = -C_{1m}\frac{\cos(r_1\lambda_m)}{\cos(r_2\lambda_m)} \tag{9.158}$$

whereas substitution of Eq. (9.158) into the second equation results in the following equation for the parameter λ_m:

$$r_1 \tan(r_1\lambda_m) = r_2 \tan(r_2\lambda_m) \tag{9.159}$$

Using Eq. (9.158), we can write the homogeneous solutions given by Eq. (9.154) as

$$F_m(\overline{y}) = C_{1m}[\cos(r_2\lambda_m)\cos(r_1\lambda_m\overline{y}) - \cos(r_1\lambda_m)\cos(r_2\lambda_m\overline{y})] \tag{9.160}$$

Finally, substituting Eq. (9.160) into Eq. (9.152) and including the constant C_{1m} into the constant C_m, we arrive at

$$w_0(\overline{x},\overline{y}) = \sum_m C_m \cosh(\lambda_m\overline{x})\overline{F}_m(\overline{y}) \tag{9.161}$$

where

$$\overline{F}_m(\overline{y}) = \cos(r_2\lambda_m)\cos(r_1\lambda_m\overline{y}) - \cos(r_1\lambda_m)\cos(r_2\lambda_m\overline{y}) \tag{9.162}$$

The constants C_m in Eq. (9.161) can be found from the boundary conditions given by Eqs. (9.129) for the plate edges $x = \pm 1$, i.e.,

$$\begin{aligned} w(\overline{x} = \pm 1) &= \sum_m C_m \cosh\lambda_m \cdot \overline{F}_m(\overline{y}) + w_p(\overline{y}) = 0 \\ \frac{\partial w}{\partial \overline{x}}(\overline{x} = \pm 1) &= \sum_m C_m\lambda_m \sinh\lambda_m \cdot \overline{F}_m(\overline{y}) = 0 \end{aligned} \tag{9.163}$$

It follows from these equations that the two mutually independent functions (w_p and 0) must be decomposed into two series with respect to the homogeneous solutions with one and the same system of constants C_{1m}. If the functions $F_m(\overline{y})$ were orthogonal and complete, this problem could not be solved. However, the functions $F_m(\overline{y})$ specified by Eq. (9.160) are of a more complicated nature, i.e., they are biorthogonal and bicomplete which, in principle, allows us to solve the problem (see Lurie and Vasiliev, 1995).

To derive the biorthogonality condition, consider Eq. (9.153) written for functions F_m and F_n such that $m \neq n$. Multiplying the equation for F_m by F_n and the equation for F_n by F_m and integrating the resulting equations from -1 to $+1$, we get

$$\begin{aligned} \int_{-1}^{1} F_m^{IV}F_n d\overline{y} + 2a^2 \int_{-1}^{1} F_m''F_n d\overline{y} + b^4 F_m F_n = 0 \\ \int_{-1}^{1} F_n^{IV}F_m d\overline{y} + 2a^2 \int_{-1}^{1} F_n''F_m d\overline{y} + b^4 F_n F_m = 0 \end{aligned} \tag{9.164}$$

Integrating by parts, with allowance for the boundary conditions, Eqs. (9.157) yield for the first equation

$$\int_{-1}^{1} F_m^{IV} F_n d\overline{y} = -\int_{-1}^{1} F_m''' F_n' d\overline{y} = \int_{-1}^{1} F_m'' F_n'' d\overline{y}$$

$$\int_{-1}^{1} F_m'' F_n d\overline{y} = \int_{-1}^{1} F_m' F_n' d\overline{y}$$

Similar relations are valid for the second equation of Eqs. (9.164). Now, subtract the second equation from the first one and take into account that $\lambda_m \neq \lambda_n$. Then,

$$\int_{-1}^{1} \left(F_m'' F_n'' - b^4 \lambda_m^2 \lambda_n^2 F_m F_n\right) d\overline{y} = 0, \quad \lambda_m \neq \lambda_n \tag{9.165}$$

The biorthogonality condition in Eq. (9.165) allows us to determine directly the constants in Eq. (9.161) only for a simply supported plate. Indeed, the boundary conditions in Eqs. (9.128) for a simply supported plate take the form

$$\begin{aligned} w(\overline{x} = \pm 1) &= \sum_m C_m \cosh \lambda_m \cdot \overline{F}_m(\overline{y}) + w_p(\overline{y}) = 0 \\ \frac{\partial^2 w}{\partial \overline{x}^2}(\overline{x} = \pm 1) &= \sum_m C_m \lambda_m^2 \sinh \lambda_m \cdot \overline{F}_m(\overline{y}) = 0 \end{aligned} \tag{9.166}$$

Differentiate twice the first of these conditions, multiply it by F_n'', subtract the second condition multiplied by $b^4 \lambda_n^2 F_n$, and integrate the result from -1 to 1 to get

$$\sum_m C_m \cosh \lambda_m \left(\int_{-1}^{1} \left(\overline{F}_m'' \overline{F}_n'' - b^4 \lambda_m^2 \lambda_n^2 \overline{F}_m \overline{F}_n\right) d\overline{y} \right) = 0$$

Applying the biorthogonality condition as per Eq. (9.165) for functions $\overline{F}_m$ and $\overline{F}_n$, we can find C_n as

$$C_n = -\frac{\int_{-1}^{1} w_p''(\overline{y}) \overline{F}_n d\overline{y}}{\cosh \lambda_n \int_{-1}^{1} \left[\left(\overline{F}_n''\right)^2 - b^4 \overline{F}_n^2\right] d\overline{y}}$$

Return now to the clamped plate. Application of the biorthogonality condition, Eq. (9.165), to the boundary conditions given by Eqs. (9.163), requires some additional transformations. First, rewrite Eq. (9.162) as

$$\overline{F}_m(\overline{y}) = u_m(\overline{y}) + v_m(\overline{y}) \tag{9.167}$$

where

$$u_m(\overline{y}) = C_{2m}\cos(r_1\lambda_m\overline{y}), \quad \upsilon_m(\overline{y}) = C_{1m}\cos(r_2\lambda_m\overline{y}) \tag{9.168}$$

in which

$$C_{1m} = -\cos(r_1\lambda_m), \quad C_{2m} = \cos(r_2\lambda_m)$$

Secondly, substitute Eqs. (9.167) and (9.168) into Eq. (9.165). Taking into account that

$$r_1^2 + r_2^2 = 2a^2, \quad r_1^2 - r_2^2 = 2\sqrt{a^4 - b^4}, \quad r_1^2 r_2^2 = b^4$$

where a^2 and b^4 are the coefficients of Eq. (9.153) and r_1 and r_2 are the roots of the corresponding characteristic equation, we can write the biorthogonality condition, Eq. (9.165), in the following form:

$$\int_{-1}^{1} \left(r_1^2 u_m u_n - r_2^2 \upsilon_m \upsilon_n\right) d\overline{y} = 0 \tag{9.169}$$

in which $m \neq n$.

Finally, rewrite the boundary conditions in Eqs. (9.163) in terms of the functions u_m and υ_m, i.e.,

$$\sum_m C_m \cosh\lambda_m \cdot (u_m + \upsilon_m) = -w_p, \quad \sum_m C_m\lambda_m \sinh\lambda_m \cdot (u_m + \upsilon_m) = 0$$

Differentiate these equations twice, taking into account that in accordance with Eqs. (9.168)

$$u_m'' = -r_1^2\lambda_m^2 u_m, \quad \upsilon_m'' = -r_2^2\lambda_m^2\upsilon_m$$

Thus,

$$\sum_m C_m\lambda_m^2 \cosh\lambda_m \cdot \left(r_1^2 u_m + r_2^2\upsilon_m\right) = w_p'' \tag{9.170}$$

$$\sum_m C_m\lambda_m^3 \sinh\lambda_m \cdot \left(r_1^2 u_m + r_2^2\upsilon_m\right) = 0 \tag{9.171}$$

Decompose Eq. (9.170) as

$$\sum_m C_m\lambda_m^2 r_1^2 \cosh\lambda_m \cdot u_m(\overline{y}) = \varphi_1(\overline{y}) \tag{9.172}$$

$$\sum_m C_m\lambda_m^2 r_2^2 \cosh\lambda_m \cdot \upsilon_m(\overline{y}) = \varphi_2(\overline{y}) \tag{9.173}$$

Here, $\varphi_1(\overline{y})$ and $\varphi_2(\overline{y})$ are some unknown functions such that

$$\varphi_1(\overline{y}) + \varphi_2(\overline{y}) = w_p'' \tag{9.174}$$

Note that if we knew the functions $\varphi_1(\bar{y})$ and $\varphi_2(\bar{y})$, we could readily find the constants C_m. Indeed, multiply Eqs. (9.172) and (9.173) by u_n and υ_n $(n \neq m)$ respectively, subtract the second equation from the first one, and integrate from -1 to 1 to get

$$\sum_m C_m \lambda_m^2 \cosh \lambda_m \int_{-1}^{1} (r_1^2 u_m u_n - r_2^2 \upsilon_m \upsilon_n) d\bar{y} = \int_{-1}^{1} (\varphi_1 u_n - \varphi_2 \upsilon_n) d\bar{y}$$

Applying Eq. (9.169), we arrive at

$$C_n = \frac{\int_{-1}^{1} (\varphi_1 u_n - \varphi_2 \upsilon_n) d\bar{y}}{\lambda_n^2 \cosh \lambda_n \int_{-1}^{1} (r_1^2 u_n^2 - r_2^2 \upsilon_n^2) d\bar{y}} \tag{9.175}$$

However, we do not know the functions $\varphi_1(\bar{y})$ and $\varphi_2(\bar{y})$ in Eqs. (9.172) and (9.173). To determine these functions, decompose Eq. (9.171) in a similar way, i.e.,

$$\sum_m C_m \lambda_m^3 r_1^2 \sinh \lambda_m \cdot u_m(\bar{y}) = \psi_1(\bar{y}) \tag{9.176}$$

$$\sum_m C_m \lambda_m^3 r_2^2 \sinh \lambda_m \cdot \upsilon_m(\bar{y}) = \psi_2(\bar{y}) \tag{9.177}$$

where

$$\psi_1(\bar{y}) + \psi_2(\bar{y}) = 0 \tag{9.178}$$

Consider Eqs. (9.172) and (9.176). Decompose the symmetric functions $\cosh \lambda_m$ and $\lambda_m \sinh \lambda_m$ into the following power series:

$$\cosh \lambda_m = \sum_{i=1}^{\infty} a_i \lambda_m^{2i}, \quad \lambda_m \sinh \lambda_m = \sum_{i=1}^{\infty} b_i \lambda_i^{2m} \tag{9.179}$$

where a_i and b_i are some coefficients, the values of which are not important for the further derivation. Then, Eqs. (9.172) and (9.176) can be presented as

$$\begin{aligned} \varphi_1(\bar{y}) &= \sum_m C_m r_1^2 \lambda_m^2 u_m(\bar{y}) \sum_i a_i \lambda_m^{2i} = r_1^2 \sum_i a_i \sum_m C_m \lambda_m^{2(i+1)} u_m(\bar{y}) \\ \psi_1(\bar{y}) &= \sum_m C_m r_1^2 \lambda_m^2 u_m(\bar{y}) \sum_i b_i \lambda_m^{2i} = r_1^2 \sum_i b_i \sum_m C_m \lambda_m^{2(i+1)} u_m(\bar{y}) \end{aligned} \tag{9.180}$$

Summation with respect to m and i is interchanged in the second part of Eqs. (9.180). Now, differentiate the functions u_m $2n$ times. Taking into account Eqs. (9.168) for u_m, we get

$$u_m^{(2n)}(\bar{y}) = (-1)^n r_1^{2n} \lambda_m^{2n} u_m(\bar{y})$$

Thus, Eqs. (9.180) after differentiation become

$$\varphi_1^{(2n)}(\bar{y}) = (-1)^n r_1^{2(n+1)} \sum_i a_i \sum_m C_m \lambda_m^{2(i+n+1)} u_m(\bar{y})$$
$$\psi_1^{(2n)}(\bar{y}) = (-1)^n r_1^{2(n+1)} \sum_i b_i \sum_m C_m \lambda_m^{2(i+n+1)} u_m(\bar{y})$$

Multiply these equations by

$$(-1)^n \frac{b_n}{r_1^{2(n+1)}} \quad \text{and} \quad (-1)^n \frac{a_n}{r_1^{2(n+1)}}$$

respectively, and sum them up with respect to n, i.e.,

$$\sum_n (-1)^n \frac{b_n}{r_1^{2(n+1)}} \varphi_1^{(2n)}(\bar{y}) = \sum_n \sum_i a_i b_n \sum_m C_m \lambda_m^{2(i+n+1)} u_m(\bar{y})$$
$$\sum_n (-1)^n \frac{a_n}{r_1^{2(n+1)}} \psi_1^{(2n)}(\bar{y}) = \sum_n \sum_i a_n b_i \sum_m C_m \lambda_m^{2(i+n+1)} u_m(\bar{y})$$

The right-hand parts of these equations are the same and, hence, so are the left-hand parts. Thus,

$$\sum_n (-1)^n \frac{b_n}{r_1^{2(n+1)}} \varphi_1^{(2n)}(\bar{y}) = \sum_n (-1)^n \frac{a_n}{r_1^{2(n+1)}} \psi_1^{(2n)}(\bar{y}) \tag{9.181}$$

Repeating the foregoing procedure for the functions $\varphi_2(\bar{y})$ and $\psi_2(\bar{y})$ in Eqs. (9.173) and (9.177), we can write the following equation similar to Eq. (9.181):

$$\sum_n (-1)^n \frac{b_n}{r_2^{2(n+1)}} \varphi_2^{(2n)}(\bar{y}) = \sum_n (-1)^n \frac{a_n}{r_2^{2(n+1)}} \psi_2^{(2n)}(\bar{y}) \tag{9.182}$$

Thus, we have four equations, Eqs. (9.174), (9.178), and (9.181), (9.182), for functions $\varphi_1(\bar{y})$, $\varphi_2(\bar{y})$, $\psi_1(\bar{y})$, and $\psi_2(\bar{y})$. However, Eqs. (9.181) and (9.182) are differential equations of infinitely high order. In principle, these equations can be solved using the method based on the algebra of pseudo-differential operators (Lurie and Vasiliev, 1995). Since the description of these techniques is rather cumbersome, we use an alternative approach allowing us to reduce the differential operators in Eqs. (9.181) and (9.182) to polynomials. The particular solution w_p specified by Eq. (9.151), being an even function which is zero at $\bar{y} = \pm 1$, can be decomposed in the following Fourier series:

$$w_p(\bar{y}) = \sum_{j=1}^{\infty} w_j \cos\left(\alpha_j \bar{y}\right), \quad \alpha_j = \frac{\pi}{2}(2j-1), \quad w_j = \frac{p_0 b^4}{24 D_2 \alpha_j^5}\left(3 - \alpha_j^2\right) \sin\left(\alpha_j \bar{y}\right) \tag{9.183}$$

In a similar way,

$$\varphi_{1,2}(\bar{y}) = \sum_j \varphi_{1j,2j} \cos\left(\alpha_j \bar{y}\right), \quad \psi_{1,2}(\bar{y}) = \sum_j \psi_{1j,2j} \cos\left(\alpha_j \bar{y}\right) \tag{9.184}$$

where, in accordance with Eqs. (9.174) and (9.178),

$$\varphi_{1j} + \varphi_{2j} = -\alpha_j^2 w_j, \quad \psi_{1j} + \psi_{2j} = 0 \tag{9.185}$$

Substituting Eqs. (9.184) into Eqs. (9.181) and (9.182), we arrive at

$$\varphi_{1j}\sum_n b_n\left(\frac{\alpha_j}{r_1}\right)^{2n} = \psi_{1j}\sum_n a_n\left(\frac{\alpha_j}{r_1}\right)^{2n}$$

$$\varphi_{2j}\sum_n b_n\left(\frac{\alpha_j}{r_1}\right)^{2n} = \psi_{2j}\sum_n a_n\left(\frac{\alpha_j}{r_2}\right)^{2n}$$

Applying the expressions for the power series in Eqs. (9.179), we get

$$\varphi_{1j}\frac{\alpha_j}{r_1}\sinh\left(\frac{\alpha_j}{r_1}\right) = \psi_{1j}\cosh\left(\frac{\alpha_j}{r_1}\right), \quad \varphi_{2j}\frac{\alpha_j}{r_2}\sinh\left(\frac{\alpha_j}{r_2}\right) = \psi_{2j}\cosh\left(\frac{\alpha_j}{r_2}\right)$$

Solving these equations in conjunction with Eqs. (9.185), we find

$$\varphi_{1j} = -w_j\beta_j r_1\sinh\left(\frac{\alpha_j}{r_2}\right), \quad \varphi_{2j} = w_j\beta_j r_2\sinh\left(\frac{\alpha_j}{r_1}\right) \tag{9.186}$$

where

$$\beta_j = \frac{\alpha_j^2}{r_1\sinh\left(\frac{\alpha_j}{r_2}\right) - r_2\sinh\left(\frac{\alpha_j}{r_1}\right)}$$

Using Eqs. (9.184) and (9.186) and applying Eq. (9.175), we arrive at the following expression for the constants in Eq. (9.152):

$$C_n = -\frac{1}{\lambda_n^2\cosh\lambda_n\int_{-1}^{1}(r_1^2u_n^2 - r_2^2\upsilon_n^2)d\bar{y}} \times\sum_{j=1}^{\infty}w_j\beta_j\left[r_1\sinh\left(\frac{\alpha_j}{r_2}\right)\int_{-1}^{1}u_n\cos\left(\alpha_j\bar{y}\right)d\bar{y} + r_2\sinh\left(\frac{\alpha_j}{r_1}\right)\int_{-1}^{1}\upsilon_n\cos\left(\alpha_j\bar{y}\right)d\bar{y}\right]$$

in which λ_n are the roots of Eq. (9.159), whereas $u_n(\bar{y})$ and $\upsilon_n(\bar{y})$ are specified by Eqs. (9.168). Calculating the integrals, we finally get

$$C_{1n} = \frac{\sum_{j=1}^{\infty}2w_j\alpha_j\beta_j\cos\left(r_1\lambda_n\right)\cos\left(r_2\lambda_n\right)\sin\alpha_j\left[\frac{r_1\sinh\left(\frac{\alpha_j}{r_2}\right)}{r_1^2\lambda_n^2-\alpha_j^2} - \frac{r_2\sinh\left(\frac{\alpha_j}{r_1}\right)}{r_2^2\lambda_n^2-\alpha_j^2}\right]}{\lambda_n\cosh\lambda_n\{r_1\cos^2(r_2\lambda_n)[r_1\lambda_n + \sin(r_1\lambda_n)\cos(r_1\lambda_n)] - r_2\cos^2(r_1\lambda_n)[r_2\lambda_n + \sin(r_2\lambda_n)\cos(r_2\lambda_n)]\}} \tag{9.187}$$

The foregoing solution corresponds to the case $D_3 > \sqrt{D_1 D_2}$ for which r_1 and r_2 are real numbers specified by Eq. (9.155). For the case $D_3 < \sqrt{D_1 D_2}$, r_1 and r_2 are complex numbers, given by Eq. (9.156), according to which

$$r_{1,2} = t_1 \mp i t_2, \quad t_{1,2} = \frac{b}{a\sqrt{2}} \sqrt{\sqrt{\frac{D_1}{D_2}} \mp \frac{D_3}{D_2}}$$

In this case, the foregoing solution should be transformed using the following relations:

$$\begin{aligned}
\sin(t_1 \mp i t_2) &= \sin t_1 \cdot \cosh t_2 \mp i \cos t_1 \cdot \sinh t_2 \\
\cos(t_1 \mp i t_2) &= \cos t_1 \cdot \cosh t_2 \mp i \sin t_1 \cdot \sinh t_2 \\
\sinh(t_1 \mp i t_2) &= \sinh t_1 \cdot \cos t_2 \mp i \cosh t_1 \cdot \sin t_2 \\
\cosh(t_1 \mp i t_2) &= \cosh t_1 \cdot \cos t_2 \mp i \sinh t_1 \cdot \sin t_2
\end{aligned}$$

For the case $D_3 = \sqrt{D_1 D_2}$, i.e., for an isotropic plate, the characteristic equation corresponding to Eq. (9.153) has double-reiterated roots $r_{1,2} = c$, where $c = b/a$. To study this case, we should put in the foregoing equations $r_1 = c$ and $r_2 = c + \varepsilon$ and go to the limit taking $\varepsilon \to 0$. For example, Eq. (9.159) for an isotropic plate reduces to

$$\sin 2c\lambda_m + 2c\lambda_m = 0 \tag{9.188}$$

This equation has only complex roots

$$2c\lambda_n = \pm r_n \pm i t_n \tag{9.189}$$

The real, r_n, and imaginary, t_n, parts of the first five roots are presented in Table 9.2. Consider, for example, a square ($a = b$) isotropic plate loaded with uniform pressure p_0. The normalized deflection at the plate center $\overline{w} = w(\overline{x} = 0, \overline{y} = 0)D_2/16p_0a^4$ calculated with the aid of the foregoing equations is $\overline{w} = 0.00128$ (Lurie and Vasiliev, 1995). The relatively accurate approximate solution presented by Timoshenko and Woinowsky-Krieger (1959) is $\overline{w} = 0.00126$.

9.4.2 Approximate solutions for classical plate theory

The exact solutions presented in the previous section, particularly the solution for the clamped plate given by Eqs. (9.152), (9.160), and (9.187), are rather cumbersome for practical applications. For this purpose, efficient approximate solutions can be constructed using applied methods of analysis (Vasiliev, 1993).

Consider a plate for which $a > b$ (see Fig. 9.17) and represent its deflection as

$$w(x, y) = W(x) \cdot f(y) \tag{9.190}$$

TABLE 9.2 Roots (Eq. 9.189) of Eq. (9.188)

n	1	2	3	4	5
r_n	4.211	10.713	17.073	23.398	29.700
t_n	2.250	3.103	3.550	3.859	4.093

Here, $f(y)$ is some function that satisfies the boundary conditions at the plate long edges $y = 0$ and $y = b$ (see Fig. 9.17) and approximates the plate deflection in the transverse direction. The function $f(y)$ can be taken as the deflection of the beam of unit width with the corresponding boundary conditions. Such functions are presented in Table 8.1. Neglecting the shear deformation, i.e., taking $S \to \infty$, and changing x to y and l to b, we get

$$f(y) = y^4 - 2by^3 + b^3y \tag{9.191}$$

for the beam with simply supported edges $y = 0$ and $y = b$ (see Fig. 9.18) and

$$f(y) = y^2(b - y)^2 \tag{9.192}$$

for the plate with clamped edges $y = 0$ and $y = b$ (see Fig. 9.20).

Since the functions in Eqs. (9.191) and (9.192) satisfy the boundary conditions, we can apply the Bubnov-Galerkin method (Grigolyuk, 1996) to obtain the approximate solutions. Consider the governing equation, Eq. (9.125). Substitute the deflections, Eq. (9.190), into Eq. (9.125), multiply it by $f(y)$, and integrate with respect to y from 0 to b to get the following ordinary differential equation for $W(x)$:

$$D_1 W^{IV} \int_0^b f^2 dy + 2D_3 W'' \int_0^b f'' f dy + D_2 W \int_0^b f^{IV} f dy = \int_0^b \overline{p} f dy \tag{9.193}$$

Using the boundary conditions for the functions given by Eqs. (9.191) and (9.192) and integrating by parts, we have

$$\int_0^b f'' f dy = -\int_0^b (f')^2 dy, \quad \int_0^b f^{IV} f dy = \int_0^b (f'')^2 dy$$

Thus, Eq. (9.193) reduces to

$$W^{IV} - 2k_1^2 W'' + k_2^4 W = k_p \tag{9.194}$$

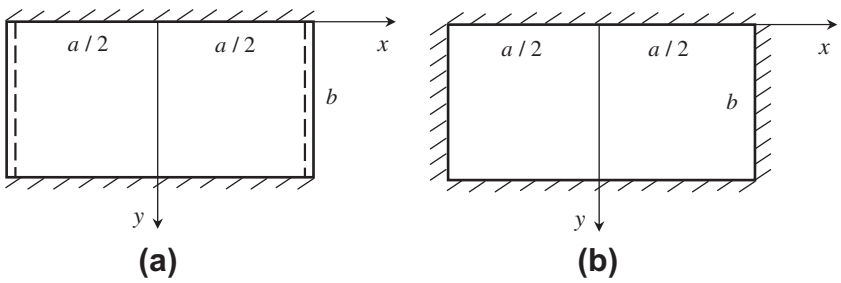


FIGURE 9.20

Plates with clamped longitudinal edges and simply supported (a) and clamped (b) transverse edges.

where

$$k_1^2 = \frac{D_3 c_2}{D_1 c_1}, \quad k_2^4 = \frac{D_2 c_3}{D_1 c_1}, \quad k_p = \frac{c_p}{D_1 c_1}$$

in which

$$c_1 = \int_0^b f^2 dy, \quad c_2 = \int_0^b (f')^2 dy, \quad c_3 = \int_0^b (f'')^2 dy, \quad c_p = \int_0^b \overline{p} f dy \tag{9.195}$$

For plate loaded with uniform pressure $\overline{p} = p_0$,

$$c_p = p_0 c, \quad c = \int_0^b f dy \tag{9.196}$$

The solution of Eq. (9.194) is specified by Eq. (9.141), i.e.,

$$W = \sum_{i=1}^{4} c_i \Phi_i(x) + W_p$$

The functions Φ_i are given in Table 9.1. For uniform pressure $\overline{p} = p_0$ and the same boundary conditions at the plate transverse edges $x = \pm a/2$ (see Figs. 9.18 and 9.20)

$$W = c_1 \Phi_1(x) + c_2 \Phi_2(x) + W_p \tag{9.197}$$

in which

$$W_p = \frac{p_0 c}{D_1 c_1}$$

The constants c_1 and c_2 can be found from the boundary conditions at $x = \pm a/2$.

If the plate longitudinal edges $(y = 0, \ y = b)$ are simply supported (Fig. 9.18), the function $f(y)$ is specified by Eq. (9.191) and the coefficients given by Eqs. (9.195) and (9.196) are

$$c_1 = 0.04921 b^9, \quad c_2 = 0.48571 b^7, \quad c_3 = 4.8 b^5, \quad c = 0.2 b^5$$

If the plate transverse edges $(x = \pm a/2)$ are also simply supported (see Fig. 9.18a), the solution in Eqs. (9.190) and (9.197) can be written as

$$w(x, y) = W_p [1 - F_1(x)](y^4 - 2by^3 + b^3 y) \tag{9.198}$$

where $F_1(x)$ is specified by Eq. (9.146).

For a plate with simply supported longitudinal edges and clamped transverse edges

$$w(x, y) = W_p [1 - F_2(x)](y^4 - 2by^3 + b^3 y) \tag{9.199}$$

(Fig. 9.18b), where $F_2(x)$ is given by Eq. (9.147).

For a plate with clamped longitudinal edges (see Fig. 9.20), the function $f(y)$ corresponds to Eq. (9.192), whereas the coefficients in Eqs. (9.195) and (9.196) become

$$c_1 = 0.001587b^9, \quad c_2 = 0.01905b^7, \quad c_3 = 0.8b^5, \quad c = 0.03333b^5$$

If the plate transverse edges are simply supported

$$w(x,y) = W_p[1 - F_1(x)]y^2(b^2 - y^2) \tag{9.200}$$

(see Fig. 9.20a), where $F_1(x)$ is given by Eq. (9.146).

Finally, for a plate with clamped edges

$$w(x,y) = W_p[1 - F_2(x)]y^2(b^2 - y^2) \tag{9.201}$$

(see Fig. 9.20b), in which $F_2(x)$ is specified by Eq. (9.147).

The simple approximate solutions obtained are typically fairly accurate. In particular, the deflection closely coincides with the corresponding exact solution, whereas the accuracy of the moment is within about 5% (Vasiliev, 1993). Approximate solutions for orthotropic plates with various boundary conditions have been presented by Whitney (1971), Dalaei and Kerr (1995), and Bhaskar and Kaushik (2004).

9.4.3 Shear deformable orthotropic symmetric plates

The behavior of shear deformable orthotropic symmetric plates under transverse bending is described by Eqs. (9.40)–(9.42). The exact solution of these equations can be found for simply supported plates (see Fig. 9.14) with the classical boundary conditions

$$w = 0, \quad M_x = 0, \quad \theta_y = 0 \quad \text{for the edges } x = constant$$
$$w = 0, \quad M_y = 0, \quad \theta_x = 0 \quad \text{for the edges } y = constant$$

For the simply supported plate shown in Fig. 9.14 with the foregoing boundary conditions, the function $W(x,y)$ in Eq. (9.40) can be taken in the form of the following series:

$$W(x,y) = \sum_m \sum_n W_{mn} \sin \lambda_m x \cdot \sin \lambda_n y \tag{9.202}$$

where $\lambda_m = \pi m/a$, $\lambda_n = \pi n/b$. The pressure $\overline{p}(x,y)$ should be decomposed into a similar series specified by Eq. (9.131). Then, substitution into Eq. (9.40) yields

$$W_{mn} = \frac{p_{mn}}{R_{mn}} \tag{9.203}$$

where

$$R_{mn} = D_{mn}\lambda_m^2 + D_{nm}\lambda_n^2 + 2\overline{D}\lambda_m^2\lambda_n^2 + (D_{mn}D_{nm} - \overline{D}\lambda_m^2\lambda_n^2)\left(\frac{\lambda_n^2}{S_x} + \frac{\lambda_m^2}{S_y}\right)$$

in which

$$D_{mn} = D_{11}\lambda_m^2 + D_{44}\lambda_n^2, \quad D_{nm} = D_{22}\lambda_n^2 + D_{44}\lambda_m^2, \quad \overline{D} = D_{12} + D_{44}$$

The rotation angles and the deflection can be found from Eqs. (9.41) and (9.42) as

$$\theta_x = \sum_m \sum_n \theta_x^{mn} \cos \lambda_m x \cdot \sin \lambda_n y$$
$$\theta_y = \sum_m \sum_n \theta_y^{mn} \sin \lambda_m x \cdot \cos \lambda_n y \tag{9.204}$$
$$w = \sum_m \sum_n w_{mn} \sin \lambda_m x \cdot \sin \lambda_n y$$

where

$$\theta_x^{mn} = -\lambda_m W_{mn}\left(1 + \frac{D_{nm}}{S_y} - \frac{\overline{D}}{S_x}\lambda_n^2\right)$$
$$\theta_y^{mn} = -\lambda_n W_{mn}\left(1 + \frac{D_{mn}}{S_x} - \frac{\overline{D}}{S_y}\lambda_m^2\right)$$
$$w_{mn} = c_{mn} W_{mn} \tag{9.205}$$

in which

$$c_{mn} = 1 + \frac{D_{mn}}{S_x} + \frac{D_{nm}}{S_y} + \frac{1}{S_x S_y}\left(D_{mn}D_{nm} - \overline{D}\lambda_m^2\lambda_n^2\right)$$

The bending moments and transverse shear forces can be found with the aid of Eqs. (9.32) and (9.34).

For plates with other boundary conditions, approximate analytical solutions are usually derived. Note that the governing equations of the theory of shear deformable plates have a special structure that allows us to simplify the problem. To study this structure, consider a semi-infinite plate with simply supported longitudinal edges as shown in Fig. 9.9. The pressure is specified by Eq. (9.111), according to which

$$\overline{p} = p_0 \sin \lambda y, \quad \lambda = \frac{\pi}{b} \tag{9.206}$$

The solution of Eq. (9.40) can be presented in the form

$$W(x, y) = F(x) \sin \lambda y$$

Substitution into Eq. (9.40) results in the following ordinary differential equation:

$$-\frac{D_1 D_{44}}{S_y}F^{VI} + \left\{D_1 + \left[\frac{D_1 D_{44}}{S_x} + \frac{1}{S_y}(D_1 D_2 - D_{12}D_3)\right]\lambda^2\right\}F^{IV}$$
$$-\left\{2D_3\lambda^2 + \left[\frac{D_1 D_{44}}{S_y} + \frac{1}{S_x}(D_1 D_2 - D_{12}D_3)\right]\lambda^4\right\}F'' + \left(D_2 + \frac{D_{44}}{S_x}\lambda^2\right)\lambda^4 F = p_0 \tag{9.207}$$

Here, D_1, D_2, and D_3 are specified by Eqs. (9.126). Recall that for isotropic plates (see Section 9.3.2), Eq. (9.207) degenerates into a set of two separate equations, Eqs. (9.113) and (9.114). For orthotropic plates, we have a unique equation of the sixth order which cannot be reduced exactly to two independent equations. However, applying the asymptotic method (Reissner, 1989, 1991), we can approximately reduce the sixth-order equation to a set of a fourth-order and second-order equations.

It follows from Section 9.3.2 that Eq. (9.207) has two solution types, i.e., a penetrating solution and a boundary-layer solution. The penetrating (or internal) part of the general solution F_i relatively slowly changes over the plate surface, which means that the derivatives of this solution $F_i^{(n)}$ are of the same order of magnitude as the function F_i. However, Eq. (9.207) contains the terms D and S in D/S which have the order of magnitude $\overline{h}^2$, where $\overline{h} = h/b$, h being the plate thickness and b the in-plane dimensions. To determine the penetration solution for relatively thin $(\overline{h} \ll 1)$ plates, these small terms can be neglected and Eq. (9.207) can be reduced to

$$D_1 F_i^{IV} - 2D_3 \lambda^2 F_i'' + D_2 \lambda^4 F_i = p_0 \tag{9.208}$$

This equation is similar to Eq. (9.113).

The boundary-layer (or edge) solution F_e is a rapidly changing function whose derivatives can be evaluated as $F_e^{(n)} = F_e/\overline{h}^{(n)}$. Taking into account that D/S is proportional to $\overline{h}^2$, we can conclude that only two terms of Eq. (9.207) (namely, the first one and the second) have the order $(1/\overline{h}^4)$. Neglecting the rest of the terms, we arrive at the following equation for the boundary-layer solution:

$$-\frac{D_1 D_{44}}{S_y} F_e^{VI} + D_1 F_e^{IV} = 0$$

Reducing the order of this equation, we finally transform it into the following form:

$$F_e'' - \frac{S_y}{D_{44}} F_e = 0 \tag{9.209}$$

which is similar to Eq. (9.114). Thus, the solution of Eq. (9.207) becomes

$$F = F_i + F_e \tag{9.210}$$

where F_i and F_e are the solutions of Eqs. (9.208) and (9.209), respectively. The total solution given by Eq. (9.210) allows us to satisfy three boundary conditions at the plate edge.

Returning to the general case, i.e., to Eq. (9.40), we can present its approximate solution in a form analogous to Eq. (9.210), i.e.,

$$W = W_i + W_e \tag{9.211}$$

where W_i can be found from the following equation:

$$D_1 \frac{\partial^4 W}{\partial x^4} + 2D_3 \frac{\partial^4 W}{\partial x^2 \partial y^2} + D_2 \frac{\partial^4 W}{\partial y^4} = \overline{p} \tag{9.212}$$

In the vicinity of the edge $x = constant$, the boundary-layer solution satisfies the following equation similar to Eq. (9.209):

$$\frac{\partial^2 W_e}{\partial x^2} - s_y^2 W_e = 0, \quad s_y^2 = \frac{S_y}{D_{44}} \tag{9.213}$$

whereas in the vicinity of the edge $y = constant$

$$\frac{\partial^2 W_e}{\partial y^2} - s_x^2 W_e = 0, \quad s_x^2 = \frac{S_x}{D_{44}} \tag{9.214}$$

Thus, the solution should be constructed separately for the edges $x = constant$ and $y = constant$.

It follows from Section 9.3.2 that for relatively thin plates whose edges are fixed with respect to deflection, the boundary-layer solution can be neglected in comparison with the penetrating solution. Naturally, in this case only two boundary conditions can be formulated at the plate edge. However, for the plates under consideration, three boundary conditions can be reduced to two as shown in Section 9.3.2. The penetrating solution can be found from Eq. (9.212), whereas the expressions for the rotation angles and deflection in Eqs. (9.41) and (9.42) are simplified to

$$\theta_x = -\frac{\partial W_i}{\partial x}, \quad \theta_y = -\frac{\partial W_i}{\partial y}, \quad w = W_i - \frac{D_1}{S_x}\frac{\partial^2 W_i}{\partial x^2} - \frac{D_2}{S_y}\frac{\partial^2 W_i}{\partial y^2} \tag{9.215}$$

The moments and the forces are

$$M_x = -\left(D_1\frac{\partial^2 W_i}{\partial x^2} + D_{12}\frac{\partial^2 W_i}{\partial y^2}\right), \quad M_y = -\left(D_2\frac{\partial^2 W_i}{\partial y^2} + D_{12}\frac{\partial^2 W_i}{\partial x^2}\right)$$

$$M_{xy} = -2D_{44}\frac{\partial^2 W_i}{\partial x \partial y}$$

$$V_x = -\frac{\partial}{\partial x}\left(D_1\frac{\partial^2 W_i}{\partial x^2} + D_3\frac{\partial^2 W_i}{\partial y^2}\right), \quad V_y = -\frac{\partial}{\partial y}\left(D_2\frac{\partial^2 W_i}{\partial y^2} + D_3\frac{\partial^2 W_i}{\partial x^2}\right)$$

Note that the foregoing set of equations for the penetrating solution in the theory of shear deformable plates has been obtained for isotropic plates by L. Donnell (1959, 1976) as a generalization of the corresponding Timoshenko (1921) beam theory. In this theory, the first term in Eqs. (9.215) is the part of the plate deflection caused by bending, whereas the last two terms take into account the part of the deflection induced by shear deformation. To obtain the penetrating solution in the theory of shear deformable plates the exact or approximate methods discussed in Sections 9.4.1 and 9.4.2 as applied in classical plate theory can be used. It is only necessary to take into account that in accordance with Donnell's interpretation W_i in Eq. (9.215) is the deflection w corresponding to classical plate theory. Thus, the approximate solutions of classical plate theory specified by Eqs. (9.198)–(9.201) are valid for the shear deformable plate theory under consideration if we change $w(x,y)$ to $W_i(x, y)$ in the left-hand parts of these equations and apply Eq. (9.215) to determine the plate deflection.

However, as shown in Section 9.3.2, the boundary-layer solution can be neglected if the parameters s_x and s_y in Eqs. (9.213) and (9.214) are much larger than the parameter λ for the penetrating solution in Eq. (9.206). If these parameters are of the same order of magnitude, the boundary-layer solution cannot be neglected in comparison with the penetrating solution. This situation usually occurs for thick sandwich plates with a shear deformable core (see the conclusion of Section 9.3.2).

Consider two particular cases for which the problem can be readily solved, i.e., square and close-to-square plates (see Fig. 9.15a) and long plates (see Fig. 9.15b).

To study square and close-to-square plates, apply the initial equilibrium equations, i.e., Eqs. (9.36) for θ_x, θ_y, and w which describe both the penetrating and the boundary-layer states of the plate. For the plates under consideration, introduce the following one-term approximations:

$$\begin{aligned} \theta_x(x,y) &= C_x \cdot \theta_{xx}(x) \cdot \theta_{xy}(y) \\ \theta_y(x,y) &= C_y \cdot \theta_{yx}(x) \cdot \theta_{yy}(y) \\ w(x,y) &= W \cdot w_x(x) \cdot w_y(y) \end{aligned} \tag{9.216}$$

in which C_x, C_y, and W are some constants and θ_{xx}, θ_{xy}, θ_{yx}, θ_{yx}, w_x, and w_y are preassigned coordinate functions that satisfy the boundary conditions. Applying the Bubnov-Galerkin method, multiply Eqs. (9.36) by $\theta_{xx}\theta_{xy}$, $\theta_{yx}\theta_{yy}$, and $w_x w_y$, respectively, and integrate the resulting equations over the plate surface (see Fig. 9.1). As a result, Eqs. (9.36) reduce to the following algebraic equations for the coefficients C_x and C_y, and

$$\begin{aligned} A_{11}C_x + A_{12}C_y + A_{13}W &= 0 \\ A_{21}C_x + A_{22}C_y + A_{23}W &= 0 \\ A_{31}C_x + A_{32}C_y + A_{33}W + A_p &= 0 \end{aligned} \tag{9.217}$$

where

$$\begin{aligned} A_{11} &= D_{11}a_1b_1 + D_{44}a_2b_2 - S_x a_2 b_1 \\ A_{12} &= \overline{D}a_3b_3, \quad A_{13} = -S_x a_4 b_4, \quad A_{21} = \overline{D}a_5 b_5 \\ A_{22} &= D_{22}a_6b_6 + D_{44}a_7b_7 - S_y a_6 b_7 \\ A_{23} &= -S_y a_8 b_8, \quad A_{31} = S_x a_9 b_9, \quad A_{32} = S_y a_{10} b_{10} \\ A_{33} &= S_x a_{11} b_{11} + S_y a_{12} b_{12}, \quad A_p = \int_0^a \int_0^b \overline{p} w_x w_y dx dy \end{aligned}$$

in which

$$a_1 = \int_0^a \theta''_{xx}\theta_{xx}dx, \quad a_2 = \int_0^a \theta^2_{xx}dx, \quad a_3 = \int_0^a \theta'_{yx}\theta_{xx}dx, \quad a_4 = \int_0^a w'_x\theta_{xx}dx$$

$$a_5 = \int_0^a \theta'_{xx}\theta_{yx}dx, \quad a_6 = \int_0^a \theta^2_{yx}dx, \quad a_7 = \int_0^a \theta''_{yx}\theta_{yx}dx, \quad a_8 = \int_0^a w_x\theta_{yx}dx$$

$$a_9 = \int_0^a \theta'_{xx}w_x dx, \quad a_{10} = \int_0^a \theta_{yx}w_x dx, \quad a_{11} = \int_0^a w''_x w_x dx, \quad a_{12} = \int_0^a w^2_x dx$$

and

$$b_1 = \int_0^b \theta^2_{xy}dy, \quad b_2 = \int_0^b \theta''_{xy}\theta_{xy}dy, \quad b_3 = \int_0^b \theta'_{yy}\theta_{xy}dy, \quad b_4 = \int_0^b w_y\theta_{xy}dx$$

$$b_5 = \int_0^b \theta'_{yy}\theta_{yy}dy, \quad b_6 = \int_0^b \theta''_{yy}\theta_{yy}dy, \quad b_7 = \int_0^b \theta^2_{yy}dy, \quad b_8 = \int_0^b w_y\theta_{yy}dx$$

$$b_9 = \int_0^b \theta_{xy}w_y dy, \quad b_{10} = \int_0^b \theta'_{yy}w_y dy, \quad b_{11} = \int_0^b w^2_y dy, \quad b_{12} = \int_0^b w''_y w_y dx$$

The solution of Eqs. (9.127) is

$$\begin{aligned}\theta_x &= \frac{A_p}{A}(A_{12}A_{23} - A_{22}A_{23})\\ \theta_y &= \frac{A_p}{A}(A_{21}A_{13} - A_{11}A_{23})\\ W &= \frac{A_p}{A}(A_{11}A_{23} - A_{12}A_{21})\end{aligned} \tag{9.218}$$

where

$$A = [(A_{32}A_{23} - A_{22}A_{33})A_{11} + (A_{22}A_{31} - A_{32}A_{21})A_{13} + (A_{21}A_{33} - A_{31}A_{23})A_{12}]$$

We take the solutions of the theory of shear deformable beams (see Table 8.1) presented in Table 9.3 as the coordinate functions in Eqs. (9.216).

Consider the second particular case, i.e., long plates as depicted in Fig. 9.15b. For such plates, we can assume that in the middle part of the plate the stress-strain state does not depend on the

TABLE 9.3 Coordinate Functions for the Plates Loaded with Uniform Pressure

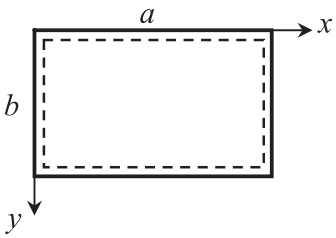
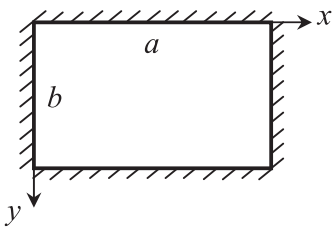
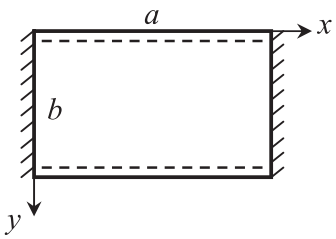
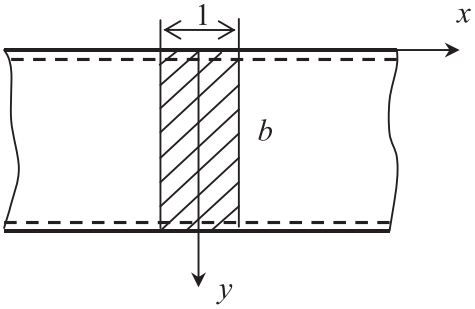
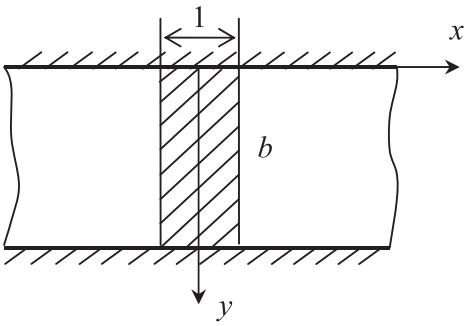
Boundary Conditions	Coordinate functions
	$w_x(x) = \theta_{yx}(x) = x^4 - 2\alpha x^3 - \frac{12D_1}{S_x}x^2 + \left(\alpha^3 + \frac{12D_1\alpha}{S_x}\right)x$ $\theta_{xx}(x) = 4x^3 - 6\alpha x^2 + \alpha^3$ $w_y(y) = \theta_{xy}(y) = y^4 - 2by^3 - \frac{12D_2}{S_y}y^2 + \left(b^3 + \frac{12D_2 b}{S_y}\right)y$ $\theta_{yy}(y) = 4y^3 - 6by^2 + b^3$
	$w_x(x) = \theta_{yx}(x) = -x^4 + 2\alpha x^3 + \left(\frac{12D_1}{S_x} - \alpha^2\right)x - \frac{12D_1\alpha x}{S_x}$ $\theta_{xx}(x) = 2x^3 - 3\alpha x^2 + \alpha^2 x$ $w_y(y) = \theta_{xy}(y) = -y^4 + 2by^3 + \left(\frac{12D_2}{S_y} - b^2\right)y - \frac{12D_2 by}{S_y}$ $\theta_{yy}(y) = 2y^3 - 3by^2 + b^2 y$
	$w_x(x) = \theta_{yx}(x) = -x^4 + 2\alpha x^3 + \left(\frac{12D_1}{S_x} - \alpha^2\right)x - \frac{12D_1\alpha x}{S_x}$ $\theta_{xx}(x) = 2x^3 - 3\alpha x^2 + \alpha^2 x$ $w_y(y) = \theta_{xy}(y) = y^4 - 2by^3 - \frac{12D_2}{S_y}y^2 + \left(b^3 + \frac{12D_2 b}{S_y}\right)y$ $\theta_{yy}(y) = 4y^3 - 6by^2 + b^3$

TABLE 9.4 Equations for Infinitely Long Orthotropic Plates Under Uniform Pressure p_0

Boundary Conditions	Equations
	$w = \frac{p_0}{24D_2}\left[b^3 - 2by^2 + y^3 + 12\frac{D_2}{S_y}(b-y)\right]y$ $\theta_y = -\frac{p_0}{24D_2}(b^3 - 6by^2 + 4y^3)$ $M_y = \frac{1}{2}p_0(b-y)y$ $V_y = \frac{1}{2}p_0(b-2y)$
	$w = \frac{p_0}{24D_2}\left[y(b-y) + 12\frac{D_2}{S_y}\right](b-y)y$ $\theta_y = -\frac{p_0}{12D_2}(2y^2 - 3by + b^2)y$ $M_y = -\frac{p_0}{12}(6y^2 - 6by + b^2)$ $V_y = -\frac{p_0}{2}(2y - b)$

x-coordinate. Then, the problem reduces to the bending of a beam of unit width, the solution for which is obtained in Chapter 8 (see Table 8.1). The basic equations for infinitely long plates are presented in Table 9.4.

As an example, consider a simply supported rectangular plate with thickness $h = 15$ mm, width $b = 250$ mm, and various aspect ratios a/b. The plate has a sandwich structure with carbon-epoxy facing layers and an aluminum honeycomb core. The plate parameters are $D_1 = D_2 = D$, $D_{12}/D = D_{44}/D = 0.25$, $D/b^2S_x = 0.04$, and $D/b^2S_y = 0.08$. The normalized maximum deflection of the plate w_m/b as a function of the aspect ratio a/b is shown in Fig. 9.21. The solid line corresponds to the exact solution, Eq. (9.203), and the dashed line shows the solution given by Eqs. (9.218) corresponding to square and close-to-square plates, whereas the dotted line demonstrates the solution for an infinitely long plate (see Table 9.4). As can be seen, for $1 \le a/b \le 1.75$ the plate can be treated as close to square and for $a/b > 3$ the solution for an infinitely long plate can be applied.

In the general case (or for $1.75 \le a/b \le 3$), the problem cannot be considerably simplified and the general equations, Eqs. (9.36), must be solved. Apply the approximate method described in Section 9.4.2 and represent the unknown functions in the following form:

$$\theta_x(x,y) = F_x(x).\theta_{xy}(y), \quad \theta_y(x,y) = F_y(x).\theta_{yy}(y), \quad w(x,y) = W(x).w_y(y) \tag{9.219}$$

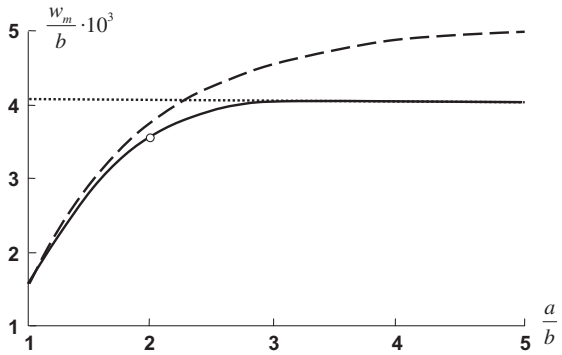


FIGURE 9.21

Dependence of the normalized maximum deflection of a simply supported rectangular plate on the aspect ratio a/b: exact solution (———), solution for a square plate (— — —), solution for an infinitely long plate (·····), numerical solution (○).

Here, F_x, F_y, and W are the unknown functions of the coordinate x, whereas the functions θ_{xy},θ_{yy}, and w_y are presented in Table 9.3 for various boundary conditions. Multiply Eqs. (9.36) by θ_{xy}, θ_{yy}, and w_y, respectively, and integrate them with respect to y from $y = 0$ to $y = b$ (see Figs. 9.18 and 9.20). As a result, we arrive at the following set of ordinary differential equations for the functions $F_x(x)$, $F_y(x)$, and $W(x)$:

$$\begin{aligned} L_{1x}(F_x) + L_{1y}(F_y) + L_{1w}(W) &= 0 \\ L_{2x}(F_x) + L_{2y}(F_y) + L_{2w}(W) &= 0 \\ L_{3x}(F_x) + L_{3y}(F_y) + L_{3w}(W) + L_p &= 0 \end{aligned} \tag{9.220}$$

where

$$L_{1x}(F_x) = \frac{1}{S_x}(D_1 a_{11} F_x'' + D_{33} b_{11} F_x) - a_{11} F_x$$

$$L_{1y}(F_y) = \frac{1}{S_x}\overline{D} a_{21} F_y', \quad L_{1w}(W) = -a_{13} W'$$

$$L_{2y}(F_y) = \frac{1}{S_y}(D_2 a_{22} F_y + D_{33} b_{22} F_y'') - b_{22} F_y$$

$$L_{2x}(F_x) = \frac{1}{S_y}\overline{D} a_{21} F_x', \quad L_{2w}(W) = -a_{23} W$$

$$L_{3x}(F_x) = S_x a_{31} F_x', \quad L_{3y}(F_y) = S_y a_{32} F_y$$

$$L_{3w}(W) = S_x a_{33} W'' + S_y W b_{33}, \quad L_p = \int_0^b \overline{p} w_y dy$$

in which

$$a_{11}=\int_0^b \theta_{xy}^2 dy,\quad b_{11}=\int_0^b \theta_{xy}''\theta_{xy} dy,\quad a_{12}=\int_0^b \theta_{yy}'\theta_{xy} dy,\quad a_{13}=\int_0^b w_y\theta_{xy} dy$$

$$a_{21}=\int_0^b \theta_{xy}'\theta_{yy} dy,\quad a_{22}=\int_0^b \theta_{yy}''\theta_{yy} dy,\quad b_{22}=\int_0^b \theta_{yy}^2 dy,\quad a_{23}=\int_0^b w_y'\theta_{yy} dy$$

$$a_{31}=\int_0^b \theta_{xy} w_y dy,\quad a_{32}=\int_0^b \theta_{yy}' w_y dy,\quad a_{33}=\int_0^b w_y^2 dy,\quad b_{33}=\int_0^b w_y'' w_y dy$$

In principle, Eqs. (9.220) can be solved analytically. They can be reduced to sixth-order ordinary differential equations and further to third-order algebraic characteristic equations, the roots of which specify the form of the general solution. This solution includes six constants which can be found from the boundary conditions for the plate edges $x=\pm a/2$ (see Fig. 9.18 or 9.20). However, it is easier to apply numerical integration of Eqs. (9.220). For the aspect ratio $a/b=2$, the result of such integration is shown in Fig. 9.21 by a circle.

9.5 BUCKLING OF ORTHOTROPIC SYMMETRIC PLATES

As known, the plates subjected to in-plane compression and shear can buckle after the load reaches some critical value. The problem of buckling is studied in this section.

9.5.1 Classical plate theory

Consider a rectangular plate simply supported at the edges and loaded with external in-plane line loads T_x, T_y, and T_{xy} (see Fig. 9.22). Under the action of in-plane compression or shear, the initial plane shape of the plate can become unstable and the plate takes a curved shape shown, for example, in Fig. 9.23. The corresponding forces that are referred to as critical loads can be found using the Euler buckling criterion, according to which the critical load is the minimum load which provides, in addition to the initial plane state of the plate, some curved shape of the plate close to this state which is balanced by the applied in-plane forces. Thus, to determine the critical load, we must induce a small

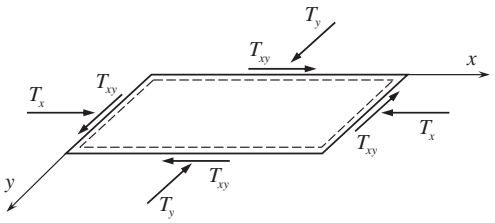


FIGURE 9.22

A plate loaded with in-plane loads.

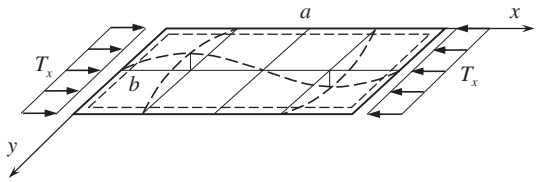


FIGURE 9.23

Buckling mode of a plate under uniaxial compression.

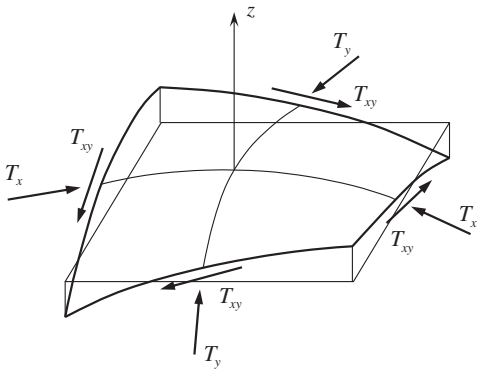


FIGURE 9.24

A deformed element of the plate reference surface.

deflection of the plate (see the dashed lines in Fig. 9.23) and find the minimum in-plane load under which the plate is in equilibrium with this load. The simplest way to derive the buckling equation which allows us to determine the critical load is to apply the method described in Section 8.4 with application to beams. Consider an element of the plate reference surface and induce small curvatures κ_x and κ_y and twist κ_{xy} deforming the element as shown in Fig. 9.24, which is similar to Fig. 8.12 drawn for the beam. It follows from Fig. 9.24 that the forces T_x, T_y, and T_{xy} now acquire a nonzero projection on the z-axis, which can be simulated by an imaginary pressure p_n which is shown in Fig. 9.25; compare Fig. 8.13 for the beam. This imaginary pressure can be found as

$$p_n = T_x\kappa_x + T_y\kappa_y + T_{xy}\kappa_{xy} \tag{9.221}$$

in which κ_x, κ_y, and κ_{xy} are specified by Eqs. (9.49). Using these equations and taking $\overline{p} = p_n$ in the equilibrium equation, Eq. (9.125) of classical plate theory, we arrive at the following buckling equation for orthotropic plates:

$$D_1\frac{\partial^4 w}{\partial x^4} + 2D_3\frac{\partial^4 w}{\partial x^2\partial y^2} + D_2\frac{\partial^4 w}{\partial y^4} + T_x\frac{\partial^2 w}{\partial x^2} + T_y\frac{\partial^2 w}{\partial y^2} + 2T_{xy}\frac{\partial^2 w}{\partial x\partial y} = 0 \tag{9.222}$$

where, as earlier, $D_1 = D_{11}$, $D_2 = D_{22}$, and $D_3 = D_{12} + 2D_{44}$. For plates that are simply supported at the edges $x = 0$, $x = a$ and $y = 0$, $y = b$ (see Fig. 9.22), the deflection can be presented in the form of

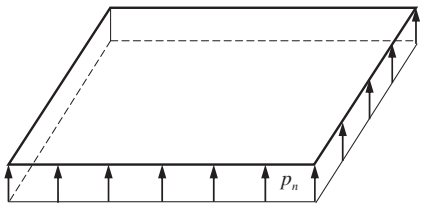


FIGURE 9.25

Imaginary pressure simulating the action of forces T_x, T_y, and T_{xy}.

double trigonometric series, i.e.,

$$w(x,y)=\sum_m\sum_n w_{mn}\sin\lambda_m x\cdot\sin\lambda_n y,\quad \lambda_m=\frac{\pi m}{a},\quad \lambda_n=\frac{\pi n}{b} \tag{9.223}$$

Each term of which satisfies the boundary conditions, Eqs. (9.128).

If the plate is subjected to uniaxial compression (see Fig. 9.23), $T_y=T_{xy}=0$ and Eq. (9.222) reduces to

$$L(w)+T_x\frac{\partial^2 w}{\partial x^2}=0,\quad L(w)=D_1\frac{\partial^4 w}{\partial x^4}+2D_3\frac{\partial^4 w}{\partial x^2\partial y^2}+D_2\frac{\partial^4 w}{\partial y^4} \tag{9.224}$$

Substitution of Eq. (9.223) into Eq. (9.224) allows us to determine the force T_x which provides the equilibrium of the plate with a nonzero deflection in Eq. (9.223), i.e.,

$$T_x=\frac{\pi^2}{b^2}L_{mn} \tag{9.225}$$

where

$$L_{mn}=D_1\lambda+2D_3n^2+D_2\frac{n^4}{\lambda} \tag{9.226}$$

in which $\lambda=(mb/a)^2$. Thus, for each combination of the half-wave numbers m and n in Eq. (9.223) for the deflection, there exists a force T_x specified by Eq. (9.225). For example, the curved shape of the plate corresponding to $m=2$ and $n=1$ is shown in Fig. 9.23 with the dashed lines. The critical force T_x^c corresponds to the minimum value of the coefficient L_{mn} with respect to $m=1,2,3\ldots$ and $n=1,2,3\ldots$. It follows from Eq. (9.226) that L_{mn} increases with an increase in n. Thus, the minimum possible value $n=1$ must be taken in Eq. (9.226) and

$$L_{mn}=L_m=D_1\lambda+2D_3+\frac{D_2}{\lambda} \tag{9.227}$$

The dependence of L_m/D_1 on the plate aspect ratio a/b for various m-values is shown in Fig. 9.26 for a carbon-epoxy angle-ply $\pm45^\circ$ rectangular plate. The solid parts of the lines correspond to the minimum values of coefficient L_m. For example, for $a/b<1$, we have the curve corresponding to $m=1$. The points of intersection of the curves in Fig. 9.26 corresponding to $(m-1)$, m, and $(m+1)$ can be found from the following conditions: $L_m(m-1)=L_m(m)$ and $L_m(m)=L_m(m+1)$. These

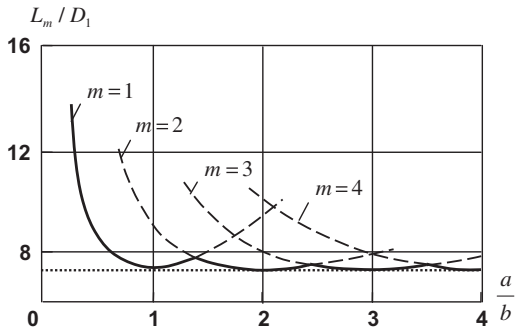


FIGURE 9.26

Dependence of L_m/D_1 on the plate aspect ratio a/b.

conditions allow us to determine m which provides the minimum value of L_m for a plate with given stiffness and geometric parameters. The corresponding value of m satisfies the following inequality:

$$m(m-1) < \frac{a^2}{b^2}\sqrt{\frac{D_2}{D_1}} < m(m+1)$$

For example, let $D_2 = D_1$ and $a/b = 1.75$. Then, the foregoing condition, i.e.,

$$m(m-1) < 3.06m(m+1)$$

is satisfied from $m = 2$ which corresponds to the plate shown in Fig. 9.23.

For $a/b \geq 2$, i.e., for relatively long plates, the approximate minimum condition $dL_m/d\lambda = 0$ can be used for L_m in Eq. (9.227). As a result, we get

$$\lambda^2 = \frac{D_2}{D_1}, \quad L_m = 2\left(\sqrt{D_1 D_2} + D_3\right) \tag{9.228}$$

For the example illustrated by Fig. 9.26, $L_m/D_1 = 7.22$. This result is depicted in Fig. 9.26 by the dotted line. Substitution of Eq. (9.228) into Eq. (9.225) yields the following final expression for the critical load:

$$T_x^c = \frac{2\pi^2}{b^2}\sqrt{D_1 D_2}\left(1 + \frac{D_3}{\sqrt{D_1 D_2}}\right) \tag{9.229}$$

For a homogeneous plate,

$$T_x^c = \frac{\pi^2 h^3}{6b^2}\left(\sqrt{\overline{E}_x \overline{E}_y} + \upsilon_{xy}\overline{E}_x + 2G_{xy}\right)$$

where

$$\overline{E}_{x,y} = \frac{E_{x,y}}{1 - \upsilon_{xy}\upsilon_{yx}}, \quad E_x \upsilon_{xy} = E_y \upsilon_{yx}$$

Consider biaxial loading with forces T_x and T_y (see Fig. 9.22). Taking $T_{xy} = 0$ in Eq. (9.222), we get

$$L(w) + T_x \frac{\partial^2 w}{\partial x^2} + T_y \frac{\partial^2 w}{\partial y^2} = 0$$

where $L(w)$ is obtained from Eqs. (9.224). Substitution of the deflection into Eq. (9.223) yields

$$T_x \lambda_m^2 + T_y \lambda_n^2 = D_1 \lambda_m^4 + 2D_3 \lambda_m^2 \lambda_n^2 + D_2 \lambda_n^4$$

Introducing the loading parameter $p = T_y/T_x$, we get Eq. (9.225) for T_x in which

$$L_{mn} = \frac{n^2 \lambda}{\lambda + p}\left(D_1 \lambda + 2D_3 + \frac{D_2}{\lambda}\right), \quad \lambda = \left(\frac{mb}{na}\right)^2 \tag{9.230}$$

For the given loading parameter p, the minimum value of L_{mn} can be found by sorting $m, n = 1, 2, 3\ldots$. Various combinations of loads T_x and T_y have been studied by Jones (2006).

For composite plates, a biaxial stress state can be induced by uniaxial loading with forces T_x only. Consider the plane state of the plate loaded in the general case with forces T_x and T_y which cause the in-plane strains ε_x^0 and ε_y^0 linked with the forces T_x and T_y by the constitutive equations, Eqs. (9.5), i.e.,

$$T_x = B_{11}\varepsilon_x^0 + B_{12}\varepsilon_y^0, \quad T_y = B_{21}\varepsilon_x^0 + B_{22}\varepsilon_y^0 \tag{9.231}$$

Assume that under compression in the x-direction with forces T_x the plate longitudinal edges $y = 0$ and $y = \mathrm{b}$ (see Fig. 9.23) can move in the y-direction. Then, $T_y = 0$ and Eqs. (9.231) yield

$$\varepsilon_y^0 = -\frac{B_{21}}{B_{22}}\varepsilon_x^0, \quad T_x = \left(B_{11} - \frac{B_{12}B_{21}}{B_{22}}\right)\varepsilon_x^0$$

The critical force for such plates is specified by Eq. (9.229). Now assume that the plate longitudinal edges are fixed, so that $\varepsilon_y^0 = 0$. Then, it follows from Eqs. (9.231) that a reactive force

$$T_y = \frac{B_{21}}{B_{11}} T_x = \upsilon_{xy} T_x$$

appears in the plate due to Poisson's effect. For composite plates, Poisson's ratio υ_{xy} depends on the material structure. For example, for $0^\circ/90^\circ$ cross-ply carbon-epoxy composite $\upsilon_{xy} = 0.03$, whereas for angle-ply $\pm 45^\circ$ composite $\upsilon_{xy} = 0.75$ and the effect of reactive biaxial loading can be significant. The corresponding critical force T_x^c can be found from Eqs. (9.225) and (9.230) if we take $p = \upsilon_{xy}$, i.e.,

$$T_x = \frac{\pi^2 n^2 \lambda}{(\lambda + \upsilon_{xy})b^2}\left(D_1 \lambda + 2D_3 + \frac{D_2}{\lambda}\right) \tag{9.232}$$

and minimize T_x with respect to the parameter λ. For an angle-ply $\pm\phi$ carbon-epoxy square plate, the dependence of the normalized critical load $\overline{T} = T_x^c(\phi)/T_x^c(\phi = 0)$ on the angle ϕ is shown in Fig. 9.27. Curve 1 corresponds to Eq. (9.229), whereas curve 2 is plotted in accordance with Eq. (9.232). As can be seen, the reactive transverse force T_y can significantly reduce the critical load. Comparison of the calculated and experimental critical loads for carbon-epoxy square plates with various υ_{xy} coefficients is presented in Table 9.5. Plate No 1 consists of 7 plies with angles 0° and $\pm 45^\circ$. Plates No 2–4 are composed of 11 plies with angles 0° and 90° (plate No 2), $\pm 45^\circ$ (plate No 3), and 0°, 90°, and $\pm 45^\circ$ (plate No 4). Plate No 5 is a cross-ply (0°, 90°) laminate consisting of 15 plies and plate No 6 has

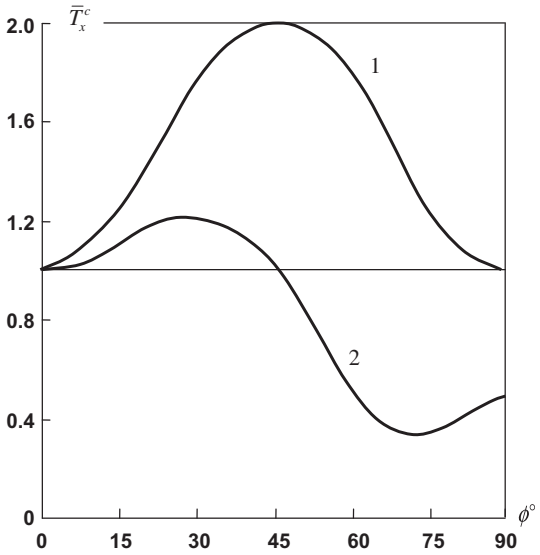


FIGURE 9.27

Dependencies of the normalized critical load for angle-ply $\pm\phi$ square carbon-epoxy plates on the ply angle ϕ as per Eq. (9.229) (curve 1) and Eq. (9.232) (curve 2).

TABLE 9.5 Calculated and Experimental Critical Loads for Square Composite Plates

Plate No	h/α	ν_{xy}	Critical Load, kN	
			Calculated	Experimental
1	0.006	0.32	1.07	1.06
2	0.009	0.03	1.95	1.86
3	0.009	0.75	3.28	3.04
4	0.009	0.22	2.45	2.45
5	0.015	0.03	8.48	8.33
6	0.02	0.15	23.32	22.93

9 plies with angles 0° and 90° and two aluminum face sheets with thickness 0.5 mm. For the plates with $\upsilon_{xy} \leq 0.3$ (Nos 1, 2, and 4–6) the critical load is calculated using Eq. (9.229), whereas for plate No 3, Eq. (9.232) is applied because Eq. (9.229) gives the load which is about 80% higher than the corresponding experimental result. It follows from Table 9.5 that Eqs. (9.229) or (9.232) predict the critical load with reasonable accuracy.

Consider the action of compression and shear. Taking $T_y = 0$ (see Fig. 9.22), generalize Eqs. (9.224) as

$$L(w) + T_x \frac{\partial^2 w}{\partial x^2} + 2T_{xy} \frac{\partial^2 w}{\partial x \partial y} = 0 \tag{9.233}$$

For a simply supported plate, apply Eq. (9.223) for the deflection and substitute it into Eq. (9.233). Using the Bubnov-Galerkin method, multiply the resulting equation by $\sin \lambda_i x \cdot \sin \lambda_j y$ and integrate it over the plate surface. Taking into account that

$$\int_0^a \sin \lambda_m x \cdot \sin \lambda_i x \, dx = \begin{cases} \dfrac{a}{2} & \text{for} \quad m = i \\ 0 & \text{for} \quad m \neq i \end{cases}$$

$$\int_0^a \cos \lambda_m x \cdot \sin \lambda_i x \, dx = \begin{cases} 0 & \text{for} \quad m = i \\ \dfrac{2ai}{\pi(i^2 - m^2)} & \text{for} \quad m + i = 2, 4, 6\ldots \\ 0 & \text{for} \quad m + i = 1, 3, 5\ldots \end{cases}$$

and the similar integrals for the y-coordinate, we arrive at the following set of coupled algebraic equations for the coefficients w_{mn}:

$$w_{mn}\left[\frac{\pi^2}{b^2}\sqrt{D_1 D_2}\left(m^4\alpha + 2m^2n^2\beta + \frac{n^4}{\alpha}\right) - m^2 T_x\right] + 32 T_{xy}\frac{amn}{\pi^2 b}\sum_i \sum_j \frac{w_{ij} ij}{(m^2 - i^2)(n^2 - j^2)} = 0 \tag{9.234}$$

where

$$\alpha = \frac{b^2}{a^2}\sqrt{\frac{D_1}{D_2}}, \quad \beta = \frac{D_3}{\sqrt{D_1 D_2}} \tag{9.235}$$

and $m \pm i = 1, 3, 5\ldots$, and $n \pm j = 1, 3, 5\ldots$. Usually, the loads T_x and T_{xy} are increased in proportion to some loading parameter p. To find the critical value of this parameter, we must use the zero condition for the determinant of Eq. (9.234) and minimize the root p of the resulting algebraic equation.

Consider the case of pure shear, taking $T_x = 0$ in Eq. (9.234). The critical shear force can be presented as

$$T_{xy}^c = K\frac{\pi^2}{ab}\sqrt{D_1 D_2} \tag{9.236}$$

(Azikov et al., 1990). The buckling coefficient calculated with the aid of Eq. (9.234) (22 terms in Eq. (9.223) have been retained) is presented in Fig. 9.28 as the function of the parameters α and β in Eqs. (9.235). As an example, consider the $\pm 45^\circ$ angle-ply carbon-epoxy plate (see Fig. 9.29) with the following parameters: $a = 196$ mm, $b = 96$ mm, $D_1 = D_2 = 0.685N/m$, and $D_3 = 1.718N/m$. For this plate, Eqs. (9.235) yield $\alpha = 0.24$ and $\beta = 2.5$ and interpolation of the curves in Fig. 9.28 gives $K = 19.8$. The corresponding experimental result is $K = 19.7$.

Note that carbon-epoxy plates loaded with shear forces are used as composite shear webs in modern aircraft structures. In the corresponding aluminum structures buckling of the shear webs is usually allowed at the limit loads, because aluminum webs can buckle many times without failure. However, this is not the case for composite webs made of relatively brittle carbon-epoxy materials.

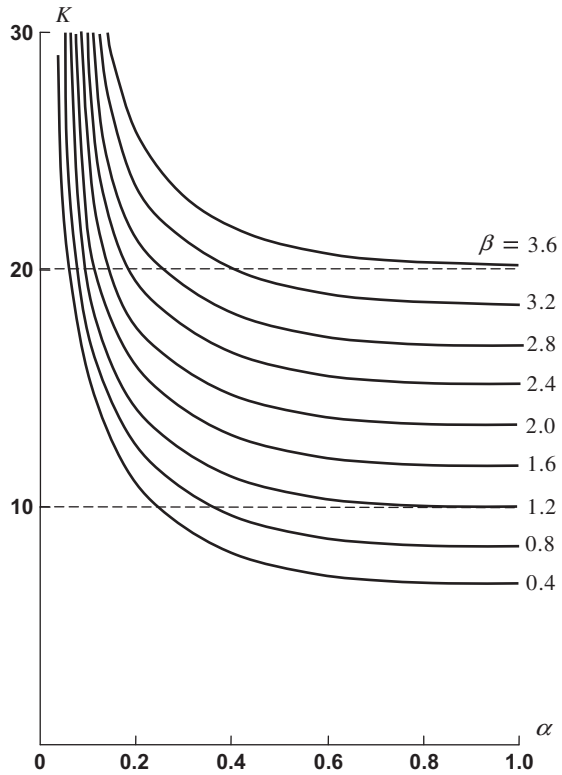


FIGURE 9.28

Dependence of the shear buckling coefficient on the parameters α and β.

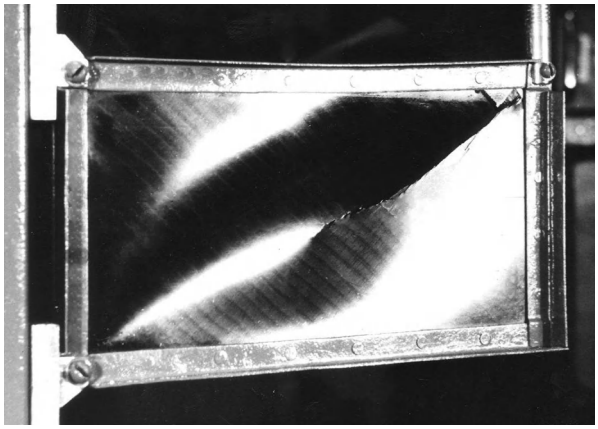


FIGURE 9.29

Buckling and failure modes of $\pm 45^\circ$ angle-ply carbon-epoxy shear web.

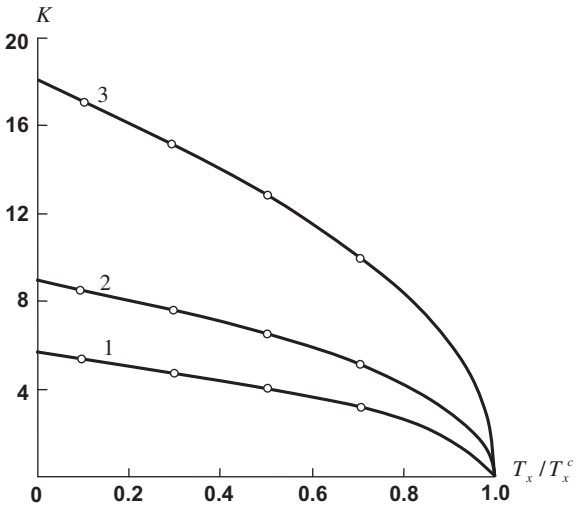


FIGURE 9.30

Dependencies of the shear buckling coefficient K on the normalized axial compressive force T_x/T_x^c as per Eq. (9.237) (———) and according to the exact solution (∘ ∘ ∘ ∘ ∘); 1 ($\alpha = 1$, $\beta = 0.2$); 2 ($\alpha = 1$, $\beta = 1$); 3 ($\alpha = 1$, $\beta = 3$)

After several cycles of loading, a crack which is parallel to the buckling lobe direction appears in the composite plate (see Fig. 9.29).

Consider the case of combined loading with compressive forces T_x and shear forces T_{xy} (see Fig. 9.22). The critical combination of the forces can be found from the following condition:

$$\frac{T_x}{T_x^c} + \left(\frac{T_{xy}}{T_{xy}^c}\right)^2 = 1 \tag{9.237}$$

in which T_x^c and T_{xy}^c are specified by Eqs. (9.229) or (9.230) and Eq. (9.236). The dependencies of the shear critical parameter K in Eq. (9.236) on the ratio T_x/T_x^c for carbon-epoxy composite plates with various values of α and β parameters are shown in Fig. 9.30. The solid lines correspond to Eq. (9.237), whereas the circles correspond to the exact solutions based on Eq. (9.234).

In conclusion, consider anisotropic plates which demonstrate specific behavior under shear. For anisotropic plates, Eqs. (9.127) for the moments become

$$\begin{aligned} M_x &= -\left(D_{11}\frac{\partial^2 w}{\partial x^2} + D_{12}\frac{\partial^2 w}{\partial y^2} + 2D_{14}\frac{\partial^2 w}{\partial x \partial y}\right) \\ M_y &= -\left(D_{21}\frac{\partial^2 w}{\partial x^2} + D_{22}\frac{\partial^2 w}{\partial y^2} + 2D_{24}\frac{\partial^2 w}{\partial x \partial y}\right) \\ M_{xy} &= -\left(D_{41}\frac{\partial^2 w}{\partial x^2} + D_{42}\frac{\partial^2 w}{\partial y^2} + 2D_{44}\frac{\partial^2 w}{\partial x \partial y}\right) \end{aligned} \tag{9.238}$$

(see Eqs. (9.5)) and the buckling equation, Eq. (9.224), is generalized as

$$D_1\frac{\partial^4 w}{\partial x^4}+2D_3\frac{\partial^4 w}{\partial x^2\partial y^2}+D_2\frac{\partial^4 w}{\partial y^4}+4D_{14}\frac{\partial^4 w}{\partial x^3\partial y}+4D_{24}\frac{\partial^4 w}{\partial x\partial y^3}+T_x\frac{\partial^2 w}{\partial x^2}+2T_{xy}\frac{\partial^2 w}{\partial x\partial y}+T_y\frac{\partial^2 w}{\partial y^2}=0$$

For simply supported plates, the deflection in Eq. (9.223) provides the absence of the deflection at the plate edges. However, it follows from Eqs. (9.223) and (9.238) that the bending moments are not zero at $x=0$, $x=a$ and $y=0$, $y=b$ (see Fig. 9.23). Nevertheless, Eq. (9.223) can be used to approximate the deflection within the framework of the Ritz method which allows us to violate the force boundary conditions (Langhaar, 1962). To use this method, consider the total potential energy of an anisotropic plate, i.e.,

$$T=\frac{1}{2}\int_0^a\int_0^b\left[M_x\frac{\partial^2 w}{\partial x^2}+M_y\frac{\partial^2 w}{\partial y^2}+2M_{xy}\frac{\partial^2 w}{\partial x\partial y}-T_x\left(\frac{\partial w}{\partial x}\right)^2-T_y\left(\frac{\partial w}{\partial y}\right)^2-2T_{xy}\,\frac{\partial w}{\partial x}\,\frac{\partial w}{\partial y}\right]dxdy \quad (9.239)$$

(Whitney, 1987). Substituting the deflection, Eq. (9.223), into Eqs. (9.238) for the moments and the expressions obtained for the moments into Eq. (9.239), we can express T in terms of w_{mn}. Applying the minimum conditions $\partial T/\partial w_{mn}=0$, we arrive at the infinite set of coupled algebraic equations whose determinant, being equal to zero, allows us, in principle, to determine the critical combination of forces T_x, T_y, and T_{xy}.

Consider three composite plates as shown in Fig. 9.31. The first plate (see Fig. 9.31a) has a $\pm\phi$ orthotropic angle-ply structure; the second and the third plates (see Figs. 9.31b and c) have unidirectional structure and are reinforced at angles $+\phi$ and $-\phi$ to the x-axis, respectively. Under compression, the second and the third plates demonstrate, as expected, similar behavior. However, under shear, their behavior is different because in the $+\phi$ plate the force T_{xy} induces tension of the fibers, whereas in the $-\phi$ plate the fibers are compressed. Recall that the stiffness of unidirectional composites in the fiber direction is much higher than the stiffness in the transverse direction. So, we can expect that the critical shear force is different for the second and third plates, though the material structure is similar.

The results of the buckling analysis are presented in Figs. 9.32 and 9.33. The critical load corresponding to axial compression is considerably higher for the angle-ply plate (curve $\pm\phi$ in Fig. 9.32), whereas for the second and the third plates it is the same (curves $+\phi$ and $-\phi$ in Fig. 9.32). The critical force corresponding to shear is the highest for the third plate (curve $-\phi$ in Fig. 9.33) for which the fibers are compressed and lowest for the second plate (curve $+\phi$ in Fig. 9.33) in which compression is directed across the fibers.

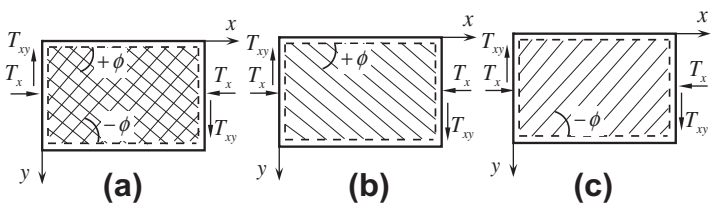


FIGURE 9.31

Angle-ply $\pm\phi$ (a) and unidirectional $+\phi$ (b) and $-\phi$ (c) composite plates under compression and shear.

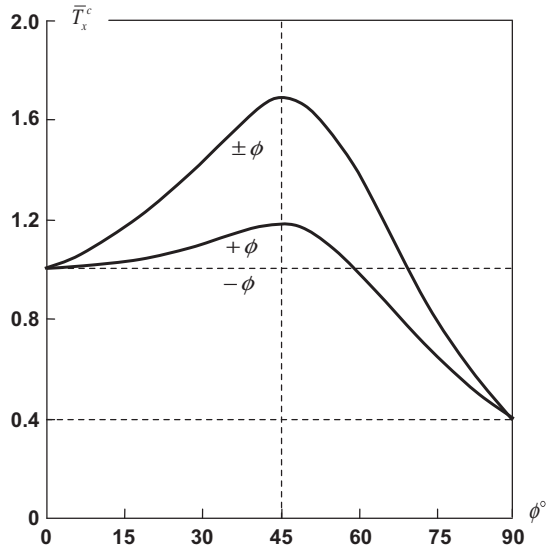


FIGURE 9.32

Dependencies of the normalized critical compressive force on the angle ϕ for $\pm\phi$ angle-ply and $+\phi$ or $-\phi$ unidirectionally reinforced plates.

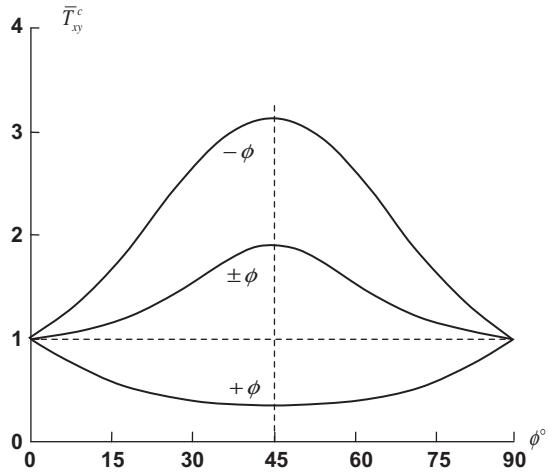


FIGURE 9.33

Dependencies of the normalized critical shear force on the angle ϕ for $\pm\phi$ angle-ply and $+\phi$ or $-\phi$ unidirectionally reinforced plates.

The foregoing buckling analysis has been undertaken for simply supported plates. For other boundary conditions, approximate solutions can be obtained approximating the plate deflection with some suitable functions which satisfy the boundary conditions. Krylov beam functions and Legendre polynomials are used for this purpose by Khaziev and Boshers (2011). Various types of loading and boundary conditions are considered by Veres and Kollar (2001), Shan and Qiao (2008), and Weaver and Nemeth (2008).

9.5.2 Theory of shear deformable plates

The foregoing results (Section 9.5.1) correspond to the classical plate theory which ignores transverse shear deformation. In practical problems, this deformation is generally negligible. However, there are at least two cases in which it should be taken into account. The first case corresponds to relatively thick plates such that the ratio of the plate thickness to the smallest in-plane dimension exceeds 0.02. Those plates with relatively low transverse shear stiffness (e.g., sandwich plates with lightweight cores) belong to the second case.

First, consider transversely isotropic plates as discussed in Section 9.3. For these plates

$$D_{11} = D_{22} = D, \quad D_{12} = \upsilon D, \quad D_{44} = \frac{1-\upsilon}{2} D, \quad S_x = S_y = S$$

and the governing equation, Eq. (9.40) for orthotropic plates, reduces to

$$D\left[\frac{D(1-\upsilon)}{2S}\Delta - 1\right]\Delta\Delta W + \overline{p} = 0 \tag{9.240}$$

For the case of bending considered in Section 9.3.2, Eq. (9.240) can be decomposed into two mutually independent equations, Eq. (9.69) and Eq. (9.76). For the buckling problem, the pressure $\overline{p}$ should be changed to the imaginary pressure p_n specified by Eq. (9.221), according to which

$$p_n = -\left(T_x\frac{\partial^2 w}{\partial x^2} + T_y\frac{\partial^2 w}{\partial y^2} + 2T_{xy}\frac{\partial^2 w}{\partial x \partial y}\right) \tag{9.241}$$

For the case of uniaxial compression with forces T_x (see Fig. 9.23), the buckling equation, following from Eqs. (9.240) and (9.241), is

$$D\left[\frac{D(1-\upsilon)}{2S}\Delta - 1\right]\Delta\Delta W - T_x\frac{\partial^2 w}{\partial x^2} = 0 \tag{9.242}$$

in which the deflection w is specified by Eq. (9.42), which for transversely isotropic plates takes the form

$$w = W - \frac{D(3-\upsilon)}{2S}\Delta W + \frac{D^2(1-\upsilon)}{2S^2}\Delta\Delta W \tag{9.243}$$

For a simply supported plate, we can present the functions W as follows:

$$W = \sum_m \sum_n W_{mn} \sin \lambda_m x \cdot \sin \lambda_n y \tag{9.244}$$

where $\lambda_m = \pi m/a$ and $\lambda_n = \pi n/b$ (see Fig. 9.23). Substituting the deflection w, Eq. (9.243), into the buckling equation, Eq. (9.242), and using Eq. (9.244) for W, we arrive at the following expression for T_x:

$$T_x = \frac{D\left(\lambda_m^2 + \lambda_n^2\right)^2}{\lambda_m^2\left[1 + \dfrac{D}{S}\left(\lambda_m^2 + \lambda_n^2\right)\right]} \tag{9.245}$$

Note that the same result can be obtained if we neglect the boundary-layer solution and consider Eqs. (9.80) and (9.82) which specify only the penetrating solution. The buckling equation, following from Eqs. (9.80), (9.82), and (9.241), can be represented by

$$D\Delta\Delta\varphi - T_x\frac{\partial^2}{\partial x^2}\left(\varphi - \frac{D}{S}\Delta\varphi\right) = 0$$

Decomposing φ into a series similar to Eq. (9.244), we arrive at Eq. (9.245) for T_x.

Consider orthotropic plates. The solution of the buckling problem can be obtained using Eqs. (9.36) in which the pressure $\overline{p}$ is changed to the imaginary pressure p_n specified by Eq. (9.241). Then, the buckling equations become

$$\begin{gathered}
L_{1x}(\theta_x) + L_{1y}\left(\theta_y\right) + L_{1w}(w) = 0 \\
L_{2x}(\theta_x) + L_{2y}\left(\theta_y\right) + L_{2w}(w) = 0 \\
L_{3x}(\theta_x) + L_{3y}\left(\theta_y\right) + L_{3w}(w) = T_x\frac{\partial^2 w}{\partial x^2} + T_y\frac{\partial^2 w}{\partial y^2} + 2T_{xy}\frac{\partial^2 w}{\partial x\partial y}
\end{gathered} \tag{9.246}$$

For simply supported plates, the angles θ_x and θ_y and the deflection w can be taken in the form of double trigonometric series, Eqs. (9.204). Substitution of these series into Eqs. (9.246) yields three homogeneous algebraic equations for the series coefficients θ_x^{mn}, θ_y^{mn}, and w_{mn}. The critical combination of loads T_x, T_y, and T_{xy} is the first combination of loads (corresponding to the minimum loading parameter according to which these loads increase) for which the determinant of the algebraic equations is zero.

Particularly, for unidirectional compression with forces T_x (see Fig. 9.23), we get

$$T_x = \frac{D_{mn}\lambda_m^2 + D_{nm}\lambda_n^2 + 2\overline{D}\lambda_m^2\lambda_n^2 + \left(D_{mn}D_{nm} - \overline{D}^2\lambda_m^2\lambda_n^2\right)\left(\dfrac{\lambda_n^2}{S_x} + \dfrac{\lambda_m^2}{S_y}\right)}{\lambda_m^2\left[1 + \dfrac{D_{mn}}{S_x} + \dfrac{D_{mn}}{S_y} + \dfrac{1}{S_xS_y}\left(D_{mn}D_{nm} - \overline{D}^2\lambda_m^2\lambda_n^2\right)\right]} \tag{9.247}$$

where, as earlier,

$$D_{mn} = D_{11}\lambda_m^2 + D_{44}\lambda_n^2, \quad D_{nm} = D_{22}\lambda_n^2 + D_{44}\lambda_m^2, \quad \overline{D} = D_{12} + D_{44}$$

$$\lambda_m = \frac{\pi m}{a}, \quad \lambda_n = \frac{\pi n}{b}$$

Ignoring the transverse shear deformation, i.e., taking $S_x \to \infty$ and $S_y \to \infty$, we arrive at Eq. (9.225) corresponding to classical plate theory. The critical load T_x^c can be found if we minimize T_x in Eq. (9.247) with respect to half-wave numbers, m, $n = 1,2,3\ldots$. The allowance for transverse shear deformation usually does not affect the critical values of half-wave numbers and they can be evaluated using the equations derived in Section 9.5.1.

The solution obtained, Eq. (9.247), can be significantly simplified if we take into account the results obtained previously for transversely isotropic plates and neglect the boundary-layer solution. Thus, determine the critical load using Eqs. (9.212) and (9.215) which specify the penetrating solution. Then, the buckling equation can be written as

$$D_1\frac{\partial^4 W_i}{\partial x^4} + 2D_3\frac{\partial^4 W_i}{\partial x^2 \partial y^2} + D_2\frac{\partial^4 W_i}{\partial y^4} + T_x\frac{\partial^2 w}{\partial x^2} + 2T_{xy}\frac{\partial^2 w}{\partial x \partial y} + Ty\frac{\partial^2 w}{\partial y^2} = 0$$

$$w = W_i - \frac{D_1}{S_x}\frac{\partial^2 W_i}{\partial x^2} - \frac{D_2}{S_y}\frac{\partial^2 W_i}{\partial y^2}$$

For simply supported plates, we can take W_i in accordance with Eq. (9.244) and for the case of unidirectional compression (T_y=0, T_{xy}=0) , derive the following expression for T_x which generalizes Eq. (9.245)

$$T_x = \frac{\pi^2}{b^2}\frac{D_1\lambda + 2D_3n^2 + D_2\dfrac{n^4}{\lambda}}{1 + \dfrac{\pi^2}{b^2}\left(\dfrac{D_1}{S_x}\lambda + \dfrac{D_2}{S_y}n^2\right)}, \quad \lambda = \left(\frac{mb}{a}\right)^2 \tag{9.248}$$

It can be readily proved that $\partial T_x/\partial n^2 > 0$, i.e., that function $T_x(\mathrm{n}^2)$ increases with increase in n^2. Thus, the minimum possible value $n = 1$ must be taken, and Eq. (9.248) reduces to

$$T_x = \frac{\pi^2}{b^2}\frac{D_1\lambda + 2D_3 + D_2\dfrac{1}{\lambda}}{1 + \dfrac{\pi^2}{b^2}\left(\dfrac{D_1}{S_x}\lambda + \dfrac{D_2}{S_y}\right)} \tag{9.249}$$

Using the minimum condition $\partial T_x/\partial\lambda = 0$, we can arrive at a quadratic equation for λ, but the corresponding solution looks rather cumbersome. For practical calculation, it is easier to apply a sorting procedure to find parameter m =1,2,3… . Consider, for example, a square ($a = b$) transversely isotropic plate for which $m = 1$, $n = 1$, and Eqs. (9.247) or (9.248) yield

$$T_c^{(1)} = \frac{4\pi^2 D}{a^2(1+2\eta)}, \quad \eta = \frac{\pi^2 D}{a^2 S}$$

For classical plate theory, $\eta = 0$ and

$$T_c^{(2)} = \frac{4\pi^2 D}{a^2}$$

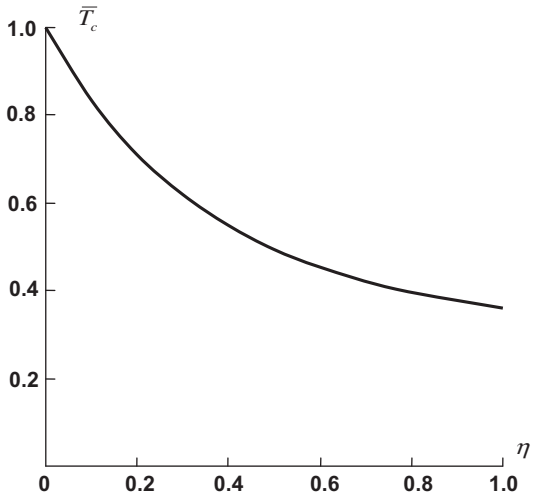


FIGURE 9.34

Dependence of the normalized critical forces on parameter η for transversely isotropic square plates.

The dependence of the normalized critical force $\overline{T}_c = \dfrac{T_c^{(1)}}{T_c^{(2)}}$ on the parameter η is presented in Fig. 9.34. Note that for homogeneous and sandwich plates the parameter η is evaluated as

$$\eta_h = \frac{\pi^2 E h^2}{12(1-\upsilon^2)Ga^2}, \quad \eta_s = \frac{\pi^2 E_f \delta h}{2G_c a^2}$$

in which E_f and δ are the modulus and the thickness of the facing layers, and G_c and h are the shear modulus and the thickness of the core of a sandwich plate. For composite plates, η_h can reach $10h^2/a^2$ and for $h/a \leq 0.05$ we have $\eta_h \leq 0.025$, so that the shear deformation is negligible. For sandwich plates η_s can reach $1000h^2/a^2$ and even for thin plates $(h/a = 0.01)$, $\eta_s = 0.1$ and the shear deformation must be taken into account.

9.6 POSTBUCKLING BEHAVIOR OF ORTHOTROPIC SYMMETRIC PLATES UNDER AXIAL COMPRESSION

It is known that rectangular plates fixed at the edges with respect to deflection can take considerable load after the onset of buckling. Consider a simply supported plate loaded with forces T_x uniformly distributed over the plate transverse edges $x = 0$ and $x = a$ (see Fig. 9.35). After buckling, the plate has a curved shape characterized by some deflection $w(x, y)$ and should be described by nonlinear

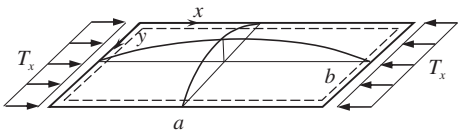


FIGURE 9.35

A simply supported plate after buckling.

equations (Vasiliev, 1993). We assume that the deflection is small so that the in-plane equilibrium equation can be taken in accordance with Eqs. (9.29) corresponding to a flat plate, i.e.,

$$\frac{\partial N_x}{\partial x}+\frac{\partial N_{xy}}{\partial y}=0, \quad \frac{\partial N_y}{\partial y}+\frac{\partial N_{xy}}{\partial x}=0 \tag{9.250}$$

where the stress resultants N_x, N_y, and N_{xy} are linked to the corresponding strains ε_x^0, ε_y^0, and γ_{xy}^0 by constitutive equations, Eqs. (9.28), according to which

$$N_x=B_{11}\varepsilon_x^0+B_{12}\varepsilon_y^0, \quad N_y=B_{21}\varepsilon_x^0+B_{22}\varepsilon_y^0, \quad N_{xy}=B_{44}\gamma_{xy}^0 \tag{9.251}$$

Here, in contrast to Eqs. (9.30), the strains allow for the plate deflection and can be written as

$$\varepsilon_x^0=\frac{\partial u}{\partial x}+\frac{1}{2}\left(\frac{\partial w}{\partial x}\right)^2, \quad \varepsilon_y^0=\frac{\partial v}{\partial y}+\frac{1}{2}\left(\frac{\partial w}{\partial y}\right)^2, \quad \gamma_{xy}^0=\frac{\partial u}{\partial y}+\frac{\partial v}{\partial x}+\frac{\partial w}{\partial x}\frac{\partial w}{\partial y} \tag{9.252}$$

(Vasiliev, 1993). Substituting Eqs. (9.252) into Eqs. (9.251) and the expressions obtained for the stress resultants into the equilibrium equations, Eqs. (9.250), we get

$$\begin{aligned}
B_{11}\frac{\partial^2 u}{\partial x^2}+B_{44}\frac{\partial^2 u}{\partial y^2}+\overline{B}\frac{\partial^2 v}{\partial x\partial y}&=-\left(B_{11}\frac{\partial w}{\partial x}\frac{\partial^2 w}{\partial x^2}+\overline{B}\frac{\partial w}{\partial y}\frac{\partial^2 w}{\partial x\partial y}+B_{44}\frac{\partial w}{\partial x}\frac{\partial^2 w}{\partial y^2}\right)\\
B_{22}\frac{\partial^2 v}{\partial y^2}+B_{44}\frac{\partial^2 v}{\partial x^2}+\overline{B}\frac{\partial^2 u}{\partial x\partial y}&=-\left(B_{22}\frac{\partial w}{\partial y}\frac{\partial^2 w}{\partial y^2}+\overline{B}\frac{\partial w}{\partial x}\frac{\partial^2 w}{\partial x\partial y}+B_{44}\frac{\partial w}{\partial y}\frac{\partial^2 w}{\partial x^2}\right)
\end{aligned} \tag{9.253}$$

where $\overline{B}=B_{12}+B_{44}$. Assume that the plate deflection corresponds to a mode of plate buckling with some unknown coefficient w_m and half-wave number m (see Fig. 9.23), i.e.,

$$w=w_m\sin\lambda_m x\sin\lambda_1 y \tag{9.254}$$

where $\lambda_m=\pi m/a$ and $\lambda_1=\pi/b$. Substituting the deflection, Eq. (9.254), into Eqs. (9.253), we can obtain the following solution of these equations:

$$\begin{aligned}
u&=-\frac{x}{B}\left(B_{22}T_x-\lambda_m^2 w_m^2\right)-\frac{w_m^2}{16\lambda_m}\left[\lambda_m^2(1-\cos 2\lambda_1 y)-\frac{B_{12}}{B_{11}}\lambda_1^2\right]\sin 2\lambda_m x\\
v&=\frac{y}{B}\left(B_{12}T_x-\lambda_1^2 w_m^2\right)-\frac{w_m^2}{16\lambda_1}\left[\lambda_1^2(1-\cos 2\lambda_m x)-\frac{B_{12}}{B_{22}}\lambda_m^2\right]\sin 2\lambda_1 y
\end{aligned} \tag{9.255}$$

(Azikov and Vasiliev, 1986) where $B = B_{11}B_{22} - B_{12}^2$. To determine w_m , apply the principle of minimum total potential energy of the plate

$$P = \int_0^a \int_0^b \left(N_x \varepsilon_x^0 + N_y \varepsilon_y^0 + N_{xy}\gamma_{xy}^0 + M_x\kappa_x + M_y\kappa_y + M_{xy}\kappa_{xy} + T_x \frac{\partial u}{\partial x} \right) dxdy \tag{9.256}$$

Here, the moments M are expressed in terms of curvatures κ as

$$M_x = D_{11}\kappa_x + D_{12}\kappa_y, \quad M_y = D_{12}\kappa_x + D_{22}\kappa_y, \quad M_{xy} = D_{44}\kappa_{xy} \tag{9.257}$$

where within the framework of classical plate theory

$$\kappa_x = -\frac{\partial^2 w}{\partial x^2}, \quad \kappa_y = -\frac{\partial^2 w}{\partial y^2}, \quad \kappa_{xy} = -2\frac{\partial^2 w}{\partial x \partial y} \tag{9.258}$$

Using Eqs. (9.251), (9.252), and (9.257), (9.258), we can write the energy P, Eq. (9.256), in terms of displacements u, v, and w. Substituting Eqs. (9.254) and (9.255) for the displacements and integrating, we can further obtain P as the following function of T_x , w_m, and λ_m. Applying the minimum condition with respect to w_m, i.e., taking $\partial P/\partial w_m = 0$, we obtain the equation for w_m whose solution is

$$w_m^2 = \frac{16B_{11}B_{22}\lambda_m^2}{B\left(B_{11}\lambda_m^4 + B_{22}\lambda_1^4\right)}(T_x - T_m) \tag{9.259}$$

in which

$$T_m = \frac{1}{\lambda_m^2}\left(D_1\lambda_m^4 + 2D_3\lambda_m^2\lambda_1^2 + D_2\lambda_1^4\right) \tag{9.260}$$

It follows from Eq. (9.259) that the deflection exists if $T_x > T_m$, where T_m in Eq. (9.260) coincides with T_x given by Eqs. (9.225) and (9.227). Minimization of T_m with respect to m gives the critical load $T_x^c = T_{m1}$ and the corresponding half-wave number m_1 specified by Eq. (9.228). Thus, if $T_x \le T_m$, $w_m = 0$ and the plate remains flat. If $T_x > T_x^c$, w_m is determined by Eq. (9.259) in which $m = m_1$. Under further loading, the so-called mode jumping can occur and the half-wave number m might increase. To find the half-wave number, substitute the displacements, Eqs. (9.255) and (9.259), into Eq. (9.256) for the total potential energy. After integration, we get

$$P = \frac{ab}{2B}T_x^2 B_{22}\left[1 + \frac{2B_{11}\lambda_m^2\lambda_1^2}{B_{11}\lambda_m^4 + B_{22}\lambda_1^4}\left(1 - \frac{T_m}{T_x}\right)^2\right] \tag{9.261}$$

The half-wave number m corresponding to the acting force T_x is found from the minimum condition for the total potential energy P. First, single out the second term in the brackets of Eq. (9.261) which depends on m and present it as follows:

$$P_1 = \frac{1}{ab\lambda_1^2}\left(P - \frac{B_{22}ab}{2B}T_x^2\right) = \frac{\lambda_m^2(T_x - T_m)^2}{B_{11}\lambda_m^4 + B_{22}\lambda_1^4} \tag{9.262}$$

Here, T_x is the acting load and T_m is the eigenvalue specified by Eq. (9.260). To demonstrate the procedure, consider an isotropic plate for which

$$D_{11} = D_{22} = D_{12} = D_{44} = D, \quad B_{11} = B_{22} = \overline{E}h, \quad \overline{E} = E/\left(1 - \upsilon^2\right)$$

For this isotropic plate, Eqs. (9.262) and (9.260) become

$$P_1 = \frac{m^2c^2}{m^4 + c^4}(T_x - T_m)^2, \quad T_m = \frac{\pi^2 Dc^2}{b^2m^2}\left(\frac{m^2}{c^2} + 1\right)^2$$

where $c = b/a$. Introduce the dimensionless functions of m

$$\widehat{p}_1(m) = \frac{P_1 b^4}{\pi^4 D^2 c^4} = \frac{m^2c^2}{m^4 + c^4}\left(\overline{T}_x - \overline{T}_m\right)^2 \tag{9.263}$$

$$\overline{T}_x = \frac{T_x b^2}{\pi^2 Dc^2}, \quad \overline{T}_m = \frac{T_m b^2}{\pi^2 Dc^2} = \frac{1}{m^2}\left(\frac{m^2}{c^2} + 1\right)^2 \tag{9.264}$$

For the plate considered as an example in Section 9.5.1, c =1.75 and $m_1 = 2$. The corresponding dimensionless critical force following from Eqs. (9.264) is $\overline{T}_2 = 1.33$. The other eigenvalues are $\overline{T}_3 = 1.723$, $\overline{T}_4 = 2.421$, and $\overline{T}_5 = 3.36$. The eigenvalues $\overline{T}_m$ $(m = 2, 3, 4, 5)$ are shown on the horizontal axis in Fig. 9.36 with dots. The curves in Fig. 9.36 show the dependencies of $\widehat{p}_1(m)$ specified by Eq. (9.263) on the dimensionless load $\overline{T}_x$ for various m-values. As can be seen, for $\overline{T}_2 \le \overline{T}_x \le \overline{T}_{23}$, we have $m = 2$. For $\overline{T}_{23} \le \overline{T}_x \le \overline{T}_3$, the minimum values of $\widehat{p}_1$ correspond to $m = 3$, for $\overline{T}_x \ge \overline{T}_{34}$, $m = 3$ changes to $m = 4$, and for $\overline{T}_x \ge \overline{T}_{45}$, we have $m = 5$. The forces $T_{m,m+1}$ at which mode jumping takes place can be found as the $\overline{T}_x$-coordinate of the point of intersection of the curves $\widehat{p}_1(m)$ corresponding to m and m+1 (see Fig. 9.36), i.e., from the condition $P(m) = P(m + 1)$. Using Eq. (9.261), we finally get

$$\left(\frac{T_x - T_m}{T_x - T_{m+1}}\right)^2 = \frac{\lambda_{m+1}^2\left(B_{11}\lambda_m^4 + B_{22}\lambda_1^4\right)}{\lambda_m^2\left(B_{11}\lambda_{m+1}^4 + B_{22}\lambda_1^4\right)} \tag{9.265}$$

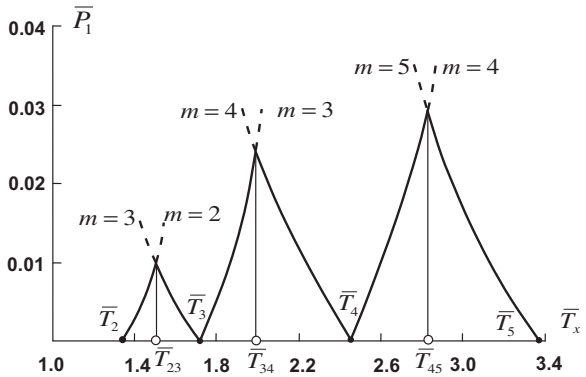


FIGURE 9.36

Dimensionless loads $\overline{T}_x$ corresponding to the eigenvalues (•) and to the mode jumping loads (○).

For the example under consideration, this equation yields $\overline{T}_{23} = 1.51$, $\overline{T}_{34} = 2.03$, $\overline{T}_{45} = 2.84$.

The half-wave number m found from Eq. (9.265) and the corresponding value of the acting load T_x are substituted into Eq. (9.259) for w_m and this value of w_m is further substituted in Eqs. (9.254) and (9.255) which specify the plate displacements. Then, using Eqs. (9.252), we can find the strains and, following the procedure described in Section 5.11, determine the strains and the stresses in the ply principal coordinates. Applying the strength criteria discussed in Chapter 6, we can evaluate the load-carrying capacity of the plate after buckling. As an example, consider a carbon-epoxy $\pm\phi$ angle-ply square plate with $a = b = 0.4$ m and $h = 1$ mm. The dependence of the ultimate force T_x^u (solid line) along with the critical force T_x^c (dashed line) on the angle ϕ is shown in Fig. 9.37. As can be seen, the optimal angle which provides the maximum load-carrying capacity (close to 0) does not coincide with the optimal angle for buckling (45°). In contrast to metal plates for which the ultimate load is much higher than the critical load, the relation between these loads for composite plates depends on the material structure.

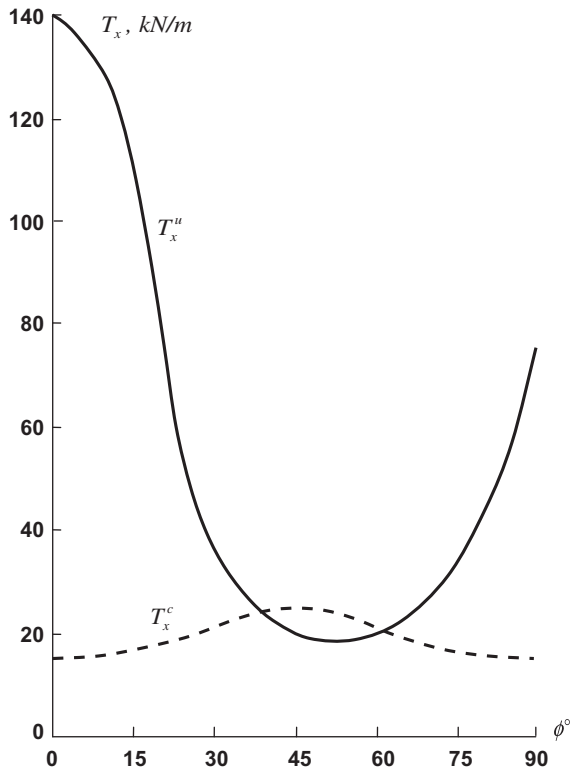


FIGURE 9.37

Dependencies of the ultimate load T_x^u and the critical load T_x^c on angle ϕ.

The foregoing approach provides reasonably accurate evaluation of the stresses and displacements of composite plates after buckling. Experimental results for 2.5 mm thick composite plates have been presented by Banks and Harvey (1979). The predicted

$$\sigma_x = \frac{N_x}{h} = -\left(\frac{T_x}{h} + \frac{B\lambda_m^2}{8B_{22}h} w_m^2 \cos 2\lambda_1 y\right)$$

and experimental distributions of σ_x along the y-coordinate of the plate (see Fig. 9.35) after buckling is shown in Fig. 9.38 for two values of the acting load. The dependence of the plate shortening $\Delta u = u(x = a) - u(x = 0)$ under the action of compressive forces T_x (see Fig. 9.35) is shown in Fig. 9.39. The knee on the curve corresponds to the plate buckling.

Numerical analysis of post-buckling behavior of composite plates has been presented by Ovesy and Assaee (2005).

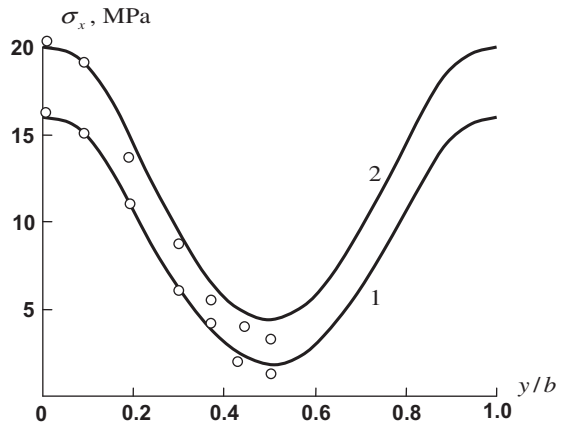


FIGURE 9.38

Theoretical (———) and experimental (○ ○ ○ ○ ○) distributions of the normal stress over the plate width after buckling for $T_x/T_x^c = 2$ (1) and $T_x/T_x^c = 2.53$ (2).

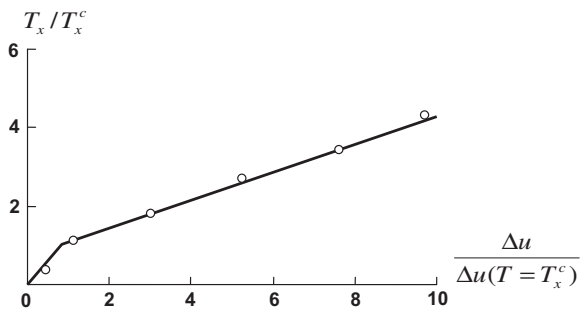


FIGURE 9.39

Theoretical (———) and experimental (○ ○ ○ ○ ○) dependencies of the plate shortening on the normalized compression load.

9.7 GENERALLY LAMINATED PLATES

The foregoing sections of this chapter are concerned with symmetrically laminated plates for which bending-stretching coupling stiffness coefficients C_{mn} in the constitutive equations, Eqs. (9.5), are zero. For generally laminated plates, these coefficients are not zero, and the plate analysis becomes much more complicated. As shown in Section 5.4, a symmetric arrangement of the layers in laminated plates provides the maximum bending stiffness for the plates with a given number of layers. It should be also taken into account that the symmetric structure of the plate substantially simplifies the plate behavior, i.e., the plate bending and in-plane loading are described by independent sets of equations and the plane remains flat before buckling under in-plane loading. In unsymmetrically laminated plates in-plane stress-strain state and bending are coupled and the plate behavior is described by a coupled set of equations which include all three displacements u, v, and w. Thus, without special reasons it does not make much sense to design unsymmetrically laminated plates. Note that the thickness of the composite ply is relatively small (0.1–0.2 mm) and tens of such plies with various orientations are usually placed to fabricate real composite plates. Thus, the possibility to make a symmetrically laminated plate practically always exists.

However, there are special cases in which the plates cannot be designed as symmetric laminates. The first class of such plates comprises plates stiffened with ribs which are usually located on one side of the plate. Being smeared over the plate surface, the ribs can be simulated by continuous layers resulting in an unsymmetrically laminated structure. For example, consider a stiffened plate shown in Fig. 9.40. The ribs in Fig. 9.40a can be approximately reduced to the layer 1 shown in Fig. 9.40b whose stiffness coefficients in the coordinates 1,2 are

$$A_{11}^{(1)} = \frac{b}{a} E_r, \quad A_{12}^{(1)} = A_{22}^{(1)} = 0$$

where E_r is the modulus of the rib material. In conjunction with the skin (layer 2 in Fig. 9.40b), the resulting structure is unsymmetric. The second group of unsymmetric structures corresponds to plates consisting of two layers, one of which is a load-carrying layer, whereas the second one protects this layer against, for example, temperature or impact loading.

9.7.1 Bending of unsymmetric plates

Consider a rectangular orthotropic plate loaded with transverse pressure as shown in Fig. 9.1. The plate behavior is described with equilibrium equations, Eqs. (9.22), (9.24), and (9.26), constitutive

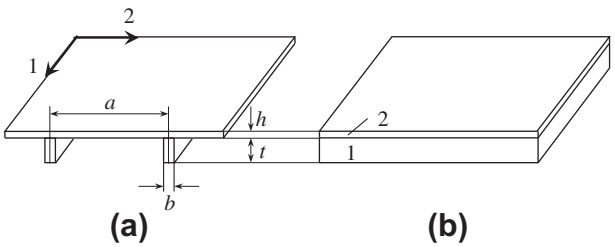


FIGURE 9.40

Reduction of a stiffened plate (a) to a laminated plate (b).

equations, Eqs. (9.16), and strain-displacement equations, Eqs. (9.3), in which the curvatures corresponding to the classical plate theory are given by Eqs. (9.49). Within the framework of classical plate theory, the constitutive equations become

$$\begin{aligned}
N_x &= B_{11}\frac{\partial u}{\partial x} + B_{12}\frac{\partial v}{\partial y} - C_{11}\frac{\partial^2 w}{\partial x^2} - C_{12}\frac{\partial^2 w}{\partial y^2} \\
N_y &= B_{12}\frac{\partial u}{\partial x} + B_{22}\frac{\partial v}{\partial y} - C_{12}\frac{\partial^2 w}{\partial x^2} - C_{22}\frac{\partial^2 w}{\partial y^2} \\
N_{xy} &= B_{44}\left(\frac{\partial u}{\partial y} + \frac{\partial v}{\partial x}\right) - 2C_{44}\frac{\partial^2 w}{\partial x \partial y} \\
M_x &= C_{11}\frac{\partial u}{\partial x} + C_{12}\frac{\partial v}{\partial y} - D_{11}\frac{\partial^2 w}{\partial x^2} - D_{12}\frac{\partial^2 w}{\partial y^2} \\
M_y &= C_{12}\frac{\partial u}{\partial x} + C_{22}\frac{\partial v}{\partial y} - D_{12}\frac{\partial^2 w}{\partial x^2} - D_{22}\frac{\partial^2 w}{\partial y^2} \\
M_{xy} &= C_{44}\left(\frac{\partial u}{\partial y} + \frac{\partial v}{\partial x}\right) - 2D_{44}\frac{\partial^2 w}{\partial x \partial y}
\end{aligned} \tag{9.266}$$

In classical plate theory, the equilibrium equations reduce to two in-plane equations, Eqs. (9.22), and Eq. (9.51) describing the plate bending. Substituting stress resultants and couples specified by Eqs. (9.266) into these three equations, we arrive at the following set of equations for u, v, and w:

$$L_1(u, v, w) = 0, \quad L_2(u, v, w) = 0, \quad L_3(u, v, w) = \overline{p} \tag{9.267}$$

in which

$$\begin{aligned}
L_1(u, v, w) &= B_{11}\frac{\partial^2 u}{\partial x^2} + B_{44}\frac{\partial^2 u}{\partial y^2} + (B_{12} + B_{44})\frac{\partial^2 v}{\partial x \partial y} - C_{11}\frac{\partial^3 w}{\partial x^3} - (C_{12} + 2C_{44})\frac{\partial^3 w}{\partial x \partial y^2} \\
L_2(u, v, w) &= B_{22}\frac{\partial^2 v}{\partial y^2} + B_{44}\frac{\partial^2 v}{\partial x^2} + (B_{12} + B_{44})\frac{\partial^2 u}{\partial x \partial y} - C_{22}\frac{\partial^3 w}{\partial y^3} - (C_{12} + 2C_{44})\frac{\partial^3 w}{\partial x^2 \partial y} \\
L_3(u, v, w) &= D_1\frac{\partial^4 w}{\partial x^4} + 2D_3\frac{\partial^4 w}{\partial x^2 \partial y^2} + D_2\frac{\partial^4 w}{\partial y^4} - C_{11}\frac{\partial^3 u}{\partial x^3} - (C_{12} + 2C_{44})\left(\frac{\partial^3 u}{\partial x \partial y^2} - \frac{\partial^3 v}{\partial x^2 \partial y}\right) - C_{22}\frac{\partial^3 v}{dy^3}
\end{aligned} \tag{9.268}$$

where, as earlier, $D_1 = D_{11}$, $D_2 = D_{22}$, and $D_3 = D_{12} + 2D_{44}$.

Consider a simply supported plate (see Fig. 9.3) and assume that the plate edges can move in the directions normal to the edges, so that the corresponding forces are zero. Then, the boundary conditions on the plate edges are, at $x = 0$ and $x = a$,

$$w = 0, \quad M_x = 0, \quad N_x = 0, \quad v = 0 \tag{9.269}$$

and at $y = 0$ and $y = b$,

$$w = 0, \quad M_y = 0, \quad N_y = 0, \quad u = 0$$

It can be proved with the aid of Eqs. (9.266) that these boundary conditions can be satisfied if we take the displacements in the form

$$\begin{aligned} u &= \sum_m \sum_n u_{mn} \cos \lambda_m x \cdot \sin \lambda_n y \\ v &= \sum_m \sum_n v_{mn} \sin \lambda_m x \cdot \cos \lambda_n y \\ w &= \sum_m \sum_n w_{mn} \sin \lambda_m x \cdot \sin \lambda_n y \end{aligned} \tag{9.270}$$

where $\lambda_m = \pi m/a$ and $\lambda_n = \pi n/b$ (see Fig. 9.1). Expanding the pressure $\overline{p}$ in a similar series specified by Eq. (9.131) and substituting the displacements, Eqs. (9.270), into the equilibrium equations, Eqs. (9.267), we arrive at the following three algebraic equations for the coefficients of Eqs. (9.270):

$$\begin{aligned} a_{11}u_{mn} + a_{12}v_{mn} + a_{13}w_{mn} &= 0 \\ a_{21}u_{mn} + a_{22}v_{mn} + a_{23}w_{mn} &= 0 \\ a_{31}u_{mn} + a_{32}v_{mn} + a_{33}w_{mn} &= p_{mn} \end{aligned} \tag{9.271}$$

in which

$$\begin{aligned} &a_{11} = B_{11}\lambda_m^2 + B_{44}\lambda_n^2, \quad a_{12} = a_{21} = \left(B_{12} + B_{44}\right)\lambda_m\lambda_n \\ &a_{22} = B_{44}\lambda_m^2 + B_{22}\lambda_n^2, \quad a_{13} = a_{31} = C_{11}\lambda_m^3 + \left(C_{12} + 2C_{44}\right)\lambda_m\lambda_n^2 \\ &a_{23} = a_{32} = C_{22}\lambda_n^3 + \left(C_{12} + 2C_{44}\right)\lambda_m^2\lambda_n \\ &a_{33} = D_1\lambda_m^4 + 2D_3\lambda_m^2\lambda_n^2 + D_2\lambda_n^4 \end{aligned} \tag{9.272}$$

The solution of Eqs. (9.271) is

$$\begin{aligned} &u_{mn} = \frac{w_{mn}}{A_1}\left(a_{13}a_{22} - a_{12}a_{23}\right), \quad v_{mn} = \frac{w_{mn}}{A_1}\left(a_{11}a_{23} - a_{12}a_{13}\right) \\ &w_{mn} = p_{mn}\frac{A_1}{A_2}, \quad A_1 = a_{11}a_{22} - a_{12}^2 \\ &A_2 = a_{33}A_1 - a_{11}a_{23}^2 - a_{22}a_{13}^2 + 2a_{12}a_{13}a_{23} \end{aligned} \tag{9.273}$$

It is possible to demonstrate a remarkable property of the solution obtained. Recall that in reducing the three-dimensional equations of the theory of elasticity to the two-dimensional equations of the plate theory, we actually reduce the plate to its reference surface located at some distance e from the lower surface of the plate. Hence, the forces N_x, N_y, and N_{xy} in plate theory are applied to the reference surface and the moments M_x, M_y, and M_{xy} are calculated with respect to this surface. Only the transverse forces V_x and V_y and the plate deflection w (see Fig. 9.41) correspond to any surface parallel to the reference surface. Thus, when formulating the boundary conditions for in-plane forces N_x, N_y, and N_{xy} or in-plane displacements u and v, we must apply the loads to the reference surface or

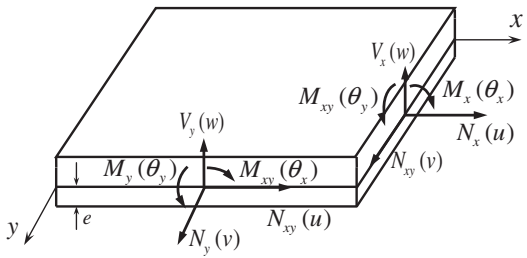


FIGURE 9.41

Forces and moments applied to the plate reference surface and the corresponding displacements u, v, w and rotation angles θ_x, θ_y.

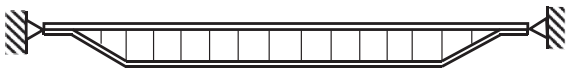


FIGURE 9.42

Sandwich plate with ramps.

fix the reference surface on the plate edges. In some cases, the location of the reference surface can be preassigned. For example, if the skin of the stiffened plate shown in Fig. 9.40 is fixed, the reference surface should be located within the skin thickness. For sandwich plates with ramps (see Fig. 9.42), the reference surface should pass through the fixed boundary contour. However, in the majority of cases the boundary conditions do not help us to identify the location of the reference surface and the coordinate e (see Fig. 9.41) can be chosen arbitrarily. Clearly, in such cases the feasible solutions for real plates must not depend on e, and this is the case for the solution given by Eqs. (9.273). Indeed, the stiffness coefficients, Eqs. (5.28) and (5.29), are

$$\begin{aligned} &B_{mn} = I^{(0)}_{mn}, \quad C_{mn} = I^{(1)}_{mn} - eI^{(0)}_{mn} \\ &D_{mn} = I^{(2)}_{mn} - 2eI^{(1)}_{mn} + e^2 I^{(0)}_{mn}, \quad I^{(r)}_{mn} = \int_0^h A_{mn} t^r dt, \quad (r = 0, 1, 2) \end{aligned} \tag{9.274}$$

where $mn = 11$, 12, 22, and 44. Substituting Eqs. (9.274) into Eqs. (9.273) for A_1 and A_2, we arrive at

$$A_1 = \left(I^{(0)}_{11}\lambda_m^2 + I^{(0)}_{44}\lambda_n^2\right)\left(I^{(0)}_{22}\lambda_m^2 + I^{(0)}_{44}\lambda_n^2\right) - \left(I^{(0)}_{12} + I^{(0)}_{44}\right)^2 \lambda_m^2\lambda_n^2$$

$$\begin{aligned} A_2 = {} & A_1\left[I^{(2)}_{11}\lambda_m^4 + 2\left(I^{(2)}_{12} + 2I^{(2)}_{44}\right)\lambda_m^2\lambda_n^2 + I^{(2)}_{22}\lambda_n^4\right] - \left(I^{(0)}_{11}\lambda_m^2 + I^{(0)}_{44}\lambda_n^2\right)\left[I^{(1)}_{22}\lambda_n^3 + \left(I^{(1)}_{12} + 2I^{(1)}_{44}\right)\lambda_m^2\lambda_n\right] \\ & - \left(I^{(0)}_{44}\lambda_m^2 + I^{(0)}_{22}\lambda_n^2\right)\left[I^{(1)}_{11}\lambda_m^3 + \left(I^{(1)}_{12} + 2I^{(1)}_{44}\right)\lambda_m\lambda_n^2\right] \\ & + 2\left(I^{(0)}_{12} + I^{(0)}_{44}\right)\left[I^{(1)}_{11}\lambda_m^2 + \left(I^{(1)}_{12} + 2I^{(1)}_{44}\right)\lambda_m\lambda_n^2\right]\left[I^{(1)}_{22}\lambda_n^3 + \left(I^{(1)}_{12} + 2I^{(1)}_{44}\right)\lambda_m^2\lambda_n\right]\lambda_m\lambda_n \end{aligned}$$

As can be seen, the terms explicitly including e disappear, whereas the integrals $I_{mn}^{(r)}$ do not depend on e. Thus, the deflection coefficient w_{mn} in Eqs. (9.273) does not depend on e either. This result is expected, since the boundary conditions given by Eqs. (9.269) actually correspond to the plate resting on thin walls which have infinitely high in-plane stiffness and are absolutely flexible with respect to the out-of-plane displacements. The conditions $N = 0$ and $M = 0$ provide zero stresses which are normal to the plate edges, whereas the conditions imposed on the displacements provide zero displacements in the plane of the edges. Obviously, the deflection of the plate with such boundary conditions must not depend on the choice of the reference surface.

To demonstrate the opposite situation, change the first two series in Eqs. (9.270) to the following ones:

$$u = \sum_m \sum_n u_{mn} \sin \lambda_m x \cdot \sin \lambda_n y, \quad \upsilon = \sum_m \sum_n \upsilon_{mn} \sin \lambda_m x \cdot \sin \lambda_n y \tag{9.275}$$

In conjunction with Eqs. (9.270) for w, these expansions correspond to the following boundary conditions. The boundary conditions on the plate edges are, at $x = 0$ and $x = a$,

$$w = 0, \quad M_x = 0, \quad u = 0, \quad \upsilon = 0$$

and at $y = 0$ and $y = b$,

$$w = 0, \quad M_y = 0, \quad \upsilon = 0, \quad u = 0$$

Thus, the in-plane displacements are zero at the plate edges. Substitution of the series for u, v, and w into Eqs. (9.267) yields

$$\begin{aligned}
&\sum_m \sum_n \left(a_{11} u_{mn} \sin \lambda_m x \cdot \sin \lambda_n y - a_{12} \upsilon_{mn} \cos \lambda_m x \cdot \cos \lambda_n y - a_{13} w_{mn} \cos \lambda_m x \cdot \sin \lambda_n y\right) = 0 \\
&\sum_m \sum_n \left(a_{21} u_{mn} \cos \lambda_m x \cdot \cos \lambda_n y - a_{22} \upsilon_{mn} \sin \lambda_m x \cdot \sin \lambda_n y + a_{23} w_{mn} \sin \lambda_m x \cdot \cos \lambda_n y\right) = 0 \\
&\sum_m \sum_n \left(a_{31} u_{mn} \cos \lambda_m x \cdot \sin \lambda_n y = a_{32} \upsilon_{mn} \sin \lambda_m x \cdot \cos \lambda_n y + (a_{33} - p_{mn}) w_{mn} \sin \lambda_m x \cdot \sin \lambda_n y\right) = 0
\end{aligned} \tag{9.276}$$

Here, the coefficients a_{ij} are specified by Eqs. (9.272). These equations cannot be directly reduced to algebraic equations similar to Eqs. (9.271). To arrive at an algebraic set of equations for u_{mn}, υ_{mn}, and w_{mn}, we can use the Bubnov-Galerkin method, i.e., multiply Eqs. (9.276) by $\sin \lambda_i x \cdot \sin \lambda_j y$ and integrate them over the plate surface area. As a result, we get an infinite set of algebraic equations for u_{mn}, υ_{mn}, and w_{mn}.

As an example, consider a square ($a = b$) cross-ply carbon-epoxy plate (see Fig. 9.43) composed of 0° and 90° layers. The plate dimensions are $a = 100$ mm and $h = 2$ mm. For uniform pressure $\overline{p} = p_0$, the maximum plate deflection corresponding to the solution given by Eqs. (9.273) is $w = 5.24 \cdot 10^6 p_0 / E_1$ in which E_1 is the longitudinal modulus of the unidirectional ply. As has been noted, this deflection does not depend on the location of the reference surface. Now assume that the reference surface coincides with the contact surface of the layers ($e = h/2$). The solution of the equation corresponding to Eqs. (9.276) in which 10 terms are retained is $w = 4.3 \cdot 10^6 p_0 / E_1$. This deflection is about 20% lower than that calculated for the simply supported plate. However, this

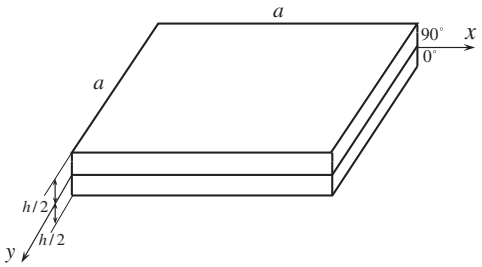


FIGURE 9.43

Two-layered cross-ply square plate.

solution depends on the coordinate of the reference surface and can hardly be used for real plates for which the location of the reference is not known.

We can expect that in addition to the solution given by Eqs. (9.273) for simply supported plates, the deflection does not depend on the location of the reference surface if the plate edges are clamped and the boundary conditions are, at $x = 0$ and $x = a$,

$$w = 0, \quad \theta_x = \frac{\partial w}{\partial x} = 0, \quad u = 0, \quad v = 0 \tag{9.277}$$

and at $y = 0$ and $y = b$,

$$w = 0, \quad \theta_y = \frac{\partial w}{\partial y} = 0, \quad u = 0, \quad v = 0$$

These boundary conditions can be satisfied if in addition to Eqs. (9.275) for u, v, the plate deflection is presented as

$$w = \sum_m \sum_n w_{mn}(1 - \cos 2\lambda_m x)(1 - \cos 2\lambda_n y) \tag{9.278}$$

where, as earlier, $\lambda_m = \pi m/a$, $\lambda_n = \pi n/b$ (see Fig. 9.1). Substitution of the displacements, Eqs. (9.275) and (9.278), into the equilibrium equations, Eqs. (9.267), results in equations similar to Eqs. (9.276) which can be solved with the aid of Bubnov-Galerkin method.

9.7.2 In-plane loading

Consider unsymmetrically laminated plates loaded by compressive forces T_x as shown in Fig. 9.23. As opposed to symmetric plates, unsymmetrically laminated plates can experience bending under compression. To allow for the in-plane loading of the plate, change the pressure $\overline{p}$ to the imaginary pressure p_n specified by Eq. (9.221). Then, the equilibrium equations, Eqs. (9.267), become

$$L_1(u, v, w) = 0, \quad L_2(u, v, w) = 0, \quad L_3(u, v, w) + T_x \frac{\partial^2 w}{\partial x^2} = 0 \tag{9.279}$$

where the operators L_1, L_2, and L_3 are specified by Eqs. (9.268).

Consider first the conditions under which the plate remains flat under in-plane loading (Leissa, 1986). Assume that

$$w = 0, \quad N_x = -T_x, \quad N_y = 0, \quad N_{xy} = 0 \tag{9.280}$$

Then, the first three equations of Eqs. (9.266) yield

$$B_{11}\frac{\partial u}{\partial x} + B_{12}\frac{\partial v}{\partial y} = -T_x, \quad B_{12}\frac{\partial u}{\partial x} + B_{22}\frac{\partial v}{\partial y} = 0, \quad \frac{\partial u}{\partial y} + \frac{\partial v}{\partial x} = 0$$

The solution of these equations is:

$$u = -\frac{T_x B_{22}}{B}x + C_1 y + C_2, \quad v = \frac{B_{12}T_x}{B}y - C_1 x + C_3 \tag{9.281}$$

where C_1, C_2, and C_3 are the constants corresponding to the plate in-plane displacements and rotation as a solid. Substituting Eqs. (9.281) into the last three equations of Eqs. (9.266), we get

$$M_x = \frac{T_x}{B}(B_{11}C_{12} - B_{22}C_{11}), \quad M_y = \frac{T_x}{B}(B_{12}C_{22} - B_{22}C_{12}), \quad M_{xy} = 0 \tag{9.282}$$

Since M_x and M_y do not depend on x and y, the moment equilibrium equations, Eqs. (9.26), show that $V_x = 0$ and $V_y = 0$. Thus, the plate is in a state of pure bending by moments specified by Eqs. (9.282) and applied at the plate edges. These moments are of a reactive nature. The unsymmetrically laminated plate, being loaded with in-plane forces T_x (see Fig. 9.23), tends to bend, but the edge moments, Eqs. (9.282), prevent this bending. Such moments can appear if the plate edges are clamped with respect to bending, i.e., if the first two boundary conditions in Eqs. (9.277) are valid at the plate edges.

Thus, unsymmetrically laminated plates clamped at the edges (clearly, this is a sliding clamp allowing nonzero in-plane displacements of the plate) remain flat under in-plane loading by uniformly distributed edge forces. Such plates can buckle and conventional methods to determine the critical loads can be used (Qatu and Leissa, 1993; Majeed and Hyer, 2005).

Consider simply supported plates. First of all, note that the equilibrium equations, Eqs. (9.279), are homogeneous and, in conjunction with the homogeneous boundary conditions, Eqs. (9.269), allow us to formulate the boundary-value problem and to find the corresponding eigenvalues for the load T_x. For symmetrically laminated plates, the lowest of these values is associated with the critical load which causes plate buckling. Consider this problem for unsymmetrically laminated plates. Substituting the displacements, Eqs. (9.270), into Eqs. (9.279), we arrive at the homogeneous set of algebraic equations, Eqs. (9.271), in which $p_{mn} = T_x\lambda_m^2 w_{mn}$. The determinant of this set must be zero, so that we arrive at the following system of eigenvalues for the load T_x:

$$T_{mn} = \frac{A_2}{\lambda_m^2 A_1} \tag{9.283}$$

in which A_1 and A_2 are specified by Eqs. (9.273). Recall that the load T_x must be applied to the reference surface with coordinate e (see Fig. 9.41) which is not specified. However, it follows from the foregoing analysis of the solution given by Eqs. (9.273) that the coefficients A_1 and A_2 do not depend on e and hence, the eigenvalues T_{mn} do not depend on e either. For the symmetrically laminated plate problem, the so-called bifurcation of the plate equilibrium takes place when T_x reaches the first

eigenvalue T_x^0. This means that for the load $T_x = T_x^c$ two equilibrium states of the plate are possible: a flat shape ($w = 0$) which is not stable for $T_x > T_x^c$ and a curved shape to which the plate is transformed as a result of buckling. However, an unsymmetrically laminated plate starts bending from the very beginning of the loading process, i.e., $w \neq 0$ for $T_x \leq T_x^c$, which means that there is no bifurcation and, hence, buckling cannot take place at the first eigenvalue specified by Eq. (9.283) (Azikov and Vasiliev, 1992; Qatu and Leissa, 1993).

Consider the initial phase of the plate bending under compression assuming that the plate deflection is small in comparison with the plate thickness. In accordance with Eqs. (9.270), the deflection of a simply supported plate can be taken in the form

$$w = \sum_m \sum_n w_{mn} \sin \lambda_m x \cdot \sin \lambda_n y \tag{9.284}$$

Substitute this expansion into the first two equilibrium equations, Eqs. (9.279), and determine u and v from these equations. Taking into account Eqs. (9.281) in which we can eliminate the plate displacements as a solid body putting $C_1 = C_2 = C_3 = 0$, we finally arrive at

$$\begin{aligned} u &= -\frac{T_x B_{22}}{B} x + \sum_m \sum_n w_{mn} \lambda_m r_{mn} \cos \lambda_m x \cdot \sin \lambda_n y \\ v &= \frac{T_x B_{12}}{B} y + \sum_m \sum_n w_{mn} \lambda_m t_{mn} \sin \lambda_m x \cdot \cos \lambda_n y \end{aligned} \tag{9.285}$$

where

$$r_{mn} = \frac{1}{B_1}\left[\left(C_{11} + \overline{C}\frac{\lambda_n^2}{\lambda_m^2}\right)\left(B_{22} + B_{44}\frac{\lambda_m^2}{\lambda_n^2}\right) - \left(C_{22}\frac{\lambda_n^2}{\lambda_m^2} + C_4\right)\overline{B}\right]$$

$$t_{mn} = \frac{1}{B_1}\left[\left(C_{22} + \overline{C}\frac{\lambda_m^2}{\lambda_n^2}\right)\left(B_{11} + B_{44}\frac{\lambda_n^2}{\lambda_m^2}\right) - \left(C_{11}\frac{\lambda_m^2}{\lambda_n^2} + C_4\right)\overline{B}\right]$$

in which

$$B_1 = B + B_{44}\left(B_{22}\frac{\lambda_n^2}{\lambda_m^2} + B_{11}\frac{\lambda_m^2}{\lambda_n^2} - 2B_{12}\right), \quad B = B_{11}B_{22} - B_{12}^2$$

$$\overline{C} = C_{12} + 2C_{44}, \quad \overline{B} = B_{12} + B_{44}$$

To determine the deflection coefficients w_{mn}, apply the principle of minimum total potential energy of the plate

$$\begin{aligned} P = \frac{1}{2}\int_0^a \int_0^b \Bigg\{ & N_x\frac{\partial u}{\partial x} + N_y\frac{\partial v}{\partial y} + N_{xy}\left(\frac{\partial u}{\partial y} + \frac{\partial v}{\partial x}\right) - M_x\frac{\partial^2 w}{\partial x^2} - M_y\frac{\partial^2 w}{\partial y^2} \\ & - 2M_{xy}\frac{\partial^2 w}{\partial x \partial y} + T_x\left[\frac{\partial u}{\partial x} - \frac{1}{2}\left(\frac{\partial w}{\partial x}\right)^2\right]\Bigg\} dxdy \end{aligned} \tag{9.286}$$

Note that in contrast to Eq. (9.256) which corresponds to the nonlinear problem, Eq. (9.286) correspond to the linearized problem and we must additionally take into account the work performed by the force T_x on the plate shortening caused by deflection. Substituting the stress resultants and couples from Eqs. (9.266) into Eq. (9.286), using Eqs. (9.284) and (9.285) for displacements, and integrating, we arrive at the total potential energy P as a function of w_{mn}. Applying the minimum condition $\partial P/\partial w_{mn} = 0$, we finally get

$$w_{mn} = \frac{T_x k_{mn}}{T_x - T_{mn}} \tag{9.287}$$

in which

$$k_{mn} = \frac{1}{B_1}\left[(B_{12}C_{12} - B_{22}C_{11})\frac{\lambda_m}{\lambda_n} + (B_{12}C_{11} - B_{22}C_{12})\frac{\lambda_n}{\lambda_m}\right], \quad m, n = 1, 3, 5, \ldots$$

and T_{mn} is specified by Eq. (9.283). Let the minimum value of $T_{mn}(m, n)$ be T_e. Then, it follows from Eq. (9.287) that the plate deflection increases infinitely while T_x approaches T_e. Consider, for example, a carbon-epoxy three-layered plate with dimensions $a = 0.4$ m and $b = 0.2$ m composed of layers with angles $\phi_1 = 0°$, $\phi_2 = \pm 45°$, and $\phi_3 = \pm 20°$ and equal thicknesses $h_1 = h_2 = h_3 = 0.26$ mm. The dependencies of the plate shortening $\Delta u = u(x = a) - u(x = 0)$ on the normalized load T_x/T_e is shown in Fig. 9.44. Curve 1 corresponds to the foregoing linearized solution, Eq. (9.287). As can be seen, Δu becomes infinitely high at $T_x/T_e = 1$, i.e., when the acting load becomes equal to the minimum eigenvalue. Clearly, this result is quite formal and does not have any physical meaning for a load that is close to T_e. Indeed, the solution, Eq. (9.287), is obtained under the condition that the deflection is small in comparison to the plate thickness and is not valid for large (moreover, infinite) deflection.

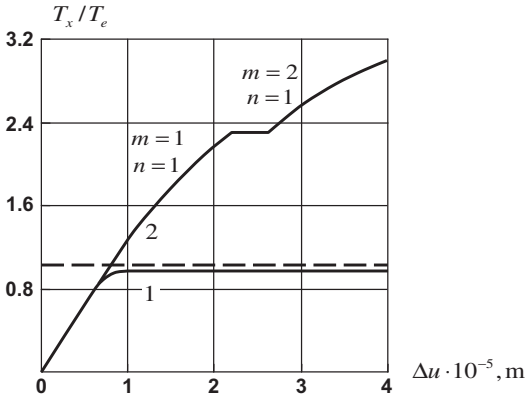


FIGURE 9.44

Dependence of the plate shortening on the normalized in-plane load: linearized (1) and nonlinear (2) solutions.

To describe large deflections, we must use the nonlinear equations presented in Section 9.6. For unsymmetrically laminated plates, Eqs. (9.253) are generalized as follows:

$$L_1(u,v,w)+B_{11}\frac{\partial w}{\partial x}\frac{\partial^2 w}{\partial x^2}+\overline{B}\frac{\partial w}{\partial y}\frac{\partial^2 w}{\partial x\partial y}+B_{44}\frac{\partial w}{\partial x}\frac{\partial^2 w}{\partial y^2}=0$$
$$L_2(u,v,w)+B_{22}\frac{\partial w}{\partial y}\frac{\partial^2 w}{\partial y^2}+\overline{B}\frac{\partial w}{\partial x}\frac{\partial^2 w}{\partial x\partial y}+B_{44}\frac{\partial w}{\partial y}\frac{\partial^2 w}{\partial x^2}=0 \tag{9.288}$$

where the operators L_1 and L_2 are specified by Eqs. (9.268).

For square or close-to-square plates ($a/b \le 1.75$), the initial deflection can be approximated by Eq. (9.254), according to which

$$w = w_m \sin \lambda_m x \cdot \sin \lambda_1 y \tag{9.289}$$

where, as earlier, $\lambda_m = \pi m/a$ and $\lambda_1 = \pi/b$. For the initial loading (at least for $T_x/T_e < 1$ in Fig. 9.44), we take $m = 1$. The problem we are going to consider is to identify the dependence $\Delta u(T_x/T_e)$ which can be different from curve 1 shown in Fig. 9.49 and to study the stability of the initial plate bending, i.e., the possibility of mode-jumping to the half-wave number m which is higher than the initial value $m = 1$ (Azikov and Vasiliev, 1992).

Substituting the deflection, Eq. (9.289), in Eqs. (9.288), we can derive the following expressions for the in-plane displacements which generalize Eqs. (9.255) for unsymmetrically laminated plates:

$$u = -\frac{x}{B}\left(B_{22}T_x+\frac{1}{8}w_m^2\lambda_m^2\right)+w_m\lambda_m r_m \cos\lambda_m x\cdot\cos\lambda_1 y$$
$$-\frac{w_m^2}{16}\left[\frac{1}{\lambda_m}\left(\lambda_m^2-\frac{B_{12}}{B_{11}}\lambda_1^2\right)-\lambda_m\cos 2\lambda_1 y\right]\sin 2\lambda_m x$$
$$v = -\frac{y}{B}\left(B_{12}T_x-\frac{1}{8}w_m^2\lambda_1^2\right)+w_m\lambda_1 t_m \sin\lambda_m x\cdot\cos\lambda_1 y \tag{9.290}$$
$$-\frac{w_m^2}{16}\left[\frac{1}{\lambda_1}\left(\lambda_1^2-\frac{B_{12}}{B_{22}}\lambda_m^2\right)-\lambda_1\cos 2\lambda_m x\right]\sin 2\lambda_1 y$$

Here, $r_m = r_{mn}$ (m, $n = 1$) and $t_m = t_{mn}$ (m, $n = 1$) are given in notations to Eqs. (9.285). Substituting the displacements, Eqs. (9.289) and (9.290), into Eq. (9.286) for the total potential energy, and integrating, we arrive at

$$P=\frac{ab}{4}\lambda_m^2\left(k_1 w_m+\frac{1}{2}k_2 w_m^2+\frac{1}{3}k_3 w_m^3+\frac{1}{4}k_4 w_m^4\right)-\frac{ab}{2B}B_{22}T_x^2 \tag{9.291}$$

where

$$k_1 = \frac{16T_x}{\lambda_m^2 ab} k_{m,} \quad k_2 = T_m - T_x$$

$$k_3 = \frac{1}{ab}\left\{\left(1 - \frac{B_{12}\lambda_1^2}{B_{11}\lambda_m^2}\right)\left[(C_{11} - B_{11}r_m)\frac{\lambda_m}{\lambda_1} + (C_{12} - B_{12}t_m)\frac{\lambda_1}{\lambda_m}\right]\right.$$

$$+ \left(\frac{\lambda_1^2}{\lambda_m^2} - \frac{B_{12}}{B_{11}}\right)\left[(C_{22} - B_{22}t_m)\frac{\lambda_1}{\lambda_m} + (C_{12} - B_{12}r_m)\frac{\lambda_m}{\lambda_1}\right]$$

$$+ \frac{\lambda_1}{\lambda_m}\left[\frac{\lambda_m^2}{\lambda_1^2}\left(C_{11} - C_{12}\frac{B_{12}}{B_{22}}\right) + \frac{\lambda_1^2}{\lambda_m^2}\left(C_{22} - C_{12}\frac{B_{12}}{B_{11}}\right) - C_{11}\frac{B_{12}}{B_{11}} - C_{22}\frac{B_{12}}{B_{11}} + 2C_{12}\right]$$

$$\left. - B\left(\frac{\lambda_m r_m}{B_{22}\lambda_1} + \frac{\lambda_1^3 t_m}{B_{11}\lambda_m^3}\right)\right\}$$

$$k_4 = \frac{B\lambda_1^2}{16}\left(\frac{\lambda_m^2}{B_{22}\lambda_1^2} + \frac{\lambda_1^2}{B_{11}\lambda_m^2}\right)$$

Here, $k_m = k_{mn}(m, n = 1)$ is given in notation to Eq. (9.287). The minimum condition, $\partial P/\partial w_m = 0$, yields the following equation for w_m:

$$k_4 w_m^3 + k_3 w_m^2 + k_2 w_m + k_1 = 0$$

This equation has one real root which specifies the plate deflection.

The half-wave number m depends on the acting load T_x and can be found by comparing the levels of the total potential energy P in Eq. (9.291) as demonstrated in Section 9.6.

For the carbon-epoxy plate considered previously as an example, the nonlinear solution is shown in Fig. 9.44 with line 2. As can be seen, the initial plate bending with $m = 1$ is not affected by the eigenvalue of the load T_e, which, as noted, does not have any physical meaning. At the load $T_x = 2.32T_e$ the bending mode corresponding to $m = 1$ changes to the mode corresponding to $m = 2$.

It should be taken into account that the behavior of in-plane loaded unsymmetrically laminated plates depends on the coordinate of the reference surface e (see Fig. 9.41) to which the load T_x is applied. Changing e, we actually move the load through the plate thickness and change the plate bending conditions. Since the location of the reference surface is usually not known, it seems reasonable to take it in accordance with the condition $C_{11} = 0$, under which the bending-stretching coupling disappears in the direction of plate loading. It follows from Eqs. (9.274) that the coordinate of the reference surface can be calculated in this case as

$$e = \frac{I_{11}^{(1)}}{I_{11}^{(0)}}$$

The foregoing procedure allows us to determine the plate displacements. Then, applying Eqs. (9.252), we can find the strains and, using the procedure described in Section 5.11, obtain the strains and the stresses in the principal coordinates of the plies. Applying the strength criteria discussed in Chapter 6, we can evaluate the load-carrying capacity of the plate.

As a numerical example, consider a square ($a = b = 0.2$ m) carbon-epoxy plate consisting of four layers with the following parameters: $\phi_1 = 0°$, $\phi_2 = \pm 30°$, $\phi_3 = \pm 60°$, $\phi_4 = 90°$, and $h_1 = h_2 = h_3 = h_4 = 0.26$ mm. For this plate, the first eigenvalue of the load is $T_e = 1.91\,\text{kN/m}$, the maximum deflection is $w = -5.82$ mm, and the ultimate load corresponding to the quadratic failure criterion, Eq. (6.11), is $T_x^u = 75.9\,\text{kN/m}$. For a symmetrically laminated plate with the same structure and thickness, the critical load is $T_x^c = 5.21\,\text{kN/m}$, the ultimate load is $T_x^u = 81.7\,\text{kN/m}$, and the deflection at the ultimate load is $w = \pm 5.66$ mm. Thus, there is no significant difference between the ultimate loads and the maximum deflections of unsymmetrically and symmetrically laminated plates composed of the same layers.

9.7.3 Shear deformable unsymmetrically laminated plates

Shear deformable unsymmetrically laminated plates are described by the most complicated equations of linear plate theory which allow for both bending-stretching coupling and transverse shear deformation. Such equations are required to analyze sandwich plates with different facing layers or sandwich plates with edge ramps (see Fig. 9.42).

To derive the corresponding governing equations, we need to use the complete set of the equations of plate theory presented in Section 9.1, i.e., equilibrium equations

$$\frac{\partial N_x}{\partial x} + \frac{\partial N_{xy}}{\partial y} = 0, \quad \frac{\partial N_y}{\partial y} + \frac{\partial N_{xy}}{\partial x} = 0 \tag{9.292}$$

$$\frac{\partial M_x}{\partial x} + \frac{\partial M_{xy}}{\partial y} - V_x = 0, \quad \frac{\partial M_y}{\partial y} + \frac{\partial M_{xy}}{\partial x} - V_y = 0 \tag{9.293}$$

$$\frac{\partial V_x}{\partial x} + \frac{\partial V_y}{\partial y} + \overline{p} = 0 \tag{9.294}$$

constitutive equations for orthotropic plates

$$\begin{aligned} N_x &= B_{11}\varepsilon_x^0 + B_{12}\varepsilon_y^0 + C_{11}\kappa_x + C_{12}\kappa_y \\ N_y &= B_{21}\varepsilon_x^0 + B_{22}\varepsilon_y^0 + C_{12}\kappa_x + C_{22}\kappa_y \\ N_{xy} &= B_{44}\gamma_{xy}^0 + C_{44}\kappa_{xy} \end{aligned} \tag{9.295}$$

$$\begin{aligned} M_x &= C_{11}\varepsilon_x^0 + C_{12}\varepsilon_y^0 + D_{11}\kappa_x + D_{12}\kappa_y \\ M_y &= C_{21}\varepsilon_x^0 + C_{22}\varepsilon_y^0 + D_{12}\kappa_x + D_{22}\kappa_y \\ M_{xy} &= C_{44}\gamma_{xy}^0 + D_{44}\kappa_{xy} \end{aligned} \tag{9.296}$$

$$V_x = S_x\gamma_x, \quad V_y = S_y\gamma_y \tag{9.297}$$

and strain-displacements equations

$$\varepsilon_x^0 = \frac{\partial u}{\partial x}, \quad \varepsilon_y^0 = \frac{\partial v}{\partial y}, \quad \gamma_{xy}^0 = \frac{\partial u}{\partial y} + \frac{\partial v}{\partial x} \tag{9.298}$$

$$\kappa_x = \frac{\partial \theta_x}{\partial x}, \quad \kappa_y = \frac{\partial \theta_y}{\partial y}, \quad \kappa_{xy} = \frac{\partial \theta_x}{\partial y} + \frac{\partial \theta_y}{\partial x} \tag{9.299}$$

$$\gamma_x = \theta_x + \frac{\partial w}{\partial x}, \quad \gamma_y = \theta_y + \frac{\partial w}{\partial y} \tag{9.300}$$

To arrive at the minimum number of the governing equations, we apply the mixed formulation of the problem. First, introduce the stress function $F(x, y)$

$$N_x = \frac{\partial^2 F}{\partial y^2}, \quad N_y = \frac{\partial^2 F}{\partial x^2}, \quad N_{xy} = -\frac{\partial^2 F}{\partial x \partial y} \tag{9.301}$$

which allows us to satisfy identically the first two equilibrium equations, Eqs. (9.292). To find the stress function, we need to use the compatibility equation which follows from Eqs. (9.298), i.e.,

$$\frac{\partial^2 \varepsilon_x^0}{\partial y^2} + \frac{\partial^2 \varepsilon_y^0}{\partial x^2} - \frac{\partial^2 \gamma_{xy}^0}{\partial x \partial y} = 0 \tag{9.302}$$

The strains that enter this equation are expressed using Eqs. (9.295). Using Eqs. (9.301) and (9.299), we finally get

$$\begin{aligned}
\varepsilon_x^0 &= b_x \frac{\partial^2 F}{\partial y^2} - b_{xy} \frac{\partial^2 F}{\partial x^2} - B_x \frac{\partial \theta_x}{\partial x} - B_{xy} \frac{\partial \theta_y}{\partial y} \\
\varepsilon_y^0 &= b_y \frac{\partial^2 F}{\partial x^2} - b_{yx} \frac{\partial^2 F}{\partial y^2} - B_y \frac{\partial \theta_y}{\partial y} - B_{yx} \frac{\partial \theta_x}{\partial x} \\
\gamma_{xy}^0 &= -b \frac{\partial^2 F}{\partial x \partial y} - c \left(\frac{\partial \theta_x}{\partial y} + \frac{\partial \theta_y}{\partial x} \right)
\end{aligned} \tag{9.303}$$

where

$$b_x = \frac{B_{22}}{B}, \quad b_y = \frac{B_{11}}{B}, \quad b_{xy} = b_{yx} = \frac{B_{12}}{B}, \quad B = B_{11} B_{22} - B_{12}^2$$

$$b = \frac{1}{B_{44}}, \quad c = \frac{C_{44}}{B_{44}}$$

$$B_x = \frac{1}{B}(B_{22} C_{11} - B_{12} C_{12}), \quad B_y = \frac{1}{B}(B_{11} C_{22} - B_{12} C_{12})$$

$$B_{xy} = \frac{1}{B}(B_{22} C_{12} - B_{12} C_{22}), \quad B_{yx} = \frac{1}{B}(B_{11} C_{12} - B_{12} C_{11})$$

Substituting the strains, Eqs. (9.303), into the compatibility equation, Eq. (9.302), we arrive at the first governing equation

$$b_y\frac{\partial^4 F}{\partial x^4}+\left(b-2b_{xy}\right)\frac{\partial^4 F}{\partial x^2\partial y^2}+b_x\frac{\partial^4 F}{\partial y^4}-B_{yx}\frac{\partial^3\theta_x}{\partial x^3}$$

$$-(B_x-c)\frac{\partial^3\theta_x}{\partial x\partial y^2}-\left(B_y-c\right)\frac{\partial^3\theta_y}{\partial x^2\partial y}-B_{xy}\frac{\partial^3\theta_y}{\partial y^3}=0 \tag{9.304}$$

To proceed, substitute Eqs. (9.303) and (9.299) into the constitutive equations for the moments, Eqs. (9.296), to get

$$M_x=D_x\frac{\partial\theta_x}{\partial x}+D_{xy}\frac{\partial\theta_y}{\partial y}+c_x\frac{\partial^2 F}{\partial y^2}+c_{xy}\frac{\partial^2 F}{\partial x^2}$$

$$M_y=D_y\frac{\partial\theta_y}{\partial y}+D_{yx}\frac{\partial\theta_x}{\partial x}+c_y\frac{\partial^2 F}{\partial x^2}+c_{yx}\frac{\partial^2 F}{\partial y^2} \tag{9.305}$$

$$M_{xy}=-c\frac{\partial^2 F}{\partial x\partial y}+D\left(\frac{\partial\theta_x}{\partial y}+\frac{\partial\theta_y}{\partial x}\right)$$

where

$$D_x=D_{11}-B_xC_{11}-B_{yx}C_{12},\quad D_y=D_{22}-B_yC_{22}-B_{xy}C_{12}$$

$$D_{xy}=D_{12}-B_{xy}C_{11}-B_yC_{12},\quad D_{yx}=D_{12}-B_{yx}C_{22}-B_xC_{12}$$

$$D=\frac{1}{B_{44}}\left(B_{44}D_{44}-C_{44}^2\right)$$

$$c_x=b_x\left(C_{11}-\frac{b_{yx}}{b_x}C_{12}\right),\quad c_y=b_y\left(C_{22}-\frac{b_{xy}}{b_y}C_{12}\right)$$

$$c_{xy}=b_y\left(C_{12}-\frac{b_{xy}}{b_y}C_{11}\right),\quad c_{yx}=b_x\left(C_{12}-\frac{b_{yx}}{b_x}C_{22}\right)$$

The remaining three equations of the governing set follow from the three equilibrium equations, Eqs. (9.293) and (9.294), if we substitute the moments from Eqs. (9.305) and the transverse shear forces from Eqs. (9.297) and (9.300), i.e.,

$$D_x\frac{\partial^2\theta_x}{\partial x^2}+\left(D+D_{xy}\right)\frac{\partial^2\theta_y}{\partial x\partial y}+D\frac{\partial^2\theta_x}{\partial y^2}+c_{xy}\frac{\partial^3 F}{\partial x^3}+(c_x-c)\frac{\partial^3 F}{\partial x\partial y^2}-S_x\left(\theta_x+\frac{\partial w}{\partial x}\right)=0 \tag{9.306}$$

$$D_y\frac{\partial^2\theta_x}{\partial y^2}+\left(D+D_{yx}\right)\frac{\partial^2\theta_x}{\partial x\partial y}+D\frac{\partial^2\theta_y}{\partial x^2}+c_{yx}\frac{\partial^3 F}{\partial y^3}+\left(c_y-c\right)\frac{\partial^3 F}{\partial x^2\partial y}-S_y\left(\theta_y+\frac{\partial w}{\partial y}\right)=0 \tag{9.307}$$

$$S_x\left(\frac{\partial\theta_x}{\partial x}+\frac{\partial^2 w}{\partial x^2}\right)+S_y\left(\frac{\partial\theta_y}{\partial y}+\frac{\partial^2 w}{\partial y^2}\right)+\overline{p}=0 \tag{9.308}$$

Thus the theory reduces to four equations, Eqs. (9.304) and (9.306)–(9.308), which include four unknown functions: F, θ_x, θ_y, and w. These equations have a total tenth order with respect to x and y variables.

For a simply supported plate with the boundary conditions at $x = 0$ and $x = a$,

$$w = 0, \quad M_x = 0, \quad N_x = 0, \quad \upsilon = 0, \quad \theta_y = 0$$

(see Fig. 9.1), and at $y = 0$ and $y = b$,

$$w = 0, \quad M_y = 0, \quad N_y = 0, \quad u = 0, \quad \theta_x = 0$$

the solution of the obtained equations can be presented in the form

$$\begin{aligned} F &= \sum_m \sum_n F_{mn} \sin \lambda_m x \cdot \sin \lambda_n y, \quad w = \sum_m \sum_n w_{mn} \sin \lambda_m x \cdot \sin \lambda_n y \\ \theta_x &= \sum_m \sum_n \theta_x^{mn} \cos \lambda_m x \cdot \sin \lambda_n y, \quad \theta_y = \sum_m \sum_n \theta_y^{mn} \sin \lambda_m x \cdot \cos \lambda_n y \end{aligned} \tag{9.309}$$

where, as earlier, $\lambda_m = \pi m/a$ and $\lambda_n = \pi n/b$. Expanding the pressure $\overline{p}$ in a similar series specified by Eq. (9.131) and substituting Eqs. (9.309) into Eqs. (9.304) and (9.306)–(9.308), we arrive at the following set of algebraic equations for the coefficients in Eqs. (9.309):

$$\begin{aligned} a_{11} F_{mn} + a_{12} \theta_x^{mn} + a_{13} \theta_y^{mn} + a_{14} w_{mn} &= 0 \\ a_{21} F_{mn} + a_{22} \theta_x^{mn} + a_{23} \theta_y^{mn} + a_{24} w_{mn} &= 0 \\ a_{31} F_{mn} + a_{32} \theta_x^{mn} + a_{33} \theta_y^{mn} + a_{34} w_{mn} &= 0 \\ a_{41} F_{mn} + a_{42} \theta_x^{mn} + a_{43} \theta_y^{mn} + a_{44} w_{mn} + p_{mn} &= 0 \end{aligned} \tag{9.310}$$

where

$$\begin{aligned} a_{11} &= b_y \lambda_m^4 + \left(b - 2b_{xy}\right) \lambda_m^2 \lambda_n^2 + b_x \lambda_n^4, \quad a_{12} = -B_{yx} \lambda_m^3 - (B_x - c) \lambda_m \lambda_n^2 \\ a_{13} &= -B_{xy} \lambda_n^3 - \left(B_y - c\right) \lambda_m^2 \lambda_n, \quad a_{14} = 0 \\ a_{21} &= -c_{xy} \lambda_m^3 - (c_x - c) \lambda_m \lambda_n^2, \quad a_{22} = -D_x \lambda_m^2 - D \lambda_n^2 - S_x \\ a_{23} &= -\left(D + D_{xy}\right) \lambda_m \lambda_n, \quad a_{24} = a_{42} = -S_x \lambda_m \\ a_{31} &= -c_{yx} \lambda_n^3 - \left(c_y - c\right) \lambda_m^2 \lambda_n, \quad a_{32} = -\left(D + D_{yx}\right) \lambda_m \lambda_n \\ a_{33} &= -D_y \lambda_n^2 - D \lambda_m^2 - S_y, \quad a_{34} = a_{43} = -S_y \lambda_n \\ a_{41} &= 0, \quad a_{44} = -S_x \lambda_m^2 - S_y \lambda_n^2 \end{aligned} \tag{9.311}$$

The solution of Eqs. (9.310) is

$$\begin{aligned} F_{mn} &= \frac{p_{mn}}{A}(a_{12}a_{23}a_{34} - a_{12}a_{33}a_{24} + a_{22}a_{33}a_{14} + a_{22}a_{13}a_{34} + a_{32}a_{13}a_{24} + a_{32}a_{23}a_{14}) \\ \theta_x^{mn} &= \frac{p_{mn}}{A}(-a_{11}a_{23}a_{34} + a_{11}a_{33}a_{24} + a_{21}a_{13}a_{34} - a_{21}a_{33}a_{14} - a_{31}a_{13}a_{24} + a_{31}a_{23}a_{14}) \\ \theta_y^{mn} &= -\frac{p_{mn}}{A}(a_{11}a_{22}a_{34} - a_{11}a_{32}a_{24} - a_{21}a_{12}a_{34} + a_{21}a_{32}a_{14} + a_{31}a_{12}a_{24} - a_{31}a_{22}a_{14}) \end{aligned} \tag{9.312}$$

$$w_{mn} = p_{mn}\frac{A_1}{A_2}$$

where

$$\begin{aligned} A = {} & a_{11}a_{22}a_{33}a_{44} - a_{11}a_{22}a_{34}a_{43} + a_{11}a_{32}a_{43}a_{24} - a_{11}a_{32}a_{23}a_{44} + a_{11}a_{42}a_{23}a_{34} \\ & - a_{11}a_{42}a_{33}a_{24} - a_{21}a_{12}a_{33}a_{44} + a_{21}a_{12}a_{34}a_{43} - a_{21}a_{32}a_{43}a_{14} \\ & + a_{21}a_{32}a_{13}a_{44} - a_{21}a_{42}a_{13}a_{34} + a_{21}a_{42}a_{33}a_{14} + a_{31}a_{12}a_{23}a_{44} \\ & - a_{31}a_{12}a_{43}a_{24} + a_{31}a_{22}a_{43}a_{14} - a_{31}a_{22}a_{13}a_{44} + a_{31}a_{42}a_{13}a_{24} \\ & - a_{31}a_{42}a_{23}a_{14} - a_{41}a_{12}a_{23}a_{34} + a_{41}a_{12}a_{33}a_{24} - a_{41}a_{22}a_{33}a_{14} \\ & + a_{41}a_{22}a_{13}a_{34} - a_{41}a_{32}a_{13}a_{24} + a_{41}a_{32}a_{23}a_{14} \end{aligned} \tag{9.313}$$

$$A_1 = -a_{11}a_{22}a_{33} + a_{11}a_{32}a_{23} + a_{21}a_{12}a_{33} - a_{21}a_{32}a_{13} - a_{31}a_{12}a_{23} + a_{31}a_{22}a_{13}$$

To study the in-plane loading under axial compression by forces T_x (see Fig. 9.23), we should change the pressure $\overline{p}$ in Eq. (9.308) to the imaginary pressure

$$p_n = -T_x\frac{\partial^2 w}{\partial x^2}$$

and apply the method described in Section 9.7.2.

9.8 References

Alfutov, N. A. (1992). On some paradoxes of the theory of thin plates. *Proc. of Russian Academy of Sciences. Mechanics of Solids, 3*, 65–72.

Ambartsumian, S. A. (1967). *Theory of Anisotropic Plates*. Moscow (in Russian): Nauka. Technomic, 1969.

Ambartsumian, S. A. (1987). *Theory of Anisotropic Plates. – Theory, Buckling and Vibrations*. Moscow (in Russian): Nauka.

Andreev, A. N., & Nemirovskii, Yu. V. (2001). *Multilayered Anisotropic Shells and Plates: Bending, Buckling, Vibrations*. Novosibirsk (in Russian): Nauka.

Ashton, J. E., & Whitney, J. M. (1970). *Theory of Laminated Plates*. Stamford CT: Technomic.

Azikov, N. S., & Vasiliev, V. V. (1986). Buckling and postbuckling behavior of compressed composite panels. *Proc. of Russian Academy of Sciences. Mechanics of Solids, 5*, 152–158.

Azikov, N. S., & Vasiliev, V. V. (1992). Compression of laminated orthotropic plates with unsymmetric structure. *Proc. of Russian Academy of Sciences. Mechanics of Solids, 4*, 157–162.

Azikov, N. S., Vasiliev, V. V., & Paterekas, A. D. (1990). Analysis of buckling and post-critical deformation of anisotropic plates under shear. *Mechanics of Composite Materials, 2*, 251–253.

Banks, W. M., & Harvey, J. M. (1979). Experimental study of stability problems in composite materials. *Stab. Probl. Eng. Struct. and Components* (pp. 1–22) London: Cardiff.

Bhaskar, K., & Kaushik, B. (2004). Simple and exact series solutions for flexure of orthotropic rectangular plates with any combination of clamped and simply supported edges. *Composite Structures, 66*, 63–68.

Bolle, L. (1947). Contribution au problĕme lineacre de flexion d'une plaque elastique. Ecole Polytechnique de l'Universite de Lausanne, Publ. No. 2. *Edition de la socie'te' du bulletin technique de la Suisse Romander* (pp. 1–32).

Brahtz, J. N. A. (1935). The stress function and photoelasticity applied to dams. *Proc. of the American Soc. of Civil Eng., 61*(7), 983–1020.

Dalali, M., & Kerr, A. D. (1995). Analysis of clamped rectangular orthotropic plates subjected to a uniform lateral load. *Int. J. Mech. Sci., 37*(5), 527–535.

Decolon, C. (2002). *Analysis of Composite Structures*. London: Hermes Penton Science.

Dekker, M. (2009). *Structural Analysis of Polymeric Composite Materials*. New York: Marcell Dekker, Inc.

Donnell, L. (1959). Shell theory. *Proc. of the 4th Midwestern Conf. on Solid Mechanics*. The Univ. of Texas (pp. 1–17).

Donnell, L. (1976). *Beams, Plates and Shells*. New York: McGraw-Hill.

Dougall, J. (1904). An analytical theory of the equilibrium of an isotropic plate. *Trans. Roy. Soc. of Edinburgh, 41*(8), 143–197.

Fadle, I. (1941). Die Seibsispannungs-Eigenwertfunctionen der Quadratischen Scheibe. *Ing-Arch, 11*(2), 125–149.

Galerkin, B. G. (1931). Elastic thick rectangular and triangular plates. *Reports of USSR Academy of Sciences (Doklady AN SSSR)* (p. 273) (in Russian).

Gay, D., Hoa, S. V., & Tsai, S. W. (2003). *Composite Materials Design and Applications*. Boca Raton: CRC Press.

Grigolyuk, E. I. (1996). *Bubnov Method – Sources, Formulations, Development*. Moscow: NII Mekhaniki MGU. (in Russian).

Hencky, H. (1947). Űber die Berücksichtigung der Schubveczerrung in ebenen Platten. *Ing-Archiv Bd, 16*. H.1, S. 72–76.

Jemielita, G. (1993). On the winding paths of the theory of plates. *Journal of Theoretical and Applied Mechanics (Mechanika Teoretyczna i Stosovana, Warsaw), 2*(31), 317–327.

Jones, R. M. (1975). *Mechanics of Composite Materials*. Washington: Hemisphere.

Jones, R. M. (1999). *Mechanics of Composite Materials*. Philadelphia: Taylor and Francis.

Jones, R. M. (2006). *Buckling of Bars, Plates, and Shells*. Blacksburg, VA: Bull Ridge Publishing.

Khaziev, A. R., & Boshers, C. D. (2011). Improved efficiency in the buckling analysis of composite laminated rectangular plates. In: *Proc. of 26th Annual Technical Conference of Canadian Association for Composite Structures and Materials*, Sept. 2011. Montreal, Quebec, Canada (CD-ROM).

Kirchhoff, G. (1850). Ŭber das Gleichgewicht und die Bewegung liner Elastischen Scheibe. *J. Reine Angew. Math. Berlin, Bd, 40*, S51–88.

Kollar, L. P., & Springer, G. S. (2003). *Mechanics of Composite Structures*. Cambridge: Cambridge University Press.

Kromm, A. (1955). Ŭber die Randquerkräfter bei gestützten Platten. *ZAMM*. Bd. 35, H. 6/7, S. 231–242.

Langhaar, H. L. (1962). *Energy Methods in Applied Mechanics*. New York: John Wiley & Sons.

Leissa, A. W. (1986). Conditions for laminated plates to remain flat under in-plane loading. *Composite Structures, 6*, 261–270.

Lekhnitskii, S. G. (1957). *Anisotropic Plates*. Moscow: Fizmatgiz (in Russian), Gordon and Breach, 1968.

Lurie, S. A. (1982). Bending of a rectangular orthotropic plate with clamped contour. *Proc. of Russian Academy of Sciences. Mechanics of Solids, 5*, 159–168.

Lurie, S. A., & Vasiliev, V. V. (1995). *The Biharmonic Problem in the Theory of Elasticity.* Amsterdam: Gordon and Breach Publishers.

Majeed, M. A., & Hyer, M. W. (2005). Mechanical behaviour of inplane-loaded unsymmetrically laminated composite plates. *Proc. of 46th AIAA/ASME/ASCE/AHS/ASC Structures, Structural Dynamics, and Material Conf,* AIAA Paper 2005–2099. (pp. 1–45).

Mindlin, R. D. (1951). Influence of rotatory inertia and shear on flexural motions of isotropic elastic plates. *J. of Appl. Mech., V, 18*(1), 31–38.

Ovesy, H. R., & Assaee, H. (2005). An investigation of the post-buckling behavior of symmetric cross-ply laminated plates using a semi-energy finite strip approach. *Composite Structures, 71*, 365–370.

Papkovich, P. F. (1941). Two problems of the theory of bending of thin elastic plates. *Applied Mathematics and Mechanics (Prikladnaya Matematika i Mekhanika, Moscow), 5*(3), 359–574.

Pelekh, B. L. (1970). Some problems of theory and analysis of anisotropic shells and plates with low shear stiffness. *Polymer Mechanics (Mekhanika Polymerov, Riga)* (4), 693–714 (in Russian).

Pikul, V. V. (1977). *General Technical Theory of Thin Elastic Plates and Shallow Shells*. Moscow: Nauka (in Russian).

Pikul, V. V. (1985). *Theory and Analysis of Laminated Structures*. Moscow: Nauka (in Russian).

Poisson, S. D. (1829). Memoire sur ĺequilibre et le movement des corps élastiques. *Memoires Paris Academie, 18*, 357–570.

Qatu, M. S., & Leissa, A. W. (1993). Buckling or transverse deflections of unsymmetrically laminated plates subjected to in-plane loads. *AIAA Journal, 31*(1), 189–194.

Reddy, J. N. (1997). *Mechanics of Laminated Composite Plates, Theory and Analysis*. Boca Raton: CRC Press.

Reddy, J. N. (2004). *Mechanics of Laminated Composite Plates and Shells, Theory and Analysis*. Boca Raton: CRC Press.

Reissner, E. (1944). On the theory of bending of elastic plates. *J. Math. Phys., 23*, 184–191.

Reissner, E. (1985). Reflections on the theory of elastic plates. *Appl. Mech. Reviews, V, 38*(11), 1453–1464.

Reissner, E. (1989). Asymptotic considerations for transverse bending of orthotropic sheardeformable plates. *Journal of Applied Mathematics and Physics (ZAMP), 40*, 543–557.

Reissner, E. (1991). On asymptotic expansions for the sixth-order linear theory problem of transverse bending of orthotropic elastic plates. *Computer Methods in Applied Mechanics and Engineering, 85*, 75–88.

Schäfer, M. (1952). Ŭber eine Verfeinerung der Klassischen Theorie dünner schwach gebegener Platten. *ZAMM, Bd 32, H, 6*. S. 161–171.

Shan, L., & Qiao, P. (2008). Explicit local buckling analysis of rotationally restrained composite plates under uniaxial compression. *Engineering Structures, 30*, 126–140.

Sheremetiev, M. P., Pelekh, B. L., & Dyachina, O. P. (1968). Study of the effect of transverse shear deformation on bending of a square plate by a concentrated force. *Applied Mechanics (Prikladnaya Mekhanika, Kiev), 4*(4), 1–7 (in Russian).

Shiff, P. A. (1883). Sur Ĺequilibre d'un Cylindre D'elastique. *Journal De Math. Pures at Appliquées, Ser, 3*. T.9. 407.

Thomson, W., & Tait, P. (1883). *Treatise on Natural Philosophy.* Cambridge: Cambridge University Press.

Timoshenko, S. P. (1921). On the correction for shear of the differential equation for transverse vibrations of prismatic bars. *Phil. Mag., Ser. 6, 41*, 744–746.

Timoshenko, S. P., & Woinowsky-Krieger, S. (1959). *Theory of Plates and Shells*. New-York: McGraw-Hill Book Co. Inc.

Todhunter, I., & Pearson, K. (1960). *A History of the Theory of Elasticity and of the Strength of Materials*. Vols. 1, 2. New York: Dover.

Tolske, F. (1938). Wasserkraftanlaneg. *Hadbibliotek fur Bauingenier, Berlin, III Teil B9* 358–408.

Uflyand, Ya. S. (1948). Wave propagation under transverse vibrations of beams and plates. *Applied Mechanics and Mathematics (Prikladnaya Mekhanika i Matematika), 12*, 287–300.

Vasiliev, V. V. (1992). On the theory of thin plates. *Proc. of Russian Academy of Sciences. Mechanics of Solids* (3), 26–47.

Vasiliev, V. V. (1993). *Mechanics of Composite Structures*. Washington: Taylor and Francis.

Vasiliev, V. V. (1998). Classical plate theory – history and contemporary analysis. *Proc. of Russian Academy of Sciences. Mechanics of Solids* (3), 46–58.

Vasiliev, V. V. (2000). Modern conceptions of plate theory. *Composite Structures, 48*, 39–48.

Veres, I. A., & Kollar, L. P. (2001). Buckling of rectangular orthotropic plates subjected to biaxial normal forces. *Journal of Composite Materials, 32*(7), 625–635.

Vinson, J. R. (2005). *Plate and Panel Structures of Isotropic, Composite and Piezoelectric Materials, Including Sandwich Structures*. Dordrecht: Springer.

Vinson, J. R., & Sierakovski, R. L. (1986). *The Behavior of Structures Composed of Composite Materials*. Dordrecht: Martinus Nijhoff Publ.

Vinson, J. R., & Sierakovski, R. L. (2004). *The Behavior of Structures Composed of Composite Materials*. Dordrecht: Kluwer Academic Publishers.

Weaver, P. M., & Nemeth, M. P. (2008). Improved design formulas for buckling of orthotropic plates under combined loading. *AIAA Journal, 46*(9), 2391–2396.

Weisshaar, T. A. (1980). Divergence of forward swept composite wings. *J. of Aircraft, 17*(6), 442–448.

Weisshaar, T. A. (1981). Aeroelastic tailoring of forward swept composite wings. *J. of Aircraft, 18*(8), 669–676.

Whitney, J. M. (1971). Fourier analysis of clamped anisotropic plates. *ASME J. Appl. Mech., 38*, 430–532.

Whitney, J. M. (1987). *Structural Analysis of Laminated Anisotropic Plates*. Lancaster: Technomic Publishing Co., Inc.

Ye, J. (2003). *Laminated Composite Plates and Shells: 3D modelling*. London: Springer.

Zhilin, P. A. (1992). On the plate theories of Poisson and Kirchhoff in the context of modern plate theory. *Proc. of Russian Academy of Sciences. Mechanics of Solids*, (3), 48–64.

Zhilin, P. A. (1995). On classical plate theory and Kelvin-Tait transformation. *Proc. of Russian Academy of Sciences. Mechanics of Solids* (4), 134–140.

CHAPTER

Thin-walled composite beams 10

The thin-walled composite beam model is widely used to simulate the behavior of engineering structural elements. The thin-walled beam is actually a cylindrical shell whose length is much greater than the dimensions of the cross section which, in turn, are much greater than the thickness of the wall. These specific features of thin-walled beams allow us to introduce a system of assumptions which, in turn, enables us to develop a relatively simple and efficient applied theory and to reduce the two-dimensional equations of shell theory to ordinary differential equations providing, as a rule, closed-form analytical solutions.

Modern composite materials are now commonly used to fabricate structural elements which can be treated as thin-walled beams. Composite thin-walled beams are discussed in the books by Vasiliev (1993), Kollar and Springer (2003), Dekker (2004), and Librescu and Song (2006).

The behavior and analysis of thin-walled beams are governed by the shape of the beam cross section, which leads to such beams being classified as one of these:

- Beams with closed cross-sectional contours (see Fig. 10.1)
- Beams with multiple cell contours (see Fig. 10.2)
- Beams with open contour of the cross section (see Fig. 10.3)

Under bending and torsion, thin-walled beams demonstrate a specific type of deformation which is referred to as cross-sectional warping, i.e., the beam cross sections do not remain in plane under loading

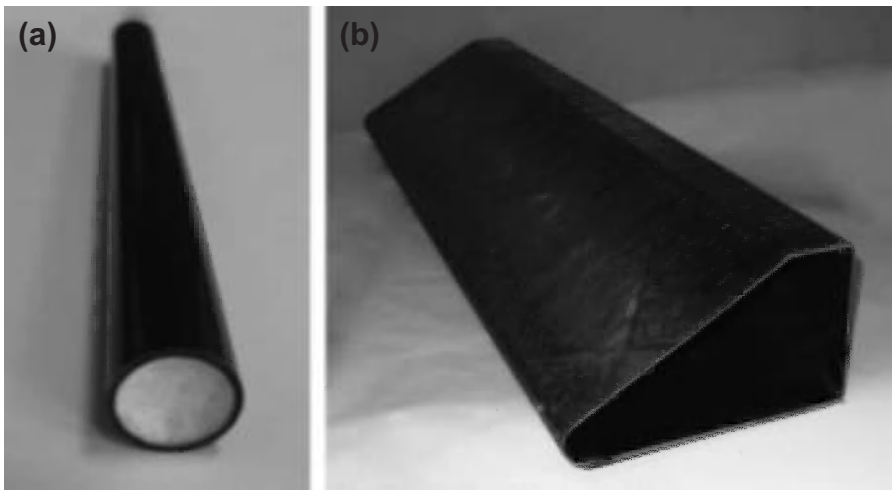


FIGURE 10.1

Composite thin-walled beams with circular (a) and polygonal (b) closed cross-sectional contours.

Advanced Mechanics of Composite Materials and Structural Elements. http://dx.doi.org/10.1016/B978-0-08-098231-1.00010-8
Copyright © 2013 Elsevier Ltd. All rights reserved.

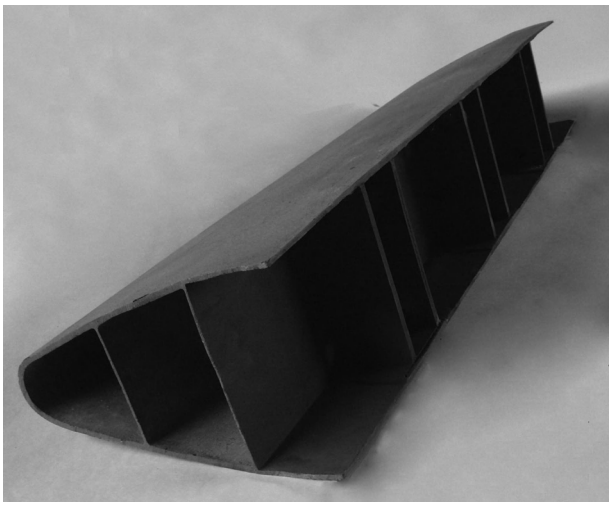


FIGURE 10.2

Composite thin-walled beam with multi-cell cross-sectional contour.

and exhibit out-of-plane axial displacements. To demonstrate such warping, consider a beam with a circular cross section and a longitudinal cut (see Fig. 10.4). Under torsion of a beam with free end cross sections, the beam cross sections, being flat before loading (dashed lines in Fig. 10.4a), do not remain in plane after loading and experience warping. As can be seen (see Fig. 10.4a), the warping is the same for all the beam cross sections. If the beam cross sections are built into absolutely rigid rings as shown in Fig. 10.4b, no warping takes place, because the rings restrain the warping of the beam cross sections. Thus, the problems of thin-walled beams' bending and torsion can be classified as the free bending and torsion problem (see Fig. 10.4a) and the restrained bending and torsion problem (see Fig. 10.4b).

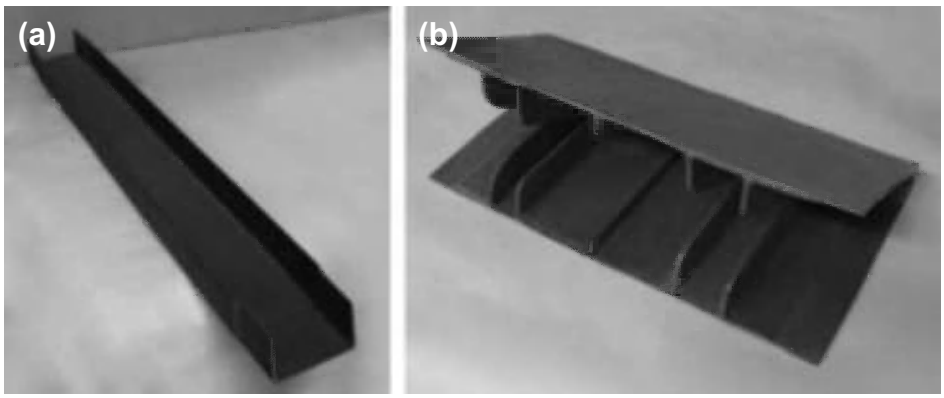


FIGURE 10.3

Composite thin-walled C-shaped beam (a) and the leading edge of an airplane wing (b) with open cross-sectional contours.

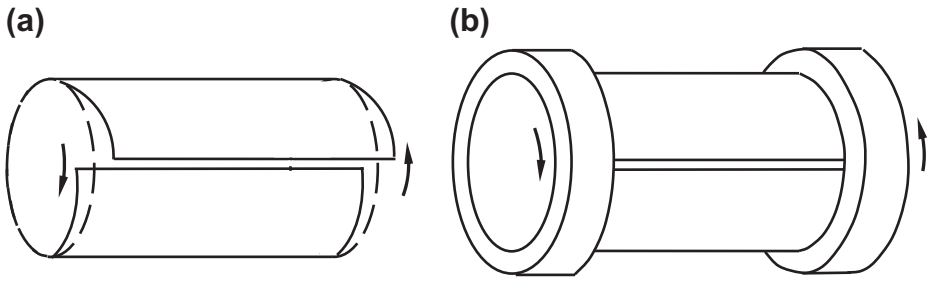


FIGURE 10.4

Free (a) and restrained (b) torsion of a circular thin-walled beam.

This chapter is concerned with the theories of composite thin-walled beams, covering free and restrained bending and torsion of beams with various shapes of the cross-sectional contour.

10.1 GEOMETRY OF THE BEAM CROSS SECTION

Consider a beam whose cross-sectional dimensions do not change along the beam axis and use a Cartesian coordinate frame x, y, z as shown in Fig. 10.5 to describe the beam. The geometry of the cross section is specified by the wall thickness h and the shape of the contour line. Introduce, as earlier (see Section 5.1), the beam reference surface located at a distance e and h–e from the inner and the outer surfaces of the beam (see Fig. 10.5). The line of intersection of this surface with the plane orthogonal to the beam axis is referred to as the cross-sectional contour. The contour coordinate s is measured along the contour from some point S as shown in Fig. 10.5, whereas the normal coordinate η is measured with the outside normal direction to the contour being positive (see Fig. 10.5). The parametric equations of the contour

$$x_e = x_e(s), \quad y_e = y_e(s) \tag{10.1}$$

satisfy the following equation:

$$\dot{x}_e^2 + \dot{y}_e^2 = 1 \tag{10.2}$$

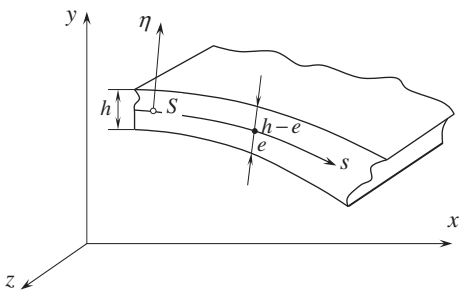


FIGURE 10.5

Normal (η) and contour (s) coordinates of the beam cross section.

where $(\therefore) = \dfrac{\partial(\ldots)}{\partial s}$. The contour curvature is specified as

$$\frac{1}{R_e} = \dot{y}_e \ddot{x}_e - \dot{x}_e \ddot{y}_e \tag{10.3}$$

in which R_e is the curvature radius. At a distance η from the contour, the arc elementary length is

$$ds_\eta = H(\eta) ds, \quad H(\eta) = 1 + \frac{\eta}{R_e} \tag{10.4}$$

where $H(\eta)$ is the Lamé coefficient. For thin-walled beams, $h \ll R_e$ and the term $\dfrac{\eta}{R_e}$ is usually neglected in comparison with unity, so that

$$H(\eta) \approx 1 \tag{10.5}$$

Consider some arbitrary point of the contour S (see Fig. 10.6) and introduce the radius $\rho = OS$ making angle α with the y-axis as shown in Fig. 10.6, the tangent vector $t = ST$, and the vector $r = OT$ which is orthogonal to the tangent vector and makes angle β with the y-axis (see Fig. 10.6). The coordinates of point S are expressed in terms of ρ and α as

$$x_e = \rho \sin \alpha, \quad y_e = \rho \cos \alpha \tag{10.6}$$

and the lengths of vectors t and r are

$$\begin{aligned} t &= \rho \sin(\beta - \alpha) = y_e \sin \beta - x_e \cos \beta \\ r &= \rho \cos(\beta - \alpha) = y_e \cos \beta + x_e \sin \beta \end{aligned} \tag{10.7}$$

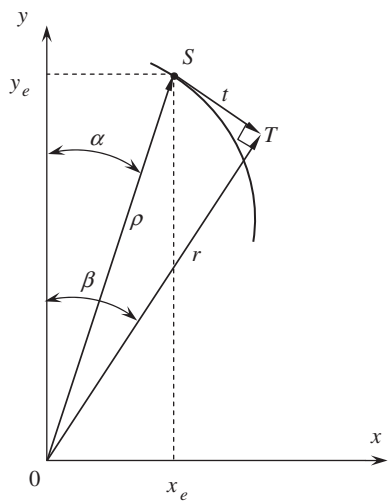


FIGURE 10.6

Radial (r, ρ) and tangent (t) vectors of the contour.

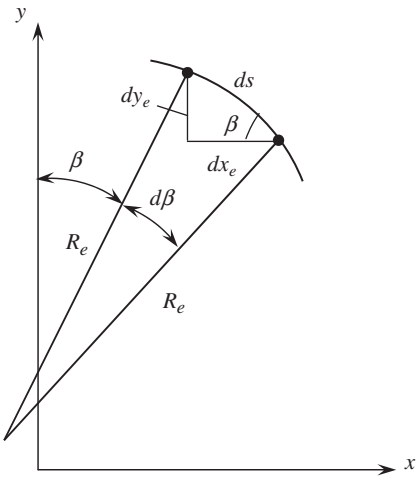


FIGURE 10.7

Element of the contour arc.

Consider the elementary arc of length ds shown in Fig. 10.7, from which it follows that

$$\sin\beta = -\frac{dy_e}{ds} = -\dot{y}_e, \quad \cos\beta = \frac{dx_e}{ds} = \dot{x}_e, \quad \frac{1}{R_e} = \frac{d\beta}{ds} = \dot{\beta} \tag{10.8}$$

These equations yield the following relations:

$$\frac{d}{ds}(\sin\beta) = \frac{\cos\beta}{R_e}, \quad \frac{d}{ds}(\cos\beta) = -\frac{\sin\beta}{R_e} \tag{10.9}$$

Differentiating Eqs. (10.7) with respect to s and using Eqs. (10.8) and (10.9), we get

$$\frac{dt}{ds} = \frac{r}{R_e} - 1, \quad \frac{dr}{ds} = -\frac{t}{R_e} \tag{10.10}$$

10.2 THE EQUATIONS OF MEMBRANE SHELL THEORY

Traditionally the theory of thin-walled beams for which Eq. (10.5) is valid is based on the equations of membrane shell theory.

The element of the beam reference surface loaded with membrane stress resultants is shown in Fig. 10.8. The corresponding equilibrium, constitutive, and strain-displacement equations are (Vasiliev, 1993):

$$\frac{\partial N_z}{\partial z} + \frac{\partial N_{zs}}{\partial s} = 0, \quad \frac{\partial N_z}{\partial s} + \frac{\partial N_{zs}}{\partial z} = 0, \quad \frac{N_s}{R_e} = 0 \tag{10.11}$$

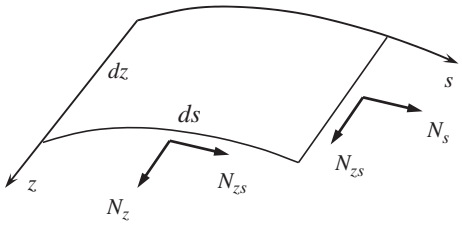


FIGURE 10.8

Membrane stress resultants acting on the element of the reference surface.

$$N_z = B_{11}\varepsilon_z + B_{12}\varepsilon_s, \quad N_s = B_{12}\varepsilon_z + B_{22}\varepsilon_s, \quad N_{zs} = B_{44}\gamma_{zs} \tag{10.12}$$

$$\varepsilon_z = \frac{\partial u_z}{\partial z}, \quad \varepsilon_s = \frac{\partial u_s}{\partial s} + \frac{u_\eta}{R_e}, \quad \gamma_{zs} = \frac{\partial u_z}{\partial s} + \frac{\partial u_s}{\partial z} \tag{10.13}$$

in which u_z, u_s, and u_η are the axial, contour, and normal displacements of a point on reference surface, respectively.

10.3 ASSUMPTIONS OF COMPOSITE BEAM THEORY

In composite beam theory, the displacements of the contour points are referred to the coordinates of the cross section x, y rather than to coordinates s, η as in Eqs. (10.13). Consider the displacement of point S in Fig. 10.9 to position S_1 which can be decomposed into the displacements referred to both

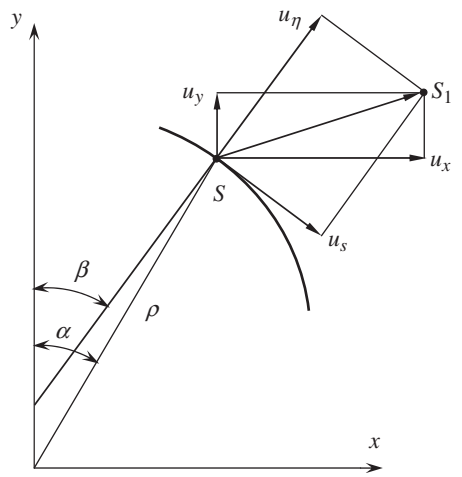


FIGURE 10.9

Displacements of the contour point S in (s, η) and (x, y) coordinate frames.

coordinate frames. It follows from Fig. 10.9 that

$$u_s = u_x \cos\beta - u_y \sin\beta, \quad u_\eta = u_x \sin\beta + u_y \cos\beta \tag{10.14}$$

These displacements are caused by two types of beam deformation. The first type of displacement corresponds to displacements and rotations of the beam cross section as a solid disk, whereas the second type of displacement is associated with the deformation (stretching and bending) of the cross-sectional contours.

The first basic assumption of this beam theory states that the displacements of the second type are negligible in comparison with the displacements of the first type. As a matter of fact, the displacements of the second type are not zero; they are just small in comparison with the displacements of the first type, which can be presented as

$$u_x = U_x(z) + \Delta u_x, \quad u_y = U_y(z) + \Delta u_y \tag{10.15}$$

Here, $U_x(z)$ and $U_y(z)$ are the displacements of the cross section as a solid in x- and y-directions, whereas Δu_x and Δu_y are caused by cross section rotation. Consider the rotation of the cross section in the xy-plane (see Fig. 10.10). If the rotation angle is Θ_z, then it follows from Fig. 10.10 that

$$\Delta u_x = \rho\Theta_z \cos\alpha, \quad \Delta u_y = -\rho\Theta_z \sin\alpha$$

Taking into account Eqs. (10.6), we get

$$\Delta u_x = y_e\Theta_z, \quad \Delta u_y = -x_e\Theta_z$$

and Eqs. (10.15) take the following final form:

$$u_x = U_x(z) + y_e\Theta_z(z), \quad u_y = U_y(z) - x_e\Theta_z(z) \tag{10.16}$$

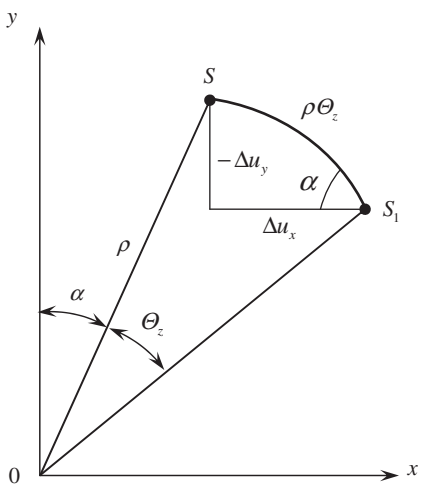


FIGURE 10.10

Displacements caused by the rotation of the cross section.

Substituting these equations into Eqs. (10.14) for u_s and u_η and using Eqs. (10.7) for t and r, we also get

$$\begin{aligned} u_s &= U_x(z)\cos\beta - U_y(z)\sin\beta + r\Theta_z(z) \\ u_\eta &= U_x(z)\sin\beta + U_y(z)\cos\beta + t\Theta_z(z) \end{aligned} \tag{10.17}$$

Thus, the in-plane displacements of the beam cross section are expressed in terms of three unknown functions of z, i.e., $U_x(z)$, $U_y(z)$, and $\Theta_z(z)$.

Consider the axial displacement u_z and present it in the following form:

$$u_z = U_z(z) + x_e\Theta_y(z) + y_e\Theta_x(z) + \Psi(z,s) \tag{10.18}$$

Here, U_z is the axial displacement and Θ_x and Θ_y are the angles of rotation of the cross section around axes x and y as a solid. The function $\Psi(z,s)$ in Eq. (10.18) is referred to as the warping function which specifies the deviation of the cross section out of the plane. In this beam theory, Eq. (10.18) is simplified in two ways.

For the problems of free bending and torsion, we assume that the warping function is the same for the whole cross section and does not depend on z (see Fig. 10.4a). Then

$$u_z = U_z(z) + x_e\Theta_y(z) + y_e\Theta_x(z) + \Psi(s) \tag{10.19}$$

For problems of restrained bending and torsion, we take Eq. (10.18) in the form

$$u_z = U_z(z) + x_e\Theta_y(z) + y_e\Theta_x(z) + f(z)\Psi(s) \tag{10.20}$$

where $f(z)$ is the unknown function and $\Psi(s)$ is the warping function corresponding to free bending or torsion of the beam.

Finally, simplify the equilibrium and the constitutive equations, i.e., Eqs. (10.11) and (10.12). It follows from the third equation of Eqs. (10.11) that $N_s = 0$ and the equilibrium equations reduce to

$$\frac{\partial N_z}{\partial z} + \frac{\partial N_{zs}}{\partial s} = 0, \quad N_{zs} = N_{zs}(s) \tag{10.21}$$

Thus, the shear stress resultant does not depend on the axial coordinate z. Since $N_s = 0$, we can use the second equation of Eqs. (10.12) to find that

$$\varepsilon_s = -\frac{B_{12}}{B_{22}}\varepsilon_z \tag{10.22}$$

and to reduce the constitutive equations to

$$N_x = B\varepsilon_z, \quad N_{zs} = B_{44}\gamma_{zs} \tag{10.23}$$

where

$$B = B_{11} - \frac{B_{12}^2}{B_{22}} \tag{10.24}$$

is the axial stiffness of the beam wall. This equation, Eq. (10.24), actually allows for the axial stiffness reduction due to Poisson's effect in the contour direction and is valid for smooth composite beams such as those shown in Fig. 10.1b and 10.3a. However, in real beams, the Poisson effect can be restricted by transverse ribs as shown in Figs. 10.2 and 10.3b or by a core filling the inner space of the beam as

shown in Fig. 10.1a. For such beams, it is generally assumed that the circumferential strain can be neglected, i.e., $\varepsilon_s = 0$ in Eqs. (10.12). In this case, the constitutive equations, Eqs. (10.12), reduce to Eqs. (10.23), in the first of which

$$B = B_{11} \tag{10.25}$$

It should be noted that thin-walled beam theory is approximate and the decision whether to use Eq. (10.24) or (10.25) for the axial stiffness depends on the actual structure of the beam.

Thus, introducing the foregoing assumptions, we can reduce the two-dimensional equations of shell theory to ordinary differential equations of beam theory which include the displacements $U_x(z)$, $U_y(z)$, and $U_z(z)$ and the rotation angles $\Theta_x(z)$, $\Theta_y(z)$, and $\Theta_z(z)$ of the beam cross section for the problem of free bending and torsion, and in addition, the function $f(z)$ for the problems of restrained bending and torsion.

10.4 FREE BENDING AND TORSION OF THIN-WALLED BEAMS WITH A CLOSED CROSS-SECTIONAL CONTOUR

Consider a beam with a closed cross-sectional contour loaded at the ends with forces and moments as shown in Fig. 10.11 and assume that the beam is in a state of free bending and torsion (restrained deformation is considered further in Section 10.4.11).

10.4.1 Axial strain and stress resultant

In the case of free bending and torsion usually studied for beams with closed cross sections, the axial stress resultant N_z can be found with the aid of Eqs. (10.22), (10.13), and (10.19), i.e.,

$$N_z = B\frac{\partial u_z}{\partial z} = B\left(U_z' + x_e\Theta_y' + y_e\Theta_x'\right) \tag{10.26}$$

As can be seen, the warping function, which does not depend on z, does not enter Eq. (10.26), which is very important for the theory of free bending.

Three functions of the z-coordinate, i.e., U_z, Θ_x, and Θ_y, can be expressed in terms of the integral axial force P_z and the bending moments H_x and H_y applied to the beam cross section (see Fig. 10.11). Using Fig. 10.12, we get

$$P_z = \int_s N_z ds, \quad H_x = \int_s N_z y_e ds, \quad H_y = \int_s N_z x_e ds \tag{10.27}$$

The index "s" under the integral shows that the integration is performed along the whole contour of the beam cross section. Substituting Eq. (10.26) into Eqs. (10.27), we arrive at the following three equations for U_z', Θ_x', and Θ_y':

$$\begin{aligned} SU_z' + S_x\Theta_x' + S_y\Theta_y' &= P_z \\ S_xU_z' + D_x\Theta_x' + D_{xy}\Theta_y' &= H_x \\ S_yU_z' + D_{xy}\Theta_x' + D_y\Theta_y' &= H_y \end{aligned} \tag{10.28}$$

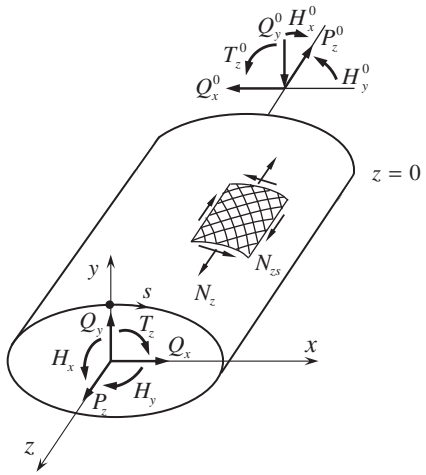


FIGURE 10.11

Thin-walled beam with closed cross-sectional contour loaded at the ends.

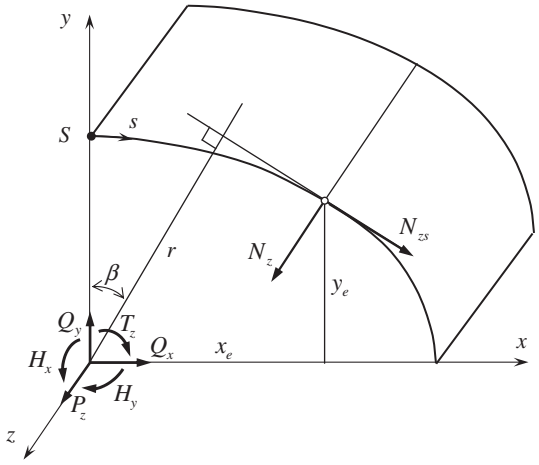


FIGURE 10.12

Reduction of stress resultants N_z and N_{zs} to the integral forces and moments.

in which

$$\begin{aligned} S &= \int_s B ds, \quad S_x = \int_s B y_e ds, \quad S_y = \int_s B x_e ds \\ D_x &= \int_s B y_e^2 ds, \quad D_y = \int_s B x_e^2 ds, \quad D_{xy} = \int_s B x_e y_e ds \end{aligned} \tag{10.29}$$

Here, S is the axial stiffness of the beam and S_x and S_y and D_x, D_y, and D_{xy} are the coupling and the bending stiffness coefficients referred to the given coordinate frame (x, y). The first equation of Eqs. (10.28) yields

$$U_z' = \frac{P_z}{S} - (x_0 \Theta_y' + y_0 \Theta_x') \tag{10.30}$$

where

$$x_0 = \frac{S_y}{S}, \quad y_0 = \frac{S_x}{S} \tag{10.31}$$

are the coordinates of the cross-sectional center. If the axial force P_z is applied at the center, it does not cause beam bending. Substituting Eq. (10.30) into the second and third of Eqs. (10.28), we get

$$\Theta_x' = \frac{k}{D_x^0}\left(\overline{H}_x - n_y \overline{H}_y\right), \quad \Theta_y' = \frac{k}{D_y^0}\left(\overline{H}_y - n_x \overline{H}_x\right) \tag{10.32}$$

Here,

$$\begin{aligned} k &= \frac{1}{1 - n_x n_y}, \quad n_x = \frac{D_{xy}^0}{D_x^0}, \quad n_y = \frac{D_{xy}^0}{D_y^0} \\ D_x^0 &= D_x - y_0^2 S, \quad D_y^0 = D_y - x_0^2 S, \quad D_{xy}^0 = D_{xy} - x_0 y_0 S \\ \overline{H}_x &= H_x - y_0 P_z, \quad \overline{H}_y = H_y - x_0 P_z \end{aligned} \tag{10.33}$$

where D_x^0, D_y^0, and D_{xy}^0 are the bending stiffness coefficients referred to the central axes of the cross section. The coefficient k depends on the symmetry of the cross section. If the cross section has one or two axes of symmetry, $D_{xy}^0 = 0$, $n_x = n_y = 0$, and $k = 1$. Substituting Eqs. (10.30) and (10.32) into Eq. (10.26), we arrive at the following final expression for the axial stress resultant:

$$N_z = B\varepsilon_z \tag{10.34}$$

in which the axial strain is

$$\varepsilon_z = \frac{P_z}{S} + k\left(\frac{\overline{H}_x}{D_x^0}\overline{y} + \frac{\overline{H}_y}{D_y^0}\overline{x}\right) \tag{10.35}$$

where

$$\overline{x} = x_e - x_0 - n_x(y_e - y_0), \quad \overline{y} = y_e - y_0 - n_y(x_e - x_0) \tag{10.36}$$

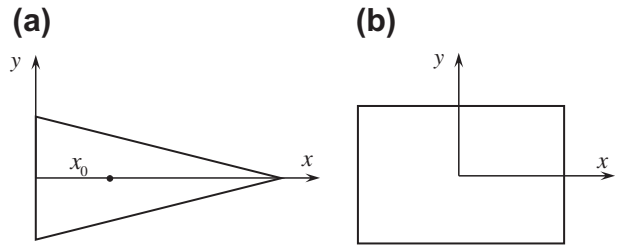


FIGURE 10.13

Cross sections with one (a) and two (b) symmetry axes.

This result, Eq. (10.35), is valid in the arbitrary coordinate frame x, y. If the cross section has one symmetry axis, e.g., axis x in Fig. 10.13a, then

$$S_x = 0, \quad D_{xy} = 0, \quad y_0 = 0, \quad D_x^0 = D_x, \quad n_x = n_y = 0, \quad k = 1$$

and

$$\varepsilon_z = \frac{P_z}{S} + \frac{H_x}{D_x} y_e + \frac{\overline{H}_y}{D_y^0}(x_e - x_0) \tag{10.37}$$

For a cross section with two symmetry axes (see Fig. 10.13b),

$$S_y = 0, \quad x_0 = 0, \quad D_y^0 = D_y$$

and

$$\varepsilon_z = \frac{P_z}{S} + \frac{H_x}{D_x} y + \frac{H_y}{D_y} x \tag{10.38}$$

The foregoing expressions for ε_z include the axial force, P_z, and the bending moments, H_x and H_y, acting in the beam cross section which must satisfy the equilibrium equations for a beam loaded at its ends (see Fig. 10.11). For the projections of the forces on axes x, y, and z, we have the following equations:

$$\frac{dQ_x}{dz} = 0, \quad \frac{dQ_y}{dz} = 0, \quad \frac{dP_z}{dz} = 0 \tag{10.39}$$

and for the moments, in a similar way

$$\frac{dH_x}{dz} - Q_y = 0, \quad \frac{dH_y}{dz} - Q_x = 0, \quad \frac{dT_z}{dz} = 0 \tag{10.40}$$

Note that Q_x, Q_y, and T_z in Eqs. (10.39) and (10.40) are the integral transverse shear forces and the torque applied to the beam cross section (see Fig. 10.12). Integrating Eqs. (10.39) and (10.40), we arrive at

$$\begin{aligned} &Q_x = Q_x^0, \quad Q_y = Q_y^0, \quad P_z = P_z^0 \\ &H_x = H_x^0 + Q_y^0 z, \quad H_y = H_y^0 + Q_x^0 z, \quad T_z = T_z^0 \end{aligned} \tag{10.41}$$

Here, the forces and the moments with subscript "0" correspond to the initial cross section $z = 0$ of the beam (see Fig. 10.11).

Thus, the axial strain ε_z and the corresponding stress resultant N_z are specified by Eqs. (10.34) and (10.35) in which the axial force P_z and the moments H_x and H_y are given by Eqs. (10.41).

10.4.2 Shear strain and stress resultant

To determine the shear stress resultant N_{zs}, substitute N_z from Eq. (10.34) into the equilibrium equation, Eq. (10.21), to get

$$\frac{\partial N_{zs}}{\partial s} = -\frac{\partial N_z}{\partial z} = -B\left(\frac{1}{S}P_z' + \frac{k\bar{y}}{D_x^0}\overline{H}_x' + \frac{k\bar{x}}{D_y^0}\overline{H}_y'\right) \tag{10.42}$$

where $(\ldots)' = d(\ldots)/dz$. Consider a closed contour shown in Fig. 10.14a and measure the contour coordinate s from some point S. Integration of Eq. (10.42) yields

$$N_{zs} = N_Q(s) + N_0 \tag{10.43}$$

where

$$N_Q(s) = -\left[\frac{1}{S}P_z'\overline{S}(s) + \frac{k}{D_x^0}\overline{H}_x'\overline{S}_x(s) + \frac{k}{D_y^0}\overline{H}_y'\overline{S}_y(s)\right] \tag{10.44}$$

in which

$$\overline{S}(s) = \int_0^s B\,ds, \quad \overline{S}_x(s) = \int_0^s B\bar{y}\,ds, \quad \overline{S}_y(s) = \int_0^s B\bar{x}\,ds \tag{10.45}$$

and N_0 is formally the integration constant. The decomposition of N_{zs} specified by Eq. (10.43) has the physical meaning demonstrated in Fig. 10.14. Consider Eq. (10.44). It follows from Eqs. (10.45) that at $s = 0$ the functions $\overline{S}(s)$ are zero and $N_Q = (s = 0) = 0$. Let $s = s_1$ where s_1 is the final value of the contour coordinate corresponding to point S in Figs. 10.14a and b. As can be readily checked,

$$\overline{S}(s = s_1) = S, \quad \overline{S}_x(s = s_1) = 0, \quad \overline{S}_y(s = s_1) = 0$$

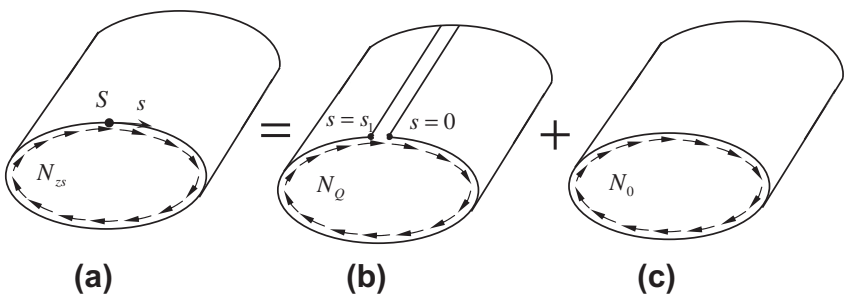


FIGURE 10.14

Decomposition of the total shear stress resultant (a) into N_Q (b) and N_O (c) components.

and Eq. (10.44) yields

$$N_Q(s = s_1) = -P_z' = 0$$

because of the third equation of Eqs. (10.39). Thus, $N_Q = 0$ at point S of the cross section, and we can imagine that to calculate N_Q we need to introduce a longitudinal cut at point S and to measure the contour coordinate s from this cut (see Fig. 10.14b). The cut is compensated by the constant shear stress resultant N_0 in Eq. (10.43) (see Fig. 10.14c). The final expression for N_Q can be derived if we substitute P_z', H_x', and H_y' following from the equilibrium equations, Eqs. (10.40), into Eq. (10.44) to get

$$N_Q = -k\left[\frac{Q_y}{D_x^0}\overline{S}_x(s) + \frac{Q_x}{D_y^0}\overline{S}_y(s)\right] \tag{10.46}$$

Here, the forces Q_x and Q_y are given by Eqs. (10.41). The stress resultant N_Q balances the transverse shear forces Q_x and Q_y. Indeed, using Fig. 10.12, we can write the following static equations:

$$\int_s N_{zs}\cos\beta\, ds = Q_x, \qquad \int_s N_{zs}\sin\beta\, ds = -Q_y \tag{10.47}$$

Substituting N_{zs} from Eq. (10.43) and taking into account that in accordance with Eqs. (10.8)

$$N_0\int_s \cos\beta\, ds = N_0\int_s \dot{x}_e ds = 0, \quad N_0\int_s \sin\beta\, ds = -N_0\int_s \dot{y}_e ds = 0$$

we get

$$\int_s N_Q\cos\beta\, ds = Q_x, \quad \int_s N_Q\sin\beta\, ds = -Q_y$$

Substituting Eq. (10.46) and using the following equations that can be obtained by integrating by parts

$$\int_s \overline{S}_x(s)\cos\beta ds = -\int_s Bx_e\bar{y}ds = -D_{xy}^0 + n_y D_y^0 = 0$$

$$\int_s \overline{S}_y(s)\sin\beta ds = -\int_s Bx_e\bar{x}ds = -D_y^0\left(1 - n_x n_y\right)$$

we can prove that the first equation of Eqs. (10.47) is satisfied identically. The same is true for the second equation, and the shear stress resultant N_Q balances the forces Q_x and Q_y acting in the beam cross section.

Thus, to determine the stress resultant N_{zs} in Eq. (10.43), we need to find N_0. For this purpose, we use the remaining equilibrium equation for the torque T_z. It follows from Fig. 10.12 that

$$\int_s N_{zs} r ds = T_z \tag{10.48}$$

where r is specified by Eqs. (10.7). Substituting N_{zs} in accordance with Eq. (10.43) into Eq. (10.48), we get

$$\int_s N_Q r ds + N_0\int_s r ds = T_z \tag{10.49}$$

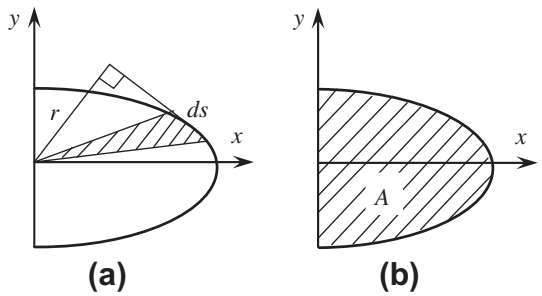


FIGURE 10.15

The elementary cross-sectional area (a) and the area bounded by the contour (b).

The function

$$d\omega = \int_s rds \tag{10.50}$$

is referred to as the elementary sectorial area and is equal to twice the area of the shaded triangular in Fig. 10.15a. Thus,

$$\int_s rds = 2A \tag{10.51}$$

where A is the area bounded by the contour (see Fig. 10.15b). Thus, Eq. (10.49) yields

$$N_0 = \frac{1}{2A}\left(T_z - \int_s N_Q rds\right) \tag{10.52}$$

Finally, substituting N_Q from Eq. (10.46) into Eq. (10.52), we arrive at the following expression for the shear stress resultant:

$$N_{zs} = Q_x F_x(s) + Q_y F_y(s) + \frac{T_z}{2A} \tag{10.53}$$

in which

$$\begin{aligned} F_x(s) &= -\frac{k}{D_y^0}\left[\overline{S}_y(s) - \frac{1}{2A}\int_s \overline{S}_y(s) rds\right] \\ F_y(s) &= -\frac{k}{D_x^0}\left[\overline{S}_x(s) - \frac{1}{2A}\int_s \overline{S}_x(s) rds\right] \end{aligned} \tag{10.54}$$

Note that, as follows from the equilibrium equations, Eqs. (10.39), Q_x, Q_y, and T_z do not depend on the axial coordinate z, and neither does the shear stress resultant N_{zs} which corresponds to the second equilibrium equation of Eqs. (10.21).

The shear strain can be found from Eqs. (10.23) and (10.53) as

$$\gamma_{zs} = \frac{1}{B_{44}}\left[Q_x F_x(s) + Q_y F_y(s) + \frac{T_z}{2A}\right] \tag{10.55}$$

In conclusion, consider pure torsion of a beam with a closed cross section. Taking $Q_x = 0$ and $Q_y = 0$ in Eq. (10.53), we get

$$N_{zs} = \frac{T_z}{2A} \tag{10.56}$$

This result is known as the Bredt equation (Timoshenko and Goodier, 1970). It follows from the foregoing derivation that the axial and the shear stress resultants N_z and N_{zs} specified by Eqs. (10.34), (10.25), and (10.53) are found using the equilibrium equations only. Thus the problem of free bending and torsion of a beam with a closed cross section is statically determinate with respect to N_z and N_{zs}.

10.4.3 Stresses in the plies of composite beams

In contrast to N_z and N_{zs} which can be found from the equilibrium equations, to determine the stresses in the plies of composite beams we need to use the compatibility conditions to distribute the stress resultants N_z and N_{zs} between the plies. Consider a laminated structure of the beam shown in Fig. 10.16. The strains in the principal ply coordinates (1, 2) can be found with the aid of Eqs. (5.130), i.e.,

$$\begin{aligned}
\varepsilon_1^{(i)} &= \varepsilon_z \cos^2\phi_i + \varepsilon_s \sin^2\phi_i + \gamma_{zs}\sin\phi_i\cos\phi_i \\
\varepsilon_2^{(i)} &= \varepsilon_z \sin^2\phi_i + \varepsilon_s \cos^2\phi_i - \gamma_{zs}\sin\phi_i\cos\phi_i \\
\gamma_{12}^{(i)} &= 2(\varepsilon_s - \varepsilon_z)\sin\phi_i\cos\phi_i + \gamma_{zs}\cos 2\phi_i
\end{aligned} \tag{10.57}$$

Here, ε_z, ε_s, and γ_{zs} are the beam strains which are the same for all the plies. The axial and shear strains ε_z and γ_{zs} are specified by Eqs. (10.35) and (10.55), whereas the contour strain ε_s depends on the beam model. For a beam with an absolutely compliant contour for which the axial stiffness corresponds to Eq. (10.24), ε_s is given by Eq. (10.22), and for the beam with absolutely rigid contour with the axial stiffness in Eq. (10.25), $\varepsilon_s = 0$.

The stresses in the plies are linked to the corresponding strains by Hooke's law, Eqs. (5.131), i.e.,

$$\sigma_1^{(i)} = \overline{E}_1^{(i)}\left(\varepsilon_1^{(i)} + \nu_{12}^{(i)}\varepsilon_2^{(i)}\right), \quad \sigma_2^{(i)} = \overline{E}_2^{(i)}\left(\varepsilon_2^{(i)} + \nu_{21}^{(i)}\varepsilon_1^{(i)}\right), \quad \tau_{21}^{(i)} = G_{12}^{(i)}\gamma_{12}^{(i)} \tag{10.58}$$

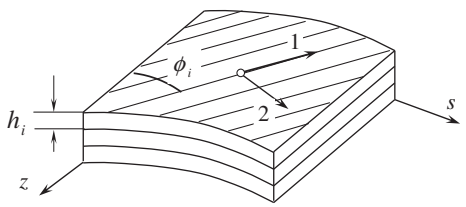


FIGURE 10.16

Laminated structure of a beam.

where, as earlier, $\overline{E}_{1,2}^{(i)} = E_{1,2}^{(i)}/(1 - v_{12}^{(i)} v_{21}^{(i)})$. The ultimate combination of stresses can be found using the strength criterion discussed in Chapter 6.

As an example, consider a circular cross section fiberglass-epoxy beam with radius $R = 100$ mm which is composed of two symmetric helical plies with angles $\phi = \pm 36^\circ$ and total thickness $h_\phi = 0.62$mm and a hoop (90°) ply with thickness $h_{90} = 0.6$mm. The elastic constants of unidirectional plies are $E_1 = 50.6$ GPa, $E_2 = 11$ GPa, $G_{12} = 4$ GPa, $v_{12} = 0.056$, and $v_{21} = 0.26$. The stiffness coefficients of the plies specified by Eqs. (4.72) are $A_{11}^{(\phi)} = 28.31$, $A_{12}^{(\phi)} = 12.11$, $A_{22}^{(\phi)} = 16.08$, $A_{44}^{(\phi)} = 13.2$ and $A_{11}^{(90)} = 11.17$, $A_{12}^{(90)} = 2.9$, $A_{22}^{(90)} = 51.37$, and $A_{44}^{(90)} = 4.0$ (GPa). For a thin wall, the membrane stiffness coefficients can be found with the aid of Eqs. (5.34) and (5.42), which yield

$$B_{mn} = A_{mn}^{(\phi)} h_\phi + A_{mn}^{(90)} h_{90}$$

The result of the calculation is $B_{11} = 24.25, B_{12} = 9.25, B_{22} = 40.79$, and $B_{44} = 10.58$(GPa•mm).

Consider the case of axial compression, for which Eq. (10.35) yields

$$\varepsilon_z = -\frac{P_z}{S}$$

in which $S = 2\pi RB$. For an absolutely rigid contour, Eq. (10.25) gives $B = B_{11}$. The corresponding function $\varepsilon_z(P_z)$ is shown in Fig. 10.17 with the solid line. For an absolutely compliant contour, B is specified by Eq. (10.24), and ε_s by Eq. (10.22). The results of this calculation are represented in Fig. 10.17 by dashed lines. As can be seen, the model with absolutely compliant contour is in better agreement with the experimental results (dots). Within the framework of this model, we have for $P_z = 40$ kN

$$\varepsilon_z = -0.29\%, \quad \varepsilon_s = 0.066\%$$

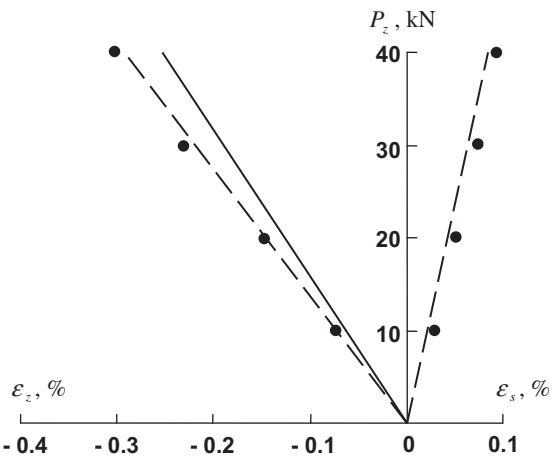


FIGURE 10.17

Dependencies of the axial (ε_Z) and contour (ε_S) strains on the axial force: analysis for absolutely rigid contour (———); analysis for absolutely compliant contour (– – – – – – –), and experiment (• • • •).

The strains in the plies following from Eqs. (10.57) are

$$\varepsilon_1^{(\phi)} = -0.151\%, \quad \varepsilon_2^{(\phi)} = -0.0051\%, \quad \gamma_{12}^{(\phi)} = \mp 0.192\%$$
$$\varepsilon_1^{(90)} = 0.066\%, \quad \varepsilon_2^{(90)} = -0.29\%, \quad \gamma_{12}^{(90)} = 0$$

Here, signs "+" and "−" correspond to the plies with angle $+\phi$ and $-\phi$, respectively. The stresses in the plies follow from Eqs. (10.58), i.e.,

$$\sigma_1^{(\phi)} = -77.7 \text{ MPa}, \ \sigma_2^{(\phi)} = 4.96 \text{ MPa}, \ \tau_{12}^{(\phi)} = \mp 7.68 \text{ MPa}$$
$$\sigma_1^{(90)} = 25.6 \text{ MPa}, \ \sigma_2^{(90)} = -30.5 \text{ MPa}, \ \tau_{12}^{(90)} = 0$$

Consider now beam torsion, for which, in accordance with Eq. (10.55),

$$\gamma_{zs} = \frac{T_z}{2AB_{44}}$$

where $A = \pi R^2$. For $T_z = 2.5$ kNm, we get $\gamma_{zs} = 0.38\%$. The calculated (solid line) and experimental (dots) values for $\gamma_{zs}(T_z)$ are shown in Fig. 10.18. The strains in the plies under such a torque are

$$\varepsilon_1^{(\phi)} = \pm 0.18\%, \quad \varepsilon_2^{(\phi)} = \mp 0.18\%, \quad \gamma_{12}^{(\phi)} = 0.12\%$$
$$\varepsilon_1^{(90)} = 0, \quad \varepsilon_2^{(90)} = 0, \quad \gamma_{12}^{(90)} = 0.38\%$$

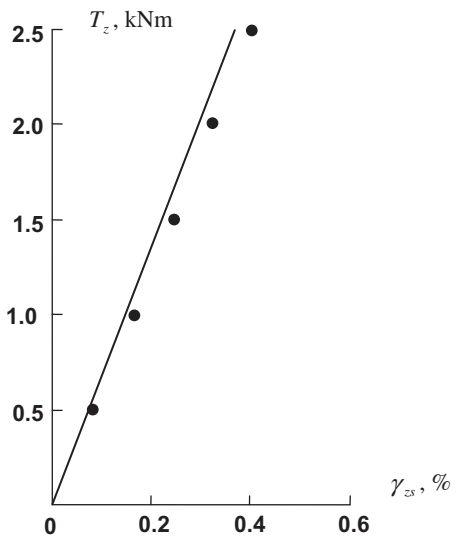


FIGURE 10.18

Dependence of the shear strain on torque: analysis (————) and experiment (• • • •).

and the stresses become

$$\sigma_1^{(\phi)} = \pm 87.3 \text{ MPa}, \quad \sigma_2^{(\phi)} = \mp 14.9 \text{ MPa}, \quad \tau_{12}^{(\phi)} = 4.8 \text{ MPa}$$
$$\sigma_1^{(90)} = 0, \quad \sigma_2^{(90)} = 0, \quad \tau_{12}^{(90)} = 15.2 \text{ MPa}$$

10.4.4 Determination of displacements

Return to Eqs. (10.30) and (10.32) and integrate them with respect to z, i.e.,

$$\begin{aligned} U_z &= U_z^0 + \frac{P_z}{S} z - x_0 \Theta_y - y_0 \Theta_x \\ \Theta_x &= \Theta_x^0 + \frac{k}{D_x^0} \int_0^z \left(\overline{H}_x - n_y \overline{H}_y\right) dz \\ \Theta_y &= \Theta_y^0 + \frac{k}{D_y^0} \int_0^z \left(\overline{H}_y - n_x \overline{H}_x\right) dz \end{aligned} \tag{10.59}$$

Here, U_x^0, Θ_x^0, and Θ_y^0 are the axial displacement and rotation angles of the beam's original cross section at $z = 0$.

To proceed, transform the constitutive equation in Eqs. (10.12) for the shear stress resultant N_{zs}. Substituting γ_{zs} in accordance with the last equation of Eqs. (10.13) and using Eqs. (10.17) for u_s in conjunction with Eq. (10.19) for u_z and Eqs. (10.8) for $\dot{x}_e$ and $\dot{y}_e$, we arrive at

$$N_{zs} = B_{44}\left[\Gamma_x \cos\beta - \Gamma_y \sin\beta + r\Theta_z' + \dot{\Psi}(s)\right] \tag{10.60}$$

where

$$\Gamma_x = \Theta_y + U_x', \quad \Gamma_y = \Theta_x + U_y' \tag{10.61}$$

Here, the functions Γ_x and Γ_y are the average shear deformations of the beam in the xz and yz planes (see Fig. 10.11). Indeed, if we neglect these deformations, using classical beam theory, and take $\Gamma_x = 0$ and $\Gamma_y = 0$, Eqs. (10.61) yield

$$\Theta_y = -U_x', \quad \Theta_x = -U_y' \tag{10.62}$$

Thus, the rotation angles of the beam cross section are equal to the slopes of the curved beam axis with a minus sign. This is typical for the classical theory of beam bending based on the assumption that the cross sections remain plane and orthogonal to the curved axis of a beam.

Integrating Eqs. (10.61), we get

$$U_x = U_x^0 + \int_0^z \left(\Gamma_x - \Theta_y\right) dz, \quad U_y = U_y^0 + \int_0^z \left(\Gamma_y - \Theta_x\right) dz \tag{10.63}$$

Here, as earlier, U_x^0 and U_y^0 are the displacements of the cross section in the x- and y-directions corresponding to the original cross section at $z = 0$.

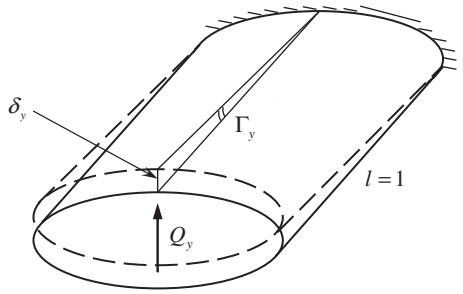


FIGURE 10.19

A cantilever beam loaded with transverse load.

Thus, to determine the beam displacements, we need to find Γ_x, Γ_y, and the twist angle Θ_z entering the foregoing equations. For this purpose, we apply Castigliano's theorem (see Section 2.11.2), according to which the displacements and the rotation angle of a beam cross section are equal to the derivatives of the beam strain energy with respect to the forces and the moment which act in this cross section. Consider a cantilever beam of unit length loaded with force Q_y as shown in Fig. 10.19 and assume that the beam deformation is associated with shear only (i.e., that all the stiffness coefficients of the beam wall B_{mn} $(mn = 11, 12, 22)$ are infinitely high except the shear stiffness B_{44}). Then, under the action of a force Q_y the loaded end of the beam experiences a deflection δ_y which is caused by shear and is equal to the shear angle Γ_y. In accordance with Castigliano's theorem,

$$\delta_y = \Gamma_y = \frac{\partial W_\sigma}{\partial Q_y} \tag{10.64}$$

in which

$$W_\sigma = \frac{1}{2}\int_s \frac{N_{zs}^2}{B_{44}} ds \tag{10.65}$$

is the strain energy induced by the shear stress resultant, N_{zs}. In a similar way, applying a force Q_x and a torque T_z to the beam in Fig. 10.19, we can write two more equations analogous to Eq. (10.64), i.e.,

$$\Gamma_x = \frac{\partial W_\sigma}{\partial Q_x}, \quad \Theta_z = \Theta_z' l = \frac{\partial W_\sigma}{\partial T_z} \tag{10.66}$$

For $l = 1$ (see Fig. 10.19), the second of these equations actually specifies Θ_z', i.e., the angle of rotation referred to the length of the beam element equal to the derivative of Θ_z with respect to z. Substituting the expression for N_{zs}, Eq. (10.53), into Eq. (10.65), we get

$$W_\sigma = \frac{1}{2}\int_s \frac{1}{B_{44}}\left[Q_x F_x(s) + Q_y F_y(s) + \frac{T_z}{2A}\right]^2 ds$$

Finally, Eqs. (10.64) and (10.66) yield

$$\begin{aligned}\Gamma_x &= c_{xx}Q_x + c_{xy}Q_y + c_{xz}T_z\\ \Gamma_y &= c_{yx}Q_x + c_{yy}Q_y + c_{yz}T_z\\ \Theta_z' &= c_{zx}Q_x + c_{zy}Q_y + c_{zz}T_z\end{aligned} \tag{10.67}$$

where

$$\begin{aligned}&c_{xx} = \int_s \frac{F_x^2(s)}{B_{44}}ds, \quad c_{xy} = c_{yx} = \int_s \frac{F_x(s)F_y(s)}{B_{44}}ds, \quad c_{yy} = \int_s \frac{F_y^2(s)}{B_{44}}ds\\ &c_{xz} = c_{zx} = \frac{1}{2A}\int_s \frac{F_x(s)}{B_{44}}ds, \quad c_{yz} = c_{zy} = \frac{1}{2A}\int_s \frac{F_y(s)}{B_{44}}ds, \quad c_{zz} = \frac{1}{4A^2}\int_s \frac{ds}{B_{44}}\end{aligned} \tag{10.68}$$

Thus, the displacements U_x, U_y, and U_z and the rotation angles Θ_x, Θ_y, and Θ_z of a beam cross section as an absolutely rigid disk are specified by Eqs. (10.59), (10.63), and (10.67).

10.4.5 Warping function

Under free bending and torsion, the beam cross sections do not remain plane, and the axial displacement of the cross-sectional contour is specified by Eq. (10.19) according to which

$$u_z = U_z(z) + x_e\Theta_y(z) + y_e\Theta_x(z) + \Psi(s) \tag{10.69}$$

To determine the warping function $\Psi(s)$, we match two expressions for the shear stress resultant N_{zs} found from the equilibrium equations, Eq. (10.53), and from the constitutive equation, Eq. (10.60). Equating the right-hand parts of these equations, we can express $\dot{\Psi}(s)$ as

$$\dot{\Psi}(s) = \frac{Q_x}{B_{44}}F_x(s) - \Gamma_x\cos\beta + \frac{Q_y}{B_{44}}F_y(s) + \Gamma_y\sin\beta + \frac{T_z}{2AB_{44}} - r\Theta_z'$$

Integrating this equation, we get

$$\Psi(s) = \Psi_b(s) + \Psi_t(s) \tag{10.70}$$

where

$$\Psi_b(s) = Q_x\int_0^s \frac{F_x(s)}{B_{44}}ds - \Gamma_x\int_0^s \cos\beta ds + Q_y\int_0^s \frac{F_y(s)}{B_{44}}ds + \Gamma_y\int_0^s \sin\beta ds \tag{10.71}$$

$$\Psi_t(s) = \frac{T_z}{2A}\int_0^s \frac{ds}{B_{44}} - \Theta_z'\int_0^s rds \tag{10.72}$$

The constant of integration is omitted because it can be included in function U_z in Eq. (10.69). According to Eq. (10.70), the warping function can be decomposed into $\Psi_b(s)$ which corresponds to bending and $\Psi_t(s)$ which corresponds to torsion of the beam.

Note that for the closed contour shown in Fig. 10.14 the warping function must be continuous, i.e.,

$$\Psi(s=0)=\Psi(s=s_1) \tag{10.73}$$

Taking into account that

$$\int_s \cos\beta\, ds=\int_s \dot{x}_e ds=0,\quad \int_s \sin\beta\, ds=-\int_s \dot{y}_e ds=0,\quad \int_s r ds=2A$$

we can reduce Eq. (10.73) to the third equation of Eqs. (10.67).

The function $\Psi(s)$ in Eq. (10.70) depends on the location of point S from which the contour coordinate s is measured and the selection of the coordinate frame x, y (see Fig. 10.12). To determine the warping function, which is invariant with respect to its coordinates, we introduce the augmented warping function as

$$W(s)=\Psi(s)+C_0+C_1x_e+C_2y_e \tag{10.74}$$

and impose the orthogonality conditions

$$\int_s W(s)Bds=0,\quad \int_s W(s)Bx_e ds=0,\quad \int_s W(s)By_e ds=0 \tag{10.75}$$

in which B is, as earlier, the axial stiffness of the wall. Substituting $W(s)$ from Eq. (10.74) into Eqs. (10.75), we arrive at the following three equations for C_0, C_1, and C_2:

$$SC_0+S_xC_1+S_yC_2=-\int_s \Psi(s)Bds$$

$$S_xC_0+D_xC_1+D_{xy}C_2=-\int_s \Psi(s)By_e ds$$

$$S_yC_0+D_{xy}C_1+D_yC_2=-\int_s \Psi(s)Bx_e ds$$

Here, the coefficients S and D are specified by Eqs. (10.29). Determining the constants C_0, C_1, and C_2 and substituting them into Eq. (10.74), we finally get

$$W(s)=\Psi(s)-\frac{1}{S}\int_s \Psi(s)Bds-k\left[\frac{y_e-y_0}{D_x^0}\int_s \Psi(s)B\bar{y}ds+\frac{x_e-x_0}{D_y^0}\int_s \Psi(s)B\bar{x}ds\right] \tag{10.76}$$

where x_0, y_0, k, and D, and $\bar{x}$ and $\bar{y}$ are given by Eqs. (10.31), (10.33), and (10.36). The warping function in Eq. (10.76) depends only on the beam geometry and mechanical properties.

10.4.6 Beams with circular and rectangular cross sections

The most widely used composite thin-walled beams have circular and rectangular cross sections (see Fig. 10.20).

Consider a beam with a circular cross section shown in Fig. 10.21. The contour coordinates s, x_e, and y_e are expressed in terms of the radius R and the angle β as

$$s=R\beta,\quad x_e=R\sin\beta,\quad y_e=R\cos\beta$$



FIGURE 10.20

Composite beams with circular and rectangular cross-sections.

The stiffness coefficients given by Eqs. (10.29) and (10.33) become

$$S = B\int_0^{2\pi} R d\beta = 2\pi RB, \quad S_x = BR^2\int_0^{2\pi} \cos\beta d\beta = 0, \quad S_y = BR^2\int_0^{2\pi} \sin\beta d\beta = 0$$

$$D_x^0 = D_x = BR^3\int_0^{2\pi} \cos^2\beta d\beta = \pi BR^3, \quad D_y^0 = D_y = BR^3\int_0^{2\pi} \sin^2\beta d\beta = \pi BR^3$$

$$D_{xy}^0 = D_{xy} = BR^3\int_0^{2\pi} \sin\beta\cos\beta\, d\beta = 0$$

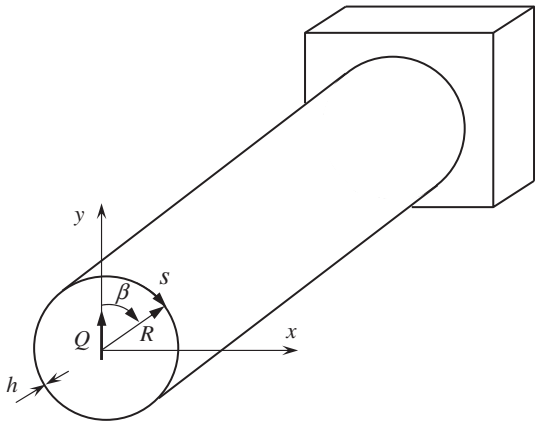


FIGURE 10.21

A beam with a circular cross section.

The axial stress resultant and strain are specified by Eqs. (10.34) and (10.35), according to which (we consider bending in the yz-plane only)

$$N_z = B\varepsilon_z = \frac{P_z}{2\pi R} + \frac{H_x}{\pi R^2}\cos\beta$$

For a circular cross section, $r = R$ and $A = \pi R^2$. Then, Eqs. (10.45) and (10.54) yield

$$\overline{S}_x(s) = BR^2\int_0^\beta \cos\beta d\beta = BR^2\sin\beta$$

$$F_y(s) = -\frac{1}{\pi BR^3}\left(BR^2\sin\beta - \frac{BR^2}{2\pi}\int_0^{2\pi}\sin\beta d\beta\right) = -\frac{\sin\beta}{\pi R}$$

(we consider the loading with a force Q_y only), and Eq. (10.53) for the shear stress resultant becomes

$$N_{zs} = \frac{1}{\pi R}\left(\frac{T_z}{2R} - Q_y\sin\beta\right)$$

Consider the displacements. For bending in the yz-plane (see Fig. 10.21), we have from Eqs. (10.59)

$$U_z = U_z^0 + \frac{P_z z}{2\pi RB}, \quad \Theta_x = \Theta_x^0 + \frac{1}{\pi BR^3}\int_0^z H_x dz$$

The compliance coefficients entering Eqs. (10.67) are

$$c_{xy} = 0, \quad c_{xz} = 0, \quad c_{yz} = 0$$

$$c_{yy} = \frac{1}{\pi^2 R B_{44}} \int_0^{2\pi} \sin^2 \beta d\beta = \frac{1}{\pi R B_{44}}, \quad c_{zz} = \frac{1}{2\pi^2 R^3 B_{44}} \int_0^{2\pi} d\beta = \frac{1}{2\pi R^3 B_{44}}$$

Then, Eqs. (10.67) yield

$$\Gamma_y = \frac{Q_y}{\pi R B_{44}}, \quad \Theta_z' = \frac{T_z}{2\pi R^3 B_{44}}$$

and according to Eqs. (10.63), the beam deflection is

$$U_y = U_y^0 - \Theta_x^0 z + \int_0^z \frac{1}{\pi R} \left(\frac{Q_y}{B_{44}} - \frac{1}{BR^2} \int_0^z H_x dz \right) dz \tag{10.77}$$

As an example, consider the cantilever beam loaded with force $Q_y = Q$ as shown in Fig. 10.21. For such a beam, Eqs. (10.41) and the boundary conditions give

$$U_y^0 = 0, \quad \Theta_x^0 = 0, \quad Q_y = Q, \quad H_x = -Q(l - z)$$

The maximum deflection $U_y^m = U_y(z = l)$ following from Eq. (10.77) is

$$U_y^m = \frac{Ql^3}{3\pi BR^3}(1 + \alpha), \quad \alpha = \frac{3BR^2}{B_{44} l^2}$$

The parameter α allows for shear deformation of the beam under bending. As can be seen, this deformation can be ignored for relatively long beams with high ratio l/R. Finally, we determine the warping functions. Using Eqs. (10.71) and (10.72), we get

$$\Psi_b(s) = Q_y \int_0^s \frac{F_y(s)}{B_{44}} ds + \Gamma_y \int_0^s \sin \beta ds = -\frac{Q_y}{\pi B_{44}} \int_0^\beta \sin \beta d\beta + \frac{Q_y}{\pi B_{44}} \int_0^\beta \sin \beta d\beta = 0$$

$$\Psi_t(s) = \frac{T_z}{2A} \int_0^s \frac{ds}{B_{44}} - \Theta_z' \int_0^s r ds = \frac{T_z}{2\pi R B_{44}} \int_0^\beta d\beta - \frac{T_z}{2\pi R B_{44}} \int_0^\beta d\beta = 0$$

Thus, bending and torsion of a beam with a closed circular cross section do not cause cross-sectional warping.

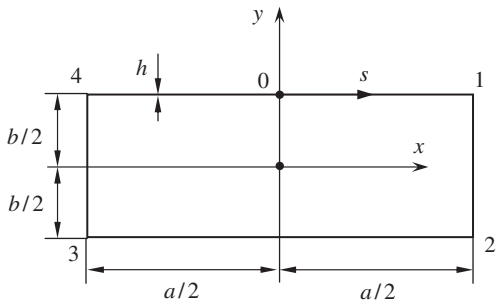


FIGURE 10.22

A rectangular cross section of a beam.

Consider the beam with a rectangular cross section shown in Fig. 10.22. Decompose the beam contour into five parts, i.e., 0 – 1, 1 – 2, 2 – 3, 3 – 4, and 4 – 0, and present the geometrical parameters of the contour for each part as

$$0-1:\ s=0,\quad x_e=x,\quad y_e=\frac{b}{2},\quad r=\frac{b}{2},\quad \beta=0$$

$$1-2:\ s=\frac{a}{2}+\left(\frac{b}{2}-y\right),\quad x_e=\frac{a}{2},\quad y_e=y,\quad r=\frac{a}{2},\quad \beta=\frac{\pi}{2}$$

$$2-3:\ s=\frac{a}{2}+b+\left(\frac{a}{2}-y\right),\quad x_e=x,\quad y_e=-\frac{b}{2},\quad r=\frac{b}{2},\quad \beta=\pi$$

$$3-4:\ s=\frac{3a}{2}+b+\left(\frac{b}{2}+y\right),\quad x_e=-\frac{a}{2},\quad y_e=y,\quad r=\frac{a}{2},\quad \beta=\frac{3\pi}{2}$$

$$4-0:\ s=\frac{3a}{2}+2b+\left(\frac{a}{2}+x\right),\quad x_e=x,\quad y_e=\frac{b}{2},\quad r=\frac{b}{2},\quad \beta=2\pi$$

The stiffness coefficients given by Eqs. (10.29) and (10.33) are

$$S=2B(a+b),\ S_x=0,\ S_y=0,\ D_{xy}^0=0$$

$$D_x^0=D_x=\frac{1}{6}Bb^2(3a+b),\ D_y^0=D_y=\frac{1}{6}Ba^2(a+3b)$$

Consider a cantilever beam loaded with force $Q_y=Q$, bending moment $H_x=M$ and torque $T_z=T$. Then, the axial stress resultant specified by Eq. (10.34) is

$$N_z=\frac{6[M-Q(l-z)]y}{b^2(3a+b)}$$

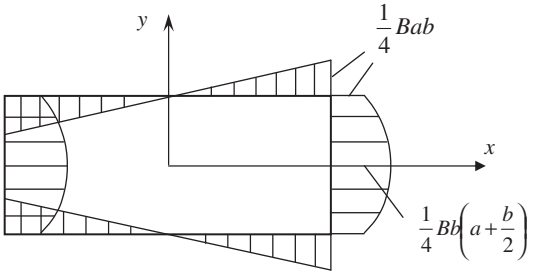


FIGURE 10.23

Distribution of function $\overline{S}_x(s)$ over the cross-sectional contour.

The function $\overline{S}_x(s)$ in Eqs. (10.45) becomes, for the different parts of the beam,

$$\overline{S}_x^{01}(s) = B\frac{b}{2}\int dx = \frac{1}{2}Bbx$$

$$\overline{S}_x^{12}(s) = \overline{S}_x^{01}\left(x=\frac{a}{2}\right) + B\int_{b/2}^{y} y(-dy) = \frac{B}{2}\left(\frac{ab}{2}+\frac{b^2}{4}-y^2\right)$$

$$\overline{S}_x^{23}(s) = \overline{S}_x^{12}\left(y=-\frac{b}{2}\right) + B\left(-\frac{b}{2}\right)\int_{a/2}^{x}(-dx) = \frac{1}{2}Bbx$$

$$\overline{S}_x^{34}(s) = \overline{S}_x^{23}\left(x=-\frac{a}{2}\right) + B\int_{-b/2}^{y} ydy = -\frac{B}{2}\left(\frac{ab}{2}+\frac{b^2}{4}-y^2\right)$$

$$\overline{S}_x^{40}(s) = \overline{S}_x^{34}\left(y=\frac{b}{2}\right) + B\frac{b}{2}\int_{-a/2}^{x} dx = \frac{1}{2}Bbx$$

The distribution of the function $\overline{S}_x(s)$ over the contour is shown in Fig. 10.23. Positive values are plotted outside the contour and negative ones inside the contour.

The function $F_y(s)$ in Eqs. (10.54) has the following form:

$$F_y(s) = -\frac{1}{D_x^0}\left[\overline{S}_x(s) - \frac{1}{2ab}\int_s \overline{S}_x(s)rds\right] = \frac{6\overline{S}_x(s)}{Bb^2(3a+b)}$$

Thus, we can find the components of the shear stress resultant as

$$N_Q = -\frac{6Q\overline{S}_x(s)}{Bb^2(3a+b)}, \quad N_0 = \frac{T}{2ab}$$

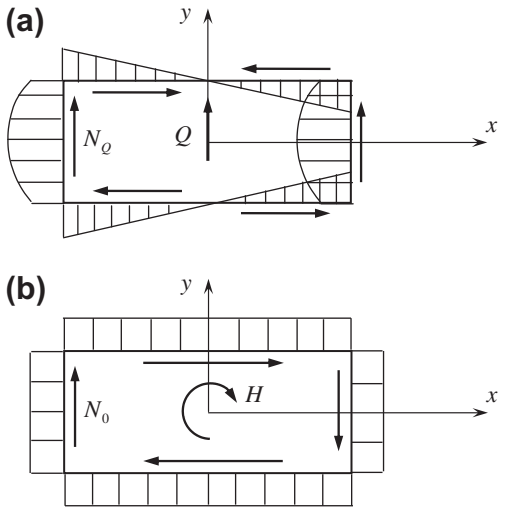


FIGURE 10.24

Distributions of N_Q (a) and N_0 (b) over the cross-sectional contour.

The distributions of these components of the shear stress resultant over the cross-sectional contour are shown in Fig. 10.24.

To determine the displacements, we need to find the compliance coefficients which enter Eqs. (10.67), i.e.,

$$c_{xy} = 0, \quad c_{xz} = 0, \quad c_{yz} = 0$$

$$c_{yy} = \frac{1}{B_{44}} \int_s F_y^2(s) ds = \frac{9}{(3a+b)^2 b^2 B_{44}} \left(\frac{b^3}{15} + \frac{ab^2}{3} + \frac{a^2 b}{2} + \frac{a^3}{6} \right)$$

$$c_{zz} = \frac{1}{4a^2 b^2 B_{44}} \int_s ds = \frac{a+b}{2a^2 b^2 B_{44}}$$

For the cantilever beam under consideration, the final expressions for the deflection and the twist angle are

$$U_y = \frac{Qz}{C_s} - \left[M - Q\left(l - \frac{z}{3}\right) \right] \frac{z^2}{2D}, \quad \Theta_z = \frac{Tz}{Dt} \tag{10.78}$$

where

$$C_s = \frac{(1+3\lambda)^2 b B_{44}}{3\left(0.2 + \lambda + 1.5\lambda^2 + 0.5\lambda^3\right)}, \quad D = \frac{1}{6} B b^3 (3\lambda + 1), \quad \lambda = \frac{a}{b} \tag{10.79}$$

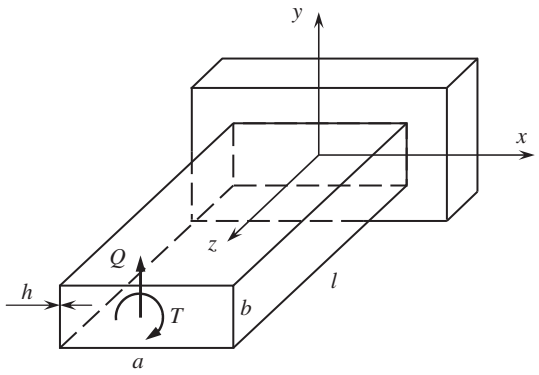


FIGURE 10.25

A cantilever beam with a rectangular cross section loaded by transverse force Q and torque T.

are the shear and bending stiffnesses of the beam and

$$D_t = \frac{2\lambda^2}{1+\lambda} b^3 B_{44} \tag{10.80}$$

is the torsional stiffness.

As an example, consider the beam experimentally studied by Smith and Chopra (1990). The cantilever beam (see Fig. 10.25) has the following dimensions: $l = 762$ mm, $a = 52.3$ mm, $b = 26$ mm, and $h = 0.76$ mm, and consists of three unidirectional axial ($\phi = 0$) carbon-epoxy plies with total thickness $h_0 = 0.38$ mm and three orthogonally reinforced plies ($\phi = 90°$) with total thickness $h_{90} = 0.38$ mm. The mechanical properties of the unidirectional ply are $E_1 = 142$ GPa, $E_2 = 9.8$ GPa, $G_{12} = 6$ GPa, $\nu_{12} = 0.029$, and $\nu_{21} = 0.42$. The stiffness coefficients of the layer are

$$A_{11}^{(0)} = \overline{E}_1, \quad A_{12}^{(0)} = \nu_{12}\overline{E}_1, \quad A_{22}^{(0)} = \overline{E}_2, \quad A_{44}^{(0)} = G_{12}$$

$$A_{11}^{(90)} = \overline{E}_2, \quad A_{12}^{(90)} = \nu_{12}\overline{E}_1, \quad A_{22}^{(90)} = \overline{E}_1, \quad A_{44}^{(90)} = G_{12}$$

where, as earlier, $\overline{E}_{1,2} = E_{1,2}/(1 - \nu_{12}\nu_{21})$. The stiffness coefficients of the beam wall

$$B_{mn} = \frac{h}{2}\left(A_{mn}^{(0)} + A_{mn}^{(90)}\right), \quad B = B_{11} - \frac{B_{12}^2}{B_{22}}$$

have the following values:

$$B_{11} = B_{22} = 58.4 \text{ MN/m}, \quad B_{12} = 3.2 \text{ MN/m}, \quad B_{44} = 4.56 \text{ MN/m}, \quad B = 58.2 \text{ MN/m}$$

The beam stiffnesses under shear, bending, and torsion specified by Eqs. (10.79) and (10.80) are

$$C_s = 158 \text{ kN}, \quad D = 1200 \text{ Nm}^2, \quad D_t = 215 \text{ Nm}^2$$

The experimental beam is loaded by a transverse force $Q = 4.448$ N and a torque $T = 0.113$ Nm (see Fig. 10.25). The deflection slope and twist angle following from Eqs. (10.78) are

$$U_y' = \left[0.028 + 2.15\left(\overline{z} - \frac{\overline{z}^2}{2}\right)\right]10^{-3},\ \Theta = 0.0004 \cdot \overline{z}$$

where $\overline{z} = z/l$. The calculated (lines) and the experimental (dots) results are presented in Fig. 10.26.

Finally, consider the warping function for a rectangular cross section. The warping function under bending is specified by Eq. (10.71), according to which

$$\Psi_b(s) = \frac{3Q}{b^2(3a+b)B_{44}}\left[\frac{2}{B}\int_0^s \overline{S}_x(s)ds + \frac{3}{3a+b}\left(\frac{b^3}{15} + \frac{ab^2}{3} + \frac{a^2b}{2} + \frac{a^3}{6}\int_0^s \sin\beta\, ds\right)\right] \tag{10.81}$$

Here, $\overline{S}_x(s)$ is shown in Fig. 10.23. It follows from Eq. (10.81) that the function $\Psi_b(s)$ is composed of two integrals whose distribution over the beam contour is presented in Fig. 10.27. As can be seen, the dependence of Ψ_b on the x-coordinate is quadratic and on the y-coordinate is cubic. The invariant form

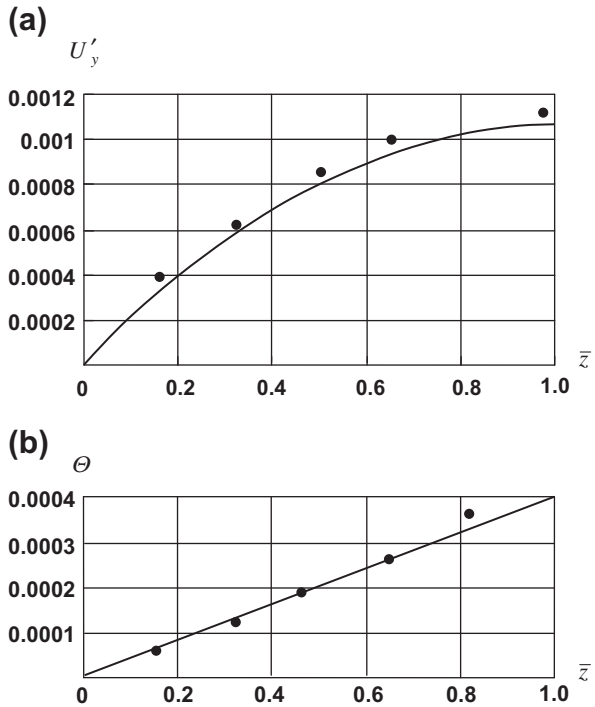


FIGURE 10.26

Dependencies of the deflection slope (a) and the twist angle (b) on the axial coordinate: analysis (———) and experiment (••••) (Smith and Chopra, 1990).

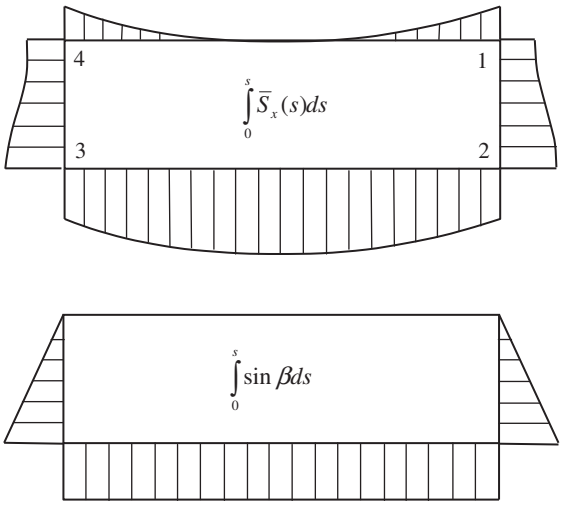


FIGURE 10.27

Distributions of the integrals in Eq. (10.81).

of the warping function is specified by Eq. (10.76), according to which

$$W_b(s) = \Psi_b(s) - \frac{1}{2(a+b)} \int_s \Psi_b(s)ds - \frac{6y}{b^2(3a+b)} \int_s \Psi_b(s)yds \tag{10.82}$$

The warping function $W_b(s)$ for the rectangular cross section is shown in Fig. 10.28. It follows from Eq. (10.81) that for $Q = 0$ we have $\Psi_b(s) = 0$, i.e., the warping of the cross section under beam bending is induced by the transverse shear force only.

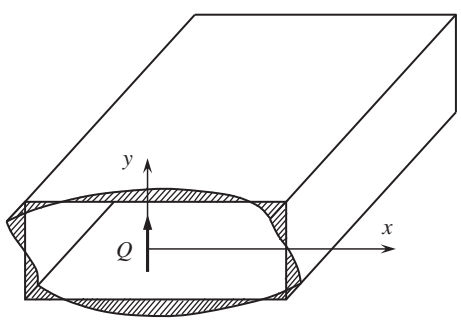


FIGURE 10.28

Warping function of a rectangular beam under transverse bending.

Under torsion, the warping function is specified by Eq. (10.72) which yields

$$\Psi_t(s) = \frac{T}{2abB_{44}}\left(\int_0^s ds - \frac{a+b}{ab}\int_0^s rds\right)$$

For the contour shown in Fig. 10.22, we have

$$\Psi_t^{01}(s) = \frac{T}{2abB_{44}}\left(\int_0^x dx - \frac{a+b}{ab}\int_0^x dx\right) = \frac{T(a-b)x}{4ab^2B_{44}}$$

$$\Psi_t^{12}(s) = \frac{T}{2abB_{44}}\left[\int_{b/2}^y (-dy) - \frac{a+b}{ab}\frac{a}{2}\int_0^y (-dy)\right] = \frac{T(a-b)y}{4ab^2B_{44}}$$

The warping function of a rectangular beam under torsion is shown in Fig. 10.29. Since

$$\int_s \Psi_t(s)ds = 0, \quad \int_s \Psi_t(s)x_e ds = 0, \quad \int_s \Psi_t(s)y_e ds = 0,$$

the function $\Psi_t(s)$ is invariant with respect to coordinate frame and $\Psi_t(s) = W_t(s)$ where

$$W_t(s) = \frac{T(a-b)}{2a^2b^2B_{44}}xy \tag{10.83}$$

For a square cross section ($a = b$) and $W_t(s) = 0$, so a square cross section does not experience warping under torsion (but it does under transverse bending). This result holds for any contour which has the shape of a regular polygon (see Fig. 10.30) for which

$$r = r_n = R\cos\alpha, \quad a_n = 2R\sin\alpha, \quad A = \frac{n}{2}a_n r_n, \quad \int_s ds = na_n$$

and $\Psi_t(s) = 0$. A thin-walled composite beam with hexagonal cross section is shown in Fig. 10.31.

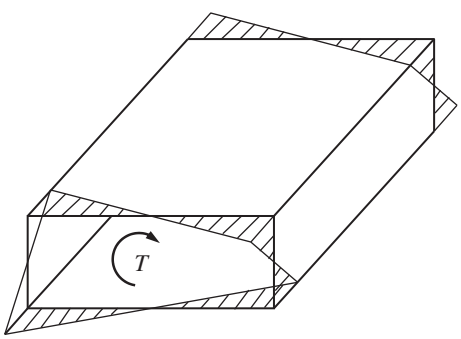


FIGURE 10.29

Warping function of a rectangular beam under torsion.

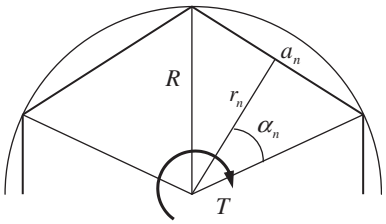


FIGURE 10.30

Cross-sectional contour in the form of a regular polygon.

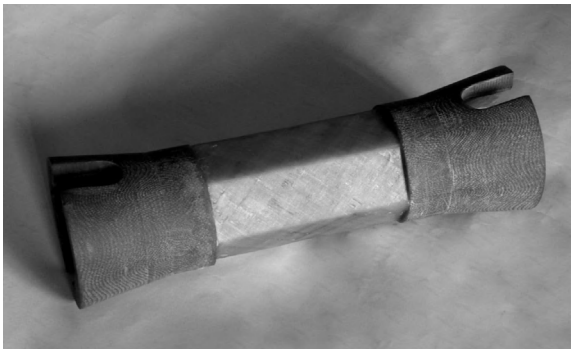


FIGURE 10.31

Composite thin-walled beam with a hexagonal cross section.

The foregoing results are valid for thin-walled beams whose stiffness coefficients do not depend on the contour coordinate s. Changing these coefficients accordingly, we can control the cross-sectional warping. Consider, for example, the rectangular cross section shown in Fig. 10.22 and assume that the shear stiffness of the horizontal walls 1 – 4 and 2 – 3 is B_{44}^a, whereas for the vertical walls 1 – 2 and 3 – 4 , it is different and is equal to B_{44}^b. Then, Eq. (10.83) can be generalized as

$$W_t(s) = \frac{Txy}{2a^2b^2}\left(\frac{a}{B_{44}^a} - \frac{b}{B_{44}^b}\right)$$

As can be seen, taking $bB_{44}^a = aB_{44}^b$, we have $W_t(s) = 0$.

10.4.7 Shear and twist center

In the general case, the forces P_z, Q_x, and Q_y applied at some arbitrary point 0 (see Fig. 10.12) induce tension, bending, and torsion of the beam. It is shown in Section 10.4.1 that if an axial force is applied at the cross-sectional center with coordinates x_0 and y_0 given by Eqs. (10.31), it does not cause any beam bending. An analogous situation occurs with respect to bending and torsion. If the transverse

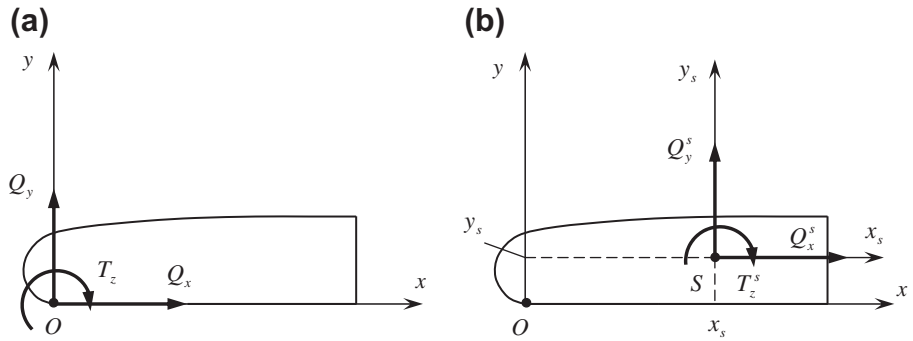


FIGURE 10.32

Cross section with forces applied at an arbitrary point *O* (a) and at the shear center *S* (b).

forces Q_x and Q_y are applied at the point called the shear center of the cross section, they do not induce the beam torsion.

To determine the coordinates of the shear center, consider the contour of a beam cross section shown in Fig. 10.32a and assume that the forces Q_x and Q_y and the torque T_z are applied at some arbitrary point O. Then, the shear deformations Γ_x and Γ_y and the derivative of the twist angle Θ_z' are specified by Eqs. (10.67), i.e.,

$$\begin{aligned}\Gamma_x &= c_{xx}Q_x + c_{xy}Q_y + c_{xz}T_z\\ \Gamma_y &= c_{yx}Q_x + c_{yy}Q_y + c_{yz}T_z\\ \Theta_z' &= c_{zx}Q_x + c_{zy}Q_y + c_{zz}T_z\end{aligned} \tag{10.84}$$

in which the coefficients c are given by Eqs. (10.68). We now introduce the shear center S with coordinates x_s, y_s and apply the transverse forces and torque to the shear center as in Fig. 10.32b. Then, the conditions of the static equivalence of the forces and torque shown in Figs. 10.32a and b are

$$Q_x^s = Q_x, \quad Q_y^s = Q_y, \quad T_z^s = T_z + x_s Q_y - y_s Q_x \tag{10.85}$$

Substitute Q_x, Q_y, and T_z from Eqs. (10.85) into the third equation of Eqs. (10.84) to get

$$\Theta_z' = (c_{xz} + y_s c_{zz})Q_x^s + \big(c_{yz} - x_s c_{zz}\big)Q_y^s + c_{zz}T_z^s \tag{10.86}$$

Since the forces Q_x^s and Q_y^s are applied at the shear center, Θ_z' must not depend on Q_x^s and Q_y^s, i.e.,

$$\Theta_z' = c_{zz}T_z^s \tag{10.87}$$

Then, Eq. (10.86) allows us to find the coordinates of the shear center as

$$x_s = \frac{c_{yz}}{c_{zz}}, \; y_s = -\frac{c_{xz}}{c_{zz}} \tag{10.88}$$

Substituting the coefficients c with their expressions, Eqs. (10.68), we finally arrive at

$$x_s = \frac{2kA}{D_x^0}\left[\frac{1}{2A}\int_s \overline{S}_x(s)rds - \left(\int_s \frac{ds}{B_{44}}\right)^{-1}\int_s \frac{\overline{S}_x(s)}{B_{44}}ds\right]$$
$$y_s = -\frac{2kA}{D_y^0}\left[\frac{1}{2A}\int_s \overline{S}_y(s)rds - \left(\int_s \frac{ds}{B_{44}}\right)^{-1}\int_s \frac{\overline{S}_y(s)}{B_{44}}ds\right] \tag{10.89}$$

Now, transform the first two equations of Eqs. (10.84) and show that if the forces Q_x^s and Q_y^s are applied at the shear center, the corresponding shear deformations Γ_x^s and Γ_y^s do not depend on the torque T_z^s. In the general case, Eqs. (10.61) yield

$$\Gamma_x = \Theta_y + U_x', \quad \Gamma_y = \Theta_x + U_y' \tag{10.90}$$

in which U_x and U_y are the displacements of point O in Fig. 10.32a. The displacements of an arbitrary point of the cross section are specified by equations analogous to Eqs. (10.16), i.e.,

$$u_x = U_x + y\Theta_z, \quad u_y = U_y - x\Theta_z$$

For the shear center, $x = x_s$ and $y = y_s$ and these equations yield

$$U_x^s = U_x + y_s\Theta_z, \quad U_y^s = U_y - x_s\Theta_z \tag{10.91}$$

where U_x^s and U_y^s are the displacements of the shear center S (see Fig. 10.32b). Solving Eqs. (10.91) for U_x and U_y and substituting the resulting expressions into Eqs. (10.90), we get

$$\Gamma_x = \left(U_x^s\right)' - y_s\Theta_z' + \Theta_y, \quad \Gamma_y = \left(U_y^s\right)' + x_s\Theta_z' + \Theta_x \tag{10.92}$$

Introduce the shear deformations Γ_x^s and Γ_y^s corresponding to the shear forces applied at the shear center using the following equations analogous to Eqs. (10.90):

$$\Gamma_x^s = \left(U_x^s\right)' + \Theta_y, \quad \Gamma_y^s = \left(U_y^s\right)' + \Theta_x \tag{10.93}$$

Then, Eqs. (10.92) become

$$\Gamma_x = \Gamma_x^s - y_s\Theta_z', \quad \Gamma_y = \Gamma_y^s + x_s\Theta_z'$$

Substitute these equations into the first two equations of Eqs. (10.84) and change Q_x, Q_y, and T_z to Q_x^s, Q_y^s, and T_z^s with the aid of Eqs. (10.85) to get

$$\Gamma_x^s = (c_{xx} + y_s c_{xz})Q_x^s + (c_{xy} - x_s c_{xz})Q_y^s + c_{xz}T_z^s + y_s\Theta_z'$$
$$\Gamma_y^s = (c_{xy} + y_s c_{yz})Q_x^s + (c_{yy} - x_s c_{yz})Q_y^s + c_{yz}T_z^s - x_s\Theta_z'$$

Substituting Θ_z' with its expression given by Eq. (10.87) and using Eqs. (10.88) for the coordinates of the shear center, we finally arrive at

$$\Gamma_x^s = c_{xx}^s Q_x^s + c_{xy}^s Q_y^s, \quad \Gamma_y^s = c_{xy}^s Q_x^s + c_{yy}^s Q_y^s \tag{10.94}$$

where

$$c_{xx}^s = c_{xx} - \frac{c_{xz}^2}{c_{zz}}, \quad c_{xy}^s = c_{xy} - \frac{c_{xz}c_{yz}}{c_{zz}}, \quad c_{yy}^s = c_{yy} - \frac{c_{yz}^2}{c_{zz}}$$

Thus, if the transverse forces are applied at the shear center, the shear deformations are specified by Eqs. (10.94) and depend only on the forces. The angle of twist is determined by Eq. (10.87).

We now introduce the twist center, i.e., the point around which the beam cross section rotates under pure torsion. Since the angles Θ_x and Θ_y are zero under pure torsion, Eqs. (10.93) yield

$$\Gamma_x^s = \left(U_x^s\right)', \quad \Gamma_y^s = \left(U_y^s\right)' \tag{10.95}$$

However, Q_x^s and Q_y^s are also zero in the case of pure torsion and it follows from Eqs. (10.94) that $\Gamma_x^s = 0$ and $\Gamma_y^s = 0$. Thus, Eqs. (10.95) show that the displacements of the shear center are zero, i.e., that the twist center coincides with the shear center. As shown by Reissner and Tsai (1972a, b), this result, in the general case, follows from the symmetry conditions for the compliance coefficients c_{ij} in Eqs. (10.84).

The coordinates of the shear and twist center depend on the cross-sectional shape and the mechanical properties of the beam material. For a cross section with one axis of symmetry, the shear center is located on this axis. If the cross section has two axes of symmetry, the shear center lies at their intersection.

As an example, consider the triangular contour shown in Fig. 10.33. Assume that the stiffness coefficients B and B_{44} do not depend on s and that $a/b = 2.5$. Since the x-axis is the axis of symmetry, $y_s = 0$ and we need to find only the coordinate x_s of the shear center. Measuring the contour coordinate from point 1 in Fig. 10.33, we get

$$x_e = s\cos\alpha, \quad y_e = s\sin\alpha, \quad \cos\alpha = 0.98, \quad \sin\alpha = 0.196, \quad s_2 = 1.02a$$

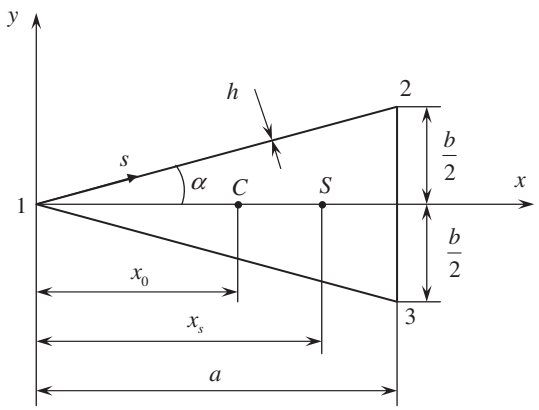


FIGURE 10.33

Triangular cross section of a beam.

The coordinate x_0 of the cross-sectional center specified by Eqs. (10.31) is

$$x_0 = \frac{S_y}{S}, \quad S_y = \int_s B x_e ds, \quad S = \int_s B ds$$

in which (see Fig. 10.33)

$$S_y^{12} = \int_0^{s_2} Bs \cos \alpha ds = 0.51 Ba^2, \quad S_y^{23} = \int_{b/2}^{-b/2} Bads = 0.4 Ba^2$$

Thus,

$$S_y = 2S_y^{12} + S_y^{23} = 1.42 Ba^2, \quad S = B(2s_2 + b) = 2.44 Ba$$

and $x_0 = 0.58a$ (see point C in Fig. 10.33).

To determine x_c, we apply the first equation of Eqs. (10.89) in which $k = 1$, $A = ab/2 = 0.2a^2$, and

$$D_x^0 = \int_s B y_e^2 ds = 2B \left(\int_0^{s_2} s^2 \sin^2 \alpha ds + \int_0^{b/2} y^2 dy \right) = \frac{Bb^2 a}{6 \cos \alpha} (1 + \sin \alpha) - 0.0325 Ba^3$$

The function

$$\overline{S}_x(s) = \int_0^s B y_e ds$$

is calculated for parts 1 – 2 and 2 – 3 of the contour as

$$\overline{S}_x^{12}(s) = B \sin \alpha \int_0^s sds = \frac{1}{2} Bs^2 \sin \alpha$$

$$\overline{S}_x^{23}(s) = \overline{S}_x^{12}(s_2) + \int_{b/2}^{y} Byds = \frac{1}{2} B \left(s_2^2 \sin \alpha + \frac{b^4}{4} - y^2 \right)$$

(see Fig. 10.33), and is shown in Fig. 10.34. Then, taking into account that $r = 0$ for parts 1 – 2 and 1 – 3 in Fig. 10.33 and $r = a$ for part 2 – 3, we have

$$\int_s \overline{S}_x(s) r ds = 2a \int_0^{b/2} \overline{S}_x^{23} dy = 0.046 Ba^3$$

$$\int_s \overline{S}_x(s) ds = 2 \left[\int_0^{s_2} \overline{S}_x^{12}(s) ds + \int_0^{b/2} \overline{S}_x^{23}(y) dy \right] = 0.115 Ba^3$$

$$\int_s ds = 2s_2 + b = 2.44a$$

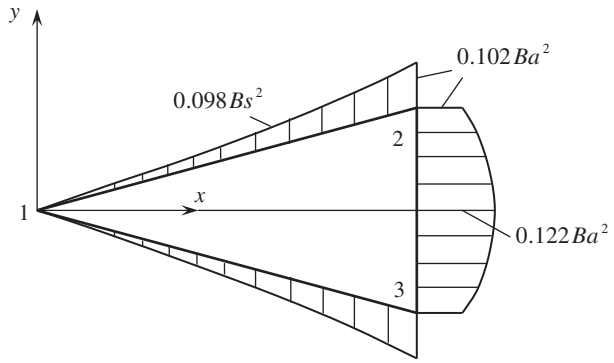


FIGURE 10.34

Distribution of the function $\overline{S}_x(s)$ over the triangular contour.

Finally, the first equation of Eqs. (10.89) yields $x_s = 0.839a$ (see the point S in Fig. 10.33).

The existence of the shear center allows us to decompose the problems of beam bending and torsion. For this purpose, the forces Q_x and Q_y acting at a given point O of the cross section (see Fig. 10.32a) are transferred to the shear center S (see Fig. 10.32b) and the torque T_z^s is calculated with the aid of the last equation of Eqs. (10.85). Then, the bending of the beam is studied independently of the torsion of the beam, and the principle of superposition is used to obtain the final solution.

The capability of being able to decompose the problem of beam bending and torsion is commonly used in practical analysis since different assumptions can be used for the bending and torsion problems to simplify the solution procedures. For example, for long beams the shear deformations induced by forces Q_x and Q_y can be ignored, taking $B_{44} \to \infty$. However, for the problem of torsion, the shear deformation must not be ignored, and the shear stiffness must be finite.

10.4.8 Anisotropic thin-walled beams

Anisotropic beams, in contrast to the orthotropic beams considered in the foregoing sections, demonstrate various coupling effects, i.e., coupling between axial tension and torsion, or between bending and torsion. These coupling effects can be used, for example, in composite aircraft structures to control the aeroelastic characteristics of composite wings (Weisshaar, 1980, 1981; Weisshaar and Foist, 1985).

In anisotropic materials, normal stresses cause both normal and shear strains and the constitutive equations for orthotropic materials, Eqs. (10.12), are generalized as

$$\begin{aligned} N_z &= B_{11}\varepsilon_z + B_{11}\varepsilon_s + B_{14}\gamma_{zs} \\ N_s &= B_{12}\varepsilon_z + B_{22}\varepsilon_s + B_{24}\gamma_{zs} \\ N_{zs} &= B_{14}\varepsilon_z + B_{24}\varepsilon_s + B_{44}\gamma_{zs} \end{aligned} \tag{10.96}$$

As earlier, we assume that $N_s = 0$. Under this condition, Eqs. (10.96) reduce to

$$N_z = B_z\varepsilon_z + B_{zs}\gamma_{zs}, \quad N_{zs} = B_{zs}\varepsilon_z + B_s\gamma_{zs} \tag{10.97}$$

where

$$B_z = B_{11} - \frac{B_{12}^2}{B_{22}}, \quad B_{zs} = B_{14} - \frac{B_{12}B_{24}}{B_{22}}, \quad B_s = B_{44} - \frac{B_{24}^2}{B_{22}} \tag{10.98}$$

Note that Eqs. (10.98) correspond to those beams with absolutely compliant cross-sectional contour for which the axial stiffness is specified by Eq. (10.24). For beams whose contour is absolutely rigid in its plane, Eq. (10.25) is generalized as

$$B_z = B_{11}, \quad B_{zs} = B_{14}, \quad B_s = B_{44} \tag{10.99}$$

To determine the normal stress resultant N_z, we express the shear strain from the second equation of Eqs. (10.97) as

$$\gamma_{zs} = \frac{N_{zs}}{B_s} - \varepsilon_z \frac{B_{zs}}{B_s} \tag{10.100}$$

and substitute it into the first equation to get

$$N_z = B_n \varepsilon_z + b_n N_{zs} \tag{10.101}$$

where

$$B_n = B_z - \frac{B_{zs}^2}{B_s}, \quad b_n = \frac{B_{zs}}{B_s} \tag{10.102}$$

Substituting the axial strain

$$\varepsilon_z = U_z' + x_e \Theta_y' + y_e \Theta_x' \tag{10.103}$$

into Eq. (10.101), we arrive at

$$N_z = B_n \left(U_z' + x_e \Theta_y' + y_e \Theta_x' \right) + b_n N_{zs} \tag{10.104}$$

In contrast to Eq. (10.26) for the orthotropic beam, the normal stress resultant N_z depends on the shear stress resultant N_{zs}. Using, as earlier, Eqs. (10.27) for the integral force and moments, we get the following equations analogous to Eqs. (10.28):

$$\begin{aligned} S U_z' + S_x \Theta_x' + S_y \Theta_y' &= P_{zn} \\ S_x U_z' + D_x \Theta_x' + D_{xy} \Theta_y' &= H_{xn} \\ S_y U_z' + D_{xy} \Theta_x' + D_y \Theta_y' &= H_{yn} \end{aligned} \tag{10.105}$$

in which

$$P_{zn} = P_z - \int_s b_n N_{zs} ds, \quad H_{xn} = H_x - \int_s b_n N_{zs} y_e ds, \quad H_{yn} = H_y - \int_s b_n N_{zs} x_e ds \tag{10.106}$$

The solution of Eqs. (10.105) is similar to Eqs. (10.30) and (10.32), i.e.,

$$\Theta_x' = \frac{k}{D_x^0}\left(\overline{H}_{xn} - n_y\overline{H}_{yn}\right)$$

$$\Theta_y' = \frac{k}{D_y^0}\left(\overline{H}_{yn} - n_x\overline{H}_{xn}\right) \tag{10.107}$$

$$U_z' = \frac{P_{zn}}{S} - \left(x_0\Theta_y' + y_0\Theta_x'\right)$$

where

$$\overline{H}_{xn} = H_{xn} - y_0P_{zn}, \quad \overline{H}_{yn} = H_{yn} - x_0P_{zn},$$

where k, D, and n and x_0 and y_0 are specified by Eqs. (10.33) and (10.31) if we change B to B_n. Substituting Eqs. (10.107) into Eq. (10.104), we have the following equation for the normal stress resultant:

$$N_z = B_n\left[\frac{P_{zn}}{S} + k\left(\frac{\overline{H}_{xn}}{D_x^0}\,\overline{y} + \frac{\overline{H}_{yn}}{D_y^0}\,\overline{x}\right)\right] + b_nN_{zs} \tag{10.108}$$

Here $\overline{x}$ and $\overline{y}$ are specified by Eqs. (10.36). Note that N_z depends on N_{zs} which enters Eq. (10.108) directly and also through P_{zn}, H_{xn}, and H_{yn} as per Eqs. (10.106). Thus, to determine N_z we need to find N_{zs}. To determine the shear stress resultant N_{zs}, apply, as earlier, the equilibrium equation in Eqs. (10.21). It follows from this equation that we need to differentiate Eq. (10.108) with respect to z. However, the second equation of Eqs. (10.21) shows that N_{zs} does not depend on z. This means that after differentiation with respect to z, all the terms with N_{zs} in Eq. (10.108) disappear and the result following from Eqs. (10.21) is

$$\frac{\partial N_{zs}}{\partial s} = -\frac{\partial N_z}{\partial_z} = -B_n\left[\frac{P_z'}{S} + k\left(\frac{\overline{H}_x'}{D_x^0}\,\overline{y} + \frac{\overline{H}_y'}{D_y^0}\,\overline{x}\right)\right] \tag{10.109}$$

where

$$\overline{H}_x = H_x - y_0P_z, \quad \overline{H}_y = H_y - x_0P_z$$

Integration of Eq. (10.109) with respect to z results in Eq. (10.43) and the final expression for N_{zs} coincides with Eq. (10.53) corresponding to the orthotropic beam, i.e.,

$$N_{zs} = Q_xF_x(s) + Q_yF_y(s) + \frac{T_z}{2A} \tag{10.110}$$

in which $F_x(s)$ and $F_y(s)$ are specified by Eqs. (10.54). Now, having found N_{zs}, we can return to Eq. (10.108) for the normal stress resultant and present the final expression as

$$N_z = B_n\left[\frac{P_z}{S} + k\left(\frac{\overline{H}_x}{D_x^0}\,\overline{y} + \frac{\overline{H}_y}{D_y^0}\,\overline{x}\right)\right] + Q_x\Phi_x(s) + Q_y\Phi_y(s) + \frac{T_z}{2A}\Phi(s) \tag{10.111}$$

where

$$\Phi_x(s) = b_n F_x(s) - \frac{B_n}{S}\int_s b_n F_x(s)ds - \frac{B_n k\bar{y}}{D_x^0}\int_s b_n F_x(s)(y_e - y_0)ds - \frac{B_n k\bar{x}}{D_y^0}\int_s b_n F_x(s)(x_e - x_0)ds$$

$$\Phi_y(s) = b_n F_y(s) - \frac{B_n}{S}\int_s b_n F_y(s)ds - \frac{B_n k\bar{y}}{D_x^0}\int_s b_n F_y(s)(y_e - y_0)ds - \frac{B_n k\bar{x}}{D_y^0}\int_s b_n F_y(s)(x_e - x_0)ds$$

$$\Phi(s) = b_n - \frac{B_n}{S}\int_s b_n ds - \frac{B_n k\bar{y}}{D_x^0}\int_s b_n(y_e - y_0)ds - \frac{B_n k\bar{x}}{D_y^0}\int_s b_n(x_e - x_0)ds$$

Thus, normal and shear stress resultants acting in anisotropic beams are specified by Eqs. (10.110) and (10.111).

To determine the displacements of anisotropic thin-walled beams, we can apply the approach described in Section 10.4.4. In-plane displacements of the beam cross section can be found, as earlier, from Eqs. (10.63), i.e.,

$$U_x = U_x^0 + \int_0^z (\Gamma_x - \Theta_y)dz, \quad U_y = U_y^0 + \int_0^z (\Gamma_y - \Theta_x)dz \tag{10.112}$$

To proceed, apply, as earlier, Castigliano's theorem. Consider a beam shown in Fig. 10.19 whose length is $l = dz$. Assume that the beam is loaded at the free end with forces P_z, Q_x, and Q_y and moments H_x, H_y, and T_z as in Fig. 10.11. Then, in accordance with Castigliano's theorem,

$$\begin{aligned} d\Theta_x &= \frac{\partial}{\partial H_x}(dW_\sigma), \quad d\Theta_y = \frac{\partial}{\partial H_y}(dW_\sigma), \quad dU_z = \frac{\partial}{\partial P_z}(dW_\sigma) \\ \Gamma_x dz &= \frac{\partial}{\partial Q_x}(dW_\sigma), \quad \Gamma_y dz = \frac{\partial}{\partial Q_y}(dW_\sigma), \quad d\Theta_z = \frac{\partial}{\partial T_z}(dW_\sigma) \end{aligned} \tag{10.113}$$

Here, the strain energy of the beam element with length dz is

$$dW_\sigma = \frac{dz}{2}\int_s (N_z\varepsilon_z + N_{zs}\gamma_{zs})ds \tag{10.114}$$

Express the normal and the shear strains in terms of the corresponding stress resultants using Eqs. (10.100) and (10.101), i.e.,

$$\varepsilon_z = \frac{1}{B_n}(N_z - b_n N_{zs}), \quad \gamma_{zs} = \frac{1}{B_n}(a_n N_{zs} - b_n N_z) \tag{10.115}$$

Here, B_n and b_n are specified by Eqs. (10.102) and

$$a_n = \frac{B_z}{B_s} \tag{10.116}$$

Substituting the strains from Eqs. (10.115) into the expression for the strain energy, Eq. (10.114), we get

$$dW_\sigma = \frac{dz}{2}\int_s \frac{1}{B_n}(N_z^2 - 2b_n N_z N_{zs} + a_n N_{zs}^2)ds$$

In the right-hand part of this equation the stress resultants N_z and N_{zs} should be expressed in terms of the forces P_z, Q_x, and Q_y and moments H_x, H_y, and T_z with the aid of Eqs. (10.111) and (10.110). Then, Eqs. (10.113) can be presented in the following explicit form (Johnson et al., 2001):

$$\begin{bmatrix} \Theta_x' \\ \Theta_y' \\ U_z' \\ \Gamma_x \\ \Gamma_y \\ \Theta_z' \end{bmatrix} = \begin{bmatrix} c_{11} & c_{12} & c_{13} & c_{14} & c_{15} & c_{16} \\ c_{21} & c_{22} & c_{23} & c_{24} & c_{25} & c_{26} \\ c_{31} & c_{32} & c_{33} & c_{34} & c_{35} & c_{36} \\ c_{41} & c_{42} & c_{43} & c_{44} & c_{45} & c_{46} \\ c_{51} & c_{52} & c_{53} & c_{54} & c_{55} & c_{56} \\ c_{61} & c_{62} & c_{63} & c_{64} & c_{65} & c_{66} \end{bmatrix} \begin{bmatrix} H_x \\ H_y \\ P_z \\ Q_x \\ Q_y \\ T_z \end{bmatrix} \tag{10.117}$$

where

$$\begin{aligned}
&c_{11} = \frac{k}{D_x^0}, \quad c_{12} = c_{21} = -k\frac{n_y}{D_x^0} = -k\frac{n_x}{D_y^0}, \quad c_{13} = c_{31} = -\frac{k}{D_x^0}y_0 + \frac{kn_x}{D_y^0}x_0 = -\frac{k}{D_x^0}y_0 + \frac{kn_y}{D_x^0}x_0 \\
&c_{14} = c_{41} = -\frac{k}{D_x^0}\int_s b_n F_x(s)\bar{y}ds, \quad c_{15} = c_{51} = -\frac{k}{D_x^0}\int_s b_n F_y(s)\bar{y}ds, \quad c_{16} = c_{61} = -\frac{k}{2AD_x^0}\int_s b_n\bar{y}ds \\
&c_{22} = \frac{k}{D_y^0}, \quad c_{23} = c_{32} = -\frac{k}{D_y^0}x_0 + \frac{kn_y}{D_x^0}y_0 = -\frac{k}{D_y^0}x_0 + \frac{kn_x}{D_y^0}y_0 \\
&c_{24} = c_{42} = -\frac{k}{D_y^0}\int_s b_n F_x(s)\bar{x}ds, \quad c_{25} = c_{52} = -\frac{k}{D_y^0}\int_s b_n F_y(s)\bar{x}ds, \\
&c_{26} = c_{62} = -\frac{k}{2AD_y^0}\int_s b_n\bar{x}ds, \quad c_{33} = \frac{1}{S} + \frac{k}{D_x^0}\left(y_0^2 - n_y x_0 y_0\right) + \frac{k}{D_y^0}\left(x_0^2 - n_x x_0 y_0\right) \\
&c_{34} = c_{43} = -\frac{1}{S}\int_s b_n F_x(s)ds + \frac{ky_0}{D_x^0}\int_s b_n F_x(s)\bar{y}ds + \frac{kx_0}{D_y^0}\int_s b_n F_x(s)\bar{x}ds \\
&c_{35} = c_{53} = -\frac{1}{S}\int_s b_n F_y(s)ds + \frac{kx_0}{D_y^0}\int_s b_n F_y(s)\bar{x}ds + \frac{ky_0}{D_x^0}\int_s b_n F_y(s)\bar{y}ds \\
&c_{36} = c_{63} = -\frac{1}{2AS}\int_s b_n ds, \quad c_{44} = \int_s \frac{1}{B_n}\left[\Phi_x^2(s) - 2b_n F_x(s)\Phi_x(s) + a_n F_x^2(s)\right]ds \\
&c_{45} = c_{54} = \int_s \frac{1}{B_n}\left[\Phi_x(s)\Phi_y(s) - b_n F_x(s)\Phi_y(s) - b_n\Phi_x(s)F_y(s) + a_n F_x(s)F_y(s)\right]ds \\
&c_{46} = c_{64} = \frac{1}{2A}\int_s \frac{1}{B_n}\left[\Phi(s)\Phi_x(s) - b_n\Phi(s)F_x(s) - b_n\Phi_x(s) + a_n F_x(s)\right]ds \\
&c_{55} = \int_s \frac{1}{B_n}\left[\Phi_y^2(s) - 2b_n F_y(s)\Phi_y(s) + a_n F_y^2(s)\right]ds \\
&c_{56} = c_{65} = \frac{1}{2A}\int_s \frac{1}{B_n}\left[\Phi(s)\Phi_y(s) - b_n\Phi(s)F_y(s) - b_n\Phi_y(s) + a_n F_y(s)\right]ds \\
&c_{66} = \frac{1}{4A^2}\int_s \frac{1}{B_n}\left[\Phi^2(s) - 2b_n\Phi + a_n\right]ds
\end{aligned} \tag{10.118}$$

The following equations, which can be checked by direct integration, have been used to derive Eqs. (10.118):

$$\int_s B_n\bar{x}ds = 0, \quad \int_s B_n\bar{y}ds = 0, \quad \int_s B_n\bar{x}^2ds = \frac{1}{k}D_y^0, \quad \int_s B_n\bar{y}^2ds = \frac{1}{k}D_x^0$$
$$\int_s B_n\bar{x}\,\bar{y}ds = -\frac{n_y}{k}D_y^0 = -\frac{n_x}{k}D_x^0, \quad \int_s \Phi(s)ds = 0$$
$$\int_s \Phi(s)\bar{x}ds = 0, \quad \int_s \Phi(s)\bar{y}ds = 0, \quad \int_s \Phi_x(s)ds = 0, \quad \int_s \Phi_x(s)\bar{x}ds = 0$$
$$\int_s \Phi_x(s)\bar{y}ds = 0, \quad \int_s \Phi_y(s)ds = 0, \quad \int_s \Phi_y(s)\bar{x}ds = 0, \quad \int_s \Phi_y(s)\bar{y}ds = 0$$

The matrix in the right-hand part of Eq. (10.117) is symmetric and contains 21 independent coefficients c_{mn}, 15 of which are located on both sides of the main diagonal and correspond to various coupling effects. Some of these effects can be eliminated by the relevant choice of coordinate frame (x, y). For example, if the beam's cross section is referred to the axes which are analogous to central and principal axes, $x_0 = y_0 = 0$ and $n_x = n_y = 0$. As a result, $c_{12} = 0$, $c_{13} = 0$, and $c_{23} = 0$ and the coupling between axial loading and bending disappears. The other 12 coupling coefficients depend on the beam material characteristics and correspond to the following coupling effects:

- Coupling between bending and shear (c_{14}, c_{45}, c_{24}, c_{25})
- Coupling between bending and torsion (c_{12}, c_{26})
- Coupling between axial loading and shear (c_{36})
- Coupling between torsion and transverse shear (c_{46}, c_{56})
- Coupling between transverse shear deformations in the xz- and yz-planes (c_{45})

As the first example, consider the beam with a circular cross section shown in Fig. 10.21. In accordance with Section 10.4.6, we have

$$x_e = R\,\sin\beta, \quad y_e = R\cos\beta, \quad s = R\beta, \quad S = 2\pi RB_n, \quad A = \pi R^2$$
$$D = D_x^0 = D_y^0 = \pi B_n R^3, \quad F_x(s) = \frac{B_n R^2}{D}\cos\beta, \quad F_y(s) = -\frac{B_n R^2}{D}\sin\beta$$

For a circular beam whose stiffness coefficients do not depend on the contour coordinate, Eqs. (10.117) reduce to

$$\begin{aligned} \Theta_x' &= c_{11}H_x + c_{14}Q_x, \quad \Gamma_x = c_{41}H_x + c_{44}Q_x \\ \Theta_y' &= c_{22}H_y + c_{25}Q_y, \quad \Gamma_y = c_{52}H_y + c_{55}Q_y \\ U_z' &= c_{33}P_z + c_{36}T_z, \quad \Theta_z' = c_{63}P_z + c_{66}T_z \end{aligned} \tag{10.119}$$

where

$$c_{11} = c_{22} = \frac{1}{\pi R^3 B_n}, \quad c_{14} = c_{41} = -c_{25} = -c_{52} = -\frac{b_n}{\pi R^2 B_n}$$
$$c_{33} = \frac{1}{2\pi RB_n}, \quad c_{36} = c_{63} = -\frac{b_n}{2\pi R^2 B_n}, \quad c_{44} = c_{55} = \frac{a_n}{\pi RB_n}$$
$$c_{66} = \frac{a_n}{2\pi R^2 B_n}$$

Consider the carbon-epoxy circular beam experimentally studied by Nixon (1987). The beam has radius $R = 20.83$ mm and thickness $h = 1.016$ mm and is composed of two unidirectional layers with angles $\phi_1 = 20^\circ$ and $\phi_2 = 70^\circ$. The thicknesses of both layers are the same and the properties of material are $E_1 = 147.1$ GPa, $E_2 = 11$ GPa, $G_{12} = 6.4$ GPa, $\nu_{12} = 0.028$, and $\nu_{21} = 0.38$. The membrane stiffness coefficients of the beam wall are specified by Eqs. (4.72), (5.53), and (5.45), according to which

$$B_{11} = B_{22} = 68.3 \text{ MN/m}, \quad B_{12} = 17.6 \text{ MN/m}, \quad B_{44} = 19.8 \text{ MN/m}$$
$$B_{14} = B_{24} = -17.6 \text{ MN/m}$$

Then, Eqs. (10.98), (10.102), and (10.116) yield

$$B_z = 63.8 \text{ MN/m}, \quad B_{zs} = -16.8 \text{ MN/m}, \quad B_s = 12.4 \text{ MN/m}$$
$$B_n = 41.1 \text{ MN/m}, \quad b_n = -1.355, \quad a_n = 5.16$$

Let the beam be loaded by an axial force $P_z = P$, transverse shear force $Q_y = Q$, and torque $T_z = T$ as shown in Fig. 10.35.

First, consider the coupling between axial loading and torsion, taking $Q = 0$. Then, the corresponding equations of Eqs. (10.119) become

$$U_z' = c_{33}P + c_{36}T, \quad \Theta_z' = c_{63}P + c_{66}T \tag{10.120}$$

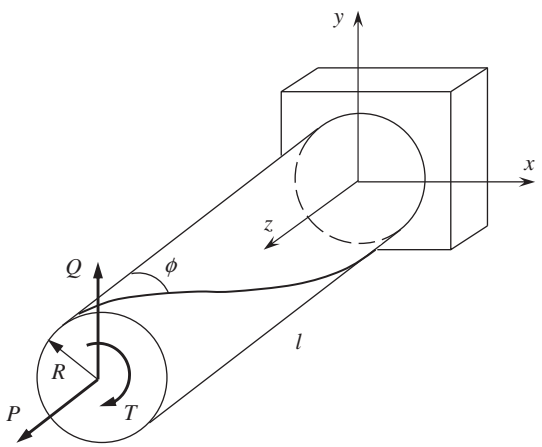


FIGURE 10.35

A cantilever circular anisotropic beam loaded with the axial force, the transverse force, and the torque.

The coefficient $c_{36} = c_{63}$ allows for coupling between tension and torsion. For the beam under consideration, the second equation of Eq. (10.120) takes the form

$$\Theta_z' = (0.121P + 2.21T)10^{-3} \text{ rad/m}$$

The dependence of Θ_z' on T for $P = 0$ (pure torsion) is shown in Fig. 10.36 with line 1, whereas the same function for $P = 4.45\ kN$ (torsion with pre-tensioning) is shown with line 2. The dots correspond to the experimental results (Nixon, 1987).

Consider the bending of a beam loaded with transverse force Q (see Fig. 10.35) which causes the bending moment

$$H = -Q(l - z) \tag{10.121}$$

The corresponding equations of Eqs. (10.119) are

$$\Theta_x' = c_{11}H, \quad \Gamma_y = c_{55}Q, \quad \Theta_y' = c_{25}Q, \quad \Gamma_x = c_{41}H \tag{10.122}$$

It follows from these equations that the beam bending in plane yz (see Fig. 10.35) caused by force Q is accompanied by bending in the orthogonal plane xz. Integrating Eqs. (10.122) with allowance for Eq. (10.121) and substituting the results in Eq. (10.112), we get for the beam shown in Fig. 10.35

$$\overline{U}_y = a_n\overline{z} + \frac{l^2}{2R^2}\left(\overline{z}^2 - \frac{1}{3}\overline{z}^3\right), \quad \overline{U}_x = b_n\overline{z}$$

where

$$\overline{U}_y = \frac{\pi RB_n}{Ql}U_y, \quad \overline{U}_x = \frac{\pi RB_n}{Ql}, \quad \overline{z} = \frac{z}{l}$$

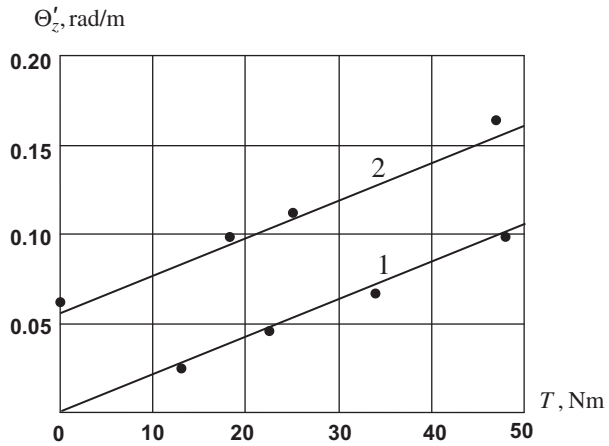


FIGURE 10.36

Dependencies of the angle of twist per unit length of the beam on torque for pure torsion (1) and for the torsion combined with the axial loading by the force P = 4.45 kN (2); (————) analysis and (••••) experiment (Nixon, 1987).

As can be seen, the deflection $\overline{U}_x(\overline{z})$ is a linear function of $\overline{z}$ which means that this deflection is caused by transverse shear. To explain this effect, note that under bending the upper part of the beam shown in Fig. 10.35 is compressed, whereas its lower part experiences tension. However, the tension and compression are coupled with the shear, and because both the loading and the material structure are antisymmetric (at $y = R$ the fibers cross the beam meridian going from the left to the right part, whereas at $y = -R$ they cross the meridian from the right side to the left), the shear deformations at $y > 0$ and $y < 0$ are of the same sign and induce bending of the beam.

Thus, it follows from the foregoing results that anisotropic thin-walled beams with mechanical properties that do not change along the cross-sectional contour demonstrate coupling between axial deformation and torsion and also coupling between bending in two orthogonal planes.

As the second example, consider a beam with a rectangular cross section (see Fig. 10.25) whose stiffness coefficients do not depend on the contour coordinate. Such beams, similarly to the circular beams discussed earlier, are described by Eqs. (10.119) in which

$$
\begin{aligned}
&c_{11} = \frac{1}{D_x},\ c_{22} = \frac{1}{D_y},\ c_{33} = \frac{1}{S},\ c_{14} = c_{41} = -\frac{1}{D_x}\int_s b_n F_x(s) y ds \\
&c_{25} = c_{52} = -\frac{1}{D_y}\int_s b_n F_y(s) x ds, \quad c_{44} = \int_s \frac{1}{B_n}\left[\Phi_x^2(s) - 2b_n F_x(s)\Phi_x(s) + a_n F_x^2(s)\right] ds \\
&c_{55} = \int_s \frac{1}{B_n}\left[\Phi_y^2(s) - 2b_n F_y(s)\Phi_y(s) + a_n F_y^2(s)\right] ds \\
&c_{36} = c_{63} = -\frac{1}{2AS}\int_s b_n ds, \quad c_{66} = \frac{1}{4A^2}\int_s \frac{1}{B_n}\left[\Phi^2(s) - 2b_n\Phi(s) + a_n\right] ds
\end{aligned}
\tag{10.123}
$$

Beams with rectangular cross sections experimentally studied by Smith and Chopra (1990) and Chandra et al. (1990) have the following dimensions (see Fig. 10.25):

$$
a = 24.2 \text{ mm}, \quad b = 13.6 \text{ mm}, \quad h = 0.76 \text{ mm}, \quad l = 762 \text{ mm} \tag{10.124}
$$

and are made of carbon-epoxy composite material with $E_1 = 142$ GPa, $E_2 = 9.8$ GPa, $G_{12} = 6$ GPa, $\nu_{12} = 0.029$, and $\nu_{21} = 0.42$.

Consider a beam whose flanges and webs are reinforced at one and the same angle, $\phi = 15°$(see Fig. 10.37a). To demonstrate the material structure, it is useful to plot the development of the beam surface as shown in Fig. 10.37b. For $\phi_1 = 15°$ and $h_1 = h$, the wall stiffness coefficients are

$$
\begin{aligned}
&B_{11} = 96.7 \text{ MN/m}, \quad B_{22} = 8.6 \text{ MN/m} \quad B_{12} = 8.95 \text{ MN/m}, \quad B_{14} = 22.7 \text{ MN/m} \\
&B_{24} = 2.74 \text{ MN/m}, \quad B_{44} = 10.3 \text{ MN/m} \\
&B_z = 87.2 \text{ MN/m}, \quad B_{zs} = 19.8 \text{ MN/m}, \quad B_s = 9.44 \text{ MN/m} \\
&B_n = 45.6 \text{ MN/m}, \quad b_n = 2.1, \quad a_n = 9.24
\end{aligned}
$$

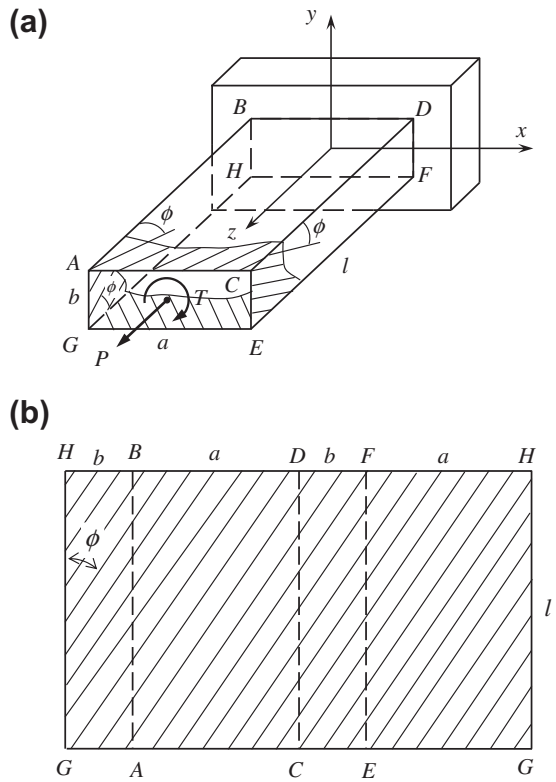


FIGURE 10.37

A beam with a rectangular cross section reinforced at angle ϕ (a) and the development of its surface (b).

For a beam loaded with axial force $P_z = P$ and torque $T_z = T$ (see Fig. 10.37a), the last equation of Eqs. (10.119) takes the following form:

$$\Theta_z' = c_{63}P + c_{66}T \tag{10.125}$$

where

$$c_{63} = -\frac{b_n}{2abB_n}, \quad c_{66} = \frac{(a+b)a_n}{2a^2b^2B_n}$$

For the experimental beam under study,

$$\Theta_z = (-0.0533P + 27.2T)10^{-3}\,\bar{z}$$

where, as earlier, $\bar{z} = z/l$. The calculated (solid line) and experimental (dots) values $\Theta_z(\bar{z})$ for $P = 4.45$ kN and $T = 0$ are shown in Fig. 10.38.

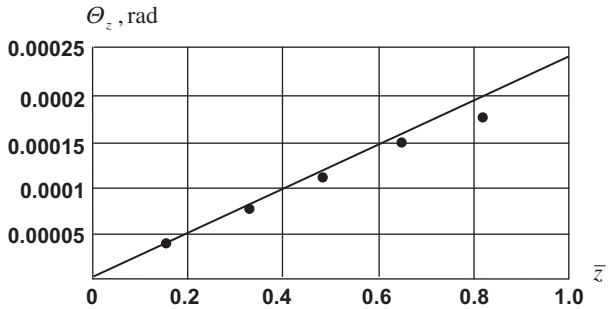


FIGURE 10.38

Dependence of the angle of twist on the axial coordinate for the beam loaded with axial force $P = 4.45$ N: analysis (————) and experiment (••••) (Chandra et al., 1990).

Consider the warping of the cross section of an anisotropic beam under tension and torsion. For such beams, Eqs. (10.119) and (10.125) yield

$$\Gamma_x = 0, \quad \Gamma_y = 0, \quad \Theta_z' = \frac{1}{2abB_n}\left(\frac{a_n}{b_n}T - b_nP\right)$$

The shear strain following from the strain-displacement equations, Eqs. (10.13), (10.17), and (10.19) for the beam under study, is

$$\gamma_{zs} = r\Theta_z' + \dot{\Psi}(s) = \frac{r}{2abB_n}\left(\frac{a_n}{b_n}T - b_nP\right) + \dot{\Psi}(s) \tag{10.126}$$

The radius r for the rectangular cross section is presented in Section 10.4.6. On the other hand, the second constitutive equation of Eqs. (10.115) yields

$$\gamma_{zs} = \frac{1}{B_n}(a_nN_{zs} - b_nN_z) \tag{10.127}$$

where in accordance with Eqs. (10.110) and (10.111)

$$N_{zs} = \frac{T}{2ab}, \quad N_z = \frac{P}{2(a+b)}$$

Equating the right-hand parts of Eqs. (10.126) and (10.127) and integrating with respect to s, we get

$$\Psi(s) = \frac{1}{2B_n}\left(\frac{a_nT}{ab} - \frac{b_nP}{a+b}\right)\left(s - \frac{a+b}{ab}\int_0^s rds\right)$$

The function $\Psi(s)$ is similar to that shown in Fig. 10.29. Note that if

$$P = \frac{a_nT}{abB_n}(a+b), \tag{10.128}$$

we have $\Psi = 0$, i.e., applying the axial force proportional to the torque in accordance with Eq. (10.128), we can eliminate the warping of the rectangular cross section of an anisotropic beam.

Consider a more complicated composite structure, i.e., a beam whose upper and lower flanges are reinforced at angles of 15° and −15°, respectively, whereas the webs are orthotropic and have a $\pm\phi$ angle-ply structure. Thus, for the upper flange *ABDC* (see Fig. 10.39a) we must take $k = 1$, $\phi_1 = 15°$, and $h_1 = h$; for the lower flange *GHFE* $k = 1$, $\phi_2 = -15°$, and $h_2 = h$; and for the webs *ABHG* and *CDFE* $k = 2$, $\phi_1 = 15°$, $\phi_2 = -15°$, and $h_1 = h_2 = h/2$. The development of the beam surface is shown in Fig. 10.39b.

The stiffness coefficients of the beam walls are presented in Table 10.1.

For a beam loaded with forces P_z, Q_x, and Q_y and moments H_x, H_y, and T_z, Eqs. (10.117) reduce to

$$\begin{aligned} \Theta_x' &= c_{11}H_x + c_{16}T_z, \quad \Gamma_x = c_{43}P_z + c_{44}Q_x \\ \Theta_y' &= c_{22}H_y, \quad \Gamma_y = c_{55}Q_y \\ U_z' &= c_{33}P_z + c_{34}Q_x, \quad \Theta_z' = c_{61}H_x + c_{66}T_z \end{aligned} \tag{10.129}$$

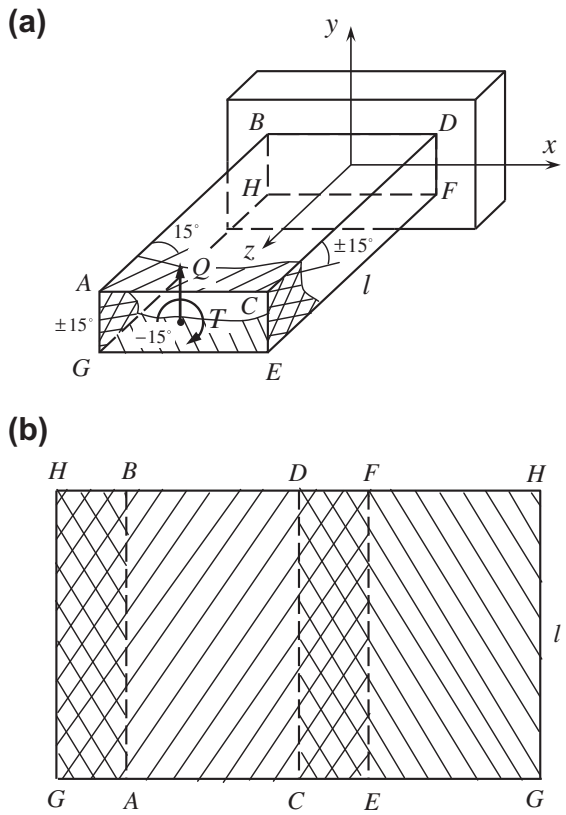


FIGURE 10.39

A beam with a rectangular cross section (a) and the development of its surface (b) showing the material structure.

TABLE 10.1 Stiffness Coefficients of the Beam Walls (see Fig. 10.39)

Stiffness Coefficient	Upper Flange ABDC	Lower Flange GHFE	Webs ABHG CDFE
B_{11}, MN/m	96.7	96.7	96.7
B_{12}, MN/m	8.95	8.95	8.95
B_{22}, MN/m	8.6	8.6	8.6
B_{44}, MN/m	10.3	10.3	10.3
B_{14}, MN/m	22.7	−22.7	0
B_{24}, MN/m	2.74	−2.74	0
B_z, MN/m	87.2	87.2	87.2
B_{zs}, MN/m	19.8	−19.8	0
B_s, MN/m	9.44	9.44	10.3
B_n, MN/m	45.6	45.6	87.2
b_n	2.1	−2.1	0
a_n	9.24	9.24	8.45

in which

$$C_{11} = \frac{1}{D_x}, \quad c_{22} = \frac{1}{D_y}, \quad c_{33} = \frac{1}{S}, \quad c_{34} = c_{43} = -\frac{1}{S}\int_s b_n F_x(s) y ds$$

$$c_{44} = \int_s \frac{1}{B_n}\left[\Phi_x^2(s) - 2b_n F_x(s)\Phi_x(s) + a_n F^2(s)\right] ds$$

$$c_{55} = \int_s \frac{1}{B_n}\left[\Phi_y^2(s) - 2b_n F_y(s)\Phi_y(s) + a_n F^2(s)\right] ds$$

$$c_{16} = c_{61} = \frac{1}{2AD_x}\int_s b_n y ds, \quad c_{66} = \frac{1}{4A^2}\int_s \frac{1}{B_n}\left[\Phi^2(s) - 2b_n\Phi(s) + a_n\right] ds$$

It follows from Eqs. (10.129) and Table 10.1 that the coefficient b_n, which has different signs for the upper and the lower flanges, gives rise to the stiffness coefficient $c_{16} = c_{61}$ which provides coupling between bending and torsion of the beam.

Consider the beam bending with force $Q_y = Q$ (see Fig. 10.39a) for which Eqs. (10.129) yield

$$\Theta_x' = -c_{11}Q(l - z), \quad \Gamma_y = c_{55}Q, \quad \Theta_z' = -c_{61}Q(l - z)$$

For the beam with dimensions specified by Eqs. (10.124), the last of these equations allows us to find the angle of twist as follows:

$$\Theta_z = 0.0044Q\left(\overline{z} - \frac{\overline{z}^2}{2}\right)$$

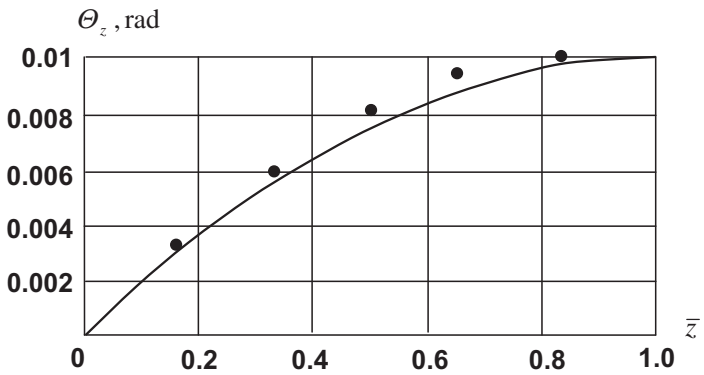


FIGURE 10.40

Dependence of the angle of twist on the axial coordinate for the beam loaded with transverse shear force $Q = 4.45$ N: analysis (————) and experiment (••••) (Smith and Chopra, 1990).

where $\overline{z} = z/l$. The function $\Theta_z(\overline{z})$ corresponding to this equation is shown in Fig. 10.40 by the solid line along with the experimental results (dots).

The torsion of the beam by torque T (see Fig. 10.39a) is accompanied by bending. The corresponding equations of Eqs. (10.129) describing this effect are

$$\Theta_x' = c_{16}T, \quad \Theta_z' = c_{66}T$$

Then, the slope of the beam deflection is

$$U_y' = \Gamma_y - \Theta_x = 0.0058T\overline{z}$$

For $T = 0.113$ Nm , the function $U_y'(\overline{z})$ is shown in Fig. 10.41 (line) along with the experimental results (dots).

10.4.9 Beams stiffened with axial ribs

We now return to orthotropic beams and consider those beams which are stiffened with axial ribs as shown in Fig. 10.42. Assume that the cross-sectional area of the rib with number "i" is a_i, its modulus is E_i, and coordinates of the rib center are x_i, y_i, and s_i (see Fig. 10.42). Introduce the reduction coefficient as follows:

$$r_i = \frac{E_i}{E_0} \tag{10.130}$$

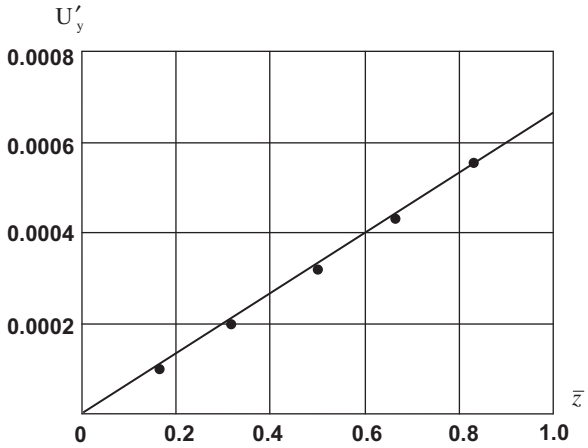


FIGURE 10.41

Dependence of the deflection slope on the axial coordinate for the beam loaded with torque T = 0.113 Nm: (————) analysis and (••••) experiment (Chandra et al., 1990).

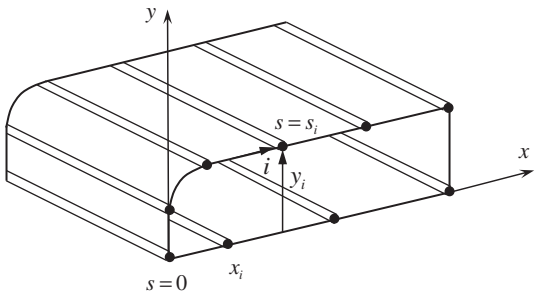


FIGURE 10.42

Thin-walled beam stiffened with axial ribs.

in which E_0 is the axial modulus of the skin. Then the stiffness coefficients of the beam cross section specified by Eqs. (10.29) are generalized as

$$\begin{aligned} S_r &= S + E_0 \sum_i r_i a_i, \quad S_{xr} = S_x + E_0 \sum_i r_i a_i y_i \\ S_{yr} &= S_y + E_0 \sum_i r_i a_i x_i, \quad D_{xr} = D_x + E_0 \sum_i r_i a_i y_i^2 \\ D_{yr} &= D_y + E_0 \sum_i r_i a_i x_i^2, \quad D_{xyr} = D_{xy} + E_0 \sum_i r_i a_i x_i y_i \end{aligned} \tag{10.131}$$

where

$$S = \int_s B_0 ds, \quad S_x = \int_s B_0 y_e ds, \quad S_y = \int_s B_0 x_e ds$$
$$D_x = \int_s B_0 y_e^2 ds, \quad D_y = \int_s B_0 x_e^2 ds, \quad D_{xy} = \int_s B_0 x_e y_e ds \tag{10.132}$$

are the stiffness coefficients of the skin, whereas B_0 is the axial stiffness of the skin. The skin modulus in Eq. (10.130) is $E_0 = B_0/h_0$, where h_0 is the skin thickness.

The axial stress resultant in the skin and the stresses in the ribs can be determined with the aid of equations analogous to Eqs. (10.34) and (10.35), i.e.,

$$N_z^s = B_0 \left[\frac{P_z}{S_r} + k \left(\frac{\overline{H}_x}{D_{xr}^0} \overline{y} + \frac{\overline{H}_y}{D_{yr}^0} \overline{x} \right) \right] \tag{10.133}$$

$$\sigma_r^{(i)} = E_i \left[\frac{P_z}{S_r} + k \left(\frac{\overline{H}_x}{D_{xr}^0} \overline{y}_i + \frac{\overline{H}_y}{D_{yr}^0} \overline{x}_i \right) \right] \tag{10.134}$$

Here, D_r^0, $\overline{x}$, and $\overline{y}$ are specified by equations which are similar to Eqs. (10.33) and (10.36). The shear stress resultant in the skin is specified by Eq. (10.53) in which the functions $\overline{S}(s)$ in Eqs. (10.45) allow for the skin's and the ribs' axial stiffnesses.

To demonstrate the procedure, consider the circular thin-walled beam with radius $R = 1000$ mm whose cross section is shown in Fig. 10.43a. The structure consists of a quasi-isotropic carbon-epoxy skin with modulus $E_0 = 70$ GPa and thickness $h_0 = 1$ mm, a system of L-beam stringers with the same modulus and cross-sectional area $a_i = a = 200$ mm^2 $(i = 1, 2, 3 \ldots 6)$, and a keel I-beam longeron made of a high-modulus carbon fiber-reinforced composite with a modulus of elasticity of 210 GPa and a cross-sectional area of 1000 mm^2. Because the cross section is symmetric with respect to the y-axis, we can consider only one half of it. The stringers and longeron are shown with dots and circles, respectively, in Fig. 10.43b. Due to the symmetry of the cross section, stringer 1 and longeron 7

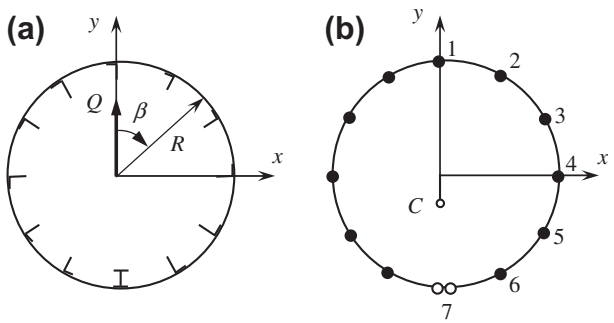


FIGURE 10.43

Actual cross section (a) and the corresponding thin-walled beam model (b).

are split into two equal parts since they are equally partitioned between both halves of the cross section.

Applying Eqs. (10.132), we get

$$S = 2\pi RB_0, \quad S_x = 0, \quad D_x = \pi B_0 R^3$$

Introduce the normalized cross-sectional areas of the ribs as

$$\overline{a}_i = \frac{a_i}{Rh_0}$$

Then, for the ribs shown in Fig. 10.43b, we have

$$\overline{a}_1 = 0.1, \quad \overline{a}_2 = \overline{a}_3 = \overline{a}_4 = \overline{a}_5 = \overline{a}_6 = 0.2, \quad \overline{a}_7 = 0.5$$

Since the modulus of the skin and the stringers 1 to 6 is the same, Eq. (10.130) yields $r_i = 1$ for $i = 1, 2, 3, 4, 5, 6$, whereas for the longeron 7, $r_7 = 3$. Using Eqs. (10.131), we find

$$S_r = 2\pi RB_0 + 2B_s R(0.1 + 5 \cdot 0.2 + 3 \cdot 0.5) = 11.48B_0R$$

$$S_{xr} = 2B_0R^2[0.1 + 0.2(0.866 + 0.5 - 0.5 - 0.866) - 3 \cdot 0.5] = -2.8B_0R^2$$

$$D_{xr} = \pi R^3 B_0 + 2B_s R^3[0.1 + 0.2(0.75 + 0.25 + 0.25 + 0.75) + 3 \cdot 0.5)] = 7.14B_0R^3$$

The coordinate of the cross-sectional center (point C in Fig. 10.43b) is

$$y_0 = \frac{S_{xr}}{S_r} = -0.244R$$

The bending stiffness of the beam is

$$D_{xr}^0 = D_{xr} - y_0^2 S_r = 6.456B_0R^3$$

The axial stress resultant in the skin and the axial stresses in the ribs induced by the bending moment H_x acting in the beam cross section $z = constant$ are specified by Eqs. (10.133) and (10.134) which reduce to

$$N_z^s = B_0 \frac{H_x}{D_{xr}^0}(y - y_0), \quad \sigma_r^{(i)} = r_i E_0 \frac{H_x}{D_{xr}^0}(y_i - y_0)$$

For the beam under consideration,

$$\sigma_z^s = \frac{N_z^s}{h_0} = 0.155 \frac{H_x}{h_0 R^2}(\cos\beta + 0.279), \quad \sigma_r^{(i)} = 0.155 r_i \frac{H_x}{h_0 R^2}(\cos\beta_i + 0.279)$$

The distribution of the normalized stresses $\overline{\sigma} = (\sigma h_0 R^2)/H_x$ over the contour of the cross section is shown in Fig. 10.44. Note that at point 7 we have two values of stresses: $\overline{\sigma} = -0.11$ in the skin and $\overline{\sigma} = -0.33$ in the longeron whose modulus is three times higher. The dashed line in Fig. 10.44 shows the location of the beam neutral axis.

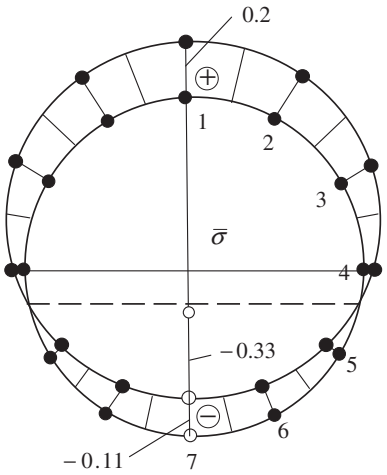


FIGURE 10.44

Distribution of the normalized axial stress $\bar{\sigma}$ over the beam cross-sectional contour.

We now determine the shear stress resultant acting in the skin. Since the beam does not experience torsion, $T_z = 0$ in Eq. (10.53) which yields

$$N_{zs} = -Q\frac{\overline{S}_{xr}(s)}{D^0_{xr}} \tag{10.135}$$

where

$$\overline{S}_{xr}(s) = \overline{S}_x(s) + \Delta\overline{S}_x \tag{10.136}$$

Here, $\overline{S}_x(s)$ corresponds to the skin and is specified by Eqs. (10.45), according to which

$$\overline{S}_x(s) = B\int_0^s (y - y_0)ds = B_0R^2(\sin\beta + 0.444\beta)$$

The second term in Eq. (10.136) corresponds to the stringers and has the following form:

$$\Delta\overline{S}_x = E_0\sum_i r_i a_i(y_i - y_0) = B_0R^2\sum_i r_i\overline{a}_i(\cos\beta_i + 0.244)$$

For the cross section shown in Fig. 10.43b, we get the following results:

At point 1 $(s = 0, \beta = 0)$ before the stringer (one half of its cross-sectional area) we have $\overline{S}^-_{xr}(0) = 0$ and after the stringer

$$\overline{S}^+_{xr}(0) = B_0R^2\overline{a}_1(1 + 0.244) = 0.1244B_0R^2$$

For part 1 – 2 $(0 \le s \le s_2, \quad 0 \le \beta \le \beta_2 = \pi/6)$

$$\overline{S}_{xr}(s) = \overline{S}_{xr}(0) + B_0R^2(\sin\beta + 0.2\beta)$$

At point 2 before the stringer $(s = s_2, \quad \beta = \beta_2)$

$$\overline{S}^{-}_{xr}(s_2) = B_0R^2\left(0.1244 + 0.5 + 0.244\frac{\pi}{6}\right) = 0.7521B_0R^2$$

At point 2 after the stringer $(s = s_2, \quad \beta = \beta_2)$

$$\overline{S}^{+}_{xr}(s_2) = 0.9741B_0R^2$$

For part 2 – 3 $(s_2 \le s \le s_3, \quad \pi/6 \le \beta \le \beta_3 = \pi/3)$

$$\overline{S}_{xr}(s) = B_0R^2[\overline{a}_1(1 + 0.244) + \overline{a}_2(\cos\beta_2 + 0.244) + \sin\beta + 0.244\beta]$$

$$= B_0R^2[0.3464 + \sin\beta + 0.244\beta]$$

At point 3 before the stringer $(s = s_3, \quad \beta = \beta_3)$

$$\overline{S}^{-}_{xr}(s_3) = B_0R^2\left(0.3464 + 0.866 + 0.244\frac{\pi}{3}\right) = 1.468B_0R^2$$

At point 3 after the stringer $(s = s_3, \quad \beta = \beta_3)$

$$\overline{S}^{+}_{xr}(s_3) = 1.617B_0R^2$$

For part 3 – 4 $(s_3 \le s \le s_4, \quad \pi/3 \le \beta \le \beta_4 = \pi/2)$

$$\overline{S}_{xr}(s) = B_0R^2[\overline{a}_1(1 + 0.244) + \overline{a}_2(\cos\beta_2 + 0.244) + \overline{a}_3(\cos\beta_3 + 0.244) + \sin\beta + 0.244\beta]$$

$$= B_0R^2[0.3464 + \overline{a}_3(\cos\beta_3 + 0.244) + \sin\beta + 0.244\beta]$$

$$= B_0R^2[0.4952 + \sin\beta + 0.244\beta]$$

At point 4 before the stringer $(s = s_4, \quad \beta = \beta_4)$

$$\overline{S}^{-}_{xr}(s_4) = B_0R^2\left(0.4952 + 1 + 0.244\frac{\pi}{2}\right) = 1.878B_0R^2$$

At point 4 after the stringer $(s = s_4, \quad \beta = \beta_4)$

$$\overline{S}^{+}_{xr}(s_4) = 1.927B_0R^2$$

For part 4 – 5 $(s_4 \le s \le s_5, \quad \pi/2 \le \beta \le \beta_5 = 2\pi/3)$

$$\overline{S}_{xr}(s) = B_0R^2[0.4952 + \overline{a}_4(\cos\beta_4 + 0.244) + \sin\beta + 0.244\beta]$$

$$= B_0R^2[0.544 + \sin\beta + 0.244\beta]$$

At point 5 before the stringer ($s = s_5, \quad \beta = \beta_5$)

$$\overline{S}_{xr}^{-}(s_5) = B_0R^2\left(0.544 + 0.866 + 0.244\frac{2\pi}{3}\right) = 1.921B_0R^2$$

At point 5 after the stringer ($s = s_5, \quad \beta = \beta_5$)

$$\overline{S}_{xr}^{+}(s_5) = 1.87B_0R^2$$

For part 5 – 6 ($s_5 \le s \le s_6, \quad 2\pi/3 \le \beta \le \beta_6 = 5\pi/6$)

$$\overline{S}_{xr}(s) = B_0R^2[0.544 + \overline{a}_5(\cos\beta_5 + 0.244) + \sin\beta + 0.244\beta]$$

$$= B_0R^2[0.4928 + \sin\beta + 0.244\beta]$$

At point 6 before the stringer ($s = s_6, \quad \beta = \beta_6$)

$$\overline{S}_{xr}^{-}(s_6) = B_0R^2\left(0.4928 + 0.5 + 0.244\frac{5\pi}{6}\right) = 1.631B_0R^2$$

At point 6 after the stringer ($s = s_6, \quad \beta = \beta_6$)

$$\overline{S}_{xr}^{+}(s_6) = 1.498B_0R^2$$

For part 6 – 7 ($s_6 \le s \le s_7, \quad 5\pi/6 \le \beta \le \beta_7 = \pi$)

$$\overline{S}_{xr}(s) = B_0R^2[0.4928 + \overline{a}_6(\cos\beta_6 + 0.244) + \sin\beta + 0.244\beta]$$

$$= B_0R^2[0.3684 + \sin\beta + 0.244\beta]$$

At point 7 before the longeron ($s = s_7, \quad \beta = \beta_7$)

$$\overline{S}_{xr}^{-}(s_7) = B_0R^2(0.3684 + 0.244\pi) = 1.134B_0R^2$$

and finally, at point 7 after the longeron (one half of its cross-sectional area)

$$\overline{S}_{xr}^{+}(s_7) = B_0R^2[1.134 + r_7\overline{a}_7(\cos\beta_7 + 0.244)] = B_0R^2[1.134 + 3\cdot0.5(-1 + 0.244)] = 0$$

Eq. (10.135) gives the following values for the shear stress resultant:
At point 1

$$N_{zs}^{-}(0) = 0\,, \quad N_{zs}^{+}(0) = -0.0193\frac{Q}{R}$$

At point 2

$$N_{zs}^{-}(s_2) = -0.116\frac{Q}{R}, \quad N_{zs}^{+}(s_2) = -0.151\frac{Q}{R}$$

At point 3

$$N_{zs}^{-}(s_3) = -0.227\frac{Q}{R}, \quad N_{zs}^{+}(s_3) = -0.25\frac{Q}{R}$$

At point 4

$$N_{zs}^{-}(s_4) = -0.291\frac{Q}{R}, \quad N_{zs}^{+}(s_4) = -0.298\frac{Q}{R}$$

At point 5

$$N_{zs}^{-}(s_5) = -0.297\frac{Q}{R}, \quad N_{zs}^{+}(s_5) = -0.29\frac{Q}{R}$$

At point 6

$$N_{zs}^{-}(s_6) = -0.253\frac{Q}{R}, \quad N_{zs}^{+}(s_6) = -0.232\frac{Q}{R}$$

At point 7

$$N_{zs}^{-}(s_7) = -0.176\frac{Q}{R}, \quad N_{zs}^{+}(s_7) = 0$$

The negative sign of the shear stress resultant means that on the right-hand part of the cross section N_{zs} acts in the direction which is opposite to the direction of the contour coordinate. On the left-hand side of the cross section, N_{zs} acts in the direction of the contour coordinate. The distribution of the normalized shear stress resultant $\overline{N} = N_{zs}R/Q$ along the contour of the beam is shown in Fig. 10.45.

It can be seen that the shear stress resultant is discontinuous in the vicinity of the stiffener. This discontinuity is illustrated in Fig. 10.46, from which it follows that the jump in the shear stress resultant N_{zs} is associated with the gradient of the force P_r in the stiffener. Indeed, it follows from the equilibrium condition for the stiffener that

$$N_{zs}^{+} - N_{zs}^{-} = \frac{dP_r}{dz}$$

For the problem of bending, the right-hand side of this equation is zero only for pure bending under which the shear flow is also zero. For transverse bending induced by shear forces Q_x or Q_y the force in

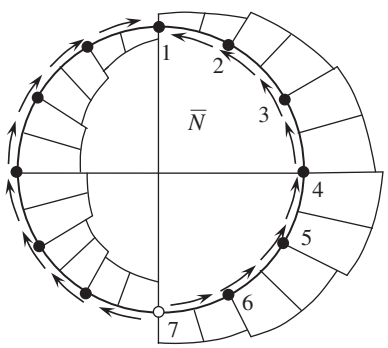


FIGURE 10.45

Distribution of the normalized shear stress resultant $\overline{N}$ over the cross-sectional contour.

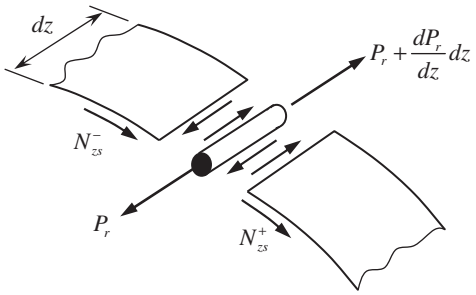


FIGURE 10.46

Interaction of a rib and skin panels.

the stiffener depends on coordinate z, and the shear flow is discontinuous in the vicinity of the stiffener. The displacements of the beam can be found using relations presented in Section 10.4.4.

10.4.10 Beams loaded with body and surface forces

The theory described in the previous sections is strictly valid only for those beams loaded at the ends. However, it can be approximately generalized for beams loaded with body and surface forces. A typical example of such a beam is a helicopter blade loaded with centrifugal and aerodynamic forces.

Consider a beam cross-sectional contour shown in Fig. 10.47 and assume that body and surface forces acting on a beam are applied at some point S of the contour and are reduced to axial forces P_z, contour forces P_s, and normal forces P_n. Within the framework of beam theory, we must reduce

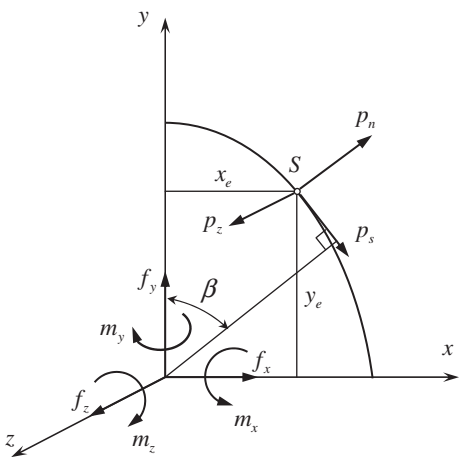


FIGURE 10.47

Reduction of body and surface forces to the beam axis.

these forces to the beam axis by introducing the following integral forces and moments (see Fig. 10.47):

$$\begin{aligned} f_x &= \int_s P_x ds, \qquad f_y = \int_s P_y ds, \qquad f_z = \int_s P_z ds \\ m_x &= \int_s P_z y_e ds, \quad m_y = \int_s P_z x_e ds, \quad m_z = \int_s \left(P_x y_e - P_y x_e\right) ds \end{aligned} \tag{10.137}$$

where

$$P_x = P_s \cos\beta + P_n \sin\beta, \quad P_y = P_n \cos\beta - P_s \sin\beta$$

The forces and moments in Eqs. (10.137) must be included in the equilibrium equations of the beam element, Eqs. (10.39) and (10.40), which are generalized as

$$\begin{aligned} &\frac{dQ_x}{dz} + f_x = 0, \qquad \frac{dQ_y}{dz} + f_y = 0, \qquad \frac{dP_z}{dz} + f_z = 0 \\ &\frac{dH_x}{dz} - Q_y + m_x = 0, \quad \frac{dH_y}{dz} - Q_x + m_y = 0, \quad \frac{dT_z}{dz} + m_z = 0 \end{aligned}$$

The general solution of these equations generalizes Eqs. (10.41), i.e.,

$$\begin{aligned} Q_x &= Q_x^0 - \int_0^z f_x dz, \quad Q_y = Q_y^0 - \int_0^z f_y dz, \quad P_z = P_z^0 - \int_0^z f_z dz \\ H_x &= H_x^0 + Q_y^0 z - \int_0^z dz \int_0^z f_y dz - \int_0^z m_x dz \\ H_y &= H_y^0 + Q_x^0 z - \int_0^z dz \int_0^z f_x dz - \int_0^z m_y dz \\ T_z &= T_z^0 - \int_0^z m_z dz \end{aligned} \tag{10.138}$$

For orthotropic beams, the axial stress resultant N_z is specified by Eqs. (10.34) and (10.35) in which P_z, H_x, and H_y are specified by Eqs. (10.138). To determine the shear stress resultant N_{zs}, we apply, as earlier, the equilibrium equation, Eq. (10.21), which for a beam loaded with distributed forces is generalized as

$$\frac{\partial N_z}{\partial z} + \frac{\partial N_{zs}}{\partial s} + P_z = 0$$

Repeating the derivation of Eq. (10.43), we finally get

$$N_{zs} = N_Q + N_P + N_0$$

where N_Q is given by Eq. (10.46) and

$$N_P = \frac{f_z}{B}\overline{S}(s) - \int_0^s P_z ds + k\left[\frac{\overline{S}_x(s)}{D_x^0}\left(m_x - y_0 f_z\right) + \frac{\overline{S}_y(s)}{D_y^0}\left(m_y - x_0 f_z\right)\right]$$

$$N_0 = \frac{1}{2A}\left[T_z - \int_s \left(N_Q + N_P\right) r ds\right]$$

The displacements of beams loaded with distributed forces can be found using the approach described in Section 10.4.4.

10.4.11 Restrained torsion and bending of beams with closed cross-sectional contours

As shown in Section 10.4.5, bending and torsion of thin-walled beams, in general, is accompanied by warping, i.e., the out-of-plane displacements of the cross-sectional points specified by Eq. (10.76) for the invariant warping function, i.e.,

$$W_{t,b}(s) = \Psi_{t,b}(s) - \frac{1}{S}\int_s \Psi_{t,b}(s) B ds - k\left[\frac{y_e - y_o}{D_x^0}\int_s \Psi_{t,b}(s) B\bar{y} ds + \frac{x_e - x_o}{D_y^0}\int_s \Psi_{t,b}(s) B\bar{x} ds\right] \tag{10.139}$$

Here, subscripts "t" and "b" correspond to torsion and bending of the beam. The warping function for the problem of torsion follows from Eq. (10.72), according to which

$$\Psi_t(s) = \frac{T_z}{2A}\int_0^s \frac{ds}{B_{44}} - \Theta_z'\int_0^s r ds \tag{10.140}$$

The warping function for the bending problem can be decomposed into two parts corresponding to bending in the xz-plane and yz-plane, i.e.,

$$\Psi_b(s) = \Psi_b^x(s) + \Psi_b^y(s) \tag{10.141}$$

in which, in accordance with Eq. (10.71),

$$\Psi_b^x(s) = Q_x\int_0^s \frac{F_x(s)}{B_{44}} ds - \Gamma_x\int_0^s \cos\beta ds, \quad \Psi_b^y(s) = Q_y\int_0^s \frac{F_y(s)}{B_{44}} ds + \Gamma_y\int_0^s \sin\beta ds \tag{10.142}$$

In the previous section we considered the problems of free bending and torsion for which the warping function does not depend on the axial coordinate and the axial displacements of the cross section caused by warping are not restricted. Now, assume that one of the beam cross sections, e.g., the cross section $z = 0$ of the beam in Fig. 10.48, is fixed. Since this cross section remains plane, its warping is constrained by the boundary conditions giving rise to additional axial and shear stresses appearing in

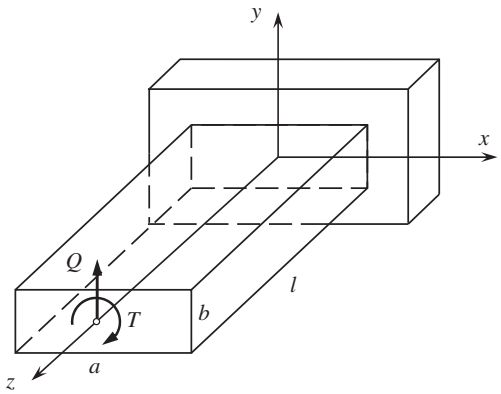


FIGURE 10.48

Torsion and bending of a cantilever beam.

the vicinity of the restricted cross section. This section is concerned with the problems of restrained torsion and bending of thin-walled beams with closed cross-sectional contours.

Note that in the considerations of free torsion and bending in the previous sections we did not separate the problem of torsion and bending, though such opportunity exists. This follows from Section 10.4.7, in which the shear center of a beam is discussed. However, for the problems of constrained torsion and bending, such separation becomes important, since the effect of restrained warping is entirely different for torsion and bending. In the case of torsion, the restrained warping results in normal stresses that do not appear under free torsion, whereas for bending problems the restrained warping results only in a redistribution of the normal and shear stresses in the beam.

To separate the problems of torsion and bending, we apply Eqs. (10.87) and (10.94), according to which

$$\Theta_z' = c_{zz} T_z^s \tag{10.143}$$

$$\Gamma_x^s = c_{xx}^s Q_x^s + c_{xy}^s Q_y^s, \quad \Gamma_y^s = c_{xy}^s Q_x^s + c_{yy}^s Q_y^s \tag{10.144}$$

Here, superscript "s" shows that the forces are applied at the shear center of the cross section.

Consider first the case of restrained torsion. Substituting Θ_z' from Eq. (10.143) into Eq. (10.140) for the warping function, using Eqs. (10.68) for coefficient c_{zz}, and taking $T_z = T_z^s$, we get

$$\Psi_t(s) = \frac{T_z^s}{2A}\left(\int_0^s \frac{ds}{B_{44}} - \frac{1}{2A}\int_0^s rds \int_s \frac{ds}{B_{44}}\right) \tag{10.145}$$

The invariant warping function W_t can be found if we substitute Eq. (10.145) into Eq. (10.139).

As has been noted, restrained warping in torsion results in a normal stress resultant N_z. Assume that the dependence of N_z on the contour coordinate s corresponds to the warping function $\overline{W}(s)$, i.e., that

$$N_z = BN(z)\overline{W}(s) \tag{10.146}$$

Here, B is the axial stiffness of the beam wall, $N(z)$ is an unknown function that needs to be determined, and $\overline{W}(s)$ is the normalized warping function (where the subscript t is omitted). Since the function $N(z)$ is not known, $\overline{W}(s)$ is the invariant warping function in Eq. (10.139) divided by any constant coefficient. For example, for a rectangular cross section, the warping function in Eq. (10.83) reduces to

$$\overline{W}(s) = xy \tag{10.147}$$

By analogy with the bending moment, we introduce the so-called bimoment (Vlasov, 1940):

$$H_w = \int_s N_z \overline{W}(s) ds \tag{10.148}$$

Substituting N_z from Eq. (10.146) into Eq. (10.148), we get

$$H_w = D_w N(z) \tag{10.149}$$

where

$$D_w = \int_s B\overline{W}^2(s) ds \tag{10.150}$$

Using Eq. (10.149), we can write Eq. (10.146) in the following final form:

$$N_z = B\frac{H_w(z)}{D_w}\overline{W}(s) \tag{10.151}$$

To determine the shear stress resultants, we use, as earlier, the equilibrium equation, Eq. (10.21), which yields

$$\frac{\partial N_{zs}}{\partial s} = -\frac{\partial N_z}{\partial z} = -B\frac{H'_w(z)}{D_w}\overline{W}(s)$$

Integrating with respect to s and determining the constant of integration from Eq. (10.48), we arrive at the following expression analogous to Eq. (10.53):

$$N_{zs} = H'_w(z)F_w(s) + \frac{T_z}{2A} \tag{10.152}$$

where

$$F_w(s) = -\frac{1}{D_w}\left[\overline{S}_w(s) - \frac{1}{2A}\int_s \overline{S}_w(s) r ds\right]$$

in which

$$\overline{S}_w(s) = \int_0^s B\overline{W}(s) ds$$

To determine the function $H_w(z)$, we apply the principle of minimum strain energy (see Section 2.11.2). The strain energy of the beam is

$$U_\sigma = \int_0^l dz \int_s \left(\frac{N_z^2}{2B} + \frac{N_{zs}^2}{2B_{44}} \right) ds \tag{10.153}$$

Substituting the stress resultants from Eqs. (10.151) and (10.152), we get the following energy functional:

$$U_\sigma = \frac{1}{2} \int_0^l \left[\frac{H_w^2}{D_w} + \left(H_w'\right)^2 D_F + \frac{S_F}{A} H_w' T_z + \frac{T_z^2}{4A^2} S_s \right] dz \tag{10.154}$$

where

$$D_F = \int_s \frac{F_w^2(s)}{B_{44}} ds, \quad S_F = \int_s \frac{F_w(s)}{B_{44}} ds, \; S_s = \int_s \frac{ds}{B_{44}}$$

The minimum conditions for the strain energy in Eq. (10.154) provide the following variational equation:

$$H_w'' - \lambda^2 H_w = 0, \; \lambda^2 = D_w D_F \tag{10.155}$$

and the natural boundary conditions for the beam ends $z = 0$ and $z = l$:

$$\left[\left(H_w' D_F + \frac{T_z}{2A} S_F \right) \delta H_w \right]_{z=0}^{z=l} = 0 \tag{10.156}$$

(see Fig. 10.48). The general solution of Eq. (10.155) is

$$H_w = C_1 \sinh \lambda z + C_2 \cosh \lambda z \tag{10.157}$$

At the end $z = l$ of the beam (see Fig. 10.48), $N_z = 0$, and hence,

$$H_w(z = l) = 0 \tag{10.158}$$

At the fixed end $z = 0$, the boundary condition given by Eq. (10.156) is equivalent to $u_z = 0$ (Vasiliev, 1993). Determining the constants C_1 and C_2 in Eq. (10.157) from the boundary conditions, Eqs. (10.156) and (10.158), we get

$$H_w = \frac{T_z S_F}{2A\lambda D_F} (\tanh \lambda l \cosh \lambda z - \sinh \lambda z)$$

Substituting this expression into Eqs. (10.151) and (10.152) for the stress resultants, we arrive at

$$N_z = \frac{T_z}{2A} B S_F \lambda (\tanh \lambda l \cosh \lambda z - \sinh \lambda z) \overline{W}(s)$$

$$N_{zs} = \frac{T_z}{2A} \left[1 + \frac{S_F}{D_F} (\tanh \lambda l \sinh \lambda z - \cosh \lambda z) F_w(s) \right]$$

As an example, consider the beam with a rectangular cross section shown in Fig. 10.48 for which $a/b = 2$ and $l/a = 5$. The beam is composed of a $\pm 45^\circ$ angle-ply carbon-epoxy layer with a thickness of 1 mm and a 90° layer with the same thickness. The warping function $\overline{w}(s)$ is specified by Eq. (10.147). The normalized normal $\overline{N}_z = N_z a^2/T_z$ and shear $N_{zs} = N_{zs}a^2/T_z$ stress resultants acting in the fixed cross section $z = 0$ (see Fig. 10.48) are shown in Fig. 10.49. It follows from Eqs. (10.150), (10.153), (10.155), for those beams whose wall stiffness does not depend on s,

$$\lambda^2 = \frac{B}{B_{44}} \int_s \overline{W}^2 ds \cdot \int_s F_w^2(s) ds$$

Thus, the rate at which the normal stress resultant reduces at a distance from the fixed cross section depends on the ratio of the axial stiffness of the wall to the shear stiffness: the higher the ratio, the higher the rate. For real beams whose axial stiffness is usually significantly higher than the shear stiffness, the normal stress resultants are usually concentrated in the vicinity of the fixed cross section. At a distance from this cross section exceeding the width of the cross section (a in Fig. 10.48), normal stress resultant usually vanishes and the beam experiences free torsion. This effect is demonstrated in Fig. 10.50 where the dependence of $\overline{N}_z$ on the axial coordinate is shown (the distance $z/l = 0.2$ corresponds to the dimension a shown in Fig. 10.48).

Under free torsion, the shear stress resultant specified by Eq. (10.56) is uniformly distributed over the cross-sectional contour (dashed line $\overline{N}_{zs} = 1$ in Fig. 10.49b). As can be seen, due to the effect of

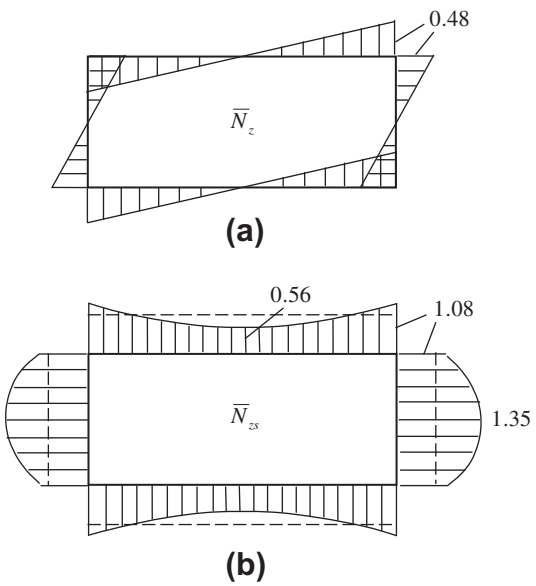


FIGURE 10.49

Distribution of the normalized normal (a) and shear (b) stress resultants over the cross-sectional contour of the beam under restrained torsion.

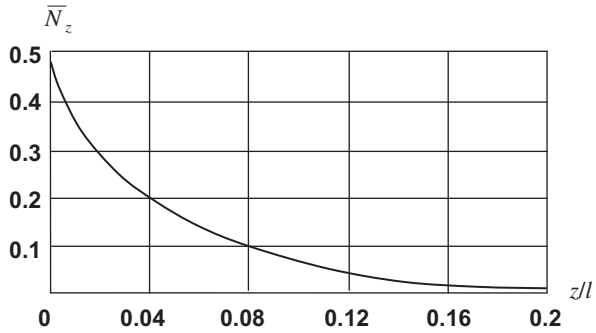


FIGURE 10.50

Dependence of the normalized normal stress resultant on the axial coordinate.

restrained warping, the maximum shear stress resultant acting in the fixed cross section $z = 0$ (see Fig. 10.49b) can be about 35% higher than in the case of free torsion.

Consider now restrained bending. For a beam loaded with transverse shear force Q (see Fig. 10.48) which induces the bending moment

$$H_x = -Q(l - z) \tag{10.159}$$

the normal stress resultant corresponding to free bending is specified by Eqs. (10.34) and (10.35) in which $P_z = 0$ and $H_y = 0$. Adding the normal stress resultant caused by the effect of restrained warping, we arrive at

$$N_z = B\left[k\frac{H_x}{D_x^0}\overline{y} + N(z)\overline{W}(s)\right]$$

where, as earlier, $N(z)$ is the unknown function and $\overline{W}(s)$ is the function proportional to the invariant warping function under free bending specified by Eqs. (10.139) and (10.142). For the beam shown in Fig. 10.48, taking $Q_x^s = 0$ and $Q_y^s = Q$ in Eqs. (10.144), we get

$$\Gamma_y^s = c_{yy}^s Q$$

Substituting this expression into the second equation of Eqs. (10.142), we can determine the warping function $\Psi_b(s)$ as

$$\Psi_b(s) = Q\left(c_{yy}^s + \int_0^s \frac{F_y(s)}{B_{44}}ds\right)$$

The invariant warping function $W(s)$ can now be found from Eq. (10.139).

Introducing the bimoment in Eq. (10.148) and taking into account that the invariant warping function is orthogonal to $\overline{y}$ (see Eqs. (10.75)), we arrive at

$$N_z = B\left[k\frac{H_x}{D_x^0}\overline{y} + \frac{H_w(z)}{D_w}\overline{W}(s)\right] \tag{10.160}$$

where H_x and D_w are specified by Eqs. (10.150) and (10.159). Repeating the derivation of Eq. (10.152) for the shear stress resultant, we finally get

$$N_{zs} = Q_y F_y(s) + H'_w F_w(s) \tag{10.161}$$

where, in accordance with Eqs. (10.54) and (10.152),

$$F_y(s) = -\frac{k}{D_x^0}\left[\overline{S}_x(s) - \frac{1}{2A}\int_s \overline{S}_x(s) r ds\right]$$

$$F_W(s) = -\frac{1}{D_w}\left[\overline{S}_w(s) - \frac{1}{2A}\int_s \overline{S}_w(s) r ds\right]$$

$$\overline{S}_x(s) = \int_0^s B\overline{y} ds, \quad \overline{S}_w(s) = \int_0^s B\overline{W} ds$$

Further analysis is similar to the derivation performed for the torsion problem. The normal and shear stress resultants, Eqs. (10.160) and (10.161), are substituted into Eq. (10.153) for the strain energy. The minimum condition results in Eq. (10.155), whose solution is specified by Eq. (10.157). The natural boundary condition becomes

$$\left[(H'_w D_F + Q S_F)\delta H_w\right]_{z=0}^{z=l} = 0 \tag{10.162}$$

where

$$D_F = \int_s \frac{F_w^2(s)}{B_{44}} ds, \quad S_F = \int_s \frac{1}{B_{44}} F_y(s) F_w(s) ds$$

For the cantilever beam shown in Fig. 10.48, at the free end $z = l$ we have $H_w = 0$, whereas for the fixed end $z = 0$, Eq. (10.162) is equivalent to the absence of axial displacements ($u_z = 0$). Satisfying the boundary conditions, we get

$$H_w = \frac{Q S_F}{\lambda D_F}(\tanh \lambda l \ \cosh \lambda z - \ \sinh \lambda z)$$

Then, the stress resultants, Eqs. (10.160) and (10.161), take the following form:

$$N_z = B\left[k\frac{H_x}{D_x^0}\overline{y} + Q\lambda S_F(\tanh \lambda l \cosh \lambda z - \ \sinh \lambda z)\overline{W}(s)\right]$$

$$N_{ZS} = Q\left[F_y(s) + \frac{S_F}{D_F}(\tanh \lambda l \sinh \lambda z - \cosh \ \lambda z) F_w(s)\right]$$

The qualitative distribution of the normal stress resultant N_z over the contour for the beam fixed cross section $z = 0$ is shown in Fig. 10.51. As can be seen, the effect of restrained bending results in some

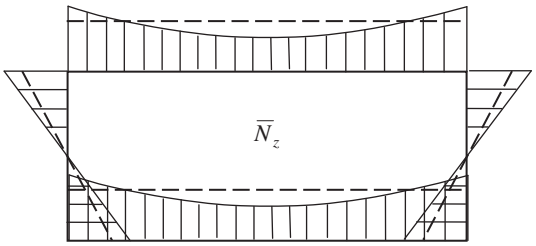


FIGURE 10.51

Distribution of the normal stress resultant over the cross-sectional contour of the beam under restrained bending.

redistribution of the stress resultant in comparison to the case of free bending (dashed line in Fig. 10.51).

10.5 BEAMS WITH MULTI-CELL CROSS-SECTIONAL CONTOURS

The theory described in Section 10.4 can be readily generalized for beams with multi-cell cross-sectional contours similar to that presented in Fig. 10.2. For confirmation, consider a wing-type rectangular beam consisting of three sections as shown in Fig. 10.52.

Since the method presented in Section 10.4.1 which allows us to determine the axial stress resultant does not depend on the shape of a beam cross section, the obtained results are valid for the beams with multi-cell cross sections as well. Thus, the axial stress resultant N_x is specified by Eqs. (10.34) and (10.35) which, for the beam shown in Fig. 10.52, yield

$$N_z = B\frac{H_x(z)}{D_x^0}y \tag{10.163}$$

where $H_x(z)$ is the bending moment acting in the beam cross section $z = constant$.

The beam shown in Fig. 10.52 can be assembled from three composite box beams made by winding and having $\phi = \pm 45^\circ$ angle-ply structure. The assembled beams can be jointed together with the aid of transverse ($\phi = 90^\circ$) plies and, finally, the flanges 1 – 4 and 5 – 8 (see Fig. 10.52) can be reinforced by

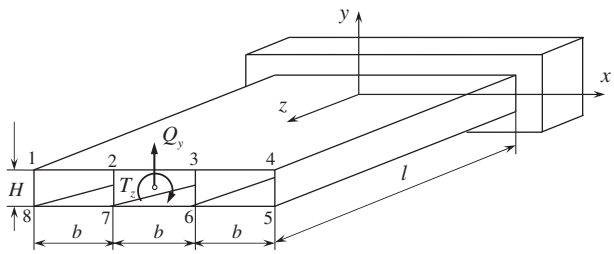


FIGURE 10.52

A beam with a multi-cell cross-sectional contour.

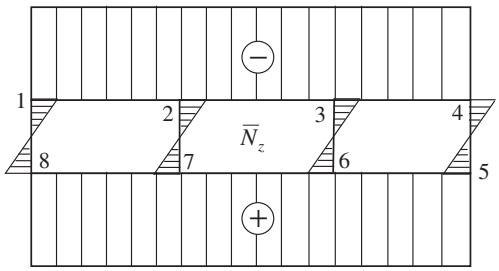


FIGURE 10.53

Distribution of the normalized axial stress resultant over the beam cross-sectional contour.

axial ($\phi = 0°$) plies. Assume that the beam is made of carbon-epoxy composite with ply thickness of 0.3 mm. Then, the thickness of the internal shear webs 2 – 7 and 3 – 6 composed of eight 45° plies is equal to 2.4 mm, and the thickness of outer shear webs 1 – 8 and 4 – 5 which have four 45° plies and two 90° plies is 1.8 mm, whereas the thickness of the flanges 1 – 4 and 5 – 8 which have four 45°, two 90°, and eight 0° plies is 4.2 mm. The membrane stiffness characteristics of the beam elements are

$$B_{11}^{1-4} = B_{11}^{5-8} = 500 \text{ MN/m}, \quad B_{44}^{1-4} = B_{44}^{5-8} = 71 \text{ MN/m}, \quad B_{11}^{1-8} = B_{11}^{4-5} = 66 \text{ MN/m}$$

$$B_{44}^{1-8} = B_{44}^{4-5} = 60 \text{ MN/m}, \quad B_{11}^{2-7} = B_{11}^{3-6} = 124 \text{ MN/m}, \quad B_{44}^{2-7} = B_{44}^{3-6} = 112 \text{ MN/m}$$

(see Fig. 10.52). For $b = 2H$ (see Fig. 10.52), the distribution of the normalized axial stress resultant $\overline{N}_z = \dfrac{N_z H^2}{H_x}$ over the contour of the cross section at z = 0 is shown in Fig. 10.53.

The specific features of a multi-cell cross section show themselves if we determine the shear stress resultant N_{zs}. As opposed to single-cell beams considered in the previous sections of this chapter, which N_{zs} is specified by Eq. (10.53) following from the equilibrium equations only, a beam with a multi-cell cross section is statically indeterminate. For a single-cell beam, we associate the point S, from which the contour coordinate is measured, with an imaginary cut of the contour as shown in Fig. 10.14. For the multi-cell contour, we must make several such cuts, the number of which is equal to the number of cells. This procedure is demonstrated in Fig. 10.54. Clearly, these cuts must be compensated with the corresponding number of unknown and, independent of s, additional stress resultants $N_0^{(i)}, i = 1, 2, 3 \ldots n$, where n is the number of cells. To express the shear stress resultants in this multi-cell beam, we introduce the auxiliary functions ω_i (see Fig. 10.55) which are equal to unity

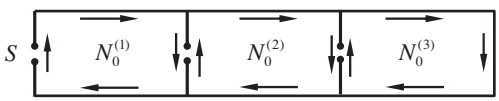


FIGURE 10.54

Reduction of a multi-cell contour to an open contour.

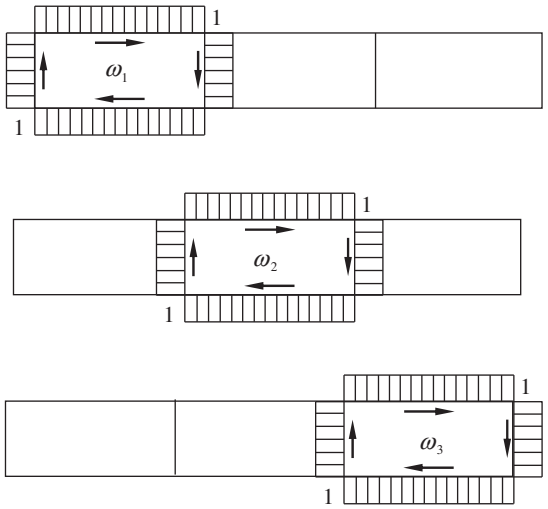


FIGURE 10.55

Auxiliary functions ω_i.

for the i-th contour and are zero for the rest of the contours. Then, Eq. (10.43) for a single-cell contour is generalized as

$$N_{zs} = N_Q + \sum_{i=1}^{n} N_0^{(i)} \omega_i \tag{10.164}$$

Here, N_Q is specified by Eq. (10.46) which for the beam shown in Fig. 10.52 reduces to

$$N_Q = -\frac{Q_y}{D_x^0} \overline{S}_x(s) \tag{10.165}$$

Since the multi-cell cross section is reduced to the corresponding open cross section (see Fig. 10.54), the function $\overline{S}_x(s)$ is plotted using the procedure described in Section 10.4.6 for a single-cell beam. For the beam under consideration (see Fig. 10.52), the function $\overline{S}_x(s)$ is presented in Fig. 10.56. As shown

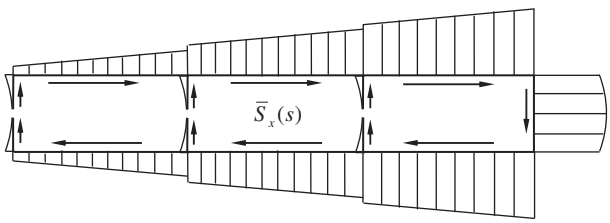


FIGURE 10.56

Function $\overline{S}_x(s)$.

in Section 10.4.2, the shear stress resultant N_Q, Eq. (10.165), balances the transverse shear force Q_y. To balance the torque T_z, we need to apply a moment equation similar to Eq. (10.49), i.e.,

$$\int_s N_Q r ds + 2\sum_{i=1}^{n} N_0^{(i)} A_i = T_z \tag{10.166}$$

where, as earlier, A_i is the area bounded by the i-th cross-sectional contour. Thus, we have one equilibrium equation, Eq. (10.166), which includes n unknown shear stress resultants $N_0^{(i)}$. This means that the problem is statically indeterminate $(n-1)$ times, and we need to derive $(n-1)$ compatibility equations to solve it. These equations can be obtained with the aid of the mixed variational principle discussed in Section 2.11.3. The energy of shear deformation for a unit beam length is

$$W_\sigma = \int_s \frac{N_{zs}^2}{2B_{44}} ds = \frac{1}{2}\int_s \left(N_Q^2 + 2N_Q \sum_{i=1}^{n} N_0^{(i)} \omega_i + \sum_{i=1}^{n}\sum_{j=1}^{n} N_0^{(i)} N_0^{(j)} \omega_i \omega_j \right) \frac{ds}{B_{44}}$$

We should minimize the energy W_σ under the condition according to which the moment equation, Eq. (10.164), is satisfied. Expanding this equation with the aid of Lagrange's multiplier Θ_z' (which is actually the angle of twist per unit length of the beam), we arrive at the following augmented functional

$$W_L = W_\sigma + \Theta_z' \left(T_z - \int_s N_Q r ds - 2\sum_{i=1}^{n} N_0^{(i)} A_i \right)$$

Minimization of this functional with respect to $N_0^{(i)}$ yields the following n equations:

$$\frac{1}{2A_i}\left(\int_s \frac{N_Q}{B_{44}} \omega_i ds + \sum_{j=1}^{n} N_0^{(j)} \int_s \frac{\omega_i \omega_j}{B_{44}} ds \right) = \Theta_z' \tag{10.167}$$

where $i = 1, 2, 3 \ldots n$. The equations obtained, Eqs. (10.167), are actually the compatibility conditions stating that the angle of twist of the i-th ($i = 1, 2, 3 \ldots n$) contour is equal to the twist angle Θ_z of the beam cross sections. These conditions seem reasonable since the beam cross section rotates in its plane as a rigid disk. Solving Eq. (10.167) for $N_0^{(i)}$, we formally get

$$N_0^{(i)} = Q_x R_x^{(i)} + Q_y R_y^{(i)} + \Theta_z' R_\Theta^{(i)} \tag{10.168}$$

where R are coefficients dependent on the beam stiffness and geometric parameters. For the beam considered as an example (see Fig. 10.52), these equations are

$$N_0^{(1)} = 0.017 \frac{Q_y}{H} + 54.8 \cdot 10^6 H \Theta_z', \quad N_0^{(2)} = 0.5 \frac{Q_y}{H} + 67.4 \cdot 10^6 H \Theta_z'$$

$$N_0^{(3)} = 0.5 \frac{Q_y}{H} + 58 \cdot 10^6 H \Theta_z'$$

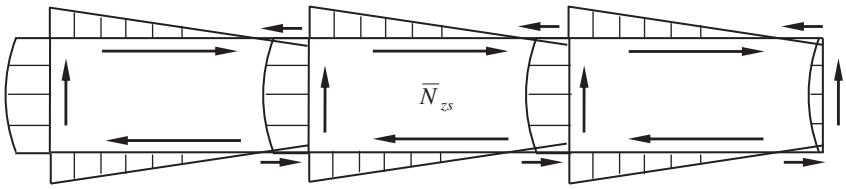


FIGURE 10.57

Distribution of the shear stress resultant over the beam cross-sectional contour.

These equations can now be substituted into the moment equation, Eq. (10.166), i.e.,

$$-6.05Q_yH + 4H^2\left(N_0^{(1)} + N_0^{(2)} + N_0^{(3)}\right) = T_z$$

which allows us to find Θ_z'. For the torque $T_z = Q_y b/2$ (see Fig. 10.52), we get $\Theta_z' = 0.14\cdot 10^{-9} Q_y/H^2$, $N_0^{(1)} = 0.25\, Q_y/H$, $N_0^{(2)} = 0.59\, Q_y/H$, and $N_0^{(3)} = 0.92\, Q_y/H$. Note that these results provide the values of $N_0^{(i)}$, whereas their directions are governed by the functions ω_i shown in Fig. 10.55. The final distribution of the normalized shear stress resultant $\overline{N}_{zs} = N_{zs}H/Q_y$ over the cross-sectional contour is shown in Fig. 10.57. The displacements and warping functions of beams with multi-cell cross sections can be determined using the approaches described in Sections 10.4.4 and 10.4.5.

To find the shear center of the beam with a multi-cell cross section, we must apply, in accordance with Section 10.4.7, the forces Q_x and Q_y at the shear center S. Consider, for example, a double-cell contour, shown in Fig. 10.58 and find the y_s coordinate of the shear center. Apply a force Q_x^s at the shear center. Then, taking $Q_y = 0$ and $Q_x = Q_x^s$ in Eqn. (10.168), we get

$$N_{0s}^{(i)} = Q_x^s R_x^{(i)}$$

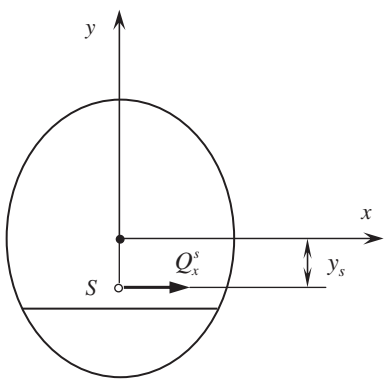


FIGURE 10.58

Shear center of a double-cell cross-sectional contour.

where $N_{0s}^{(i)}$ are the stress resultants $N_0^{(i)}$ corresponding to the force Q_x applied at the shear center. Now, use the moment equation, Eq. (10.166), in which $T_z = -Q_x^s y_s$ and $N_0^{(i)} = N_{0s}^{(i)}$, i.e.,

$$\int_s N_Q r ds + 2Q_x^s \sum_{i=1}^{n} R_x^{(i)} A_i = -Q_x^s y_s$$

where, in accordance with Eq. (10.46),

$$N_Q = -k \frac{Q_x^s}{D_y^0} \overline{S}_y(s)$$

Solving the equation for y_s, we get

$$y_s = \frac{k}{D_y^0} \int_s \overline{S}_y(s) r ds - 2 \sum_{i=1}^{n} R_x^{(i)} A_i$$

Since the cross section shown in Fig. 10.58 is symmetric, $x_s = 0$. In the general case, the coordinate x_s can be found using the earlier approach to determine the y_s coordinate of the shear center.

10.6 BEAMS WITH OPEN CROSS-SECTIONAL CONTOURS

Consider now beams with open cross-sectional contours as shown in Fig. 10.3. As opposed to beams with closed cross-sectional contours, such beams have two free axial edges, $s = 0$ and $s = s_1$ (see Fig. 10.59), which determine specific features of the beam behavior and analysis.

10.6.1 Transverse bending

Since the method applied to determine the axial stress resultant N_z and described in Section 10.4 does not depend on the shape of the beam cross section, the results obtained in that section, i.e., Eqs. (10.34) and (10.35), hold for beams with open cross-sectional contour. The index "s" in the integrals in Eqs. (10.29) means that the integration is performed from $s = 0$ up to $s = s_1$ (see Fig. 10.59).

Consider the shear stress resultant N_{zs} specified, in the general case, by Eq. (10.43), i.e.,

$$N_{zs} = N_Q(s) + N_0$$

in which $N_0 = N_{zs}(s = 0)$. However, for beams with open cross sections, the edge $s = 0$ is free of shear stresses (see Fig. 10.59) and $N_0 = 0$. Thus, in accordance with Eq. (10.46),

$$N_{zs} = N_Q(s) = -k \left[\frac{Q_y}{D_x^0} \overline{S}_x(s) + \frac{Q_x}{D_y^0} \overline{S}_y(s) \right] \tag{10.169}$$

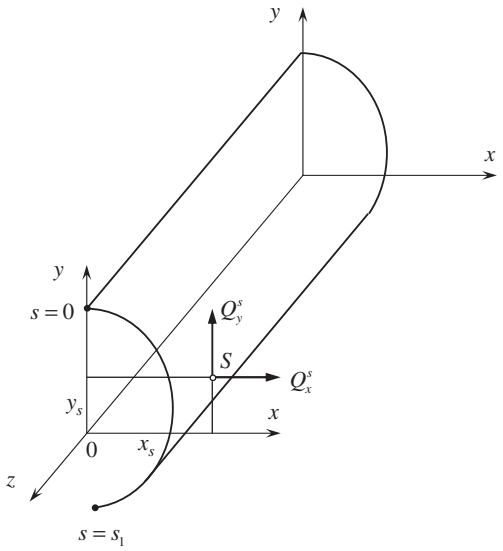


FIGURE 10.59

A thin-walled beam with an open cross-sectional contour.

Recall that in Section 10.4.2 the component of the shear stress resultant N_0 is found from the moment equilibrium equation, Eq. (10.49). Taking $N_0 = 0$ in that equation, we get

$$\int_s N_Q r ds = T_z \tag{10.170}$$

However, no external torque is applied to the beam shown in Fig. 10.59. Thus, to satisfy Eq. (10.170), we need to assume that the forces Q_x and Q_y are applied at some point S, which is called the shear center of the beam with an open contour. These forces create a torque with respect to point 0 (see Fig. 10.59)

$$T_z = Q_x^s y_s - Q_y^s x_s \tag{10.171}$$

Substituting Eqs. (10.169) and (10.171) into Eq. (10.170), we have

$$k\left[\frac{Q_y^s}{D_x^0}\int_s \overline{S}_x(s) r ds + \frac{Q_x^s}{D_y^0}\int_s \overline{S}_y(s) r ds\right] = Q_y^s x_s - Q_x^s y_s$$

This equation must be valid if $Q_x^s = 0$, $Q_y^s \neq 0$, and $Q_y^s = 0$, $Q_x^s \neq 0$. It follows from these conditions that the coordinates of the shear center are

$$x_s = \frac{k}{D_x^0}\int_s \overline{S}_x(s) r ds, \quad y_s = -\frac{k}{D_y^0}\int_s \overline{S}_y(s) r ds \tag{10.172}$$

As the first example, consider a C-shaped beam shown in Fig. 10.60a and find the coordinate x_s. Since the contour is symmetric with respect to the x-axis, $y_s = 0$ and we can consider only one half of the

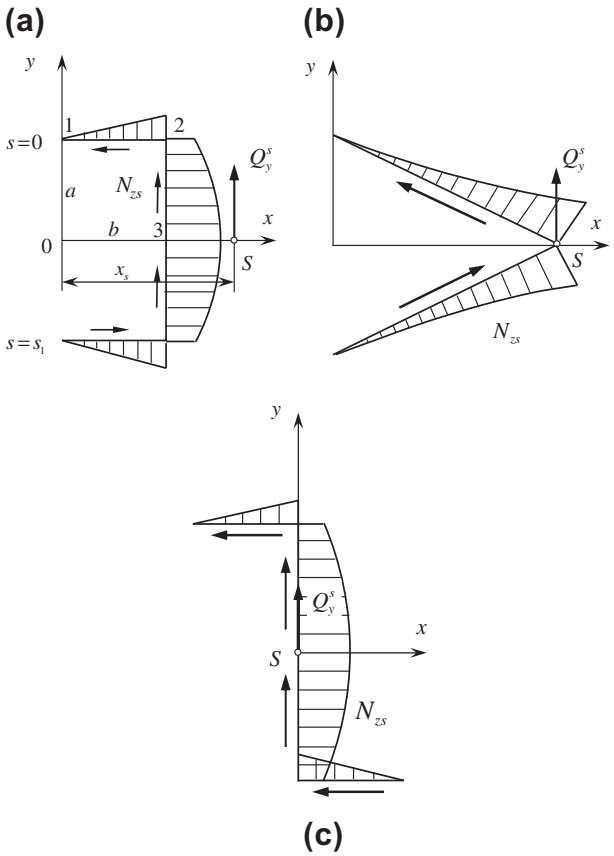


FIGURE 10.60

Shear centers of C-shaped (a), triangular-shaped (b), and Z-shaped (c) beams.

contour consisting of parts 1 – 2 and 2 – 3. For a symmetrical contour, $k = 1$ and Eqs. (10.29) and (10.33) yield

$$D_x^0 = \int_s By^2 ds = 2B\left[\int_0^b a^2 dx + \int_a^0 y^2(-dy)\right] = 2a^2B\left(b + \frac{a}{3}\right)$$

The function $\overline{S}_x(s)$ in Eqs. (10.45) is

$$\overline{S}_x^{12}(s) = \int_0^s Byds = Bax$$

$$\overline{S}_x^{23}(s) = B\left[ab + \int_a^y y(-dy)\right] = B\left[ab + \frac{1}{2}\left(a^2 - y^2\right)\right]$$

The distribution of the shear stress resultant, Eq. (10.169), over the cross-sectional contour is shown in Fig. 10.60a. For the part 1 – 2 of the contour, we have $r = a$, whereas for the part 2 – 3, $r = b$. Then, the first equation of Eqs. (10.172) yields

$$x_s = \frac{2B}{D_x^0}\left[\int_0^b a^2 x dx + \int_a^0 b\left(ab + \frac{a^2 - y^2}{2}\right)(-dy)\right] = \frac{9b^2 + 2ab}{2(a + 3b)}$$

For $a = b$, we have $x_s = 1.375b$, i.e., the shear center is located outside the contour.

In a similar way, we can find the shear stress resultants for the triangular-shaped (see Fig. 10.60b) and z-shaped (see Fig. 10.60c) cross sections. Applying the first equation of Eqs. (10.172), we can prove that for both sections, $x_s = 0$.

Deformations of the model beams with cross sections shown in Fig. 10.60 are presented in Fig. 10.61 (Cheremukhin, 1969). In Fig. 10.61a, the force is applied at the point which is located to the left of the shear center; in Fig. 10.61b, the force acts at the shear center; and in Fig. 10.61c, the force is applied at the point which is located to the right of the shear center. As can be seen, if the force is applied at the shear center, the beam does not experience bending.

To demonstrate the application of the second equation of Eqs. (10.172), consider a circular cross section with a cut shown in Fig. 10.62. For a circular cross section,

$$k = 1, \quad r = R, \quad D_y^0 = \pi B R^3$$

$$\overline{S}_y(s) = \int_0^s B x ds = BR^2 \int_0^\beta \sin\beta d\beta = BR^2(1 - \cos\beta)$$

and the second equation of Eqs. (10.172) yields $y_s = 2R$ (see Fig. 10.62).

It should be noted that Eqs. (10.172) for the coordinates of the shear center are derived assuming that the beam's wall thickness is infinitely small. Actual coordinates of real beams with a finite wall thickness may be different from the values obtained using Eqs. (10.172).

Assuming that the forces Q_x^s and Q_y^s are applied at the shear center and, hence, the beam does not experience torsion, we can determine the displacements of the beam. The displacements of the beam cross section U_x, U_y, and U_z and the rotation angles Θ_x and Θ_y can be found with the aid of Eqs. (10.59) and (10.63) which include the shear deformations Γ_x and Γ_y. Applying the approach described in Section 10.4.4, we can obtain the following expressions similar to Eqs. (10.67):

$$\Gamma_x = c_{xx}Q_x^s + c_{xy}Q_y^s, \quad \Gamma_y = c_{yx}Q_x^s + c_{yy}Q_y^s$$

where

$$c_{xx} = \frac{k^2}{\left(D_y^0\right)^2}\int_s \overline{S}_y^2(s)\frac{ds}{B_{44}}, \quad c_{yy} = \frac{k^2}{\left(D_x^0\right)^2}\int_s \overline{S}_x^2(s)\frac{ds}{B_{44}}$$

$$c_{xy} = c_{yx} = \frac{k^2}{D_x^0 D_y^0}\int_s \overline{S}_x(s)\overline{S}_y(s)\frac{ds}{B_{44}}$$

Now, a natural question arises as to what happens if the forces Q_x and Q_y are not applied at the shear center and the beam experiences torsion. This problem cannot be solved within the framework of the beam model

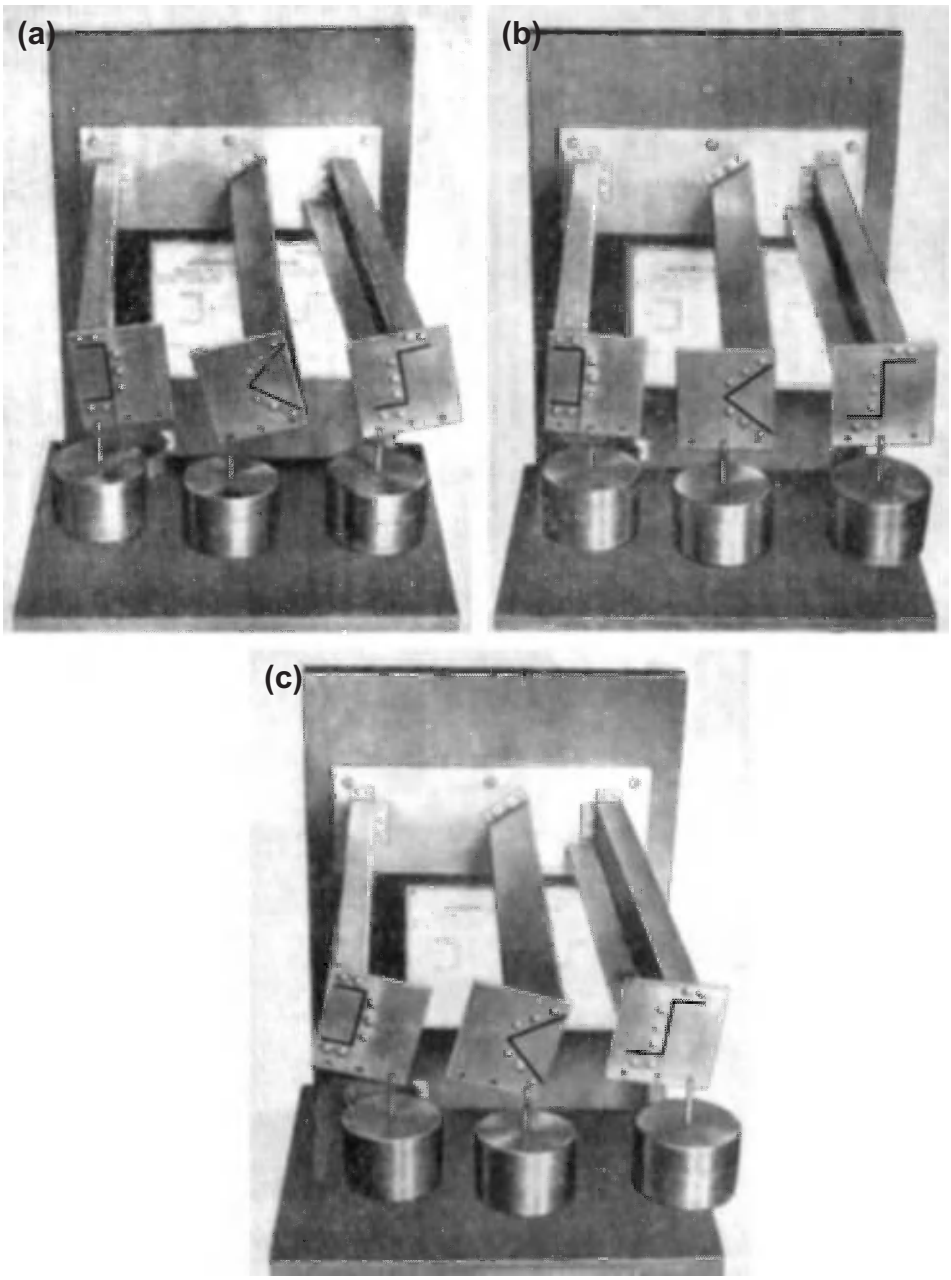


FIGURE 10.61

Models demonstrating the deformations of C-shaped, triangular-shaped, and Z-shaped beams under bending with the force applied to the left of the shear center (a), to the shear center (b), and to the right of the shear center (c).

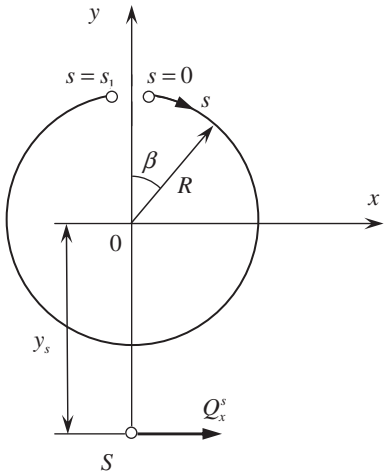


FIGURE 10.62

Shear center of a circular cross section with a cut.

used in the foregoing sections. It should be emphasized that this shortcoming should be attributed to the beam model and not to the physical beam itself. It follows from Fig. 10.61a and c that a beam with an open cross section can resist torsion (although its torsional stiffness is relatively low); however, the study of the problem of torsion would require the development of a more complicated beam model.

10.6.2 Free torsion of beams with open cross-sectional contours

The main shortcoming of the beam model considered in the previous sections is associated with using the equations of membrane shell theory (Section 10.2) to describe the beam behavior. To demonstrate this drawback, consider a homogeneous beam whose stiffness characteristics do not change through the wall thickness. Within the framework of membrane shell theory, the shear stress τ_{zs} is uniformly distributed through the thickness as shown in Fig. 10.63a, giving rise to the shear stress resultant $N_{zs} = \tau_{zs}h$, which is referred to as the shear flow in application to metal beams. This model is quite adequate for thin-walled beams with closed cross-sectional contours (see Fig. 10.63a) and has been widely used in the foregoing sections of this chapter.

However, for beams whose cross-sectional contours are open (see Fig. 10.63b), the shear flow does not exist. The shear stress τ_{zs} is linearly distributed through the beam wall thickness giving rise to a twisting moment M_{zs}. Moreover, in the vicinity of the beam's free longitudinal edges, the shear stress is orthogonal to the cross-sectional contour, which results in a transverse shear force V_z (see Fig. 10.63b).

Thus, to describe torsion of thin-walled beams with open contours, we need to apply the equations of shell theory which allows for moments and transverse shear forces as shown in Fig. 10.64. The corresponding equilibrium equations for the problem of torsion become

$$\frac{\partial N_{sz}}{\partial s} = 0, \quad \frac{\partial M_{sz}}{\partial s} - V_z = 0 \tag{10.173}$$

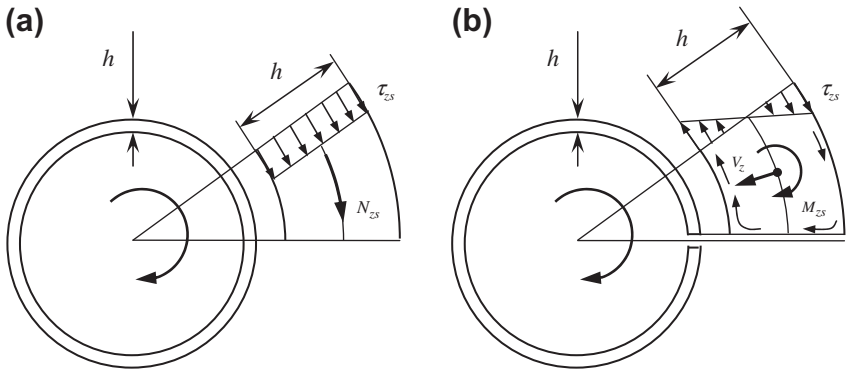


FIGURE 10.63

Distribution of shear stresses through the wall thickness for beams with closed (a) and open (b) cross-sectional contours.

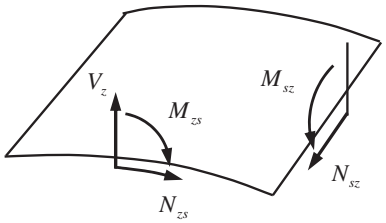


FIGURE 10.64

Forces and moments acting on the element of the reference surface of a beam with open contour.

(Vasiliev, 1993). However, there is one more effect that should be taken into account. To demonstrate this effect, consider a beam with an open cross-sectional contour *EF* as shown in Fig. 10.65 and simulate it with a single-cell sandwich cross section *ABCD*. For a beam with a closed contour *ABCD*, Bredt's formula given by Eq. (10.56) is valid, so that

$$T_z = 2AN_{zs} = \pi RhN_{zs} \tag{10.174}$$

Now assume that the wall thickness h is small. Then, the effect of the shear stress resultant N_{zs} can be reflected by couples $m = N_{zs}h$ uniformly distributed along the contour *EF* (see Fig. 10.65) and

$$T_z = \frac{1}{2}\pi RhN_{zs}$$

The right-hand part of this equation is one half of the corresponding part of Eq. (10.174) and, hence, it is not correct, because, in deriving it, we neglect the difference in the lengths of arcs *AD* and *BC*

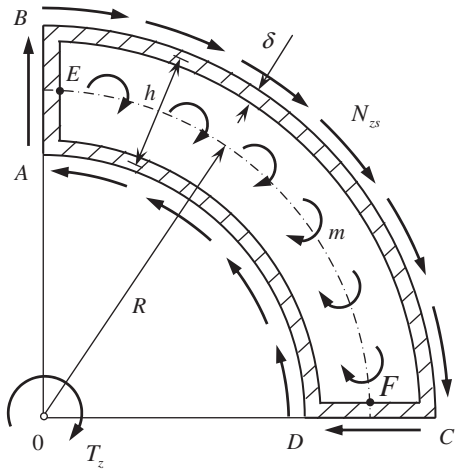


FIGURE 10.65

A model of a thin-walled beam with an open cross section.

assuming that the radius of both arcs is R. However, it is $(R - h/2)$ for AD and $(R + h/2)$ for BC. With this in mind, we get

$$T_z = \frac{\pi}{2}\left[\left(R + \frac{h}{2}\right)^2 - \left(R - \frac{h}{2}\right)^2\right]N_{zs} = \pi R h N_{zs}$$

which is consistent with Eq. (10.174). Thus, in addition to Eqs. (10.173), we should take into account that the Lamé coefficient H cannot be taken equal to unity in accordance with Eq. (10.5), and should be specified by Eqs. (10.4), which yield

$$H = 1 + \frac{\eta}{R_e} = 1 + \frac{t - e}{R_e} \tag{10.175}$$

where t is counted from zero to h (see Fig. 5.8) and e is the coordinate of the reference surface showing the location of the contour arc with the radius R_e.

The constitutive equations allowing for these effects can be written as

$$\begin{aligned}
N_{zs} &= B_{44}^{11}\varepsilon_{zs} + B_{44}^{12}\varepsilon_{sz} + C_{44}^{11}\kappa_{zs} + C_{44}^{12}\kappa_{sz} \\
N_{sz} &= B_{44}^{21}\varepsilon_{zs} + B_{44}^{22}\varepsilon_{sz} + C_{44}^{21}\kappa_{zs} + C_{44}^{22}\kappa_{sz} \\
M_{zs} &= C_{44}^{11}\varepsilon_{zs} + C_{44}^{12}\varepsilon_{sz} + D_{44}^{11}\kappa_{zs} + D_{44}^{12}\kappa_{sz} \\
M_{sz} &= C_{44}^{21}\varepsilon_{zs} + C_{44}^{22}\varepsilon_{sz} + D_{44}^{21}\kappa_{zs} + D_{44}^{22}\kappa_{sz} \\
V_z &= S_z\gamma_z
\end{aligned} \tag{10.176}$$

(Vasiliev, 1993). The strain-displacement equations are

$$\varepsilon_{zs} = \frac{\partial u_s}{\partial z}, \quad \varepsilon_{sz} = \frac{\partial u_z}{\partial s}, \quad \kappa_{zs} = \frac{\partial \theta_s}{\partial z}, \quad \kappa_{sz} = \frac{\partial \theta_z}{\partial s}$$
$$\theta_z = \gamma_z - \frac{\partial u_\eta}{\partial z}, \quad \theta_s = \frac{u_s}{R_e} - \frac{\partial u_\eta}{\partial s} \tag{10.177}$$

Here, u_z, u_s, and u_η are the displacements of the point lying at the contour line in z, s and η -directions (see Fig. 10.5), θ_z and θ_s are the angles of rotation of the line normal to the reference surface in ηz – and ηs – planes, and γ_z is the transverse shear deformation of the beam wall. The stiffness coefficients of the wall in Eqs. (10.176) are specified by the following equations similar to Eqs. (5.28)

$$B_{44}^{11} = I_0, \quad C_{44}^{11} = I_1 - eI_0, \quad D_{44}^{11} = I_2 - 2eI_1 + e^2 I_0$$
$$B_{44}^{22} = J_0, \quad C_{44}^{22} = J_1 - eJ_0, \quad D_{44}^{22} = J_2 - 2eJ_1 + e^2 J_0 \tag{10.178}$$
$$B_{44}^{12} = B_{44}^{21} = K_0, \quad C_{44}^{12} = C_{44}^{21} = K_1 - eK_0, \quad D_{44}^{12} = D_{44}^{21} = K_2 - 2eK_1 + e^2 K_0$$

where

$$I_r = \int_0^h A_{44} H t^r dt, \quad J_r = \int_0^h \frac{t^r}{H} A_{44} dt, \quad K_r = \int_0^h A_{44} dt \quad (r = 0, 1, 2) \tag{10.179}$$

and H is specified by Eq. (10.175). The transverse shear stiffness of the beam wall in the last equation of Eqs. (10.176) is similar to Eq. (5.22), i.e.,

$$S_x = \frac{h^2}{\int_0^t \frac{dt}{G_{z\eta}}} \tag{10.180}$$

In Eqs. (10.179), $A_{44} = G_{zs}$, i.e., the stiffness coefficient is equal to the shear modulus of the beam material, whereas $G_{z\eta}$ in Eq. (10.180) is the transverse shear modulus of the beam wall in the ηz-plane (see Fig. 10.5). For laminated beams (see Fig. 5.10), in accordance with Section 5.3, we get

$$I_r = \frac{1}{r+1} \sum_{i=1}^{k} H_i G_{zs}^{(i)} \left(t_i^{r+1} - t_{i-1}^{r+1} \right)$$
$$J_r = \frac{1}{r+1} \sum_{i=1}^{k} \frac{1}{H_i} G_{zs}^{(i)} \left(t_i^{r+1} - t_{i-1}^{r+1} \right)$$
$$K_r = \frac{1}{r+1} \sum_{i=1}^{k} G_{zs}^{(i)} \left(t_i^{r+1} - t_{i-1}^{r+1} \right), \quad r = 0, 1, 2 \tag{10.181}$$
$$S_x = h^2 \left(\sum_{i=1}^{k} \frac{t_i - t_{i-1}}{H_i G_{z\eta}^{(i)}} \right)^{-1}, \quad H_i = 1 + \frac{1}{2R_e} (t_{i-1} + t_i - 2e)$$

Recall that in accordance with Section 5.10, the coordinate of the reference surface e (see Figs. 5.8 and 5.10) can be preassigned in such a way that one of the coupling coefficients C_{mn} in Eqs. (10.178) becomes zero. Let this coefficient be $C_{44}^{12} = C_{44}^{21}$. Then

$$e = \frac{K_1}{K_0} = \frac{\int_0^h G_{zs} t dt}{\int_0^h G_{zs} dt} \tag{10.182}$$

If this equation is valid, we can use Eq. (10.175) and transform the equation for B_{44}^{11} in Eqs. (10.178) as

$$B_{44}^{11} = \int_0^h \left(1 + \frac{t-e}{R_e}\right) G_{zs} dt = \int_0^h G_{zs} dt + \frac{1}{R_e}(K_1 - eK_0) = \int_0^h G_{zs} dt = B_{44}^{12}$$

Thus, if e satisfies Eq. (10.182), we have

$$B_{44}^{11} = B_{44}^{12} = B_{44}^{21} = B_{44}, \quad C_{44}^{12} = C_{44}^{21} = 0 \tag{10.183}$$

Consider the strain-displacement equations, Eqs. (10.177). The displacements of the cross-sectional contour points u_s and u_η are specified by Eqs. (10.17) in which, for the case of free torsion, $U_x = 0$ and $U_y = 0$, so that

$$u_s = r\Theta_z(z), \quad u_\eta = t\Theta_z(z) \tag{10.184}$$

where r and t are specified by Eqs. (10.7). Substituting Eqs. (10.184) in Eqs. (10.177) and taking into account Eqs. (10.10), we get

$$\begin{aligned} &\varepsilon_{zs} = r\Theta_z', \quad \varepsilon_{sz} = \dot{u}_z, \quad \theta_z = \gamma_z - t\Theta_z' \\ &\theta_s = \left(\frac{r}{R_e} - \dot{t}\right)\Theta_z = \Theta_z, \quad \kappa_{zs} = \Theta_z', \quad \kappa_{sz} = \dot{\gamma}_z - \dot{t}\Theta_z' \end{aligned} \tag{10.185}$$

where $(\ldots)' = d(\ldots)/dz$ and $(\dot{}) = d(\ )/ds$. Using Eqs. (10.183) and (10.185), we can present the constitutive equations, Eqs. (10.176), in the following form:

$$\begin{aligned} N_{zs} &= \left(rB_{44} + C_{44}^{11}\right)\Theta_z' + B_{44}\dot{u}_z \\ N_{sz} &= \left(rB_{44} - \dot{t}C_{44}^{22}\right)\Theta_z' + B_{44}^{22}\dot{u}_z + C_{44}^{22}\dot{\gamma}_z \\ M_{zs} &= \left(rC_{44}^{11} + D_{44}^{11} - \dot{t}D_{44}^{12}\right)\Theta_z' + D_{44}^{12}\dot{\gamma}_z \\ M_{sz} &= \left(D_{44}^{12} - \dot{t}D_{44}^{22}\right)\Theta_z' + C_{44}^{22}\dot{u}_z + D_{44}^{22}\dot{\gamma}_z \\ V_z &= S_z\gamma_z \end{aligned} \tag{10.186}$$

Consider now the first equilibrium equation in Eqs. (10.173), according to which the shear stress resultant N_{sz} acting in the longitudinal planes $s = constant$ of the beam (see Fig. 10.64) does not

depend on s. However, on the beam's free edges $s = 0$ and $s = s_1$ (see Fig. 10.59), $N_{sz} = 0$. Thus, $N_{zs} = 0$ and the second equation of Eqs. (10.186) allows us to determine $\dot{u}_z$ as

$$\dot{u}_z = -\frac{1}{B_{44}^{22}}\left[\left(rB_{44} - \dot{\imath}C_{44}^{22}\right)\Theta_z' + C_{44}^{22}\dot{\gamma}_z\right] \tag{10.187}$$

Substituting Eq. (10.187) into the first and the fourth equations of Eqs. (10.186), we get

$$N_{zs} = \left(rB_r + C_{44}^{11}\right)\Theta_z' + \frac{B_{44}}{B_{44}^{22}}C_{44}^{22}\left(\dot{\imath}\Theta_z' - \dot{\gamma}_z\right), \quad M_{sz} = (D_r - \dot{\imath}D)\Theta_z' + D\dot{\gamma}_z \tag{10.188}$$

where

$$B_r = B_{44}\left(1 - \frac{B_{44}}{B_{44}^{22}}\right), \quad D_r = D_{44}^{12} - \frac{rB_{44}}{B_{44}^{22}}C_{44}^{22}, \quad D = D_{44}^{22} - \frac{1}{B_{44}^{22}}\left(C_{44}^{22}\right)^2$$

It follows from Eqs. (10.186) and (10.188) that the stress resultants and couples N_{zs}, N_{sz} and M_{zs}, M_{sz} depend on Θ_z', which is actually a constant, and on γ_z, which is a function of s for the case of free torsion. To determine the function $\gamma_z(s)$, apply the second equilibrium equation of Eqs. (10.173). Substituting M_{sz} and V_z from Eqs. (10.188) and (10.186), we arrive at the following equation:

$$D\ddot{\gamma}_z + \dot{D}\dot{\gamma}_z - S_z\gamma_z = \left(\dot{\imath}\ddot{D} + \dot{\imath}\dot{D} - \dot{D}_r\right)\Theta_z' \tag{10.189}$$

whose solution specifies the function $\gamma_z(s)$. The solution of Eq. (10.189) includes two constants of integration that can be found from the boundary conditions at the longitudinal edges of beam $s = 0$ and $s = s_1$ (see Fig. 10.59). For the free edges, $M_{sz}(s = 0) = 0$, and $M_{sz}(s = s_1) = 0$ where M_{sz} is specified by the second equation of Eqs. (10.188).

The constant angle of twist per unit length Θ_z' can be now found from the moment equation that follows from Fig. 10.66, i.e.,

$$T_z = \int_0^{s_1}(rN_{zs} + tV_z + M_{zs})ds \tag{10.190}$$

in which N_{zs}, V_z, and M_{zs} are specified by Eqs. (10.186) and (10.188).

Finally, we need to determine the warping function. The axial displacement of the point A (see Fig. 10.67) located at a distance η from the contour line can be written in accordance with Eqs. (5.2) as

$$w_z(s) = u_z(s) + \eta\theta_z(s) \tag{10.191}$$

where $u_z(s)$ is the axial displacement of the contour which can be found by integration of Eq. (10.187), i.e.,

$$u_z = u_z^0 - \int_0^s \frac{1}{B_{44}^{22}}\left[\left(rB_{44} - \dot{\imath}C_{44}^{22}\right)\Theta_z' + C_{44}^{22}\dot{\gamma}_z\right]ds \tag{10.192}$$

in which $u_z^0 = u_z(s = 0)$ and θ_z is the angle of rotation of the normal to the contour line in the plane $z\eta$ specified by Eqs. (10.185), i.e.,

$$\theta_z = \gamma_z - t\Theta_z' \tag{10.193}$$

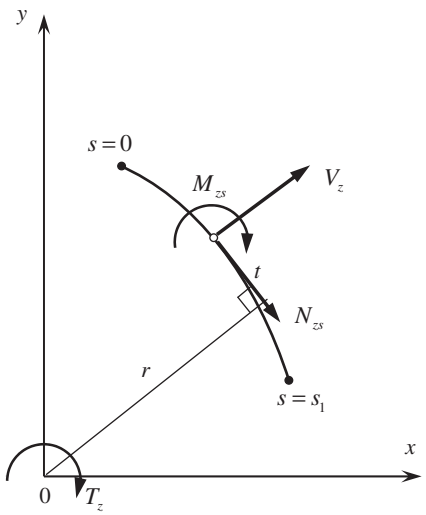


FIGURE 10.66

Forces and moment acting in the beam cross section under free torsion.

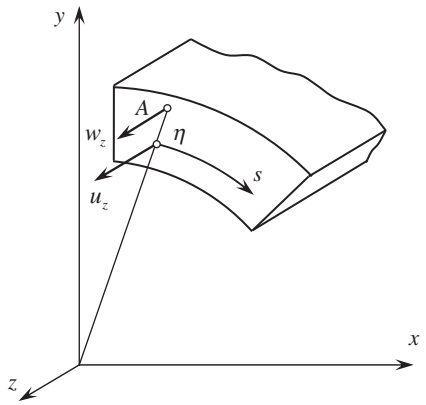


FIGURE 10.67

Axial displacement of the cross-sectional point.

It follows from Eq. (10.191) that when subjected to pure torsion the open cross section of the beam experiences two warping effects. The first one is the warping of the contour line ($\eta = 0$) specified by Eq. (10.192). The second effect is the warping of the cross section with respect to the contour line which is determined by Eq. (10.193).

In the general case, Eq. (10.189) can only be solved numerically. However, there exist two important particular cases for which an analytical solution can be found: beams whose cross-sectional

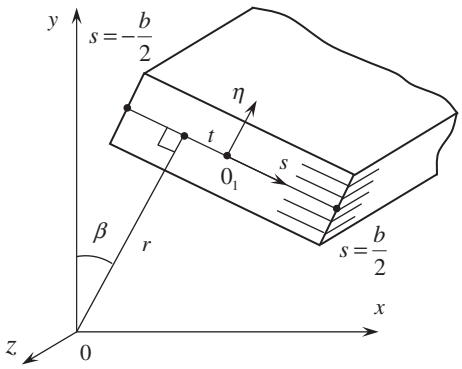


FIGURE 10.68

Axial displacement of the cross-sectional point.

contour is a straight line and beams having a circular contour line. Keeping in mind that the majority of the actual contour lines can be approximated by segments of straight lines and circles, we now consider these particular cases.

A beam with a solid rectangular cross section referred to arbitrary coordinate frame x , y, z is shown in Fig. 10.68. The contour line is straight. Counting the s-coordinate from the center of the cross section O_1 and using Figs. 10.66 and 10.68, we get

$$r = constant, \quad \beta = constant, \quad t = -s$$

Then, Eqs. (10.178) yield

$$B_{44}^{11} = B_{44}^{12} = B_{44}^{21} = B_{44}^{22} = B_{44} = K_0$$

$$C_{44}^{11} = C_{44}^{12} = C_{44}^{21} = C_{44}^{22} = 0$$

$$D_{44}^{11} = D_{44}^{12} = D_{44}^{21} = D_{44}^{22} = D_{44} = K_2 - 2eK_1 + e^2K_0$$

where $K_r (r = 0, 1, 2)$ and e are specified by Eqs. (10.179) and (10.182).

Note that a similar problem is discussed in Section 5.5 and some of the results obtained are repeated here for the sake of completeness. For the beam under study, Eq. (10.189) becomes

$$\ddot{\gamma}_z - k^2\gamma_z = 0, \quad k^2 = \frac{S_z}{D} \tag{10.194}$$

Where $D = D_{44}$. The solution of Eq. (10.194) is

$$\gamma_z = C_1 \sinh ks + C_2 \cosh ks \tag{10.195}$$

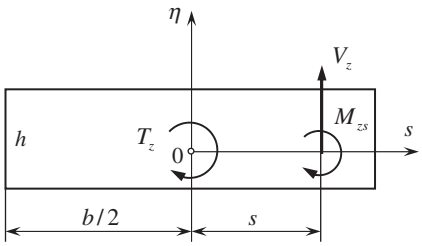


FIGURE 10.69

Forces and moments acting in the beam cross section.

and Eqs. (10.186) and (10.188) give the following expressions for the stress resultants and couples:

$$\begin{aligned} N_{zs} &= N_{sz} = 0 \\ M_{zs} &= M_{sz} = D_{44}\left(2\Theta_z' + \dot{\gamma}_z\right) \\ V_z &= S_z\gamma_z \end{aligned} \tag{10.196}$$

Consider a beam with free edges $s = \pm b/2$ (see Fig. 10.68). Moving point O_1 to point O, we arrive at the cross section shown in Fig. 10.69 for which $r = 0$. Determining C_1 and C_2 in Eq. (10.195) from the boundary conditions $M_{sz}(s = \pm b/2) = 0$, we find from Eqs. (10.196)

$$M_{zs} = 2D_{44}\Theta_z'\left(1 - \frac{\cosh ks}{\cosh \lambda}\right), \quad V_z = -\frac{2S_z \sinh ks}{k \cosh \lambda}\Theta_z' \tag{10.197}$$

where

$$\lambda = \frac{1}{2}kb = \frac{b}{2}\sqrt{\frac{S_z}{D_{44}}} \tag{10.198}$$

To determine Θ_z', apply the moment equation, Eq. (10.190), which takes the form

$$T_z = \int_{-b/2}^{b/2} (M_{zs} - sV_z)ds$$

Substituting for M_{zs} and V_z their expressions, Eqs. (10.197), we arrive at

$$T_z = D_t\Theta_z' \tag{10.199}$$

in which

$$D_t = 4D_{44}b\left(1 - \frac{\tanh \lambda}{\lambda}\right) \tag{10.200}$$

is the torsional stiffness of the beam.

The warping of the beam cross section is specified by Eq. (10.191). It follows from Eq. (10.192) that $u_z = u_z^0$ and if the point O in Fig. 10.69 is fixed, $u_z = 0$. Thus, there is no warping of the cross-sectional contour line $\eta = 0$ (see Fig. 10.69) which remains straight under torsion. Substituting γ_z and Θ_z' into Eqs. (10.193) and (10.191), we get

$$w_z = \Theta_z'\left(\frac{2\sinh ks}{k\cosh\lambda} + s\right)\eta$$

The distribution of w_z over the cross section as well as the dependencies of M_{zs} and V_z, given by Eqs. (10.197), on s, are shown in Fig. 10.70.

For a homogeneous beam with height h,

$$D_{44} = \frac{1}{12}G_{zs}h^3, \quad S_z = G_{z\eta}h$$

(see Fig. 10.69) and Eq. (10.200) yields

$$D_t = \frac{1}{3}G_{zs}bh^3\left(1 - \frac{\tanh\lambda}{\lambda}\right), \quad \lambda = \frac{b}{h}\sqrt{\frac{3G_{z\eta}}{G_{zs}}} \tag{10.201}$$

For an isotropic beam, $G_{z\eta} = G_{zs}$, $\lambda = \dfrac{b\sqrt{3}}{h}$ and

$$D_t = Gbh^3\overline{D}_t, \quad \overline{D}_t = \frac{1}{3}\left(1 - \frac{\tanh\lambda}{\lambda}\right)$$

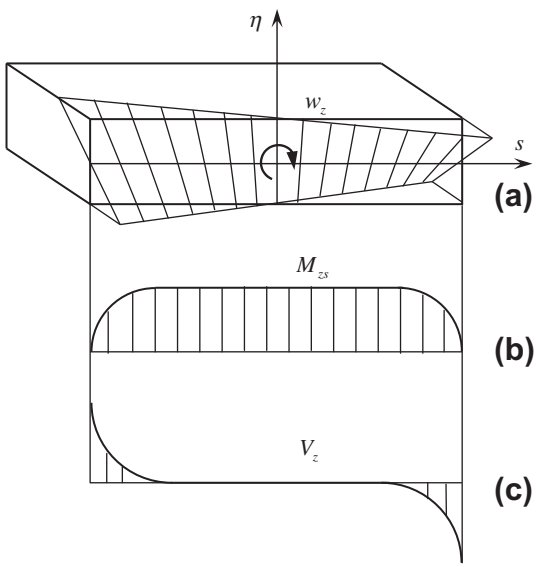


FIGURE 10.70

Warping function (a), twisting moment (b), and transverse shear force (c) for a solid rectangular beam.

TABLE 10.2 Exact (D_t^e) and Approximate ($\overline{D}_t$) Values of the Torsional Stiffness Coefficient

b/h	1.0	1.2	1.4	1.6	1.8	2.0
D_t^e	0.1406	0.1661	0.1869	0.2037	0.2174	0.2287
$\overline{D}_t$	0.1525	0.1779	0.1980	0.2140	0.2268	0.2373
b/h	2.5	3.0	3.5	4.0	4.5	5.0
D_t^e	0.2494	0.2633	0.2735	0.2810	0.2868	0.2914
$\overline{D}_t$	0.2564	0.2692	0.2783	0.2852	0.2906	0.2948
b/h	5.5	6.0	7.0	8.0	10.0	∞
D_t^e	0.2952	0.2984	0.3035	0.3071	0.3124	0.3333
$\overline{D}_t$	0.2983	0.3013	0.3058	0.3093	0.3141	0.3333

The function $\overline{D}_t$ of the ratio b/h along with the exact solution of Arutyunyan and Abramyan (1963) is presented in Table 10.2. As can be seen, Eq. (10.201) has reasonable accuracy (the error is 8.5%) even for beams with square cross sections ($h = b$), whereas for $b \geq 5h$ the error is less than 1%.

For thin-walled beams with a high ratio of b/h, Eq. (10.200) for the torsional stiffness can be simplified and presented in the following approximate form:

$$D_t = 4D_{44}b \tag{10.202}$$

To apply this equation, consider a sandwich beam consisting of isotropic layers. The thickness of each layer is h (see Fig. 10.71) such that $b \gg h$. The shear moduli of the outer and inner layers are G_1 and G_2, respectively. Taking $t_1 = h$, $t_2 = 2h$, and $t_3 = 3h$ in Eqs. (10.181), we get

$$K_0 = h(2G_1 + G_2), \quad K_1 = \frac{3h^2}{2}(2G_1 + G_2), \quad K_2 = \frac{h^3}{3}(20G_1 + 7G_2)$$

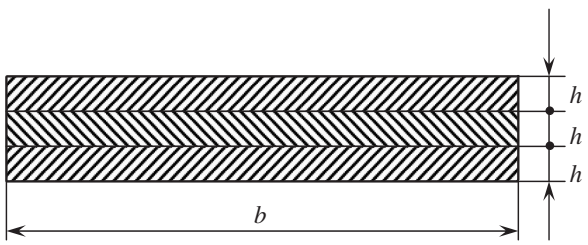


FIGURE 10.71

Cross section of a sandwich beam.

Then the corresponding equation of Eqs. (10.178) yields

$$D_{44} = \frac{h^3}{12}(26G_1 + G_2)$$

and, in accordance with Eq. (10.202),

$$D_t = \frac{h^3}{3}(26G_1 + G_2)$$

This result coincides with the exact solution obtained by Lekhnitskii (1971).

For practical analysis, Eq. (10.202) is usually generalized for beams with arbitrary open cross-sectional contour as

$$D_t = 4\int_0^l D_{44}ds \tag{10.203}$$

in which l is the length of the contour line.

Consider beams with circular cross-sectional contour (see Fig. 10.72) for which

$$r = R, \quad t = 0, \quad R_e = R, \quad H = 1 + \frac{t-e}{R}$$

and Eqs. (10.186), (10.188) become

$$\begin{aligned} N_{zs} &= \left(RB_r + C_{44}^{11}\right)\Theta_z' - \frac{B_{44}}{B_{44}^{22}}C_{44}^{22}\dot{\gamma}_z \\ M_{zs} &= \left(RC_{44}^{11} + D_{44}^{11}\right)\Theta_z' + D_{44}^{12}\dot{\gamma}_z \\ M_{sz} &= D_r\Theta_z' + D\dot{\gamma}_z \\ V_z &= S_z\gamma_z \end{aligned} \tag{10.204}$$

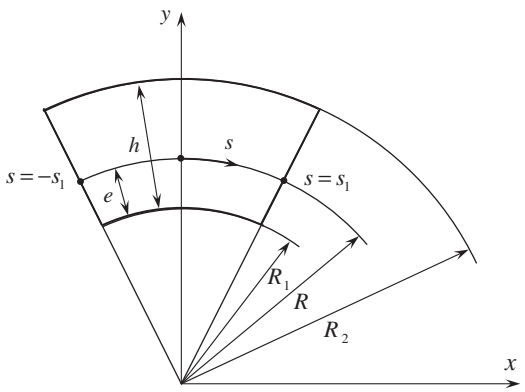


FIGURE 10.72

Circular cross section of a beam.

As for the beam with a rectangular cross section considered previously, Eq. (10.189) reduces to Eq. (10.194), whose solution satisfying the symmetry condition for the cross section shown in Fig. 10.72 is

$$\gamma_z = C_3 \sinh ks, \quad k^2 = \frac{S_z}{D} \tag{10.205}$$

in which the constant C_3 is determined from the boundary condition $M_{sz}(s = s_1) = 0$. Finally, we get

$$\gamma_z = -\frac{D_r \Theta_z'}{kD \cosh \lambda} \sinh ks, \quad \lambda = s_1 \sqrt{\frac{S_z}{D}} \tag{10.206}$$

The moment equation, Eq. (10.190), becomes

$$T_z = 2 \int_0^{s_1} (RN_{zs} + M_{zs}) ds$$

and can be reduced to Eq. (10.199), in which

$$D_t = 2s_1 \left(2C_{44}^{11} R + D_{44}^{11} + B_r R^2\right) - \frac{2D_r^2}{Dk} \tanh \lambda \tag{10.207}$$

As an example, consider a homogeneous cylindrical beam with a cut whose cross section is shown in Fig. 10.73. To use the solution given by Eq. (10.206), we must count the contour coordinate s from point O. For the beam under study,

$$s_1 = \pi R, \quad G_{zs} = G, \quad G_{z\eta} = G_1, \quad e = \frac{h}{2}$$

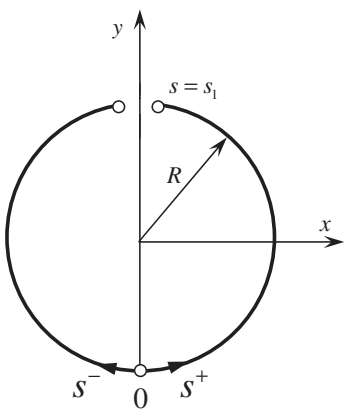


FIGURE 10.73

Circular cross-sectional contour with a cut.

in which h is the beam thickness and

$$B_{44} = Gh, \quad B_{44}^{22} = GRp, \quad C_{44}^{11} = \frac{Gh^3}{12R}, \quad C_{44}^{22} = GR^2(\overline{h} - p)$$
$$D_{44}^{11} = D_{44}^{12} = \frac{Gh^3}{12}, \quad D_{44}^{22} = GR^3(p - \overline{h}), \quad S_z = \frac{h^2 G_1}{Rp} \tag{10.208}$$

where

$$p = \ln\frac{1 + \overline{h}/2}{1 - \overline{h}/2}, \quad \overline{h} = \frac{h}{R}$$

For an isotropic beam ($G_1 = G$), the exact solution of this problem is given by A. Föppl and L. Föppl (1928) and has the form

$$D_t = cGR_1^4$$

in which the coefficient c depends on the ratio R_1/R_2 (see Fig. 10.72). The exact values of this coefficient, c_e, along with approximate values for c_1 following from Eq. (10.207), are presented in Table 10.3 for various ratios R_1/R_2. The coefficient c_2 corresponds to Eq. (10.203), according to which

$$D_t = 8\pi R D_{44} = \frac{2\pi}{3} GRh^3 \tag{10.209}$$

As can be seen, c_1 values practically coincide with c_e for all the beams, whereas Eq. (10.203) provides reasonably accurate results for beams with $h/R < 0.5$.

Consider the warping functions. To simplify the analysis, assume that $h/R \ll 1$. Then, the stiffness coefficients in Eq. (10.208) become

$$B_{44} = B_{44}^{22} = Gh, \quad C_{44}^{11} = -C_{44}^{22} = \frac{Gh^3}{12R}, \quad D_{44}^{11} = D_{44}^{12} = D_{44}^{22} = \frac{Gh^3}{12}, \quad S_z = Gh$$

so that

$$D = \frac{Gh^3}{12}, \quad D_r = \frac{Gh^3}{6}, \quad k^2 = \frac{12}{h^2}$$

Taking $u_z(s = 0) = 0$ (see Fig. 10.73), we have from Eq. (10.192)

$$u_z = -\pi R \Theta_z' s \tag{10.210}$$

TABLE 10.3 Exact and Approximate Coefficients of the Torsional Stiffness for a Cylindrical Beam with a Cut

R_1/R_2	0.1	0.2	0.3	0.4	0.5	0.6	0.7	0.8	0.9
h/R	1.636	1.333	1.077	0.857	0.667	0.5	0.363	0.222	0.105
c_e	0.725	0.570	0.420	0.291	0.183	0.101	0.045	0.014	0.0019
c_1	0.728	0.574	0.426	0.294	0.183	0.102	0.046	0.014	0.0019
c_2	0.84	0.643	0.467	0.317	0.196	0.107	0.048	0.015	0.0019

Note that the small term proportional to $(h/R)^3$ is neglected in this equation. The equation obtained, Eq. (10.210), specifies the warping of the cross-sectional contour line. This type of warping is shown in Fig. 10.4a. The second type of warping, i.e., the warping of the beam wall with respect to the contour line, follows from Eqs. (10.191), (10.193), and

$$w_z = \eta\gamma_z = -\frac{\Theta_z' h \sinh ks}{\sqrt{3}\cosh\lambda}\eta$$

where $\lambda = \pi Rk$ and $-h/2 \le \eta \le h/2$. This type of warping is similar to that shown in Fig. 10.70a.

Finally, using the foregoing example, evaluate the torsional stiffness. For a circular beam with an open cross-sectional contour (see Fig. 10.73) the torsional stiffness is approximately specified by Eq. (10.209). For a circular beam with a closed contour (without the cut shown in Fig. 10.73) considered in Section 10.4.6,

$$D_t = \frac{1}{C_{zz}} = 2\pi GR^3 h$$

which is $3R^2/h^2$ higher than that following from Eq. (10.209).

Thus, beams with open cross sections, in principle, can be used under torsion; however, their torsional stiffness is rather low.

Consider those beams whose contour line can be approximated by a combination of straight lines and circles using the angle-shaped beam shown in Fig. 10.74 as an example. For the circular part of the beam, i.e., for s_1 changing from 0 to $s_1 = \pi R/4$, Eqs. (10.204) and (10.205) yield

$$N_{zs}^c = \left(RB_r + C_{44}^{11}\right)\Theta_z' - \frac{B_{44}^{12}}{B_{44}^{22}}C_{44}^{22}C_3 k_c \cosh k_c s_1$$

$$M_{zs}^c = \left(RC_{44}^{11} + D_{44}^{11}\right)\Theta_z' + D_{44}^{12}C_3 k_c \cosh k_c s_1$$

$$M_{sz}^c = D_r\Theta_z' + DC_3 k_c \cosh k_c s_1$$

$$V_z^c = S_z C_3 \sinh k_c s_1$$

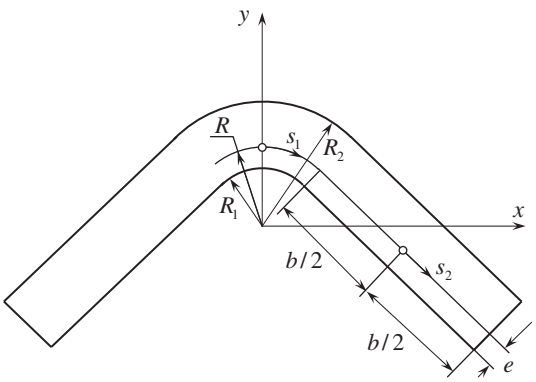


FIGURE 10.74

Angle-shaped thin-walled beam.

We also need the equations for the axial displacement u_z and angle of rotation θ_z that follow from Eqs. (10.192) and (10.193), i.e.,

$$u_z^c = -\int_0^{s_1}\left(\frac{B_{44}}{B_{44}^{22}}R\Theta_z' + C_{44}^{22}C_3k_c\cosh k_cs_1\right)ds_1$$

$$\theta_z^c = C_3\sinh k_cs_1$$

We take $u_z^c(s_1=0)=0$, fixing the beam with respect to its axial displacement as a solid.

For the rectangular part of the cross section (see Fig. 10.74), the contour coordinate s_2 changes from $-b/2$ to $b/2$, $r=R+e$, and $t=-s_2$, and Eqs. (10.195), (10.196), (10.192/10.193) yield

$$N_{zs}^r = 0, \quad M_{zs}^r = M_{sz}^r = D_{44}[2\Theta_z' + k_r(C_1\cosh k_rs_2 + C_2\sinh k_rs_2)]$$

$$V_z^r = S_z(C_1\sinh k_rs_2 + C_2\cosh k_rs_2)$$

$$u_z^r = u_z^0 - (R+e)\Theta_z's_2$$

$$\theta_z^r = C_1\sinh k_rs_2 + C_2\cosh k_rs_2 + \Theta_z's_2$$

The solution obtained includes four constants: C_1, C_2, C_3, and u_z^0 which can be found from the following boundary conditions:

$$M_{sz}^c(s_1=\pi R/4) = M_{sz}^r(s_2=-b/2), \quad M_{sz}^r(s_2=b/2)=0$$

$$u_z^c(s_1=\pi R/4) = u_z^r(s_2=-b/2), \quad \theta_z^c(s_1=\pi R/4) = \theta_z^r(s_2=-b/2)$$

The coordinate of the reference surface e specified by Eq. (10.182) is the same for the circular and rectangular parts of the cross section.

Finally, to determine the angle of rotation per unit length Θ_z', we need to apply the moment equation, Eq. (10.190), which takes the form

$$T_z = 2\int_0^{\pi R/4}\left(RN_{zs}^c + M_{zs}^c\right)ds_1 + 2\int_{-b/2}^{b/2}\left(M_{zs}^r - s_2V_z^r\right)ds_2$$

The expression for the torsional stiffness is rather cumbersome and is not presented here. The dependence of the normalized torsional stiffness of the isotropic beam

$$\overline{D}_t = \frac{D_t}{Gh^3l},$$

where l is the length of the contour line on the ratio b/h is shown in Fig. 10.75 (line) along with the exact theory of elasticity solution (dots) presented by Arutyunyan and Abramyan (1963).

10.6.3 Restrained torsion of beams with open cross-sectional contours

Consider those beams whose cross-sectional warping is restrained by their supports. In such beams, similar to the beams with closed cross sections discussed in Section 10.4.4, restrained warping results

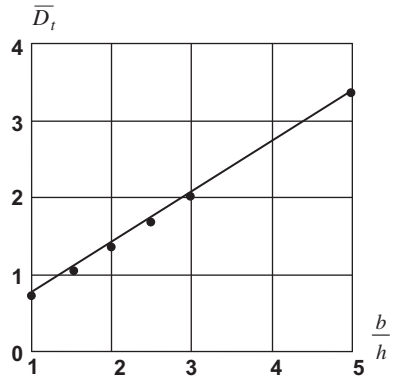


FIGURE 10.75

Dependence of the normalized torsional stiffness of an angle-shaped isotropic beam (———) and exact solution of the theory of elasticity (•••).

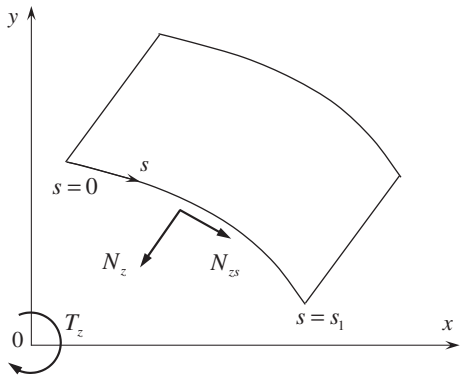


FIGURE 10.76

Normal and shear stress resultant acting in the beam cross section under restrained torsion.

in axial normal stress resultants N_z and additional shear stress resultants N_{zs} (see Fig. 10.76) which appear in the vicinity of the fixed cross section. The simplest theory of restrained torsion is based, as discussed in Section 10.4.4, on membrane shell theory equivalent to that presented in Section 10.2. Thus, we neglect the bending stiffness of the beam wall, taking bending (D_{mn}) and coupling (C_{mn}) stiffness coefficients equal to zero and allowing for membrane stiffness coefficients (B_{mn}) only. First, determine the warping function for the beam with an open cross section. Taking $C_{44} = 0$ in Eq. (10.192), we get

$$u_z = u_z^0 - \Theta_z' \omega(s) \tag{10.211}$$

where

$$\omega(s) = \int_0^s r ds \tag{10.212}$$

is the so-called sectorial characteristic of the cross section in which r is specified by Eqs. (10.7). Now, we need to introduce the normalized warping function which is discussed in Section 10.4.5 and does not depend on the particular coordinate frame to which the beam cross section is referred (see Fig. 10.76). For this purpose, we use Eq. (10.20) for u_s and generalize Eq. (10.211) as

$$u_z = U_z(z) + x_e \Theta_y(z) + y_e \Theta_x(z) - \omega(s)\Theta'_z(z) \tag{10.213}$$

Then, the axial strain can be expressed as

$$\varepsilon_z = \frac{\partial u_z}{\partial z} = U'_z + x_e \Theta'_y + y_e \Theta'_x - \omega(s)\Theta''_z(z) \tag{10.214}$$

and the axial normal stress resultant is

$$N_z = B\varepsilon_z \tag{10.215}$$

where, as earlier, B is the axial stiffness coefficient of the beam wall. Since the beam experiences only torsion, the axial force P_z and the bending moments H_x and H_y are zero and Eqs. (10.27) which specify these force and moments yield

$$\int_s N_z ds = 0, \quad \int_s N_z y_e ds = 0, \quad \int_s N_z x_e ds = 0$$

Substituting N_z in accordance with Eqs. (10.214) and (10.215), we arrive at the following equations similar to Eqs. (10.30) and (10.32):

$$\begin{aligned} U'_z &= \frac{S_\omega}{S}\Theta''_z - \left(y_0 \Theta'_x + x_0 \Theta'_y\right) \\ \Theta'_x &= \frac{k}{D_x^0}\left(S_{\omega x}^0 - n_y S_{\omega y}^0\right)\Theta''_z \\ \Theta'_y &= \frac{k}{D_y^0}\left(S_{\omega y}^0 - n_x S_{\omega x}^0\right)\Theta''_z \end{aligned} \tag{10.216}$$

in which x_0, y_0, S, D_x^0, D_y^0, n_x, n_y, and k are specified by Eqs. (10.29), (10.31), (10.33), and

$$S_\omega = \int_s B\omega ds, \quad S_{\omega x} = \int_s B\omega y_e ds, \quad S_{\omega y} = \int_s B\omega x_e ds$$

$$S_{\omega x}^0 = S_{\omega x} - y_0 S_\omega, \quad S_{\omega y}^0 = S_{\omega y} - x_0 S_\omega$$

Substitution of Eq. (10.216) into Eqs. (10.214) and then into Eq. (10.215) yields

$$N_z = B\left[\frac{S_\omega}{S} + k\left(\frac{S^0_{\omega x}}{D^0_x}\overline{y} + \frac{S^0_{\omega y}}{D^0_y}\overline{x}\right) - \omega(s)\right]\Theta''_z \tag{10.217}$$

where $\overline{x}$ and $\overline{y}$ are given by Eqs. (10.36). Integration of Eqs. (10.216) with respect to z and substitution into Eq. (10.213) results in the following expression for the axial displacement of the beam contour line:

$$\begin{aligned} u_z = {} & u^0_z + (x - x_0)\Theta^0_y + (y - y_0)\Theta^0_x \\ & + k\left[\frac{x - x_0}{D^0_y}\left(S^0_{\omega y} - n_x S^0_{\omega x}\right) + \frac{y - y_0}{D^0_x}\left(S^0_{\omega x} - n_y S^0_{\omega y}\right)\right]\Theta'_z + \left[\frac{S_\omega}{S} - \omega(s)\right]\Theta'_z \end{aligned} \tag{10.218}$$

Here, u^0_z, Θ^0_x, and Θ^0_y are the axial displacement and the angles of rotation of the beam as a solid. The shear stress resultant N_{zs} can be found, as earlier, from the equilibrium equation in Eqs. (10.21). Substituting N_z from Eq. (10.217) and integrating with respect to s, we arrive at

$$N_{zs} = -F_\omega(s)\Theta'''_z \tag{10.219}$$

where

$$F_\omega(s) = \frac{S_\omega}{S}\overline{S}(s) - \overline{S}_\omega(s) + k\left[\frac{S^0_{\omega x}}{D^0_x}\overline{S}_x(s) + \frac{S^0_{\omega y}}{D^0_y}\overline{S}_y(s)\right]$$

in which

$$\overline{S}_\omega(s) = \int_o^s B\omega(s)ds$$

and the functions $\overline{S}(s)$, $\overline{S}_x(s)$, and $\overline{S}_y(s)$ are specified by Eqs. (10.45). Since $F_\omega(s = 0) = 0$, N_{zs} is zero at the edge $s = 0$ of the beam (see Fig. 10.76). For the edge $s = s_1$ (see Fig. 10.76), $\overline{S}(s = s_1) = S$, $\overline{S}_x(s = s_1) = 0$, $\overline{S}_y(s = s_1) = 0$, and Eq. (10.219) yields $N_{zs}(s = s_1) = 0$, hence satisfying the boundary condition for the free edge $s = s_1$. Applying Eqs. (10.47) for Q_x and Q_y, we can prove that $Q_x = Q_y = 0$, which is as expected since we consider a beam under pure torsion.

The shear stress resultant, Eq. (10.219), is statically equivalent to the following torque:

$$T_\omega = \int_s N_{zs} r ds = -D_\omega \Theta'''_z \tag{10.220}$$

where

$$D_\omega = \int_s F_\omega(s) r ds \tag{10.221}$$

The total torque T_z (see Fig. 10.76) consists of T_ω and T_f, i.e.,

$$T_z = T_\omega + T_f \tag{10.222}$$

in which

$$T_f = D_t \Theta_z' \tag{10.223}$$

where D_t is the beam torsional stiffness under free torsion determined in Section 10.6.2. Substituting Eqs. (10.220) and (10.223) into Eq. (10.222), we arrive at the following final equation for the angle of twist:

$$\Theta_z''' - k_\omega^2 \Theta_z' = -\frac{T_z}{D_\omega}, \quad k_\omega^2 = \frac{D_t}{D_\omega} \tag{10.224}$$

For $T_z = constant$, the solution of this equation is

$$\Theta_z = \frac{T_z z}{D_t} + C_1 \sinh k_\omega z + C_2 \cosh k_\omega z + C_3 \tag{10.225}$$

The constants of integration C_1, C_2, and C_3 are found from the boundary conditions.

As an example, consider a cantilever beam with a circular contour line and a cut as shown in Fig. 10.77. At the beam fixed end $z = 0$, we have $u_z = 0$, and Eq. (10.218) yields $u_z^0 = 0$, $\Theta_x^0 = 0$, $\Theta_y^0 = 0$, and $\Theta_z'(z = 0) = 0$. The angle of twist of the fixed cross section $z = 0$ must also be zero, so that $\Theta_z(z = 0) = 0$. At the beam end $z = l$ (see Fig. 10.77), $N_z = 0$, and, in accordance with Eq. (10.217), $\Theta_z''(z = l) = 0$. Thus, the constants entering Eq. (10.225) can be found from the boundary conditions $\Theta_z(z = 0) = 0$, $\Theta_z'(z = 0) = 0$, and $\Theta_z''(z = l) = 0$. Finally, the solution given by Eq. (10.225) takes the form

$$\Theta_z = \frac{T_z}{k_\omega D_t}[k_\omega z - \sinh k_\omega z + (\cosh k_\omega z - 1)\tanh k_\omega l] \tag{10.226}$$

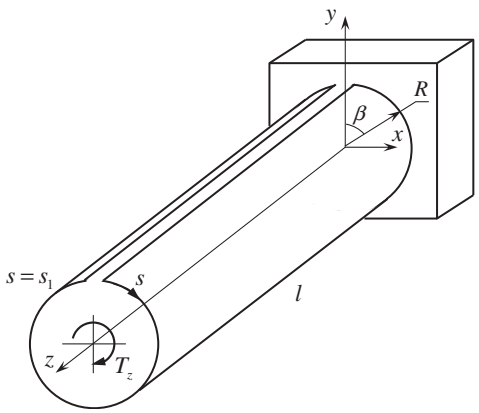


FIGURE 10.77

Cantilever circular beam under torsion.

For the circular cross section shown in Fig. 10.77, we have

$$x_0 = 0, \quad y_0 = 0, \quad \overline{x} = x, \quad \overline{y} = y, \quad k = 1$$

$$\omega(s) = R^2\beta, \quad S = 2\pi BR, \quad S_\omega = 2\pi^2 BR^3, \quad S^0_{\omega x} = 0, \quad S^0_{\omega y} = -2\pi BR^4$$

$$D^0_x = D^0_y = \pi BR^3$$

$$\overline{S}(s) = BR\beta, \quad \overline{S}_\omega(s) = \frac{1}{2}BR^3\beta^2, \quad \overline{S}_x(s) = BR^2 \sin\beta, \quad \overline{S}_y(s) = BR^2(1 - \cos\beta)$$

The torsional stiffnesses specified by Eqs. (10.203) and (10.221) are

$$D_t = 8D_{44}\pi R, \quad D_\omega = \frac{2}{3}(\pi^2 - 6)\pi BR^5$$

where, for a homogeneous wall, $D_{44} = B_{44}h^2/12$ and $B = B_{11}$. Then, Eqs. (10.217) and (10.219) yield, for normal and shear stress resultants,

$$N_z = BR^2(\pi - 2\sin\beta - \beta)\Theta''_z$$

$$N_{zs} = -BR^3\left(\pi\beta - \frac{1}{2}\beta^2 - 2 + 2\cos\beta\right)\Theta''_z$$

where $\Theta_z(z)$ is specified by Eq. (10.226). The distributions of the normalized axial and shear stress resultants are shown in Fig. 10.78.

To evaluate the torsional stiffness of the beam, consider a carbon-epoxy beam, shown in Fig. 10.77. The beam is composed of $\pm 45^\circ$ plies with the total thickness of 1.2 mm and of axial plies with the same

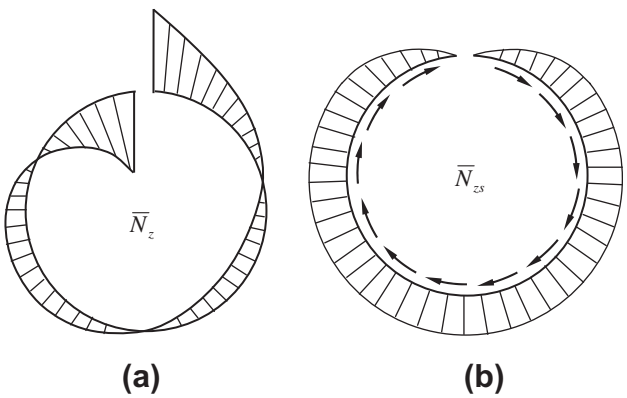


FIGURE 10.78

Distribution of the normalized axial (a) and shear (b) stress resultants over the cross-sectional circular contour with a cut.

total thickness. The beam radius and length are $R = 100\,\text{mm}$ and $l = 20R$. The angle of rotation of the beam end $z = l$ can be presented as

$$\Theta_z^l = \frac{T_z}{D}$$

where D is the torsional stiffness of the beam with length l. For a beam without a cut,

$$D = D_1 = \frac{2\pi}{l} B_{44} R^3$$

which in the present example gives $D_1 = 195\,\text{kNm}$. For a beam with a cut under free rotation,

$$D = D_2 = \frac{2\pi}{3l} B_{44} R h^2$$

which gives $D_2 = 0.04\,\text{kNm}$. For a beam with restrained torsion,

$$D = D_3 = \frac{2\pi B_{44} R h^2}{3l\left(1 - \frac{1}{\lambda}\tanh\,\lambda\right)}, \quad \lambda = k_{\omega l}$$

which yields $D_3 = 5.6\,\text{kNm}$. Thus, restrained torsion allows us to increase the beam stiffness by a factor of 140 in comparison with free torsion, though this stiffness is about 35 times lower than the stiffness of a beam with a closed cross section.

10.7 References

Arutyunyan, N. Kh., & Abramyan, B. L. (1963). *Torsion of Elastic Solids*. Moscow: Fizmatgiz (in Russian).

Chandra, R., Stemple, A. D., & Chopra, I. (1990). Thin-walled composite beams under bending, torsional, and extensional loads. *Journal of Aircraft, 27*(7), 619–626.

Cheremukhin, A. M. (1969). *Selected Papers*. Moscow: Mashinostroenie (in Russian).

Dekker, M. (2004). *Structural Analysis of Polymeric Composite Materials*. New York: Marcell Dekker, Inc.

Föppl, A., & Föppl, L. (1928). *Drang und Zwang. Band 2, Zweite Auflage*. München and Berlin: Verlag von B. Oldenbourg.

Johnson, E. R., Vasiliev, V. V., & Vasiliev, D. V. (2001). Anisotropic thin-walled beams with closed cross-sectional contours. *AIAA Journal, 39*(12), 2389–2393.

Kollar, L. P., & Springer, G. S. (2003). *Mechanics of Composite Structures*. Cambridge: Cambridge University Press.

Lekhnitskii, S. G. (1971). *Torsion of Anisotropic and Inhomogeneous Beams*. Moscow: Nauka (in Russian).

Librescu, L., & Song, O. (2006). *Thin-walled Composite Beams*. Dordrecht: Springer.

Nixon, M. W. (1987). Extension-twist coupling of composite circular tubes with application to tilt rotor blade design. *Proc. of 28th Structures, Structural Dynamics and Materials Conf.* (Monterey, CA). Part 1, (pp. 295–303). Washington, DC: AIAA.

Reissner, E., & Tsai, W. T. (1972). Pure bending, stretching, and twisting of anisotropic cylindrical shells. *Journal of Applied Mechanics, 39*, 148–154, Ser. E, No 1.

Reissner, E., & Tsai, W. T. (1972a) and (1972b). On the determination of the centers of twist and of shear for cylindrical shell beams. Transactions of ASME. *Journal of Applied Mechanics* 1098–1102, December.

Smith, E. C., & Chopra, I. (1990). Formulation and evaluation of an analytic model for composite box-beams. *Proc. of the 31st AIAA/ASME/ASCE/AHS/ASC Structures, Structural Dynamics, and Material Conf.* (pp. 759–782). Washington, DC: AIAA.

Timoshenko, S. P., & Goodier, J. N. (1970). *Theory of Elasticity* (3rd ed.). New York: McGraw-Hill

Vasiliev, V. V. (1993). *Mechanics of Composite Structures*. Washington: Taylor & Francis.

Vlasov, V. Z. (1940). *Thin-walled Elastic Beams*. Moscow: Stroiizdat (in Russian).

Weisshaar, T. A. (1980). Divergence of forward swept composite wings. *Journal of Aircraft, 17*(6), 442–448.

Weisshaar, T. A. (1981). Aeroelastic tailoring of forward swept composite wings. *Journal of Aircraft, 18*(8), 669–676.

Weisshaar, T. A., & Foist, B. L. (1985). Vibration tailoring of advanced composite lifting surfaces. *Journal of Aircraft, 22*(2), 141–147.

CHAPTER

Circular cylindrical shells 11

Composite materials are widely used to fabricate cylindrical shells which can be the structural elements in pipes (see Fig. 11.1), storage tanks (see Fig. 11.2), cisterns for transportation (see Fig. 11.3), pressure vessels (see Fig. 11.4), rocket components (see Fig. 11.5), etc. The theory of cylindrical shells and its application to the analysis of cylindrical structures is described in numerous publications, among which are the books by Ambartsumyan (1961), Korolev (1965), Vasiliev et al. (1993, 2009), Elpatievskii and Vasiliev (1972), Paliy and Spiro (1977), Alfutov et al. (1984), Pikul (1985, 2009), Khoma (1986), Rasskazov et al. (1986), Khoroshun et al. (1988), Kollar and Springer (2003), Ye (2003), and Reddy (2004). This chapter is concerned with those problems which are specific for composite cylindrical shells.



FIGURE 11.1

Elements of composite pipes.

Advanced Mechanics of Composite Materials and Structural Elements. http://dx.doi.org/10.1016/B978-0-08-098231-1.00011-X
Copyright © 2013 Elsevier Ltd. All rights reserved.

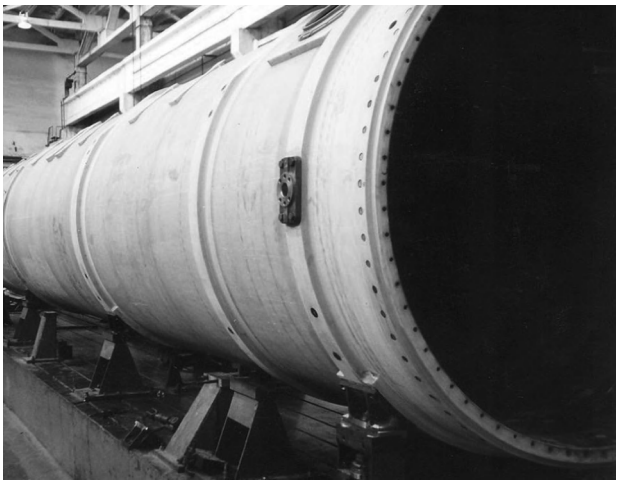


FIGURE 11.2

A large composite storage tank.

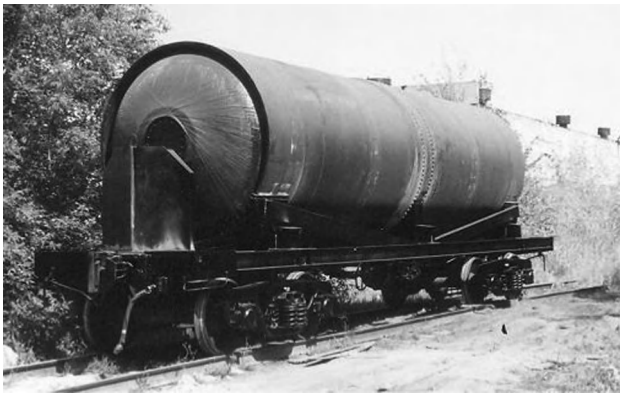


FIGURE 11.3

Composite cistern.

11.1 GOVERNING EQUATIONS AND APPLIED SHELL THEORIES

Consider a cylindrical shell with radius R, length l, and thickness h loaded as shown in Fig. 11.6 in which p is the internal pressure, q is the external pressure, and N are the axial forces uniformly distributed over the end cross section. The shell reference surface is referred to surface coordinates x and y. The shell is described by the following set of governing equations (Vasiliev, 1993).

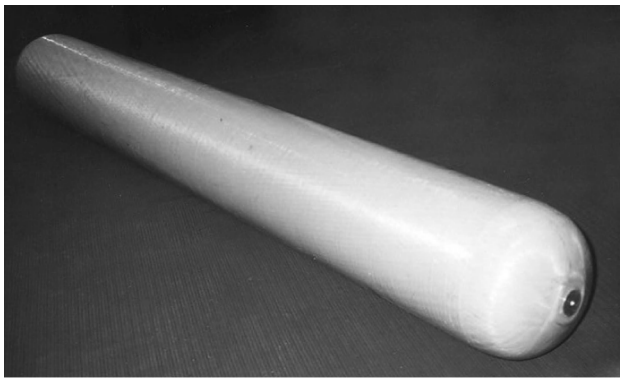


FIGURE 11.4

Cylindrical composite pressure vessel.



FIGURE 11.5

Cylindrical composite sections of the USSR Pioneer (left) and US Pershing (right) rockets in the National Air and Space Museum in Washington, DC.

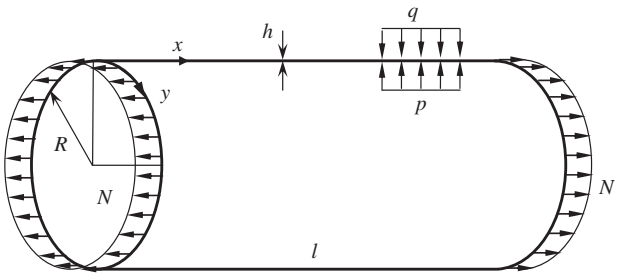


FIGURE 11.6

Loading of the cylindrical shell.

The equilibrium equations are

$$\frac{\partial N_x}{\partial x}+\frac{\partial N_{xy}}{\partial y}+p_x=0 \tag{11.1}$$

$$\frac{\partial N_y}{\partial y}+\frac{\partial N_{xy}}{\partial x}+\frac{V_y}{R}+p_y=0 \tag{11.2}$$

$$\frac{\partial M_x}{\partial x}+\frac{\partial M_{xy}}{\partial y}-V_x=0, \quad \frac{\partial M_y}{\partial y}+\frac{\partial M_{xy}}{\partial x}-V_y=0 \tag{11.3}$$

$$\frac{\partial V_x}{\partial x}+\frac{\partial V_y}{\partial y}-\frac{N_y}{R}+\overline{p}=0, \quad \overline{p}=p-q \tag{11.4}$$

These equations include the stress resultants and couples acting on the element of the reference surface shown in Fig. 11.7, and surface forces p and q. For an orthotropic material, the stress resultants and

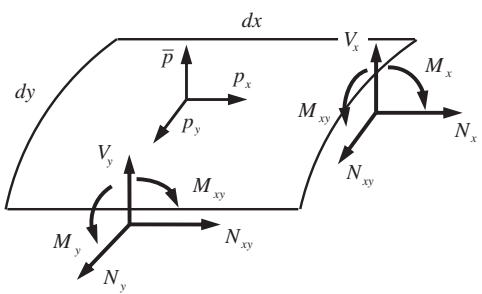


FIGURE 11.7

Stress resultants and couples acting on the element of the reference surface.

couples are linked with the generalized strains (strains and curvature changes) by the constitutive equations which have the form

$$\begin{aligned}
N_x &= B_{11}\varepsilon_x + B_{12}\varepsilon_y + C_{11}\kappa_x + C_{12}\kappa_y \\
N_y &= B_{12}\varepsilon_x + B_{22}\varepsilon_y + C_{12}\kappa_x + C_{22}\kappa_y \\
N_{xy} &= B_{44}\gamma_{xy} + C_{44}\kappa_{xy} \\
M_x &= C_{11}\varepsilon_x + C_{12}\varepsilon_y + D_{11}\kappa_x + D_{12}\kappa_y \\
M_y &= C_{12}\varepsilon_x + C_{22}\varepsilon_y + D_{12}\kappa_x + D_{22}\kappa_y \\
M_{xy} &= C_{44}\gamma_{xy} + D_{44}\kappa_{xy} \\
V_x &= S_x\gamma_x, \quad V_y = S_y\gamma_y
\end{aligned} \tag{11.5}$$

whereas the generalized strains (strains ε, γ and curvature changes κ) are expressed in terms of displacements as

$$\varepsilon_x = \frac{\partial u}{\partial x}, \quad \varepsilon_y = \frac{\partial v}{\partial y} + \frac{w}{R}, \quad \gamma_{xy} = \frac{\partial u}{\partial y} + \frac{\partial v}{\partial x} \tag{11.6}$$

$$\kappa_x = \frac{\partial \theta_x}{\partial x}, \quad \kappa_y = \frac{\partial \theta_y}{\partial y}, \quad \kappa_{xy} = \frac{\partial \theta_x}{\partial y} + \frac{\partial \theta_y}{\partial x} \tag{11.7}$$

$$\theta_x = \gamma_x + \omega_x, \quad \theta_y = \gamma_y + \omega_y, \quad \omega_x = -\frac{\partial w}{\partial x}, \quad \omega_y = \frac{v}{R} - \frac{\partial w}{\partial y} \tag{11.8}$$

Here, u, v, and w are the axial, circumferential, and radial displacements of the reference surface, $\theta_x, \theta_y,$ and ω_x, ω_y are the angles of rotation of the normal and the tangent to the reference surface in the axial and circumferential sections of the shell, and γ_x and γ_y are the transverse shear deformations.

The most widely used simplified version of this theory is the engineering theory of cylindrical shells (the so-called Mushtary-Donnell-Vlasov theory) in which some small terms are ignored in the equilibrium and strain-displacement equations. In particular, the term V_y/R is omitted in Eq. (11.2) and the corresponding term v/R in Eqs. (11.8) for ω_y is ignored. As a result, these equations are simplified to

$$\frac{\partial N_y}{\partial y} + \frac{\partial N_{xy}}{\partial x} + p_y = 0, \quad \omega_y = -\frac{\partial w}{\partial y} \tag{11.9}$$

This engineering theory is widely used to solve nonlinear and linearized buckling problems for cylindrical shells. For nonlinear problems, Eq. (11.4) for $\overline{p}$ is generalized as

$$\overline{p} = p - q - N_x\frac{\partial \omega_x}{\partial x} - N_{xy}\left(\frac{\partial \omega_x}{\partial y} + \frac{\partial \omega_y}{\partial x}\right) - N_y\frac{\partial \omega_y}{\partial y} \tag{11.10}$$

whereas Eqs. (11.6) for $\varepsilon_x, \varepsilon_y,$ and γ_{xy} have the form

$$\varepsilon_x = \frac{\partial u}{\partial x} + \frac{1}{2}\omega_x^2, \quad \varepsilon_y = \frac{\partial v}{\partial y} + \frac{w}{R} + \frac{1}{2}\omega_y^2, \quad \gamma_{xy} = \frac{\partial u}{\partial y} + \frac{\partial v}{\partial x} + \omega_x\omega_y \tag{11.11}$$

It follows from Eqs. (11.10) and (11.11) that the equations of nonlinear theory take into account the rotation of the shell element shown in Fig. 11.7. Application of Eq. (11.10) in conjunction with the linear equations for $\varepsilon_x, \varepsilon_y,$ and γ_{xy}, i.e., Eqs. (11.6), results in a nonlinear theory which takes into

account only the curvature changes of the shell element, whereas the strains and the angles of rotation are assumed to be small in comparison with unity (Vasiliev, 1993).

The simplest version of the theory is the membrane theory in which the bending and coupling stiffness coefficients of the shell wall D and C are ignored in comparison to the membrane stiffness coefficients B. Taking $C_{mn} = 0$ and $D_{mn} = 0$ in Eqs. (11.5), we get

$$N_x = B_{11}\varepsilon_x + B_{12}\varepsilon_y, \quad N_y = B_{12}\varepsilon_x + B_{22}\varepsilon_y, \quad N_{xy} = B_{44}\gamma_{xy} \tag{11.12}$$

where $\varepsilon_x, \varepsilon_y$, and γ_{xy} are specified by Eqs. (11.6). Since the moments M and the transverse shear forces V are zero in this membrane shell theory, the equilibrium equations, Eqs. (11.1)–(11.4), reduce to the following form:

$$\frac{\partial N_x}{\partial x} + \frac{\partial N_{xy}}{\partial y} + p_x = 0, \quad \frac{\partial N_y}{\partial y} + \frac{\partial N_{xy}}{\partial x} + p_y = 0, \quad N_y = \overline{p}R \tag{11.13}$$

The application of the membrane theory is limited by the fourth order of the governing equations, Eqs. (11.6), and (11.12), (11.13), with respect to coordinates x and y. The solution of these equations can satisfy only four boundary conditions at the shell edges $x = 0$ and $x = l$ (see Fig. 11.6) that should be imposed on membrane stress resultants N_x and N_y or displacements u and v. The boundary conditions restricting the shell normal deflection w cannot be satisfied within the framework of the membrane theory.

There are two ways to improve the membrane shell theory and to allow for the boundary conditions with respect to w, both involving the possibility to increase the order of the governing differential equations at least by two.

The first of these ways is to apply the nonlinear membrane theory using Eq. (11.10) for $\overline{p}$ in Eqs. (11.13). It follows from Eqs. (11.8) that Eq. (11.10) for $\overline{p}$ includes the second derivatives of the deflection, thus allowing us to derive a sixth-order set of equations.

The second way is associated with the so-called semi-membrane theory proposed by V.Z. Vlasov (1949). This semi-membrane theory of cylindrical shells is based on a number of assumptions that significantly simplify the equations of the general theory. In particular, it is assumed that the circumferential strain $\varepsilon_y = 0$ and the axial bending and twisting moments M_x and M_{xy} are neglected in comparison to the circumferential moment M_y. Actually, the semi-membrane theory models the shell as a system of rings joined with bars as shown in Fig. 11.8. To derive the equations of semi-membrane

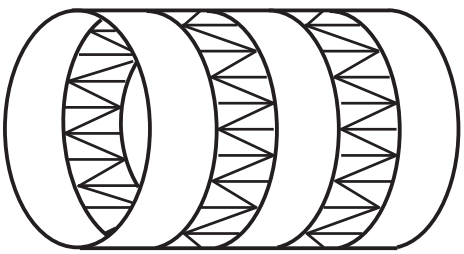


FIGURE 11.8

A physical model corresponding to the semi-membrane theory of cylindrical shells.

theory, consider the constitutive equations, Eqs. (11.5), and introduce some assumptions concerning the stiffness coefficients of the shell wall. First of all, neglect the coupling coefficients taking $C_{11} = C_{12} = C_{44} = 0$ and determine the coordinate of the reference surface e from the condition $C_{22} = 0$ (see Section 5.10). Using Eqs. (5.28), we have

$$e = \frac{I_{22}^{(1)}}{I_{22}^{(0)}} \tag{11.14}$$

(see Fig. 5.8), where

$$I_{22}^{(1)} = \int_0^h A_{22} t dt, \quad I_{22}^{(0)} = \int_0^h A_{22} dt$$

Furthermore, assume that the circular cross-sectional contour is inextensible, i.e., that the circumferential membrane stiffness coefficient B_{22} is infinitely high. Then, the second equation of Eqs. (11.5) yields $\varepsilon_y = 0$ and in accordance with the second equation of Eqs. (11.6)

$$\frac{\partial v}{\partial y} + \frac{w}{R} = 0 \tag{11.15}$$

Neglect also the axial, bending, and twisting stiffnesses of the shell wall taking $D_{11} = D_{12} = D_{44} = 0$. Then, the corresponding equations of Eqs. (11.5) give $M_x = 0, M_{xy} = 0$ and the first equation of Eqs. (11.3) yields $V_x = 0$. The remaining equations form the following set of equations of the semi-membrane theory of cylindrical shells:

$$\begin{aligned} &\frac{\partial N_x}{\partial x} + \frac{\partial N_{xy}}{\partial y} + p_x = 0, \quad \frac{\partial N_y}{\partial y} + \frac{\partial N_{xy}}{\partial x} + \frac{V_y}{R} + p_y = 0 \\ &\frac{\partial M_y}{\partial y} - V_y = 0, \quad \frac{\partial V_y}{\partial y} - \frac{N_y}{R} + \overline{p} = 0 \end{aligned} \tag{11.16}$$

$$N_x = B_{11}\varepsilon_x, \quad N_{xy} = B_{44}\gamma_{xy}, \quad M_y = D_{22}\kappa_y, \quad V_y = S_y\gamma_y \tag{11.17}$$

$$\varepsilon_x = \frac{\partial u}{\partial x}, \quad \gamma_{xy} = \frac{\partial u}{\partial y} + \frac{\partial v}{\partial x}, \quad \kappa_y = \frac{\partial \theta_y}{\partial y}, \quad \theta_y = \gamma_y + \omega_y, \quad \omega_y = \frac{v}{R} - \frac{\partial w}{\partial y} \tag{11.18}$$

As opposed to the equations of the general theory, Eqs. (11.1)–(11.8), that have the tenth order with respect to coordinates x and y, the order of equations of the semi-membrane theory, Eqs. (11.15)–(11.18), is four for the x-variable and eight for the y-variable. Decomposing the solution into trigonometric series with respect to the y-variable, we arrive at a fourth-order ordinary differential equation with respect to the x-variable that can be solved analytically. Numerous applications have demonstrated the high efficiency of the semi-membrane theory for the solution of static and buckling problems in the theory of cylindrical shells.

11.2 CYLINDRICAL SHELLS WHOSE STRESS-STRAIN STATE DOES NOT DEPEND ON THE AXIAL COORDINATE

Consider one-dimensional problems described by ordinary differential equations with respect to the y-variable. Such problems arise for infinitely long cylindrical shells or circular rings that are studied in the subsequent sections.

11.2.1 Circular rings

Composite rings (see Fig. 11.9) are widely used to reinforce cylindrical shells (see Fig. 11.2). Under the action of forces applied to the ring, we can neglect the load-carrying capacity of the shell and consider a separate ring loaded with radial ($\overline{p}$) and tangential (p_y) forces as shown in Fig. 11.10. For this ring, the governing equations, Eqs. (11.1)–(11.8), become

$$N_y' + \frac{V_y}{R} + p_y = 0, \quad M_y' - V_y = 0, \quad V_y' - \frac{N_y}{R} + \overline{p} = 0 \tag{11.19}$$

$$N_y = B_{22}\varepsilon_y, \quad M_y = D_{22}\kappa_y, \quad V_y = S_y\gamma_y \tag{11.20}$$

$$\varepsilon_y = \frac{\partial v}{\partial y} + \frac{w}{R}, \quad \kappa_y = \theta_y', \quad \theta_y = \gamma_y + \omega_y, \quad \omega_y = \frac{v}{R} - \frac{\partial w}{\partial y} \tag{11.21}$$

Here, $(\ldots)' = d(\ldots)/dy$. The coordinate of the reference surface e (see Fig. 11.10) is specified by Eq. (11.14) and the stiffness coefficients are

$$B_{22} = I_{22}^{(0)}, \quad D_{22} = I_{22}^{(2)} - \frac{\left(I_{22}^{(1)}\right)^2}{I_{22}^{(0)}}, \quad S_y = h^2\left(\int_0^h \frac{dt}{bG_{yz}}\right)^{-1} \tag{11.22}$$



FIGURE 11.9

Composite rings.

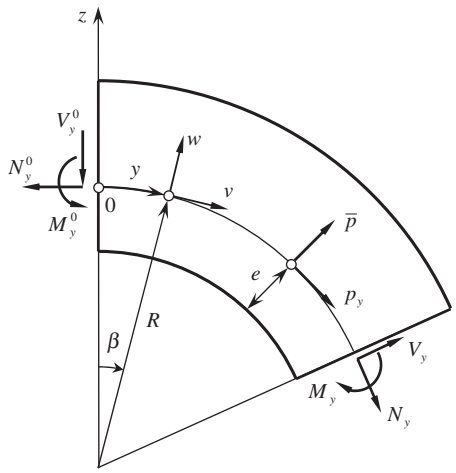


FIGURE 11.10

Element of a circular ring.

where

$$I_{22}^{(r)} = \int_0^h bA_{22}t^r dt \quad (r = 0, 1, 2) \tag{11.23}$$

Note that Eq. (11.23) takes into account that the ring width b may, in general, depend on the z-coordinate (see Fig. 11.10).

Consider the three equilibrium equations, Eqs. (11.19), that include three unknown functions, i.e., the axial and transverse forces N_y and V_y, and the bending moment M_y shown in Fig. 11.10. The first equation yields

$$V_y = -R(N_y' + p_y) \tag{11.24}$$

Substituting this result into the third equation of Eqs. (11.19), we get

$$N_y'' + k^2 N_y = k\overline{p} - p_y', \quad k = \frac{1}{R}$$

The solution of this equation is

$$N_y = C_1 \sin ky + C_2 \cos ky + \sin ky \int_0^y (\overline{p} - Rp_y') \cos kydy - \cos ky \int_0^y (\overline{p} - Rp_y') \sin kydy \tag{11.25}$$

Eliminating V_y from the first two equations of Eqs. (11.19), we get

$$M_y' + RN_y' + p_y = 0$$

Integration yields

$$M_y = C_3 - RN_y - R\int_0^y p_y dy \tag{11.26}$$

Thus, the forces V_y and N_y and the moment M_y are specified by Eqs. (11.24)–(11.26). Express the constants of integration $C_1, C_2,$ and C_3 in terms of the initial values of the forces and the moment $N_y^0 = N_y(y=0),\ V_y^0 = V_y(y=0),$ and $M_y^0 = M_y(y=0)$ (see Fig. 11.10). Then, the final expressions for N_y, V_y, and M_y become

$$\begin{aligned} N_y &= N(y)\cos ky - V(y)\sin ky \\ V_y &= V(y)\cos ky + N(y)\sin ky \\ M_y &= M_y^0 + RN_y^0 + RV(y)\sin ky - RN(y)\cos ky - R\int_0^y p_y dy \end{aligned} \tag{11.27}$$

where

$$N(y) = N_y^0 - \int_0^y (\overline{p}\sin ky + p_y \cos ky)dy$$

$$V(y) = V_y^0 - \int_0^y (\overline{p}\cos ky - p_y \sin ky)dy$$

For a closed ring, the solution must be periodic, so that

$$N_y(y = 2\pi R) = N_y^0, \quad V_y(y = 2\pi R) = V_y^0, \quad M_y(y = 2\pi R) = M_y^0$$

Then, Eqs. (11.27) provide the following conditions for the applied loads:

$$\int_0^{2\pi R} (\overline{p}\sin ky + p_y \cos ky)dy = 0, \quad \int_0^{2\pi R} (\overline{p}\cos ky - p_y \sin ky)dy = 0, \quad \int_0^{2\pi R} p_y dy = 0$$

which ensure the equilibrium of the ring as a solid.

To determine the displacements v, w, and the angle of rotation θ_y, apply Eqs. (11.20) and (11.21) that yield

$$\frac{\partial v}{\partial y} + \frac{w}{R} = \frac{N_y}{B_{22}}, \quad \theta_y' = \frac{M_y}{D_{22}}, \quad \theta_y - \frac{v}{R} + w' = \frac{V_y}{S_y} \tag{11.28}$$

The first and the third of these equations give

$$\begin{aligned} w &= \frac{RN_y}{B_{22}} - R\frac{\partial v}{\partial y}, \\ \theta_y &= \frac{V_y}{S_y} + \frac{v}{R} - w' \end{aligned} \tag{11.29}$$

Substituting w into the second equation and the expression obtained for θ_y into the second equation of Eqs. (11.28), we arrive at

$$v''' + k^2 v' = \frac{M_y}{RD_{22}} - \frac{V_y'}{RS_y} + \frac{N_y''}{B_{22}}$$

Using Eqs. (11.27) for N_y, V_y, and M_y to eliminate the derivatives from the right-hand part of this equation, we get

$$v''' + k^2 v' = k^2 F(y) \tag{11.30}$$

in which

$$F(y) = f(y) - \frac{p_y' R^2}{B_{22}}, \quad f(y) = \frac{RM_y}{D_{22}} - \left(\frac{1}{B_{22}} + \frac{1}{S_y}\right)\left(N_y - \overline{p}R\right)$$

where M_y and N_y are specified by Eqs. (11.27). The general solution of Eq. (11.30) is

$$v = C_4 + C_5 \sin ky \; C_6 \cos ky + \int_0^y F(y)dy$$
$$- \sin ky \int_0^y F(y) \sin ky \, dy - \cos ky \int_0^y F(y) \cos ky \, dy$$

The constants of integration $C_4,\ C_5,$ and C_6 can be expressed in terms of the initial displacements and angle of rotation of the beam cross section $v_0 = v(y=0), w_0 = w(y=0),$ and $\theta_0 = \theta_y(y=0)$. Using Eqs. (11.29) to determine w and θ_y, we finally get

$$\begin{aligned} v &= U(y) \cos ky - W(y) \sin ky + R\Theta(y) \\ w &= \frac{RN_y}{B_{22}} + W(y) \cos ky + U(y) \sin ky \\ \theta_y &= \Theta(y) + V_y\left(\frac{1}{B_{22}} + \frac{1}{S_y}\right) + \frac{Rp_y}{B_{22}} \end{aligned} \tag{11.31}$$

where

$$U(y) = v_0 - RC_0 - \int_0^y f(y) \cos kydy + \frac{R^2 p_y}{B_{22}} \cos ky + \frac{R}{B_{22}} \int_0^y p_y \sin kydy$$

$$W(y) = w_0 - \frac{RN_y^0}{B_y} + \int_0^y f(y) \sin kydy - \frac{R^2 p_y}{B_{22}} \sin ky + \frac{R}{B_{22}} \int_0^y p_y \cos kydy$$

$$\Theta(y) = C_0 + \frac{1}{R} \int_0^y f(y)dy - \frac{Rp_y}{B_{22}}, \quad C_0 = \theta_0 - V_y^0\left(\frac{1}{B_{22}} + \frac{1}{S_y}\right)$$

For closed rings, the following continuity conditions must be satisfied:

$$v(y = 2\pi R) = v_0, \quad w(y = 2\pi R) = w_0, \quad \theta_y(y = 2\pi R) = \theta_0$$

Substituting Eqs. (11.31), we get

$$\int_0^{2\pi R} f(y) \sin ky dy = 0, \quad \int_0^{2\pi R} f(y) \cos ky dy = 0, \quad \int_0^{2\pi R} f(y) dy = 0$$

These conditions should be used to determine the initial forces and moment N_y^0, V_y^0, and M_y^0 in a closed ring, whereas the initial displacements v_0, w_0, and the initial angle of rotation θ_0 of the ring cross section can be found if we fix an arbitrary cross section of the ring. If the cross section $y = 0$ is fixed, then $v_0 = w_0 = \theta_0 = 0$.

As an example, consider the ring loaded with two forces P applied as shown in Fig. 11.11. In accordance with the symmetry conditions, we must take

$$N_y^0 = 0, \quad V_y^0 = \frac{P}{2}, \quad v_0 = 0, \quad \theta_0 = 0, \quad v\left(y = \frac{\pi R}{2}\right) = 0, \quad \theta_y\left(y = \frac{\pi R}{2}\right) = 0$$

Then, Eqs. (11.27) and (11.31) give

$$\begin{aligned} &N_y = \frac{P}{2} \sin ky, \quad V_y = -\frac{P}{2} \cos ky, \quad M_y = \frac{PR}{2\pi}(2 - \pi \sin ky) \\ &w_0 = 0.0745 \frac{PR^3}{D_{22}} \left[1 + 5.3 \frac{D}{R^2}\left(\frac{1}{B_{22}} + \frac{1}{S_y}\right)\right] \end{aligned} \tag{11.32}$$

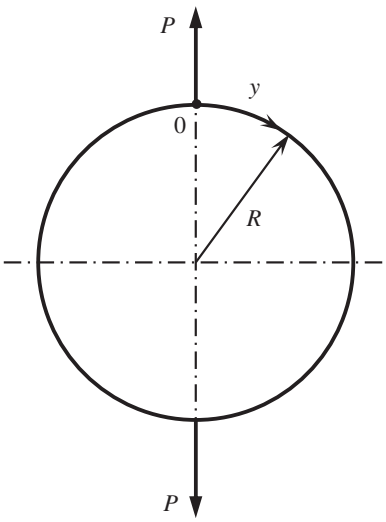


FIGURE 11.11

A ring loaded with two self-balanced forces.

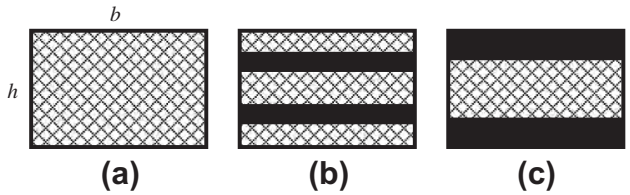


FIGURE 11.12

Rectangular cross section of fiberglass fabric-epoxy ring (a) reinforced with carbon-epoxy layers (b, c).

For the homogeneous beam with a rectangular cross section as shown in Fig. 11.12a,

$$B_{22} = Ebh, \quad D_{22} = \frac{1}{12}Ebh^3, \quad S_y = Gbh$$

and the radial displacement of point 0 in Fig. 11.11 specified by Eq. (11.32) becomes

$$w_0 = 0.0745\frac{12PR^3}{Ebh^3}\left[1 + 0.44\frac{h^2}{R^2}\left(1 + \frac{E}{G}\right)\right] \tag{11.33}$$

The first term in the parenthesis multiplied by $(h/R)^2$ takes into account the deformation of the beam axial line and is negligible for thin rings. Ignoring this deformation, i.e., taking $B_{22} \to \infty$, we can simplify the solution and reduce Eqs. (11.31) to the form

$$\begin{aligned} v &= U(y)\cos ky - W(y)\sin ky + R\Theta(y) \\ w &= W(y)\cos ky + U(y)\sin ky \\ \theta_y &= \Theta(y) + \frac{V_y}{S_y} \end{aligned} \tag{11.34}$$

where

$$U(y) = v_0 + R\theta_0 + \frac{RV_y^0}{S_y} - \int_0^y f(y)\cos ky dy$$

$$W(y) = w_0 + \int_0^y f(y)\sin ky dy$$

$$\Theta(y) = \theta_0 - \frac{V_y^0}{S_y} + \frac{1}{R}\int_0^y f(y)dy, \quad f(y) = \frac{RM_y}{D_{22}} - \frac{1}{S_y}\left(N_y - \overline{p}R\right)$$

The term including E/G in Eq. (11.33) allows for the transverse shear deformation. Taking $S_y \to \infty$, we can neglect this deformation. Then, Eqs. (11.34) are further simplified as follows

$$v = v_0 \cos ky + R\theta_0(1 - \cos ky) - w_0 \sin ky + R\int_0^y \frac{M_y}{D_{22}}dy$$
$$- R\cos ky \int_0^y \frac{M_y}{D_{22}} \cos kydy - R \sin ky \int_0^y \frac{M_y}{D_{22}} \sin ky\, dy$$
$$w = w_0 \cos ky + (v_0 - R\theta_0) \sin ky + R \cos ky \int_0^y \frac{M_y}{D_{22}} \sin kydy - R \sin ky \int_0^y \frac{M_y}{D_{22}} \cos ky\, dy$$
$$\theta_y = \theta_0 + \int_0^y \frac{M_y}{D_{22}}dy$$

These equations, in contrast to the foregoing Eqs. (11.31) and (11.34), are valid for the rings whose bending stiffness D_{22} depends on y.

Experimental verification of this solution has been undertaken for the rings with parameters $h/R = 0.105$ and $b/h = 1.5$. The rings were made of fiberglass fabric (see Fig. 11.12a) and were reinforced by carbon fibers (dark layers in Fig. 11.12b and c). The calculated dependencies of the ring deflections at point 0 (see Fig. 11.11) on the applied load P corresponding to Eqs. (11.32) are presented in Fig 11.13 by solid lines along with the experimental results (circles).

11.2.2 Infinitely long cylindrical panel

Consider an infinitely long cylindrical composite panel (see Fig. 11.14) loaded with internal pressure simulating, e.g., a skin panel of an airplane fuselage. To describe the behavior of the panel, we apply the engineering theory of cylindrical shells, i.e., simplify the governing equations in accordance with Eqs. (11.9). As a consequence of the high strength of modern composite materials, the ratio h/R for such panels is generally small so that the transverse shear deformation can be neglected and we can take $S_y \to \infty$. However, for the same reason, the bending stiffness of the panel wall is also small and we should allow for the local curvature of the panel caused by bending. To take this effect into account, we need to apply Eq. (11.10) which yields, in conjunction with the second equation of Eqs. (11.9), the following expression for $\overline{p}$ for the panel shown in Fig. 11.14:

$$\overline{p} = p - N_y \frac{\partial^2 w}{\partial y^2}$$

Finally, we assume that the coordinate of the reference surface e corresponds to Eq. (11.14), so that $C_{22} = 0$. As a result, the governing equations describing the behavior of the panel shown in Fig. 11.14 can be written as

$$N_y' = 0, \quad M_y' - V_y = 0, \quad V_y' - N_y\left(\frac{1}{R} - w''\right) + p = 0 \tag{11.35}$$

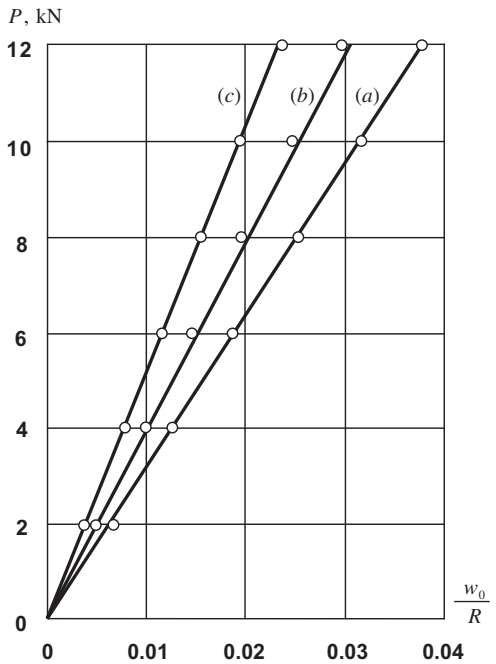


FIGURE 11.13

Dependencies of the ring deflection on the applied force corresponding to the cross sections shown in Fig. 11.12a–c: (———) analysis and (◦◦◦) experiment.

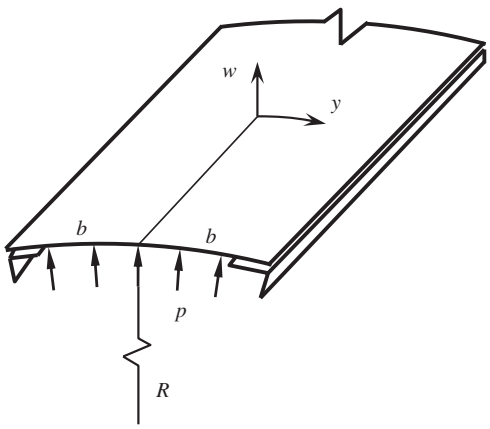


FIGURE 11.14

Infinitely long cylindrical panel under internal pressure.

$$N_y = B_{22}\left(v' + \frac{w}{R}\right), \quad M_y = -D_{22}w'' \tag{11.36}$$

The first equation of Eqs. (11.35) yields $N_y = N = constant$ and the third equation, being transformed with the aid of the second equation, becomes

$$M_y'' - N\left(\frac{1}{R} - w''\right) + p = 0 \tag{11.37}$$

The term in parenthesis is actually the curvature of the panel in the deformed state. Substituting M_y in accordance with Eqs. (11.36), we arrive at the following equation:

$$w^{IV} - k^2 w'' = \frac{p}{D_{22}}(1-\lambda), \quad k^2 = \frac{N}{D_{22}}, \quad \lambda = \frac{N}{pR} \tag{11.38}$$

The general solution of this equation is

$$w = C_1 + C_2 y + C_3 \sinh ky + C_4 \cosh ky - \frac{y^2(1-\lambda)}{2R\lambda}$$

Due to the symmetry conditions (see Fig. 11.14), $C_2 = C_3 = 0$, so that

$$w = C_1 + C_4 \cosh ky - \frac{y^2(1-\lambda)}{2R\lambda} \tag{11.39}$$

The integration constants C_1 and C_4 in Eq. (11.39) can be found from the boundary conditions at the panel edges $y = \pm b$ (see Fig. 11.14).

For simply supported edges, $w = w'' = 0$ at $y = \pm b$ and the solution in its final form is

$$w = \frac{1-\lambda}{R\lambda}\left[\frac{1}{2}\left(b^2 - y^2\right) - \frac{\cosh kb - \cosh ky}{k^2 \cosh kb}\right] \tag{11.40}$$

For clamped edges, $w = w' = 0$ at $y = \pm b$ and

$$w = \frac{1-\lambda}{R\lambda}\left[\frac{1}{2}\left(b^2 - y^2\right) - \frac{b}{k \sinh kb}(\cosh kb - \cosh ky)\right] \tag{11.41}$$

The circumferential displacement v can be found by integration of the first equation of Eqs. (11.36). Taking into account that $N_y = N$ and $v(y = 0) = 0$, we get

$$v = \frac{Ny}{B_{22}} - \frac{1}{R}\int_0^y w dy \tag{11.42}$$

At the fixed edges $y = \pm b/2$ (see Fig. 11.14), we have $v = 0$ and Eq. (11.42) yields the following equation for N:

$$\frac{Nb}{B_{22}} = \frac{1}{R}\int_0^b w dy \tag{11.43}$$

in which w is substituted in accordance with Eqs. (11.40) or (11.41). Thus, for simply supported edges, we have

$$\frac{\lambda N}{B_{22}(1-\lambda)} - \frac{b^2}{3R^2} = \frac{1}{k^2R^2}\left(\frac{1}{kb}\tanh kb - 1\right)$$

and for clamped edges

$$\frac{\lambda N}{B_{22}(1-\lambda)} - \frac{b^2}{3R^2} = \frac{b}{kR^2}\left(\frac{1}{kb} - \operatorname{cotanh} kb\right) \tag{11.44}$$

As an example, consider a fuselage panel. Since the panel shown in Fig. 11.14 is jointed along the stringers with the adjacent panel, the isolated panel behaves as if it is clamped at the edges $y = \pm b$ and is described by Eqs. (11.41) and (11.44). The carbon-epoxy panel has a cross-ply $0/90^\circ$ structure with thicknesses $h_0 = 0.8$ mm and $h_{90} = 1.6$ mm, and ratios $h/R = 0.0012$, $b/R = 0.075$. The calculated dependence of the normalized deflection $\overline{w} = w/w_0$, in which $w_0 = pR^2/B_{22}$ is the deflection corresponding to the linear membrane shell theory, on the y-coordinate is shown in Fig. 11.15 by curve 1.

We can compare the solution obtained previously with the linear solution based on the equations that ignore the curvature change under loading. The corresponding governing equation can be obtained from Eq. (11.37) if we neglect w'' in comparison with $1/R$. Then, Eq. (11.38) takes the form

$$w^{IV} = \frac{p}{D_{22}}(1-\lambda)$$

and its solution satisfying the boundary conditions $w(y = \pm b) = w'(y = \pm b) = 0$ is

$$w = \frac{(1-\lambda)p}{24D_{22}}\left(b^2 - y^2\right)^2 \tag{11.45}$$

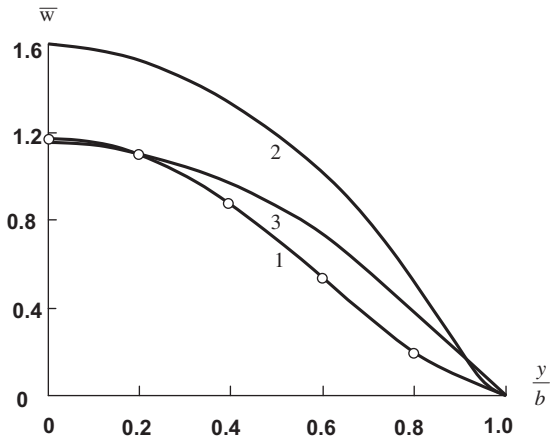


FIGURE 11.15

Dependencies of the normalized deflection on the y-coordinate corresponding to the nonlinear solution, Eq. (11.41) (curve 1), linear solution, Eq. (11.45) (curve 2), nonlinear membrane solution, Eq. (11.46) (curve 3), and complete nonlinear solution (∘∘∘).

The equation for the stress resultant N, Eq. (11.43), yields

$$N = \frac{pR}{1 + \dfrac{45D_{22}R^2}{B_{22}b^4}}$$

The linear solution given by Eq. (11.45) is shown in Fig. 11.15 by curve 2. As can be seen, the difference to the nonlinear solution (curve 1) is significant.

Since the bending stiffness of the panel wall D_{22} is relatively small, we can apply the nonlinear membrane theory based on Eqs. (11.10), and (11.12), (11.13). The corresponding governing equation follows from Eq. (11.37) if we take $M_y = 0$. Then, Eq. (11.38) reduces to

$$w'' = -\frac{1-\lambda}{R\lambda}$$

The solution of this equation satisfying the boundary conditions $w(y = \pm b) = 0$ is

$$w = \frac{1-\lambda}{2\lambda R}\left(b^2 - y^2\right) \tag{11.46}$$

The equation for N, i.e., Eq. (11.43), reduces to the following quadratic equation:

$$\lambda^2 = \eta(1-\lambda), \quad \eta = \frac{B_{22}b^2}{3pR^3}$$

whose solution is

$$\lambda = \frac{N}{pR} = \frac{1}{2}\left[\sqrt{\eta(\eta+4)} - \eta\right]$$

The membrane solution, i.e., Eq. (11.46), is shown in Fig. 11.15 by curve 3. As can be seen, this solution predicts the maximum deflection with fair accuracy, though it cannot, naturally, satisfy the boundary condition $w'(y = \pm b)$ for the clamped edge.

Finally, we can apply the complete nonlinear equations to the problem under study. As has been noted, Eq. (11.37) takes into account only the first-order nonlinear effect associated with the change of the panel curvature under loading. If in addition to this the deflection is not small in comparison with the panel width $2b$ (see Fig. 11.14), we must use Eq. (11.11) for ε_y and change the first equation of Eqs. (11.30) to the following one:

$$N_y = B_{22}\left[v' + \frac{w}{R} + \frac{1}{2}(w')^2\right]$$

Then, the solution is specified, as earlier, by Eq. (11.39), but Eq. (11.43) for N is generalized as

$$\frac{Nb}{B_{22}} = \frac{1}{R}\int_0^b w dy + \frac{1}{2}\int_0^b (w')^2 dy$$

The corresponding solution is shown in Fig. 11.15 with circles. As can be seen, its deviation from the solution given by Eq. (11.41) (curve 1) is negligible.

In conclusion note that a problem similar to that considered earlier has been studied by Boitnott et al. (1985).

11.3 AXISYMMETRIC DEFORMATION OF CYLINDRICAL SHELLS

Consider one more one-dimensional problem: deformation of cylindrical shells whose stress-strain state does not depend on the circumferential coordinate y. Such shells are typical structural elements of composite pipes and pressure vessels (see Figs. 11.1 and 11.4).

Let the shell be loaded with internal, p, and external, q, pressure and axial forces N that do not depend on y as shown in Fig. 11.16. If the shell displacements, forces, and moment depend on the x-coordinate only, the governing equations, Eqs. (11.1)–(11.8), reduce to

$$N_x' = 0, \quad M_x' - V_x = 0, \quad V_x' - \frac{N_y}{R} + \overline{p} = 0 \tag{11.47}$$

$$\begin{aligned} N_x &= B_{11}\varepsilon_x + B_{12}\varepsilon_y + C_{11}\kappa_x, \quad N_y = B_{12}\varepsilon_x + B_{22}\varepsilon_y + C_{12}\kappa_x \\ M_x &= C_{11}\varepsilon_x + C_{12}\varepsilon_y + D_{11}\kappa_x, \quad V_x = S_x\gamma_x \end{aligned} \tag{11.48}$$

$$\varepsilon_x = u', \quad \varepsilon_y = \frac{w}{R}, \quad \kappa_x = \theta_x', \quad \theta_x = \gamma_x + \omega_x, \quad \omega_x = -w' \tag{11.49}$$

Here $(\ldots)' = d(\ldots)/dx$. The stiffness coefficients in Eqs. (11.48) are

$$B_{mn} = I_{mn}^{(0)}, \quad C_{mn} = I_{mn}^{(1)} - eI_{mn}^{(0)}, \quad D_{11} = I_{11}^{(2)} - 2eI_{11}^{(1)} + e^2 I_{11}^{(0)}$$

$$S_x = h^2\left(\int_0^h \frac{dt}{G_{xz}}\right)^{-1}, \quad I_{mn}^{(r)} = \int_0^h A_{mn}t^r dt \tag{11.50}$$

where $mn = 11, 12, 22$ and $r = 0, 1, 2$, whereas e is an arbitrary coordinate of the reference surface. Allow for the first-order nonlinear effect by applying Eq. (11.10) in the following form:

$$\overline{p} = p - q + N_x w'' \tag{11.51}$$

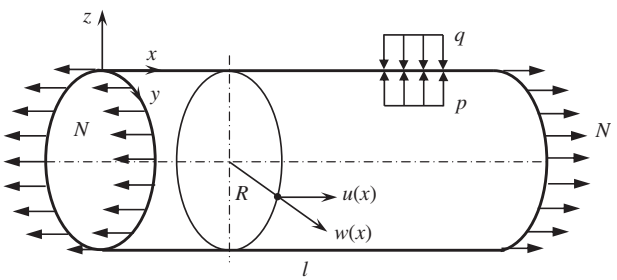


FIGURE 11.16

Axisymmetrically loaded cylindrical shell.

The last term of this equation allows us to take into account the meridian curvature which takes place under load.

We now reduce the set of equations, Eqs. (11.47)–(11.49), to one governing equation for the shell deflection w. The first equilibrium equation of Eqs. (11.47) in conjunction with Fig. 11.16 yields $N_x = N$, where N is the applied axial force. Then, the first constitutive equation in Eqs. (11.48) and Eqs. (11.49) allow us to determine

$$u' = \frac{1}{B_{11}}\left(N - B_{12}\frac{w}{R} - C_{11}\theta_x'\right) \tag{11.52}$$

Substitute this result into Eqs. (11.48) for N_y and M_x. Using Eqs. (11.49), we get

$$N_y = \frac{B_{12}}{B_{11}}N + B\frac{w}{R} + C\theta_x', \quad M_x = \frac{C_{11}}{B_{11}}N + C\frac{w}{R} + D\theta_x' \tag{11.53}$$

where

$$B = B_{22} - \frac{B_{12}^2}{B_{11}}, \quad C = C_{12} - \frac{B_{12}C_{11}}{B_{11}}, \quad D = D_{11} - \frac{C_{11}^2}{B_{11}} \tag{11.54}$$

From the third equilibrium equation in Eqs. (11.47) where $\overline{p}$ is specified by Eq. (11.51) in which $N_x = N$ we find

$$V_x' = \frac{N_y}{R} - Nw'' - p + q$$

Substitute N_y from Eqs. (11.53), i.e.,

$$V_x' = \frac{1}{R}\left(\frac{B_{12}}{B_{11}}N + B\frac{w}{R} + C\theta_x'\right) - Nw'' - p + q \tag{11.55}$$

The constitutive equation in Eqs. (11.48) for V_x in conjunction with Eq. (11.49) for θ_x yields

$$\theta_x = \frac{V_x}{S_x} - w' \tag{11.56}$$

Differentiation and substitution of Eq. (11.55) results in the equation which allows us to express θ_x' as

$$\theta_x' = \frac{1}{1-c}\left[\frac{1}{S_x}\left(\frac{B_{12}N}{RB_{11}} + B\frac{w}{R^2} - p + q\right) - \left(1 + \frac{N}{S_x}\right)w''\right]$$

where $c = C/RS_x$. Using this equation, we can eliminate θ_x' from Eqs. (11.53) for M_x and Eq. (11.55) for V_x' and present them as

$$\begin{aligned} M_x &= \frac{D}{1-c}\left\{\left[\frac{C_{11}}{D}(1-c) + \frac{B_{12}}{RS_x}\right]\frac{N}{B_{11}} + \left[\frac{C}{D}(1-c) + \frac{B}{RS_x}\right]\frac{w}{R} - \left(1 + \frac{N}{S_x}\right)w'' - \frac{1}{S_x}(p-q)\right\} \\ V_x' &= \frac{1}{1-c}\left\{\frac{B_{12}N}{RB_{11}} + B\frac{w}{R^2} - p + q - \left[\frac{C}{R}\left(1 + \frac{N}{S_x}\right) + N\right]w''\right\} \end{aligned} \tag{11.57}$$

Finally, differentiating the second equilibrium equation of Eqs. (11.47) and substituting Eqs. (11.57), we arrive at the following governing equation:

$$w^{IV} - 2k_1^2 w'' + k_2^4 w = k_p \tag{11.58}$$

where

$$\begin{gathered} k_1^2 = \frac{1}{2D_s}\left[\frac{BD}{R^2 S_x} + N(1+c) + \frac{C}{R}(2-c)\right], \quad k_2^4 = \frac{B}{R^2 D_s} \\ k_p = \frac{1}{D_s}\left[p - q - \frac{B_{12}N}{RB_{11}} - \frac{D_s}{S_x}(p'' - q'')\right], \quad D_s = D\left(1 + \frac{N}{S_x}\right) \end{gathered} \tag{11.59}$$

The general solution of Eq. (11.58) is

$$w = \sum_{i=1}^{4} C_i \Phi_i(x) + w_p \tag{11.60}$$

in which C_i are the constants of integration and w_p is the particular solution which for constant internal pressure $p = p_0$ has the following form:

$$w_p = \frac{R}{D}\left(p_0 R - \frac{B_{12}N}{B_{11}}\right) \tag{11.61}$$

Having found the deflection, Eq. (11.60), we can further determine the bending moment M_x using Eqs. (11.57); then the transverse shear force V_x can be found from the second equilibrium equation of Eqs. (11.47) and the angle of rotation θ_x can be determined from Eq. (11.56). The axial displacement u can be obtained by integrating Eq. (11.52).

Return to Eqs. (11.50) which specify the stiffness coefficients and include the unknown coordinate of the reference surface e. Though the stiffness coefficients C_{mn} and D_{mn} depend on e, the generalized stiffness coefficients B, C, and D in Eqs. (11.54) which enter the formulas for the coefficients given by Eqs. (11.59) do not depend on e. Indeed, substituting Eqs. (11.50) into Eqs. (11.54), we get the expressions

$$\begin{gathered} B = \frac{1}{I_{11}^{(0)}}\left[I_{11}^{(0)} I_{22}^{(0)} - \left(I_{12}^{(0)}\right)^2\right], \quad C = \frac{1}{I_{11}^{(0)}}\left[I_{11}^{(0)} I_{12}^{(1)} - I_{12}^{(0)} I_{11}^{(1)}\right] \\ D = \frac{1}{I_{11}^{(0)}}\left[I_{11}^{(0)} I_{11}^{(2)} - \left(I_{11}^{(1)}\right)^2\right] \end{gathered} \tag{11.62}$$

which do not include e. Thus, the obtained deflection does not depend on the location of the reference surface. This location affects only the axial displacement u in Eq. (11.52) since u is the displacement of the points on the reference surface to which the axial forces N are applied.

The possible solutions $\Phi_i(x)$ in Eq. (11.60) are presented in Table 9.1. For relatively short shells and $k_2 > k_1$, the functions $\Phi_i(x)$ are specified by Eqs. (9.143). For relatively long shells, the other form of these solutions can be used, i.e., for $k_2 > k_1$

$$\begin{aligned} \Phi_1(x) &= e^{-rx}\cos tx, \quad \Phi_2(x) = e^{-rx}\sin tx \\ \Phi_3(x) &= e^{rx}\cos tx, \quad \Phi_4(x) = e^{rx}\sin tx \end{aligned} \tag{11.63}$$

where

$$r=\sqrt{\frac{1}{2}\left(k_2^2+k_1^2\right)},\quad t=\sqrt{\frac{1}{2}\left(k_2^2-k_1^2\right)}$$

The derivatives of the functions in Eqs. (11.63) can be expressed in terms of these functions as follows

$$\Phi_1'=-(t\Phi_2+r\Phi_1),\quad \Phi_2'=t\Phi_1-r\Phi_2$$
$$\Phi_1''=\alpha\Phi_1+\beta\Phi_2,\quad \Phi_2''=\alpha\Phi_2-\beta\Phi_1$$
$$\Phi_1'''=-r\gamma\Phi_1+t\eta\Phi_2,\quad \Phi_2'''=-r\gamma\Phi_2-t\eta\Phi_1$$

where

$$\alpha=r^2-t^2,\quad \beta=2rt,\quad \gamma=r^2-3t^2,\quad \eta=t^2-3r^2$$

The constants C_1-C_4 in Eq. (11.60) can be found from the following natural boundary conditions at the shell edges $x=0$ and $x=l$:

$$N\delta u=0,\quad M_x\delta\theta_x=0,\quad (V_x+Nw')\delta w=0 \tag{11.64}$$

(see Fig. 11.16). These equations are equivalent to two static boundary conditions imposed on the bending moment M_x and generalized transverse force (V_x+Nw') which includes the projection of the axial force N on the shell radius, or to three kinematic boundary conditions for axial displacement u, the angle of rotation θ_x, and the deflection w.

The governing equation, Eq. (11.58), allows for two specific effects: geometric nonlinearity which shows itself through the terms including N in the expression for k_1 and transverse shear deformation which is associated with the stiffness coefficient S_x. Consider some particular cases.

11.3.1 Linear theory of shear deformable shells

For relatively thick composite shells, the transverse shear deformation can be important, whereas the nonlinear terms can be neglected. Then, Eqs. (11.59) become

$$k_1^2=\frac{1}{2DR}\left[\frac{BD}{S_x}+C(2-c)\right],\quad k_2^4=\frac{B}{R^2D},\quad c=\frac{C}{RS_x}$$
$$k_p=\frac{1}{D}\left[p-q-\frac{B_{12}N}{RB_{11}}-\frac{D}{S_x}(p''-q'')\right] \tag{11.65}$$

and the terms including the product Nw'' should be omitted in Eqs. (11.57). The third boundary condition in Eqs. (11.64) reduces to $V_x\delta w=0$.

11.3.2 Linear classical shell theory

In classical shell theory, $S_x\to\infty$ and Eqs. (11.65) are further simplified as

$$k_1^2=\frac{C}{DR},\quad k_2^4=\frac{B}{DR^2},\quad k_p=\frac{1}{D}\left(p-q-\frac{B_{12}N}{RB_{11}}\right) \tag{11.66}$$

11.3.3 Nonlinear classical theory

In the equations of this theory, the coefficient k_1 includes, in addition to the corresponding expression in Eqs. (11.66), a term incorporating the axial force N, i.e.,

$$k_1^2 = \frac{1}{2D}\left(\frac{2C}{R} + N\right), \quad k_2^4 = \frac{B}{DR^2}, \quad k_p = \frac{1}{D}\left(p - q - \frac{B_{12}N}{RB_{11}}\right) \tag{11.67}$$

and the natural boundary conditions are specified by Eqs. (11.64).

11.3.4 Nonlinear membrane theory

Taking $D = 0$, $S_x \to \infty$, and $C = 0$, we arrive at the following equation

$$w'' - k^2 w = k_N \tag{11.68}$$

where

$$k^2 = \frac{BR^2}{N}, \quad k_N = \frac{B_{12}N}{RB_{11}} - p + q$$

For the case of internal pressure, i.e., $p = p_0$, $q = 0$, the solution of Eq. (11.68) is

$$w = C_1 e^{-kx} + C_2 e^{kx} = \frac{N}{BR^2}\left(p_0 - \frac{B_{12}N}{RB_{11}}\right) \tag{11.69}$$

The constants of integration C_1 and C_2 can be found from the third boundary condition in Eqs. (11.64), i.e.,

$$V_N \delta w = 0 \tag{11.70}$$

according to which we should specify at the shell edges either w or the projection of the axial force $V_N = Nw'$ on the shell radius.

11.3.5 Examples

As the first example, consider a cylindrical shell made of fiberglass fabric with the following properties:

$$E_1 = 18.1 \text{ GPa}, \quad E_2 = 23 \text{ GPa}, \quad G_{xz} = 2.3 \text{ GPa}, \quad \upsilon_{12} = 0.16, \quad \upsilon_{21} = 0.21$$

The shell normalized thickness is $\overline{h} = h/R = 0.03$. The shell is loaded with uniform internal pressure $p_0 = 2$ MPa. The end $x = 0$ (see Fig. 11.16) is clamped, whereas the end $x = l$ is closed with a dome, so that $N = p_0 R/2$. As has been noted, the solution does not depend on the coordinate of the reference surface e; however, the initial equations do depend on this coordinate. For the homogeneous shell under consideration, the equations take the simplest form if we take $e = h/2$, i.e., if the reference surface coincides with the middle surface. Then the stiffness coefficients of the shell wall become

$$B_{11} = \overline{E}_1 h, \quad B_{12} = \upsilon_{12}\overline{E}_1 h, \quad B_{22} = \overline{E}_2 h, \quad D_{11} = \frac{1}{12}\overline{E}_1 h^3, \quad S_x = G_{xz} h$$

where $\overline{E}_{1,2} = E_{1,2}/(1 - \upsilon_{12}\upsilon_{21})$. Then, Eqs. (11.54) and (11.59) yield

$$B = E_2 h, \quad C = 0, \quad D = \frac{1}{12}\overline{E}_1 h^3, \quad D_s = D(1+\lambda), \quad \lambda = \frac{p_0 R}{2G_{xz}h}$$

The coefficients given by Eqs. (11.59) for the shell under study are

$$k_1^2 = \frac{3}{1+\lambda}\left(\frac{E_2}{6G_{xz}R^2} + \frac{p_0 R}{\overline{E}_1 h^3}\right), \quad k_2^4 = \frac{12E_2}{\overline{E}_1 R^2 h^2 (1+\lambda)}, \quad k_p = \frac{12p_0}{\overline{E}h^3(1+\lambda)}\left(1 - \frac{\upsilon_{12}}{2}\right)$$

For a long shell, the deflection is specified by Eqs. (11.60), (11.61), and (11.63) and can be presented as

$$w = e^{-rx}(C_1 \cos tx + C_2 \sin tx) + w_p \tag{11.71}$$

where

$$w_p = \frac{p_0 R^2}{2E_2 h}(2 - \upsilon_{12})$$

for the clamped end $x = 0$, Eqs. (11.64) yield the following boundary conditions: $w\ (0) = 0$ and $\theta_x(0) = 0$. To apply these boundary conditions, we need to make use of the equation for θ_x which follows from Eqs. (11.47) and (11.56), i.e.,

$$\theta_x = \frac{V_x}{S_x} - w' = \frac{M_x'}{S_x} - w' \tag{11.72}$$

where M_x and w are specified by Eqs. (11.57) and (11.71). Finally, the constants of integration in Eqs. (11.71) are

$$C_1 = -w_p, \quad C_2 = -\mu w_p, \quad \mu = \frac{r\left(1 - \dfrac{\eta E_2}{G_{xz}}\right) + \eta(1+\lambda)r\left(r^2 - 3t^2\right)}{t\left(1 - \dfrac{\eta E_2}{G_{xz}}\right) - \eta(1+\lambda)t\left(t^2 - 3r^2\right)}, \quad \eta = \frac{\overline{E}_1 h^2}{12R^2 G_{xz}} \tag{11.73}$$

and the solution given by Eq. (11.71) becomes

$$w = w_p\left[1 - e^{-rx}(\cos tx + \mu \sin tx)\right] \tag{11.74}$$

If we neglect the transverse shear deformation taking $G_{xz} \to \infty$, then $\lambda = 0$ and $\eta = 0$, and Eqs. (11.73) and (11.74) yield the solution corresponding to nonlinear classical theory, i.e.,

$$w = w_p\left[1 - e^{-rx}\left(\cos tx + \frac{r}{t}\sin tx\right)\right] \tag{11.75}$$

Furthermore, if we neglect the nonlinear term we arrive at the classical solution

$$w = w_p\left[1 - e^{-rx}(\cos rx + \sin rx)\right], \quad r^2 = \frac{1}{h}\sqrt{\frac{3E_2}{\overline{E}_1}} \tag{11.76}$$

The dependencies of the normalized deflection $\overline{w} = w/w_p$ on the axial coordinate $\overline{x} = x/R$ corresponding to the solutions given by Eqs. (11.74)–(11.76) along with experimental data are shown in Fig. 11.17. As can be seen, all three solutions are in fair agreement with the experimental results. Thus, the simplest, i.e., the classical theory can be used to study the shell under consideration. It should be noted that this shell is relatively thick ($h/R = 0.03$), its bending stiffness $D_{11} = 138\ \text{GPa}\cdot\text{mm}^3$ is rather high, and the ratio $E_1/G_{xz} = 7.86$ is moderate.

The situation can be different for composite pressure vessels made by filament winding. Due to the high strength of modern composite materials, the thickness and, hence, the bending stiffness of the shell wall can be rather small. As a result, transverse shear deformation can be neglected, whereas the nonlinear effect should be taken into account.

As the second example, consider the cylindrical section of the fiberglass pressure vessel with a steel ring shown in Figs. 11.18 and 11.19. The shell is composed of an inner $\pm 36^\circ$ angle-ply layer with thickness $h_\phi = 1.2$ mm and an outer 90° circumferential layer with thickness $h_{90} = 0.86$ mm. The stiffness coefficients of the layers, specified by Eqs. (4.72), are

$$A_{11}^{\phi} = 22.41\ \text{GPa}, \quad A_{12}^{\phi} = 7.72\ \text{GPa}, \quad A_{22}^{\phi} = 10.2\ \text{GPa}$$
$$A_{11}^{90} = 6.9\ \text{GPa}, \quad A_{12}^{90} = 1.45\ \text{GPa}, \quad A_{22}^{90} = 57.9\ \text{GPa}$$

The integrals $I_{mn}^{(r)}$ in Eqs. (11.50) for the layered wall, i.e.,

$$I_{mn}^{(r)} = \frac{1}{r+1}\left\{A_{mn}^{\phi} h_\phi^r + A_{mn}^{90}\left[\left(h_\phi + h_{90}\right)^r - h_\phi^r\right]\right\}, \quad (r = 0, 1, 2)$$

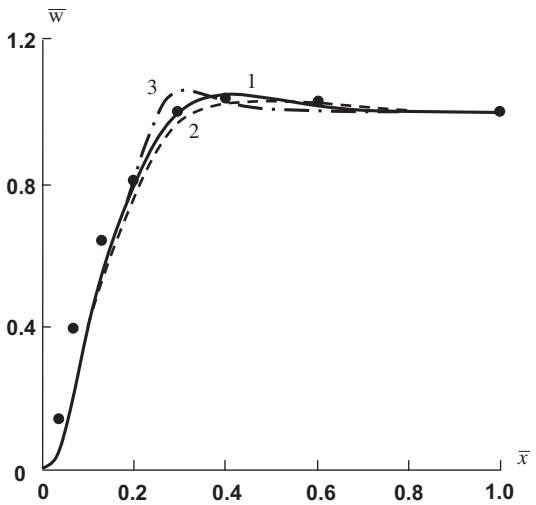


FIGURE 11.17

Dependence of the normalized deflection on $\overline{x}$ for the clamped cylindrical shell:
1 (——) nonlinear solution with transverse shear deformation, Eq. (11.74);
2 (– – –) nonlinear solution without transverse shear deformation, Eq. (11.75);
3 (— · — · —) classical solution, Eq. (11.76);
(•) experimental data.

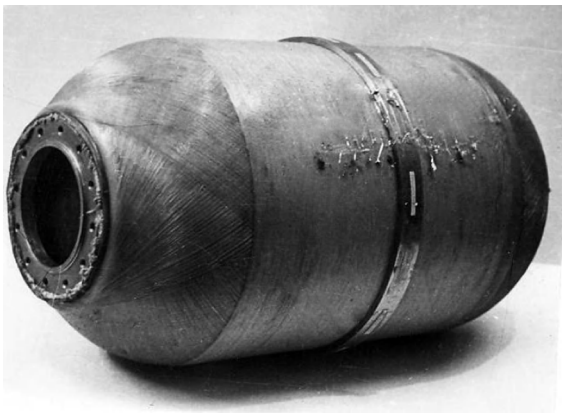


FIGURE 11.18

Composite pressure vessel with a steel ring.

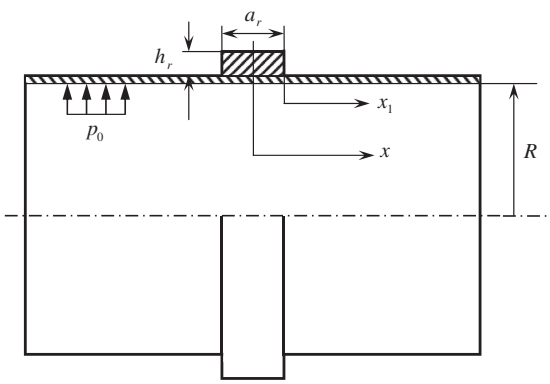


FIGURE 11.19

Cylindrical shell with a ring.

have the following values:

$$I_{11}^{(0)} = 32.83 \text{ GPa}\cdot\text{mm}, \quad I_{12}^{(0)} = 10.5 \text{ GPa}\cdot\text{mm}, \quad I_{22}^{(0)} = 61.45 \text{ GPa}\cdot\text{mm}$$
$$I_{11}^{(1)} = 25.81 \text{ GPa}\cdot\text{mm}^2, \quad I_{11}^{(2)} = 34.5 \text{ GPa}\cdot\text{mm}^3$$

To simplify the equations, we determine the coordinate of the reference surface from the following condition:

$$C_{11} = I_{11}^{(1)} - eI_{11}^{(0)} = 0$$

which yields $e = 0.8$ mm. Then, according to Eqs. (11.50), the stiffness coefficients become

$$B_{11} = 32.83 \text{ GPa}\cdot\text{mm}, \quad B_{12} = 10.5 \text{ GPa}\cdot\text{mm}, \quad B_{12} = 61.45 \text{ GPa}\cdot\text{mm}$$

$$C_{11} = 0, \quad C_{12} = -0.7 \text{ GPa}\cdot\text{mm}^2, \quad D_{11} = 14.21 \text{ GPa}\cdot\text{mm}^3$$

The shell radius is $R = 100$ mm and the ratio $h/R = 0.0206$. Since this ratio is relatively small, we neglect the transverse shear deformation, i.e., take $S_x \to \infty$. Then, the generalized stiffness coefficients in Eqs. (11.54) become

$$B = 58.1 \text{ GPa}\cdot\text{mm}, \quad C = -0.7 \text{ GPa}\cdot\text{mm}^2, \quad D = 14.21 \text{ GPa}\cdot\text{mm}^3$$

The shell deflection in the vicinity of the ring is specified by the following equation analogous to Eq. (11.71):

$$w = e^{-11.9\bar{x}_1}(C_1 \cos 7.75\bar{x}_1 + C_2 \sin 7.75\bar{x}_1) + w_p \tag{11.77}$$

in which, in accordance with Eq. (11.61),

$$w_p = \frac{p_0 R}{2B}\left(2 - \frac{B_{12}}{B_{11}}\right) \tag{11.78}$$

For $p_0 = 4.8$ MPa, $w_p = 0.7$ mm. The normalized axial coordinate $\bar{x}_1 = x_1/R$ in Eq. (11.77) is counted from the edge of the ring as shown in Fig. 11.19.

The constants C_1 and C_2 in Eq. (11.77) can be determined from the boundary conditions

$$w(\bar{x}_1 = 0) = w_r, \quad \theta_x(\bar{x}_1 = 0) = 0 \tag{11.79}$$

Here, $\theta_x = -w'$ and w_r is the deflection of the ring (see Fig. 11.19) which can be determined as

$$w_r = \frac{R_r^2}{B_r}\left[p_0 + \frac{2}{a_r} V_n(\bar{x}_1 = 0)\right] \tag{11.80}$$

Here, $R_r = 104$ mm is the ring radius, $B_r = A_{22}h + E_r h_r$ is the ring stiffness in which $E_r = 206$ GPa and $h_r = 4$ mm, $a_r = 18.8$ mm, and in accordance with the third equation of Eqs. (11.64),

$$V_n = V_x + \frac{p_0 R}{2} w' \tag{11.81}$$

The final expression for the shell deflection is

$$\overline{w} = \frac{w}{w_p} = 10^{-2}\left[1 - e^{-11.9\bar{x}_1}(0.843 \cos 7.75\bar{x}_1 + 1.286 \sin 7.75\bar{x}_1)\right] \tag{11.82}$$

This solution is shown in Fig. 11.20 by solid line 1.

If we neglect the nonlinear effect, we arrive at the solution corresponding to classical shell theory which has the form

$$\overline{w} = 10^{-2}\left[1 - e^{-9.84\bar{x}_1}(0.843 \cos 10.25\bar{x}_1 + 0.814 \sin 10.25\bar{x}_1)\right] \tag{11.83}$$

This solution is demonstrated in Fig. 11.20 by the dashed/dotted curve 2.

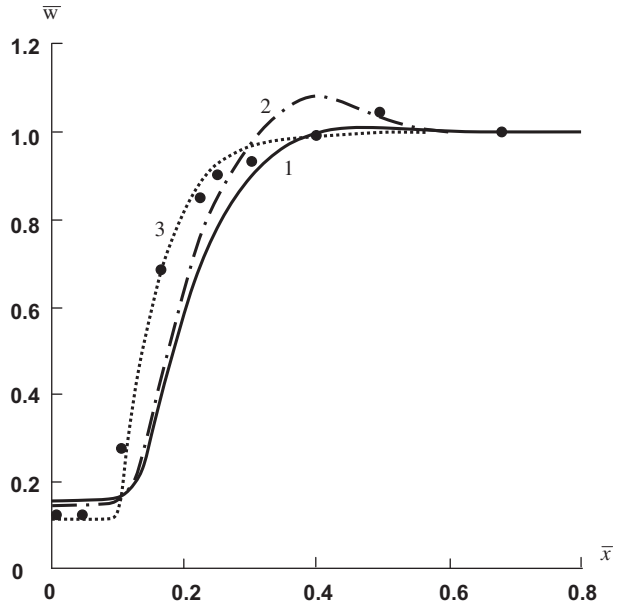


FIGURE 11.20

Dependence of the shell normalized deflection on the axial coordinate:
1 (——) nonlinear solution, Eq. (11.82);
2 (— · —) classical solution, Eq. (11.83);
3 (·····) membrane nonlinear solution, Eq. (11.84);
(•••) experimental data.

Finally, apply the nonlinear membrane theory discussed in Section 11.3.4. For the shell under study, the solution given by Eq. (11.69) has the following form:

$$w = C_1 e^{-kx_1} + w_p$$

where $k^2 = BR/2p_0$ and w_p is specified by Eq. (11.78). The constant of integration C_1 can be found from the first boundary condition in Eqs. (11.79) in which w_r is given by Eq. (11.80) and $V_x = 0$ in Eq. (11.81). For the shell under consideration, the deflection

$$\overline{w} = 10^{-2}\left(1 - 0.886e^{-15.56\overline{x}_1}\right) \tag{11.84}$$

is shown in Fig. 11.20 by dotted line 3. It follows from Fig. 11.20 that the best agreement with experimental results (dots) is demonstrated by the nonlinear membrane solution, Eq. (11.84). The reason for this is discussed in Section 4.4.2. Under the action of internal pressure, cracks appear in the matrix of unidirectional plies (see Fig. 4.36). As a result, the bending stiffness of the shell wall becomes rather low and the shell behaves as a system of flexible fibers.

11.3.6 Anisotropic shells

Consider axisymmetric deformation of anisotropic cylindrical shells. Under the action of axial tension or internal pressure such a shell experiences torsion, i.e., demonstrates the coupling effects that can be used to design flexible structural elements in robots and manipulators. For anisotropic shells, Eqs. (11.47)–(11.49) are generalized as

$$\begin{gathered} N_x' = 0, \quad N_{xy}' + \frac{V_y}{R} = 0, \quad M_x' - V_x = 0 \\ M_{xy}' - V_y = 0, \quad V_x' - \frac{N_y}{R} + \overline{p} = 0 \end{gathered} \tag{11.85}$$

$$\begin{aligned} N_x &= B_{11}\varepsilon_x + B_{12}\varepsilon_y + B_{14}\gamma_{xy} + C_{11}\kappa_x + C_{14}\kappa_{xy} \\ N_y &= B_{12}\varepsilon_x + B_{22}\varepsilon_y + B_{24}\gamma_{xy} + C_{12}\kappa_x + C_{24}\kappa_{xy} \\ N_{xy} &= B_{14}\varepsilon_x + B_{24}\varepsilon_y + B_{44}\gamma_{xy} + C_{14}\kappa_x + C_{44}\kappa_{xy} \\ M_x &= C_{11}\varepsilon_x + C_{12}\varepsilon_y + C_{14}\gamma_{xy} + D_{11}\kappa_x + D_{14}\kappa_{xy} \\ M_{xy} &= C_{14}\varepsilon_x + C_{24}\varepsilon_y + C_{44}\gamma_{xy} + D_{14}\kappa_x + D_{44}\kappa_{xy} \end{aligned} \tag{11.86}$$

$$\varepsilon_x = u', \quad \varepsilon_y = \frac{w}{R}, \quad \gamma_{xy} = v', \quad \kappa_x = -w'', \quad \kappa_{xy} = \frac{v'}{R} \tag{11.87}$$

Note that the foregoing equations, Eqs. (11.85)–(11.87), correspond to classical shell theory.

The first equilibrium equation of Eqs. (11.85), as earlier, yields $N_x = N$, where N are the axial forces applied to the end cross section (see Fig. 11.16). Eliminating V_y from the second and fourth equilibrium equations of Eqs. (11.85) and integrating the resulting equations, we get

$$N_{xy} + \frac{M_{xy}}{R} = C_1 \tag{11.88}$$

in which C_1 is the constant of integration. Assume that in addition to the axial forces N the shell ends are loaded with shear forces S. Then, at the shell ends $x = 0$ and $x = l$ we have $N_{xy} = S$ and $M_{xy} = 0$. Thus, $C_1 = S$ in Eq. (11.88) and

$$N_x = N, \quad N_{xy}R + M_{xy} = SR$$

Substituting N_x, N_{xy} and M_{xy} from Eqs. (11.86) and using Eqs. (11.87), we arrive at

$$\begin{aligned} B_{11}u' + \overline{B}_{14}v' + B_{12}\frac{w}{R} - C_{11}w'' &= N \\ \overline{B}_{14}u' + \tilde{B}_{44}v' + B_{24}\frac{w}{R} - \overline{C}_{14}w'' &= S \end{aligned} \tag{11.89}$$

where

$$\overline{B}_{mn} = B_{mn} + \frac{C_{mn}}{R}, \quad \overline{C}_{mn} = C_{mn} + \frac{D_{mn}}{R}, \quad \tilde{B}_{44} = \overline{B}_{44} + \frac{\overline{C}_{44}}{R}$$

Solving Eqs. (11.89) for u' and v' and substituting the resulting expressions into Eqs. (11.86) for N_y and M_x, we have

$$N_y = B_y\frac{w}{R} - C_{xy}w'' + \overline{N}, \quad M_x = C_{xy}\frac{w}{R} - D_x w'' + \overline{M} \tag{11.90}$$

where

$$B_y = B_{22} - \frac{1}{B_x}\left(B_{11}\overline{B}_{24}^2 + B_{12}^2\tilde{B}_{44} - 2B_{12}\overline{B}_{13}\overline{B}_{24}\right), \quad B_x = B_{11}\tilde{B}_{44} - \overline{B}_{14}^2$$

$$C_{xy} = C_{12} - \frac{1}{B_x}\left(B_{11}\overline{B}_{24}\overline{C}_{14} + B_{12}C_{11}\tilde{B}_{44} - \overline{B}_{14}\overline{B}_{24}C_{11} - B_{12}\overline{B}_{14}\overline{C}_{14}\right)$$

$$D_x = D_{11} - \frac{1}{B_x}\left(\tilde{B}_{44}C_{11}^2 + B_{11}\overline{C}_{14}^2 - 2\overline{B}_{14}C_{11}\overline{C}_{14}\right)$$

$$\overline{N} = \frac{1}{B_x}\left[\left(B_{12}\tilde{B}_{44} - \overline{B}_{14}\overline{B}_{24}\right)N + \left(B_{11}\overline{B}_{24} - B_{12}\overline{B}_{14}\right)S\right]$$

$$\overline{M} = \frac{1}{B_x}\left[\left(\tilde{B}_{44}C_{11} - \overline{B}_{14}\overline{C}_{14}\right)N + \left(B_{11}\overline{C}_{14} - \overline{B}_{14}C_{11}\right)S\right]$$

Now, using the third and the last equilibrium equations of Eqs. (11.85), we get

$$M_x'' - \frac{N_y}{R} + \overline{p} = 0$$

Substituting Eqs. (11.90), we arrive at the following governing equation:

$$D_x w^{IV} - \frac{2}{R}C_{xy}w'' + \frac{B_y}{R^2}w = \overline{p} - \frac{\overline{N}}{R}$$

The solution of this equation is similar to the solution of Eq. (11.58) for an orthotropic shell. It follows from the foregoing results that the deflection w and the axial displacement u of anisotropic cylindrical shells are accompanied by circumferential displacement v.

11.4 GENERAL LOADING CASE

Consider a cylindrical shell shown in Fig. 11.6 and assume that the acting loads depend on both x and y coordinates. The applied methods of analysis for such shells are discussed below.

11.4.1 Classical shell theory

The majority of applied problems are studied within the framework of classical shell theory which ignores transverse shear deformations ($S_x \to \infty$ and $S_y \to \infty$ in Eqs. (11.5)). Thus, the constitutive equations for transverse shear forces vanish and these forces are found from the equilibrium equations, Eqs. (11.3), as

$$V_x = \frac{\partial M_x}{\partial x} + \frac{\partial M_{xy}}{\partial y}, \quad V_y = \frac{\partial M_y}{\partial y} + \frac{\partial M_{xy}}{\partial x} \tag{11.91}$$

Substituting Eqs. (11.8) into the rest of equilibrium equations, Eqs. (11.2) and (11.4), we arrive at the following three equations:

$$\begin{aligned}&\frac{\partial N_x}{\partial x}+\frac{\partial N_{xy}}{\partial y}+p_x=0,\quad \frac{\partial N_y}{\partial y}+\frac{\partial N_{xy}}{\partial x}+\frac{1}{R}\left(\frac{\partial M_y}{\partial y}+\frac{\partial M_{xy}}{\partial x}\right)+p_y=0\\&\frac{N_y}{R}-\frac{\partial^2 M_x}{\partial x^2}-2\frac{\partial^2 M_{xy}}{\partial x\partial y}-\frac{\partial^2 M_y}{\partial y^2}=\overline{p}\end{aligned}\tag{11.92}$$

Since the transverse shear strains $\gamma_x=\gamma_y=0$, Eqs. (11.8) yield the following expressions for the angles of rotation:

$$\theta_x=-\frac{\partial w}{\partial x},\quad \theta_y=\frac{v}{R}-\frac{\partial w}{\partial y}\tag{11.93}$$

Now, substituting the strain-displacement equations, Eqs. (11.6), (11.7) and (11.93), into the constitutive equations, Eqs. (11.5), and the resulting expressions for the stress resultants and couples into the equilibrium equations, Eqs. (11.92), we derive the following three equations in terms of displacements u, v, and w:

$$L_1^s(u,v,w)+p_x=0,\quad L_2^s(u,v,w)+p_y=0,\quad L_3^s(u,v,w)=\overline{p}\tag{11.94}$$

Here

$$L_i^s(u,v,w)=L_i(u,v,w)+L_i^R(u,v,w)\quad (i=1,2,3)$$

are the differential operators which are composed of the corresponding operators for plates L_i given by Eqs. (9.268) and additional operators

$$\begin{aligned}L_1^R(u,v,w)&=\frac{1}{R}\left[(C_{12}+C_{44})\frac{\partial^2 v}{\partial x\partial y}+B_{12}\frac{\partial w}{\partial x}\right]\\L_2^R(u,v,w)&=\frac{1}{R}\left[(C_{12}+C_{44})\frac{\partial^2 u}{\partial x\partial y}+\left(2C_{44}+\frac{D_{44}}{R}\right)\frac{\partial^2 v}{\partial x^2}+\left(2C_{22}+\frac{D_{22}}{R}\right)\frac{\partial^2 v}{\partial y^2}\right.\\&\quad\left.+\left(B_{22}+\frac{C_{22}}{R}\right)\frac{\partial w}{\partial y}-(D_{12}+2D_{44})\frac{\partial^3 w}{\partial x^2\partial y}-D_{22}\frac{\partial^3 w}{\partial y^3}\right]\\L_3^R(u,v,w)&=\frac{1}{R}\left[B_{12}\frac{\partial u}{\partial x}+\left(B_{22}+\frac{C_{22}}{R}\right)\frac{\partial v}{\partial y}-(D_{12}+2D_{44})\frac{\partial^3 v}{\partial x^2\partial y}\right.\\&\quad\left.-D_{22}\frac{\partial^3 v}{\partial y^3}+B_{22}\frac{w}{R}-2\left(C_{12}\frac{\partial^2 w}{\partial x^2}+C_{22}\frac{\partial^2 w}{\partial y^2}\right)\right]\end{aligned}\tag{11.95}$$

The derived equations, Eqs. (11.94), can be readily solved for closed shells with simply supported ends $x=0$ and $x=l$ (see Fig. 11.6). To be specific, assume that the meridional section $y=0$ (see Fig. 11.6) is the plane of shell symmetry (if this is not the case, the shell can be rotated around the axis). Then,

since the solution must be periodic with respect to coordinate y, it can be presented in the form of a trigonometric series, i.e.,

$$\begin{aligned} u &= \sum_{n=0}^{\infty} u_n(x)\cos\lambda_n y, \quad v = \sum_{n=1}^{\infty} v_n(x)\sin\lambda_n y \\ w &= \sum_{n=0}^{\infty} w_n(x)\cos\lambda_n y, \quad \lambda_n = n/R \end{aligned} \tag{11.96}$$

For simply supported shells, the following boundary conditions must be satisfied at the shell ends $x = 0$ and $x = l$:

$$w = 0, \quad v = 0, \quad N_x = 0, \quad M_x = 0 \tag{11.97}$$

To satisfy these boundary conditions, we can take in Eqs. (11.96)

$$\begin{aligned} u_n(x) &= \sum_{m=1}^{\infty} u_{mn}\cos\lambda_m x, \quad v_n(x) = \sum_{m=1}^{\infty} v_{mn}\sin\lambda_m x \\ w_n(x) &= \sum_{m=1}^{\infty} w_{mn}\sin\lambda_m x, \qquad \lambda_m = \frac{\pi m}{l} \end{aligned} \tag{11.98}$$

Assume that $p_x = p_y = 0$ and decompose $\overline{p}$ into similar trigonometric series with coefficients p_{mn}. Substitution of the foregoing series in Eqs. (11.94) results in three algebraic equations for the amplitudes u_{mn}, v_{mn}, and w_{mn} that can be determined as

$$\begin{aligned} u_{mn} &= \frac{p_{mn}}{C}(c_{13}c_{22} - c_{12}c_{23}), \quad v_{mn} = \frac{p_{mn}}{C}(c_{12}c_{13} - c_{11}c_{23}) \\ w_{mn} &= \frac{p_{mn}}{C}\left(c_{11}c_{22} - c_{12}^2\right) \end{aligned} \tag{11.99}$$

where $c_{ij} = a_{ij} + b_{ij}$ are the coefficients which are composed of coefficients for plates a_{ij} in Eqs. (9.272) and additional coefficients

$$\begin{aligned} b_{11} &= 0, \quad b_{12} = \frac{1}{R}(c_{12} + c_{44})\lambda_m\lambda_n, \quad b_{13} = \frac{1}{R}B_{12}\lambda_m \\ b_{22} &= \frac{1}{R}\left[\left(2C_{44} + \frac{D_{44}}{R}\right)\lambda_m^2 + \left(2C_{22} + \frac{D_{22}}{R}\right)\lambda_n^2\right] \\ b_{23} &= \frac{1}{R}\left[\left(B_{22} + \frac{C_{22}}{R}\right)\lambda_n + (D_{12} + 2D_{44})\lambda_m^2\lambda_n + D_{22}\lambda_n^3\right] \\ b_{33} &= \frac{1}{R}\left[\frac{B_{22}}{R} + 2\left(C_{12}\lambda_m^2 + C_{22}\lambda_n^2\right)\right] \end{aligned} \tag{11.100}$$

and

$$C = c_{33}\left(c_{11}c_{22} - c_{12}^2\right) - c_{11}c_{23}^2 - c_{22}c_{13}^2 + 2c_{12}c_{13}c_{23}$$

If the shell ends are not simply supported, i.e., the boundary conditions differ from those given by Eqs. (11.97), substitution of Eqs. (11.96) into Eqs. (11.94) results in three ordinary differential equations for functions $u_n(x)$, $v_n(x)$, and $w_n(x)$. The overall order of these equations is eight and a solution cannot be found in the general case. Note that application of numerical integration also encounters some problems. It follows from Fig. 11.17 that a boundary-layer solution which vanishes rapidly with distance from the fixed edge of a shell can be found for a shell with fixed ends. For relatively long shells, the stresses acting in the vicinity of the ends $x = 0$ and $x = l$ practically do not interact and the fundamental solutions of the corresponding equation become linearly dependent. This results in a weakly posed computational process. To overcome this computational problem the so-called sweep methods have been developed (Godunov, 1961; Abramov, 1961) and applied to shell structures (Valishvili, 1976; Biderman, 1977).

11.4.2 Engineering shell theory

As stated in Section 11.1, reasonable accuracy of the solution can be achieved by applying the equations of simplified engineering theory, Eq. (11.9), instead of the corresponding general equations (11.2) and (11.8). Within the framework of engineering theory, the differential operators given by Eqs. (11.95) are simplified as

$$L_1^R(u,v,w) = \frac{B_{12}}{R}\frac{\partial w}{\partial x}, \quad L_2^R(u,v,w) = \frac{B_{22}}{R}\frac{\partial w}{\partial y}$$

$$L_3^R(u,v,w) = \frac{1}{R}\left[B_{12}\frac{\partial u}{\partial x} + B_{22}\left(\frac{\partial v}{\partial y} + \frac{w}{R}\right) - 2\left(C_{12}\frac{\partial^2 w}{\partial x^2} + C_{22}\frac{\partial^2 w}{\partial y^2}\right)\right]$$

For simply supported shells, the coefficients presented by Eqs. (11.100) become

$$b_{11} = 0, \quad b_{12} = 0, \quad b_{22} = 0, \quad b_{13} = \frac{1}{R}B_{12}\lambda_m, \quad b_{23} = \frac{1}{R}B_{22}\lambda_n$$

$$b_{33} = \frac{1}{R}\left[\frac{B_{22}}{R} + 2\left(C_{12}\lambda_m^2 + C_{22}\lambda_n^2\right)\right]$$

The equations of the engineering theory have simpler coefficients compared to the equations of the general theory; however, the order of these equations is the same. Hence, the computation problems are the same as those typical for the general theory.

11.4.3 Semi-membrane shell theory

The solution can be significantly simplified using the semi-membrane theory of cylindrical shells described by Eqs. (11.15)–(11.18). To avoid duplication in the derivations, we consider here shear deformable shells (such shells are discussed further in Section 11.4.4) and then arrive at the classical version of the theory by taking $S \to \infty$ in the resultant equations.

For closed shells, decompose the unknown functions entering the equations of the semi-membrane theory into the following trigonometric series:

$$\begin{Bmatrix} u, & w \\ N_x, \quad N_y, & M_y \\ \varepsilon_x, & \kappa_y \end{Bmatrix} = \sum_{n=1}^{\infty} \begin{Bmatrix} u_n(x), & w_n(x) \\ N_n(x), \quad T_n(x), & M_n(x) \\ \varepsilon_n(x), & \kappa_n(x) \end{Bmatrix} \cos \lambda_n y$$

$$\begin{Bmatrix} v \\ N_{xy}, \quad V_y \\ \gamma_{xy}, \quad \gamma_y \end{Bmatrix} = \sum_{n=1}^{\infty} \begin{Bmatrix} v_n(x) \\ S_n(x), \quad V_n(x) \\ \gamma_{xy}^{(n)}(x), \quad \gamma_n(x) \end{Bmatrix} \sin \lambda_n y \tag{11.101}$$

where, as earlier, $\lambda_n = n/R$. Assuming that the shell is loaded with surface forces p_y and $\overline{p}$ $(p_x = 0)$, decompose these forces in a similar way, i.e.,

$$p_y = \sum_{n=1}^{\infty} q_n(x) \sin \lambda_n y, \quad \overline{p} = \sum_{n=1}^{\infty} p_n(x) \cos \lambda_n y \tag{11.102}$$

Note that the terms with $n = 0$ are omitted in Eqs. (11.101) and (11.102). Such terms correspond to the axisymmetric problem which cannot be studied within the framework of semi-membrane theory and should be solved separately using the equations presented in Section 11.3. Substituting the series given by Eqs. (11.101) and (11.102) into Eqs. (11.15)–(11.18) for the semi-membrane theory, we arrive at the following set of ordinary differential equations:

$$\lambda_n v_n + \frac{w_n}{R} = 0 \tag{11.103}$$

$$N_n' + \lambda_n S_n = 0, \quad S_n' - \lambda_n T_n + \frac{1}{R} V_n + q_n = 0 \tag{11.104}$$

$$\lambda_n M_n + V_n = 0, \quad \lambda_n V_n - \frac{1}{R} T_n + p_n = 0 \tag{11.105}$$

$$N_n = B_{11} u_n', \quad S_n = B_{44} \left(v_n' - \lambda_n u_n \right) \tag{11.106}$$

$$M_n = D_{22} \lambda_n \left(\gamma_n + \frac{1}{R} v_n + \lambda_n w_n \right), \quad V_n = S_y \gamma_n \tag{11.107}$$

in which $(\ldots)' = d(\ldots)/dx$. We now reduce the resultant set of equations, Eqs. (11.103)–(11.107), to one governing equation for w_n.

First, Eq. (11.103) allows us to express v_n in terms of w_n as

$$v_n = -\frac{w_n}{R \lambda_n} \tag{11.108}$$

Substituting v_n and γ_n from Eq. (11.108) and the second equation of Eqs. (11.107) into the first equation, we have

$$M_n = D_{22} \lambda_n \left[\frac{V_n}{S_y} + \left(n^2 - 1 \right) \frac{w_n}{R^2} \right] \tag{11.109}$$

The first equation of Eqs. (11.105) yields $V_n = -\lambda_n M_n$. Substitute this result into Eq. (11.109) to get

$$M_n = D_n w_n, \quad D_n = \frac{D_{22}\left(n^2-1\right)}{R^2\left(1+\lambda_n^2\dfrac{D_{22}}{S_y}\right)} \tag{11.110}$$

Then,

$$V_n = -\lambda_n M_n = -D_n \lambda_n w_n \tag{11.111}$$

and

$$\gamma_n = \frac{V_n}{S_y} = -\lambda_n \frac{D_n}{S_y} w_n \tag{11.112}$$

Expressing T_n from the second equation of Eqs. (11.105) and substituting V_n from Eq. (11.111), we find

$$T_n = R\left(p_n - \lambda_n^2 D_n w_n\right) \tag{11.113}$$

Using the second equation of Eqs. (11.104), we can determine S_n'. Transforming the resulting equation with the aid of Eqs. (11.111) and (11.113), we arrive at

$$S_n' = \lambda_n R\left(\overline{p}_n - \frac{n^2-1}{R^2} D_n w_n\right), \quad \overline{p}_n = p_n - \frac{q_n}{\lambda_n R} \tag{11.114}$$

Differentiate the second constitutive equation of Eqs. (11.106), substitute Eqs. (11.108) and (11.114) for υ_n and S_n', and express u_n' as

$$u_n' = \frac{R}{B_{44}}\left(\frac{n^2-1}{R^2} D_n w_n - \overline{p}_n\right) - \frac{1}{R\lambda_n^2} w_n'' \tag{11.115}$$

Then, the first constitutive equation of Eqs. (11.106) yields

$$N_n = \frac{RB_{11}}{B_{44}}\left(\frac{n^2-1}{R^2} D_n w_n - \overline{p}_n\right) - \frac{B_{11}}{R\lambda_n^2} w_n'' \tag{11.116}$$

Finally, differentiating the first equilibrium equation of Eqs. (11.104) and substituting S_n' and N_n from Eqs. (11.114) and (11.116), we arrive at the following governing equation:

$$w_n^{IV} - 2k_1^2 w_n'' + k_2^4 w_n = k_p \tag{11.117}$$

in which

$$k_1^2 = \frac{\lambda_n^2\left(n^2-1\right)D_n}{2B_{44}}, \quad k_2^4 = \frac{D_n}{B_{11}}\lambda_n^4\left(n^2-1\right), \quad k_p = \frac{n^4}{R^2 B_{11}}\overline{p}_n - \frac{n^2}{B_{44}}\overline{p}_n''$$

In contrast to the equations of the general and engineering theories discussed in Sections 11.4.1 and 11.4.2, Eq. (11.117) can be solved analytically. It is analogous to Eq. (11.58) whose solution is considered in Section 11.3. The general solution of Eq. (11.117) includes four constants of integration which can be found from the boundary conditions that are imposed on the shell axial and circumferential displacements u and v or on the axial and shear stress resultants N_x and N_{xy}. Note that if the shell edge is fixed with respect to the circumferential displacement, i.e., if $v = 0$ at the edge, then, in accordance with Eq. (11.108), $w = 0$. Thus, the semi-membrane theory allows us to fix the shell edge with respect to both displacements v and w. To formulate the boundary conditions for N_x and u or for N_{xy} and v, we can use Eq. (11.116) or (11.108), which specifies N_n and v_n in terms of w_n. However, we cannot use Eqs. (11.114) and (11.115) because they specify the derivatives of S_n and u_n. The expression for S_n can be derived from the first equilibrium equation of Eqs. (11.104) if we substitute N_n from Eq. (11.116), i.e.,

$$S_n = \frac{1}{\lambda_n} N_n' = \frac{B_{11}}{R\lambda_n^3} w_n''' - \frac{RB_{11}}{\lambda_n B_{44}} \left(\frac{n^2 - 1}{R^2} D_n w_n' - \overline{p}_n' \right) \tag{11.118}$$

The axial displacement can be found from the second constitutive equation of Eqs. (11.106) if we use Eq. (11.118) for S_n and Eq. (11.108) for v_n. The result is

$$u_n = \frac{B_{11}R}{\lambda_n^2 B_{44}^2} \left(\frac{n^2 - 1}{R^2} D_n w_n' - \overline{p}_n' \right) - \frac{B_{11} w_n'''}{R\lambda_n^4 B_{44}} - \frac{w_n'}{R\lambda_n^2} \tag{11.119}$$

The derived equations correspond, as has been noted, to the theory of shear deformable shells. For the semi-membrane theory corresponding to classical shell theory, we must take $S_y \to \infty$. As can be seen, in this case only the expression for D_n in Eqs. (11.110) is changed as follows:

$$D_n^0 = \frac{D_{22}}{R^2} \left(n^2 - 1 \right)$$

For the first terms in Eqs. (11.101), i.e., for $n = 1$ Eq. (11.117) reduces to

$$w_1^{IV} = \frac{\overline{p}_1}{R^2 B_{11}} - \frac{\overline{p}_1''}{B_{44}} \tag{11.120}$$

This equation has the polynomial solution which describes the shell bending as a beam with absolutely rigid cross-sectional contour. Such a problem is discussed in Chapter 10 in application to thin-walled beams.

For $n \geq 2$, the solution of Eq. (11.117) is given by Eq. (11.60), i.e.,

$$w_n = \sum_{i=1}^{4} A_i \Phi_i(x) + w_p \tag{11.121}$$

The solution in Eq. (11.121) in conjunction with the solution in Eq. (11.60) for the axisymmetric problem and the solution of Eq. (11.120) for the beam-type bending problem allows us to consider a wide class of practical problems of analysis for cylindrical shells. As an example, formulate the problem of analysis for a shell fixed at $x = 0$ and loaded with axial force P at point $x = l$, y = 0 as

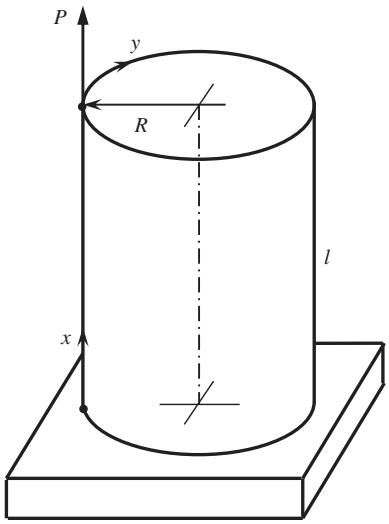


FIGURE 11.21

Cantilever cylindrical shell loaded with concentrated axial force.

shown in Fig. 11.21. Decompose the axial force acting in the cross section $x = l$ of the shell into the following trigonometric series:

$$q_x = q_0 + q_1 \cos \lambda_1 y + \sum_{n=2}^{\infty} q_n \cos \lambda_n y \tag{11.122}$$

where

$$q_0 = \frac{P}{2\pi R}, \quad q_1 = q_n = \frac{P}{\pi R}$$

The load component q_0 is uniformly distributed over the shell cross section. The corresponding component of the shell stress-strain state can be found using Eq. (11.58) for the axisymmetric problem in which $N = q_0$. The integration constants C_i in Eq. (11.60) can be determined from the following boundary conditions:

$$w(0) = 0, \quad \theta_x(0) = 0, \quad M_x(l) = 0, \quad V_x(l) = 0$$

(see Fig. 11.21). One more constant which appears after the integration of Eq. (11.52) for u' can be found from the boundary condition $u(0) = 0$.

The solution component corresponding to q_1 in Eq. (11.122) is the result of integration of Eq. (11.120). To find the four constants of integration, we should use the following boundary conditions:

$$u(0) = 0, \quad v(0) = w(0) = 0, \quad N_1(l) = q_1, \quad S_1(l) = 0$$

Finally, the solutions corresponding to q_n ($n \geq 2$) in Eq. (11.122) follow from Eq. (11.117) of semi-membrane theory. The four constants A_i in Eq. (11.121) can be obtained from the four boundary conditions, which are

$$u_n(0) = 0, \quad v_n(0) = w_n(0) = 0, \quad N_n(l) = q_n, \quad S_n(l) = 0$$

Thus the problem is approximately reduced to three ordinary differential equations of the fourth order, i.e., Eqs. (11.58), (11.117), and (11.120) which can be solved analytically.

For relatively long shells, only the polynomial solution of Eq. (11.120) which describes the beam-type bending of a shell penetrates from the loaded cross section $x = l$ to the fixed cross section $x = 0$ (see Fig. 11.21), whereas the solutions of Eqs. (11.58) and (11.117) are localized in the vicinity of the shell ends $x = 0$ and $x = l$. This is expected, since the self-balanced stresses corresponding to the load components q_n in Eq. (11.122) must vanish at a distance from the loaded end. This demonstrates the principal difference between membrane and semi-membrane shell theories. Membrane shells have zero bending stiffnesses. Taking $D_n = 0$ in the coefficients of Eq. (11.117), we arrive at Eq. (11.120) for w_n. This equation has only polynomial solutions which do not vanish at a distance from the loaded end. Thus, the membrane theory of cylindrical shells, in general, cannot be used to study relatively long shells.

11.4.4 Membrane shell theory

The membrane theory of cylindrical shells can be used for long and infinitely long shells whose stress-strain state does not depend on coordinates. Consider the shell loaded with uniform pressures p and q and axial forces N as shown in Fig. 11.16. For such shells, the equilibrium equations, Eqs. (11.13), yield

$$N_x = N, \quad N_y = \overline{p}R, \quad N_{xy} = 0 \tag{11.123}$$

Substituting these equations into the constitutive equations, Eqs. (11.12), and solving the resulting equations for the strains, we have

$$\varepsilon_x = \frac{1}{B_{11}B}(B_{22}N - B_{12}\overline{p}R), \quad \varepsilon_y = \frac{1}{B_{11}B}(B_{11}\overline{p}R - B_{12}N) \tag{11.124}$$

Note that the shell deflection $w = \varepsilon_y R$ coincides with the particular solution, Eq. (11.61), of the governing equation for the axisymmetric problem, Eq. (11.58).

For the cylindrical parts of pressure vessels with end domes, $\overline{p} = p$, $N = pR/2$, and Eqs. (11.123) and (11.124) reduce to

$$N_x = \frac{pR}{2}, \quad N_y = pR \tag{11.125}$$

$$\varepsilon_x = \frac{pR}{2B_{11}B}(B_{22} - 2B_{12}), \quad \varepsilon_y = \frac{pR}{2B_{11}B}(2B_{11} - B_{12}) \tag{11.126}$$

11.4.5 Shear deformable shell theory

The main applications of the theory of shear deformable cylindrical shells are associated with the analysis of sandwich shells with lightweight core and composite facing layers which can have different thicknesses and stiffnesses. To simplify the problem, we consider such shells within the framework of

the engineering shell theory discussed in Section 11.1. It is important to note that the equations of the general shell theory simplified in accordance with Eqs. (11.9) practically coincide with Eqs. (9.292)–(9.300) presented in Section 9.7.3 in application to unsymmetrically laminated plates. The only differences show themselves in the equilibrium equation, Eq. (11.4), which includes the term N_y/R and in the strain-displacement equation in Eqs. (11.6) for ε_y which contains the term w/R. For plates, $R \to \infty$ and both terms vanish.

Following the derivation presented in Section 9.7.3, we introduce the stress function $F(x, y)$ as in Eqs. (9.301), i.e.,

$$N_x = \frac{\partial^2 F}{\partial y^2}, \quad N_y = \frac{\partial^2 F}{\partial x^2}, \quad N_{xy} = -\frac{\partial^2 F}{\partial x \partial y}$$

The stress function is found from the compatibility equation, Eq. (9.302), which is generalized as

$$\frac{\partial^2 \varepsilon_x}{\partial y^2} + \frac{\partial^2 \varepsilon_y}{\partial x^2} - \frac{\partial^2 \gamma_{xy}}{\partial x \partial y} = \frac{1}{R}\frac{\partial^2 w}{\partial x^2}$$

Finally, the set of the governing equations analogous to Eqs. (9.304), (9.306)–(9.308), becomes

$$\begin{aligned}
&b_y \frac{\partial^4 F}{\partial x^4} + (b - 2b_{xy}) \frac{\partial^4 F}{\partial x^2 \partial y^2} + b_x \frac{\partial^4 F}{\partial y^4} - \frac{1}{R}\frac{\partial^2 w}{\partial x^2} - B_{yx}\frac{\partial^3 \theta_x}{\partial x^3} - (B_x - c)\frac{\partial^3 \theta_x}{\partial x \partial y^2} \\
&\quad -(B_y - c)\frac{\partial^3 \theta_y}{\partial x^2 \partial y} - B_{xy}\frac{\partial^3 \theta_y}{\partial y^3} = 0 \\
&D_x \frac{\partial^2 \theta_x}{\partial x^2} + (D + D_{xy})\frac{\partial^2 \theta_y}{\partial x \partial y} + D\frac{\partial^2 \theta_x}{\partial y^2} + c_{xy}\frac{\partial^3 F}{\partial x^3} + (c_x - c)\frac{\partial^3 F}{\partial x \partial y^2} - S_x\left(\theta_x + \frac{\partial w}{\partial x}\right) = 0 \\
&D_y \frac{\partial^2 \theta_y}{\partial y^2} + (D + D_{yx})\frac{\partial^2 \theta_x}{\partial x \partial y} + D\frac{\partial^2 \theta_y}{\partial x^2} + c_{yx}\frac{\partial^3 F}{\partial y^3} + (c_y - c)\frac{\partial^3 F}{\partial x^2 \partial y} - S_y\left(\theta_y + \frac{\partial w}{\partial y}\right) = 0 \\
&S_x\left(\frac{\partial \theta_x}{\partial x} + \frac{\partial^2 w}{\partial x^2}\right) + S_y\left(\frac{\partial \theta_y}{\partial y} + \frac{\partial^2 w}{\partial y^2}\right) - \frac{1}{R}\frac{\partial^2 F}{\partial x^2} + \overline{p} = 0
\end{aligned} \tag{11.127}$$

The stiffness and compliance coefficients in these equations are given in Section 9.7.3. The four equations obtained, Eqs. (11.127), include four unknown functions, i.e., F, θ_x, θ_y, and w.

For cylindrical shells with simply supported ends $x = 0$ and $x = l$ (see Fig. 11.6), the solution can be presented in the form of trigonometric series similar to those given by Eqs. (11.96) and (11.98), i.e.,

$$\begin{aligned}
F &= \sum_{m=1}^{\infty}\sum_{n=0}^{\infty} F_{mn} \sin \lambda_m x \cos \lambda_n y, \quad \theta_x = \sum_{m=1}^{\infty}\sum_{n=0}^{\infty} \theta_x^{mn} \cos \lambda_m x \cos \lambda_n y \\
\theta_y &= \sum_{m=1}^{\infty}\sum_{n=0}^{\infty} \theta_y^{mn} \sin \lambda_m x \sin \lambda_n y, \quad w = \sum_{m=1}^{\infty}\sum_{n=0}^{\infty} w_{mn} \sin \lambda_m x \cos \lambda_n y
\end{aligned} \tag{11.128}$$

in which, as earlier, $\lambda_m = \pi m/l$ and $\lambda_n = n/R$. Substitution of Eqs. (11.128) into Eqs. (11.127) results in four algebraic equations, Eqs. (9.310), for F_{mn}, θ_x^{mn}, θ_y^{mn}, and w_{mn}. However, in contrast to

Eqs. (9.309) for plates, Eqs. (11.128) contain different combinations of trigonometric functions and some of the coefficients a_{ij} in Eqs. (9.310) are also different and have the following form:

$$\begin{aligned} a_{13} &= B_{xy}\lambda_n^3 + (B_y - c)\lambda_m^2\lambda_n, \quad a_{14} = a_{41} = \frac{1}{R}\lambda_m^2 \\ a_{23} &= (D + D_{xy})\lambda_m\lambda_n, \quad a_{31} = c_{yx}\lambda_n^3 + (c_y - c)\lambda_m^2\lambda_n \\ a_{32} &= (D + D_{yx})\lambda_m\lambda_n, \quad a_{34} = a_{43} = S_y\lambda_n \end{aligned} \tag{11.129}$$

The rest of the coefficients are the same as those given by Eqs. (9.310). The solution of these equations is presented in Section 9.7.3.

For shells with a symmetric structure, the coupling coefficients C_{mn} in the constitutive equations are zero and we should take

$$\begin{aligned} &B_x = 0, \ B_y = 0, \ B_{xy} = B_{yx} = 0, \ D_x = D_{11}, \ D_y = D_{22}, \ D_{xy} = D_{yx} = D_{12} \\ &D = D_{44}, \ c_x = 0, \ c_y = 0, \ c_{xy} = c_{yx} = 0 \end{aligned}$$

in Eqs. (11.127). As an example, consider a cylindrical shell made of fiberglass fabric and having the following parameters: $R = 112$ mm, $l = 265$ mm, $h = 3.53$ mm; and material properties are $E_x = 19.6$ GPa, $E_y = 30.5$ GPa, $G_{xy} = 4.75$ GPa, $G_{xz} = G_{yz} = 2.06$ GPa, $\upsilon_{xy} = 0.14$, and $\upsilon_{yx} = 0.09$. The shell is simply supported and loaded with a concentrated load P at the point $x = l/2$, $y = 0$ as shown in Fig. 11.22. Decomposing the load into the double trigonometric series, we have

$$\overline{p} = \sum_{m=1}^{\infty}\sum_{n=0}^{\infty} p_{mn} \sin \lambda_m x \cos \lambda_n y$$

where

$$\begin{aligned} p_{m0} &= (-1)^{\frac{1}{2}(m+3)}\frac{P}{\pi R l} \quad (m = 1, 3, 5\ldots) \\ p_{mn} &= (-1)^{\frac{1}{2}(m+3)}\frac{2P}{\pi R l} \quad (m = 1, 3, 5\ldots; \ n = 1, 2, 3\ldots) \end{aligned}$$

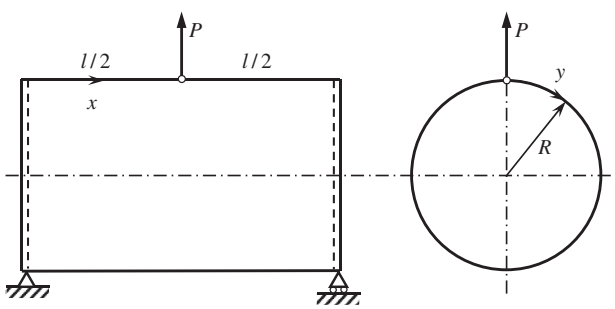


FIGURE 11.22

Simply supported cylindrical shell under the action of a concentrated radial force.

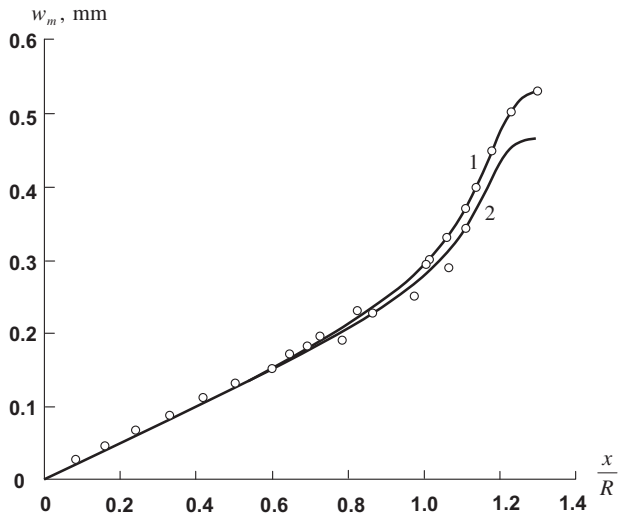


FIGURE 11.23

Dependence of the shell maximum deflection on the axial coordinate: shear deformable shell theory (1), classical shell theory (2), experiment (∘∘∘).

and the rest of coefficients p_{mn} are zero. The calculated dependencies of the shell maximum deflection $w_m = w(x = l/2, y = 0)$ on the axial coordinate are shown in Fig. 11.23 along with the experimental results (circles). Curves 1 and 2 correspond to the shear deformable shell theory and the classical shell theory, respectively. As can be seen, there is not too much of a difference between the results obtained based on the two theories. The relative shell thickness $h/R = 0.0316$, whereas the ratios $E_1/G_{xz} = 9.51$ and $E_2/G_{xz} = 14.8$ are rather low, and the transverse shear deformation is not significant for the shell under study. As has been noted, the most pronounced effect of the transverse shear deformation is observed in sandwich shells with lightweight cores.

Cylindrical shells whose ends are not simply supported can be efficiently studied with the aid of semi-membrane shell theory as discussed in Section 11.4.3.

11.5 BUCKLING OF CYLINDRICAL SHELLS UNDER AXIAL COMPRESSION

Cylindrical shells compressed in the axial direction can experience buckling. Consider the possible buckling modes.

11.5.1 Column-type buckling

Long shells can experience a column-type buckling as shown in Fig. 8.18. The critical value of the total axial force $P = 2\pi RT$ can be found using the approach described in Section 8.5 of Chapter 8 as

$$P_{cr} = \frac{P_E}{1 + P_E/S}$$

where

$$P_E = k\frac{\pi^2 D}{l^2}$$

is the Euler critical force for a compressed column. The coefficient k depends on the boundary conditions at the shell ends $x = 0$ and $x = l$ (see Fig. 8.18). If the end cross section can rotate (see Fig. 8.18a), then $k = 1$. For a cantilever shell whose end $x = 0$ is fixed, and the force P acts on the free end (see Fig. 8.18b), we have $k = 1/4$. For clamped shells whose end cross sections cannot rotate (see Fig. 8.18c), we get $k = 4$. The bending stiffness of the shell D and the transverse shear stiffness S are determined as discussed in Section 10.4.6 of Chapter 10 and have the following forms: $D = \pi BR^3$ and $S = \pi RB_{44}$ in which B and B_{44} are the membrane axial and shear stiffness coefficients of the shell wall.

11.5.2 Axisymmetric buckling mode

Assume that the buckling mode of a shell fixed at the ends $x = 0$ and $x = l$ is axisymmetric, i.e., that the shell deflection w caused by buckling does not depend on the coordinate y (see Fig. 11.24). Then, the buckling equation follows from Eq. (11.58) if we take $N = -T_s$ and $k_p = 0$, i.e.,

$$D\left(1 - \frac{T_s}{S_x}\right)w^{IV} + \left[T_s(1+c) - \frac{C}{R}(2-c) - \frac{BD}{R^2 S_x}\right]w'' + \frac{B}{R^2}w = 0, \quad c = \frac{C}{RS_x} \tag{11.130}$$

where the stiffness coefficients B, C, and D are specified by Eqs. (11.54). If the shell is simply supported at the ends $x = 0$ and $x = l$ (see Fig. 11.24), the deflection can be presented in the following form:

$$w = \sum_{m=1}^{\infty} w_m \sin \lambda_m x \tag{11.131}$$

where $\lambda_m = \pi m/l$. Substituting the deflection, Eq. (11.131), into the buckling equation, Eq. (11.130), we can express T_s as

$$T_s = \frac{D\lambda_m^4 + \dfrac{\lambda_m^2}{R}\left[C(2-c) + \dfrac{BD}{RS_x}\right] + \dfrac{B}{R^2}}{\lambda_m^2\left(1 - c + \dfrac{D}{S_x}\lambda_m^2\right)} \tag{11.132}$$

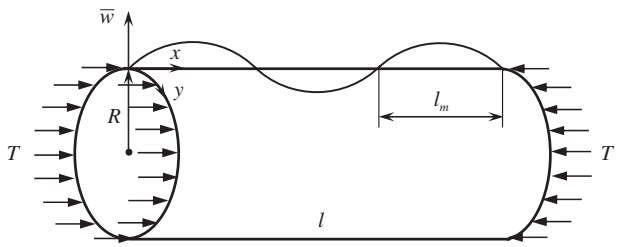


FIGURE 11.24

Cylindrical shell loaded with axial compressive forces T.

Applying the minimum condition, i.e., $\partial T/\partial\lambda_m^2 = 0$, we get

$$\lambda_m^2 = \frac{\dfrac{1}{S_x} + \sqrt{\dfrac{(1-c)R}{BD}\left[(1-c)R - \dfrac{C(2-c)}{S_x}\right] + \dfrac{c}{S_x^2}}}{\dfrac{R^2}{B}(1-c) + \dfrac{CR}{BS_x}(2-c) - \dfrac{D}{S_x^2}} \tag{11.133}$$

The critical load is specified by Eq. (11.132) in which λ_m^2 should be substituted from Eq. (11.133). Note that Eqs. (11.132) and (11.133) include the stiffness coefficients B, C, and D which, in accordance with Eqs. (11.62), do not depend on the coordinate of the reference surface e. However, the axial forces T_s (see Fig. 11.24) are applied to the reference surface of the shell. Thus, we can conclude that the critical load does not depend on the location of the surface to which the forces T_s are applied.

Neglecting the transverse shear deformation, i.e., taking $S_x \to \infty$, we can reduce Eqs. (11.132) and (11.133) to

$$T_s = D\lambda_m^2 + \frac{C}{R} + \frac{B}{R^2\lambda_m^2}, \quad \lambda_m^2 = \frac{1}{R}\sqrt{\frac{B}{D}} \tag{11.134}$$

and find

$$T_s^{cr} = \frac{1}{R}\left(2\sqrt{BD} + C\right) \tag{11.135}$$

For symmetrically laminated shells, $C = 0$ and

$$T_s^{cr} = \frac{2}{R}\sqrt{BD}, \quad \lambda_m^2 = \frac{1}{R}\sqrt{\frac{B}{D}} \tag{11.136}$$

For homogeneous shells,

$$B = E_y h, \quad C = 0, \quad D = \overline{E}_x\frac{h^3}{12}, \quad \overline{E}_x = \frac{E_x}{1 - \upsilon_{xy}\upsilon_{yx}}$$

and Eqs. (11.134) and (11.135) yield

$$T_s^{cr} = \frac{h^2}{R\sqrt{3}}\sqrt{\overline{E}_x E_y}, \quad \lambda_m^2 = \frac{2\sqrt{3}}{Rh}\sqrt{\frac{E_y}{\overline{E}_x}} \tag{11.137}$$

For an isotropic shell, $E_x = E_y = E, \upsilon_{xy} = \upsilon_{yx} = \upsilon$, and Eqs. (11.136) reduce to the classical results

$$T_s^{cr} = \frac{Eh^2}{R\sqrt{3(1-\upsilon^2)}}, \quad \lambda_m^2 = \frac{2\sqrt{3(1-\upsilon^2)}}{Rh} \tag{11.138}$$

Note that the foregoing equations for the critical load are valid for relatively long shells whose length is greater than the length of the half-wave

$$l_m = \pi/\lambda_m \tag{11.139}$$

(see Fig. 11.24).

It has been shown that the foregoing results obtained for simply supported shells are also valid for clamped shells whose length is larger than l_m given by Eqs. (11.139) (Vasiliev, 2011). Indeed, consider for the sake of brevity symmetrically laminated shells and assume that $S_x \to \infty$. Taking $N = -T_s$ and $\overline{p} = 0$ in Eq. (11.58), we arrive at the following equation:

$$w^{IV} + 2k_1^2 w'' + k_2^4 w = k_p \tag{11.140}$$

where

$$k_1^2 = \frac{T_s}{2D}, \quad k_2^4 = \frac{B}{R^2 D}, \quad k_p = \frac{B_{12} T_s}{R B_{11} D} \tag{11.141}$$

This equation describes the nonlinear deformation of a shell under axial compression. Introduce the loading parameter

$$\overline{T}_s = \frac{T_s}{T_s^{cr}} \tag{11.142}$$

where T_s^{cr} is specified by Eqs. (11.136). Then the coefficients in Eqs. (11.141) become

$$k_1^2 = \overline{T}_s \lambda, \quad k_2^2 = \lambda, \quad k_p = \frac{2B_{12}}{B_{11}} \overline{T}_s \lambda, \quad \lambda = \frac{1}{R}\sqrt{\frac{B}{D}} \tag{11.143}$$

The form of the solution of Eq. (11.140) which is discussed in Sections 9.4.1 and 11.3 depends on the relationship between the coefficients k_1 and k_2 given by Eqs. (11.143).

If $\overline{T}_s < 1$, i.e., the load is less than the critical value, $k_1 < k_2$ and the solution of Eq. (11.140) is

$$w = e^{-rx}(C_1 \cos tx + C_2 \sin tx) + e^{rx}(C_3 \cos tx + C_4 \sin tx) + w_p \tag{11.144}$$

where

$$r = \sqrt{\frac{\lambda}{2}(1 - \overline{T}_s)}, \quad t = \sqrt{\frac{\lambda}{2}(1 + \overline{T}_s)}, \quad w_p = \frac{2B_{12}\overline{T}_s}{B_{11}\lambda}$$

If the load is equal to the critical value, i.e., $\overline{T}_s = 1$, we have $k_1^2 = k_2^2 = \lambda$ and the solution to Eq. (11.140) becomes

$$w = (C_1 + C_2 x)\cos\sqrt{\lambda}x + (C_3 + C_4 x)\sin\sqrt{\lambda}x + w_p \tag{11.145}$$

And finally, for $\overline{T}_s > 1$, i.e., for $k_1 > k_2$, we have

$$w = C_1 \cos \alpha_1 x + C_2 \cos \alpha_2 x + C_3 \sin \alpha_1 x + C_4 \sin \alpha_2 x + w_p \tag{11.146}$$

where

$$\alpha_{1,2} = \sqrt{\left(\overline{T}_s \pm \sqrt{\overline{T}_s^2 - 1}\right)\lambda}$$

As an example, consider an isotropic shell with the following parameters:

$$R/h = 50, \quad l/R = 2, \quad \upsilon = 0.3 \tag{11.147}$$

For a simply supported shell, the constants of integration C_1-C_4 are found from the boundary conditions $w = w'' = 0$ at $x = 0$ and $x = l$ (see Fig. 11.24). The solution specified by Eq. (11.144) for $\overline{T}_s = 0.5$ is shown in Fig. 11.25a by curve 1 (note that the deflection has been scaled by a factor of ten; the actual maximum deflection is $w_m = 0.0023R$). For $\overline{T}_s = 1$ the solution given by Eq. (11.145) corresponds to curve 2. The maximum deflection is $w_m = 0.025R$, i.e., ten times greater than for $\overline{T}_s = 0.5$. If we increase the load by 1%, i.e., take $\overline{T}_s = 1.01$, the solution presented by Eq. (11.146) corresponds to curve 3 and the maximum deflection becomes $w_m = 0.04R$. Under further loading, the deflection rapidly increases, e.g., for $\overline{T}_s = 1.05$ we have $w_m = 0.74R$, which definitely is not correct because the theory resulting in Eq. (11.140) cannot describe a shell deflection which is comparable with the shell radius.

For clamped shells, the constants of integration C_1-C_4 are found from the boundary conditions $w = w' = 0$ at $x = 0$ and $x = l$ (see Fig. 11.24). The results of the calculation are presented in Fig. 11.25b. For $\overline{T}_s = 0.5$ (curve 1), the maximum deflection is $w_m = 0.00018R$, for $\overline{T}_s = 1$ (curve 2), $w_m = 0.0072R$, for $\overline{T}_s = 1.01$ (curve 3), $w_m = 0.009R$, and for $\overline{T}_s = 1.05, w_m = 0.013R$.

It follows from the foregoing analysis (which is not in fact the buckling analysis, since there is no bifurcation of the shell equilibrium state) that for a load T_s that is less than the critical value T found from the conventional buckling analysis, the shell experiences radial deformation due to Poisson's effect (w_p) and local bending in the vicinity of the ends. When the load T_s is higher than T_s^{cr}, the shell deflection becomes a periodic function whose amplitude rapidly increases with an increase in T_s. Thus, we can consider that T_s^{cr} is the critical load. It is important that we do not need to solve Eq. (11.140) in order to find T_x^{cr}. The solution of this equation becomes periodic if the roots r of the characteristic equation

$$r^4 + 2k_1^2 r^2 + k_2^4 = 0 \tag{11.148}$$

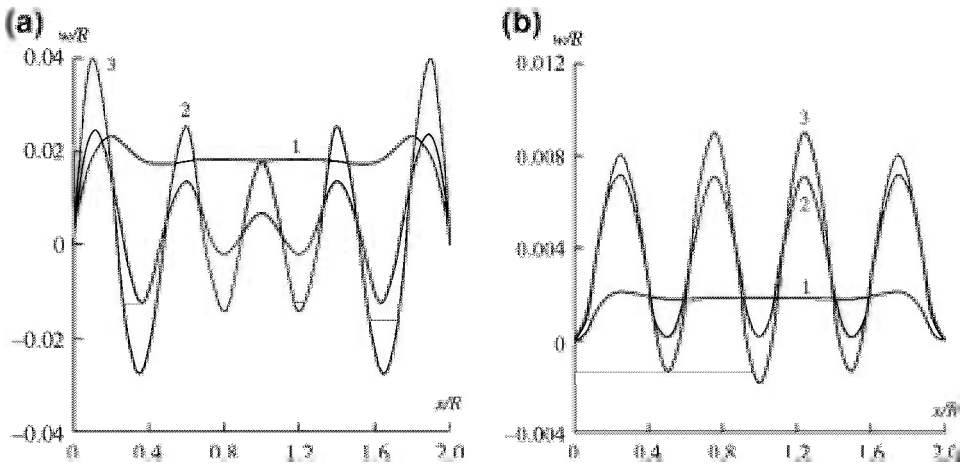


FIGURE 11.25

Dependencies of the normalized deflection on the axial coordinate for simply supported (a) and clamped (b) shells:
1 – solution of Eq. (11.144) (10w, $\overline{T} = 0.50$)
2 – solution of Eq. (11.145) (w, $\overline{T} = 1.0$)
3 – solution of Eq. (11.146) (w, $\overline{T} = 1.01$)

are imaginary numbers. The minimum value of load, or the minimum value of coefficient k_1 in Eqs. (11.141) for which it occurs, can be found from the condition $k_1 = k_2 = k$. In this case, Eq. (11.148) reduces to the following equation:

$$\left(r^2 + k^2\right)^2 = 0$$

which has only imaginary roots. Using Eqs. (11.141) and applying the condition $k_1 = k_2$, we have

$$T_s = \frac{2}{R}\sqrt{BD} \tag{11.149}$$

which coincides with Eq. (11.136) for the critical load. It is important that the result obtained, Eq. (11.149), does not depend on the boundary conditions.

However, there are two particular cases for which Eq. (11.149) is not valid. The first case corresponds to short shells for which $l < l_m$, where l_m is specified by Eq. (11.139). If λ_m is given by the second equation of Eqs. (11.138), we have

$$l_m = \frac{\pi\sqrt{Rh}}{\sqrt[4]{12(1-\upsilon^2)}}$$

For the shell with parameters given by Eqs. (11.147) considered as an example, $l_m = 0.244R$, i.e., the shell length is much less than the radius. For a short shell with length $l = 0.2R$ which is less than l_m, the dependencies of the normalized deflection on the axial coordinate corresponding to $\overline{T}_s = 1$ are shown in Fig. 11.26 for a simply supported shell (line 1) and for a clamped shell (the deflection corresponding

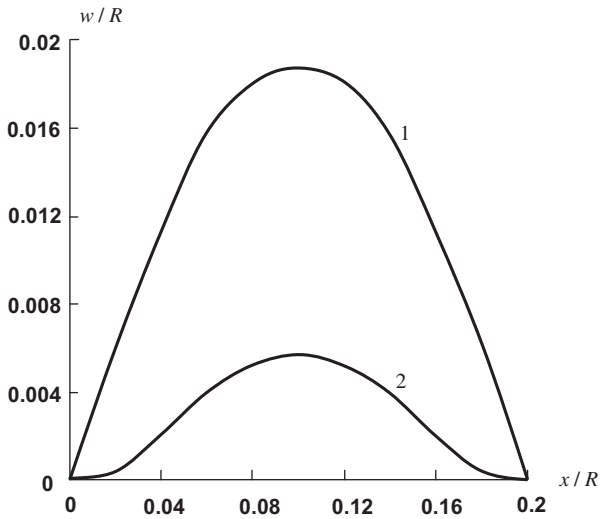


FIGURE 11.26

Dependencies of the normalized deflection on the axial coordinate for simply supported (curve 1, w) and clamped (curve 2, $10w$) shells corresponding to $\overline{T}_s = 1$.

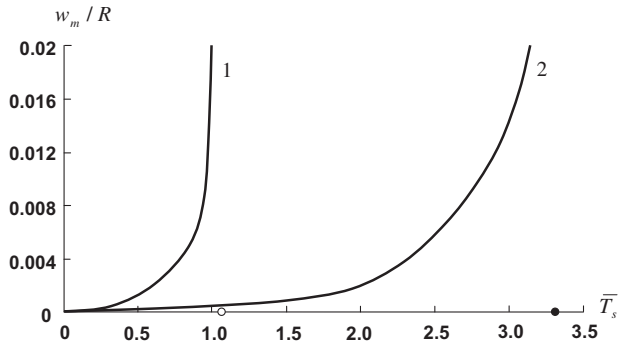


FIGURE 11.27

Dependencies of the normalized maximum deflection on the loading parameter for simply supported (1) and clamped (2) shells.

to curve 2 is multiplied by 10). As can be seen, the curves are not periodic. The maximum normalized deflections of the simply supported (line 1) and clamped (line 2) shells as functions of the loading parameter $\overline{T}_s$ are plotted in Fig. 11.27. Note that for a short ($l < l_m$) simply supported cylindrical shell, the critical load is specified by Eq. (11.132) in which we should take $m = 1$. For a symmetrically laminated shell, the first equation of Eqs. (11.136) must be changed to

$$T_{ss}^{cr} = \frac{\pi^2 D}{l^2} + \frac{Bl^2}{\pi^2 R^2} \tag{11.150}$$

For the isotropic shell with parameters given by Eqs. (11.147), the loading parameter specified by Eq. (11.142) becomes $\overline{T}_s = 1.081$ and is shown on the $\overline{T}_s$-axis in Fig. 11.27 with a circle. As can be seen, the shell deflection (curve 1 in Fig. 11.27) becomes rather high in the vicinity of this circle. To derive the equation analogous to Eq. (11.150) for a clamped shell, consider the buckling equation following from Eq. (11.140) for symmetrically laminated shells if we take $k_p = 0$, i.e.,

$$Dw^{IV} + T_s w'' + \frac{B}{R^2} w = 0 \tag{11.151}$$

and approximate the shell deflection with the following function

$$w = w_0 \left(1 - \cos \frac{2\pi x}{l}\right) \tag{11.152}$$

which satisfies the boundary conditions for clamped shells. Substituting Eq. (11.152) into Eq. (11.151) and using the Bubnov-Galerkin method, i.e., multiplying Eq. (11.151) by the coordinate function given by Eq. (11.152) and integrating from $x = 0$ to $x = l$, we can finally find

$$T_{sc}^{cr} = 4\frac{\pi^2 D}{l^2} + \frac{3Bl^2}{4\pi^2 R^2} \tag{11.153}$$

For the isotropic shell considered as an example, we get from Eq. (11.142) that $\overline{T}_s = 3.239$. This result is shown on the $\overline{T}_s$-axis in Fig. 11.27 with a dot. As can be seen, the maximum shell deflection for the clamped shell (curve 2 in Fig. 11.27) becomes rather high in the vicinity of the dot. Thus, we can conclude that Eqs. (11.150) and (11.153) specify the critical loads for simply supported and clamped shells whose length is less than l_m in Eq. (11.139). Naturally, for such short shells the critical load depends on the boundary conditions.

The second particular case for which Eq. (11.149) cannot be used to determine the critical load corresponds to those shells whose edges $x = 0$ and $x = l$ are not fixed with respect to the shell deflection, i.e., the load T is applied to the free end edges of the shell. For such shells, buckling occurs in the vicinity of the free edge and the shell deflection is not periodic (Kilchevsky, 1942).

11.5.3 Nonsymmetric buckling mode

We can apply the method discussed earlier to study nonsymmetric buckling of a cylindrical shell which has a symmetric structure and is described by the equations of the classical theory, Eqs. (11.94). To derive the buckling equation for a shell compressed by axial forces T_n, we must change the pressure $\overline{p}$ in accordance with Eq. (11.10) and take

$$\overline{p} = -T_n \frac{\partial^2 w}{\partial x^2} \tag{11.154}$$

Using Eq. (11.154), taking $C_{mn} = 0$, and applying the engineering shell theory discussed in Section 11.4.2, we can write Eqs. (11.94) in the following form:

$$\begin{aligned}
&B_{11}\frac{\partial^2 u}{\partial x^2} + B_{44}\frac{\partial^2 u}{\partial y^2} + (B_{12} + B_{44})\frac{\partial^2 v}{\partial x \partial y} + \frac{B_{12}}{R}\frac{\partial w}{\partial x} = 0 \\
&B_{22}\frac{\partial^2 v}{\partial y^2} + B_{44}\frac{\partial^2 v}{\partial x^2} + (B_{12} + B_{44})\frac{\partial^2 u}{\partial x \partial y} + \frac{B_{22}}{R}\frac{\partial w}{\partial y} = 0 \\
&D_1\frac{\partial^4 w}{\partial x^4} + 2D_3\frac{\partial^4 w}{\partial x^2 \partial y^2} + D_2\frac{\partial^4 w}{\partial y^4} + \frac{1}{R}\left[B_{12}\frac{\partial u}{\partial x} + B_{22}\left(\frac{\partial v}{\partial y} + \frac{w}{R}\right)\right] + T_n\frac{\partial^2 w}{\partial x^2} = 0
\end{aligned} \tag{11.155}$$

where, as earlier, $D_1 = D_{11}$, $D_2 = D_{22}$, and $D_3 = D_{12} + 2D_{44}$. Irrespective of the boundary conditions at the shell ends, present the solution of Eqs. (11.155) in the following form:

$$u = u_0 e^{rx}\cos\lambda y, \quad v = v_0 e^{rx}\sin\lambda y, \quad w = w_0 e^{rx}\cos\lambda y \tag{11.156}$$

where $\lambda = n/R$. Substitution of Eq. (11.156) into Eqs. (11.155) results in three algebraic equations for u_0, v_0, and w_0, i.e.,

$$\begin{aligned}
&\left(B_{11}r^2 - B_{44}\lambda^2\right)u_0 + (B_{12} + B_{44})r\lambda v_0 + \frac{B_{12}}{R}rw_0 = 0\\
&-(B_{12} + B_{44})r\lambda u_0 + \left(B_{44}r^2 - B_{22}\lambda^2\right)v_0 - \frac{B_{22}}{R}\lambda w_0 = 0\\
&\frac{1}{R}(B_{12}ru_0 + B_{22}\lambda v_0) + \left(D_1r^4 - 2D_3r^2\lambda^2 + D_2\lambda^4 + \frac{B_{22}}{R} + T_nr^2\right)w_0 = 0
\end{aligned} \tag{11.157}$$

Solving the first two equations of Eqs. (11.157) for u_0 and v_0, we get

$$\begin{aligned}
u_0 &= \frac{rB_{44}}{RB_1}\left(B_{12}r^2 + B_{22}\lambda^2\right)w_0\\
v_0 &= \frac{\lambda}{RB_1}\left[B_{22}\left(B_{11}r^2 - B_{44}\lambda^2\right) - B_{12}(B_{12} + B_{44})r^2\right]w_0
\end{aligned} \tag{11.158}$$

where

$$B_1 = \left(B_{11}r^4 - B_2r^2\lambda^2 + B_{22}\lambda^4\right), \quad B_2 = \frac{B_{11}B}{B_{44}} - 2B_{12}, \quad B = B_{22} - \frac{B_{12}^2}{B_{11}}$$

Substituting Eqs. (11.158) into the third equation of Eqs. (11.157), we arrive at the following equation for the force T_n:

$$B_1\left(D_1r^4 - 2D_3r^2\lambda^2 + D_2\lambda^4 + T_nr^2\right) + \frac{B}{R^2}B_{11}r^4 = 0 \tag{11.159}$$

The other form of this equation is

$$a_1r^8 + a_2r^6 - a_3r^4 + a_4r^2 + a_5 = 0 \tag{11.160}$$

where

$$\begin{aligned}
&a_1 = B_{11}D_1, \quad a_2 = B_{11}T_n - (B_1D_1 + 2B_{11}D_3)\lambda^2\\
&a_3 = B_1\lambda^2T_n - (B_{11}D_2 + 2B_1D_3 + B_{22}D_1)\lambda^4\\
&a_4 = B_{22}\lambda^4T_n - (B_1D_2 + 2B_{22}D_3)\lambda^6, \quad a_5 = B_{22}D_2\lambda^8
\end{aligned} \tag{11.161}$$

As discussed in Section 11.5.3, shell buckling occurs if the solutions given by Eqs. (11.156) become periodic functions of x, which means that Eq. (11.160) must have imaginary roots. Take $r^2 = s$ and reduce Eq. (11.160) to

$$a_1s^4 + a_2s^3 - a_3s^2 + a_4s + a_5 = 0 \tag{11.162}$$

If r is an imaginary number, then Eq. (11.162) must have a negative real root s. Now take $s = -t$ and write Eq. (11.162) as

$$a_1t^4 - a_2t^3 - a_3t^2 - a_4t + a_5 = 0 \tag{11.163}$$

Thus, if Eq. (11.160) has imaginary roots r, then Eq. (11.163) must have positive real roots t. Assume that T_n in Eqs. (11.161) is relatively small so that coefficients a_2, a_3, and a_4 are negative. Then, all the coefficients of Eq. (11.163) are positive; hence, it cannot have positive roots and the shell buckling does not occur. If T_n in Eqs. (11.161) is relatively high, the coefficients a_2, a_3, and a_4 can be positive. Then, Eq. (11.163) has two changes of signs, and according to the Cartesian Rule (Korn and Korn, 1961) it can have two positive roots, which shows that the shell can buckle. The corresponding load can be found from Eq. (11.159) which yields

$$T_n = D_1 t + 2D_3\lambda^2 + D_2\frac{\lambda^4}{t} + \frac{BB_{11}t}{R^2\left(B_{11}t^2 + B_1 t\lambda + B_{22}\lambda^4\right)} \tag{11.164}$$

Here t and λ are real and positive numbers. The critical force can be determined by minimization of the load T_n given by Eq. (11.164) with respect to the parameters t and λ.

Analytical minimization in Eq. (11.164) is possible for homogeneous shells for which

$$B_{mn} = A_{mn}h, \quad D_{mn} = \frac{1}{12}A_{mn}h^3 \tag{11.165}$$

and Eq. (11.164) reduces to

$$T_n = \frac{h^2}{12}\left[B_{11}t + 2(B_{12} + 2B_{44})\lambda^2 + B_{22}\frac{\lambda^4}{t}\right] + \frac{BB_{11}t}{R^2\left[B_{11}t^2 + \left(\dfrac{BB_{11}}{B_{44}} - 2B_{12}\right)t\lambda + B_{22}\lambda^4\right]} \tag{11.166}$$

The minimum condition $\partial T_n/\partial\lambda^2 = 0$ yields

$$\lambda^2 = \sqrt{\frac{B_{11}}{B_{22}}}\cdot t \tag{11.167}$$

whereas the minimum condition $\partial T_n/\partial t = 0$ gives

$$t^2 = \frac{1}{R^2h^2}\cdot\frac{3B_{44}}{B_{11}\left(B_{12} + 2B_{44} + \sqrt{B_{11}B_{22}}\right)\left(\dfrac{1}{2B_{44}} + \dfrac{1}{B_{12} + \sqrt{B_{11}B_{22}}}\right)} \tag{11.168}$$

To derive this equation we have used the following decomposition:

$$B_{11}B_{22} - B_{12}^2 = \left(\sqrt{B_{11}B_{22}} + B_{12}\right)\left(\sqrt{B_{11}B_{22}} - B_{12}\right)$$

Finally, substituting λ and t from Eqs. (11.167) and (11.168) into Eq. (11.166), we have

$$T_n^{cr} = \frac{\sqrt{2}h}{\sqrt{3}R}\sqrt{B_{44}\left(\sqrt{B_{11}B_{22}} + B_{12}\right)} \tag{11.169}$$

For a homogeneous shell

$$B_{11} = \overline{E}_x h, \quad B_{12} = \upsilon_{xy}\overline{E}_x h, \quad B_{22} = \overline{E}_y h, \quad B_{44} = G_{xy}h$$

and Eq. (11.169) reduces to

$$T_n^{cr} = \frac{h^2}{R}\sqrt{\frac{2G_{xy}\left(\sqrt{E_xE_y} + \upsilon_{xy}E_x\right)}{3\left(1 - \upsilon_{xy}\upsilon_{yx}\right)}} \tag{11.170}$$

Compare this result with Eq. (11.137) which specifies the critical load T_s^{cr} for axisymmetric buckling. Substituting Eqs. (11.137) and (11.170) into the inequality $T_n^{cr} \le T_s^{cr}$, we have

$$G_{xy} \le \frac{E_xE_y}{2\left(\sqrt{E_xE_y} + \upsilon_{xy}E_x\right)} = \frac{\sqrt{E_xE_y}}{2\left(1 + \sqrt{\upsilon_{xy}\upsilon_{yx}}\right)} \tag{11.171}$$

The second part of Eq. (11.171) can be obtained if we use the symmetry condition of elastic constants ($\upsilon_{xy}E_x = \upsilon_{yx}E_y$) and the following relation:

$$\upsilon_{xy}E_x = \sqrt{\upsilon_{xy}\upsilon_{yx}E_xE_y}$$

Thus, the critical force T_n^{cr} corresponding to nonsymmetric buckling is less than the force T_s^{cr} causing symmetric buckling if the shear modulus of the material satisfies the condition in Eq. (11.171). For isotropic shells, $G = E/2(1 + \upsilon)$ and the critical load is the same for both buckling modes, i.e.,

$$T_s^{cr} = T_n^{cr} = T_{cr} = \frac{Eh^2}{R\sqrt{3(1 - \upsilon^2)}} \tag{11.172}$$

As in the case of axisymmetric buckling, the calculated critical load does not depend on the boundary conditions at the shell ends $x = 0$ and $x = l$ (see Fig. 11.24). The limitations are the same as those in the axisymmetric problem. First, the foregoing results are not valid for short shells whose length l is less than the length of the half-wave $\sqrt{t}$, where t is specified by Eq. (11.168). Secondly, the results are not valid for the shells that buckle in the vicinity of the end edges. Such buckling can occur if the shell edge is not fixed with respect to the deflection w (Karmishin et al., 1975).

To support the results obtained, consider an isotropic shell whose critical force T_{cr} is specified by Eq. (11.172) and let the critical load for shells with arbitrary boundary conditions be

$$T_{cr}^a = kT_{cr} \tag{11.173}$$

The dependence of the coefficient k on the length parameter

$$\alpha_l = \frac{l}{\sqrt{Rh}}\sqrt[4]{3(1 - \upsilon^2)} \tag{11.174}$$

is presented in Fig. 11.28 (adapted from Volmir, 1967). Curve 1 corresponds to simply supported shells and curves 2 and 3 correspond to clamped shells with different membrane boundary conditions. In particular, for curve 2, the shear stress resultant N_{xy} is zero at the end edges, whereas for curve 3, the circumferential displacement υ is zero. As can be seen, for long shells $k = 1$ and the critical load does not depend on the boundary conditions.

The foregoing results correspond to shells with symmetric structures for the wall. Consider the problem of buckling for laminated cylindrical shells with an arbitrary structure for the shell wall and apply the engineering version of classical shell theory as discussed in Section 11.4.2. For simply supported shells, the displacements can be presented in the form of trigonometric series given by

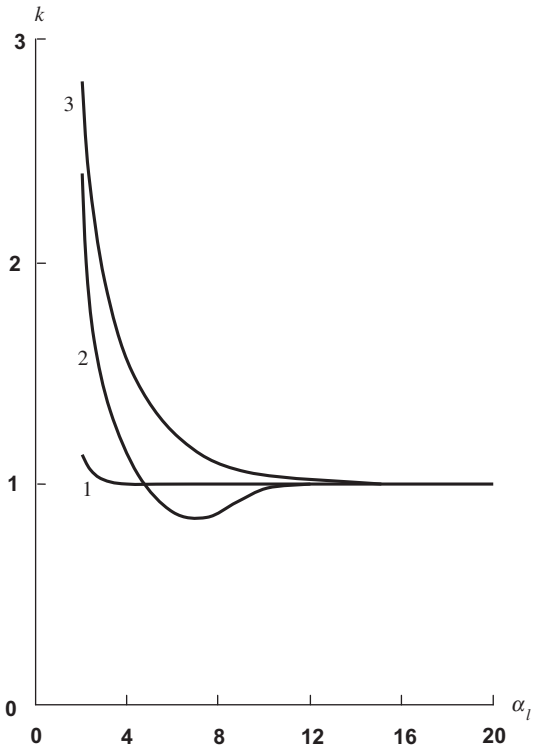


FIGURE 11.28

Dependence of parameter k in Eq. (11.173) on the length factor α_l in Eq. (11.174) for the shells with various boundary conditions:
simply supported shell (curve 1, $w = w'' = v = N_x = 0$);
clamped shell (curve 2, $w = w' = u = N_{xy} = 0$);
clamped shell (curve 3, $w = w' = v = N_x = 0$).

Eqs. (11.96) and (11.98). For the problem of buckling under axial compression, the pressure $\overline{p}$ is specified by Eq. (11.154). Taking into account the decomposition of the shell deflection in Eqs. (11.96) and (11.98), we get for nonsymmetric buckling

$$w = \sum_{m=1}^{\infty} \sum_{n=1}^{\infty} w_{mn} \sin \lambda_m x \cos \lambda_n y, \quad \lambda_m = \frac{\pi m}{l}, \quad \lambda_n = \frac{n}{R} \tag{11.175}$$

Then, Eq. (11.154) yields

$$\overline{p} = \sum_{m} \sum_{n} p_{mn} \sin \lambda_m x \cos \lambda_n y$$

where

$$p_{mn} = T_n \lambda_m^2 w_{mn} \tag{11.176}$$

Substituting this result into the solution for w_{mn} in Eqs. (11.99), we finally get

$$T_n = \frac{1}{\lambda_m^2}\left[c_{33} - \frac{c_{11}c_{23}^2 + c_{22}c_{13}^2 - 2c_{12}c_{13}c_{23}}{c_{11}c_{22} - c_{12}^2}\right] \tag{11.177}$$

where

$$c_{11} = B_{11}\lambda_m^2 + B_{44}\lambda_n^2, \quad c_{12} = \left(B_{12} + B_{44} + \frac{C_{12} + C_{44}}{R}\right)\lambda_m\lambda_n$$

$$c_{13} = C_{11}\lambda_m^3 + (C_{12} + 2C_{44})\lambda_m\lambda_n^2 + \frac{1}{R}B_{12}\lambda_m$$

$$c_{22} = B_{44}\lambda_m^2 + B_{22}\lambda_n^2 + \frac{1}{R}\left[\left(2C_{44} + \frac{D_{44}}{R}\right)\lambda_m^2 + \left(2C_{22} + \frac{D_{22}}{R}\right)\lambda_n^2\right]$$

$$c_{23} = C_{22}\lambda_n^3 + (C_{12} + 2C_{44})\lambda_m^2\lambda_n + \frac{1}{R}\left[\left(B_{22} + \frac{C_{22}}{R}\right)\lambda_n + (D_{12} + 2D_{44})\lambda_m^2\lambda_n + D_{22}\lambda_n^3\right]$$

$$c_{33} = D_1\lambda_m^4 + 2D_3\lambda_m^2\lambda_n^2 + D_2\lambda_n^4 + \frac{1}{R}\left[\frac{B_{22}}{R} + 2\left(C_{12}\lambda_m^2 + C_{22}\lambda_n^2\right)\right]$$

The critical load can be determined by minimization of T_n in Eq. (11.177) with respect to λ_m and λ_n. Note that the result does not depend on the coordinate of the reference surface e.

Finally, consider the general case, i.e., nonsymmetrically laminated and shear deformable shells discussed in Section 11.4.5. The critical load can be found if we substitute p_{mn} from Eq. (11.176) into the solution, Eqs. (9.312), for w_{mn}, i.e.,

$$T_n = \frac{1}{\lambda_m^2}\frac{A}{A_1} \tag{11.178}$$

Here, A and A_1 are specified by Eqs. (9.313), whereas the coefficients a_{mn} in these equations are given by Eqs. (11.129) and (9.311). The critical load can be determined by minimization of the right-hand part of Eq. (11.178) with respect to the numbers of half-waves m and n.

In conclusion, recall that for isotropic shells the calculated axial critical force is usually three to four times higher than the corresponding experimental values. This discrepancy is normally associated with shape imperfections in the metal shells. In this respect, composite cylindrical shells are in a more favorable situation. Composite materials are elastic and composite shells do not exhibit the residual shape imperfections that can occur as a result of occasional actions in the process of assembling, testing, and transporting the structures. Nevertheless, there is a difference between the

calculated and experimental critical loads for composite shells as well. To cover this difference, the so-called knock-down factors are introduced in the shell design. For composite cylindrical shells, the theoretical critical axial force is usually reduced by the factor 0.6 to match the experimental results.

11.6 BUCKLING OF CYLINDRICAL SHELLS UNDER EXTERNAL PRESSURE

Consider a cylindrical shell loaded with an external pressure as shown in Fig. 11.29. When the pressure q reaches the critical value q_{cr}, the shell buckles with one half-wave of the deflection in the axial direction and several half-waves in the circumferential direction. Thus, the shell experiences mainly circumferential bending and we can apply the semi-membrane shell theory described in Sections 11.1 and 11.4.3 which ignores bending of the wall in the axial direction.

The buckling equation follows from Eq. (11.117) if we take in accordance with Eqs. (11.8) and (11.10)

$$\overline{p} = -N_y \frac{\partial \omega_y}{\partial y} = -N_y \left(\frac{1}{R} \frac{\partial v}{\partial y} - \frac{\partial^2 w}{\partial y^2} \right)$$

For a shell loaded with an external pressure q, Eqs. (11.125) of the membrane shell theory yield $N_y = -qR$. Decomposing the shell displacements v and w in accordance with Eqs. (11.101), we arrive at the following coefficients from Eqs. (11.102) for the pressure $\overline{p}$:

$$p_n = qR\lambda_n \left(\frac{v_n}{R} + \lambda_n w_n \right)$$

Finally, expressing v_n in terms of w_n with the aid of Eq. (11.103), we have

$$p_n = \frac{q}{R} \left(n^2 - 1 \right) w_n \tag{11.179}$$

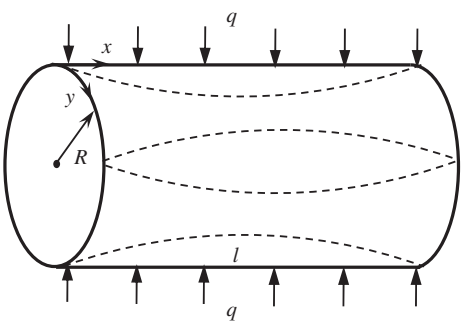


FIGURE 11.29

Cylindrical shell loaded with external pressure q.

Substituting p_n into Eq. (11.117) for w_n, we arrive at the following buckling equation:

$$w_n^{IV} + 2k_1^2 w_n'' - k_2^4 w_n = 0 \tag{11.180}$$

where

$$k_1^2 = \frac{n^2-1}{2B_{44}}\lambda_n^2(qR - D_n), \quad k_2^4 = \frac{\lambda_n^4}{B_{11}}\left(n^2-1\right)(qR - D_n)$$

and, as before, $\lambda_n = n/R$.

The solution of Eq. (11.180) is

$$w_n = C_1 \cosh rx + C_2 \sinh rx + C_3 \cos tx + C_4 \sin tx$$

where

$$r = \sqrt{\sqrt{k_1^4 + k_2^4} - k_1^2}, \quad t = \sqrt{\sqrt{k_1^4 + k_2^4} + k_1^2}$$

The boundary conditions at the shell ends $x = 0$ and $x = l$ allow us to arrive at a set of four algebraic equations for the constants of integration C_1−C_4. For the buckling problem, these equations are homogeneous and thus, to have a nonzero solution, we must equate the determinant of this set of equations to zero. This condition provides the equation for q which is in the coefficients of Eq. (11.180) and, hence, the parameters r and t. The critical pressure can be found by minimizing q with respect to the number of half-waves n.

11.6.1 Simply supported shells

For shells with simply supported edges $x = 0$ and $x = l$ (see Fig. 11.29), we must take $w_n = 0$ (which is equivalent to $v_n = 0$ in accordance with Eq. (11.103)) and $N_x = 0$, where N_x is given by Eq. (11.116). Using Eqs. (11.116) and (11.179), we get the following boundary conditions for a simply supported shell: $w_n = w_n'' = 0$. These boundary conditions can be satisfied if we take

$$w_n = w_n^0 \sin\frac{\pi x}{l} \tag{11.181}$$

Substituting Eq. (11.181) into Eq. (11.180), expressing q, and using Eqs. (11.110) for D_n, we get

$$q = \frac{D_{22}\left(n^2-1\right)}{R^3\left(1 + \dfrac{\lambda_n^2 D_{22}}{S_y}\right)} + \frac{\pi^4 R}{n^2 l^4 (n^2-1)\left(\dfrac{\lambda_n^2}{B_{11}} + \dfrac{\pi^2}{l^2 B_{44}}\right)} \tag{11.182}$$

The critical pressure can be found by minimization of the right-hand part of Eq. (11.182) with respect to n ($\lambda_n = n/R$).

The calculated pressure, Eq. (11.182), allows for transverse shear deformation which is important only for sandwich shells with lightweight cores. If this is not the case, we can take $S_y \to \infty$ and reduce Eq. (11.182) to

$$q = \frac{D_{22}}{R^3}\left(n^2 - 1\right) + \frac{\pi^4 R}{n^2 l^4 (n^2 - 1)\left(\dfrac{\lambda_n^2}{B_{11}} + \dfrac{\pi^2}{l^2 B_{44}}\right)} \tag{11.183}$$

This result can be further simplified. It follows from direct calculations that the critical load corresponding to the buckling mode shown in Fig. 11.29 is practically not affected by in-plane shear deformation. Neglecting this deformation, i.e., taking $B_{44} \to \infty$ in Eq. (11.183), we have

$$q = \frac{D_{22}}{R^3}\left(n^2 - 1\right) + \frac{\pi^4 B_{11} R^3}{l^4 n^4 (n^2 - 1)} \tag{11.184}$$

To obtain the analytical result, it is usually assumed that $n^2 \gg 1$ in Eq. (11.184). Then, neglecting unity in comparison with n^2, we find

$$q = \frac{D_{22} n^2}{R^3} + \frac{\pi^4 B_{11} R^3}{l^4 n^6}$$

Applying the minimum condition, i.e., taking $\partial q / \partial n^2 = 0$, we finally arrive at

$$n^2 = \frac{\pi R}{l}\sqrt[4]{\frac{3B_{11}R^2}{D_{22}}}, \quad q_{cr} = \frac{4\pi}{lR}\sqrt[4]{\frac{B_{11}D_{22}^3}{27R^2}} \tag{11.185}$$

11.6.2 Infinitely long shells

The critical pressure for an infinitely long cylindrical shell follows from Eq. (11.182) if we take $l \to \infty$, i.e.,

$$q = \frac{D_{22}\left(n^2 - 1\right)}{R^3\left(1 + \dfrac{\lambda_n^2 D_{22}}{S_y}\right)}$$

The minimum q-value corresponds to the minimum n-value which is equal to 2. Then,

$$q_{cr} = \frac{3D_{22}}{R^3\left(1 + \dfrac{4D_{22}}{R^2 S_y}\right)}$$

Neglecting transverse shear deformation, i.e., taking $S_y \to \infty$, we arrive at the classical result

$$q_{cr} = \frac{3D_{22}}{R^3}$$

For homogeneous shells,

$$D_{22} = \frac{E_y h^3}{12\left(1 - \upsilon_{xy}\upsilon_{yx}\right)}$$

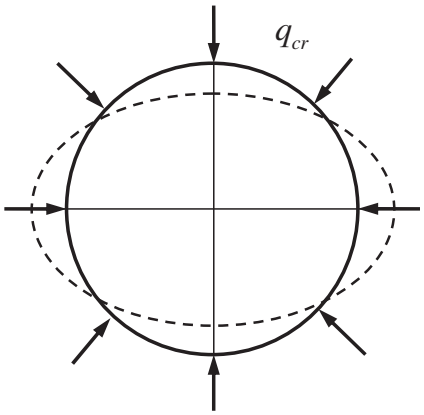


FIGURE 11.30

The buckling mode of an infinitely long shell under the action of external pressure.

and

$$q_{cr} = \frac{E_y h^3}{4R^3\left(1 - \upsilon_{xy}\upsilon_{yx}\right)} \tag{11.186}$$

The buckling mode is shown in Fig. 11.30.

11.6.3 Hydrostatic pressure

In the case of hydrostatic external pressure q, the shell is loaded with membrane axial and circumferential forces which follow from Eqs. (11.125), i.e.,

$$N_x = -\frac{1}{2}qR\,, \quad N_y = -qR \tag{11.187}$$

To evaluate the critical loads, consider an infinitely long homogeneous shell, for which Eqs. (11.137) and (11.186) yield the following critical stresses:

$$\sigma_x^{cr} = \frac{T_s^{cr}}{h} = \frac{h}{R\sqrt{3}}\sqrt{\frac{E_x E_y}{1 - \upsilon_{xy}\upsilon_{yx}}}\,, \quad \sigma_y^{cr} = \frac{q_{cr}R}{h} = \frac{E_y h^2}{4R^2\left(1 - \upsilon_{xy}\upsilon_{yx}\right)}$$

As can be seen, the ratio $\sigma_y^{cr}/\sigma_x^{cr}$ is proportional to h^2/R^2, which means that σ_y^{cr} is much less than σ_x^{cr}.

This difference explains the effect of shell shape imperfections on the critical load in axial compression. Indeed, if the shell has some initial deflection directed inwardly in the shell, the axial forces T (see Fig. 11.24) are statically equivalent, in accordance with Eq. (11.154), to the external pressure under which the critical stress is very low, and significantly reduces the axial critical stress. This analysis allows us to conclude that any shape imperfections in the shell geometry affect the critical value of the external pressure much less than the critical axial load. This conclusion is confirmed by experimental critical pressures, which agree with the theoretical results much better than those for the axial critical forces.

Thus, we can assume that under hydrostatic loading the buckling mode is the same as for the case of lateral pressure (see Fig. 11.29). For the prebuckling stress resultants given by Eqs. (11.187), Eq. (11.10) yields

$$\overline{p} = -qR\left(\frac{1}{2}\frac{\partial^2 w}{\partial x^2} + \frac{1}{R}\frac{\partial v}{\partial y} - \frac{\partial^2 w}{\partial y^2}\right)$$

and the buckling equation, Eq. (11.180), is generalized as

$$\left(1 - \frac{qRn^2}{2B_{44}}\right)w_n^{IV} + \left[\frac{qRn^4}{2R^2B_{11}} + \frac{n^2-1}{B_{44}}\lambda_n^2(qR - D_n)\right]w_n'' - \frac{\lambda_n^4}{B_{11}}\left(n^2-1\right)(qR - D_n)w_n = 0$$

For a simply supported shell, the hydrostatic pressure can be found from the following equation:

$$qR\left(\frac{\pi^2R^2}{2l^2} + n^2 - 1\right) = \frac{D_{22}\left(n^2-1\right)^2}{R^2\left(1 + \lambda_n^2\dfrac{D_{22}}{S_y}\right)} + \frac{\pi^4R^2}{n^2l^4\left(\dfrac{\lambda_n^2}{B_{11}} + \dfrac{\pi^2}{B_{44}l^2}\right)}$$

The critical pressure can be determined by minimizing q with respect to $n = 2, 3, 4\ldots$. Neglecting the shear deformation, i.e., taking $S_y \to \infty$ and $B_{44} \to \infty$, we get the following result generalizing Eq. (11.184):

$$q = \frac{1}{\dfrac{\pi^2R^2}{2l^2} + n^2 - 1}\left[\frac{D_{22}}{R^3}\left(n^2-1\right)^2 + \frac{\pi^4R^3B_{11}}{n^4l^4}\right] \tag{11.188}$$

As previously, neglect unity in comparison with n^2 and substitute n^2 from Eqs. (11.185) assuming that the axial force does not change n, and it can be taken from the solution for the lateral pressure case. Then, Eq. (11.188) yields the following approximate equation for the critical hydrostatic pressure:

$$q_{cr}^h = \frac{q_{cr}}{1 + \dfrac{\pi R}{2l}\sqrt[4]{\dfrac{D_{22}}{3B_{11}R^2}}}$$

Here, q_{cr} is specified by Eqs. (11.185). As can be seen, an additional axial force reduces the critical pressure.

11.7 References

Alfutov, N. A., Zinoviev, P. A., & Popov, B. G. (1984). *Analysis of Multilayered Composite Plates and Shells*. Moscow (in Russian): Mashinostroenie.

Ambartsumyan, S. A. (1961). *Theory of Anisotropic Shells*. Moscow (in Russian): Fizmatgiz.

Abramov, A. A. (1961). On translation of boundary conditions for systems of linear ordinary differential equations (variant of the sweep method). *Journal of Computational Mathematics and Mathematical Physics, 1*(3), 542–545 (in Russian).

Biderman, V. L. (1977). *Mechanics of Thin-Walled Structures*. Moscow (in Russian): Mashinostroenie.

Boitnott, R. L., Johnson, E. R., & Starnes, J. H., Jr. (1985). Nonlinear analysis of infinitely long graphite-epoxy cylindrical panels loaded with internal pressure. In *Proceedings of 26th AIAA/ASME/ASCE/AHS Structures, Structural Dynamics, and Materials Conference* (pp. 15–17). Orlando, Florida, April 1985. AIAA, New York, N.Y., pp. 593–604.

Elpatievskii, A. N., & Vasiliev, V. V. (1972). *Strength of Cylindrical Shells Made of Reinforced Materials*. Moscow (in Russian): Mashinostroenie.

Godunov, S. K. (1961). On numerical solutions of the boundary problems for the systems of ordinary differential equations. *Progress in Mathematical Sciences, 16*(3), 171–174 (in Russian).

Karmishin, A. V., Lyaskovets, V. A., Myachenkov, V. I., & Frolov, A. N. (1975). *Statics and Dynamics of Thin-Walled Shell Structures*. Moscow (in Russian): Mashinostroenie.

Kilchevsky, N. A. (1942). On axisymmetric deformation and elastic buckling of a circular pipe under the action of axial compressive forces. *Applied Mathematics and Mechanics, 6*(6), 497–508 (in Russian).

Khoma, I. Yu (1986). *Generalized Theory of Anizotropic Shells*. Kiev (in Russian): Naukova Dumka.

Khoroshun, L. P., Kozlov, S. V., Ivanov, Yu. A., & Koshevoi, I. K. (1988). *Generalized Theory of Nonhomogeneous Through-the-thickness Plates and Shells*. Kiev (in Russian): Naukova Dumka.

Kollar, L. P., & Springer, G. S. (2003). *Mechanics of Composite Structures*. Cambridge: Cambridge University Press.

Korn, G. A., & Korn, T. M. (1961). *Mathematical Handbook for Scientists and Engineers*. New York: McGraw Hill Book Company Inc.

Korolev, V. I. (1965). *Laminated Anisotropic Plates and Shells Made of Reinforced Plastics*. Moscow (in Russian): Mashinostroenie.

Paliy, O. M., & Spiro, V. E. (1977). *Anisotropic Shells in Shipbuilding*. Leningrad (in Russian): Sudostroenie.

Pikul, V. V. (1985). *Theory and Analysis of Laminated Structures*. Moscow (in Russian): Nauka.

Pikul, V. V. (2009). *Mechanics of Shells*. Vladivostok (in Russian): Dalnauka.

Rasskazov, A. O., Sokolovskaya, I. N., & Shulga, N. A. (1986). *Theory and Analysis of Laminated Orthotropic Plates and Shells*. Kiev (in Russian): Vischa Shkola.

Reddy, J. N. (2004). *Mechanics of Laminated Composite Plates and Shells – Theory and Analysis* (2nd ed.). Boca Raton: CRC Press.

Valishvili, N. V. (1976). *Computer Methods of Analysis for Shells of Revolution*. Moscow (in Russian): Mashinostroenie.

Vasiliev, V. V. (1993). *Mechanics of Composite Structures*. Washington: Taylor and Francis.

Vasiliev, V. V. (2009). *Composite Pressure Vessels: Analysis, Design, and Manufacturing*. Blacksburg VA, USA: Bull Ridge Publishing.

Vasiliev, V. V. (2011). To the problem of buckling of cylindrical shell under axial compression. *Proceedings of Russian Academy of Sciences, Mechanics of Solids, 2*, 5–15.

Vlasov, V. Z. (1949). *General Shell Theory and its Technical Applications*. Moscow – Leningrad (in Russian): GITTL. [English translation: NASA TT F-99, NASA, Washington, D.C. April 1964].

Volmir, A. S. (1967). *Stability of Deformable Systems*. Moscow (in Russian): Nauka.

Ye, J. (2003). *Laminated Composite Plates and Shells*. London: Springer.

CHAPTER

Optimal composite structures 12

Advanced composite materials are characterized by their high specific strength and stiffness and, in combination with automatic manufacturing processes, make it possible to fabricate composite structures with high levels of weight and cost efficiency. The replacement of metal alloys by composite materials, in general, reduces a structure's mass by 20–30%. However, in some special cases, the number of which progressively increases, the combination of material directional properties with design concepts utilizing these properties, being supported by the advantages of modern composite technology, provides a major improvement in structural performance. Such efficiency is demonstrated by composite structures of uniform strength in which the load is taken by uniformly stressed fibers.

12.1 OPTIMAL FIBROUS STRUCTURES

To introduce composite structures of uniform strength, consider a laminated panel shown in Fig. 12.1 and loaded with in-plane forces N_x, N_y, and N_{xy} uniformly distributed along the panel edges. Let the laminate consist of k unidirectional composite layers characterized with thicknesses h_i and fiber orientation angles ϕ_i $(i = 1,\ 2,\ 3,\ \ldots,\ k)$. For a plane stress state, the stacking sequence of the layers is not important.

To derive the optimality criterion specifying the best structure for the panel in Fig. 12.1, we first use the simplest monotropic model of a unidirectional composite (see Section 3.3) assuming that the forces $N_x,\ N_y$, and N_{xy} are taken by the fibers only. For a design analysis, this is a reasonable approach because the transverse and shear strengths of a unidirectional composite ply (stresses $\overline{\sigma}_2$ and $\overline{\tau}_{12}$) are much lower than the ply strength in the longitudinal direction (stress $\overline{\sigma}_1$). Using Eqs. (4.68) in which we put $\sigma_2 = 0$ and $\tau_{12} = 0$, we can write the following equilibrium equations relating the applied forces to the stresses $\sigma_1^{(i)}$ in the direction of the fibers of the ith layer:

$$\begin{aligned} N_x &= \sum_{i=1}^{k} \sigma_x^{(i)} h_i = \sum_{i=1}^{k} \sigma_1^{(i)} h_i \cos^2 \phi_i, \\ N_y &= \sum_{i=1}^{k} \sigma_y^{(i)} h_i = \sum_{i=1}^{k} \sigma_1^{(i)} h_i \sin^2 \phi_i, \\ N_{xy} &= \sum_{i=1}^{k} \tau_{xy}^{(i)} h_i = \sum_{i=1}^{k} \sigma_1^{(i)} h_i \sin \phi_i \cos \phi_i \end{aligned} \tag{12.1}$$

Advanced Mechanics of Composite Materials and Structural Elements. http://dx.doi.org/10.1016/B978-0-08-098231-1.00012-1
Copyright © 2013 Elsevier Ltd. All rights reserved.

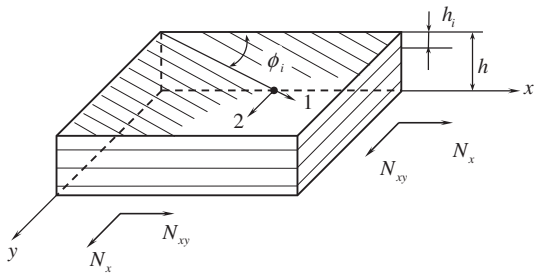


FIGURE 12.1

A laminated plate in a plane state of stress.

The strain $\varepsilon_1^{(i)}$ in the fiber direction in the ith layer can be expressed in terms of strains in coordinates x, y with the aid of the first equation of Eqs. (4.69). Using the constitutive equations for the monotropic model of a ply, Eqs. (3.61), we arrive at

$$\sigma_1^{(i)} = E_1 \varepsilon_1^{(i)} = E_1(\varepsilon_x \cos^2 \phi_i + \varepsilon_y \sin^2 \phi_i + \gamma_{xy} \sin \phi_i \cos \phi_i) \tag{12.2}$$

where it is assumed that the layers are made of one and the same material.

Consider the design problem and stipulate, for example, that the best structure for the laminate is that which provides the minimum total thickness

$$h = \sum_{i=1}^{k} h_i \tag{12.3}$$

for the given combination of loads. Thus, we should minimize the laminate thickness in Eq. (12.3) subject to the constraints imposed by Eqs. (12.1) and (12.2). To solve this problem, we can use the method of Lagrange multipliers, according to which we should introduce multipliers λ and minimize the following augmented function:

$$\begin{aligned} L = \sum_{i=1}^{k} h_i &+ \lambda_x \left(N_x - \sum_{i=1}^{k} \sigma_1^{(i)} h_i \cos^2 \phi_i \right) + \lambda_y \left(N_y - \sum_{i=1}^{k} \sigma_1^{(i)} h_i \sin^2 \phi_i \right) \\ &+ \lambda_{xy} \left(N_{xy} - \sum_{i=1}^{k} \sigma_1^{(i)} h_i \sin \phi_i \cos \phi_i \right) \\ &+ \sum_{i=1}^{k} \lambda_i \left[\sigma_1^{(i)} - E_1 \left(\varepsilon_x \cos^2 \phi_i + \varepsilon_y \sin^2 \phi_i + \gamma_{xy} \sin \phi_i \cos \phi_i \right) \right] \end{aligned}$$

with respect to the design variables h_i, ϕ_i and multipliers λ, i.e.,

$$\frac{\partial L}{\partial h_i} = 0, \quad \frac{\partial L}{\partial \phi_i} = 0, \quad \frac{\partial L}{\partial \lambda_x} = \frac{\partial L}{\partial \lambda_y} = \frac{\partial L}{\partial \lambda_{xy}} = \frac{\partial L}{\partial \lambda_i} = 0 \tag{12.4}$$

Minimization with respect to λ gives, obviously, the constraints in Eqs. (12.1) and (12.2), whereas the first two of Eqs. (12.4) yield

$$\sigma_1^{(i)} (\lambda_x \cos^2 \phi_i + \lambda_y \sin^2 \phi_i + \lambda_{xy} \sin \phi_i \cos \phi_i) = 1 \tag{12.5}$$

$$h_i\sigma_1^{(i)}\left[(\lambda_y-\lambda_x)\sin 2\phi_i+\lambda_{xy}\cos 2\phi_i\right]=E_1\lambda_i\left[(\varepsilon_y-\varepsilon_x)\sin 2\phi_i+\varepsilon_{xy}\cos 2\phi_i\right] \tag{12.6}$$

The solution of Eq. (12.6) is

$$\lambda_x=E_1\varepsilon_x\frac{\lambda_i}{h_i\sigma_1^{(i)}},\quad \lambda_y=E_1\varepsilon_y\frac{\lambda_i}{h_i\sigma_1^{(i)}},\quad \lambda_{xy}=E_1\gamma_{xy}\frac{\lambda_i}{h_i\sigma_1^{(i)}}$$

These equations allow us to conclude that

$$\frac{\lambda_i}{h_i\sigma_1^{(i)}}=\frac{\lambda_x}{E_1\varepsilon_x}=\frac{\lambda_y}{E_1\varepsilon_y}=\frac{\lambda_{xy}}{E_1\gamma_{xy}}=\frac{1}{c^2}$$

where c is a constant. Substituting λ_x, λ_y, and λ_{xy} from these equations into Eq. (12.5) and taking into account Eq. (12.2), we have

$$\left(\sigma_1^{(i)}\right)^2=c^2 \tag{12.7}$$

This equation has two solutions: $\sigma_1^{(i)}=\pm c$.

Consider the first case, i.e., $\sigma_1^{(i)}=c$. Adding the first two equations of Eqs. (12.1) and taking into account Eq. (12.9), we have

$$h=\frac{1}{c}(N_x+N_y)$$

Obviously, the minimum value of h corresponds to $c=\overline{\sigma}_1$, where $\overline{\sigma}_1$ is the ultimate stress. Thus, the total thickness of the optimal plate is

$$h=\frac{1}{\overline{\sigma}_1}(N_x+N_y) \tag{12.8}$$

Taking now $\sigma_1^{(i)}=\overline{\sigma}_1$ in Eqs. (12.1) and eliminating $\overline{\sigma}_1$ with the aid of Eq. (12.8), we arrive at the following two optimality conditions in terms of the design variables and acting forces:

$$\sum_{i=1}^{k}h_i\left(N_x\sin^2\phi_i-N_y\cos^2\phi_i\right)=0 \tag{12.9}$$

$$\sum_{i=1}^{k}h_i\left[\left(N_x+N_y\right)\sin\phi_i\cos\phi_i-N_{xy}\right]=0 \tag{12.10}$$

Thus, $2k$ design variables, i.e., k values of h_i and k values of ϕ_i, should satisfy these three equations, Eqs. (12.8)–(12.10). All possible optimal laminates have the same total thickness in Eq. (12.8). As follows from Eq. (12.2), the condition $\sigma_1^{(i)}=\overline{\sigma}_1$ is valid, in the general case, if $\varepsilon_x=\varepsilon_y=\varepsilon$ and $\gamma_{xy}=0$. Applying Eqs. (4.69) to determine the strains in the principal material coordinates of the layers, we arrive at the following result: $\varepsilon_1=\varepsilon_2=\varepsilon$ and $\gamma_{12}=0$. This means that the optimal laminate is the structure of uniform stress and strain in which the fibers in each layer coincide with the directions of principal strains. An important feature of the optimal laminate follows from the last equation of Eqs. (4.168) which yields $\phi_i'=\phi_i$. Thus, the optimal angles do not change under loading.

Introducing the new variables

$$\overline{h}_i = \frac{h_i}{h}, \quad n_y = \frac{N_y}{N_x}, \quad n_{xy} = \frac{N_{xy}}{N_x}, \quad \lambda = \frac{1}{1+n_y}$$

and taking into account that

$$\sum_{i=1}^{k} \overline{h}_i = 1 \tag{12.11}$$

we can transform Eqs. (12.8)–(12.10) that specify the structural parameters of the optimal laminate to the following final form

$$h = \frac{N_x}{\lambda \overline{\sigma}_1} \tag{12.12}$$

$$\sum_{i=1}^{k} \overline{h}_i \cos^2\phi_i = \lambda, \quad \sum_{i=1}^{k} \overline{h}_i \sin^2\phi_i = \lambda n_y \tag{12.13}$$

$$\sum_{i=1}^{k} \overline{h}_i \sin\phi_i \cos\phi_i = \lambda n_{xy} \tag{12.14}$$

For uniaxial tension in the x-direction, we have $n_y = n_{xy} = 0,\ \lambda = 1$. Then, Eqs. (12.13) yield $\phi_i = 0$ ($i = 1, 2, 3, \ldots, k$) and Eq. (12.12) gives the obvious result $h = N_x/\overline{\sigma}$.

To describe tension in two orthogonal directions x and y, we should put $n_{xy} = 0$. It follows from Eq. (12.14) that the laminate structure in this case should be in-plane symmetric, i.e., each ply with angle $+\phi_i$ should be accompanied by a ply of the same thickness but with angle $-\phi_i$.

Consider, for example, uniform biaxial tension such that $N_x = N_y = N$, $N_{xy} = 0$, $n_y = 1$, $n_{xy} = 0$, and $\lambda = 0.5$. For this case, Eqs. (12.12) and (12.13) yield

$$h = \frac{2N}{\overline{\sigma}_1}, \quad \sum_{i=1}^{k} \overline{h}_i \cos 2\phi_i = 0 \tag{12.15}$$

The natural structure for this case corresponds to the cross-ply laminate for which $k = 2$, $\phi_1 = 0^\circ$, and $\phi_2 = 90^\circ$ (Fig. 12.2a). Then, the second equation of Eqs. (12.15) gives the evident result $\overline{h}_1 = \overline{h}_2$.

Consider the first equation, from which it follows that the total thickness of the optimal laminate is twice the thickness of a metal plate of the same strength under the same loading conditions. This result is expected because, in contrast to isotropic materials, the monotropic layer can work in only one direction, i.e., along the fibers. So, we need to have the 0° layer to take $N_x = N$ and the same, but 90°, layer to take $N_y = N$. From this we can conclude that the directional character of a composite ply's stiffness and strength is actually a material shortcoming rather than an advantage. The real advantages of composite materials are associated with their high specific strength provided by thin fibers (see Section 3.2.1), and if we had isotropic materials with such high specific strength, no composites would be developed and implemented.

Return now to the second equation of Eqs. (12.15) which shows that, in addition to a cross-ply laminate, there exists an infinite number of optimal structures. For example, this equation is

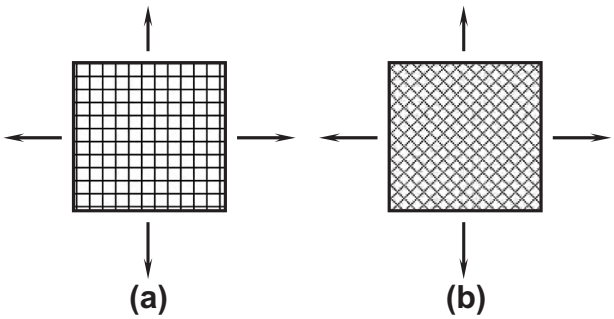


FIGURE 12.2

Cross-ply (a) and ±45° angle-ply (b) optimal structures for uniform tension.

satisfied for a symmetric ±45° angle-ply laminate (Fig. 12.2b). Moreover, all the quasi-isotropic laminates discussed in Section 5.7 and listed in Table 5.3 satisfy the optimality conditions for uniform tension.

A loading case, which is important for actual applications, corresponds to a cylindrical pressure vessel, as considered in Section 6.3. The winding of such a vessel is shown in Fig. 7.63. For this type of loading,

$$N_x = \frac{1}{2}pR, \quad N_y = pR, \quad N_{xy} = 0$$

where N_x and N_y are the axial and circumferential stress resultants, respectively, p is the internal pressure, and R is the cylinder radius. Thus, we have $n_y = 2$ and $\lambda = 1/3$. Since $N_{xy} = 0$, the structure of the laminate is symmetric with respect to the cylinder meridian, and Eqs. (12.12)–(12.14) can be reduced to

$$h = \frac{3pR}{2\overline{\sigma}_1} \tag{12.16}$$

$$\sum_{i=1}^{k} \overline{h}_i \left(3\cos^2\phi_i - 1\right) = 0 \tag{12.17}$$

Comparing Eq. (12.16) with the corresponding expression for the thickness of a metal pressure vessel, which is $h_m = pR/\overline{\sigma}$, we can see that the thickness of an optimal composite vessel is 1.5 times greater than h_m. Nevertheless, because of their higher strength and lower density, composite pressure vessels are significantly lighter than metal ones. To show this, consider pressure vessels with radius $R = 100$ mm made of different materials and designed for a burst pressure $p = 20$ MPa. The results are listed in Table 12.1. As can be seen, the thickness of a glass-epoxy vessel is the same as that for a steel vessel, because the factor 1.5 in Eq. (12.16) is compensated by the composite's strength which is 1.5 times higher than the strength of steel. However, the density of a glass-epoxy composite is much lower than the density of steel, and as a result, the mass of unit surface area of the composite vessel is only 27% of the corresponding value for a steel vessel. The most promising materials for pressure vessels are aramid and carbon composites, which have the highest specific tensile strength (see Table 12.1).

TABLE 12.1 Parameters of Metal and Composite Pressure Vessels.

Parameter	Material					
	Steel	**Aluminum**	**Titanium**	**Glass-Epoxy**	**Carbon-Epoxy**	**Aramid-Epoxy**
Strength, $\overline{\sigma}$, $\overline{\sigma}_1$ (MPa)	1200	500	900	1800	2000	2500
Density, ρ (g/cm^3)	7.85	2.7	4.5	2.1	1.55	1.32
Thickness of the vessel, h_m, h (mm)	1.67	4.0	2.22	1.67	1.5	1.2
Mass of the unit surface area, ρh (kg/m^2)	13.11	10.8	10.0	3.51	2.32	1.58

Consider Eq. (12.17) which shows that there can exist an infinite number of optimal laminates with one and the same thickness specified by Eq. (12.16).

The simplest is a cross-ply laminate having $k = 2$, $\phi_1 = 0°$, $h_1 = h_0$, $\phi_2 = 90°$, and $h_2 = h_{90}$. For this structure, Eq. (12.17) yields $h_{90} = 2h_0$. This result seems obvious because $N_y/N_x = 2$. For symmetric $\pm\phi$ angle-ply laminate, we should take $k = 2$, $h_1 = h_2 = h_\phi/2$, $\phi_1 = +\phi$, and $\phi_2 = -\phi$. Then,

$$\cos^2\phi = \frac{1}{3}, \quad \phi = \phi_0 = 54.44°$$

As a rule, helical plies are combined with circumferential plies as in Fig. 7.63. For this case, $k = 3$, $h_1 = h_2 = h_\phi/2$, $\phi_1 = -\phi_2 = \phi$, $h_3 = h_{90}$, $\phi_3 = 90°$, and Eq. (12.17) gives

$$\frac{h_{90}}{h_\phi} = 3\cos^2\phi - 1 \tag{12.18}$$

Since the thickness cannot be negative, this equation is valid for $0 \le \phi \le \phi_0$. For $\phi_0 \le \phi \le 90°$, the helical layers should be combined with an axial one, i.e., we should put $k = 3$, $h_1 = h_2 = h_\phi/2$, $\phi_1 = -\phi_2 = \phi$, $h_3 = h_0$, and $\phi_3 = 0°$. Then,

$$\frac{h_0}{h_\phi} = \frac{1}{2}(1 - 3\cos^2\phi) \tag{12.19}$$

The dependencies corresponding to Eqs. (12.18) and (12.19) are presented in Fig. 12.3. As an example, consider a filament-wound pressure vessel whose parameters are listed in Table 6.1. The cylindrical part of the vessel shown in Figs. 4.14 and 6.22 consists of a $\pm 36°$ angle-ply helical layer and a circumferential layer whose thicknesses $h_1 = h_\phi$ and $h_2 = h_{90}$ are presented in Table 6.1. The ratio h_{90}/h_ϕ for two experimental vessels is 0.97 and 1.01, whereas Eq. (12.18) gives for this case $h_{90}/h_\phi = 0.96$ which shows that both vessels are close to optimal structures.

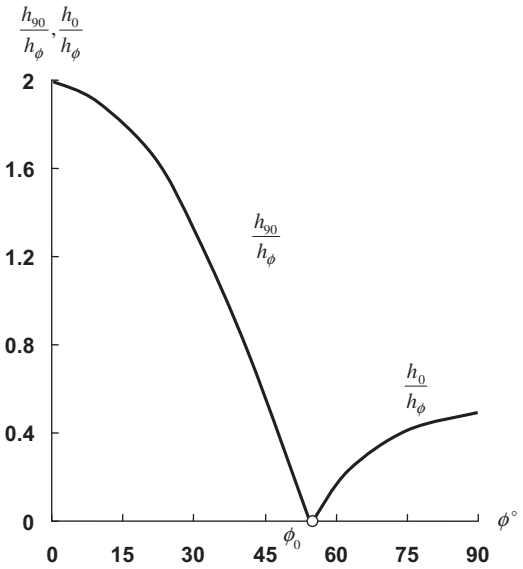


FIGURE 12.3

Optimal thickness ratios for a cylindrical pressure vessel consisting of $\pm\phi$ helical plies combined with circumferential (90°) or axial(0°) plies.

Laminates reinforced with uniformly stressed fibers can exist provided some restrictions are imposed on the acting forces N_x, N_y, and N_{xy}. Such restrictions follow from Eqs. (12.13) and (12.14) under the conditions that $\overline{h}_i \geq 0$, $0 \leq \sin^2\phi_i$, and $\cos^2\phi_i \leq 1$ and have the form

$$0 \leq \lambda \leq 1, \quad -\frac{1}{2} \leq \lambda n_{xy} \leq \frac{1}{2}$$

In particular, Eqs. (12.13) and (12.14) do not describe the case of pure shear for which only the shear stress resultant, N_{xy}, is not zero. This is quite reasonable because the strength condition $\sigma_1^{(i)} = \overline{\sigma}_1$ under which Eqs. (12.12)–(12.14) are derived is not valid for shear inducing tension and compression in angle-ply layers.

To study in-plane shear of the laminate, we should use both solutions of Eq. (12.7) and assume that for some layers, e.g., with $i = 1, 2, 3, \ldots, n-1$, $\sigma_1^{(i)} = \overline{\sigma}_1$ whereas for the other layers ($i = n, n+1, n+2, \ldots, k$), $\sigma_1^{(i)} = -\overline{\sigma}_1$. Then, Eqs. (12.1) can be reduced to the following form:

$$N_x + N_y = \overline{\sigma}_1\left(h^+ - h^-\right) \tag{12.20}$$

$$N_x - N_y = \overline{\sigma}_1\left(\sum_{i=1}^{n-1} h_i^+ \cos 2\phi_i - \sum_{i=n}^{k} h_i^- \cos 2\phi_i\right) \tag{12.21}$$

$$N_{xy} = \frac{1}{2}\overline{\sigma}_1\left(\sum_{i=1}^{n-1} h_i^+ \sin 2\phi_i - \sum_{i=n}^{k} h_i^- \sin 2\phi_i\right) \tag{12.22}$$

where

$$h^+ = \sum_{i=1}^{n-1} h_i^+, \quad h^- = \sum_{i=n}^{k} h_i^-$$

are the total thicknesses of the plies with tensile and compressive stresses in the fibers, respectively.

For the case of pure shear ($N_x = N_y = 0$), Eqs. (12.20) and (12.21) yield $h^+ = h^-$ and $\phi_i = \pm 45^\circ$. Then, assuming that $\phi_i = +45^\circ$ for the layers with $h_i = h_i^+$, whereas $\phi_i = -45^\circ$ for the layers with $h_i = h_i^-$, we get from Eq. (12.22)

$$h = h^+ + h^- = \frac{2N_{xy}}{\overline{\sigma}_1}$$

The optimal laminate, as follows from the foregoing derivation, corresponds to a $\pm 45^\circ$ angle-ply structure as shown in Fig. 12.2b.

12.2 COMPOSITE LAMINATES OF UNIFORM STRENGTH

Consider again the panel in Fig. 12.1 and assume that the unidirectional plies or fabric layers that form the panel are orthotropic, i.e., in contrast to the previous section, we do not now neglect stresses σ_2 and τ_{12} in comparison with σ_1 (see Fig. 3.29). Then, the constitutive equations for the panel in a plane stress state are specified by the first three equations in Eqs. (5.35), i.e.,

$$\begin{aligned} N_x &= B_{11}\varepsilon_x + B_{12}\varepsilon_y + B_{14}\gamma_{xy} \\ N_y &= B_{21}\varepsilon_x + B_{22}\varepsilon_y + B_{24}\gamma_{xy} \\ N_{xy} &= B_{41}\varepsilon_x + B_{42}\varepsilon_y + B_{44}\gamma_{xy} \end{aligned} \tag{12.23}$$

where, in accordance with Eqs. (4.72), (5.28), and (5.42),

$$\begin{aligned} B_{11} &= \sum_{i=1}^{k} h_i \left(\overline{E}_1^{(i)} \cos^4\phi_i + \overline{E}_2^{(i)} \sin^4\phi_i + 2E_{12}^{(i)} \sin^2\phi_i \cos^2\phi_i \right) \\ B_{12} = B_{21} &= \sum_{i=1}^{k} h_i \left[\overline{E}_1^{(i)} \nu_{12}^{(i)} + \left(\overline{E}_1^{(i)} + \overline{E}_2^{(i)} - 2E_{12}^{(i)} \right) \sin^2\phi_i \cos^2\phi_i \right] \\ B_{22} &= \sum_{i=1}^{k} h_i \left(\overline{E}_1^{(i)} \sin^4\phi_i + \overline{E}_2^{(i)} \cos^4\phi_i + 2E_{12}^{(i)} \sin^2\phi_i \cos^2\phi_i \right) \\ B_{14} = B_{41} &= \sum_{i=1}^{k} h_i \left(\overline{E}_1^{(i)} \cos^2\phi_i - \overline{E}_2^{(i)} \sin^2\phi_i - E_{12}^{(i)} \cos 2\phi_i \right) \sin\phi_i \cos\phi_i \\ B_{24} = B_{42} &= \sum_{i=1}^{k} h_i \left(\overline{E}_1^{(i)} \sin^2\phi_i - \overline{E}_2^{(i)} \cos^2\phi_i + E_{12}^{(i)} \cos 2\phi_i \right) \sin\phi_i \cos\phi_i \end{aligned} \tag{12.24}$$

$$B_{44} = \sum_{i=1}^{k} h_i \left[\left(\overline{E}_1^{(i)} + \overline{E}_2^{(i)} - 2\overline{E}_1^{(i)} \nu_{12}^{(i)} \right) \sin^2\phi_i \cos^2\phi_i + G_{12}^{(i)} \cos^2 2\phi_i \right]$$

and $\overline{E}_{1,2}^{(i)} = \dfrac{E_{1,2}^{(i)}}{1 - \nu_{12}^{(i)}\nu_{21}^{(i)}}$, $E_{12}^{(i)} = \overline{E}_1^{(i)}\nu_{12}^{(i)} + 2G_{12}^{(i)}$.

In the general case, the panel can consist of layers made from different composite materials. Using the optimality criterion developed in the previous section for fibrous structures, we consider that the fibers in each layer are directed along the lines of principal strains, or principal stresses, because $\tau_{12}^{(i)} = G_{12}\gamma_{12}^{(i)}$ for an orthotropic layer and the condition $\gamma_{12}^{(i)} = 0$ is equivalent to the condition $\tau_{12}^{(i)} = 0$ (see Section 2.4). Using the third equation in Eqs. (4.69), we can write these conditions as

$$2(\varepsilon_y - \varepsilon_x) \sin\phi_i \cos\phi_i + \gamma_{xy} \cos 2\phi_i = 0 \tag{12.25}$$

This equation can be satisfied for all the layers if we take

$$\varepsilon_x = \varepsilon_y = \varepsilon, \quad \gamma_{xy} = 0 \tag{12.26}$$

Then, Eqs. (12.23) yield

$$N_x = (B_{11} + B_{12})\varepsilon, \quad N_y = (B_{21} + B_{22})\varepsilon, \quad N_{xy} = (B_{41} + B_{42})\varepsilon$$

These equations allow us to find the strain, i.e.,

$$\varepsilon = \frac{N_x + N_y}{B_{11} + 2B_{12} + B_{22}} \tag{12.27}$$

and to write two relationships specifying the optimal structural parameters of the laminate:

$$(B_{11} + B_{12})N_y - (B_{21} + B_{22})N_x = 0$$
$$(B_{41} + B_{42})(N_x + N_y) - (B_{11} + 2B_{12} + B_{22})N_{xy} = 0$$

Substitution of B_{mn} from Eqs. (12.24) results in the following explicit form of these conditions:

$$\sum_{i=1}^{k} h_i \left[\overline{E}_1^{(i)} \left(1 + \nu_{12}^{(i)}\right) \left(N_x \sin^2\phi_i - N_y \cos^2\phi_i \right) + \overline{E}_2^{(i)} \left(1 + \nu_{21}^{(i)}\right) \left(N_x \cos^2\phi_i - N_y \sin^2\phi_i \right) \right] = 0 \tag{12.28}$$

$$\sum_{i=1}^{k} h_i \left\{ \left(N_x + N_y \right) \left(\overline{E}_1^{(i)} - \overline{E}_2^{(i)} \right) \sin\phi_i \cos\phi_i - N_{xy} \left[\overline{E}_1^{(i)} \left(1 + \nu_{12}^{(i)}\right) + \overline{E}_2^{(i)} \left(1 + \nu_{21}^{(i)}\right) \right] \right\} = 0$$

To determine the stresses that act in the optimal laminate, we use Eqs. (4.69) and (12.26) that specify the strains in the principal material coordinates of the layers as $\varepsilon_1 = \varepsilon_2 = \varepsilon$, $\gamma_{12} = 0$. Applying the

constitutive equations, Eqs. (4.56), substituting ε from Eq. (12.27), and writing the result in explicit form with the aid of Eqs. (12.24), we arrive at

$$\sigma_1^{(i)} = \frac{\overline{E}_1^{(i)}}{S_i}\left(1 + \nu_{12}^{(i)}\right)\left(N_x + N_y\right)$$

$$\sigma_2^{(i)} = \frac{\overline{E}_2^{(i)}}{S_i}\left(1 + \nu_{21}^{(i)}\right)\left(N_x + N_y\right)$$

$$\tau_{12}^{(i)} = 0 \tag{12.29}$$

where

$$S_i = \sum_{i=1}^{k} h_i\left[\overline{E}_1^{(i)}\left(1 + \nu_{12}^{(i)}\right) + \overline{E}_2^{(i)}\left(1 + \nu_{21}^{(i)}\right)\right]$$

is the laminate stiffness coefficient.

If all the layers are made from the same material, Eqs. (12.28) and (12.29) are simplified as

$$\sum_{i=1}^{k} h_i\left[N_x \sin^2\phi_i - N_y \cos^2\phi_i + n\left(N_x \cos^2\phi_i - N_y \sin^2\phi_i\right)\right] = 0$$

$$\sum_{i=1}^{k} h_i\left[m\left(N_x + N_y\right) \sin\phi_i \cos\phi_i - \left(1 + n\right)N_{xy}\right] = 0 \tag{12.30}$$

$$\sigma_1^{(i)} = \sigma_1 = \frac{N_x + N_y}{h(1+n)}, \quad \sigma_2^{(i)} = \sigma_2 = \frac{n\left(N_x + N_y\right)}{h(1+n)}, \quad \tau_{12}^{(i)} = 0 \tag{12.31}$$

in which

$$n = \frac{E_2(1+\nu_{21})}{E_1(1+\nu_{12})}, \quad m = \frac{E_1 - E_2}{E_1(1+\nu_{12})}, \quad h = \sum_{i=1}^{k} h_i$$

Laminates of uniform strength exist under the following restrictions:

$$\frac{n}{1+n} \le \frac{N_x}{N_x + N_y} \le \frac{1}{1+n}, \quad \left|\frac{N_{xy}}{N_x + N_y}\right| \le \frac{1-n}{2(1+n)}$$

For the monotropic model of a unidirectional ply considered in the previous section, $n = 0$, $m = 1$, and Eqs. (12.30) reduce to Eqs. (12.9) and (12.10).

To determine the thickness of the optimal laminate, we should use Eqs. (12.31) in conjunction with one of the strength criteria discussed in Chapter 6. For the simplest case, using the maximum stress criterion in Eqs. (6.2), the thickness of the laminate can be found from the following conditions: $\sigma_1 = \overline{\sigma}_1$ or $\sigma_2 = \overline{\sigma}_2$, so that

$$h_1 = \frac{N_x + N_y}{(1+n)\overline{\sigma}_1}, \quad h_2 = \frac{n\left(N_x + N_y\right)}{(1+n)\overline{\sigma}_2} \tag{12.32}$$

TABLE 12.2 Parameters of Typical Advanced Composites.

	Fabric-Epoxy Composites			Unidirectional-Epoxy Composites				
Parameter	**Glass**	**Carbon**	**Aramid**	**Glass**	**Carbon**	**Aramid**	**Boron**	**Boron-Al**
$\overline{\sigma}_2/\overline{\sigma}_1$	0.99	0.99	0.83	0.022	0.025	0.012	0.054	0.108
n	0.85	1.0	1.0	0.28	0.1	0.072	0.11	0.7

Obviously, for the optimal structure, we would like to have $h_1 = h_2$. However, this can happen only if material characteristics meet the following condition:

$$\frac{\overline{\sigma}_2}{\overline{\sigma}_1} = n = \frac{E_2(1+\nu_{21})}{E_1(1+\nu_{12})} \tag{12.33}$$

The results of calculations for typical materials whose properties are listed in Tables 3.5 and 4.6 are presented in Table 12.2. As can be seen, Eq. (12.33) is approximately valid for fabric composites whose stiffness and strength in the warp and fill directions (see Section 4.7) are controlled by fibers of the same type. However, for unidirectional polymeric and metal matrix composites, whose longitudinal stiffness and strength are governed by the fibers and whose transverse characteristics are determined by the matrix properties, $\overline{\sigma}_2/\overline{\sigma}_1 << n$. In accordance with Eqs. (12.32), this means that $h_1 << h_2$, and the ratio h_2/h_1 varies from 12.7 for glass-epoxy to 2.04 for boron-epoxy composites. Now, return to the discussion presented in Section 4.4.2 from which it follows that in laminated composites transverse stresses σ_2 reaching their ultimate value, $\overline{\sigma}_2$, cause cracks in the matrix, which do not result in failure of the laminate whose strength is controlled by the fibers. To describe such a laminate with cracks in the matrix (provided the cracks are allowable for the structure under design), we can use the monotropic model of the ply and, hence, the results of the optimization presented in Section 12.1.

Consider again the optimality condition Eq. (12.25). As can be seen, this equation can be satisfied not only by strains in Eqs. (12.26), but also if we take

$$\tan 2\phi_i = \frac{\gamma_{xy}}{\varepsilon_x - \varepsilon_y} \tag{12.34}$$

Since the left-hand side of this equation is a periodic function with period π, Eq. (12.34) determines two angles, i.e.,

$$\phi_1 = \phi = \frac{1}{2}\tan^{-1}\frac{\gamma_{xy}}{\varepsilon_x - \varepsilon_y}, \quad \phi_2 = \frac{\pi}{2} + \phi \tag{12.35}$$

Thus, the optimal laminate consists of two layers, and the fibers in both layers are directed along the lines of principal stresses. Suppose that the layers are made of the same composite material and have the same thickness, i.e., $h_1 = h_2 = h/2$, where h is the thickness of the laminate. Then, using Eqs. (12.24) and (12.35) and, we can show that $B_{11} = B_{22}$ and $B_{24} = -B_{14}$ for this laminate. After some transformation involving elimination of γ^0_{xy} from the first two equations of Eqs. (12.23) with the

aid of Eq. (12.34) and similar transformation of the third equation from which ε_x^0 and ε_y^0 are eliminated, using again Eq. (12.34), we get

$$N_x = (B_{11} + B_{14}\tan 2\phi)\varepsilon_x^0 + (B_{12} - B_{14}\tan 2\phi)\varepsilon_y^0$$
$$N_y = (B_{12} - B_{14}\tan 2\phi)\varepsilon_x^0 + (B_{11} + B_{14}\tan 2\phi)\varepsilon_y^0$$
$$N_{xy} = \Big(B_{44} + B_{14}\cot 2\phi\Big)\gamma_{xy}^0$$

Upon substitution of coefficients B_{mn} from Eqs. (12.24) we arrive at

$$N_x = \frac{h}{2}\Big[(\overline{E}_1 + \overline{E}_2)\varepsilon_x^0 + (\overline{E}_1\nu_{12} + \overline{E}_2\nu_{21})\varepsilon_y^0\Big]$$
$$N_y = \frac{h}{2}\Big[(\overline{E}_1\nu_{12} + \overline{E}_2\nu_{21})\varepsilon_x^0 + (\overline{E}_1 + \overline{E}_2)\varepsilon_y^0\Big]$$
$$N_{xy} = \frac{h}{4}\Big[\overline{E}_1(1 - \nu_{12}) + \overline{E}_2(1 - \nu_{21})\Big]\gamma_{xy}^0$$

Introducing average stresses $\sigma_x = N_x/h$, $\sigma_y = N_y/h$, and $\tau_{xy} = N_{xy}/h$ and solving these equations for strains, we have

$$\varepsilon_x^0 = \frac{1}{E}(\sigma_x - \nu\sigma_y), \quad \varepsilon_y^0 = \frac{1}{E}(\sigma_y - \nu\sigma_x), \quad \gamma_{xy}^0 = \frac{\tau_{xy}}{G} \tag{12.36}$$

where

$$E = \frac{1}{2(E_1 + E_2)}\left[2E_1E_2 + \frac{E_1^2\big(1 - \nu_{12}^2\big) + E_2^2\big(1 - \nu_{21}^2\big)}{1 - \nu_{12}\nu_{21}}\right] \tag{12.37}$$
$$\nu = \frac{E_1\nu_{12} + E_2\nu_{21}}{E_1 + E_2}, \quad G = \frac{E}{2(1 + \nu)}$$

Changing strains for stresses in Eqs. (12.35), we can write the expression for the optimal orientation angle as

$$\phi = \frac{1}{2}\tan^{-1}\frac{2\,\tau_{xy}}{\sigma_x - \sigma_y} \tag{12.38}$$

It follows from Eqs. (12.36) that a laminate consisting of two layers reinforced along the directions of principal stresses behaves like an isotropic layer, and Eqs. (12.37) specify the elastic constants of the corresponding isotropic material. For typical advanced composites, these constants are listed in Table 12.3 (the properties of unidirectional plies are taken from Table 3.5). Comparing the elastic moduli of the optimal laminates with those for quasi-isotropic materials (see Table 5.4), we can see that for polymeric composites the characteristics of the first group of materials are about 40% higher than those for the second group. However, it should be emphasized that whereas the properties of quasi-isotropic laminates are universal material constants, the optimal laminates demonstrate characteristics shown in Table 12.3 only if the orientation angles of the fibers are found from Eqs. (12.35) or (12.38) and correspond to a particular distribution of stresses σ_x, σ_y, and τ_{xy}.

It can be noted from Table 12.3 that the modulus of a carbon-epoxy laminate is close to the modulus of aluminum, whereas the density of the composite material is lower by a factor of 1.7. This is

TABLE 12.3 Effective Elastic Constants of an Optimal Laminate.

Property	Glass-Epoxy	Carbon-Epoxy	Aramid-Epoxy	Boron-Epoxy	Boron-Al	Carbon-Carbon	Al_2O_2-Al
Elastic modulus, E (GPa)	36.9	75.9	50.3	114.8	201.1	95.2	205.4
Poisson's ratio, ν	0.053	0.039	0.035	0.035	0.21	0.06	0.176

the theoretical weight saving factor that can be expected if we change from aluminum to carbon-epoxy composite in a thin-walled structure. Since the stiffness of both materials is approximately the same, to find the optimal orientation angles of the fibers, we can substitute in Eq. (12.38) the stresses acting in the aluminum prototype structure. A composite structure designed in this way will have approximately the same stiffness as the prototype structure and, as a rule, higher strength because carbon composites are stronger than aluminum alloys.

To evaluate the strength of the optimal laminate, we should substitute strains from Eqs. (12.36) into Eqs. (4.69) and thence, these strains in the principal material coordinates of the layers, into constitutive equations, Eqs. (4.56), that specify the stresses σ_1 and $\sigma_2(\tau_{12} = 0)$ acting in the layers. Applying the appropriate failure criterion (see Chapter 6), we can evaluate the laminate strength.

Comparing Tables 1.1 and 12.3, we can see that boron-epoxy optimal laminates have approximately the same stiffness as titanium (but are lighter by a factor of about 2). Boron-aluminum can be used to replace steel with a weight saving factor of about 3.

For preliminary evaluation, we can use a monotropic model of unidirectional plies neglecting the stiffness and load-carrying capacity of the matrix. Then, Eqs. (12.37) take the following simple form:

$$E = \frac{E_1}{2}, \quad \nu = 0, \quad G = \frac{E_1}{4} \tag{12.39}$$

As an example, consider an aluminum shear web with thickness $h = 2$ mm, elastic constants $E_a = 72$ GPa and $\nu_a = 0.3$, and density $\rho_a = 2.7$ g/cm^3. This panel is loaded with shear stress τ. Its shear stiffness is $B_{44}^a = 57.6$ GPa•mm and the mass of a unit surface is $m_a = 5.4$ kg/m^2 . For the composite panel, taking $\sigma_x = \sigma_y = 0$ in Eq. (12.38) we have $\phi = 45^\circ$. Thus, the composite panel consists of $+45^\circ$ and -45° unidirectional layers of the same thickness. The total thickness of the laminate is $h = 2$ mm, i.e., the same as for an aluminum panel. Substituting $E_1 = 140$ GPa and taking into account that $\rho = 1.55$ g/cm^3 for a carbon-epoxy composite, which is chosen to substitute for aluminum, we get $B_{44}^c = 70$ GPa•mm and $m_c = 3.1$ kg/m^3. The stresses acting in the fiber directions of the composite plies are $\sigma_1^c = \pm 2\tau$. Thus, the composite panel has a 21.5% higher stiffness and its mass is only 57.4% of the mass of a metal panel. The composite panel also has higher strength because the longitudinal strength of unidirectional carbon-epoxy composite under tension and compression is more than twice the shear strength of aluminum.

The potential performance of the composite structure under discussion can be enhanced if we use different materials in the layers with angles ϕ_1 and ϕ_2 specified by Eqs. (12.35). According to the derivation of Obraztsov and Vasiliev (1989), the ratio of the layers' thicknesses is

$$\frac{h_2}{h_1} = \frac{\bar{E}_1^{(1)} - \bar{E}_2^{(1)}}{\bar{E}_1^{(2)} - \bar{E}_2^{(2)}}$$

and the elastic constants in Eqs. (12.37) are generalized as

$$\overline{E} = \frac{E}{1-\nu^2} = \frac{\bar{E}_1^{(1)}\bar{E}_1^{(2)} - \bar{E}_2^{(1)}\bar{E}_2^{(2)}}{\bar{E}_1^{(1)} + \bar{E}_1^{(2)} - \bar{E}_2^{(1)} - \bar{E}_2^{(2)}}$$

$$\nu = \frac{\bar{E}_1^{(1)}\bar{E}_1^{(2)}\left(\nu_{12}^{(1)} + \nu_{12}^{(2)}\right) - \bar{E}_2^{(1)}\bar{E}_2^{(2)}\left(\nu_{21}^{(1)} + \nu_{21}^{(2)}\right)}{\bar{E}_1^{(1)}\overline{E}_1^{(2)} - \overline{E}_2^{(1)}\overline{E}_2^{(2)}}$$

Superscripts 1 and 2 correspond to layers with orientation angles ϕ_1 and ϕ_2, respectively.

12.3 OPTIMAL DESIGN OF LAMINATES

The foregoing sections of this chapter are concerned with composite laminates of uniform strength which can exist under special loading conditions only. In the general case, the optimal structure can be found using numerical methods. Optimization of composite materials and structures using analytical and numerical methods are discussed by Obraztsov et al. (1977), Obraztsov and Vasiliev (1989), Teters et al. (1978), Tsai (1987), Banichuk et al. (1988), Narusberg and Teters (1988), Kanibolotsky and Urzhumtsev (1989), Vasiliev and Gurdal (1999), and Gurdal et al. (1999).

In their application to laminated composite structures, the numerical methods of optimization, which have been widely developed and used, encounter serious problems. To demonstrate the nature of these problems, consider the laminate in the general plane stress state shown in Fig. 12.1. The laminate consists of k layers with unknown thicknesses h_i and orientation angles ϕ_i ($i = 1, 2, 3 \ldots k$). Thus, we have $2k$ unknown structural parameters and, moreover, the number of layers k is not known either. As follows from Section 12.1, the optimal structure of a laminated composite is not unique. For example, two equations, Eqs. (12.9) and (12.10), link $2k$ unknown structural parameters h_i and ϕ_i and, being satisfied, provide an infinite number of optimal laminates with one and the same total thickness h. Applying a numerical method of optimization, we use an iterative procedure starting from an initial approximation of the design item and improving it by the process of optimization. For the composite laminate with multiple optimal solutions, this process will converge to an occasional optimal design dependent on the initial approximation. The complete set of optimal solutions can be found by direct sorting of initial approximations; however, sorting of the design variables, i.e., thicknesses h_i and angles ϕ_i, does not require any specific optimization procedure, because the optimal parameters can be found by direct matching of the laminate thickness h corresponding to the particular values of h_i and ϕ_i. Such an optimization process, proposed by Vasiliev and Khaziev (2009), is applied further to optimize composite laminates.

For orthotropic laminates with symmetric structures, the constitutive equations, Eqs. (12.23), can be presented in the following form:

$$N_x = h\left(\overline{B}_{11}\varepsilon_x + \overline{B}_{12}\varepsilon_y\right), \quad N_y = h\left(\overline{B}_{12}\varepsilon_x + \overline{B}_{22}\varepsilon_y\right), \quad N_{xy} = h\overline{B}_{44}\gamma_{xy} \tag{12.40}$$

Here,

$$\overline{B}_{mn} = \sum_{i=1}^{k} \overline{h}_i A_{mn}^{(i)}, \quad \overline{h}_i = \frac{h_i}{h}$$

$$A_{11}^{(i)} = \overline{E}_2 + R_{11}c_i + R_{12}c_i^2, \quad A_{22}^{(i)} = \overline{E}_1 - R_{21}c_i + R_{12}c_i^2$$

$$A_{12}^{(i)} = \overline{E}_1\nu_{12} + R_{12}c_i(1-c_i), \quad A_{44}^{(i)} = G_{12} + R_{12}c_i(1-c_i), \quad c_i = \cos^2\phi_i$$

$$R_{11} = 2\big(\overline{E}_1\nu_{12} - \overline{E}_2 + 2G_{12}\big), \quad R_{12} = \big(1-2\nu_{12}\big)\overline{E}_1 + \overline{E}_2 - 4G_{12}$$

$$R_{21} = 2\big[\big(1-\nu_{12}\big)\overline{E}_1 - 2G_{12}\big]$$

Solving Eqs. (12.40) for strains, we have

$$\varepsilon_x = \frac{1}{\overline{B}h}(\overline{B}_{22}N_x - \overline{B}_{12}N_y), \quad \varepsilon_y = \frac{1}{\overline{B}h}(\overline{B}_{11}N_y - \overline{B}_{12}N_x), \quad \gamma_{xy} = \frac{N_{xy}}{\overline{B}_{44}} \tag{12.41}$$

$$\overline{B} = \overline{B}_{11}\overline{B}_{22} - \overline{B}_{12}^2$$

The strains in the principal coordinates of the ply 1, 2 (see Fig. 4.18) for those plies with angles $\pm\phi_i$ with respect to axis x (see Fig. 12.1) are specified by Eqs. (4.69) which yield

$$\begin{aligned}
\varepsilon_{1i}^{\pm} &= \varepsilon_x c_i + \varepsilon_y(1-c_i) \pm \gamma_{xy}\sqrt{c_i(1-c_i)} \\
\varepsilon_{2i}^{\pm} &= \varepsilon_x(1-c_i) + \varepsilon_y c_i \mp \gamma_{xy}\sqrt{c_i(1-c_i)} \\
\gamma_{12i}^{\pm} &= \gamma_{xy}(2c_i-1) \pm 2(\varepsilon_y - \varepsilon_x)\sqrt{c_i(1-c_i)}
\end{aligned} \tag{12.42}$$

The stresses in the plies with angles $\pm\phi_i$ follow from Hooke's law, i.e.,

$$\sigma_{1i}^{\pm} = \overline{E}_1\big(\varepsilon_{1i}^{\pm} + \nu_{12}\varepsilon_{2i}^{\pm}\big), \quad \sigma_{2i}^{\pm} = \overline{E}_2\big(\varepsilon_{2i}^{\pm} + \nu_{21}\varepsilon_{1i}^{\pm}\big), \quad \tau_{12i}^{\pm} = G_{12}\gamma_{12i}^{\pm} \tag{12.43}$$

Substituting the strains from Eqs. (12.42) into Eqs. (12.43), we arrive at the following expressions for the stresses:

$$\begin{aligned}
\sigma_{1i}^{\pm} &= \frac{\overline{E}_1}{\overline{B}h}\Bigg((\nu_{12}\overline{B}_{22} - \overline{B}_{12})N_x + (\overline{B}_{11} - \nu_{12}\overline{B}_{12})N_y \\
&\qquad + \Big[(\overline{B}_{22} + \overline{B}_{12})N_x - (\overline{B}_{11} + \overline{B}_{12})N_y\Big](1-\nu_{12})c_i \pm N_{xy}\frac{\overline{B}}{\overline{B}_{44}}(1-\nu_{12})\sqrt{c_i(1-c_i)}\Bigg) \\
\sigma_{2i}^{\pm} &= \frac{\overline{E}_2}{\overline{B}h}\Bigg((\overline{B}_{22} - \nu_{21}\overline{B}_{12})N_x + (\nu_{21}\overline{B}_{11} - \overline{B}_{12})N_y \\
&\qquad - \Big[(\overline{B}_{22} + \overline{B}_{12})N_x - (\overline{B}_{11} + \overline{B}_{12})N_y\Big](1-\nu_{21})c_i \mp N_{xy}\frac{\overline{B}}{\overline{B}_{44}}(1-\nu_{21})\sqrt{c_i(1-c_i)}\Bigg) \\
\tau_{12i}^{\pm} &= \frac{G_{12}}{\overline{B}h}\left(N_{xy}\frac{\overline{B}}{\overline{B}_{44}}(2c_i-1) \mp 2\big[\big(\overline{B}_{22} + \overline{B}_{12}\big)N_x - \big(\overline{B}_{11} + \overline{B}_{12}\big)N_y\big]\sqrt{c_i(1-c_i)}\right)
\end{aligned} \tag{12.44}$$

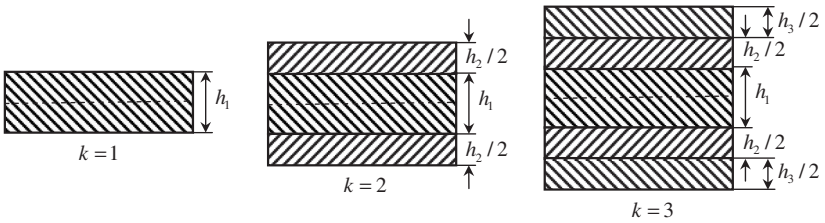


FIGURE 12.4

Laminates composed of one ($k = 1$), three ($k = 2$), and five ($k = 3$) layers.

Thus, the strains of the laminate loaded in accordance with Fig. 12.1 and the stresses in the plies are specified, in the general case, by Eqs. (12.42) and (12.44).

Further, we consider the optimization of symmetric laminates consisting of one, three, and five symmetrically arranged layers. Since the structure is symmetric, we have, respectively, $k = 1$, $k = 2$, and $k = 3$ (see Fig. 12.4). Each layer has an angle-ply $\pm\phi_i$ structure and is orthotropic.

12.3.1 Optimization under strength constraints

Since the signs of the stresses are not known, the ply strength is evaluated with the aid of the polynomial strength criterion valid both for tension and compression and given by Eq. (6.15), i.e.,

$$\sigma_1^i\left(\frac{1}{\overline{\sigma}_1^+}-\frac{1}{\overline{\sigma}_1^-}\right)+\sigma_2^i\left(\frac{1}{\overline{\sigma}_2^+}-\frac{1}{\overline{\sigma}_2^-}\right)+\frac{\left(\sigma_1^i\right)^2}{\overline{\sigma}_1^+\overline{\sigma}_1^-}+\frac{\left(\sigma_2^i\right)^2}{\overline{\sigma}_2^+\overline{\sigma}_2^-}+\left(\frac{\tau_{12}^i}{\overline{\tau}_{12}}\right)^2\le 1 \tag{12.45}$$

Substituting the stresses from Eqs. (12.44) into Eq. (12.45), we arrive at the following strength constraints:

$$\frac{r_i}{h^2}+\frac{s_i}{h}\le 1 \qquad (i=1,2,3\ \ldots\ k) \tag{12.46}$$

where

$$\begin{aligned}
r_i=&\frac{1}{\overline{\sigma}_1^+\overline{\sigma}_1^-}\left(\frac{\overline{E}_1}{\overline{B}}\right)^2\Big\{\left(\nu_{12}\overline{B}_{22}-\overline{B}_{12}\right)N_x+\left(\overline{B}_{11}-\nu_{12}\overline{B}_{12}\right)N_y\\
&+\left[\left(\overline{B}_{22}+\overline{B}_{12}\right)N_x-\left(\overline{B}_{11}+\overline{B}_{12}\right)N_y\right](1-\nu_{12})c_i\pm N_{xy}\frac{\overline{B}}{\overline{B}_{44}}(1-\nu_{12})\sqrt{c_i(1-c_i)}\Big\}^2\\
&+\frac{1}{\overline{\sigma}_2^+\overline{\sigma}_2^-}\left(\frac{\overline{E}_2}{\overline{B}}\right)^2\Big\{\left(\overline{B}_{22}-\nu_{21}\overline{B}_{12}\right)N_x+\left(\nu_{21}\overline{B}_{11}-\overline{B}_{12}\right)N_y\\
&-\left[\left(\overline{B}_{22}+\overline{B}_{12}\right)N_x-\left(\overline{B}_{11}+\overline{B}_{12}\right)N_y\right](1-\nu_{21})c_i\mp N_{xy}\frac{\overline{B}}{\overline{B}_{44}}(1-\nu_{21})\sqrt{c_i(1-c_i)}\Big\}^2\\
&+\left(\frac{G_{12}}{\overline{\tau}_{12}\overline{B}}\right)^2\Big\{N_{xy}\frac{\overline{B}}{\overline{B}_{44}}(2c_i-1)\mp 2\left[\left(\overline{B}_{22}+\overline{B}_{12}\right)N_x-\left(\overline{B}_{11}+\overline{B}_{12}\right)N_y\right]\sqrt{c_i(1-c_i)}\Big\}^2
\end{aligned} \tag{12.47}$$

$$s_i = \frac{\overline{E}_1}{\overline{B}}\left(\frac{1}{\overline{\sigma}_1^+} - \frac{1}{\overline{\sigma}_1^-}\right)\Big\{(\nu_{12}\overline{B}_{22} - \overline{B}_{12})N_x + (\overline{B}_{11} - \nu_{12}\overline{B}_{12})N_y$$
$$+\big[(\overline{B}_{22} + \overline{B}_{12})N_x - (\overline{B}_{11} + \overline{B}_{12})N_y\big](1-\nu_{12})c_i \pm N_{xy}\frac{\overline{B}}{\overline{B}_{44}}(1-\nu_{12})\sqrt{c_i(1-c_i)}\Big\}$$
$$+\frac{\overline{E}_2}{\overline{B}}\left(\frac{1}{\overline{\sigma}_2^+} - \frac{1}{\overline{\sigma}_2^-}\right)\Big\{(\overline{B}_{22} - \nu_{21}\overline{B}_{12})N_x + (\nu_{21}\overline{B}_{11} - \overline{B}_{12})N_y$$
$$-\big[(\overline{B}_{22} + \overline{B}_{12})N_x - (\overline{B}_{11} + \overline{B}_{12})N_y\big](1-\nu_{21})c_i \mp N_{xy}\frac{\overline{B}}{\overline{B}_{44}}(1-\nu_{21})\sqrt{c_i(1-c_i)}\Big\}$$

Thus, we need to determine $\overline{h}_i$, ϕ_i, and the minimum value of the laminate thickness satisfying the strength constraints given by Eq. (12.46) for all the layers. Note that the normalized layer thickness must satisfy the following condition:

$$\sum_{i=1}^{k} \overline{h}_i = 1 \tag{12.48}$$

To be specific, consider a carbon-epoxy composite material with the following properties: $E_1 = 143$ GPa, $E_2 = 10$ GPa, $G_{12} = 6$ GPa, $\nu_{21} = 0.3$, $\overline{\sigma}_1^+ = 2172$ MPa, $\overline{\sigma}_1^- = 1558$ MPa, $\overline{\sigma}_2^+ = 54$ MPa, $\overline{\sigma}_2^- = 186$ MPa, and $\overline{\tau}_{12} = 87$ MPa. To describe various loading cases, normalize the acting loads as

$$N_x = N \bullet \overline{N}_x, \quad N_y = N \bullet \overline{N}_y, \quad N_{xy} = N \bullet \overline{N}_{xy}$$

where

$$|\overline{N}_x| + |\overline{N}_y| + |\overline{N}_{xy}| = 1$$

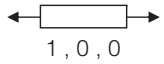
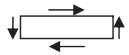
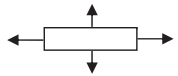
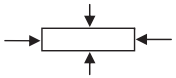
and N is an arbitrary factor which is preassigned here as the load causing failure of a 1 mm thick unidirectional composite layer under tension, i.e., $N = 2.172 \bullet 10^6$ N/m. The results of the calculations are presented in Table 12.4.

Consider first the laminate consisting of one layer ($k = 1$ in Fig. 12.4). In accordance with Eq. (12.48), $\overline{h}_1 = 1$ and we have only one design variable ϕ_1. The strength constraint for $i = 1$ becomes an equality from which it follows that the thickness that should be minimized with respect to ϕ_1 is

$$h^{(1)} = h = \frac{1}{2}\left(s_1 + \sqrt{s_1^2 + 4r_1}\right) \tag{12.49}$$

Consider the case of uniaxial tension (Case 1 in Table 12.4). In contrast to the obvious solution ($\phi_1 = 0$ and $h = 1$ mm) following from the maximum stress criterion ($\sigma_1 \le \overline{\sigma}_1$), we have $\phi_1 = 6.49^\circ$ and $h = 0.97$ mm. The difference in results is attributed to the form of the strength criterion in Eq. (12.45) which allows for the stress interaction. Indeed, if we plot the function $h(\phi_1)$ shown in Fig. 12.5 for small angles ϕ_1, we can conclude that the optimal angle is not zero.

TABLE 12.4 Optimal Structure of Carbon-Epoxy Composite Panels Consisting of One $(k = 1)$, Three $(k = 2)$, and Five $(k = 3)$ Layers Under Various Loading Conditions.

Loading Case $\overline{N}_x, \overline{N}_y, \overline{N}_{xy}$	Optimal Structural Parameters					
	$k = 1$		$k = 2$		$k = 3$	
	ϕ°	h, mm	$\overline{h}_i,\ \phi_i^\circ$	h, mm	$\overline{h}_i,\ \phi_i^\circ$	h, mm
1  1 , 0 , 0	6.49	0.97	–	0.97	–	0.97
2  -1 , 0 , 0	0	1.39	$\overline{h}_1 = 0.95,\ \overline{h}_2 = 0.05$ $\phi_1 = 0,\ \phi_2 = 90$	1.36	–	1.36
3  0 , 0 , 1	45	5.25	–	5.25	–	5.25
4  0.5 , 0.5 , 0	45	3.29	$\overline{h}_1 = 0.85,\ \overline{h}_2 = 0.15$ $\phi_1 = 40,\ \phi_2 = 85$ $\phi_1 = 50,\ \phi_2 = 5$ $\overline{h}_1 = \overline{h}_2 = 0.5$ $\phi_1 = \phi,\ \phi_2 = 90 - \phi$	3.29 3.29	–	3.29
5  -0.5 , -0.5 , 0	45	1.31	$\overline{h}_1 = 0.85,\ \overline{h}_2 = 0.15$ $\phi_1 = 40,\ \phi_2 = 85$ $\phi_1 = 50,\ \phi_2 = 0$ $\overline{h}_1 = 0.65,\ \overline{h}_2 = 0.35$ $\phi_1 = 30,\ \phi_2 = 80$ $\phi_1 = 35,\ \phi_2 = 65$ $\phi_1 = 55,\ \phi_2 = 25$ $\phi_1 = 60,\ \phi_2 = 10$ $\overline{h}_1 = 0.55,\ \overline{h}_2 = 0.45$ $\phi_1 = 20,\ \phi_2 = 80$ $\phi_1 = 70,\ \phi_2 = 10$ $\overline{h}_1 = \overline{h}_2 = 0.5$ $\phi_1 = \phi,\ \phi_2 = 90 - \phi$	1.31 1.31 1.31 1.31	–	1.31

6	0.33 , 0.33 , 0.33	45	3.48	–	3.48	–	3.48
7	-0.33, -0.33, 0.33	45	1.48	–	1.48	–	1.48
8	-0.5 , 0.5 , 0	90	5.81	$\overline{h}_1 = 0.64,\ \overline{h}_2 = 0.36$ $\phi_1 = 90,\ \phi_2 = 0$	2.4	–	2.4
9	0.5 , 0 , 0.5	26.76	4.01	–	4.01	–	4.01
10	-0.5 , 0 , 0.5	24.53	5.43	$\overline{h}_1 = 0.71,\ \overline{h}_2 = 0.29$ $\phi_1 = 53.2,\ \phi_2 = 0$	3.82	$\overline{h}_1 = 0.28,\ \overline{h}_2 = 0.03$ $\overline{h}_3 = 0.69$ $\phi_1 = 0,\ \phi_2 = 63.3$ $\phi_3 = 52.6$	3.82
11	-0.33, 0.33, 0.33	71.26	5.48	$\overline{h}_1 = 0.76,\ \overline{h}_2 = 0.24$ $\phi_1 = 64.1,\ \phi_2 = 0$	3.88	$\overline{h}_1 = 0.4,\ \overline{h}_2 = 0.2$ $\overline{h}_3 = 0.4$ $\phi_1 = 76.8,\ \phi_2 = 0$ $\phi_3 = 50.1$	3.88

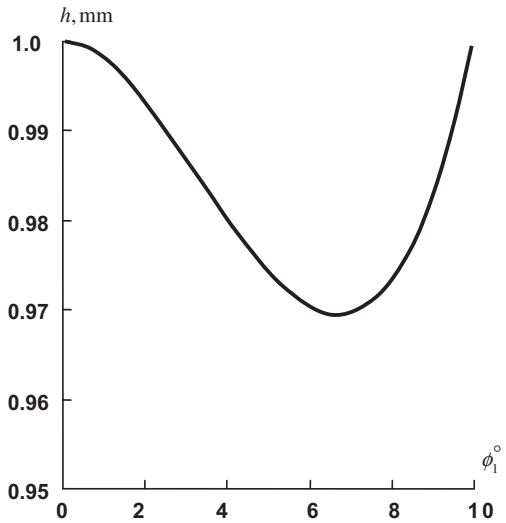


FIGURE 12.5

Dependence of the thickness on the layer angle.

Consider the case $k = 2$, i.e., the sandwich laminate shown in Fig. 12.4. Taking into account that in accordance with Eqs. (12.48), $\overline{h}_2 = 1 - \overline{h}_1$, and applying Eqs. (12.46) for $i = 1$ and $i = 2$ as equalities, we can find two values of the laminate thickness, i.e.,

$$h^{(1)} = \frac{1}{2}\left(s_1 + \sqrt{s_1^2 + 4r_1}\right), \quad h^{(2)} = \frac{1}{2}\left(s_2 + \sqrt{s_2^2 + 4r_2}\right) \tag{12.50}$$

in which $s_i(\overline{h}_1,\ c_1,\ c_2)$ and $r_i(\overline{h}_1,\ c_1,\ c_2)$ are specified by Eqs. (12.47). Of the two thickness values $h^{(1)}$ and $h^{(2)}$ we must select the largest and minimize it with respect to $\overline{h}_1,\ c_1,$ and c_2. The results are presented in Table 12.4 ($k = 2$). It follows from this table that for the loading cases 1, 3, 6, 7, and 9, calculation gives $\overline{h}_1 = 1$ and $\overline{h}_2 = 0$ and the sandwich laminate reduces to the single-layered structure. For the cases 4 and 5 for which an analytical solution can be found (see Section 12.2), a number of optimal solutions can exist for $k = 2$ and the laminate thickness is the same as that for $k = 1$. There are only four loading cases (2, 8, 10, and 11) for which the solution corresponding to $k = 2$ delivers a smaller thickness than that given by the solution for $k = 1$.

For higher values of k, the solution by direct sorting of the structural parameters encounters considerable computational problems. However, calculations show that by increasing the number of layers we do not improve the structure. It follows from Table 12.4 that only two loading cases (10 and 11) for which the solutions for $k = 3$ do not degenerate to the solutions corresponding to $k = 2$ have been found. In both cases, the optimal thickness of laminate is the same for $k = 2$ and $k = 3$.

Thus, for the majority of applications, the optimal laminate structure can be found within the class of symmetric sandwich laminates.

12.3.2 Optimization under strength and buckling constraints

Consider a laminate subjected to uniaxial compression with force $N_x = -T_x$ ($N_y = N_{xy} = 0$) as in Figs. 9.22 and 12.1. Applying the strength constraint only, we arrive at the result presented in Table 12.4 (Case 1), i.e., to a single-layered structure with angle $\phi_1 = 6.49^\circ$. However, the plate can buckle under the critical load specified by Eq. (9.229) which can be written as

$$T_x^c = K_c \frac{h^3}{b^2} \tag{12.51}$$

where the coefficient K_c is

$$K_c = 2\pi^2 \sqrt{\overline{D}_1 \overline{D}_2} \left(1 + \frac{\overline{D}_3}{\sqrt{\overline{D}_1 \overline{D}_2}} \right)$$

for relatively long plates ($a/b \geq 2$) and depends on the ratio a/b in accordance with Fig. 9.26 for relatively short plates. As previously, $\overline{D}_1 = \overline{D}_{11}$, $\overline{D}_2 = \overline{D}_{22}$, $\overline{D}_3 = \overline{D}_{12} + 2\overline{D}_{44}$, and the normalized bending stiffness coefficients for symmetric laminates in Fig. 12.4 (see Section 5.4) are

$$k = 1 \qquad \overline{D}_{mn}^{(1)} = \frac{1}{12} A_{mn}$$

$$k = 2 \qquad \overline{D}_{mn}^{(2)} = \overline{D}_{mn}^{(1)} + \frac{1}{12} A_{mn}^{(2)} \overline{h}_2 \left(3\overline{h}_1^2 + 3\overline{h}_1 \overline{h}_2 + \overline{h}_2^2 \right)$$

$$k = 3 \qquad \overline{D}_{mn}^{(3)} = \overline{D}_{mn}^{(2)} + \frac{1}{12} A_{mn}^{(3)} \overline{h}_3 \left[3\left(\overline{h}_1 + \overline{h}_2 \right)^2 + 3\left(\overline{h}_1 + \overline{h}_2 \right) \overline{h}_3 + \overline{h}_3^2 \right]$$

If we apply only the buckling constraint for a single-layered plate, we get, in accordance with Fig. 9.27, (curve 1) $\phi_1 = 45^\circ$.

To apply both the strength and the buckling constraints we need to supplement the strength constraints given by Eqs. (12.49) and (12.50) with the buckling constraints following from Eq. (12.51), i.e.,

$$h^{(c)} = \sqrt[3]{\frac{b^2 T_x}{K_c}},$$

select the maximum value of the laminate thickness (of $h^{(i)}$ and $h^{(c)}$) and minimize it with respect to the structural parameters. As previously, minimization is performed by direct sorting of $\overline{h}_i$ and ϕ_i. For the carbon-epoxy composite laminates considered in Section 12.3.1 and a plate with width $b = 0.15$ m and various aspect ratios a/b, the results of the optimization are presented in Table 12.5. As can be seen, allowance for both constraints increases the angle of the single-layered ($k = 1$) structure in comparison with the design under strength constraints only, and reduces this angle compared to the case where only the buckling constraint is imposed. In sandwich laminates ($k = 2$), both constraints can be met by two layers and the laminate thickness can be reduced. If we further increase the number of layers ($k = 3$), the laminate thickness is practically the same. Thus, the results obtained allow us to conclude that the optimal laminate designed for compression is close to the sandwich symmetric structure in which the middle layer provides the strength and its reinforcement angle is close to 0, whereas the outer layers ensure buckling resistance and have an angle for the reinforcement orientation close to 45°.

TABLE 12.5 Optimal Structural Parameters of the Laminated Plates Subjected to Axial Compression Under Strength and Buckling Constraints.

Structural Parameters		a/b				
		1.0	1.25	1.5	1.75	2.0
$k = 1$	ϕ_1°	24.2	24.8	24.9	22.9	24.8
	h, mm	6.2	6.4	6.5	6.4	6.4
$k = 2$	ϕ_1°	3.6	12.7	12.5	3.4	3.6
	ϕ_2°	45.7	50.0	44.4	40.9	45.7
	$\overline{h}_1$	0.24	0.27	0.32	0.27	0.24
	$\overline{h}_2$	0.76	0.73	0.68	0.73	0.76
	h, mm	5.8	5.7	5.7	5.8	5.8
$k = 3$	ϕ_1°	1.3	2.4	2.5	0.9	1.4
	ϕ_2°	10.3	52.5	79.3	10.8	10.3
	ϕ_3°	45.3	48.8	45.0	44.5	45.5
	$\overline{h}_1$	0.08	0.21	0.14	0.08	0.08
	$\overline{h}_2$	0.18	0.43	0.13	0.18	0.18
	$\overline{h}_3$	0.74	0.36	0.73	0.74	0.74
	h, mm	5.8	5.7	5.7	5.8	5.8

12.4 APPLICATION TO OPTIMAL COMPOSITE STRUCTURES

As stated in the introduction to this chapter, there exist special composite structures for which the combination of the specific properties of modern composites with the appropriate design concepts and potential of composite technology provide a major improvement to these structures in comparison with the corresponding metal prototypes. Three such special structures, i.e., geodesic filament-wound pressure vessels, composite flywheels, and an anisogrid lattice structure, are described in this section.

12.4.1 Composite pressure vessels

As the first example of the application of the foregoing results, consider filament-wound membrane shells of revolution that are widely used as pressure vessels (Vasiliev, 2009), solid propellant rocket motor cases, tanks for gases and liquids, etc. (See Figs. 4.14 and 7.63.) The shell is loaded by a uniform internal pressure p and axial forces T uniformly distributed along the contour of the shell cross-section $r = r_0$ as in Fig. 12.6. The equations for meridional, N_α, and circumferential, N_β, stress resultants acting in the shell follow from the corresponding free body diagrams of the shell element and can be written as

$$N_\alpha = -Q\frac{\left[1+(z')^2\right]^{1/2}}{rz'} \tag{12.52}$$

$$N_\beta = -\frac{1}{z'}\left[1+(z')^2\right]^{1/2}\left\{pr - \frac{Qz''}{z'\left[1+(z')^2\right]}\right\}$$

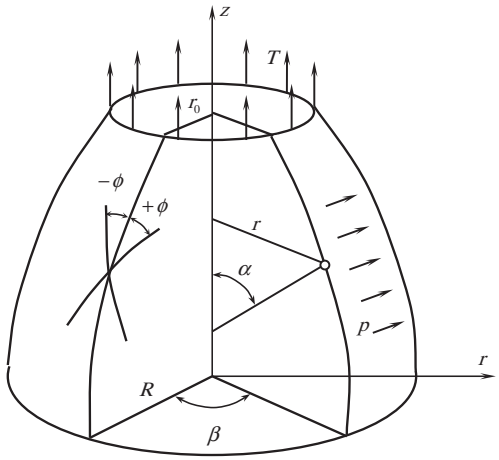


FIGURE 12.6

Axisymmetrically loaded membrane shell of revolution.

(see, e.g., Vasiliev, 1993), where $z(r)$ specifies the form of the shell meridian, $z' = dz/dr$, and

$$Q = Tr_0 + \frac{p}{2}\left(r^2 - r_0^2\right) \tag{12.53}$$

Let the shell be made by winding an orthotropic tape at angles $+\phi$ and $-\phi$ with respect to the shell meridian as in Fig. 12.6. Then, N_α and N_β can be expressed in terms of the stresses σ_1, σ_2, and τ_{12}, referred to the principal material coordinates of the tape with the aid of Eqs. (4.68), i.e.,

$$\begin{aligned} N_\alpha &= h\left(\sigma_1 \cos^2\phi + \sigma_2 \sin^2\phi - \tau_{12} \sin 2\phi\right) \\ N_\beta &= h\left(\sigma_1 \sin^2\phi + \sigma_2 \cos^2\phi + \tau_{12} \sin 2\phi\right) \end{aligned} \tag{12.54}$$

in which h is the shell thickness. The stresses σ_1, σ_2, and τ_{12} are related to the corresponding strains by Hooke's law, Eqs. (4.55), as

$$\varepsilon_1 = \frac{1}{E_1}(\sigma_1 - \nu_{21}\sigma_2), \quad \varepsilon_2 = \frac{1}{E_2}(\sigma_2 - \nu_{12}\sigma_1), \quad \gamma_{12} = \frac{\tau_{12}}{G_{12}} \tag{12.55}$$

whereas strains ε_1, ε_2, and γ_{12} can be expressed in terms of the meridional, ε_α, and circumferential, ε_β, strains of the shell using Eqs. (4.69), i.e.,

$$\begin{aligned} \varepsilon_1 &= \varepsilon_\alpha \cos^2\phi + \varepsilon_\beta \sin^2\phi \\ \varepsilon_2 &= \varepsilon_\alpha \sin^2\phi + \varepsilon_\beta \cos^2\phi \\ \gamma_{12} &= \left(\varepsilon_\beta - \varepsilon_\alpha\right) \sin 2\phi \end{aligned} \tag{12.56}$$

Since the right-hand parts of these three equations include only two strains, ε_α and ε_β, there exists a compatibility equation linking ε_1, ε_2, and γ_{12}. This equation is

$$(\varepsilon_1 - \varepsilon_2)\sin 2\phi + \gamma_{12}\cos 2\phi = 0$$

Writing this equation in terms of stresses with the aid of Eqs. (12.55), we have

$$\left[\frac{\sigma_1}{E_1}(1+\nu_{21}) - \frac{\sigma_2}{E_2}(1+\nu_{12})\right]\sin 2\phi + \frac{\tau_{12}}{G_{12}}\cos 2\phi = 0$$

In conjunction with Eqs. (12.54), this equation allows us to determine the stresses as

$$\sigma_1 = \frac{1}{2hC}\left\{(N_\alpha + N_\beta)\left[1 + \frac{2G_{12}}{E_2}(1+\nu_{12})\tan^2 2\phi\right] + \frac{N_\alpha - N_\beta}{\cos 2\phi}\right\}$$

$$\sigma_2 = \frac{1}{2hC}\left\{(N_\alpha + N_\beta)\left[1 + \frac{2G_{12}}{E_1}(1+\nu_{21})\tan^2 2\phi\right] - \frac{N_\alpha - N_\beta}{\cos 2\phi}\right\} \tag{12.57}$$

$$\tau_{12} = \frac{G_{12}\tan 2\phi}{hC\cos 2\phi}\left[N_\beta\left(\frac{1+\nu_{21}}{E_1}\sin^2\phi + \frac{1+\nu_{12}}{E_2}\cos^2\phi\right)\right.$$

$$\left. -N_\alpha\left(\frac{1+\nu_{21}}{E_1}\cos^2\phi + \frac{1+\nu_{12}}{E_2}\sin^2\phi\right)\right]$$

where

$$C = 1 + G_{12}\left(\frac{1+\nu_{21}}{E_1} + \frac{1+\nu_{12}}{E_2}\right)\tan^2 2\phi$$

Now assume, in accordance with the results presented in the previous section, that the optimal shell is reinforced along the lines of principal stresses, i.e., in such a way that $\tau_{12} = 0$. In accordance with the last equation of Eqs. (12.55), for such a shell $\gamma_{12} = 0$ and, as follows from Eqs. (12.56), $\varepsilon_\alpha = \varepsilon_\beta = \varepsilon_1 = \varepsilon_2$.

Putting $\tau_{12} = 0$ in the last equation of Eqs. (12.57), we can conclude that for the optimal shell

$$\frac{N_\beta}{N_\alpha} = \frac{1 - (1-n)\cos^2\phi}{n + (1-n)\cos^2\phi} \tag{12.58}$$

where as previously

$$n = \frac{E_2(1+\nu_{21})}{E_1(1+\nu_{12})} \tag{12.59}$$

Substituting N_α and N_β from Eqs. (12.52) into Eq. (12.58), we arrive at the following equation for the meridian of the optimal shell:

$$\frac{rz''}{z'\left[1+(z')^2\right]}=\frac{pr^2}{Q}-\frac{1-(1-n)\cos^2\phi}{n+(1-n)\cos^2\phi} \tag{12.60}$$

The first two equations of Eqs. (12.57) yield the following expressions for stresses acting in the tape of the optimal shell:

$$\sigma_1=\frac{\sigma_2}{n}=\frac{N_\alpha}{h[n+(1-n)\cos^2\phi]},\quad \tau_{12}=0 \tag{12.61}$$

Taking into account that in accordance with Eqs. (12.57)

$$\sigma_1+\sigma_2=\frac{1}{h}(N_\alpha+N_\beta),$$

we arrive at the following relationships:

$$\sigma_1=\frac{N_\alpha+N_\beta}{h(1+n)},\quad \sigma_2=\frac{n(N_\alpha+N_\beta)}{h(1+n)},\quad \tau_{12}=0$$

which coincide with Eqs. (12.31).

Substituting N_α from the first equation of Eqs. (12.52) into Eqs. (12.61), we have

$$\sigma_1 h=-\frac{Q\left[1+(z')^2\right]^{1/2}}{rz'[n+(1-n)\cos^2\phi]} \tag{12.62}$$

Assume that the optimal shell is a structure of uniform stress. Differentiating Eqs. (12.62) with respect to r and taking into account that according to the foregoing assumption $\sigma_1=constant$, we arrive at the following equation in which z'' is eliminated with the aid of Eq. (12.60):

$$\frac{d}{dr}\left\{rh\left[n+(1-n)\cos^2\phi\right]\right\}-h\left[1-(1-n)\cos^2\phi\right]=0 \tag{12.63}$$

This equation specifies either the thickness or the orientation angle of the optimal shell.

Consider two particular cases. First, consider a fabric tape of variable width $w(r)$ being laid up on the surface of the mandrel along the meridians of the shell of revolution to be fabricated. Then, $\phi=0$, and Eq. (12.63) takes the form

$$\frac{d}{dr}(rh)-nh=0$$

The solution of this equation is

$$h=h_R\left(\frac{r}{R}\right)^{n-1} \tag{12.64}$$

where $h_R = h(r = R)$ is the shell thickness at the equator $r = R$ (see Fig. 12.6). Assuming that there is no polar opening in the shell ($r_0 = 0$) or that it is closed ($T = pr_0/2$), we have from Eq. (12.53) $Q = pr^2/2$. Substituting this result into Eqs. (12.60) and (12.62), we obtain

$$\frac{rz''}{z'\left[1 + (z')^2\right]} = 2 - n \tag{12.65}$$

$$\sigma_1 = -\frac{pr}{2z'h}\sqrt{1 + (z')^2} \tag{12.66}$$

Integrating Eq. (12.65) with the condition $1/z' = 0$ for $r = R$, which means that the tangent line to the shell meridian is parallel to the axis z at $r = R$ (see Fig. 12.6), we arrive at

$$z' = -\frac{r^{2-n}}{\sqrt{R^{2(2-n)} - r^{2(2-n)}}} \tag{12.67}$$

Further integration results in the following parametric equation for the shell meridian:

$$\frac{r}{R} = (1 - t)^{\lambda}$$

$$\frac{z}{R} = \lambda \int_0^t t^{-\frac{1}{2}}(1 - t)^{-\lambda} dt = \lambda B_x\left(\frac{1}{2}, \quad 1 - \lambda\right)$$

$$\lambda = \frac{1}{2(2 - n)}$$

Here, B_x is the β-function (or the Euler integral of the first type). The constant of integration is found from the condition $z(r = R) = 0$. Meridians corresponding to various n numbers are presented in Fig. 12.7. For $n = 1$ the optimal shell is a sphere, whereas for $n = 2$ it is a cylinder. As follows from Eq. (12.64), the thickness of the spherical ($n = 1$) and cylindrical ($n = 2$ and $r = R$) shells is constant. Substituting Eqs. (12.64) and (12.67) into Eq. (12.66) and taking into account Eqs. (12.61), we have

$$\sigma_1 = \frac{\sigma_2}{n} = \frac{pR}{2h_R}$$

This equation allows us to determine the shell thickness at the equator ($r = R$), h_R, by matching σ_1 or σ_2 with material strength characteristics.

As has been noted already, the shells under study can be made by laying up fabric tapes of variable width, $w(r)$, along the shell meridians. The tape width can be related to the shell thickness, $h(r)$, as

$$kw(r)\delta = 2\pi r h(r) \tag{12.68}$$

where k is the number of tapes in the shell cross section (evidently, k is the same for all the cross sections) and δ is the tape thickness. Substituting $h(r)$ from Eq. (12.64), we get

$$w(r) = \frac{2\pi\, h_R r^n}{\kappa\delta\, R^{n-1}}$$

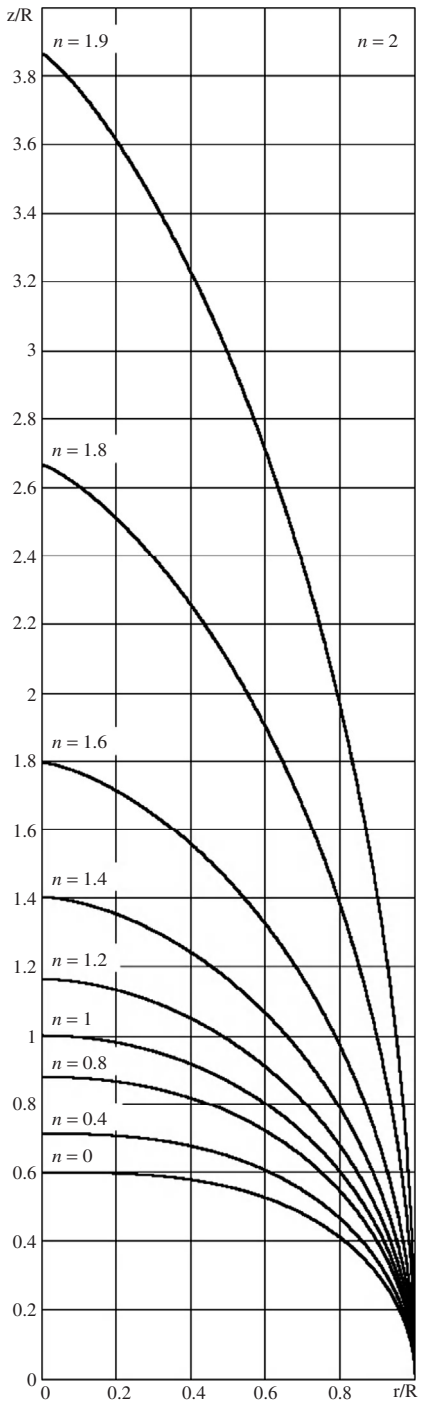


FIGURE 12.7

Meridians of optimal composite shells.

Consider the second special case: a shell made by winding unidirectional composite tapes at angles $\pm\phi$ with respect to the shell meridian (see Fig. 12.6). The tape width, w_0, does not depend on r, and its thickness is δ. Then, the relevant equation similar to Eq. (12.68) can be written as

$$\frac{kw_0\delta}{\cos\phi\,(r)} = 2\pi r h(r)$$

where k is the number of tapes with angles $+\phi$ and $-\phi$. Thus, the shell thickness is

$$h(r) = \frac{kw_0\delta}{2\pi\, r\cos\phi\,(r)} \tag{12.69}$$

This can be expressed in terms of the thickness value at the shell equator $h_R = h(r = R)$ as

$$h(r) = h_R\frac{R\cos\phi_R}{r\cos\phi\,(r)} \tag{12.70}$$

where $\phi_R = \phi\,(r = R)$. It should be noted that this equation is not valid for the part of the shell in which the tapes are completely overlapped close to the polar opening.

Substituting $h(r)$ from Eq. (12.70) into Eq. (12.63), we arrive at the following equation for the tape orientation angle:

$$r\frac{d\phi}{dr}\cdot\frac{\sin\phi\,\left[n-\left(1-n\right)\cos^2\phi\right]}{\cos\phi\,\left[1-\left(1-n\right)\cos^2\phi\right]} = 1$$

The solution of this equation that satisfies the boundary condition $\phi\,(r = R) = \phi_R$ is as follows:

$$r\left[1-\left(1-n\right)\cos^2\phi\,(r)\right]^{\frac{1-n}{2}}\cos^n\phi\left(r\right) = R\left[1-\left(1-n\right)\cos^2\phi_R\right]^{\frac{1-n}{2}}\cos^n\phi_R \tag{12.71}$$

Consider monotropic filament-wound shells. As noted in the previous section, the simplest and sufficiently adequate model of unidirectional fibrous composites for design problems is the monotropic model, which ignores the stiffness of the matrix. For this model, we should take $n = 0$ in the foregoing equations. Particularly, Eq. (12.71) yields in this case

$$r\sin\phi\,(r) = R\sin\phi_R \tag{12.72}$$

This is the equation of a geodesic line on the surface of revolution. Thus, in optimal filament-wound shells the fibers are directed along the geodesic trajectories. This substantially simplifies the winding process because the tape placed on the surface under tension automatically takes the form of the geodesic line, provided there is no friction between the tape and the surface. As follows from Eq. (12.72), for $\phi = 90^\circ$, the tape touches the shell parallel circle with radius

$$r_0 = R\sin\phi_R \tag{12.73}$$

and a polar opening of this radius is formed in the shell (see Fig. 12.6).

Transforming Eq. (12.60) with the aid of Eqs. (12.72) and (12.73) and taking $n = 0$, we arrive at the following equation which specifies the meridian of the optimal filament wound shell:

$$\frac{z''}{z'\left[1 + (z')^2\right]} = \frac{2r}{r^2 - \eta^2} - \frac{r_0^2}{r\left(r^2 - r_0^2\right)} \tag{12.74}$$

where

$$\eta^2 = r_0^2 - \frac{2T}{p} r_0$$

Integrating Eq. (12.74) with due regard to the condition $1/z'(R) = 0$ which, as earlier, requires that for $r = R$ the tangent to the meridian be parallel to z-axis, we have

$$z' = -\frac{r(r^2 - \eta^2)\sqrt{R^2 - r_0^2}}{\sqrt{R^2(r^2 - r_0^2)(R^2 - \eta^2)^2 - r^2(R^2 - r_0^2)(r^2 - \eta^2)^2}} \tag{12.75}$$

Using this equation to transform Eq. (12.62) in which we take $n = 0$ and substituting h from Eq. (12.70), we obtain the following equation for the longitudinal stress in the tape:

$$\sigma_1 = \frac{p\left(R^2 - r_0^2\right) + 2r_0 T}{2Rh_R \cos^2 \phi_R} \tag{12.76}$$

As can be seen, σ_1 does not depend on r, and the optimal shell is a structure reinforced by uniformly stressed fibers.

Such fibrous structures are referred to as isotensoids. To study the types of isotensoids corresponding to the loading shown in Fig. 12.6, factor the expression in the denominator of Eq. (12.75). The result can be presented as

$$z' = -\frac{r\left(r^2 - \eta^2\right)}{\sqrt{\left(R^2 - r^2\right)\left(r^2 - r_1^2\right)\left(r^2 + r_2^2\right)}} \tag{12.77}$$

where

$$r_{1,2}^2 = \left(\frac{R^2}{2} - \eta^2\right)\left\{\sqrt{\frac{R^2}{R^2 - r_0^2}\left[1 + \frac{\left(3R^2 - 4\eta^2\right)r_0^2}{\left(R^2 - 2\eta^2\right)^2}\right]} \pm 1\right\} \tag{12.78}$$

It follows from Eq. (12.77) that the parameters R and r_1 are the maximum and minimum distances from the meridian to the rotation axis. Meridians of isotensoids corresponding to various loading conditions are shown in Fig. 12.8. For $p = 0$, i.e., under axial tension, a hyperbolic shell is obtained with the meridian determined as

$$r^2 - z^2 \tan^2 \phi_R = R^2$$

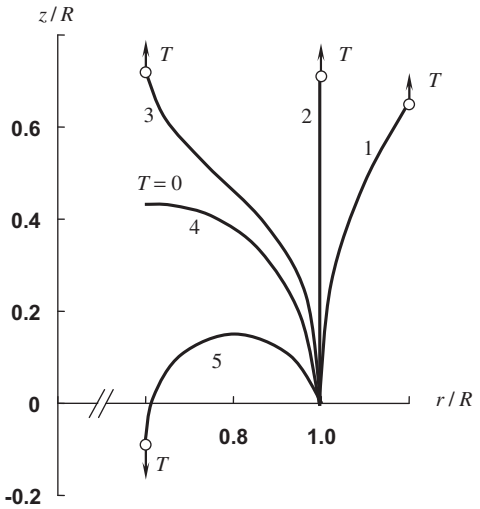


FIGURE 12.8

Isotensoids corresponding to various loading conditions.

This meridian corresponds to line 1 in Fig. 12.8. For $\phi_R = 0$, the hyperbolic shell degenerates into a cylinder (line 2). Curve 3 corresponds to $T = pr_0/2$, i.e., to a shell for which the polar opening of radius r_0 is closed. For the special angle $\phi_R = \phi_0 = 54°44'$, the shell degenerates into a circular cylindrical shell (line 2) as discussed in Section 12.1. For $T = 0$, i.e., in the case of an open polar hole, the meridian has the form corresponding to curve 4. The change in the direction of axial forces T yields a toroidal shell (line 5). Performing integration of Eq. (12.77) and introducing dimensionless parameters

$$\overline{r} = \frac{r}{R}, \quad \overline{z} = \frac{z}{R}, \quad \overline{r}_0 = \frac{r_0}{R}, \quad \overline{\eta} = \frac{\eta}{R},$$

we finally arrive at

$$\overline{z} = \frac{k_2 - \overline{\eta}^2}{\sqrt{1 - k_2}} F(k, \theta) + \sqrt{1 - k_2}\, E(k, \theta) \tag{12.79}$$

where

$$F(k, \theta) = \int_0^\theta \frac{d\theta}{\sqrt{1 - k^2 \sin^2\theta}}, \quad E(k, \theta) = \int_0^\theta \sqrt{1 - k^2 \sin^2 \theta} d\theta$$

are the first-kind and the second-kind elliptic integrals and

$$k_{1,2} = \left(\frac{1}{2} - \overline{\eta}^2\right)\left\{ \pm \sqrt{\frac{1}{1 - \overline{r}_0^2}\left[1 + \frac{3 - 4\overline{\eta}^2}{\left(1 - 2\overline{\eta}^2\right)^2}\right]} - 1 \right\}$$

$$k^2 = \frac{1-k_1}{1-k_2},\ \sin\theta = \sqrt{\frac{1-\overline{r}^2}{1-k_1}}$$

As an application of the foregoing equations, consider the optimal structure for the end closure of the pressure vessel shown in Fig. 4.14. The cylindrical part of the vessel consists of a $\pm\phi_R$ angle-ply layer with thickness h_R that can be found from Eq. (12.76) in which we should take $T = pr_0/2$, and a circumferential $(\phi = 90^\circ)$ layer whose thickness is specified by Eq. (12.18), i.e.,

$$h_{90} = h_R\left(3\cos^2\phi_R - 1\right)$$

The polar opening of the dome (see Fig. 4.14) is closed. So $T = pr_0/2$, $\overline{\eta} = 0$, and the dome meridian corresponds to curve 3 in Fig. 12.8. As has already been noted, upon winding an opening of radius r_0 is formed at the shell apex. However, the analysis of Eq. (12.77) for r_1 that determines the minimum distance from the meridian to the z-axis (see Fig. 12.9) shows that r_1 is equal to r_0 only if a shell has an open polar hole (curve 4 in Fig. 12.8). For a pressure vessel whose polar hole is closed, $r_1 \geq r_0$ and the equality takes place only for $\phi = 0$, i.e., for $r_1 = r_0 = 0$. In real vessels, polar holes are closed with rigid polar bosses as shown in Fig. 12.10. The meridian of the shell under consideration can be divided into two segments. For $R \geq r \geq b$, the meridian corresponds to curve 3 in Fig. 12.8 for which $T = pr_0/2$ and $\eta = 0$. In Fig. 12.9, this segment of the meridian is shown by a solid line. The meridian segment $b \geq r \geq r_0$, where the shell touches the polar boss, corresponds to curve 4 in Fig. 12.8 for which $T = 0$. In Fig. 12.9, this segment of the meridian is indicated by the dashed line. The radius b in Figs 12.9 and 12.10 can be set as the coordinate of an inflection point of this curve determined by the condition $z''(r = b) = 0$. Differentiating Eq. (12.77) and taking $\eta = 0$ for the closed polar opening, we get

$$b = \sqrt{\frac{3}{2}}\cdot r_0 = 1.225 r_0$$

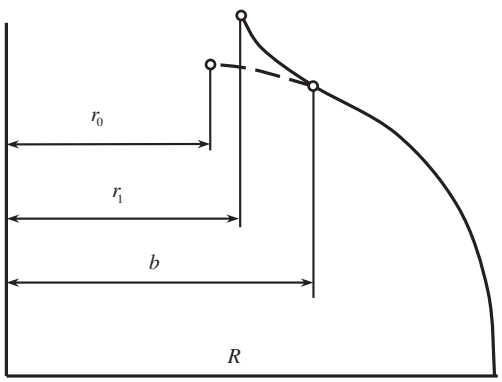


FIGURE 12.9

Combined meridian of the pressure vessel dome.

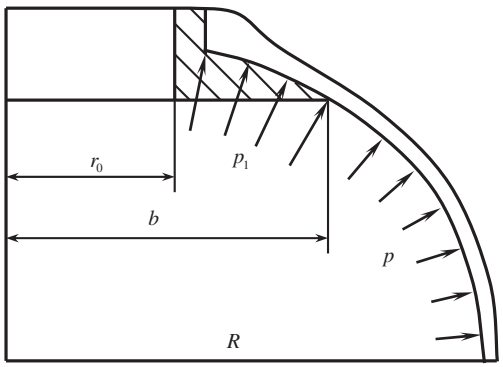


FIGURE 12.10

Isotensoid dome with a polar boss.

Since the segment $(b - r_0)$ is relatively small, we can assume that the contact pressure p_1 between the shell and the boss is uniform. Then, from the condition of boss equilibrium (the hole in the boss is closed), we have

$$p_1 = \frac{pb^2}{b^2 - r_0^2} \tag{12.80}$$

Constructing the combined meridian, we should take into account that functions $z(r)$ and $z'(r)$ must be continuous for $r = b$. Finally, using Eqs. (12.77) and (12.79), we obtain, for $R \geq r \geq b$ $(T = pr_0/2,\ \eta = 0)$,

$$z' = -\frac{r^3\sqrt{R^2 - r_0^2}}{\sqrt{R^6\left(r^2 - r_0^2\right) - r^6\left(R^2 - r_0^2\right)}} \tag{12.81}$$

and

$$\overline{z} = \frac{k_2}{\sqrt{1 - k_2}}F(k, \theta_1) + \sqrt{1 - k_2}E(k, \theta_1)$$

where

$$k_{1,2} = \frac{1}{2}\left(\pm\sqrt{\frac{1 + 3\overline{r}_0^2}{1 - \overline{r}_0^2}} - 1\right), \quad \sin\theta_1 = \sqrt{\frac{1 - \overline{r}^2}{1 - k_1}}, \quad k^2 = \frac{1 - k_1}{1 - k_2}$$

and for $b \geq r \geq r_0$ $(T = 0,\ \eta = r_0)$,

$$z' = -\frac{rb^2\sqrt{\left(r^2 - r_0^2\right)\left(R^2 - r_0^2\right)}}{\sqrt{R^6\left(b^2 - r_0^2\right)^2 - r^2b^4(r^2 - r_0^2)(R^2 - r_0^2)}} \tag{12.82}$$

and

$$\overline{z} = -\frac{m_1}{\sqrt{m_1+m_2}}\left[F(m,\theta_2) - F(m,\theta_2^*)\right] + \sqrt{m_1+m_2}\left[E(m,\theta_2) - E(m,\theta_2^*)\right] + \frac{k_2}{\sqrt{1-k_2}}F(k,\theta_1^*) + \sqrt{1-k_2}E(k,\theta_1^*)$$

where

$$m_{1,2} = \frac{\overline{r}_0^2}{2}\left[\sqrt{1 - \frac{4(\overline{b}^2 - \overline{r}_0^2)^2}{\overline{b}^4\overline{r}_0^4(1-\overline{r}_0^2)}} \pm 1\right], \quad m^2 = \frac{m_2}{m_1+m_2}$$

$$\cos\theta_2 = \sqrt{\frac{\overline{r}^2 - \overline{r}_0^2}{m_2}}, \quad \sin\theta_1^* = \sqrt{\frac{1-\overline{b}^2}{1-k_1}}$$

$$\cos\theta_2^* = \sqrt{\frac{\overline{b}^2 - \overline{r}_0^2}{m_2}}, \quad \overline{b} = \frac{b}{R}$$

Meridians plotted in accordance with equations Eqs. (12.81) and (12.82) and corresponding to various values of the parameter $\overline{r}_0$ specifying the radius of the polar opening (which is closed) are presented in Fig. 12.11. The curve $\overline{r}_0 = 0$ corresponds to a shell reinforced along the meridians and is the same as the curve for $n = 0$ in Fig. 12.7. This isotensoid shape can be readily obtained experimentally if we load a balloon reinforced along the meridians with internal pressure as shown in Fig. 12.12.

Stresses acting along the fibers of the shells whose meridians are presented in Fig. 12.11 are determined by Eq. (12.62) in which we should take $n = 0$. Substituting h from Eq. (12.70) and ϕ from Eqs. (12.72) and (12.73), we should consider two segments of the meridian. For the first segment, we take $T = pr_0/2$ and z' in accordance with Eq. (12.81), whereas for the second one we substitute z' from Eq. (12.82) and put $T = 0$, $p = p_1$, where p_1 is specified by Eq. (12.80). For both segments, we arrive at the same result, i.e.,

$$\sigma_1 = \frac{pR}{2h_R\cos^2\phi_R}$$

The shell mass and internal volume can be found as

$$M = 2\pi\rho h_R\cos\phi_R\int_{r_0}^{R}\sqrt{1+(z')^2}\,\frac{dr}{\cos\phi}$$

$$V = \pi\int_{r_0}^{R} z'r^2dr$$

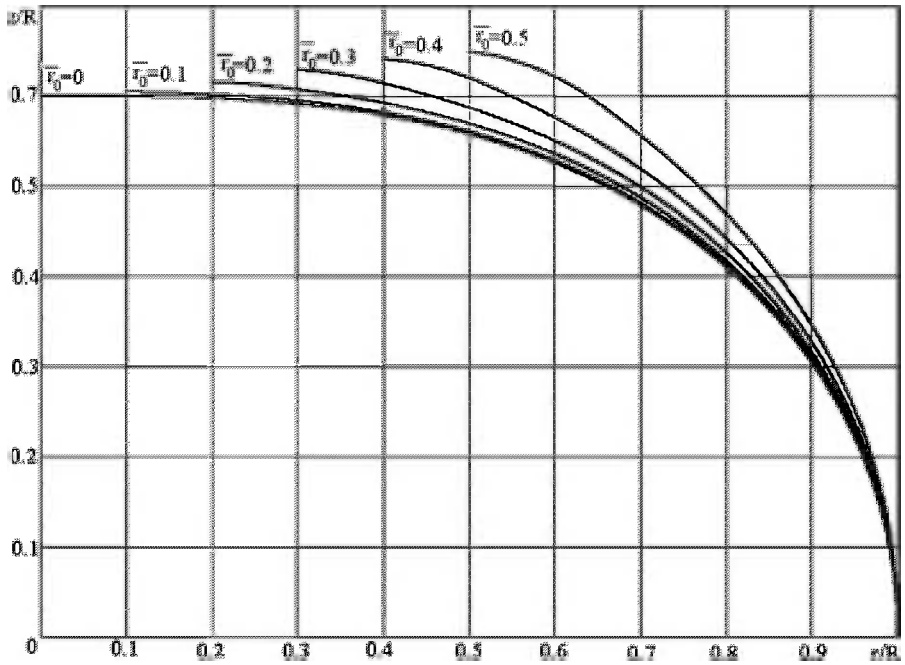


FIGURE 12.11

Meridians of isotensoids corresponding to various normalized radii of the polar openings $\overline{r}_0 = r_0/R$.

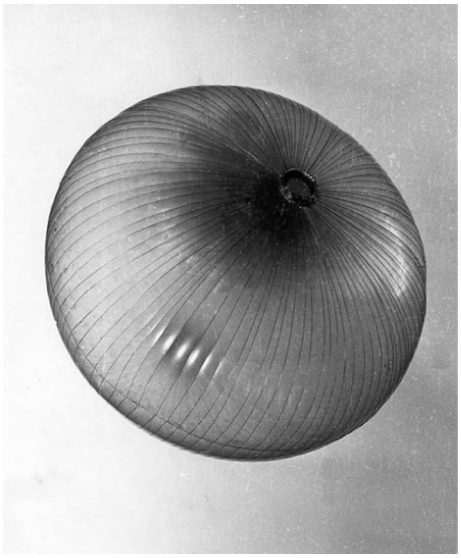


FIGURE 12.12

A model isotensoid reinforced along the meridians.

where ρ is the density of the material. The mass of a composite pressure vessel is often evaluated by using the parameter μ in the equation

$$M = \mu \frac{p_u V}{\overline{\sigma}_1/\rho}$$

Here, p_u is the ultimate pressure, and $\overline{\sigma}_1/\rho$ is the specific strength of the material. The variation of the parameter μ and the normalized internal volume $\overline{V} = V/R^3$ as a function of the radius of the polar opening are shown in Fig. 12.13.

The weight efficiency of composite pressure vessels is usually evaluated by the following parameter:

$$k_w = \frac{\overline{p}V}{M} \tag{12.83}$$

in which $\overline{p}$ is the burst pressure. If we use the old metric units, i.e., measure $\overline{p}$ in kg/mm^2, V in liters, and M in kg, the parameter k_w in Eq. (12.83) is measured in km and is analogous to the material specific strength k_σ given by Eq. (1.2). For the pressure vessel shown in Fig. 12.14 which consists of a thin aluminum liner and an aramid-epoxy composite layer, k_w is close to 35 km. Filament-wound composite pressure vessels are discussed in more detail by Vasiliev (2009).

12.4.2 Spinning composite disks

As the second example of an optimal composite structure, consider a disk rotating around its axis with an angular velocity ω. Let the disk be reinforced with fibers making angles $+\phi$ and $-\phi$ with the radius as in Fig. 12.15 and find the optimal trajectories of the fibers (Kyser, 1965; Obraztsov and Vasiliev, 1989). The radial, N_r, and circumferential, N_β, stress resultants are related to the stresses σ_1 acting in the composite material along the fibers by Eqs. (12.54). Using the monotropic material model and putting $\sigma_2 = 0$ and $\tau_{12} = 0$ in these equations, we get

$$N_r = h\sigma_1 \cos^2\phi, \quad N_\beta = h\sigma_1 \sin^2\phi \tag{12.84}$$

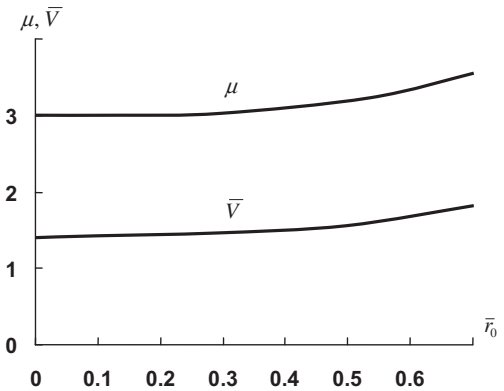


FIGURE 12.13

Mass efficiency parameter μ and the normalized internal volume $\overline{V} = V/R^3$ of the isotensoid pressure vessel as functions of the polar opening radius.

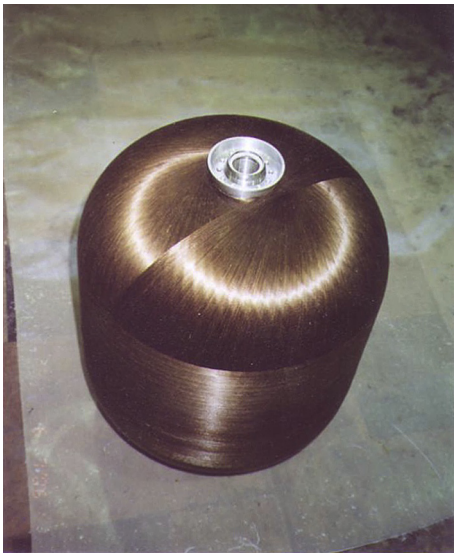


FIGURE 12.14

Filament-wound composite pressure vessel.

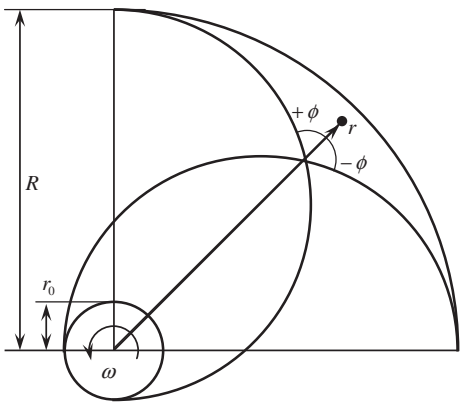


FIGURE 12.15

Fibers' trajectories in the spinning disk.

Consider a disk element shown in Fig. 12.16. The equilibrium condition yields

$$(rN_r)' - N_\beta + F_r = 0 \tag{12.85}$$

where $(\ldots)' = d(\ldots)/dr$ and $F_r = \rho h \omega^2 r^2$ with ρ being the material density. The disk thickness is specified by Eq. (12.69), i.e.,

$$h(r) = \frac{k w_0 \delta}{2\pi r \cos\phi} \tag{12.86}$$

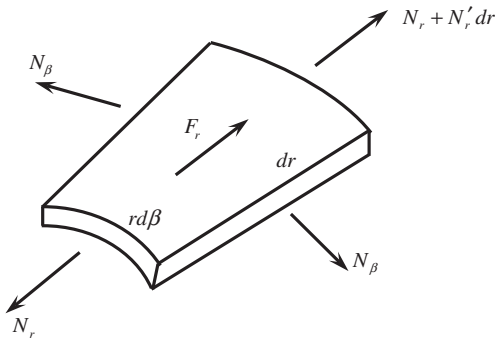


FIGURE 12.16

Forces acting on the disk element.

where k is the number of fibrous tapes passing through the circumference $r =$ constant, and w_0 and δ are the tape width and thickness.

For a disk of uniform strength, we take $\sigma_1 = \overline{\sigma}_1$ in which $\overline{\sigma}_1$ is the ultimate stress for the unidirectional composite under tension along the fibers. Correspondingly, we take $\omega = \overline{\omega}$, where $\overline{\omega}$ is the ultimate angular velocity of the disk. Then, substituting Eq. (12.86) into Eqs. (12.84) and the calculated stress resultants N_r and N_β into Eq. (12.85), we arrive at the following equation for the fiber angle:

$$r\phi' \sin\phi \cos\phi + \sin^2\phi = \frac{1}{\overline{\sigma}_1}\rho\overline{\omega}^2 r^2 \tag{12.87}$$

The solution of this equation must satisfy the boundary conditions. For a disk with radius R and with a central opening of radius r_0 as in Fig. 12.15, we must have $N_r = 0$ at $r = r_0$ and $r = R$. Taking into account the first expression in Eqs. (12.84), we arrive at the following boundary conditions for Eq. (12.87):

$$\phi\,(r = r_0) = \frac{\pi}{2}, \quad \phi\,(r = R) = \frac{\pi}{2} \tag{12.88}$$

Since Eq. (12.87) is of the first order, its solution can, in general, satisfy only one of these conditions. Using the second condition in Eqs. (12.88), we get

$$\sin\phi = \frac{R}{r}\sqrt{1 - \frac{\lambda}{2}\left(1 - \frac{r^4}{R^4}\right)} \tag{12.89}$$

where

$$\lambda = \frac{\rho\overline{\omega}^2 R^2}{\overline{\sigma}_1} \tag{12.90}$$

Applying the first condition in Eqs. (12.88), we arrive at the following equation specifying the parameter λ:

$$\lambda = \frac{2}{1 + \left(\frac{r_0}{R}\right)^2} \tag{12.91}$$

In conjunction with Eq. (12.90), this result enables us to determine the maximum value of the disk angular velocity, i.e.,

$$\overline{\omega}^2 = \frac{2\overline{\sigma}_1}{\rho R^2\left(1 + \overline{r}_0^2\right)} \tag{12.92}$$

where $\overline{r}_0 = r_0/R$. It follows from Eq. (12.92) that the maximum value for the ultimate angular velocity corresponds to $\overline{r}_0 = 0$, i.e., to a disk without a central opening, for which Eq. (12.92) reduces to

$$\overline{\omega}_m^2 = \frac{2\overline{\sigma}_1}{\rho R^2} \tag{12.93}$$

Note that relatively small central openings have practically no effect on the ultimate angular velocity. For example, for $\overline{r}_0 = 0.1$, Eq. (12.92) gives $\overline{\omega}$ which is only 0.005% less than the maximum value $\overline{\omega}_m$ following from Eq. (12.93).

For further analysis, we take $\overline{r}_0 = 0$ and consider disks without a central opening. Then, Eq. (12.91) yields $\lambda = 2$, and Eq. (12.89) for the fiber angle becomes

$$\sin\phi = \frac{r}{R} \tag{12.94}$$

To find the fiber trajectory, consider Fig. 12.17 showing the tape element in Cartesian x, y and polar r, β coordinate frames. As follows from the figure,

$$x = r\sin\beta, \quad y = r\cos\beta, \quad \tan\phi = \frac{rd\beta}{dr} \tag{12.95}$$

Applying the last equation of Eqs. (12.95) and using Eq. (12.94) for ϕ, we arrive at the following differential equation:

$$\frac{d\beta}{dr} = \frac{1}{\sqrt{R^2 - r^2}}$$

whose general solution is

$$\sin\left(\beta - \beta_0\right) = \frac{r}{R} \tag{12.96}$$

in which β_0 is the constant of integration. Changing β and r to x and y with the aid of Eqs. (12.95), we can write Eq. (12.96) in Cartesian coordinates as

$$\left(x - \frac{R}{2}\cos\beta_0\right)^2 + \left(y - \frac{R}{2}\sin\beta_0\right)^2 = \frac{R^2}{4}$$

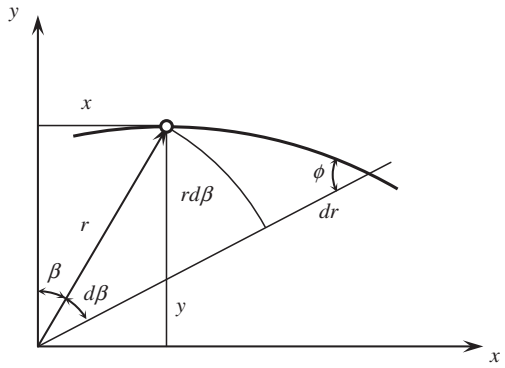


FIGURE 12.17

A tape element in Cartesian and polar coordinate frames.

For each value of β_0, this equation specifies a circle with radius $R/2$ with its center located on the circumference $r = R/2$. Changing β_0, we get the system of circles shown in Fig. 12.18.

Composite disks can be efficiently used as inertial accumulators of mechanical energy: flywheels, such as that shown in Fig. 12.19. Note that the disk in Fig. 12.19 can be made using the technology described in Section 4.5.2. The disk composite structure is made by winding onto an inflated elastic mandrel similar to that shown in Fig. 12.12. After the shell, with the appropriate winding patterns, is fabricated, the pressure is continuously reduced and the shell is compressed in the axial direction between two plates. Once the shell is transformed into a disk, the resin in the composite material is cured.

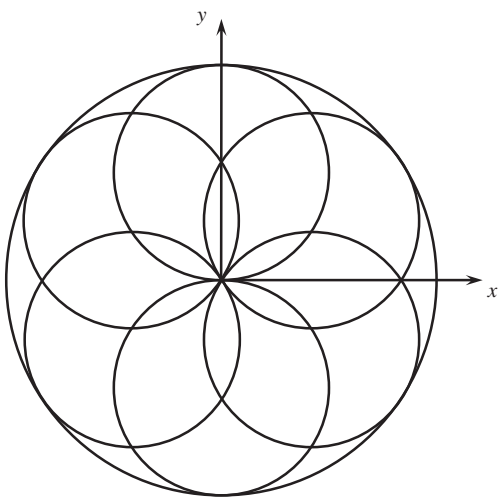


FIGURE 12.18

Fiber patterns in the spinning optimal composite disk.

The maximum kinetic energy that can be stored and the mass of the disk are

$$KE = \pi\overline{\omega}^2\rho\int_0^R hr^3dr, \quad M = 2\pi\rho\int_0^R hrdr$$

Substituting h in accordance with Eq. (12.86) and using Eq. (12.94) for the winding patterns, we get

$$KE = \frac{\pi}{8}R^3\rho\overline{\omega}^2kw_0\delta, \quad M = \frac{\pi}{2}R\rho\, kw_0\delta \tag{12.97}$$

where k, w_0, and δ are specified in notations to Eq. (12.86). Transforming Eqs. (12.97) for KE with the aid of the corresponding equation for M, we have

$$KE = \frac{1}{4}MR^2\overline{\omega}^2$$

Substituting $\overline{\omega}$ from Eq. (12.93), we finally arrive at

$$KE = \frac{M\overline{\sigma}_1}{2\rho}$$

Introducing the linear circumferential velocity at the outer circumference $r = R$ of the disk as $\overline{v}_R = \overline{\omega}R$ and using Eq. (12.93) for $\overline{\omega}$, we obtain the following result

$$\overline{v}_R = \sqrt{\frac{2\overline{\sigma}_1}{\rho}} \tag{12.98}$$

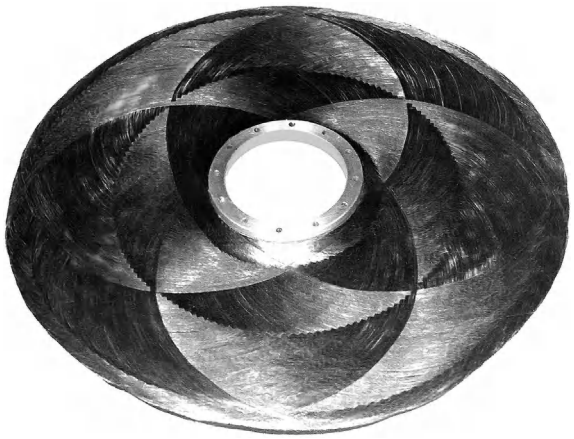


FIGURE 12.19

Carbon-epoxy flywheel.

TABLE 12.6 Maximum Values of the Circumferential Velocities for Fibrous Composite Disks of Uniform Strength.

Composite Material	Glass-Epoxy	Carbon-Epoxy	Aramid-Epoxy
$\overline{v}_R$, (m/s)	1309	1606	1946

which means that $\overline{v}_R$ depends only on the material's longitudinal specific strength $(\overline{\sigma}_1/\rho)$. The results of calculations for the composites whose properties are listed in Table 3.5 are presented in Table 12.6. Note that in order to use Eq. (12.98) for $\overline{v}_R$ we must substitute $\overline{\sigma}_1$ in $\mathrm{N/m^2}$, ρ in $\mathrm{kg/m^3}$, and take into account that $1\ \mathrm{N} = 1\ \mathrm{kg \cdot m\ /s^2}$.

12.4.3 Anisogrid composite lattice structures

Anisogrid (anisotropic grid) composite lattice structures (Vasiliev et al., 2001, 2012; Vasiliev and Razin, 2001, 2006) are usually made in the form of a cylindrical or conical shell consisting of helical and circumferential (hoop) unidirectional composite ribs formed by continuous winding. The manufacturing process includes the following main steps illustrated in Fig 12.20:

- The mandrel is covered with an elastic coating formed of silicon rubber and having the grooves for the ribs (see Fig. 12.20a)
- Unidirectional carbon tows impregnated with resin are wound into the grooves forming a system of helical, hoop, and, in some cases, axial ribs which are covered with thin composite skin, also made by winding (see Fig. 12.20b)
- After curing, the mandrel is removed and the elastic coating is pulled out as shown in Fig. 12.20c, resulting in an integral composite structure (see Fig. 12.20d)

Anisogrid structures are widely used as interstage (see Fig. 12.21) and spacecraft (see Fig. 12.22) structures (Bakhvalov et al., 2005).

Cylindrical anisogrid lattice structures with given diameter D and length L are characterized by six design variables (Fig. 12.23), i.e.:

- The shell thickness (the height of the rib cross-section), h
- The angle of helical ribs with respect to the shell meridian, ϕ
- The widths of the helical and the circumferential (hoop) ribs cross sections, δ_h and δ_c (for the structure in Fig. 12.23, δ_c is the total width of the adjacent hoop ribs)
- The spacings of the helical and the hoop ribs, a_h and a_c, taken along the normal elements to the axes

The ribs are the principal load-bearing elements of the structure, whereas the skin, the presence of which can be justified by design requirements, is not considered as a load-bearing element in the design of lattice structures. Moreover, the skin thickness, being treated as a design variable, degenerates in the process of optimization because the skin contribution to the mass of the structure is higher than that to the structural strength and stiffness. Thus, the optimal lattice structure design does not

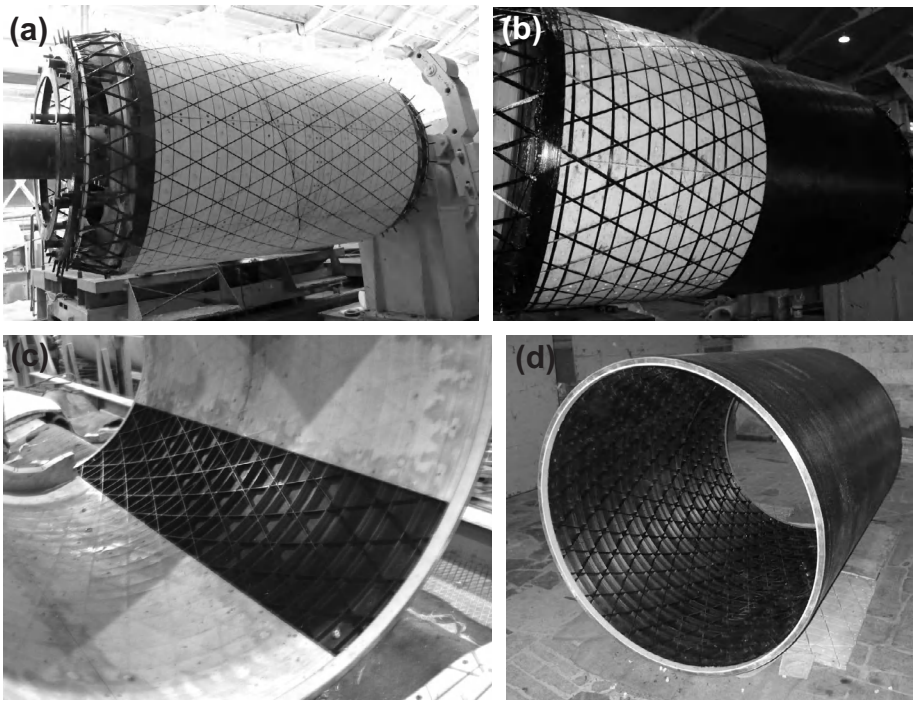


FIGURE 12.20

Fabrication of a composite lattice structure: (a) winding of the ribs, (b) winding of the skin, (c) removal of elastic coating, and (d) fabricated structure.

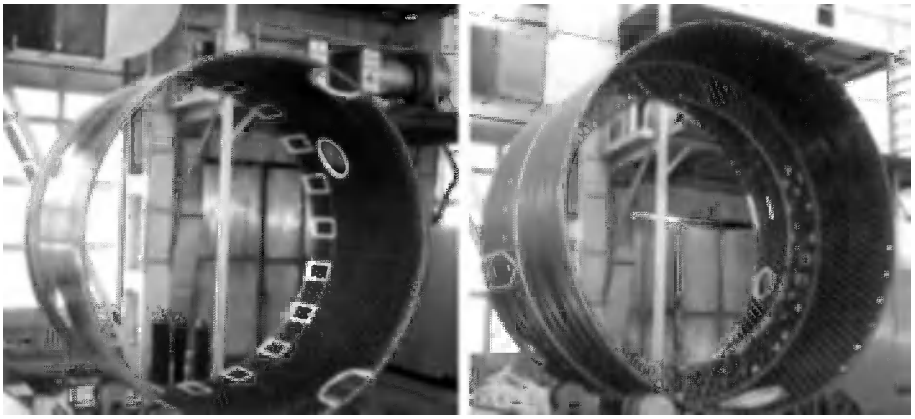


FIGURE 12.21

Four meter diameter interstage composite lattice structures.

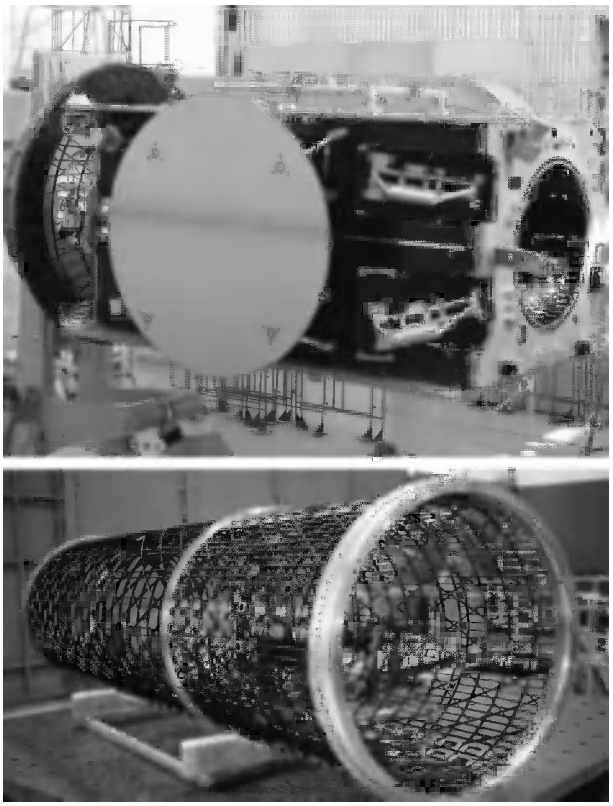


FIGURE 12.22

Composite lattice spacecraft structures.

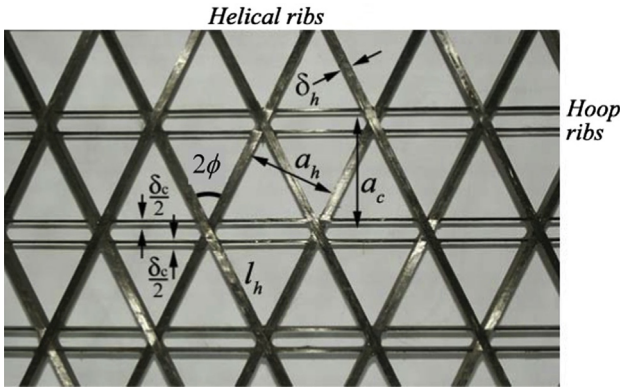


FIGURE 12.23

Lattice structure.

require a skin. If the actual structure needs a skin, its thickness and composition are preassigned to meet the operational and manufacturing requirements.

High performance and weight efficiency in composite lattice structures are provided by unidirectionally reinforced ribs that have a high strength and stiffness. In comparison with the known isogrid structures (Rehfield et al., 1980), consisting of helical and circumferential ribs forming equilateral triangles and having the same cross-sectional dimensions, the anisogrid structures under consideration provide additional mass savings because the thicknesses of the helical and circumferential ribs are different and are found, as well as the angle of the helical ribs, in the process of optimal design.

Anisogrid carbon-epoxy lattice structures are normally designed for axial compression as the main loading case.

Consider the design of a cylindrical lattice shell with given diameter, D, and length, L. The shell is loaded by an axial compressive force, $P = 2\pi RT$ (see Fig. 11.24). For the shell referred to axial coordinate x and circumferential coordinate y, the constitutive equations, Eqs. (5.5), can be presented as

$$\begin{aligned} N_x &= B_{11}\varepsilon_x^0 + B_{12}\varepsilon_y^0, \quad N_y = B_{21}\varepsilon_x^0 + B_{22}\varepsilon_y^0, \quad N_{xy} = B_{44}\gamma_{xy}^0 \\ M_x &= D_{11}\kappa_x + D_{12}\kappa_y, \quad M_y = D_{21}\kappa_x + D_{22}\kappa_y, \quad M_{xy} = D_{44}\kappa_{xy} \end{aligned} \tag{12.99}$$

in which, in accordance with Eqs. (4.194), and (5.36) for the stiffness coefficients,

$$\begin{gathered} B_{11} = 2E_h h\overline{\delta}_h c^4, \quad B_{12} = B_{21} = B_{44} = 2E_h h\overline{\delta}_h c^2 s^2, \quad B_{22} = 2E_h h\overline{\delta}_h s^4 + E_c h\overline{\delta}_c \\ D_{mn} = B_{mn}h^2/12 \end{gathered} \tag{12.100}$$

Here, subscripts "h" and "c" correspond to the helical and circumferential ribs and

$$\overline{\delta}_h = \frac{\delta_h}{a_h}, \quad \overline{\delta}_c = \frac{\delta_c}{a_c}, \quad c = \cos\phi, \quad s = \sin\phi \tag{12.101}$$

The mass of the structure consists of the mass of helical and circumferential ribs, i.e.,

$$M = M_h + M_c, \quad M_h = n_h L_h h\delta_h \rho_h, \quad M_c = n_c L_c h\delta_c \rho_c$$

Here,

$$n_h = \frac{2\pi}{a_h}Dc, \quad n_c = \frac{L}{a_c} \tag{12.102}$$

(see Fig. 12.23) are the numbers of helical and circumferential ribs in the shell with diameter D and length L, and

$$L_h = \frac{L}{c}, \quad L_c = \pi D$$

are the lengths of the ribs. Finally, we get

$$M = \pi DLh\rho_h\left(2\overline{\delta}_h + \overline{\rho}\overline{\delta}_c\right) \tag{12.103}$$

where $\overline{\rho} = \rho_c/\rho_h$ and ρ_c and ρ_h are the densities of the circumferential and helical ribs.

To design the lattice structure, we must find the structural parameters, i.e., h, ϕ, δ_h, δ_c, a_h, and a_c, delivering the minimum value of the mass of the structure in Eq. (12.103) and satisfying the set of constraints providing:

- Sufficient strength in the helical ribs under compression
- Local stability of the segments of helical ribs between the points of intersection (nodal points)
- Global stability of the lattice shell under axial compression

Consider the foregoing constraints. The stresses σ_h acting in helical ribs which take an axial compressive force P can be found using the free-body diagram, i.e.,

$$P = n_h \sigma_h h \delta_h \cos\phi$$

Using Eqs. (12.102) for n_h and notations in Eqs. (12.101), we get

$$\sigma_h = \frac{P}{2\pi D h \overline{\delta}_h c^2} \tag{12.104}$$

Thus, the strength constraint $\sigma_h \leq \overline{\sigma}$, in which $\overline{\sigma}$ is the strength of the helical rib under compression, can be written as

$$P \leq 2\pi D h \overline{\delta}_c c^2 \overline{\sigma} \tag{12.105}$$

Helical ribs can experience local buckling under compression which shows itself as a local bending of the rib segments between the nodal points. For two typical lattice structures in the first of which circumferential ribs divide the spacing between the nodal points of helical ribs in two equal parts, whereas in the second one circumferential ribs are located on both sides of the nodal points, local buckling of helical ribs is presented in Fig. 12.24. The critical stress causing local buckling is determined by the Euler formula given by Eq. (8.71), i.e.,

$$\sigma_{cr} = \frac{T_E}{A_h} = k \frac{\pi^2 E_h I_h}{l_h^2 A_h} \tag{12.106}$$

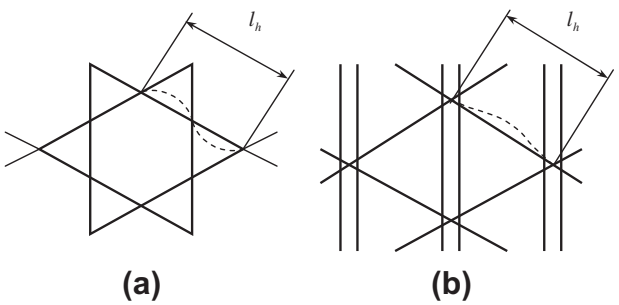


FIGURE 12.24

Local buckling of helical ribs in the lattice structure with circumferential ribs located between the nodal points (a) and in the vicinity of nodal points (b).

The thickness of the lattice structures h is usually greater than the width of the helical ribs δ_c, and local buckling occurs in the plane of the lattice structure. In this case, the moment of inertia and the area of the rib cross section are

$$I_h = \frac{h}{12}\delta_h^3, \quad A_h = h\delta_h \tag{12.107}$$

The length of the rib segment l_h shown in Figs. 12.23 and 12.24 can be expressed in terms of the design variables as

$$l_h = \frac{a_h}{\sin 2\phi} \tag{12.108}$$

and the parameter k in Eq. (12.106) is a coefficient depending on the boundary conditions. In general, k depends on the mutual location and bending stiffnesses of the helical and circumferential ribs. For the structures shown in Figs. 12.24a and 12.24b, $k = 1.55$ and 1.15, respectively.

The local buckling constraint has the form $\sigma_h \leq \sigma_{cr}$ in which σ_h is the stress in the helical ribs specified by Eq. (12.104). Using Eqs. (12.107) and (12.108), we finally obtain

$$P \leq \frac{2}{3}\pi^3 k E_h D h \bar{\delta}_h^3 s^2 c^4 \tag{12.109}$$

Consider the global (shell-type) buckling constraint. Under axial compression, lattice cylindrical shells experience two modes of buckling: axisymmetric, shown in Fig. 11.24, and nonsymmetric, demonstrated in Fig. 12.25. The critical loads corresponding to axisymmetric and nonsymmetric buckling are specified by Eqs. (11.136) and (11.169). Taking into account that the bending

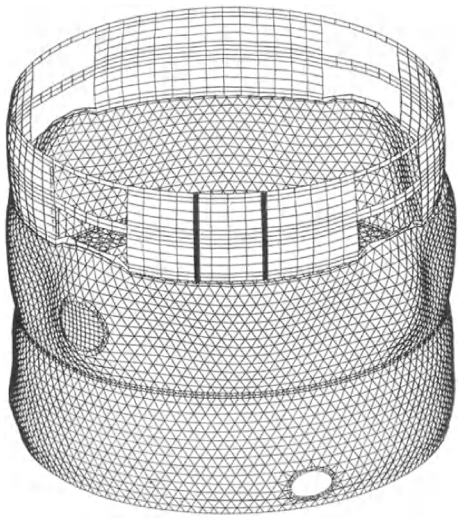


FIGURE 12.25

Nonsymmetric buckling of a lattice interstage structure.

stiffness for lattice structures D_{mn} can be expressed in terms of the membrane stiffnesses B_{mn} with the aid of the last expression in Eqs. (12.100), we can arrive at the following equations for the critical axial forces corresponding to the axisymmetric, P^a_{cr}, and nonsymmetric, P^n_{cr}, modes of buckling:

$$P^a_{cr} = \frac{2\pi}{\sqrt{3}} h \sqrt{B_{11}B_{22} - B_{12}^2}, \quad P^n_{cr} = \frac{2\pi\sqrt{2}}{\sqrt{3}} h \sqrt{B_{44}\left(B_{12} + \sqrt{B_{11}B_{22}}\right)}$$

Substituting stiffnesses B_{mn} in accordance with Eqs. (12.100), we get

$$P^a_{cr} = \frac{2\pi\sqrt{2}}{\sqrt{3}} h^2 c^2 \sqrt{E_h E_c \overline{\delta}_h \overline{\delta}_c} \tag{12.110}$$

$$P^n_{cr} = \frac{4\pi\sqrt{2}}{\sqrt{3}} E_h h^2 \overline{\delta}_h c^2 s^2 \sqrt{1 + \sqrt{1 + \frac{E_c \overline{\delta}_c}{2E_h \overline{\delta}_h s^4}}} \tag{12.111}$$

Clearly, the lowest value of P_{cr} specified by Eqs. (12.110) and (12.111) should be selected for the design. Using Eqs. (12.110) and (12.111), we arrive at the following condition:

$$P^a_{cr} \le P^n_{cr} \quad \text{if} \quad s \le \frac{1}{2} \sqrt[4]{\frac{E_c \overline{\delta}_c}{E_h \overline{\delta}_h}} \tag{12.112}$$

As shown below, buckling of typical lattice structures corresponds to the axisymmetric mode because P^a_{cr} is usually less than P^n_{cr}. So, the global buckling constraint $P \le P_{cr}$ can be taken in the form

$$P \le \frac{2\pi\sqrt{2}}{\sqrt{3}} h^2 c^2 \sqrt{E_h E_c \overline{\delta}_h \overline{\delta}_c} \tag{12.113}$$

Thus, we should minimize the mass of the structure M in Eq. (12.103) subject to the constraints given by Eqs. (12.105), (12.109), and (12.113). As can be seen, the structure under consideration is specified by four design variables: h, ϕ, $\overline{\delta}_h$, and $\overline{\delta}_c$. The main problem we face is associated with the fact that the constraints in Eqs. (12.105), (12.109), and (12.113) are written in the form of inequalities. To convert them to equalities, let us introduce safety factors $n \ge 1$ for all the modes of failure, i.e., for fracture of the helical ribs under compression, n_s, global buckling, n_b, and local buckling, n_l. As a result, the constraints can be re-written in the following form:

$$\frac{2\pi}{Pn_s} D\overline{\sigma}\, h \overline{\delta}_h c^2 = 1 \tag{12.114}$$

$$\frac{2\pi\sqrt{2}}{\sqrt{3}Pn_b} h^2 c^2 \sqrt{E_h E_c \overline{\delta}_h \overline{\delta}_c} = 1 \tag{12.115}$$

$$\frac{2\pi^3 k}{3Pn_l} E_h D h \overline{\delta}_h^3 c^4 s^2 = 1 \tag{12.116}$$

We should also take into account that

$$c^2 + s^2 = 1 \tag{12.117}$$

The idea of the method of minimization of safety factors (Vasiliev and Razin, 2001) is implemented as follows. We apply Eqs. (12.114)–(12.117) to express the design variables in terms of the safety factors and minimize the mass of the structure with respect to both sets of unknown variables: the design parameters and the safety factors. If one of the parameters n is equal to unity, the corresponding constraint is active. If $n = n_0 > 1$, the constraint is satisfied with some additional safety factor n_0. For active constraints, the function $M(n)$ has positive gradients, so to optimize the structure, we should take $n = 1$, and no further optimization is required. So, following this procedure, we should express h, ϕ, $\overline{\delta}_h$, and $\overline{\delta}_c$ in terms of the safety factors n_s, n_b, and n_l. Using Eq. (12.114), we get

$$c^2 = \frac{Pn_s}{2\pi D\overline{\sigma}\, h\overline{\delta}_h} \tag{12.118}$$

Substitution of this result into Eqs. (12.115) and (12.116) yields

$$\frac{\overline{\delta}_c}{\overline{\delta}_h} = \frac{3D^2 n_b^2 \overline{\sigma}^2}{2n_s^2 E_h E_c h^2} \tag{12.119}$$

$$s^2 = \frac{6n_l D\overline{\sigma}^2 h}{\pi k P n_s^2 E_h \delta_h} \tag{12.120}$$

Substituting further Eqs. (12.118) and (12.120) into Eq. (12.117), we obtain

$$\overline{\delta}_h = \frac{6n_l\overline{\sigma}^2 Dh}{\pi k P n_s^2 E_h} + \frac{Pn_s}{2\pi D\overline{\sigma} h} \tag{12.121}$$

Now, Eqs. (12.119) and (12.121) enable us to express the mass of the structure, Eq. (12.103), in terms of only one design variable, i.e., the shell thickness h:

$$M = L\rho_c\left(\frac{12D^2 n_l\overline{\sigma}^2 h^2}{Pn_s^2 k E_h} + \frac{3Pn_b^2 D^2\overline{\sigma}\,\overline{\rho}}{4n_s E_h E_c h^2} + \frac{9D^4\overline{\sigma}^4 n_l n_b\overline{\rho}}{Pn_s^4 k E_h^2 E_c} + \frac{Pn_s}{\overline{\sigma}}\right) \tag{12.122}$$

Applying the condition $\partial M/\partial h = 0$, we have

$$h^4 = \frac{P^2 n_b^2 n_s\overline{\rho}}{16n_l E_c\overline{\sigma}} \tag{12.123}$$

Substituting this result into Eq. (12.122), we arrive at

$$M = L\rho_c\left(\frac{9D^4\overline{\sigma}^4 n_l n_b^2\overline{\rho}}{Pn_s^4 k E_h} + \frac{6D^2\overline{\sigma}\, n_b}{n_s E_h}\sqrt{\frac{n_l\overline{\sigma}\,\overline{\rho}}{kn_s E_c}} + \frac{Pn_s}{\overline{\sigma}}\right) \tag{12.124}$$

It follows from this equation that the mass of the structure M increases with an increase in the buckling safety factors n_b and n_l, and to minimize the mass, we must take the minimum allowable values of these factors, i.e., $n_b = 1$ and $n_l = 1$. This means that the buckling constraints in Eqs. (12.115) and (12.116) are active. To find the strength safety factor n_s, we need to put $\partial M/\partial n_s = 0$, where M is defined by Eq. (12.124). As a result, we have

$$n_s = \overline{\sigma}\left(\frac{144D^4\overline{\rho}}{P^2kE_h^2E_c}\right)^{1/5} \tag{12.125}$$

Take into account that $n_s \geq 1$. Then, equation Eq. (12.125) yields

$$P \leq P_s = \frac{12D^2\overline{\sigma}^2}{E_h}\sqrt{\frac{\overline{\sigma}\,\overline{\rho}}{kE_c}} \tag{12.126}$$

So, we have two design cases. For $P < P_s$, we have $n_s > 1$, and the strength constraint, Eq. (12.114), is not active. There exists some safety factor for this mode of failure specified by Eq. (12.125). For $P > P_s$, we have $n_s = 1$, and the strength constraint becomes active, so all three constraints are active in this case.

To study these two cases, introduce the following mass and force parameters:

$$m = \frac{4M}{\pi D^2 L}, \quad p = \frac{4P}{\pi D^2} \tag{12.127}$$

Then, Eq. (12.126) gives

$$p_s = \frac{4P_s}{\pi D^2} = \frac{48\overline{\sigma}^2}{\pi E_h}\sqrt{\frac{\overline{\sigma}\,\overline{\rho}}{kE_c}} \tag{12.128}$$

Consider the case $p \leq p_s$. Substituting n_s specified by Eq. (12.125) into Eqs. (12.118; and 12.123/12.124) and using Eq. (12.127), we arrive at the following equations for the parameters of the optimal structure:

$$\begin{gathered}
\overline{h} = \frac{h}{D} = \frac{1}{4}\left(\frac{48\pi^4k^2\overline{\rho}^3}{E_hE_c^3}p^4\right)^{1/10} \\
\tan\phi = \frac{1}{2}, \quad \phi = 26.565^\circ \\
\overline{\delta}_h = \frac{5}{4\pi}\left(\frac{108\pi^2E_c}{k^4E_h^3\overline{\rho}}p^2\right)^{1/10} \\
\overline{\delta}_c = \frac{\overline{\delta}_c}{2\overline{\rho}} \\
m = \frac{25\rho_h}{8}\left(\frac{72\overline{\rho}\,p^3}{\pi^2kE_h^2E_c}\right)^{1/5}
\end{gathered} \tag{12.129}$$

Consider the case $p \geq p_s$, repeating the derivation of Eqs. (12.129) and taking $n_s = 1$, so that we have

$$\begin{gathered}
\overline{h} = \frac{h}{D} = \left(\frac{\pi^2 k\overline{\rho}}{\mathrm{E_c}\overline{\sigma}} p^2\right)^{1/4} \\
\tan^2 \phi = \frac{p_s}{4p} \\
\overline{\delta}_h = \frac{2}{\pi \sin 2\phi}\sqrt{\frac{3\overline{\sigma}}{kE_h}} \\
\overline{\delta}_c = \frac{p_s \overline{\delta}_h}{2\overline{\rho}\, p} \\
m = \frac{p\rho_h}{\overline{\sigma}}\left(1 + \frac{p_s}{4p}\right)^2
\end{gathered} \tag{12.130}$$

For $p = p_s$ Eqs. (12.129) and (12.130) yield the same results. Note that these equations are universal ones, i.e., they do not include the structural dimensions.

Eqs. (12.129) and (12.130) are valid subject to the conditions in Eqs. (12.112). Substituting the parameters following from Eqs. (12.130) in the second of these conditions, we can conclude that the axisymmetric mode of shell buckling exists if

$$p \leq p_0 = p_s \sqrt{\frac{1}{2}\left(\sqrt{\frac{2E_h\overline{\rho}}{E_c}} + \sqrt{\frac{2E_h\overline{\rho}}{E_c} - 1}\right)} \tag{12.131}$$

Analysis of this result confirms that the calculated value of p_0 corresponds to an axial force that is usually higher than the typical loads for existing aerospace structures.

As an example, consider an interstage section of a space launcher with $D = 4$ m designed to withstand an axial force $P = 15$ MN. The ribs are made from carbon-epoxy composite with the following properties: $E_h = E_c = 90$ GPa, $\overline{\sigma} = 450$ MPa, and $\rho_h = \rho_c = 1450$ kg/m^3. Calculating p, p_s, and p_0 using Eqs. (12.127/12.128); and (12.131), we get $p = 1.2$ MPa, $p_s = 1.45$ MPa, and $p_0 = 1.6$ MPa. As can be seen, $p < p_s$ and the optimal parameters of the structure are specified by Eqs. (12.129) which give the following results:

$$\overline{h} = 0.009, \quad \phi = 26.565^\circ, \quad \overline{\delta}_h = 0.05$$
$$\overline{\delta}_c = 0.025, \quad m = 6.52 \text{ kg/m}^3$$

Consider a design in which there are 120 helical ribs in the shell cross section and the lattice structure corresponds to that shown in Fig. 12.24b. In this case, the calculation yields $a_h = 188$ mm and $a_c = 210$ mm. For a structure with $D = 4$ m, we have $h = 36$ mm, $\delta_h = 9.4$ mm, and $\delta_c = 2.35$ mm. The mass of the unit surface is 6.52 kg/m^2. To confirm the high weight efficiency of this lattice structure, note that the composite section with this mass corresponds to a smooth or stringer-stiffened aluminum shell with the effective thickness $h = 2.4$ mm. The axial stress induced in this shell by an axial force $P = 15$ MN is about 500 MPa, which is higher than the yield stress of typical aluminum alloys.

In conclusion, omitting the derivation, we can present the optimal parameters of lattice cylindrical shells for which the loading parameter p in Eqs. (12.127) is higher than p_0 specified by Eq. (12.131). Buckling of such structures is nonsymmetric and the critical force is determined by Eq. (12.111). For $p \geq p_0$, the optimal structural parameters are

$$\overline{h} = \frac{\pi p}{16\overline{\sigma}}\sqrt{\frac{kE_c p_s}{3\overline{\sigma} p_0}}, \quad \tan^2\phi = \frac{p_s}{4p_0}$$

$$\overline{\delta}_c = \frac{2}{\pi \sin 2\phi}\sqrt{\frac{3\overline{\sigma}}{kE_c}}, \quad \overline{\delta}_h = \frac{p_s p_0 \overline{\delta}_c}{\rho_h p^2}\left(\frac{p_0^2}{p^2} - \frac{1}{2}\right)$$

and the normalized mass of the optimal structure is

$$m = \frac{p\rho_c}{\overline{\sigma}}\left(1 + \frac{p_s}{4p}\right)^2\left[1 + \frac{p_0 p_s}{2p^2}\left(\frac{p_0^2}{p^2} - 1\right)\right]$$

The foregoing results are obtained with the aid of the method of minimization of safety factors proposed by Vasiliev and Razin (2001). Optimization of lattice cylindrical shells by means of a geometric programming method has been undertaken by Bunakov (1999), whereas numerical methods have been applied by Totaro (2011).

Optimization is based on the continuum model of lattice structures within the framework of which the ribs are smeared over the shell surface and which is valid for relatively dense and regular systems of ribs. The study of composite lattice structures simulated by a discrete model according to which the structure is treated as a system of beam-type finite elements has been undertaken by Morozov et al. (2011a, b). The correspondence between continuum and discrete models of composite lattice structures has been discussed by Azarov (2012).

12.5 References

Azarov, A. V. (2012). Continuum and discrete models of lattice composite cylindrical shells. *Mechanics of Composite Materials and Structures, 18*(1), 121–130.

Bakhvalov, Yu. O., Molochev, V. P., Petrovskii, S. A., Barynin, V. A., Vasiliev, V. V., & Razin, A. F. (2005). Proton-M composite interstage structures: design, manufacturing and performance. In *Proc. European Conf. Aerospace Sci.*, July 4–7, 2005, Moscow [CD-ROM].

Banichuk, N. V., Kobelev, V. V., & Rikards, R. B. (1988). *Optimization of Composite Structural Elements*. Moscow (in Russian): Mashinostroenie.

Bunakov, V. A. (1999). Design of axially compressed cylindrical shells with lattice stiffeners. In V. V. Vasiliev, & Z. Gurdal (Eds.), *Optimal Structural Design* (pp. 207–246). Lancaster PA: Technomic Publ. Co.

Gurdal, Z., Haftka, R. T., & Hajela, P. (1999). *Design and Optimization of Laminated Composite Materials*. New York: John Wiley & Sons, Inc.

Kanibolotsky, M. A., & Urzhumtsev, Yu. S (1989). *Optimal Design of Laminated Structures*. Novosibirsk (in Russian): Nauka.

Kyser, A. C. (1965). Uniform-stress spinning filamentary disk. *AIAA Journal*, 1313–1316, July.

Morozov, E. V., Lopatin, A. V., & Nesterov, V. A. (2011a). Finite-element modelling and buckling analysis of anisogrid composite lattice cylindrical shells. *Composite Structures, 93*, 308–323.

Morozov, E. V., Lopatin, A. V., & Nesterov, V. A. (2011b). Buckling analysis and design of anisogrid composite lattice conical shells. *Composite Structures, 93*, 3150–3162.

Narusberg, V. L., & Teters, G. A. (1988). *Stability and Optimization of Composite Shells*. Zinatne: Riga (in Russian).

Obraztsov, I. F., & Vasiliev, V. V. (1989). Optimal design of composite structures. In C. T. Herakovich, & Yu. M. Tarnopol'skii (Eds.), *Handbook of Composites: Vol. 2. Structure and Design* (pp. 3–84). Amsterdam: Elsevier.

Obraztsov, I. F., Vasiliev, V. V., & Bunakov, V. A. (1977). *Optimal Reinforcement of Composite Shells of Revolution*. Moscow (in Russian): Mashinostroenie.

Rehfield, L. W., Deo, R. B., & Renierg, G. D. (1980). Continuous filament advanced composite isogrid: a promising design concept. *Fibrous Composites in Structural Design.* Plenum Publ Corp, 215–239.

Teters, G. A., Rikards, R. B., & Narusberg, V. L. (1978). *Optimization of Laminated Composite Shells*. Riga (in Russian): Zinatne.

Totaro, G. (2011). *Multilevel optimization of anisogrod lattice structures for aerospace applications*. PhD Thesis. Delft University.

Tsai, S. W. (1987). *Composite Design* (3rd ed.). Dayton OH: Think Composites.

Vasiliev, V. V. (1993). *Mechanics of Composite Strucrtures*. Washington: Taylor & Francis.

Vasiliev, V. V. (2009). *Composite Pressure Vessels: Analysis, Design and Manufacturing*. Blacksburg VA: Bull Ridge Publishing.

Vasiliev, V. V., & Gurdal, Z. (Eds.). (1999). *Optimal Design. Theory and Applications to Materials and Structures*. Lancaster PA: Technomic Publishing Co.

Vasiliev, V. V., Barynin, V. A., & Razin, A. F. (2001). Anisogrid lattice structures – survey of development and application. *Composite Structures, 54*, 361–370.

Vasiliev, V. V., & Razin, A. F. (2001). Optimal design of filament-wound anisogrid composite lattice structures. In *Proc. 16th Annual Tech. Conf. American Society for Composites*. September 9–12, 2001, Blacksburg, VA, USA (CD-ROM).

Vasiliev, V. V., & Razin, A. F. (2006). Anisogrid composite lattice structures for spacecraft and aircraft applications. *Composite Structures, 76*, 182–189.

Vasiliev, V. V., & Khaziev, A. R. (2009). Optimal design of composite laminates. *Mechanics of Composite Materials and Structures, 15*(1), 3–16.

Vasiliev, V. V., Barynin, V. A., & Razin, A. F. (2012). Anisogrid composite lattice structures: development and aerospace applications. *Composite Structures, 94*, 1117–1127.

Author Index

Note: Page numbers with "f" denote figures.

A

Abdel-Jawad, Y. A., 76–78
Abramov, A. A., 717
Abramyan, B. L., 672, 677
Abu-Farsakh, G. A., 76–78
Abu-Laila, Kh. M, 76–78
Adams, R. D., 394
Adkins, J. E., 129
Alexandrov, A. Ya., 266–267, 484–485
Alfutov, N. A., 210–211, 500–501, 685
Ambartsumyan, S. A., 467–468, 470–471, 487, 685
Anderson, J. A., 396
Andreev, A. N., 487
Andreevskaya, G. D., 119–121
Anihovskaya, L. I., 275
Annin, B. D., 302–304
Aoki, T., 87
Apinis, R. P., 396
Artemchuk, V. Ya., 365–367
Arutyunyan, N. Kh., 672, 677
Ashkenazi, E. K., 313
Ashton, J. E., 294–295, 487
Assaee, H., 564
Azarov, A. V., 795
Azikov, N. S., 551, 563, 571–572, 574
Azzi, V. D., 187

B

Baev, L. V., 302–304
Baker, A., 27
Banichuk, N. V., 758
Banks, W. M., 564
Bannister, M. K., 332
Barbero, E. J., 310–312
Barnes, J. A., 360–362
Barynin, V. A., 785
Bazant, Z. P., 338
Belyankin, F. P., 302–304
Bert, C. W., 440
Bhaskar, K., 537
Biderman, V. L., 717
Birman, V., 440
Bogdanovich, A. E., 15, 92
Boitnott, R. L., 703
Bolle, L., 487
Bolotin, V. V., 478–479
Boshers, C. D., 556
Bowles, K. J., 426–427
Brahtz, J. N. A, J, 526
Bryukker, L. E., 266–267, 484–485
Bucci, R. J., 275
Bulavs, F. Ya., 95, 119, 229, 300, 376–377, 388–389
Bulters, P. B. M., 275
Bunakov, V. A., 758, 795

C

Callus, P. J., 332
Camanho, P. P., 332, 338, 344–346
Carlile, D. R., 346
Carrera, E., 478–480
Cervera, M. A., 338
Chamis, C. C., 158–160
Chandra, R., 632f, 636f
Chang, F. K., 346–348
Chang, K. Y., 346
Chen, H.-J., 267–269
Chen, J. F., 333, 338–341, 344–348
Chen, J. L., 333, 335–336, 338–339
Cheng, J. H., 346–348
Cheremukhin, A. M., 660
Cherevatsky, A. S., 206–207
Chiao, C. C., 391
Chiao, T. T., 75, 187–188
Chopra, I., 613, 614f, 630, 632f, 635f, 636f
Chou, T. W., 15, 398
Chulkov, P. P., 479
Crasto, A. S., 114–115
Curtis, A. R., 114

D

Dávila, C. G., 332, 338, 344–346
Dalaei, M., 537
Davis, G. W., 406
De Baere, I., 332
Decolon, C., 487
Degrieck, J., 332
Dekker, M., 435, 585
Dementyeva, L. A., 275
Deo, R. B., 788
Donaldson, S. L., 346
Donnell, L., 540
Dougall, J, 526
Doxsee, L., 408
Drucker, D. C., 333
Dudchenko, A. A., 187
Dutton, S., 27
Dyachina, O. P., 506–507

E

Egorov, N. G., 119–121
Elpatievskii, A. N., 182–183, 187, 479, 685

F

Fadle, I., 526
Faria, R., 338
Farrow, G. J., 360–362
Fink, A., 275
Foist, B. L., 622
Föppl, A., 675
Föppl, L., 675
Fredell, R. S., 275
Fridlyander, I. N., 275
Frolov, A. N., 735
Fukuda, H., 15, 75

G

Galerkin, B. G., 500–501
Gay, D., 435
Gere, J. M., 109–114
Gilman, J. J., 58–59
Godunov, S. K., 717
Goens, E., 440
Gol'denblat, I. I., 299–300, 302–304, 315–317, 319–320
Goldenveizer, A. L., 472
Golovkin, G. S., 121
Gong, X. J., 152–156, 164
Goodey, W. J., 15–16, 65
Goodier, J. N., 600
Gorushkin, V. A., 275
Green, A. E., 129
Griffith, A. A., 60
Grigolyuk, E. I., 479, 535–536
Gudmundson, P., 187
Gunnik, J. W., 275
Gunyaev, G. M., 119
Gurdal, Z., 39–40, 758
Gurvich, M. R., 95, 119, 229, 300, 376–377, 388–389
Gutans, Yu. A, 61–62

H

Ha, S. K, 365–367
Haftka, R. T., 758
Hahn, H. T., 150, 187, 299–300
Hajela, P., 758
Hamilton, J. G., 361–362
Haresceugh, R. I., 114
Harvey, J. M., 564
Hashin, Z., 94, 187, 299–300, 333, 337
Hencky, H., 487
Herakovich, C. T., 147, 151, 169
Herbech, L., 275
Hetherington, N. W., 391
Hinton, M. J., 299–300
Hoa, S. V., 435
Horst, P., 275
Hurtado, J. A., 332, 341
Hwang, W., 403
Hwang., J. H., 403
Hyer, M. W., 428, 571

I

Ilyushin, A. A., 143–144
Ishida, T., 400
Ivanov, Yu. A., 685
Ivanovskii, V. S., 420

J

Jackson, D., 360–362
Jemielita, G., 487
Jeong, T. H., 87
Johnson, E. R., 626
Jones, R. M., 92, 97–98, 109–114, 148, 306–307, 487

K

Kaddour, A. S., 299–300
Kanagawa, Y., 400
Kanibolotsky, M. A., 758
Kanovich, M. Z., 122–123
Karmishin, A. V., 294–295, 735
Karpinos, D. M., 18–20
Katarzhnov, Yu. I., 308–309
Kaushik, B., 537
Kawai, M., 346
Kawase, Y., 346
Kelly, D., 27
Kerr, A. D., 537
Kharchenko, E. F., 121
Khaziev, A. R., 556, 758
Khoma, I. Yu., 685
Khonichev, V. I., 396
Khoroshun, L. P., 685
Kilchevsky, N. A., 732
Kim, H. G., 87
Kim, R. Y., 114–115
Kincis, T. Ya., 95, 115
Kingston-Lee, D. M., 359–360
Kirchhoff, G., 501–502
Ko, F. K., 15
Kobelev, V. V., 758
Kolesnikov, B., 275
Kollar, L. P., 435, 556, 585, 685
Koltunov, M. A., 122–123
Kondo, K., 87
Kopnov, V. A., 299–300, 302–304, 315–317, 319–320
Korn, G. A., 734
Korn, T. M., 734
Korolev, V. I., 685
Koshevoi, I. K., 685
Kozlov, S. V., 685
Krikanov, A. A., 216–218
Kromm, A., 506–507
Kruklinsh, A. A., 95, 119, 229, 300, 376–377, 388–389
Kurshin, L. M., 266–267, 484–485
Kwon, D., 403
Kyriakides, S., 332
Kyser, A. C., 779

L

Ladeveze, P., 332
Lafarie-Frenot, M. C., 332, 349–350
Lagace, P. A., 95, 198–199, 207–208
Langhaar, H. L., 553–554
Lapczyk, I., 332, 341
Lapotkin, V. A., 365–367
Le Dantec, E., 332
Leach, D. C., 346
Lee, C. S., 403
Lee, D. J., 87
Leissa, A. W., 571–572
Lekhnitskii, S. G., 478–479, 487, 673
Librescu, L., 585
Limonov, V. A., 396
Long, A. C., 27
Lopatin, A. V., 795
Lubliner, J., 332, 334
Lungren, J. E., 187
Lurie, S. A., 472, 526–528, 530–534
Lyaskovets, V. A., 735

M

Maa, R. H., 346–348
Maimi, P., 332, 338, 344–346
Majeed, M. A., 571
Margolin, G. G., 302–304
Masuko, Y., 346
Matzenmiller, A., 332, 334
Mayugo, J. A., 332, 338, 344–346
Mikelsons, M. Ya., 61–62, 396
Mileiko, S. T., 78
Mindlin, R. D., 440, 487
Miyazawa, T., 75
Moore, D. R., 346
Morozov, E. V., 164–165, 240, 287–288, 306, 333, 338–341, 346–348, 429–432, 795
Mortensen, A., 27
Mueller, L. N., 275
Murakami, S., 400
Myachenkov, V. I., 735

N

Nanyaro, A. P., 313
Narusberg, V. L., 758
Narzullaev, B. N., 390–391
Natrusov, V. I., 122–123
Negishi, R., 346
Nemeth, M. P., 556
Nemirovskii, Yu. V., 487
Nesterov, V. A., 795
Ni, R. G., 394
Nixon, M. W., 628–629, 629f
Novichkov, Yu. N., 478–479

O

Obraztsov, I. F., 757–758, 779
Oh, B. H., 338
Ohrloff, N., 275
Ovesy, H. R., 564

P

Pagano, N. J., 235–240
Paliy, O. M., 685
Papadopoulos, D. S., 426–427
Papkovich, P. F., 526
Pastore, C. M., 15, 92
Paterekas, A. D., 551
Patterson, J. M., 361–362
Pearson, K., 504
Pelekh, B. L., 505–507
Peters, S. T., 15, 27, 95
Phillips, L. M., 359–360
Pikul, V. V., 487
Pinho, S. T., 338
Pleshkov, L. V., 122–123
Poisson, S. D., 501–502
Polyakov, V. A., 15, 18–20, 233, 235
Popkova, L. K., 429–432
Popov, B. G., 685
Prevo, K. M., 361–362
Prohaska, J. L., 275
Protasov, V. D., 394, 398–399
Prusakov, A. P., 266–267, 484–485

Q

Qatu, M. S., 571–572
Qiao, P., 556

R

Rach, V. A., 420
Rasskazov, A. O., 685
Razin, A. F., 216–218, 785, 792, 795
Reddy, J. N., 465–467, 470–471, 479–480, 487, 685
Reese, E., 398
Rehfield, L. W., 788
Reifsnaider, K. L., 187
Reismann, H., 450–454
Reissner, E., 440, 487, 502, 504, 620
Renierg, G. D., 788
Rikards, R. B., 758
Rogers, E. F., 359–360
Roginskii, S. L., 119–123
Rosen, B. W., 94
Rowlands, R. E., 299–300
Roze, A. V., 87, 421–422
Rui, Y., 346

S

Sakata, I. F., 406
Salov, O. V., 191
Salov, V. A., 188, 191
Sandler, V. S., 275
Schäfer, M., 506–507
Schulte, K., 398
Schulte, R. W., 275
Scott, R. A., 346–348
Senatorova, O. G., 275
Shan, L., 556
Shankar, K., 333, 338–341, 346–348
Shen, S. H., 368–370
Sheremetiev, M. P., 506–507

Sherry, R. J., 391
Shiff, P. A., 526
Shokin, G. I., 275
Shulga, N. A., 685
Sibiryakov, A. V., 412
Sidelnikov, V. V., 275
Sierakowski, R. L., 435, 487
Simms, I. J., 360–362
Sirotkin, O. S., 275
Skudra, A. M., 95, 119, 229, 300, 376–377, 388–389
Sluys, L. J., 332
Smith, E. C., 613, 614f, 630, 635f
Sobol', L. A., 365–367
Soden, P. D., 299–300
Sokolovskaya, I. N., 685
Song, O., 585
Soutis, C., 365–367
Spiro, V. E., 685
Springer, G. S., 346–348, 365–370, 376, 435, 585, 685
Sridharan, S., 336
Stemple, A. D., 632f, 636f
Strife, J. R., 361–362
Sukhanov, A. V., 365–367
Sun, C. T., 333, 335–336, 344–346

T

Tait, P., 501–502
Tamuzh, V. P., 394, 396, 398–399
Tan, S. C., 346
Tarnopol'skii, Yu. M., 15, 18–20, 63, 87, 95, 115, 233, 235, 421–422
Tatarnikov, O. V., 288, 306
Taylor, R. L., 332, 334
Tennyson, R. C., 313
Teters, G. A., 758
Thomson, W., 501–502
Tikhomirov, P. V., 76–78
Timoshenko, S. P., 109–114, 440, 500–501, 511, 530–534, 540, 600
Todhunter, I., 504
Toland, R. H., 299–300
Tolcke, F., 526
Tomatsu, H., 75
Totaro, G., 795
Touchard, F., 332, 349–350
Tsai, S. W., 150, 152–156, 187, 267–269, 299–300, 310–312, 371, 374, 376, 396, 435, 758
Tsai, W. T., 620
Tsushima, E., 400
Turkmen, D., 365–367

U

Uflyand, Ya. S., 461–462, 487
Urzhumtsev, Yu. S., 758

V

Valishvili, N. V., 717
Van Der Meer, F. P., 332
Van Fo Fy (Vanin), G. A., 88f, 91
Van Paepegem, W., 332
Varshavskii, V. Ya, 116–117
Vasiliev, D. V., 626
Vasiliev, V. V., 18–20, 39–40, 63, 164–165, 182–183, 187–188, 191, 216–218, 233, 235, 240, 266–267, 320, 322–323, 412, 435, 472, 477, 479, 487, 505–506, 526–528, 530–534, 537, 551, 559–563, 571–572, 574, 585, 589–590, 626, 663–665, 685, 757–758, 766–767, 779, 785, 792, 795
Verchery, G., 152–156, 164, 292–294
Veres, I. A., 556
Vermeeren, C. A. J. R., 275
Verpoest, I., 408
Vicario, A. A., Jr., 299–300
Vinson, J. R., 435, 487
Vlasov, B. F., 467
Vlasov, V. Z., 690–691
Vlot, A., 275
Vogler, T. J., 332
Volmir, A. S., 735
Vorobey, V. V., 275, 288, 306

W

Wada, A., 15
Wang, C. M., 465–467
Wang, J., 332
Weaver, P. M., 556
Weisshaar, T. A., 622
Wharram, G. E., 313
Whitford, L. E., 235–240
Whitney, J. M., 294–295, 487, 537, 553–554
Winn, V. M., 336
Woinowsky-Krieger, S., 500–501, 511, 530–534
Woolstencroft, D. H., 114
Wostenholm, G., 360–362
Wu, E. M., 299–300, 310–312

Y

Yakushiji, M., 15
Yates, B., 360–362
Yatsenko, V. F., 302–304
Ye, J., 685
Yoon, K. J., 346
Yushanov, S. P., 76–78

Z

Zabolotskii, A. A., 116–117
Zahlan, N., 346
Zhigun, I. G., 15, 18–20, 233, 235
Zhilin, P. A., 501–502
Zhurkov, S. N., 390–391
Zinoviev, P. A., 210–211, 685

Subject Index

Note: Page numbers followed by "f" denote figures; "t" tables.

A

Advanced composites, 9
  alumina fibers, 13
  B_4C fibers, 13–14
  boron fibers, 12–13
  carbon fibers, 11–12
  ceramic fibers, 13
  extended chain polyethylene fibers, 12
  continuous glass fibers, 9–10
  high-performance structures, 11
  HM and HS carbon fibers, 12
  man-made metal alloys, 14
  metal fibers, 14
  modern high-modulus carbon fibers, 11
  monolithic glass, 10
  natural fibers, 14t
  organic fibers, 12
  processability, 15
  quartz fibers, 10
  reinforcing elements, 14
  SiC fibers, 13
  stress-strain diagrams, 10f
  temperature degradation, 11f
  temperature dependence, 13f
  tests, 15
  unidirectional tow, 15
Aging, 374–375, 376f
  theory, 387
Al_2O_3 fibers. *See* Alumina fibers
ALOR. *See* Aluminum and organic fibers
Alumina fibers (Al_2O_3 fibers), 13
Aluminum alloy
  plastic Poisson's ratio dependency, 137f
  secant modulus dependency, 137f
  stress-strain diagram for, 136f
  tangent modulus dependency, 137f
Aluminum and organic fibers (ALOR), 275
Angle-ply circumferential winding, 216–218, 217f
  circumferential layer thickness, 218–221
  circumferential tow linear velocity, 218–221
  manufacturing parameters, 218–221, 220t
  material mechanical properties, 218, 220t
  material moduli dependencies, 221f
  material tensile strength dependencies, 221f
  parameters, 218f
  stiffness and strength of material, 222
  stresses and strains, 222
Angle-ply laminate, 748–749
Angle-ply layer, 274–275, 431–432, 431f
Angle-ply orthotropic layer, 196
  of filament wound shell, 196f
  free-edge effects, 211–212
    in angle-ply specimen, 212
    angle-ply specimen dependency, 216
    axial strain, 214–215
    constitutive equations, 212–214
    governing equation for problem, 214–215
    interlaminar shear stiffness, 215
    model simulating plies' interactions, 213f
    strength dependency, 217f
    stress distribution, 215–216, 216f
    symmetric plies deformation, 212f
    transverse shear deformation, 212–214
    transverse shear stress, 212–214
  linear elastic model, 196–197
    angle-ply layer shear modulus, 199
    carbon-epoxy layer moduli dependencies, 198–199, 198f
    constitutive equations, 196–197
    deformation and stresses, 199f
    in-plane shear modulus, 199–200
  nonlinear elastic models, 200
    algebraic equations, 203–205
    angle after deformation, 203–205
    angle-ply layer stress-strain diagrams, 206f, 207f
    angle-ply specimen failure mode, 210f
    angle-ply two-matrix composite stress-strain diagrams, 201f
    carbon-epoxy layer stress-strain diagrams, 209f, 210f, 211f
    curved angle-ply pipe, 207f
    dependencies of normalized stresses, 209f
    equilibrium equations, 205
    global coordinate frame, 203–205
    linear element, 202f
    longitudinal strain simplification, 205–206
    manufacturing process, 206–207
    material nonlinearity, 200–202
    matrix cracking effect, 207–208
    stress and ply orientation angle dependencies, 212f
    stress-strain diagrams for transverse tension, 208f
    transverse normal stress, 209–211
    two-matrix glass-epoxy composite, 200
    uniaxial tension problem, 205–206
  two symmetric plies forming, 196f
Angles of rotations, 244
Anisogrid composite lattice structures
  axial coordinate and circumferential coordinate, 788
  axial force, 794
  axial stress, 794
  axisymmetric mode, 791, 794
  carbon-epoxy lattice structures, 788
  composite lattice spacecraft structures, 787f
  composite lattice structure fabrication, 786f
  free-body diagram, 789
  helical and circumferential ribs, 788
  helical ribs, 789
  interstage, 785, 786f
  lattice structures thickness, 790
  load-bearing element, 785–788
  local buckling constraint, 790
  manufacturing process, 785
  mass and force parameters, 793
  nonsymmetrical buckling lattice interstage structure, 790–791, 790f
  optimal structural parameters, 795
  rib segment length, 790
  safety factors minimization method, 792
  strength constraint, 789, 793
  structural parameters, 789
  structure mass, 788, 791–792
Anisotropic laminated plates, 487, 487f
  boundary conditions on plate surfaces, 490–492
  constitutive equations, 488–489
    for plate bending problem, 492–493
  in-plane stresses, 488–489
  for orthotropic plate, 490
  plane stress state, 490–492
  in plate theory, 487
  stiffness coefficients, 489–490
  strain-displacement equations, 492–493
  stress resultants and couples, 488f
  transverse shear stress distribution, 489–490
  see also Generally laminated plates
Anisotropic shells
  classical shell theory, 713
  coupling effects, 713
  equilibrium equation, 713
  orthotropic shell, 714
Anisotropic thin-walled beams, 622
  axial stiffness, 623
  beam bending, 629
  beam deflection, 630
    slope, 635
  for beam loaded with forces, 633–634
  beam torsion, 635
  beam with rectangular cross section, 630, 631f
    angle of twist dependencies, 634–635, 635f
    function for, 630, 632–633
    material structure, 630, 633f
    stiffness coefficients, 633–634, 634t
    surface development, 633f
  cantilever circular anisotropic beam, 628f
  carbon-epoxy circular beam, 628
  Castigliano's theorem, 625
  coupling effects, 627–628
  direct integration, 627
  equation for experimental beam, 631
  expression for strain energy, 625
  forces and moments, 626
  isotropic beam, 624–625
  loaded with axial force, 631

Anisotropic thin-walled beams (*Continued*)
  normal stress resultant, 623–624
  normal stresses, 622–623
  shear strain, 632
  shear stress resultant, 624–625
  stiffness coefficients, 627
  twist angle dependencies, 629f, 632f
  see also Closed cross-sectional contour
Antisymmetric laminates, 284
  angle-ply structure, 285, 285f, 288
  carbon-phenolic cylindrical shells, 288
  in composite technology, 286
  constitutive equations, 287
  coupling stiffness coefficients, 287
  cross-ply layer, 284–285, 285f
  filament-wound cylinders, 286f
  using finite-element models, 288
  solid modelling and finite-element analysis, 287–288
  T-segment, 286
  see also Symmetric laminates
Antisymmetric structure, 427–428
Approximation strength criteria, 301, 309–310
  experimental data, 310–312
  glass-epoxy
    tubular specimen failure mode, 309f
    unidirectional composite, 312f
  polynomial criterion, 310–312
  polynomial strength criteria, 313
  second-order polynomials, 310f
ARALL. *See* Aramid fibers and aluminum
Aramid fibers, 12, 99–100
Aramid fibers and aluminum (ARALL), 275
Aramid-epoxy composite material, 8
Aromatic polyamide fiber. *See* Aramid fibers
AS4/PEEK $(\pm 45^\circ)_{2s}$ composite laminates
  comparison, 350f
  numerical simulations, 350
  unidirectional AS4/PEEK CFRP material, 349–350
Axial loading, 441
Axial ribs beam, stiffness with, 635–637
  actual cross section, 637f
  axial stress resultant, 637–638
  for bending problem, 642
  circular thin-walled beam, 637
  deflection slope dependency, 636f
  normalized axial stresses distribution, 638, 639f
  normalized cross-sectional areas, 638
  normalized shear stress resultant distribution, 642f
  rib and skin panel interaction, 643f
  shear stress resultant, 639, 641–642
  stringer effect, 639–641
  thin-walled beam model, 636f, 637f
Axial strain resultant, 593, 597
  beam axial stiffness, 595
  bending stiffness coefficients, 595
  cross sections with symmetry axes, 596, 596f
  final expression for, 595
  reduction to integral forces and moments, 594f
Axial stress, 470–471
  resultant, 593
    axial stiffness of beam, 595
    bending stiffness coefficients, 595
    cross sections with symmetry axes, 596, 596f
    final expression for, 595
    reduction to integral forces and moments, 594f
Axial vibrations, 459–461
Axisymmetric buckling mode
  Bubnov-Galerkin method, 731–732
  clamped shells, 728
  conventional buckling analysis, 729–730
  cylindrical shell loaded with axial compressive forces, 726f
  homogeneous shells, 727
  isotropic shell, 727, 732
  laminated shells, 727
  loading parameter, 728
  minimum condition, 727
  normalized deflection dependencies
    axial coordinate, 729f, 730f
    on loading parameter, 731f
  shell deflection, 726
  see also Nonsymmetric buckling mode
Axisymmetric deformation, 703f
  anisotropic shells, 713
  axial coordinate normalization, 711, 712f
  bending moment, 705
  composite pressure vessel with steel ring, 710f
  constant internal pressure, 705
  constitutive equation, 704
  cylindrical shell, 707–708
    with ring, 710f
  kinematic boundary conditions, 706
  layers stiffness coefficients, 709
  linear classical shell theory, 706
  long shell, 708
  meridian curvature, 704
  nonlinear classical theory, 707–708
  nonlinear effect, 709
  nonlinear membrane theory, 707
  normalized deflection dependencies, 709, 709f
  one-dimensional problem, 703
  reference surface coordinate, 710–711
  ring deflection, 711
  shear deformable shells linear theory, 706
  shell, 703
    deflection, 704, 711–712
    radius, 711
    short and long, 705–706
  specific effects, 706
  stiffness coefficients, 703, 705

B

B_4C fibers. *See* Boron carbide fibers
Balanced laminates, 274–275
Ballistic limit. *See* projectile velocity
Barely visible impact damage (BVID), 401
Beam cross section geometry, 587–588
  arbitrary point, 588
  contour arc element, 589f
  contour curvature, 588
  cross-sectional contour, 587–588
  elementary arc, 589
  normal and contour coordinates, 587f
  radial and tangent, 588f
Beam strength, 447–450
  axial stress, 450
  maximum deflection, 450
  shear stress, 450
  stiffness coefficients, 449–450
Beams and plates refined theories
  axial displacement, 474–475, 479f, 480
  beam deflection, 475
  bending moment, 468–469
  bi-harmonic equation, 478–479
  boundary-layer solutions, 479–480
  cantilever beam, 464
  cantilever sandwich beam, 480–484, 480f
  clamped end beam, 474
  composite beam, 464
  displacements, 467–468
  free-body diagram, 472
  higher-order theories, 467
  layer interface surfaces, 480
  load-carrying layers, 479
  nonzero roots equation, 476t
  normal and shear stresses, 471
  normal stress distributions, 477f
  penetrating solution, 475
  sandwich beam
    free-body diagrams, 482f
    maximum deflections, 484–485, 484t
  shear stress, 473–474, 477–478
  static variables, 465–467
  transverse normal strain, 484
  trigonometric series, 469–470
  see also Plate theory
Bi-harmonic equation, 478–479
Boron carbide fibers (B_4C fibers), 13–14
Boron fibers, 12–13
Boron-aluminum, 757
Boron-aluminum unidirectional composite, 151, 152f
Boron-epoxy optimal laminates, 757
Bredt equation, 600
Bubnov-Galerkin method, 535–536, 731–732
Buckling constraints
  bending stiffness, 765
  critical load, 765
  laminated plates optimal structural parameters, 766t
  single-layered plate, 765
  strength constraints, 765
BVID. *See* Barely visible impact damage

C

Cantilever beam, 464, 465f, 472
Carbon fibers, 11–12
  HM and HS, 12

modern high-modulus, 11
pitch-based carbon fibers, 11–12
Carbon-carbon composites, 20–21
Carbon-carbon conical shell, 26, 27
Carbon-epoxy composite material, 56
Carbon-epoxy flywheel, 783, 784f
Carbon-epoxy laminate, 756–757
Carbon-epoxy lattice spacecraft, 231f
Carbon-phenolic cylindrical shells, 288
Cartesian coordinate frame, 38, 143–144
Cartesian coordinates, 29–30, 29f
Castigliano's formulae, 129–132
Castigliano's theorem, 50, 604
CDM. *See* Continuum damage mechanics
Ceramic composites, 20
Ceramic fibers, 13
extended chain polyethylene fibers, 12
CHFF. *See* Composites with high fiber fraction
Circular cross section, beam with, 606, 607f, 608f
axial stress resultant and strain, 608
beam displacements, 608
compliance coefficients, 609
maximum deflection, 609
stiffness coefficients, 607
warping functions, 609
Circular cylindrical shells, 685
axisymmetric deformation, 703
bending moment, 705
constant internal pressure, 705
constitutive equation, 704
kinematic boundary conditions, 706
meridian curvature, 704
one-dimensional problem, 703
shell deflection, 703–704
short and long shells, 705–706
specific effects, 706
stiffness coefficients, 703, 705
circular rings, 692
beam cross section, 695
circular ring element, 693f
closed ring, 694, 696
composite rings, 692
deformation, 697
dependencies ring deflection, 699f
displacements and angle of rotation, 694
equilibrium equations, 693
integration, 694
laminated beams rectangular cross sections, 697, 697f
reference surface coordinate, 692–693
ring arbitrary cross section, 696
ring equilibrium, 694
rings with parameters, 698
self-balanced forces, 696f
symmetry conditions, 696
transverse shear deformation, 698
classical shell theory, 714
composite materials, 685
infinitely long cylindrical panel, 698
circumferential displacement, 700
clamped edges, 700
deformed state, 700
first-order nonlinear effect, 702
fuselage panel, 701
integration constants, 700
internal pressure, 699f
linear solution, 701
membrane solution, 702
nonlinear membrane theory, 702
normalized deflection dependencies, 701f, 702
panel behavior, 698
quadratic equation, 702
reference surface coordinate, 698–700
symmetry conditions, 700
one-dimensional problems, 692
shell theories, 686–691
Circular rings
beam cross section, 695
circular ring element, 693f
closed ring, 694, 696
composite rings, 692
deformation, 697
dependencies ring deflection, 699f
displacements and angle of rotation, 694
equilibrium equations, 693
integration constants, 694
laminated beams rectangular cross sections, 697, 697f
reference surface coordinate, 692–693
ring arbitrary cross section, 696
ring equilibrium, 694
rings with parameters, 698
self-balanced forces, 696f
symmetry conditions, 696
transverse shear deformation, 698
Circumferential winding, 418f, 419f
aramid-epoxy unidirectional composites, 420f
carbon-epoxy composite dependence, 423, 423f
direct correlation, 418–420
filament winding, 420
material stiffness reduction, 420
normalized modulus reduction, 422f
ply waviness, 423
regular waviness, 421–422
tape preliminary tension, 420, 421f
Clamped plates, 526
biorthogonality condition, 528–530
boundary conditions, 527–528, 530–534
decomposing symmetric functions, 530–534
homogeneous solutions, 527–528
normalized coordinates, 526–527, 526f
Classical plate theory, 496–497
algebraic equations for coefficients, 550–551
anisotropic plates, 553–554
approximate minimum condition, 548–549
approximate solutions, 534, 537
Bubnov-Galerkin method, 535–536
clamped longitudinal edges, plate with, 535f, 536–537
clamped transverse edge, plate with, 536
neglecting shear deformation, 534–535
simply supported longitudinal edge, plate with, 536
approximate solutions, 556
biaxial stress state, 549–550
boundary conditions, 499
boundary problem in, 501–502
buckling analysis results, 554
buckling equation for orthotropic plates, 545–547
buckling mode, 546f, 552f
carbon-epoxy plates, 551–553
clamped plates, 526
biorthogonality condition, 528–530
boundary conditions, 527–528, 530–534
decomposing symmetric functions, 530–534
double-reiterated roots, 530–534, 534t
homogeneous solutions, 527–528
normalized coordinates, 526–527, 526f
composite plates, 554, 554f
compression and shear action, 550–551
critical loads, 545–547
for square composite plates, 550t
critical shear force, 551
exact solutions, 519
failure modes, 552f
features, 497–499
imaginary pressure, 547f
minimum value coefficient, 547–548, 548f
neglecting transverse shear deformation, 519–520
normalized compressive force dependencies, 555f
normalized critical load dependencies, 549–550, 550f
normalized shear force dependencies, 555f
normalized transverse shear force distribution, 500f
plate loaded with in-plane loads, 545f
plate reference surface deformed element, 546f
plate torsion problem, 499
plate with sine pressure, 498f
shear buckling coefficient dependencies, 552f, 553f
shear forces, 496–497
simply supported plates, 520–521, 520f
boundary conditions, 525–526
with clamped transverse edges, 525f
close-to-square rectangular plate, 521f
convergence of series, 521–522
long rectangular plate, 521f, 522
with longitudinal edges, 525f
normalized deflection dependency, 522f
at opposite edges, 522–524
orthotropic plates, 524–525
rectangular plate with, 523f
solutions of differential equation, 524t, 525
support reactions, 500f
transformations, 500–502
transverse shear forces, 497–499

Classical plate theory (*Continued*)
uniaxial compression, 547–548
variational equation, 499
Classical shell theory
amplitudes algebraic equations, 716
differential operators, 715
equilibrium equations, 715
rotation angles, 715
strain-displacement equations, 715
transverse shear deformations, 714
trigonometric series, 715–716
see also Shell theories
Closed cross-sectional contour
axial stress resultant, 593
axial stiffness of beam, 595
bending stiffness coefficients, 595
cross sections with symmetry axes, 596, 596f
final expression for, 595
reduction to integral forces and moments, 594f
beam displacements, 603, 605
average shear deformations, 603
beam element length, 604
cantilever beam with transverse load, 604f
Castigliano's theorem, 604
cross section, 603
beam stiffness with axial ribs, 635–637
actual cross section, 637f
axial stress resultant, 637–638
for bending problem, 642
circular thin-walled beam, 637
deflection slope dependency, 636f
distribution of normalized axial stresses, 638, 639f
normalized cross-sectional areas, 638
normalized shear stress resultant distribution, 642f
rib and skin panel interaction, 643f
shear stress resultant, 639, 641–642
stringer effect, 639–641
thin-walled, 636f
thin-walled beam model, 637f
beam with, 593
beams loaded with body and surface forces, 643
axial stress resultant, 644–645
body and surface force reduction, 643f
forces and moments, 644
circular cross section, beam with, 606, 607f, 608f
axial stress resultant and strain, 608
beam displacements, 608
compliance coefficients, 609
maximum deflection, 609
stiffness coefficients, 607
warping functions, 609
composite beams
axial and contour dependencies, 601f
axial compression, 601
beam torsion, 602–603
circular cross section fiberglass-epoxy beam, 601
laminated structure, 600f
shear strain dependence, 602f
strains in plies, 602
stresses in plies, 600–601
rectangular cross section, beam with, 606, 607f, 610f
axial stress resultant, 610
beam displacements, 612
beam stiffnesses, 613
composite thin-walled beam, 617f
cross-sectional contour in regular polygon, 617f
decomposing beam contour, 610
deflection slope dependency, 614f
expressions for deflection, 612–613
function distribution, 611, 611f, 612f
integral distributions, 615f
loaded by transverse force and torque, 613f
shear stress resultant components, 611
square cross section, 616
stiffness coefficients, 610, 617
torsional stiffness, 613
twist angle dependency, 614f
warping function, 614–616
restrained bending, 645, 650
bimoment, 650–651
normal shear resultants, 651
normal stress resultants, 651, 652f
restrained torsion, 645
bimoment, 647
of cantilever beam, 646f
integration constant, 647
normalized normal stress resultants, 649, 649f, 650f
normalized shear stress resultants, 649, 649f
normalized warping function, 647
restrained warping, 646
shear center of beam, 646
shear stress resultants, 647
strain energy, 648
stress resultants, 648
warping function, 645–646
shear center, 617–618
coordinates, 618–620
cross section, 618f
displacements, 619
forces, 618
shear deformations, 620
Bredt equation, 600
shear stress resultant, 597–598
area bounded by contour, 599f, 599
contour coordinate value, 597–598
decomposition, 597f
elementary cross-sectional area, 599, 599f
equilibrium equation, 598–599
expression for, 599
static equations, 598
thin-walled beam loaded at ends, 594f
twist center, 617–618, 620
beam triangular cross section, 620f
bending and torsion problems, 622
coordinates, 620–621
existence, 622
function distribution, 622f
stiffness coefficients, 620
warping function, 605
continuous function, 606
integration constant, 605–606
rectangular beam under torsion, 616f
rectangular beam under transverse bending, 615f
see also Multi-cell cross-sectional contour; Thin-walled composite beams
Coefficients of thermal expansion (CTE), 358
Column-type buckling, 725–726
Compliance matrix, 44
Composite beam theory assumptions
axial stiffness reduction, 592–593
contour point displacements, 590–591, 590f
displacements by cross section rotation, 591f
equilibrium and constitutive equation simplification, 592
reducing shell theory 2D equations, 593
Composite beams
axial and contour dependencies, 601f
axial compression, 601
beam torsion, 602–603
circular cross section fiberglass-epoxy beam, 601
laminated structure, 600f
plies
strains in, 602
stresses in, 600–601
shear strain dependence, 602f
Composite beams free vibrations, 462f
axial compressive force, 464
beam deflection, 462–463
flexural vibrations, 461–462
laminated composite structures, 459–461
rotatory inertia effect, 463
vibration coupling effect, 463
Composite columns buckling
axial force, 457, 457f
critical force, 459
Euler formula, 457–459
shear mode, 459
Composite laminates, 343
AS4/PEEK
composite, 346
and model parameters, 348t
comparison, 349t
composite layup function, 343
load *vs*. displacement curves, 348f
nonlinearity or plasticity, 343
plastic model parameters, 344–346
predicted load *vs*. displacement curves, 349f
principal damage model, 346–348
rectangular laminates, 343
T300/1034-C and model parameters, 345t
tensile failure stresses, 346, 347t
Composite lattice
shear web structure, 232f
spacecraft structures, 787f
structure fabrication, 786f

Composite layer mechanics
  angle-ply
    circumferential winding, 216–222, 217f
    orthotropic layer, 196–216
  fabric layers, 223–229
  isotropic layer, 125–144
  laminated structure of composite pipe, 125, 126f
  lattice layer, 230–231
  orthogonally reinforced orthotropic layer, 169–196
  spatially reinforced layers, 232–240
  unidirectional
    anisotropic layer, 152–169
    orthotropic layer, 144–151
Composite materials, 9, 685, 745
  composite cistern, 686f
  composite pipe elements, 685f
  cylindrical composite pressure vessel, 687f
  fibers for advanced composites
    alumina fibers, 13
    B_4C fibers, 13–14
    boron fibers, 12–13
    carbon fibers, 11–12
    ceramic fibers, 13
    extended chain polyethylene fibers, 12
    continuous glass fibers, 9–10
    high-performance structures, 11
    HM and HS carbon fibers, 12
    man-made metal alloys, 14
    metal fibers, 14
    modern high-modulus carbon fibers, 11
    monolithic glass, 10
    natural fibers, 14t
    organic fibers, 12
    processability, 15
    quartz fibers, 10
    reinforcing elements, 14
    SiC fibers, 13
    stress-strain diagrams, 10f
    temperature degradation, 11f
    temperature dependence, 13f
    tests, 15
    unidirectional tow, 15
  filled materials, 9
  large composite storage tank, 686f
  matrix materials, 15
    boron-aluminum unidirectional composite material, 18–20
    carbon tow strength, 16t
    carbon-carbon composites, 20–21
    ceramic composites, 20
    cured epoxy resins with T_g, 18f
    matrices, 17
    matrix properties, 16–17
    normalized longitudinal moduli, 19f
    in polymeric composites, 20
    polymeric matrices, 17
    stiffness of matrix, 15–16
    stress-strain curves for aluminum, 19f
    tensile strength temperature dependence, 20f
    testing of straight tow, 16f
    thermo-mechanical curves, 17–18
    thermoplastic matrices, 17
    typical cured epoxy matrix, 17f
    widespread metal matrices, 18
  processing
    carbon-carbon conical shell, 27
    catamaran yacht Ivan-30 made, 24f
    fabricated by braiding, 23–25
    fabrication processes, 27
    filament winding, 23
    4D spatial structure, 26f
    heating and stages, 26
    heterogeneous media, 21
    hybrid materials, 21–22
    lay-up and fiber placement technology, 23
    linear structure, 22–23
    machine making prepreg, 22f
    made by pultrusion and braiding, 23f
    material macrostructure, 22
    pipe manufacturing by circumferential winding, 24f
    plane laminated structure, 23
    pressure vessel geodesic winding, 25f
    RTM, 26
    small plane made by filament winding, 25f
    spatial macrostructure, 25–26
    VARTM, 26
    wet, dry or prepreg processes, 21
  reinforced materials, 9
  see also Structural materials
Composite ply, 53–55
Composite pressure vessels
  axisymmetrically loaded membrane revolution shell, 767f
  combined meridian, 776–777
  filament-wound composite pressure vessel, 780f
  first-kind and second-kind elliptic integrals, 774–775
  geodesic line, 772
  hyperbolic shell, 774
  isotensoids, 773
  monotropic model, 772
  optimal composite shells meridians, 771f
  optimal filament wound shell, 773
  optimal shell, 768
    meridian, 769
    stresses expressions, 769
  polar opening, 772
  pressure vessel dome, 775, 775f
  shell element, 766
  shell mass and internal volume, 777–779
  shell meridian, 767
    parametric equation, 770
    tangent line, 770
  shell thickness, 770, 772
  stresses, 768
  tape material coordinates, 767
  tape orientation angle, 772
Composite rings, 692, 692f
Composite structure, 243
Composite thin-walled C-shaped beam, 586f
Composite tows, 443, 444f
Composites with high fiber fraction (CHFF), 121
Consistent tangent stiffness matrix, 341
Constitutive equations, 2
Continuous glass fibers, 9–10
Continuum damage mechanics (CDM), 332
Convolution theorem. *See* Laplace transformation
Cooling process, 426–427
Cross-ply laminate, 748–749
Cross-ply layer, 171f
  with crack in transverse ply, 176f
  nonlinear phenomenological model, 182–183
  in plane stress state, 183f
  stress-strain diagram, 181–182
  transverse shear, 173f
Cross-sectional contour, 587–588
Cross-sectional warping, 585–586
CTE. *See* Coefficients of thermal expansion
Cyclic loading
  anisotropic materials, 396
  aramid-epoxy composite material's, 395f
  carbon-epoxy composites fatigue strength, 397f
  cyclic bending, 397–398
  cyclic tension, 396
  dissipation factor, 394, 395f
  energy dissipation in conjunction, 394
  fabric composites, 398, 399f
  glass-fabric-epoxy-phenolic composite elastic modulus, 399, 400f
  low-cycle fatigue, 398, 399f
  material strength, 396
  stiffness degradation, 400
  stress acting, 392–394
  stress concentration, 394, 396f
  viscoelastic and elasticmaterials, 393f
Cylindrical drive shaft, 323f
Cylindrical shells buckling
  under axial compression
    axisymmetric buckling mode, 726
    column-type buckling, 725–726
  under external pressure, 738
    buckling equation, 738
    cylindrical shell loaded with external pressure, 738f
    hydrostatic pressure, 741
    infinitely long shells, 740
    simply supported shells, 739

D

Damage initiation criterion, 337
Damage model
  damage evolution
    damage energy, 338–339
    damage surface, 338
    loading/unloading stress strain curves, 339, 339f
  damage initiation criteria, 337
  propagation criteria, 337
Deformation theory of plasticity, 133–134
  constitutive equations, 137–138, 141, 143–144

Deformation theory of plasticity (*Continued*)
increments of plastic strains, 142–143
plastic potential, 134–135
plastic strains, 133–134
successive loading method, 141
uniaxial tension, 135–137
uses, 144
Delamination, 409
Displacement-controlled loading, 343

E

Elastic energy. *See* Potential energy
Elastic material, 42
Elastic model, 3–4, 3f
Elastic solution method, 138, 139f
Elastic-plastic material model, 6, 7f
Elastic-viscoelastic analogy, 386
Elementary composite layer
axial circumferential strains, 326f
cylindrical drive shaft, 322–323, 323f
dependencies of strains, 327
failure criteria
approximation strength criteria, 301, 309–313
interlaminar strength, 320
maximum stress and strain criteria, 301–309
microphenomenological approach, 300
plane stress state, 301
structural failure criteria, 301
tensor strength criteria, 313–320
filament-wound fiberglass pressure vessels, 327t
using maximum stress criterion, 323
polynomial criterion, 324
practical strength evaluation, 321
comparing, 321
composite drive shafts with test fixtures, 322f
failure criteria, 321–322
laminate strength, 321
two-layered cylindrical shell, 324
Elementary composite layer
maximum strain failure criterion, 307–309
maximum stress criterion, 301–302
carbon-carbon unidirectional composite, 306f
carbon-epoxy test tubular specimens, 303f
fabric composites, 306–307
failure envelope, 304f, 305f
failure surface corresponding, 303f
glass-fabric-epoxy test tubular specimens, 302f
glass-phenolic fabric composite, 305f
stress dependence, 307f
structural elements, 302–304
unidirectional glass-epoxy composite, 308f
unidirectional ply, 308–309
warp and filling yarns, 302–304
Energy conservation law, 415–416
Engineering shell theory
reasonable accuracy, 717
shells coefficients, 717
Engineering theory. *See* Mushtary-Donnell-Vlasov theory
Environmental, special loading, and manufacturing effects, 353
Equilibrium equations, 688
Euler formula, 457–459

F

Fabric composites, 398
Fabric layers
apparent modulus of elasticity, 223–225
braided fabric structure, 228–229, 228f
carbon fabric tape, 223f
composite hull of boat, 224f
composite leading edge of aeroplane, 224f
diamond fabric structure, 228–229, 228f
fabric composites
properties, 226t
stiffness and strength, 225
fabric structure unit cell, 225f
fabrics shaping, 227–228
shear modulus, 229
stiffness and strength characteristics, 229
stress-strain curves
for fiberglass fabric composite, 227f
for fiberglass knitted composites, 228f
textile performing role, 223
typical knitted structures, 227f
weave patterns, 225, 226f
see also Lattice layer
Failure surface, 299
in stress space, 300f
thin-walled tubular specimens, 301
Fatigue diagrams
carbon-carbon composite material, 397f
unidirectional
aramid-epoxy composite, 398f
carbon-epoxy composite, 398f
FGM. *See* Functionally graded material
Fiber ineffective length, 74
Fiber metal laminates (FML), 275
carbon-epoxy laminate, 275f
GLARE aircraft skin of variable thickness, 276f
metal-composite laminate, 276–277, 277f
metals and composites, 275
shortcomings, 276
Fiber-matrix interaction
fiber strength statistical aspects
bundle of fibers, 63
bundles strength, 63–64, 64t
carbon bundles, 64f
fiber bundle tension, 63f
strength deviation, 62–63
strength distribution for boron fibers, 63f
strength variation, 64–65, 65t
theoretical strength, 61–62
fracture toughness, 78
brittle, ductile and metal alloys, 78f
crack stopping mechanism, 80f
fiber-matrix interfaces, 78
fracture toughness and strength, 79f
static strength dependence, 79f
structural materials, 79–80
stress diffusion in fiber interaction
analytical solution, 73–74
carbon-epoxy ply with parameters, 74
composite bundles, 65
constitutive equations, 68
dry bundles and composite bundles, 65t
equilibrium equations, 66
geometric interpretation, 70f
matrix stiffness, 66
normal stress distribution, 74f, 75f, 76f
perturbation, 68
qualitative results, 76–78
shear and normal stresses, 71–72
shear strain in matrix layer, 68f
shear stress distribution, 76f, 77f
using single-fiber fragmentation test, 75
stresses acting in fibers and matrix layers, 67f
unidirectional glass-epoxy composites, 75
unidirectional ply with broken fiber, 66f
variation coefficient, 66t
theoretical and actual strength
Atoms' interaction curve, 59, 59f
boron fibers strength on fiber length, 62f
composite materials, 57
fiber with crack, 60–61, 60f
glass fibers, 61
high-carbon steel wire strength, 58f
material microstructure or macrocracks, 61
material model, 58f
Physics of Solids, 58–59
Fibers mechanical properties, 5t
Fibrous technology, 21–22
Fick's law, 368–370
Filament winding, 23, 420
Filament-wound composite pressure vessel, 145f, 780f
Filled materials, 9
First-order ply model, 355
First-order shear deformation theory, 465–467
FML. *See* Fiber metal laminates
Four-layered quasi-isotropic carbon-epoxy laminate, 328f, 330
Fourier series, 368–370
Fourier's law, 353–354
Fracture toughness, 78
brittle, ductile and metal alloys, 78f
crack stopping mechanism, 80f
fiber-matrix interfaces, 78
fracture toughness and strength, 79f
static strength dependence, 79f
structural materials, 79–80
Free torsion of beams, 662
analytical solution, 668–669
angle of rotation, 667, 677
angle-shaped thin-walled beam, 676, 676f
arbitrary coordinate frame, 669
arbitrary open cross-sectional contour, 673
axial displacement, 668f, 669f
beam cross section warping, 671

beam displacements, 665
beam thickness, 674–675
beam torsional stiffness, 670
beams with circular cross-sectional contour, 673–674, 674f
boundary conditions, 677
circular cross section of beam, 673f
constant angle of twist, 667
constitutive equations, 664–665
equation
for axial displacement, 677
for homogeneous beam, 671
for isotropic beam, 671
equilibrium equation, 666–667
expression
for stress resultants, 669–670
for torsional stiffness, 677
forces and moments, 663f, 668f, 670f
homogeneous cylindrical beam, 674–675
for isotropic beam, 675
Lamé coefficient, 663–664
for laminated beams, 665
moment equation, 670, 674
sandwich beam cross section, 672f
shear stress, 662
distribution, 663f
resultant, 663
single-cell sandwich cross section *ABCD*, 663
strain-displacement equations, 666
stress resultants, 667
thin-walled beam model, 664f
thin-walled beam torsion, 662
torsional stiffness
coefficient values, 672, 672t, 675t
evaluation, 676
transverse shear stiffness, 665
twisting moment, 662
warping function, 671f, 675–676
see also Open cross-sectional contours
Free-edge effects, 211–212
in angle-ply specimen, 212
angle-ply specimen dependency, 216
axial strain, 214–215
constitutive equations, 212–214
governing equation for problem, 214–215
interlaminar shear stiffness, 215
model simulating plies' interactions, 213f
strength dependency, 217f
stresses distribution, 215–216, 216f
symmetric plies deformation, 212f
transverse shear
deformation, 212–214
stress, 212–214
Frequency histogram, 62–63
Functionally graded material (FGM), 243–244

G

Generally laminated plates, 565
boundary conditions, 569–570
constitutive equations, 565–566
cross-ply carbon-epoxy plate, 569–570, 570f
forces and moments, 568f
in-plane displacements, 569
in-plane loading, 570
for carbon-epoxy plate, 575
deflection coefficients, 572–573
expressions for in-plane displacements, 574–575
large deflections, 574
plate shortening dependency, 573f
reference surface coordinate, 575–576
simply supported plates, 571–573
square carbon-epoxy plate, 576
square or close-to-square plates, 574
unsymmetrically laminated plates, 571
reference surface, 566–569
sandwich plate with ramps, 568f
shear deformable unsymmetrically laminated plates, 576
constitutive equations, 576–579
equilibrium equations, 576–579
for simply supported plate, 579–580
strain-displacements equations, 576–579
simply supported plate, 566–569
stiffened plate reduction to, 565, 565f
unsymmetric plate bending, 565–566
Glass fibers, 9–10
Glass transition temperature (T_g), 17–18
Glass-epoxy composite material, 122
Glass-fabric-epoxy test tubular specimens, 302f

H

Helical ribs, 789
local buckling, 789f
Hereditary constitutive theory, 377–378, 378f
High performance fibers, 12
High-modulus carbon fiber (HM carbon fiber), 12
High-modulus carbon-epoxy composite, 359–360
High-strength carbon fiber (HS carbon fiber), 12
Higher-order theories, 467
HM carbon fiber. *See* High-modulus carbon fiber
Homogeneous layer
stiffness coefficients, 254–255, 254f
see also Nonhomogeneous anisotropic layer
Hooke's law, 125–126, 358, 380–381, 436–437, 759
HS carbon fiber. *See* High-strength carbon fiber
Hybrid composites, 116
composites with high fiber fraction
aramid-epoxy CHFF, 121
aramid-epoxy composite, 120f, 121t
composites with high fiber fraction, 121
tensile longitudinal strength, 119–121, 120f
experimental dependencies, 117f
first-order microstructural model, 116f
hybrid carbon-glass epoxy unidirectional composite, 119f
inverse linear dependence, 117–118
longitudinal modulus *vs.* ultimate tensile strain, 118f
micromechanics, 116–117
stress-strain diagrams, 118f
threshold value, 119
Hybrid materials, 21–22
Hydrostatic pressure
axial and circumferential forces, 741
critical loads, 741
critical pressure, 742
prebuckling stress resultants, 742
shell shape imperfections, 741
Hygrothermal effects
aramid-epoxy composites, 375f
Arrhenius relationship, 374
laminated composite material, 369f
material aging, 374–375
material behavior, 371
material mass increase, 371
moisture
absorption, 368–370
concentration distribution, 372f, 373f
content dependence, 373f, 374f, 375f
polymeric composites, 373
second boundary condition, 370
slope, 371
thermal effects, 374
see also Temperature effects

I

Impact loading
aluminum layers, 414
aramid fabrics, 417–418
ballistic limit, 415t, 416
carbon-epoxy plates, 405f
clamping fixture for compression test, 403f
composite airframe structure, 401, 401f
composite panel, 402f
compression strength dependence, 408, 408f
delamination, 409
area, 403, 404f
energy dependencies, 406f
drop-weight mass, 407
energy dissipation, 407
extrapolation, 403
fabric membrane, 416
flying projectile, 414–415
force-deflection diagrams, 416f
homogeneous layer, 410–411
impact test, 414f, 415f
impactor and plate interaction, 407f
interlaminar conditions, 412
interlaminar stress dependence, 412, 412f
kinetic energy, 401–403
laminate under impact load, 410f
laminates structure, 413f
load *vs.* plate shortening under compression, 409f
load-carrying structures, 404–406
material delamination, 409–410
normal stress, 413f
projectile velocity, 415–416

Impact loading (*Continued*)
quasi-static test, 416
residual velocity dependence, 416–417, 417f
steel impactor
energy, 406
and hail ice, 406, 406t
stress-strain diagrams, 411–412
surface layers local buckling, 409f
tensile and compressive waves, 411f
thin fabric skin damage, 405f
thin-walled composite laminates, 401
wave interaction, 412–414
see also Barely visible impact damage (BVID)
In-plane displacements, 425–426
In-plane loading, 570
for carbon-epoxy plate, 575
deflection coefficients, 572–573
expressions for in-plane displacements, 574–575
large deflections, 574
plate shortening dependency, 573f
reference surface coordinate, 575–576
simply supported plates, 571–573
square carbon-epoxy plate, 576
square or close-to-square plates, 574
unsymmetrically laminated plates, 571
In-plane shear, 104–107
parameter dependence, 104f
pure shear simulation in square frame, 106f
test fixture
for transverse tension and compression, 105f
for unidirectional tubular specimens, 106f
tubular specimen for shear test, 107f
Infinitely long cylindrical panel
circumferential displacement, 700
clamped edges, 700
deformed state, 700
first-order nonlinear effect, 702
fuselage panel, 701
integration constants, 700
internal pressure, 699f
linear solution, 701
membrane solution, 702
nonlinear membrane theory, 702
normalized deflection dependencies, 701f, 702
panel behavior, 698
quadratic equation, 702
reference surface coordinate, 698–700
symmetry conditions, 700
Infinitely long shells, 741f
critical pressure, 740
homogeneous shells, 740–741
Inhomogeneous orthotropic layers
coupling coefficients, 274
elementary cross-ply couples, 273
membrane stiffnesses, 273
Integration algorithm, 340
closest point return mapping algorithm, 340
damage variable, 340
nonlinear system, 340
stress-strain relationship, 340
Interlaminar strength, 320, 321f
Interstage composite lattice structure, 231f
Invariant strength criteria, 315
Isochrone stress-strain diagrams, 376–377, 377f
Isotensoids, 773, 778f
boss equilibrium, 776
with internal pressure, 776–777
loading conditions, 774f
meridians, 773, 777
with polar boss, 776f
polar openings, 778f, 779, 779f
Isotropic layer, 125, 129f
composite drive shaft, 127f
composite pressure vessel
aluminum liner for, 127f
thermoplastic liners for, 128f
linear elastic model
Hooke's law, 125–126
three-dimensional stress state, 126–129
see also Lattice layer

L

Lagrange multipliers, 50–51
method, 746
Lamina. *See* Ply
Laminated beam bending
airplane fuselage, 445–447
beam deflections, 447
beam dimensions, 447–450
beam problem solutions, 448t
dependencies, 447
I-beam, 448f
layer coordinates, 449f
load terms, 444–445
shear force distributions, 446f
transverse shear deformation, 445
Laminated composite beams and columns, 435
axial loading, 441
beam bending, 441
beam element stress state, 436–437, 436f
beam loaded with surface end forces and moment, 435, 435f
equilibrium equations, 440–441
force distribution, 440
reference plane, 437–439
sandwich beam cross section, 440, 440f
shear correction factor, 440
shear stress, 440
stiffness coefficients
composite tows, 443
homogeneous or quasihomogeneous beams, 442–443
laminated beam with layers, 444f
laminated cross section, 443f
rectangular cross-sections, 442f
shear stress, 443
Laminated composite plates, 487
anisotropic laminated plate theory equations, 487–493
generally laminated plates, 565–580
orthotropic plate equations, 493–495
orthotropic symmetric plate
bending, 519–545
buckling, 545–559
postbuckling behavior, 559–564
plate theory equation analysis, 495–519
Laminates, allowable stresses for
biaxial loading with stresses, 330–331
composite pressure vessel failure mode, 328f
failure envelops
for biaxial loading, 331f
for uniaxial tension and compression, 332f
failure of matrix, 329
four-layered quasi-isotropic carbon-epoxy laminate, 330
laminate loaded with normal and shear stresses, 328f
modern fibrous composites, 331
operational loading parameter calculation, 329–330
progressive failure
CDM, 332
constitutive equations, 333–335
damage development process, 333
damage model, 337–339
nonlinearity and irreversible deformations, 333
nonlinearity or plasticity, 332
numerical analyses, 343–350
numerical implementation, 340–343
plastic damage model, 333
plastic model, 335–336
postfailure behavior, 333
using strength criterion, 327
uniaxial tension with stresses, 331
unidirectional fibrous composite ply, 327–328
Laminates mechanics
antisymmetric laminates, 284
angle-ply structures, 285, 285f, 288
carbon-phenolic cylindrical shells, 288
in composite technology, 286
constitutive equations, 287
coupling stiffness coefficients, 287
cross-ply layer, 284–285, 285f
filament-wound cylinders, 286f
using finite-element models, 288
solid modelling and finite-element analysis, 287–288
T-segment, 286
orthotropic laminates engineering stiffness coefficients, 260–272
quasi-homogeneous laminates, 272
angle-ply layers, 274–275
fiber metal laminates, 275–277
identical homogeneous layers, 272–273
inhomogeneous orthotropic layers, 273–274
quasi-isotropic laminates, 277–284
reference plane coordinate, 292
homogeneous and symmetric structures, 292–294
layer coordinates, 293f

practical analysis, 294–295
pre-assigned stacking-sequences, 294
sandwich structures, 288–291
axial and circumferential strains, 290f
composite sandwich panel with honeycomb core, 290f
composite sandwich rings with foam core, 291f
filament-wound structures, 289t
finite-element models and deformed shapes, 289f
sandwich laminate with two laminated facings, 291f
stiffness coefficients
arbitrary *i*th layer, 255–256
coefficients, 256
homogeneous layer, 254–255
laminate structure, 256f
nonhomogeneous anisotropic layer, 243–254
transverse shear forces, 257
transverse shear stiffnesses, 256–257
stresses in laminates
compatible deformation, 296
constitutive equations, 295
material axes, 295
unidirectional plies, 295–296
symmetric laminates, 257–259
layer coordinates, 258f
maximum bending stiffness, 260
middle plane coordinates, 259f
symmetric and antisymmetric components, 259–260
Laminates optimal design
buckling constraints
bending stiffness, 765
critical load, 765
laminated plates optimal structural parameters, 766t
single-layered plate, 765
strength constraints, 765
Hooke's law, 759
numerical methods, 758
optimization, 758
carbon-epoxy composite material, 761, 762t
layer thickness normalization, 761
ply strength, 760
sandwich laminate, 764
strength constraints, 760–761
structural parameters sorting, 764
thickness dependence, 764f
uniaxial tension, 761
orthotropic laminates, 758
strains, 759–760
stresses, 759
symmetric laminates optimization layers, 760, 760f
Laplace transformation, 383–384
Lattice layer, 230
carbon-epoxy lattice spacecraft, 231f
composite lattice shear web structure, 232f
geometric parameters, 232f
interstage composite lattice structure, 231f
structure formation, 230–231
winding of, 230f
see also Orthogonally reinforced orthotropic layer
Lattice structure, 787f
Lay-up processes, 23
Linear classical shell theory, 706
Linear elastic model, 42–43
angle-ply orthotropic layer, 196–197
angle-ply layer shear modulus, 199
constitutive equations, 196–197
deformation and stresses, 199f
dependencies of carbon-epoxy layer moduli, 198–199, 198f
in-plane shear modulus, 199–200
isotropic layer
Hooke's law, 125–126
three-dimensional stress state, 126–129
linear elastic material, 4
stress-strain diagram, 4f
material model, 132–133
orthogonally reinforced orthotropic layer, 170–172
stiffness coefficients, 172–173
total shear strains, 172–173
total thickness of layer, 170–172
unidirectional anisotropic layer
apparent modulus, 168
carbon-epoxy strip deflection, 168, 168f
compliance coefficients, 156–158
composite dependencies, 164f
constitutive equations, 152–156
coupling stiffness dependencies of, 159f
elastic constants of anisotropic materials relationship, 164
forces and moments effect, 167f
for free tension, 166
in-plane shear modulus, 158–160, 163
invariant stiffness characteristics, 156–158
normalized apparent modulus dependence, 168
normalized strain dependencies, 161f
off-axis tension, 165f
off-axis test, 160f, 165
shear-extension coupling coefficient, 162
stiffness coefficients, 152–156, 158
tensile and shear stiffness dependencies, 159f
transformation for strains, 152–156
unidirectional composites, 163–164
unidirectional layer deformation, 160f, 161
unidirectional orthotropic layer
constitutive equations, 144–147
filament-wound composite pressure vessel, 145f
transverse normal stress, 144–147
transverse shear modulus, 147f, 147t
for unidirectional composites, 147
Linear-viscoelastic material behavior, 377–378
Linearization methods, 138
Load-carrying layers, 479
Longitudinal compression
compatible fiber-matrix deformation, 113f
deformation of fiber, 111f
epoxy composite characteristics, 108t
fiber local buckling in unidirectional ply, 110f
fracture modes, 114–115
microstructural models, 107
shear failure under compression, 108f
shear stress calculation, 107–108
strain concentration factor, 109f
strength of composites under, 115
transverse extension and fiber local buckling, 109f
transverse extension failure mode, 108f
typical ply element, 110f
unidirectional carbon-epoxy composite under, 115f
unidirectional composite strength, 114
see also Transverse compression
Longitudinal tension
characteristics for, 99
strength and stiffness under, 97–98
unidirectional
aramid-epoxy composite material, 99f
carbon-epoxy composite material, 98f
composites, 95–97
glass-epoxy composite material, 97f
see also Transverse tension
Low-cycle fatigue, 398

M

Man-made metal alloys, 14
Manufacturing effects, composite materials, 418
circumferential winding, 418f, 419f
aramid-epoxy unidirectional composites, 420f
carbon-epoxy composite dependence, 423, 423f
direct correlation, 418–420
filament winding, 420
material stiffness reduction, 420
normalized modulus reduction, 422f
ply waviness, 423
regular waviness, 421–422
tape preliminary tension, 420, 421f
shrinkage effects
angle-ply layer, 431–432, 431f
characteristics, 432
glass-epoxy composite, 429–430
material shrinkage, 428
residual strains dependence, 430f
strains, 429
unidirectional circumferential layer, 429f
warping and laminates bending
angle-ply antisymmetric panel, 429f
antisymmetric structure, 427–428
asymmetric laminates, 424
cooling process, 426–427
cross-ply antisymmetric panel, 425f
displacements, 428
in fabrication process, 424
in-plane displacements, 425–426

Manufacturing effects, composite materials (*Continued*)
orthotropic cross-ply laminate, 424–425
polymeric composite panel, 424
symmetric laminates, 424
transverse modulus dependence, 427f
Material aging, 374–375
Materials, 1
Matrix materials, 15, 79–80
boron-aluminum unidirectional composite material, 18–20
carbon tows strength, 16t
carbon-carbon composites, 20–21
ceramic composites, 20
cured epoxy resins with T_g, 18f
matrices, 17
matrix properties, 16–17
normalized longitudinal moduli, 19f
in polymeric composites, 20
polymeric matrices, 17
stiffness of matrix, 15–16
stress-strain curves for aluminum, 19f
tensile strength temperature dependence, 20f
testing of straight tow, 16f
thermo-mechanical curves, 17–18
thermoplastic matrices, 17
typical cured epoxy matrix, 17f
widespread metal matrices, 18
Membrane shell theory
equations, 589
beam reference surface element, 589–590
membrane stress resultants, 590f
long and infinitely long shells, 722
pressure vessels cylindrical parts, 722
shell deflection, 722
strains equations, 722
see also Semi-membrane shell theory
Membrane theory, 690
application, 690
differential equations, 690
see also Semi-membrane theory
Metal fibers, 14
Metal matrix composites, 365–367
Metal-composite laminates, 277f
Micromechanical analysis
actual and admissible states, 93–94
actual stress-strain state, 94–95
applications, 95
comparison, 87
constitutive equation, 86–87
elastic constants, 81
first-order models, 83–85, 84f
higher-order microstructural models, 91
under in-plane loading, 80f
isotropic matrix, 91
longitudinal and transverse strains, 85–86
matrix material specimens, 81f
matrix specimen testing, 82f
mechanical characteristics, 81–82
microcomposite
material, 82–83
specimen gripped at ends, 84f
specimen overwrapped over discs, 83f
normalized in-plane shear modulus, 88f
normalized longitudinal modulus, 87f
normalized transverse modulus on fiber volume fraction, 88f
qualitative analysis, 91–92
second-order models, 89–91, 89f
simplest or zero-order model, 83
structural element, 90f
transverse tension, 92–93
unidirectional composite ply, 80–81
Micromechanics
ply
actual and admissible states, 93–94
actual stress-strain state, 94–95
applications, 95
comparison, 87
constitutive equation, 86–87
elastic constants, 81
first-order models, 83–85, 84f
higher-order microstructural models, 91
under in-plane loading, 80f
isotropic matrix, 91
longitudinal and transverse strains, 85–86
matrix material specimens, 81f
matrix specimen testing, 82f
mechanical characteristics, 81–82
microcomposite material, 82–83
microcomposite specimen gripped at ends, 84f
microcomposite specimen overwrapped over discs, 83f
normalized in-plane shear modulus, 88f
normalized longitudinal modulus, 87f
normalized transverse modulus on fiber volume fraction, 88f
qualitative analysis, 91–92
second-order models, 89–91, 89f
simplest or zero-order model, 83
structural element, 90f
transverse tension, 92–93
unidirectional composite ply, 80–81
unidirectional composite ply, 80–81
actual and admissible states, 93–94
actual stress-strain state, 94–95
applications, 95
comparison, 87
constitutive equation, 86–87
elastic constants, 81
first-order models, 83–85, 84f
higher-order microstructural models, 91
under in-plane loading, 80f
isotropic matrix, 91
longitudinal and transverse strains, 85–86
matrix material specimens, 81f
matrix specimen testing, 82f
mechanical characteristics, 81–82
microcomposite material, 82–83
microcomposite specimen gripped at ends, 84f
microcomposite specimen overwrapped over discs, 83f
normalized in-plane shear modulus, 88f
normalized longitudinal modulus, 87f
normalized transverse modulus on fiber volume fraction, 88f
qualitative analysis, 91–92
second-order models, 89–91, 89f
simplest or zero-order model, 83
structural element, 90f
transverse tension, 92–93
Microphenomenological approach, 300
Modern composite materials, 585
Modern high-modulus carbon fibers, 11
Moisture absorption, 368–370
Moisture diffusion, 368–370
Monotropic model, 772
Multi-cell cross-sectional contour
augmented functional minimization, 655
auxiliary functions, 653–654, 654f
beams with, 652–653, 652f
coordinate of beam, 657
features of, 653–654
function, 654f
Lagrange's multiplier, 655
membrane stiffness characteristics, 652–653
moment equation, 656–657
normalized axial stress resultant distribution, 653f
reduction of, 653f, 654–655
shear center of beam, 656–657, 656f
shear stress resultant distribution, 656f
see also Open cross-sectional contours; Thin-walled composite beams
Mushtary-Donnell-Vlasov theory, 689

N

Natural fibers, 14
mechanical properties, 14t
Newton flow law, 380–381
Newton's method, 139f, 140
Nonhomogeneous anisotropic layer, 243–244
stiffness coefficients
actual and approximate distributions, 248f
arbitrary point coordinates, 253f
basic deformations, 245f
coefficients with subscripts, 247
conjunction with Hooke's law, 247–248
constitutive equations, 246, 250–251
displacement decomposition, 244f
element, 243f
using energy method, 251–252
using equations, 253–254
in-plane displacements, 244
in-plane strains, 244–245
minimum strain energy, 252–253
normal deflection, 244
stress resultants and couples, 246–247, 246f
for transverse shear, 248–251
transverse shear of strip with unit width, 251f
transverse shear stresses to stress resultants, 249f
see also Homogeneous layer
Nonlinear bending
beam axis curved element, 451f
beam deflection, 450–454

beam deflection under eccentric tension, 456f
bending and bending-stretching beam, 451f
imaginary pressure, 452f
laminated beam eccentric tension, 454–455, 455f
maximum deflection dependencies, 454f
maximum stress
dependencies, 455f
normalization, 454
rotation angle and bending moment, 455–456
Nonlinear classical theory, 707
Nonlinear elastic models, 129, 147–148
aluminum alloy
plastic Poisson's ratio dependency, 137f
secant modulus dependency, 137f
stress-strain diagram for, 136f
tangent modulus dependency, 137f
angle-ply orthotropic layer, 200
algebraic equations, 203–205
angle after deformation, 203–205
angle-ply layer stress-strain diagrams, 206f, 207f
angle-ply specimen failure mode, 210f
angle-ply two-matrix composite stress-strain diagrams, 201f
carbon-epoxy layer stress-strain diagrams, 209f, 210f, 211f
curved angle-ply pipe, 207f
dependencies of normalized stresses, 209f
equilibrium equations, 205
global coordinate frame, 203–205
linear element, 202f
longitudinal strain simplification, 205–206
manufacturing process, 206–207
material nonlinearity, 200–202
matrix cracking effect, 207–208
stress and ply orientation angle dependencies, 212f
stress-strain diagrams for transverse tension, 208f
transverse normal stress, 209–211
two-matrix glass-epoxy composite, 200
uniaxial tension problem, 205–206
Cartesian coordinate frame, 143–144
Castigliano's formulae, 129–132
complementary elastic potential, 129–132, 131f
deformation theory of plasticity, 133–134
constitutive equations of, 137–138, 141, 143–144
increments of plastic strains, 142–143
plastic potential, 134–135
plastic strains, 133–134
successive loading method, 141
uniaxial tension, 135–137
uses, 144
elastic potential, 131f, 133–134
elastic solution method, 138, 139f
linear elastic material model, 132–133
linearization methods, 138
loading path in stress space, 143f
material model, 4
Newton's method, 139f, 140
nonlinear stress-strain diagram, 132–133
orthogonally reinforced orthotropic layer, 173
boundary and interface conditions, 176–178
carbon-epoxy cylindrical pressure vessel, 184–185
circumferential strain dependence, 186–187, 187f
composite pressure vessel element, 185f
crack system in transverse ply, 179, 179f
cracks in circumferential layer, 176f
cross-ply laminate tension, 174, 174f
elastic constants, 185–186
expressions for stresses, 176–178, 180
failure in transverse, 175
glass-epoxy sandwich layer, 176–178, 182f
minimum strain energy, 176–178
normalized normal stress variation, 179f
normalized shear distribution, 181f
normalized stress distribution, 180f
stiffness coefficients, 185–186
strain calculation, 186
strain determination procedure, 183–184
strains and stresses in plies, 185–186
stress decomposition, 175–176
total stresses, 186
transverse normal stress distribution, 181f
transverse ply stress-strain diagram, 182f
ultimate stresses, 175t
unidirectional ply stress-strain diagrams, 183–184, 183f
polymeric materials, 129
proportional loading, 143–144
strain intensity, 133–134, 141–142
stress-strain curve
approximation, 131f
for polymeric film, 130f
successive loading method, 139f, 140–141
Taylor series, 132
uniaxial tension, 142–143
unidirectional anisotropic layer, 169
stress-strain diagram, 170f, 171f
two-matrix fiberglass composite, 169
unidirectional orthotropic layer
boron-aluminum unidirectional composite, 151, 152f
independent uniaxial loading, 151
material behavior under elementary loading, 148
nonlinear behavior in composite materials, 150
notations for stresses and strains, 151
pronounced nonlinear elastic behavior, 148–149
sixth-order approximation, 148–149
strain decomposition, 150–151
two-matrix unidirectional composite, 150f
for unidirectional composites, 148–149
variable elasticity parameter method, 139–140, 139f
see also Isotropic layer
Nonlinear membrane theory, 690, 707
Nonlinear theory, 689–690
Nonsymmetric buckling mode
arbitrary boundary conditions, 735
Cartesian rule, 734
coefficient dependence on length factor, 735, 736f
critical load, 737
decomposition, 734
displacements, 735–736
elastic constants symmetry condition, 735
engineering shell theory, 732–733
homogeneous shell, 734–735
real and positive numbers, 734
shear modulus, 735
shell buckling equation, 732–733
see also Axisymmetric buckling mode
Numerical integration algorithms, 340
closest point return mapping algorithm, 340
computational procedure
damage corrector, 343
elastic predictor, 342
initial conditions, 342
plastic corrector, 342–343
user subroutine UMAT, 344f
user-defined materials, 342–343
consistent tangent stiffness matrix, 341
damage variable, 340
nonlinear system, 340
stress-strain relationship, 340
viscous regularization scheme, 341

O

Open cross-sectional contours
beams with, 657
restrained torsion of beams, 677–679
axial displacement, 680
axial normal stress resultant, 679
axial strain, 679
bending stiffness, 677–679
cantilever circular beam, 681, 681f
circular cross section, 682
equation for angle of twist, 681
expression for axial displacement, 680
normal and shear stress resultant, 678f
normalized axial stress resultants, 682f
normalized shear stress resultants, 682f
normalized torsional stiffness dependence, 678f
sectorial characteristics, 679
shear stress resultant, 680
torsional stiffnesses, 682–683
total torque, 680–681
thin-walled beam with, 658f
transverse bending, 657
beam displacements, 660
with C-shaped beam, 658–659, 659f
model beam deformations, 660, 661f
shear center of beam, 658
shear center of circular cross section, 660–662, 662f
shear stress resultant, 657, 660

Optimal composite structures, 745
  application, 766
  composite materials, 745
  laminates optimal design, 758
  optimal fibrous structures, 745
  uniform strength composite laminates, 752–753
Optimal fibrous structures
  cross-ply and angle-ply laminate, 748–749, 749f
  cylindrical pressure vessel, 749
  helical plies, 750
  high specific strength, 748
  Lagrange multipliers method, 746
  laminate in-plane shear, 751–752
  laminated plate, 746f
  metal pressure vessel thickness, 749, 750t
  optimal laminate, 747
  optimal plate total thickness, 747
  optimal thickness ratios, 751f
  optimality conditions, 747
  strain, 746
  structural parameters, 748
  tension in orthogonal directions, 748
  uniaxial tension, 748
  unidirectional composite monotropic model, 745
  uniform biaxial tension, 748
Optimal shell, 768
  meridian, 769
  stresses expressions, 769
Organic fibers, 12
Orthogonally reinforced orthotropic layer, 169–170
  composites with controlled cracks, 191–193
    carbon-epoxy composite, 193–196
    dependencies of coefficients, 194f
    expression for stress in transverse ply, 193–196
    function dependencies, 195f
    relative transverse ply thickness function, 195f
  cross-ply layer, 171f
    with crack in transverse ply, 176f
    nonlinear phenomenological model, 182–183
    in plane stress state, 183f
    stress-strain diagram of, 181–182
    transverse shear of, 173f
  linear elastic model, 170–172
    stiffness coefficients, 172–173
    total shear strains, 172–173
    total thickness of layer, 170–172
  nonlinear elastic models, 173
    boundary and interface conditions, 176–178
    carbon-epoxy cylindrical pressure vessel, 184–185
    circumferential strain dependence, 186–187, 187f
    composite pressure vessel element, 185f
    crack system in transverse ply, 179, 179f
    cracks in circumferential layer, 176f
    cross-ply laminate tension, 174, 174f
    elastic constants, 185–186
    expressions for stresses, 176–178, 180
    failure in transverse, 175
    glass-epoxy sandwich layer, 176–178, 182f
    minimum strain energy, 176–178
    normalized normal stress variation, 179f
    normalized shear distribution, 181f
    normalized stress distribution, 180f
    stiffness coefficients, 185–186
    strain calculation, 186
    strain determination procedure, 183–184
    strains and stresses in plies, 185–186
    stress decomposition, 175–176
    total stresses, 186
    transverse normal stress distribution, 181f
    transverse ply stress-strain diagram, 182f
    ultimate stresses, 175t
    unidirectional ply stress-strain diagrams, 183–184, 183f
  two-matrix composites, 187
    acoustic emission intensity, 192f
    composite fiber properties, 188
    composite fibers of, 191
    conventional cross-ply glass-epoxy layer, 191, 192f
    glass-epoxy unidirectional composite properties, 191t
    longitudinal strength dependency, 189f
    mechanical characteristics, 190–191
    microstructure of, 190f
    solutions to analysis problem, 187–188
    stress-strain curves for epoxy matrices, 188f
    stress-strain curves for transverse tension, 189f
    stress-strain diagram of deformable epoxy matrix, 190f
    synthesizing composite materials, 188
    two-matrix cross-ply glass-epoxy layer, 191, 192f
  see also Spatially reinforced layers
Orthotropic cross-ply laminate, 424–425
Orthotropic laminates
  stiffness coefficients, 260
    bending-stretching coupling effects, 262–263
    constitutive equations, 269–272
    cross-section, 262f
    element under torsion deformation, 265f
    using equation, 261
    forces and moments, 261–262
    forces and moments acting, 271f
    laminate membrane and bending, 272
    laminated element under tension, 261f
    laminated strip torsion, 269f
    reference plane, 264
    sandwich structures, 266–267, 266f, 267t
    shear and torsion, 263–264, 263f
    shear stiffness coefficient, 267–269
    strip cross-section, 270f
    tension and bending, 260f
    transverse shear deformation effects, 267–269, 269t
    transverse shear forces, 265–266, 265f
  see also Quasi-homogeneous laminates
Orthotropic layers, 299, 360–361
  composite laminates, 300
  failure surface, 300f
  in plane stressed state, 299f
Orthotropic plate equations, 493
  coupling stiffness coefficients, 494
  maximum bending stiffness, 493
  nonsymmetric plates, 493
  using operational method, 494–495
  symmetric plates, 493
Orthotropic symmetric plate bending
  classical plate theory
    approximate solutions for, 534–537
    clamped plates, 526–534
    exact solutions of, 519
    neglecting transverse shear deformation, 519–520
    simply supported plates, 520–526
  shear deformable orthotropic symmetric plates, 537–538
    algebraic equations for coefficients, 540–542
    approximate analytical solutions, 538–540
    approximate method, 543–545
    boundary-layer solution, 539–540
    coordinate functions for plates, 542t
    equations for infinitely long orthotropic plates, 543t
    using long plates, 542–543
    normalized maximum deflection dependency, 544f
    ordinary differential equation, 538
    penetrating solution, 539–540
    rotation angles and deflection, 537–538
    simply supported rectangular plate, 543
    square and close-to-square plates, 540–542
Orthotropic symmetric plate buckling
  classical plate theory
    algebraic equations for coefficients, 550–551
    anisotropic plates, 553–554
    approximate minimum condition, 548–549
    approximate solutions, 556
    biaxial stress state, 549–550
    buckling analysis results, 554
    buckling and failure modes, 552f
    buckling equation for orthotropic plates, 545–547
    buckling mode of plate, 546f
    carbon-epoxy plates, 551–553
    composite plates, 554, 554f
    compression and shear action, 550–551
    critical loads, 545–547, 550t
    critical shear force, 551
    deformed element of plate reference surface, 546f
    imaginary pressure, 547f

minimum value of coefficient, 547–548, 548f
normalized compressive force dependencies, 555f
normalized critical load dependencies, 549–550, 550f
normalized shear force dependencies, 555f
plate loaded with in-plane loads, 545f
shear buckling coefficient dependencies, 552f, 553f
uniaxial compression, 547–548
shear deformable plate theory, 556
buckling equation, 556–559
normalized critical force dependency, 557–558, 559f
orthotropic plates, 557
transversely isotropic plates, 556–558
for unidirectional compression, 557–558
see also Transversely isotropic plates
Orthotropic symmetric plate postbuckling behavior, 559–563
critical load dependency, 563f
dimensionless functions, 559–563
dimensionless loads, 562f
half-wave number, 563
mode jumping, 559–563
normal stress distributions, 564f
numerical analysis of post-buckling behavior, 564
plate shortening dependencies, 564f
simply supported plate after buckling, 560f
stresses and displacements evaluation, 564
ultimate load dependency, 563f

P

PAN. *See* Polyacrylonitrile
PAN-based fibers, 11–12
Phenomenological homogeneous model
actual material behavior prediction, 122
biaxial compression, 122f
first-order micromechanical model, 122
ply, 122
stresses acting in fibers and matrix, 123
Phenomenological theory, 30
Pitch-based carbon fibers, 11–12
Plane laminated structure, 22–23
Plastic damage model, 333
Plastic model
equivalent stress, 335–336
internal forces, 335
isotropic hardening law, 336
one-parameter plastic potential, 335
plastic strain rate, 336
plastic yield function, 335
Plate theory
anisotropic laminated plates, 487
classical plate theory, 496–502
equations analysis, 494–495
shear deformable plate theory, 502–519
Ply, 53
architecture
actual fiber distribution, 54f
carbon-epoxy composite material, 56
composite ply, 53–55
fibers and matrix, 56
hexagonal fiber distribution, 55f
layer-wise fiber distribution, 55f
square fiber distribution, 54f
strength and stiffness, 56
tape, 53
ultimate fiber arrays, 56–57, 57f
unidirectional ply, 53f
composite, 53–55
mechanical properties, 95
in-plane shear, 104–107
longitudinal compression, 107–115
longitudinal tension, 95–99
transverse compression, 115
transverse tension, 99–103
micromechanics
actual and admissible states, 93–94
actual stress-strain state, 94–95
applications, 95
comparison, 87
constitutive equation, 86–87
elastic constants, 81
first-order models, 83–85, 84f
higher-order microstructural models, 91
under in-plane loading, 80f
isotropic matrix, 91
longitudinal and transverse strains, 85–86
matrix material specimens, 81f
matrix specimen testing, 82f
mechanical characteristics, 81–82
microcomposite material, 82–83
microcomposite specimen gripped at ends, 84f
microcomposite specimen overwrapped over discs, 83f
normalized in-plane shear modulus, 88f
normalized longitudinal modulus, 87f
normalized transverse modulus on fiber volume fraction, 88f
qualitative analysis, 91–92
second-order models, 89–91, 89f
simplest or zero-order model, 83
structural element, 90f
transverse tension, 92–93
unidirectional composite ply, 80–81
tape, 53
unidirectional, 53f
Poisson's effect, 384–385
Polyacrylonitrile (PAN), 11–12
Polyethylene fibers, 12
Polymeric composites, 353
Polymeric matrices, 17, 376–377
Potential energy, 3–4
Prepreg process, 21
Principal damage model, 346–348
Principal material axes, 299
Progressive failure modeling and analysis
CDM, 332
constitutive equations
compression and tension effects, 334–335
damaged and undamaged composite materials, 334
elastic and plastic strain parts, 334
fiber-reinforced composite materials, 333–334
irreversible deformations, 335
shear stiffness reduction, 335
damage development process, 333
damage model
damage evolution, 338–339
damage initiation criteria, 337
propagation criteria, 337
nonlinearity and irreversible deformations, 333
nonlinearity or plasticity, 332
numerical analyses, 343
AS4/PEEK $(\pm 45^\circ)_{2s}$ composite laminates, 349–350, 350f
composite laminates with through holes, 343–348
geometry and boundary conditions, 345f
numerical implementation, 340
computational procedure, 342–343
consistent tangent stiffness matrix, 341
integration algorithm, 340
viscous regularization, 341–342
plastic damage model, 333
plastic model
equivalent stress, 335–336
internal forces, 335
isotropic hardening law, 336
one-parameter plastic potential, 335
plastic strain rate, 336
plastic yield function, 335
postfailure behavior, 333
Projectile velocity, 415–416
Pyrolysis, 11–12

Q

Quartz fibers, 10
Quasi-homogeneous laminates, 272
angle-ply layers, 274–275
fiber metal laminates, 275
carbon-epoxy laminate, 275f
GLARE aircraft skin of variable thickness, 276f
metal-composite laminate, 276–277, 277f
metals and composites, 275
shortcomings, 276
identical homogeneous layers, 272–273
inhomogeneous orthotropic layers
coupling coefficients, 274
elementary cross-ply couples, 273
membrane stiffnesses, 273
Quasi-isotropic laminates, 277–278
angles properties, 279t
carbon and boron fibers, 280
under compression, 283–284
elasticity and Poisson's ratio modulus, 280t
experimental stress-strain diagram, 280–282, 281f
modern composite airplanes, 284
in plane stress state, 278–279
principal ply directions, 280–282
stiffness coefficients and elastic constants, 283

Quasi-isotropic laminates (*Continued*)
stiffness coefficients calculations, 278–279
theoretical stress-strain diagram, 282
unidirectional plies, 280

R

Rectangular cross section, beam with, 606, 607f, 610f, 630, 631f
angle of twist dependencies, 634–635, 635f
axial stress resultant, 610
beam displacements, 612
beam stiffnesses, 613
composite thin-walled beam, 617f
cross-sectional contour in regular polygon, 617f
decomposing beam contour, 610
deflection slope dependency, 614f
distribution of function, 611, 611f, 612f
distributions of integrals, 615f
expressions for deflection, 612–613
function for, 630, 632–633
loaded by transverse force and torque, 613f
material structure, 630, 633f
shear stress resultant components, 611
square cross section, 616
stiffness coefficients, 610, 617, 633–634, 634t
surface development, 633f
torsional stiffness, 613
twist angle dependency, 614f
warping function, 614–616
Reference plane, 243–244
coordinate, 292
homogeneous and symmetric structures, 292–294
layer coordinates, 293f
practical analysis, 294–295
pre-assigned stacking-sequences, 294
Reinforced materials, 9
Relative humidity (RH), 368–370
Resin infusion process (RI process), 26
Resin transfer molding (RTM), 26
Restrained bending, 645, 650
bimoment, 650–651
normal shear resultants, 651
normal stress resultants, 651, 652f
Restrained torsion, 645
axial displacement, 680
axial normal stress resultant, 679
axial strain, 679
of beams, 677–679
bending stiffness, 677–679
bimoment, 647
of cantilever beam, 646f
cantilever circular beam, 681, 681f
circular cross section, 682
constant of integration, 647
equation for angle of twist, 681
expression for axial displacement, 680
normal and shear stress resultant, 678f
normalized axial stress resultants, 682f
normalized normal stress resultants, 649, 649f, 650f
normalized shear stress resultants, 649, 649f, 682f
normalized torsional stiffness dependence, 678f
normalized warping function, 647
restrained warping, 646
sectorial characteristics, 679
shear center of beam, 646
shear stress resultants, 647, 680
strain energy of beam, 648
stress resultants, 648
torsional stiffnesses, 682–683
total torque, 680–681
warping function, 645–646
RH. *See* Relative humidity
RI process. *See* Resin infusion process
Rotations. *See* Angles of rotations
Roving. *See* Unidirectional tow
RTM. *See* Resin transfer molding

S

Sandwich beam
free-body diagrams, 482f
maximum deflections, 484–485, 484t
Sandwich structures, 266–267, 288–291
axial and circumferential strains, 290f
composite sandwich
panel with honeycomb core, 290f
rings with foam core, 291f
filament-wound structures, 289t
finite-element models and deformed shapes, 289f
parameters, 267t
sandwich laminate with two laminated facings, 291f
three-layered and two-layered laminates, 266f
Secant, 4
Second-order models, 89–91, 89f
Second-order tensor criterion, 315
Semi-membrane shell theory
axial displacement, 720
cantilever cylindrical shell, 720–721, 721f
closed shells, 718
constants of integration, 720
first equilibrium equation, 719
ordinary differential equations, 718, 722
shear deformable shells, 717, 720
shell beam-type bending, 722
shell bending, 720
shell stress-strain state, 721
see also Membrane shell theory
Semi-membrane theory, 690–691
applications, 691
cross-sectional contour, 691
equations, 691
physical model, 690f
see also Membrane theory
Shear center, 617–618
coordinates of, 618–620
cross section, 618f
displacements, 619
forces, 618
shear deformations, 620
Shear deformable orthotropic symmetric plates, 537–538
algebraic equations for coefficients, 540–542
approximate analytical solutions, 538–540
approximate method, 543–545
boundary-layer solution, 539–540
coordinate functions for plates, 542t
equations for infinitely long orthotropic plates, 543t
using long plates, 542–543
normalized maximum deflection dependency, 544f
ordinary differential equation, 538
penetrating solution, 539–540
rotation angles and deflection, 537–538
simply supported rectangular plate, 543
square and close-to-square plates, 540–542
Shear deformable plate theory, 502, 556
bending moment
dependency, 518f
distribution, 514f
boundary conditions, 505–507
buckling equation, 556–559
clamped plate, 511
concentrated corner force, 509–511
cylindrical bending of plate, 512
equations, 503–504
for relatively thin plates, 509–511
for transverse shear force, 504–505
normalized critical force dependency, 557–558, 559f
normalized deflection dependency, 518f
orthotropic plates, 557
penetrating solution, 502–503, 507–509
physical interpretation, 505–506
plate behavior, 511
plate deflection
exact solutions for, 517
penetrating solution, 517
solution to classical plate theory, 517
plate supported at edge, 513–515
plate with clamped edge, 515–517
rotation angles of plate element, 504–505
rotational potential, 503–505
semi-infinite plate, 512, 512f
shear deformation, 518–519
shear forces distribution, 513–515, 516f
sixth-order plate theory, 519
square plate with cosine pressure, 507–509, 507f
transverse shear deformation effect, 519
transverse shear force
distribution of, 510f
expression for, 509–511
transversely isotropic plates, 556–558
twisting moments distribution, 515f
for unidirectional compression, 557–558
Shear deformable shell theory
coupling coefficients, 724–725
linear theory, 706

radial force concentration, 724f
sandwich shells analysis, 722–723
shell maximum deflection dependence, 725f
stiffness and compliance coefficients, 723
stress function, 723
trigonometric series form, 723–724
Shear deformable unsymmetrically laminated plates, 576
constitutive equations for orthotropic plates, 576–579
equilibrium equations, 576–579
for simply supported plate, 579–580
strain-displacements equations, 576–579
Shear strain resultant, 597–598, 600
Bredt equation, 600
Shear stress resultant, 597–598
area bounded by contour, 599, 599f
contour coordinate value, 597–598
decomposition, 597f
elementary cross-sectional area, 599, 599f
equilibrium equation, 598–599
expression for, 599
static equations, 598
Shell meridian, 767
parametric equation, 770
tangent line, 770
Shell theories, 686
cylindrical shell loading, 688f
equilibrium equations, 688
membrane theory, 690
nonlinear theory, 689–690
reference surface, 689
semi-membrane theory, 690–691
stress resultants and couples, 688–689, 688f
see also Classical shell theory
Shrinkage effects
angle-ply layer, 431–432, 431f
characteristics, 432
glass-epoxy composite, 429–430
material shrinkage, 428
residual strains dependence, 430f
strains, 429
unidirectional circumferential layer, 429f
Silicon carbide (SiC), 13
fibers, 13
Simply supported beam, 465f
Simply supported plates, 520–521, 520f
close-to-square rectangular plate, 521f
convergence of series, 521–522
long rectangular plate, 521f, 522
at opposite edges, 522–524
boundary conditions, 525–526
with clamped transverse edges, 525f
with longitudinal edges, 525f
normalized deflection dependency, 522f
orthotropic plates, 524–525
rectangular plate with, 523f
solutions of differential equation, 524t, 525
Simply supported shells
boundary conditions, 739
critical load, 740
critical pressure, 739
transverse shear deformation, 739–740
Solid mechanics, 29, 40
Cartesian coordinate frame, 38
compatibility equations, 39–40
strain-displacement equations, 39
constitutive equations
additional displacements, 40–41
additional strains, 40
compliance matrix, 44–45
elastic material, 42
finite expression, 44
internal variables, 41–42
linear elastic model, 42–43
orthotropic material, 45–46
simplest material model, 45–46
specific strain energy, 45–46
displacements and strains
coordinate component displacements, 35
displacement of infinitesimal linear element, 35–38, 36f
linear strain-displacement equations, 35–38
equilibrium equations
differential equilibrium equations, 31–32
forces on elementary tetrahedron, 31–32, 31f
integral equation, 32
integral equilibrium equations, 31–32
in tetrahedron, 31
kinematic field, 40
principal stresses, 34–35
linear algebraic equations, 34
under shear, 35, 35f
stress transformations, 34
problem formulations, 46–47
small strain transformation, 38
static field, 40
stress transformation
rotation of coordinate frame, 32–33, 33f
shear stress, 33
stresses
Cartesian coordinates, 29–30, 29f
phenomenological theory, 30
on planes, 30, 30f
variational principles
kinematically admissible field, 47–48
minimum strain energy principle, 49–50
minimum total potential energy principle, 48–49
mixed variational principles, 50–51
statically admissible stress field, 47–48
Space telescope, 357–358, 357f, 364
angle-ply carbon-epoxy external skin, 357
carbon-epoxy lattice layer, 357
internal skin
aluminum foil, 358
aramid fabric, 358
Spatial structure, 22, 25–26
4D spatial structure, 26f
Spatially reinforced layers, 232
coefficients for compliance matrix, 235–240
elastic constant dependencies, 240f
formation by bulk materials, 233
formation by unidirectional composite material, 235–240
global structural coordinate frame, 236f
multi-dimensional
composite structure properties, 235
reinforced materials, 233f
orientation angles in spatial composite structure, 239f
for planar structures, 240
spatially reinforced structure
4D, 234f
5D, 235f
3D, 234f
stiffness matrix, 235–240
three-point bending test, 236f
triaxial reinforcement, 233
see also Unidirectional anisotropic layer
Spatially reinforced structure
4D, 26f, 234f
5D, 235f
3D, 234f
Spinning composite disks, 780f
angular velocity, 782
boundary conditions, 781
carbon-epoxy flywheel, 783, 784f
differential equation, 782
disk element, 780–781, 781f
fiber angle, 781–782
fiber patterns, 783, 783f
fibers optimal trajectories, 779
linear circumferential velocity, 784–785, 785t
maximum kinetic energy, 784
small central openings, 782
tape element in Cartesian and polar coordinate frames, 782, 783f
winding patterns, 784
Stiffness degradation, 400, 400f
Strain energy. *See* Potential energy
Strength analysis, 299–300
Stress diffusion in fibers interaction
analytical solution, 73–74
carbon-epoxy ply with parameters, 74
composite bundles, 65
strength, 65t
constitutive equations, 68
dry bundle strength, 65t
equilibrium equations, 66
geometric interpretation, 70f
matrix stiffness, 66
normal stresses distribution, 74f, 75f, 76f
perturbation, 68
qualitative results, 76–78
shear and normal stresses, 71–72
shear strain in matrix layer, 68f
shear stress distribution, 76f, 77f
using single-fiber fragmentation test, 75
stresses acting in fibers and matrix layers, 67f
transform equilibrium equations, 68–71
unidirectional glass-epoxy composites, 75
unidirectional ply with broken fiber, 66f
variation coefficient, 66t

Stress relaxation, 381–382, 382f
Stress-strain curves, 3f
  of deformable epoxy matrix, 190f
  elastic material, 3–4
  for elastic-plastic material, 7f
  for epoxy matrices, 188f
  for fiberglass fabric composite, 227f
  for fiberglass knitted composites, 228f
  linear elastic material, 4, 4f
  for transverse tension, 189f
Structural materials, 1
  aramid-epoxy composite material, 8
  bar under tension, 2, 2f
  constitutive equation, 7–8
  dependence of force, 8–9, 8f
  elastic-plastic material model, 6
  high stiffness, 1
  Hooke's law, 4
  lack of material strength, 1
  material stiffness and strength, 1–2
  mechanical characteristics, 4
  mechanical properties, 5t
  nonlinear elastic material model, 4
  secant and tangent moduli, 7f
  specific modulus, 4
  specific strength, 2
  stress and strain interrelation, 2
  stress-strain curve, 3f
    elastic material, 3–4
    for elastic-plastic material, 7f
    linear elastic material, 4, 4f
  structure's design, 1
  time-sensitive material, 7
  see also Composite materials
Successive loading method, 139f, 140–141
Symmetric laminates, 257–259
  layer coordinates, 258f
  maximum bending stiffness, 260
  middle plane coordinates, 259f
  symmetric and antisymmetric components, 259–260
  see also Antisymmetric laminates; Orthotropic laminates

T

Taylor series, 132
Temperature effects, 353
  polymeric composites, 353
  thermal conductivity
    composite materials coefficients, 356t
    heat flow, 353–354, 356f
    heat transfer, 355
    orthotropic ply, 355–357
    space telescope, 357–358
    temperature distribution in laminate, 354f
    unidirectional composite ply, 355
  thermoelasticity
    constitutive equations, 362
    high-modulus carbon-epoxy composite, 359–360
    layers stiffness coefficients, 364
    layers thermal coefficients, 365–367
    orthotropic layer, 360–361
    temperature distribution, 358
    temperature strains, 358
    temperature variation, 363–364
    thermal expansion coefficients, 361–362, 361f, 363f
    thermal strains dependencies, 366f
    thermoelastic behavior, 359
  see also Hygrothermal effects
Tensor strength criteria, 313–315
  invariant strength criteria, 315
  orthotropic material, 313f
  pure shear in coordinates, 315–317, 316f
  second and fourth rank strength tensors, 319–320
  second-order tensor criterion, 315
  tensor-polynomial strength criteria, 320
  transformation matrix form, 317–319
Tensor-polynomial strength criteria, 320
T_g. *See* Glass transition temperature
Thermal conductivity
  composite materials coefficients, 356t
  heat flow, 353–354, 356f
  heat transfer, 355
  orthotropic ply, 355–357
  space telescope, 357–358
  temperature distribution in laminate, 354f
  unidirectional composite ply, 355
Thermoelasticity
  constitutive equations, 362
  high-modulus carbon-epoxy composite, 359–360
  layer stiffness coefficients, 364
  layer thermal coefficients, 365–367
  orthotropic layer, 360–361
  stiffness and strength dependencies
    unidirectional carbon-epoxy composites, 367f
    unidirectional glass-polypropylene composites, 368f
  temperature distribution, 358
  temperature strains, 358
  temperature variation, 363–364
  thermal expansion coefficients, 361–362, 361f, 363f
  thermal strain dependencies, 366f
  thermoelastic behavior, 359
Thermoplastic matrices, 17–18
Thermoset
  epoxy matrices, 17–18
  polymers, 17
Thermostable structures, 116
Thin nonhomogeneous layer, 243–244
Thin-walled composite beams, 585
  beam cross section geometry, 587–588
    arbitrary point of contour, 588
    contour arc element, 589f
    contour curvature, 588
    cross-sectional contour, 587–588
    elementary arc, 589
    normal and contour coordinates, 587f
    radial and tangent of contour, 588f
  behavior and analysis classification, 585
  with circular closed cross-sectional contours, 585f
  composite beam theory assumptions
    axial stiffness reduction, 592–593
    contour point displacements, 590–591, 590f
    displacements by cross section rotation, 591f
    equilibrium and constitutive equation simplification, 592
    reducing shell theory 2D equations, 593
  composite thin-walled C-shaped beam, 586f
  cross-sectional warping, 585–586
  free and restrained torsion, 587f
  with hexagonal cross section, 617f
  membrane shell theory equations, 589
    beam reference surface element, 589–590
    membrane stress resultants, 590f
  with multi-cell cross-sectional contour, 586f
  with polygonal closed cross-sectional contours, 585f
Third-order theory, 467–468, 470–471
Three-point bending test, 236f
TIGR. *See* Titanium and graphite fibers
Time-dependent loading effects
  cyclic loading
    anisotropic materials, 396
    aramid-epoxy composite temperature, 395f
    carbon-epoxy composites fatigue strength, 397f
    cyclic bending, 397–398
    cyclic tension, 396
    dissipation factor, 394, 395f
    energy dissipation in conjunction, 394
    fabric composites, 398, 399f
    glass-fabric-epoxy-phenolic composite elastic modulus, 399, 400f
    low-cycle fatigue, 398, 399f
    material strength, 396
    stiffness degradation, 400
    stress acting, 392–394
    stress concentration, 394, 396f
    viscoelastic and elastic materials, 393f
  durability
    curves approximation, 389–390, 390f
    long-term strength, 390
    material damage accumulation, 388–389
    material lifetime dependencies, 391, 392f
    predicted and experimental lifetimes, 392t
    tensile strength, 391
  impact loading
    aluminum layers, 414
    aramid fabrics, 417–418
    ballistic limit, 415t, 416
    carbon-epoxy plates, 405f
    clamping fixture for compression test, 403f
    composite airframe structure, 401, 401f
    composite panel, 402f
    compression strength dependence, 408, 408f
    delamination, 409
    delamination area, 403, 404f

delamination energy dependencies, 406f
drop-weight mass, 407
energy dissipation, 407
extrapolation, 403
fabric membrane, 416
flying projectile, 414–415
force-deflection diagrams, 416f
homogeneous layer, 410–411
impact test, 414f, 415f
impactor and plate interaction, 407f
interlaminar conditions, 412
interlaminar stress dependence, 412, 412f
kinetic energy, 401–403
laminate under impact load, 410f
laminates structure, 413f
load *vs*. plate shortening under compression, 409f
load-carrying structures, 404–406
material delamination, 409–410
normal stress, 413f
projectile velocity, 415–416
quasi-static test, 416
residual velocity dependence, 416–417, 417f
steel impactor and hail ice, 406, 406t
steel impactor energy, 406
stress-strain diagrams, 411–412
surface layers local buckling, 409f
tensile and compressive waves, 411f
thin fabric skin damage, 405f
thin-walled composite laminates, 401
wave interaction, 412–414
viscoelasticity
aging theory, 387
aramid-epoxy composite, 377f
circumferential strain dependence on time, 389f
creep compliance, 378–379, 379f, 387
elastic viscoelastic analogy, 386
exponential approximation, 379–380
Laplace transformation, 383–384, 386–387
linear-viscoelastic material behavior, 377–378
material axes, 384–385
material creep, 381, 382f
nonlinear hereditary theory, 388
normalized shear strain, 386, 387f
one-term exponential approximation, 382–383
polymeric fibers, 388
polymeric matrices, 376–377
relaxation modulus, 378
stress relaxation, 381–382
three-element mechanical model, 380–381, 380f
unidirectional glass-epoxy composite, 380f
Titanium and graphite fibers (TIGR), 275
Transcendental equation, 450–454
Transverse bending, 657
beam displacements, 660
with C-shaped beam, 658–659, 659f
model beam deformations, 660, 661f
shear center
of beam, 658
of circular cross section, 660–662, 662f
shear stress resultant, 657, 660
Transverse compression
failure under, 115f
strength, 115
see also Longitudinal compression
Transverse tension
composite ring on eight-sector test fixture, 102f
failure modes, 103f
mandrel for test rings, 101f
material failure under, 99–100
material strength on fiber volume fraction, 104f
normalized longitudinal strength on fiber volume fraction, 101f
polymeric and metal matrices, 102–103
qualitative analysis, 100–102
strength and stiffness under, 103
two-, four-, and eight-sector test fixtures, 102f
unidirectional boron-epoxy composite material, 100f
see also Longitudinal tension
Transversely isotropic plates
orthotropic symmetric plate bending, 519–545, 520f
plate theory
classical plate theory, 496–502
equations analysis, 494–495
shear deformable plate theory, 502–519
Twist center, 617–618, 620
beam triangular cross section, 620f
bending and torsion problems, 622
coordinates of, 620–621
distribution of function, 622f
existence of, 622
stiffness coefficients, 620
Two-dimensional braiding (2D braiding), 22–23
Two-matrix composites, 187
acoustic emission intensity, 192f
composite fiber properties, 188
composite fibers of, 191
conventional cross-ply glass-epoxy layer, 191, 192f
glass-epoxy unidirectional composite properties, 191t
longitudinal strength dependency, 189f
mechanical characteristics, 190–191
microstructure of, 190f
solutions to analysis problem, 187–188
stress-strain curves
for epoxy matrices, 188f
for transverse tension, 189f
stress-strain diagram of deformable epoxy matrix, 190f
synthesizing composite materials, 188
two-matrix cross-ply glass-epoxy layer, 191, 192f

U

Ultimate fiber arrays, 56–57, 57f
Unidirectional anisotropic layer, 152
composite layer, 153f
of composite pressure vessel, 153f
linear elastic model
apparent modulus, 168
carbon-epoxy strip deflection, 168, 168f
compliance coefficients, 156–158
composite dependencies, 164f
constitutive equations, 152–156
coupling stiffness dependencies, 159f
elastic constants of anisotropic materials relationship, 164
forces and moments effect, 167f
for free tension, 166
in-plane shear modulus, 158–160, 163
invariant stiffness characteristics, 156–158
normalized apparent modulus dependence, 168
normalized strain dependencies, 161f
off-axis tension, 165f
off-axis test, 160f, 165
shear-extension coupling coefficient, 162
stiffness coefficients, 152–156, 158
tensile and shear stiffness dependencies, 159f
transformation for strains, 152–156
unidirectional composites, 163–164
unidirectional layer deformation, 160f, 161
nonlinear models, 169
stress-strain diagram, 170f, 171f
two-matrix fiberglass composite, 169
Unidirectional composite properties, 96t
Unidirectional orthotropic layer, 144, 145f
linear elastic model
constitutive equations, 144–147
filament-wound composite pressure vessel, 145f
transverse normal stress, 144–147
transverse shear modulus, 147f, 147t
for unidirectional composites, 147
nonlinear models, 147–148
boron-aluminum unidirectional composite, 151, 152f
independent uniaxial loading, 151
material behavior under elementary loading, 148
nonlinear behavior in composite materials, 150
notations for stresses and strains, 151
pronounced nonlinear elastic behavior, 148–149
sixth-order approximation, 148–149
strain decomposition, 150–151
two-matrix unidirectional composite, 150f
for unidirectional composites, 148–149
Unidirectional ply, 53f
fiber-matrix interaction
fiber strength statistical aspects, 61–65
fracture toughness, 78–80
stress diffusion in fibers interaction, 65–78
theoretical and actual strength, 57–61

Unidirectional ply (*Continued*)
hybrid unidirectional ply, 116
composites with high fiber fraction, 119–121
experimental dependencies, 117f
first-order microstructural model, 116f
hybrid carbon-glass epoxy unidirectional composite, 119f
inverse linear dependence, 117–118
longitudinal modulus *vs.* ultimate tensile strain, 118f
micromechanics, 116–117
threshold value, 119
typical stress-strain diagrams for, 118f
mechanical properties, 95
in-plane shear, 104–107
longitudinal compression, 107–115
longitudinal tension, 95–99
transverse compression, 115
transverse tension, 99–103
unidirectional composites, 96t
micromechanics
actual and admissible states, 93–94
actual stress-strain state, 94–95
applications, 95
comparison, 87
constitutive equation, 86–87
elastic constants, 81
first-order models, 83–85, 84f
higher-order microstructural models, 91
under in-plane loading, 80f
isotropic matrix, 91
longitudinal and transverse strains, 85–86
matrix material specimens, 81f
matrix specimen testing, 82f
mechanical characteristics, 81–82
microcomposite material, 82–83
microcomposite specimen gripped at ends, 84f
microcomposite specimen overwrapped over discs, 83f
normalized in-plane shear modulus, 88f
normalized longitudinal modulus, 87f
normalized transverse moduluson fiber volume fraction, 88f
qualitative analysis, 91–92
second-order models, 89–91, 89f
simplest or zero-order model, 83
structural element, 90f
transverse tension, 92–93
unidirectional composite ply, 80–81
phenomenological homogeneous model
actual material behavior prediction, 122
biaxial compression, 122f
first-order micromechanical model, 122
ply, 122
stresses acting in fibers and matrix, 123
ply architecture
actual fiber distribution, 54f
carbon-epoxy composite material, 56
composite ply, 53–55
fibers and matrix, 56
hexagonal fiber distribution, 55f
layer-wise fiber distribution, 55f
square fiber distribution, 54f
strength and stiffness, 56
tape, 53
ultimate fiber arrays, 56–57, 57f
Unidirectional tow, 15
Uniform strength composite laminates
advanced composites parameters, 755, 755t
boron-epoxy optimal laminates, 757
carbon-epoxy laminate, 756–757
coefficients, 756
composite materials, 753
composite panel, 757
laminate optimal structural parameters, 753
laminate thickness, 754
optimal laminate elastic constants, 756, 757t
optimal orientation angle, 756
optimal structure, 755
optimality condition, 755
periodic function, 755
plane stress state, 752–753
ratio layers' thicknesses, 757–758
restrictions, 754
strains, 756
stresses, 753–756
unidirectional plies, 757

V

Vacuum-assisted RTM (VARTM), 26
Variable elasticity parameter method, 139–140, 139f
VARTM. *See* Vacuum-assisted RTM
Vibration coupling, 463
Viscoelasticity
aging theory, 387
aramid-epoxy composite, 377f
creep compliance, 378–379, 379f, 387
elastic-viscoelastic analogy, 386
exponential approximation, 379–380
Laplace transformation, 383–384, 386–387
linear-viscoelastic material behavior, 377–378
material axes, 384–385
material creep, 381, 382f
nonlinear hereditary theory, 388
normalized shear strain, 386, 387f
one-term exponential approximation, 382–383
polymeric fibers, 388
polymeric matrices, 376–377
relaxation modulus, 378
stress relaxation, 381–382
three-element mechanical model, 380–381, 380f
unidirectional glass-epoxy composite, 380f
Viscous regularization scheme, 341

W

Warping function, 605
constant of integration, 605–606
continuous function, 606
rectangular beam under torsion, 616f
rectangular beam under transverse bending, 615f
Wet process, 21
Widespread metal matrices, 18

Y

Yarn, 15

Z

Zhurkov equation, 390–391